Contrast Media & Molecular Imaging

Machine Learning Techniques for Medical Radiological and Nuclear Medicine Imaging

Lead Guest Editor: M. Pallikonda Rajasekaran
Guest Editors: V Muneeswaran and G. Saravana Kumar

Machine Learning Techniques for Medical Radiological and Nuclear Medicine Imaging

Machine Learning Techniques for Medical Radiological and Nuclear Medicine Imaging

Lead Guest Editor: M. Pallikonda Rajasekaran
Guest Editors: V Muneeswaran and G. Saravana Kumar

Contents

Contents

Contents

Contents

Hindawi
Contrast Media & Molecular Imaging
Volume 2023, Article ID 9875603, 1 page
https://doi.org/10.1155/2023/9875603

Retraction

Retracted: Artificial Intelligence-Based MRI in Diagnosis of Injury of Cranial Nerves of Premature Infant and Its Correlation with Inflammation of Placenta

Contrast Media & Molecular Imaging

Received 31 October 2023; Accepted 31 October 2023; Published 1 November 2023

This article has been retracted by Hindawi following an investigation undertaken by the publisher [1]. This investigation has uncovered evidence of one or more of the following indicators of systematic manipulation of the publication process:

(1) Discrepancies in scope
(2) Discrepancies in the description of the research reported
(3) Discrepancies between the availability of data and the research described
(4) Inappropriate citations
(5) Incoherent, meaningless and/or irrelevant content included in the article
(6) Peer-review manipulation

The presence of these indicators undermines our confidence in the integrity of the article's content and we cannot, therefore, vouch for its reliability. Please note that this notice is intended solely to alert readers that the content of this article is unreliable. We have not investigated whether authors were aware of or involved in the systematic manipulation of the publication process.

Wiley and Hindawi regrets that the usual quality checks did not identify these issues before publication and have since put additional measures in place to safeguard research integrity.

We wish to credit our own Research Integrity and Research Publishing teams and anonymous and named external researchers and research integrity experts for contributing to this investigation.

The corresponding author, as the representative of all authors, has been given the opportunity to register their agreement or disagreement to this retraction. We have kept a record of any response received.

References

[1] G. Liao, "Artificial Intelligence-Based MRI in Diagnosis of Injury of Cranial Nerves of Premature Infant and Its Correlation with Inflammation of Placenta," *Contrast Media & Molecular Imaging*, vol. 2022, Article ID 4550079, 9 pages, 2022.

Hindawi
Contrast Media & Molecular Imaging
Volume 2022, Article ID 6495568, 7 pages
https://doi.org/10.1155/2022/6495568

Research Article

Diagnostic Value of Image Features of Magnetic Resonance Imaging in Intracranial Hemorrhage and Cerebral Infarction

Wencai Tang,[1] **Fangyi Zeng**,[2] **and Guangtang Zhao**[1]

[1]*Department of Radiology, The Second Affiliated Hospital of Hainan Medical University, Haikou 570000, Hainan, China*
[2]*Department of Radiology, Hainan Danzhou People's Hospital, Danzhou 571700, Hainan, China*

Correspondence should be addressed to Guangtang Zhao; zhaoguangtang1825@hainmc.edu.cn

Received 11 April 2022; Revised 9 June 2022; Accepted 13 June 2022; Published 12 July 2022

Academic Editor: M. Pallikonda Rajasekaran

This study aimed to investigate the differential diagnosis value of routine magnetic resonance imaging (MRI) and magnetic resonance diffusion-weighted imaging (DWI) in hyperacute intracranial hemorrhage (HICH) and hyperacute cerebral infarction (HCI). Fifty-five patients with HICH were set as group A, and 55 patients with HCI were selected as group B. All the patients underwent routine MRI and DWI examinations. The morphological distribution and signal characteristics (low, high, or mixed) of the lesions in the two groups were recorded. The diagnostic accuracy, sensitivity, and specificity of routine MRI and DWI were compared for distinguishing HICH and HCI. The results suggested that the lesions in patients with HICH were mainly manifested as mixed signals (40 cases), while those in patients with HCI showed high signals (48 cases). HICH occurred in the basal ganglia in 44 cases, in the brain stem in 6 cases, in the cerebellum in 4 cases, in the cerebral cortex in 0 cases, and in the corpus callosum in 1 case. HCI occurred in the basal ganglia area, brain stem, cerebellum, cerebral cortex, and corpus callosum in 5, 3, 35, 12, and 0 cases, respectively. The diagnostic accuracy, specificity, and sensitivity of DWI for HICH and HCI were significantly higher than those of routine MRI ($P < 0.05$). It was indicated that compared with routine MRI, DWI was more effective in the diagnosis of HICH and HCI, with clearer and more accurate images and better diagnostic performance.

1. Introduction

Stroke, also known as a cerebrovascular accident, is an acute cerebrovascular disease. It is a group of diseases that cause brain tissue damage due to sudden rupture of blood vessels in the brain or the inability of blood to flow into the brain due to vascular obstruction, including ischemic and hemorrhagic stroke [1–3]. Statistically, the incidence of ischemic stroke is higher than that of hemorrhagic stroke, accounting for about 65% of all strokes [4, 5]. Stroke occurs in people more than 40 years old, more men than women; in severe cases, it can cause death. Stroke can also be divided into intracranial hemorrhage and cerebral infarction, of which cerebral infarction is caused by cerebral thrombosis, atherosclerosis, cardioembolic embolism, etc. These result in the sudden interruption of blood flow in the cerebral blood vessels, causing local brain tissue necrosis and thereby forming symptoms of neurological deficits. Intracerebral hemorrhage is caused by the spontaneous rupture and hemorrhage of cerebral blood vessels, which causes the blood in vessels to overflow into the parenchymal cells of the brain, resulting in necrosis and swelling of the patient's brain tissue [6, 7]. Clinically, intracerebral hemorrhage and cerebral infarction that occur within 6 hours are called hyperacute intracranial hemorrhage (HICH) and hyperacute cerebral infarction (HCI). However, there are obvious differences between the two, and the treatment options are also completely different [8]. Therefore, the accurate identification of HICH and HCI within 3–6 hours of onset has a great influence on the effectiveness of treatment for patients.

In recent years, with the rapid development of medical imaging technology, various imaging methods can not only indicate morphological changes in brain tissue but also provide information on cerebral blood flow and metabolism, playing an important role in early diagnosis and treatment [9–12]. Computerized tomography (CT) utilizes precise and accurate X-ray beams, gamma rays, ultrasonic waves, etc., together with highly sensitive detectors, to scan a certain part of the human body one plane by one plane. It has the characteristics of fast scanning and clear images. It is often used in the clinical diagnosis of stroke, but with low sensitivity [13, 14]. Magnetic resonance imaging (MRI) can map the internal structure of an object according to the different attenuation of the released energy in different structural environments inside the material as well as the emitted electromagnetic waves detected in a gradient magnetic field. Taking advantage of the high resolution, multi-parameters, and so on, it has also been gradually applied to the clinical diagnosis of stroke, but there are certain limitations as well [15–17]. Diffusion-weighted imaging (DWI), as a new MRI method, is different from traditional T1-weighted imaging (T1WI) and T2-weighted imaging (T2WI). It can describe the diffusion process of molecules (especially water molecules) in biological tissues through specific MRI sequences and software to generate images from the resulting data [18, 19]. At present, most of the studies on the diagnosis by DWI are aimed at the symptoms of cerebral infarction, and the diagnostic effect of cerebral hemorrhage is not completely clear.

To sum up, imaging techniques are common to diagnose stroke, but there are differences in the application effects of various imaging techniques to a certain extent. It is necessary to choose the most reliable examination method. Thus, 55 patients with HICH were included in group A, while 55 patients with HCI were included in group B. Routine MRI and DWI examinations were performed on all the patients, and the pathological diagnosis results were used as the gold standards. The diagnostic accuracy, sensitivity, and specificity of routine MRI and DWI for HICH and HCI were calculated to innovatively explore the diagnostic performance of different MRI imaging techniques for HICH and HCI.

2. Materials and Methods

2.1. Research Objects. Fifty-five patients with HICH and 55 patients with HCI were chosen as the research objects, as they were admitted to the hospital from October 2020 to December 2021. The 55 cases with HICH were included in group A, and the 55 cases with HCI were in group B. This study had been approved by the ethics committee of the hospital, and all patients participated voluntarily and signed informed consent forms.

Inclusion criteria: if the patients could offer complete basic information, had no contraindications to MRI examination, signed the informed consent, and were older than 20 years old.

Exclusion criteria: if the patients were complicated with mental illness, complicated with heart, liver, and kidney dysfunction, or complicated with diseases of the blood system. Patients had poor compliance in examinations, or they withdrew from the project due to personal reasons.

2.2. Imaging Methods. The patients were examined with a fiber-optic superconducting 1.5 T magnetic resonance instrument. Scanning parameters for routine MRI and DWI (coronal T1WI, coronal T2WI, and fluid-attenuated inversion recovery (FLAIR)) are listed in Table 1.

2.3. Image Processing. The obtained images under routine MRI and DWI were read by two senior radiologists using a double-blind method. After the image data were sent to the General Electric workstation, the hematoma or infarction locations were selected in the original window for image correction. The apparent diffusion coefficient (ADC) maps were obtained after processing, and the ADC values of the lesions of HICH and HCI were measured. With $0.8 \times 10^{-3}\,\mathrm{mm}^2$ taken as the boundary, there were two intervals of $0.4–0.8 \times 10^{-3}\,\mathrm{mm}^2$ and $0.8–1.2 \times 10^{-3}\,\mathrm{mm}^2$.

2.4. Observation Indicators. The general data of the patients (male to female ratio, average age, average height, average weight, proportion of high blood pressure, proportion of diabetes, and proportion of smoking history) were recorded. The images of patients with HICH and HCI were compared, and the morphological distribution and the low, high, or mixed signal characteristics of the lesions were also recorded. The diagnostic accuracy, sensitivity, and specificity of routine MRI and DWI for HICH and HCI were calculated with pathological diagnosis results as the gold standards. The ADC values of patients with HICH and HCI were compared as well.

2.5. Statistical Methods. The SPSS 19.0 statistical software was used for data processing. Measurement data were expressed as mean ± standard deviation ($\pm S$), while enumeration data were expressed as percentage (%). One-way analysis of variance was adopted for the pairwise comparisons of the indicators of patients between group A and group B. The difference was statistically significant at $P < 0.05$.

3. Results

3.1. Comparison of General Data. Figure 1 showed the comparison of the patients' general data between the two groups. The ratio of male to female, the average age, the average height, the average weight, the proportion of high blood pressure, the proportion of diabetes, and the proportion of smoking history in group A were all not significantly different from those in group B ($P > 0.05$).

3.2. Imaging of Patients with HICH and HCI. Figure 2 displays the images of a patient with HICH. There was oxygenated hemoglobin in the right lateral ventricle, which had a slight effect on the MRI signal. T1WI showed a low signal, T2WI showed a high signal, but the T2WI signal was uneven. The images of a patient with HCI were presented in Figure 3. The lesion was shown with an obvious high signal, together with the strip-shaped high signal shadow inside.

Table 1: Imaging scan parameters.

Parameters	Routine MRI	T_2WI	T_1WI	FLAIR
Slice thickness	1.5 mm	5 mm	1.2 mm	1.2 mm
Slice spacing	5 mm	1.5 mm	4 mm	4 mm
Matrix	256 × 256	256 × 185	256 × 185	256 × 185
Field of view	150 × 220 mm	220 × 220 mm	220 × 220 mm	220 × 220 mm
Time of echo/time of repetition	580 ms/35 ms	660 ms/40 ms	660 ms/40 ms	660 ms/40 ms

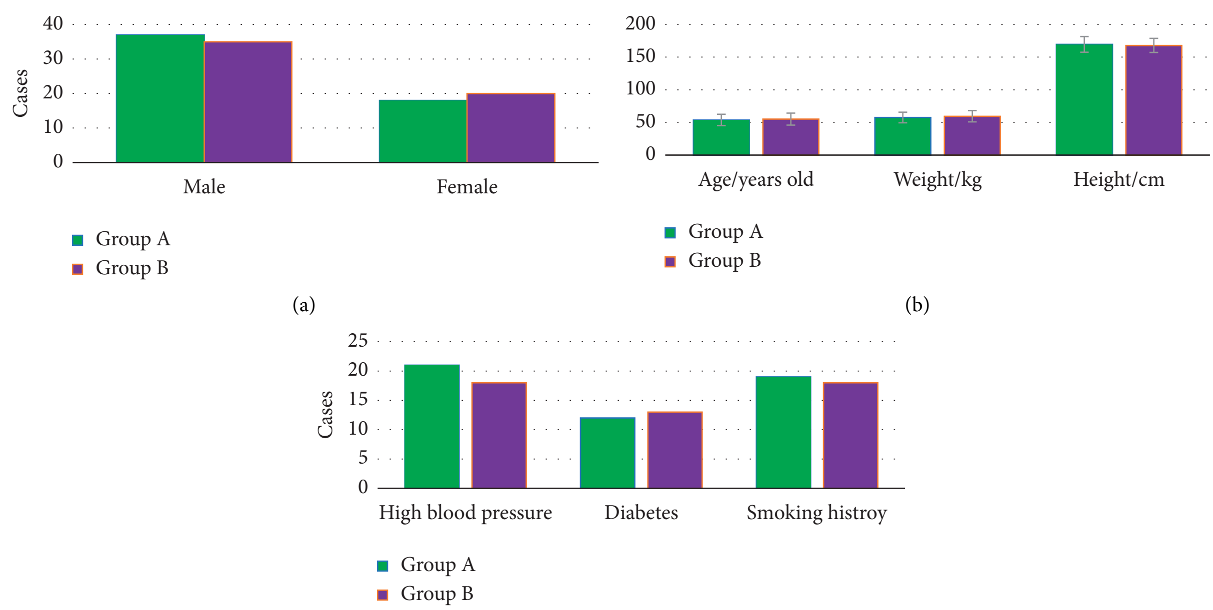

Figure 1: Comparison of the general data of patients in the two groups. (a) The comparison of gender; (b) age, height, and weight comparison; (c) proportion of high blood pressure, diabetes, and smoking history comparison.

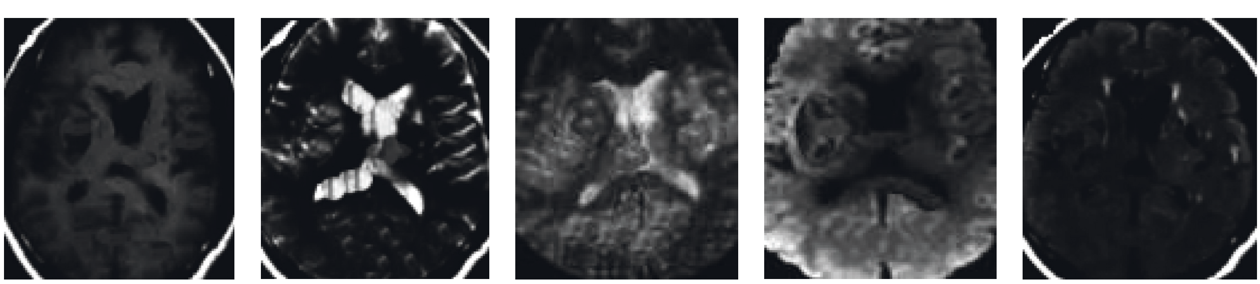

(a) (b) (c) (d) (e)

Figure 2: Imaging data of a patient with HICH. (a–e): T1WI, T2WI, pressurized-water T2WI, DWI, and FLAIR, respectively.

3.3. Signal Comparison of Lesions. In Figure 4, the signals of the lesions in patients were compared between the two groups. The lesions in patients with HICH were dominated by mixed signals. 40 cases were shown under DWI (72.73%) and 21 cases were under routine MRI (38.18%); the difference was considered to be statistically significant ($P < 0.05$). The lesions in patients with HCI were mainly shown as high signals, among which 48 cases were shown under DWI, accounting for 87.27%. 30 cases were shown by routine MRI, which accounted for 54.55%, and the difference was also of statistical significance ($P < 0.05$).

3.4. Comparison of ADC Values. The ADC values of the two groups of patients were compared in Figure 5. There were 12 patients in group A whose ADC value was in the range of $0.4–0.8 \times 10^{-3}\ \mathrm{mm}^2$, and 43 patients whose ADC value was $0.8–1.2 \times 10^{-3}\ \mathrm{mm}^2$. In group B, the ADC value of

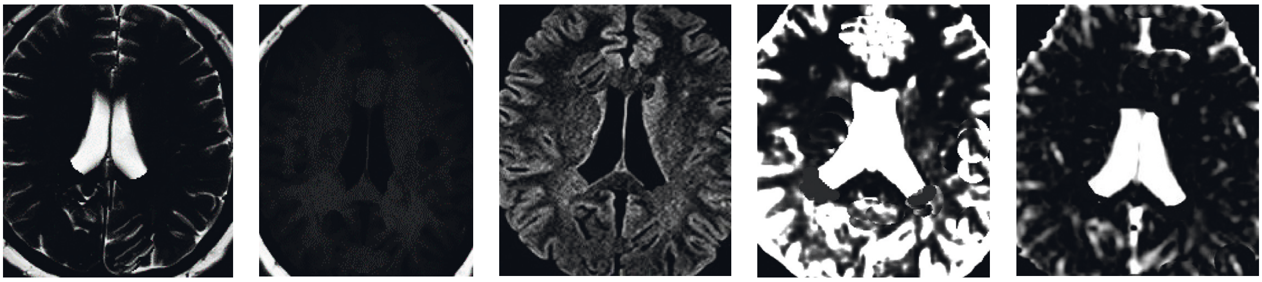

(a) (b) (c) (d) (e)

Figure 3: Imaging data of a patient with HCI. (a–e): T1WI, T2WI, pressurized-water T2WI, DWI, and FLAIR, respectively.

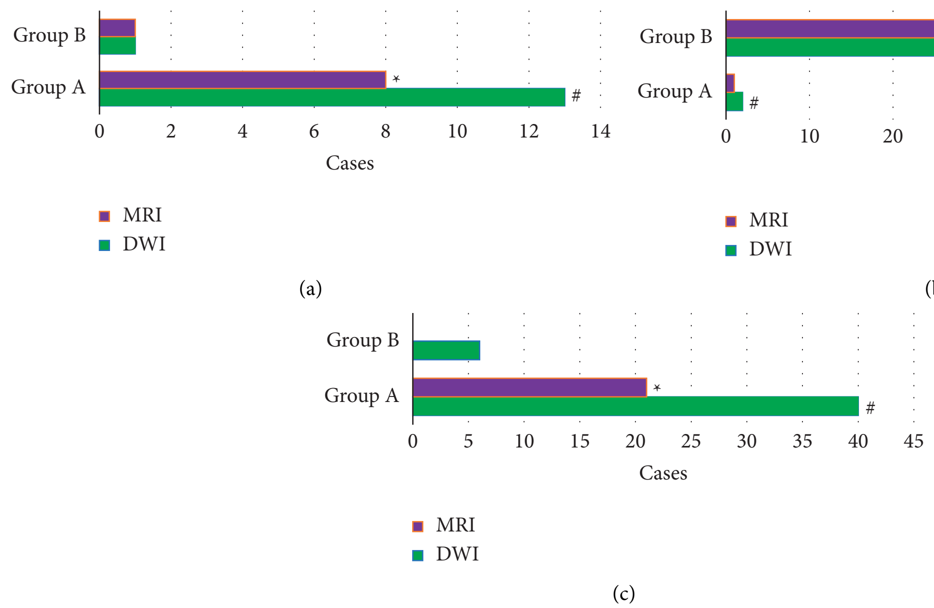

Figure 4: Comparison of the signals of the lesions in the two groups of patients. (a–c) showed the comparison of low signal, high signal, and mixed signal, respectively. *Compared with the corresponding signal under DWI, $P < 0.05$; #compared with that in group B $P < 0.05$.

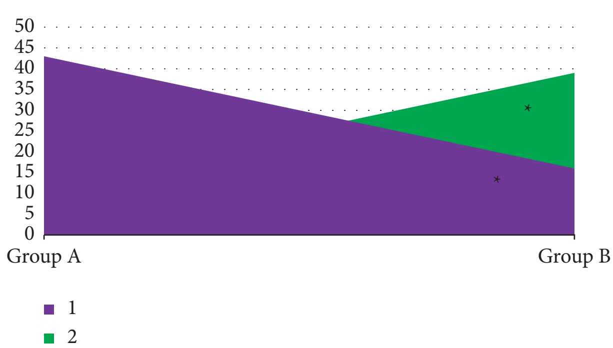

Figure 5: Comparison of ADC values between the two groups of patients. 1 stood for $0.4–0.8 \times 10^{-3}\,\text{mm}^2$, and 2 meant $0.8–1.2 \times 10^{-3}\,\text{mm}^2$. *Compared with the data of group A $P < 0.05$.

$0.4–0.8 \times 10^{-3}\,\text{mm}^2$ was found in 43 cases and that of $0.8–1.2 \times 10^{-3}\,\text{mm}^2$ was found in 16 cases. There was a statistically significant difference in ADC value between group A and group B ($P < 0.05$).

3.5. Comparison of Imaging Examination Performance. Figure 6 displays the comparison of the diagnostic accuracy, sensitivity, and specificity between the two groups as well as between routine MRI and DWI. For diagnosing HICH by routine MRI, the accuracy was 73.12%, the sensitivity was 79.66%, and the specificity was 65.37%. The diagnostic accuracy, sensitivity, and specificity of DWI were 96.33%, 92.65%, and 85.15%, respectively. For HCI, the diagnostic accuracy of routine MRI was 65.81%, the diagnostic sensitivity was 81.45%, and the diagnostic specificity was 70.32%. The diagnostic accuracy, sensitivity, and specificity of DWI for HCI were 97.14%, 90.74%, and 82.45%, respectively. The accuracy, specificity, and sensitivity of DWI for diagnosing both HICH and HCI were significantly higher than those of routine MRI, showing statistically significant differences ($P < 0.05$).

3.6. Comparison of the Lesion Locations in the DWI Examination. Figure 7 shows the comparison of lesion locations in the two groups in the DWI examination. In DWI examination, HICH occurred in the basal ganglia,

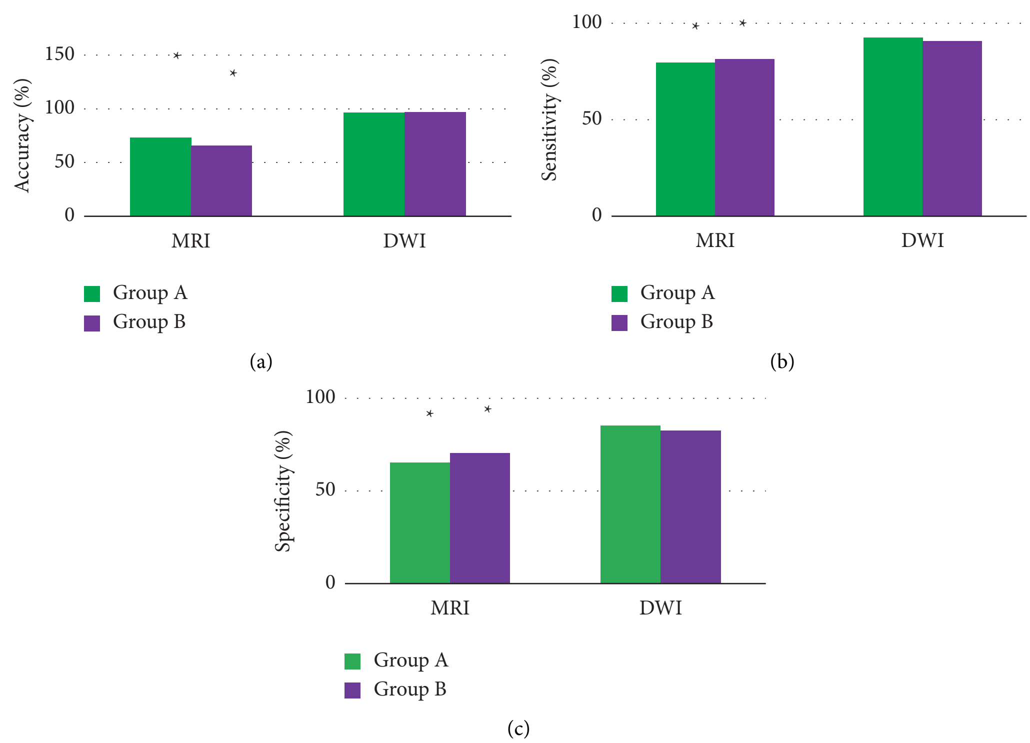

Figure 6: Comparison of the diagnostic accuracy, sensitivity, and specificity of the two groups by routine MRI and DWI. (a) Comparison of the accuracy; (b) the sensitivity; (c) the specificity. *Compared with the data under DWI, $P < 0.05$.

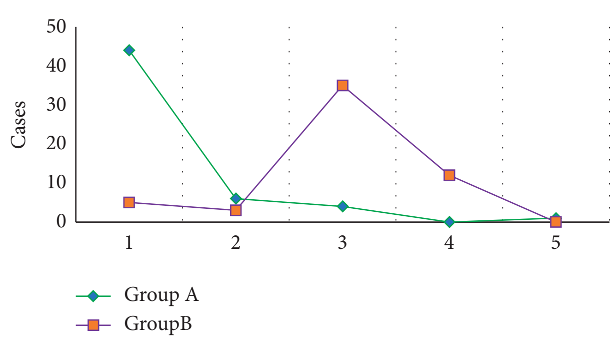

Figure 7: Comparison of lesion locations in the DWI examination between two groups. 1–5 represented the basal ganglia, brainstem, cerebellum, cerebral cortex, and corpus callosum, respectively.

brain stem, cerebellum, cerebral cortex, and corpus callosum in 44, 6, 4, 0, and 1 cases, respectively. HCI occurred in those locations in 5 cases, 3 cases, 35 cases, 12 cases, and 0 cases, respectively.

4. Discussion

Stroke is a common clinical disorder of cerebral blood circulation, generally divided into cerebral infarction and intracerebral hemorrhage. If the diseases occur within 6 hours, it is called the hyperacute phase [20, 21]. Clinically, the optimal treatment time for stroke is 3–6 hours, in which the best prognosis can be achieved for patients. However, because the clinical manifestations of cerebral infarction and intracerebral hemorrhage are similar, the treatment options are different. It is necessary to seek an efficient and high-precision method to distinguish HICH from HCI [22]. The commonly used clinical examination methods are CT and MRI techniques, but the diagnostic sensitivity of both CT and routine MRI is not high. It is prone to missing and misdiagnosing some cases, which will lead to delay and aggravation of the patients' condition [23, 24]. Different from the traditional MRI technology, DWI can use the pulse sequence sensitive to the diffusion movement to detect the diffusion motion state of water molecules in the tissue and then express it in MRI images. Therefore, 55 patients with HICH and 55 patients with HCI, admitted to the hospital from October 2020 to December 2021, were included as the research objects. The patients with HICH and HCI were in group A and group B, respectively, and all of them experienced routine MRI and DWI examinations. First, the general data of the patients in two groups were compared, and it was known that the ratio of males to females, the average age, the average height, the average weight, the proportion of high blood pressure, the proportion of diabetes, and the proportion of smoking history in group A were not remarkably different from those in group B ($P > 0.05$). Such a result provided a feasibility for subsequent analyses, and the results would be reliable [25].

From the images, the oxygenated hemoglobin was observed in the right lateral ventricle of patients with HICH. The low signal was shown on T1WI and the high signal on T2WI, but the signal on T2WI was uneven. The lesion in HCI patients showed obvious high signal with strip-shaped high signal shadow insides. It was indicated that the signal levels of HICH and HCI were different in MRI images

[26, 27]. The quantitative data showed that the lesions in patients with HICH were dominated by mixed signals (40 cases), while those in patients with HCI were dominated by high signals (48 cases). These were consistent with what the above images presented, further confirming that there were significant differences in the signal of lesions. In terms of lesion location, 44 HICH cases had their lesion in the basal ganglia, 6 cases in the brain stem, 4 cases in the cerebellum, 0 cases in the cerebral cortex, and 1 case in the corpus callosum. There were 5, 3, 35, 12, and 0 HCI cases that had lesions in the basal ganglia, the brain stem, the cerebellum, the cerebral cortex, and the corpus callosum, respectively. Thus, it could be concluded that HICH mostly occurred in the basal ganglia region, while HCI occurred in the cerebellum and cerebral cortex mostly, showing the very distinct difference between the two [28].

In addition, the performances of routine MRI and DWI were also compared in the detection of HICH and HCI. For HICH, there were 40 cases of mixed signal under DWI, accounting for 72.73%; and 21 cases of mixed signal under MRI, accounting for 38.18%. The difference was statistically significant ($P < 0.05$). For HCI, 48 cases were observed with high signal under DWI (87.27%), 30 cases with high signal under MRI (54.55%), and the difference was of statistical significance ($P < 0.05$). These indicated that DWI images had a significant effect on the clearer and more accurate display of HICH and HCI, showing a high signal of HCI and a mixed signal of HICH. DWI had a high reference significance for the differential diagnosis of the two diseases. The diagnostic accuracy, specificity, and sensitivity of DWI for HICH and HCI were significantly higher than those of routine MRI, with differences of statistical significance ($P < 0.05$). This was similar to the findings of Zhao et al. [29], suggesting that DWI could better show the functional and physiological changes of water molecules in human tissues. Therefore, DWI was superior to routine MRI in the detection of both the diseases.

5. Conclusion

The diagnostic value of routine MRI and DWI was discussed in 55 patients with HICH and 55 patients with HCI. The lesions in patients with HICH showed mixed signals mainly, which were mostly in the basal ganglia. The lesions in patients with HCI were represented by high signals and were mostly in the cerebellum and cerebral cortex. DWI produced clearer and more accurate images than routine MRI for the display of HICH and HCI, showing high-signal characteristics of HCI and mixed-signal characteristics of HICH. The diagnostic accuracy, sensitivity, and specificity of DWI were also higher. However, there were still some unresolved issues in this research. The sample size of the patients included was small and the source was single, and there was also a lack of long-term data on the prognosis of patients. The impact of the DWI examination on the prognosis of patients was not discussed. The patient samples would be re-included in the future for a deeper analysis. In conclusion, the results provided data reference for the imaging differentiation of HICH and HCI.

Data Availability

The data used to support the findings of this study are available from the corresponding author upon request.

Conflicts of Interest

The authors declare that they have no conflicts of interest.

Authors' Contributions

Wencai Tang and Fangyi Zeng contributed equally to this work.

References

[1] H. Kimura, "Stroke," *Brain and Nerve*, vol. 72, no. 4, pp. 311–321, 2020.

[2] M. El-Koussy, G. Schroth, C. Brekenfeld, and M. Arnold, "Imaging of acute ischemic stroke," *European Neurology*, vol. 72, no. 5-6, pp. 309–316, 2014.

[3] A. Knight-Greenfield, N. Nario, and A. Gupta, "Causes of acute stroke," *Radiologic Clinics of North America*, vol. 57, no. 6, pp. 1093–1108, 2019.

[4] A. O. de Mendivil, A. Alcalá-Galiano, M. Ochoa, E. Salvador, and J. M. Millán, "Brainstem stroke: anatomy, clinical and radiological findings," *Seminars in Ultrasound, CT and MRI*, vol. 34, no. 2, pp. 131–141, 2013.

[5] A. Bersano, M. Kraemer, A. Burlina et al., "Heritable and non-heritable uncommon causes of stroke," *Journal of Neurology*, vol. 268, no. 8, pp. 2780–2807, 2021.

[6] C. Z. Simonsen, T. M. Leslie-Mazwi, and G. Thomalla, "Which imaging approach should Be used for stroke of unknown time of onset," *Stroke*, vol. 52, no. 1, pp. 373–380, 2021 Jan.

[7] N. M. Murray, M. Unberath, G. D. Hager, and F. K. Hui, "Artificial intelligence to diagnose ischemic stroke and identify large vessel occlusions: a systematic review," *Journal of Neurointerventional Surgery*, vol. 12, no. 2, pp. 156–164, 2020 Feb.

[8] M. Sparaco, L. Ciolli, and A. Zini, "Posterior circulation ischemic stroke-a review part II: imaging and acute treatment," *Neurological Sciences*, vol. 40, no. 10, pp. 2007–2015, 2019.

[9] R. Suri, F. Rodriguez-Porcel, K. Donohue et al., "Post-stroke movement disorders: the clinical, neuroanatomic, and demographic portrait of 284 published cases," *Journal of Stroke and Cerebrovascular Diseases*, vol. 27, no. 9, pp. 2388–2397, 2018 Sep.

[10] Z. Lv, L. Qiao, Q. Wang, and F. Piccialli, "Advanced machine-learning methods for brain-computer interfacing," *IEEE/ACM Transactions on Computational Biology and Bioinformatics*, vol. 18, no. 5, pp. 1688–1698, 2021.

[11] Y. Inatomi, M. Nakajima, T. Yonehara, and Y. Ando, "Ipsilateral hemiparesis in ischemic stroke patients," *Acta Neurologica Scandinavica*, vol. 136, no. 1, pp. 31–40, 2017.

[12] Z. C. Yu, S. U. Amin, M. Alhussein, and Z. H. Lv, "Research on disease prediction based on improved DeepFM and IoMT," *IEEE Access*, vol. 9, no. 99, pp. 39043–39054, 2021.

[13] M. Hu, Y. Zhong, S. Xie, H. Lv, and Z. Lv, "Fuzzy system based medical image processing for brain disease prediction," *Frontiers in Neuroscience*, vol. 15, Article ID 714318, 2021.

[14] M. P. Amatangelo, "Cryptogenic stroke," *Critical Care Nursing Clinics of North America*, vol. 32, no. 1, pp. 37–50, 2020.

[15] A. Ferrara, "Computed tomography in stroke diagnosis, assessment, and treatment," *Radiologic Technology*, vol. 91, no. 5, 2020.

[16] S. X. Xie, Z. C. Yu, and Z. H. Lv, "Multi-Disease prediction based on deep learning: a survey," *Computer Modeling in Engineering and Sciences*, vol. 128, no. 2, pp. 489–522, 2021.

[17] D. Dolotova, V. Donitova, I. Arhipov et al., "A platform for collection and analysis of image data on stroke," *Studies in Health Technology and Informatics*, vol. 262, pp. 312–315, 2019.

[18] R. G. Hart, H. C. Diener, S. B. Coutts et al., "Embolic strokes of undetermined source: the case for a new clinical construct," *The Lancet Neurology*, vol. 13, no. 4, pp. 429–438, 2014.

[19] G. Wang, T. Song, Q. Dong, M. Cui, N. Huang, and S. Zhang, "Automatic ischemic stroke lesion segmentation from computed tomography perfusion images by image synthesis and attention-based deep neural networks," *Medical Image Analysis*, vol. 65, Article ID 101787, 2020.

[20] R. Yang, Y. Zhang, M. Xu, and J. Ma, "Image features of magnetic resonance angiography under deep learning in exploring the effect of comprehensive rehabilitation nursing on the neurological function recovery of patients with acute stroke," *Contrast Media and Molecular Imaging*, vol. 2021, pp. 1–9, 2021.

[21] L. D'Anna, F. T. Filippidis, K. Harvey, E. Korompoki, and R. Veltkamp, "Ischemic stroke in oral anticoagulated patients with atrial fibrillation," *Acta Neurologica Scandinavica*, vol. 145, no. 3, pp. 288–296, 2022.

[22] A. Kitsiou, F. Zuhorn, R. Wachter, C. W. Israel, W. R. Schäbitz, and A. Rogalewski, "Embolischer Schlaganfall mit ungeklärter Emboliequelle (ESUS) - klassifikation einer neuen Schlaganfallentität," *DMW - Deutsche Medizinische Wochenschrift*, vol. 146, no. 06, pp. 403–409, 2021.

[23] A. Nutakki, M. Chomba, L. Chishimba et al., "Risk factors and outcomes of hospitalized stroke patients in Lusaka, Zambia," *Journal of the Neurological Sciences*, vol. 424, Article ID 117404, 2021.

[24] V. Bates, "Outpatient neuroimaging of stroke," *Neurologic Clinics*, vol. 27, no. 1, pp. 139–170, 2009, viii.

[25] X. Ayrignac, N. Gaillard, C. Carra-Dallière, and P. Labauge, "Microangiopathie cérébrale: du diagnostic à la prise en charge small vessel disease of the brain: diagnosis and management," *La Revue de Medecine Interne*, vol. 41, no. 7, pp. 469–474, 2020.

[26] F. Boustia, A. Crespy, K. Janot, and D. Herbreteau, "Prise en charge endovasculaire de l'accident vasculaire cérébral ischémique aigu," *La Presse Médicale*, vol. 48, no. 6, pp. 664–671, 2019.

[27] A. Y. X. Yu, M. D. Hill, and S. B. Coutts, "Should minor stroke patients be thrombolyzed? A focused review and future directions," *International Journal of Stroke*, vol. 10, no. 3, pp. 292–297, 2015.

[28] L. Bao, S. Zhang, X. Gong, and G. Cui, "Trousseau syndrome related cerebral infarction: clinical manifestations, laboratory findings and radiological features," *Journal of Stroke and Cerebrovascular Diseases*, vol. 29, no. 9, Article ID 104891, 2020.

[29] D. Zhao, J. Zhu, Q. Cai, F. Zeng, X. Fu, and K. Hu, "The value of diffusion weighted imaging-alberta stroke program early CT score in predicting stroke-associated pneumonia in patients with acute cerebral infarction: a retrospective study," *PeerJ*, vol. 10, Article ID e12789, 2022.

Hindawi
Contrast Media & Molecular Imaging
Volume 2022, Article ID 1541980, 16 pages
https://doi.org/10.1155/2022/1541980

Review Article

Review on Hybrid Segmentation Methods for Identification of Brain Tumor in MRI

Khurram Ejaz,[1] Mohd Shafry Mohd Rahim,[2] Muhammad Arif,[1] Diana Izdrui,[3] Daniela Maria Craciun,[3] and Oana Geman[3]

[1]*Department of Computer Science and Information Technology, The University of Lahore, Lahore, Pakistan*
[2]*University of Technology Malaysia, Johor Bahru, Malaysia*
[3]*Faculty of Physical Education and Sport, Stefan Cel Mare University of Suceava, Suceava, Romania*

Correspondence should be addressed to Muhammad Arif; arifmuhammad36@hotmail.com

Received 30 December 2021; Accepted 22 April 2022; Published 11 July 2022

Academic Editor: M. Pallikonda Rajasekaran

Modalities like MRI give information about organs and highlight diseases. Organ information is visualized in intensities. The segmentation method plays an important role in the identification of the region of interest (ROI). The ROI can be segmented from the image using clustering, features, and region extraction. Segmentation can be performed in steps; firstly, the region is extracted from the image. Secondly, feature extraction performed, and better features are selected. They can be shape, texture, or intensity. Thirdly, clustering segments the shape of tumor, tumor has specified shape, and shape is detected by feature. Clustering consists of FCM, K-means, FKM, and their hybrid. To support the segmentation, we conducted three studies (region extraction, feature, and clustering) which are discussed in the first line of this review paper. All these studies are targeting MRI as a modality. MRI visualization proved to be more accurate for the identification of diseases compared with other modalities. Information of the modality is compromised due to low pass image. In MRI Images, the tumor intensities are variable in tumor areas as well as in tumor boundaries.

1. Introduction

Medical imaging provides potential information and an easy visualization of diseases such as brain tumors to doctors and biomedical experts. The accurate identification of brain tumors requires a visualization of the disease area. Superior quality of visualization is possible on the MRI modality when the image processing technique or soft computing technique is used [1]. Tumor segmentation is possible with different soft clustering techniques and also with traditional image processing techniques. They help to identify accurate features for clinical analysis. Hence, segmentation techniques are helpful for the identification of the region of interest (ROI). The studies [2, 3] revealed that MRI faced numerous challenges for the identification of diseases.

Segmentation of medical imaging is not straightforward; it required sequence. Firstly, this was due to the MRI image being a low pass information image, and therefore more enhancements were required. Moreover, MRI dataset experiences data complexity issues. For cases of complex dataset, feature selection was required for the identification of relevant features for MRI images. Even though the images were enhanced, the ROI was still compromised due to the poorly managed intensities [4]. Moreover, although continuous tumor intensities were easy to detect, in certain situations, the segmentation process still requires special mechanisms for favorable results.

2. Related Work

In the comparative study, the literature of various previous studies was compared in terms of their efficient problem-solving capabilities. This comparative study is divided into three sections: (1) enhancement and region extraction, (2) feature reduction and selection, and (3) segmentation. Other literature studies have been considered for better segmentation results.

Here, image extraction is helpful as a pre-step in segmentation. Region extraction is also equally important. In a study, the pre-enhancement step is proposed where spackle noise is handled as compared to the Otsu algorithm. The study [3] preprocesses the image and handles the noisy images with localization. Noise of MRI image is tackled, region of interest is found out through feature extraction, and classification of cells is calculated [5]. In another study, different modalities were reviewed, and it was deduced that MRI segmentation is more challenging due to the low pass and high pass [6]. The confidence region is important to enhance the shape of a tumor with multiple parameters just like the classification of an image pixel to estimate the region of interest [7]. An improved Sobel edge detection algorithm, which draws close contour to extract the accurate region of a brain tumor, is proposed [3]. In this proposed algorithm, the bias correction field estimating the inhomogeneous intensities using two multiplicative components has a biased correction field and the input image. Reference [8] suggests that, for biomedical applications, software is used to check the active contour internal energy as well as external energy using the Marr, gradient vector flow, and vector field convolution methods [9]. In [10], a multilevel Otsu threshold enhances the image with determining 41 significant intensity points and assigns them threshold; then, using combination, they are enhanced by the algorithm.

In another study, an image enhancement was performed with denoising, watershed, and visual analysis of the image by connected components, and finally the image was evaluated [11]. A histogram was used as a formal analysis of the image, and the intensity of the brain tumor image was corrected by applying standard deviation.

In the given study, they mentioned the model about normalized the images, and obtained the information from the normalized image. The white portion in normalized image was enhanced and easily visible [12]. The MICCAI BraTS brain tumor dataset contained many aspects with a good set of data in comparison to other datasets. This processed brain tumor dataset then underwent a skull (cranium) stripping process of the image, where it was removed by the ITK tool kit [13]. Region scale fitting was enhanced where the edge stop function was improved. Hence, the region of interest denoises the noisy region [14]. In this study, the FCM was used to enhance the edges of the brain tumor image [15]. This method smoothly detected the inner contour versus the outer contour, while examining the start and end of the contour point. Hence, the background evolved smoothly from the foreground of the image [16]. There was a need for improvement of the edges of the brain tumor [17]. Furthermore, another study detected the edges of the region of interest (ROI) through the Bayesian contour, which also produced the measurement area and volume of ROI [11]. In another study, hyperintense lesion was dealt with through a combination of Gaussian mixture model, synthetic image, and support vector machine [18]. In [19], more focus has been made on the multi-contrast scan in which the variation of tumor stages is presented, 65 algorithms have been tested, and not a single algorithm has produced any good performance to classify the intensities properly. In addition, in another study, the accurate identification of a brain tumor was performed through the combination of growing region, segmentation, gray level cooccurrence matrix (GLCM) feature extraction, and classification through probabilistic neural network (PNN) [20, 21].

In [22], the enhanced Darwinian particle swarm optimization was compared with the PSO for the enhancement of the brain tumor image. The glioma tumor feature detection was classified using the Gaussian mixture model (GMM) in [23]. The initial learning rate improved the performance of self-organizing map (SOM) for the generation of a better dataset classification and results as suggested by [24]. Hence, the latest technologies have not improved the confidence region of brain tumor detection.

In the blow mentioned concepts, features like shape, texture, and intensity played an important role as an intermediate process between image enhancement and segmentation. Features were extracted from datasets, complex dataset values were classified, and hence classification features were able to be reduced. Therefore, the study needed certain feature selection criteria. The features were combined with other supervised and unsupervised algorithms. A better segmentation was achieved through the best texture-based feature by checking the entropy. With the SVM feature classification, the tumorous and nontumorous images were identified [25]. In [26], SOM was improved with its weights, and therefore its capabilities were improved for relevant feature selection. Furthermore, weighted SOM was improved at this level, and it did not require preprocessing. Furthermore, a higher classification accuracy feature was selected in [27]. Additionally, the study [28] contained accounts about the multiple kernels that selected the relevant features from the dataset. They were classified by SVM, and after the classification process, they assigned a label to each image with accuracy. In [24], there was an important step that was improved by using the Gaussian function that resulted in good performance. Another study [23] revealed that a Gaussian 43 mixture model showed the best feature accuracy on the heterogeneous tumor region as compared to the latest technology of PCA and wavelet. In [29], shape-based features were extracted with major axis, minor axis, area, circularity, and two-classifier decision tree algorithm, C4.5. The multilayer perceptron showcased the best classification accuracy. This kind of study was helpful in the analysis of image enhancement. At first, the image is segmented through the Berkeley wavelet algorithm. Next, the texture features were extracted and classified. The image was classified as tumorous and nontumorous accurately [30]. The major portion of [31] was about the analysis of an image labeled as tumorous and nontumorous. The first image was segmented through the execution of morphological operation, and the next image then underwent a texture feature extraction. Those extracted features were classified as tumorous and nontumorous.

In [31], the method was claimed to have improved the segmentation the Histogram of Oriented Gradients (HOGs) feature used to capture the variation of pixel values and these values are classified through the SVM. In [32], the segmentation was performed through the Spiking Pulse-Coupled Neural Network (SPCNN) with feature extraction through fast discrete curvelet transformation, reduction through PCA + LDA (linear discriminant analysis), and classification through probabilistic neural network. In [33], the features were extracted through two-dimensional discrete transformation wavelet and reduced through probabilistic principal component analysis, and the image was classified using AdaBoost algorithm. In [34], the classifier was improved where SWT was combined with PCA for dimension reduction, with four classifiers on SVM improved. In this referenced study, shape, texture, and intensity-based features were extracted, reduced, and classified. For feature reduction, principal component analysis was used. As the images hold high dimensionality, they will expand the computation time and the storage capacity. And they are classified as 2D extracted feature, whereas 3D extraction results in time consumption of 44 features [35]. In [36], multi-contrast images were analyzed through unsupervised algorithm, where efficient brain tumor structure was achieved [36]. In [37], numerous researchers cited here selected the optimal features with a combination of binary particle swarm optimization with mutation time variations. Additionally, in another study, the HOG feature-based classifier was suggested to detect brain tumor images [20]. Another study [38] revealed an updated self-organizing map, an improvement to SOM, which provided better feature classification as compared to the-state-of-the-art SOM. In [39], the nuclei-based neural network classified the tumor with the help of the proposed features. In [40], improved classification was proposed from the selected feature, and it was found to be helpful in the segmentation of brain tumor. Moreover, textural features were helpful for the detection of tumor types such as malignant or benign [41]. However, the review of the referenced studies showed that not a single study was able to select the best deterministic feature for segmentation.

Notably, segmentation is found to be a significant process for the exclusion of the tumor region in brain MRI. For segmentation, the detection of tumor-like feature is crucial, but the task is difficult especially when the intention is to detect a tumor automatically. The segmentation of medical images can be viewed by different methods. Surveys have been conducted to check both techniques of image processing under the umbrella of segmentation and different modalities of medical imaging [42]. Medical imaging is used for the analysis of image segmentation of the related 45 regions being analyzed, and it is based on different application techniques such as region-based, classification, or hybrid methods [43]. The segmentation can be also achieved through good statistical calculation, computational application on the dataset, and confusion matrix with its derivations [44]. It has been acknowledged that there is a conventional technique of segmentation which removes noise over boundaries of an MR image using filters [45]. Automatic segmentation becomes challenging if there are a variety of tumor tissues in the image [46]. Furthermore, in [47], an image was segmented through two phases. The first phase was to limit the image by using a histogram. The second phase involved the extraction of the tumor where an automatic seed was automatically adjusted. Hence, pixel-based segmentation was obtained [47]. In addition to these studies, image registration was a faster technique for segmentation as compared to active contour. In addition, with the cranium removal (skull stripped) image, the registration performance increases. The study [48] determined the complete enhancement of the tumor shape from a longitudinal analysis of the image. Moreover, this technique provided favorable results because of random regularization of image energy method applied. Therefore, extreme variation of intensities was easily managed [49]. In [50], a hyperintense MRI image FLAIR was used, and a small lesion was measured for clinical application. The small lesion was significant for the visualization of a small lesion of heterogonous shape of tumor. Based on [18], the heterogonous issue lies in the T2 weighted image, with the same intensity, a small lesion was also determined with the Gaussian mix model. This detection method identified the intensity outside the mean. In [51], three contributions were achieved; for one axial image, the brain's left and right parts were analyzed through unsupervised learning.

The second contribution was to enable the independent intensity normalization of an image, and the third was the segmentation of the brain tumor image through CNN. Multi-cascaded convolution neural network (MCCNN) with the combination of coarse fine-grain segmentation method produced a good segmentation, but these 46 segmentations were more enhanced with the connected conditional random field (CRF) [52]. In [53], the tumor was segmented using CNN and local as well as global features. With the reduction of the parameters, the issue of overfitting was also managed. The study was chosen to fine-tune the contour for registration. It enabled the descriptor extraction of an image block. Thus, adaptive matching was obtained. This process was a fully automatic process for the segmentation of brain tumors [54].

Another study explicated a two-phase process; in phase one, random forest algorithm generated a classified segmentation which was combined with the level set for delineation of the tumor boundaries [55]. This referenced method was good for the enhancement of the region of interest. It reduced the noise of signal-to-noise ratio. Firstly, the GLCM along with DWT was applied for denoising process. Then, a probabilistic neural network was used to identify the patch. After that, the segmentation analysis was made through classification [21]. The contrast resulting from the combination of criterion, fuzzy C-means and spatial technique produced an impactful segmentation. With this combination, the segmentation was addressed, and the outliner issue was also resolved [56]. In [1], the SOM performed initial clustering, which included the FKM and memberships at an average and soft computing techniques apart from artificial intelligence, which have been combined for new biomedical applications in present day. The soft computing techniques were then compared with their state-of-the-art techniques for performance measurement perspective.

Unsupervised learning plays an important role. According to [57], an unsupervised multi-objective algorithm was proposed. The target pixels were extracted in clusters. With the mentioned step, the region of interest (ROI) was segmented. According to [36], one unsupervised algorithm was applied for identification of contrast intensities. In comparison with the contrast, a deep learning neural network approach was proposed to segment region of interest (ROI); this practice of research was done for the purpose of automation, and the segmentation speed of the proposed algorithm was good for a number of brain tumor images. Manual practice was discouraged.

Different state-of-the-art literature exists; for example, [29] segments the tumor using deep learning neural network. U-Net is a deep learning model. This network was used for automation purpose. This automatic algorithm is compared with other state-of-the-art techniques. In another study [58], the 3D feature of images is taken as input, and then the input image is segmented through deep learning CNN. In another study, CNN 4.55 is combined with optimized parameters; CNN 4.55 is good for classification of the MRI feature; for more optimization, t-test is used for identification of the accurate classification parameter in disease image [58].

In [59], the K-means cluster is combined with morphological operation. The result of the combination of both techniques is segmentation of region of interest (inner information of tumor). In [60], a segmentation technique was suggested with combination of KFC and HCSD. KFCM segments the tumor pixel; this technique also gives the details of nontumorous pixels; however, HCSD segments the tumor pixel cluster. In another study, the tumorous pixels are extracted and then detected for accurate identification of accurate class of tumor cells in MRI images [61]. Twenty (20) matrices are evaluated to measure the accurate performance of the algorithm, fuzzy cluster values are compared with ground truth reality image, and then 20 parameters help to evaluate the results [62].

In line with the above study, three types of techniques, namely, hybrid-based technique, learning-based technique, and atlas-based technique, were used for the segmentation of tumor pixels, with the evaluation metrics being Dice and Jaccard [63]. In other research, the PSO and EDPSO are compared across 48 instances, and the results are verified for both classification and segmentation [22]. In another study, an unsupervised learning algorithm was proposed. The reason for the design of this algorithm was multiobjective.

In [64], both K-means and SOM are combined where SOM identifies the scattered pixel and K-means identifies hard clustering values of pixels. In [52], the multi-cascaded neural network offers portion segmentation. The multi-cascaded neural network with random forest was proposed, and this hybrid approach is compared with the random forest.

According to [53], the neural network is trained for segmentation using local and global feature. The results are improved with CNN parameter named as max pooling. In another study, contour was drawn around the boundaries of tumor for identification of tumor region [54]. In [56], a local based FCM algorithm (LCFCM_S) identifies the region with robust outlier. In another study, two phases are included for segmentation; in the first phase, voxel based classifier along with random forest is used, and in the second phase, active contours are identified using level set method (LSM) [55]. In addition, [65] reviewed the segmentation methods over MRI images.

In [66], the effective segmentation is performed through a series of steps. K-means cluster and FCM clusters are combined, the resultant cluster is further combined with morphological operation, and morphological operation is performed for thresholding of tumor pixels. In [42], different modalities like MRI and CT scan are discussed; these modalities can be further segmented and classified. In [1], traditional image processing is compared with soft computing. In [67], the segmentation of image is performed through K-means and analyzed through HOG feature along with SVM classifier for detection of brain image. An image was segmented by K-means segmentation with preprocessing of brain MRI.

In another study, the brain tumor image is segmented through combination of modified FCM (MFCM) and Bacteria Foraging Optimization (BFO) [68]. In [4], FKM is combined with SOM for identification of tumor boundaries, with the performance evaluation performed utilizing comparison parameters such as Dice overlap index (DOI), Jaccard index (JI), sensitivity, specificity, peak signal-to-noise ratio (PSNR), mean squared error (MSE), and computational time in addition to the memory needs for processing the magnetic resonance (MR) brain images. DOI and JI gave the voxel similarity, whereas the MSE and PSNR indicated the quality of image with numeric value. In this study, automatic detection of the tumor region in MR brain images was achieved and possessed a positive effect in assisting radio surgeons in identifying the precise topographical location of tumor region. In a study by Rahim et al. [69], local features were extracted for region detection, and eigenvectors were used for segmentation. Furthermore, in [70], a review was conducted on soft clustering, tradition image processing, and artificial neural network (ANN). In [71], it was revealed that automatic pathological analysis possessed greater value than manual image analysis, especially when the focus was on accuracy or time. In another study, a review was conducted to check the segmentation and evaluation methods for identification of disease [72]. In [63], for dedicated kind of method for MRI, segmentation of brain tumor (glioma) was suggested in a survey. In another study, a specific general classification-based segmentation was suggested with evaluation parameters like Dice and Jaccard.

In [73], segmentation is performed through deep learning on glioma images, and analysis of tumor is done through classification of glioma images as compared to normal cell images. In [74], a tumor is segmented through localization, then thresholding is performed, and at last statistical evaluation is performed. In [75], a study was conducted with a combination of SCM and modified SVM and modified FCM which provided a better segmentation of the brain tumor.

In another study, FLAIR sequence of MRI is segmented through the CNN technique. Another technique named as Simultaneous Truth Estimation (STAPLE) is used to generate the ground truth images. In [58], a cascade of 2.5D CNN was proposed for segmentation with classes of

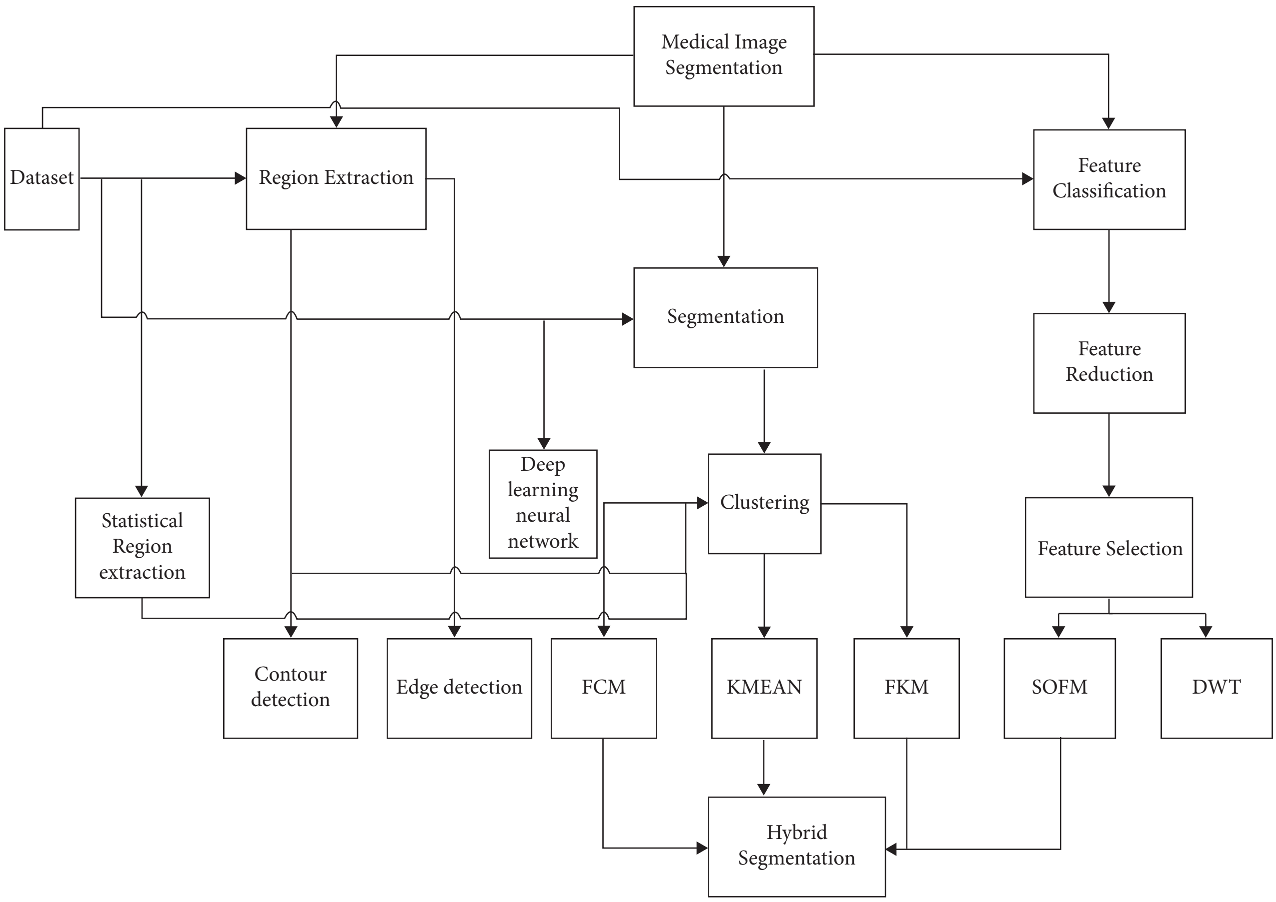

Figure 1: Process of medical image segmentation.

intensities of the brain tumor. In [76], very special deep learning technique, which assigns label to the global tumor images as compared to the detailed tumor image, was proposed. In [77], K-means is combined with CNN; in parallel for segmentation, the accuracy with unsupervised learning is more accurate as compared to supervised learning and CNN. In [78–84], segmentation methods are compared with deep learning. Hence, it is emphasized that not a single study among the referenced ones was capable of solving the issues of variation of intensities, extreme intensities, and features clustering.

In another study, efficient segmentation is performed with the combination of SOFM and FKM.

In studies like [85–91], segmentation and classification play an important role for identification of disease in medical imaging.

Figure 1 shows the design of the research process; this figure is a kind of pre-map of the review work. Furthermore, datasets of medical images are acquired. Then, those images are input to the preprocessing phase. In this phase, tumor region is extracted using the mentioned traditional image processing techniques. Furthermore, the higher-dimensional features of the big dataset images are reduced to small set. From small set, a set of specific features was selected through the mentioned techniques in Figure 1. The images of the big datasets are segmented through the preferred clustering techniques. All of the three phases are combined at the level of hybrid segmentation.

3. Dataset and Processing

Dataset and processing include the details of modalities like magnetic resonance imaging (MR). Modality information can be published or unpublished. It includes the details of MRI and MRI based dataset. The discussion can be seen in Section 3.1 and Section 3.2.

3.1. Magnetic Resonance Imaging (MRI). Out of the different kinds of image modalities in existence, three modalities have been identified as being frequently used: the application of X-ray, computed tomography (CT), and magnetic resonance imaging (MRI). Notably, the MRI can be easily distinguished from the other two modalities. CT scan is more similar to MRI as both are able to view the internal structure of the physique. However, unlike MRI which utilizes a powerful magnet and radio waves to function, the CT scan employs a sophisticated X-ray system to capture a 360-degree image of the targeted internal body area and organs. The targeted human organ is exposed to the X-rays. During the process of CT scan, a person must be laid down on a sliding table, and the machine rotates for capturing cross-sectional images of the body. Meanwhile, X-rays utilize electromagnetic waves with a wavelength of approximately 0.01 to 10 nanometers. Pretibial *l* edema (PTE) indicates signs of abnormal level of fluid in the human body. All the three mentioned image modalities (X-ray, CT, and MRI) are medical imaging tests used in medical image processing. In medical imaging science, MRI is superior in many instances in comparison to X-rays and CT scan [92].

The main purpose of medical imaging is to process internal organ visualization. It is used to diagnose ailments. It is a must to possess prior knowledge regarding the chemistry of the human body before capturing images. A human body consists of matters termed as atoms. An atom consists of three elements: an electron, nucleus, and proton, where electrons revolve around the nuclei. Modalities give a powerfully aligned margin around the nuclei within the body.

The variable magnetic field inside the body that causes the atoms to resonate is called the nuclear magnetic resonance (NMR). The nuclei produce a strong magnetic field. The scanner detects the magnetic field and produces an image [42]. The MRI employs the same physical effect as the nuclear magnetic resonance (NMR).

The human body normally consists of water (H_20), composed of 2 hydrogen atoms (H_2) and one oxygen atom. The hydrogen nuclei (protons) will align with the magnetic field of 0.2 to 3 tesla. The scanner produces a strong magnetic field that creates varying magnetic fields, and because protons are part of atoms, they will absorb varying energy from the variable field created by the scanner. They flip their spins when the field is turned off and gradually return to the normal spin which is called precession. The return of energy will produce a radio frequency that is measured by the receiver in a scanner, and this will create an image. The protons in the different parts of the body will return to their normal spin at different rates, and this enables the scanner to distinguish different tissues, assisted by the setting of the scanner which produces a contrast that enables this differentiation of the tissues. MRI is used for testing healthy and also abnormal cells and tissues with the use of microwaves that are spread over the internal organs of the human body to obtain an image of the targeted organ as shown in Figure 2.

In Figure 2, an MRI machine is presented with its components such as magnets that produce magnetic fields in the body, and the scanner will create the image. MRI provides magnetic field and X-rays such as radio frequency (RF) pulses; it is not recommended during radiation for the first diagnosis. For safety measures, the doctor goes through an MRI magnet. MRI uses an implanted magnet that heats up the field. Therefore, before the patient is examined, it is important to check and evaluate the implanted magnet properly and the patient's risk factors, for safety measures.

When a continuous magnetic ray is directed onto the patient, the ray penetrates through, and this sensation is felt by the patient. In addition, the flipping of a magnet used in MRI procedure produces a certain sound/beep noise; thus, for protection, it is necessary to insulate the room. The radiofrequency rays are transmitted by the scanner, and the body absorbs those radiations, thereby limiting the rays of the scanner. The future of the MRI with the advancement of science magnet flip has been modified, and now more magnets can be used. The enhancement of organ imaging

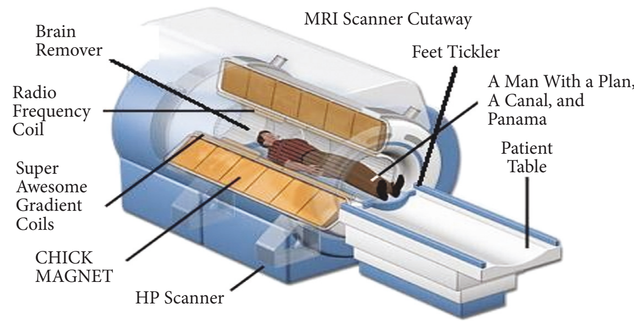

Figure 2: Architecture of MRI machine (source: [93]).

with quantitative technique has enabled an image of the brain up to 1 mm be obtained. This permits doctors to perform analyses on brains.

Molecules tend to diffuse in a parallel manner along the fibers. A technique known as Digital Tensor Imaging (DTI) measures the parallel diffusion. Functional magnetic resonance imaging (fMRI) is a kind of MRI that checks the functional activity in the brain and measures the flow of blood toward other parts of the body. The fMRI basically measures the blood oxygen level depending on the contrast because the neurons of the body are active and contain more oxygen levels and vice versa. Most researchers employ the fMRI with DTI for examination and evaluation purposes. Nevertheless, for this current case study, the researchers ascertained that the MRI is adequate as the MRI quality of image is acknowledged to have undergone improvements. This current research study has identified the MRI as having sufficient accuracy to detect brain tumors, which is the focus of this study.

The brain tumor detection was realized through the modality of the MRI; an abnormal mass or cell collection in a particular part of the body is called a tumor. When this process is found in the brain, it is termed as a brain tumor. Furthermore, any tumor can be either benign (noncancerous) or malignant (cancerous). Both types have the potential to grow inside the brain, and their growth subsequently creates pressure within the brain, which is life threating. Brain tumors are classified into two main classes, primary and secondary. When tumors reside in the brain, they are termed as primary benign. When they spread to other parts such as the lungs and chest, they are termed as secondary tumors in which metastasis is formed, and this leads to the spread of the tumor. The risk factors of brain tumor are dependent upon age, race, family history, and race. The symptoms of brain tumors are vomiting, headache, confusion, and weakness.

Generally, doctors initiate their examination by checking the condition of the brain through the MRI. If a tumor is found, the doctor will then set out on further examination to determine whether the tumor is benign or malignant.

The MRI measures the size of the tumor in the brain after detailed imaging of the brain is executed. Before the imaging, a patient is given an injection into the vein which works as a tracer. The tracer helps to highlight the region of interest (ROI), which is ensued by detail MRI to detect a tumor.

T1 and T2 are important relaxation time factors as they can separate the tissues. The time constant for the z-axis plan is termed as the T1 parameter, whereas the time constant for the xy-axis plan is termed as the T2 parameter. T1 is greater than T2 element in the biological factor. T1 relaxation time difference produces a T1 weighted image, whereas the T2 relaxation time difference produces a T2 image. To determine the protons in every tissue, the sum of the protons in each tissue is taken per unit and is termed as proton density (PD) image.

During MRI, six items are employed with six components, and they are (1) coil, (2) shim coil, (3) radio frequency coil, (4) receiver coil, (5) gradient coil, and (6) computer. The CT scan and X-ay are both one-dimensional planes, whereas the MRI consists of three-dimensional planes. One of the dimensional planes consists of the axial plane, with the orientation of the image direction is from the head to feet. The next dimensional plane is the sagittal plane, with the orientation of the image plane from the back to the front of the human body. The third and final dimensional plane is the coronal *l* plane, with the orientation of the image plane from left arm to right arm. All of the images from the dimensional planes mentioned can be used for medical analysis of the internal body that enables doctors to perform clinical analysis. MRI does not perform ionization radiation. With short T relaxation time, fat signal typically appears bright in most significant clinical imaging sequences and can conceal the latent pathology such as edema, inflammation, or enhancing tumors. The visualization of the interior representation of a human body is akin to the internal tissues; it can be seen in Figure 2.

One of the disadvantages of the MRI images is the production of a noisy image. Occasionally, the image features are overlapped. In instances when a disease is discovered through the analysis of an image, the presence of overlapping features will pose problems to the clarity of the case. Furthermore, the MRI is considered as very expensive in comparison to modalities such as the X-ray. The aspect ratio of original image is 4 : 3. The most important benefit of MRI is its 3-dimensional image details.

The standard means of producing the information of the brain is using the brain imaging technique that presents the image of the brain in digital or MRI film format. There are many applied benefits of these images, for example, in clinical purposes such as diagnosis systems or forensic purposes such as human identification systems.

3.2. MRI Dataset. The MRI dataset can be found in both published and unpublished datasets. The published dataset is accessible online, whereas the unpublished ones need to be made available. Previously available published dataset is the Harvard brain tumor repository (such as https://www.med.harvard.edu/AANLIB/home.html). The main disadvantage of using this dataset images is the availability of skull (cranium) images. Presently available dataset is the MICCAI BraTS brain tumor dataset which consists of images of the brain with the exclusion of the skull (cranium) in the images [13]. Ground truth images are also available in the dataset. Scientists worldwide will enhance the dataset annually [19].

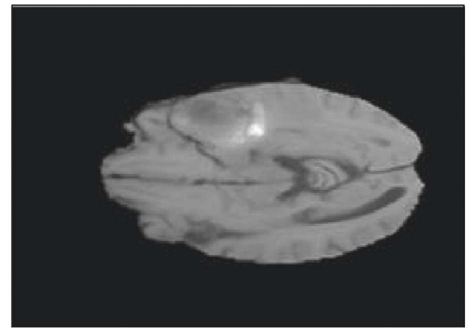

Figure 3: Image of T1 (BraTS17_13_2_1).

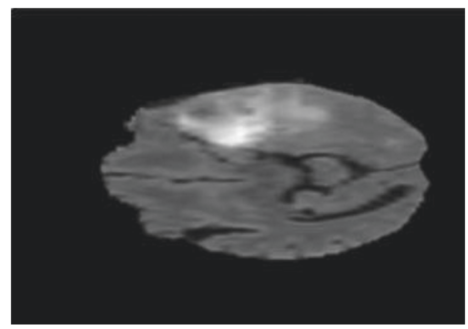

Figure 4: Image of FLAIR (BraTS17_13_2_1).

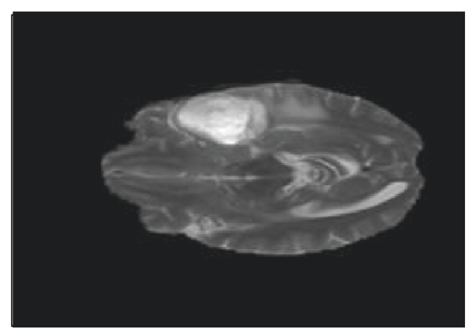

Figure 5: Image of T2 (BraTS17_13_2_1).

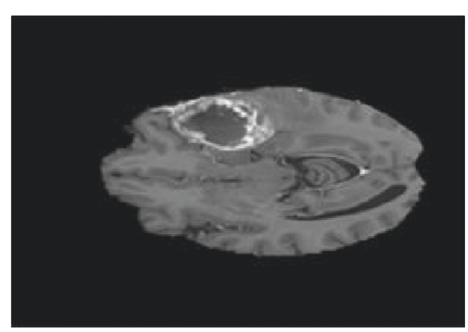

Figure 6: Image of T1CE (BraTS17_13_2_1).

In Figures 3–6, four sequences of images are provided. They are termed as T1, FLAIR, T2, and T1CE. They indicate intensity-wise information in the dataset. They are also labeled based on their intensities. T1 provides the details of enhancing tumor core, while T2 and FLAIR provides the

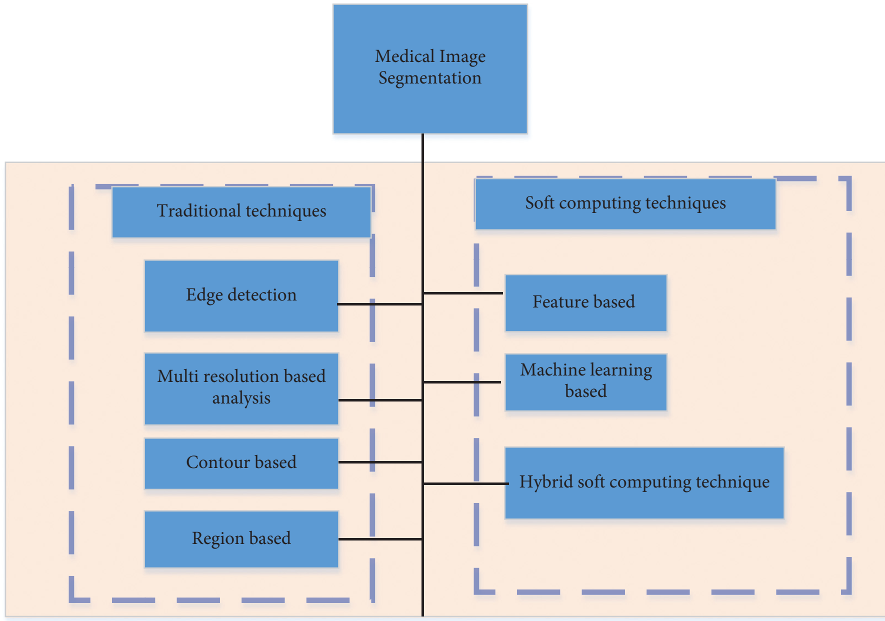

Figure 7: Soft computing and image segmentation approaches.

details of edema, and T1CE provides the details of enhancement as well as the complete shape of the tumor.

4. Approach

The segmentation and analysis of the brain tumor images with high accuracy using MRI are enabled through two methods, which are image processing and soft computing [94].

Image processing penetrates deep inside the tumor and is based on image information, whereas soft computing analyzes the image intelligently. With soft computing, the number of brain tumor image can provide the features of the image. Figure 7 illustrates seven types of segmentations which are contour-based, region-based, multi-resolution-based, machine learning-based, and hybrid soft computing-based segmentations. Contour involves curve analysis of the shape. Region-based segmentation explores the information inside the edges. Statistical-based segmentation is used for investigation purposes and is divided into two groups; they are the clustering and the predictive modeling. Multi-resolution-based segmentation creates the objects through the employment of an iterative algorithm. Meanwhile, the machine learning techniques are used to divide the information of the image. However, different from the traditional techniques, soft computing employs the clustering techniques which provide information of the image; the techniques are combined in hybrid.

5. Image Enhancement

The term image enhancement refers to the improvement of the image appearance or to the improvement of the contrast and visibility of features of concern. In addition, image enhancement is the development of digital images to produce suitable results for analysis or demonstration; clustering gives particular information. These techniques perform the analyses of images. The enhancement of a medical image is important as it helps radiologists or surgeons to identify the abnormalities in human organs. The main medical image enhancement categories include the spatial domain methods and frequency domain methods.

Image enhancement provides brightness to an image by making changes in pixel values or by transformation of pixel values, and this has been accomplished with equations and formula. As Fourier transformation (FT) is also an example of image enhancement, the values of the pixel will be changed.

$$f \longrightarrow g, \tag{1}$$

$$S = T(r). \tag{2}$$

Equation (1) shows a one-to-one function, where T is the transformation of domain f to domain g with pixel, and the transformation pixels' intensity can be within the range $[0\text{–}2k^{-1}]$. In (2), T is the transformation of r intensities. These intensities are formed with the mapping function. S is the variable in which the intensity values will be stored. Other transformations can enhance the image. Furthermore, T transformation has been used by logarithmic transformation, power transformation, and piece-wise linear image transformation and for intensity transformation of image [95].It can be seen in Figure 8 where one T1 image is input, and Figure 9 is the enhanced image.

6. Segmentation

In image processing, an image is an input, and after processing, the processed image is returned. The output is an image with attributes. The segmentation is carried out by subdividing an image into its parts or objects. This process of subdivision will be carried out till the problem is solved. Two

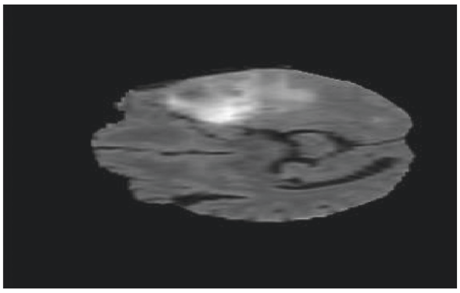

Figure 8: Input T1 sequence image.

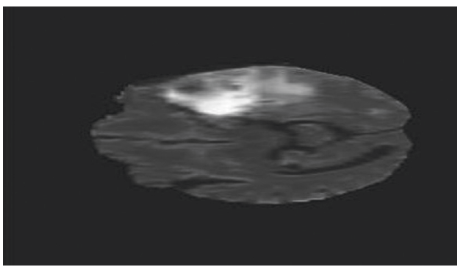

Figure 9: Image enhancement of Figure 8.

properties of segmentation exist. These are continuous and discontinuous segmentation.

Segmentation can be seen by means of image processing and by soft computing. By using image processing, the intensity of detecting features is enabled by using line, edge, and point. The intensity of an image is also addressed through the soft computing methods. Some methods are represented in Table 1.

The segmentation methods are used for detecting features based on sharp local intensities and the type of feature that they can isolate such as edges, isolated lines, and isolated point edges which are found over the pixels where the intensity changes abruptly so as to reveal the connected edges of a pixel. An edge detector can be used to locate and identify an object. The line may be viewed as an edge segment in which the intensity of the background of either side is higher or lighter than the intensity of the line pixel. Points are line, and one point in width or height will be single pixel [95]. In the following paragraph, segmentation methods are discussed clearly by means of image processing and soft computing.

The study [97] indicated the cluster techniques K-means and fuzzy C-means (FCM) which were combined for tumor segmentation. The K-means functions rapidly, whereas FCM performs accurate segmentation of a brain tumor. Thus, the functions of these two techniques were combined to produce the K-means integrated with fuzzy C-means (KIFCM) approach, which was proposed for segmentation. Another study [74] of automatic segmentation of tumor from T2 is performed with statistical operation. This statistical-based segmentation enhanced the low intensities of an image. In addition, in a study [98] on a brain tumor detection method, the method involved the combination of steps such as preprocessing, segmentation through neural network, and image analysis that was performed though Gabor filter and Bayesian neural network classifier. In addition to the aforementioned studies, another study [2] revealed that the MRI was the widely preferred and used method of medical imaging. In this study, the statistical evaluation consists of the mean, median, mode, variance, and standard deviation. The mathematical *l* formulation was also discussed, where it facilitated the identification of the statistical features of an MRI image and aided the segmentation. In [99], the supervoxel (volume elements) was over-segmented. Congruent with this, the supervoxel of an image was compared to the supervoxel of the atlas (for multi-atlas segmentation of brain MR images). Accordingly, from the MRI supervoxel images, labels were transferred to the atlas. In another study [100], the automated localization of a brain tumor in the MRI that employed potential cluster was compared to the K-means clustering algorithm. The research suggested that future work could address the calculation of the appropriate number of N clusters to locate one or more tumors. This depends mainly on the relative total intensity of the tumor regions with respect to the total intensity of the image.

6.1. Segmentation Performance. The performance of an image processing algorithm is improved with segmentation. In the majority of studies, the image processing technique is combined with segmentation such as edge detection and is coupled with intensity thresholding. Image segmentation based on morphology is a good technique to be used for brain tumor identification. The segmentation techniques work with different types of image processing such as histogram equalization, filters, region of interest, classification, morphological operation, dominant gray level run length, feature selection, feature extraction, region growing, K-means clustering, expectation maximum, and fuzzy logic [41].

6.2. Threshold. Threshold is about mapping the intensity value of the corresponding pixel value. If TR is applied to pixels in the neighborhood yield and the (x, y) value of output, then g is equal to the neighbor with an origin at (x, y). Thus, segmentation directly focuses on the characteristics of an image such as region-based intensity and property.

6.2.1. Threshold and Its Types. For the identification of intensity, consider a histogram T1. The histogram corresponds to the image in such a way that the background light and object pixels have intensity values that are grouped into two dominant modes. For global thresholding, T is constant over the image. For variable thresholding, T1 changes the image completely. It is also known that variable thresholding is also termed as local thresholding, where T1 at any point of the (x, y) can depend on the neighbor's mean of average. If T1 depends on the spatial coordinate of (x, y) in the variable thresholding, the term will be referred to as adaptive thresholding or dynamic thresholding. If the threshold problem involves certain histogram and the histogram has three threshold classes, one of the classes is for the

Table 1: Segmentation techniques.

Sr. no.	References	Techniques
1	[96]	Histogram, fuzzy c-means, and K-means
2	[42]	Thresholding, region growing, clustering, classifiers, Bayesian approach, deformable methods, atlas guided approach, edge-based methods, and compression-based method
3	[43]	Thresholding, histogram, region of interest (ROI), clustering techniques, classification techniques, expectation maximization, and graph cut
4	[45]	Image texturing and range filters
5	[46]	Dominant gray level run length

background and two of the classes are for the objects; such classification is known as multi-thresholding classification.

6.2.2. Region-Based Segmentation. The objective of segmentation is to partition an image into regions. The problem of finding boundaries of a region based on discontinuities is that the threshold is accomplished based on pixel distribution property, such as intensity via color. However, through advancements made in the field, segmentation of tumor region can be found directly [101].

A method known as region growing can assist in the identification of the seed based on the similarities of the neighboring pixels and on the predefined seeds. Seed selection is based on particular criteria. If there are no criteria available, then the study will compute each node and the same property of seed will be processed for region growing. The formation of clusters posits such a seed nearest to the centroid. There is a need for some descriptor based on certain color intensities or texture, or useful information. The descriptor will look for similar colors only, but not for their connectivity. Hence, the possibility for region growing is misleading.

Region growing will stop if no pixel satisfies the growth rate or due to the similarity of colors or texture. Therefore, considering the historical account of the pixel, it checks the likeness among the candidate pixels. Such a description is partially available [101].

6.2.3. Histogram. In a histogram, an image in which the intensity levels are separately identified is generated. These intensity levels are derived from different ranges of pixel values. The complete ranges of intensities are available in the histogram. These intensities consist of a dynamic range which helps to increase the contrast of the gray scale level. Histogram equalization is the transformation of discrete distributive intensities into discrete distributive intensities. To normalize a histogram, each of its values is divided by the total number of pixels in an image. In histogram equalization, each value of the histogram is modified or the contrast of every value is calculated. It produces a linear trend to the cumulative distributive function (CDF) which is associated with the image. The processing of CDF relies on histogram equalization. Linear CDF results in a uniform histogram [102].

6.2.4. Dominant Gray Level. This technique is mainly used for feature extraction. The dominant gray level run length matrix (DGLRLM) is based on the calculation or it is the computation of the gray level found in different channels or lengths. Different gray level run length or the different consequences of gray level run are applied in this study. Run length is used for segmentation; this technique is based on the gray level run, which is defined as a collinear that is connected to a set of pixels, all possessing the same gray level. The length of the run is the number of pixel points in every run or iteration [101].

6.2.5. Range Filter. In the local subrange filter, statistical subrange of different intensities within the window was used. The range distance is the statistical measure of the sample variation. The edge is a discontinuity in mean intensity. If the variation in the local range is small, minor computation is needed. The local range distance is considered large if a region has large discontinuities at the intensity level. Hence, range filter detects the intensity values among the edges within the window. The output range may be max or min, where the range values are multiplied by a certain constant to affect a clear picture of edges. Local range filter needs less amount of time for execution because it has a small input as a range filter for segmentation through creating structure element for extraction of neighbor range value [47].

6.2.6. Morphological Operation. The above-mentioned study was developed for binary images and later extended to the gray scale function and images. The fundamental morphological operations are erosion, dilation, opening, and closing. These operations are helpful to remove the cranium from the brain tumor image. They are very strong features of image processing. With these, the images' pixels can be added to or removed from the MRI image [101].

6.3. Feature Extraction. Feature extraction extracts the cluster that indicated the predicted tumor at the output. The extracted cluster is introduced to the threshold process. It may be the binary mask over the complete image. It makes the dark pixel darker and the white one whiter or brighter. In the threshold coding, each transformation coefficient is compared with threshold T2. If the value is less than that, it is compared with other thresholds and assigned zero. However, if it is more than threshold T, then it will be considered as effective.

The difference between feature selection and feature extraction is that for feature selection, the feature is of the subset of the original feature set. Meanwhile, in feature extraction, a new feature subset is built from the original one.

6.3.1. Feature Selection. Feature selection is a process that selects a subset of features relevant to the application. With the help of feature selection, it enables the search for a subset of features in this study.

The criterion of selection is the extent of classification accuracy, based on the optimization subset of the feature chosen. This is performed for reduction of the data dimensions and computation time and an increase in the classification accuracy. The selection of a subset feature from the total number of features is based on the optimization criteria [43].

6.4. Feature Classification. A feature classification is considered as an important step in the medical imaging process for the identification of a brain tumor. There are various classifiers available. Based on the curtained phenomena, the extracted feature labels are evaluated. The K-means helps the accuracy of the feature classification. With the following studies, a critical discussion on feature classification will assist in the analysis for the best feature classification and their combination.

The ensuing discussion will be very helpful for the detection of brain tumor images. To detect brain tumors with MRI, it is important to achieve feature classification accuracy. Thus, if the accuracy has been achieved completely, then the accuracy from all of the three planes, namely, the z-axis termed as axial images of MRI, the y-axis image termed as the coronal plane, and the x-axis termed as the sagittal, is ensured.

In the prior discussion, classification and novel hybrid classifier were discussed for the detection of normal and abnormal brain incidences. In the majority of the studies, 100 per cent of classification accuracy is achieved after performing the experiments. In [103], a series of steps over image such as the wavelet transformation were performed. At different levels, features were then reduced by using principal component analysis (PCA) which is a dimensionality-reduction method for feature extraction. Finally, the backpropagation neural network (BP-NN) was employed, and it has been revealed that the accuracy over the axial z-axis images was more than 90 per cent. Henceforth, the modern classification and combinations of brain MRI images were invented. According to Zhang, [104], the proposed "weighted" type Fourier transformation (WFRFT) + principal component analysis (PCA) + generalize eigenvalue proximal SVM (GEPSVM), WFRFT + PCA_twin SVM (TSVM), indicated better results.

In addition, further advancements in the field brought forth the successful invention used for automatic abnormal brain detection that employed improved classifiers with the combination of quantum behaved particle swarm optimization (QPSO), kernel support vector machine (KSVM), and wavelet energy, obtaining the best results comparatively. Secondly, the wavelet energy feature was the best for abnormal brain detection through CAD (Computer Aided Diagnose) [105, 106]. After the application of a 5-fold cross validation technique, the KSVM PSO was applied over the trained data; optimal KSVM revealed the state of t normal or abnormal brain. Thus, this technique was applied to 90 images, with a 97.7 per cent accuracy, which is a higher accuracy in comparison to backpropagation neural network (BP-NN) (86.22%) and RBF-NN (91.33%) [107, 108]. In another study, for the automatic classification of brain MR images into normal or abnormal, the wavelet, SVM, and BBO were used. The results of this study showed comparatively better accuracy, 97.78 per cent, than that of other studies using the biogeography-based optimization.

Table 2: Combination of classification technique and classification accuracy.

Sr. no.	Referenced studies	Techniques
1	[103]	DWT, SWT
2	[105]	Artificial B colony algorithm DWT PCA K-fold stratified cross validation FNN classifier
3	[107]	SCAB Fourier transformation, DWT, BNN
4	[110]	DWT, PCA, SVM Kernel-SVM (KSVM) K-fold technique

KSVM (BBO-KSVM) technique [105] is a combination of biogeography-based optimization and particle swarm optimization, and it is used to train the FNN. In [107], the stationary wavelet transformation (SWT) produced better results. The classification results were 98.5 per cent with a combination of adaptive comparative particle swarm optimization (ADCPSO) and fuzzy neural network (FNN) derived from over 160 images from the Harvard site, and neural network has been applied [107]. Scalable Chaotic Artificial Bee Colony algorithm classifies normal and abnormal brains of T1 weight images with an accuracy of 100 per cent [109]. In [110], automatic detection of tumorous and nontumorous images was performed with 99 per cent accuracy through the combination of DWT, PCA, and LS classifier. An automated and intelligent medical decision support system is in use for brain MRI scan classification. Hence, the optimal classifier combination demonstrated a higher classification accuracy of MRI brain tumor images for identification. In Table 2, a combination of feature extraction, reduction, selection, and classification is given. From the abovementioned details, their classification accuracy can be observed.

6.4.1. Overlap Accuracy (OA). Overlap accuracy is determined by the statistical measure where the closeness of an image or object is measured. The overlap accuracy calculates the extent of the overlap of the white portion and how much overlap of the white portion occurs among two images of black and white. One image is a ground truth reality image, and another image is a segmented image. It is determined that images have complete overlap when the segmented image perfectly matches the ground truth reality image. With black and white input images where foreground is white and background is black, the conditions are as follows: If the segmented foreground white pixels overlap with the ground truth of the foreground, the image will then be considered as true positive, and the pixels will be labeled as foreground and indicate the tumor portion. In another case, the background portion will show up as black pixels of the tumor image when they overlap with the background black pixels of the ground truth image, where the image will then be considered as true negative. When the foreground pixels in the segmented image overlap with the background of ground truth, the image will then be considered as false positive. In another case, when the segmented image background overlaps with the foreground of ground truth reality image, the image will be considered as false negative.

$$A = \text{segmented image}, \tag{3}$$

$$B = \text{ground truth reality image}, \tag{4}$$

$$\text{total image area} = A * B, \tag{5}$$

$$OA = \left(\frac{\text{total image area}}{A}\right) * 100. \tag{6}$$

Equation (3) is the segmented or the test image, and this segmented image is stored in A. Equation (4) shows the ground truth reality image, and it is stored in variable B. The total image area is the product, and this is shown in (5) and is formed with the combination of (3) and (4). Finally, (6) returns the percentage of the overlap of the white foreground segmented pixel with the white foreground ground truth pixel and is formed with the combination of (3) and (4).

7. Discussion

From the content of the article, it was found that region extraction, feature selection, and hybrid segmentation were the most applied methods. They played important roles in medical image processing (MIP). Similarly, better techniques have been proposed in the field of MIP. However, MIP was still lacking in areas pertaining to region extraction, confidence element extraction, and segmentation; therefore, time was needed to invent new methods or extend existing ones. Notably, dataset is an important element in the field of MIP. Datasets like Harvard brain tumor repository and BraTS brain tumor challenge are helpful for experimentation. A huge amount of experimentation has been performed, but issues persist and were visualized when the sequence of image (FLAIR, T1, T2, T1CE) was analyzed. In BraTS brain tumor dataset, the tumor core region was enhanced by the T1 sequence; thus, it is important to analyze this region. It can be seen in article [20] that the edema region, complete tumor region, and enhancing tumor region show the tumor areas with different labels. Due to the intensities, a labeled image seems to be challenging.

The scope of the mentioned issues is crucial, as the issues are opening new horizon which needs inventions and improvements. Firstly, the MRI image region extraction was executed through confidence interval, but it was inadequate for the identification of complete tumor pixels. These pixels are required in enhancing tumor core. If tumor pixels can be identified, the probability of tumor region identification increases. Therefore, in [111], the confidence region was needed for the accurate identification of enhancing tumor. Secondly, in another suggested study, SOM selection assigned weight to the features, but improvement was required to select the best single feature. These features must be highly accredited feature on the dataset. Due to the high cost of processing, the feature selection algorithm needed improvement. Accurate features are needed to assist in the segmentation of tumors [26].

In some other studies, hybrid segmentation algorithm was used. Segmentation was achieved, but extreme variations or extending intensities of intensity were an open question. Extreme intensities of tumor were mixed with other normal brain intensities [52]. Therefore, there were issues in the hybrid segmentation methods when the algorithm performed segmentation. A hybrid unsupervised learning algorithm was required for managing the extreme variation of intensities [68].

8. Conclusion

MRI modality is compared with other modalities like CT scan, X-rays, and PET scan. Different state-of-the-art studies over brain tumor detection are available, like, feature selection and segmentation technique. Where the region extraction techniques identifies region of brain tumor and features are extracted and selected from the image dataset. Segmentation gives region of interest after series of steps. Concepts are more specific on MRI like MR imaging, MRI dataset, MRI enhancement, segmentation, feature extraction, comparative studies, and discussion on the basis of critical analysis. We can see after comparative analysis of techniques that the article highlights issues of variation of intensity, which needs to be extracted from a certain region of brain; secondly, feature selection is important aspect from big datasets, and the specific feature selection from state of the SOFM is another challenge. Finally, segmentation is required for extreme variation of intensities on the tumor boundaries.

Data Availability

No data were used to support this study.

Conflicts of Interest

The authors declare that they have no conflicts of interest.

References

[1] S. S. Chouhan, A. Kaul, and U. P. Singh, "Soft computing approaches for image segmentation: a survey," *Multimedia Tools and Applications*, vol. 77, no. 21, Article ID 28483, 2018.

[2] E. P. Kumar, V. M. Kumar, and M. Sumithra, "Tumour detection in brain MRI using improved segmentation algorithm," in *Proceedings of the 2013 Fourth International Conference on Computing, Communications and Networking Technologies (ICCCNT)*, July, 2013.

[3] A. Aslam, E. Khan, and M. S. Beg, "Improved edge detection algorithm for brain tumor segmentation," *Procedia Computer Science*, vol. 58, pp. 430–437, 2015.

[4] G. Vishnuvarthanan, M. P. Rajasekaran, P. Subbaraj, and A. Vishnuvarthanan, "An unsupervised learning method with a clustering approach for tumor identification and tissue segmentation in magnetic resonance brain images," *Applied Soft Computing*, vol. 38, pp. 190–212, 2016.

[5] S. Swamy and P. Kulkarni, "Image processing for identifying brain tumor using intelligent system," *Int. J. Innov. Res. Sci. Eng. Technol*, vol. 4, no. 11, 2015.

[6] M. Angulakshmi and G. Lakshmi Priya, "Automated brain tumour segmentation techniques- A review," *International Journal of Imaging Systems and Technology*, vol. 27, no. 1, pp. 66–77, 2017.

[7] K. K. Reddy, "Confidence guided enhancing brain tumor segmentation in multi-parametric MRI," in *Proceedings of the 2012 9th Ieee International Symposium on Biomedical Imaging (Isbi)*, May, 2012.

[8] C. Li, J. C. Gore, and C. Davatzikos, "Multiplicative intrinsic component optimization (MICO) for MRI bias field estimation and tissue segmentation," *Magnetic Resonance in Imaging*, vol. 32, no. 7, pp. 913–923, 2014.

[9] S. D. Oberhelman, "Active Contours Implementation," Open Access Master's Theses, 2018.

[10] S. Banerjee, S. Mitra, and B. Uma Shankar, "Single seed delineation of brain tumor using multi-thresholding," *Information Sciences*, vol. 330, pp. 88–103, 2016.

[11] P. Dhage, M. Phegade, and S. Shah, "Watershed segmentation brain tumor detection," in *Proceedings of the 2015 International Conference on Pervasive Computing (ICPC)*, January, 2015.

[12] R. T. Shinohara, E. M. Sweeney, J. Goldsmith et al., "Statistical normalization techniques for magnetic resonance imaging," *NeuroImage: Clinica*, vol. 6, pp. 9–19, 2014.

[13] S. Bauer, T. Fejes, and M. Reyes, "A skull-stripping filter for ITK," *Insight Journal*, vol. 2012, 2013.

[14] C. Liu, W. Liu, and W. Xing, "An improved edge-based level set method combining local regional fitting information for noisy image segmentation," *Signal Processing*, vol. 130, pp. 12–21, 2017.

[15] D. N. George, H. B. Jehlol, and A. S. A. Oleiwi, "Brain tumor detection using shape features and machine learning algorithms," *International Journal of Advanced Research in Computer Science and Software Engineering*, vol. 5, no. 10, pp. 454–459, 2015.

[16] K. Ding and L. Xiao, "A simple method to improve initialization robustness for active contours driven by local region fitting energy," 2018, https://arxiv.org/abs/1802.10437.

[17] A. Zotin, K. Simonov, M. Kurako, Y. Hamad, and S. Kirillova, "Edge detection in MRI brain tumor images based on fuzzy C-means clustering," *Procedia Computer Science*, vol. 126, pp. 1261–1270, 2018.

[18] C. Bowles, C. Qin, R. Guerrero et al., "Brain lesion segmentation through image synthesis and outlier detection," *NeuroImage: Clinica*, vol. 16, pp. 643–658, 2017.

[19] B. H. Menze, A. Jakab, S. Bauer et al., "The multimodal brain tumor image segmentation benchmark (BRATS)," *IEEE Transactions on Medical Imaging*, vol. 34, no. 10, pp. 1993–2024, 2015.

[20] N. A. Khan, "A method for tumour detection on brain MRI image by implementing SVM," *International Journal of Computer Science and Information Security*, vol. 14, no. 8, p. 154, 2016.

[21] N. Varuna Shree and T. N. R. Kumar, "Identification and classification of brain tumor MRI images with feature extraction using DWT and probabilistic neural network," *Brain informatics*, vol. 5, no. 1, pp. 23–30, 2018.

[22] V. Vijay, A. Kavitha, and S. R. Rebecca, "Automated brain tumor segmentation and detection in MRI using enhanced darwinian particle swarm optimization(EDPSO)," *Procedia Computer Science*, vol. 92, pp. 475–480, 2016.

[23] A. Chaddad, "Automated feature extraction in brain tumor by magnetic resonance imaging using Gaussian mixture models," *International Journal of Biomedical Imaging*, vol. 2015, Article ID 868031, 11 pages, 2015.

[24] W. Natita, W. Wiboonsak, S. Wiboonsak, and S. Dusadee, "Appropriate learning rate and neighborhood function of self-organizing map (SOM) for specific humidity pattern classification over Southern Thailand," *International Journal of Modeling and Optimization*, vol. 6, no. 1, pp. 61–65, 2016.

[25] L. Jin, L. Min, J. Wang, W. Fangxiang, T. Liu, and Y. Pan, "A survey of MRI-based brain tumor segmentation methods," *Tsinghua Science and Technology*, vol. 19, no. 6, pp. 578–595, 2014.

[26] A. Starkey, A. U. Ahmad, and H. Hamdoun, "Automated feature identification and classification using automated feature weighted self organizing map (FWSOM)," in *IOP Conference Series: Materials Science and Engineering*IOP Publishing, Bristol, UK, 2017.

[27] N. Gupta and P. Khanna, "A non-invasive and adaptive CAD system to detect brain tumor from T2-weighted MRIs using customized Otsu's thresholding with prominent features and supervised learning," *Signal Processing: Image Communication*, vol. 59, pp. 18–26, 2017.

[28] N. Nabizadeh and M. Kubat, "Brain tumors detection and segmentation in MR images: Gabor wavelet vs. statistical features," *Computers & Electrical Engineering*, vol. 45, pp. 286–301, 2015.

[29] H. Dong, "Automatic brain tumor detection and segmentation using U-Net based fully convolutional networks," in *Annual Conference on Medical Image Understanding and Analysis*Springer, Berlin/Heidelberg, Germany, 2017.

[30] N. B. Bahadure, A. K. Ray, and H. P. Thethi, "Image analysis for MRI based brain tumor detection and feature extraction using biologically inspired BWT and SVM," *International Journal of Biomedical Imaging*, vol. 2017, 12 pages, Article ID 9749108, 2017.

[31] B. Devkota, A. Alsadoon, P. Prasad, A. Singh, and A. Elchouemi, "Image segmentation for early stage brain tumor detection using mathematical morphological reconstruction," *Procedia Computer Science*, vol. 125, pp. 115–123, 2018.

[32] D. R. Nayak, R. Dash, B. Majhi, and V. Prasad, "Automated pathological brain detection system: a fast discrete curvelet transform and probabilistic neural network based approach," *Expert Systems with Applications*, vol. 88, pp. 152–164, 2017.

[33] D. R. Nayak, R. Dash, and B. Majhi, "Brain MR image classification using two-dimensional discrete wavelet transform and AdaBoost with random forests," *Neurocomputing*, vol. 177, pp. 188–197, 2016.

[34] X. X. Zhou, J. F. Yang, H. Sheng et al., "Combination of stationary wavelet transform and kernel support vector machines for pathological brain detection," *Simulation*, vol. 92, no. 9, pp. 827–837, 2016.
[35] A. S. Am and P. Augustine, "Efficient brain tumor classification using PCA and SVM," *International Journal of Research in Engineering, IT and Social Sciences*, vol. 7, pp. 1–7, 2017.
[36] O. Puonti, J. E. Iglesias, and K. Van Leemput, "Fast and sequence-adaptive whole-brain segmentation using parametric Bayesian modeling," *NeuroImage*, vol. 143, pp. 235–249, 2016.
[37] S. Wang, P. Phillips, J. Yang, P. Sun, and Y. Zhang, "Magnetic resonance brain classification by a novel binary particle swarm optimization with mutation and time-varying acceleration coefficients," *Biomedical Engineering/ Biomedizinische Technik*, vol. 61, no. 4, pp. 431–441, 2016.
[38] M. Abdelsamea, M. H. Mohamed, and M. Bamatraf, "An effective image feature classiffication using an improved som," 2015, https://arxiv.org/abs/1501.01723.
[39] Y. Zheng, Z. Jiang, F. Xie et al., "Feature extraction from histopathological images based on nucleus-guided convolutional neural network for breast lesion classification," *Pattern Recognition*, vol. 71, pp. 14–25, 2017.
[40] A. Veeramuthu, S. Meenakshi, and V. P. Darsini, "Brain image classification using learning machine approach and brain structure analysis," *Procedia Computer Science*, vol. 50, pp. 388–394, 2015.
[41] A. P. Ag and S. Pattar, "Textural feature extraction and analysis for brain tumors using MRI," *International Journal of Scientific and Research Publications*, vol. 7, no. 8, 2017.
[42] S. Masood, M. Sharif, A. Masood, M. Yasmin, and M. Raza, "A survey on medical image segmentation," *Current Medical Imaging Reviews*, vol. 11, no. 1, pp. 3–14, 2015.
[43] A. Norouzi, M. S. M. Rahim, A. Altameem et al., "Medical image segmentation methods, algorithms, and applications," *IETE Technical Review*, vol. 31, no. 3, pp. 199–213, 2014.
[44] A. Ahirwar, "Study of techniques used for medical image segmentation and computation of statistical test for region classification of brain MRI," *International Journal of Information Technology and Computer Science*, vol. 5, no. 5, pp. 44–53, 2013.
[45] A. Rajaei, "Medical Image Texture Segmentation Usingrange Filter," in *Proceedings of the The First International Conference on Information Technology Convergence and Services*, Coimbatore, India, January, 2012.
[46] A. Padma, "Automatic classification and segmentation of brain tumor in CT images using optimal dominant gray level run length texture features," *International Journal of Advanced Computer Science and Applications*, vol. 2, no. 10, 2011.
[47] R. A. Jasmine and P. A. J. Rani, "A two phase segmentation algorithm for MRI brain tumor extraction," in *Proceedings of the 2016 International Conference on Control, Instrumentation, Communication and Computational Technologies (ICCICCT)*, December, 2016.
[48] M. Uhlich, R. Greiner, B. Hoehn et al., "Improved brain tumor segmentation via registration-based brain extraction," *Forecasting*, vol. 1, no. 1, pp. 59–69, 2018.
[49] S. Bauer, "Integrated spatio-temporal segmentation of longitudinal brain tumor imaging studies," in *International MICCAI Workshop on Medical Computer Vision*Springer, Berlin/Heidelberg, Germany, 2013.
[50] S. Bakas, H. Akbari, A. Sotiras et al., "Advancing the cancer genome atlas glioma MRI collections with expert segmentation labels and radiomic features," *Scientific Data*, vol. 4, no. 1, Article ID 170117, 2017.
[51] P. Dvořák, "Brain Tumor Detection and Segmentation in Multisequence MRI," Ph. D. Thesis, 2015.
[52] K. Hu, Q. Gan, Y. Zhang et al., "Brain tumor segmentation using multi-cascaded convolutional neural networks and conditional random field," *IEEE Access*, vol. 7, Article ID 92615, 2019.
[53] M. Malathi and P. Sinthia, "Brain tumour segmentation using convolutional neural network with tensor flow," *Asian Pacific Journal of Cancer Prevention*, vol. 20, no. 7, pp. 2095–2101, 2019.
[54] M. A. Tehrani and R. Sablatnig, *The Coarse-To-Fine Contour-Based Multimodal Image Registration*, FH-Steyr, Wehrgrabengasse 1-3, 4400 Steyr, Austria, 2005.
[55] L. Lefkovits and S. Lefkovits, "Two-phase MRI Brain Tumor Segmentation Using Random Forests and Level Set Methods," in *Proceedings of the International Conference in Central Europe on Computer Graphics, Visualization and Computer Vision'2017*, Kumaracoil, India, January, 2018.
[56] X. L. Jiang, Q. Wang, B. He, S. J. Chen, and B. L. Li, "Robust level set image segmentation algorithm using local correntropy-based fuzzy c-means clustering with spatial constraints," *Neurocomputing*, vol. 207, pp. 22–35, 2016.
[57] S. Saha, A. K. Alok, and A. Ekbal, "Brain image segmentation using semi-supervised clustering," *Expert Systems with Applications*, vol. 52, pp. 50–63, 2016.
[58] G. Wang, S. Li, T. Ourselin, and T. Vercauteren, "Automatic brain tumor segmentation based on cascaded convolutional neural networks with uncertainty estimation," *Frontiers in Computational Neuroscience*, vol. 13, p. 56, 2019.
[59] J. A. Shah and S. Suralkar, "Brain tumor detection from MRI images using fuzzy C-means segmentation," *Int J Adv Res Comput Commun Eng*, vol. 5, no. 6, 2016.
[60] R. Shanker and M. Bhattacharya, "Brain tumor segmentation of normal and lesion tissues using hybrid clustering and hierarchical centroid shape descriptor," *Computer Methods in Biomechanics and Biomedical Engineering: Imaging & Visualization*, vol. 7, 2019.
[61] S. M. Anwar, S. Yousaf, and M. Majid, "Brain tumor segmentation on Multimodal MRI scans using EMAP Algorithm," in *Proceedings of the 2018 40th Annual International Conference of the IEEE Engineering in Medicine and Biology Society (EMBC)*, July, 2018.
[62] A. A. Taha and A. Hanbury, "Metrics for evaluating 3D medical image segmentation: analysis, selection, and tool," *BMC Medical Imaging*, vol. 15, no. 1, p. 29, 2015.
[63] S. González-Villà, A. Oliver, S. Valverde, L. Wang, R. Zwiggelaar, and X. Lladó, "A review on brain structures segmentation in magnetic resonance imaging," *Artificial Intelligence in Medicine*, vol. 73, pp. 45–69, 2016.
[64] K. Jalali, M. Heydari, and A. Tanavar, "Image Segmentation with Improved Distance Measure in SOM and K Means Algorithms," *Journal of Mathematics and Computer Science*, vol. 8, 2014.
[65] G. Kaur and J. Rani, *MRI Brain Tumor Segmentation Methods-A Review*, 2016.
[66] S. Dhurkunde and S. Patil, "Segmentation of brain tumor in magnetic resonance images using various techniques," *Int. J. Innov. Res. Sci. Eng. Technol*, vol. 5, pp. 1039–1046, 2016.
[67] S. R. Telrandhe, A. Pimpalkar, and A. Kendhe, "Brain tumor detection using object labeling algorithm & SVM,"

International Engineering Journal For Research & Development, vol. 2, pp. 2–8, 2015.

[68] A. Vishnuvarthanan, M. P. Rajasekaran, V. Govindaraj, Y. Zhang, and A. Thiyagarajan, “Development of a combinational framework to concurrently perform tissue segmentation and tumor identification in T1 - W, T2 - W, FLAIR and MPR type magnetic resonance brain images,” *Expert Systems with Applications*, vol. 95, pp. 280–311, 2018.

[69] M. S. M. Rahim, A. Rehman, F. Kurniawan, and T. Saba, “Ear biometrics for human classification based on region features mining,” *Biomedical Research*, vol. 28, no. 10, pp. 4660–4664, 2017.

[70] S. S. Chouhan, A. Kaul, and U. P. Singh, “Image segmentation using computational intelligence techniques: review,” *Archives of Computational Methods in Engineering*, vol. 26, no. 3, pp. 533–596, 2019.

[71] S. H. Shirazi, S. Naz, M. I. Razzak, A. I. Umar, and A. Zaib, “Automated pathology image analysis,” in *Soft Computing Based Medical Image Analysis*, pp. 13–29, Elsevier, Amsterdam, Netherlands, 2018.

[72] L. Dora, S. Agrawal, R. Panda, and A. Abraham, “State-of-the-art methods for brain tissue segmentation: a review,” *IEEE reviews in biomedical engineering*, vol. 10, pp. 235–249, 2017.

[73] A. Işın, C. Direkoğlu, and M. Şah, “Review of MRI-based brain tumor image segmentation using deep learning methods,” *Procedia Computer Science*, vol. 102, pp. 317–324, 2016.

[74] K. Sudharani, T. Sarma, and K. S. Prasad, “Advanced morphological technique for automatic brain tumor detection and evaluation of statistical parameters,” *Procedia Technology*, vol. 24, pp. 1374–1387, 2016.

[75] A. M. Nichat and S. Ladhake, “Brain tumor segmentation and classification using modified FCM and SVM classifier,” *International Journal of Advanced Research in Computer and Communication Engineering*, vol. 5, no. 4, pp. 73–76, 2016.

[76] M. Havaei, A. Davy, D. Warde-Farley et al., “Brain tumor segmentation with deep neural networks,” *Medical Image Analysis*, vol. 35, pp. 18–31, 2017.

[77] E. Ahn, “Unsupervised feature learning with K-means and an ensemble of deep convolutional neural networks for medical image classification,” 2019, https://arxiv.org/abs/1906.03359.

[78] K. Ejaz, M. Shafry, A. Rehman et al., “Segmentation method for pathological brain tumor and accurate detection using MRI,” *International Journal of Advanced Computer Science and Applications*, vol. 9, no. 8, pp. 394–401, 2018.

[79] K. Ejaz, M. S. M. Rahim, U. I. Bajwa, H. Chaudhry, A. Rehman, and F. Ejaz, “Hybrid segmentation method with confidence region detection for tumor identification,” *IEEE Access*, vol. 9, Article ID 35256, 2021.

[80] K. Ejaz, “An unsupervised learning with feature approach for brain tumor segmentation using magnetic resonance imaging,” in *Proceedings of the 2019 9th International Conference on Bioscience, Biochemistry and Bioinformatics*, New York, NY, USA, January, 2019.

[81] K. Ejaz, “An Image-Based Multimedia Database and Efficient Detection Though Features,” *VFAST Transactions on Software Engineering*, vol. 7, no. 1, 2019.

[82] U. Asghar, M. Arif, K. Ejaz, D. Vicoveanu, D. Izdrui, and O. Geman, “An improved COVID-19 detection using GAN-based data augmentation and novel QuNet-based classification,” *BioMed Research International*, vol. 2022, Article ID 8925930, 9 pages, 2022.

[83] S. Natarajan, V. Govindaraj, R. Venkata Rao Narayana et al., “A novel triple-level combinational framework for brain anomaly segmentation to augment clinical diagnosis,” *Computer Methods in Biomechanics and Biomedical Engineering: Imaging & Visualization*, vol. 10, no. 1, pp. 96–111, 2022.

[84] S. Natarajan, V. Govindaraj, Y. Zhang et al., “Minimally parametrized segmentation framework with dual metaheuristic optimisation algorithms and FCM for detection of anomalies in MR brain images,” *Biomedical Signal Processing and Control*, vol. 78, Article ID 103866, 2022.

[85] M. Arif, F. M. Philip, F. Ajesh, D. Izdrui, M. D. Craciun, and O. Geman, “Automated detection of nonmelanoma skin cancer based on deep convolutional neural network,” *Journal of Healthcare Engineering*, vol. 2022, Article ID 6952304, 15 pages, 2022.

[86] K. Mohammadi, S. Shamshirband, C. W. Tong, M. Arif, D. Petković, and S. Ch, “A new hybrid support vector machine-wavelet transform approach for estimation of horizontal global solar radiation,” *Energy Conversion and Management*, vol. 92, pp. 162–171, 2015.

[87] A. S. Al-Waisy, M. A. Al-Fahdawi, K. H. Mohammed et al., “COVID-CheXNet: hybrid deep learning framework for identifying COVID-19 virus in chest X-rays images,” *Soft Computing*, pp. 1–16, 2020.

[88] S. Iqbal, C. Zhang, M. Arif, M. Hassan, and S. Ahmad, “A new fuzzy time series forecasting method based on clustering and weighted average approach,” *Journal of Intelligent and Fuzzy Systems*, vol. 38, no. 5, pp. 6089–6098, 2020.

[89] A. Muhammad and W. Guojun, “Segmentation of calcification and brain hemorrhage with midline detection,” in *Proceedings of the 2017 IEEE International Symposium on Parallel and Distributed Processing with Applications and 2017 IEEE International Conference on Ubiquitous Computing and Communications (ISPA/IUCC)*, Guangzhou, China, December, 2017.

[90] M. Arif, F. Ajesh, S. Shamsudheen, O. Geman, D. Izdrui, and D. Vicoveanu, “Brain tumor detection and classification by MRI using biologically inspired orthogonal wavelet transform and deep learning techniques,” *Journal of Healthcare Engineering*, vol. 2022, Article ID 2693621, 18 pages, 2022.

[91] V. E. Balas, *Biomedical Engineering Tools For Management For Patients With COVID-19*, Academic Press, Cambridge, MA, USA, 2021.

[92] C. S. Kidwell, “Comparison of MRI and CT for detection of acute intracerebral hemorrhage,” *JAMA*, vol. 292, no. 15, p. 1823, 2004.

[93] J. R. Schrieffer, M. Davidson, J. Brooks, William, and Moulton, *MRI: A Guided Tour*, 2012.

[94] E. S. A. El-Dahshan, H. M. Mohsen, K. Revett, and A. B. M. Salem, “Computer-aided diagnosis of human brain tumor through MRI: a survey and a new algorithm,” *Expert Systems with Applications*, vol. 41, no. 11, pp. 5526–5545, 2014.

[95] G. Singh, A. Pokhriyal, and S. Lehri, “Neuro-fuzzy model based classification of handwritten Hindi modifiers,” *International Journal of Application or Innovation in Engineering & Management (IJAIEM)*, vol. 3, no. 6, pp. 311–325, 2014.

[96] A. Bansal and S. Kaur, “Segmentation of brain tumour in magnetic resonance images in time domain-study of previous work,” *The International Journal of Science and Technoledge*, vol. 3, no. 8, p. 241, 2015.

[97] E. Abdel-Maksoud, M. Elmogy, and R. Al-Awadi, "Brain tumor segmentation based on a hybrid clustering technique," *Egyptian Informatics Journal*, vol. 16, no. 1, pp. 71–81, 2015.

[98] H. Mohsen, E. S. A. El-Dahshan, E. S. M. El-Horbaty, and A. B. M. Salem, "Classification using deep learning neural networks for brain tumors," *Future Computing and Informatics Journal*, vol. 3, no. 1, pp. 68–71, 2018.

[99] H. Wang and P. A. Yushkevich, "Multi-atlas segmentation without registration: a supervoxel-based approach," in *International Conference on Medical Image Computing and Computer-Assisted Intervention*Springer, Berlin, Germany, 2013.

[100] I. Cabria and I. Gondra, "Automated localization of brain tumors in MRI Using Potential-K-means clustering algorithm," in *Proceedings of the 2015 12th Conference on Computer and Robot Vision*, June, 2015.

[101] S. P. Woods, J. D. Rippeth, E. Rippeth et al., "Deficient strategic control of verbal encoding and retrieval in individuals with methamphetamine dependence," *Neuropsychology*, vol. 19, no. 1, pp. 35–43, 2005.

[102] D. Coltuc, P. Bolon, and J. M. Chassery, "Exact histogram specification," *IEEE Transactions on Image Processing*, vol. 15, no. 5, pp. 1143–1152, 2006.

[103] Y. Zhang, Z. Dong, L. Wu, and S. Wang, "A hybrid method for MRI brain image classification," *Expert Systems with Applications*, vol. 38, no. 8, Article ID 10049, 2011.

[104] Y. D. Zhang, S. Chen, S. H. Wang, J. F. Yang, and P. Phillips, "Magnetic resonance brain image classification based on weighted-type fractional Fourier transform and nonparallel support vector machine," *International Journal of Imaging Systems and Technology*, vol. 25, no. 4, pp. 317–327, 2015.

[105] G. Yang, Y. Zhang, J. Yang et al., "Automated classification of brain images using wavelet-energy and biogeography-based optimization," *Multimedia Tools and Applications*, vol. 75, no. 23, pp. 15601–15617, 2016.

[106] Y. Zhang, G. Ji, J. Ji et al., "Preliminary research on abnormal brain detection by wavelet-energy and quantum- behaved PSO," *Technology and Health Care*, vol. 24, no. s2, pp. S641–S649, 2016.

[107] Y. D. Zhang, S. Wang, and L. Wu, "A novel method for magnetic resonance brain image classification based on adaptive chaotic PSO," *Progress In Electromagnetics Research*, vol. 109, pp. 325–343, 2010.

[108] Y. Zhang, S. Wang, G. Ji, Z. Ji, and Z. Dong, "An MR brain images classifier system via particle swarm optimization and kernel support vector machine," *The Scientific World Journal*, vol. 2013, Article ID 130134, 9 pages, 2013.

[109] Y. D. Zhang, L. Wu, and S. Wang, "Magnetic resonance brain image classification by an improved artificial bee colony algorithm," *Progress In Electromagnetics Research*, vol. 116, pp. 65–79, 2011.

[110] M. F. Siddiqui, A. W. Reza, and J. Kanesan, "An automated and intelligent medical decision support system for brain MRI scans classification," *PLoS One*, vol. 10, no. 8, Article ID e0135875, 2015.

[111] P. Buenestado and L. Acho, "Image segmentation based on statistical confidence intervals," *Entropy*, vol. 20, no. 1, p. 46, 2018.

Hindawi
Contrast Media & Molecular Imaging
Volume 2022, Article ID 4795307, 9 pages
https://doi.org/10.1155/2022/4795307

Research Article

Classification Algorithms for Brain Magnetic Resonance Imaging Images of Patients with End-Stage Renal Disease and Depression

Yan Cheng,[1] Tengwei Liao,[2] and Nailong Jia[3]

[1]*Department of Nephrology, The Third People's Hospital of Zhengzhou, Zhengzhou 453000, Henan, China*
[2]*The First Clinical Medical College, Guangzhou University of Chinese Medicine, Guangzhou 510405, China*
[3]*Department of Radiology, The Second Affiliated Hospital of Hainan Medical College, Haikou 570311, Hainan, China*

Correspondence should be addressed to Nailong Jia; dbhui013@hainmc.edu.cn

Received 11 April 2022; Accepted 13 June 2022; Published 6 July 2022

Academic Editor: M Pallikonda Rajasekaran

This study was aimed to explore the relationship between depression and brain function in patients with end-stage renal disease (ESRD) complicated with depression based on brain magnetic resonance imaging (MRI) image classification algorithms. 30 people in the healthy control group and 70 people in the observation group were selected as the research objects. First, the preprocessing algorithms were applied on MRI images. With the depression classification algorithm based on deep learning, the features were extracted from the capsule network to construct a classification network, and the network structure was compared to obtain the difference in the distribution of brain lesions. Different classifiers and degree centrality, functional connection, low-frequency amplitude ratio, and low-frequency amplitude were selected to analyze the effectiveness of features. In the deep learning method, the neural network model was constructed, and feature extraction and classification network were carried out. The classification layer was based on the capsule network. The results showed that the correct rate of the deep learning feature extraction network structure combined with the capsule network classification was 82.47%, the recall rate was 83.69%, and the accuracy was 88.79%, showing that the capsule network can improve the heterogeneity of depression. The combination of fractional amplitude of low-frequency fluctuation (fALFF), DC, and amplitude of low-frequency fluctuation (ALFF) can achieve the accuracy of 100%. In summary, MRI images showed that patients with depression may have neurological abnormalities in the white matter area. In this study, the classification algorithm based on brain MRI images can effectively improve the classification performance.

1. Introduction

With the continuous development of the economy and the continuous advancement of social development, China has also accelerated its entry into an aging society, and the number of people with poor sleep quality, anxiety, and depression is also increasing [1]. With the advancement of dialysis technology and the implementation of medical insurance, more and more end-stage renal disease (SRD) patients are receiving hemodialysis treatment, and their survival time is relatively longer [2]. According to relevant statistics, about 1.8%–23% of women and 1.1%–15% of men in the general population have depression, and the proportion of depression in ESRD is 20%–30% [3]. Depression seriously affects the physical and mental health of patients, and severely ill people will have thoughts of committing suicide. Physical complications and abnormal signs of ESRD patients, such as blood system, bone disease, and cardiovascular disease, have attracted special attention. An ESRD patient will have abnormal mental or neurological syndromes such as anxiety, depression, neurasthenia, and fear [4]. It is often easier to be ignored. Depression can cause the patient's mood or mood to be low, lack of interest, and suicidal tendencies, somatic symptoms such as sleep disturbance, appetite disturbance, sexual dysfunction, and non-specific somatic diseases such as pain and general discomfort. Depression generally affects the life of patients through the patient's concern for their own health, deterioration of nutritional status, abnormal immune function, medication and dialysis compliance, and low response to stress state [5, 6].

The etiology of depression in ESRD patients is caused by physical factors, social and psychological factors and other factors. Uremia toxins and complications can induce or aggravate the depression symptoms of ESRD patients. Marital relationship, economic pressure, and social support can also aggravate the depressive symptoms of ESRD patients [7, 8]. Diffusion tensor imaging (DTI) is a new type of diagnostic method developed on the basis of diffusion-weighted imaging, which can accurately describe the expansion direction and amplitude of water molecules. DTI can also show the path of white matter fiber tracts in vivo. The data obtained by DTI can be used to reconstruct the three-dimensional microscopic directional map of the white matter fiber tracts of the brain. This method of imaging is called diffusion tensor tractography (DTT) [9]. DTT imaging is a new technology developed on the basis of diffusion-weighted imaging. Six directions are added to the diffusion sensitivity gradient, and the diffusion state of water molecules is described based on the three-dimensional space. With the rapid development of imaging technology, DTT plays an important role in the diagnosis and treatment of brain diseases [10]. This imaging method is based on the similarity of the shape and direction of the diffuse ellipsoid between adjacent voxels. It is very useful for the analysis of the integrity and directionality of the central nerve fiber network [11].

At this stage, segmentation algorithms in the field of computer vision have many applications in the segmentation of image features, but they have not formed a sign of evaluating the quality of the algorithm. Machine learning based on computer intelligence is easier to recognize and analyze data [12, 13]. Intelligent segmentation of MRI image boundaries and features uses functional parameters to extract feature contours, and the image data obtained through image segmentation is more scientific, providing effective reference value for disease prediction [14, 15]. Compared with other medical images, MRI can provide doctors with more brain information based on the collected data and design different scan parameters to make a good diagnosis of the disease. The preprocessing of MRI images can largely eliminate morphological differences between individuals, as well as machine noise mixed in during the acquisition process and physiological noise caused by non-cerebral neural activities. The extraction of MRI image features can effectively describe the gray matter of the brain or brain neural activity from different angles, which is also a way to analyze and diagnose the brain structure of patients with depression [16, 17]. Brain MRI images of depression patients can clearly distinguish the difference between the two through MRI images, and pathological research on MRI with the help of machine learning methods can become an important content in computer-aided diagnosis [18].

In this study, the MRI images of patients with ESRD complicated with depression were firstly processed with algorithms, and then features were extracted. The classifier design and fusion algorithm from multiple perspectives were adopted to analyze the impacts of different characteristics on the brain function of patients, aiming to provide a reference for the treatment of patients with depression in the clinic.

2. Methods

2.1. Research Objects. In this study, ESRD patients who were hospitalized from June 2018 to December 2020 were selected and defined as the observation group. They all meet the diagnostic criteria of major depression in the American Diagnostic and Statistical Manual of Mental Disorders (4^{th} Edition). The specific items included (i) 18–68 years old, Han nationality, and right-handed; (ii) the total score was ≥18 evaluated using the 17^{th} edition of the Hamilton Depression Scale; (iii) before enrollment, the patients had not used antidepressant or antipsychotic drugs, and none of the patients had alcohol dependence, hypertension, diabetes, schizophrenia, and epilepsy, etc., There were 70 cases that met the inclusion criteria, including 26 males and 44 females; and their age ranged from 32 to 63 years old, with an average of 51.56 ± 2.74 years old. The patient's course of illness was 2–12 months, and the dialysis time was 7–10 months. There were 14 cases of polycystic kidney disease, 13 cases of chronic interstitial nephritis, 16 cases of obstructive nephropathy, 15 cases of hypertensive nephropathy, and 32 cases of chronic glomerulonephritis. The general condition of the patient was recorded in detail.

The inclusion criteria were defined as follows: patients who met the ESRD diagnostic criteria and aged ≥18 years old; patients with complaints of mental abnormalities, unconscious disorders, and sleep disorders; patients with good understanding and communication skills; and patients who were volunteer to join this study.

The exclusion criteria were given as follows: patients who had a history of severe mental disorders and those who did not cooperate; patients whose image analysis results were affected by factors such as serious image motion artifacts; patients who were unable to take care of themselves, were slurred in speech, were seriously ill, etc.,; patients who cannot cooperate with the investigation or who did not agree to participate in the investigation; and patients whose kidney DTI images showed renal abnormalities, changes around the kidney, and diseases of the collective system.

Healthy control group: employees and healthy volunteers were recruited. The inclusion criteria were given as follows: (i) no drugs had been used before enrollment; (ii) individuals and families had no current or ever suffered mental disorders;(iii) no obvious traumatic brain injury;(iv) no MRI contraindications; (v) no obvious medical disease; and (vi) the patient voluntarily participated in the study to understand the content of the study. 30 healthy people were studied, including 12 males and 18 females, aged 22–57 years old, with an average of 53.09 ± 2.38 years old.

This study had been approved by the ethics committee of the hospital. All patients and their families had signed the informed consent forms.

2.2. Assessment Using Scale. The Chinese version of the Hamilton Rating Scale for Anxiety (HAMA) (14^{th} version) was selected to evaluate the anxiety of the two groups of subjects. Both Chinese version scales were widely used in clinical and scientific research, and their validity and reliability were very good.

2.3. MRI Scan Image Parameters. In this study, all patients and healthy controls received 3.0T superconducting MRI whole body scanner, using 8-channel head coils for MRI scanning. Before the scan, we described the examination process in detail to the patients, made the patients supine, and advised them to use earplugs to reduce the impact of equipment noise and maintain steady breathing. The scanning sequence included T1 fast-recovery fast spin-echo (FSE) (FRFSE) sequence and DTI sequence. The same level and positioning were adopted, the positioning line was parallel to the anterior commissure-posterior commissure (AC-PC) plane, and the whole brain was scanned from the base of the skull to the top of the skull. The scan time was about 20 minutes. The scanning parameters were described as follows. For cranial horizontal axis FSE sequence T1WI: time of echo (TE) was 15–25 ms, and time of repetition (TR) was 500 ms. For FSE T2WI: the TE and TR were 90–120 ms and 2500 ms, respectively; layer thickness was 8 mm, and layer spacing was 2 mm. DWI scanning used a single excitation plane echo sequence, using 2 dispersion b values (0–1000 s/mm^2): the field of view (FOV) was 24 cm × 24 cm, matrix was 256 × 128, layer thickness was 8 mm, layer spacing was 2 mm, three perpendiculars to each other dispersion sensitive gradient direction, and the TR/TE was 6000/110 ms. The DTI sequence scan also used a single excitation plane echo sequence, the horizontal axis scan, the dispersion sensitive gradient direction was 13, t and the TR/TE was 10000/110 ms. The FOV was 24 cm × 24 cm, matrix was 256 × 128, layer thickness was 5 mm, layer spacing was 0 mm, NEX = 1, and the scanning time was 160 seconds. The obtained MRI images were sent to the workstation, and the images were processed using Function II software.

2.4. Image Analysis. The data obtained from MRI scans were used in the software and 3.0T MRI scanner. Two experienced doctors with 5 years of working experience in the diagnostic imaging department were invited to select random double-blind principles to analyze the DTI images of patients. The diagnosing physicians read the film without knowing the general clinical data of the patients. First of all, the quality of the image was evaluated, and artifacts and noises in the image were removed to avoid affecting the doctor's diagnosis of DTI. The morphology and DTI images that met the diagnostic requirements were included in the final DTI image analysis, the ADC and FA of the kidneys were finally measured, and the abnormalities of the kidneys were observed.

2.5. Image Standardization. Image standardization was done to eliminate the differences in the morphology of individual brains and interference and analyze the fixed points of MRI images. The standardization process of MRI images is shown in Figure 1 below.

2.6. Feature Extraction of Image. In the feature extraction of MRI images, the intensity of each voxel in the brain changed with time series. The changing information can be used to describe the brain nerve activity from different angles. The commonly used variable characteristics mainly included degree centrality, regional homogeneity, low-frequency amplitude, functional connection, and low-frequency amplitude ratio. These features can prove whether the brain nerve activity was normal, and these features were also different in the extraction stage of different preprocessing processes. The extraction stage of different features in the MRI image preprocessing process is shown in Figure 2.

Functional connectivity refers to changes in the brain with mental illness, which can reflect the increase or decrease of the connection between the brain function network areas. Different areas of the brain have different perceptions of functions such as hearing, cognitive control, emotional understanding, and vision. Researchers generally look at the brain as a complex network. Each area is a node of the brain network, and the connection node is the functional connection of the brain. Many researchers have produced maps of different brain regions, which are divided into 246 or 116 brain regions. After MRI images are standardized, automatic anatomical markings are made in the Montreal Neurological Institute (MNI) space, which are used more in research. Based on this, the brain regions were divided with automatic anatomical markers in this study. First, the average value of the signal hydroxyl groups was calculated at different moments in the brain regions, as shown in Figure 1.

$$Xi = \sum Xg. \tag{1}$$

Xi represents the ith brain area and Xg represents the signal intensity of voxel g in the brain area, then, the Pearson correlation coefficient f^{ij} between the two brain areas is expressed as follows:

$$f^{ij} = \frac{\operatorname{cov}(Xi, Xj)}{\varphi(Xi)\varphi(Xj)} = \frac{\sum[(Xi[t] - \overline{X}i)(Xj[t] - \overline{X}j)]}{\sqrt{\sum[Xi[t] - \overline{X}i)^2 (Xj[t] - \overline{X}j)^2}}. \tag{2}$$

In equation (2), *Xi[t]* and *Xj[t]* represents the regional average signal intensity of brain area i and brain area j at time t, respectively; $\overline{X}i$ and $\overline{X}j$ refers to the time average signal intensity of brain area i and brain area j in the entire time series, respectively. The function connection matrix is as follows:

$$R_c = \begin{bmatrix} f_{11} f_{12} f_{13} \cdots f_{1N} \\ f_{21} f_{22} f_{23} \cdots f_{2N} \\ \cdots \\ f_{N1} f_{N2} f_{N3} \cdots f_{NN} \end{bmatrix}. \tag{3}$$

In the equation above, N represents the size of the matrix, and N also represents the number of brain regions in the map. If $N = 116$, the brain is divided into 116 brain regions and below equation is obtained:

$$f_{ij} = f_{ji}. \tag{4}$$

Then, it is necessary to extract the functional connection of the triangular area in the matrix. The extraction of functional connection features still depends on the structure of the brain network Atlas.

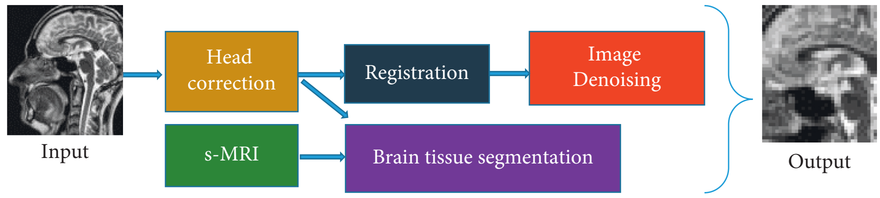

FIGURE 1: Schematic diagram of the standardization process of resting MRI images.

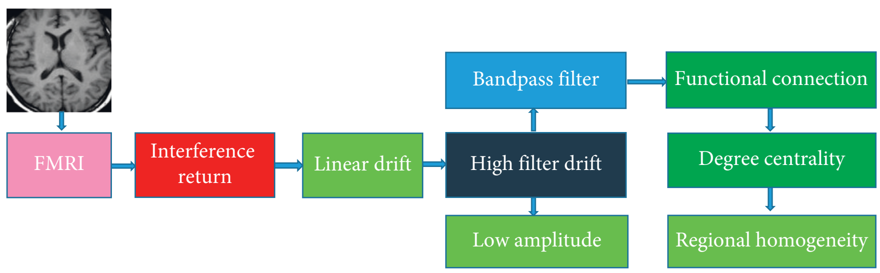

FIGURE 2: Feature extraction in preprocessing.

2.7. Degree Centrality and Regional Homogeneity. Degree centrality represents the association between a given voxel and the whole brain voxel. If certain nodes in the brain are abnormal, some areas cannot be matched with healthy people's nodes consistently, which will lead to mental illness. In the contrast center feature extraction, the connectivity of the brain is measured by the number of strong correlation connections of brain voxels, and the correlation between different voxels is expressed as an equation.

$$f_{ij} = \frac{\sum\left[\left(X_i[t] - \overline{X}_i\right)\left(X_j[t] - \overline{X}_j\right)\right]}{\sqrt{\sum\left[X_i[t] - \overline{X}_i\right)^2\left(X_j[t] - \overline{X}_j\right)^2}}. \quad (5)$$

$X_i[t]$ and $X_j[t]$ represents the regional average signal intensity of brain area i and brain area j at time t, respectively; and the average time voxel signal intensity of the ith and jth voxel positions are denoted as $\overline{X}i$ and $\overline{X}j$, respectively.

If there were n voxels in the MRI image, an undirected unweighted adjacency matrix of $n * n$ size can be constructed according to the coefficients, and the centrality measure of voxel i is shown in the following equation:

$$d_{ij} = \begin{cases} 1 f_{ji} > 0.25, i \neq j, \\ 0\text{other}, \end{cases} \quad (6)$$

$$Db_{ij} = \sum d_{ij}, j = 1, 2, \ldots N, i \neq j. \quad (7)$$

The correlation coefficient between voxels ij in equation (6) represents the number of other voxels connected with each voxel, and the feature is extracted.

Regional homogeneity is the abnormality of neural activity on the basis of brain lesions, which reflects the degree of synchronization of the voxel field signals of the FMRI data in the time series. Feature extraction itself has a smoothing effect and did not require Gaussian filtering. Feature acquisition was achieved by calculating voxels and neighboring voxels. The equation is as follows:

$$Q_i = \frac{\sum_i X_i[t]^2 - N\sum_i X_i[t]^2}{(1/12)v\left(N^3 - N\right)}. \quad (8)$$

$X_i[t]$ represented the voxel intensity at the ith voxel position at time t, V represents the number of selected domain intensity voxels, and N reached the total number of voxels.

Amplitude of low-frequency fluctuation (ALFF) can be used to detect the difference in neuronal activity between depressed patients and healthy people. When the low-frequency amplitude was calculated, the image was band-pass filtered. The energy range of the filtered signal was (0.001–0.08), and the frequency spectrum calculation equation is as follows:

$$X_i[h] = \sum_{i=1}^{n} X_i[k]e^{j(2\pi/N)hk}. \quad (9)$$

X_i represents the frequency spectrum calculated by the Fourier transform of the time series of voxel i.

The low-frequency amplitude of the voxel is calculated as follows:

$$ALEE_i = \sum_K \sqrt{X_i[k]^2}, K \in \left[0.01\frac{2\pi}{f_s^2}, 0.08\frac{2\pi}{f_s^2}\right]. \quad (10)$$

In equation (10), fs represents the sampling frequency.

The feature extraction of fALFF was based on the problem that the low-frequency amplitude of the physiological noise signal in the periphery of the large blood vessel, and the brain cistern was higher than the low-frequency amplitude of the brain nerve signal. The ratio of the total amplitude of the low frequency to the total amplitude of the entire frequency range is as follows.

$$FALEE_i = \frac{\sum_K \sqrt{X_i[k]^2}}{(1/N)\sum_{h=0}^{N-1}\sqrt{X_i[k]^2}}, K \in \left[0.01\frac{2\pi}{f_s^2}, 0.08\frac{2\pi}{f_s^2}\right]. \quad (11)$$

The low-frequency amplitude can suppress the physiological noise brought by the large blood vessels. When the low-frequency amplitude was close to the high-frequency amplitude, the equation (11) can inhibit it.

2.8. Classification Algorithm Based on Deep Learning. Many clinical MRI images in the study of patients with depression have large feature dimensions, and the disease response of mental disorders exists in all corners of the brain. In some areas, there are a large number of initial features that do not interfere with each other. To extract features in a very large space, a good classifier is needed to select the optimal feature subset. In the designed classifier, the classification model is used to classify new samples. In the deep learning algorithm, the Capsule Network (CapsNet) is an emerging neural network architecture. Compared with the convolutional neural network (CNN), the CapsNet has stronger generalization ability and does not require a lot of training. Some precise details can be better preserved, such as the position, inclination, thickness, and size of the object's rotation. It can also enhance the feature extraction ability of network details without an additional process of losing and then recovering. The capsule network can be simple a unified architecture completes different visual tasks. As shown in Figure 3, after a standard convolutional layer ReLU Conv1 with a step size of 1 was inputted, it would generate 256 channels for feature images. Then, a modified capsule convolutional layer was inputted to generate an 8-dimensional vector instead of a table volume. The length of each vector ||L2|| represents the possibility that the input image belongs to 10 categories.

The optimization of network parameters is different from general neural networks. The CapsNet uses dynamic routing to back-propagate and iteratively update the parameters of each layer. The calculation equation of the loss function is as follows:

$$L_p = T_p \max\left(0, m^+ - \left\|V_p\right\|\right)^2 + \lambda\left(1 - T_p\right)\max\left(0, \left\|V_p\right\| - m^-\right)^2. \quad (12)$$

In the above equation (12), P represents the classification category index, m^+ and m^- takes values 0.9 and 0.1, respectively. When the sample type is P, when T_P is set to 1, the loss function is expressed as follows:

$$L_p = \max\left(0, m^+ - \left\|V_p\right\|\right)^2. \quad (13)$$

The value of T_P is close to 0.9, and the loss function is close to 0, which is also the model result that the network hopes to train.

If the sample category is not P, the loss function is given as follows:

$$L_p = \lambda \max\left(0, \left\|V_p\right\| - m^-\right)^2. \quad (14)$$

The appearance of the λ value reduced the loss value that did not appear in the P category, and thus, avoiding the initial loss from being too large, resulting in the shrinking of the length of all output vectors. The overall loss can be expressed as below equation (15):

$$L^{(i)} = \sum_P L_p{}^{(i)}. \quad (15)$$

2.9. Statistical Methods. SPSS21.0 statistical software was adopted to perform statistical analysis on DTI parameters. Measurement data conforming to the normal distribution were represented by mean ± standard deviation ($\bar{x} \pm s$), and non-conforming count data were represented in the form of frequency or percentage (%). $\alpha = 0.05$ was undertaken as the test level for comparison between groups. When $P < 0.05$, the difference was considered to be statistically significant.

3. Results

3.1. General Data of Patients. The comparison of the demographic data of the two groups of study subjects showed that there was no statistical difference between the healthy control group and the depression group in terms of gender, education level, age, and marital status ($P < 0.05$) (Table 1).

The general information of the observation group is shown in Table 2. The main occupations were workers, farmers, civil servants or institutions, self-employed, and teachers. The main sources of expenses were municipal medical insurance, provincial medical insurance at their own expense, and rural cooperative medical care.

3.2. Network Classification Results. The neural network model was constructed in the deep learning method, and the feature extraction and classification network were performed. The classification layer was based on the capsule network. The experimental results of the CNN feature extraction network structure and the CapsNet classification are shown in Figure 4. The correct rate of the constructed network was 82.47%, the recall rate was 83.69%, and the accuracy was 88.79%. It showed that the CapsNet can improve the heterogeneity of depression, which was suitable for the classification of MRI images.

3.3. Multi-Feature Ensemble Classification Results. The idea of ensemble learning is to integrate multiple feature classification models to classify depression. In order to maximize the classification performance, fALFF, DC, and ALFF were aggregated, and the prediction results of the combined model were weighted and averaged to obtain the final classification result. It can be observed from the results shown in Figure 5 that the combination of the three can achieve the accuracy of 100%. Compared with the other two forms, the combination of the three had significant difference ($P < 0.05$).

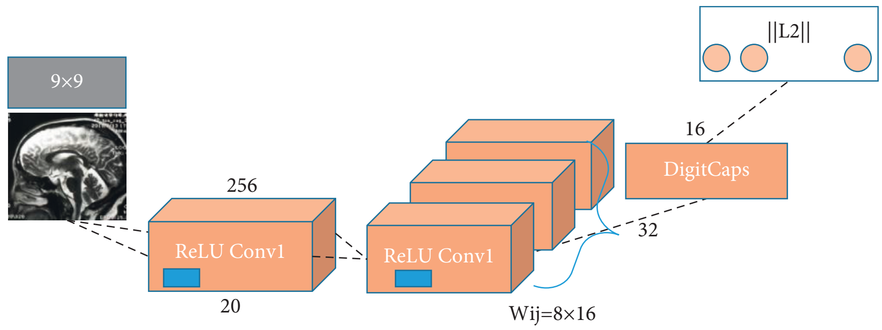

FIGURE 3: Classification algorithm of CapsNet.

TABLE 1: Comparison on general data of patients in two groups.

Item	Depression group	Healthy control group	P value
Number of cases	70	30	—
Age (years old)	51.56 ± 2.74	53.09 ± 2.38	—
Gender	—	—	0.574
Number of males	26	12	—
Number of females	44	18	—
Marital status	—	—	0.879
Unmarried	14	7	—
Married	56	23	—
Education level (years)	12.24 ± 3.65	15.24 ± 2.61	0.243
HAMD (scores)	26.37 ± 4.36	3.37 ± 1.13	—
HAMA (scores)	21.43 ± 5.21	2.41 ± 1.42	—

TABLE 2: General data of patients.

Category	Number	Profession	Number	Average age	Source of expenses	Number
Polycystic kidney	14	Worker	26	50.06 ± 3.13	Own expense	8
Chronic interstitial nephritis	13	Farmer	12	42.60 ± 4.04	District medical insurance	8
Obstructive nephropathy	11	Civil servants	8	31.56 ± 5.78	City medical insurance	11
Hypertensive nephropathy	10	Self-employed	15	46.56 ± 2.28	Social medical insurance	14
Chronic glomerulonephritis	22	Teacher	9	31.06 ± 3.62	Rural cooperative medical	29
Total	70	—	70	51.56 ± 2.74	—	—

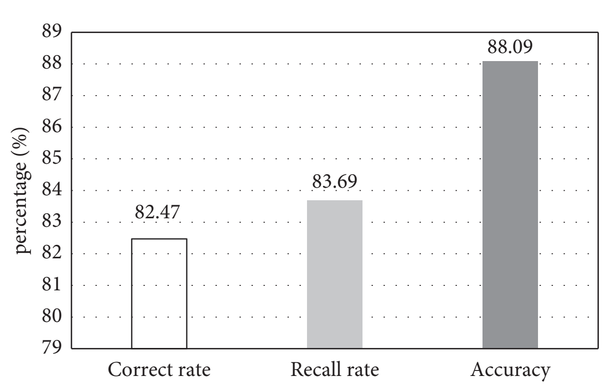

FIGURE 4: Network classification results.

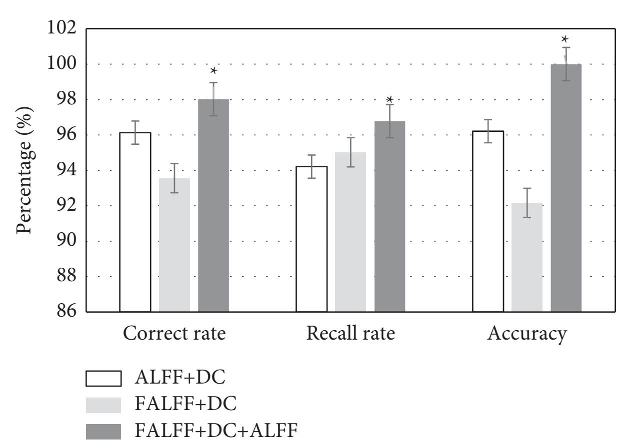

FIGURE 5: Integrated classification results. *compared with the other two groups, $^{*}P < 0.05$.

3.4. MRI Images. The healthy patients were selected to observe MRI images. Figure 6 shows the images on MRI showing no obvious structural abnormalities. Figure 6(a) is a cross-sectional MRI image of the main structures of the brain, which can show structures such as the

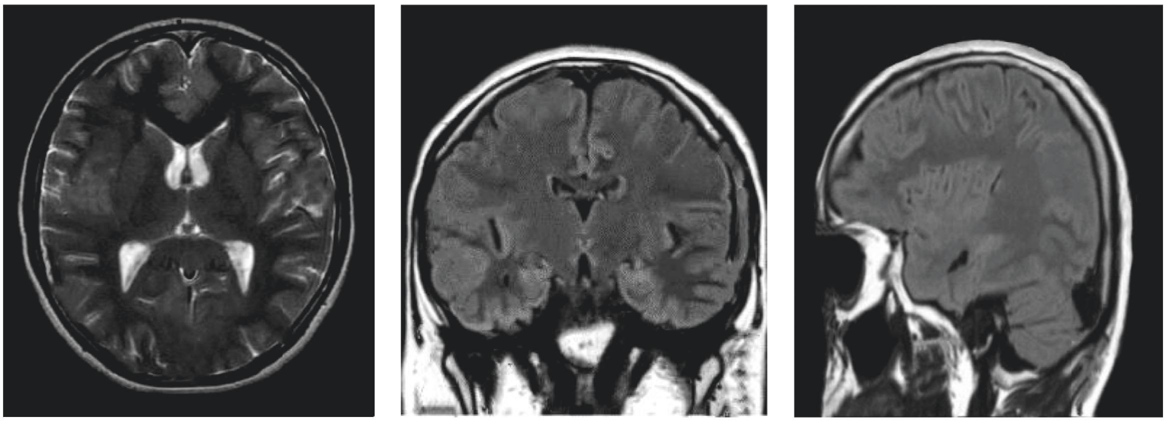

(a) (b) (c)

FIGURE 6: MRI images of healthy people.

interhemispheric fissure of the frontal lobe and the superior cerebral vein. Figure 6(b) shows a normal axial image of the brain lobes, with the frontal lobe occupying 2/3 of the upper layer of the cerebral hemisphere, and the occipital lobe near the posterior horn of the lateral ventricle. Figure 6(c) shows a craniocerebral anomaly, clearly showing the middle cerebral artery in the middle frontal gyrus of the craniocerebral gyrus and in the center of the semiovale.

Figure 7 shows an image of a male patient in the observation group. Figure 7(a) is a side view of the brain, and an MRI image shows a disorder of the central nervous system. Figures 7(b) and 7(c) show the "tiger stripe sign", T1WI shows a streak-like structure with low signal in the high-signal area, and the MRI signal shows abnormal lobular transverse shape. The lesions are mainly concentrated in the hypothalamus, and there are abnormalities in the hypothalamus pituitary gland in the sellar region. The arrow in the figure marks the location of the lesion. Butterfly pituitary stalk moved backward with uniform signal strength. The red arrows in Figure 7 indicat the location of the lesions.

3.5. Registration Image of MRI Image. The images in Figure 8 are from a 52-year-old male patient. After the image was processed by the algorithm, the definition was higher. The blue line in the figure shows the process of image registration by the instrument. After the objective function was optimized, the image registration was performed according to the selection of the parameters, and the example effect is shown in Figure 8. The image was registered from the structural master image. Figure 8(a) shows that the registration line is parallel to the line connecting the frontal lobes on both sides. Figure 8(b) shows the parallel anterior fossa floor. Figure 8(c) shows where the configuration line is located in the frontal lobe.

3.6. Comparison of White Matter FA. The anisotropy score (FA) was used to quantitatively measure the size of the third anisotropy of water molecules in the white matter fiber bundles. It was positively correlated with the integrity of the myelin sheath, the compactness and parallelism of the fibers, and can reflect the completeness of structure of the white matter. Compared with the healthy group, the main manifestations of the observation group were the right posterior cingulate gyrus, the right lingual gyrus, the right prefrontal lobe, the medial marginal lobe of the right upper gyrus, and the right talus gyrus. The specific results are listed in Table 3.

4. Discussion

ESRD is a disease that cannot be cured. Patients need to rely on dialysis to maintain their lives. During the entire treatment process, the patient's psychology will produce various emotional distress.

Relevant studies have shown that 50%–80% of ESRD patients have different types and degrees of sleep disorders. Sleep disorders and anxiety in patients with depression complement each other and promote each other. The two have good compliance. People with severe depression sometimes have suicidal tendencies, which increase the economic burden of society and families [19]. Health status affects the quality of life of patients, and what they want to do produces resistance in thought and life. Family support can improve patients' depression and anxiety caused by dialysis, and effectively improve patients' treatment compliance. Yoong et al. [20] found that 49.9% of ESRD patients experienced increased depression, and 45.4% of de-ESRD patients experienced increased anxiety during treatment. The high proportion of anxiety and depression emphasized the importance of detection and care for ESRD patients during dialysis care. Reckert et al. [21] reported that depressive symptoms are relatively common in ESRD patients and have a great correlation with morbidity and mortality. Depression and anxiety symptoms are related to the gender, employment status, and physical activity of ESRD patients. Anxiety symptoms are also closely related to body mass index, and physical activity can be used as a protective factor for patients with ESRD. In the study, workers accounted for the highest occupational proportion of ESRD patients (40%), and the least proportion was teachers, the proportion was 10%. The number of patients in each occupation is different,

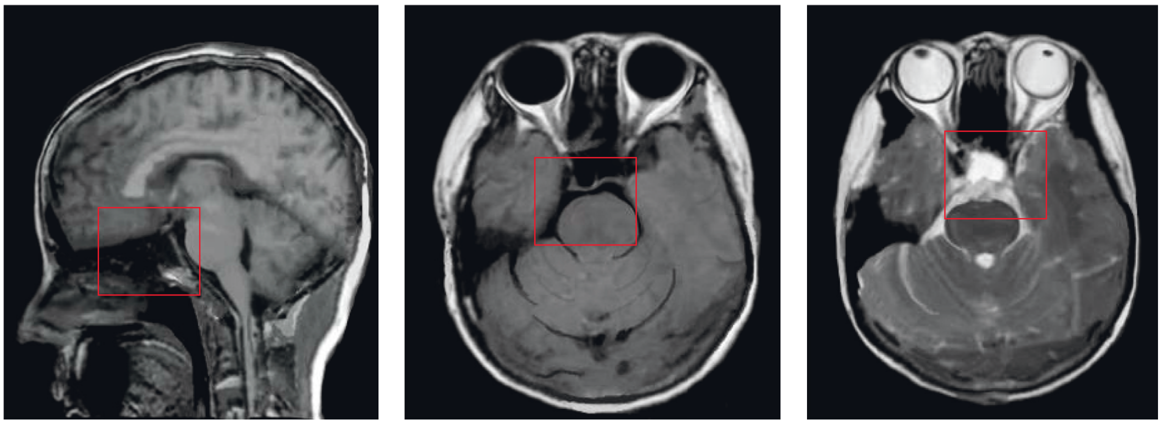

(a) (b) (c)

Figure 7: MRI images of a patient.

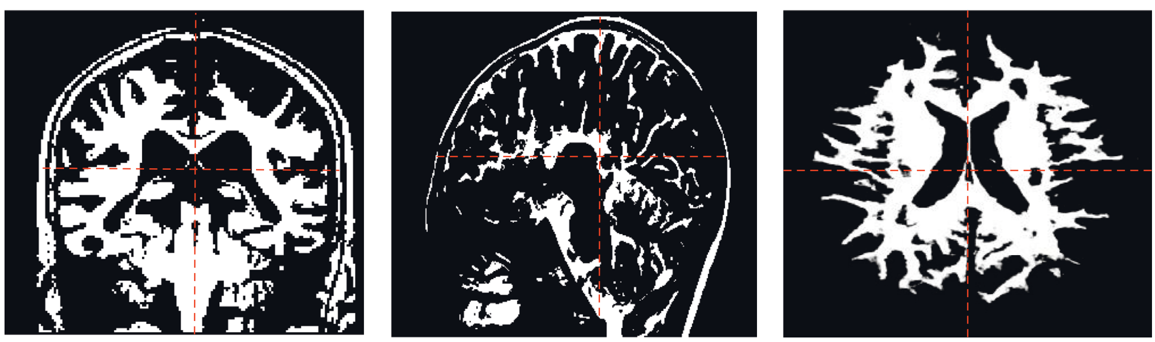

(a) (b) (c)

Figure 8: MRI image registration example.

Table 3: Comparison of white matter FA between the two groups.

Brain area with decreased FA value	Voxel (mm^2)	Z	T	P
Right posterior cingulate back	14	3.425	3.912	<0.01
Right lingual gyrus	23	4.501	3.822	<0.01
Right frontal lobe	31	3.921	3.401	<0.01
Medial marginal lobe of upper right side	48	3.465	3.612	<0.01
Right talar gyrus	121	3.987	3.608	<0.01

and the emotions generated are different, which may be related to the nature of the job itself.

As a non-invasive imaging method, DTI can reflect the directional diffusion of water molecules in the tissue by measuring partial anisotropy, and it can also evaluate the translation of water molecules in various directions by measuring ADC [22, 23]. MRI images of the brain of patients with depression showed that the patients' hippocampus, insula, and amygdala were abnormal, and the frontal cortex, cingulate gyrus, hippocampus, and striatum of unidirectional depression were reduced in volume [24]. In recent years, studies have confirmed that the introduction of intelligent algorithms, such as deep learning, into medical images has a great effect on image quality improvement, lesion recognition, and extraction and segmentation [25]. It was found in this study that the FA value decreased, and the spatial attention and memory of depression patients decreased.

5. Conclusion

In this study, based on the classification algorithm of deep learning, a network structure was constructed to extract and classify patient MRI images. In the deep learning method, a neural network model was constructed to perform feature extraction and classification network. The classification layer was based on capsule network with high accuracy. The algorithm of this study could effectively classify the features of the concave region. Research on classification algorithms based on brain MRI images requires more research, and the number is bound to increase. In the future, more good algorithms should be effectively verified to provide reference for computer-aided diagnosis in clinical practice.

Data Availability

The data used to support the findings of this study are available from the corresponding author upon request.

Conflicts of Interest

The authors declare no conflicts of interest.

References

[1] B. Mehdi, H. Kaveh, and V. F. Ali, "Implantable cardioverter-defibrillators in patients with ESRD: complications, management, and literature review," *Current Cardiology Reviews*, vol. 15, no. 3, pp. 161–166, 2019.

[2] E. J. Rajan and S. Subramanian, "The effect of depression and anxiety on the performance status of end-stage renal disease patients undergoing hemodialysis," *Saudi Journal of Kidney Diseases and Transplantation*, vol. 27, no. 2, pp. 331–334, 2016.

[3] Y. Hou, X. Li, L. Yang et al., "Factors associated with depression and anxiety in patients with end-stage renal disease receiving maintenance hemodialysis," *International Urology and Nephrology*, vol. 46, no. 8, pp. 1645–1649, 2014.

[4] R. W. Schouten, G. L. Haverkamp, W. L. Loosman et al., "Anxiety symptoms, mortality, and hospitalization in patients receiving maintenance dialysis: a cohort study," *American Journal of Kidney Diseases*, vol. 74, no. 2, pp. 158–166, 2019.

[5] W. Dziubek, J. Kowalska, M. Kusztal et al., "The level of anxiety and depression in dialysis patients undertaking regular physical exercise training - a preliminary study," *Kidney & Blood Pressure Research*, vol. 41, no. 1, pp. 86–98, 2016.

[6] V. Semaan, S. Noureddine, and L. Farhood, "Prevalence of depression and anxiety in end-stage renal disease: a survey of patients undergoing hemodialysis," *Applied Nursing Research*, vol. 43, pp. 80–85, 2018.

[7] D. C. S. D. Brito, E. L. Machado, I. A. Reis, L. P. D. F. D. Carmo, and M. L. Cherchiglia, "Depression and anxiety among patients undergoing dialysis and kidney transplantation: a cross-sectional study," *Sao Paulo Medical Journal*, vol. 137, no. 2, pp. 137–147, 2019.

[8] H. Moradi, E. Streja, and N. D. Vaziri, "ESRD-induced dyslipidemia-Should management of lipid disorders differ in dialysis patients?" *Seminars in Dialysis*, vol. 31, no. 4, pp. 398–405, 2018 Jul.

[9] E. Gyengesi, E. Calabrese, M. C. Sherrier, G. A. Johnson, G. Paxinos, and C. Watson, "Semi-automated 3D segmentation of major tracts in the rat brain: comparing DTI with standard histological methods," *Brain Structure and Function*, vol. 219, no. 2, pp. 539–550, 2014.

[10] K. M. Hasan, F. G. Moeller, and P. A. Narayana, "DTI-based segmentation and quantification of human brain lateral ventricular CSF volumetry and mean diffusivity: validation, age, gender effects and biophysical implications," *Magnetic Resonance Imaging*, vol. 32, no. 5, pp. 405–412, 2014.

[11] C. A. Elliott, H. Danyluk, K. E. Aronyk et al., "Intraoperative acquisition of DTI in cranial neurosurgery: readout-segmented DTI versus standard single-shot DTI," *Journal of Neurosurgery*, vol. 133, no. 4, pp. 1210–1219, 2020.

[12] S. Inokuchi, N. Fujita, H. Hasegawa et al., "[Frontal base penetrating brain injury by a gardening scissors:A case report]," *Noshinkeigeka*, vol. 46, no. 11, pp. 999–1005, 2018.

[13] A. Morice, F. Kolb, A. Picard, N. Kadlub, and S. Puget, "Reconstruction of a large calvarial traumatic defect using a custom-made porous hydroxyapatite implant covered by a free latissimus dorsi muscle flap in an 11-year-old patient," *Journal of Neurosurgery: Pediatrics*, vol. 19, no. 1, pp. 51–55, 2017.

[14] S. M. K. Hasan, M. Ahmad, and M. Ahmad, "Two-step verification of brain tumor segmentation using watershed-matching algorithm," *Brain Informatics*, vol. 5, no. 2, p. 8, 2018 Aug 14.

[15] V. Sivakumar and N. Janakiraman, "A novel method for segmenting brain tumor using modified watershed algorithm in MRI image with FPGA," *Biosystems*, vol. 198, 2020.

[16] W. Wieclawek, "3D marker-controlled watershed for kidney segmentation in clinical CT exams," *BioMedical Engineering Online*, vol. 17, no. 1, p. 26, 2018.

[17] T. A Fosu, W. Guo, D. Jeter, C. M. Mizutani, N. Stopczynski, and R. Sousa-Neves, "3D clumped cell segmentation using curvature based seeded watershed," *Journal of Imaging*, vol. 2, no. 4, p. 31, 2016.

[18] H. J. Otero, J. S. C. Toro, C. L. Maya, K. Darge, and S. D. Serai, "DTI of the kidney in children: comparison between normal kidneys and those with ureteropelvic junction (UPJ) obstruction," *Magnetic Resonance Materials in Physics, Biology and Medicine*, vol. 33, no. 1, pp. 63–71, 2020.

[19] C. Christodoulou, V. Efstathiou, P. Ferentinos, A. Poulios, A. Papadopoulou, and A. Douzenis, "Comparative study of hostility in depressive patients with and without a suicide attempt history," *Psychology Health & Medicine*, vol. 22, no. 7, pp. 866–871, 2017.

[20] R. K. Yoong, N. Mooppil, E. Y. Khoo et al., "Prevalence and determinants of anxiety and depression in end stage renal disease (ESRD). A comparison between ESRD patients with and without coexisting diabetes mellitus," *Journal of Psychosomatic Research*, vol. 94, pp. 68–72, 2017.

[21] A. Reckert, J. Hinrichs, H. Pavenstädt, B. Frye, and G. Heuft, "Prävalenz und Korrelate von Angst und Depression bei Hämodialysepatienten," *Zeitschrift für Psychosomatische Medizin und Psychotherapie*, vol. 59, no. 2, pp. 170–188, 2013.

[22] L. Tang, Y. Wen, Z. Zhou, K. M. von Deneen, D. Huang, and L. Ma, "Reduced field-of-view DTI segmentation of cervical spine tissue," *Magnetic Resonance Imaging*, vol. 31, no. 9, pp. 1507–1514, 2013.

[23] S. Rajan, J. Brettschneider, and J. F. Collingwood, "Regional segmentation strategy for DTI analysis of human corpus callosum indicates motor function deficit in mild cognitive impairment," *Journal of Neuroscience Methods*, vol. 345, 2020.

[24] A. J. Asman, C. B. Lauzon, and B. A. Landman, "Robust inter-modality multi-atlas segmentation for PACS-based DTI quality control," *SPIE Proceedings*, vol. 8674, p. 8674, 2013.

[25] L. Wang, C. Chang, Z. Liu, J. Huang, C. Liu, and C. Liu, "A medical image fusion method based on SIFT and deep convolutional neural network in the SIST domain," *J Healthc Eng*, vol. 21, p. 2021, Article ID 9958017, 2021.

Hindawi
Contrast Media & Molecular Imaging
Volume 2022, Article ID 5313238, 7 pages
https://doi.org/10.1155/2022/5313238

Research Article

Diffusion-Weighted Imaging Image Combined with Transcranial Doppler Ultrasound in the Diagnosis of Patients with Cerebral Infarction and Vertigo

Ying Lv,[1] **Yijie Zhang**,[2] **and Jun Wu**[3]

[1]*Department of Neurology and Psychiatry, Beijing Shijitan Hospital, Capital Medical University, Beijing 100038, China*
[2]*Department of Emergency, Beijing Shijitan Hospital, Capital Medical University, Beijing 100038, China*
[3]*Department of Community Medical Center, Beijing Shijitan Hospital, Capital Medical University, Beijing 100038, China*

Correspondence should be addressed to Ying Lv; lvying@bjsjth.cn

Received 12 April 2022; Revised 18 May 2022; Accepted 24 May 2022; Published 30 June 2022

Academic Editor: M Pallikonda Rajasekaran

This study aimed at exploring the application value of diffusion-weighted imaging (DWI) combined with transcranial Doppler (TCD) in the diagnosis of patients with cerebral infarction and vertigo (CI + V). In this article, using a retrospective case-control study, 100 CI + V patients (CI + V group) were examined by DWI combined with TCD. Seventy cases of noncerebral infarction with vertigo (control group) who were hospitalized at the same time were collected for clinical data analysis and comprehensive evaluation of each index. The results showed that in patients with CI + V, the abnormal rate of blood vessels was proportional to the size of the lesion, and the abnormal rate of blood vessels in the large-area infarction group (97%) was much higher than that of the small-area infarct group (62%) and the lacunar infarction group (51%). The overall abnormal rate of blood vessels in the CI + V group (71%) was greatly higher than that in the control group (15%), showing a statistically and extremely great difference ($P < 0.01$). In short, DWI can effectively extract lesion-related data, and combined with TCD examination, the clinical diagnosis of CI + V can be more accurately performed, which had a positive impact on the clinical work of CI + V. This work provided some reference for the clinical effective diagnosis method of CI + V.

1. Introduction

Cerebral infarction is also known as ischemic stroke, and it is a common cerebrovascular disease (CVD). It is caused by the obstruction of blood supply to the brain tissue area, which leads to cerebral tissue ischemia and hypoxia, resulting in clinical brain tissue necrosis and corresponding neurological deficits [1, 2]. Most of the patients are middle-aged and elderly people, and the clinical cause is generally intracranial or cervical aortic atherosclerosis caused by a variety of factors [3, 4]. The early clinical symptoms mainly include dizziness, blackness, and numbness in different parts of the body, and there are life-threatening risks in the middle and late stages [5, 6]. Cerebral infarction is often accompanied by vertigo, which is a pseudo-vertigo caused by systemic diseases. The patient feels his body is wandering without obvious foreign objects or self-rotating sensation. For people with high incidence, the initial diagnosis and treatment of cerebral infarction are very necessary. Clinically, brain structure imaging and cerebrovascular imaging are usually used for diagnosis, which generally include cranial computed tomography (CT), and cranial magnetic resonance imaging (MRI), diffusion-weighted imaging (DWI), and transcranial Doppler ultrasound (TCD) [7].

Among them, cranial CT is the most convenient and commonly used. It can detect some subtle early ischemic changes within 6 hours of onset, but it is hard to distinguish after 2–3 weeks and lacks sensitivity to the posterior brainstem and cerebellum lesions [8]. Cranial MRI can clearly image these two parts, but it is difficult to detect lesions within a few hours of onset. The diagnostic detection rate of early acute CI + V by conventional CT and MRI is low with poor sensitivity, which can meet the requirements of clinical medical diagnosis and treatment. TCD uses blood flow velocity to assess the blood flow status, thereby inferring changes in local cerebral blood flow. It is a commonly used noninvasive inspection method to detect intracranial and extracranial vascular stenosis or occlusion [9, 10]. However, some researchers believe that the results of TCD are subjectively affected by the operator and are not as accurate as magnetic resonance angiography (MRA), digital subtraction angiography (DSA), and other invasive examination methods. DWI is an MRI function imaging technology. With the application of high field-strength MRI machine, it is the only MRI technology that can reflect the diffusion of water molecules and possesses high sensitivity. DWI can not only detect the early ischemic location, but also clearly show some small infarcts, which are mainly used for the diagnosis of ultra-early cerebral ischemia [11].

Therefore, in the above context, a retrospective investigation was conducted on CI + V patients who were examined jointly by DWI and TCD and 70 non-CI + V patients were hospitalized at the same time, to explore whether DWI combined with TCD has good clinical diagnostic value in CI + V, and to provide theoretical basis for the further promotion and application of this combined examination program.

2. Materials and Methods

2.1. Research Objects. A total of 100 patients hospitalized for CI + V from May 2018 to December 2020 in hospital were selected as subjects, including 60 males and 40 females, with an average age of 65 ± 10.5 years. Seventy cases of non-cerebral infarction patients with vertigo were enrolled at the same time, including 44 males and 26 females, with an age range of 63.5 ± 9.7 years. All patients underwent head CT or MRI examination and were excluded from cerebrovascular diseases. There was no statistical significance in general clinical data with patients in the CI + V group. All subjects were divided into the CI + V group and the control group. The CI + V group was divided into three groups according to the lesion area presented by imaging examination. There were 31 patients with large-area cerebral infarction ($>15\,cm^2$), 46 patients with small-area cerebral infarction ($<5\,cm^2$), and 23 patients with lacunar cerebral infarction. The clinical data were analyzed by a retrospective case-control study. All the subjects agreed to sign informed consents, and this study had been approved by the ethics committee of hospital.

Inclusion criteria are as follows: the patients who were diagnosed according to the diagnostic criteria given in the 2010 Chinese Guidelines for the Diagnosis and Treatment of Ischemic Stroke; patients who received DWI in combination with TCD within 48 hours after admission; patients with no previous history of cerebral infarction; and patients without serious organic disease.

Exclusion criteria are as follows: patients with otogenic vertigo, ocular vertigo, or dizziness caused by psychological effects, emotional anxiety, and depression; patients with chronic subdural hematoma and other diseases; pregnant and lactating women; and unable to perform correlation analysis due to unknown medical records.

2.2. TCD Inspection Plan. All subjects were examined by a transcranial Doppler analyzer with a pulse probe frequency of 2 MHz. Through the examination, the subject's information was acquired, including anterior cerebral artery (ACA), middle cerebral artery (MCA), posterior cerebral artery (PCA), bilateral vertebral artery (VA), and basilar artery (BA). In addition, the average blood flow velocity (Vm), vascular pulsatility index (PI), peak systolic blood flow velocity (Vs), peak diastolic blood flow velocity (Vd), etc., were also determined

2.3. DWI Inspection Plan. 1.5 T magnetic resonance scanner was used for TCD underwent cranial MRI, which was used to conventionally scan the transverse $T2$-weighted imaging ($T2$WI), $T1$-weighted imaging ($T1$WI), coronal $T2$WI, sagittal $T1$WI, DWI, and $T2^*$WI. The parameters were set as follows: DWI—repetition time was 5,000 ms, echo time was 90 ms, scanning layer thickness was 6 mm, layer spacing was 1 mm, matrix was $200\,mm \times 220\,mm$; and $T2^*$WI—repetition time was 450 ms, echo time was 2.53 ms, scanning layer thickness was 6 mm, layer spacing was 1 mm, and matrix was $220\,mm \times 200\,mm$.

2.4. Image Processing Scheme. Texture feature parameters in DWI images were extracted by full quantitative post-processing software, which were read and analyzed by two experienced professional physicians. By standardizing and calibrating DWI images, the signal characteristics of each sequence position on the lesion in the CI + V group were observed. The image was segmented, and the relevant texture feature parameters were obtained. The apparent diffusion coefficient (ADC) values of all subjects in the relevant area were measured. All data were calculated automatically by computer software.

2.5. Statistical Analysis. SPSS 24.0 software was used for statistical analysis, the measurement data were expressed as mean ± standard deviation ($\bar{x} \pm s$), and the χ^2 test was adopted for comparison between groups. The Kolmogorov–Smirnov test was applied to analyze whether the experimental data were consistent with the Gaussian distribution. If it was consistent, the t-test was used. $P < 0.05$ meant that the difference was statistically significant. Origin 8.0 was adopted for drawing.

3. Results

3.1. DWI Results of Typical Cases. A 55-year-old female patient presented with recurrent headache, dizziness, and limb weakness for more than 2 years, poor mobility, and worsening blurred vision for 3 weeks. On admission, DWI examination showed that the left lesion showed an obvious high signal, and the clinical diagnosis was acute cerebral infarction in the left basal ganglia with vertigo (Figure 1).

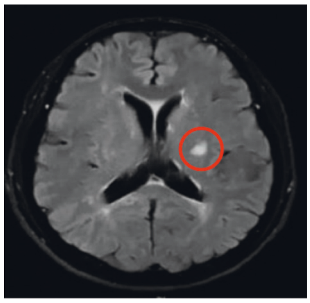

Figure 1: DWI imaging results of a typical case. The red circle marked the infarcted area.

3.2. Comparison of Blood Vessel Conditions among the Subgroups of Patients in the CI + V Group

3.2.1. Comparison of Blood Vessel Conditions of Patients between Large-Area Infarction Group and Small-Area Infarction Group. As shown in Figure 2, there were 31 patients in the large-area infarction group and 46 patients in the small-area infarction group. Among them, there were 8 patients in the large-area infarction group and 7 patients in the small-area infarction group with increased blood flow velocity; and 19 cases were in the large-area infarction group and 20 cases were in the small-area infarction group with decreased blood flow velocity; there were 3 cases in the large-area infarction group and 2 cases in the small-area infarction group without blood flow signal.; and there were 1 case in the large-area infarction group and 17 cases in the small-area infarction group with normal blood vessels. The abnormal rate of blood vessels in the large-area and the small-area infarction groups was 97% and 62%, respectively. It suggested that the DWI combined with TCD examination showed that the abnormal rate of blood vessels of cerebral infarction was directly proportional to the size of the lesion, and the abnormal rate of blood vessels of the large-area infarction group was observably higher than that of the small-area infarct group, showing a statistically significant difference ($P < 0.05$).

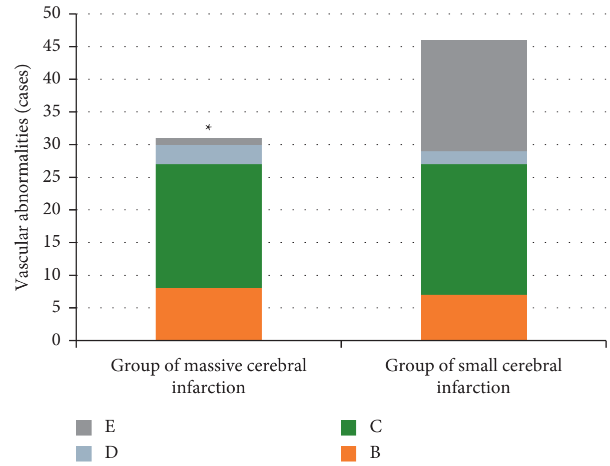

Figure 2: Comparison of blood vessel conditions of patients between large-area infarction group and small-area infarction group. *B*, *C*, *D*, and *E* in the figure referred to increased blood flow velocity, decreased blood flow velocity, without blood flow signal, and normal blood vessels, respectively. *The difference in the abnormal rate of blood vessels of patients in the two groups was statistically obvious, $P < 0.05$.

3.2.2. Comparison of Blood Vessel Conditions of Patients between Large-Area Infarction Group and Lacunar Infarction Group. As shown in Figure 3, there were 23 patients in the lacunar infarction group, including 4 patients with increased blood flow velocity, 7 patients with decreased blood flow velocity, 1 patient without blood flow signal, and 11 cases with normal blood vessels. The abnormal rate of blood vessels in the lacunar infarction group was 51%. Thus, the abnormal rate of blood vessels in the large-area infarction group was visibly higher than that in the lacunar infarction group after DWI combined with TCD examination, and the difference was statistically obvious ($P < 0.05$).

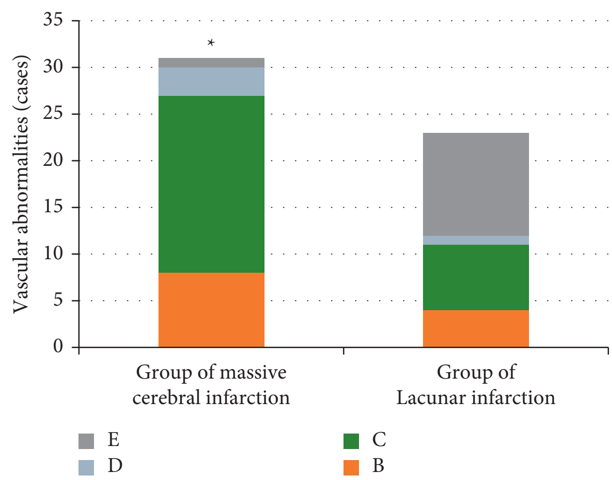

Figure 3: Comparison of blood vessel conditions of patients between large-area infarction group and lacunar infarction group. *B*, *C*, *D*, and *E* referred to increased blood flow velocity, decreased blood flow velocity, without blood flow signal, and normal blood vessels, respectively. *The difference in the abnormal rate of blood vessels of patients in the two groups was statistically obvious, $P < 0.05$.

3.2.3. Comparison of Blood Vessel Conditions of Patients between Small-Area Infarction Group and Lacunar Infarction Group. As illustrated in Figure 4, the abnormal rate of blood vessels in the small-area infarction group was 62% and that in the lacunar infarction group was 51%. It indicated that the DWI combined with TCD suggested that the difference in the abnormal rate of blood vessels between the two groups was not statistically significant ($P < 0.05$).

3.3. Comparison on Blood Vessel Condition of Patients in the CI + V Group and the Control Group. As shown in Figure 5, there were a total of 100 patients with CI + V, including 19 cases with increased blood flow velocity, 46 cases with decreased blood flow velocity, 6 cases with no blood flow

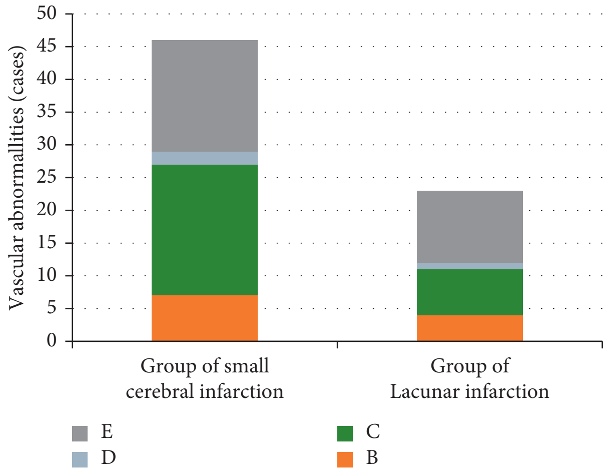

Figure 4: Comparison of blood vessel conditions of patients between the small-area infarction group and lacunar infarction group. *B*, *C*, *D*, and *E* referred to increased blood flow velocity, decreased blood flow velocity, without blood flow signal, and normal blood vessels, respectively.

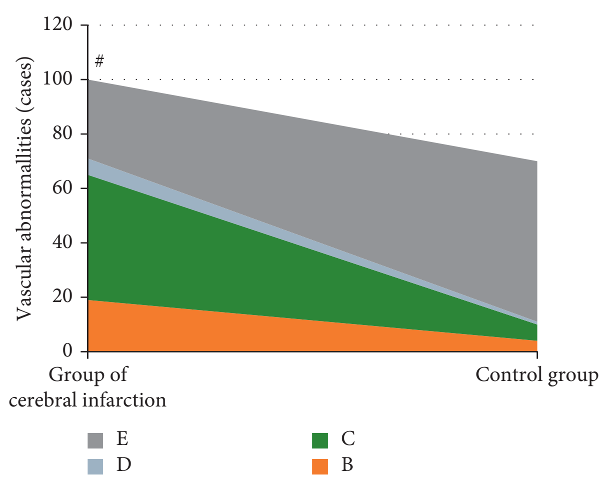

Figure 5: Comparison on the blood vessel condition of patients in the CI + V group and the control group. *B*, *C*, *D*, and *E* referred to increased blood flow velocity, decreased blood flow velocity, without blood flow signal, and normal blood vessels, respectively. #The difference in the abnormal rate of blood vessels of patients in the two groups was statistically obvious, $P < 0.01$.

signal, and 29 cases with normal blood vessels. Thus, the abnormal rate of blood vessels was 71%. A total of 70 patients in the control group included 4 cases with increased blood flow velocity, 6 cases with decreased blood flow velocity, 1 case with no blood flow signal, and 59 cases with normal blood vessels, so the abnormal rate of blood vessels was 15%. The DWI combined with TCD examination showed that the abnormal rate of blood vessels in the CI + V group was much higher than that in the control group, and the difference was extremely and statistically obvious ($P < 0.01$).

3.4. Comparison of DWI Combined with TCD, CT, and MRI in Locating Lesions. As shown in Figures 6 and 7, among the 100 patients with cerebral infarction and vertigo, CT and

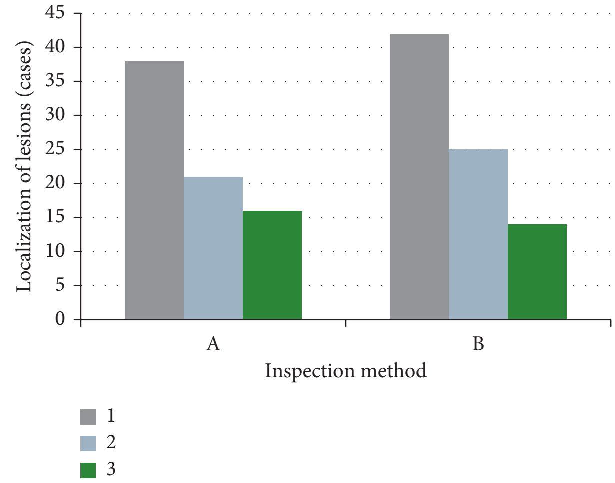

Figure 6: Comparison of DWI combined with TCD, CT, and MRI in locating lesions. A referred to the results of DWI combined with TCD; B showed the results of CT and MRI. 1, 2, and 3 referred to the number of patients with infarction of the internal carotid artery system, infarction of the vertebral base arterial system, and the ischemic infarction of the marginal zone between adjacent blood vessels, respectively.

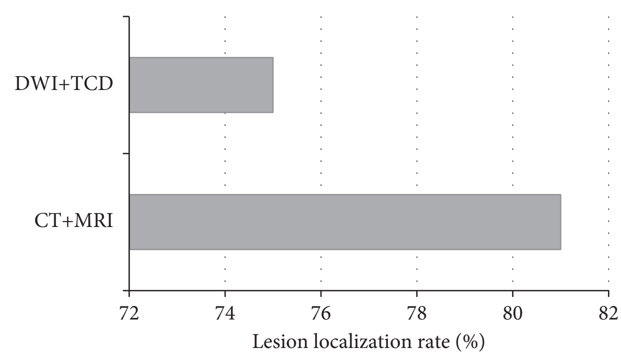

Figure 7: Comparison of lesion localization rates between the two methods.

MRI can locate the lesions in 81 cases. Among them, 42 cases had internal carotid artery system infarction, 25 cases had vertebrobasilar system infarction, and 14 cases had ischemic infarction in the border zone between adjacent blood supply areas. DWI combined with TCD could locate the lesions in 75 cases, including 38 cases of internal carotid artery system infarction, 21 cases of vertebrobasilar system infarction, and 16 cases of border zone ischemia between adjacent blood supply areas. It meant that there was no significant difference between DWI combined with TCD and CT and MRI in locating lesions (75% and 81%, respectively), and there was no statistical significance ($P > 0.05$).

3.5. DWI Combined with TCD to Detect the Blood Flow Velocity in the CI + V Group. The blood flow velocity of patients in the CI + V group detected by DWI combined with TCD is illustrated in Figures 8 and 9. There were 19 cases with increased blood flow velocity and 46 cases decreased blood flow velocity.

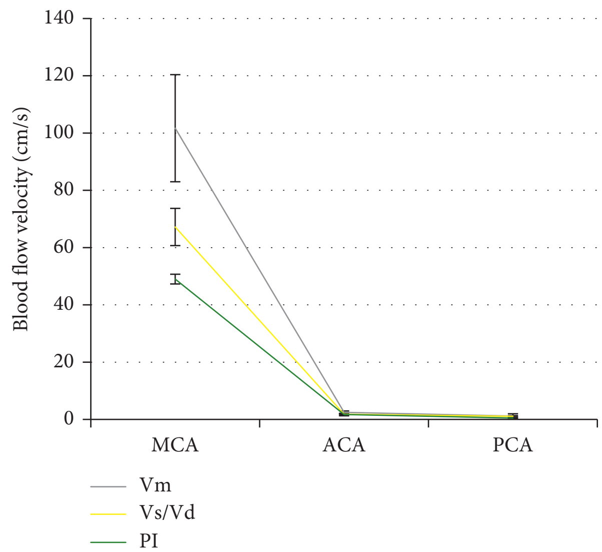

FIGURE 8: The specific conditions of patients with increased blood flow velocity.

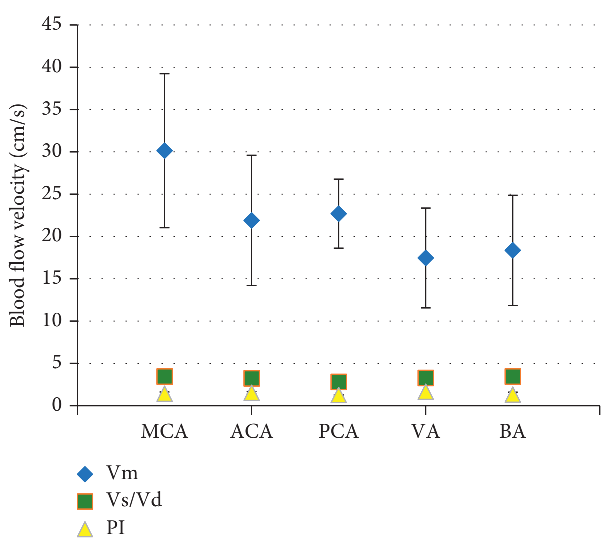

FIGURE 9: The specific conditions of patients with decreased blood flow velocity.

For patients with increased blood flow velocity: in MCA, Vm was 101.7 ± 18.7 cm/s, Vs/Vd was 2.46 ± 0.5, and PI was 1.17 ± 0.8; in ACA, Vm was 67.2 ± 6.5 cm/s, Vs/Vd was 1.83 ± 0.2, and PI was 1.09 ± 0.24; and in PCA, Vm was 49 ± 1.7 cm/s, Vs/Vd was 1.7 ± 0.44, and PI was 0.49 ± 0.33.

For patients with decreased flood flow velocity: in MCA, Vm was 30.14 ± 9.1 cm/s, Vs/Vd was 3.46 ± 0.2, and PI was 1.43 ± 0.19; in ACA, Vm was 21.9 ± 7.7 cm/s, Vs/Vd was 3.24 ± 0.28, and PI was 1.53 ± 0.16; in PCA, Vm was 22.7 ± 4.08 cm/s, Vs/Vd was 2.82 ± 0.14, and PI was 1.27 ± 0.04; in VA, Vm was 17.46 ± 5.9 cm/s, Vs/Vd was 3.28 ± 0.61, and PI was 1.65 ± 0.9; and in BA, Vm was 18.36 ± 6.51 cm/s, Vs/Vd was 3.46 ± 0.77, and PI was 1.32 ± 0.28.

3.6. Composition of ADC Value of Patients in the CI + V Group and the Control Group. As shown in Figure 10, the patients in the CI + V group showed low ADC values; and ADC values of patients in the large-area cerebral infarction group, small-area cerebral infarction group, and the lacunar infarction group were $0.000421 \pm 0.000069\,mm^2/s$, $0.000419 \pm 0.000072\,mm^2/s$, and $0.000432 \pm 0.000075\,mm^2/s$, respectively. The ADC of patients in the control group was $0.000975 \pm 0.000014\,mm^2/s$. It suggested that the ADC values of the large-area cerebral infarction group, the small-area cerebral infarction group, and the lacunar infarction group were not statistically different ($P > 0.05$), while the difference in ADC values between the CI + V group and the control group was statistically significant ($P < 0.05$).

3.7. The Specific Situation of Patients with Clinical Vertigo. As revealed in Figure 11, there were 48 cases of isolated vertigo (including 37 cases of transient attacks and 11 cases of persistent attacks) and 52 cases of nonisolated vertigo (including 28 cases of transient attacks and 24 cases of persistent attacks).

During the experiment, 6 cases suffered from ambiguity, 8 cases suffered from eyelid movement, 14 cases suffered from body numbness, 19 cases suffered from mild hemiplegia, and 3 cases suffered from other symptoms (Figures 12 and 13).

4. Discussion

Cerebral infarction, also known as ischemic stroke, is a kind of cerebral blood circulation disorder. It is the most common type of cerebral vascular disease, which is caused by ischemia and hypoxia [12, 13]. It is more common in middle-aged and elderly patients. The general clinical diagnosis is based on brain structure imaging and cerebrovascular imaging. Among them, TCD is a noninvasive examination method used to evaluate the hemodynamics of the skull base arteries, which can more sensitively reflect the functional status of the cerebrovascular [14, 15], but it has some shortcomings, which is embodied that it fails to guarantee the incident angle of ultrasound, reducing the accuracy of repeated measurement of blood flow velocity. DWI can detect the size and location of the lesion in the ultra-early stage of onset, and it can also detect some small infarcts in the brainstem and cerebellum [16–18].

A retrospective study was conducted on 100 CI + V patients who underwent DWI combined with TCD examination to obtain effective data information from THEIR DWI images. The results showed that in patients with CI + V, the abnormal rate of blood vessels was directly proportional to the size of the lesion. The abnormal rate of blood vessels in the large-area infarction group was much higher than that in the small-area infarction group and the lacunar infarction group, showing statistically obvious differences ($P < 0.05$). In addition, the overall abnormal rate of blood vessels in the CI + V group was obviously higher than that in the control

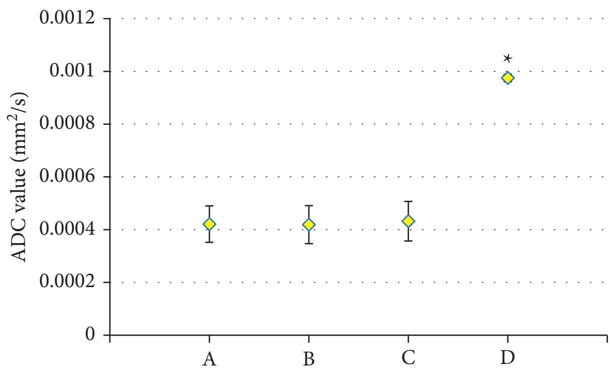

Figure 10: Composition of the ADC value of patients in the CI + V group and the control group. A, B, C, and D referred to the ADC values of patients in the large-area cerebral infarction group, small-area cerebral infarction group, the lacunar infarction group, and the control group, respectively. *The ADC value between the CI + V group and the control group showed a statistically great difference, $P < 0.05$.

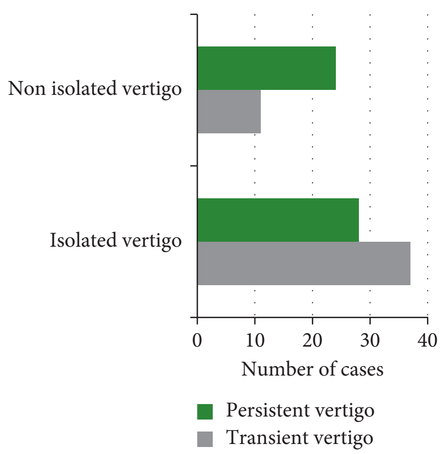

Figure 11: The specific situation of patients with clinical vertigo.

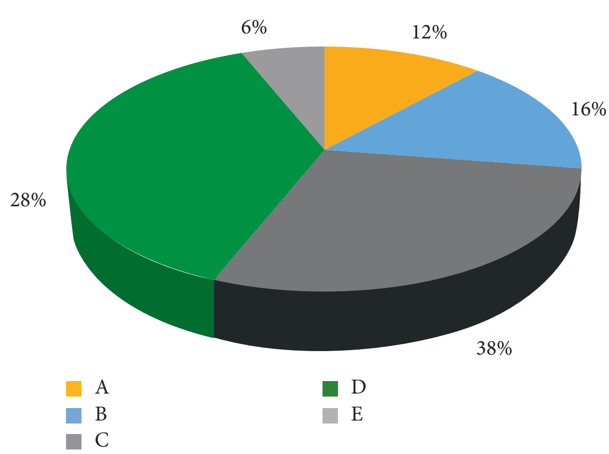

Figure 12: The specific symptoms of patients with clinical vertigo.

group, and the difference was extremely and statistically significant ($P < 0.01$). For patients with vertigo symptoms during the experiment, their clinical manifestations were also consistent with the diagnosis of vertigo. Takahashi [19]

Figure 13: The specific symptoms of patients with clinical vertigo. A–E in the figure represented to the ambiguity, eyelid movement, body numbness, mild hemiplegia, and other symptoms, respectively.

ever pointed out in the article that the success of the treatment of CI + V depended on whether the function of ischemic zone can be recovered as early as possible. However, traditional CT and MRI were both unable to accurately determine the location and scope of lesions at early stage. Consequently, clinical diagnosis becomes difficult. DWI could diagnose CI + V accurately, thus guiding clinical treatment, which was consistent with the conclusion of the research. Snider et al. [20] demonstrated the values of TCD in diagnosing and treating CI + V. TCD showed high accuracy of diagnosing CI + V with quick and convenient operation as well as no trauma. TCD helped people understand the functional state of intracranial vascular preliminary. The examination results showed significant guidance meaning for the early diagnosis and assessment of CI + V.

5. Conclusion

A retrospective study was conducted on 100 CI + V patients who underwent DWI combined with TCD examination. It was found that the information of the cerebral infarction lesions extracted suggested that in patients with CI + V, the abnormal rate of blood vessels in the large-area infarction group was obviously higher than that in the small-area infarction group and the lacunar infarction group, showing statistical differences ($P < 0.05$); and compared with the control group, the overall abnormal rate of blood vessels in the CI + V group was highly statistically significant ($P < 0.01$). The deficiency is that there are only a few samples included in the final study due to the different quality level and degree of perfection of each case. Moreover, as this study is a retrospective study, there are many uncontrollable factors, so the results have certain limitations. In future studies, the sample size will be expanded to further explore this topic. In conclusion, DWI combined with TCD has a good application value in the diagnosis of CI + V, providing a theoretical basis for the clinical work of CI + V.

Data Availability

The data used to support the findings of this study are available from the corresponding author upon request.

Conflicts of Interest

The authors declare no conflicts of interest.

References

[1] H. Takeda, T. Yamaguchi, H. Yano, and J. Tanaka, “Microglial metabolic disturbances and neuroinflammation in cerebral infarction,” *Journal of Pharmacological Sciences*, vol. 145, no. 1, pp. 130–139, 2021 January.

[2] J. Ye, Z. Sun, and W. Hu, “Roles of astrocytes in cerebral infarction and related therapeutic strategies,” *Zhejiang Da Xue Xue Bao Yi Xue Ban*, vol. 47, no. 5, pp. 493–498, 2018 May 25, Chinese.

[3] Z. Lv and L. Qiao, “Analysis of healthcare big data,” *Future Generation Computer Systems*, vol. 109, pp. 103–110, 2020.

[4] W. Rojsanga, K. Sawanyawisuth, V. Chotmongkol, S. Tiamkao, K. Kongbonkiat, and N. Kasemsap, “Clinical risk factors predictive of thrombotic stroke with large cerebral infarction,” *Neurology International*, vol. 11, no. 2, p. 7941, 2019 June 18.

[5] W. Sun, G. Li, X. Zeng et al., “Clinical and imaging characteristics of cerebral infarction in patients with nonvalvular atrial fibrillation combined with cerebral artery stenosis,” *Journal of Atherosclerosis and Thrombosis*, vol. 25, no. 8, pp. 720–732, 2018 August 1.

[6] A. Wallin, E. Kapaki, M. Boban et al., “Biochemical markers in vascular cognitive impairment associated with subcortical small vessel disease - a consensus report,” *BMC Neurology*, vol. 17, no. 1, p. 102, 2017 May 23.

[7] W. Zhang, J. Cheng, Y. Zhang, K. Wang, and H. Jin, “Analysis of CT and MRI combined examination for the diagnosis of acute cerebral infarction,” *Journal of the College of Physicians and Surgeons Pakistan*, vol. 29, no. 09, pp. 898-899, 2019 September.

[8] J. Fu, M. Zeng, F. Shen et al., “Effects of action observation therapy on upper extremity function, daily activities and motion evoked potential in cerebral infarction patients,” *Medicine (Baltimore)*, vol. 96, no. 42, p. e8080, 2017 October.

[9] S. Xie, Z. Yu, and Z. Lv, “Multi-disease prediction based on deep learning: a survey,” *Computer Modeling in Engineering and Sciences*, vol. 128, no. 2, pp. 489–522, 2021.

[10] F. Wadehn and T. Heldt, “Adaptive maximal blood flow velocity estimation from transcranial Doppler echos,” *IEEE Journal of Translational Engineering in Health and Medicine*, vol. 8, pp. 1–11, Article ID 1800511, 2020 July.

[11] T. Yuan, G. Ren, X. Hu et al., “Added assessment of middle cerebral artery and atrial fibrillation to FLAIR vascular hyperintensity-DWI mismatch would improve the outcome prediction of acute infarction in patients with acute internal carotid artery occlusion,” *Neurological Sciences*, vol. 40, no. 12, pp. 2617–2624, 2019 December.

[12] X. Jin, Y. Zou, J. Zhai, J. Liu, and B. Huang, “Refractory Mycoplasma pneumoniae pneumonia with concomitant acute cerebral infarction in a child,” *Medicine (Baltimore)*, vol. 97, no. 13, p. e0103, 2018 March.

[13] H. Ikenouchi, T. Yoshimoto, and M. Ihara, “Postprandial cerebral infarction,” *Journal of Clinical Neuroscience*, vol. 94, pp. 38–40, 2021 December.

[14] C. Robba, D. Cardim, M. Sekhon, K. Budohoski, and M. Czosnyka, “Transcranial Doppler: a stethoscope for the brain-neurocritical care use,” *Journal of Neuroscience Research*, vol. 96, no. 4, pp. 720–730, 2018 April.

[15] Y. Cao, X. Song, L. Wang, Y. Qi, Y. Chen, and Y. Xing, “Transcranial Doppler combined with quantitative electroencephalography brain function monitoring for estimating the prognosis of patients with posterior circulation cerebral infarction,” *Frontiers in Neurology*, vol. 12, Article ID 600985, 2021 May 17.

[16] P. Yue, W. Dongmei, L. Zhenzhou, Y. Wu, and J. I. Zhong, “[Diffusion-weighted imaging hyperintensity is reversible in large middle cerebral artery infarction following thrombectomy:a case report],” *Nan Fang Yi Ke Da Xue Xue Bao*, vol. 40, no. 4, pp. 459–462, 2020 April 30.

[17] M. Takahashi, M. Hashimoto, and M. Uehara, “Preparation of a small acute-phase cerebral infarction phantom for diffusion-weighted imaging,” *Japanese Journal of Radiological Technology*, vol. 74, no. 6, pp. 531–538, 2018, Japanese.

[18] Y. Li, J. Zhao, Z. Lv, and J. Li, “Medical image fusion method by deep learning,” *International Journal of Cognitive Computing in Engineering*, vol. 2, no. 2, pp. 21–29, 2021 June.

[19] M. Takahashi, “4. Preparation of a small h cerebral infarction phantom in diffusion-weighted imaging,” *Nippon Hoshasen Gijutsu Gakkai Zasshi*, vol. 77, no. 8, 858 pages, 2021, Japanese.

[20] S. B. Snider, I. Migdady, S. L. LaRose et al., “Transcranial-Doppler-Measured vasospasm severity is associated with delayed cerebral infarction after subarachnoid hemorrhage,” *Neurocritical Care*, vol. 36, no. 3, pp. 815–821, 2021 November.

Hindawi
Contrast Media & Molecular Imaging
Volume 2022, Article ID 1968189, 9 pages
https://doi.org/10.1155/2022/1968189

Research Article

Diffusion-Weighted Imaging Combined with Perfusion-Weighted Imaging under Segmentation Algorithm in the Diagnosis of Melanoma

Chuankui Shi,[1] **Peng Ge**,[2] **Yuping Zhao**,[2] **and Guobao Huang**[3]

[1]*Department of Dermatology, Qilu Children's Hospital of Shandong University, Jinan 250022, Shandong, China*
[2]*Burn and Plastic Surgery, The People's Hospital of Zhangqiu Area, Zhangqiu Area, Jinan 250200, Shandong, China*
[3]*Burn and Plastic Surgery, Central Hospital Affiliated to Shandong First Medical University, Jinan 250013, Shandong, China*

Correspondence should be addressed to Guobao Huang; 201957020002@sdu.edu.cn

Received 3 December 2021; Revised 28 May 2022; Accepted 2 June 2022; Published 27 June 2022

Academic Editor: M Pallikonda Rajasekaran

This study is aimed at exploring the value of magnetic resonance diffusion-weighted imaging (DWI) combined with perfusion-weighted imaging (PWI) for diagnosing melanoma under a three-dimensional (3D) hybrid segmentation algorithm. 40 patients with melanoma were collected as research objects and subjected to magnetic resonance imaging (MRI) examination. A segmentation model was constructed and the original images were input. The noise contained in the images was preprocessed and normalized, and the mixed level set segmentation was performed after linear fusion of the images. Imaging findings were analyzed to find that the combined diagnosis of DWI and PWI with a 3D hybrid segmentation algorithm had the advantage of being clear and accurate. 10 primary cases were detected, which occurred in the cerebral meninges; 30 cases of metastases occurred inside the skull, mostly adjacent to the surface of the brain. The typical T1-weighted imaging (T1WI) and T2-weighted imaging (T2WI) of melanoma showed high signal and low signal, respectively, and the enhanced scan showed obvious enhancement. Atypical melanoma was manifested variously in MRI; a few had cystic necrosis, and an enhanced scan of the solid area revealed significant enhancement. Patients with multiple metastatic melanomas mainly showed low signal on DWI, and patients with primary or single metastatic melanoma mainly showed high signal or mixed high signal. Patients with perfusion imaging showed high perfusion on PWI. The 3D hybrid segmentation algorithm helped to improve the accuracy of DWI combined with PWI in the diagnosis of melanoma. This work provided a certain reference for the clinical diagnosis of melanoma.

1. Introduction

Melanoma generally refers to malignant melanoma in clinical practice, which is a kind of malignant tumor derived from melanocytes. Its pathogenesis is not yet clear. Relevant studies indicate that its occurrence and development are closely related to the genes, the environment, or the genes together with the environment. The occurrence of this disease is relatively insidious, and the prognosis of patients is poor [1]. Malignant melanoma is more common in adults over 30 years old and is slightly less in men than women. It usually occurs in skin, mucous membranes, and organs, but it can also occurs in the eyes, nasal cavity, and the brain sometimes. It can be newly caused by dysplastic nevus, and the malignant transformation of junctional nevus and congenital or acquired benign melanocytic nevus, accounting for about 3% of all tumors [2, 3]. Signs of malignant transformation are generally manifested as the increase of the pigment volume, the darkening of the color, the sudden growth, and the appearance of inflammation, ulcers, and bleeding of the nevus [4]. In recent years, the incidence and mortality of malignant melanoma have increased gradually, and the age of death is even smaller than that of other solid tumors. Early clinical diagnosis of some melanomas is relatively difficult, and puncture or biopsy is not recommended [5].

Histopathological examination is the gold standard for diagnosing melanoma, and imaging examinations can accurately locate and quantitatively analyze the lesions. These are helpful for the selection of treatment plans, prediction of therapeutic effect, and follow-up in the latter period, having clinical significance. Computed tomography is a common imaging method in clinical practice. However, some patients think that it is not sensitive to early limited-stage metastases of melanoma, has a low benefit rate, and cannot display limbs and other body parts. Conventional magnetic resonance imaging (MRI) gives a better resolution for soft tissues without radiation and can analyze the tissue source and signal characteristics of lesions on purpose, which is of great value in diagnosing melanoma [6, 7]. It can obtain information such as blood flow, metabolism, and biochemistry and display microscopic images and data noninvasively. Thus, the diagnosis of cancer can be focused on microscopic changes rather than morphology, and the biological characteristics of cancer tissues can be better displayed. It also makes the detailed information of the cancer tissues fully known, and the diagnosis rate and treatment rate can be improved [8, 9]. Diffusion-weighted imaging (DWI) and perfusion-weighted imaging (PWI) have fully demonstrated their application value and potential in the brain, liver, and prostate cancers. It was suggested that they could be used for the differentiation of benign and malignant cancers, the monitoring of postoperative recurrence, and the efficacy analysis of radiotherapy and chemotherapy, etc. [10]. DWI is an ideal method to detect the diffusion movement of water molecules in living tissues by using diffusion-sensitive gradients. An apparent diffusion coefficient is a physical quantity of the diffusion ability of water molecules that is used to quantitatively describe the diffusion movement of water molecules in the tissues [11]. PWI appeared with the rapid imaging sequence of MRI. It is an imaging technique that noninvasively evaluates the blood perfusion of the tissues by observing and comparing the early characteristics of tissue distribution [12].

In image processing, there are countless algorithms that can be applied for segmentation. The earliest method used for automatic segmentation of cerebral tumor is traditional machine learning, in which the threshold algorithm, clustering algorithm, and deformation mode algorithm are more commonly used than other machine learning algorithms [13, 14]. Automatic brain tumor segmentation technology has been a hot research topic in recent years, especially that based on multimodal three-dimensional (3D) image segmentation. The high precision and low deviation of the segmentation method have become common goals in surgical plans [15]. The technology can meet the needs of clinical medical treatment and has high segmentation accuracy and research prospects [16, 17]. However, many existing methods around the world are on the basis of a single modality, so their segmentation accuracy and reliability are not very high. Thus, the 3D hybrid segmentation algorithm was innovatively applied to DWI and PWI, and the diagnostic data of intracranial melanoma were expounded. This provided a theoretical basis for further understanding of melanoma and improved the accuracy of clinical diagnosis.

2. Materials and Methods

2.1. General Data. In this study, 40 patients with central nervous melanoma were included, and they were admitted to hospital from September 2019 to September 2020. All the patients, including 30 males and 10 females, were 37–68 years old with an average age of 44.35 ± 9.78. At the time of visiting doctor, patients with symptoms like nausea, vomiting, dizziness, headache, weakness of the limbs, visual disturbances, and confusion of consciousness had lesions in the brain. Meanwhile, the patients with stiff necks accompanied by soreness had lesions in the spinal canal. The informed consents were signed by the patients and their families. This study has been approved by the ethics committee of the hospital.

The inclusion criteria were as follows: patients were diagnosed clearly by histopathological examination; Patients had the complete clinical and pathological data; Patients had a good physical condition generally. The exclusion criteria were as follows: patients with incomplete pathological diagnosis data and those who cannot cooperate with MRI examination were excluded.

2.2. Instruments and Examination Methods. A 3.0 T MRI examination was performed. The head was scanned with T1WI, T2WI, water suppression, enhanced scanning, and DWI combined with PWI, respectively; and the spinal canal was scanned with T1WI, T2WI, fat suppression, and enhanced scanning. The MRI enhanced scanning contrast agent was gadolinium diethylenetriamine pentaacetic acid (Gd-DTPA), and the intravenous injection dose was 0.1 mmol/kg of weight. The scanning parameters are detailed in Table 1.

2.3. Multimodal 3D Image Hybrid Segmentation Algorithm for Intracranial Melanoma. The traditional fuzzy C-means clustering algorithm had the defects of a large amount of calculation and a long running time for large data samples. Therefore, an improved method was proposed to reduce the number of iterations required for the algorithm convergence, and the data sets involved in the iterations were compressed. Therefore, the running time of each iteration process could be reduced, the operation speed of the fuzzy C-means algorithm was improved, and the clustering effect of the algorithm was not affected. The clustering segmentation algorithm of 3D fast fuzzy C-means (FFCM) was carried out by the FFCM, through which the data was divided into c categories. For an $P \times Q \times W$ image, it is assumed that $\{g_i, i = 1, 2, \ldots, n; n = P \times Q \times W\}$ was the set of pixel intensity values in the image histogram, $\{u_j, j = 1, 2, \ldots, c\}$ was the set of cluster centers, and $\mu_j(g_i)$ was the membership function of g_i belonging to category j. Thus, the objective function of FFCM is expressed in the following equation:

$$J_f = \sum_{j=1}^{c} \sum_{i=1}^{n} \left[\mu_j(g_i)\right]^r \left\|g_i - u_j\right\|^2, \tag{1}$$

$$\begin{gathered}\sum_{j=1}^{c} \mu_j(g_i) = 1, \forall i, \\ 0 \le \mu_j(g_i) \le 1, \quad \forall i, j.\end{gathered} \tag{2}$$

Table 1: Scanning parameters for the head and spine MRI.

Position	Scanning items	Scanning parameters	Sequence
Head	T1WI	Time of repetition (TR): 2000 ms, time of echo (TE): 9 ms	
	T2WI	TR: 3000 ms, TE: 98 ms	
	Water suppression	TR: 7000 ms, TE: 93 ms Time of inversion (TI): 2500 ms	Fluid attenuated inversion recovery (FLAIR)
	DWI	TR: 5000 ms, TE: 90 ms	
	PWI	TR: 1500 ms, TE: 60 ms Slice thickness: 5 mm	
Spinal canal	T1WI	TR: 420 ms, TE: 9 ms	
	T2WI	TR: 3000 ms, TE: 113 ms	
	Fat suppression	TR: 330 ms, TE: 41 ms TI: 220 ms Slice thickness: 3 mm	Turbo inversion recovery magnitude (TIRM)

Together with the equation (2), the FFCM algorithm could be carried out. In the equations, $\|\bullet\|$ represented the 2-norm, r represented 1-constant>1, which were used to control the fuzzy degree of clustering.

Because the MRI image of intracranial melanoma was extremely complex, a 3D hybrid level set algorithm was applied to integrate the surface and volume information. The zero set of the embedding function ϕ was used to represent the active contour $C = \{Y|\phi(Y) = 0\}$, and the points inside and outside the contour had the positive or negative values. Then the function of minimum need is defined in the following equation:

$$\mathrm{Min}\varepsilon(\phi) = -\alpha\int_{\Omega}(U-\mu)W(\phi)\mathrm{d}\Omega + \beta\int_{\Omega}k|\nabla W(\phi)|\mathrm{d}\Omega. \tag{3}$$

U represented the 3D image to be segmented in the equation (3). $k = \exp(-c|\nabla U|^2)$ was the surface feature map related to the 3D image gradient, c was the control slope, $W(\phi)$ was the Heaviside function, Ω was the 3D image area, and α and β were the predefined weights to balance the two items. Then μ stood for the predefined parameter indicating the lower limit of the gray level of the target image.

$\overrightarrow{Q}$ was defined as the normal vector pointing to the outside of the surface, and then the explicit surface evolution partial differential equation of the active contour could be expressed as the following equation:

$$C_t = \alpha(U-\mu)\overrightarrow{Q} - \beta\langle\nabla_k\overrightarrow{Q}\rangle + \beta k\kappa\overrightarrow{Q}. \tag{4}$$

In the equation (4), $\overrightarrow{Q} = -\nabla\phi/|\nabla\phi|$, the curvature $\kappa = \mathrm{div}(\nabla\phi/|\nabla\phi|)$, and $\langle\cdot,\cdot\rangle$ were the inner product. Since only the geometric changes of the curved surface were of interest in the segmentation, it could be observed that all points on the curved surface moved in the normal direction through the equation (4). The first term of the equation (4) represented the transfer item between the expansion motion of the inner surface area and the contraction motion of the outer surface area in the target image. The second term represented the advection item of surface movement in the vector field caused by the gradient k, which drew the surface to the boundary of the target object. The third term represented the k-weighted curvature flow of the gradient feature map, meaning that the weak part of the support surface was with a smooth boundary.

In the level set, $C_t = \gamma\overrightarrow{Q}$ and $\phi_t = \gamma|\nabla\phi|$ represented the same surface change. If ϕ was a signed distance function, the derivative of the level set $|\nabla\phi| = 1$ embedding function over time was described as the following equation:

$$\phi_t = \alpha(U-\mu) + \beta\mathrm{div}(k\nabla\phi). \tag{5}$$

For the process of multimodal 3D image hybrid segmentation algorithm, firstly, the MRI images of T1, T2, and T1ce models were input. Because there was noise in the image itself, the image is preprocessed with median filtering and gray stretching. The gray stretching was applied under the 3D FFCM algorithm, through which partial boundary information could be effectively retained. Then linear fusion was used, and the fused image was for 3D FFCM clustering segmentation. The part with larger gray value in the clustered image was extracted by automatic threshold value, the under-segmented part of intracranial melanoma was then obtained, and finally the mixed level set was used for the segmentation. The flowchart and the main steps of segmentation are shown in Figure 1 and 2.

According to the algorithm flow, the image segmentation steps are shown in Figure 2. Images 2(a)–2(c) represented the original images of FLAIR, T2, and T1C, respectively. Image 2(d) represented the image obtained after fusion, and images 2(e)–2(g) are processed by FFCM, the automatic threshold, and the mixed level set, respectively. Image 2(h) was the final image obtained.

3. Results

3.1. General Data of Patients. Among the 40 patients in this study, 5 cases had the primary lesion in the cerebral meninges, 5 cases had that in the spinal meninges, and 30 cases had intracranial metastatic melanoma. 25 cases and 5 cases had skin and eyeballs as the primary lesion location, respectively. Figure 3 shows the pictures of melanoma in some patients.

3.2. Primary Melanoma. There were 10 cases with primary melanoma in this study. 5 patients were with melanoma in the cerebral meninges and the other 5 with melanoma in the

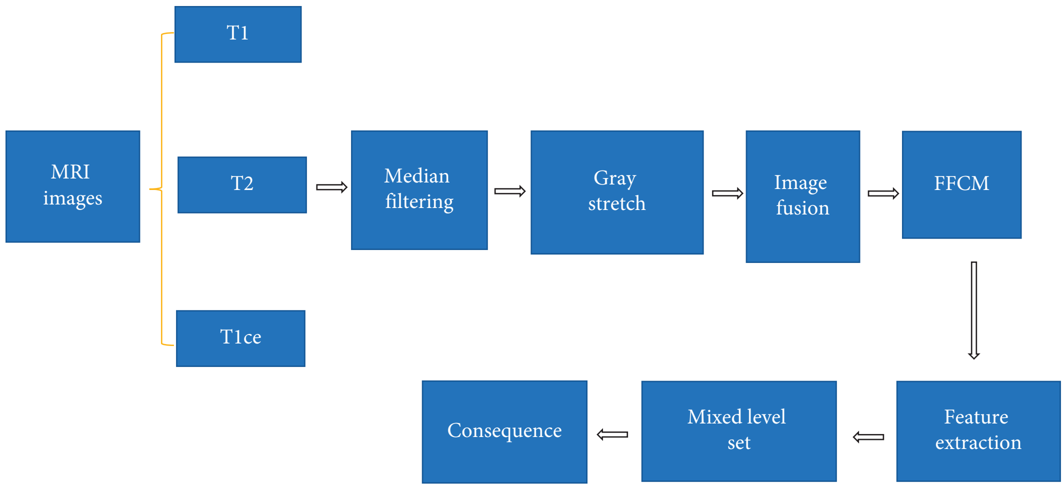

Figure 1: Flowchart of the 3D image hybrid segmentation algorithm.

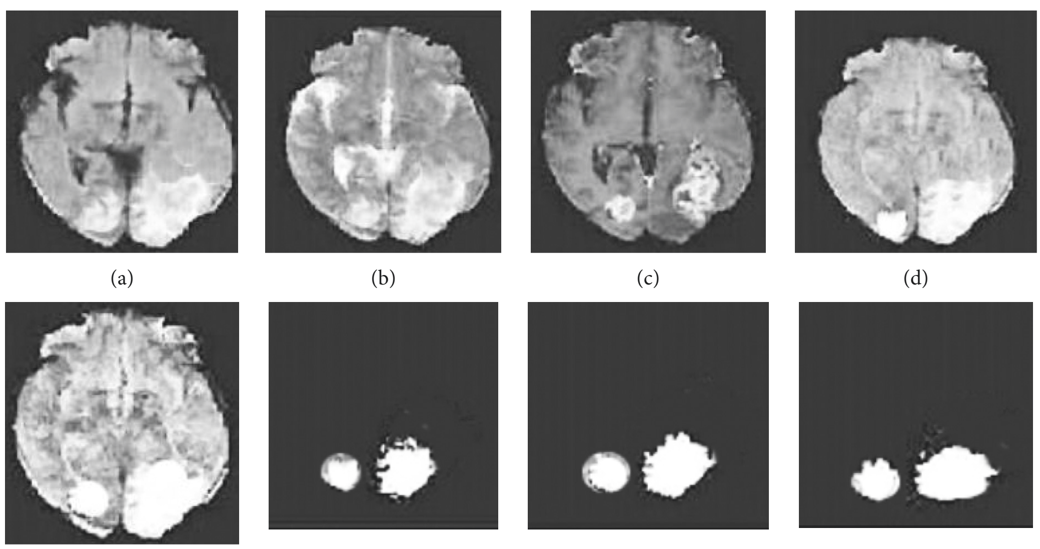

(a) (b) (c) (d)

(e) (f) (g) (h)

Figure 2: Diagram of the main segmentation steps of intracranial melanoma.

cervical spinal cord. The imaging findings are shown in Table 2 and Figure 4.

From Table 2 and Figure 4, it was found that the primary cerebral meningeal melanoma showed a uniform magnetic signal. A high signal was found on T1WI and T2WI, and a slightly high signal on DWI. As the enhancement scanning was carried out, the lesion area was obviously enhanced, with thickened and enhanced adjacent meningeal nodules and obvious peripheral edema. The PWI suggested that the rCBV of the lesion area of interest was increased. For the primary cervical meningeal melanoma, a typical magnetic signal was found, with a high signal on T1WI and a low signal on T2WI. The adjacent spinal cord suffered from compression; the arachnoid submembrane space was widened; the lesion was obviously enhanced under enhancement scanning, and the dural tail sign of spinal meninges could be observed.

3.3. Metastatic Melanoma. There were 30 cases with intracranial metastatic melanoma, including 25 patients with the primary lesion in the skin and 5 patients with the primary lesion in the eyeballs. 20 patients of them were diagnosed with solitary lesion, and 10 patients with multiple lesions. The results of their imaging examinations are shown in Table 3, Figure 5, and6.

From Table 3, Figure 5, and 6, it is observed that most of the patients among the 30 cases with intracranial metastatic melanoma had metastases close to the brain surface, and only a small part of the metastases was located deep. Mild or moderate edema was found around the lesions. The solitary lesions of 20 patients were determined to be of capsule-solid mixed type, with different MRI signals. There were 10 of them who had a low or equally low signal on T1WI and a high or equally high signal on T2WI; and the other 10 patients had mixed signals on T1WI and T2WI. DWI

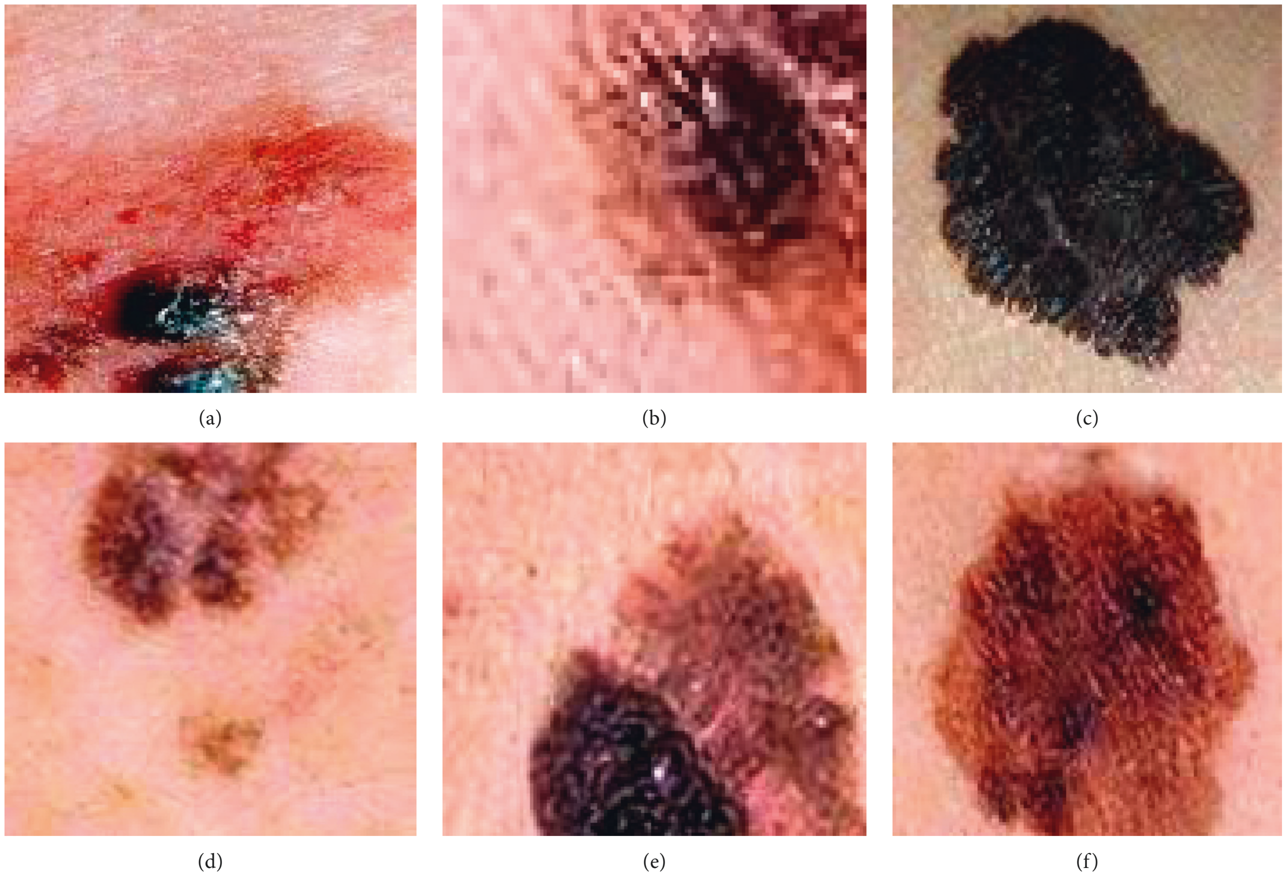

Figure 3: Images of melanoma in some patients. (a) Melanoma with raised skin lesions; (b) keratinized melanoma; (c) dyspigmentation; (d) melanoma with irregular borders; (e) 2 or more colors; (f) greater than 5 mm in its diameter.

Table 2: Imaging results of primary melanoma.

		High signal	Slightly high signal	Low signal
Cerebral meninges	T1WI	√		
	T2WI	√		
	DWI		√	
	PWI	The relative cerebral blood volume (rCBV) of the lesion area of interest was increased.		
Cervical spinal meninges	T1WI	√		
	T2WI			√

showed high signal or mixed high signal, and significant lesion enhancement was found in all patients under enhancement scanning. For the 10 patients with multiple lesions, their melanomas were all solid, with uniform and typical magnetic signals. Low signal was shown on DWI, and increased rCBV was found on PWI.

3.4. Pathological Manifestations. All the patients were diagnosed with melanoma through surgical pathology. The pathological images of some patients are shown in Figure 7.

From Figure 7, most patients had lesions complicated with bleeding. Some patients underwent immunohistochemical test, and the results suggested S-100 protein, malignant melanin-related antigen (HMB45), and Melan-1 were all positive.

4. Discussion

The relevant literature stated that primary melanoma of the central nervous system is rare, and it proposed three basic diagnostic conditions, including no melanoma on the skin and eyeballs, no melanoma history of tumor resection, and no melanoma metastasis in internal organs [18]. All the diagnoses of primary melanoma in this study met the above conditions. According to the different locations of the lesions, primary melanoma can be divided into melanoma that diffusely invades the cerebral (spinal) membranes and parenchymal melanoma. The former is more common, mainly because of the widespread existence of melanoma cells in the body, such as the cranial base, brainstem, optic chiasma, dura mater of each lobe of the brain, and spinal membrane [18, 19]. In this study, nodular thickening of the cerebral

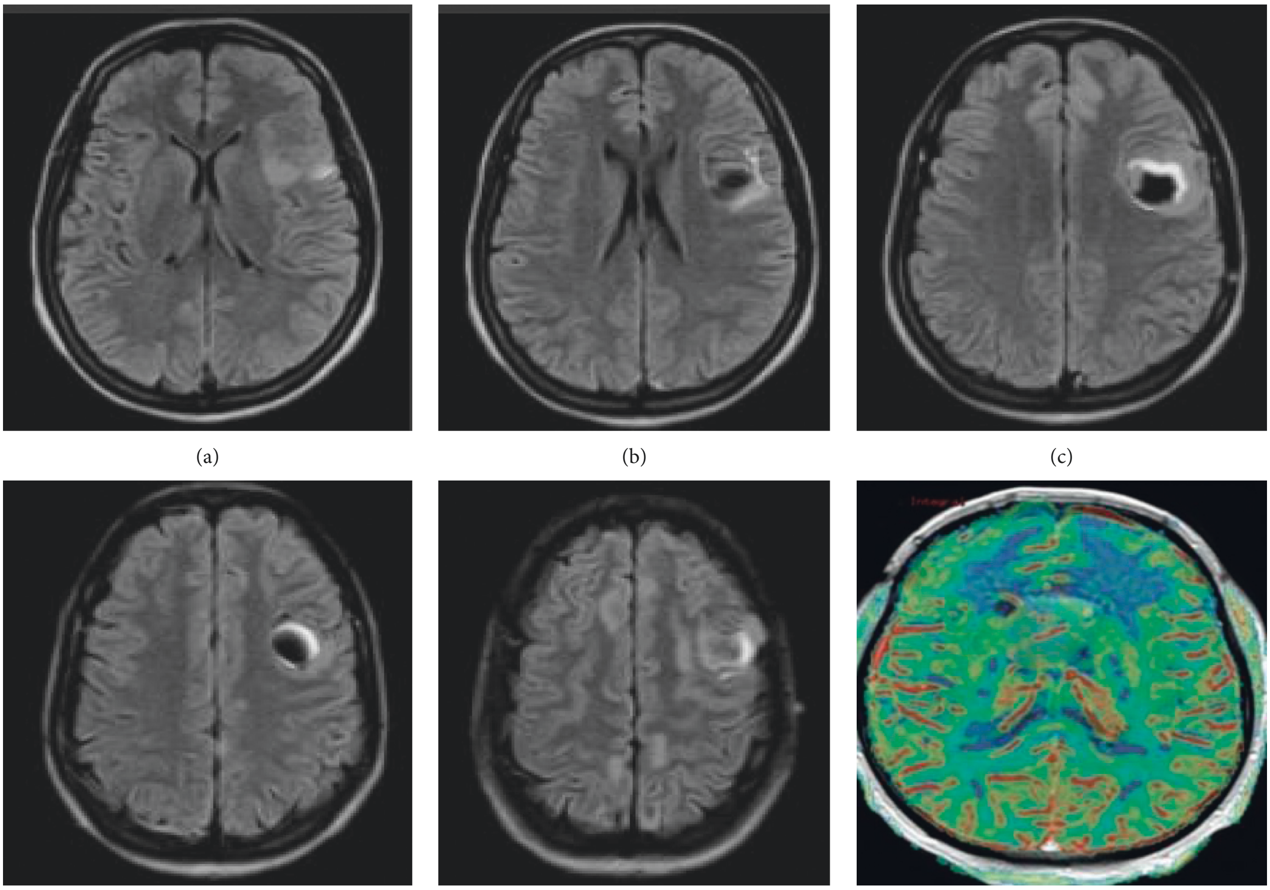

(a) (b) (c)

(d) (e) (f)

Figure 4: MRI images of primary intracranial melanoma. (A) (B), (C), and (D) : T1WI, T2WI, DWI, and PWI images of cerebral meninges region, respectively. (E) (F) : cervical spinal meninges region, respectively.

Table 3: Imaging results of intracranial metastatic melanoma.

		High or equally high signal	Low or equally low signal	Mixed signal	Low signal
Solitary	T1WI		√		
	T2WI	√		√	
	DWI	All equally high signals or mixed high signal			
Multiple	DWI				√
	PWI	Increasing rCBV on the solid parts of lesions			

meninges was observed in cases with primary meningopathy, and obvious enhancement was found during enhanced scanning near the cerebral meninges and sulcus. It was indicated that the meninges were diffusely invaded, and the dural tail sign was only limited to the spinal meninges without any obvious diffusion. It was also suspected that it is because the patients had symptoms of spinal cord compression in the early stages of the rapid growth of the tumor, but due to the timely resection, there was no diffusion to the spinal cord.

MRI shows great differences in the presentation of melanoma, and it can be divided into four types. The first is the melanin type, with T1WI and T2WI with high signal and low signal, respectively. The second is the nonpigmented type, as T1WI and T2WI show equally low signal and equally high signal, respectively. The third is mixed type with the mixed signals; and the fourth is the blood type, with only hemorrhage manifested [20, 21]. When the melanoma is rich in melanin, MRI will be very typical, as T1WI and T2WI showed high signal and low signal, respectively [22]. In this study, the primary spinal meningeal melanoma just belonged to the melanin type. However, the MRI of most melanomas is not typical, and the bleeding and melanin content in the tumor tissues are the main factors in determining the signal of melanoma. Relevant studies have found that to make MRI typical, there must be more than 10% melanocyte content in the tissue. In such a condition, T1WI and T2WI show high signal and low signal, respectively. Peripheral blood vessels are susceptible to melanoma invasion to cause bleeding, but the bleeding signal changes

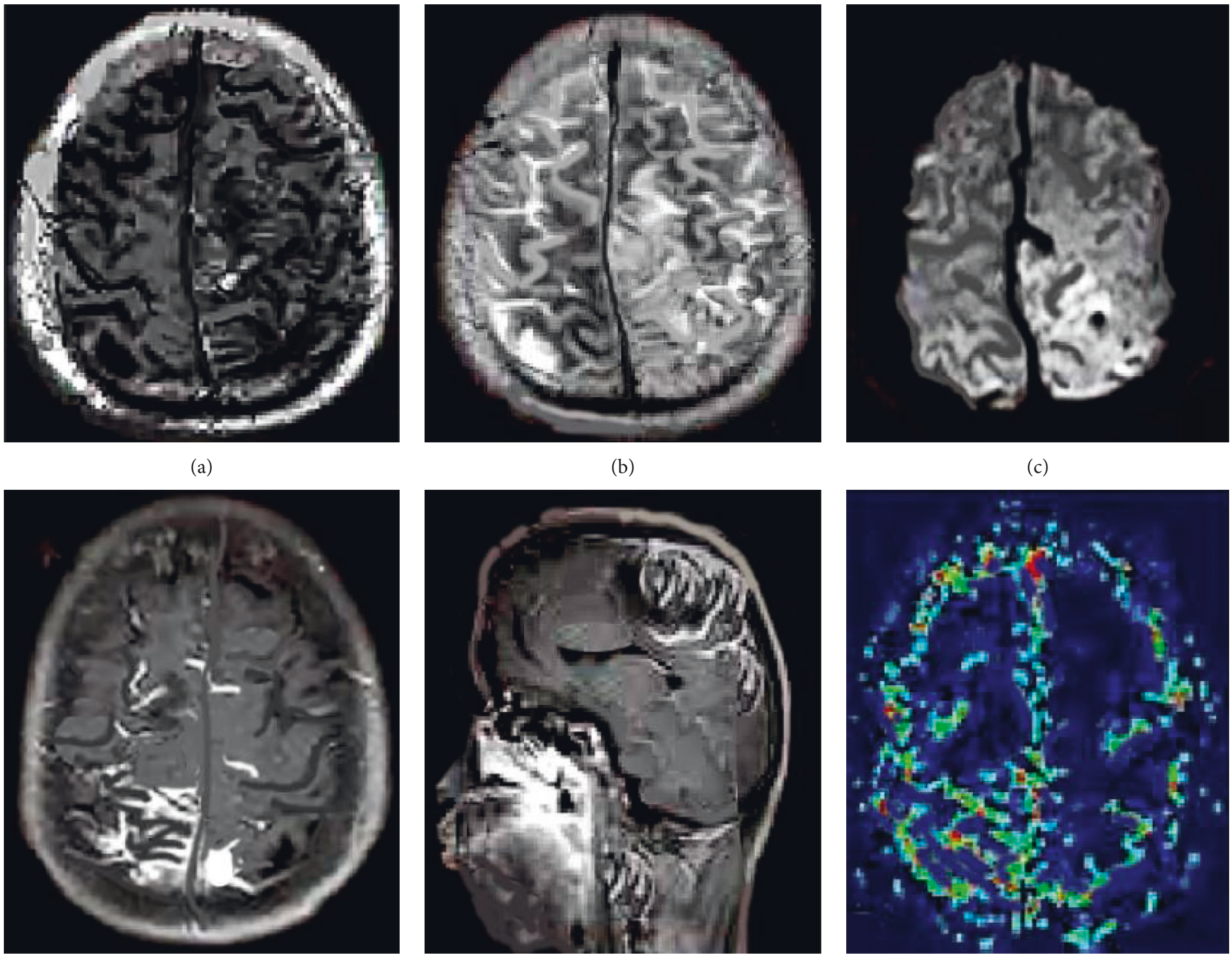

(a) (b) (c)
(d) (e) (f)

Figure 5: MRI images of single intracranial metastatic melanoma.

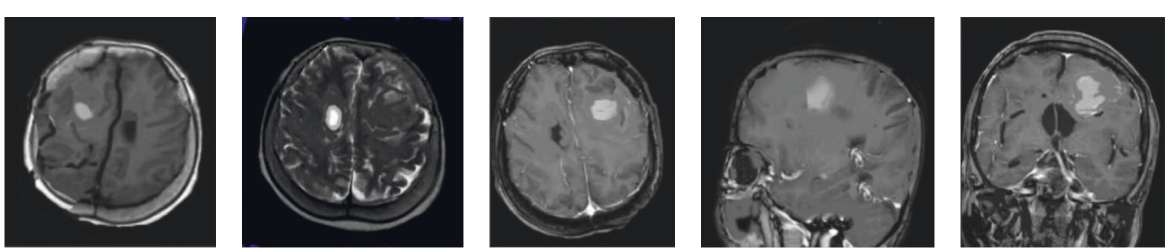

(a) (b) (c) (d) (e)

Figure 6: MRI images of multiple intracranial metastatic melanomas.

over time, which usually masks the paramagnetic effect of melanin [23, 24]. Among the cases in this study, the signal characteristics of primary meningeal melanoma may be related to the complex tumor signals in the theory.

Metastatic melanoma is more common in the central nervous system, which is the third largest intracranial metastatic tumor, only after that of lung cancer and breast cancer. It may occur in every part of the central nervous system, especially the junctions of the cortex and medulla. The MRI signal performance of it is similar to that of primary melanoma and is also related to bleeding and the content of melanin in tumor tissue [25, 26]. In this study, 30 cases of metastatic melanoma occurred in the brain, most of which were close to the brain surface, and a small portion were located in the deep part of the brain, with various MRI manifestations. 10 cases of multiple metastases with typical signals were all solid ones, and 20 cases of solitary metastases had cystic changes of different degrees. Among the 20 cases,

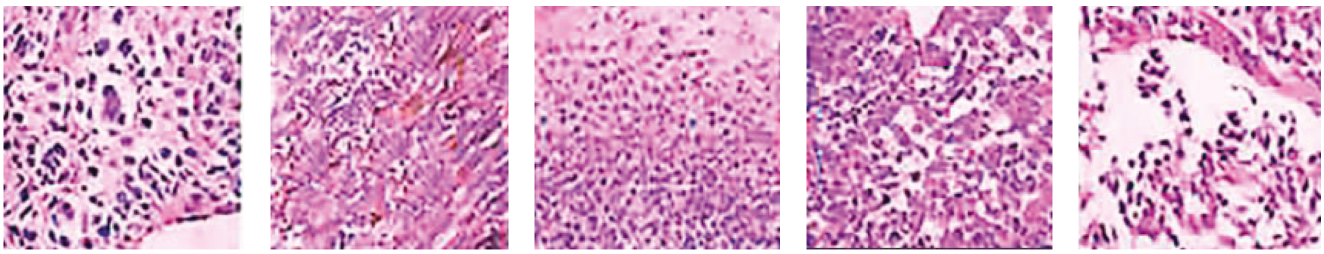

(a) (b) (c) (d) (e)

Figure 7: Pathological images of melanoma of some patients (× 200).

10 cases were determined to be nonpigmented, with the T1WI and T2WI of low or equally low and high or equally high signal, respectively. The other 10 cases with mixed signals might be related to intracranial bleeding. Melanoma with intracranial metastasis is clinically diagnosed as stage IV, and the survival period is only about 1 year. Therefore, it is particularly important for the accurate identification of the primary melanoma in clinical practice. Intracranial melanoma metastases frequently occur at the junction of the cortex and medulla, mostly with multiple lesions, and primary melanoma mostly occurs in the cerebral meninges. For patients who are highly suspected of having melanoma, their melanoma history should be carefully investigated.

PWI of MRI is applied for the evaluation of the angiogenesis in brain tissues, by measuring cerebral blood volume; while DWI can be used for the analysis of specific tissues. However, the diagnosis of melanoma by PWI combined with DWI is rarely reported at home and abroad [27, 28]. In this study, some patients underwent DWI scanning with the results showing diverse signal manifestations. Primary or solitary metastases showed high or equally high signals of varying degrees, and multiple metastases was shown low signals. Under PWI scanning, rCBV was showed to increase, which suggested the high tumor perfusion. Such results were of some predictive significance for the diagnosis of melanoma.

5. Conclusion

In this work, a multimodal 3D image hybrid segmentation algorithm was utilized for observing the MRI findings of melanoma patients. It was discovered that the MRI manifestations of most melanoma patients were complex and diverse, showing different low, high, or mixed signals. DWI combined with PWI examination under the 3D hybrid segmentation algorithm had the advantages of great clarity and accuracy, providing certain value in the diagnosis of melanoma. The disadvantage was that the sample size of this work was small, which needed further supplementation and improvement in the future. This work offered a theoretical reference for the clinical diagnosis and treatment of melanoma.

Data Availability

The data used to support the findings of this study are available from the corresponding author upon request.

Conflicts of Interest

The authors declare that there are no conflicts of interest.

Acknowledgments

This work was supported by Rongxiang Regenerative Medicine Foundation of Shandong University (2019SDRX-08).

References

[1] R. Cabrera and F. Recule, "Unusual clinical presentations of malignant melanoma: a review of clinical and histologic features with special emphasis on dermatoscopic findings," *American Journal of Clinical Dermatology*, vol. 19, no. S1, pp. 15–23, 2018.

[2] M. Fujimoto, I. Matsuzaki, K. Nishitsuji et al., "Adipophilin expression in cutaneous malignant melanoma is associated with high proliferation and poor clinical prognosis," *Laboratory Investigation*, vol. 100, no. 5, pp. 727–737, 2020.

[3] A. Mastoraki, D. Schizas, I. Giannakodimos et al., "Malignant melanoma of the breast: controversies in the diagnosis and therapeutic management of a rare nosologic entity," *International Journal of Dermatology*, vol. 59, no. 9, pp. 1057–1064, 2020.

[4] N. Yang, J. Lu, Y. Lu, J. Guo, and H. Wang, "Primary malignant melanotic melanoma and hypomelanotic melanoma of the female urethra: case series and a review of the literature in China," *Melanoma Research*, vol. 29, no. 1, pp. 59–64, 2019.

[5] E. Harrington, B. Clyne, N. Wesseling et al., "Diagnosing malignant melanoma in ambulatory care: a systematic review of clinical prediction rules," *BMJ Open*, vol. 7, no. 3, Article ID e014096, 2017.

[6] J.-W. Shao, J.-H. Yin, S.-T. Xiang, Q. He, H. Zhou, and W. Su, "CT and MRI findings in relapsing primary malignant melanoma of the lacrimal sac: a case report and brief literature review," *BMC Ophthalmology*, vol. 20, no. 1, p. 191, 2020.

[7] M. Kawaguchi, H. Kato, H. Tomita et al., "MR imaging findings for differentiating cutaneous malignant melanoma from squamous cell carcinoma," *European Journal of Radiology*, vol. 132, Article ID 109212, 2020.

[8] J. H. Francis, F. Catalanotti, J. Landa, C. A. Barker, A. N. Shoushtari, and D. H. Abramson, "Hepatic abnormalities identified by staging MRI and accuracy of MRI of patients with uveal melanoma," *British Journal of Ophthalmology*, vol. 103, no. 9, pp. 1266–1271, 2019.

[9] M. G. Jaarsma-Coes, T. A. Goncalves Ferreira, G. R. van Haren, M. Marinkovic, and J.-W. M. Beenakker, "MRI enables accurate diagnosis and follow-up in uveal melanoma patients

after vitrectomy," *Melanoma Research*, vol. 29, no. 6, pp. 655–659, 2019.

[10] F. Mosavi, G. Ullenhag, and H. Ahlström, "Whole-body MRI including diffusion-weighted imaging compared to CT for staging of malignant melanoma," *Upsala Journal of Medical Sciences*, vol. 118, no. 2, pp. 91–97, 2013.

[11] E. Gumeler, S. Parlak, G. Yazici, E. Karabulut, H. Kiratli, and K. K. Oguz, "Single shot echo planar imaging (ssEPI) vs single shot turbo spin echo (ssTSE) DWI of the orbit in patients with ocular melanoma," *British Journal of Radiology*, vol. 94, no. 1118, Article ID 20200825, 2021.

[12] G. S. Young and K. Setayesh, "Spin-echo echo-planar perfusion MR imaging in the differential diagnosis of solitary enhancing brain lesions: distinguishing solitary metastases from primary glioma," *American Journal of Neuroradiology*, vol. 30, no. 3, pp. 575–577, 2009.

[13] M. Hu, Y. Zhong, S. Xie, H. Lv, and Z. Lv, "Fuzzy system based medical image processing for brain disease prediction," *Frontiers in Neuroscience*, vol. 15, Article ID 714318, 2021.

[14] N. Fan, S. Yuan, P. Du et al., "Design of a robot-assisted system for transforaminal percutaneous endoscopic lumbar surgeries: study protocol," *Journal of Orthopaedic Surgery and Research*, vol. 15, no. 1, p. 479, 2020.

[15] S. Xie, Z. Yu, and Z. Lv, "Multi-disease prediction based on deep learning: a survey," *Computer Modeling in Engineering and Sciences*, vol. 128, no. 2, pp. 489–522, 2021.

[16] M. G. Jaarsma-Coes, T. A. Ferreira, G. P. M. Luyten, and J. W. M. Beenakker, "Reaction on "Ocular ultrasound versus MRI in the detection of extrascleral extension in a patient with choroidal melanoma"," *BMC Ophthalmology*, vol. 19, no. 1, p. 193, 2019.

[17] Z. Lv and L. Qiao, "Analysis of healthcare big data," *Future Generation Computer Systems*, vol. 109, pp. 103–110, 2020.

[18] M. J. Sladden, O. E. Nieweg, J. Howle, B. J. Coventry, and J. F. Thompson, "Updated evidence based clinical practice guidelines for the diagnosis and management of melanoma: definitive excision margins for primary cutaneous melanoma," *Medical Journal of Australia*, vol. 208, no. 3, pp. 137–142, 2018.

[19] D. Chen, P. Wawrzynski, and Z. Lv, "Cyber security in smart cities: a review of deep learning-based applications and case studies," *Sustainable Cities and Society*, vol. 66, Article ID 102655, 2020.

[20] F. Piscioli, T. Pusiol, and L. Roncati, "Nowadays a histological sub-typing of thin melanoma is demanded for a proper patient management," *Journal of Plastic, Reconstructive & Aesthetic Surgery*, vol. 69, no. 11, pp. 1563-1564, 2016.

[21] Y. Zeng, Y. Zeng, H. Yin et al., "Exploration of the immune cell infiltration-related gene signature in the prognosis of melanoma," *Aging (Albany NY)*, vol. 13, no. 3, pp. 3459–3482, 2021.

[22] Y. Su, X. Xu, P. Zuo et al., "Value of MR-based radiomics in differentiating uveal melanoma from other intraocular masses in adults," *European Journal of Radiology*, vol. 131, Article ID 109268, 2020.

[23] Y.-K. Kim, J. W. Choi, H.-J. Kim et al., "Melanoma of the sinonasal tract: value of a septate pattern on precontrast T1-weighted MR imaging," *American Journal of Neuroradiology*, vol. 39, no. 4, pp. 762–767, 2018.

[24] J. Liu, J. Chen, Y. Zha, Y. Huang, and F. Zeng, "Magnetic resonance imaging (MRI) differential diagnosis of meningiomas using ANOVA," *Contrast Media and Molecular Imaging*, vol. 10, p. 2021, Article ID 4799116, 2021 Jul.

[25] S. Tang, J. Zuo, H. Zhang, Z. Wu, and B. Liang, "Spinal metastatic melanoma with unknown primary lesions presenting as radiculopathy: case report and literature review," *World Neurosurgery*, vol. 140, pp. 320–324, 2020.

[26] P. M. LoRusso, K. Schalper, and J. Sosman, "Targeted therapy and immunotherapy: emerging biomarkers in metastatic melanoma," *Pigment Cell & Melanoma Research*, vol. 33, no. 3, pp. 390–402, 2020.

[27] K. Askaner, A. Rydelius, S. Engelholm et al., "Differentiation between glioblastomas and brain metastases and regarding their primary site of malignancy using dynamic susceptibility contrast MRI at 3T," *Journal of Neuroradiology*, vol. 46, no. 6, pp. 367–372, 2019.

[28] M. A. McDonald, P. Sanghvi, J. Bykowski, and G. A. Daniels, "Unmasking of intracranial metastatic melanoma during ipilimumab/nivolumab therapy: case report and literature review," *BMC Cancer*, vol. 18, no. 1, p. 549, 2018.

Hindawi
Contrast Media & Molecular Imaging
Volume 2022, Article ID 9383982, 9 pages
https://doi.org/10.1155/2022/9383982

Research Article

Stereotactic Surgery of Parkinson's Disease with Magnetic Resonance Imaging under Three-Dimensional Mark Point Positioning Algorithm

Yuan Jia,[1] **Zengguang Wang**,[2] **Xiang Sun**,[1] **and Yipin Zhou**[1]

[1]*Department of Neurosurgery, Tianjin Third Central Hospital, Tianjin 300170, China*
[2]*Department of Neurosurgery, Tianjin Medical University General Hospital, Tianjin 300052, China*

Correspondence should be addressed to Yipin Zhou; 201409040137@stu.sdnu.edu.cn

Received 4 April 2022; Revised 20 May 2022; Accepted 26 May 2022; Published 26 June 2022

Academic Editor: M. Pallikonda Rajasekaran

This research aimed to study the application of magnetic resonance imaging (MRI) under three-dimensional mark point positioning algorithm in stereotactic surgery for Parkinson's disease (PD) and improve clinical treatment effect. Eighty patients with PD in Tianjin Medical University General Hospital were selected as the research objects and randomly divided into two groups. The three-dimensional mark point positioning algorithm was applied to perform feature positioning on the MRI images of PD patients, and the international unified Parkinson's disease rating scale (UPDRS) was assessed before and after single-target surgery of the two groups. There was a significant difference in the postoperative treatment effect between the two groups compared with the preoperative one ($P < 0.05$). Among the patients in the observation group, 37 cases were marked as markedly effective, accounting for 92.5% of the total group; 1 case was ineffective and 2 cases were improved, accounting for 2.5% and 5%, respectively. In the control group, 35, 2, and 3 cases were assessed as markedly effective, ineffective, and improved, accounting for 87.5%, 5%, and 7.5%, respectively. The overall curative effect of the observation group was better than that of the control group, and the difference was significant ($P < 0.05$). The MRI manifestations of PD patients were diversified. MRI under the three-dimensional mark point positioning algorithm had a high value for the stereotactic treatment of PD patients, which was beneficial to the clinical surgery.

1. Introduction

Parkinson's disease (PD) is also called paralysis agitans, which is a neurodegenerative disease with relatively insidious onset and slow course [1, 2]. Most PD patients are sporadic cases, and a small number of patients with the family history account for 10%. The pathological mechanism of PD mainly lies in glial cell proliferation in different degrees of the substantia nigra pars compacta with dopamine, and the loss of some neurons. However, how this pathology causes PD exactly is still not very clear. The degeneration and death of the neurons need to be further explored, and other reasons such as aging, environmental factors, genetics, and oxidative stress have not yet been clearly known at current [3, 4]. For the population who are attacked by PD at the age of 60 years, relevant data show that there is a certain connection between the disease and aging. However, there is no such a trend in the 65-year-old group, and the morbidity is not high in the 65-year-olds. Therefore, more research is needed on how the neurons of PD patients change [5–7]. The clinical diagnosis of PD mainly relies on symptoms, signs, routine blood sample examinations, medical history, and so on [8]. In the examination of head, magnetic resonance imaging (MRI) and computerized tomography (CT) show no characteristic changes [9]. At present, there is no cure for PD, and the main treatment method is a combination of drugs and surgery. Stereotactic surgery is a method for the treatment of PD [10]. With the rapid development of imaging and neuroelectrophysiology, the use of brain stereotaxic technology to treat PD has become an important treatment method. Stereotactic surgery is safe and effective for PD, and the precise positioning of the target can improve the surgical efficacy and reduce complications.

The motor system of PD patients is abnormal, and the lack of dopamine in the brain causes the dysfunction of cortex-striatum-cortex circuits. How the network with the complex process works and how it performs abnormally are still uncertain. At present, resting-state functional MRI has been used in the research of PD pathology and has shown certain effects. MRI can locate in multiple directions and has high resolution for soft tissues, so that it is widely used for the diagnosis of many diseases clinically [11, 12]. MRI would lead to fewer complications in stereotactic surgery, with less loss and a relatively simpler method [13, 14]. Examination results of MRI can be observed at multiple angles, multiple slices, and multiple directions. The computer system can convert the anatomical mark points into coordinate values, eliminating measurement errors, and can display the morphological structure of the soft tissues of the craniofacial region clearly without radiation. Although MRI can clearly show the structure of the brain tissues, there are relatively few studies on MRI in examining the brain of PD patients [15, 16]. In the clinical practice, there are differences in the position of the two-dimensional image displayed, and the left and right of the anatomical image cannot overlap well, so there is the distortion in image. This also causes error in a certain degree in the diagnosis, resulting in misdiagnosis and missed diagnosis. The two-dimensional image cannot fully show the real anatomy, and the detection result is not correct enough [17]. Three-dimensional imaging in MRI images can clearly show the exact anatomical positioning, display the measurement of the image accurately, and locate the lesion on the three-dimensional brain image of the patients clearly [18, 19].

In the case of clear 3D MRI images, this study constructed a method for locating anatomical markers in the brain, combined with the accurate positioning of surgical targets, which provided a basis for the development of single-scan MRI image parameters and improved surgical efficacy, thus segmenting MRI images, analyzing the characteristics of PD patients from different directions, reducing the incidence of patient complications, and improving the accuracy of surgery.

2. Materials and Methods

2.1. Research Object. Retrospective analysis of PD patients in Tianjin Medical University General Hospital was made, and those patients were chosen as the research objects. The modern multifunctional video therapy equipment and high-precision brain stereotaxic instrument were used to treat the PD patients who joined the study. 40 patients who underwent three-dimensional mark point positioning surgery were included in the observation group. The age of the patients was 42 ± 72 years with an average age of 51.23 ± 3.24 years, and the course of disease was (11 ± 7). 16 patients out of them had the PD of tremor type, 9 patients had the tetanic PD, and 15 patients had the mixed PD. Another 40 patients in the control group received ordinary surgical treatment. They aged 41 ± 69 years with an average age of 49.23 ± 2.67 years and course of disease of (12 ± 4). 19 of them suffered from tremor PD, 11 patients had the tetanic type, and 10 patients were classified into the mixed type. This study had been approved by ethics committee of hospital, and all the study objects and their families were informed and voluntarily agreed to participate in this study.

The following inclusion criteria were formulated: All study objects were evaluated by experienced neurologists using the unified Parkinson's disease rating scale (UPDRS). The patients offered complete general clinical information. They met the treatment indications and had not interrupted all treatment in the hospital. All the objects self-cooperated with the diagnosis and treatment.

Exclusion criteria were as follows: The patients had language communication disorders, serious diseases like organic diseases of the hematopoietic system, or mental illnesses. Patients had a poor compliance in the treatment. Patients stopped treatment for some cause. Patients had systemic infections or brain diseases in other parts of the body.

2.2. MRI Image Acquisition Method. The patients stopped taking levodopa drugs 1 day before the surgery. On the day of the surgery, a stereotactic frame was laid down on the patient's head, and a high-resolution MRI examination was made. For functional positioning, the CRW stereotaxic system utilized was the Leksell system of Elekta AB, Sweden. Brain MRI was performed with 1.5T magnetic resonance machine by Signa, GE Corporation. The receiving coil was an abdominal phased array winding coil, while the radio frequency transmitting coil was a body coil. The sagittal and axial planes were selected for the positioning of the target point under direct vision. The scanning plane was required to be parallel to the anterior commissure-posterior commissure (AC-PC). The coordinates of the target nuclei were located with the midpoint of AC-PC as the original point, $X = \pm 10$–± 13 mm, $Y = -1$ to -2 mm, and $Z = -2$ to -6 mm. The selected conventional coronal and sagittal parameters were as follows. Time of repetition (TR)/time of echo (TE) = (3500–3800) ms/130 ms; for T2WI signal, fat saturation fast recovery fast spin echo (fs FRFSE) was X, number of excitations (NEX) = 2–4, the field of view (FOV) = 26. For the sectional spin echo-echo planar imaging (SE-EPI) sequence of diffusion-weighted imaging (DWI), $b = 700$, TR/TE = 4000 ms/73 ms. For the cross-sectional T1WI signal, fat-saturated fast-spin echo (fs FSE) was XL, TR/TE = 400 ms/8 ms, NEX = 2, and FOV = 32. For the cross-sectional T2WI signal, fs FRFSE was XL, TR/TE = 4000 ms/130 ms, NEX = 4, and FOV = 32.

2.3. Mark Point Behavior Algorithm. Directed against digital image algorithm for straight line and circular feature detection, image mark point algorithm has been applied in a lot of research worldwide. For straight line features, Paul Hough proposed a transformation method to detect straight lines in binary images. If the variable XY was regarded as a constant, the linear equation in Figure 1(a) was transformed into the

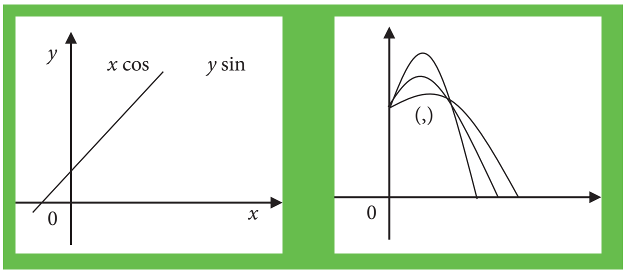

Figure 1: Representation of the same straight line in the parameter space of the image space domain.

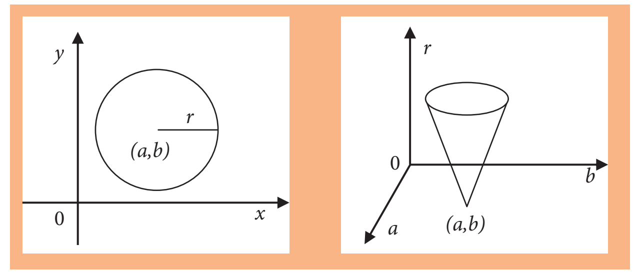

Figure 2: Schematic diagram of duality in image space and parameter space.

parameter space. Then, it was transformed again into a cluster of sinusoids in the parameter space, as shown in Figure 1(b). The edge points of the binary image can be adopted to determine the straight-line equation, which was that the Hough transform was used to detect the straight line.

For the detection of circular mark points, the algorithm was introduced and extended to detect circles, ellipses, and parabolic curves with analytical expression $f(x, y)$ according to the equations. It was assumed that the center of the circle was $O(a, b)$ and the radius was r, and the detection of the circular mark points was carried out in the discretized space. The three-dimensional accumulation array $A(a, b, r)$ was established, and after any point (x_i, y_i) on the circumference in the image space was transformed into the parameter space, the corresponding value of r could be computed with the changes of center of the circle in the parameters. It was accumulated on point A, and finally a three-dimensional cone was formed in the parameter space (Figure 2).

On the basis of positioning of the center of the circular mark points, the flow of mark point positioning and matching is shown in Figure 3. First, the coordinate position of point AB was determined, and the collinearity of multiple points was found. The mark point module utilized one-mark point matching module in the image acquisition channel, which matched the mark points in a certain order.

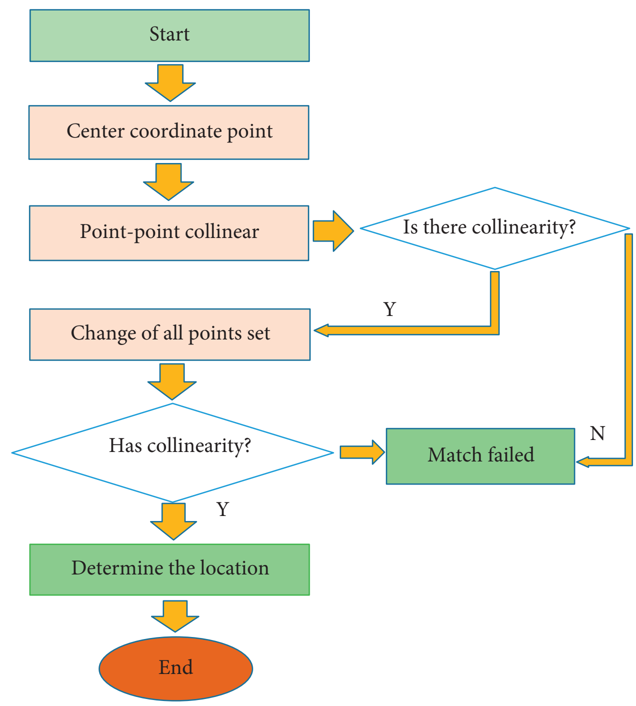

Figure 3: Flowchart of mark point matching.

2.4. Surgical Operating Methods. Surgical target positioning was carried out in the control group. After the CRW stereotaxic head coil was installed, MRI scanning was performed in the sagittal, transverse, and coronal planes. The target was determined by the image direct positioning method combined with coordinate value positioning, and the target coordinates were calculated. As the microelectrodes and electrophysiological recording system produced by FHC Inc. were used, the functional positioning of the anatomically positioned targets was made and confirmed.

In the observation group, stereotaxic surgery and MRI anatomical positioning were given. The puncture path was designed to avoid the cerebral ventricles and cerebral sulcus blood vessels as much as possible. Before surgery, the scalp incision was cut according to the designed puncture path under local anesthesia, the skull was drilled, and the puncture was performed through the bone hole. The hard channel of the puncture sleeve was indwelled, the recording electrode was implanted at the target coordinates through the puncture sleeve, and the discharges of neurons in different positions were recorded. Satisfactory subthalamic nucleus (STN) and substantia nigra spontaneous discharge signals were obtained, which showed high-frequency and high-amplitude cell discharges with high background noise and tremor-related cells. Electrophysiological recording of STN targets was made, eliminating the influence of image drift and brain tissue displacement caused by intraoperative cerebrospinal fluid loss. After the position of the target point was determined, the stimulating electrode was implanted, and the discharge stimulation was conducted while the patient kept awake. The self-reported symptoms and symptom changes of the patients after the electrical stimulation were recorded under electrical stimulations in different frequencies and amplitudes, for the setting and adjustment of the electrical stimulation parameters in the later stage. The initial stimulation parameters were generally set to a frequency of 130 Hz, a pulse width of 60 μs, and a voltage of 1.0–1.5 V. The stimulation voltage was adjusted according to the patient's tolerance and response, generally not exceeding 3.0 V. As the recording was completed, the stimulation was stopped, and the stimulating electrode was fixed. MRI was performed for checking and verifying the position of electrode implantation, and it was observed whether the intracranial hemorrhage or other complications occurred. Afterwards, general anesthesia was given. A saccular space was freed subcutaneously of the right chest, and the stimulation pulser was embedded. The subcutaneous tunnel from the right chest incision to the cephalic incision was connected and penetrated, and the connecting wire was embedded to connect the stimulating electrode and the stimulation pulser. The program controller was used in vitro for detecting the connection of the deep brain stimulation system. After the connection was detected to work normally, the system was shut down temporarily, and the incisions were sutured. Levodopa drugs were retaken in the preoperative dose after surgery. The cerebral edema subsided, and the microdamage effect disappeared 1 month after surgery.

The curative effect of PD patients was judged depending on their emotional state, mental state, and behavior pattern. The side effects of drugs, motor function, activities of daily living, and so forth were also evaluated. Patients' status was assessed 1 month before surgery and 1 month after surgery, respectively; the dose of medication remained unchanged after surgery. With the equation preoperative UPDR–postoperative UPDRS/preoperative UPDRS × 100%, it was evaluated whether the symptoms were improved.

2.5. Image Processing. Noise would reduce the signal-to-noise ratio of the image, in which edge detection cannot be performed well. This affects the accuracy and speed of marking seriously. Therefore, it is necessary to denoise the obtained images. Noise interference must be avoided before the mark point positioning, and the identification of mark points was needed after edge detection. The wavelet change was developed by the Fourier transform, with the square integrated in the real number domain of the signal W. The Fourier change was $\widehat{W}$, W, and $\widehat{W}$, which can decay fast enough. Then, the function equation was generated.

$$ab(w)\frac{1}{\sqrt{a}}\left(\frac{tb}{a}\right). \tag{1}$$

In equation (1), b was the translation factor and a was the expansion factor. After the wavelet was established and satisfied, the continuous integrable function $f(W)$ in the real number domain was expressed as the following equation:

$$f(w) = \frac{1}{c}\frac{1}{a^2}wf(a,b)\left(\frac{tb}{a}\right)\mathrm{d}a\mathrm{d}b. \tag{2}$$

2.6. Statistical Analysis. SPSS19.0 was used for statistical analysis of the data in this study. The measurement data was expressed in the form of mean ± standard deviation, and the nonconforming enumeration data were expressed in the frequency (%). t-test was adopted to compare differences in the data, and $P < 0.05$ indicated that the difference was statistically significant.

3. Results and Analysis

3.1. Preprocessing of MRI Images. The results of brain MRI imaging analysis showed that after the image was denoised, Figure 4(b) had a higher clarity than Figure 4(a). Noise reduced the signal-to-noise ratio of the image. After denoise, the mark points in the image could be clear positioned, and edge detection could also be performed for mark point recognition.

3.2. MRI Image under Three-Dimensional Mark Point Positioning Algorithm. MRI of PD patients was evaluated, and the results are shown in Figure 5. Figures 5(a)–5(c) clearly show the brain structure as well as the diseased location of the PD patient in different axial positions. Figures 5(d)–5(f) are the effect diagrams using three-dimensional mark point positioning to process the MRI images in different axial positions. It could be observed that it realized the positioning of the diseased location of the patient.

3.3. Positioning Effect of MRI Images. For the MRI images of patients in the observation group, the correlation coefficient distribution within the XYZ axes of the anatomical points is shown in Figure 6. The anatomical points were distributed within the patients with a correlation coefficient ≥0.9, and the correlation coefficient between the Y axis and the Z axis was also ≥0.9. It suggested that the repeatability was very high, and the stability was great.

Eight three-dimensional mark points in the brain MRI image were selected, respectively, with the same positioning accuracy and the same Talairach grid system of each set of data. The transformation parameters of the global registration were also the same. Figure 7 shows that, for the main body classification of lateral brain and lateral ventricle, the positioning mark point 55 had a large error.

The positioning errors of different mark points were selected in the clinical data and the Brain web data set. The statistical results of the positioning errors of different mark point models are shown in Figure 8. The mark point models had a small effect on the accuracy of the mark points in this study.

3.4. Evaluation and Comparison of UPDRS for Patients before and after Surgery. The curative effect of patients was counted with the data one month after surgery. The UPDRS evaluation results of patients in the two groups before and after single-target surgery are shown in Figure 9. The curative effect of the two groups after surgery was significantly different from that before surgery, and the difference was significant ($P < 0.05$). The overall curative effect of the observation group was significantly better than that of the control group. The long-term effect was still to be observed in the follow-up.

3.5. Comparison of the Curative Effects. As shown in Table 1, 37 cases in the observation group had the markedly effective effect, accounting for 92.5% of all the PD patients in the observation group. 1 case showed the ineffective effect and 2 cases showed the improved effect, accounting for 2.5% and

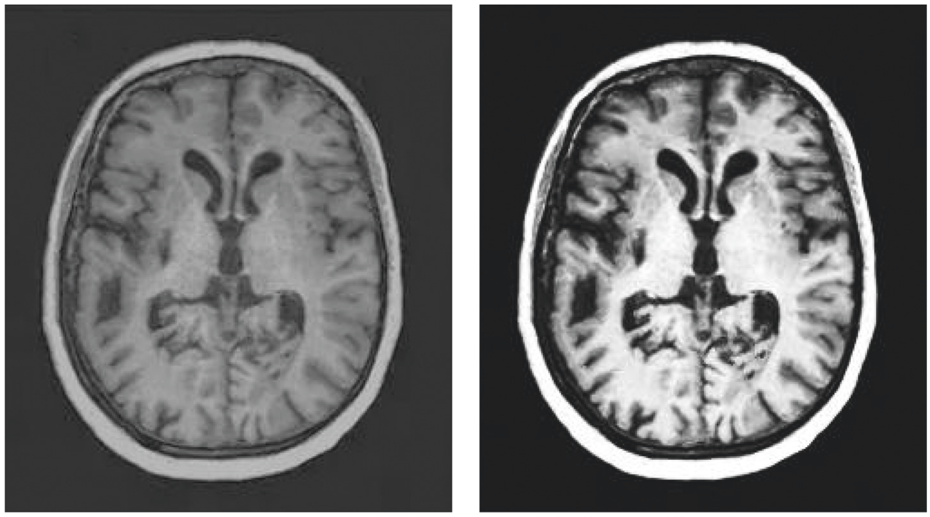

(a) (b)

Figure 4: Comparison of image denoise processing.

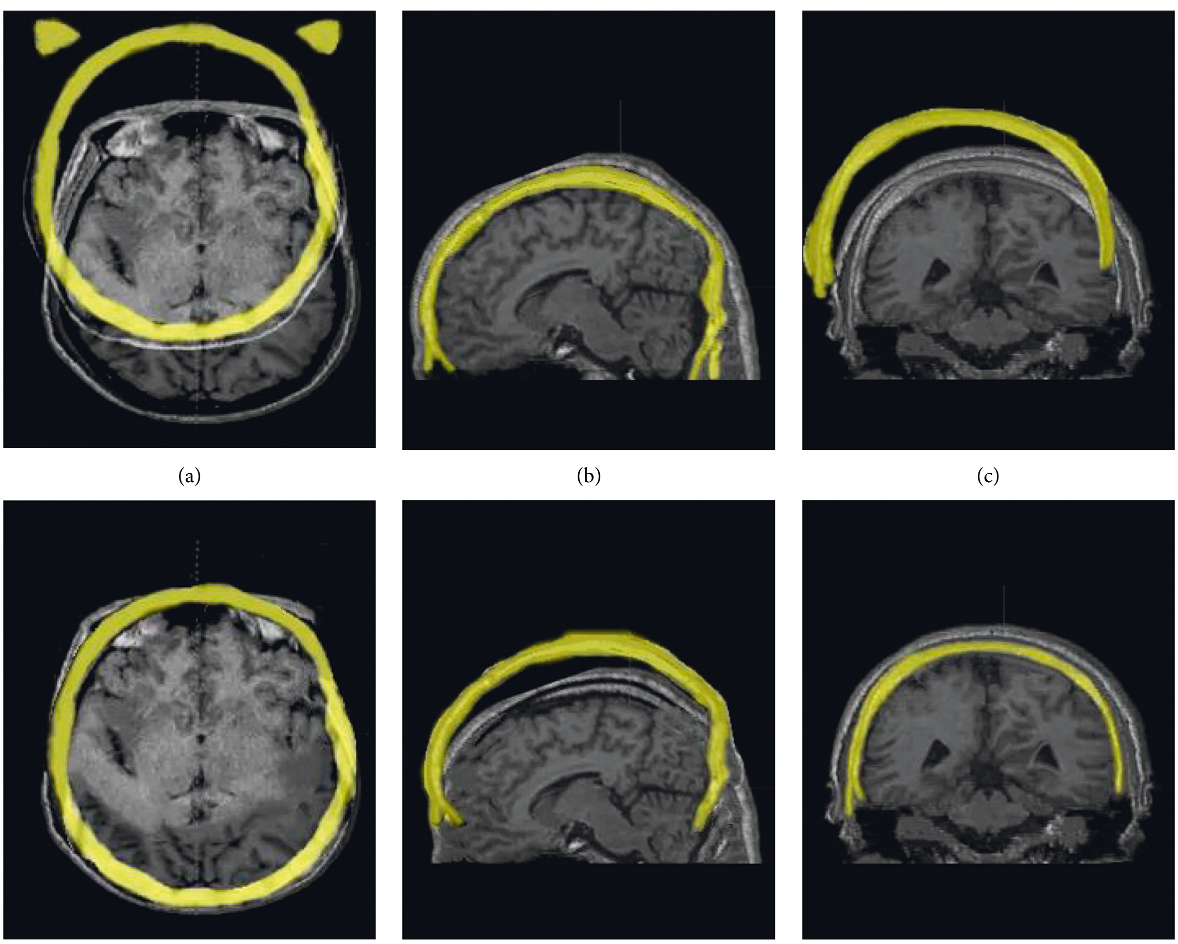

(a) (b) (c)

(d) (e) (f)

Figure 5: MRI images under the three-dimensional mark point positioning algorithm.

5%, respectively. In the control group, 35 cases had markedly effective effect, 2 cases went with ineffective effect, and 3 cases were improved, which accounted for 87.5%, 5%, and 7.5%, respectively. The overall curative effect of patients in the observation group was significantly different from that in the control group ($P < 0.05$).

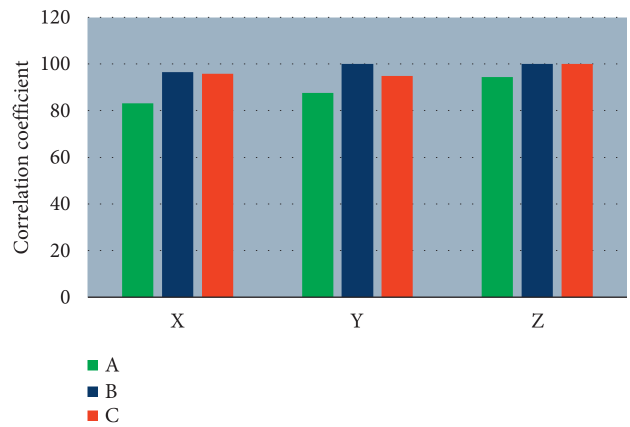

FIGURE 6: Correlation coefficient distribution within the XYZ axes in the observation group. ABC indicates different anatomical points.

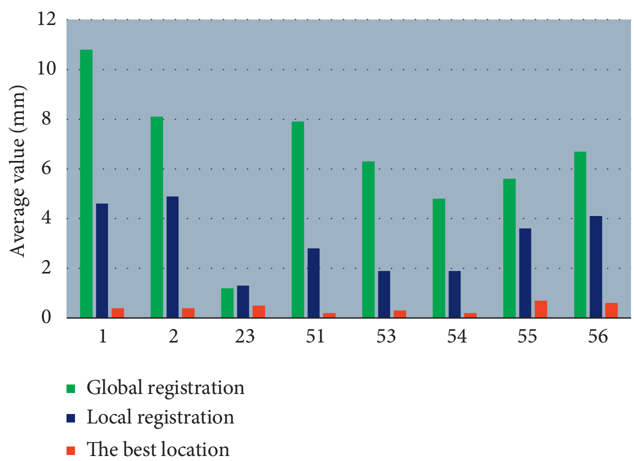

FIGURE 7: Analysis results of the positioning error of each step for the mark points in the data set.

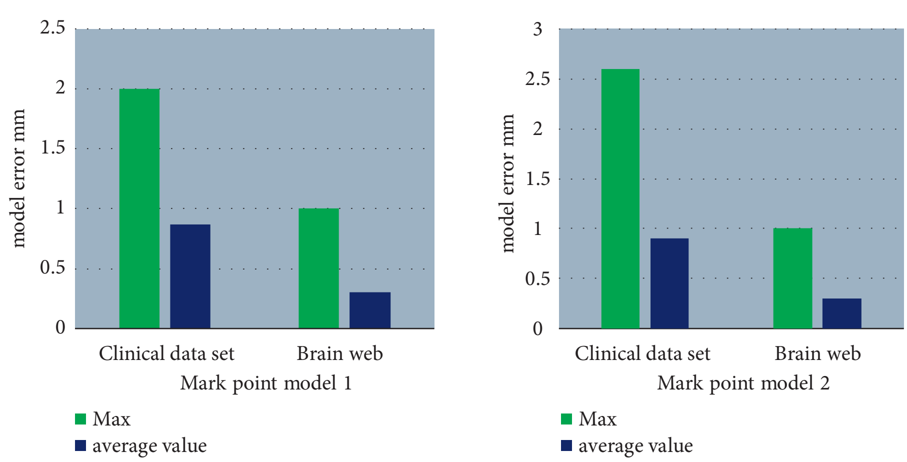

FIGURE 8: Statistical results of positioning errors of different mark point models.

4. Discussion

PD cannot be completely cured, and it progresses slowly. Stereotactic surgery has become a fixed surgical method for the treatment of PD, having a significant effect on eliminating tremor and tetany. Chronic electrical stimulation to deep brain, gene therapy, brain core damage, and nerve tissue transplantation are all surgical treatments [20]. Li et al. [21] used a machine learning method of spatial coupling penalty to analyze the MRI images of PD patients

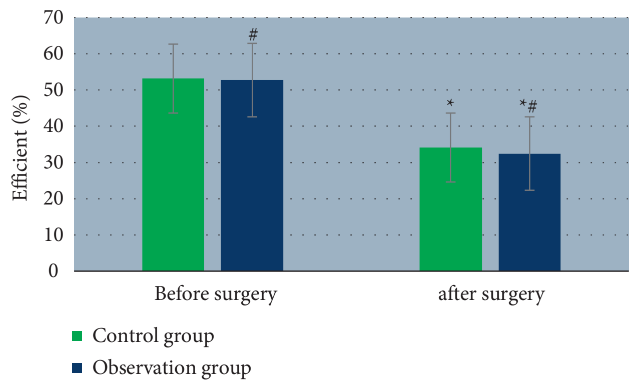

Figure 9: The ability of MRI to diagnose the depth of myometrial invasion. The symbol # indicates the significant difference between the two groups before and surgery ($P < 0.05$) and $*$ indicates that before surgery and after surgery in the same group ($P < 0.05$).

Table 1: Comparison of curative effects in the two groups.

Groups	Markedly effective		Ineffective		Improved	
Observation group	37	92.5%	1	2.5%	2	5.0%
Control group	35	87.5%	2	5.0%	3	7.5%
Chi-square			7.939			
P value			0.001			

and found that MRI images can well identify the ROI of PD patients. Intracranial responses in patients may predict outcomes. Kotecha et al. [22] demonstrated that stereotactic radiosurgery can be very good for the treatment of brain metastases. PD cannot be cured under any surgical treatment, so a surgery is aimed to relieve the condition of patients and improve symptoms, thereby the course of disease would be prolonged and the pain of patients would be reduced. Therefore, not all patients are suitable for stereotactic surgery, which is also the reason why the surgical result cannot reach 100% in a lot of research. Many factors in the surgical treatment play a corresponding role in the diagnosis and treatment of the disease, including the patients' condition, degree of cooperation, clinical experience, and general function status; the selection of the target during the surgery depends on clinical experience of the physicians [23]. Furlanetti et al. [24] experimented with stereotaxic imaging to reduce the duration and cost of image acquisition without compromising accuracy. In this study, 37 patients (92.5%) in stereotactic surgery had an effect markedly effective. Some scholars stated that stereotactic surgery has contraindications for patients over 70 years old, but the age is not a decisive factor. In this study, there is a 71-year-old male patient who underwent the bilateral surgery, and it also showed a good result after surgery. In stereotactic surgery, the installation of the stereotactic instrument should be standard and adjusted to the best position that the patients felt the most comfortable. During the surgery, fixed personnel were selected for projection to ensure the surgery went smoothly. The treatment of PD in China has been carried out with deep brain stimulation surgery, which is nondestructive with relatively few side effects and complications. The curative effect of stereotactic surgery has been affirmed in many studies. This study also proved the effectiveness of the surgery. It costs less and is suitable for promotion at the grassroots level.

MRI can perform imaging in multiple planes, without radiation, and the soft tissue resolution in the images is good. It has shown good results in stereotactic surgery. Functional MRI analyzes the entire brain area from the perspective of functional integration, determines the directionality among brain areas, and connects the brain areas of interest in the model. In this process, it is affected by functional imaging and neuroanatomy, and the "seed point" is generally chosen for functional connection analysis method to discuss the functional connection of PD patients or normal brains in the resting state [25, 26]. Ryman and Poston [27] used biomarkers to explore the neuropathology of PD patients, and the functional characteristics of dopamine in the brain were shown through MRI image analysis. The results of this study showed that MRI had the clear images and high resolution, giving a high accuracy for PD imaging. In stereotactic surgery, 37 cases were treated as markedly effective, accounting for 92.5%. The three-dimensional mark point positioning algorithm was of important clinical significance in MRI imaging of PD patients.

5. Conclusion

In this study, the three-dimensional mark point positioning algorithm was applied to the MRI of PD patients, which improved the efficiency of image feature extraction and classification of patients effectively. It was suggested that MRI was significantly improved with a markedly effective rate of 92.5% in stereotactic surgery. Although the mark point positioning algorithm had good results, it cannot achieve 100% in accurate positioning with unavoidable errors. In practical applications, there were still shortcomings such as the inability of test data to completely eliminate the interference of subjective factors, so the indicators can be standardized in further research. As the images selected in this study were relatively single, image anatomical points can be analyzed from multiple angles in the future, and more samples can also be added to expand the study of PD patients.

Data Availability

The data used to support the findings of this study are available from the corresponding author upon request.

Conflicts of Interest

The authors declare no conflicts of interest.

Authors' Contributions

Yuan Jia and Zengguang Wang are contributed equally to this work.

Acknowledgments

This work was supported by Tianjin Science and Technology Planning Project (No. 20YFZCSY00010).

References

[1] E. Fiorenzato, A. P. Strafella, J. Kim et al., "Dynamic functional connectivity changes associated with dementia in Parkinson's disease," *Brain*, vol. 142, no. 9, pp. 2860–2872, 2019.

[2] G. Carey, M. Görmezoğlu, J. J. A. Jong et al., "Neuroimaging of anxiety in Parkinson's disease: a systematic review," *Movement Disorders*, vol. 36, no. 2, pp. 327–339, 2021.

[3] G. E. C. Thomas, L. A. Leyland, A.-E. Schrag, A. J. Lees, J. Acosta-Cabronero, and R. S. Weil, "Brain iron deposition is linked with cognitive severity in Parkinson's disease," *Journal of Neurology, Neurosurgery & Psychiatry*, vol. 91, no. 4, pp. 418–425, 2020.

[4] B. Bluett, E. Bayram, and I. Litvan, "The virtual reality of Parkinson's disease freezing of gait: a systematic review," *Parkinsonism & Related Disorders*, vol. 61, pp. 26–33, 2019.

[5] L. Griffanti, J. C. Klein, K. Szewczyk-Krolikowski et al., "Cohort profile: the oxford Parkinson's disease centre discovery cohort MRI substudy (OPDC-MRI)," *BMJ Open*, vol. 10, no. 8, Article ID e034110, 2020.

[6] C. W. Christine, K. S. Bankiewicz, A. D. Van Laar et al., "Magnetic resonance imaging-guided phase 1 trial of putaminal AADC gene therapy for Parkinson's disease," *Annals of Neurology*, vol. 85, no. 5, pp. 704–714, 2019.

[7] N. Wright, A. Alhindi, C. Millikin et al., "Elevated caudate connectivity in cognitively normal Parkinson's disease patients," *Scientific Reports*, vol. 10, no. 1, Article ID 17978, 2020.

[8] K. Bharti, A. Suppa, S. Tommasin et al., "Neuroimaging advances in Parkinson's disease with freezing of gait: a systematic review," *NeuroImage: Clinica*, vol. 24, Article ID 102059, 2019.

[9] O. Zarnowski, S. Ziton, R. Holmberg et al., "Functional MRI findings in personality disorders: a review," *Journal of Neuroimaging*, vol. 31, no. 6, pp. 1049–1066, 2021.

[10] A. Sejnoha Minsterova, P. Klobusiakova, A. Pies et al., "Patterns of diffusion kurtosis changes in Parkinson's disease subtypes," *Parkinsonism & Related Disorders*, vol. 81, pp. 96–102, 2020.

[11] A. R. Khan, N. M. Hiebert, A. Vo et al., "Biomarkers of Parkinson's disease: striatal sub-regional structural morphometry and diffusion MRI," *NeuroImage: Clinica*, vol. 21, Article ID 101597, 2019.

[12] O. Ekizoglu, A. Er, M. Bozdag, N. Moghaddam, and S. Grabherr, "Forensic age estimation based on fast spin-echo proton density (FSE PD)-weighted MRI of the distal radial epiphysis," *International Journal of Legal Medicine*, vol. 135, no. 4, pp. 1611–1616, 2021.

[13] C. Dreher, P. Linde, J. Boda-Heggemann, and B. Baessler, "Radiomics for liver tumours," *Strahlentherapie und Onkologie*, vol. 196, no. 10, pp. 888–899, 2020.

[14] M. Cathomas, N. Mertineit, C. Kim-Fuchs, A. Lachenmayer, and M. H. Maurer, "Value of MRI/CT image fusion for targeting "invisible" lesions in stereotactic microwave ablation (smwa) of malignant liver lesions: a retrospective analysis," *CardioVascular and Interventional Radiology*, vol. 43, no. 10, pp. 1505–1514, 2020.

[15] Y. Fang, L.-Y. Gu, J. Tian et al., "MRI-visible perivascular spaces are associated with cerebrospinal fluid biomarkers in Parkinson's disease," *Aging (Albany NY)*, vol. 12, no. 24, pp. 25805–25818, 2020.

[16] X. Guan, X. Xu, and M. Zhang, "Region-specific iron measured by MRI as a biomarker for Parkinson's disease," *Neuroscience Bulletin*, vol. 33, no. 5, pp. 561–567, 2017.

[17] Y. Zeighami, S.-M. Fereshtehnejad, M. Dadar, D. L. Collins, R. B. Postuma, and A. Dagher, "Assessment of a prognostic MRI biomarker in early de novo Parkinson's disease," *NeuroImage: Clinica*, vol. 24, Article ID 101986, 2019.

[18] S. Shinde, S. Prasad, Y. Saboo et al., "Predictive markers for Parkinson's disease using deep neural nets on neuromelanin sensitive MRI," *NeuroImage: Clinica*, vol. 22, Article ID 101748, 2019.

[19] A. Vo, W. Sako, K. Fujita et al., "Parkinson's disease-related network topographies characterized with resting state functional MRI," *Human Brain Mapping*, vol. 38, no. 2, pp. 617–630, 2017.

[20] A. Moussavi, S. Mißbach, C. Serrano Ferrel et al., "Comparison of cine and real-time cardiac MRI in rhesus macaques," *Scientific Reports*, vol. 11, no. 1, Article ID 10713, 2021.

[21] C. Li, X. Wang, G. Du et al., "Folded concave penalized learning of high-dimensional MRI data in Parkinson's disease," *Journal of Neuroscience Methods*, vol. 357, Article ID 109157, 2021.

[22] R. Kotecha, J. M. Kim, J. A. Miller et al., "The impact of sequencing PD-1/PD-L1 inhibitors and stereotactic radiosurgery for patients with brain metastasis," *Neuro-Oncology*, vol. 21, no. 8, pp. 1060–1068, 2019.

[23] J. Karlsson and G. Bertolizio, "Anesthesia Service provision for MRI: is shifting the technique enough?" *Pediatric Anesthesia*, vol. 31, no. 9, pp. 916-917, 2021.

[24] L. Furlanetti, H. Hasegawa, A. Oviedova et al., "O-arm stereotactic imaging in deep brain stimulation surgery workflow:

a utility and cost-effectiveness analysis," *Stereotactic and Functional Neurosurgery*, vol. 99, no. 2, pp. 93–106, 2021.

[25] R. C. Helmich, D. E. Vaillancourt, and D. J. Brooks, "The future of brain imaging in Parkinson's disease," *Journal of Parkinson's Disease*, vol. 8, no. s1, pp. S47–S51, 2018.

[26] A. P. Strafella, N. I. Bohnen, J. S. Perlmutter et al., "Molecular imaging to track Parkinson's disease and atypical parkinsonisms: new imaging frontiers," *Movement Disorders*, vol. 32, no. 2, pp. 181–192, 2017.

[27] S. G. Ryman and K. L. Poston, "MRI biomarkers of motor and non-motor symptoms in Parkinson's disease," *Parkinsonism & Related Disorders*, vol. 73, pp. 85–93, 2020.

Hindawi
Contrast Media & Molecular Imaging
Volume 2022, Article ID 2629868, 8 pages
https://doi.org/10.1155/2022/2629868

Research Article

Effect Evaluation of Perioperative Fast-Track Surgery Nursing for Tibial Fracture Patients with Computerized Tomography Images under Intelligent Algorithm

Mengmeng Zhang,[1] **Chuanbo Li**,[1] **and Fulan Rao**[2]

[1]*Department of Orthopaedics, People's Hospital of Chongqing Banan District, Chongqing 401320, China*
[2]*Department of Nursing, People's Hospital of Chongqing Banan District, Chongqing 401320, China*

Correspondence should be addressed to Mengmeng Zhang; 2018010100179@jlxy.nju.edu.cn

Received 13 March 2022; Revised 18 May 2022; Accepted 23 May 2022; Published 24 June 2022

Academic Editor: V. Muneeswaran

This study aimed to study the application value of computerized tomography (CT) images under the graph cut algorithm in the effect evaluation of perioperative fast-track surgery (FTS) nursing in tibial fracture. In this study, 80 tibial fracture patients in the perioperative period were selected as the research objects. These objects were randomly divided into two groups according to the examination method. In group A, routine CT examination was performed; in group B, CT examination under the graph cut algorithm was applied. The imaging results showed that there were still 16 cases with collapse of group A and 34 cases with collapse of group B; the difference was statistically significant ($P < 0.05$). As for 16 cases with collapse in both groups, the average collapse shown in group A was about 2.79 ± 1.31 mm, while that in group B was 5.51 ± 1.88 mm, with a statistically significant difference ($P < 0.05$). The average broadening in the images of group A was 3.17 ± 1.41 mm and that of group B was 5.72 ± 1.83 mm, suggesting that the difference was statistically significant ($P < 0.05$). The broadening distance of 3-4 mm was mainly shown in the images of group A and that of 5-8 mm was shown in group B, with a statistical difference ($P < 0.05$). In terms of the total score, there were 26, 44, 8, and 2 cases that were assessed as excellent, good, common, and bad, respectively, in group A, while 44 cases were assessed as good and 36 cases were assessed as common in group B, which were significantly different ($P < 0.05$). In summary, the graph cut algorithm not only had a good segmentation effect and segmentation efficiency but also could improve the evaluation of CT images for perioperative FTS nursing effect in patients with tibial fracture.

1. Introduction

A tibial fracture is one of the most common types of long tubular bone fractures, accounting for 10% to 15% of systemic fractures [1]. Because the tibias are very close to the ground, it is more likely to be knocked, crushed, or hit by direct violence. Therefore, open fractures are often caused by more serious contaminations, as infections are prone to occur and the wounds are difficult to heal [2]. The current methods of treating tibial fractures mainly include the surgical ones and nonsurgical ones [3, 4]. Nonsurgical methods include small splint external fixation and plaster external fixation; surgical methods mainly include internal fixations with interlocking intramedullary nails, general compression steel plates, external fixators, and locking compression plates combined with minimally invasive percutaneous plate osteosynthesis [5, 6]. If the treatment measures are unreasonable, it will cause many complications with the higher possibility of the disunion of fracture and skin necrosis [7]. Therefore, in addition to the basic rigorous monitoring after tibial fracture surgery, early fast-track surgery (FTS) nursing can reduce the possibility of complications significantly [8].

FTS was first proposed by Danish surgeon Henrik Kehlet in the 1990s. It refers to a number of improved perioperative nursing measures, to alleviate various adverse reactions of patients after surgery, reduce the length of hospital stays, and achieve the rapid recovery [9, 10]. FTS is a result of the continuous improvement of nutrition, surgery, nursing, anesthesiology, and other disciplines in the perioperative period. At present, FTS has been widely used in the nursing of orthopedic patients in perioperative period and has achieved quite great effects [11]. However, there is no sufficient research to prove the specific extent of joint recovery after FTS nursing of fracture patients in the perioperative period.

Clinically, the accurate measurement of the articular surface plays an important role in the evaluation of the recovery effect after fracture surgery. Computerized tomography (CT) and three-dimensional reconstruction technology can not only determine the degree and scope of joint surface damage accurately but also measure the distance of intra-articular bone splitting and the width or depth of collapse [12]. However, the previous semi-automatic segmentation methods of CT have the disadvantage that it is difficult to capture the true contours of the target. Thus, finding a more practical segmentation method is one of the major research directions in the field of medical image segmentation nowadays [13]. The proposed graph cuts algorithm, a machine intelligence algorithm, provides a new method for solving the practical issues of image segmentation; its wide application also promotes the improvement and perfection in itself continuously [14].

Therefore, CT under the graph cuts algorithm was utilized in this research, to evaluate the recovery of tibial fractures. Compared with routine CT, the application effect of intelligent algorithm-based CT and its application value in the evaluation of perioperative FTS nursing for patients with tibial fractures were discussed. This method had a reference value for the evaluation of perioperative recovery in patients with tibial fractures in the future.

2. Methodology

2.1. Research Objects. From May 2019 to December 2021, 80 patients with tibial fracture in the perioperative period were selected for this study. After FTS nursing was given, the recovery effect of their tibias was evaluated. The patients were randomly divided into two groups according to the detection methods, with routine CT examination in group A and CT examination under the graph cuts algorithm in group B. The examination results were compared. The patients included in the study signed the informed consent forms, and the experiments had been approved by the ethics committee of hospital.

Inclusion criteria were composed of the following. (1) the tibia fracture of patients was the primary fracture, and the joint motion before the fracture was not significantly different from that of the healthy limbs. (2) The fracture was a nonpathological fracture. (3) There was no ipsilateral fracture of both patella and distal femur. Exclusion criteria were listed as follows. (1) The patients had the complicated other acute or chronic osteomyelitis, or septic arthritis at the fracture site in the past. (2) Patients suffered from skin and soft tissue damage that had a great impact on knee function. (3) They had osteoarthritis, rheumatoid arthritis, or other arthritis before knee surgery on the ipsilateral tibial fracture.

2.2. Nursing. Patients in the group A were given routine rehabilitation nursing guidance, including admission education, preoperative nursing, intraoperative cooperation, postoperative nursing, and rehabilitation guidance.

The patients in group B were treated with the FTS nursing in addition to the routine rehabilitation nursing. The FTS team was formed, which was composed of orthopedic doctors, rehabilitation specialists, and responsible nurses. The orthopedic doctors propagandized the needs of the clinical prognosis, nursing priorities, and difficulties of tibial fracture patients to nursing staff and rehabilitation specialists and carried out health education and on-the-job training to improve their clinical nursing skills. Preoperative rehabilitation guidance was given as well. The preoperative fasting time for patients was shortened, and 200 mL 125% glucose injection was given two hours before the surgery. As different degrees of pain the patients with tibial fractures suffered from were taken into consideration, the pain level of the patients after surgery was evaluated. Targeted pain management strategies were formulated based on the pains of the patients including massaging the patients' extremities and adjusting the tightness of the splint reasonably, to avoid affecting the local blood supply circumstance and leading to local swelling and pain. For patients with high pain tolerance, their physical and mental health and treatment compliance could be improved by diverting their attention; they could be given analgesic measures to avoid the increase in the risk of complications due to pain factors. Daily rehabilitation exercise was a gradual progress, and passive and active exercises in bed after surgery were the main ones. It was recommended that patients got out of bed early, and the reasonable rehabilitation training plan should be designed based on the patients' physical outcome. The communication with the family members of patients was strengthened and the ability of accelerated supervision was improved, to help patients implement rehabilitation exercises safely and smoothly and ensure the quality of rehabilitation.

2.3. Graph Cuts Algorithm under Threshold Marker Automatic Generation. For the previous image cutting method, the corresponding histogram model was constructed by setting the foreground and background markers under manual interaction; the attributes of the remaining unmarked pixels were evaluated based on the model, to determine the area items [15]. However, in the modern age where intelligence, automation, and accuracy have been improved continuously, an image segmentation algorithm that can achieve segmentation automation or tend to be automated is needed, especially for complex and fuzzy medical images. Therefore, the graph cut algorithm that was suitable for the segmentation of bone tissue in CT images was applied under threshold marker automatic generation, to make up for the shortcomings of traditional graph cutting algorithms that required manual setting of foreground and background markers.

A grayscale image $E(x, y)$ with L (usually $L = 256$) gray levels was given; x and y represented the width and the height of the image, respectively. n was set as the total number of pixels in the image E, n_i was the number of pixels whose gray value was i, and p_i was the probability when the gray value was i. Then, the following equations were obtained:

$$p_i = \frac{n_i}{n}, \tag{1}$$

$$\sum_{i=0}^{L-1} p_i = 1 \tag{2}$$

A threshold t was given, and the image E was divided into two parts: background and foreground, which were represented by C_0 and C_1, respectively. As $C_0 = \{0, 1, 2, \ldots, t\}$ and $C_1 = \{t+1, t+2, \ldots, L-1\}$, the distribution probabilities w_0 and w_j of C_0 and C_1, respectively, were expressed by the following equations:

$$w_0 = \sum_{i=0}^{t} p_i, \tag{3}$$

$$w_1 = \sum_{i=t+1}^{L-1} p_i. \tag{4}$$

$w_0 + w_1 = 1$. The distribution mean values m_0 and m_1 of C_0 and C_1 were then expressed by the following equations:

$$m_0 = \sum_{i=0}^{t} i\frac{p_i}{w_0}, \tag{5}$$

$$m_1 = \sum_{i=t+1}^{L-1} i\frac{p_i}{w_1}. \tag{6}$$

The distribution variances s_0^2 and s_1^2 of C_0 and C_1, respectively, were expressed by the following equations:

$$s_0^2 = \frac{1}{w_0}\sum_{i=0}^{t} p_i \cdot (i - m_0)^2, \tag{7}$$

$$s_1^2 = \frac{1}{w_1}\sum_{i=t+1}^{L-1} p_i \cdot (i - m_1)^2. \tag{8}$$

The information entropy H_0 and H_1 of C_0 and C_1, respectively, were expressed by the following equations:

$$H_0 = -\sum_{i=0}^{t} \frac{P_i}{W_0} \cdot \log\frac{P_i}{W_0}, \tag{9}$$

$$H_1 = -\sum_{i=t+1}^{L-1} \frac{P_i}{W_1} \cdot \log\frac{P_i}{W_1}. \tag{10}$$

For the maximum entropy threshold segmentation, the sum of the information entropies of the foreground and background was maximized, so that the optimal threshold suitable for the image was obtained. In the image, the sum of entropy $f(t)$ of the foreground and background could be expressed by the following equation:

$$f(t) = H_0 + H_1. \tag{11}$$

Therefore, the optimal threshold t^* met the equation as follows:

$$t^* = \arg\left\{\max_{0 \le t \le L-1} f(t)\right\}. \tag{12}$$

For the minimum entropy threshold segmentation, a mixture Gaussian model was introduced by assuming that both foreground and background obeyed the Gaussian distribution. Then, the binary segmentation was transformed into the minimizing Gaussian distribution fitting issue. The solution objective function $J(t)$ was worked out with the idea of minimum classification error, as expressed in the following equation:

$$J(t) = 1 + w_0 \cdot \log\frac{S_0^2}{W_0^2} + w_1 \cdot \log\frac{S_1^2}{W_1^2}. \tag{13}$$

The optimal threshold t^* was finally obtained by minimizing $J(t)$, as the following equation shows:

$$t^* = \arg\left\{\min_{0 \le t \le L-1} J(t)\right\}. \tag{14}$$

In this work, the obtained tibial CT images of 4 cases were randomly selected for image evaluation experiment. To compute the Dice similarity coefficient, one of the image evaluation criteria, M was set as the set of image pixels under the gold standard for manual segmentation, and N was the set of all image pixels obtained by the semi-automatic or automatic segmentation algorithm. Then, the Dice similarity coefficient was obtained through the following equation:

$$\mathrm{Dice}(M, N) = \frac{2|M \cap N|}{|M| + |N|}. \tag{15}$$

If M and N did not intersect, the Dice similarity coefficient was 0; if M and N intersect completely, the Dice similarity coefficient was 1.

Because the consumed time of each sample was difficult to count, and there were errors among the time for each operation, the efficiency in this study is referred to as the

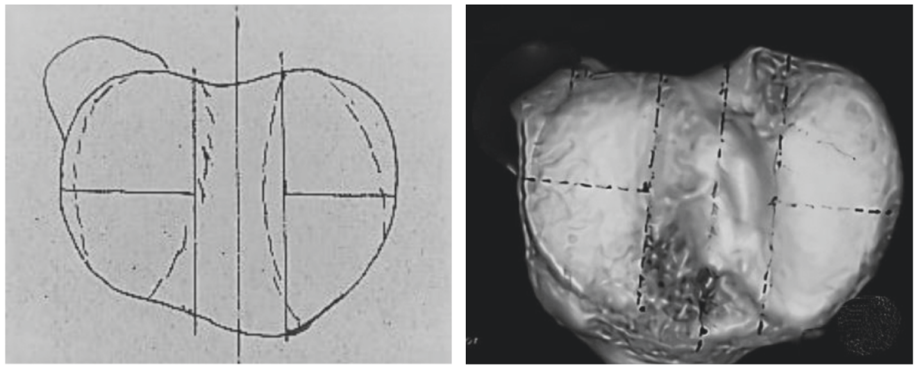

Drawing segmentation Actual image segmentation

Figure 1: Area division of articular surface. (a) Drawing segmentation. (b) Actual image segmentation.

time consumed by the computer to participate in the calculation and execution.

2.4. CT Examination Methods. The CT instrument was applied for examination. 6, 12, and 18 months after the FTS nursing, CT examinations were performed on the patients participating in this study. The degree of fracture comminution, the size of the injured area, and the degree of displacement were measured and evaluated; meanwhile, the corresponding imaging scores were worked out.

The patients took the supine position on the examination table, with the legs together and the patella facing up. CT scanning range was 5 cm above the femoral condyle and 10 cm below the tibial articular surface, with the voltage of 120 kV, the current of 240 mA, the scanning thickness of 2–5 mm, and the reconstruction thickness of 0.625~1.25 mm. The multiplanar reconstruction and surface mask imaging were then performed.

As for the calculation of the damage area of the tibial articular plateau surface, on the top view image of the three-dimensional reconstruction of the tibia, a longitudinal line was drawn in the middle of the intercondylar crest, and then, two straight lines parallel to the longitudinal line were drawn on both sides of the base of the intercondylar eminence. The tibial articular surface was divided into the medial and lateral weight-bearing articular areas and the intercondylar eminence area, and then, a horizontal line perpendicular to the longitudinal line was drawn in the middle. The medial and lateral articular areas were further divided into anterolateral area, anteromedial area, posterolateral area, and posteromedial area. Thus, the articular surface was divided into five areas, including the intercondylar eminence area and the four articular areas. The damage area was calculated according to the number of damaged articular areas. The area division is shown in Figure 1.

2.5. Imaging Scores. For the score of tibial articular surface displacement, the Rasmussen anatomical scoring criteria for tibial condyle fracture reduction were used. The total displacement score was 18 points, if the patients held an excellent degree of joint displacement, it was 18 points; if the degree was good, it was 12–17 points; if the degree was common, it was 6–11 points; and if the degree was bad, it was 0–5 points. The details are shown in Table 1.

Table 1: Scores for tibial articular surface displacement.

Fracture types	Degree	Score	Grade
Articular surface collapse	None	6 points	Excellent
	5 mm	4 points	Good
	6–10 mm	2 points	Common
	>10 mm	0 point	Bad
Tibial articular surface broadening	None	6 points	Excellent
	<5 mm	4 points	Good
	6–10 mm	2 points	Common
	>10 mm	0 point	Bad
Angular deformity (varus or valgus)	None	6 points	Excellent
	$<10^{\circ}$	4 points	Good
	$10–20^{\circ}$	2 points	Common
	$>20^{\circ}$	0 point	Bad

For the damage areas and degree of tibial comminution of tibial articular plateau surface, the scores are shown in Table 2. The total imaging score was 30 points, and the excellent grade was rated 28–30 points; the good grade ranged between 20 and 27 points; the common grade ranged between 10 and 19 points; and the bad was rated 0–9 points.

2.6. Statistical Methods. SPSS 22.0 was used to process and analyze the collected data. The paired-samples t-test was adopted for the difference in data results between the two groups. When $P < 0.05$, the difference was significant with a statistical significance. The chi-square test was adopted to analyze the enumeration data, and the Spearman's rank correlation test was used for the correlation analysis.

3. Research Results

3.1. Evaluation of Image Reconstruction Results. The segmentation results of knee joint bone tissue slices are shown in Figure 2. Figure 2(a) shows the original image, Figure 2(b) shows the segmentation result under the traditional algorithm, and Figure 2(c) shows the segmentation result under the graph cuts algorithm with the automatic threshold mark. It could be observed from Figure 2 that when the foreground was complex and scattered, the number of seed points that

Table 2: Scores for damage areas and degree of tibial comminution of tibial articular surface.

Types	Degree	Score	Grade
Damage areas	Intercondylar eminence area	6 points	Excellent
	1-2 areas	4 points	Good
	3 areas	2 points	Common
	4 areas	0 point	Bad
Degree of tibial comminution	0 fracture fragment	6 points	Excellent
	1 fracture fragment	4 points	Good
	2 fracture fragments	2 points	Common
	≥3 fracture fragments	0 point	Bad

Note: "0 fracture fragment" means that the fracture line passed through the intercondylar eminence area rather than the articular surface area. "1 fracture fragment" means that there was only one fracture line passing through the articular surface area and so on for each degree of tibial comminution.

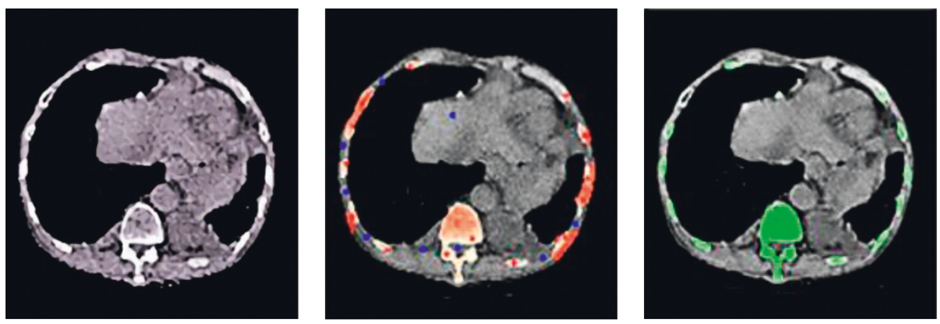

(a) (b) (c)

Figure 2: Comparison of CT image effects under algorithm reconstruction.

needed to be marked was significantly increased and was more complex in the traditional algorithm. It brought more interference to image analysis. The graph cuts algorithm based on threshold is more accurate and has better segmentation effect.

The graph cuts algorithm, which generated threshold markers automatically, did better in image segmentation and was more efficient in algorithm efficiency. In particular, when the foreground was scattered with a large number of distributions in the whole image, it could not only avoid the insufficient foreground and background markers required by the image segmentation algorithm but also make up for the shortcoming of producing "holes" and isolated points under the threshold segmentation algorithm to a certain extent. As shown in Figure 3, this made the entire segmentation more automated, and the segmentation results were more accurate.

It could be known from the equation (15) that, when the Dice similarity coefficient was larger, the difference between the real and standard image segmentation results was smaller. The smaller the Dice similarity coefficient was, the larger the difference. Therefore, as shown in Figure 4, the algorithm in this study offered a greater improvement in the effect of image segmentation, compared with traditional algorithm segmentation.

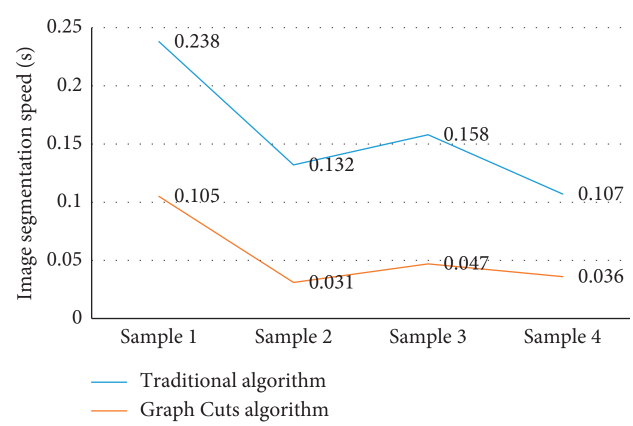

Figure 3: Image segmentation speed(s) of the different algorithms.

3.2. Tibial Displacement Degrees. 16 cases were found with the tibial plateau collapse in group A, while 34 cases were found with the tibial plateau collapse in group B, with the statistically significant difference ($P < 0.05$). For the 16 cases with collapse in both groups, the average collapse was about 2.79 ± 1.31 mm in group A and 5.51 ± 1.88 mm in group B, showing the statistically significant difference ($P < 0.05$). Figure 5 shows the comparison intuitively.

For the plateau broadening distance, there were 26 cases in group A and 15 cases in group B. The specific broadening distances are shown in Figure 6. For the 30 cases with broadened tibia shown in group B, it could be found through the images in group A as well, so that there was no significant difference ($P > 0.05$). The degrees of broadening were different. In the 30 cases, the average broadening distance was 3.17 ± 1.41 mm in group A and 5.72 ± 1.83 mm in group B; the difference was statistically significant ($P < 0.05$).

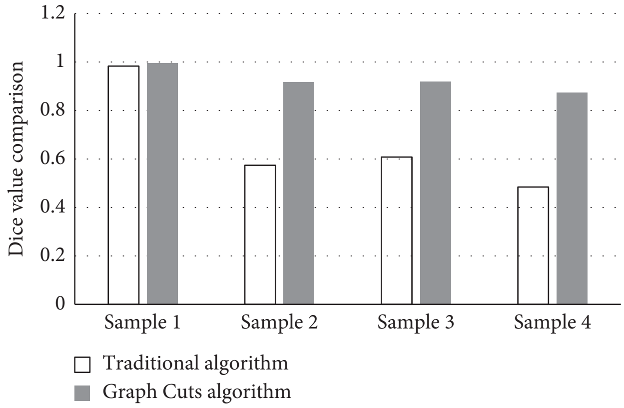

Figure 4: Comparison of the Dice similarity coefficients between two algorithms.

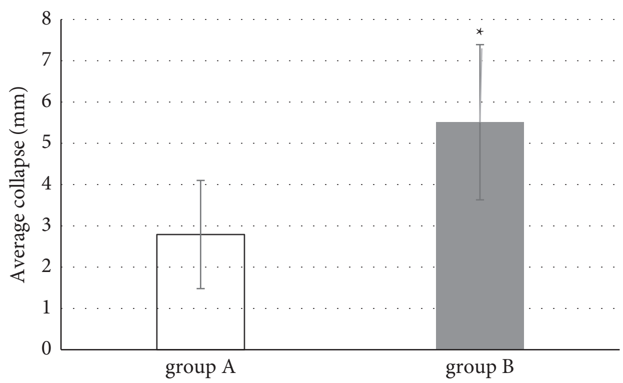

Figure 5: Comparison of the detection results of tibial collapse degree between two groups. *compared with the data in group A, $P < 0.05$.

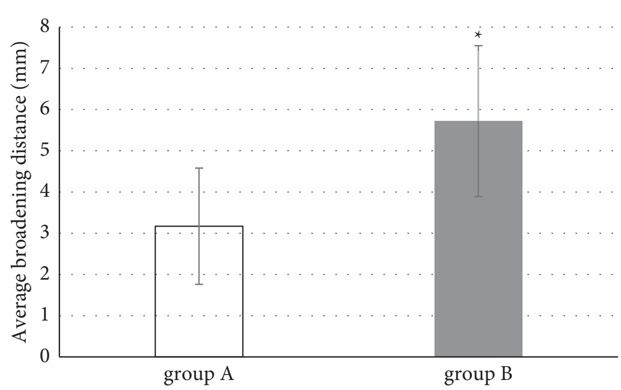

Figure 6: Comparison of the detected tibial broadening distance between two groups. *compared with the data of group A, $P < 0.05$.

3.3. Damage Area of Articular Surface of Tibial Plateau. The images in group A showed 6 cases with 1 damage area and 42 cases with 2 damage areas and 2 cases with ≥3 damage areas. In the images in group B, there were 12 cases with 1 damage area, 48 cases with 2 damage areas, and 12 cases with ≥3 damage areas. The significant difference could be found between the two groups ($P < 0.05$), which is shown in Figure 7.

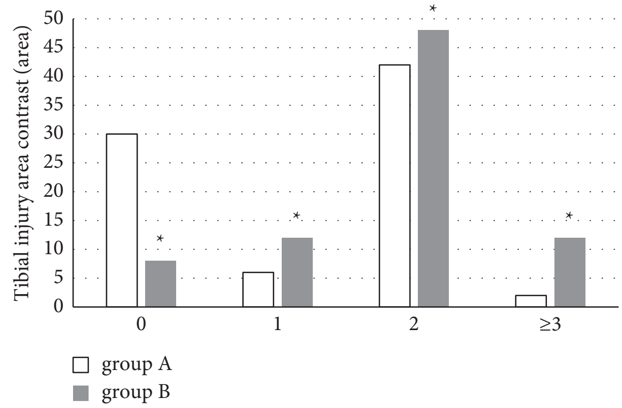

Figure 7: Comparison of the detected tibial damage area between two groups. *compared with that of group A, $P < 0.05$.

3.4. Degree of Tibial Comminution of Tibial Articular Plateau Surface. From the images in group A, 30 cases had no damage in articular surface, while in group B, only 8 cases had no articular surface damage, suggesting a statistically significant difference ($P < 0.05$). In terms of degree of tibial comminution, there were 18 cases with 1 fracture fragment, 24 cases with 2 fracture fragments, and 8 cases with ≥3 fracture fragments in group A. In group B, there were 24 cases with 1 fracture fragment, 14 cases with 2 fracture fragments, and 34 cases with ≥3 fracture fragments, with a significant difference between the two groups ($P < 0.05$). The comparison is shown in Figure 8.

3.5. Scores of Plateau Displacement Degree. As shown in Figure 9, there were 38 cases in excellent, 34 cases in good, 6 cases in common, and 2 cases in bad in group A, while the numbers of patients with excellent, good, common, and bad were 22, 34, 6, and 2, respectively. There was no statistically obvious difference in the numbers of patients in bad and common between the two groups ($P > 0.05$), while the numbers of patients in excellent and good showed observable differences ($P < 0.05$). The average score of the two groups was about 1.43 ± 1.37 points, and the difference was statistically significant ($P < 0.05$).

3.6. The Total Scores. The total score reflected the scores of the entire tibial plateau fracture after treatment. From the images in group A, 26 cases were rated as excellent, 44 cases were rated as good, 8 cases were rated as common, and 2 cases were rated as bad; in group B, 44 cases and 36 cases were rated to be good and common, respectively, which had the significant differences ($P < 0.05$). As shown in Figure 10, the average score of group A was 24.98 ± 3.76 and that of group B was 21.03 ± 3.88; there was a significant difference between the two groups ($P < 0.05$).

4. Discussion

Three-dimensional CT reconstruction was formed by the combination of advanced image reconstruction technology overseas and CT scanning in the late 1980s. It can display the

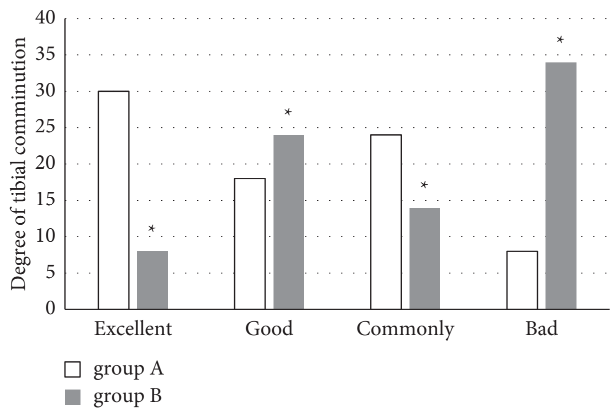

Figure 8: Comparison of the degrees of tibial comminution between two groups. Excellent, good, common, and bad meant that 0, 1, 2, and ≥3 fracture fragments were found, respectively. *compared with those in group A, $P < 0.05$.

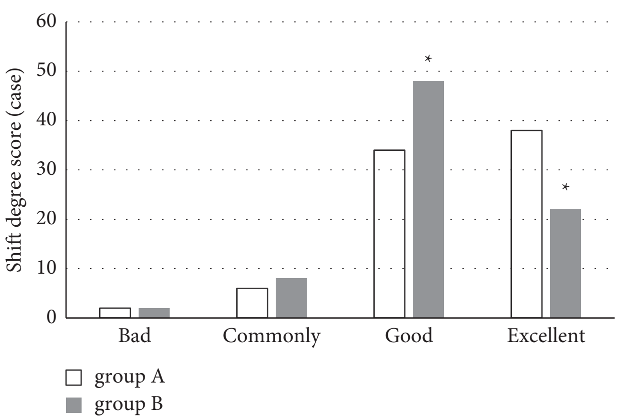

Figure 9: Comparison of displacement degree scores between two groups. *the scores of two groups were compared, $P < 0.05$.

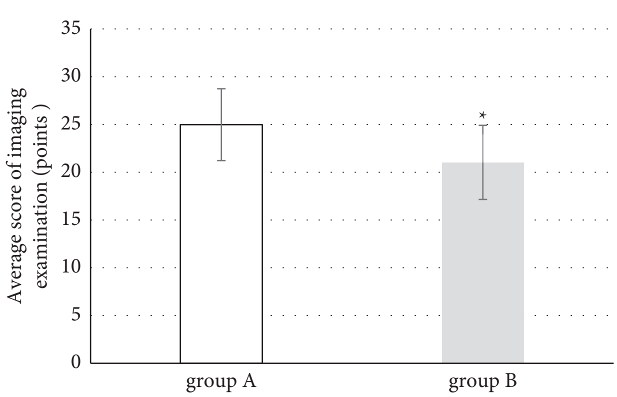

Figure 10: Comparison of the total imaging scores between the two groups. *the scores of two groups were compared, $P < 0.01$.

characteristics of fractures visually and three-dimensionally and play an important role in clinical diagnosis, evaluation, and treatment [16]. CT and three-dimensional reconstruction allow to observe the articular surface from any angle, to know comprehensively about the intra-articular injury [17]. Tibial fractures are complicated as the articular surface and the overlap of the fracture fragments are involved. CT and three-dimensional reconstruction technology can be used not only to determine the range and degree of the fracture of the tibial articular plateau surface accurately but also to measure the distance of the fracture and the depth and width of the collapse [18, 19]. In this study, the graph cuts algorithm under the intelligent algorithm was introduced to reconstruct the traditional CT images, to evaluate the recovery of tibial fracture patients after FTS nursing in the perioperative period, and to explore the application value of the graph cuts algorithm.

The algorithm image reconstruction results showed that the threshold-based graph cuts algorithm segmentation was more accurate with better effect. In the efficiency, this algorithm is more efficient, especially when the foreground was scattered and quite distributed throughout the whole image. It made the segmentation process more automatic, and the segmentation results were more accurate [20]. The Dice similarity coefficient was significantly improved as well compared with that under the traditional algorithm, which proved that the graph cuts algorithm could realize the segmentation of bone tissue CT images effectively. The results showed 16 cases with collapses in group A and 34 cases with collapses in group B; the average collapse in group A was about 2.79 ± 1.31 mm and that in group B was 5.51 ± 1.88 mm. It could be explained that the CT reconstruction under the graph cuts algorithm could show the subtle fracture signs in the tibia. The average broadening in group A was 3.17 ± 1.41 mm and that in group B was 5.72 ± 1.83 mm; the difference was statistically significant ($P < 0.05$). In group A, 6 cases were shown with 1 damage area and 42 cases with 2 areas; in group B, 8 and 48 cases were shown with 1 and 2 damage areas, respectively; there were significant differences between two groups ($P < 0.05$).

In this study, it was believed that CT under the graph cuts algorithm had a better effect to display the number of fracture fragments and evaluate the degree of fracture comminution more accurately. Compared with those in group B, the traditional CT photography is inferior in showing the damage areas and the degree of comminution of the tibial articular plateau surface. In the bird's eye view of images in group B, it was clearly shown the direction of the fracture lines and the number of fracture fragments of the articular surface, which made it more accurate to evaluate the effect of nursing and the recovery of the patients' tibia.

5. Conclusion

As it was aimed at the defect that traditional algorithms needed to mark foreground and background points manually in medical image segmentation, in this study, the graph cuts algorithm was applied to reconstruct traditional CT images. The results showed that the algorithm guaranteed the quality of segmentation, meanwhile improved the segmentation efficiency. It could evaluate the degrees of tibial displacement, articular surface damage areas, and the degree of comminution more accurately, for the patients with tibial fracture after perioperative FTS nursing. Therefore, the algorithm could be used to evaluate the effect of nursing effectively, with a clinical promotion value. Due to the limitation of conditions, the sample size included was small, and the comparison method was simplex. It was necessary to increase the sample size and increase the comparison methods in the future, which would make the results more feasible.

Data Availability

The data used to support the findings of this study are available from the corresponding author upon request.

Conflicts of Interest

The authors declare no conflicts of interest.

References

[1] B. Rudran, C. Little, A. Wiik, and K. Logishetty, "Tibial plateau fracture: anatomy, diagnosis and management," *British Journal of Hospital Medicine*, vol. 81, no. 10, pp. 1–9, 2020.

[2] D. R. Ramponi and T. McSwigan, "Tibial plateau fractures," *Advanced Emergency Nursing Journal*, vol. 40, no. 3, pp. 155–161, 2018.

[3] K. D. Duan and J. R. Huang, "[Progress in diagnosis and treatment of posterior condylar fracture of tibial plateau]," *Zhong Guo Gu Shang*, vol. 32, no. 12, pp. 1173–1176, 2019.

[4] L. Lin, Y. Liu, C. Lin et al., "Comparison of three fixation methods in treatment of tibial fracture in adolescents," *ANZ Journal of Surgery*, vol. 88, no. 6, pp. E480–E485, 2018.

[5] M. Erschbamer, P. Gerhard, H. Klima, B. Ellenrieder, K. Zdenek-Lehnen, and K. Giesinger, "Distal tibial derotational osteotomy with external fixation to treat torsional deformities: a review of 71 cases," *Journal of Pediatric Orthopaedics B*, vol. 26, no. 2, pp. 179–183, 2017.

[6] B. A. Zelle, K. H. Dang, and S. S. Ornell, "High-energy tibial pilon fractures: an instructional review," *International Orthopaedics*, vol. 43, no. 8, pp. 1939–1950, 2019.

[7] J. Mthethwa and A. Chikate, "A review of the management of tibial plateau fractures," *Musculoskeletal Surgery*, vol. 102, no. 2, pp. 119–127, 2018.

[8] A. Bagherifard, P. Arasteh, M. Salehpour et al., "COVID-19 among patients with orthopedic surgery: our experience from the Middle East," *Journal of Orthopaedic Surgery and Research*, vol. 16, no. 1, p. 336, 2021.

[9] K. Gromov, B. B. Kristensen, C. C. Jørgensen, T. B. Hansen, H. Kehlet, and H. Husted, "[Fast-track total knee arthroplasty]," *Ugeskr Laeger*, vol. 179, no. 38, 2017.

[10] Y. Wu, M. Xu, and Y. Ma, "Fast-track surgery in single-hole thoracoscopic radical resection of lung cancer," *Journal of B.U.ON.: Official Journal of the Balkan Union of Oncology*, vol. 25, no. 4, pp. 1745–1752, 2020.

[11] C. Samama, "Fast-track procedures in major orthopaedic surgery: is Venous thromboembolism prophylaxis still mandatory?" *Thrombosis and Haemostasis*, vol. 119, no. 01, pp. 003–005, 2019.

[12] A. R. Vosoughi, M. L. T. Jayatilaka, B. Fischer, A. P. Molloy, and L. W. Mason, "CT analysis of the posteromedial fragment of the posterior malleolar fracture," *Foot & Ankle International*, vol. 40, no. 6, pp. 648–655, 2019.

[13] S. Wang, D. M. Yang, R. Rong, X. Zhan, and G. Xiao, "Pathology image analysis using segmentation deep learning algorithms," *American Journal Of Pathology*, vol. 189, no. 9, pp. 1686–1698, 2019.

[14] Q. Huang, H. Ding, X. Wang, and G. Wang, "Fully automatic liver segmentation in CT images using modified graph cuts and feature detection," *Computers in Biology and Medicine*, vol. 95, pp. 198–208, 2018.

[15] K. B. Girum, G. Créhange, R. Hussain, and A. Lalande, "Fast interactive medical image segmentation with weakly supervised deep learning method," *International Journal of Computer Assisted Radiology and Surgery*, vol. 15, no. 9, pp. 1437–1444, 2020.

[16] X. Gong, Z.-Y. Pan, J. Chen, S. Yang, T. Jiang, and Y.-M. Shen, "Application of 3D reconstruction through CT to measure the abdominal cavity volume in the treatment of external abdominal hernia," *Hernia*, vol. 25, no. 4, pp. 971–976, 2021.

[17] R. P. Blom, B. Hayat, R. M. A. Al-Dirini et al., "Posterior malleolar ankle fractures," *The Bone & Joint Journal*, vol. 102-B, no. 9, pp. 1229–1241, 2020.

[18] M. Arduini, F. Mancini, P. Farsetti, A. Piperno, and E. Ippolito, "A new classification of peri-articular heterotopic ossification of the hip associated with neurological injury: 3D CT scan assessment and intra-operative findings," *The Bone & Joint Journal*, vol. 97-B, no. 7, pp. 899–904, 2015.

[19] M. Luxenhofer, N. Beisemann, M. Schnetzke et al., "Diagnostic accuracy of intraoperative CT-imaging in complex articular fractures - a cadaveric study," *Scientific Reports*, vol. 10, no. 1, p. 4530, 2020.

[20] C. Platero and M. C. Tobar, "A multiatlas segmentation using graph cuts with applications to liver segmentation in CT scans," *Computational and Mathematical Methods in Medicine*, vol. 2014, Article ID 182909, 16 pages, 2014.

Hindawi
Contrast Media & Molecular Imaging
Volume 2022, Article ID 5161703, 10 pages
https://doi.org/10.1155/2022/5161703

Research Article

Effect Evaluation of Dexmedetomidine Intravenous Anesthesia on Postoperative Agitation in Patients with Craniocerebral Injury by Magnetic Resonance Imaging Based on Sparse Reconstruction Algorithm

Xue Feng[1], **Binbin Zhao**[1], **and Yongqiang Wang**[2]

[1]*Department of Anesthesia Surgery, First Affiliated Hospital, Heilongjiang University of Traditional Chinese Medicine, Harbin 150040, Heilongjiang, China*
[2]*Department of Outpatient, Harbin Red Cross Central Hospital, Harbin 150076, Heilongjiang, China*

Correspondence should be addressed to Yongqiang Wang; 2015042023@stu.gzucm.edu.cn

Received 22 March 2022; Revised 1 June 2022; Accepted 3 June 2022; Published 23 June 2022

Academic Editor: M. Pallikonda Rajasekaran

The effect of dexmedetomidine on postoperative agitation of patients with craniocerebral injury was investigated based on magnetic resonance imaging (MRI) with the sparse reconstruction algorithm. Sixty patients with craniocerebral injury who underwent tracheal intubation and craniotomy hematoma removal under general anesthesia in hospital were selected as the research objects. Patients were randomly and averagely divided into the normal saline group (group A) and the dexmedetomidine (DEX) group (group B). DEX was added to patients in group A during anesthesia. Other operations in group B were the same as those in group A, where DEX needed to be used was replaced by an equal amount of the normal saline. All patients received the MRI examination, and the images were processed by using the sparse reconstruction algorithm. After the surgery, some indexes, such as hemodynamics (mean arterial pressure (MAP) and hear rate (HR)), the Riker sedation agitation score, the Ramsay sedation score, and the visual analogue scale (VAS) score were recorded and compared. The results showed that the MRI image quality processed by sparse reconstruction algorithm was observably improved. After reconstruction, the sharpness of the image was significantly improved, and the distinction between lesions and tissues was also increased. The Riker sedation agitation score and the incidence of agitation in group A were greatly lower than those in group B (16% VS 76%, $P < 0.05$). The Ramsay sedation score of group A was manifestly higher than that of group B. The cases of postoperative nausea, vomiting, chills, delirium, and bradycardia in group A were 2, 1, 1, 0, and 1, respectively. The cases of postoperative nausea, vomiting, chills, delirium, and bradycardia in group B were 3, 9, 6, 5, and 0, respectively. The cases of chills and delirium in group A were observably less than those in group B ($P < 0.05$). In conclusion, based on the sparse reconstruction algorithm, the MRI technology and DEX had high adoption value in preventing postoperative agitation of patients with craniocerebral injury. Compared with group B, the hemodynamics of patients in group A was more stable.

1. Introduction

In recent years, the incidence of craniocerebral injury is increasing gradually. At present, it has become a relatively common clinical acute trauma, and it is also one of the most common causes of patients' death in both the emergency department and the neurosurgery department [1]. Currently, the main method for clinical treatment for craniocerebral injury is the craniotomy evacuation of the hematoma. The craniotomy evacuation of hematoma is generally performed under tracheal intubation and general anesthesia, which can not only cause hemodynamic fluctuations but also lead to a linear increase in the incidence of agitation in patients during awakening [2]. A large number of clinical data show that patients with craniocerebral injury often have complications, such as the fluctuation of heart rate and blood pressure and the dysphoria after craniotomy. In some serious cases, patients even have secondary cerebral ischemia and hypoxia, which further aggravates brain tissue injury [3]. Hence, the appropriate sedation therapy for patients with craniocerebral injury can reduce various stress reactions caused by tracheal stimulation. The treatment of sedation and analgesia has become an essential treatment for patients with craniocerebral injury [4]. Nevertheless, the sedative and analgesic drugs generally cause respiratory depression, effect on consciousness, and pupil light reflex, which usually bring great interference to the doctor's judgment [5]. Dexmedetomidine (DEX) produces dose-dependent sedation that is similar to the status of natural sleep. Simultaneously, it also has abirritation, diuretic effect, and anti-sympathetic activity as well as a protective effect on the heart, brain, and kidney [6]. DEX has been widely used in clinical treatment, and its efficacy has been recognized by the majority of doctors. However, there are few clinical investigations on the effect of DEX on postoperative agitation in patients with craniocerebral injury, which needs to be further explored.

Computed tomography (CT) is a commonly used imaging method for the diagnosis of the craniocerebral injury. CT provides great help for the diagnosis of craniocerebral injury, and it has many advantages, such as low cost and scanning time. However, the CT scan cannot detect the skull base, posterior fossa, and non-hemorrhagic injuries [7]. Due to its inability to examine shear injuries of white matter, corpus callosum, and brainstem, the CT scan has little help in the examination of the patients with severe illness and does not show substantial advantages in the long-term prognosis [8]. With the continuous development and progress of imaging technology, magnetic resonance imaging (MRI) has been rapidly developed, which provides the reference and basis for the diagnosis of craniocerebral injury. According to domestic and overseas investigations, MRI can reveal more detailed lesions than CT. Besides, hemorrhagic and non-hemorrhagic injuries can also be clearly distinguished. Zhao et al. (2019) studied the diagnostic effect of MRI on patients with craniocerebral injury, and the results showed that the accuracy of MRI in diagnosing craniocerebral injury could reach 93% [9]. MRI has high specificity and sensitivity in the diagnosis of cortical, brainstem, and cerebellum injuries [10].

MRI technology has been widely applied in modern clinical medicine. Nonetheless, the long imaging time of MRI has always been a vital problem that restricts its further development. The average imaging time of the latest third-generation cone-beam CT is within a few seconds, that of the spiral CT is even faster at about 1 second, and that of the conventional MRI is at about 15 to 30 seconds [11]. The main factors that affect MRI imaging are analyzed, which are mainly classified into the machine-scanning time and the image reconstruction time. Recently, computer technology has developed rapidly, and it has achieved good results in the MRI image reconstruction [12]. Currently, the unpaid image reconstruction time has been reduced to the order of milliseconds [13]. The artificial intelligence (AI) algorithm was applied for the processing of MRI images and evaluation of patients with craniocerebral injury under DEX intravenous anesthesia. The effect of DEX on patients' postoperative agitation was analyzed. This was of great significance for the promotion and adoption of the AI algorithm in the medical field and for the reduction of the incidence of postoperative agitation and other adverse reactions in patients under general anesthesia.

2. Methods

2.1. Research Objects. Sixty patients with craniocerebral injury who underwent tracheal intubation and craniotomy hematoma removal under general anesthesia in hospital from January 2020 to March 2021 were selected as the research objects. There were 36 male patients and 24 female patients, with a mean age of 44.7 ± 11.3 years old. Patients were randomly and averagely divided into the normal saline group (group A) and the dexmedetomidine (DEX) group (group B). All the patients signed the informed consent, and the experiment satisfied the requirements of medical ethics.

The inclusion criteria were as follows. I. Patients diagnosed with craniocerebral injury by CT and MRI; II. Patients with a Glass score (GCS) of 9 to 12 points at admission; III. Patients with admission time of 1 to 6 hours; IV. Patients who were no younger than 18 years old. The exclusion criteria were as follows. I. Patients who needed a second surgery; II. Patients with other severe injuries; III. Patients with insufficiency of liver, kidney, lung, and heart; IV. Patients who took a long-term use of psychotropic drugs; V. Patients with severe allergies; VI. Patients with drug addiction or alcoholism; VII. Patients with physical disabilities; VIII. Those with mental disorders or illnesses that cannot communicate with the doctor.

2.2. Anesthesia Methods. All patients received intramuscular injections of 0.5 mg and atropine and 0.1 g phenobarbital 30 minutes before surgery. After patients entered the operating room, they received oxygen through a mask with an oxygen flow rate of 3 L/min. Routine indexes were detected, such as heart rate, non-invasive blood pressure, pulse oxygen saturation, and electrocardiogram. After patients calmed down, their vital signs were measured three times, and the average value was calculated as the basic value. The peripheral venous channel was established for two weeks, and the compound sodium chloride injection was given. Continuous arterial pressure was monitored and recorded through the routine arteria dorsalis pedis catheterization. At the beginning of anesthesia induction, patients in group A were intravenously pumped with Dex1μg/kg for no less than 10 minutes. Patients in group B were given the same volume of normal saline intravenously at the same speed and time.

For anesthesia induction, midazolam 0.1 mg/kg and sufentanil 0.5 μg/kg were injected intravenously successively. After patients lost consciousness, they were injected with cisatracurium besilate 0.2 mg/kg and propofol (Di ShiNing) 2 mg/kg. After 3 minutes of pressurized nitrogen removal and oxygen delivery, the orotracheal intubation was performed under direct vision. After confirmation, ventilation was controlled by connecting the A5 anesthesia machine. Tidal volume was set at 8 ml/kg, oxygen flow was set at 1.5 L/min, respiratory rate was set at 12 times/min, and inhalation/respiration ratio was 1 : 2.

For the maintenance of anesthesia, the maintenance amount of DEX0.5 μg/kg.h was intravenously pumped in group A, and the same volume of normal saline was pumped at the same speed in group B. Both groups received the continuous intravenous pumping of propofol 4–12 mg/kg.h, cisatracurium besilate 1.5 μg/kg.min, and remifentanil 0.05-2ug/kg·min to maintain anesthesia. Compound sodium chloride injection and hydroxyethyl starch 130/0.4 sodium chloride injection were used. During the surgery, respiratory parameters were adjusted according to the results of arterial blood gas detection, and the partial pressure of end-tidal pressure of carbon dioxide (PETC02) was maintained at 30–40 mmHg. The infusion speed of anesthetics was adjusted according to the arterial blood pressure, and the fluctuation of arterial pressure was controlled within 30% of the base value. The infusion of muscle relaxant and DEX was stopped simultaneously when the galea aponeurotica was sutured in the surgery.

After the surgery, all anesthetic drugs were stopped. The tracheal tube was removed after patients became conscious and reached extubation indexes.

2.3. MRI Examination. 1.5 T MRI equipment was adopted to perform a general scan of the head. The detailed scanning parameters were as follows. The T2 weighted imaging (T2WI)/fast spin echo (FSE), T1 weighted imaging (T1WI)/IR transverse axis, and T1WI/IR sagittal. For T2WI, the time of repetition (TR) was 4000 ~ 4500 ms and the time of echo (TE) was 100 ms; for T1WI, it was 1750 ms. The layer thickness was 6 ~ 8 mm, and the layer interval was 0.5 ~ 1.0 mm. Nex was 1 ~ 2 times, the matrix was 384 × 256, and the field of view (FoV) was 24 cm.

All patients underwent axial, sagittal, and coronal scans. MRI images were evaluated by three senior radiologists who had no prior knowledge of patients' injury history or disease. If there was any dispute about the three-dimensional judgment, the three radiologists needed to discuss and make the conclusion. The number, location, and signal intensity of the injury were recorded. Scans were generally performed 1–39 days after injury. The scanning time ranged from about 17 to 35 minutes. Sedation and endotracheal intubation were required in some patients during the examination. Blood pressure and high concentration of peripheral blood pressure required continuous monitoring.

2.4. MRI Image Processing Based on Sparse Reconstruction Algorithm. A sparse reconstruction algorithm was proposed according to the characteristics of the back-projection algorithm. Firstly, the algorithm was optimized. Then, in the following equation, according to the properties of trigonometric functions, sines and cosines of angles that differed by 90 degrees were converted.

$$\begin{aligned} sin(\alpha+90) &= cos(\alpha)cos(\alpha+90) = -sin(\alpha),\\ sin(\alpha+180) &= -\sin(\alpha)cos(\alpha+180) = -\cos(\alpha),\\ \sin(\alpha+270) &= -cos(\alpha)\cos(\alpha+270) = sin(\alpha). \end{aligned} \tag{1}$$

According to the following equations, sine and cosine operations of $(\beta-\phi)$ were simplified.

$$U(r,\phi,\beta) = \frac{D + r\sin(\beta-\phi)}{D}, \tag{2}$$

$$s' = D\frac{r\cos(\beta-\phi)}{D + r\sin(\beta-\phi)}. \tag{3}$$

In equations (2) and (3), the values of β and ϕ ranged from 0 to 360 degrees. The reconstruction area was divided into four quadrants, and the projection data was also divided into four regions according to the projection angle, namely, $0<\beta_1\le 90, 90<\beta_2\le 180, 180<\beta_3\le 270, 270<\beta_4\le 360$. Four spots were selected during the reconstruction, namely, $E(r,\phi), E_1(r,\phi+90), E_2(r,\phi+180), E_3(r,\phi+270)$. These four spots belonged to the four quadrants, and the values of r were equal. Besides, their ϕ values differed by 90 degrees in turn.

Reconstruction steps after remodeling were as follows.

Firstly, for the spot $E(r,\phi)$ in the first quadrant, when $0<\beta_1\le 90$, $r\sin(\beta_1-\phi)$ and $r\cos(\beta_1-\phi)$ were calculated. Then, according to equations (2) and (3), U and s' were calculated as shown in the following equations.

$$U(r,\phi,\beta_1) = \frac{D + r\sin(\beta_1-\phi)}{D}, \tag{4}$$

$$s'(r,\phi,\beta_1) = D\frac{r\cos(\beta_1-\phi)}{D + r\sin(\beta_1-\phi)}. \tag{5}$$

Secondly, in the following equation, for the spot $E1(r,\phi+90)$, $\beta_2=\beta_1+90$ was set, and the values of r were set to be equal.

$$\beta_2-(\phi+90) = \beta_1+90-\phi-90 = \beta_1-\phi. \tag{6}$$

Hence, for the spot $E(r,\phi)$ in the first quadrant, there was only one corresponding spot $E1(r,\phi+90)$ in the second quadrant. The U and s' of the two spots corresponded to each other. For $\beta_2=\beta_1+180$, U and s' of $E2(r,\phi+180)$ were equal to those of $E(r,\phi)$. For $\beta_4=\beta_1+270$, U and s' of $E3(r,\phi+270)$ were equal to those of $E(r,\phi)$. The following equations showed the calculation methods.

$$\begin{aligned} U(r,\phi,\beta_1) &= U(r,\phi+90,\beta_2)\\ &= U(r,\phi+180,\beta_3)\\ &= U(r,\phi+270,\beta_4). \end{aligned} \tag{7}$$

$$\begin{aligned} s'(r,\phi,\beta_1) &= s'(r,\phi+90,\beta_2)\\ &= s'(r,\phi+270,\beta_4). \end{aligned} \tag{8}$$

In this step, the values of U and s' of the four spots were calculated once only, which helped save the time.

Thirdly, in the following equations, when $0 < \beta_1 \leq 90$, the values of U and s' of $E1(r, \phi + 90)$ in the second quadrant were calculated.

$$\begin{aligned} U(r, \phi + 90, \beta_1) &= \frac{D + r\sin(\beta_1 - \phi - 90)}{D} \\ &= \frac{D - r\cos(\beta_1 - \phi)}{D}, \end{aligned} \tag{9}$$

$$\begin{aligned} s'(r, \phi + 90, \beta_1) &= D\frac{r\cos(\beta_1 - \phi - 90)}{D + r\sin(\beta_1 - \phi - 90)} \\ &= D\frac{r\sin(\beta_1 - \phi)}{D - r\cos(\beta_1 - \phi)}. \end{aligned} \tag{10}$$

$r\sin(\beta_1 - \phi)$ and $r\cos(\beta_1 - \phi)$ were both obtained in the first step, so a floating point operation was performed in this step. Then, the following equations were obtained.

$$\begin{aligned} U(r, \phi + 90, \beta_1) &= U(r, \phi + 180, \beta_2) \\ &= U(r, \phi + 270, \beta_3) \\ &= U(r, \phi, \beta_4). \end{aligned} \tag{11}$$

$$\begin{aligned} s'(r, \phi + 90, \beta_1) &= s'(r, \phi + 180, \beta_2) \\ &= s'(r, \phi + 270, \beta_3) \\ &= s'(r, \phi, \beta_4). \end{aligned} \tag{12}$$

The values of U and s' for spots $E2(r, \phi + 180)$ and $E3(r, \phi + 270)$ could be calculated in the similar way.

After image reconstruction, the mean square error (MSE), peak signal-to-noise ratio (PSNR), structural similarity (SSIM), and other indicators were used to quantitatively evaluate the image reconstruction effect. The specific calculation methods of the three indicators were as follows:

$$\mathrm{MSE} = \frac{1}{mn}\sum_{i=0}^{m-1}\sum_{j=0}^{n-1}[I(i,j) - K(i\cdot j)]^2, \tag{13}$$

$$\begin{aligned} \mathrm{PSNR} &= 10\cdot\log_{10}\left(\frac{\mathrm{MAX}_I^2}{\mathrm{MSE}}\right) \\ &= 20\cdot\log_{10}\left(\frac{\mathrm{MAX}_I}{\sqrt{\mathrm{MSE}}}\right), \end{aligned} \tag{14}$$

$$\mathrm{SSIM}(x, y) = \frac{(2\mu_x\mu_y + c_1)(2\sigma_{xy} + c_2)}{(\mu_x^2) + \mu_y^2 + c_1(\sigma_x^2 + \sigma_y^2 + c_2)}. \tag{15}$$

2.5. Observation Index. Firstly, respiratory recovery time, wake-up time, and extubation time were recorded. Secondly, heart rate (HR) (times/min) and mean arterial pressure (MAP) (mmHg) were recorded immediately after awakening (T1), immediately after extubation (T2), 5 minutes (T3), 30 minutes (T4), 60 minutes (T5), and 120 minutes (T6) after extubation in the two groups. Thirdly, the Riker sedation agitation scores of patients in the two groups at 6 postoperative time points were recorded [14]. Fourthly, the degree and incidence of agitation were recorded from the end of surgery to 120 minutes after extubation. Fifthly, the Ramsay sedation score of the patients in the two groups at 6 postoperative points was recorded [15]. Sixthly, the visual analogue scale (VAS) scores of patients in the two groups at 6 postoperative points were recorded. Seventhly, the total amount of remifentanil and propofol used in the two groups was recorded, and the average dose used in each group was calculated. Finally, the incidence of adverse reactions from the end of surgery to 120 minutes after extubation in the two groups was recorded.

2.6. Statistical Analysis. From thisSPSS 22.0 was used for data statistics and analysis. Mean ± standard deviation ($x \pm s$) was how measurement data were expressed. Comparison between the two groups was performed by t test. Analysis of variance was used for the comparisons within the groups. Enumeration data were tested by χ^2 test. The difference was statistically considerable with $P < 0.05$.

3. Results

3.1. Patients' Classic Images. Figure 1 shows the images of typical cases. The MRI images processed by the sparse reconstruction algorithm had higher sharpness and more prominent details on the edges of lesions compared with the unprocessed MRI images, which indicated that the image quality was obviously improved.

3.2. Quantitative Evaluation of Algorithm Image Reconstruction Effect. Figure 2 shows the quantitative evaluation results of the image reconstruction effect of the traditional algorithm and the new algorithm proposed in this work. Analysis of Figure 2 showed that the MSE, PSNR, and SSIM of the traditional algorithm were 150, 32, and 0.77, respectively; while those of the new algorithm were 120, 44, and 0.92, respectively. It can be known that there was a significant difference in the indicators of the two algorithms ($P < 0.05$). This suggested that the performance of the new algorithm proposed in this work was significantly better than the traditional algorithm in the reconstruction of MRI images of patients with craniocerebral injury.

3.3. Comparison of the General Recovery Time. Figure 3 shows the statistical results of postoperative respiratory recovery time, wake-up time, and extubation time of patients in the two groups. The respiratory recovery time, wake-up time, and extubation time in group A were 5.33 ± 1.3, 6.57 ± 2.4, and 10.1 ± 3.3, respectively. The respiratory recovery time, wake-up time, and extubation time in group B were 5.41 ± 2.2, 6.38 ± 1.4, and 10.3 ± 2.7, respectively. There was insignificant difference in the general recovery time between the two groups ($P > 0.05$).

3.4. Comparison of Hemodynamic Data. Figure 4 shows the comparison of hemodynamics between the two groups at each time point. HR of group A at T1, T2, T3, T4, T5, and T6 were 100 ± 5.5, 113 ± 6.8, 102 ± 7.7, 101 ± 7.1, 91 ± 6.6, and 99 ± 7.3, respectively. MAP of group A at T1, T2, T3, T4, T5,

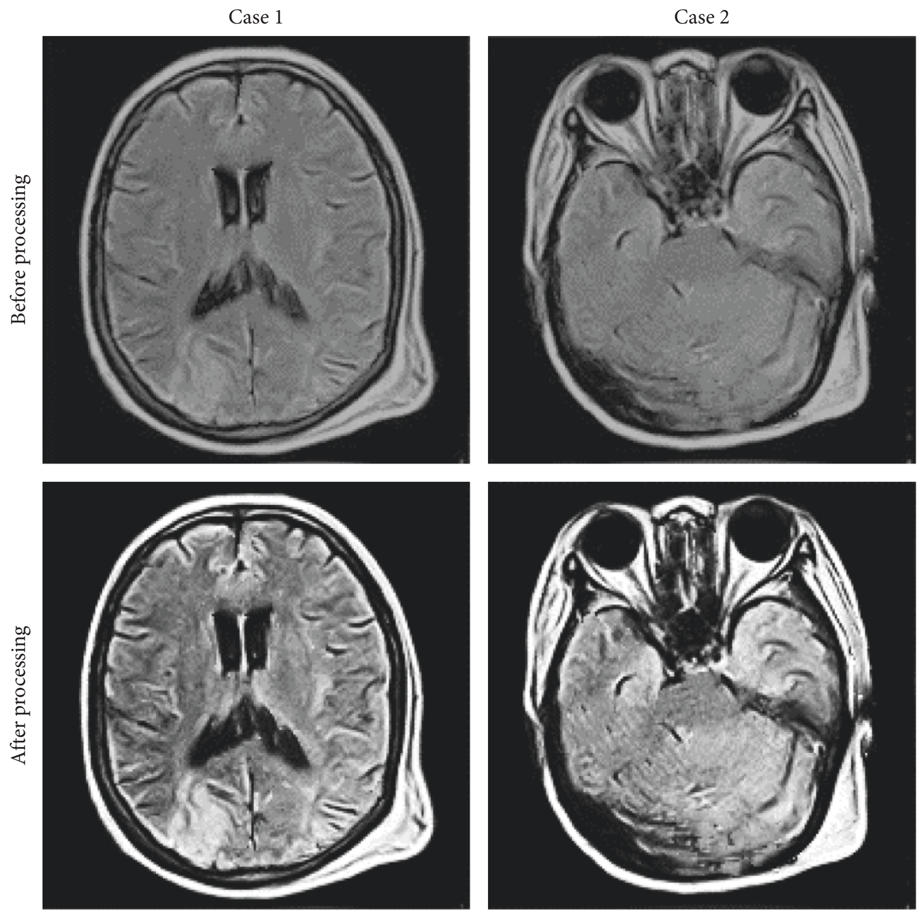

Figure 1: Presentation of images of typical cases.

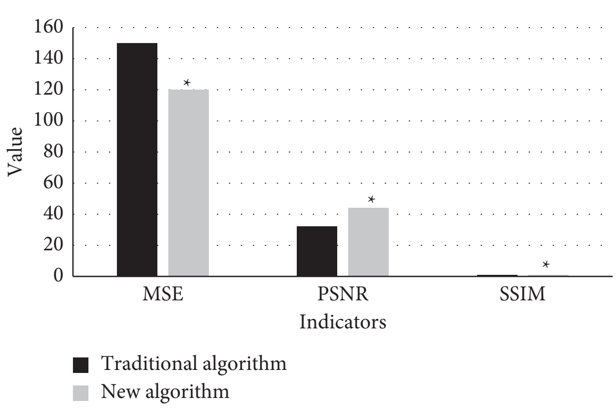

Figure 2: Quantitative evaluation of algorithm image reconstruction effect. *Compared with the traditional algorithm, $P < 0.05$.

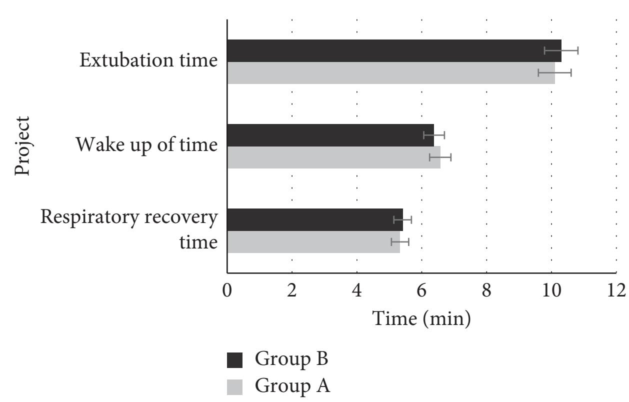

Figure 3: Comparison of the general recovery time between the two groups.

and T6 were 100 ± 5.7, 104 ± 6.1, 98 ± 8.1, 93 ± 9.2, 87 ± 6.6, and 82 ± 7.7, respectively. In group B, HR at T1, T2, T3, T4, T5, and T6 were 112 ± 6.8, 126 ± 7.4, 113 ± 4.9, 109 ± 6.3, 103 ± 8.8, and 96 ± 9.1, respectively. MAP of group B at T1, T2, T3, T4, T5, and T6 were 108 ± 7.8, 118 ± 8.8, 107 ± 6.9, 101 ± 7.6, 93 ± 6.3, and 84 ± 7.2, respectively. The comparison between the two groups showed that there were significant differences in HR and MAP at each time point within 60 minutes ($P < 0.05$).

3.5. Comparison of the Riker Sedation Agitation Scores after the Surgery. Figure 5 shows the comparison of the Riker sedation agitation scores of patients in the two groups after the surgery. In group A, the Riker sedation agitation scores at T1, T2, T3, T4, T5, and T6 were 2.8 ± 0.3, 3.8 ± 0.1, 3.4 ± 0.4, 3.1 ± 0.3, 3 ± 0.2, and 2.8 ± 0.5, respectively. In group B, the Riker sedation agitation scores at T1, T2, T3, T4, T5, and T6 were 4.1 ± 0.3, 4.7 ± 0.4, 4.2 ± 0.2, 3.8 ± 0.3, 3.6 ± 0.22, and 3.22 ± 0.31, respectively. The difference was statistically considerable in the Riker

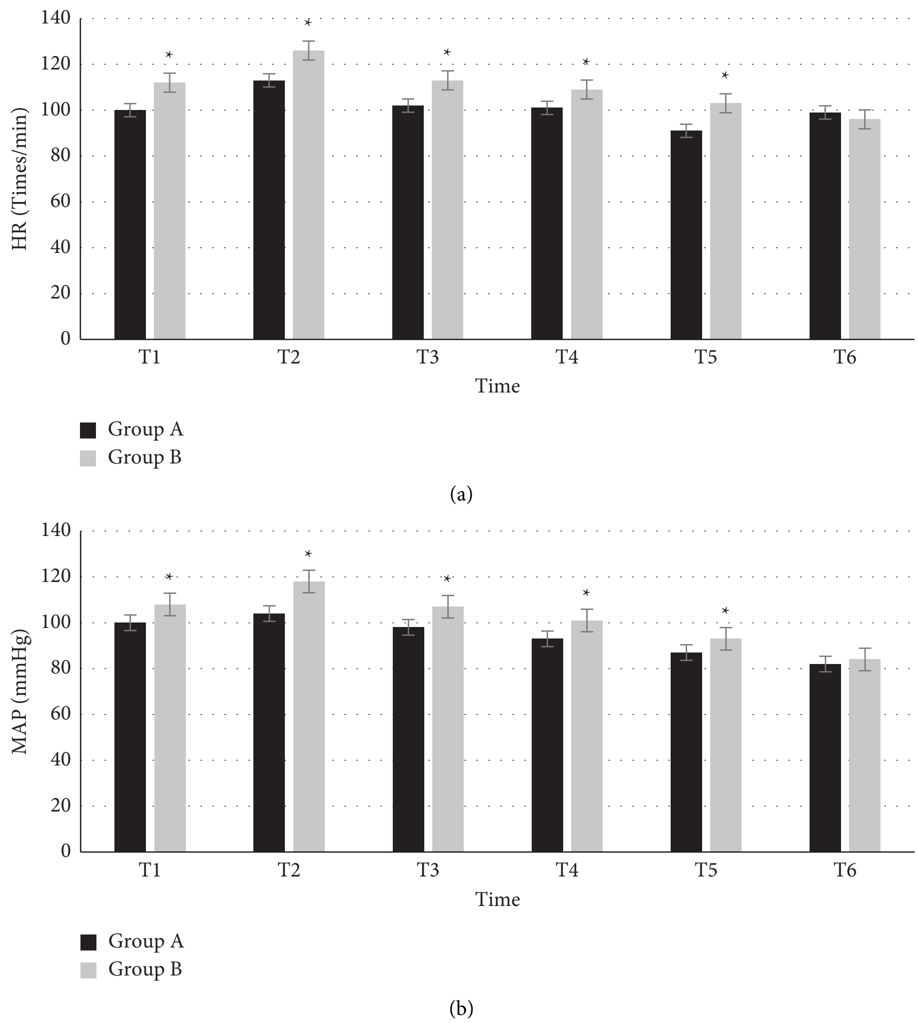

FIGURE 4: Comparison of hemodynamic data between the two groups at each time point. *Compared with group A, $P < 0.05$.

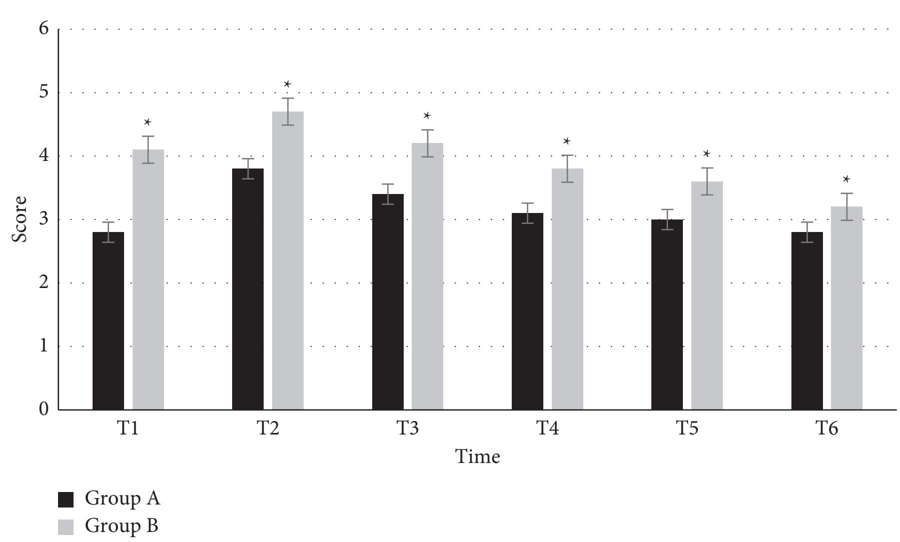

FIGURE 5: Comparison of the Riker sedation agitation scores at each time point between the two groups. *Compared with group A, $P < 0.05$.

sedation agitation score within 60 minutes between the two groups ($P < 0.05$).

3.6. Comparison of the Incidence of Agitation. Table 1 shows the comparison of the incidence of agitation between the two groups. The incidence of agitation was 16% in group A and that was 76% in group B. The incidence of agitation in group A was remarkably lower than that in group B ($P < 0.05$).

3.7. The Ramsay Sedation Score. Figure 6 shows the comparison of the Ramsay sedation scores between the two groups at each time. The Ramsay sedation scores at T1, T2, T3, T4, T5, and T6 in group A were 2 ± 0.1, 1.3 ± 0.3, 1.8 ± 0.2, 1.6 ± 0.5, 1.4 ± 0.7, and 2.1 ± 0.4, respectively. In group B, the Ramsay sedation scores at T1, T2, T3, T4, T5, and T6 were 2.7 ± 0.4, 2 ± 0.3, 2.6 ± 0.2, 2.9 ± 0.1, 3 ± 0.3, and 2.2 ± 0.4, respectively. There was a statistically significant difference in the Ramsay sedation scores within 60 minutes between the two groups ($P < 0.05$).

3.8. Comparison of the VAS Scores at Each Time Point. Figure 7 shows the comparison of the VAS scores at each time point between the two groups. The VAS scores of group A at T1, T2, T3, T4, T5, and T6 were 2 ± 0.2, 2.6 ± 0.3, 3.2 ± 0.5, 4.3 ± 0.4, 4.9 ± 0.2, and 5.5 ± 0.3, respectively. The VAS scores of group B at T1, T2, T3, T4, T5, and T6 were 3 ± 0.2, 3.9 ± 0.4, 4.8 ± 0.6, 5.2 ± 0.3, 5.8 ± 0.2, and 6 ± 0.5, respectively. Within 60 minutes, the VAS scores of group A were evidently higher than those of group B at each time point ($P < 0.05$).

3.9. Comparison of Dosages of Remifentanil and Propofol. Figure 8 shows the comparison of dosages of remifentanil and propofol between two groups. The average dosage of remifentanil and propofol in group A were 0.11 ± 0.01 and 0.073 ± 0.03, respectively. The average dosage of remifentanil and propofol in group B were 0.33 ± 0.02 and 0.17 ± 0.015, respectively. The average dosage of remifentanil and propofol in group A were markedly lower than those in group B ($P < 0.05$).

3.10. Comparison of Postoperative Adverse Reactions between the Two Groups. Figure 9 shows the comparison of postoperative adverse reactions between the two groups. The cases of postoperative nausea, vomiting, chills, delirium, and bradycardia in group A were 2, 1, 1, 0, and 1, respectively. The cases of postoperative nausea, vomiting, chills, delirium, and bradycardia in group B were 3, 9, 6, 5, and 0, respectively. The cases of chills and delirium in group A were observably less than those in group B ($P < 0.05$).

4. Discussion

Postoperative agitation is defined as the over-excitability of patients during the waking period under anesthesia with ether, cyclopropane, and ketamine. Its main clinical manifestations are unconscious movements of the body, uncontrollable crying, irrational language, and excited agitation. Agitation occurs for several reasons, such as surgically related factors, anesthetic factors, and adverse stimuli. At present, the mechanism of postoperative agitation cannot be precisely explained [16, 17]. Some scholars believe that the occurrence of postoperative agitation is related to the different degrees of inhibition of the central nervous system by anesthetic drugs [11, 18]. Postoperative agitation is a common but difficult complication to be controlled. Postoperative agitation is dangerous in patients with craniocerebral injury. It can not only interfere with the observation of postoperative conditions but also seriously affect the respiratory and circulatory functions of patients and further lead to a substantial increase in intracranial pressure [19, 20]. The probability of intracranial hemorrhage also increases, and postoperative agitation also induces secondary brain injury like the aggravation of cerebral edema. Moreover, patients have such problems as disturbance of consciousness, which leads to the occurrence of accidents during the removal of the tracheal tube, urinary tube, and drainage tube. This will not only bring safety threats to patients but also increase the difficulty of postoperative nursing [21].

Table 1: Comparison of the incidence of agitation between the two groups.

Grading	Group A	Group B
3	5	2
4	20	5
5	3	7
6	2	9
7	0	7
Incidence of agitation (%)	16	76*

*Compared with group A, $P < 0.05$.

Sedative and analgesic therapy can reduce restlessness and stress response, which plays a crucial role in improving the prognosis of patients with craniocerebral injury [22]. Benzodiazepines, propofol, and opioids are often used in the clinic to reduce the occurrence of agitation. However, these drugs have such side effects as respiratory depression and urinary retention. These side effects have a great interference effect on the clinical observation of patients' conditions, so its clinical adoption is limited to a certain extent. DEX is a kind of $\alpha 2$ adrenergic receptor agonist that is discovered and applied late in the clinic. It has a unique effect of calming but not inhibiting respiration [23], so it is widely used in the clinic. The craniotomy evacuation of the hematoma is a very common and vital treatment for patients with craniocerebral injury. Effective sedative and analgesic therapy after the surgery can effectively prevent agitation in patients who have undergone neurosurgical operations [24]. DEX can reduce the excitability of the sympathetic nervous system and reduce the hemodynamic changes caused by the stress response, which plays the role of analgesia and sedation. Consequently, it is applied in the anesthesia and surgery of patients with craniocerebral injury. Patients with traumatic brain injury were selected as the research subjects in this work to observe the effect of dexmedetomidine on postoperative agitation. The results showed that compared with group B, patients in group A were hemodynamically more

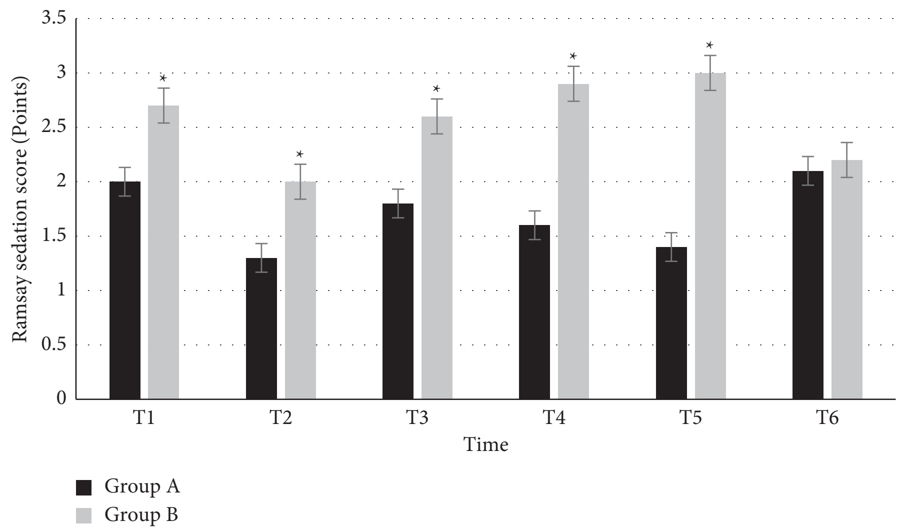

Figure 6: Comparison of the Ramsay sedation scores between the two groups at each time. *Compared with group A, $P < 0.05$.

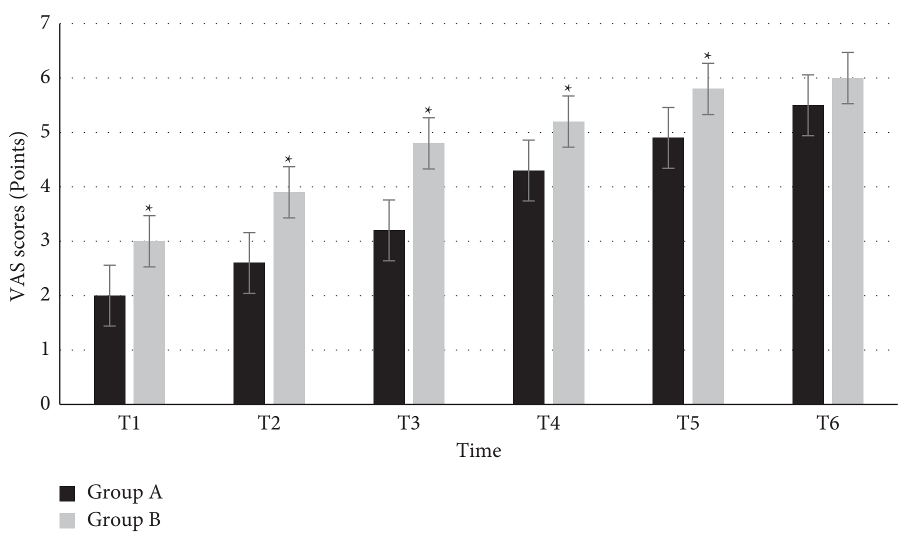

Figure 7: Comparison of the VAS scores at each time point between the two groups. *Compared with group A, $P < 0.05$.

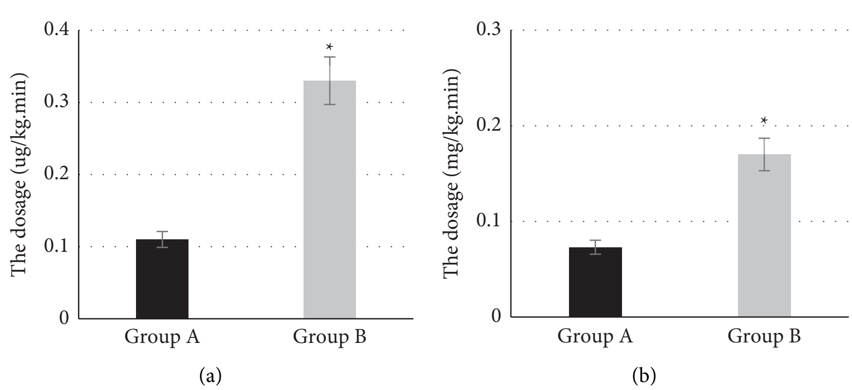

Figure 8: Comparison of dosages of remifentanil and propofol between two groups. *Compared with group A, $P < 0.05$.

stable. The scores of Rick sedation and the incidence of agitation in group A were significantly lower than those in group B. The Ramsay sedation score in group A was significantly higher than that in group B, and the incidence of postoperative complications in group A was also significantly lower than that in group B. Therefore, DEX has

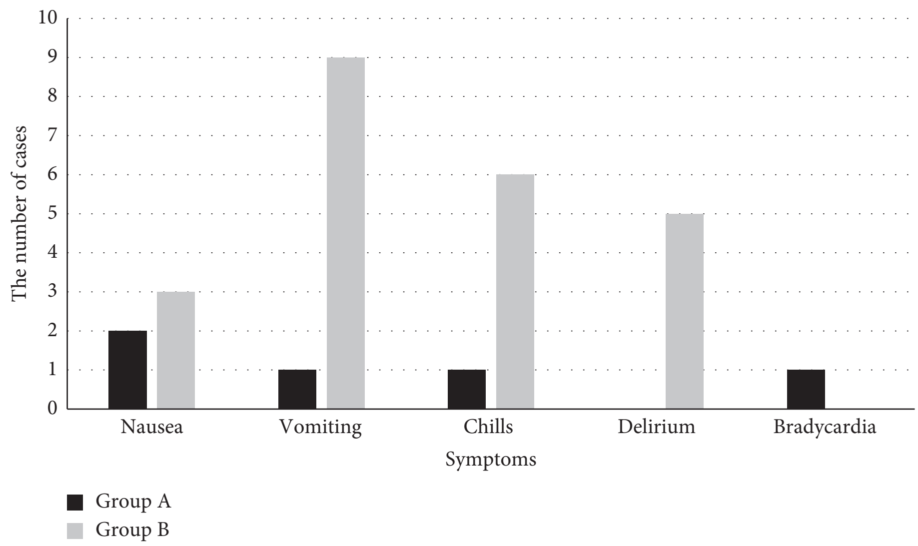

Figure 9: The conditions of postoperative adverse reactions in the two groups.

high clinical application value in reducing postoperative agitation in patients with craniocerebral injury.

Accurate diagnosis of the craniocerebral injury is of great significance to the treatment of the disease. Only by an accurate judgment of the degree of injury can correct treatment measures be taken. Imaging techniques play an important role in the diagnosis of these diseases, among which CT and MRI are more commonly used and more concerned. According to many investigations, MRI is more sensitive than CT in the diagnosis of craniocerebral injury, and MRI also has great advantages in the evaluation of the prognosis of craniocerebral injury [25]. In recent years, with the rapid development of computer technology, the combination of computer technology and other technologies becomes the main trend of the development of various fields. In the medical field, all kinds of medical image processing technology are explored, and there is quite good progress in computer technology applied in the field of medical image processing [26]. In the image processing of MRI, the sparse reconstruction algorithm is of great concern [27]. The MRI images of all patients were processed by sparse reconstruction algorithm, and the value of this algorithm in processing MRI images was studied. The results showed that the quality of MRI images processed by the sparse reconstruction algorithm was significantly improved. Compared with the traditional algorithm, the sparse reconstruction algorithm had better performance in image processing. This shows that the MRI based on sparse reconstruction algorithm also has good performance in the diagnosis of traumatic brain injury.

5. Conclusion

Patients with craniocerebral injury were selected as research objects. The effect of DEX on postoperative agitation was observed. The sparse reconstruction algorithm was used to process MRI images of all patients, and the value of the algorithm in processing MRI images was explored. The results reflected that the quality of MRI images processed by the sparse reconstruction algorithm was evidently improved. Compared with group B, the Riker sedation agitation score, the Ramsay sedation score, hemodynamics, and other indexes of group A were better. In conclusion, DEX had a high clinical adoption value in reducing postoperative agitation in patients with craniocerebral injury. Besides, MRI based on sparse reconstruction algorithm had good performance in the diagnosis of the craniocerebral injury. There were still some limitations in this work. For example, it only studied the image reconstruction performance of two algorithms, and many excellent algorithms had not been introduced. Therefore, the algorithm proposed in this work was not an optimal processing algorithm. In addition, it only analyzed and showed the results of MRI examinations and failed to compare with other examination methods, which may lead to certain errors in the research results. In the future study and work, it would study and improve the above problems, and continue such research in a comprehensive and in-depth manner.

Data Availability

The data used to support the findings of this study are available from the corresponding author upon request.

Conflicts of Interest

The authors declare no conflicts of interest.

References

[1] S. W. Roberson, M. B. Patel, W. Dabrowski, E. W. Ely, C. Pakulski, and K. Kotfis, "Challenges of delirium management in patients with traumatic brain injury: from pathophysiology to clinical practice," *Current Neuropharmacology*, vol. 19, no. 9, pp. 1519–1544, 2021.

[2] D. Karakaya, C. Cakir-Aktas, S. Uzun, F. Soylemezoglu, and M. Mut, "Tailored therapeutic doses of dexmedetomidine in

evolving neuroinflammation after traumatic brain injury," *Neurocritical Care*, vol. 36, no. 3, pp. 802–814, 2021.

[3] V. Bilodeau, M. Saavedra-Mitjans, A. J. Frenette et al., "Safety of dexmedetomidine for the control of agitation in critically ill traumatic brain injury patients: a descriptive study," *Journal of Clinical Pharmacy and Therapeutics*, vol. 46, no. 4, pp. 1020–1026, 2021.

[4] X. Feng, W. Ma, J. Zhu, W. Jiao, and Y. Wang, "Dexmedetomidine alleviates early brain injury following traumatic brain injury by inhibiting autophagy and neuroinflammation through the ROS/Nrf2 signaling pathway," *Molecular Medicine Reports*, vol. 24, no. 3, p. 661, 2021.

[5] G.-R. Huang and F.-G. Hao, "Dexmedetomidine inhibits inflammation to alleviate early neuronal injury via TLR4/NF-κB pathway in rats with traumatic brain injury," *Critical Reviews in Eukaryotic Gene Expression*, vol. 31, no. 1, pp. 41–47, 2021.

[6] F. Soltani, S. Tabatabaei, F. Jannatmakan et al., "Comparison of the effects of haloperidol and dexmedetomidine on delirium and agitation in patients with a traumatic brain injury admitted to the intensive care unit," *Anesthesiology and Pain Medicine*, vol. 11, no. 3, Article ID e113802, 2021.

[7] D. Sun, J. Wang, X. Liu, Y. Fan, M. Yang, and J. Zhang, "Dexmedetomidine attenuates endoplasmic reticulum stress-induced apoptosis and improves neuronal function after traumatic brain injury in mice," *Brain Research*, vol. 1732, Article ID 146682, 2020.

[8] Z. Zhao, Y. Ren, H. Jiang, and Y. Huang, "Dexmedetomidine inhibits the PSD95-NMDA receptor interaction to promote functional recovery following traumatic brain injury," *Experimental and Therapeutic Medicine*, vol. 20, no. 6, p. 1, 2020.

[9] O. Karaca and G. Doğan, "The effects of dexmedetomidine in increased intestinal permeability after traumatic brain injury: an experimental study," *Ulusal travma ve acil cerrahi dergisi = Turkish journal of trauma & emergency surgery: TJTES*, vol. 26, no. 1, pp. 15–20, 2020.

[10] H. Li, C. Lu, W. Yao, L. Xu, J. Zhou, and B. Zheng, "Dexmedetomidine inhibits inflammatory response and autophagy through the circLrp1b/miR-27a-3p/Dram2 pathway in a rat model of traumatic brain injury," *Aging*, vol. 12, no. 21, Article ID 21705, 2020.

[11] Q. Ding, X. Zhang, and P. Chen, "Intraoperative dexmedetomidine in peripheral or emergency neurologic surgeries of patients with mild-to-moderate traumatic brain injuries: a retrospective cohort study," *Dose-response: A Publication of International Hormesis Society*, vol. 18, no. 2, Article ID 1559325820920119, 2020.

[12] S. Musick and A. Alberico, "Neurologic assessment of the neurocritical care patient," *Frontiers in Neurology*, vol. 12, Article ID 588989, 2021.

[13] Y. I. Sysoev, V. A. Prikhodko, R. T. Chernyakov, R. D. Idiyatullin, P. E. Musienko, and S. V. Okovityi, "Effects of alpha-2 adrenergic agonist mafedine on brain electrical activity in rats after traumatic brain injury," *Brain Sciences*, vol. 11, no. 8, p. 981, 2021.

[14] J. W. Branstetter, K. L. Ohman, D. W. Johnson, and B. W. Gilbert, "Management of paroxysmal sympathetic hyperactivity with dexmedetomidine and propranolol following traumatic brain injury in a pediatric patient," *Journal of Pediatric Intensive Care*, vol. 09, no. 01, pp. 064–069, 2020.

[15] J. Peng, F. He, C. Qin, Y. Que, R. Fan, and B. Qin, "Intraoperative dexmedetomidine versus midazolam in patients undergoing peripheral surgery with mild traumatic brain injuries: a retrospective cohort analysis," *Dose-response: A Publication of International Hormesis Society*, vol. 18, no. 2, Article ID 1559325820916342, 2020.

[16] N. Kii, A. Sawada, Y. Yoshikawa, S. Tachibana, and M. Yamakage, "Dexmedetomidine ameliorates perioperative neurocognitive disorders by suppressing monocyte-derived macrophages in mice with preexisting traumatic brain injury," *Anesthesia & Analgesia*, vol. 134, no. 4, pp. 869–880, 2022.

[17] M. K. Teah, G. K. Chan, M. T. F. Wong, and T. B. Yeap, "Treatment of benzodiazepine withdrawal syndrome in a severe traumatic brain injury patient," *BMJ Case Reports*, vol. 14, no. 1, Article ID e238318, 2021.

[18] K. Unchiti, P. Leurcharusmee, A. Samerchua, T. Pipanmekaporn, N. Chattipakorn, and S. C. Chattipakorn, "The potential role of dexmedetomidine on neuroprotection and its possible mechanisms: evidence from in vitro and in vivo studies," *European Journal of Neuroscience*, vol. 54, no. 9, pp. 7006–7047, 2021.

[19] M. Baserga, T. L. DuPont, B. Ostrander et al., "Dexmedetomidine use in infants undergoing cooling due to neonatal encephalopathy (dice trial): a randomized controlled trial: background, aims and study protocol," *Frontiers in Pain Research*, vol. 2, Article ID 770511, 2021.

[20] W. Huang, Y. Qin, and X. Dai, "[Breakthroughs in global critical care medicine 2019]," *Zhonghua Wei Zhong Bing Ji Jiu Yi Xue*, vol. 32, no. 1, pp. 1–7, 2020, Chinese.

[21] A. Kabi, S. Tandon, and P. T. Kandy, "Extradural anesthesia in a case of mild head injury," *Cureus*, vol. 13, no. 7, Article ID e16475, 2021.

[22] N. García-Méndez, M. Briceño-Santana, A. Totomoch-Serra et al., "The hemodynamic effects of diazepam versus dexmedetomidine in the treatment of alcohol withdrawal syndrome: a randomized clinical trial," *Medicina Clínica*, vol. 157, no. 12, pp. 561–568, 2021.

[23] T. Jeffcote, T. Weir, J. Anstey, R. Mcnamara, R. Bellomo, and A. Udy, "The impact of sedative choice on intracranial and systemic physiology in moderate to severe traumatic brain injury," *Journal of Neurosurgical Anesthesiology*, vol. 25, 2022.

[24] L. Yang, H. Wu, F. Yang et al., "Identification of candidate genes and pathways in dexmedetomidine-induced neuroprotection in rats using RNA sequencing and bioinformatics analysis," *Annals of Palliative Medicine*, vol. 10, no. 1, pp. 372–384, 2021.

[25] M. Grigg-Damberger, O. Hussein, and T. Kulik, "Sleep spindles and K-complexes are favorable prognostic biomarkers in critically ill patients," *Journal of Clinical Neurophysiology*, vol. 47, 2022.

[26] F. Li, X. Wang, Z. Deng, X. Zhang, P. Gao, and H. Liu, "Dexmedetomidine reduces oxidative stress and provides neuroprotection in a model of traumatic brain injury via the PGC-1α signaling pathway," *Neuropeptides*, vol. 72, pp. 58–64, 2018.

[27] B. Zheng, S. Zhang, Y. Ying et al., "Administration of Dexmedetomidine inhibited NLRP3 inflammasome and microglial cell activities in hippocampus of traumatic brain injury rats," *Bioscience Reports*, vol. 38, no. 5, Article ID BSR20180892, 2018.

Hindawi
Contrast Media & Molecular Imaging
Volume 2022, Article ID 3544735, 8 pages
https://doi.org/10.1155/2022/3544735

Research Article

Magnetic Resonance Cholangiopancreatography to Evaluate Improvement Effect of FXR Regulating Bile Acid on Hepatocellular Carcinoma with Obstructive Jaundice

Liu Wang, Shi Liu, and Yuanyuan Li

Department of General Surgery, The Third Affiliated Hospital of Qiqihar Medical University, Qiqihar 161000, Heilongjiang, China

Correspondence should be addressed to Liu Wang; 2016218131@smail.jsut.edu.cn

Received 11 April 2022; Revised 1 June 2022; Accepted 3 June 2022; Published 23 June 2022

Academic Editor: M. Pallikonda Rajasekaran

This research aimed at exploring the improvement effect of Farnesoid X receptor (FXR) regulating bile acid (BA) on hepatocellular carcinoma with obstructive jaundice under magnetic resonance cholangiopancreatography (MRCP). Forty-eight hepatocellular carcinoma patients with obstructive jaundice who were examined in hospital were selected as the study group, and another 10 healthy volunteers who were examined at the same period were selected as the control group. The patients were treated with FXR inhibitor, and the therapeutic effect was observed. The results showed that after treatment, the AST content and TBIL content in serum of the study group were 123.5 ± 4.9 U/L and $1.8 \pm 0.3\ \mu$mol/L, respectively, which were significantly lower than those before treatment, $P < 0.05$; the ALT content and AST content in serum in patients with high obstruction were significantly lower than those before treatment, and the K^+ content was significantly higher than that before treatment ($P < 0.05$). The ALT, AST, and TBIL contents in serum in patients with low obstruction were significantly lower than those before treatment ($P < 0.05$). Apparent diffusion coefficient (ADC) was $1.17 \pm 0.49 \times 10^{-3}\ mm^2/s$ in patients with moderate jaundice and $1.20 \pm 0.27 \times 10^{-3}\ mm^2/s$ in patients with severe jaundice, compared with that before treatment, and the difference was statistically significant ($P < 0.05$). Based on FXR, it can regulate BA synthesis and metabolism, restore BA metabolic homeostasis, effectively play a hepatoprotective role, reduce bilirubin content in the body, and improve jaundice injury, which has application value.

1. Introduction

Hepatocellular carcinoma with obstructive jaundice is defined as obstruction of bile excretion and cholestasis due to invasion or compression of the hepatobiliary duct or common bile duct by various direct or indirect causes, which is clinically characterized by hyperbilirubinemia, yellow staining of tissues or body fluids, and bile duct dilatation [1]. Obstructive jaundice can be divided into benign and malignant obstructive jaundice [2]. The hilar bile duct is often used as the demarcation line for the two, and the causes of obstruction can be direct compression of the bile duct by the primary tumor around the liver, gallbladder, bile duct, pancreas, and ampulla, or obstruction caused by tumor metastasis invading the bile duct at other sites [3]. The core problem of jaundice damage to the body is a series of organ dysfunctions with liver damage as the source caused by persistent and progressive obstruction of the biliary tract. Persistent obstruction makes bile unable to enter the intestine normally, and a large amount of bilirubin stasis in the liver, and then a large amount of bilirubin into the blood, forming hyperbilirubinemia, at this time with the impact of malignant tumors, so that the body produces a series of pathophysiological disorders [4]. Relevant studies have shown that degeneration, necrosis, and intrahepatic cholestasis occur in hepatocytes when bile duct obstruction occurs for 3 to 5 days, and with the persistence of bile duct obstruction, bile canalicular proliferation, fibrosis, and even biliary cirrhosis occur [5].

Imaging examinations such as ultrasound, CT, MRI, and endoscopic retrograde cholangiopancreatography (ERCP) are used for the diagnosis and differential diagnosis of calculous obstructive jaundice, especially magnetic resonance imaging (MRI) has been widely used for the detection and characterization of liver lesions, and the evaluation of tumor treatment effects [6]. Magnetic resonance cholangiopancreatography (MRCP) can clearly show the location of obstruction and the number of stones, but it can only provide morphological information of the liver and biliary system, but cannot reflect the functional status of the liver. Because liver dysfunction caused by persistent cholestasis is an important manifestation of obstructive jaundice, the evaluation of liver function in clinical practice is mainly through serum biochemical monitoring [7–9]: (1) protein metabolic function monitoring; (2) plasma coagulation factor determination; (3) serum bilirubin determination, which is an important indicator to assess the degree of jaundice; (4) bile acid (BA) metabolism detection, which is synthesized by cholesterol in the liver, and the determination of which can reflect the synthesis, uptake, and secretion function of hepatocytes, and is related to biliary excretion function; (5) liver function test, indocyanine green (ICG) retention test; and (6) detection of serum enzymes and isoenzymes.

BAs are a general term for a large group of cholanic acids found in bile. As the main component of bile, they often exist in the form of sodium or potassium, which is called bile salt [10]. The BAs are to form mixed micelles through the characteristics of their surfactants to promote the dissolution, digestion, and absorption of fat and fat-soluble vitamins; it can also maintain the homeostasis of cholesterol in the body by promoting the absorption of intestinal nutrients and the secretion of cholesterol in bile, thereby protecting the liver and other tissue cells from the toxicity of high cholesterol; it can protect the intestine, remove endotoxin, act as a chemical barrier of the intestinal mucosa, and maintain the stability of the intestinal microbiome under normal physiological conditions, and most BAs have a significant antibacterial effect on *Staphylococcus aureus* and *Escherichia coli* [11]. In recent years, through the study of BA metabolism, it has been found that BA is not only an energy-derived substance in the body, but also an important signaling molecule, which is involved in the regulation of glucose and lipid metabolism, energy metabolism, and inflammation in the enterohepatic circulation system and peripheral organs by activating different signaling pathways [12].

With the in-depth study of metabolism, scholars have found that in addition to the general physiological function of BA metabolism, it can also indirectly regulate many biological processes of the body. When the homeostasis of BA metabolism in the brain-enterohepatic axis is destroyed, it can cause a series of diseases, which are closely related to the hepatobiliary system, nervous system, etc. It has become a research hotspot in liver disease, encephalopathy, metabolic diseases, etc. [13]. Nuclear receptor Farnesoid X receptor (FXR) is the most important receptor that controls BA metabolism and is involved in affecting the enterohepatic circulation system. By regulating the expression of related key enzymes and target genes, FXR is involved in the regulation of BA synthesis, efflux, metabolism, intake, and transport, which is of great significance for reducing the toxicity of BAs to the liver, maintaining the homeostasis of BAs, maintaining body homeostasis, and exerting a protective effect on the liver [14]. FXR is widely distributed in various tissues such as liver, intestine, adipose tissue, vascular wall, pancreas, and kidney, especially highly expressed in tissues and organs closely related to BA metabolism such as liver and intestine, which can regulate the absorption, metabolism, and secretion of BAs [15].

Therefore, patients with obstructive jaundice due to liver cancer were selected as the study subjects to regulate BA changes in patients by FXR inhibitor treatment and to observe its therapeutic effect on obstructive jaundice injury with the help of MRI cholangiopancreatography. It provides data and theoretical support for the evaluation of the therapeutic effect of obstructive jaundice injury in liver cancer in the future clinical practice.

2. Research Methods

2.1. Study Subjects. Forty-eight hepatocellular carcinoma patients with obstructive jaundice who were examined in hospital from January 2019 to June 2021 were selected as the study group, including 20 males and 28 females, with an average age of 52.61 ± 9.59 years. All patients were treated with FXR inhibitors and could be classified according to the serum bilirubin content as mild jaundice: 34–170 μmmol/L, moderate jaundice: 170–240 μmmol/L, and severe jaundice: >340 μmmol/L. According to the site of obstruction, it was divided into high obstruction and low obstruction. Another 10 healthy volunteers examined in the Hospital during the same period were selected as the control group, including 5 males and 5 females, with a mean age of 46.74 ± 7.92 years. The families of the patients signed the informed consent form, and the trial process was approved by the ethics committee of hospital.

Inclusion criteria are as follows: (1) biochemical tests suggested elevated serum bilirubin; (2) imaging diagnosis showed benign intrahepatic and/or extrahepatic bile duct stone obstruction; (3) intrahepatic or extrahepatic bile duct stones confirmed by surgery; and (4) liver cancer confirmed by pathological examination. Exclusion criteria are as follows: patients with other chronic liver diseases.

2.2. Detection of Total Bile Acid (TBA) Level. Blood samples were collected from veins in the morning (fasting), and serum was separated and placed at 20°C for examination. Basic principle: the level of TBA was determined by the double antibody sandwich method. The extracted TBA was added into the micropores of the coated monoclonal antibody and combined with the HRP-labeled TBA body to form an antibody-antigen-enzyme-labeled antibody complex. After thorough washing, the substrate TMB was added for color development. TMB changed from blue to yellow under the catalysis of HRP and acid, and the color depth was positively correlated with the TBA content in the sample. The OD value was measured at 450 nm by enzyme labeling instrument, and the concentration of TBA in the sample was calculated by the established TBA standard curve [16].

2.3. Upper Abdominal MRI and Laboratory Tests for Liver Function. 3.0 T magnetic resonance scanner was used. Each patient was fasted for 6–8 hours before the examination, and the patient's breathing was trained before the scan, so that the patient can better cooperate with the breath-holding. Routine MRI scanning was performed in the supine, head-forward position, the upper abdomen was surrounded by an abdominal phase-controlled display coil, and routine T1WI, T2WI, coronal T2, and MRCP scans of the liver were performed. DWI examination was performed with the body coil as the radiofrequency transmit coil and receive coil, using the SE-EPI sequence and prospective acquisition correction (PACE), axial, TR: 5,900 ms, TE: 83 ms, slice thickness: 6.59 mm, interval: 1 mm, field of view: 284×376 mm, matrix: 115×192, NEX = 1. The b value (diffusion-sensitive gradient coefficient) was taken as 50, 400, and 800 s/mm^2.

All MRDWI images automatically generated apparent diffusion coefficient (ADC) maps by magnetic resonance postprocessing workstation, and two experienced MRI diagnostic experts jointly evaluated the image quality and measured the ADC values of the liver in the qualified scanning images. Since the left lobe of the liver was susceptible to cardiac motion, the circular region of interest (ROI) for measuring the ADC value of the liver parenchyma was located at the level near the hilum of the right lobe of the liver, with each circular ROI area of 79 mm^2 (1 cm in diameter), which contained about 776 voxels, and the visible hepatic vasculature should be avoided as much as possible during measurement.

The laboratory examination of the liver function of all patients was to draw 5 mL blood from elbow vein when fasting and analyze it automatically by the Beckman Coulters automatic biochemical instrument; the time between laboratory examination and MRI examination was less than 48 hours. Laboratory test indicators included alanine aminotransferase (ALT), aspartate aminotransferase (AST), serum total bilirubin (TBIL), and electrolytes (Na^+, K^+).

2.4. Statistical Methods. SPSS 22.0 statistical software was used for data management and statistical analysis. Measurement data were expressed as mean ± standard deviation, means were compared using the t-test, and categorical variables were compared using x^2 test, with $P < 0.05$ considered statistically significant.

3. Results

3.1. General Information. Fifty-eight subjects were included, including 25 males and 33 females. After examination, there were 26 cases of high biliary obstruction and 22 cases of low biliary obstruction; There were 8 cases of mild jaundice, 24 cases of moderate jaundice, and 16 cases of severe jaundice (Table 1 and Figure 1).

3.2. Changes in BA Levels. The detection results of serum TBA showed that the content of serum TBA was 13.5 ± 0.4 mmol/L and intrahepatic TBA was 34.6 ± 0.6 mmol/L in the control group. The serum TBA was 11.2 ± 0.6 mmol/L, and intrahepatic TBA was 12.4 ± 1.8 mmol/L in the study group before treatment. Compared with the control group, the content in the study group decreased significantly, and the difference was statistically significant ($P < 0.05$). After treatment, the content of serum TBA and intrahepatic TBA in the study group were 12.8 ± 0.5 mmol/L and 28.3 ± 1.2 mmol/L,

Table 1: General information of patients.

Group	Cases	Age/years old	Male/cases	Female/cases
Study group	48	52.61 ± 9.59	20	28
Control group	10	46.74 ± 7.92	5	5

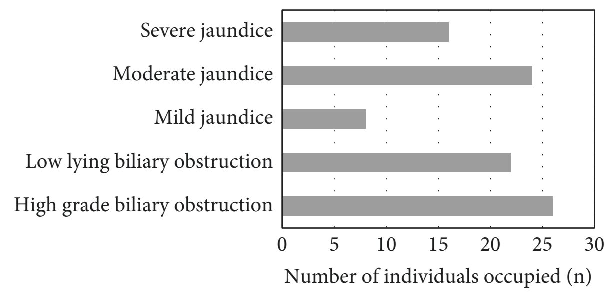

Figure 1: Basic information of patients.

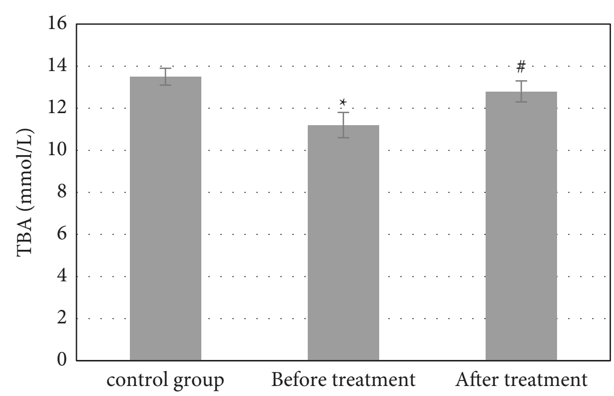

Figure 2: Changes in the serum TBA content. *Compared with the control group, $P < 0.05$; #compared with that before treatment, $P < 0.05$.

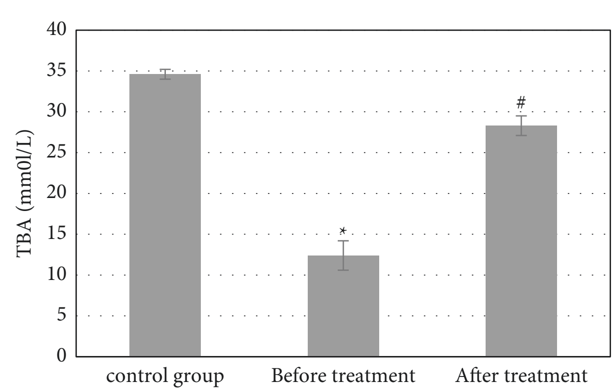

Figure 3: Changes of the intrahepatic TBA content. *Compared with the control group, $P < 0.05$; #compared with that before treatment, $P < 0.05$.

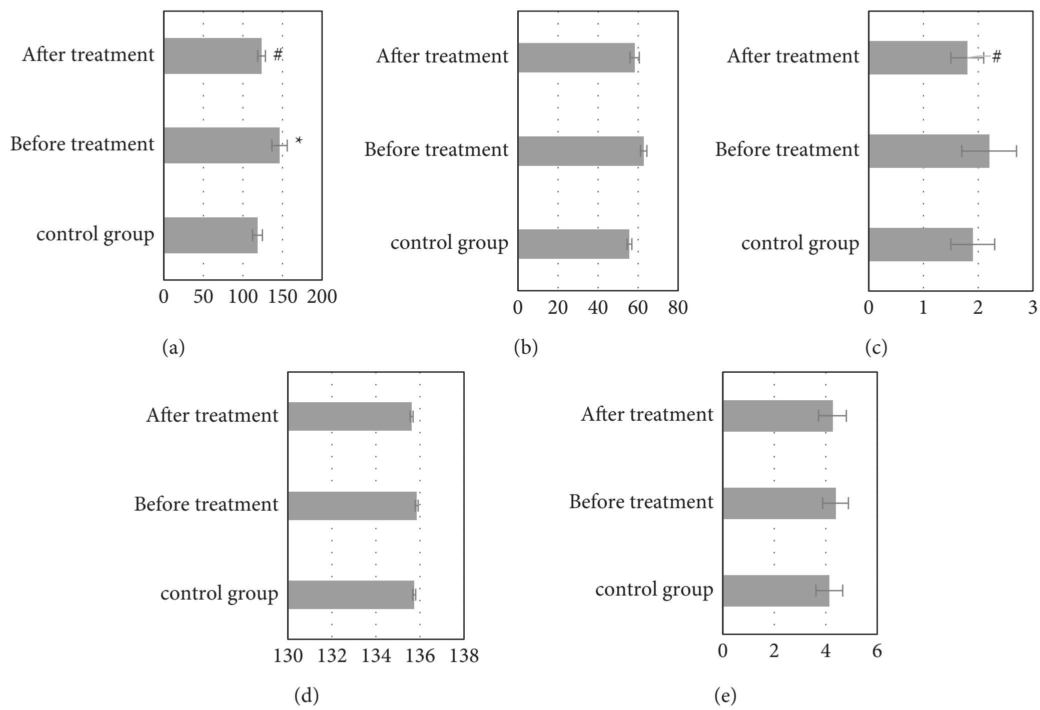

FIGURE 4: Changes in various indexes of the liver function test. *Compared with the control group, $P < 0.05$; #compared with that before treatment, $P < 0.05$. (a) AST (U/L). (b) ALT (U/L). (c) TBIL (umol/L). (d) Na+ (mmol/L). (e) K+ (mmol/L).

which increased significantly compared with that before treatment, with a statistically significant difference ($P < 0.05$). Although there was a difference compared with the control group, it was not significant, $P > 0.05$ (Figures 2 and 3).

3.3. Laboratory Test Results. The contents of AST, ALT, TBIL, Na^+, and K^+ in the serum of the control group were 118.4 ± 6.2 U/L, 55.7 ± 1.2 U/L, $1.9 \pm 0.4\,\mu$mol/L, 135.74 ± 4.76 mmol/L, and 4.14 ± 0.52 mmol/L, respectively; before treatment, the content of AST in the serum of the study group was 146.3 ± 9.7 U/L, which was significantly higher than that of the control group, and the difference was statistically significant ($P < 0.05$). Although other contents increased or decreased in varying degrees, the difference was not statistically significant ($P > 0.05$). After treatment, the content of AST in serum was 123.5 ± 4.9 U/L, which was significantly lower than that before treatment, $P < 0.05$. The content of TBIL was $1.8 \pm 0.3\,\mu$mol/L, which was significantly lower than that ($2.2 \pm 0.5\,\mu$mol/L) before treatment, $P < 0.05$. There was no significant change in other contents (Figure 4).

3.4. Changes of Liver Function at Different Obstruction Sites. The detection results of the changes in liver function in patients with obstruction at different sites showed that after treatment, the serum ALT content of 55.7 ± 31.6 U/L, AST content of 66.4 ± 42.4 U/L, and TBIL content of $215.4 \pm 136.32\,\mu$mol/L in patients with high obstruction were significantly decreased compared with those before treatment, and the differences had statistical significance ($P < 0.05$); the K^+ content of 4.13 ± 0.4 mmol/L was significantly increased compared with that before treatment, and the difference had statistical significance ($P < 0.05$) (Figure 5). The serum ALT content of 47.4 ± 32.8 U/L, AST content of 56.1 ± 25.9 U/L, and TBIL content of $142.5 \pm 123.6\,\mu$mol/L in patients with low obstruction were significantly decreased compared with those before treatment, and the differences were statistically significant, $P < 0.05$ (Figure 6).

3.5. MRI Test Results. The results of MRI showed that ADC was $1.34 \pm 0.32 \times 10^{-3}\,mm^2/s$ in the control group, $1.24 \pm 0.44 \times 10^{-3}\,mm^2/s$ in patients with mild jaundice before treatment, $1.18 \pm 0.67 \times 10^{-3}\,mm^2/s$ in patients with moderate jaundice, and $1.02 \pm 0.66 \times 10^{-3}\,mm^2/s$ in patients with severe jaundice; compared with the control group, the difference was statistically significant ($P < 0.05$); ADC was $1.17 \pm 0.49 \times 10^{-3}\,mm^2/s$ in patients with moderate jaundice and $1.20 \pm 0.27 \times 10^{-3}\,mm^2/s$ in patients with severe jaundice after treatment; compared with that before treatment, the difference was statistically significant ($P < 0.05$). Although ADC values were slightly increased in patients with mild jaundice, compared with those before treatment, the difference was not statistically significant ($P > 0.05$) (Figure 7).

4. Discussion

FXR regulates the synthesis of BAs in a tissue-specific manner. High levels of ligands activate the expression of hepatic FXR. FXR inhibits the synthesis of BAs in the classical pathway by inducing the expression of target gene atypical nuclear receptor small heterodimer partner (SHP)

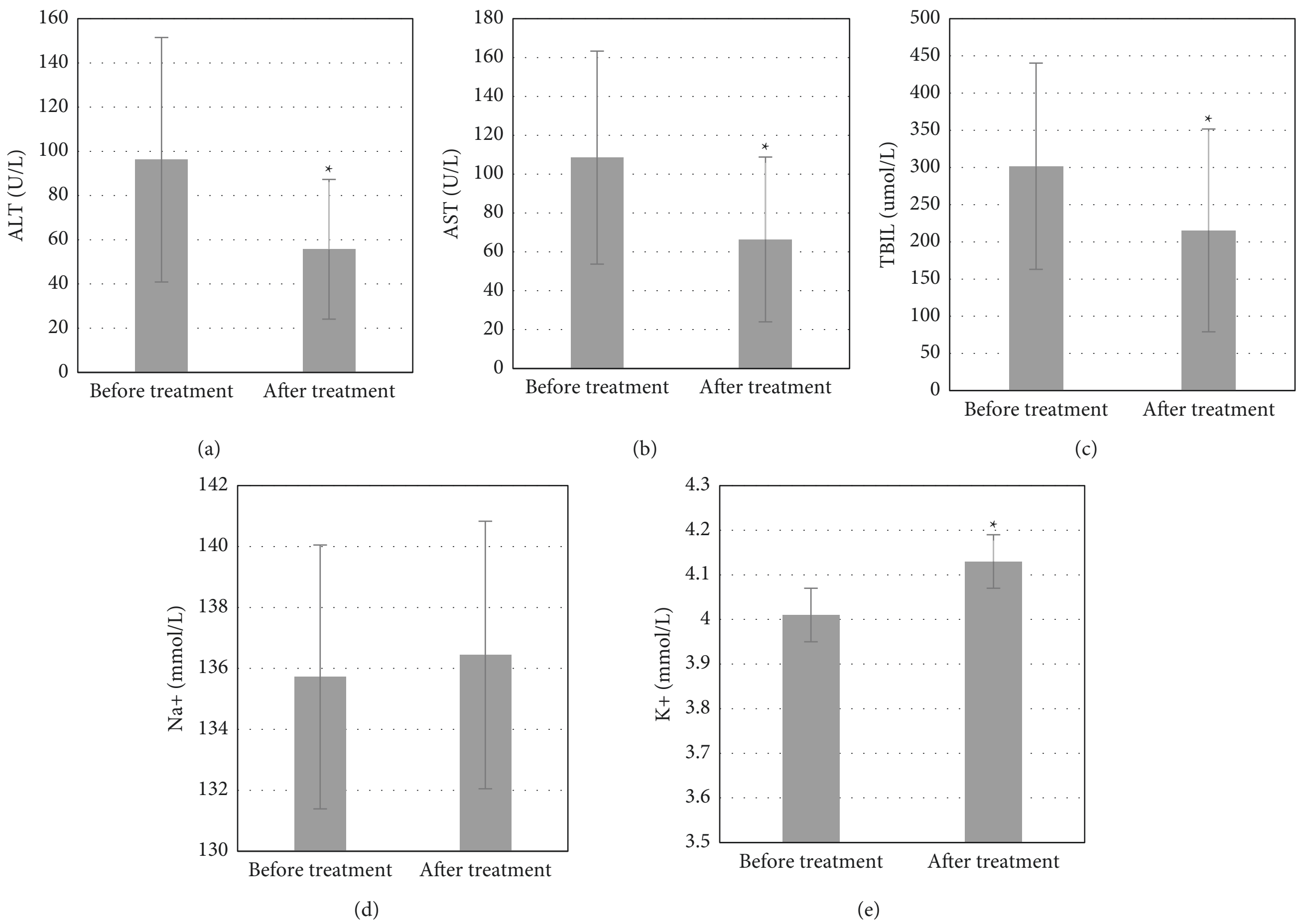

Figure 5: Changes of liver function in patients with high obstruction. *Compared with that before treatment, $P < 0.05$.

and further inhibiting the expression of rate limiting enzyme CYP7A1. The inhibition of the classical pathway often feeds back the activation of alternative pathway synthase [17]. The results of serum TBA content detection in patients with hepatocellular carcinoma and obstructive jaundice treated with FXR inhibitor showed that the serum TBA content was 13.5 ± 0.4 mmol/L and the intrahepatic TBA content was 34.6 ± 0.6 mmol/L in the control group. The serum TBA content was 11.2 ± 0.6 mmol/L, and the intrahepatic TBA content was 12.4 ± 1.8 mmol/L before treatment in the study group, which was significantly decreased compared with the control group, and the difference had statistical significance ($P < 0.05$); the serum TBA content was 12.8 ± 0.5 mmol/L, and the intrahepatic TBA content was 28.3 ± 1.2 mmol/L after treatment in the study group, which was significantly increased compared with that before treatment, and the difference had statistical significance ($P < 0.05$). Studies have shown that liver injury causes BA intestinal and hepatic circulation disorders and BA secretion disorders in the liver, blood BA levels increased significantly, and an increased BA reflux rate causes the increase in TBA levels in ileum [14]. FXR-based regulation of BAs is effective in the treatment of liver injury.

Studies have shown that elevated transaminases and serum bilirubin may present with obstructive jaundice when the left and right hepatic ducts are obstructed at the same time or the common hepatic duct is obstructed, and patients may present with only elevated transaminases and normal serum total bilirubin when one hepatic duct is obstructed alone [18]. The detection results showed that serum AST, ALT, TBIL, Na^+, and K^+ contents in the control group were 118.4 ± 6.2 U/L, 55.7 ± 1.2 U/L, 1.9 ± 0.4 μmol/L, 135.74 ± 4.76 mmol/L, and 4.14 ± 0.52 mmol/L, respectively; the serum AST content in the study group before treatment was 146.3 ± 9.7 U/L, significantly higher than that in the control group, and the difference had a statistical significance ($P < 0.05$); after treatment, the serum AST content was 123.5 ± 4.9 U/L, significantly lower than that before treatment, and the difference had statistical significance ($P < 0.05$); the TBIL content was 1.8 ± 0.3 μmol/L, significantly lower than 2.2 ± 0.5 μmol/L before treatment, and the difference had statistical significance ($P < 0.05$). The decrease in transaminase and serum bilirubin in the patient's body suggested that the obstructive jaundice was effectively improved. This is similar to the results of a simulation experiment by Yan-Xi et al. [19]. The detection results of the changes of liver function in patients at different obstruction sites showed that after treatment, the serum ALT content of 55.7 ± 31.6 U/L, AST content of 66.4 ± 42.4 U/L, and TBIL content of 215.4 ± 136.32 μmol/L in patients with high

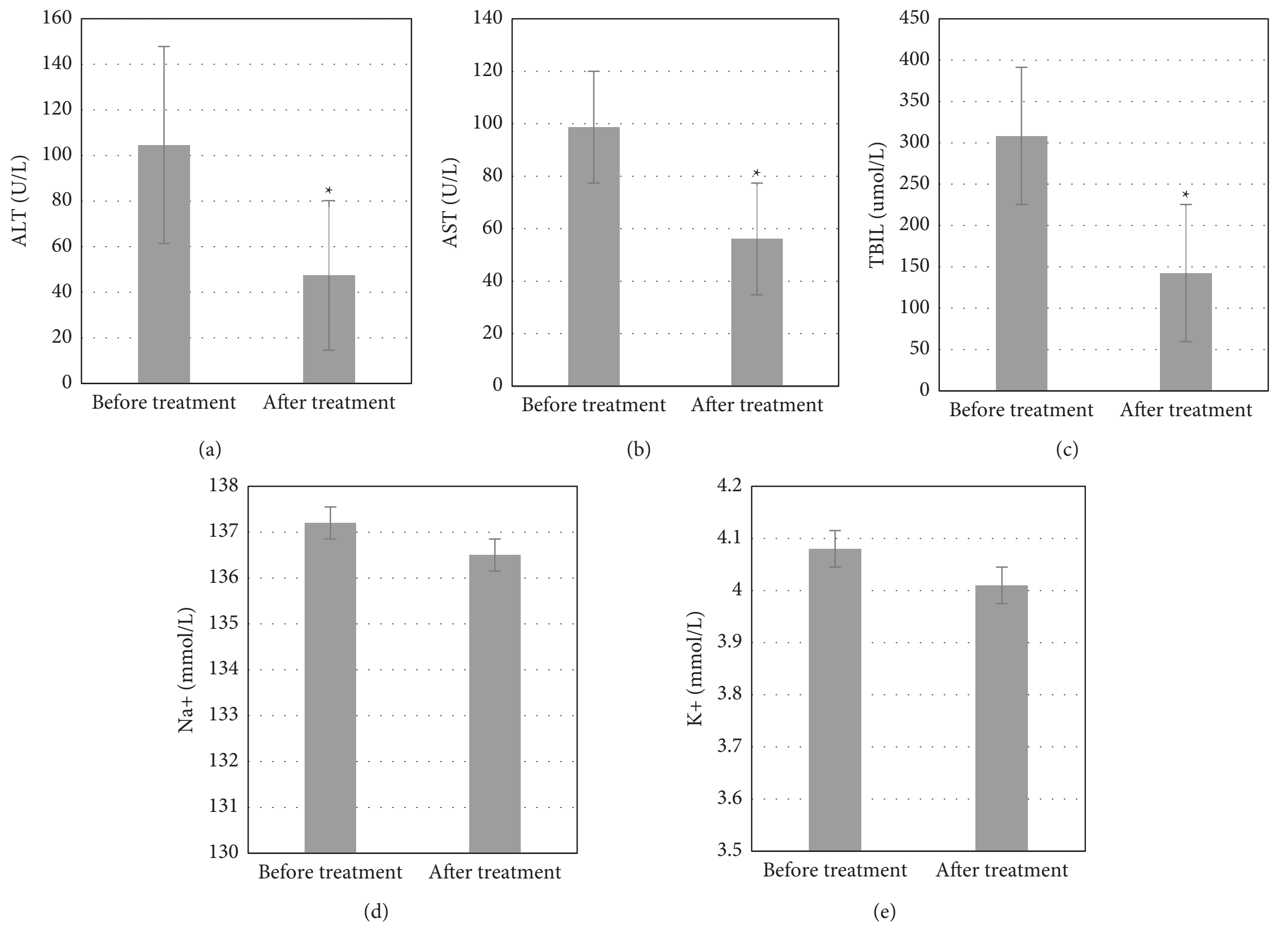

Figure 6: Changes of liver function in patients with low obstruction. *Compared with that before treatment, $P < 0.05$.

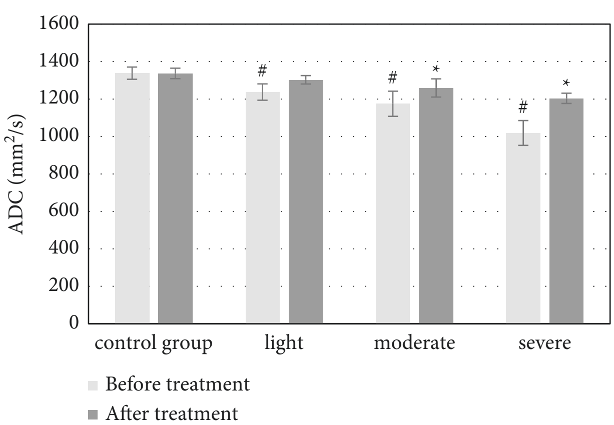

Figure 7: Changes in the ADC value before and after treatment. *Compared with that before treatment, $P < 0.05$; #compared with the control group, $P < 0.05$.

obstruction were significantly decreased compared with those before treatment; the differences had statistical significance ($P < 0.05$); the serum ALT content of 47.4 ± 32.8 U/L, AST content of 56.1 ± 25.9 U/L, and TBIL content of $142.5 \pm 123.6\,\mu$mol/L in patients with low obstruction were significantly decreased compared with those before treatment; the differences had statistical significance ($P < 0.05$).

Diffusion is an irregular thermal movement process of water molecules, also known as Brownian motion, which can reflect the water molecule movement of human tissues and organs by measuring the ADC value, and then reflect the physiological and pathological characteristics of body tissue structure [20]. The results of MRI showed that ADC was $1.34 \pm 0.32 \times 10^{-3}\,mm^2/s$ in the control group, $1.24 \pm 0.44 \times 10^{-3}\,mm^2/s$ in patients with mild jaundice, $1.18 \pm 0.67 \times 10^{-3}\,mm^2/s$ in patients with moderate jaundice, and $1.02 \pm 0.66 \times 10^{-3}\,mm^2/s$ in patients with severe jaundice before treatment, and the difference was statistically significant compared with the control group, $P < 0.05$; ADC was $1.17 \pm 0.49 \times 10^{-3}\,mm^2/s$ in patients with moderate jaundice and $1.20 \pm 0.27 \times 10^{-3}\,mm^2/s$ in patients with severe jaundice after treatment, and the difference was statistically significant compared with that before treatment, $P < 0.05$. The possible mechanisms were analyzed as follows: (1) due to the increase in serum bilirubin, bile salts, and plasma endotoxin concentration, the apoptosis of hepatocytes was accelerated: the Na^+-K^+ ATPase activity of hepatocytes was inhibited, resulting in cytotoxic edema and bile duct. Bile duct epithelial proliferation and a small amount of irregular capillary network was formed around the new bile duct, which increased the cell density and decreased the intercellular space, limiting the diffusion movement of water molecules; (2) the role of increased pressure in the upper bile duct of obstruction and cytokines released by macrophages, bile duct epithelial proliferation, and capillary network formation around the new bile duct, so that the cell density increased and the intercellular space became smaller, further leading to limited water molecule diffusion; (3) cholestasis and inflammatory cell infiltration, resulting in liver microarchitecture destruction and remodeling, caused microcirculatory pathway disorders, intrahepatic microthrombosis, and reduced hepatic effective blood flow, resulting in decreased measured ADC values. However, although the ADC values of patients with mild jaundice increased slightly, there was no significant difference compared with those before treatment, with no statistical significance, $P > 0.05$. It may be because in mild jaundice, after obstruction, the serum bilirubin level was slightly increased, the pressure in the bile duct was increased, the bile canaliculi were dilated, the microvilli were reduced, the normal structure of desmosomes was destroyed, and the bile solute molecules in bile canaliculi diffuse or reflux to the surrounding, causing osmotic pressure changed; a large number of water molecules entered the intercellular space, resulting in increased intercellular space and increased diffusion movement of water molecules, which counteracted with the factors limiting the movement of water molecules and made the increased measured ADC value. When bilirubin continued to rise, factors that limited the movement of water molecules dominated, resulting in reduced ADC values.

5. Conclusion

FXR inhibitor was used to regulate BA in the treatment of obstructive jaundice injury in liver cancer, and the therapeutic effect was detected by MRI cholangiopancreatography. The results showed that the regulation of BA based on FXR could regulate the reabsorption of BA, accelerate the circulation of BA, restore the homeostasis of BA metabolism, play a hepatoprotective role, reduce bilirubin content in the body, and improve jaundice injury, which has application value. However, due to the limitation of experimental conditions, the included sample size is small, there is no significant difference in the changes of some data, and the liver function is strong and the physiological and pathological changes are complex, resulting in that the measurement of the ADC value is affected. Therefore, it still needs to further expand the sample size for further study and confirmation.

Data Availability

The data used to support the findings of this study are available from the corresponding author upon request.

Conflicts of Interest

The authors declare no conflicts of interest.

Acknowledgments

This work was supported by the Qiqihar City Science and Technology Plan Joint Guidance Project (category of project no. LHYD-2021073).

References

[1] E. T. Pavlidis and T. E. Pavlidis, "Pathophysiological consequences of obstructive jaundice and perioperative management," *Hepatobiliary and Pancreatic Diseases International*, vol. 17, no. 1, pp. 17–21, 2018 February.

[2] Y. S. Vinnik, R. A. Pakhomova, L. V. Kochetova, E. A. Voronova, V. V. Kozlov, and A. K. Kirichenko, "Predictors of hepatic insufficiency in obstructive jaundice," *Khirurgiia*, no. 3, pp. 37–41, 2018, Russian.

[3] E. H. Kim, H. G. Lee, J. S. Oh, H. J. Chun, and B. G. Choi, "Extraluminal recanalization of bile duct anastomosis obstruction after liver transplantation," *Journal of Vascular and Interventional Radiology*, vol. 29, no. 10, pp. 1466–1471, 2018 October.

[4] A. G. Feldman and R. J. Sokol, "Recent developments in diagnostics and treatment of neonatal cholestasis," *Seminars in Pediatric Surgery*, vol. 29, no. 4, Article ID 150945, 2020 August.

[5] A. Sokal, A. Sauvanet, B. Fantin, and V. de Lastours, "Acute cholangitis: diagnosis and management," *Journal of Visceral Surgery*, vol. 156, no. 6, pp. 515–525, 2019 December.

[6] C. J. Zech, A. Ba-Ssalamah, T. Berg et al., "Consensus report from the 8th international forum for liver magnetic resonance imaging," *European Radiology*, vol. 30, no. 1, pp. 370–382, 2020 January.

[7] M. Guarino, V. Cossiga, and F. Morisco, "The interpretation of liver function tests in pregnancy," *Best Practice & Research Clinical Gastroenterology*, vol. 44-45, Article ID 101667, 2020 February - April.

[8] B. M. Metra, F. F. Guglielmo, D. L. Halegoua-DeMarzio, J. M. Civan, and D. G. Mitchell, "Beyond the liver function tests: a radiologist's guide to the liver blood tests," *RadioGraphics*, vol. 42, no. 1, pp. 125–142, 2022 January-February.

[9] C. Keerl and C. Bernsmeier, *Therapeutische Umschau. Revue therapeutique*, vol. 77, no. 8, pp. 371–378, 2020, German.

[10] E. R. McGlone and S. R. Bloom, "Bile acids and the metabolic syndrome," *Annals of Clinical Biochemistry*, vol. 56, no. 3, pp. 326–337, 2019 May.

[11] J. Y. L. Chiang and J. M. Ferrell, "Bile acids as metabolic regulators and nutrient sensors," *Annual Review of Nutrition*, vol. 39, pp. 175–200, 2019 August 21.

[12] A. L. Ticho, P. Malhotra, P. K. Dudeja, R. K. Gill, and W. A. Alrefai, "Intestinal absorption of bile acids in health and disease," *Comprehensive Physiology*, vol. 10, no. 1, pp. 21–56, 2019 December 18.

[13] S. Fiorucci, E. Distrutti, A. Carino, A. Zampella, and M. Biagioli, "Bile acids and their receptors in metabolic disorders," *Progress in Lipid Research*, vol. 82, Article ID 101094, 2021 April.

[14] D. J. Shin and L. Wang, "Bile acid-activated receptors: a review on FXR and other nuclear receptors," *Handbook of Experimental Pharmacology*, vol. 256, pp. 51–72, 2019.

[15] J. Y. L. Chiang and J. M. Ferrell, "Bile acid metabolism in liver pathobiology," *Gene Expression*, vol. 18, no. 2, pp. 71–87, 2018 May 18.

[16] M. Sun, Q. W. Yu, T. Xiang, Z. Z. Jiang, and L. Y. Zhang, "[2, 3, 5, 4′-Tetrahydroxystibane-2-O-β-D-glucoside induces liver injury by disrupting bile acid homeostasis and phospholipids efflux]," *Zhongguo Zhongyao Zazhi*, vol. 46, no. 1, pp. 139–145, Article ID 33645063, Chinese, 2021 January.

[17] J. Y. L. Chiang and J. M. Ferrell, "Bile acid receptors FXR and TGR5 signaling in fatty liver diseases and therapy," *American*

Journal of Physiology - Gastrointestinal and Liver Physiology, vol. 318, no. 3, pp. G554–G573, 2020 March 1.

[18] S. Uemura, R. Higuchi, T. Yazawa, W. Izumo, T. Otsubo, and M. Yamamoto, "Level of total bilirubin in the bile of the future remnant liver of patients with obstructive jaundice undergoing hepatectomy predicts postoperative liver failure," *J Hepatobiliary Pancreat Sci*, vol. 27, no. 9, pp. 614–621, 2020 September.

[19] L. I. Yan-Xi, L. I. Xiao-Peng, G. U. Jian et al., "[Study on protective mechanism of Tibetan medicine Ershiwuwei Songshi Pills on cholestatic liver injury in rats based on FXR signaling pathway]," *Zhongguo Zhongyao Zazhi*, vol. 45, no. 21, pp. 5273–5279, 2020 November, Chinese.

[20] F. Nalaini, F. Shahbazi, S. M. Mousavinezhad, A. Ansari, and M. Salehi, "Diagnostic accuracy of apparent diffusion coefficient (ADC) value in differentiating malignant from benign solid liver lesions: a systematic review and meta-analysis," *British Journal of Radiology*, vol. 94, no. 1123, Article ID 20210059, 2021 July 1.

Hindawi
Contrast Media & Molecular Imaging
Volume 2022, Article ID 5707231, 9 pages
https://doi.org/10.1155/2022/5707231

Research Article

Magnetic Resonance Imaging Data Features to Evaluate the Efficacy of Compound Skin Graft for Diabetic Foot

Chunlei Wang[1] **Xiaomei Yu**[1] **Ying Sui**[2] **Junhui Zhu**[1] **Bo Zhang**[1] **and Yongtao Su**[2]

[1]*Department of Burn Skin Surgery, PKUcare Luzhong Hospital, Zibo 255400, Shandong, China*
[2]*Innovation Research Institute, Shandong University of Traditional Chinese Medicine, Jinan 250355, Shandong, China*

Correspondence should be addressed to Yongtao Su; 161843328@masu.edu.cn

Received 15 February 2022; Revised 9 May 2022; Accepted 10 May 2022; Published 13 June 2022

Academic Editor: M. Pallikonda Rajasekaran

This study aimed to analyze the role of magnetic resonance imaging (MRI) data characteristics based on the deep learning algorithm in evaluating the treatment of diabetic foot (DF) with composite skin graft. In this study, 78 patients with DF were randomly rolled into the experimental group (composite skin graft) and control group (autologous skin graft) with 39 patients in each group. MRI scans were performed before and after treatment to compare the changes of experimental observation indicators such as healing time, recurrence rate, and scar score. The results showed that T1-weighted imaging (T1WI) of the scanning sequence was considerably increased in the experimental group after treatment. The signal intensity of fat-suppressed T2-weighted imaging (T2WI) and fat-suppressed T1WI enhancement sequences was considerably decreased ($P < 0.05$). In addition, compared with the control group, the recurrence rate, healing time, and scar score in the experimental group were considerably decreased ($P < 0.05$). The accuracy, specificity, and sensitivity of MRI imaging information in evaluating the therapeutic effect of DF patients were 85.2%, 89.75%, and 86.47%, respectively. According to the specificity and sensitivity, the subject operating characteristic curve was drawn, and the area under the curve was determined to be 0.838. In summary, MRI image data characteristics based on the deep learning algorithm can provide auxiliary reference information for the efficacy evaluation of compound skin transplantation for DF.

1. Introduction

In recent years, with the rapid growth of the incidence of diabetes, the number of diabetic foot (DF) patients has gradually increased [1]. DF is a very serious complication caused by diabetes, usually manifested as infection of the lower limbs, ulcers, and even the destruction of deep tissue and bone marrow. Pathological changes involve neuropathy and peripheral vascular lesions of the lower limbs. The disease is characterized by a long period of disease, which is often difficult to cure, high treatment cost, and a very high recurrence rate, thus bringing serious burden and harm to patients and families all over the world [2–5]. According to statistics, in 2003, the number of diabetes patients in the world was close to 200 million, while in 2014, the number of diabetes patients has exceeded 400 million. At this rate, the number of diabetes patients in the world will exceed 600 million by 2035 [6–8]. In China, the number of diabetes patients is also increasing rapidly. The literature reported that the incidence of diabetes in China was only 0.67% in 1980. In 2013, the incidence of diabetes has increased to more than 10%, which means that 10-11 out of 100 randomly selected people in China have diabetes. The incidence of DF is also high, and there are about 8 DF patients in every 100 people [9, 10]. Clinical DF is often difficult to cure, and the mechanism is that the DF patients lack growth factors required for normal healing. DF patients increased proteolytic activity, resulting in a rapid increase in matrix metalloproteinase concentration, so that the wound could not heal normally. The function of fibroblasts in patients is limited, resulting in the difficulty of normal synthesis of collagen and abnormal blood vessel formation, resulting in affected wound healing. In DF patients, the normal activity of white blood cells in the body inhibited, and sufficient neutrophils cannot gather around the wound, leading to the failure of the antiinfection function of the wound site and the limitation of blood supply, thus affecting wound healing [11–14].

Slow healing of DF ulcer seriously affects the quality of life of patients. Therefore, the treatment and management of DF patients is particularly important [15].

The treatment of DF mainly includes medical treatment and surgical treatment. First, according to the situation of DF wounds, different methods of debridement and dressing change should be appropriately given to remove local bacteria or infected microorganisms to promote wound healing, and systemic antibiotic treatment should be given to patients at the same time [16, 17]. After long-term conservative medical treatment, the wound will not heal for a long time and even the infection will be aggravated. At that time, it is necessary to use surgical treatment to remove the necrotic limbs, remove the potential infection foci, and avoid the development of DF into sepsis. Skin grafting is an operation with significant efficacy for the repair of large areas of wounds and is a good choice for the healing of diabetic foot wounds [18–20]. Skin grafting is often used to repair DF ulcers in clinical practice. When simple skin grafting is adopted to repair wounds, such as medium or full thickness skin, the survival rate of full thickness skin transplantation is often low due to the existence of granulation wounds. After medium thick skin transplantation, the healing barrier of donor site will be caused, resulting in the generation of new surface. Thick blade skin transplantation can solve the problem of low survival rate. However, due to the lack of dermis after skin grafting, the friction resistance and pressure resistance of the surface are poor, and it is easy to cause secondary ulceration. Composite skin transplantation can solve the above problems. In this study, acellular allogeneic dermal matrix and autologous skin combined with skin grafting were used to treat DF patients. Acellular allogenic dermal matrix refers to the fixation and cross-linking of allogenic skin extracellular matrix with solid agent treatment. Then, chelating agents and trypsin were used to remove the epidermis, and DNA and RNA enzymes and chemical agents were used to treat the reticular acellular allogenic dermis to reduce the cellular immune response [21].

Diabetes can be diagnosed and observed by X-ray, computed tomography (CT), magnetic resonance imaging (MRI), and other influencing methods. X-rays are an economical method and are often used to evaluate bone infection, but changes in the bone usually do not show up until 1-2 weeks after infection. The density resolution of CT is higher than that of X-ray, but compared with MRI, the early changes of the lesions displayed by CT are obviously inferior. MRI and CT examination have the same price, high soft tissue resolution, and spatial resolution, which can diagnose abnormal changes of bone early and can accurately diagnose the range of lesions and whether there is infection, providing a reliable basis for the selection of clinical plans. Therefore, MRI has unique advantages in the diagnosis of DF. There are many imaging features around ulcer skin of DF. Computer vision algorithms can make use of these visual symbols to distinguish and use deep learning-based methods for medical image analysis, and processing has become an important part of imaging diagnosis. It plays a crucial role in detecting a variety of diseases, including DF ulcers. As a target detection algorithm, the single shot detector (SSD) is one of the main target detection frameworks. With high speed and accuracy, it can detect objects on different feature maps at different scales, resist changes in object size to a certain extent, and give more robustness to the network. Methods and technologies based on deep learning have been widely applied in the medical field and have a high clinical application value [22].

In this research, DF patients meeting the requirements were selected and divided into the experimental group and control group. Different methods were used for treatment, and MRI scanning and clinical indicators were observed and compared to comprehensively evaluate the application value of MRI imaging information based on the deep learning algorithm in the curative effect of compound skin transplantation for diabetic foot, so as to provide a feasible plan for the clinical treatment of DF.

2. Materials and Methods

2.1. The Research Objects. In this study, 78 patients with DF admitted to hospital from January 10, 2018, to May 10, 2020, were selected and divided into the experimental group and control group according to their treatment intention, with 39 patients in each group. Composite skin graft and autologous skin graft were adopted for treatment in the experimental group and control group, respectively. This study had been approved by the ethics committee of hospital, and the patients' families had been informed of this study and signed informed consent.

Inclusion criteria were as follows: patients diagnosed with DF according to diagnostic criteria, patients had been treated with combined skin graft/autologous skin graft, patients older than 18 years, patients who had signed informed consent, and patients with contraindications were not examined.

Exclusion criteria were as follows: patients with other serious underlying diseases, patients with severe allergic constitution, patients with obesity, patients with lower limb amputation, patients whose family members did not agree or sign informed consent, and patients with poor coordination or did not accept follow-up.

2.2. Treatment Methods. Patients in the experimental group were treated with compound skin graft. First, debridement was performed to remove the necrotic skin, subcutaneous tissue, tendon, fascia, and necrotic bone. Then, the skin wound was covered with VSD dressing, and the negative pressure sealing drainage technology was used to keep the VSD unobstructed by periodic flushing. VSD was replaced regularly until the necrotic tissue at the depth of the wound was removed and the granulation tissue was fresh and full. For skin grafting, the acellular allogenic dermal matrix prepared was taken and washed with normal saline for three times. The size of the wound was compared and trimmed, not exceeding the edge of the wound. Acellular allogenic dermal matrix was fixed on the wound surface with net face up and dermal face down to make it closely fit without leaving gaps. The skin of the leg was taken with an electric skin knife, transplanted on the wound surface, and fixed. It was washed with normal saline to make it closely fit, leaving no dead cavity. Then, VSD material was covered on the surface again, and negative pressure was applied to seal drainage. The patency of the VSD was checked regularly every day, and the affected limb was kept in a high position. VSD material was removed 7–10 days later, and the survival of skin grafting was observed. Dressing change and nursing were continued on time until the wound healed completely. The control group was treated with autologous skin graft. Autologous skin graft thickness was about 0.4 mm. Other treatments were the same as compound skin graft.

2.3. MRI Scan. 3.0 T MR imaging scanning instrument was used for scanning. Sagittal plane, transverse plane, and coronal plane scanning were performed according to the lesion site of the foot. Special coil for the foot was adopted. The scanning sequence included T1-weighted Imaging (T1WI), T2-weighted Imaging (T2WI), and fat-suppressed T1WI. Enhancement scan was performed about 3 min after the gadolinium contrast agent was injected. The injection volume was calculated according to 0.1 mmoL/kg, and the injection rate was 2.5 mL/s. Specific scanning parameters are shown in Figure 1.

2.4. Deep Learning Algorithm Model. As an excellent target detection model, the single shot detector (SSD) has been widely used. SSD uses feature graphs from multiple convolutional layers to perform boundary box regression and target category prediction. Target detection is carried out at different convolutional layers in combination with features extracted from feature graphs of different sizes, so as to improve the accuracy of detecting small objects in size. The specific flowchart is shown in Figure 2.

The original photos were first input to obtain feature maps of different scales. Four prior frames were set, namely, predetermined frames of the target. Feature maps of different sizes corresponded to prior frames of different sizes. The side length of the smaller prior frame was set as x, the side length of the larger prior frame as $\sqrt{x \times d}$, and the aspect ratio as Ar. Then, the length (C) of the rectangular frame can be expressed by

$$C = \sqrt{Ar} \times x. \tag{1}$$

The width (K) of the rectangular box is expressed by

$$K = \frac{1}{\sqrt{Ax} \times x}. \tag{2}$$

x and d are determined by

$$M_0 = Mx + \frac{Md - Mx}{s - 1} (a - 1). \tag{3}$$

The range of a is shown in

$$a \in [1, s]. \tag{4}$$

In equation (4), s represents the number of feature maps. When Ar is 1, a scale will be added, as shown in

$$M_0 = \sqrt{M_0 \times M_{0+1}}. \tag{5}$$

Based on the average accuracy of the test means in different test sets, the accuracy of SSD ranged from 67.0% to 78.8%. SSD has the dual guarantee of accuracy and detection rate. The algorithm proposes that it has a variety of width-to-height ratio prior frames, which makes it have a good detection effect for all kinds of objects of different sizes.

2.5. Evaluation Indexes. Basic data collected from the two groups were compared and analyzed, including age, sex, course of disease, body mass index, and glycosylated hemoglobin (HbAlC), and Wagner grading of DF was performed using MRI scan. According to the overall cardiac function parameters obtained from MRI scans, the changes of T1WI, fat-suppressed T2WI, and enhancement sequences of MRI scans were observed and compared between the two groups to analyze the relationship between MRI intensity signal and therapeutic effect after combined skin graft treatment. The wound healing of patients in the two groups was recorded, and the time from surgical treatment to wound healing was recorded and compared. The total number of cases was S, the number of cases was C, and the complete healing rate R was calculated according to

$$R = \frac{c}{s} \times 100\%. \tag{6}$$

The healing time of the donor skin area was recorded and compared. The healing state was determined when the wound surface of the donor skin area was gradually epithelialized, and the skin surface was dry. Scar status was recorded and compared between the two groups. The patients were scored in terms of skin graft softness, color, thickness, and vascular distribution using the Vancouver Scar Scale. For the calculation and statistics of the recurrence rate, the patients were followed up after discharge, and the recurrence rate of the two groups of patients was calculated. The number of patients with reulcer at the same site was denoted as G, the total number of patients in each group was denoted as S, and the recurrence rate F was calculated according to

$$F = \frac{G}{S} \times 100\%. \tag{7}$$

In this study, experimental observation results after transplantation treatment were used as the reference standard, and three common indicators were used to evaluate the ability of MRI image data characteristics to evaluate the therapeutic effect of DF patients. Accuracy, specificity, and sensitivity were calculated in the following equations.

$$\text{Accuracy} = \frac{TA + TB}{TA + FC + TB + FD}, \tag{8}$$

$$\text{Specificity} = \frac{TB}{FC + TB}, \tag{9}$$

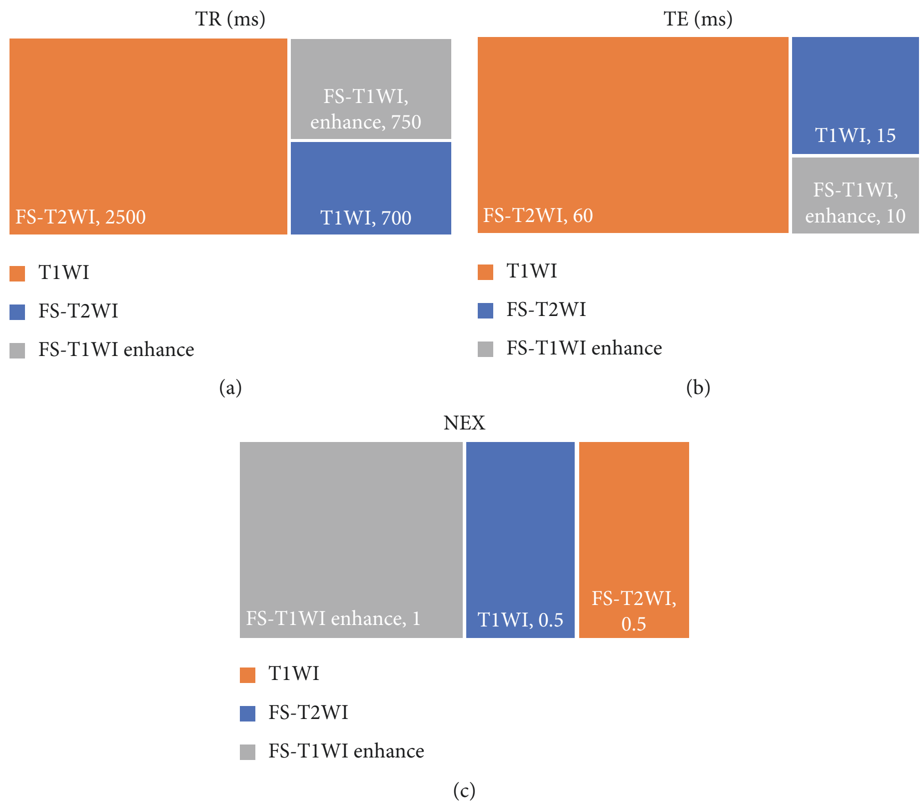

Figure 1: MRI scanning parameters. (a) The repetition time of each scan sequence. (b) The echo time of each scan sequence. (c) The length of echo chain of each scan sequence.

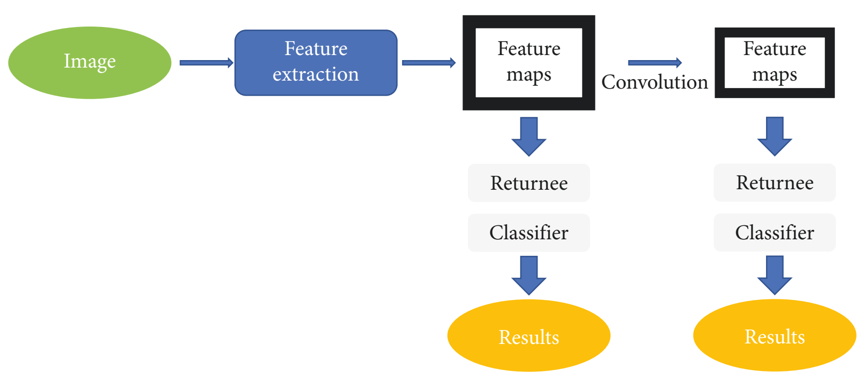

Figure 2: SSD detection flowchart.

$$\text{Sensitivity} = \frac{TA}{FD + TA}. \tag{10}$$

Among them, *TA* is true positive, indicating that the diagnosis result is positive, which is positive. *TB* refers to true negative, indicating that the diagnosis is negative, but negative. *FC* is false positive, meaning that the diagnosis is positive, but negative. *FD* is false negative, which means the actual result is positive and the diagnostic result is negative.

Receiver operating characteristic (ROC) curve was used to represent the ability of MRI image data characteristics to evaluate the therapeutic effect of DF patients. According to ROC, the area under ROC curve (AUC) was determined.

2.6. Statistical Methods. All experimental data were statistically analyzed by the SPSS 24.0 software. The measurement data were expressed by mean ± standard deviation ($\overline{x} \pm s$), and the counting data were statistically inferred by the χ^2 test. If the measurement data conformed to normal distribution, the t-test was adopted. $P < 0.05$ was statistically significant.

3. Results

3.1. MRI Imaging Results. Figure 3 shows MRI images of different DF patients in different planes. Figure 3(a) shows a 55-year-old male DF patient who had suffered from diabetes for 11 years with swollen feet and ulcers. Figure 3(b) shows a

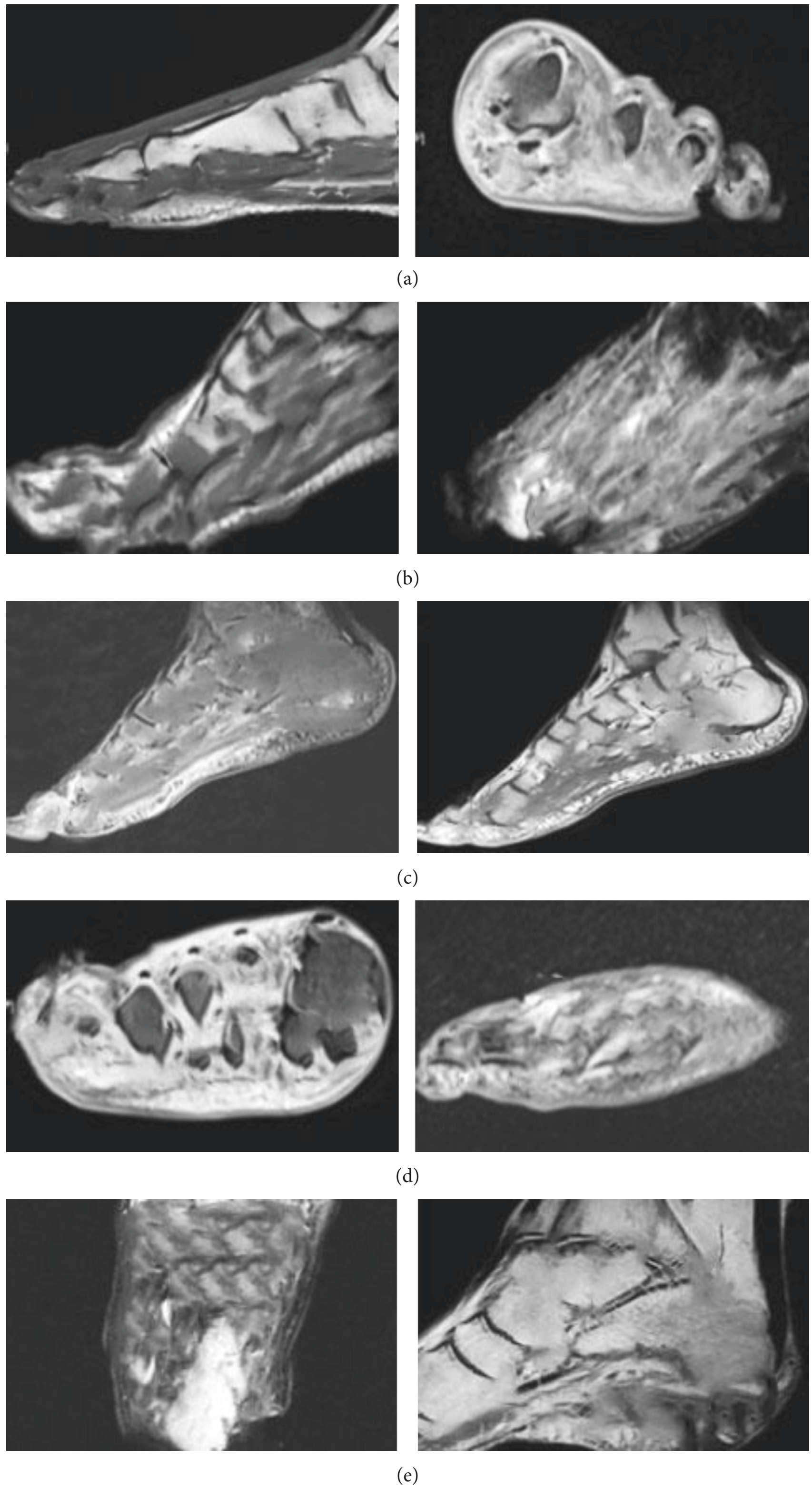

FIGURE 3: MRI images of different DF patients.

DF patient, male, 57 years old, with observed skin continuity interruption, abscess, and sinus tract. Figure 3(c) shows a DF patient, male, 64 years old, with high blood glucose level for 8 years. Both feet were broken and admitted to hospital for treatment. Figure 3(d) shows a 63-year-old male DF patient with elevated blood glucose for 13 years, who was hospitalized with foot ulcer and discharge. Figure 3(e) shows a deep penetrating skin ulcer and sinus tract on the plantar.

3.2. SSD Algorithm Target Detection. In Figure 4, the SSD target detection model was used to accurately locate and extract features of wounds requiring skin grafting in MRI images, which was also applicable to target detection with different aspect ratios.

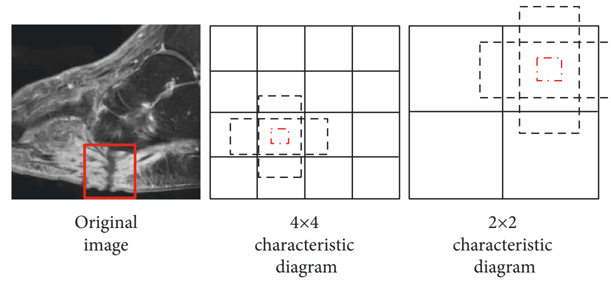

Figure 4: SSD target detection.

3.3. Comparison of Basic Data between the Two Groups. Through comparison, there were no substantial differences in age, gender, course of disease, body mass index, HbAlC, and Wagner grading between the two groups ($P < 0.05$, Figure 5).

3.4. Comparison Results of MRI Scanning Sequence Signal. MRI scan sequence signal intensity of patients before and after treatment was obtained. Comparative analysis showed that T1WI signal intensity of the experimental group was considerably increased after treatment, while the signal intensity of fat-inhibited T2WI and fat-suppressed T1WI enhanced sequence was considerably decreased ($P < 0.05$, Figure 6).

3.5. Results of Experimental Indicators after Treatment. The results showed that compared with the control group, there was no statistical difference in the wound healing time and complete healing rate in the experimental group ($P > 0.05$), while the recurrence rate, healing time of the donor skin area, and scar score were considerably decreased ($P < 0.05$). The specific results are shown in Figures 7 and 8.

3.6. MRI Imaging Information Evaluation Effectiveness. Through calculation of accuracy, specificity, and sensitivity, it was found that MRI imaging information had high accuracy, specificity, and sensitivity in evaluating the therapeutic effect of DF patients, which were 85.2%, 89.75%, and 86.47%, respectively. ROC curves were drawn based on MRI imaging information to evaluate the specificity and sensitivity of therapeutic effects in DF patients (Figure 9). Meanwhile, AUC was determined to be 0.838 according to ROC.

4. Discussion

At present, the number of patients with diabetes is increasing. As one of the most serious complications of diabetes, DF brings serious economic and mental burden to patients and their families. It is estimated that the number of diabetes patients in the world will exceed 600 million in 2035. DF has a long disease cycle, difficult to cure, high treatment cost, and high recurrence rate. Studies reported that every 20 seconds, a DF patient faces amputation, which seriously affects the quality of life of the patient, and the 5-year mortality rate of the patient after amputation is more than 50%. Therefore, the timely treatment and management of DF patients is crucial [23]. Skin grafting can help DF patients repair ulcers. Skin grafting alone often leads to the low survival rate of full thickness skin transplantation due to the existence of granulation wounds. After medium thick skin transplantation, the healing barrier of donor site will be caused, resulting in the generation of new surface. Thick blade skin transplantation can solve the problem of the low survival rate. However, due to the lack of dermis after skin grafting, the friction resistance and pressure resistance of the surface are poor, which is easy to cause secondary rupture. In this study, acellular allogeneic dermal matrix and autologous skin combined with skin grafting for wound repair can overcome the above problems in DF patients [20]. MRI has great advantages in distinguishing various types of soft tissue infection and distinguishing between tissue and bone marrow. It can detect abnormal bone marrow signals early and accurately identify the range of soft tissue infection. Therefore, MRI can be used as an important means for routine diagnostic examination and posttreatment efficacy evaluation of DF to help optimize and improve the quality of life of patients with DF [24].

A total of 78 DF patients were selected as research subjects and divided into the experimental group (composite skin graft) and control group (autologous skin graft). MRI scanning was performed before and after treatment to compare the changes of MRI signal sequence intensity and other image data characteristics of patients, as well as the changes of experimental observation indicators such as healing time, recurrence rate, and scar score. This study aimed to analyze the application value of MRI image data features based on the deep learning algorithm in evaluating the treatment of DF with compound skin graft. The results showed that there were no substantial differences in age, gender, course of disease, body mass index, HbAlC, and Wagner grading between the two groups ($P > 0.05$), which increased the comparability of MRI image data in the evaluation of treatment efficacy between the two groups after treatment. The comparison analysis of the scanning sequence signal intensity of patients obtained by MRI scan before and after treatment showed that the T1WI signal intensity of the experimental group was considerably increased after treatment, while the signal intensity of fat-suppressed T2WI and fat-suppressed T1WI enhanced sequence was considerably decreased ($P < 0.05$). This indicated that there were differences in the intensity of MRI scan sequence T1WI, fat-suppressed T2WI, and fat-suppressed T1WI enhancement sequence before and after treatment, which were closely related to the treatment effect. Compared with the control group, there was no statistical difference in the wound healing time and complete healing rate of the experimental group ($P < 0.05$), while the

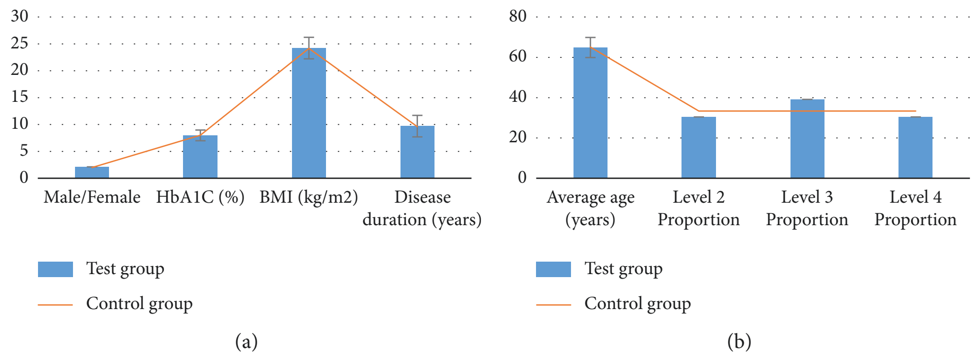

Figure 5: Comparison of basic data between the two groups. (a) The comparison results of gender ratio, HbAlC, body mass index, and disease course between the two groups. (b) The comparison results of average age and proportion of patients in Wagner classification between the two groups.

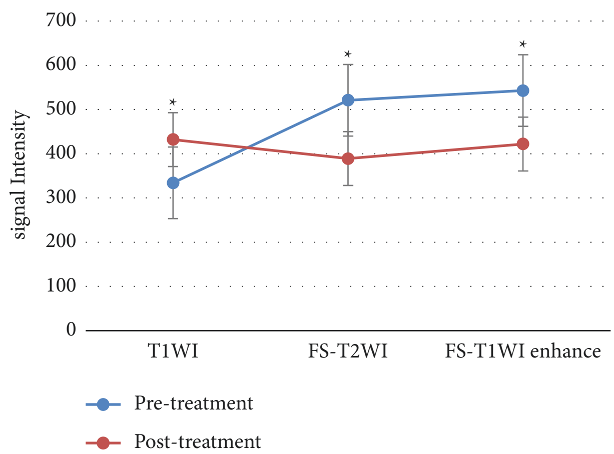

Figure 6: Changes in MRI sequence signal intensity before and after treatment. *Substantial difference, $P < 0.05$.

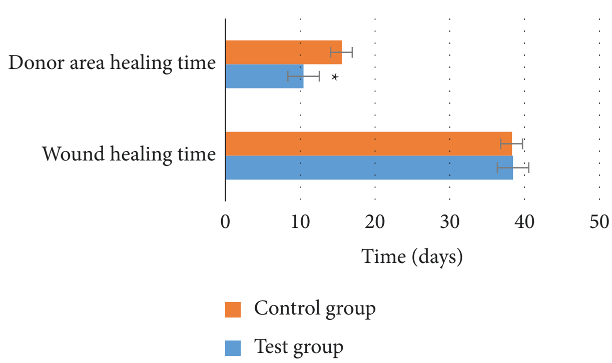

Figure 7: Comparison of wound healing time and donor site healing time between the two groups after treatment. *Substantial difference, $P < 0.05$.

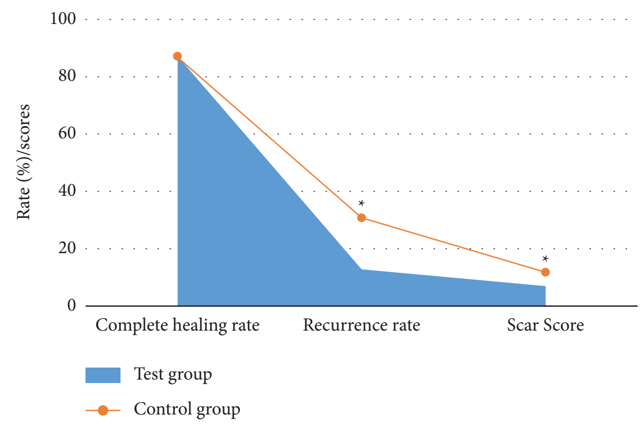

Figure 8: Comparison of complete healing rate, recurrence rate, and scar score between the two groups after treatment. *Substantial difference, $P < 0.05$.

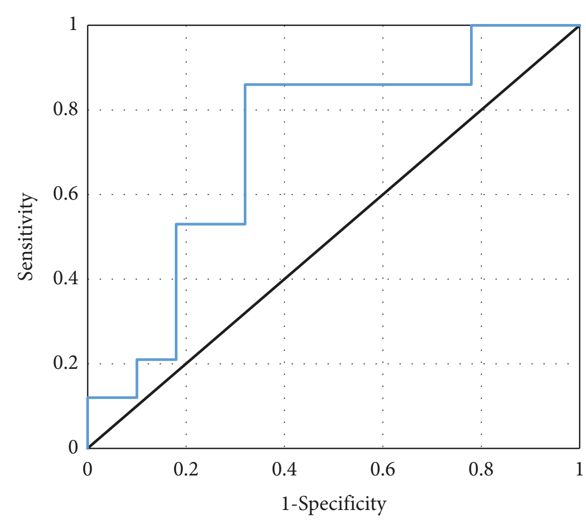

Figure 9: ROC curve results of MRI image data characteristics.

recurrence rate, healing time of the donor skin area, and scar score were considerably decreased ($P < 0.05$). This was consistent with the research results of Campitiello et al. [25]. After acellular treatment, the composite skin was fused with the body, resulting in the formation of epidermis and basement membrane, complete dermis structure, and less infiltration of inflammatory cells, which did not affect normal wound healing. Lantis et al. [26] also pointed out that due to DF end blood supply obstacles and factors of local high sugar, the recurrence rate was high, and the integrity of the skin was restored after transplantation of the composite skin, promoting capillary and normal expression of growth factors and cytokines and improving local microvascular environment, so the recurrence rate was also decreased. Through calculation of accuracy, specificity, and sensitivity, it was found that MRI imaging information had high accuracy, specificity, and sensitivity in evaluating the therapeutic effect of DF patients, which were 85.2%, 89.75%, and 86.47%, respectively. The specificity and sensitivity of the therapeutic effect of DF were evaluated according to MRI imaging information, and ROC curve was plotted. AUC was determined to be 0.838 according to ROC, indicating that the characteristics of MRI image data can provide a reference for the evaluation of the therapeutic effect after compound skin transplantation for DF. Some studies evaluated the correlation between diagnosis and treatment performance of DF image MRI and laboratory examination. It was found that MRI could be used to monitor and evaluate the curative effect of treating DF. As a noninvasive monitoring method, it is simple to operate and very sensitive and accurate to the pathological changes of DF patients, which is consistent with the results of this study [27]. In short, MRI image data features based on the deep learning algorithm can provide auxiliary information for the efficacy evaluation of compound skin transplantation for DF, which has a great application value.

5. Conclusion

In this study, DF patients in the experimental group and the control group were treated with compound skin graft and autologous skin graft, respectively. MRI was used to compare the signal sequence intensity, clinical healing time, recurrence rate, scar score, and other indicators of the two groups. The results showed that T1WI, fat-inhibited T2WI, and enhanced sequence signal intensity of MRI scan were correlated with the therapeutic effect. The accuracy, specificity, and sensitivity of MRI image data characteristics to evaluate the therapeutic effect of diabetic foot were high, which could provide a reference for the evaluation of the therapeutic effect of DF after compound skin transplantation. The deficiency of the study is that the sample size is small, which is relatively single, and does not have randomness and wide applicability. In the future study, multisite, multitype, and large sample size analysis and research will be considered. In conclusion, this work provides some reference for the treatment of diabetic foot transplantation.

Data Availability

The data used to support the findings of this study are available from the corresponding author upon request.

Conflicts of Interest

The authors declare that they have no conflicts of interest.

Authors' Contributions

Chunlei Wang and Xiaomei Yu contributed equally to this work.

References

[1] G. V. Carro, R. Saurral, E. L. Witman et al., "Diabetic foot attack. Pathophysiological description, clinical presentation, treatment and outcomes," *Medicina*, vol. 80, no. 5, pp. 523–530, 2020.

[2] R. Reardon, D. Simring, B. Kim, J. Mortensen, D. Williams, and A. Leslie, "The diabetic foot ulcer," *Australian Journal of General Practice*, vol. 49, no. 5, pp. 250–255, 2020.

[3] A. J. Pérez-Panero, M. Ruiz-Muñoz, A. I. Cuesta-Vargas, and M. González-Sánchez, "Prevention, assessment, diagnosis and management of diabetic foot based on clinical practice guidelines," *Medicine*, vol. 98, no. 35, Article ID e16877, 2019.

[4] L. Coffey, C. Mahon, and P. Gallagher, "Perceptions and experiences of diabetic foot ulceration and foot care in people with diabetes: a qualitative meta-synthesis," *International Wound Journal*, vol. 16, no. 1, pp. 183–210, 2019.

[5] U. Riedel, E. Schüßler, D. Härtel, A. Keiler, S. Nestoris, and H. Stege, "Wundbehandlung bei Diabetes und diabetischem Fußulkus," *Hautarzt, Der*, vol. 71, no. 11, pp. 835–842, 2020.

[6] L. Slahor and L. Iselin, "Der diabetische fuss (diabetic foot syndrome) (diabetic foot syndrome)," *Therapeutische Umschau*, vol. 77, no. 7, pp. 339–346, 2020 Sep.

[7] S. V. Yalla, R. T. Crews, N. A. Patel, T. Cheung, and S. Wu, "Offloading for the diabetic foot," *Clinics in Podiatric Medicine and Surgery*, vol. 37, no. 2, pp. 371–384, 2020.

[8] Y. Wang, T. Shao, J. Wang et al., "An update on potential biomarkers for diagnosing diabetic foot ulcer at early stage," *Biomedicine & Pharmacotherapy*, vol. 133, Article ID 110991, 2021.

[9] Z. Lv and L. Qiao, "Analysis of healthcare big data," *Future Generation Computer Systems*, vol. 109, pp. 103–110, 2020.

[10] A. N. Wadee, M. H. F. Aref, A. A. Nassar, I. H. Aboughaleb, and S. M. Fahmy, "The influence of low-intensity laser irradiation versus hyperbaric oxygen therapy on transcutaneous oxygen tension in chronic diabetic foot ulcers: a controlled randomized trial," *Journal of Diabetes and Metabolic Disorders*, vol. 20, no. 2, pp. 1489–1497, 2021.

[11] M. Aalaa, N. Mehrdad, S. Bigdeli, A. Dehnad, Z. Sohrabi, and K. S. Arabshahi, "Challenges and expectations of diabetic foot care from the patients' point of views," *Journal of Diabetes and Metabolic Disorders*, vol. 20, no. 2, pp. 1111–1118, 2021.

[12] E. M. Hossam, A. H. K. Alserr, C. N. Antonopoulos, A. Zaki, and W. Eldaly, "Autologous platelet rich plasma promotes the healing of non-ischemic diabetic foot ulcers. A randomized controlled trial," *Annals of Vascular Surgery*, vol. 82, no. 21, pp. 165–171, 2022.

[13] R. Collins, T. Burrows, H. Donnelly, and P. E. Tehan, "Macronutrient and micronutrient intake of individuals with diabetic foot ulceration: a short report," *Journal of Human Nutrition and Dietetics*, vol. 18, 2021.

[14] B. Bedriñana-Marañón, M. Rubio-Rodríguez, M. Yovera-Aldana, E. Garcia-Villasante, and I. Pinedo-Torres, "Association between the diabetes mellitus duration and the severity of diabetic foot disease in hospitalized patients in Latin America," *The International Journal of Lower Extremity Wounds*, vol. 10, Article ID 153473462110632, 2021.

[15] H. K. Nair, N. W. Ahmad, A. Ismail et al., "Maggot debridement therapy to treat hard-to-heal diabetic foot ulcers: a single-centre study," *Journal of Wound Care*, vol. 30, no. Sup12, pp. S30–S36, 2021.

[16] X. Lim, L. Zhang, Q. Hong et al., "Novel home use of mechanical negative pressure wound therapy in diabetic foot

ulcers," *Journal of Wound Care*, vol. 30, no. 12, pp. 1006–1010, 2021.

[17] S. Worasakwutiphong, T. Termwattanaphakdee, T. Kamolhan, P. Phimnuan, A. Sittichokechaiwut, and J. Viyoch, "Evaluation of the safety and healing potential of a fibroin-aloe gel film for the treatment of diabetic foot ulcers," *Journal of Wound Care*, vol. 30, no. 12, pp. 1020–1028, 2021.

[18] W. W. Jifar, S. A. Atnafie, and S. Angalaparameswari, "A review: matrix metallopeptidase-9 nanoparticles targeted for the treatment of diabetic foot ulcers," *Journal of Multidisciplinary Healthcare*, vol. 14, pp. 3321–3329, 2021.

[19] L. G. Felix, A. E. O. d Mendonça, I. K. F. Costa, S. H. D. S. Oliveira, A. M. d Almeida, and M. J. G. O. Soares, "Knowledge of primary care nurses before and after educational intervention on diabetic foot," *Revista gaucha de enfermagem*, vol. 42, Article ID e20200452, 2021.

[20] B. Colak, S. Yormaz, I. Ece, and M. Sahin, "Can intralesional epidermal growth factor reduce skin graft applications in patients with diabetic foot ulcer?" *Journal of the American Podiatric Medical Association*, vol. 111, no. 5, 2021.

[21] Z. Hu, J. Zhu, X. Cao et al., "Composite skin grafting with human acellular dermal matrix scaffold for treatment of diabetic foot ulcers: a randomized controlled trial," *Journal of the American College of Surgeons*, vol. 222, no. 6, pp. 1171–1179, 2016.

[22] S. Xie, Z. Yu, and Z. Lv, "Multi-disease prediction based on deep learning: a survey," *Computer Modeling in Engineering and Sciences*, vol. 128, no. 2, pp. 489–522, 2021.

[23] E. Jafarzadeh, R. Soheilifard, and A. Ehsani-Seresht, "Design optimization procedure for an orthopedic insole having a continuously variable stiffness/shape to reduce the plantar pressure in the foot of a diabetic patient," *Medical Engineering & Physics*, vol. 98, pp. 44–49, 2021.

[24] Y. Li, J. Zhao, Z. Lv, and J. Li, "Medical image fusion method by deep learning," *International Journal of Cognitive Computing in Engineering*, vol. 2, no. 2, pp. 21–29, 2021.

[25] F. Campitiello, M. Mancone, M. Cammarota et al., "Acellular dermal matrix used in diabetic foot ulcers: clinical outcomes supported by biochemical and histological analyses," *International Journal of Molecular Sciences*, vol. 22, no. 13, p. 7085, 2021.

[26] J. C. Lantis, R. Snyder, A. M. Reyzelman et al., "Fetal bovine acellular dermal matrix for the closure of diabetic foot ulcers: a prospective randomised controlled trial," *Journal of Wound Care*, vol. 30, no. Sup7, pp. S18–S27, 2021.

[27] K. P. Iyengar, V. K. Jain, M. K. Awadalla Mohamed, R. Vaishya, and S. Vinjamuri, "Update on functional imaging in the evaluation of diabetic foot infection," *Journal of Clinical Orthopaedics and Trauma*, vol. 16, pp. 119–124, 2021.

Hindawi
Contrast Media & Molecular Imaging
Volume 2022, Article ID 8950600, 11 pages
https://doi.org/10.1155/2022/8950600

Research Article

Artificial Intelligence Algorithm in Classification and Recognition of Primary Hepatic Carcinoma Images under Magnetic Resonance Imaging

Zehua He[1] **Qingqiang Huang**[2] **Yingyang Liao**[3] **Xiaojie Xu**[4] **Qiulin Wu**[4] **Yuanle Nong**[4] **Ningfu Peng**[4] **and Wanrong He**[5]

[1]*Department of General Surgery, Langdong Hospital of Guangxi Medical University, Nanning 530022, Guangxi, China*
[2]*Department of Radiology, Guigang City People's Hospital, Guigang 537100, Guangxi, China*
[3]*Department of Nutrition, Affiliated Tumor Hospital of Guangxi Medical University, Nanning 530021, Guangxi, China*
[4]*Department of Hepatobiliary Surgery, Affiliated Tumor Hospital of Guangxi Medical University, Nanning 530021, Guangxi, China*
[5]*Department of Gastroenterology, People's Hospital of Guangxi Zhuang Autonomous Region, Nanning 530021, Guangxi, China*

Correspondence should be addressed to Wanrong He; 1401040303@xs.hnit.edu.cn

Received 22 March 2022; Revised 10 May 2022; Accepted 12 May 2022; Published 7 June 2022

Academic Editor: M. Pallikonda Rajasekaran

This study aimed to discuss the application value of the bias field correction algorithm in magnetic resonance imaging (MRI) images of patients with primary hepatic carcinoma (PHC). In total, 52 patients with PHC were selected as the experimental group and divided into three subgroups: mild (15 cases), moderate (19 cases), and severe (18 cases) according to pathological grading. Another 52 patients with hepatic nodules in the same period were included in the control group. All the patients underwent dynamic contrast-enhanced (DCE) MRI examination, and the image qualities of MRI before and after bias field correction were compared. The DCE-MRI perfusion parameters were measured, including the transport constant Ktrans, reverse rate constant Kep, extravascular extracellular volume fraction (Ve), plasma volume (Vp), microvascular density (MVD), hepatic artery perfusion index (HPI), mean transit time of contrast agent (MTT), time to peak (TTP), blood volume (BV), hepatic arterial perfusion (HAP), full perfusion (FP), and portal venous perfusion (PVP). It was found that the sensitivity (93.63%), specificity (71.62%), positive predictive value (95.63%), negative predictive value (71.62%), and accuracy (90.01%) of MRI examination processed by the bias field correction algorithm were all significantly greater than those before processing ($P < 0.05$). The Ktrans, Kep, Ve, Vp, and MVD of patients in the experimental group were significantly larger than those of the control group, and severe group> moderate group> mild group ($P < 0.05$). HPI, MTT, TTP, BV, and HAP of patients in the experimental group were also significantly greater than those of the control group, which was shown as severe group > moderate group > mild group ($P < 0.05$). FP and PVP of the experimental group were significantly lower than those of the control group, and severe group < moderate group < mild group ($P < 0.05$). It was suggested that in MRI images of patients with PHC, the bias field correction algorithm could significantly improve the diagnosis rate. Each perfusion parameter was related to the pathological grading, which could be used to evaluate the prognosis of patients.

1. Introduction

Primary hepatic carcinoma (PHC) is one of the common malignant tumors in humans, and its mortality has been high [1]. According to the *Global Cancer Report 2014* issued by World Health Organization, the deaths due to liver cancer in China account for about 51% of that globally. It ranks second in the mortality of malignant tumors in rural areas in China and ranks the third in cities [2]. Hepatic carcinoma mostly occurs in the context of hepatitis and liver cirrhosis in China. Hepatitis, cirrhosis, and liver cancer are three steps experienced by many patients. Due to the poor reserve function of the liver, the antitumor immune function of the body is low, and the prognosis is also poor. Therefore, early diagnosis and effective treatment are the keys to improving the prognosis of patients with hepatic carcinoma [3, 4].

It has been shown that the histopathological grading of PHC is related to its degree of infiltration and distant metastasis and is the main influencing factor for its prognosis [5]. Thus, early diagnosis, accurate pathological grading, and timely treatment of PHC are the keys to prolonging the survival time of patients with liver cancer [6]. A hepatic biopsy is currently the gold standard for pathological grading of PHC. In addition to sampling errors, this invasive procedure may bring certain risks to patients, such as infection, hemorrhage, and even the spread of cancer cells. Therefore, it is particularly important to find a noninvasive, repeatable, and highly accurate examination method for clinical diagnosis and treatment. The most common diagnostic method for PHC is imaging examination. Currently, there are real-time ultrasound, histopathological examination, computed tomography (CT), magnetic resonance imaging (MRI), angiography, radionuclide imaging, and so on [7, 8].

Histopathological examination is the gold standard for the diagnosis of liver cancer, but it is necessary to combine it with clinical evidence in the pathological diagnosis. This is to comprehensively understand hepatitis B virus (HBV) and hepatitis C virus (HCV) infections in patients, the detection results of other tumor markers, and the imaging features of hepatic space occupying lesions [9]. With the rapid development of imaging technology, ultrasound and CT have become the common methods for clinical diagnosis, with easy operations and affordable cost. But if the imaging features of the hepatic space occupying lesions are not typical, it may be missed or misdiagnosed. MRI showed more and more prominent advantages in the diagnosis of PHC. Its good resolution of tissues, multisection, multiparameter observation, relatively nontoxic contrast agent, no radiation, nontrauma, and other characteristics make MRI the optimal choice for imaging diagnosis of PHC [10]. In the past, the diagnosis of PHC by MRI mainly focused on morphological changes according to the imaging features of the tumor, such as T2 weighted imaging (T2WI) hyperintensity, diffusion-weighted imaging (DWI) hyperintensity, pseudocapsule sign, and rapid wash-in and wash-out enhancement. Thereby, tumors can be easily distinguished from nontumor nodules, but the degree of pathological differentiation of tumors cannot be accurately inferred. With the continuous development of functional MRI technology, it can not only reflect histological characteristics such as microcirculation state and cell density of tumors but also reflect cell metabolism and biochemical information of tumors [11, 12]. This makes it possible to assess the pathological grading of PHC accurately using MRI.

Dynamic contrast-enhanced (DCE) imaging technology is a three-dimensional volumetric thin-slice scanning on the ground of the T1 weighted imaging (T1WI) sequence. The magnetic resonance contrast agent is injected into the venous bolus for repeated, multistage, and rapid scanning, which allows MRI to detect the situation of blood perfusion in internal organs and tissues and obtain multiple perfusion parameter information through relevant analysis by the processing software [13]. DCE-MRI can quantitatively evaluate the properties of blood vessels in tissues. It has been reported that this technique can accurately assess the level of tumor tissue microcirculation, as well as capillary permeability and hepatic artery blood supply ratio in hepatic malignant tumor tissues [14].

With the development and application of deep learning, deep learning models can replace traditional machine learning algorithms to automatically extract lesion features and achieve lesion classification and identification [15]. Hepatic MRI bias field correction is mainly to deal with image grayscale inhomogeneity caused by radiofrequency field inhomogeneity and other factors. The bias field correction algorithm utilized the estimation of the bias field and the corresponding spatial information, which could well deal with the impact of the image bias field on the segmentation. A hepatic bias field correction algorithm was put forward on the basis of grayscale preservation, which ensured that the corrected image retained the grayscale information of the original image to the greatest extent. Hepatic tissue segmentation was performed on the corrected images, and evaluation parameters like segmentation were used to reflect the performance of the bias field correction algorithm [16, 17]. To sum up, the hepatic MRI images of patients were processed under the bias field correction algorithm. The correlation was analyzed between multiphase DCE-MRI perfusion parameters and microvascular density (MVD) and pathological grading of PHC patients, which was to provide a certain theoretical basis for the diagnosis of PHC.

2. Materials and Methods

2.1. General Data of Patients. In this study, 52 patients with PHC admitted to the hospital from July 2019 to July 2021 were included in the experimental group. Another 52 patients with benign hepatic nodules admitted during the same period were chosen as the control group. The inclusion criteria of patients were as follows. The clinical symptoms and histopathological examination results of the patients were in line with the diagnostic criteria for PHC formulated in *PHC Diagnosis and Treatment Standards (Edition 2011)* [18]. The patients were willing to undergo a DCE-MRI examination, and they all had the first-time onset. All the patients and their families fully understood the situation and signed the informed consent, and this study was approved by the ethics committee of the hospital.

The exclusion criteria below were followed. Patients had cancer tissue infiltration or metastasis to other tissues or organs. Patients had dysfunction of other important organs, such as heart, lung, and kidney. Patients were complicated with severe immune system diseases, infectious diseases, or infectious diseases. Patients had contraindications to DCE-MRI.

The general data of the two groups of patients are shown in Table 1 for details. There was no significant difference in gender, age, and average age between the two groups ($P > 0.05$), which made the research was of comparability.

Table 1: General data of patients in the two groups.

Groups	Males	Females	Age	Average age
Experimental group	32 cases	20 cases	(19–76) years old	(57.14 ± 5.45) years old
Control group	30 cases	22 cases	(17–78) years old	(56.17 ± 5.29) years old
P value	0.081	0.094	—	0.083

2.2. DCE-MRI Examination Method. The patients underwent a DCE-MRI examination after respiratory function training. Then 1.5 T MRI instrument was used, and the abdominal phased array coil was set to 8 channels. The abdominal belt was used to adjust the breathing state of the patients. Dynamic, fast, and enhanced scanning were performed, respectively. For scanning parameters, the field of view (FOV) was set to be (350×320) mm, time of echo (TE) was 1.5 ms, time of repetition (TR) was 4.2 ms, the interlayer spacing was 0, the layer thickness was 3.6 mm of the (320×195) matrix, and the number of excitations was 1. Only the flip angles (3°, 9°, and 25°) needed to be adjusted; during enhanced scanning, a total of 50 dynamic cycles were scanned, each cycle lasted about 6 seconds with 30 layers, and the whole process lasted about 5 minutes. The scanning parameters were set as follows: FOV = (215×284) mm, TE = 1.35 ms, TR = 3.2 ms, slice thickness = 3.24 mm, the matrix was sized as 521×521, and the number of excitation was 2. In the second scanning, the contrast agent gadolinium diamine of 0.2 mL/kg was injected from the median cubital vein at a rate of about 4 mL/s. In total, 20 mL of normal saline was injected at the same rate after the injection. DCE scanning required the patients to hold their breath throughout the procedure, with only light and rapid ventilation.

2.3. Bias Field Correction Algorithm. MRI bias field correction was an algorithm model under local coherence, global intensity, and spatial continuity information. It could keep the grayscale of images consistent before and after correction. Its objective function was shown as follows:

$$\begin{aligned} A_{\text{our}} &= A_{\text{MPFCM}} + \gamma \sum_{k=1}^{m} \left(1 - h_k\right)^2 \\ &= \sum_{i=1}^{d} \sum_{k=1}^{m} v_{ik}^{n} N_{ik} + \gamma \sum_{k=1}^{m} \left(1 - h_k\right)^2. \end{aligned} \tag{1}$$

In the equation, $N_{ik} = \sum_{a \in M_i} \omega_{kp} [(\alpha \sum_{r \in \Omega} T_i(r)) \| I_{kp} - h_r u_i \|^2 + (1-\alpha) \sum_{r \in O_k} K(r-k) \| I_{kp} - h_r u_i \|^2]$. Ω represents the whole hepatic MRI image with background noise removed. O_k represents the local area of the grayscale value of the k-th pixel in the image. The membership template function was expressed as $V = [v_{ik}]$, which was used to describe the degree to which the pixel belonged to a certain cluster. $g_{kp} \in [0,1]$ refers to the local spatial continuity weight, which stands for the influence of domain pixels. $T_i(r), i = 1, 2, \ldots, d; r = 1, 2, \ldots, m$ represents the label function, which was the intensity information for this image and guided the correct clustering. I_{kp} is the filtered image after background noises were removed, and it was obtained by multiplying the membership template with the original image. $U = \{u_1, u_2, \ldots, u_d\}$ is the clustering center. $\alpha (0 \leq \alpha \leq 1)$ stands for a positive value to balance global intensity with local intensity. Parameter $n > 1$, d represents the number of clusters, and m is the total number of pixels in the image. The weighted function $K(r-k)$ also represents a truncated Gaussian kernel function, which reflects the influence of the center pixel r on the surrounding pixels, and its value decreased as the distance from the center r to the neighbor pixels k increased. $\gamma > 0$ is to balance the effects of the intensity and intensity-preserving constraints mentioned above.

In the energy minimization equation, $\sum_{r \in \Omega} T_i(r) \| I_{kp} - h_r u_i \|^2$ refers to the global intensity of the image, which was to ensure the correct clustering of each pixel in the image. The term $\sum_{r \in O_k} K(r-k) \| I_{kp} - h_r u_i \|^2$ is used to guarantee the smoothness of the bias field under the local intensity of the image. $\sum_{k=1}^{m} (1 - h_k)^2$ is the constraint term proposed to ensure the grayscale of the image after bias field correction, ensuring the grayscale consistency of the image before and after bias field correction; that is, the corrected image (I/h) and the original image have the same grayscale. $g_{kp} \in [0,1]s$ indicates the local spatial continuity weight, which was the influence of neighbor pixels. In the image space domain, a pixel k had a spatial coordinate (n_k, m_k), and a pixel p in the neighborhood had a spatial coordinate (n_p, m_p), then the local spatial weight information could be expressed as follows:

$$\omega_{kp} = \left\{ \frac{-\exp \delta_{kp}}{\sum_{p \in M_k} \left(-\exp \delta_{kp}\right)} \right\} \exp\left(-\max\left(\left|m_p - m_k\right|, \left|n_p - n_k\right|\right)\right). \tag{2}$$

In this equation,

$$\delta_{kp} = \frac{\left\{ \left[\left(\sum_{p' \in (M_k/s)} \left(I_{p'} - I_p\right)^2 / \left(m_k - 1\right) \right) + \left(I_p - I_k\right)^2 \right]^{(1/2)} - \left(\sum_{p \in M_k} \left[\left(\sum_{p' \in (M_k/s)} \left(I_{p'} - I_p\right)^2 / \left(m_k - 1\right) \right) + \left(I_p - I_k\right)^2 \right]^{(1/2)} / m_k \right) \right\}}{k}, \tag{3}$$

where k represents a constant and δ_{kp} is the same when the image pixel value was multiplied by a constant.

The parameters V, U, and h could be obtained by minimizing the energy function A_{our}. In this process, when solving one parameter, the other two parameters could be kept unchanged, which was the same as the standard D-means clustering method. Therefore, the parameters V, U, and h could be obtained by making the first derivative of the objective function A_{our} equal 0, respectively. The iteration of parameters was applied to estimate the bias field h, and the corrected image of the bias field could be obtained by I/h. Since the energy function A_{our} was a convex function to its variables, the method proposed here was robust to initialize parameters.

The membership function was solved at first.

The first-order partial derivative of the energy function A_{our} to the parameter V was computed, and the result was made equal to 0. Then the following equation was worked out:

$$\frac{\partial A_{\text{our}}}{\partial v_{ik}} = \sum_{i=1}^{d} \frac{\partial}{\partial v_{ik}} \sum_{k=1}^{m} v_{ik}^{n} N_{ik} = 0. \tag{4}$$

The variable v_{ik} was determined by the following equation:

$$\left\{ \frac{\partial v_{ik}}{\partial v_{ik}} = n v^{n-1} N_{ik} \right\}_{v_{ik}=v_{ik}^{*}} = 0. \tag{5}$$

Because V in the energy function A_{our} needed to satisfy the constraint term $\sum_{i=1}^{d} v_{ik} = 1, v_{ik} \in [0,1]$, the following equation was obtained:

$$v_{ik}^{*} = \left\{ \sum_{a=1}^{d} \left[\left(\frac{N_{ik}}{N_{ak}} \right)^{1/n-1} \right] \right\}^{-1}. \tag{6}$$

Next, the clustering center was solved.

The first-order partial derivative of the energy function A_{our} to the parameter U was solved, and the result was made equal to 0, then the following equation was obtained:

$$\frac{\partial A_{\text{our}}}{\partial u_i} = \sum_{k=1}^{m} v_{ik}^{n} \frac{\partial N_{ik}}{\partial u_i} = 0. \tag{7}$$

The variable u_i was determined by the following equation:

$$\left\{ \frac{\partial A_{\text{our}}}{\partial u_i} = \sum_{k=1}^{m} v_{ik}^{n} \frac{\partial N_{ik}}{\partial u_i} \right\}_{u_i=u_i^{*}} = 0. \tag{8}$$

Then the solution of u_i was calculated through the following equation:

$$u_i^{*} = \frac{\sum_{k=1}^{m} v_{ik}^{n} I_k \left((1-\alpha)(h * K) + \alpha h T_i \right)}{\sum_{k=1}^{m} v_{ik}^{n} \left((1-\alpha)\left(h^2 * K\right) + \alpha h^2 T_i \right)}. \tag{9}$$

In the equation, the symbol $*$ refers to the convolution operator. $I = \sum_{p \in M_k} (\omega_{kp} \cdot I_{kp}) / \sum_{p \in M_k} \omega_{kp}$, and I is the hepatic MRI image after background noises were removed. I_k represents the grayscale value of the k-th pixel in the filtered image I.

Finally, the bias field estimation was performed.

The energy function A_{our} was utilized to find the first-order partial derivative of the bias field parameter h, and it was set equal to 0, then equation equation could be worked out:

$$\frac{\partial A_{\text{our}}}{\partial h_k} = \sum_{i=1}^{d} \frac{\partial}{\partial h_k} \sum_{k=1}^{m} v_{ik}^{n} N_{ik} + \gamma \frac{\partial}{\partial h_k} \sum_{k=1}^{m} \left(1 - h_k\right)^2 = 0. \tag{10}$$

The variable h_k was determined by the following equation:

$$\left\{ \sum_{i=1}^{d} \frac{\partial}{\partial h_k} v_{ik}^{n} N_{ik} + \gamma \frac{\partial}{\partial h_k} \left(1 - h_k\right)^2 \right\}_{h_k = h_k^{*}} = 0. \tag{11}$$

Therefore, the bias field h_k could be expressed as follows:

$$h_k^{*} = \frac{\alpha I A_1^{(1)} + (1-\alpha)\left(\left(I A_2^{(1)} * K\right)\right) + \gamma m}{\alpha A_1^{(1)} + (1-\alpha)\left(\left(I A_2^{(1)} * K\right)\right) + \gamma m}. \tag{12}$$

In the equation (12), $A_1^{(1)} = \sum_{i=1}^{d} v_i^n u_i T_i$, $A_1^{(2)} = \sum_{i=1}^{d} v_i^n u_i^2 T_i$, $A_2^{(1)} = \sum_{i=1}^{d} v_i^n u_i$, $A_2^{(2)} = \sum_{i=1}^{d} v_i^n u_i^2$, and v_i represents the membership degree of category i.

The experimental steps of this method are described in Figure 1.

(1) Parameters V, U, and h and other parameters were initialized.
(2) The membership template function I_{mask} was calculated.
(3) The membership matrix was updated by multiplying equation (6) and the membership template function I_{mask}.
(4) The global variable $T_i(r)$ was updated.
(5) The cluster center was updated via equation (9).
(6) The bias field was updated through equation (12).
(7) It was judged whether the convergence condition $\|U_{\text{new}} - U_{\text{old}}\| < \varepsilon$ was satisfied, where ε is a very small number. If it was satisfied, the calculation was stopped; if not, the calculation was continued with steps (3) to (6).

2.4. Pathological Judgment Standards. The patients in the experimental group were graded with Edmondson–Steiner's tumor pathological grading method [19]. The pathological grading was performed according to the size and morphology of tumor cells, nuclear size, basophilic cytoplasmic staining, nuclear staining depth, and cytoplasmic ratio. Differentiation grade I referred to the tumor cells arranged in fascicles; grade II referred to the tumor cells that were shown eosinophilic with rich cytoplasm, large nuclei, and dark staining. Grade III meant that the nuclear staining degree was deeper than that of grade II, and tumor giant cells appeared. For grade IV, the tumor cells were shown with less cytoplasm, larger nuclei, darker staining, lacking of intercellular connections, and low differentiation. According to the grading of pathological conditions, grade I belonged to the mild group, grades II-III were in the moderate group, and grade IV was in the severe group.

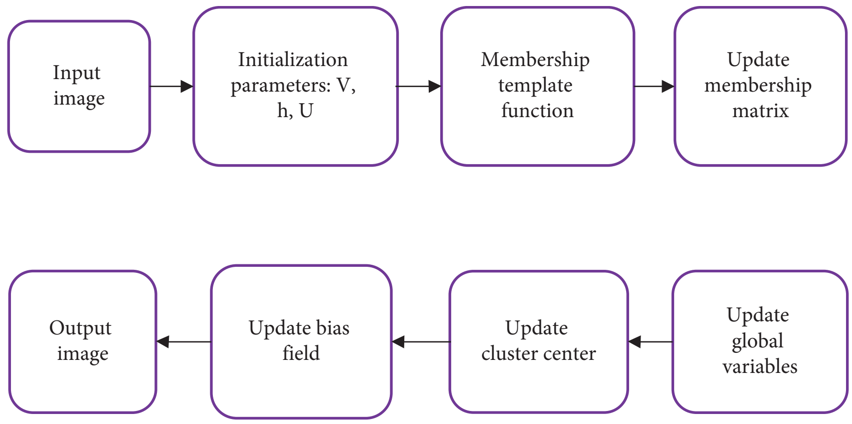

Figure 1: Schematic diagram of the algorithm flow.

2.5. Observation Indicators. After the DCE-MRI scanning, processing software was used to analyze the measurement results as the two-chamber Tofts model was selected. During the period, necrotic tissue and blood vessel areas were avoided. The maximum microvascular density (MVD) was selected under a low power lens, while the number of microvessels was calculated under a high power lens. Double-blind counts were performed by two experienced radiologists, respectively; then the average value of MVD was taken. Three regions of interest were selected to measure the plasma volume (Vp), the extravascular extracellular volume fraction (Ve), and the transport constant Ktrans from intracellular to extracellular space. The reverse rate constant Kep from extracellular to intravascular space, hepatic artery perfusion index (HPI), mean transit time (MTT) of contrast agent, time to peak (TTP), blood volume (BV), full perfusion (FP), hepatic arterial perfusion (HAP), and portal venous perfusion (PVP) were used to determine the mean value of the three fields of view.

2.6. Statistical Methods. SPSS19.0 was applied for statistical analysis. The enumeration data were expressed as a percentage (%). The measurement data Ktrans, Kep, Ve, Vp, MVD, HPI, MTT, TTP, BV, FP, HAP, and PVP were expressed as mean ± standard deviation $(x\,(\_)\ \pm s)$. The differences in the measurement data among the three groups were analyzed by variance analysis. The *t*-test and Pearson method were adopted to analyze the differences in measurement data between two groups. When $P < 0.05$, the difference was statistically significant.

3. Results

3.1. MRI Results of Liver Cancer Patients. Figure 2 shows the MRI images of a 64-year-old male patient with hepatic carcinoma. In Figure 2 below, the images a, b, c, and d were the MRI images of the PHC patient before being processed by the bias field correction algorithm, while images e, f, g, and h were the MRI images after the bias field correction algorithm processing. Images a and e were the MRI images, images b and f were the T1WI images, images c and g were the T2WI images, and images d and h were the DWI images.

After being processed by the bias field correction algorithm, the sensitivity, specificity, positive predictive value, negative predictive value, and accuracy of MRI examination were 93.63%, 71.62%, 95.63%, 71.62%, and 90.01%, respectively. These were all significantly greater than those before processing $(P < 0.05)$, and the differences were of statistical significance, which could be discovered in Figure 3 for details.

3.2. Comparison of Ktrans, Kep, Ve, Vp, and MVD in Patients between the Two Groups. Ktrans, Kep, Ve, Vp, and MVD of patients in the experimental group were significantly greater than those in the control group $(P < 0.05)$, suggesting that the differences were statistically significant. The details are shown in Figure 4.

3.3. Comparison of Ktrans, Kep, Ve, Vp, and MVD among Subgroups of Patients in the Experimental Group. With the pathological judgment standards, the patients in the experimental group were divided into three subgroups, namely, the mild group (15 cases), the moderate group (19 cases), and the severe group (18 cases). Ktrans, Kep, Ve, Vp, and MVD of the severe group > those of the moderate group > those of the mild group $(P < 0.05)$, and all the differences were considered to be statistically significant. Figure 5 shows the comparisons in detail.

3.4. Comparison of HPI, MTT, TTP, BV, FP, HAP, and PVP between the Two Groups of Patients. HPI, MTT, TTP, BV, FP, HAP, and PVP of patients were compared between the experimental group and the control group. HPI, MTT, TTP, BV, and HAP of patients in the experimental group were significantly higher than those of the control group $(P < 0.05)$. FP and PVP of the experimental group were significantly lower than those of the control group $(P < 0.05)$, which were all displayed in Figures 6 and 7.

3.5. Comparison of HPI, MTT, TTP, BV, FP, HAP, and PVP of Patients in Each Subgroup of the Experimental Group. The levels of HPI, MTT, TTP, BV, and HAP in the severe group >

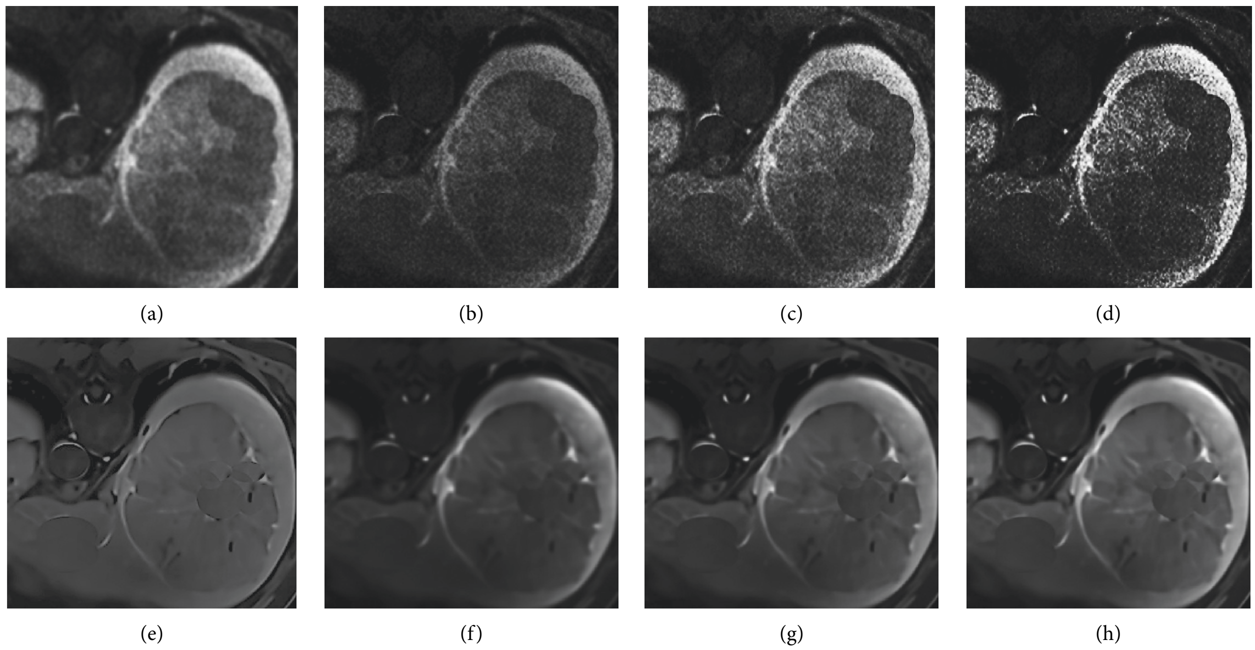

FIGURE 2: MRI images of a PHC patient before and after processing by the bias field correction algorithm.

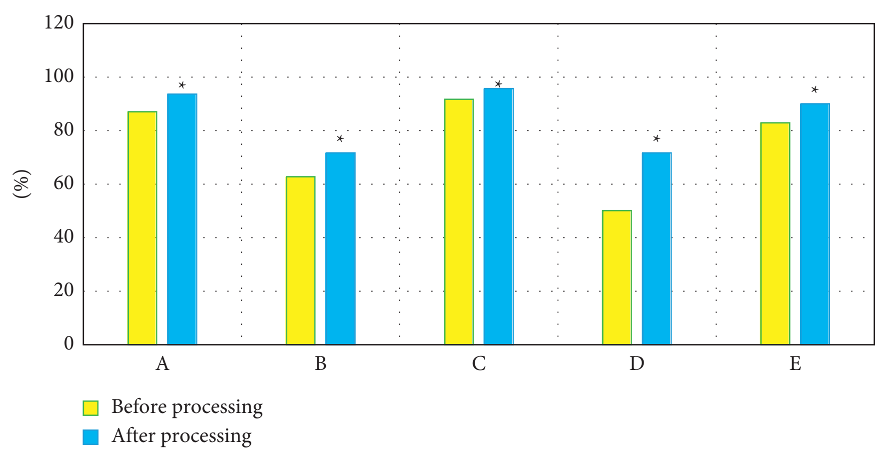

FIGURE 3: MRI results before and after the bias field correction processing. A, B, C, D, and E indicated sensitivity, specificity, positive predictive value, negative predictive value, and accuracy, respectively. *Compared with those before processing, $P < 0.05$.

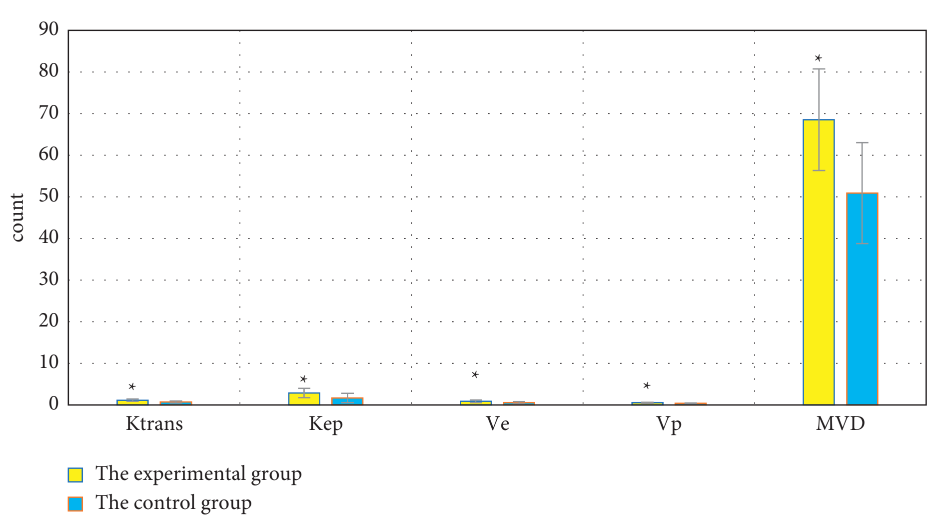

FIGURE 4: Comparison of Ktrans, Kep, Ve, Vp, and MVD between the two groups. *Compared with those of the control group, $P < 0.05$.

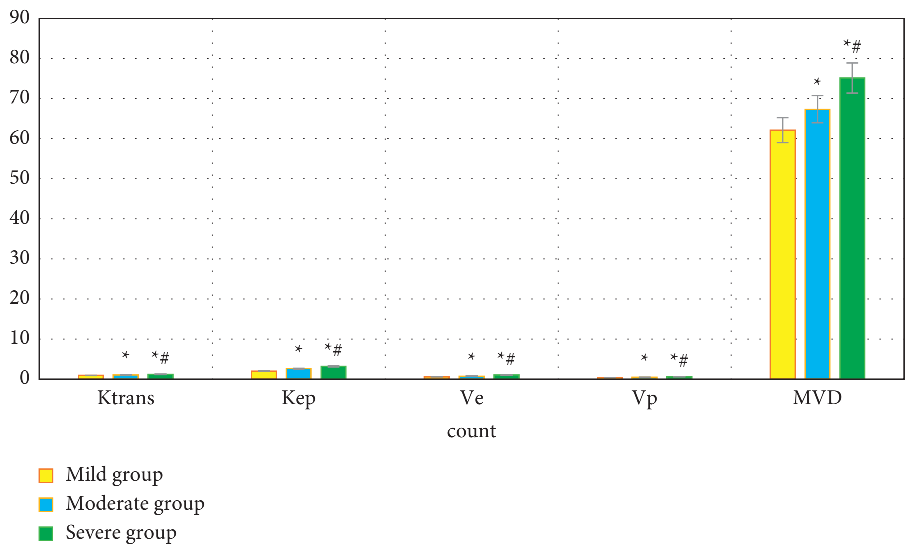

Figure 5: Comparison of Ktrans, Kep, Ve, Vp, and MVD in each subgroup of patients in the experimental group. *Compared with the data of the mild group, $P < 0.05$; #compared with those of the moderate group, $P < 0.05$.

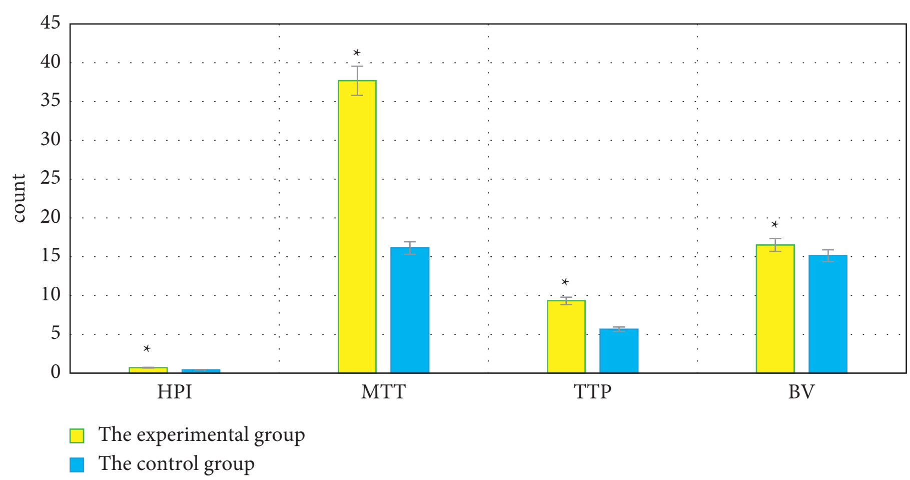

Figure 6: Comparison of HPI, MTT, TTP, and BV between the two groups of patients. *Compared with the responding data of the control group, $P < 0.05$.

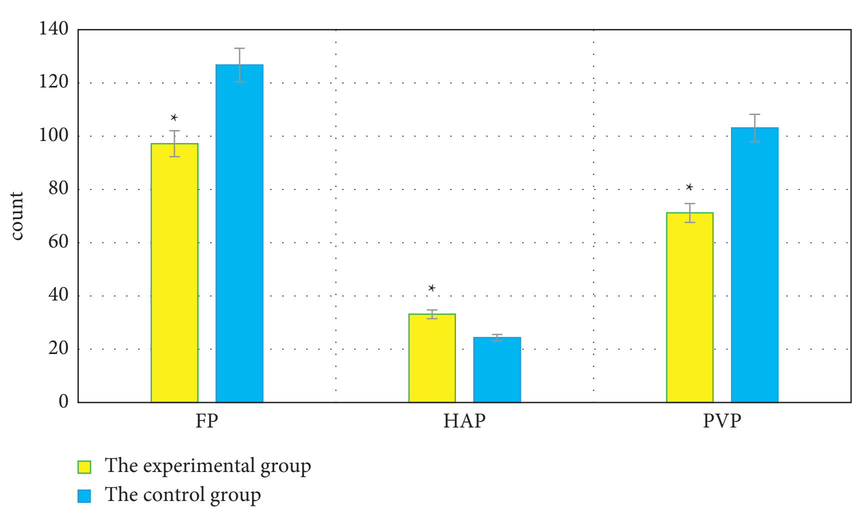

Figure 7: Comparison of FP, HAP, and PVP between the two groups of patients. *Compared with the control group, $P < 0.05$.

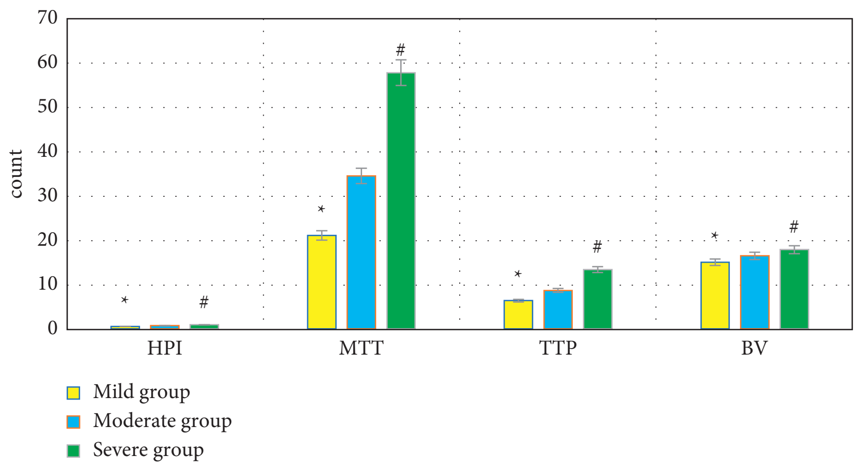

FIGURE 8: Comparison of HPI, MTT, TTP, and BV of patients in each subgroup of the experimental group. *Compared with the data of the moderate group, $P < 0.05$; #compared with the data of the moderate group, $P < 0.05$.

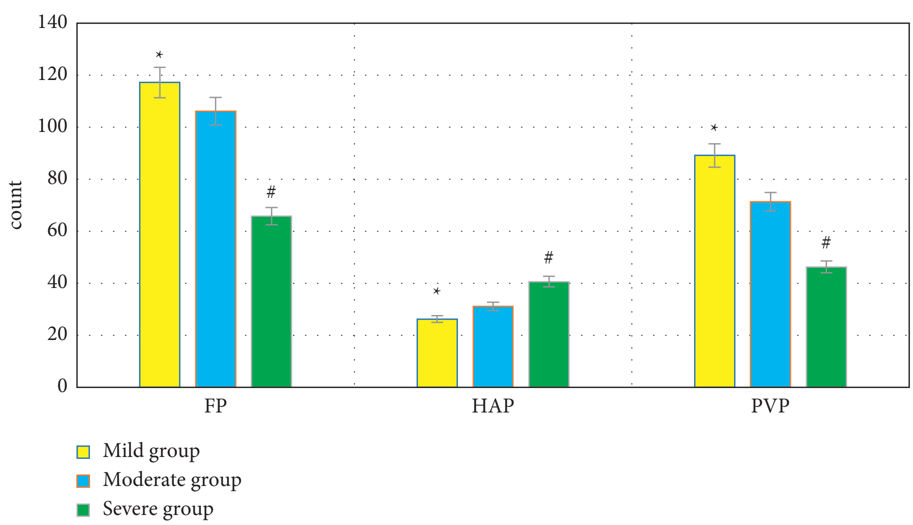

FIGURE 9: Comparison of FP, HAP, and PVP in each subgroup of the experimental group. *Compared with the data of the moderate group, $P < 0.05$; #compared with the data of the moderate group, $P < 0.05$.

those in the moderate group > those in the mild group, $P < 0.05$. FP and PVP in the severe group < those in the moderate group < those in the mild group, $P < 0.05$. All the differences were of statistical significance, as observed in Figures 8 and 9.

3.6. Correlation Analysis of Hepatic DCE-MRI Perfusion Parameters and MVD in PHC Patients in Experimental Group. Hepatic DCE-MRI perfusion parameters Ktrans, Kep, Ve, Vp, HPI, MTT, TTP, BV, and HAP were positively correlated with MVD in the experimental group ($P < 0.05$). FP and PVP were negatively correlated with MVD in the group ($P < 0.05$). The differences were suggested to be statistically significant, as shown in Figure 10 in detail.

4. Discussion

DCE-MRI is a noninvasive imaging technique. It is to inject a paramagnetic contrast agent into the blood vessel after the T1 is shortened. If the imaging is repeated, the change in the signal intensity in the tissue can be measured. As the diffusion time of the contrast agent increases, the peripheral tissues are monitored. After being processed by professional software, the quantitative parameter technology can be applied to measure the pathological changes in blood perfusion, and this technology has been increasingly used to evaluate the vascular permeability and the tumor microcirculation [20, 21].

The level of MVD can reflect the formation of new blood vessels in tumor tissues. The permeability of new blood vessels in immature tumors is higher, and the permeability of new blood vessels is related to the dynamic enhanced detection method of DCE-MRI [22]. It has been reported that with the increase of the tumor tissue volume and the degree of differentiation of PHC, the arterial blood supply also increases accordingly, and the hepatic sinusoids may present a capillary state. Because the morphological basis of tumor tissue growth and infiltration lies in blood vessels, the

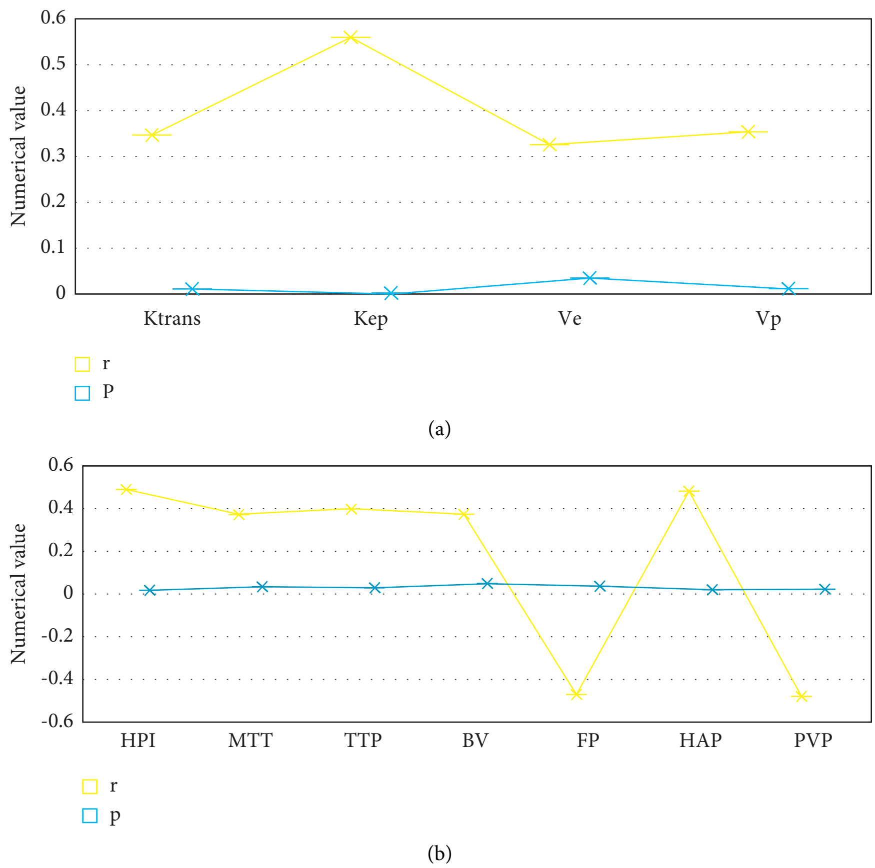

Figure 10: Correlation between hepatic DCE-MRI perfusion parameters and MVD in PHC patients in the experimental group. (a) showed the correlation between parameters Ktrans, Kep, Ve, and Vp and MVD, while (b) showed the correlation between parameters HPI, MTT, TTP, BV, FP, HAP, and PVP and MVD.

new tumor tissues and blood vessels can provide nutrients. If the blood vessels are immature, their permeability is higher; the contrast agent injected in DCE-MRI examinations has a small molecular weight and is easy to exudate from blood vessels into the extracellular space [23, 24]. It was found in this research that the sensitivity, specificity, positive predictive value, negative predictive value, and accuracy of MRI diagnosis processed by the bias field correction algorithm were 93.63%, 71.62%, 95.63%, 71.62%, and 90.01%, respectively. All of the results were remarkably greater than those before processing as $P < 0.05$, which indicated that compared with the simple MRI images, the diagnostic performance of MRI under the bias field correction algorithm was more excellent.

The blood flow velocity, which can be reflected as Ktrans on the vascular permeability, is used to indicate the permeability of the microvessels in the cancer tissues. The rate of contrast agent infiltration from the extracellular space to the intravascular space of the blood vessels is regarded as Kep. The volume ratio of contrast agent leaks into the extravascular interstitial space to the extracellular volume is denoted as Ve. Ktrans, Kep, and Ve increase if the vascular permeability around the tumor tissue increases [25]. It was found that Ktrans, Kep, Ve, Vp, and MVD of the experimental group were significantly higher than those of the control group, $P < 0.05$ with statistically significant differences. In the subgroups, Ktrans, Kep, Ve, Vp, and MVD of the severe group > those of the moderate group > those of the mild group, and $P < 0.05$, indicating the differences were statistically significant. It was suggested that the quantitative perfusion parameters of PHC patients by DCE-MRI examination were greatly related to the MVD and lesion severity of patients, which was similar to the results of Liu and Qian [26].

Some scholars have reported that the hepatic lobular structure is damaged in patients with PHC, regenerative nodules and a large number of fibrous tissue hyperplasia are shown, and even the blood circulation path is changed [27]. The portal vein reflux is not smooth, the hepatic arteriovenous shunt occurs, the hepatic blood flow resistance increases, and the PVP can be reduced. Under the action of fibrous cords, hepatic veins and portal vein branches in patients with PHC are occluded and narrowed, and a large number of collagen fibers are deposited in the intercellular space of hepatocytes. The flow time of the contrast agent in the liver is prolonged, which increases MTT and TTP. As blood flow resistance increases, the blood flow through the portal vein decreases and the proportion of hepatic artery blood flow in the total hepatic circulation increases, resulting in a decrease in FP and an increase in HPI [28]. It was found that HPI, MTT, TTP, BV, and HAP of the experimental group were significantly higher than those of the control group ($P < 0.05$), while FP and PVP were significantly lower ($P < 0.05$); the differences were computed to be statistically significant. The levels of HPI, MTT, TTP, BV, and HAP in patients were shown that those of the severe group > the moderate group > the mild group ($P < 0.05$). In FP and PVP, those of the severe group < the moderate group < the mild group ($P < 0.05$); the differences were all of statistical significance. It could be suggested that the quantitative perfusion parameters of PHC patients by DCE-MRI were significantly related to the incidence of portal vein thrombosis in patients. With the aggravation of PHC lesions, the risk of portal vein thrombosis increased, HPI, MTT, TTP, BV, and HAP increased, while FP and PVP decreased. These results were exactly similar to the findings of Song et al. [29].

5. Conclusion

The hepatic MRI images of the patients were processed under the bias field correction algorithm. The correlation was also analyzed between the perfusion parameters of multiphase DCE-MRI and MVD and pathological grades of PHC patients to assist the clinical diagnosis of PHC. The results showed that the sensitivity, specificity, positive predictive value, negative predictive value, and accuracy of MRI were significantly improved after processing the bias field correction algorithm. DCE-MRI could evaluate the microcirculation status of PHC patients objectively and quantitatively, and the changes of quantitative perfusion parameters were significantly correlated with MVD and pathological grades. Quantitative perfusion parameters detected by DCE-MRI could evaluate MVD level and pathological grading, which was worthy of further promotion. However, only 52 cases with PHC were included in this work, the sample size was small and the source was single, which might affect the results. The image processing performance of the bias field correction algorithm also needed to be further analyzed. The research would need to be expanded in the future so as to verify the conclusion with more clinical experiments.

Data Availability

The data used to support the findings of this study are available from the corresponding author upon request.

Conflicts of Interest

The authors declare no conflicts of interest.

Authors' Contributions

Zehua He and Qingqiang Huang contributed equally to this work.

Acknowledgments

This work was supported by the Natural Science Foundation of Guangxi (2021GXNSFBA075040) and the Natural Science Foundation of China (81560460/H1602).

References

[1] A. Nakano, K. Hirabayashi, H. Yamamuro et al., "Combined primary hepatic neuroendocrine carcinoma and hepatocellular carcinoma: case report and literature review," *World Journal of Surgical Oncology*, vol. 19, no. 1, p. 78, 2021.

[2] J.-X. Mao, F. Teng, K.-Y. Sun, C. Liu, G.-S. Ding, and W.-Y. Guo, "Two-in-one: a pooled analysis of primary hepatic neuroendocrine carcinoma combined/collided with hepatocellular carcinoma," *Hepatobiliary and Pancreatic Diseases International*, vol. 19, no. 4, pp. 399–403, 2020.

[3] X. Zhou, L. Fang, X. Meng, and W. Luo, "Treatment of primary hepatic carcinoma through ultrasound-guided microwave ablation," *Nigerian Journal of Clinical Practice*, vol. 22, no. 10, pp. 1408–1411, 2019.

[4] P. Song, Y. Hai, W. Ma et al., "Arsenic trioxide combined with transarterial chemoembolization for unresectable primary hepatic carcinoma," *Medicine*, vol. 97, no. 18, Article ID e0613, 2018.

[5] H.-Y. Jiang, J. Chen, C.-C. Xia, L.-K. Cao, T. Duan, and B. Song, "Noninvasive imaging of hepatocellular carcinoma: from diagnosis to prognosis," *World Journal of Gastroenterology*, vol. 24, no. 22, pp. 2348–2362, 2018.

[6] G. Özgün, N. Haberal Reyhan, B. H. Özdemir, and M. Haberal, "Liver transplant for hepatocellular carcinoma: pathologic point of view," *Experimental and Clinical Transplantation :Official Journal of the Middle East Society for Organ Transplantation*, vol. 15, no. Suppl 2, pp. 50–54, 2017 Mar.

[7] Z. Xuan, N. Wu, C. Li, and Y. Liu, "Application of contrast-enhanced ultrasound in the pathological grading and prognosis prediction of hepatocellular carcinoma," *Translational Cancer Research*, vol. 10, no. 9, pp. 4106–4115, 2021 Sep.

[8] X.-H. Li, Q. Liang, T.-W. Chen, J. Wang, and X.-M. Zhang, "Diagnostic value of imaging examinations in patients with primary hepatocellular carcinoma," *World Journal of Clinical Cases*, vol. 6, no. 9, pp. 242–248, 2018.

[9] L. Mulazzani and M. Alvisi, "Imaging findings of hepatic epithelioid hemangioendothelioma and fibrolamellar hepatocellular carcinoma: a critical appraisal of current literature about imaging features of two rare liver cancers," *Translational Cancer Research*, vol. 8, no. S3, pp. S297–S310, 2019 Apr.

[10] H.-H. Chong, L. Yang, R.-F. Sheng et al., "Multi-scale and multi-parametric radiomics of gadoxetate disodium-enhanced MRI predicts microvascular invasion and outcome in patients with solitary hepatocellular carcinoma ≤ 5 cm," *European Radiology*, vol. 31, no. 7, pp. 4824–4838, 2021 Jul.

[11] K. Lv, X. Cao, Y. Dong, D. Geng, and J. Zhang, "CT/MRI LI-RADS version 2018 versus CEUS LI-RADS version 2017 in the diagnosis of primary hepatic nodules in patients with high-risk hepatocellular carcinoma," *Annals of Translational Medicine*, vol. 9, no. 13, p. 1076, 2021 Jul.

[12] X. Ji, S. Zhou, P. Yang, F. Liu, Y. Li, and H. Li, "Value of ultrasound combined with MRI in the diagnosis of primary and recurrent hepatocellular carcinoma," *Oncology Letters*, vol. 18, no. 6, pp. 6180–6186, 2019 Dec.

[13] J. H. Park, M.-S. Park, S. J. Lee et al., "Contrast-enhanced US with perfluorobutane for hepatocellular carcinoma surveillance: a multicenter diagnostic trial (scan)," *Radiology*, vol. 292, no. 3, pp. 638–646, 2019.

[14] Q. Song, Y. Guo, X. Yao et al., "Comparative study of evaluating the microcirculatory function status of primary small HCC between the CE (DCE-MRI) and Non-CE (IVIM-DWI)

MR Perfusion Imaging," *Abdominal Radiology*, vol. 46, no. 6, pp. 2575–2583, 2021.

[15] S. Wu, K. Roberts, S. Datta et al., "Deep learning in clinical natural language processing: a methodical review," *Journal of the American Medical Informatics Association*, vol. 27, no. 3, pp. 457–470, 2020.

[16] R. Keesman, T. N. van de Lindt, C. Juan-Cruz et al., "Correcting geometric image distortions in slice-based 4D-MRI on the MR-linac," *Medical Physics*, vol. 46, no. 7, pp. 3044–3054, 2019 Jul.

[17] S. Ruschke, H. Eggers, H. Kooijman et al., "Correction of phase errors in quantitative water-fat imaging using a monopolar time-interleaved multi-echo gradient echo sequence," *Magnetic Resonance in Medicine*, vol. 78, no. 3, pp. 984–996, 2017.

[18] R. Kutlu and S. Karatoprak, "Radioembolization for hepatocellular carcinoma in downstaging and bridging for liver transplantation," *Journal of Gastrointestinal Cancer*, vol. 51, no. 4, pp. 1157–1164, 2020.

[19] L. Zhou, J.-A. Rui, W.-X. Zhou, S.-B. Wang, S.-G. Chen, and Q. Qu, "Edmondson-Steiner grade: a crucial predictor of recurrence and survival in hepatocellular carcinoma without microvascular invasio," *Pathology, Research & Practice*, vol. 213, no. 7, pp. 824–830, 2017 Jul.

[20] M. Rata, K. Khan, D. J. Collins et al., "DCE-MRI is more sensitive than IVIM-DWI for assessing anti-angiogenic treatment-induced changes in colorectal liver metastases," *Cancer Imaging*, vol. 21, no. 1, p. 67, 2021.

[21] Y. Sun, Q. Zhu, M. Huang, D. Shen, Y. Zhou, and Q. Feng, "Liver DCE-MRI registration based on sparse recovery of contrast agent curves," *Medical Physics*, vol. 48, no. 11, pp. 6916–6929, 2021 Nov.

[22] C. Kim, J.-Y. Suh, C. Heo et al., "Spatiotemporal heterogeneity of tumor vasculature during tumor growth and anti-angiogenic treatment: MRI assessment using permeability and blood volume parameters," *Cancer Medicine*, vol. 7, no. 8, pp. 3921–3934, 2018.

[23] J. M. Franklin, B. Irving, B. W. Papiez et al., "Tumour subregion analysis of colorectal liver metastases using semi-automated clustering based on DCE-MRI: Comparison with histological subregions and impact on pharmacokinetic parameter analysis," *European Journal of Radiology*, vol. 126, Article ID 108934, 2020.

[24] K. E. Pitman, K. M. Bakke, A. Kristian, and E. Malinen, "Ultra-early changes in vascular parameters from dynamic contrast enhanced MRI of breast cancer xenografts following systemic therapy with doxorubicin and liver X receptor agonist," *Cancer Imaging*, vol. 19, no. 1, p. 88, 2019.

[25] T. T. Dündar, E. Cetinkaya, İ. Yurtsever, Ö. Uysal, and A. Aralaşmak, "Follow-up of high-grade glial tumor; differentiation of posttreatment enhancement and tumoral enhancement by DCE-MR perfusion," *Contrast Media and Molecular Imaging*, vol. 2022, no. 1, Article ID 6948422, 2022.

[26] D. Liu and H. F. Qian, "Dynamic contrast-enhanced magnetic resonance imaging permeability parameters monitor the early response to bevacizumab plus chemotherapy in colorectal cancer patients with liver metastases," *Zhongguo Yi Xue Ke Xue Yuan Xue Bao*, vol. 40, no. 2, pp. 256–263, 2018.

[27] T. Zhang, G. Ding, H. Wang et al., "miR-497 targets VEGF signal pathway to regulate proliferation, invasion and migration of hepatocellular carcinoma cells: a primary study using DEC-MRI," *J BUON*, vol. 26, no. 2, pp. 418–428, 2021.

[28] W. Zhang, H. J. Chen, Z. J. Wang, W. Huang, and L. J. Zhang, "Dynamic contrast enhanced MR imaging for evaluation of angiogenesis of hepatocellular nodules in liver cirrhosis in N-nitrosodiethylamine induced rat model," *European Radiology*, vol. 27, no. 5, pp. 2086–2094, 2017.

[29] D. Song, Y. Wang, W. Wang et al., "Using deep learning to predict microvascular invasion in hepatocellular carcinoma based on dynamic contrast-enhanced MRI combined with clinical parameters," *Journal of Cancer Research and Clinical Oncology*, vol. 147, no. 12, pp. 3757–3767, 2021 Dec.

Hindawi
Contrast Media & Molecular Imaging
Volume 2022, Article ID 6168528, 9 pages
https://doi.org/10.1155/2022/6168528

Research Article

Prognosis Analysis and Perioperative Research of Elderly Patients with Non-Muscle-Invasive Bladder Cancer under Computed Tomography Image of Three-Dimensional Reconstruction Algorithm

Hongying Ke[1], **Dandan Qiu**[2], **and Zhicheng Cong**[3]

[1]*Department of Geriatrics, Zhejiang Hospital, Hangzhou 310000, Zhejiang, China*
[2]*Department of Urology, The First Affiliated Hospital of Zhejiang Chinese Medical University, Hangzhou 310000, Zhejiang, China*
[3]*Department of Urology, Zhejiang Hospital, Hangzhou 310000, Zhejiang, China*

Correspondence should be addressed to Zhicheng Cong; 2011030334@mail.sdufe.edu.cn

Received 15 February 2022; Revised 5 May 2022; Accepted 10 May 2022; Published 6 June 2022

Academic Editor: M Pallikonda Rajasekaran

To analyze the application value of computed tomography (CT) based on a three-dimensional reconstruction algorithm in perioperative nursing research and prognosis analysis of non-muscle-invasive bladder cancer (NMIBC), a retrospective study was performed on 124 patients with NMIBC who underwent surgical treatment in the hospital. All patients underwent CT examination based on the three-dimensional reconstruction algorithm before surgery, and transurethral resection of the bladder tumor was performed. The patients receiving conventional care were classified as the control group, and those receiving comprehensive care were classified as the case group, and the recovery status and recurrence of the two groups were compared. The results showed that the accuracy, specificity, and sensitivity of CT imaging information based on the three-dimensional reconstruction algorithm for NMIBC patients were 89.38, 93.77, and 84.39, respectively. The incidence of bladder spasm (9.68%), bladder flushing time (1.56 d), and retention of drainage tube time (2.68 d) in the case group were obviously lower compared with the control group (30.65%, 2.32 d, and 5.19 d) ($P < 0.05$). Serum BLCA-1 (3.72 ng/mL) and CYFRA21-1 (5.68 μg/mL) in the case group were significantly lower than those in the control group, with a statistically considerable difference ($P < 0.05$). Compared with the control group, the scores of role function (89.82 points), emotional function (84.76 points), somatic function (79.23 points), and social function (73.93 points) in the case group were observably higher ($P < 0.05$). In addition, one year after the operation, CT examination showed that the recurrence rate in the case group (6.45%) was significantly lower than that in the control group (22.58%) ($P < 0.05$). Therefore, CT detection based on the three-dimensional reconstruction algorithm was particularly important for preoperative diagnosis, prognosis, and recurrence monitoring of NMIBC patients. It could provide great clinical value for the diagnosis and prognosis monitoring of NMIBC.

1. Introduction

In recent years, the incidence rate of bladder cancer has been increasing. As the most common malignant tumor of the urinary system, it brought great threat and harm to patients both at home and abroad [1, 2]. North America, North Africa, and Europe are the most frequent areas of bladder cancer worldwide. Egypt has the highest incidence rate of cancer in the world. In addition, statistics showed that in 2010, the number of new bladder cancer patients in the United States increased to 70 thousand, and the number of new patients reached more than 80 thousand in 2018. The number of new cases and deaths increased annually in China. The incidence rate of bladder cancer was the first [3–6]. Clinically, it can be divided into transitional cell carcinoma, adenocarcinoma, squamous cell carcinoma, small cell carcinoma, metastatic carcinoma, and mixed types of cancer according to the tissue source of bladder cancer, among which transitional cell carcinoma is the most common [7–10].

Clinically, most patients with bladder cancer are NMIBC, and surgical treatment is the most effective and widely used treatment method [11–14]. NMIBC has the possibility of further developing into invasive bladder cancer. Therefore, the choice of surgical treatment for NMIBC aroused wide discussion and attention. A large number of researchers thought that radical cystectomy with radical cystectomy for NMIBC patients could significantly reduce the risk of recurrence of bladder cancer. However, great trauma was caused by this surgical method to the patient's body, and a variety of complications occurred in severe cases. In addition, the limitation of surgical indications was extremely strict, so its scope of clinical application was affected and could not be widely popularized [15, 16]. Iqbal et al. [17] investigated the incidence, risk factors, and survival outcomes associated with the pathologic rise from noninvasive to muscle-invasive bladder cancer after robot-assisted radical cystectomy. They found that patients with noninvasive bladder cancer who underwent surgical treatment had an increased incidence of muscle-invasive bladder cancer, which was associated with worse survival outcomes. Türk et al. [18] retrospectively analyzed the case data from 530 patients who underwent radical cystectomy or pelvic lymphadenectomy by selected surgeons between May 2005 and April 2016. They found that patients with early radical cystectomy had better disease-free survival and overall survival time than patients with pelvic lymphadenectomy. In recent years, transurethral resection of bladder tumors has appeared in the sight of researchers and doctors and has gradually developed into the main treatment method for patients with NMIBC [19, 20]. Transurethral resection of bladder tumors has many advantages, including less trauma, repeatable treatment, and rapid recovery. However, the risk of postoperative recurrence in patients with NMIBC after this operation was high [21–23].

Computed tomography (CT) is one of the most commonly used methods for the diagnosis of bladder cancer. Preoperative diagnosis can improve the accuracy of preoperative staging and detect the recurrence of bladder cancer after operation [24–26]. Conventional CT often uses two-dimensional slice observation, so many spatial data are lost, and the structural and morphological display of cancerous tissue is not complete and sufficient [27]. Imaging doctors cannot intuitively make accurate and objective judgments based on the observed images, which may lead to wrong diagnosis [28]. Three-dimensional images can completely, stereoscopically, and intuitively reproduce the tumor tissue morphology and structure. CT detection based on the three-dimensional reconstruction algorithm is helpful for clinicians to further observe and analyze, obtain more detailed information, and diagnose the disease more accurately and quickly [29].

To analyze the application value of CT images based on the three-dimensional reconstruction algorithm in perioperative nursing research and prognosis analysis of elderly patients with NMIBC, 124 patients with NMIBC were selected in this study. The patients were diagnosed by CT detection based on the three-dimensional reconstruction algorithm before operation. After the operation, the patients were divided into case group and control group for rapid comprehensive nursing and routine nursing. The recovery status of the two groups was analyzed and compared. In addition, the recurrence was detected by CT scanning, so as to evaluate the reference value of CT image information based on the three-dimensional reconstruction algorithm in preoperative diagnosis, postoperative nursing, and recurrence monitoring of NMIBC patients.

2. Materials and Methods

2.1. Research Object. A retrospective study was performed on 124 patients with NMIBC who underwent surgical treatment in the hospital from February 2, 2018, to June 2, 2020. The age of the patients was 55–75 years. They were divided into two groups, 62 in each group. All patients underwent transurethral resection of the bladder tumor. The patients in the case group received comprehensive nursing after the operation, and the patients in the control group took routine nursing measures. This study was approved by the medical ethics committee of the hospital, and all patients and their families signed informed consent.

Inclusion criteria were as follows: (1) patients with NMIBC diagnosed by imaging, CT, and pathology; (2) the patients who were in good condition without other serious organ diseases; (3) patients who cooperate with CT examination; (4) patients without any contraindications; and (5) the age range was 55–75 years.

Exclusion criteria were as follows: (1) patients with critical condition and survival less than half a year; (2) patients with other malignant tumors; (3) patients with mental illness who cannot be treated with surgery; and (4) patients whose family members did not consent and did not sign the informed consent.

2.2. Computed Tomography Imaging Examination. All patients underwent a CT imaging examination. The range between the bottom of the bladder and the ischial tubercle was included in the scanning position. Before scanning, the patient was instructed by the doctor to drink a large amount of water to keep the bladder in a full state. First, the plain scanning mode was performed, and iohexol (300 mg/mL) was injected at a uniform speed. The patients were scanned in enhanced mode after 45 s, and the delayed scan was completed after 5 min.

2.3. Three-Dimensional Reconstruction Algorithm. In this study, the improved marching cubes (MC) algorithm was used to reconstruct three-dimensional images. Multiple contour lines were set for all CT slices and were named $L1$, $L2, \ldots, Ln$. Each voxel (a, b, c) in the data was assigned to the function $f(a, b, c)$. When (a, b, c) was outside all contour lines, it was expressed as

$$f(a, b, c) = -1. \tag{1}$$

When (a, b, c) was above any contour line, it was expressed as

$$f(a, b, c) = 0. \tag{2}$$

When (a, b, c) was within any contour line, it was expressed as the following equation:

$$f(a, b, c) = 1. \tag{3}$$

Each point may have a result of 0, −1, or 1. When the edge interface passed through the vertex whose function $f(a, b, c)$ was 0 and if the values of two vertex functions $f(a, b, c)$ located on an edge were different signs, the edge interface would intersect with the edge. If the values of two vertex functions $f(a, b, c)$ located on an edge were different signs, the edge interface would not intersect with the edge. When an edge interface intersected with an edge, the midpoint of the edge was usually taken as the intersection point, and different intersection points were connected in order to obtain the reconstructed surface. The function $f(a, b, c)$ of each vertex would have three cases: 0, −1, and 1. In addition, the normal direction of the vertex could be calculated by the central difference method, and the state value of the vertex could be displayed according to the function $f(a, b, c)$. Then, the normal direction is shown as follows:

$$\begin{aligned} M_a &= \frac{f(a-1,b,c) - f(a+1,b,c)}{2}, \\ M_a &= \frac{f(a,b-1,c) - f(a,b+1,c)}{2}, \\ M_a &= \frac{f(a,b,c-1) - f(a,b,c+1)}{2}. \end{aligned} \tag{4}$$

The triangular surface generated after three-dimensional reconstruction needed to be simplified by the deletion algorithm so as to improve the speed of model reconstruction. The priority function was expressed as Y, as shown in the following equation:

$$Y(s) = C_t T(s) + C_x X(s) + C_g G(s). \tag{5}$$

In equation (5), s was the edge to be processed, and the flatness of the triangle connected with s was expressed as $T(s)$. The normal direction of this kind of triangle could be expressed as

$$\dot{L}_i \, (i = 1, 2, \ldots\ldots, n). \tag{6}$$

Then,

$$T(s) = Max\left(1 - \dot{L}_i \dot{L}_j\right). \tag{7}$$

In the equation (7), $G(s)$ was the length of one side s and $X(s)$ was the shape coefficient of the triangle with side s connected.

2.4. Surgical Treatment. All patients with NMIBC were given general anesthesia. Transurethral resection of the bladder tumor was performed at the bladder lithotomy site. Different parameters of the resection mirror were set. The electrocoagulation power and resection power were 60–80 W and 80 W, respectively. The resection range was 1 cm away from the edge of the tumor base to ensure complete resection of the tumor base. During the operation, the superficial muscle layer or the whole layer of the bladder wall could be selected according to the specific situation. When the tumor was too large, the protrusion tissue was first removed, then the tumor base was completely removed, and electrocautery was used to stop bleeding.

2.5. Postoperative Nursing Process. After the operation, the patients in the case group and the control group were treated with comprehensive nursing and routine nursing. Routine nursing: electrocardiographic (ECG) monitoring was performed 24 hours after the operation to observe the changes in blood pressure, respiration, pulse, and other parameters. Comprehensive nursing intervention in the case group: on the basis of routine nursing, psychological health counseling was conducted. Besides, timely communicating with patients and their families, popularizing medical-related knowledge, and instructing the significance of postoperative bladder flushing should be conducted, so as to alleviate the tension of patients and make patients cooperate with treatment in a good emotional state. Nursing care of bladder flushing: attention should be paid to the flushing operation, and the changes in flushing fluid should be timely monitored. Nurses and family members should timely react with doctors. The temperature, dosage, and flushing speed of flushing fluid were controlled as required. Nursing of drainage tube: the drainage tube was properly fixed to ensure its patency in the whole process, bladder spasm was prevented, the change of drainage fluid was monitored in real time, and the drainage speed was controlled. Nurses and family members should timely communicate with doctors for adjustment in time.

2.6. Observation and Evaluation Indicators. The general basic data of the two groups were collected, analyzed, and compared, including average age, proportion of men and women, course of disease, average tumor diameter, and proportion of patients with single and multiple tumors.

Based on the pathological examination results, three common index CT images based on the three-dimensional reconstruction algorithm were selected to evaluate the preoperative diagnostic effect of NMIBC patients, namely, accuracy, specificity, and sensitivity. The calculation methods are shown in the following equations:

$$\begin{aligned} \text{accuracy} &= \frac{A + B}{A + C + B + D}, \\ \text{specificity} &= \frac{B}{C + B}, \\ \text{sensitivity} &= \frac{A}{D + A}. \end{aligned} \tag{8}$$

In the above equation, A was true positive, indicating that the diagnostic result was positive and actually positive; B meant true negative, indicating that the diagnosis result was negative and actually negative; C was false positive, meaning that the diagnostic result was positive and actually negative; D was false negative, indicating that the actual result was positive and the diagnostic result was negative.

A receiver operating characteristic (ROC) curve was used to represent the diagnostic ability of CT information for patients with NMIBC, and the area under the curve (AUC) was determined according to ROC.

A self-rating anxiety scale (SAS) [30] was used to evaluate the psychological status of the two groups. The total score was 100. The higher the score was, the more serious the anxiety state was. The frequency of bladder spasm, bladder flushing time, and indwelling time of the drainage tube were recorded and compared between the two groups. The changes of tumor markers of bladder cancer specific antigen-1 (BLCA-1) and cyto-keratin 19 fragment antigen 21-1 (CYFRA21-1) were recorded in two groups of patients after operation. The quality of life of patients at 6 months after operation was evaluated by using the European Cancer Research and Treatment Organization quality of life core questionnaire. The scores were determined by five aspects: role, body, emotion, social, and cognitive function. The higher the score was, the better the quality of life of patients after operation was. The postoperative complications of the two groups were recorded and compared, and the complications such as electroresection syndrome, urinary tract infection, and massive hemorrhage were observed and analyzed. One year after the operation, CT image scanning based on the three-dimensional reconstruction algorithm was performed to check the recurrence of the two groups.

2.7. Statistical Methods. SPSS software was used to analyze the data. The data conforming to normal distribution was expressed by mean $\pm s$, and the measurement data was expressed by t-test, chi-square test, ($\chi 2$) was used to indicate the counting data, and $P < 0.05$ indicated that there was a statistical difference.

3. Results

3.1. Comparison Results of Basic Conditions of Patients. The basic conditions of the two groups were recorded and compared. It was found that there was no significant difference between the case group and the control group in terms of average age, proportion of male patients, average tumor diameter, duration of disease, and number distribution of patients with multiple tumors ($P < 0.05$). In addition, there was no significant difference between the two groups in the proportion of patients with hematuria, frequent urination, urgent urination, dysuria, and obvious weight loss ($P < 0.05$). The specific results are illustrated in Figures 1 and 2.

3.2. Computed Tomography Imaging Results of Patients. Figure 3 shows the CT image of a 57-year-old male. There were multiple multicolor lumps on the left lateral wall and left posterior wall of the bladder. The largest one was located 2.5 cm above the left ureter, with a wide base. There was necrosis on the tumor surface, and the rest of the bladder mucosa was smooth.

Figure 4 shows the CT image of a 63-year-old male. There was a papillary mass on the left posterior wall of the bladder, with 3×3 cm in size and a broad base close to the right ureteral opening. The vascular pedicle was clear.

3.3. Diagnostic Ability of Computed Tomography Images. By calculating the accuracy, specificity, and sensitivity, it was found that the accuracy, specificity, and sensitivity of CT imaging information based on the three-dimensional reconstruction algorithm in diagnosing NMIBC patients were 89.38, 93.77, and 84.39, respectively. The specific results are revealed in Figure 5.

The ROC curve was drawn according to the specificity and sensitivity of CT imaging information in diagnosing NMIBC patients, as shown in Figure 6. In addition, the AUC was determined to be 0.871 according to the ROC.

3.4. SAS Score Results of Two Groups. After treatment, the SAS scores of the two groups were measured. The results showed that the scores of the case group were significantly lower than those of the control group ($P < 0.05$). The specific results are shown in Figure 7.

3.5. Comparison of the Incidence of Bladder Spasm, Bladder Flushing, and Indwelling Time of Drainage Tube between the Two Groups. The incidence of bladder spasm, bladder flushing, and indwelling time of the drainage tube in the two groups were recorded and compared. The results indicated that the incidence of bladder spasm (9.68%), bladder flushing time (1.56 d), and retention of drainage tube time (2.68 d) in the case group were obviously lower compared to the control group (30.65%, 2.32 d, and 5.19 d) ($P < 0.05$). The specific results are shown in Figure 8.

3.6. Comparison of Tumor Markers between the Two Groups. The levels of tumor markers after operation in the two groups were recorded and compared. The results showed that serum BLCA-1 (3.72 ng/mL) and CYFRA21-1 (5.68 μg/mL) in the case group were signally lower than those in the control group, with a statistically considerable difference ($P < 0.05$). Figure 9 illustrates the specific results.

3.7. Comparison of Quality of Life Scores between the Two Groups. The postoperative quality of life indexes of the two groups were recorded and compared. The results showed that, in contrast to the control group, the scores of role function (89.82 points), emotional function (84.76 points), somatic function (79.23 points), and social function (73.93 points) in the case group were markedly higher ($P < 0.05$). The specific results are shown in Figure 10.

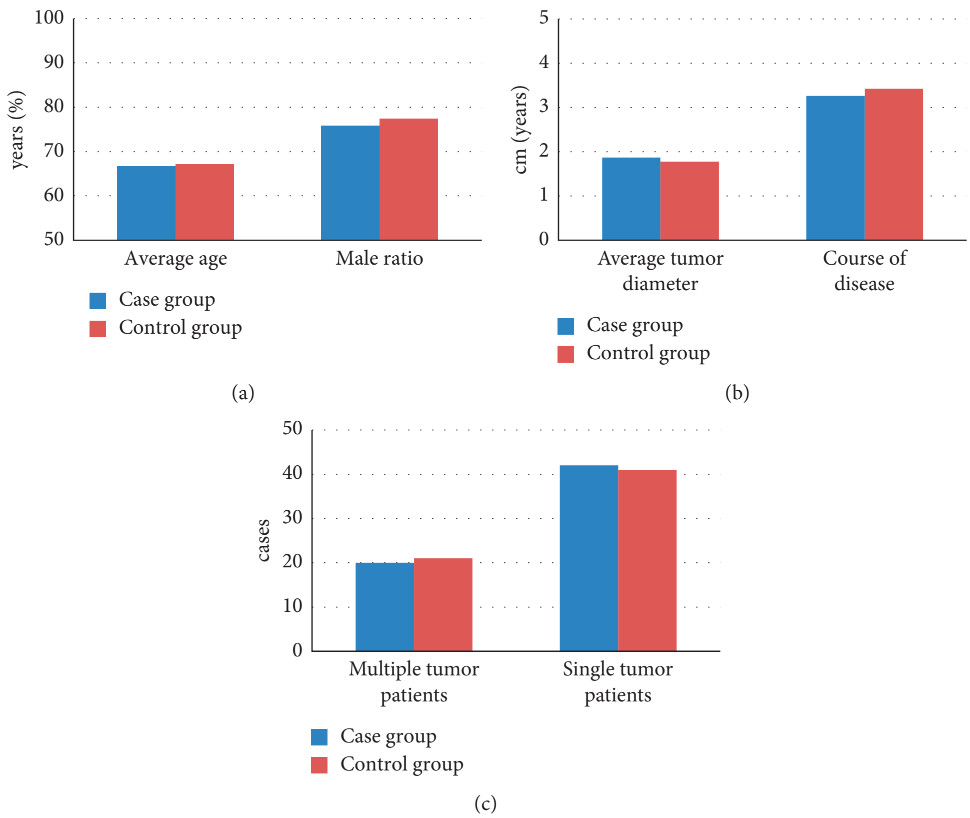

FIGURE 1: Comparison results of basic conditions of two groups of patients. (a) The comparison of average age and the male ratio between the two groups; (b) the comparison of average tumor diameter and course of disease between the two groups; (c) the comparison of the number of patients with multiple and single tumors between the two groups.

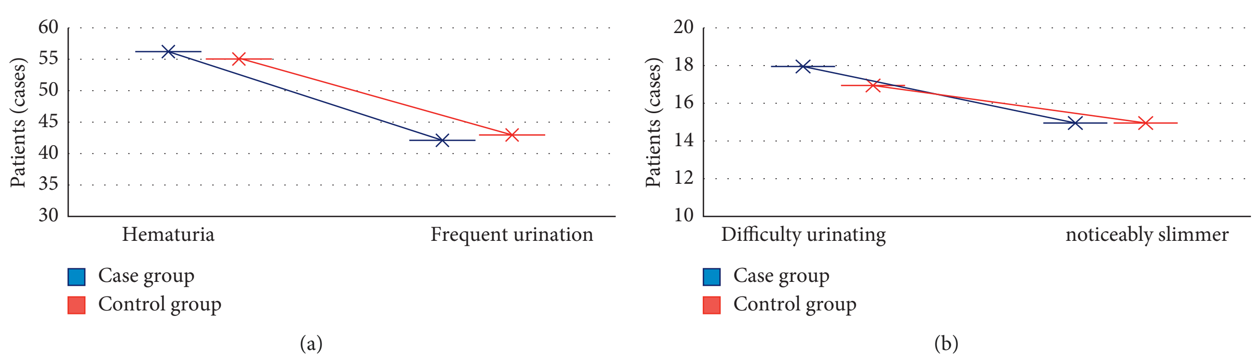

FIGURE 2: Comparison of clinical symptoms between the two groups. (a) The comparison of the number of patients with hematuria, frequent urination, and urgent urination in the two groups; (b) the comparison of the number of patients with dysuria and significant weight loss in the two groups.

3.8. Comparison of Postoperative Complications and Recurrence Rate between the Two Groups. The postoperative complications of the two groups were recorded and compared. The results showed that compared with the control group, the number of patients with postoperative urinary tract infection and electroresection syndrome in the case group was significantly lower ($P < 0.05$), and there was no urethral stricture in the two groups. In addition, one year after the operation, CT examination showed that the recurrence rate in the case group (6.45%) was significantly lower than that in the control group (22.58%) ($P < 0.05$). Figure 11 suggests the specific results.

4. Discussion

At present, the incidence rate and mortality rate of bladder cancer are increasing, and it has the characteristics of high malignancy and poor prognosis. It has seriously damaged the physical and mental health of patients. In men, bladder cancer has been ranked fifth in cancer mortality rate, and in

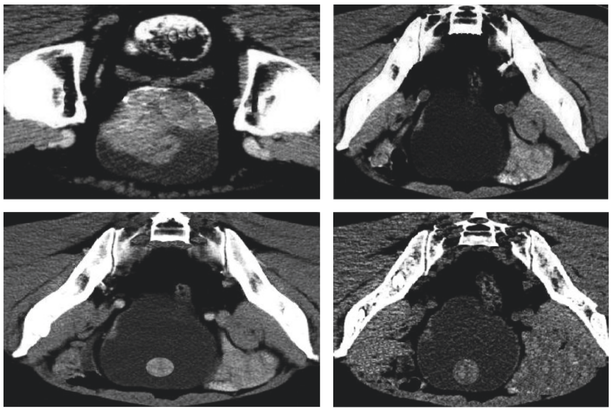

Figure 3: The CT image of a 57-year-old male patient, with a history of high blood pressure.

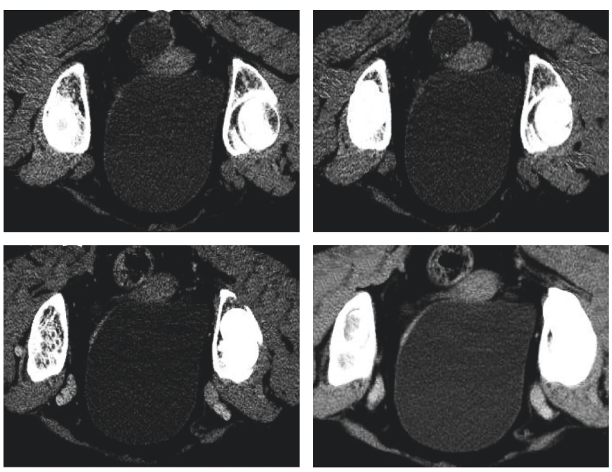

Figure 4: The CT image of a 63-year-old male patient. The general condition was good, and he was admitted after 8 days of hematuria.

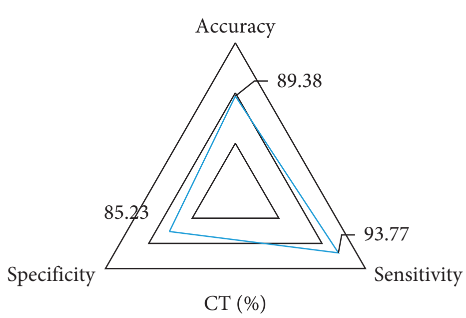

Figure 5: Evaluation of the ability of CT imaging information to diagnose NMIBC patients.

women, it has been ranked in the top ten. Therefore, timely diagnosis and effective treatment of bladder cancer are particularly important [31]. About 70% of the clinical patients are NMIBC patients, but non-muscle-invasive bladder cancer patients also have a higher risk of metastasis. Surgical treatment is the main means of clinical treatment for bladder cancer. Preoperative diagnosis of bladder tumor by CT is very important for determining the stage, location, and size of the bladder tumor. CT is one of the common methods for

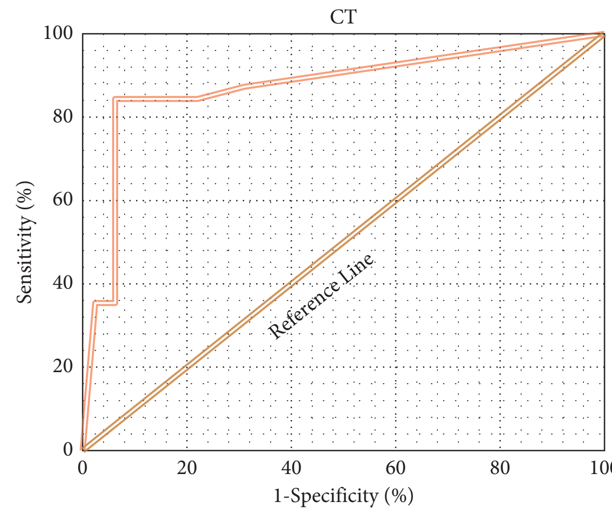

Figure 6: ROC curve results of NMIBC patients diagnosed by CT imaging information.

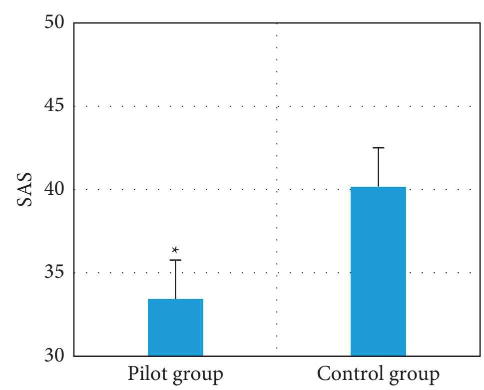

Figure 7: Comparison of SAS scores between the two groups. ∗ indicates significant difference, $P < 0.05$.

the clinical diagnosis of bladder cancer. Preoperative diagnosis can improve the accuracy of preoperative staging and can detect the recurrence of bladder cancer. CT detection based on a three-dimensional reconstruction algorithm is helpful for clinicians to further observe and analyze, obtain more deep information, and confirm the operation plan more accurately and quickly [32]. To analyze the application value of CT image based on three-dimensional reconstruction algorithm in perioperative nursing research and prognosis analysis of elderly patients with NMIBC in urology, 124 patients with NMIBC were selected and divided into case group and control group. Before operation, CT detection based on the three-dimensional reconstruction algorithm was used to diagnose the tumor. The results showed that there was no significant difference in the average age, the proportion of male patients, the average tumor diameter, the length of disease course, and the number distribution of patients with multiple tumors ($P < 0.05$). In addition, there was no significant difference between the two groups in the proportion of patients with hematuria, frequent urination, urgent urination, dysuria, and obvious weight loss ($P < 0.05$), which showed that the basic

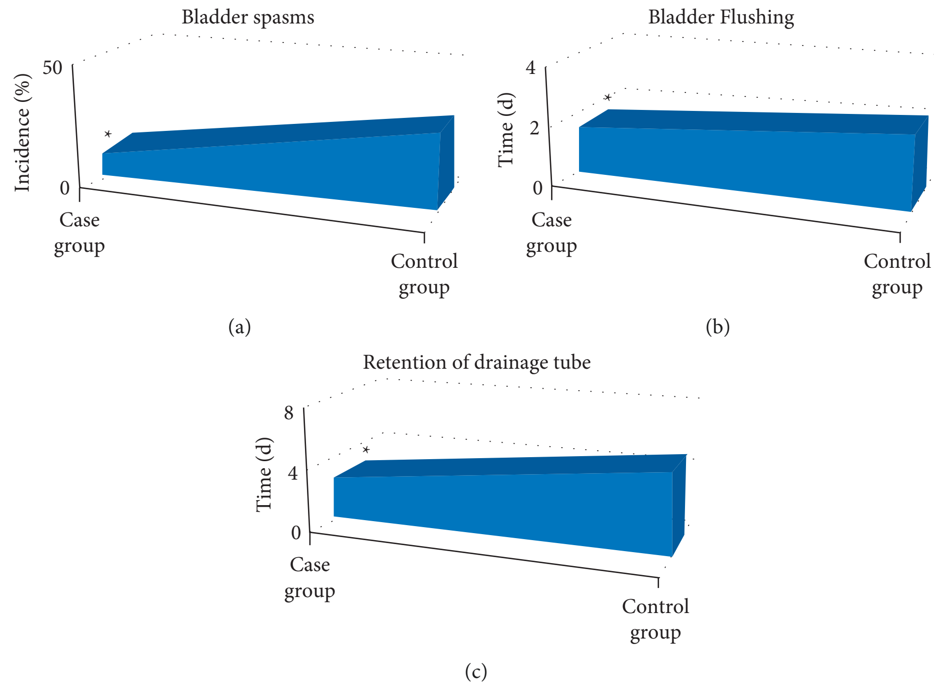

FIGURE 8: Comparison of the incidence of bladder spasm, bladder flushing, and indwelling time of drainage tube between the two groups. (a) The comparison of the incidence of bladder spasm between the two groups; (b) the comparison of bladder flushing time between the two groups; (c) the comparison of the retention time of the bladder drainage tube between the two groups. ∗ indicates a significant difference: $P < 0.05$.

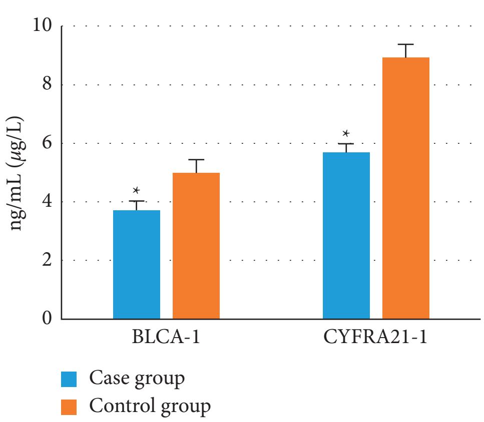

FIGURE 9: Comparison of tumor markers in serum between the two groups. ∗ indicates significant difference, $P < 0.05$.

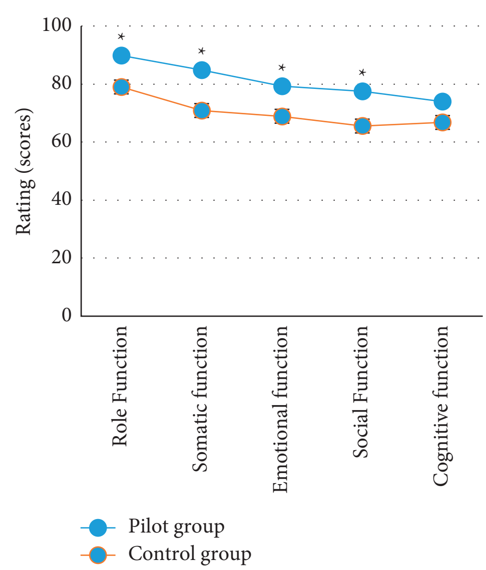

FIGURE 10: Quality of life score results of two groups of patients. ∗ indicates significant difference, $P < 0.05$.

conditions of the two groups were the same and increased the comparability of follow-up parameters. By calculating the accuracy, specificity, and sensitivity, it was found that the accuracy, specificity, and sensitivity of CT imaging information based on the three-dimensional reconstruction algorithm in diagnosing NMIBC patients were 89.38, 93.77, and 84.39, respectively. The ROC curve was drawn according to the specificity and sensitivity of CT imaging information in diagnosing NMIBC patients, and the AUC was determined to be 0.871 according to ROC. This indicated that the CT image based on the three-dimensional reconstruction algorithm had a strong diagnostic ability for NMIBC patients. The results of comparative analysis of the two diagnostic methods of CT and pathology in multiple bladder cancer pathologies showed that the coincidence rate between CT diagnosis and pathological diagnosis was high. It could provide a reference for the clinical diagnosis of MNIBC patients, which was more consistent with the results of this study [33].

In this study, the patients were divided into case group and control group for rapid comprehensive nursing and

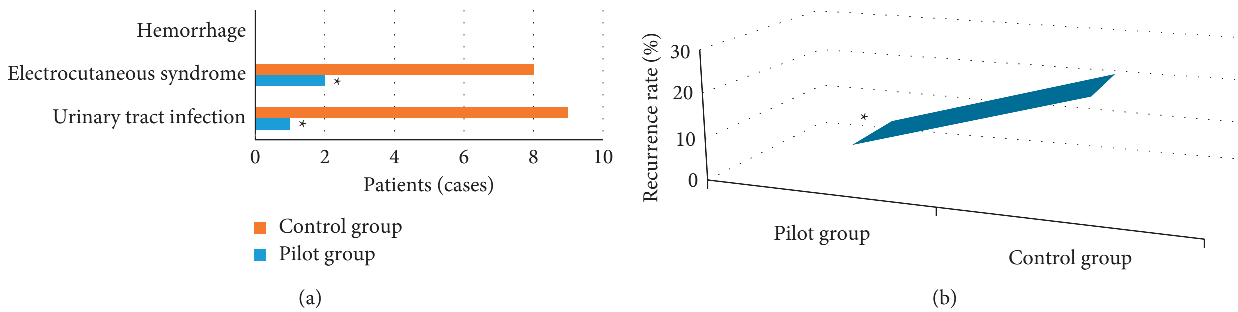

Figure 11: Comparison of postoperative complications and recurrence between the two groups. (a) The comparison results of complications between the two groups; (b) the comparison results of postoperative recurrence between the two groups. $*$ indicates significant difference, $P < 0.05$.

routine nursing. The recovery status of the two groups was analyzed and compared. The recurrence was detected by CT scanning, so as to evaluate the reference value of CT image information based on the three-dimensional reconstruction algorithm in preoperative diagnosis, postoperative nursing, and recurrence monitoring of NMIBC patients. The results showed that after surgical treatment and nursing, compared with the control group, the SAS score in the case group was significantly lower ($P < 0.05$). The incidence of bladder spasm in the case group was significantly lower, the bladder flushing and drainage tube retention time were significantly shorter ($P < 0.05$), and the tumor markers BLCA-1 and CYFRA21-1 in the serum of the case group were significantly lower ($P < 0.05$). The scores of emotional function, physical function, and social function increased significantly ($P < 0.05$), and there was no significant difference in cognitive function between the two groups ($P > 0.05$). Compared with the control group, the number of patients with postoperative urinary tract infection and electroresection syndrome in the case group decreased significantly ($P < 0.05$). There was no urethral stricture in both groups. In addition, one year after the operation, CT examination showed that the recurrence rate of patients in the case group was significantly lower than that in the control group ($P < 0.05$), indicating that postoperative comprehensive nursing was particularly important for patients with NMIBC. CT detection could play a great role in the postoperative detection and prognosis evaluation of NMIBC. In some studies, the recurrence rate of patients with NMIBC decreased significantly after surgical treatment and one year after comprehensive nursing, which was consistent with the results of this study [34]. In conclusion, CT detection based on a three-dimensional reconstruction algorithm was particularly important for preoperative diagnosis, prognosis, and recurrence monitoring of NMIBC patients.

5. Conclusion

124 patients with NMIBC received CT examination based on the three-dimensional reconstruction algorithm and received rapid comprehensive care and conventional care. The results showed that CT images based on the three-dimensional reconstruction algorithm had a strong diagnostic ability for NMIBC patients, and postoperative comprehensive care was particularly crucial for NMIBC patients. Besides, CT detection could play a huge role in postoperative detection and prognosis assessment of NMIBC. Postoperative comprehensive nursing could not only shorten the bladder flushing and retention of drainage tube time of NMIBC patients but also reduce the postoperative recurrence rate and improve the prognosis. The deficiency of this study was that the sample size of the research object had a single source and did not have randomness and wide applicability. In the future research, multilocation and multitype sample size analysis and research will be considered, so as to provide a more practical and effective reference for CT imaging examination and its monitoring in preoperative diagnosis, prediction, and recurrence of NMIBC patients.

Data Availability

The data used to support the findings of this study are available from the corresponding author upon request.

Conflicts of Interest

The authors declare no conflicts of interest.

Acknowledgments

This work was supported by the Zhejiang Medical and Health Science and Technology Project (no. 2021423910).

References

[1] A. T. Lenis, P. M. Lec, K. Chamie, and M. Mshs, “Bladder cancer,” *JAMA*, vol. 324, no. 19, pp. 1980–1991, 2020.

[2] V. G. Patel, W. K. Oh, and M. D. Galsky, “Treatment of muscle-invasive and advanced bladder cancer in 2020,” *CA: A Cancer Journal for Clinicians*, vol. 70, no. 5, pp. 404–423, 2020.

[3] S. Siracusano, R. Rizzetto, and A. B. Porcaro, “Bladder cancer genomics,” *Urologia Journal*, vol. 87, no. 2, pp. 49–56, 2020.

[4] A. Richters, K. K. H. Aben, and L. A. L. M. Kiemeney, “The global burden of urinary bladder cancer: an update,” *World Journal of Urology*, vol. 38, no. 8, pp. 1895–1904, 2020.

[5] M. Pecoraro, M. Takeuchi, H. A. Vargas et al., “Overview of VI-rads in bladder cancer,” *American Journal of Roentgenology*, vol. 214, no. 6, pp. 1259–1268, 2020.

[6] A. T. Lenis, P. M. Lec, and K. Chamie, “Bladder cancer.” *JAMA*, vol. 324, no. 19, p. 2006, 2020.

[7] J. Hamad, H. McCloskey, M. I. Milowsky, T. Royce, and A. Smith, “Bladder preservation in muscle-invasive bladder cancer: a comprehensive review,” *International Braz J Urol*, vol. 46, no. 2, pp. 169–184, 2020.

[8] R. Cao, L. Yuan, B. Ma, G. Wang, W. Qiu, and Y. Tian, “An EMT-related gene signature for the prognosis of human bladder cancer,” *Journal of Cellular and Molecular Medicine*, vol. 24, no. 1, pp. 605–617, 2020.

[9] B. Jordan and J. J. Meeks, “T1 bladder cancer: current considerations for diagnosis and management,” *Nature Reviews Urology*, vol. 16, no. 1, pp. 23–34, 2019.

[10] C. Alifrangis, U. McGovern, A. Freeman, T. Powles, and M. Linch, “Molecular and histopathology directed therapy for advanced bladder cancer,” *Nature Reviews Urology*, vol. 16, no. 8, pp. 465–483, 2019.

[11] M. Minoli, M. Kiener, G. N. Thalmann, M. Kruithof-de Julio, and R. Seiler, “Evolution of urothelial bladder cancer in the context of molecular classifications,” *International Journal of Molecular Sciences*, vol. 21, no. 16, p. 5670, 2020.

[12] C. Seidl, “Targets for therapy of bladder cancer,” *Seminars in Nuclear Medicine*, vol. 50, no. 2, pp. 162–170, 2020.

[13] R. López-Cortés, S. Vázquez-Estévez, J. Á Fernández, and C. Núñez, “Proteomics as a complementary technique to characterize bladder cancer,” *Cancers*, vol. 13, no. 21, p. 5537, 2021.

[14] A. Plata, F. Guerrero-Ramos, C. Garcia et al., “Long-term experience with hyperthermic chemotherapy (HIVEC) using mitomycin-C in patients with non-muscle invasive bladder cancer in Spain,” *Journal of Clinical Medicine*, vol. 10, no. 21, p. 5105, 2021.

[15] S. R. Unsworth-White, M. O. Kitchen, and R. T. Bryan, “Immunotherapy for non-muscle-invasive bladder cancer: from the origins of BCG to novel therapies,” *Future Oncology*, vol. 18, no. 1, pp. 105–115, 2022.

[16] R. Nadal, A. B. Apolo, D. M. Girardi, N. M. Hahn, and J. Bellmunt, “Systemic therapy issues: immunotherapy in nonmetastatic urothelial cancer,” *Urologic Oncology: Seminars and Original Investigations*, vol. S1078-1439, no. 20, Article ID 30477, 2020.

[17] U. Iqbal, A. S. Elsayed, Z. Jing et al., “Upstaging and survival outcomes for non-muscle invasive bladder cancer after radical cystectomy: results from the international robotic cystectomy consortium,” *Journal of Endourology*, vol. 35, no. 10, pp. 1541–1547, 2021.

[18] H. Türk, S. Ün, A. Cinkaya, H. Kodaz, M. Parvizi, and F. Zorlu, “Effect of delayed radical cystectomy for invasive bladder tumors on lymph node positivity, cancer-specific survival and total survival,” *Tumori Journal*, vol. 104, no. 6, pp. 434–437, 2018.

[19] W. Choi, K. Lombardo, S. Patel et al., “A molecular inquiry into the role of antibody-drug conjugates in Bacillus calmette-guérin-exposed non-muscle-invasive bladder cancer,” *European Urology*, vol. 81, no. 2, Article ID 02077, 2022.

[20] Z. Li, X. Li, R. Tang, and L. Zhang, “Apriori algorithm for the data mining of global cyberspace security issues for human participatory based on association rules,” *Frontiers in Psychology*, vol. 11, Article ID 582480, 2021.

[21] M. A. Han, P. Maisch, J. H. Jung et al., “Intravesical gemcitabine for non-muscle invasive bladder cancer: an abridged Cochrane Review,” *Investigative and Clinical Urology*, vol. 62, no. 6, pp. 623–630, 2021.

[22] D. M. Carrión, J. Gómez Rivas, A. Aguilera Bazán et al., “The benefit of a neoadjuvant instillation of chemotherapy in non-muscle invasive bladder cancer: interim analysis of the PRECAVE randomized clinical trial,” *Archivos Españoles de Urología*, vol. 74, no. 9, pp. 883–893, 2021.

[23] X. Zhang, H. Shen, and Z. Lv, “Deployment optimization of multi-stage investment portfolio service and hybrid intelligent algorithm under edge computing,” *PLoS One*, vol. 16, no. 6, Article ID e0252244, 2021.

[24] S. Xie, Z. Yu, and Z. Lv, “Multi-disease prediction based on deep learning: a survey,” *Computer Modeling in Engineering and Sciences*, vol. 128, no. 2, pp. 489–522, 2021.

[25] J. Tamihardja, S. Cirsi, P. Kessler et al., “Cone beam CT-based dose accumulation and analysis of delivered dose to the dominant intraprostatic lesion in primary radiotherapy of prostate cancer,” *Radiation Oncology*, vol. 16, no. 1, p. 205, 2021.

[26] M. Hu, Y. Zhong, S. Xie, H. Lv, and Z. Lv, “Fuzzy system based medical image processing for brain disease prediction,” *Frontiers in Neuroscience*, vol. 15, Article ID 714318, 2021.

[27] M. Nakagawa, T. Naiki, A. Naiki-Ito et al., “Usefulness of advanced monoenergetic reconstruction technique in dual-energy computed tomography for detecting bladder cancer,” *Japanese Journal of Radiology*, vol. 40, no. 2, pp. 177–183, 2021.

[28] J.-H. Choi, K.-H. Yoo, D.-G. Lee, G.-E. Min, G.-Y. Kim, and T.-S. Choi, “A case of incidental schwannoma mimicking necrotic metastatic lymph node from bladder cancer,” *Medicina*, vol. 57, no. 7, p. 728, 2021.

[29] K. Takayama, S. Narita, Y. Terai, R. Saito, and T. Habuchi, “Cancer antigen 15-3 serum level as a biomarker for advanced micropapillary urothelial carcinoma of the bladder: a case report,” *Case Reports in Oncology*, vol. 14, no. 2, pp. 1019–1024, 2021.

[30] D. A. Dunstan and N. Scott, “Norms for zung’s self-rating anxiety scale,” *BMC Psychiatry*, vol. 20, no. 1, p. 90, 2020.

[31] J. Han, X. Gu, Y. Li, and Q. Wu, “Mechanisms of BCG in the treatment of bladder cancer-current understanding and the prospect,” *Biomedicine & Pharmacotherapy*, vol. 129, Article ID 110393, 2020.

[32] S. Tenninge, H. Mogos, E. Eriksson et al., “Control computerized tomography in neoadjuvant chemotherapy for muscle invasive urinary bladder cancer has no value for treatment decisions and low correlation with nodal status,” *Scandinavian Journal of Urology*, vol. 55, no. 6, pp. 455–460, 2021.

[33] N. Ishibashi, T. Maebayashi, M. Sakaguchi, T. Aizawa, and M. Okada, “Bladder filling volume variation between the first and second day of planning computed tomography for prostate cancer radiation therapy and correlation with renal function,” *Asia-Pacific Journal of Clinical Oncology*, vol. 21, 2021.

[34] F. Verghote, L. Poppe, S. Verbeke et al., “Evaluating the impact of 18F-FDG-PET-CT on risk stratification and treatment adaptation for patients with muscle-invasive bladder cancer (EFFORT-MIBC): a phase II prospective trial,” *BMC Cancer*, vol. 21, no. 1, p. 1113, 2021.

Hindawi
Contrast Media & Molecular Imaging
Volume 2022, Article ID 2574451, 9 pages
https://doi.org/10.1155/2022/2574451

Research Article

Computed Tomography Image under Artificial Intelligence Algorithm to Evaluate the Nursing and Treatment Effect of Pemetrexed Combined Platinum-Based Chemotherapy on Elderly Lung Cancer

Qing Gu and Shu'e Li

Department of General Medicine, The First Affiliated Hospital of Suzhou University, Suzhou 215006, Jiangsu, China

Correspondence should be addressed to Shu'e Li; lishue@suda.edu.cn

Received 22 February 2022; Revised 3 May 2022; Accepted 16 May 2022; Published 6 June 2022

Academic Editor: M Pallikonda Rajasekaran

This study was to evaluate the clinical efficacy of pemetrexed combined with platinum-based chemotherapy in the treatment of elderly lung cancer using electronic computed tomography (CT) images based on artificial intelligence algorithms. In this study, 80 elderly patients with lung cancer treated were selected and randomly divided into two groups: patients treated with pemetrexed combined with cisplatin were included in the pemetrexed group and patients treated with docetaxel combined with cisplatin were included in the docetaxel group, with 40 cases in each group. The DenseNet network was compared with the Let Net-5 and ResNet model and applied to the CT images of 80 elderly patients with lung cancer. The diagnosis accuracy of the DenseNet network (97.4%) was higher than that of the Let Net-5 network (80.1%) and ResNet model (95.5%). Carcinoembryonic antigen (CEA), cytokeratin fragment antigen 21–1 (CYFRA 21–1), and squamous cell-associated antigen (SCC) after chemotherapy in the pemetrexed group and docetaxel group were all lower than those before chemotherapy, showing statistically obvious differences ($P < 0.05$). The satisfaction degree of nursing care in the pemetrexed group (92.67%) was significantly higher than that in the docetaxel group (85.62%), and the difference was statistically significant ($P < 0.05$). Adverse reactions such as fatigue, diarrhea, and neutrophils in the pemetrexed group were lower than those in the docetaxel group, and the difference was statistically great ($P < 0.05$). The DenseNet convolutional neural network has high diagnostic accuracy; methotrexate combined with platinum chemotherapy can improve the chemotherapy effect in elderly patients with lung cancer, with low degree of adverse reactions and good overall tolerance, which can be used as the first-line treatment for elderly patients with lung cancer.

1. Introduction

Lung cancer is the malignant tumor with the highest morbidity and mortality in the world, and it is increasing year by year [1, 2]. Nonsquamous non-small cell lung cancer (NSCLC) is a common pathological type of lung cancer. Because of its insidious onset and rapid disease progression, patients are usually in the advanced stage when diagnosed, and 50% of the elderly are over 65 years old, and most of them are in the advanced stage, so they cannot be treated by surgery [3–5]. For a long time, platinum-containing dual-drug chemotherapy has been the first-line standard treatment for patients with advanced NSCLC without driver gene mutations. Pemetrexed combined with platinum chemotherapy has been approved to be the first-line treatment way by the Food and Drug Administration of the United States for the treatment of patients with advanced nonsquamous NSCLC [6]. In China, pemetrexed combined with platinum-based chemotherapy is more widely used in nonsquamous NSCLC patients. At present, the efficacy and safety of pemetrexed combined with platinum in the first-line treatment of nonsquamous NSCLC patients have not been clearly evaluated.

In recent years, with the development of medical image informatics, digging out image features and analyzing clinical information from medical images has gradually attracted the attention of clinicians [7–9]. Studies have confirmed that computed tomography (CT) scans have the advantages of noninvasive and repeated examinations and can evaluate the efficacy of tumors based on tumor size, enhancement characteristics, and density changes [10]. After chemotherapy, the efficacy of chemotherapy can be assessed noninvasively based on the patient's clinical indicators, CT indicators, and histological indicators, and a personalized treatment plan suitable for the patient can be selected, which can provide a good reference for new treatment methods.

The function of automatic search and representation by artificial intelligence is very useful in the medical field. The main features can be extracted by artificial intelligence, and CT images can be classified without human intervention. The newly developed DenseNet is a convolutional neural network (CNN) with dense connection function, in which any two layers are directly connected; the input of each layer is the union of the outputs of all the previous layers, and the characteristic map of this layer is also the input of all the subsequent layers [11]. Wan et al. (2021) [12] found that DenseNet is more efficient than a convolutional neural network, which is mainly reflected in the reduction of computation and the reuse of features in all layers of the network. DenseNet can effectively detect and classify pulmonary nodules in CT images for accurate diagnosis.

In this study, 80 elderly patients with lung cancer were selected, and the artificial intelligence algorithms were innovatively combined with CT images to segment and calibrate the elderly patients with lung cancer so as to explore the efficacy of pemetrexed combined with platinum-based chemotherapy in the treatment of lung cancer and truly realize the desire of "early detection, early diagnosis, early treatment, and early cure."

2. Research Objects and Grouping

2.1. Research Objects. In this study, 80 elderly patients with lung cancer (aged > 60 years old) in the hospital from January 2019 to September 2020 were selected as the research objects. In addition, all research objects were diagnosed as lung cancer using percutaneous lung puncture, bronchoscopy biopsy, lymph node biopsy, and other biopsies of metastatic lesions. They were randomly divided into two groups, patients treated with pemetrexed combined with cisplatin were included in the pemetrexed group (40 cases aged 62~83 years old) and patients treated with docetaxel combined with cisplatin were included in the docetaxel group (40 cases aged 61~85 years old). There was no significant difference in age and gender between the two groups of patients ($P > 0.05$), and they were comparable (Table 1). This study had been approved by the ethics committee of hospital, and the patients and their families understand the situation of the study and sign the informed consent forms.

Table 1: Clinical characteristics of the two groups of patients before treatment (n, %).

		Pemetrexed group ($n = 40$)	Docetaxel group ($n = 40$)	P value
Average age (years old)		73.2 ± 12.5	74.5 ± 13.8	>0.05
Gender	Males	26 (65%)	24 (60%)	>0.05
	Females	14 (35%)	16 (40%)	>0.05
PS score	0	6 (15%)	9 (22.5%)	>0.05
	1	33 (82.5%)	24 (60%)	>0.05
	2	1 (2.5%)	7 (17.5%)	>0.05

Inclusion criteria are as follows: patients with the systemic function status score (PS score) standard of below 2 points; patients whose estimated survival time was more than 3 months; patients whose liver and kidney function and blood routine before chemotherapy were in the normal range; and patients without severe qualitative lesions in important organs.

Exclusion criteria are as follows: patients who were ≤60 years old; patients with unclear clinical stage; patients with less than 2 cycles of chemotherapy; patients who did not cooperate; and patients with malignant tumors of other parts.

2.2. Treatment Schemes. Pemetrexed group: 40 patients with lung cancer started to take folic acid tablets 7 days before receiving pemetrexed chemotherapy (400 μg/d) for continuous 21 days. They were given VitB12 (1000 μg/time) intramuscular injection at the same time 7 days before chemotherapy, once every 21 days. Dexamethasone (4 mg) was taken orally 1 day before chemotherapy and 1st day and 2nd day after chemotherapy to prevent skin rash and allergies. Pemetrexed (500 mg/m^2) was given in the form of intravenous infusion on the first day; cisplatin (70 mg/m^2), intravenous infusion, was given on the first time. One cycle included 21 days.

Docetaxel group: the patients were given dexamethasone (5 mg) intravenously before chemotherapy, and docetaxel (75 mg/m^2) and cisplatin (70 mg/m^2) were intravenously injected on the first day, with 21 days for a cycle. Measures to prevent vomiting were given during chemotherapy. The blood picture was rechecked once a week, tumor markers and biochemical indicators were rechecked before each chemotherapy, and CT imaging was performed to evaluate the curative effect after 2 cycles of chemotherapy.

2.3. Evaluation Criteria. The curative effect was evaluated according to the solid tumor curative effect evaluation standard RECIST 1.1 given by World Health Organization (WHO) [13]. In this study, CT scans were used to evaluate the changes in the size of the measurable nodules before and after treatment. The imaging examination before treatment showed that there were 1 or more measurable lesions. All patients had at least 2 cycles of chemotherapy. The curative effect was evaluated after 2 cycles of chemotherapy and compared with the lesion before treatment. It should detect the serum tumor markers (carcinoembryonic antigen (CEA), cytokeratin fragment antigen 21–1 (CYFRA 21–1), and squamous cell-associated antigen (SCC)). In addition, the chest and abdomen were performed with the enhanced CT, and then it should continue to the next round according to RECIST standards treatment.

Evaluation indicators of target lesions included complete remission (CR), partial remission (PR), stable disease (SD), and disease progression (PD).

The response rate (RR) (RR = CR + PR), disease control rate (DCR) (DCR = CR + PR + SD), time to progression (TTP), median survival time (MST), and progression-free survival (PFS) were detected. The follow-up was performed using a combination of outpatient and telephone follow-up. During the follow-up, the survival time (months) of all patients was recorded.

2.4. CT Scan. The patient was in a supine position with the head advanced, and a 16-slice spiral CT scanner was used. Before the examination, the patient was trained to breathe and hold his breath calmly to eliminate tension. Local plain scan was performed on the mass and determine the largest level of the lesion on the plain scan image. Scanning conditions were set as follows: 120 kV, 200 mA, 1.0 s/r, acquisition layer thickness of 1 mm × 16, reconstruction interval of 7 mm, reconstruction layer thickness of 7 mm, and pitch of 15. Dynamic scanning was performed on selected layers according to cross-sectional positioning. Perfusion scanning conditions were set as follows: 120 kV, 200 mA, 1.0 s/r, field of view (FOV) of 40, matrix of 512 × 512, acquisition layer thickness of 2 mm × 4, and interval of 1 s. 50 mL of 300 mg/mL iohexo was injected intravenously in front of the elbow, 21 G × 3/4 intravenous indwelling needle was embedded through median cubital vein puncture, with the rate of 4 mL/s, delay of 6 s, and data acquisition of 32 s, generating 128 layers of perfusion images. After the completion of the perfusion scan, 50 mL of contrast medium was injected again at a rate of 2 mL/s, with a delay of 25 seconds for routine enhanced scan.

2.5. Nursing Methods. Psychological nursing should be implemented for all patients. Nursing staff should understand and support patients, meet their reasonable needs, fully mobilize the enthusiasm of patients' spouses or family members, assist patients with treatment with a good attitude, and respond to various adverse reactions in a timely manner.

Before administration, patients and family members should be informed that chemotherapy drugs may cause side effects such as leukopenia and thrombocytopenia. The importance of vitamin B12 and folic acid should be explained, the compliance of patients with self-medication outside the hospital has to be improved, patients should be encouraged to drink more water, urine output should be maintained above 2000 mL, and the color and nature of urine should be paid attention to.

Patients have different degrees of skin rash and itching, and the head, face, and trunk are more common. Oral antihistamines or hormone antiallergic drugs can be used for nursing, and antibiotics can be taken orally in a short time to prevent infection. Patients are advised to wear soft and breathable clothes, keep their skin clean, and if skin rash or itching occurs, they should avoid scratching and rubbing irritating drugs locally. Hydrocortisone or dexamethasone ointment can be applied for external treatment.

According to the nursing of gastrointestinal reaction, antiemetic drugs such as granisetron and metoclopramide should be used on time and correctly before treatment to prevent the occurrence of nausea and vomiting. It is important to reduce bad stimulation, create a good living environment, and keep the indoor air fresh and the temperature appropriate. Dietary guidance should be given. For patients with diarrhea, the number and characteristics of defecation should be recorded. Compound phenethylpiperidine can be taken orally to reduce gastrointestinal peristalsis. For patients with dehydration symptoms, water and electrolytes should be added intravenously.

Cisplatin has obvious toxic and side effects on kidney, and active hydration and diuresis during chemotherapy are the keys to prevent kidney damage. On the day of application of cisplatin, the hydration volume should be >2000 mL and furosemide 20 mg or 20% mannitol 125 mL should be given for diuresis. In order to ensure continuous renal perfusion and maintain the infusion time for more than 14 hours, patients should be encouraged to drink more water and keep sufficient urine output and the 24-hour urine output should be >2000 mL.

2.6. CT Image Based on DenseNet. DenseNet is a dense connection mechanism that connects all layers to each other. That is, the input of each layer in the network is the output of all the previous layers [14]. Figure 1 showed the dense connection mechanism of the DenseNet.

If there were N layers in the DenseNet, there were $N(N-1)/2$ connections in the entire DenseNet CNN. DenseNet is not only densely structured but also can improve network efficiency by connecting feature maps of different layers.

The output of the traditional convolutional neural network (CNN) in the N layer was given as follows:

$$x_n = T_n(x_{n-1}). \tag{1}$$

In (1), x represented output and T_n represented a nonlinear transformation function, which was a series of comprehensive operations such as batch normalization (BN), ReLU activation function, pooling operation, and Conv convolution operation. In the DenseNet, the identity function from the input of the previous layer was added:

$$x_n = T_n(x_{n-1}) + x_{n-1}. \tag{2}$$

At the same time, all the previous layers were taken as input:

$$x_n = T_n([x_0, x_1, \ldots, x_{n-1}]). \tag{3}$$

Parameters of DenseNet were shown in Table 2.

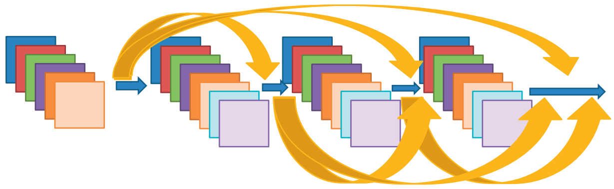

Figure 1: The dense connection mechanism of the DenseNet.

Table 2: Parameters of DenseNet.

Layer	Output size	Parameter
Convolution	112×112	7×7 conv, stide2
Pooling	56×56	3×3 max pool, stide2
Dense block	56×56	$\begin{pmatrix} 1 \times 1conv \\ 3 \times 3conv \end{pmatrix} \times 6$
Transition layer	56×56	1×1 conv
	28×28	2×2 average pool, stide2
Dense block	28×28	$\begin{pmatrix} 1 \times 1\text{conv} \\ 3 \times 3\text{conv} \end{pmatrix} \times 12$
Classification layer	1×1	7×7 global average pool

2.7. Image Analysis and Processing. The two-dimensional (2D) images of the CT image sequence of 80 patients with nodules were extracted. The CT image was segmented, the candidate position was taken as the center to obtain the image block, and the cross-section, sagittal plane, and coronal plane were extracted. Due to the size of most nodules, the receptive field size of each image block was set to 64×64. The CT values were cut to (–1000–400 HU) and normalized to (0, 1). The average gray value was subtracted to fit the DenseNet.

2.8. Setting for Algorithm Comparison. The ratio of the training set to the test set was 8 : 2, and these two sets of pictures were used as the input of the DenseNet. When the model was trained, the network growth speed k was set to 32, the compression rate of the transition layer between different blocks was set to 0.5, the learning rate was set to 0.01, and the dropout rate was set to 0.3. The optimizer used the batch gradient descent method. In order to make the conclusion more convincing, the DenseNet network was compared with Let Net-5 and ResNet models in this study.

2.9. Statistical Methods. SPSS (Statistical Product and Service Solutions) 22.0 was adopted as the analysis and statistical software for statistical analysis. The count data were expressed in percentage (%),the data conforming to the normal distribution was expressed in $\overline{x} \pm s$, and the t-test was used to verify. The results were statistically significant when $P < 0.05$.

3. Results

3.1. Results of Image Segmentation Algorithms. There were 156 malignant nodules in 80 elderly lung cancer patients. The DenseNet network was compared with Let Net-5 and ResNet models to diagnose malignant nodules. The results showed that the Let Net-5 network detected 125 malignant nodules, the ResNet network detected 149 malignant nodules, and the DenseNet network detected 152 malignant nodules. The diagnosis accuracy of the DenseNet network (97.4%) was higher than that of the Let Net-5 network (80.1%) and ResNet model (95.5%), and there was no statistical difference ($P > 0.05$), as shown in Figure 2. The diagnostic accuracy of DenseNet was better than other typical models, which proved the effectiveness of DenseNet in diagnosing malignant nodules.

The CT image was segmented based on the DenseNet, and the results were shown in Figure 3. It was found that the DenseNet showed a more accurate and higher definition for the number of nodules diagnosed.

3.2. Clinical Efficacy and Survival. The RRs of the pemetrexed group and the docetaxel group were 28.5% and 16.78%, respectively; the DCRs were 63.5% and 62.8%, respectively; and the 1-year survival rates were 38.6% and 30.4%, respectively, showing statistically obvious differences. The follow-up time for all patients was 6–24 months. Among them, the TTP of the pemetrexed group was 3.2 months and the MST was 8.7 months; the TTP of the docetaxel group was 3.6 months, and the MST was 9.2 months. There was no statistically significant difference in TTP and MST between the two groups of patients, as shown in Figure 4.

3.3. CT Imaging Changes of Lung Cancer before and after Chemotherapy. The imaging features of lung cancer showed an irregular flaky consolidation at the tip and posterior segment of the lung, and the lesion was shrunken; dilated bronchioles were seen inside, with clear edges and long burrs; bilateral thoracic cavity, horizontal fissure, and bilateral oblique fissure showed fluid density shadow; left lower lung tissue was compressed, and middle and lower lobe scattered in the parenchymal zone in the right lung. In addition, the left atrium and left ventricle were enlarged, and multiple lymph nodes in the mediastinum were enlarged, as shown in Figure 5(a). CT was rechecked after chemotherapy. The lung cancer patients in the remission group had shrunken masses, unclear borders, and open atelectasis, as shown in Figure 5(b).

3.4. Determination of Tumor Markers. CEA, CYFRA21-1, and SCC after chemotherapy in the pemetrexed group and docetaxel group were lower than before chemotherapy, and the differences were statistically significant ($P < 0.05$). In addition, there was no significant difference in CEA, CYFRA21-1, and SCC before and after chemotherapy in the pemetrexed group and docetaxel group ($P > 0.05$), as illustrated in Figure 6.

3.5. Nursing Satisfaction. The satisfaction degree of nursing care in the pemetrexed group (92.67%) was significantly higher than that in the docetaxel group (85.62%), and the difference was statistically significant ($P < 0.05$), as shown in Figure 7.

3.6. Adverse Reactions. The main adverse reactions of the two groups of patients were insomnia, skin rash, cardiotoxicity,

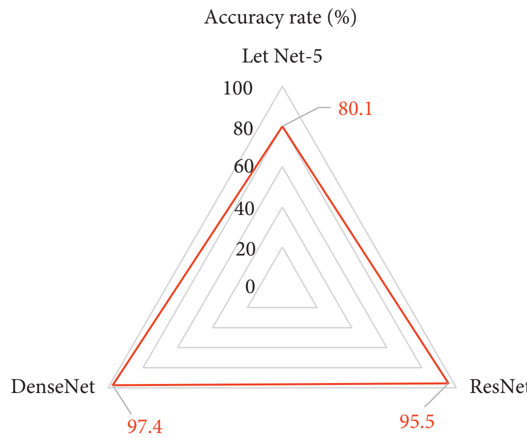

FIGURE 2: Comparison of the diagnostic test results of lung malignant nodules.

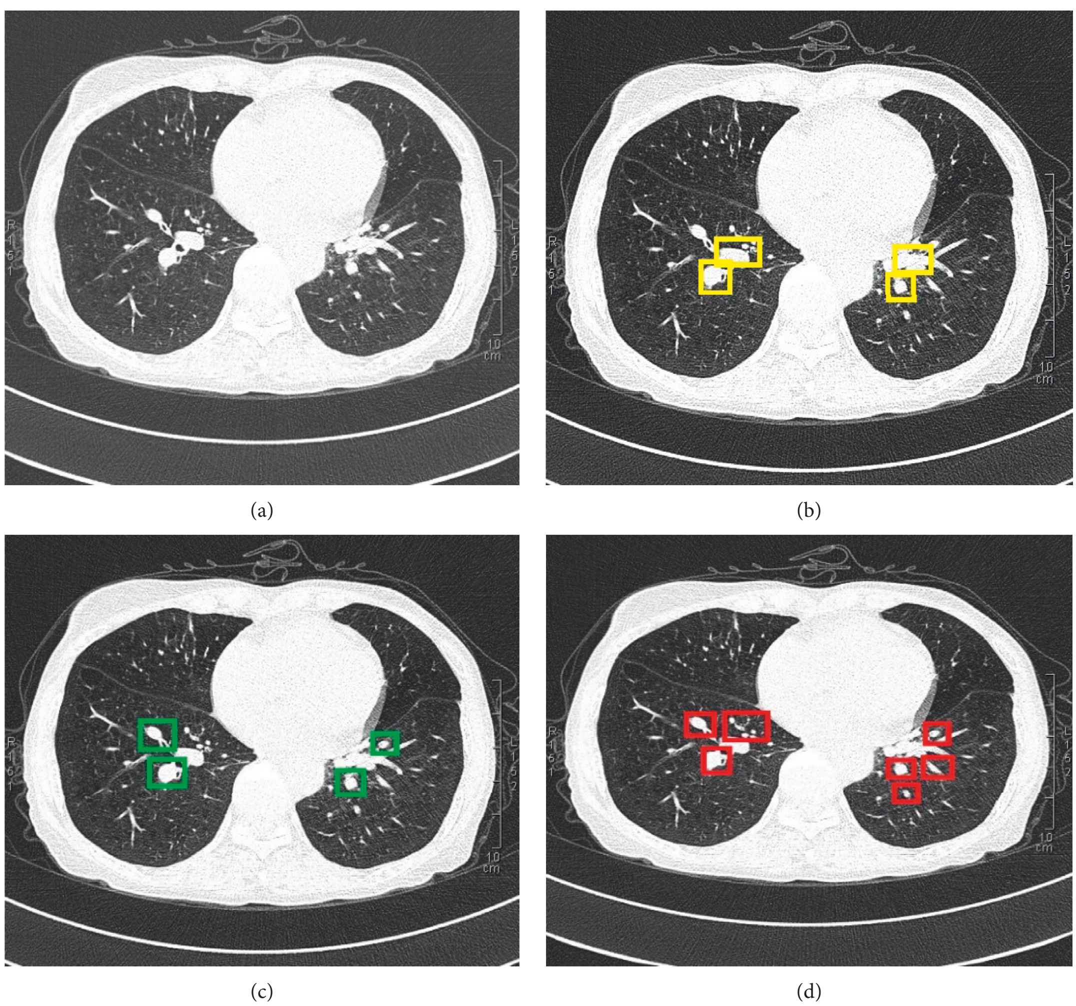

FIGURE 3: Comparison of CT image segmentation results. (a) Original CT image; (b) Image segmented by Let Net-5 network; (c) Image segmented by ResNet; (d) Image segmented by the DenseNet.

nephrotoxicity, liver toxicity, fatigue, hair loss, constipation, diarrhea, nausea and vomiting, thrombocytopenia, neutrophils, anemia, etc. Adverse reactions such as fatigue, diarrhea, and neutrophils in the pemetrexed group were lower than those in the docetaxel group, and the difference was statistically significant ($P < 0.05$), while the difference in other adverse reactions was not statistically obvious ($P > 0.05$). The adverse reactions were shown in Figure 8.

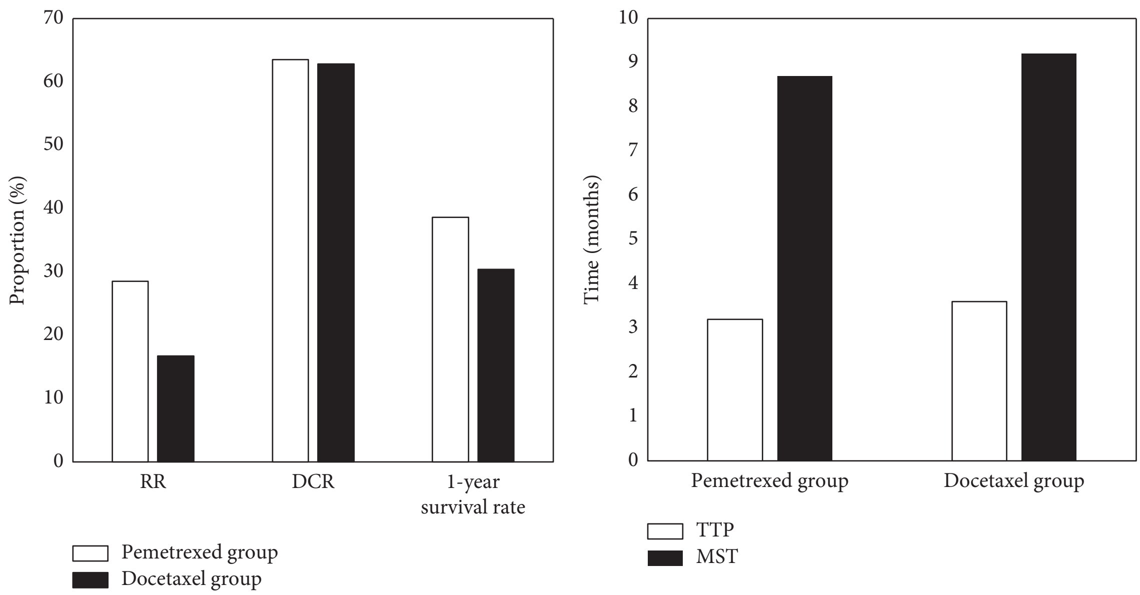

(a) (b)

Figure 4: Comparison of clinical efficacy between two groups. (a) Comparison of clinical efficacy; (b) Comparison of survival.

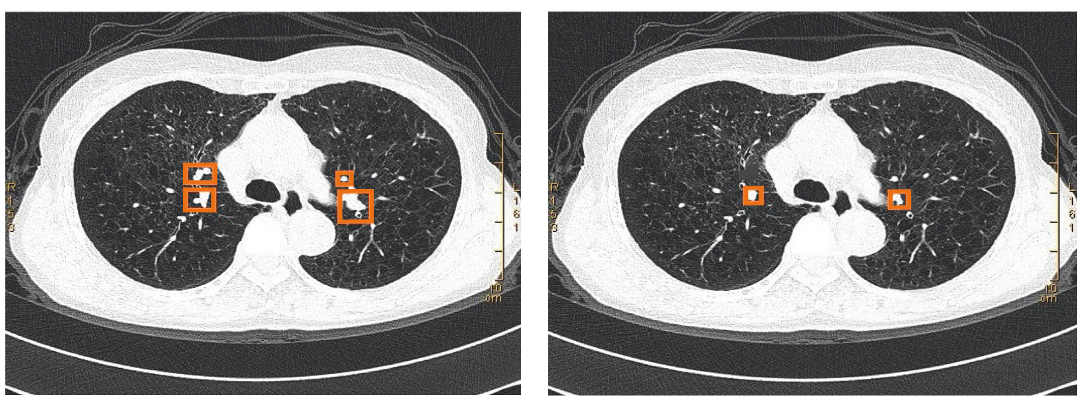

(a) (b)

Figure 5: Changes in lung cancer CT images before and after chemotherapy. Male, 79 years old, patient with lung cancer. (a) Before chemotherapy, the CT image showed the distribution of nodular soft tissue density masses at the posterior and lower right hilum (the size was about 0.8 cm in diameter, the edges were slightly under-rectified, and there was no obvious swollen lymphoma in the mediastinum). (b) After chemotherapy, CT images showed that the posterior and lower right hilum nodules were significantly smaller than before treatment, with a diameter of about 0.4 cm, blurred edges, reduced right lung volume, and no obvious lymphadenopathy in the mediastinum.

4. Discussion

Early diagnosis of lung cancer is very difficult. Most patients are already in the middle and late stages when they are diagnosed, especially elderly patients. They even have distant metastases and miss the chance of radical surgery. With the aging of the population intensifying, the incidence of lung cancer among the elderly is increasing [15]. Due to the weakening of the physiological functions of the elderly, liver reserves, renal clearance, and lung function are greatly reduced, and hematopoietic function is attenuated. If other organ diseases are combined at the same time, the chemotherapy tolerability of elderly lung cancer patients will decrease. The continuous updating of chemotherapy drugs in recent years has brought good clinical effects for the treatment of elderly lung cancer patients [16]. Therefore, this study used a comprehensive approach of chemotherapy combined with radiotherapy for patients with advanced NSCLC. The platinum-containing dual-drug combination chemotherapy regimen for the treatment of advanced NSCLC had been affirmed by a number of studies at home and abroad, and its clinical efficacy and survival rate had been greatly improved. This study retrospectively analyzed the changes of CEA, CYFRA 21–1, and SCC tumor markers, and explored the clinical efficacy of pemetrexed combined with platinum on NSCLC chemotherapy.

Pemetrexed shows the characteristics of low toxicity, high efficiency, and extensive antitumor properties. It was

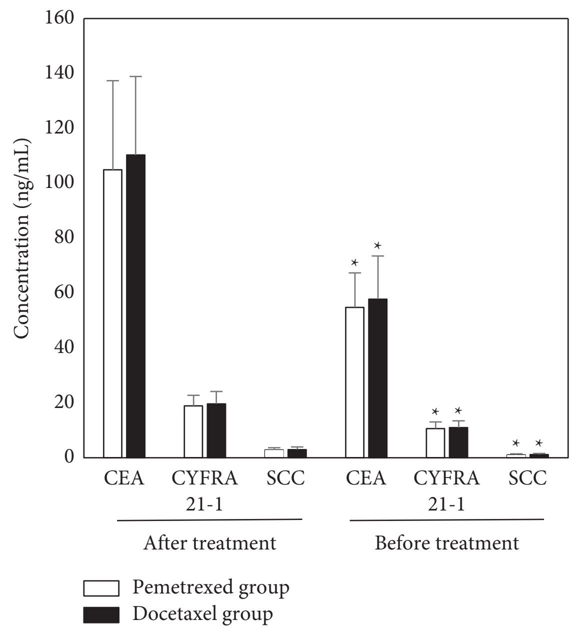

Figure 6: Tumor marker levels before and after treatment. *Compared with the levels before treatment, $P < 0.05$.

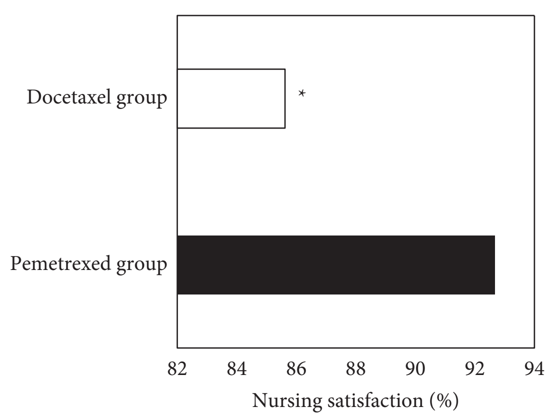

Figure 7: Comparison of nursing satisfaction. *Compared with the pemetrexed group, $P < 0.05$.

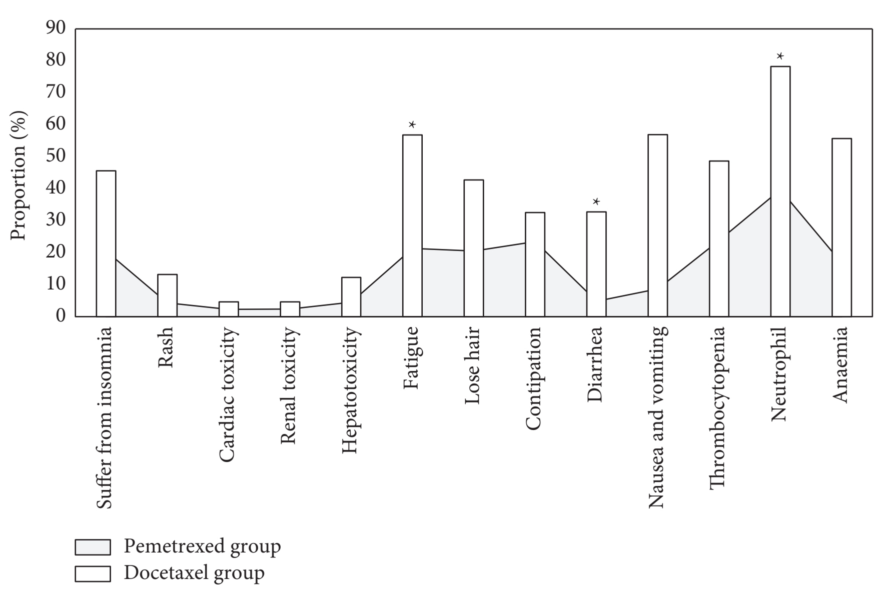

Figure 8: Comparison of adverse reactions between the two groups. *Compared with the pemetrexed group, $P < 0.05$.

approved by the Food and Drug Administration of the United States in 2004 for the second-line treatment of advanced NSCLC. Previous clinical studies have shown that pemetrexed used in the second-line treatment of lung cancer exhibits a good remission rate and overall survival advantage. Gadgeel [17] found that pemetrexed and docetaxel have different therapeutic effects for different histological types, while pemetrexed treats NSCLC patients with PFS longer. Cisplatin is a nonspecific antitumor drug targeting the cell cycle and is currently widely used in clinical practice. Cisplatin is still active on anaerobic cells and aerobic cells, so it has a radiosensitization effect [10, 18, 19].

CEA is the most commonly used tumor marker in clinical practice, and its level is related to tumor metastasis and recurrence. Studies have shown that about 20% of lung cancer patients have higher CEA levels, which means that dynamic monitoring of CEA levels can reflect the clinical efficacy of lung cancer [20]. CYFRA21-1 is a fragment of cytokeratin 19, which is very common in patients with NSCLC. The RR of advanced NSCLC imaging assessment of chemotherapy is positively correlated with the assessment of CEA and CYFRA21-1. SCC is not elevated in small cell lung cancer, but it is abnormally elevated in lung squamous cell carcinoma. The detection of SCC can help differentiate NSCLC [21]. CEA, CYFRA21-1, and SCC in the pemetrexed group and docetaxel group after chemotherapy were lower than those before chemotherapy ($P < 0.05$). It shows that pemetrexed combined with cisplatin has a good effect in the treatment of NSCLC, which is consistent with the research results of Chen et al. (2020) [22]. Pemetrexed inhibits the activities of the above three key enzymes through multiple targets, reduces the synthesis of purines and pyrimidines, and ultimately inhibits the production of tumor cell DNA. In particular, tumor cells stagnate during the DNA synthesis stage of mitosis, leading to tumor cell apoptosis and achieving the goal of antitumor.

The folic acid and vitamin B12 were given accurately before chemotherapy to reduce bone marrow suppression and accurately take dexamethasone to reduce the occurrence of skin toxicity. Medical staff should closely observe the toxic and side effects of drugs, deal with them promptly if they find undesirable conditions, strengthen patients' psychological care and health knowledge education, and obtain the support and cooperation of patients' families. Adverse reactions such as fatigue, diarrhea, and neutrophils in the pemetrexed group were lower than those in the docetaxel group, and the differences were statistically obvious ($P < 0.05$). The results showed that there were no serious adverse reactions in the two groups of patients after treatment, and the adverse reactions of pemetrexed combined with cisplatin were mild.

5. Conclusion

In this study, 80 patients with lung cancer were selected as the research objects, and the clinical efficacy of pemetrexed combined with platinum and docetaxel chemotherapy was compared under the guidance of CT images based on DenseNet. DenseNet convolutional neural network has high diagnostic accuracy; methotrexate combined with platinum chemotherapy can improve the chemotherapy effect in elderly patients with lung cancer, with a low degree of adverse reactions and good overall tolerance, which can be used as the first-line treatment for elderly patients with lung cancer. The shortcoming of this study was that the number of included cases was small and data bias could not be ruled out. In the later stage, further research was needed to explore the differences in the efficacy and adverse reactions of the two programs and to provide a basis for individualized treatment of patients. In conclusion, it was confirmed in this study that pemetrexed combined with cisplatin showed good clinical efficacy in the treatment of elderly lung cancer and was worthy of promotion.

Data Availability

The data used to support the findings of this study are available from the corresponding author upon request.

Conflicts of Interest

The authors declare no conflicts of interest.

References

[1] T. S. Mok, Y.-L. Wu, M.-J. Ahn et al., *New England Journal of Medicine*, vol. 376, no. 7, pp. 629–640, 2017 February 16.

[2] V. A. Papadimitrakopoulou, T. S. Mok, J. Y. Han et al., "Osimertinib versus platinum-pemetrexed for patients with EGFR T790M advanced NSCLC and progression on a prior EGFR-tyrosine kinase inhibitor: AURA3 overall survival analysis," *Annals of Oncology*, vol. 31, no. 11, pp. 1536–1544, 2020 November.

[3] M. C. Garassino, S. Gadgeel, E. Esteban et al., "Patient-reported outcomes following pembrolizumab or placebo plus pemetrexed and platinum in patients with previously untreated, metastatic, non-squamous non-small-cell lung cancer (KEYNOTE-189): a multicentre, double-blind, randomised, placebo-controlled, phase 3 trial," *The Lancet Oncology*, vol. 21, no. 3, pp. 387–397, 2020 March.

[4] M. Nishio, H. Saito, K. Goto et al., "IMpower132: atezolizumab plus platinum-based chemotherapy vs chemotherapy for advanced NSCLC in Japanese patients," *Cancer Science*, PMCID, vol. 112, no. 4, pp. 1534–1544, 2021.

[5] V. A. Papadimitrakopoulou, J. Y. Han, M. J. Ahn et al., "Epidermal growth factor receptor mutation analysis in tissue and plasma from the AURA3 trial: osimertinib versus platinum-pemetrexed for T790M mutation-positive advanced non-small cell lung cancer," *Cancer*, vol. 126, no. 2, pp. 373–380, 2020 January 15.

[6] J. C. Soria, D. S. W. Tan, R. Chiari et al., "First-line ceritinib versus platinum-based chemotherapy in advanced ALK -rearranged non-small-cell lung cancer (ASCEND-4): a randomised, open-label, phase 3 study," *The Lancet*, vol. 389, no. 10072, pp. 917–929, 2017.

[7] C. S. Lu, C. W. Lin, Y. H. Chang et al., "Antimetabolite pemetrexed primes a favorable tumor microenvironment for immune checkpoint blockade therapy," *J Immunother Cancer*, vol. 8, no. 2, Article ID e001392, 2020 November.

[8] H. Kenmotsu, N. Yamamoto, T. Yamanaka et al., "Randomized phase III study of pemetrexed plus cisplatin versus vinorelbine plus cisplatin for completely resected stage II to IIIA nonsquamous non-small-cell lung cancer," *Journal of Clinical Oncology*, vol. 38, no. 19, pp. 2187–2196, 2020 July 1.

[9] C. Zhou, G. Chen, Y. Huang et al., "Camrelizumab plus carboplatin and pemetrexed versus chemotherapy alone in chemotherapy-naive patients with advanced non-squamous non-small-cell lung cancer (CameL): a randomised, open-label, multicentre, phase 3 trial," *The Lancet Respiratory Medicine*, vol. 9, no. 3, pp. 305–314, 2021 March.

[10] N. Singh, M. Baldi, J. Kaur et al., "Timing of folic acid/vitamin B12 supplementation and hematologic toxicity during first-line treatment of patients with nonsquamous non-small cell lung cancer using pemetrexed-based chemotherapy: the PEMVITASTART randomized trial," *Cancer*, vol. 125, no. 13, pp. 2203–2212, 2019 July 1.

[11] Z. Lv, L. Qiao, Q. Wang, and F. Piccialli, "Advanced machine-learning methods for brain-computer interfacing," *IEEE/ACM Transactions on Computational Biology and Bioinformatics*, vol. 18, no. 5, pp. 1688–1698, 2021 September-October.

[12] Z. Wan, Y. Dong, Z. Yu, H. Lv, and Z. Lv, "Semi-supervised support vector machine for digital twins based brain image fusion," *Frontiers in Neuroscience*, vol. 15, Article ID 705323, 2021 July 9.

[13] H. Asahina, K. Tanaka, S. Morita et al., "A phase II study of osimertinib combined with platinum plus pemetrexed in patients with EGFR-mutated advanced non-small-cell lung cancer: the OPAL study (NEJ032C/LOGIK1801)," *Clinical Lung Cancer*, vol. 22, no. 2, pp. 147–151, 2021 March.

[14] M. Hu, Y. Zhong, S. Xie, H. Lv, and Z. Lv, "Fuzzy system based medical image processing for brain disease prediction," *Frontiers in Neuroscience*, PMCID, vol. 15, Article ID 714318, 2021 July 30.

[15] N. A. Rizvi, M. D. Hellmann, J. R. Brahmer et al., "Nivolumab in combination with platinum-based doublet chemotherapy for first-line treatment of advanced non-small-cell lung cancer," *Journal of Clinical Oncology*, vol. 34, no. 25, pp. 2969–2979, 2016 September 1.

[16] Z. S. Noor, J. W. Goldman, W. E. Lawler et al., "Luminespib plus pemetrexed in patients with non-squamous non-small cell lung cancer," *Lung Cancer*, vol. 135, pp. 104–109, 2019 September.

[17] S. M. Gadgeel, J. P. Stevenson, C. J. Langer et al., "Pembrolizumab and platinum-based chemotherapy as first-line therapy for advanced non-small-cell lung cancer: phase 1 cohorts from the KEYNOTE-021 study," *Lung Cancer*, vol. 125, pp. 273–281, 2018 November.

[18] G. Yang, H. Xu, L. Yang et al., "Apatinib in combination with pemetrexed-platinum chemotherapy for chemo-naive non-squamous non-small cell lung cancer: a phase II clinical study," *Lung Cancer*, vol. 147, pp. 229–236, 2020 September.

[19] S. S. Paik, I. K. Hwang, M. J. Park, and S. H. Lee, "Pemetrexed continuation maintenance versus conventional platinum-based doublet chemotherapy in EGFR-negative lung adenocarcinoma: retrospective analysis," *Tuberculosis and Respiratory Diseases*, vol. 81, no. 2, pp. 148–155, 2018 April.

[20] X. Zhang, J. Lu, J. Xu et al., "Pemetrexed plus platinum or gemcitabine plus platinum for advanced non-small cell lung cancer: final survival analysis from a multicentre randomized phase II trial in the East Asia region and a meta-analysis," *Respirology*, vol. 18, no. 1, pp. 131–139, 2013 January.

[21] T. Hang, L. Yang, X. Zhang et al., "Peroxisome proliferator-activated receptor γ improves pemetrexed therapeutic efficacy in non-squamous non-small cell lung cancer," *Am J Transl Res*, vol. 13, no. 4, pp. 2296–2307, 2021 April 15.

[22] C. Y. Chen, K. Y. Chen, J. Y. Shih, and C. J. Yu, "Clinical factors associated with treatment toxicity of pemetrexed plus platinum in elderly patients with non-small cell lung cancer," *Journal of the Formosan Medical Association*, vol. 119, no. 10, pp. 1506–1513, 2020 October.

Hindawi
Contrast Media & Molecular Imaging
Volume 2022, Article ID 8728468, 10 pages
https://doi.org/10.1155/2022/8728468

Research Article

Optimized Deconvolutional Algorithm-based CT Perfusion Imaging in Diagnosis of Acute Cerebral Infarction

Xiaoxia Chen[1] **Xiao Bai**[2] **Xin Shu**[3] **Xucheng He**[3] **Jinjing Zhao**[4] **Xiaodong Guo**[5] **and Guisheng Wang**[1]

[1]*Department of Radiology, the Third Medical Centre, Chinese PLA General Hospital, Beijing 100039, China*
[2]*Department of Geriatric, the Third Medical Centre, Chinese PLA General Hospital, Beijing 100039, China*
[3]*Department of Dermatology, the Third Medical Centre, Chinese PLA General Hospital, Beijing 100039, China*
[4]*Department of Neurology, PLA 305 Hospital, Beijing 100017, China*
[5]*Department of Radiology, the Fifth Medical Centre, Chinese PLA General Hospital, Beijing 100039, China*

Correspondence should be addressed to Guisheng Wang; wanggsh@alumni.itp.ac.cn

Received 4 February 2022; Revised 3 May 2022; Accepted 4 May 2022; Published 4 June 2022

Academic Editor: M Pallikonda Rajasekaran

To apply deconvolution algorithm in computer tomography (CT) perfusion imaging of acute cerebral infarction (ACI), a convolutional neural network (CNN) algorithm was optimized first. RIU-Net was applied to segment CT image, and then equipped with SE module to enhance the feature extraction ability. Next, the BM3D algorithm, Dn CNN, and Cascaded CNN were compared for denoising effects. 80 patients with ACI were recruited and grouped for a retrospective analysis. The control group utilized the ordinary method, and the observation group utilized the algorithm proposed. The optimized model was utilized to extract the feature information of the patient's CT images. The results showed that after the SE module pooling was added to the RIU-Net network, the utilization rate of the key features was raised. The specificity of patients in observation group was 98.7%, the accuracy was 93.7%, and the detected number was (1.6 ± 0.2). The specificity of patients in the control group was 93.2%, the accuracy was 87.6%, and the detected number was (1.3 ± 0.4). Obviously, the observation group was superior to the control group in all respects ($P < 0.05$). In conclusion, the optimized model demonstrates superb capabilities in image denoising and image segmentation. It can accurately extract the information to diagnose ACI, which is suggested clinically.

1. Introduction

Cerebral infarction is a cerebrovascular disease common in elderly people. It is always accompanied by chronic diseases, such as hypertension, hyperlipidemia, and diabetes. If not treated timely, it will seriously affect brain function. Epidemiological data show that acute cerebral infarction (ACI) accounts for about 50%–60% of all cerebrovascular diseases, whose mortality rate is 10%–15% [1]. Acute ischemic cerebral infarction is a common acute cerebrovascular disease, which mainly refers to the complete obstruction of the cerebral artery, the main trunk of the vertebrobasilar artery, and other branches, eventually resulting in the necrosis of the blood supply area of the brain tissue. Cerebral ischemia can cause irreversible damage to the function of brain tissue. The increase in infarct size will trigger a space-occupying effect. Acute cerebral infarction followed by hemorrhagic or hemorrhagic transformation is also one factor affecting its prognosis and treatment [2]. Related studies have found that the occurrence of ACI hemorrhage is associated with the integrity of the brain microvascular structure, that is, the blood-brain barrier. The increase of microvascular permeability in the ischemic area increases the amount of red blood cells leaking from the blood vessel [3]. Acute cerebral infarction has high fatality rate and disability rate [4]. Timely diagnosis is imperative for enhancing the prognosis [5].

CT examination can clearly show the size, location, and shape of ACI, and it is also economical, simple, and fast [6]. After CT examination, doctors can judge the treatment timing and treatment methods according to the size and

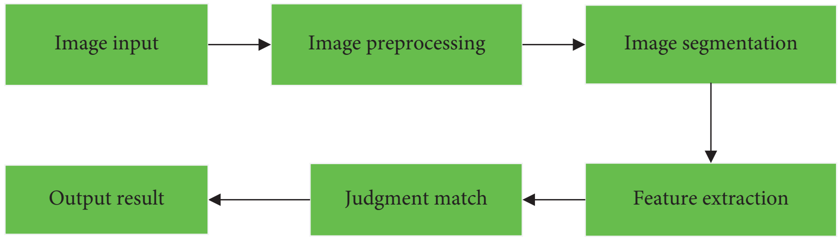

Figure 1: Traditional image recognition process.

number of the lesions [7]. Early CT detectors only performed perfusion scans at some slices, and failed to cover the whole brain, limiting their clinical applications and promotion. Dual-source computed tomography (DSCT) is a device under mature 64-slice CT, with a brilliant enhancement in time resolution, which is 83 ms, lower than 0.1s of cardiac imaging. CT scanning lifts the time resolution, and it has become a noninvasive diagnosis of cerebral infarction. Image feature extraction via different mathematical algorithms can position the lesion with a high running speed [8]. Dual-source CT is divided into plain scan, enhanced scan, and vascular examination. However, its definition was not high enough in traditional CT images. The inaccurate image segmentation also becomes a disadvantage in disease diagnosis. The application of intelligent algorithms in CT images could help display clear CT images and realize denoising. Many detection systems use deep networks to extract features for pixel classification. Convolutional neural networks (CNNs) are utilized in image segmentation, classification, and target positioning [9]. Reducing the size of the convolution kernel can faster the running speed of CNN [10]. The CNN was optimized in the study. RIU-Net was utilized to extract convolution features, equipped with the SE module to enhance feature extraction, and expected to provide novel approach for diagnosis of ACI.

2. Materials and Methods

2.1. Research Subjects. Eighty patients treated in the hospital from June 2018 to June 2020 were rolled into the control group (25 male + 20 female, (68.0 ± 3.2) years) and observation group (26 male + 14 female, (63.8 ± 3.4) years). This research had been approved of ethics committee of hospital, and the patients all signed the informed consent forms.

Inclusion criteria are as follows: (i) those diagnosed as ACI after examination; (ii) those having settled in the region for no less than 5 years; (iii) those admitted to the hospital within three days after the attack, and the examination interval between the two devices was within two hours; (iv) those having stroke for the first time; (v) those meeting the diagnostic criteria for ischemic stroke by the Fourth National Cerebrovascular Disease Academic Conference; and (vi) those having CT examinations during emergency visits.

Exclusion criteria are as follows: (i) those who cannot receive CT scan; (ii) mental illnesses such as vascular dementia and Lewy body dementia; (iii) incomplete clinical and imaging data; (iv) organ dysfunction; (v) patients with transient cerebral insufficiency and hypocalcemia convulsions; (vi) patients with severe organ complications; and (vii) patients with other types of cerebral ischemia.

2.2. Image Recognition. Image recognition is an important branch of computer vision in which the computer analyzes the image and makes corresponding judgments. Humans get 90% of the information from the vision. With the advent of the computer era, deep learning for image recognition and judgment process also develops constantly, along with the development of the Internet. Figure 1 shows the traditional image recognition process, mainly including the image input, preprocessing, feature extraction, and target recognition. Due to the complexity of image and the limitations of algorithms, the speed of image recognition is slow and the effect is not so satisfactory. The combination of artificial intelligence technology and image recognition has become a hot topic.

With the development of computer information technology, CNN arises. CNN demonstrates significant advantages in image and video identification using less pretreatment. It can learn and filter image features, and is widely utilized in natural language processing. In this study, the artificial neural network is incorporated in the existing image recognition process to optimize it. After image processing, feature extraction is performed. The artificial neural network model can reduce the complexity and redundancy, and SE module can enhance feature extraction. To include RIU network in SE can enhance the network accuracy. Figure 2 presents the image recognition flowchart.

2.3. CNN. CNN is formed by fully connected networks. Each neuron is connected to another through input and output assigned weights, which are proportional to the number of neurons in each layer. Image is generally a three-dimensional matrix, including length, width, and the channel number. With multiple layers, CNN requires a huge amount of calculation. With the improvement of image pixels, the required weight matrix is also increasing. As the pixel of the input image grows to 1000×1000 and the number of neurons in the middle layer reaches 1M, 10^{12} pieces of data are needed to represent a simple two-layer fully connected network. In Figure 3, each neuron is connected to all the pixels in the image, and the matrix transformation is completed first. The pixel feature of a point is largely related to that of its surrounding pixels and less related to that of the point far away. The image itself has space information. After optimization, the weight coefficient

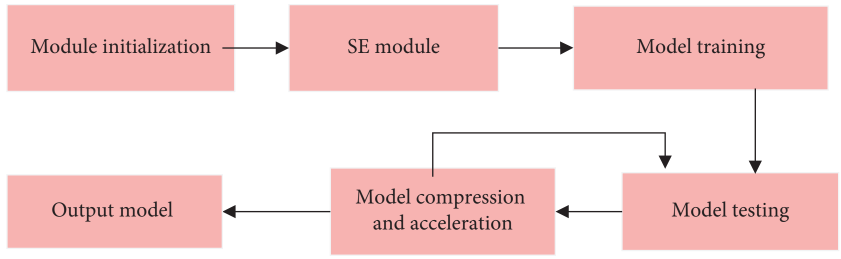

Figure 2: Schematic diagram of image recognition flowchart.

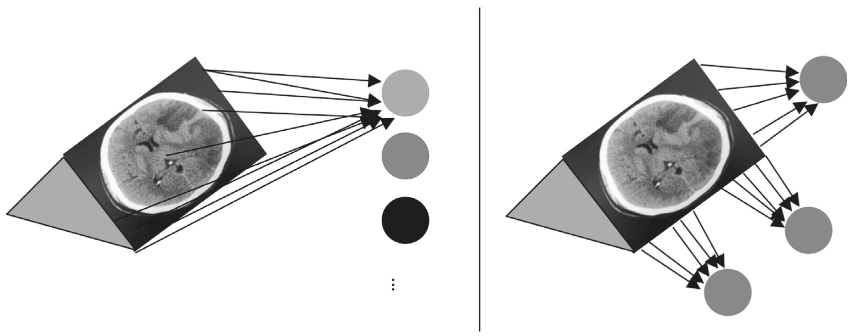

Figure 3: Schematic diagrams of full connection and convolutional form.

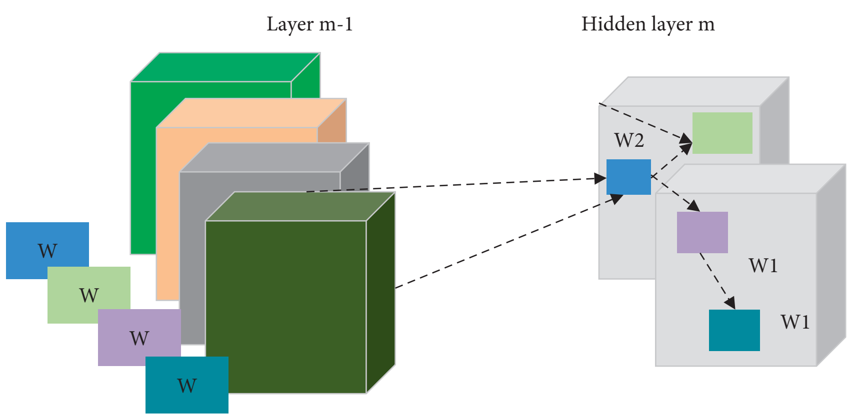

Figure 4: The calculation process of CNN.

of the CNN network is reduced, and the pixel is also increased.

After the convolutional layer and pooling layer of CNN are added to the network, the input layer is also different. Input layer input the three-dimensional image information as image input. If H is the height of an image, W is the width of it, and C is the number of input images, a color image with a size of 360×360 is represented as a column vector with a size of $360 \times 360 \times 3$. CNN network with the three-dimensional input of $360 \times 360 \times 3$ maintains the original spatial information of the image. The convolution layer obtains the eigenvalue matrix through the convolution operation. The input matrix is the current convolution layer's input. The convolution kernel refers to weight matrix of each layer in CNN, and the weight matrix is represented by the size of the weight from input matrix neuron to output matrix neuron.

The input matrix at layer m is the output matrix at layer m-1. The size of the image is $H_{in} \times W_{in} \times 4$. Figure 4 shows the weight matrix. It is a $2 \times 2 \times 4 \times 2$ matrix, where 2 suggest 2 output channels, 4 indicates 4 input channels, 2×2 is the size of adjacent region corresponding to the input image. At W1, it is obtained by multiplying the $2 \times 2 \times 4$ convolution kernel with the corresponding point of the matrix. The matrix features output by the CNN network are expressed as follows.

$$Ci,\, j,\, k = \sum_{m=(h/2)}^{m=(h/2)} \sum_{m=(h/2)}^{m=(h/2)} F\left(I_{i+m,j+n,k} w_{m,n,k}\right). \quad (1)$$

After the convolution calculation is completed, the neuron completes the nonlinear operation in a complex way. F represents the activation function, and Sigmoid is generally utilized as the activation function. Different movements cause different neural units to be activated.

After the pooling layer inputs the feature map, the complexity of the calculation is reduced. The pooling of a convolutional kernel of $h \times w$ is expressed by (2). The

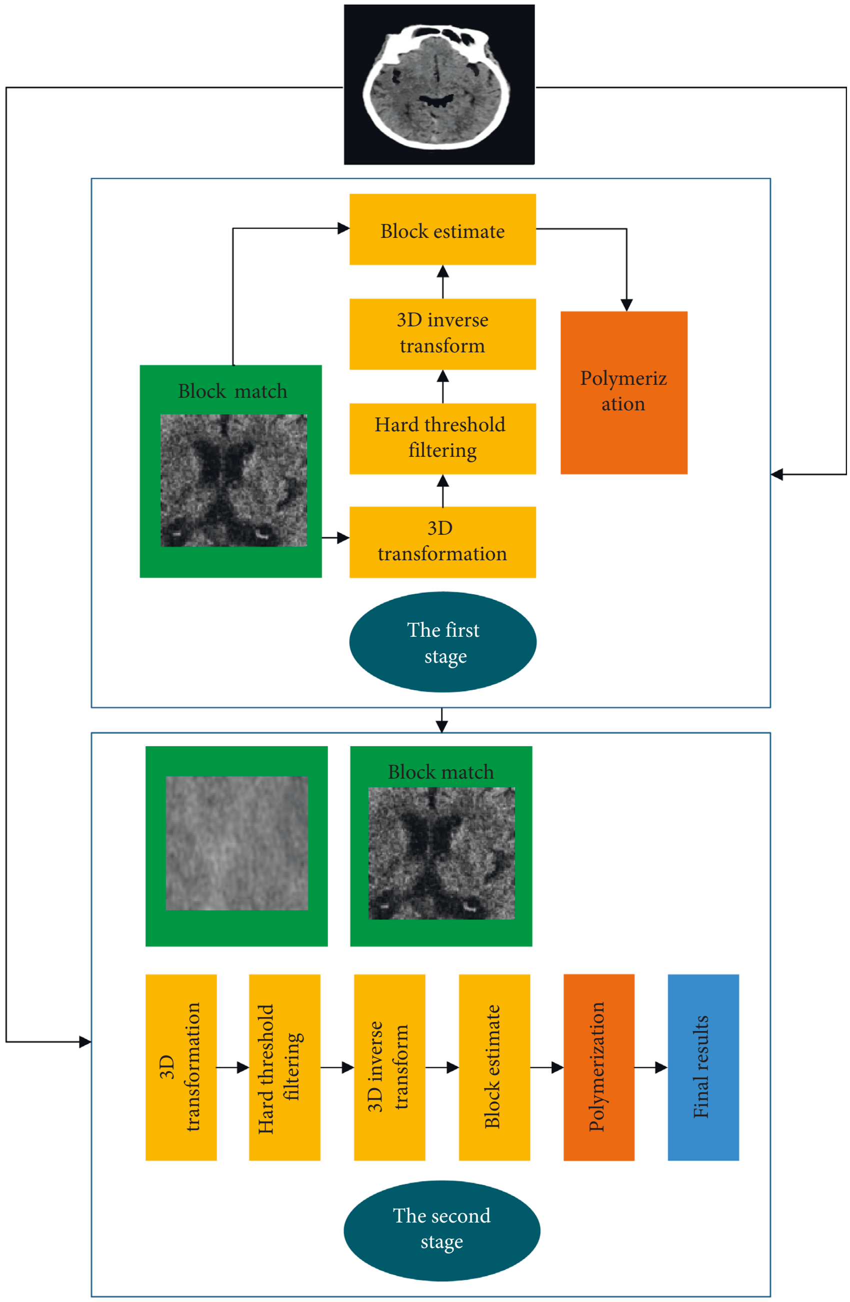

Figure 5: Schematic diagram of BM3D.

parameters in the network are decreased, which in turn reduces the computation amount. Thus, it can maintain the invariance of the feature map for small shifts in the input.

$$\left(\frac{H}{h}\right) \times \left(\frac{W}{w}\right). \tag{2}$$

Each output represents an expansion of the receptive field by a factor of $h \times w$. The receptive field is expanded and then it enables the use of more surrounding information. The full connection layer is in line with the full connection of the neural network to ensure the consistency of output.

For the optimization of CNN network, the problems of fitting and underfitting need to be solved first so that the network can obtain the optimal performance in training. To make a set of weight parameters Q to approach the ideal weight Q^*, the generalization equation is as follows:

$$MSE(Q) = E\left(\left(Q^* - Q\right)^2\right) = E\left(\left(Q^* - Q\right)^2\right) + \mathrm{VAR}\left(Q^*\right). \tag{3}$$

On the premise of ignoring noise, generalization error can be regarded as the combination of deviation and variance to measure the fitting ability of the network. A smaller deviation represents better fitting ability of the network to the data. The variance describes the overall disturbance of the network. A larger variance means that the network is more unstable and larger fluctuation in results (Figure 5).

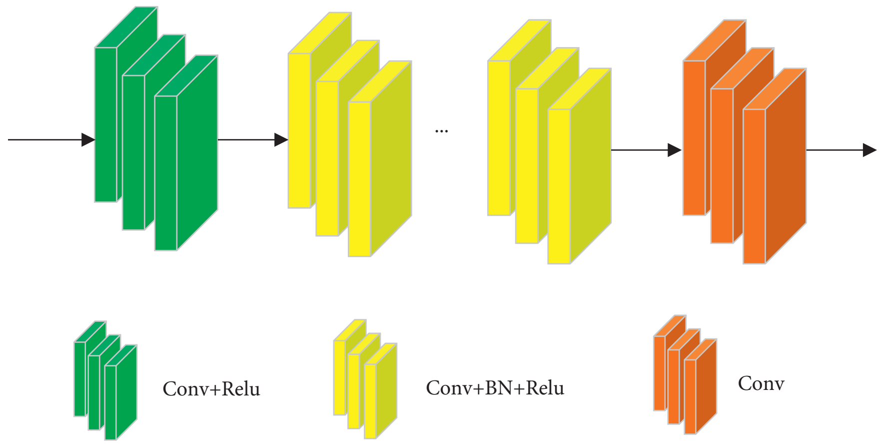

FIGURE 6: DnCNN structure.

2.4. Image denoising. There are many classic denoising methods, such as nonlocal denoising algorithms, full variational regularization, and block-matching and 3Dfitering (BM3D) algorithms. The overall operation of BM3D is relatively complicated. It mainly uses the similarity of image blocks to group them, and then carries out filtering operation on each image block to turn them to the two-dimensional form, and finally weighs and averages all similar images. The process is shown in Figure 6. It includes two stages. The first stage is to select reference blocks for the input image, and arrange all similar image blocks to form a three-dimensional matrix. Next, filtering is performed for two-dimensional transformation. Finally, the fused image blocks are put back in the original position. In the second stage, the original image and the result image are input. The three-dimensional matrix obtained is the same as that of the first stage.

2.5. Denoising Model. Denoising problems based on convolutional networks include IRCNN, FFDNet, RED-CNN, DnCNN, etc.

The denoising model expresses the low-dose CT image as follows:

$$\chi = \varphi(\mathrm{y}). \tag{4}$$

$\chi \in \mathrm{W}^{\mathrm{m}\times\mathrm{n}}$ represents a low-dose noise image, $\mathrm{y} \in \mathrm{W}^{\mathrm{m}\times\mathrm{n}}$ represents a normal image, and $\varphi \mathrm{W}^{\mathrm{m}\times\mathrm{n}}$ is a mapping from a normal image to a noise image.

CNN-based image denoising is to find a function f, expressed as follows:

$$F = \arg\min \|\mathrm{F}(x) - y\|_2^2. \tag{5}$$

F is the approximate value of φ^{-1}, and it represents the CNN. With more than two layers and sufficient parameters, the CNN can fit any functions. Theoretically, $F = \varphi^{-1}$ exists.

2.6. DnCNN and Cascaded Structure. The structure of DnCNN is shown in Figure 6. DnCNN was originally utilized to process Gaussian noise. The network does not include any sampling process, and performs denoising directly on the original image to ensure the denoising effects.

In Figure 7, the DnCNN structure is optimized to a multilevel structure, namely, the Cascaded CNN structure. The denoising result of the previous layer and the original image are utilized as the input of the next layer. The artifact can be further processed in the next layer, and the next layer uses the original input information, which can well avoid the loss of information. A deeper number of BLOCKs can produce better performance.

2.7. Residual Neural Network Structure. If X is input in CNN, the arbitrary mapping of the network is expressed as $M(X)$. The ordinary convolutional network uses stacking learning $M(X)$, while the residual neural network (RNN) no longer directly maps $M(X)$, and the ideal mapping equation is as follows:

$$F(X) = M(X) - X. \tag{6}$$

After the complex ideal mapping $M(x)$ is converted into residual $F(x)$ for learning, the learning objective between multiconvolutional layers is changed. When multilayer convolution operations are performed to approximate residuals, the network learns to output a residual function, $F(X) = M(X) - X$. If $F(x) = 0$, the optimization objective function approximates an identity mapping, rather than 0. To find the identity map is easier than to reproduce a mapping function. It suggests that compared to common network structure, RNN can learn information from more and deeper layers.

In feature extraction, the equations of information processing and image texture are shown as below.

Mean (i-mean) is defined as follows:

$$\overline{\mathrm{x}} = \frac{1}{n}\sum_{i=1}^{n} x_i. \tag{7}$$

Skewness (i-skewness) is calculated as follows:

$$D = \frac{(1/n)\sum_{i=1}^{n}(x_i - \overline{x})^2}{\left(\sqrt{(1/n)\sum_{i=1}^{n}(x_i - \overline{x})^2}\right)^3}. \tag{8}$$

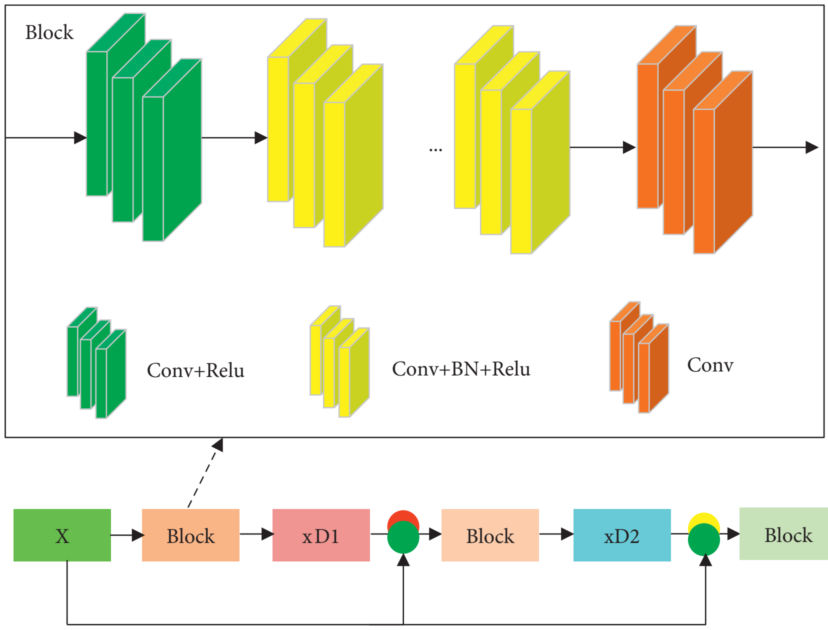

FIGURE 7: The Cascaded CNN structure.

I-kurtosis is calculated as follows:

$$K = \frac{(1/n)\sum_{i=1}^{n}(x_i - \overline{x})4}{\left((1/n)\sum_{i=1}^{n}(x_i - \overline{x})^2\right)^2} - 3. \tag{9}$$

The loss function is optimized as below, where F is the actual data, and E represents the output predicted by the model. |E∩F| is an intersection of two sets. |E|, |F|, |E ∩ F| refer to the number size. *D1* is then calculated, as shown in Figure 8. The equations are as follows:

$$\begin{aligned} \text{DIce} &= \frac{2|E \cap F|}{|E| + |F|}, \\ &= \frac{2\sum_i^N e_i f_i}{\sum_i^N e_i^2 + \sum_i^N f_i^2}, \\ \text{DIce}_{\text{distance}} &= 1 - \frac{2|E \cap F|}{|E| + |F|}, \\ &= \frac{2\sum_i^N e_i f_i}{\sum_i^N e_i^2 + \sum_i^N f_i^2}. \end{aligned} \tag{10}$$

The Dice model focuses on |E∩F|. The enhanced model avoids oversegmentation. Equation (11) shows the undersegmentation, and equation (12) is the oversegmented predicted outcome.

$$\text{New DIce} = \frac{2|E\cap F| - |E\cap F| - |E\cap F|}{|E| + |F|}, \tag{11}$$

$$= \frac{2\sum_i^N e_i f_i - \sum_i^N (1 - e_i) f_i - \sum_i^N e_i (1 - f_i)}{\sum_i^N e_i^2 + \sum_i^N f_i^2}. \tag{12}$$

The change of the convolution structure is expressed in

$$\frac{H \times W \times D_K \times D_K \times M + H \times W \times M \times N}{H \times W \times D_K \times D_K \times M \times N} = \frac{1}{N} + \frac{1}{D_K \times D_K}. \tag{13}$$

2.8. Scan Method and Scan Parameters. 256-slice spiral CT was used. Patient was informed of the examination procedure and precautions in detail before scanning. Treatment plans for allergic reactions should be formulated in advance. The height and weight of the patient were accurately recorded before the examination, and a trocar was inserted into the anterior elbow vein. During the examination, the patient was instructed not to tilt the head, and not to speak or swallow to keep the body still, which can ensure good imaging results.

The head scanning requires a layer thickness of 5 mm, a tube voltage of 120 KV, and a tube current of 100 mA. The CT whole brain perfusion scan was performed under the reciprocating dynamic scan mode. The contrast agent was injected into the anterior elbow vein using a high-pressure syringe (double-barreled) at a flow rate of 4-5 mL/s, and 20 mL of normal saline was injected at 4-5 mL/s. The perfusion scan program began as the contrast agent was injected, with the tube voltage set to 80kv, and the tube current set to 125 mA. The matrix is 512 × 512, the scanning thickness is 5 mm, and the scanning is from the top of the brain to the side of the foot. The time is 45s, with about 20 cycles. After the scan, allergic reactions were observed in time, and the patient was asked to drink water to promote the discharge of the contrast agent.

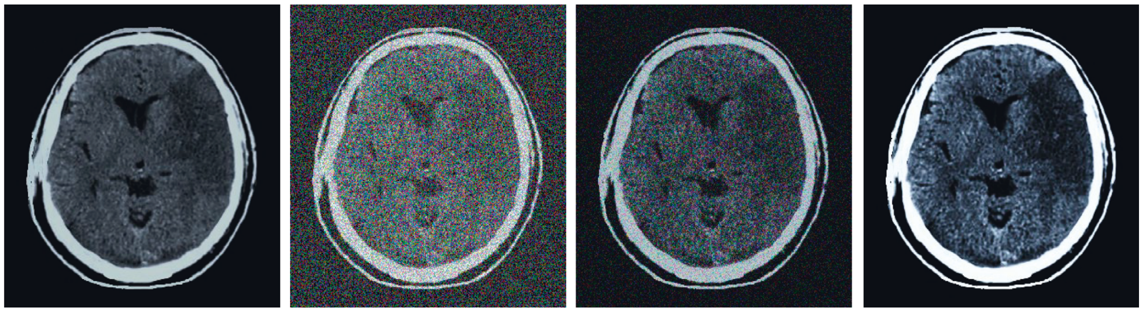

Figure 8: Comparison of CT images of the brain.

The perfusion scan images were transferred to workstation, and processed by the deconvolution algorithm. The software automatically output the image of cerebral perfusion parameters, and then the abnormal perfusion area was divided by 3 physicians with over 5 years of experience. Any inconsistencies were solved through negotiation with a senior physician.

2.9. Image Segmentation. Image segmentation can accurately diagnose diseases and locate lesions. Image segmentation and computer aided diagnosis can clearly identify the unclear area of the edge. A CT is a three-dimensional image of the human body. Region-based segmentation algorithm uses the gray uniformity of the same region to identify different regions of the image. Mapped to a standardized Montreal Neurological Society space, the image is divided into white matter, gray matter, and cerebrospinal fluid. Next, the target data is smoothed. Figure 9 shows the flowchart of CT image segmentation by convolutional network. First, the original image is processed to segment the crane-less head, and then the image is standardized. Noise reduction and anticounterfeiting follow to obtain a smooth image, and finally the segmented image is obtained.

2.10. Statistical Methods. The data were processed by SPSS21.0. The measurement data (normal distribution) were the form of mean ± SD ($\overline{x} \pm s$), and relative frequency and frequency (%) were how nonconforming count data was indicated. The T-test was performed, χ^2 test was performed for quality comparison, and $P < 0.05$ was the threshold for considerable difference.

3. Results

3.1. Image Comparison. Figure 8 showed the comparison of an original image and a low-dose image. It was found that the low-dose image had more particles than the original image, and the denoising effects were not good. BM3D and Cascaded CNN both exhibited obvious denoising effects, but BM3D was better. However, some areas were still not presented.

3.2. Performance Comparison on the Test Set. Table 1 listed the performance comparison between high-dose, low-dose, and BM3D denoising methods in a test set. BM3D parameter $\varphi = 4$. Other parameters are consistent with the simulation experiment.

In Figure 10, the 115 slices of the CT image were analyzed. It was noted that the BM3D method was too smooth. The low-dose and high-dose white dots in the orange box were very light, and the white plots disappeared when using the BM3D method.

3.3. The Segmentation of Brain CT Images. In Figure 11, the CT images of ACI, RISEU-Net network, RISEU-Net-N network, and RIU-Net network were used to segment the cerebral infarct area. The enhanced RISEU-Net network segmented CT image effectively.

3.4. Efficacy. The specificity, accuracy, and detected numbers were compared. In Table 2, the specificity, accuracy, and detected numbers in the observation group were superior to controls ($P < 0.05$).

4. Discussion

Both the incidence and mortality of cerebral infarction are on the rise [11]. The most common cerebral infarction is atherosclerosis, and the corresponding in situ thrombus leads to insufficient blood supply to brain tissue, resulting in neurological dysfunction. The brain is intolerant to ischemia and hypoxia. The blood supply interruption for 5 minutes will cause irreparable injury [12]. Imaging is an important part of the clinical diagnosis of ACI, and rapid and accurate diagnosis is a prerequisite for timely treatment [13]. It is reported that plain CT scan takes 22 hours to present the results of ACI [14, 15]. CT perfusion imaging is a functional imaging. Studies have found that abnormalities can be displayed after 30 minutes of cerebral ischemia. Some researchers use perfusion parameters to determine the severity of ACI, and use different algorithms to detect the efficacy. Different algorithms use different perfusion parameters, and there is a good correlation between the blood flow and blood volume of the diseased tissue measured by the deconvolution algorithm and the maximum slope method.

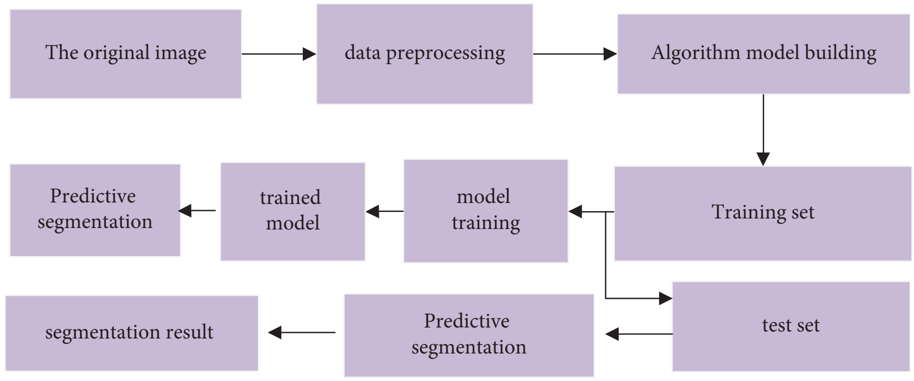

Figure 9: Flow chart of image segmentation.

Table 1: Comparison of denoising performance.

Method	PSNR	RMSE	SSLM
BM3D	32.46	9.786	32.68
Low dose	29.14	14.00	0.826
High dose	33.01	9.052	0.948

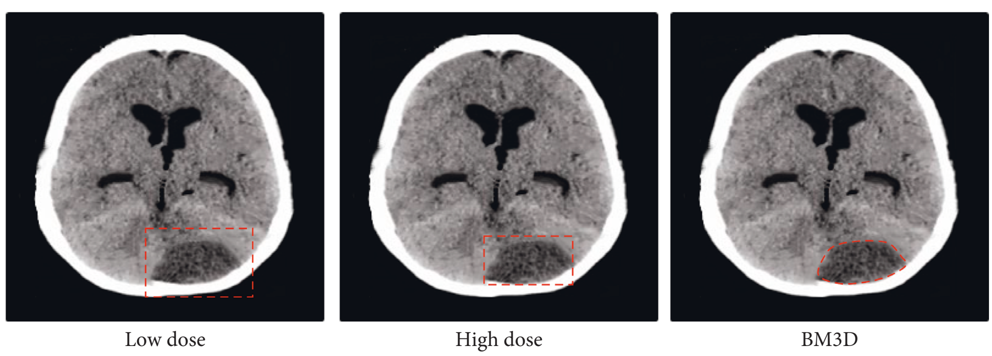

Figure 10: Slice effect diagram.

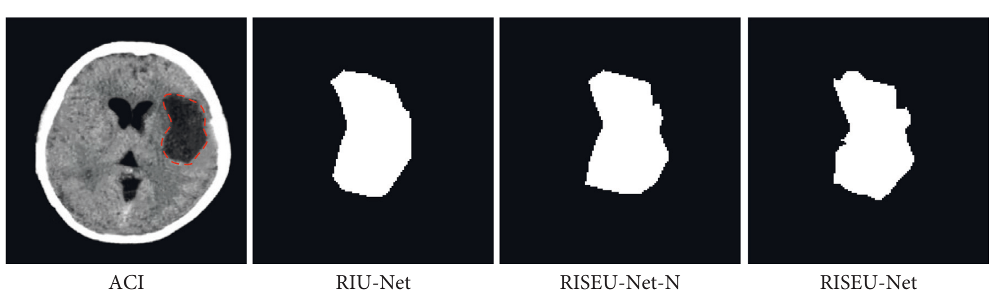

Figure 11: ACI CT images and segmentation results.

Deep learning is widely utilized. The evacuation design of buildings was simulated using a deep learning-based model, and the accuracy of the CNN model was verified by introducing auxiliary image prediction training and tracking sequence prediction training algorithm After image classification, the lesion's location is displayed clearly, and the features are extracted accurately [16, 17]. Shelhamer et al. (2017) utilized natural images to segment semantics [18]. Pereira et al. (2019) applied CNN in the segmentation of brain tumor images [19]. The specific locations in the convolutional layer were merged to create a new image [20, 21]. The optimized CNN algorithm was utilized, and RIU-Net was applied to segment CT image. The features of images could be clearly shown. CT images of the patients in observation group were clearer than those in the control group with less noise. Some scholars have applied the CNN in feature extraction. Coordinates are set in the lesion area to form a preselected detection frame, and then, the suspicious

Table 2: Efficacy of two groups.

	Sensitivity (%)	Number of lesions detected	Accuracy (%)
Control group	93.2	1.3 ± 0.4	87.6
Observation group	98.7*	$1.6 \pm 0.2^*$	93.7*

*The difference was statistically significant ($P < 0.05$).

part is classified, which makes up for the shortcomings of the traditional method, and can detect the location of the lesion accurately. The model was optimized by deep learning [22]. The optimized model was defined as the RIU-net network, and it was then equipped with SE module, to enhance the feature extraction image [20]. The BM3D algorithm was compared with DnCNN and Cascaded CNN, and it was concluded that the BM3D algorithm had better denoising effects. SE module pooling was added into the RIU-Net network. The utilization of CT image features was remarkably enhanced. The specificity of the observation group reached 93.7%, while that of the control group was 87.6%. The result indicated that the optimized network showed significant capacities in image denoising and segmentation and could offer accurate information for ACI patients. The optimized network used in the research showed excellent effects in image denoising.

5. Conclusion

A CNN algorithm was enhanced and adopted for CT image segmentation of patients with ACI. Next, the SE module was supplemented to RIU-Net to enhance the extraction ability. It was found that the model's accuracy was 96.7% for image segmentation. The BM3D algorithm had better denoising effects compared to DnCNN and optimized Cascaded CNN. The deep learning model demonstrated superb capabilities in CT image denoising and segmentation. However, some limitations should be noted. The sample size was insufficient, and the segmentation did not reach 100%. Later, abundant samples are necessary to verify the findings of the study. In conclusion, a theoretical basis is given for extraction of lesion features in CT images [23, 24].

Data Availability

The data used to support the findings of this study are available from the corresponding author upon request.

Conflicts of Interest

The authors declare no conflicts of interest.

Authors' Contributions

Xiaoxia Chen and Xiao Bai contributed equally to this work.

Acknowledgments

This work was supported by the National Key R&D Program of China (No. 2019YFC0118104), National Natural Science Foundation of China (No. 82001808), Capital's Clinical Applied Research Project (No. Z181100001718013), and Beijing Municipal Science and Technology Commission (No. Z211100002921047).

References

[1] Y. Guan, P. Wang, Q. Wang et al., "Separability of acute cerebral infarction lesions in CT based radiomics: toward artificial intelligence-assisted diagnosis," *BioMed Research International*, vol. 2020, Article ID 8864756, 2020.

[2] J. J. Heit, G. Zaharchuk, and M. Wintermark, "Advanced neuroimaging of acute ischemic stroke," *Neuroimaging Clinics of North America*, vol. 28, no. 4, pp. 585–597, 2018.

[3] Y. Zhao, Y. Zhang, and Y. Yang, "Acute cerebral infarction with adenomyosis in a patient with fever: a case report," *BMC Neurology*, vol. 20, no. 1, p. 210, 2020.

[4] Z. A. King, K. N. Sheth, W. T. Kimberly, and J. M. Simard, "Profile of intravenous glyburide for the prevention of cerebral edema following large hemispheric infarction: evidence to date," *Drug Design, Development and Therapy*, vol. 12, pp. 2539–2552, 2018.

[5] X. Wen, Y. Li, X. He et al., "Prediction of malignant acute middle cerebral artery infarction via computed tomography radiomics," *Frontiers in Neuroscience*, vol. 14, p. 708, 2020.

[6] J. S. Kim, V. Arvind, E. K. Oermann et al., "Predicting surgical complications in patients undergoing elective adult spinal deformity procedures using machine learning," *Spine Deformity*, vol. 6, no. 6, pp. 762–770, 2018.

[7] A. M. Dawud, K. Yurtkan, and H. Oztoprak, "Application of deep learning in neuroradiology: brain haemorrhage classification using transfer learning," *Computational Intelligence and Neuroscience*, vol. 2019, Article ID 4629859, 12 pages, 2019.

[8] A. T. Vanli, I. Ünal, and D. Özdemir, "Normal complex contact metric manifolds admitting a semi symmetric metric connection," *Applied Mathematics and Nonlinear Sciences*, vol. 5, no. 2, pp. 49–66, 2020.

[9] L. Zhou and D. Q. Kou, "Correlation between acute myocardial infarction complicated with cerebral infarction and expression levels of MMP-2 and MMP-9," *European Review for Medical and Pharmacological Sciences*, vol. 23, no. 1, pp. 297–302, 2019.

[10] P. Luo and J. Li, "Dual-source computed tomography image information under deep learning algorithm in evaluation of coronary artery lesion in children with Kawasaki disease," The Journal of Supercomputing, Dordrecht, Netherlands, 2021.

[11] T. Wang, Y. Gong, Y. Shi, R. Hua, and Q. Zhang, "Feasibility of dual-low scheme combined with iterative reconstruction technique in acute cerebral infarction volume CT whole brain perfusion imaging," *Experimental and Therapeutic Medicine*, vol. 14, no. 1, pp. 163–168, 2017.

[12] Y. Xin, S. Shi, G. Yuan, Z. Miao, Y. Liu, and Y. Gu, "Application of CT imaging in the diagnosis of cerebral hemorrhage and cerebral infarction nerve damage," *World Neurosurgery*, vol. 138, pp. 714–722, 2020.

[13] N. Hecht, M. Schrammel, K. Neumann et al., "Perfusion-dependent cerebral autoregulation impairment in hemispheric stroke," *Annals of Neurology*, vol. 89, no. 2, pp. 358–368, 2021.

[14] R. Liu, X. Yu, L. Zhang et al., "Computed tomography (CT) imaging evaluation of integrated traditional Chinese medicine cooperative therapy in treating acute cerebral infarction," *Medicine*, vol. 99, no. 18, Article ID e19998, 2020.

[15] Y. Chen, S. Hu, H. Mao, W. Deng, and X. Gao, "Application of the best evacuation model of deep learning in the design of public structures," *Image and Vision Computing*, vol. 102, Article ID 103975, 2020.

[16] B. Zang, L. Ding, Z. Feng et al., "CNN-LRP: understanding convolutional neural networks performance for target recognition in SAR images," *Sensors*, vol. 21, no. 13, p. 4536, 2021.

[17] C. ShanWei, S. LiWang, N. T. Foo, and A. R. Dzati, "A CNN based handwritten numeral recognition model for four arithmetic operations," *Procedia Computer Science*, vol. 192, pp. 4416–4424, 2021.

[18] E. Shelhamer, J. Long, and T. Darrell, "Fully convolutional networks for semantic segmentation," *IEEE Transactions on Pattern Analysis and Machine Intelligence*, vol. 39, no. 4, pp. 640–651, 2017.

[19] S. Pereira, A. Pinto, J. Amorim, A. Ribeiro, V. Alves, and C. A. Silva, "Adaptive feature recombination and recalibration for semantic segmentation with fully convolutional networks," *IEEE Transactions on Medical Imaging*, vol. 38, no. 12, pp. 2914–2925, 2019.

[20] N. Rashid, L. Chen, M. Dautta, A. Jimenez, P. Tseng, and M. A. Al Faruque, "Feature augmented hybrid CNN for stress recognition using wrist-based photoplethysmography sensor," in *Proceedings of the 2021 43rd Annual International Conference of the IEEE Engineering in Medicine & Biology Society (EMBC)*, vol. 2021, pp. 2374–2377, Mexico, November 2021.

[21] E. Essa, D. Aldesouky, S. E. Hussein, and M. Z. Rashad, "Neuro-fuzzy patch-wise R-CNN for multiple sclerosis segmentation," *Medical, & Biological Engineering & Computing*, vol. 58, no. 9, pp. 2161–2175, 2020.

[22] Z. Cai, N. Vasconcelos, and R.-C. N. N. Cascade, "High quality object detection and instance segmentation," *IEEE Transactions on Pattern Analysis and Machine Intelligence*, vol. 43, no. 5, pp. 1483–1498, 2021.

Hindawi
Contrast Media & Molecular Imaging
Volume 2022, Article ID 1703250, 9 pages
https://doi.org/10.1155/2022/1703250

Research Article

Spiral Computed Tomography Imaging Analysis of Positioning of Lumbar Spinal Nerve Anesthesia under the Concept of Enhanced Recovery after Surgery

Xue Feng[1], **Binbin Zhao**[1], **and Yongqiang Wang**[2]

[1]*Department of Anesthesia Surgery, First Affiliated Hospital,Heilongjiang University of Traditional Chinese Medicine, Harbin 150040, Heilongjiang, China*
[2]*Department of Outpatient, Harbin Red Cross Central Hospital, Harbin 150076, Heilongjiang, China*

Correspondence should be addressed to Yongqiang Wang; 2015042023@stu.gzucm.edu.cn

Received 22 March 2022; Revised 2 May 2022; Accepted 4 May 2022; Published 3 June 2022

Academic Editor: M Pallikonda Rajasekaran

The objective of this research was to explore the effect of perioperative anesthesia management for patients based on the concept of enhanced recovery after surgery (ERAS) and the application value of the computed tomography (CT) localization method in lumbar spinal nerve anesthesia, reducing the damage caused by anesthesia. One hundred and twenty patients who underwent the lumbar spinal anesthesia in lower limb surgery were selected as the research subjects. According to puncture positioning and nursing intention, the patients were classified into the control group with 30 patients (method of anatomical landmarks), CT group with 50 patients (the CT localization), and ERAS group with 40 patients (the CT localization and the ERAS management). The effects of the anesthesia positioning method and the ERAS management were compared and analyzed. The results showed that d (0.32) and r (0.27) of exponential filtering function were notably smaller than those of R-L filtering function ($d = 0.40$, $r = 0.39$) and of S-R filtering function ($d = 0.37$, $r = 0.36$) ($P < 0.05$). Puncture time ((9.23 ± 0.32) min vs. (13.11 ± 0.45) min), puncture direction change (20% vs. 33.33%), abnormal puncture sensation (22% vs. 40%), and nerve root touch (4% vs. 23.33%) in the CT group were all lower than those in the control group. The proportion of Degree I anesthesia effect (94%) of the CT group was greatly higher than that of the control group (76.67%) ($P < 0.05$). The VAS score, time of activity and gastrointestinal function recovery, and the incidence of adverse reactions (2.5% vs. 28%) in the ERAS group were lower than those in the CT group ($P < 0.05$). All in all, the CT localization method can improve the difficulty of anesthesia puncture and improve the anesthetic effect; the ERAS nursing concept can improve the postoperative pain of patients and contribute to the prognosis of patients and have a good clinical value.

1. Introduction

Intraspinal anesthesia (lumbar spinal nerve anesthesia) is a kind of local anesthesia, which is currently very common in clinic. According to the different injection positions, it can be divided into epidural anesthesia, combined spinal epidural anesthesia, and subarachnoid anesthesia (also known as spinal anesthesia/lumbar anesthesia) [1–3]. Lumbar spinal nerve anesthesia is widely used in cesarean section, lower limb surgery, hemorrhoidectomy, and the supplementary treatment of cardiovascular diseases [4, 5]. The positioning of lumbar spinal nerve anesthesia has always been the focus of clinical attention because the correct lumbar space positioning is crucial to ensure the effect of anesthesia and reduce nerve injury. Currently, the method of anatomical landmarks is often used clinically. However, this method is highly dependent on patients' bony landmarks on the body surface, so it is difficult to apply it to patients with obesity or spinal/spinous deformity [6]. Hence, the method of imaging localization becomes another common method of lumbar positioning [7]. In addition, surgery usually brings great trauma and perioperative risk to patients, so the enhanced recovery after surgery (ERAS) is designed to reduce the perioperative stress and trauma [8]. ERAS is an integration of multidisciplinary interventions based on the theories of anesthesiology, surgical methods, and pain control. The ERAS concept is proposed in the joint surgery department and is successfully implemented in some gastrointestinal procedures. At present, the ERAS concept is applied for perioperative anesthesia management, with some good adoption results [9, 10].

Computed tomography (CT) localization has a clear imaging, which can not only evaluate the puncture plane but also show the malformation of the spine, so it helps facilitate the customization of the puncture path and improve safety [11]. Nevertheless, due to the existence of ionizing radiation, the clinical adoption of CT localization is limited to a certain extent [12]. Clinically, the low-dose CT can reduce the radiation of the conventional CT scans to 1/6–1/4 of the original, but the image quality is affected. Presently, image reconstruction by algorithms is a common method to improve the low-dose CT images, and the typical algorithm is the filtered back projection (FBP) algorithm [13]. However, when the FBP algorithm is used to reconstruct CT images, it is relatively important to select the filtering function, because an appropriate function has a vital impact on the reconstruction results and speed. The exponential filtering function can retain the characteristics of the image well [14], and it has a good adoption effect.

In summary, patients who needed lumbar spinal nerve anesthesia were selected as research subjects. The accuracy of CT localization method was evaluated by using low-dose CT scanning for puncture positioning. Moreover, the ERAS concept was used for perioperative anesthesia management of patients, and its clinical application value was analyzed to provide better effect for patients, reduce the damage caused by anesthesia, and improve the quality of life of patients.

2. Methods

2.1. Research Subjects. One hundred and twenty patients who received lower limb surgery in the hospital from March 2019 to March 2021 with the need for lumbar spinal nerve anesthesia were selected as the research subjects. There were 78 male patients and 42 female patients, who ranged in age from 30 to 56 years old, with an average age of (46.23 ± 12.11) years old. Their weight ranged from 45 kg to 80 kg, with an average weight of (61.11 ± 26.85) kg. Patients were classified into the control group, CT group, and ERAS group by consulting their anesthesia puncture positioning and nursing intention. In the control group, 30 patients received anesthesia puncture positioning by the conventional method of anatomical landmarks. In the CT group, 50 patients received CT scanning for puncture positioning. Besides, 40 patients in the ERAS group underwent perioperative anesthesia management with the CT localization combined with the ERAS concept. The adoption effects of the two anesthesia positioning methods in the control group and the CT group were compared and analyzed. The effects of the ERAS concept on perioperative anesthesia management for patients' postoperative recovery in the CT group and the ERAS group were compared and analyzed. This study had been approved by ethics committee of the hospital, and the patients and their families understand the situation of the study and sign the informed consent forms.

The inclusion criteria were as follows. (i) Patients who could receive the surgery under lumbar spinal nerve anesthesia through the evaluation of examination. (ii) Patients without the contraindications to anesthesia. (iii) Patients with age over 25 years old. (iv) Patients who signed the informed consent.

The exclusion criteria were as follows. (i) Patients with the resistance to anesthesia. (ii) Patients with other serious diseases, such as dysfunction of heart, liver, and kidney, blood diseases, and tumor diseases. (iii) Patients who did not complete the full experiment. (iv) Patients in pregnancy.

2.2. Reconstruction Algorithm of Low Dose CT

2.2.1. FBP Algorithm. The "filtered" in the FBP algorithm refers to the data correction of CT image back-projection reconstruction. The simple back-projection reconstruction algorithm produces "star-like" artifacts, resulting in the decrease of CT image quality and the unclear display after reconstruction. The specific steps of the FBP algorithm are as follows.

First, the one-dimensional Fourier method is used to transform the projected data (at a certain angle) q. The transformed data are denoted as $Q(\omega)$.

$$Q(\omega) = q \cdot w^{-j2\omega} dt(\infty, -\infty). \tag{1}$$

In (1), w represents the projection angle and ω represents the Fourier coefficient.

Second, the one-dimensional weight factor β and $Q(\omega)$ are multiplied, and (2) is obtained.

$$Q(\omega) \bullet \beta = q \bullet w^{-j2\omega} \times \beta dt(\infty, -\infty). \tag{2}$$

Then, (3) shows that after the one-dimensional Fourier transform of $Q(\omega) \bullet \beta$, $R(\omega \bullet \beta)$ is obtained.

$$R(\omega \bullet \beta) = Q(\omega) \times E(\omega)\beta w^{-j2\omega}(\infty, -\infty). \tag{3}$$

Finally, in (4), all the modified functions $R(\omega \bullet \beta)$ of 0°–180° are back-projected, and the fault image $F(x, y)$ is obtained.

$$F(x, y) = \begin{cases} \int_0^{180} R(\omega \bullet \beta) dw, \\ \downarrow, \\ \int_0^{180} R(\omega \bullet \beta)(x \cos w + y \sin w) dw. \end{cases} \tag{4}$$

2.2.2. Filter. The effect of the filter has a direct influence on the image quality after the reconstruction. Accordingly, the quality of the filter is closely related to the choice of the filter function. The principle of the filtering function is selecting a window function $W(\beta)$. Currently, the R-L filter and S-L filter are pervasive.

(5) and (6) show the filtering function of the R-L filter.

$$F_{R-L}(\beta) = \begin{cases} |\beta| W(\beta), \\ \Downarrow, \\ |\beta| rect(\beta/2U), \end{cases} \quad (5)$$

$$\mathrm{rect}(\beta/2U) = \begin{cases} 1 \in |\beta| < U = 1/2d, \\ 0 \in \text{others}. \end{cases} \quad (6)$$

(7) shows the filtering function of the S-L filter.

$$F_{S-L}(\beta) = 1/2\left[(4U/180)^2 \left(\frac{1 - 4U\sin 360U}{1 - (4U)^2} \right) \right]. \quad (7)$$

In equations (5)–(7), U represents the projection angle. Both the R-l filter and S-L filter have certain defects. For instance, the former produces an obvious Gibbs phenomenon [15], and the latter has a poor quality of low-frequency image reconstruction. Hence, the exponential window function is proposed as a filtering function to study, and its expression is shown in (8) and (9).

$$W(\beta) = e^{-a|\beta/2U|}, |\beta| < U, \quad (8)$$

$$W(\beta) = 0, |\beta| \geq U. \quad (9)$$

In (8) and (9), e expresses the constant and a expresses the parameter. When the value of a is different, the obtained filtering function is different. When $a = 0$, $F_{R-L}(\beta)$ can be obtained. When $a = 0.64$, the results are close to $F_{S-L}(\beta)$. Consequently, the exponential window function has the characteristics of R-L, S-L, and other filtering functions.

2.2.3. Image Evaluation Index. Normalized mean square distance (d) and normalized mean absolute distance (r) were used to evaluate the effect of reconstructed images guided by the three filtering functions.

Equ. (10) shows the expression of the normalized mean square distance (d).

$$d = \left[\frac{\sum_{i=1}^{N} \sum_{j=1}^{M} \left(m_{ij} - r_{ij} \right)^2}{\sum_{i=1}^{N} \sum_{j=1}^{M} \left(m_{ij} - \overline{m} \right)^2} \right]^{1/2}. \quad (10)$$

Equ. (11) shows the expression of the normalized mean absolute distance (r).

$$r = \left[\frac{\sum_{i=1}^{N} \sum_{j=1}^{M} \left| m_{ij} - r_{ij} \right|}{\sum_{i=1}^{N} \sum_{j=1}^{M} \left| m_{ij} \right|} \right]. \quad (11)$$

In (10) and (11), i expresses the rows in the image, j expresses the columns in the image, m expresses the pixel density of the object model, r expresses the pixel density of the reconstructed image, $\overline{m}$ expresses the mean density of the object model, and $N * M$ expresses the image pixels. The larger the values of d and r were, the larger the error between the reconstructed image and the original object model image was.

2.3. Anesthesia Positioning and Puncture. The method of anatomical landmarks was selected according to the basic situation of patients. The soft tissue depression positioning method was suitable for obese people. The C_7 positioning method was suitable for patients without spinal deformity, and the compound anatomic marker positioning method was suitable for patients with spinal abnormalities.

For the CT localization, the 64-slice spiral CT scanner was employed for examination. The patient was placed in the conventional supine position with both knees flexed in the right position. The scanning parameters included tube voltage 120 kV, tube current 200 mA, layer thickness 3–5 mm, and screw pitch 1 : 1. The scanning sites were from the third lumbar vertebra (L3) to the first sacral vertebra (S1). The puncture position and the angle and route of the needle insertion were determined by the CT images.

For the puncture, the anesthesia puncture kit combined lumbar and epidural puncture kit (disposable, model) was used, whose specifications were AS-E/SII, and the registered standard of the medical device of the People's Republic of China was 20153660652. Besides, the epidural puncture needle (1.6 mm × 80 mm) was used as well as the lumbar anesthesia puncture needle (0.5 mm × 113 mm).

2.4. Anesthesia Management under the ERAS Concept. The patients' psychophysiological status was concerned before the surgery. Psychological counseling was performed on the patients with psychological conditions to prevent the occurrence of psychological stress. Patients were constantly reminded to abstain from drinking and fasting. If the patient had constipation, the defecation was induced within 1-2 hours before surgery. An empty stomach was maintained from 8 hours before anesthesia, and water was forbidden from 6 hours before anesthesia. If there were patients with poor gastrointestinal function, the bladder was guided to be empty to prevent postoperative hypoglycemia or vomiting.

After the surgery, the patient's position was noticed. The patient needed to keep the supine position for 6–8 hours to reduce the pressure of the spinal cord cavity, reduce cerebrospinal fluid leakage, and avoid the occurrence of headache after lumbar anesthesia. For the diet notice, cotton swabs were used to moisten the patient's lips to relieve thirst. After 6 hours, liquid food in small amounts was allowed, and it was gradually increased to the normal. The recovery conditions of consciousness, complexion, respiration, and lower limbs' muscle strength were observed. The pain degree of patients was assessed, according to which the different methods of analgesia were given. If the degree of pain was mild, the method of distracting attention was implemented. If it was severe, painkillers were taken under the doctor's advice or a pain relief pump could be used.

2.5. Observation Indexes. The time required for anesthesia puncture, the number of cases of puncture direction change, puncture sensation, nerve root contact, and the anesthesia effect were all observed in the control group and the CT group. The anesthetic effect was evaluated by the rating standard of clinical effect of intraspinal anesthesia (Table 1).

Table 1: Rating standard of clinical effect of intraspinal anesthesia.

Degree	Anesthesia	Pain	Muscle	Hemodynamics	Adjuvant drugs	Surgery
I	Perfect	Painless	Relaxed	Stable	Not required	Easy
II	Nearly perfect	Mild	Not good enough	Fluctuant	Required	Nearly easy
III	Imperfect	Obvious	Poor	Obvious fluctuation	Required	Fair

The recovery indexes such as the condition of out-of-bed activity and the recovery time of gastrointestinal function were recorded. The visual analog scale (VAS) scores of 2 h, 6 h, 12 h, 24 h, and 48 h after surgery were evaluated and recorded. Figure 1 shows the scoring method. The incidence of adverse reactions, such as gastrointestinal reaction, hypoglycemia, restlessness, infection, and abnormal cardiac function in the two groups was observed.

2.6. Statistical Method. SPSS 22.0 was employed for data processing. The quantity statistics were expressed by $x \pm s$. The t-test and the χ^2 test were used. The percentage (%) was how the statistics of numbers were expressed. The difference was statistically significant with $P < 0.05$.

3. Results

3.1. Reconstruction Effects of Different Filtering Functions. Figure 2 shows the comparison between normalized mean square distance (d) and normalized mean absolute distance (r) of reconstructed images by the exponential filtering function, the R-L filtering function, and the S-R filtering function. Both d (0.32) and r (0.27) of the exponential filtering function were lower than those of the R-L filtering function ($d = 0.40$, $r = 0.39$) and the S-R filtering function ($d = 0.37$, $r = 0.36$) ($P < 0.05$). Figure 3 shows the comparison of the effect images after CT image reconstruction. The reconstructed image quality guided by the exponential filtering function was remarkably better than that guided by the other two filtering functions.

3.2. Comparison of the General Data. Figure 4 shows the comparison of gender, age, and weight distribution of general data of patients in the three groups. There were insignificant differences in gender distribution, average age, and average weight among the three groups ($P > 0.05$), which reflected that the experiment had certain feasibility.

3.3. Puncture. The time required for puncture, the number of patients with puncture direction change, the abnormal puncture sensation, and the occurrence of nerve root contact in the control group and the CT group were analyzed (Figure 5). In the control group, the puncture time was (13.11 ± 0.45) min, the number of patients with puncture direction change was 10 (33.33%), 12 patients (40%) had abnormal puncture sensation, and 7 patients (23.33%) had nerve root contact. In the CT group, the puncture time was (9.23 ± 0.32) min, the number of patients with puncture direction change was 10 (20%), 11 patients (22%) had abnormal puncture sensation, and 2 patients (4%) had nerve root contact. The results showed that the puncture time, the number of patients with puncture direction change, the abnormal puncture sensation, and the occurrence of nerve root contact in the CT group were all lower than those in the control group ($P < 0.05$).

3.4. Anesthesia Effect. Among the 30 patients in the control group, there were 23 (76.67%) patients with the anesthesia effect of Degree I, 3 (10%) patients with that of Degree II, 3 (10%) patients with that of Degree III, and only 1 patient with that of Degree IV. Among the 50 patients in the CT group, there were 47 (94%) patients with anesthesia effect of Degree I, 3 (6%) patients with that of Degree II, 0 (0%) patient with that of Degree III, and 0 (0%) patient with that of Degree IV. According to comparison and analysis, the proportion of Degree I in the CT group was significantly higher than that in the control group ($P < 0.05$) (Figure 6).

3.5. VSA Score. In Figure 7, the VAS scores of 2 h, 6 h, 12 h, 24 h, and 48 h after surgery were compared between the CT group and the ERAS group. The VAS scores of 2 h, 6 h, 12 h, 24 h, and 48 h after surgery in the CT group were (3.01 ± 0.89), (2.77 ± 0.59), (2.65 ± 0.78), (2.21 ± 0.74), and (1.61 ± 0.72), respectively. The VAS scores of 2 h, 6 h, 12 h, 24 h, and 48 h after surgery in the ERAS group were (1.57 ± 0.66), (1.29 ± 0.45), (1.35 ± 0.28), (0.89 ± 0.64), and (0.61 ± 0.60), respectively. The VAS scores in the ERAS group were lower than those in the CT group during the whole postoperative period ($P < 0.05$).

3.6. Rehabilitation Index and Adverse Reactions. Among the 50 patients in the CT group, the mean activity time and the recovery time of gastrointestinal function were (39.88 ± 6.04) hours and (11.98 ± 0.44) hours, respectively. Among the 40 patients in the ERAS group, the mean activity time and gastrointestinal function recovery time were (25.14 ± 4.74) hours and (5.69 ± 0.49) hours, respectively. The required time in the ERAS group was markedly shorter than that in the CT group ($P < 0.05$). As for the adverse reactions, in the CT group, 5 (10%) patients had gastrointestinal reactions, 2 (4%) had hypoglycemia, 3 (6%) had restlessness, 2 (4%) had the infection, and 2 (4%) had an abnormal cardiac function, and the total incidence of adverse reactions was 28%. In the ERAS group, only one (2.5%) patient had gastrointestinal reactions, and nobody had hypoglycemia, restlessness, the infection, and an abnormal cardiac function, with a total incidence of 2.5%. The total incidence of the ERAS group was observably lower than that of the CT group ($P < 0.05$) (Figure 8).

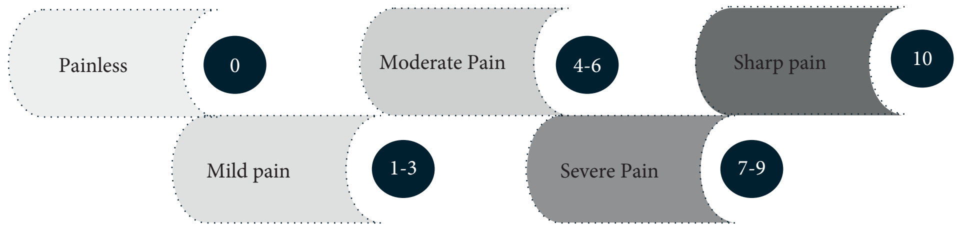

Figure 1: Scoring method of VAS.

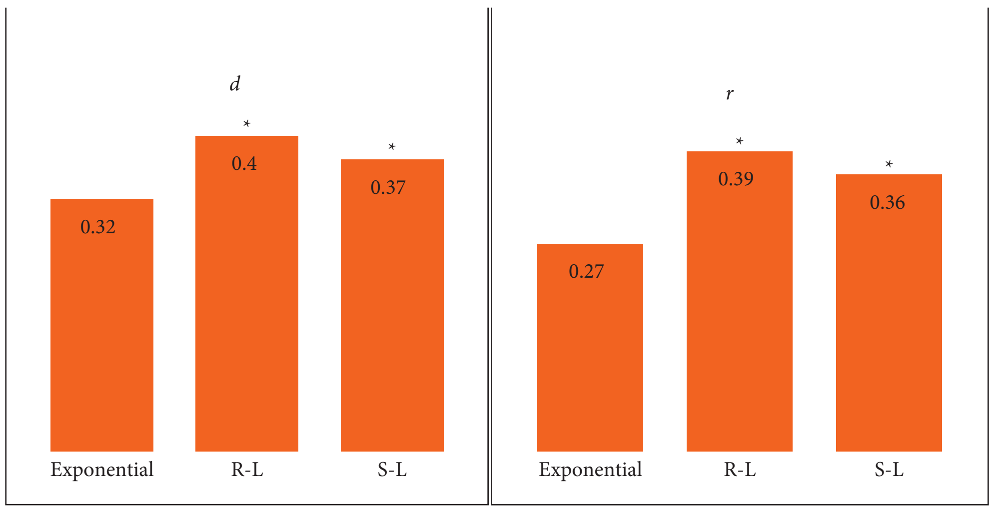

Figure 2: Values of (d) and (r) of different filtering functions. * Compared with the exponential filtering function, $P < 0.05$.

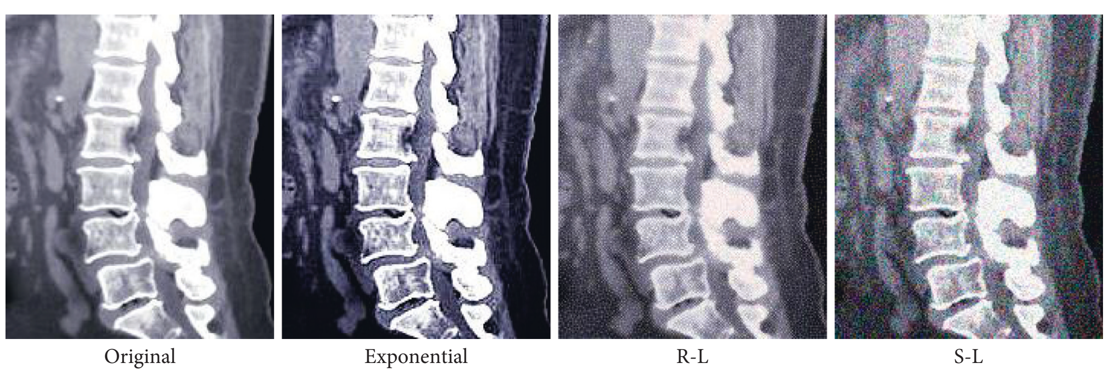

Figure 3: Effect images after reconstruction.

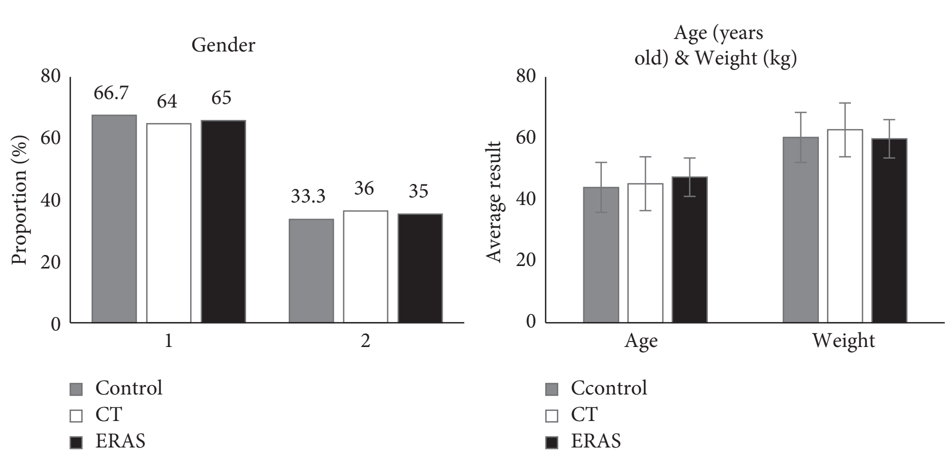

Figure 4: Comparison of general data. 1: male; 2: female.

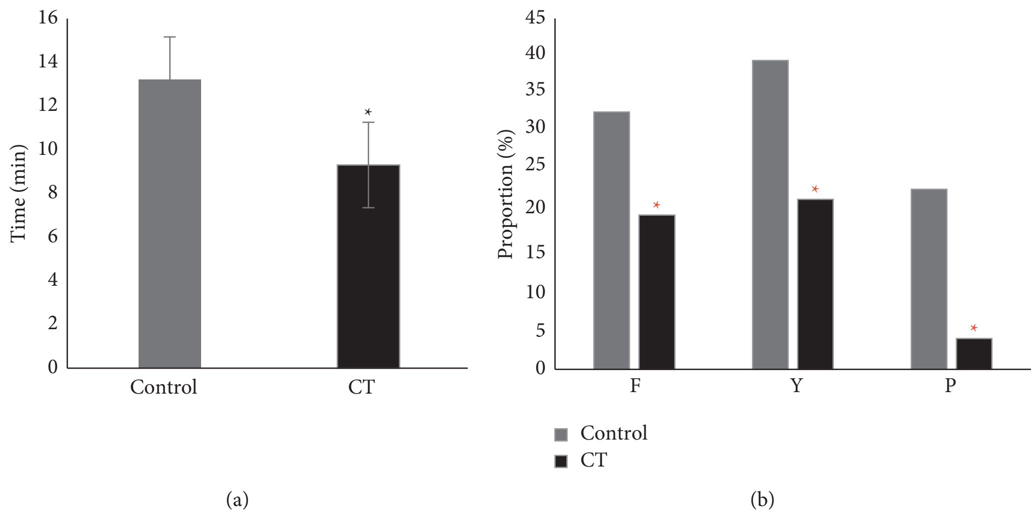

Figure 5: Comparison of puncture conditions. (a) Time required for puncture; (b) puncture condition (number of cases with changed direction (F), abnormal sensation of puncture (Y), and nerve root touch (P)). * indicates that there is a statistically significant difference in the time required for puncture and the number of cases with changed direction compared with the control group ($P < 0.05$).

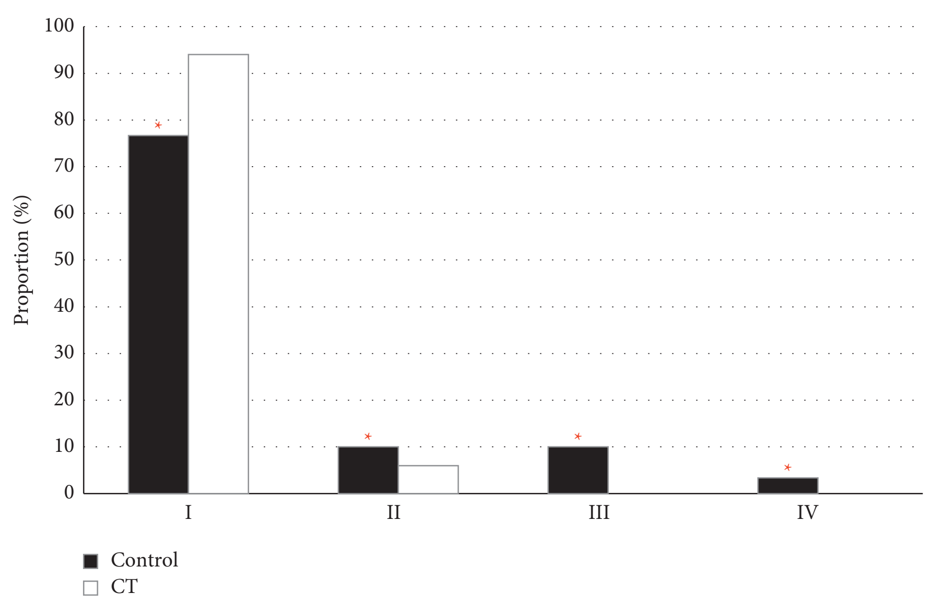

Figure 6: Comparison of anesthesia effect. * Compared with CT group, $P < 0.05$.

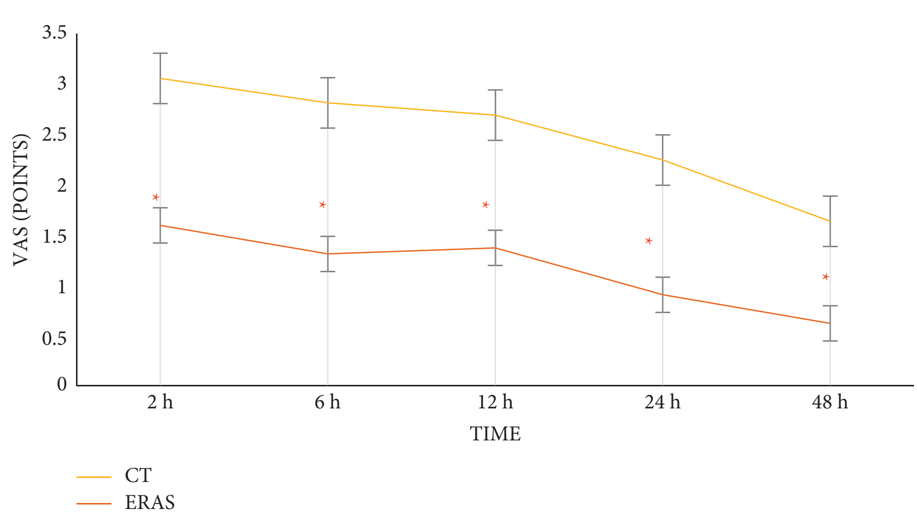

Figure 7: VAS score. * Compared with CT group, $P < 0.05$.

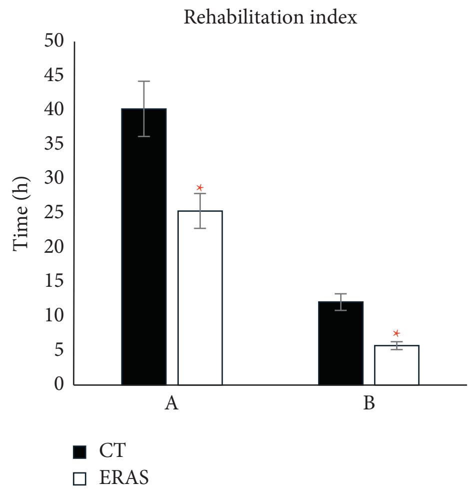

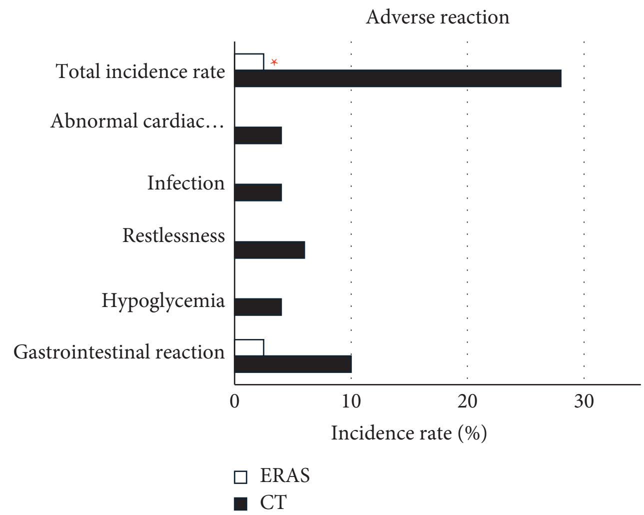

Figure 8: Comparisons of the rehabilitation index and the incidence of adverse reactions. (a) Activity time and (b) recovery time of gastrointestinal function. * Compared with CT group in ambulation time, intestinal function recovery time, and incidence of adverse reactions, $P < 0.05$.

4. Discussion

Lumbar spinal nerve anesthesia has been widely used as a common method of local anesthesia. Accurate puncture positioning and puncture path are of great significance for the reduction of anesthetic effects and adverse reactions. With the development of imaging technology, CT scanning localization has become one of the key technologies, and it is also one of the themes of the experiment.

In the experiment, there was ionizing radiation in the conventional CT examination. Consequently, the low dose CT scanning technology and the FBP algorithm were used to reconstruct CT images to prevent the degradation of the image display effect. The performance of the FBP algorithm was related to the filtering function. Furthermore, the exponential filtering function could keep the good reconstruction characteristic of the FBP algorithm [16]. The values of d (0.32) and r (0.27) of exponential filtering function were manifestly smaller than those of the R-L filtering function ($d = 0.40$, $r = 0.39$) and the S-R filtering function ($d = 0.37$, $r = 0.36$) ($P < 0.05$). The results reflected that the error between the reconstructed image and the original image of the exponential filtering function was smaller than that of both the R-L filtering function and the S-R filtering function, with the ideal reconstructed image quality, which was consistent with the above research results.

Based on the above results, the anesthesia puncture process and the anesthesia effect were compared between the method of anatomical landmarks and the CT localization. The incidence of puncture time (9.23 ± 0.32) min vs. (13.11 ± 0.45) min), puncture direction change (20% vs. 33.33%), abnormal puncture sensation (22% vs. 40%), and nerve root contact (4% vs. 23.33%) in the CT group were lower than those in the control group. The proportion of Degree I anesthesia effect (94%) of the CT group was signally higher than that of the control group (76.67%) ($P < 0.05$). The CT localization had a good adoption value in lumbar spinal nerve anesthesia positioning. According to many clinical investigations, the improper intraspinal anesthesia puncture brings adverse consequences to patients, while the imaging puncture positioning brings benefits to patients to a certain extent [17, 18]. The value of CT examination in lumbar spinal anesthesia is investigated. The results show that the success rate of surgery is higher in patients with the CT examination than in those without [19]. Sun et al. [20] found that imaging technology was an effective and tolerable method for the guidance of local anesthesia.

In recent years, it has been proposed that if there is no nursing intervention during the perioperative period of anesthesia, patients will often have serious physiological and psychological reactions after surgery, which are not conducive to their prognosis [21]. The ERAS concept is thus mentioned and applied to ensure the quality of nursing during the recovery of anesthesia [22]. Perioperative nursing with the ERAS concept can effectively improve patients' pain and facilitate postoperative recovery [23, 24]. Moreover, in this work, the VAS scores in the ERAS group were lower than those in the CT group at all the postoperative periods, and the time required for activity and gastrointestinal function recovery in the ERAS group was greatly shorter than that in the CT group ($P < 0.05$). Anesthesia nursing under the ERAS concept had the effect of improving patients' pain and promoting patients' postoperative recovery, which was consistent with the above research results. Besides, the total incidence of adverse reactions in the ERAS group (2.5%) was significantly lower than that in the CT group (28%) ($P < 0.05$). Mancel et al. [25] proposed that the implementation of ERAS nursing in different surgical procedures helped reduce the overall complications and the recovery time. Chiu et al. [26] proposed that ERAS nursing could improve the analgesic effect and reduce the occurrence of some adverse reactions like nausea and vomiting. Hence, the good adoption prospect of the ERAS concept in the perioperative period was reflected.

5. Conclusion

The adoption value of the CT localization in lumbar spinal nerve anesthesia positioning was analyzed under the ERAS concept, and the effect of perioperative anesthesia management under the ERAS concept was evaluated. The results proved that the CT localization was helpful to improve the difficulty of anesthesia puncture as well as the anesthesia effect. The ERAS nursing could improve postoperative pain and contribute to patients' prognosis, both of which had a favorable clinical adoption value. However, the radiation in the CT scanning used in this work cannot be eliminated at present, so the selection of research subjects is limited, resulting in an incomplete study population. This deficiency needs to be improved and broken through in subsequent explorations. The ERAS concept has good development prospects in clinical disease care, and it is worthy of further clinical exploration.

Data Availability

The data used to support the findings of this study are available from the corresponding author upon request.

Conflicts of Interest

The authors declare that they have no conflicts of interest.

References

[1] T. Zhang, Y. Ma, L. Liu et al., "Comparison of clinical effects of general anesthesia and intraspinal anesthesia on total hip arthroplasty," *American Journal of Tourism Research*, vol. 13, no. 7, pp. 8241–8246, 2021 Jul 15.

[2] J Serino, A. R. Galivanche, J. N. Grauer, M. Haynes, V. Karas, and C. J. Della Valle, "General versus neuraxial anesthesia in revision surgery for periprosthetic joint infection," *The Journal of Arthroplasty*, vol. 21, 2022.

[3] T. Zheng, P. Ye, W. Wu et al., "Minimum local anesthetic dose of ropivacaine in real-time ultrasound-guided intraspinal anesthesia for lower extremity surgery: a randomized controlled trial," *Annals of Translational Medicine*, vol. 8, no. 14, 2020 Jul.

[4] P. Wang, X. Chen, J. Zhang, and Y. Ma, "Continuous epidural anesthesia with double catheters for cesarean section in a patient with severe pulmonary hypertension," *Medicine*, vol. 100, no. 47, Article ID e27979, 2021 Nov 24.

[5] C.-n. Wei, X.-y. Chang, J.-h. Dong, and Q.-h. Zhou, "Remifentanil for carboprost-induced adverse reactions during cesarean delivery under combined spinal-epidural anesthesia," *Frontiers in Pharmacology*, vol. 11, p. 980, 2020 Jun 30.

[6] J. M. McGaugh, J. M. Brismée, G. S. Dedrick, E. A. Jones, and P. S. Sizer, "Comparing the anatomical consistency of the posterior superior iliac spine to the iliac crest as reference landmarks for the lumbopelvic spine: a retrospective radiological study," *Clinical Anatomy*, vol. 20, no. 7, pp. 819–825, 2007 Oct.

[7] G. C. Feigl, C. Mattersberger, W. Rosmarin, R. Likar, and C. Avila González, "Lumbale CT-gezielte Radiofrequenzablationen des Ramus medialis rami dorsalis nervi spinalis," *Schmerz, Der*, vol. 32, no. 2, pp. 99–104, 2018 Apr.

[8] G. Nelson, J. Bakkum-Gamez, E. Kalogera et al., "Guidelines for perioperative care in gynecologic/oncology: enhanced Recovery after Surgery (ERAS) Society recommendations-2019 update," *International Journal of Gynecological Cancer*, vol. 29, no. 4, pp. 651–668, 2019 May.

[9] E. Melloul, K. Lassen, D. Roulin et al., "Guidelines for perioperative care for pancreatoduodenectomy: enhanced recovery after surgery (ERAS) recommendations 2019," *World Journal of Surgery*, vol. 44, no. 7, pp. 2056–2084, 2020 Jul.

[10] D. T. Engelman, W. Ben Ali, J. B. Williams et al., "Guidelines for perioperative care in cardiac surgery," *JAMA Surgery*, vol. 154, no. 8, pp. 755–766, 2019 Aug 1.

[11] W. Zhang, P. Xia, S. Liu et al., "A coordinate positioning puncture method under robot-assisted CT-guidance: phantom and animal experiments," *Minimally Invasive Therapy & Allied Technologies*, vol. 31, no. 2, pp. 206–215, 2020.

[12] G. Noid, D. Schott, E. Paulson, J. Zhu, J. Shah, and X. A. Li, "Technical Note: using virtual noncontrast images from dual-energy CT to eliminate the need of precontrast CT for x-ray radiation treatment planning of abdominal tumors †," *Medical Physics*, vol. 48, no. 3, pp. 1365–1371, 2021 Mar.

[13] M. J. Willemink and P. B. Noël, "The evolution of image reconstruction for CT-from filtered back projection to artificial intelligence," *European Radiology*, vol. 29, no. 5, pp. 2185–2195, 2019 May.

[14] V. Patel, S. Subhra Bhattacharjee, and N. V. George, "Convergence analysis of adaptive exponential functional link network," *IEEE Transactions on Neural Networks and Learning Systems*, vol. 32, no. 2, pp. 882–891, 2021 Feb.

[15] A. Glos, A. Krawiec, and Ł. Pawela, "Asymptotic entropy of the Gibbs state of complex networks," *Scientific Reports*, vol. 11, no. 1, p. 311, 2021 Jan 11.

[16] M. Hu, Y. Zhong, S. Xie, H. Lv, and Z. Lv, "Fuzzy system based medical image processing for brain disease prediction," *Frontiers in Neuroscience*, vol. 15, p. 714318, 2021 Jul 30.

[17] B. C. Demilew, A. Tesfaw, A. Tefera, B. Getnet, K. Essa, and A. Aemero, "Incidence and associated factors of postdural puncture headache for parturients who underwent cesarean section with spinal anesthesia at Debre Tabor General Hospital, Ethiopia; 2019," *SAGE Open Med*, vol. 9, Article ID 20503121211051926, 2021.

[18] R. Yin, Y. Zhu, Z. Su et al., "Catastrophic thoracolumbar spinal massive hematoma triggered by intraspinal anesthesia puncture," *Medicine*, vol. 98, no. 41, Article ID e17553, 2019 Oct.

[19] H. Liu, M. Brown, L. Sun et al., "Complications and liability related to regional and neuraxial anesthesia," *Best Practice & Research Clinical Anaesthesiology*, vol. 33, no. 4, pp. 487–497, 2019 Dec.

[20] Y. Sun, W. Wang, Q. Zhang et al., "Local anesthesia for percutaneous US/CT-guided bipolar radiofrequency ablation of small renal masses: a safe and feasible alternative," *Urologic Oncology: Seminars and Original Investigations*, vol. 39, no. 10, 2021 Oct.

[21] American College of Obstetricians and Gynecologists' Committee on Practice Bulletins—Obstetrics, "ACOG practice bulletin No. 209: obstetric analgesia and anesthesia," *Obstetrics & Gynecology*, vol. 133, no. 3, pp. e208–e225, 2019 Mar.

[22] T. W. Wainwright, M. Gill, D. A. McDonald et al., "Consensus statement for perioperative care in total hip replacement and total knee replacement surgery: enhanced Recovery after

Surgery (ERAS) Society recommendations," *Acta Orthopaedica*, vol. 91, no. 1, pp. 3–19, 2020 Feb.

[23] U. O. Gustafsson, M. J. Scott, M. Hubner et al., "Guidelines for perioperative care in elective colorectal surgery: enhanced recovery after surgery (ERAS) society recommendations: 2018," *World Journal of Surgery*, vol. 43, no. 3, pp. 659–695, 2019 Mar.

[24] J. Simpson, X. Bao, and A. Agarwala, "Pain management in enhanced recovery after surgery (ERAS) protocols," *Clinics in Colon and Rectal Surgery*, vol. 32, no. 02, pp. 121–128, 2019 Mar.

[25] L. Mancel, K. Van Loon, and A. M. Lopez, "Role of regional anesthesia in enhanced recovery after surgery (ERAS) protocols," *Current Opinion in Anaesthesiology*, vol. 34, no. 5, pp. 616–625, 2021 Oct 1.

[26] C. Chiu, P. Aleshi, L. J. Esserman et al., "Improved analgesia and reduced post-operative nausea and vomiting after implementation of an enhanced recovery after surgery (ERAS) pathway for total mastectomy," *BMC Anesthesiology*, vol. 18, no. 1, p. 41, 2018 Apr 16.

Hindawi
Contrast Media & Molecular Imaging
Volume 2022, Article ID 1711456, 9 pages
https://doi.org/10.1155/2022/1711456

Research Article

K-Space Data Reconstruction Algorithm-Based MRI Diagnosis and Influencing Factors of Knee Anterior Cruciate Ligament Injury

Rui Chang [1], Angang Chen [1], Xiang Li [1], Xiaoqiang Song [1], Benqiang Zeng [1], Liping Zhang [1], and Wanying Deng [2]

[1]*Department of Orthopaedics, The People's Hospital of Wenjiang, Chengdu 611130, Sichuan, China*
[2]*Department of Neurorehabilitation, Affiliated Sichuan Provincial Rehabilitation Hospital of Chengdu University of TCM, Chengdu 611130, Sichuan, China*

Correspondence should be addressed to Wanying Deng; 1927101205@siit.edu.cn

Received 21 March 2022; Revised 9 May 2022; Accepted 11 May 2022; Published 1 June 2022

Academic Editor: M Pallikonda Rajasekaran

This study was aimed at investigating the diagnostic value of MRI based on K-space data reconstruction algorithm for anterior cruciate ligament (ACL) injury of knee joint and the influencing factors of ligament injury. 96 patients with ACL injury of knee joint were selected, and they were randomly divided into two groups: group A (arthroscopy) and group B (MRI examination), and another 96 healthy volunteers in the same period were selected as the control group. The test results of each indicator were compared. The results showed that the signal-to-noise ratio (SNR) of SMASH algorithm was higher than that of sum of squares (SOS) algorithm. In group A, there were 66 positive and 30 negative tests, and in group B, there were 56 positive and 40 negative tests ($P < 0.05$). The intercondylar fossa width, the intercondylar fossa width index, and the ratio of tibial intercondylar eminence width to intercondylar fossa width in group B were lower than those in the control group ($P < 0.05$). Compared with the traditional SOS algorithm, SMASH algorithm can improve the image quality, reduce the impact of damage data on the final synthesis image, and improve the image SNR. In clinical work, the ratio of the width of tibial intercondylar eminence to the width of femoral intercondylar fossa can be measured by imaging data to evaluate the matching between tibial intercondylar eminence and femoral intercondylar fossa, so as to evaluate the risk of ACL rupture.

1. Introduction

Anterior cruciate ligament (ACL) is the main component of the knee joint, one of the largest and most complex joints in the human body. It can effectively prevent excessive tibial forward movement and maintain the normal function of the knee joint under the combined action of other tissues of the knee joint [1]. Therefore, ACL injury of knee joint and meniscus injury of knee joint are the most common [2]. If the function and characteristics of ACL are examined from the perspectives of biomechanics, human anatomy, and human kinematics, it will be found that ACL injury presents considerable complexity and variability from the aspects of combined injury, injury mechanism, and sick population [3]. Without timely diagnosis and treatment after ACL injury, complications such as knee joint rotation instability, knee meniscus injury, and traumatic arthritis may occur, which may affect the normal function of the knee joint of patients and cause serious problems in daily life. In addition, the swelling and pain of the knee joint at the early stage of injury may interfere with the clinical examination and diagnosis [4]. It is difficult to accurately determine the severity or type of ACL injury, especially on the premise of rapid diagnosis and timely treatment.

The clinical diagnosis of ACL injury is mostly based on three progressive levels [5]. First, the clinical attending physician relies on face-to-face understanding of the patient's injury history and on-site physical examination to make a preliminary diagnosis. There are many inspection methods in physical examination. Generally, the physical examination experiments include the anterior drawer test, the Lachman test, and the pivot-shift test [6]. The second is the implementation of auxiliary examination methods. Arthrography, ultrasonography, and other examinations have been used to diagnose ACL injury in different historical periods, but they have not become the mainstream means due to their invasiveness, sensitivity, specificity, and accuracy [7]. Since the 1980s, MRI technology, which has been applied to the imaging diagnosis of knee soft tissue injury, has become one of the preferred imaging methods for initial diagnosis with its noninvasive, fast, powerful multiplanar tomography and high differentiation of soft tissue [8]. The recent development of related technologies has also significantly promoted the diagnostic application of MRI; in particular, some recent studies have shown that the progress of technology has made MRI more refined and accurate in the degree of fault segmentation [9]. Arthroscopy, as the "gold standard" of soft tissue injury such as ACL of knee joint, has great diagnostic advantages of intuitive and accurate diagnosis and clear qualification and positioning, but after all, it cannot become the preferred method as an invasive operation [10].

MRI technology uses the characteristics of nuclear spin motion to obtain the morphological images of human tissues, being widely used in clinical diagnosis. However, magnetic resonance imaging (MRI) needs long time, so it cannot meet the requirements of fast imaging such as brain function imaging and cardiac dynamic imaging [11]. However, parallel MRI uses the spatial position information of the phased array coil instead of the number of phase encoding steps, which can greatly improve the imaging speed and ensure the image quality and high spatial resolution [12]. The sum of squares (SOS) algorithm is considered to be the optimal image synthesis method without knowing the exact sensitivity of each phased array coil. However, the SOS algorithm uses the same weight to synthesize the images of each coil and cannot suppress the external noise well, resulting in the problems of signal deviation and low signal-to-noise ratio (SNR) of the final image [13]. Therefore, simultaneous acquisition of spatial harmonics (SMASH) reconstruction algorithm was introduced in detail as a representative of parallel imaging algorithm based on K-space domain. The smoothing filter was used to denoise the reconstructed image of each phased array coil, and then the sensitivity of each coil was used as the weight of image synthesis [14].

Therefore, by arthroscopic diagnosis, MRI based on K-space SMASH reconstruction algorithm was used for imaging diagnosis of patients. The application effect was explored by comparing the detection results. In addition, compared with the healthy population, the possible influencing factors in knee ligament injury were explored to provide data support for the prevention and diagnosis of knee cruciate ligament injury in clinical practice.

2. Research Methods

2.1. Research Objects. In this study, 96 patients with ACL injury of knee joint in hospital from September 2018 to September 2020 were randomly selected, with unlimited age and gender. A total of 96 patients, 44 males and 52 females, were finally included. They were randomly divided into two groups: group A (arthroscopy) and group B (MRI examination), and another 96 healthy volunteers in the same period were selected as the control group. All the objects signed informed consent, and this study had been approved by the ethics committee of hospital.

Inclusion criteria are as follows: clinical tests have at least one of the positive signs of the three basic tests (anterior drawer test, Lachman test, and pivot-shift test) and have a history of trauma and clinical symptoms such as joint swelling and pain. Exclusion criteria are as follows: patients with clear history of knee joint, such as tuberculous arthritis, rheumatoid arthritis, intra-knee tumor, or knee surgery.

2.2. Examination Methods

2.2.1. Clinical Examination. In the anterior drawer test, the patient was in a supine position. The knee flexion was 90°, and the hip flexion was 45°. The examiner fixed the patient's feet and pulled the patient's lower legs from posterior to anterior by holding the upper end of the lower legs with both hands.

In the Lachman test, knee flexion was 15°; the examiner seized the lower end of the patient's femur and pulled the upper end of the tibia from posterior to anterior with the other hand. The anterior drawer test and Lachman test were graded according to the following criteria: degree I: the tibial anteversion of the injured side increased by 1–5 mm and had a good termination point compared with the healthy side; degree II: the gap between the two sides was 6–10 mm, with flexible termination point; degree III: the gap was greater than 10 mm, without termination point.

In the Pivot-shift test (MacIntosh method), the patient was in supine position; the examiner placed one hand on the lateral side of the patient's knee, grasped the heel with the other hand to internally rotate the lower leg, everted the knee, and gradually flexed the knee joint from 0° position. When the affected knee was out of the buttoning-locking position, the lateral condyle of the tibia began to be gradually subluxated anteriorly, and when the knee was slowly flexed up to about 30°, the tibia suddenly reduced posteriorly and there was a sense of dislocation. The positive graduation of the test is as follows: degree I was slippage, degree II was dislocation, degree III was temporary interlocking. The clinical examination part was only used as preliminary screening, so it was only judged to be positive and negative.

There was at least one positive sign; then, it could be classified as a suspected case, and the second step of the examination was performed, that is, MRI examination.

2.2.2. MRI Examination. An MRI machine and an SE sequence were used for relevant conventional scans.

The MRI findings of complete ACL injury include direct and indirect signs. The direct signs were interrupted ACL continuity, irregular and wavy ACL shape, abnormally increased signal in and around the ligament, no normal hypointense ligament fibers seen, reduced ACL inclination, and no parallel walking to the Blumensaat line. Indirect signs included posterior cruciate ligament curvature greater than 0.39, bone contusion on the posterolateral surface of the tibial plateau, depression of the lateral femoral notch greater than 1.5 mm, anterior displacement of tibial greater than 5 mm, and posterior displacement of the posterior horn of the lateral meniscus. According to the MRI findings of partial ACL injury, the ligament morphology was normal, while localized abnormal signals appeared in the ligament; some ligament fibers were curved or wavy.

2.3. Measurement of Relevant Anatomical Parameters. Measurement of relevant anatomical parameters of femoral intercondylar notch was performed using 3.0T MRI scanner, with slice thickness of 2 mm. The patient was placed in supine position. The knee joint was naturally extended in non-weight-bearing state. The sagittal, coronal, and axial scans of the knee joint were performed. On coronal images, the level at which the medial and lateral femoral condyles maintained continuity and the popliteal groove could be observed was selected as the level at which the intercondylar notch width index was measured. The intercondylar notch width index = the width of the intercondylar notch at the level of the popliteal groove/the width of both condyles at the same level.

Measurement of anatomical parameters related to tibial intercondylar augmentation was carried out as follows: the patient was placed in the supine position with the knee joint naturally extended in a non-weight-bearing state, and X-ray examination was performed on the knee joint. The height of the medial and lateral apices of the tibial intercondylar eminence and the width of the tibial intercondylar eminence were measured on intact anteroposterior radiographs of the knee. First, the connecting line between the most concave point of the medial tibial plateau and the most convex point of the lateral tibial plateau was used as the joint line, and vertical lines were made from the apices of the medial and lateral tibial intercondylar eminence to the joint line. The length of these two vertical lines was the medial height of the tibial intercondylar eminence and the lateral height of the tibial intercondylar eminence, and the distance between the two vertical lines and the intersection point of the joint line was the width of the tibial intercondylar eminence.

2.4. Parallel Imaging Reconstruction Algorithm Based on K-Space Domain. K-space is Fourier space, also known as spatial frequency space or raw data space, which is the filling space of the original data of magnetic resonance signal with spatial positioning coding information [15].

For two-dimensional K-space, the unit is spatial frequency, which is expressed by the number of cycles cm^{-1} or $H_z \cdot \mathrm{cm}^{-1}$, and is described by two mutually perpendicular vectors, K_x, K_y; that is, K-space is the space defined by the two coordinate components K_x, K_y. The line with $K_y = 0$ is called zero Fourier line, the Fourier line close to $K_y = 0$ is called low spatial frequency Fourier line, and that far away from $K_y = 0$ is called high spatial frequency Fourier line. Thus, the K-plane region can be divided into low-frequency Fourier space and high-frequency Fourier space.

The conversion relationship between K-space and data space is in a uniform applied magnetic field; the magnetic resonance signal is directly proportional to the transverse magnetization vector, but in a nonuniform applied magnetic field space or in the presence of gradient magnetic field, the magnetic resonance signal is related not only to the proton spin density, but also to its spatial position. It is supposed that the vector form of the two-dimensional space coordinate where the sample is located, is $\underset{r}{\longrightarrow} = (x, y)$; the proton spin density in unit space is $\rho(\underset{r}{\longrightarrow}) = \rho(x, y)$; the time of repetition (TR) is long enough; and the time of echo (TE) is short enough. The expression of magnetic resonance signal $S(t)$ is as follows:

$$S(t) = \int \rho\left(\underset{r}{\longrightarrow}\right) e^{-i2\pi\gamma \int_0^t G(t')\mathrm{d}t'} d^2 \underset{r}{\longrightarrow}. \tag{1}$$

In (1), γ is the magnetogyric ratio, and $G(t')$ is the gradient field. K-space is $\underset{K}{\longrightarrow} = \underset{K}{\longrightarrow}(t) = \gamma \int_0^t G(t')\mathrm{d}t'$; then, the following equation can be obtained:

$$S\left(\underset{K}{\longrightarrow}\right) = \int \rho\left(\underset{r}{\longrightarrow}\right) e^{-i2\pi K(t) d^2 \underset{r}{\longrightarrow}}. \tag{2}$$

Under the condition of $\underset{K}{\longrightarrow} = \underset{K}{\longrightarrow}(t) = \gamma \int_0^t G(t')\mathrm{d}t'$, the proton spin density represented as $\rho(\underset{r}{\longrightarrow})$ of the object in the original coordinate $\underset{r}{\longrightarrow}$ and the acquired signal represented as $S \underset{K}{\longrightarrow}$ of the object in K-space are Fourier transform pair: $S \underset{K}{\longrightarrow}$ is the Fourier transform of $\rho(\underset{r}{\longrightarrow})$; $\rho(\underset{r}{\longrightarrow})$ is the inverse Fourier transform of $S \underset{K}{\longrightarrow}$. Therefore, the original coordinate $\underset{r}{\longrightarrow}$ with unit as cm will correspond to the spatial frequency coordinate $\underset{K}{\longrightarrow}$ with unit as $H_z \cdot \mathrm{cm}^{-1}$. Figure 1 shows the process from level matrix to K-space. In Figure 1, x and y represent frequency coding and phase coding, FOV_x and FOV_y are the field of vision in x and y directions, and ΔT_s is the sampling interval. ΔK_x and ΔK_y are the intervals of K-space along the x and y directions.

In (2), $\underset{K}{\longrightarrow}$ and $\underset{r}{\longrightarrow}$ are two-dimensional vectors, so the gradient field corresponding to the two coordinate components in K-space in MRI technology can be expressed as follows:

$$\underset{K}{\longrightarrow} = \underset{K}{\longrightarrow}(t) = \left[K_x(t'), K_y(t')\right]. \tag{3}$$

The component form is as follows:

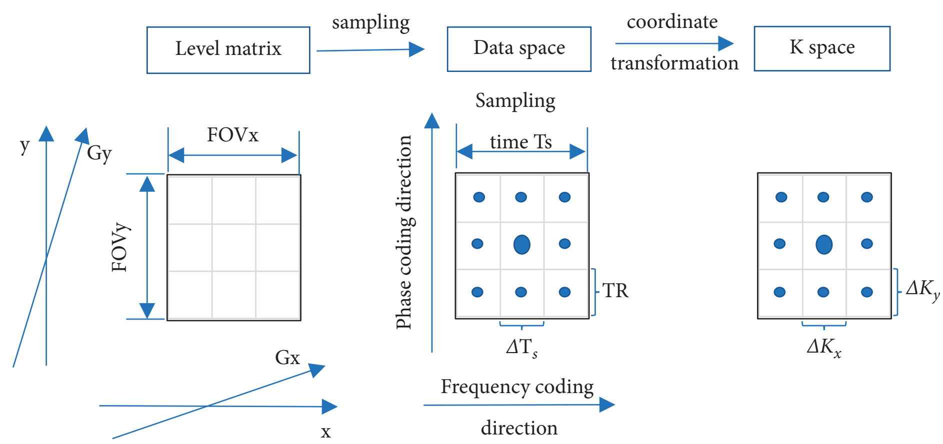

Figure 1: Process from level matrix to K-space.

$$K_x = K_x(t') = \gamma \int_0^t G_x(t')dt', K_y = K_y(t') = \gamma \int_0^t G_y(t')dt'. \tag{4}$$

For the case where the gradient field change rate is constant, (4) can be expressed as follows:

$$\begin{aligned} K_x &= \gamma G_x t, \\ K_y &= \gamma G_y t. \end{aligned} \tag{5}$$

The conversion equation of converting the coordinates of data space into spatial frequency domain can be deduced as follows:

$$\begin{aligned} \Delta K_x &= \frac{\gamma G_x \Delta T_s}{2\pi} = \frac{1}{\mathrm{FOV}_x}, \\ \Delta K_y &= \frac{\gamma G_y \Delta T_s}{2\pi} = \frac{1}{\mathrm{FOV}_y}. \end{aligned} \tag{6}$$

Parallel imaging based on K-space domain uses the K-space data collected by each phased array coil and the fitted weighting coefficient to recover the unsampled data in K-space, obtain the full K-space data of each phased array coil, and then carry out inverse Fourier transform to reconstruct the final image of each phased array coil [16]. SMASH reconstruction algorithm was introduced as a representative of parallel imaging algorithm based on K-space domain.

The SMASH reconstruction algorithm mainly uses the linear combination of phased array coil sensitivities to recover the K-space phase coded line data lost due to undersampling [17], and its brief schematic diagram is shown in Figure 2.

It is supposed that there is a group of phased array coils, each phased array coil has its unique sensitivity $S_i(x, y)$, and a mixed sensitivity $S_m^{\mathrm{comp}}(x, y)$ can be obtained through the linear combination of coils. The linear combination equation is as follows:

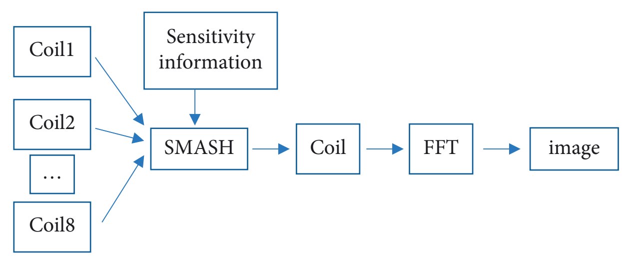

Figure 2: Schematic diagram of SMASH.

$$S_m^{\mathrm{comp}}(x, y) = \sum_{i=1}^{N_c} w_i^{(m)} S_i(x, y). \tag{7}$$

In (7), m is the ordinal number of spatial harmonics. $m = -R/2, -R/2 + 1, \ldots 0, 1, \ldots R/2$, $w_i^{(m)}$ are the weight coefficients of the i coil to the m harmonic. N_c is the number of coils forming the array. It is supposed that the weight coefficient $w_i^{(m)}$ and coil sensitivity $S_i(x, y)$ are as follows:

$$\sum_{i=1}^{N_c} w_i^{(m)} S_i(x, y) \approx e^{-2\pi j m \Delta k_y y}. \tag{8}$$

The only unknown $w_i^{(m)}$ in (8) is calculated by $S_i(x, y)$ merging with $e^{jm\Delta k_y y}$.

It is supposed that $I_i(k_x, k_y)$ is the K-space data collected by the i coil; then, the result of Fourier transform after sensitivity coefficient $S_i(x, y)$ weighting by the proton spin density $\rho(x, y)$ is as follows:

$$I_i(k_x, k_y) = \int\int S_i(x, y)\rho(x, y) e^{-2\pi j (k_x y + k_y y)} \mathrm{d}x\mathrm{d}y. \tag{9}$$

In two-dimensional MRI, the magnetic resonance signal detected by the receiving coil can be described as the following equation in Fourier space.

$$I(k_x, k_y) = \int\int \rho(x, y) e^{-2\pi j (k_x y + k_y y)} \mathrm{d}x\mathrm{d}y. \tag{10}$$

$I_i(k_x, k_y)$ is weighted by $w_i^{(m)}$; the phase coded line data lost in K-space can be obtained.

$$I_m^{\mathrm{comp}}\left(k_x, k_y\right) = \sum_{i=1}^{N_c} w_i^{(m)} I_i\left(k_x, k_y\right), \tag{11}$$

$$\begin{aligned} I_m^{\mathrm{comp}}\left(k_x, k_y\right) &= \sum_{i=1}^{N_c} \int\int S_i(x, y)\rho(x, y)e^{-2\pi j\left(k_x y + k_y y\right)}\mathrm{d}x\mathrm{d}y \\ &= \int\int \rho(x, y)e^{-2\pi j\left(k_x y + k_y y\right)}\mathrm{d}x\mathrm{d}y. \end{aligned} \tag{12}$$

Finally, the following equation is obtained:

$$I_m^{\mathrm{comp}}\left(k_x, k_y\right) = I\left(k_x, k_y + m\Delta k_y\right). \tag{13}$$

Equations (11)–(13) show that the linear combination of data collected by each coil can be used to generate K-space displacement, which is similar to the traditional phase coding method using gradient magnetic field. The advantage of this is that the increase of data used for fitting improves the accuracy and robustness of linear weight coefficient estimation, and several additional rows of autocalibration signal (ACS) lines located in the center of K-space can be used for image reconstruction, which will improve the quality of reconstructed image.

2.5. Evaluation Method of Reconstructed Image. The goal of MRI is to obtain medical images with minimum error. According to the methods used to evaluate the quality of image synthesis methods from different principles and entry points, it can be divided into two classical categories, namely, qualitative analysis criteria and quantitative analysis criteria. The performance of the algorithm was measured through the qualitative analysis of reconstructed image comparison and the two quantitative evaluation algorithms of SNR and error image (ERR).

SNR mainly reflects the image quality through the ratio of signal intensity to noise intensity. It is an important index to measure the image quality. Its calculation equation is as follows:

$$\mathrm{SNR} = 20 \times \lg \frac{\sum_{x,y}\left|I_{\mathrm{rec}}(x, y)\right|}{\sum_{x,y}\left|I_{\mathrm{rec}}(x, y) - I_{\mathrm{ref}}(x, y)\right|^2}. \tag{14}$$

I_{rec} is the reconstructed image, and I_{ref} is the reference image.

ERR mainly reflects the proximity between the reconstructed image and the reference image in the form of the absolute value of the difference. It intuitively reflects the reconstruction accuracy of the algorithm.

$$\mathrm{ERR} = \sum_{j=1}^{N_x}\sum_{i=1}^{N_y}\left|I_{i,j}^{\mathrm{rec}}(x, y) - I_{i,j}^{\mathrm{ref}}(x, y)\right|. \tag{15}$$

$I_{\mathrm{rec}}(x, y)$ represents the reconstructed image, $I_{\mathrm{ref}}(x, y)$ represents the reference image, and N_x and N_y are the number of pixels.

2.6. Statistical Methods. SPSS 22.0 software was used. The measurement data were expressed by independent sample *t*-test, and the counting data were expressed by χ^2 test. The difference was statistically meaningful with $P < 0.05$. The number of true positive cases refers to the number of ACL injuries diagnosed by arthroscopy or MRI. The number of false positive cases refers to the number of ACL injuries diagnosed by arthroscopy or MRI. The number of true negative cases refers to the number of ACL injuries diagnosed by arthroscopy or MRI. The number of false negative cases refers to the number of ACL injuries diagnosed by arthroscopy or MRI.

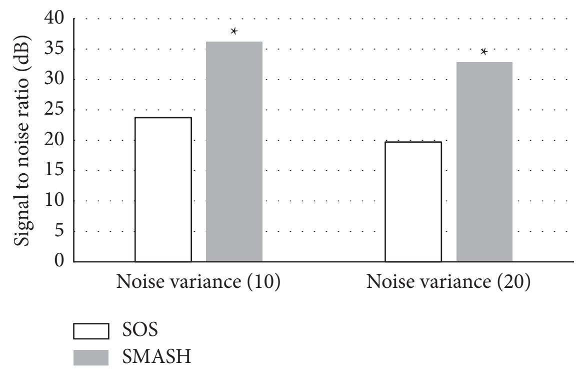

Figure 3: SNR of images synthesized by different algorithms. *Compared with SOS algorithm, $P < 0.05$.

3. Results

3.1. Image Reconstruction Result. The SNR of SMASH was higher than that of SOS. According to the definition of SNR, the larger the SNR, the higher the tissue signal strength and image clarity. This suggested that SMASH algorithm could improve image quality and had superiority (Figure 3).

Similarly, the difference image between the synthesized image and the reference image of the two algorithms was simulated (Figure 4). By comparison, there was almost no background noise in the difference image between the synthesized image and the reference image of the SMASH algorithm, and the ERR was almost invisible, which further illustrated the effectiveness and universal applicability of the improved algorithm. The reconstruction of knee joint image is shown in Figure 5, and the image processed by SMASH algorithm is obviously clearer.

3.2. Analysis of the Results of Different Methods. With arthroscopy as the standard, 66 tests were positive and 30 tests were negative. According to the MRI diagnosis results based on K-space data reconstruction algorithm, 56 tests were positive and 40 tests were negative; the difference between the two groups was statistically significant, $P < 0.05$ (Figure 6).

The two examination methods were plotted as ROC curves, and the area under the ROC curve for arthroscopy was 0.617, standard error 0.7, 95% confidence interval of area (0.766, 0.957) (0.408, 0.716), sensitivity 0.603, and misdiagnosis rate 0.149; the area under ROC curve of MRI detection based on K-space reconstruction algorithm was slightly lower than that of arthroscopy (Figure 7).

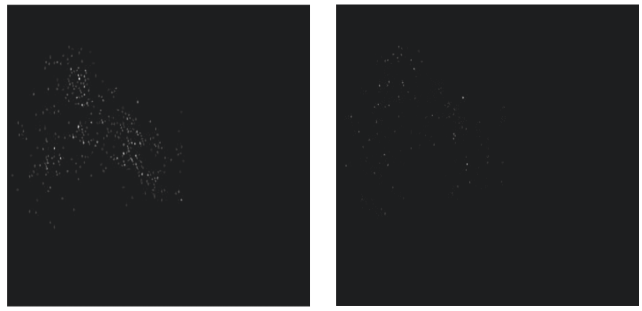

(a) (b)

Figure 4: Difference image of algorithms. (a) SOS algorithm. (b) SMASH algorithm.

Original image SOS algorithm processing SMASH algorithm processing

Figure 5: Image comparison of knee cruciate ligament injury.

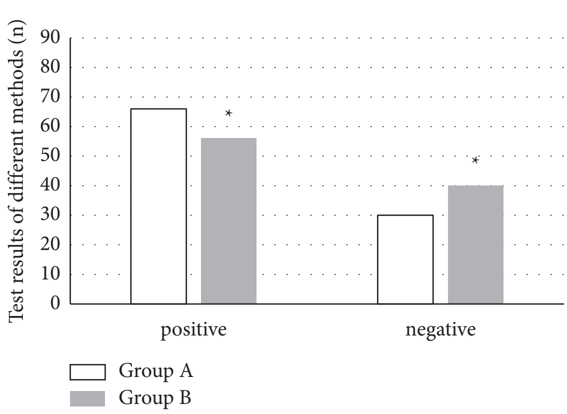

Figure 6: Diagnostic results of different methods for cruciate ligament injury. *Compared with group A, $P < 0.05$.

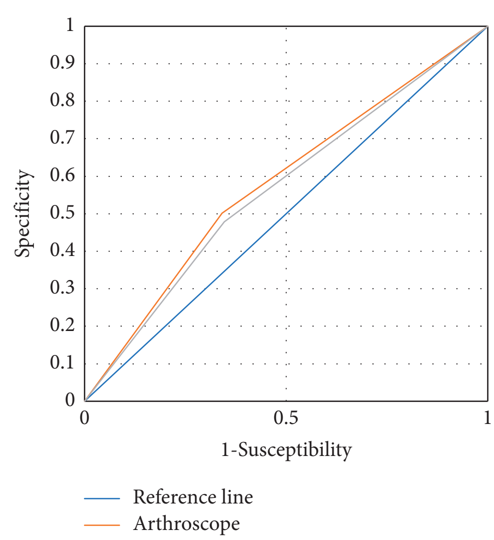

Figure 7: ROC curve.

3.3. Comparison of Anatomic Parameters. There was no significant difference in the width of femoral condyle between the two groups ($P > 0.05$). The width of intercondylar fossa, intercondylar fossa width index, and the ratio of tibial intercondylar eminence width to intercondylar fossa width in group B were lower than those in the control group ($P < 0.05$) (Figures 8 and 9).

4. Discussion

In the past, the SOS algorithm used to synthesize the reconstructed images of each phased array coil with equal weight greatly affected the final image quality. In addition, it could not well suppress the external noise, and the final image had problems such as signal deviation and reduced SNR [18]. Aiming at remedying its shortcomings, the K-space-based SMASH reconstruction algorithm is applied. First, the reconstructed images of each phased array coil are denoised using a smoothing filter, and then the final images are synthesized by using the coil sensitivity as a weight. The

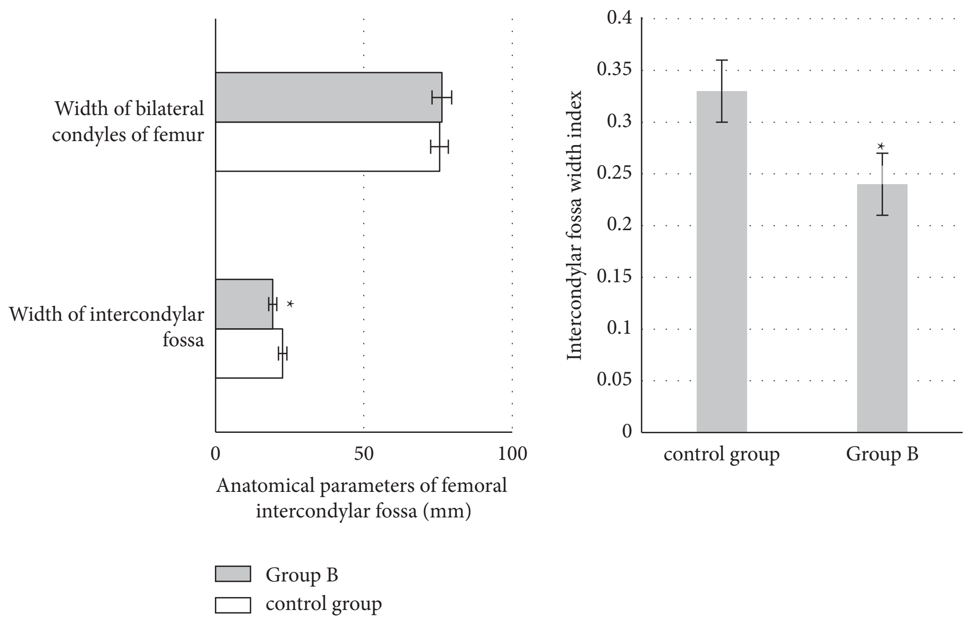

Figure 8: Measurement results of related anatomical parameters of femoral intercondylar fossa. *Compared with the control group, $P < 0.05$.

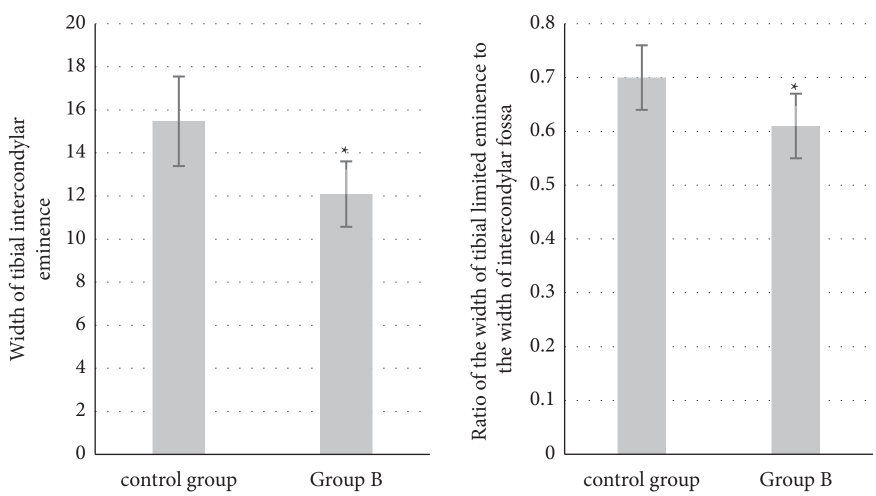

Figure 9: Measurement results of anatomical parameters related to tibial intercondylar eminence. *Compared with the control group, $P < 0.05$.

experimental results show that the SNR of the SMASH algorithm is higher than that of the SOS algorithm; there is almost no background noise in the difference image between the synthesized image and the reference image of the SMASH algorithm, and the error image is almost invisible. This shows that the SMASH algorithm can improve the image quality, has superiority, can effectively reduce the impact of corrupted data on the final synthetic image, can effectively eliminate the artifacts in the image, and can improve the image SNR.

The patients were examined by MRI based on SMASH algorithm. The results of arthroscopic examination showed that the number of positives was 66 and the number of negatives was 30. The results of MRI diagnosis based on K-space data reconstruction algorithm showed that the number of positives was 56 and the number of negatives was 40. The difference between the two groups had statistical significance ($P < 0.05$). After the experiment, the reasons were considered and summarized in combination with the relevant literature: the direction during MRI scanning was not parallel to the ACL, and the number of upper layers of section imaging was small; the hematoma of the surrounding tissues of patients in the acute phase would cause artifacts; the volume effect caused artifacts, affecting the judgment [19].

The ACL is an important structure to maintain the stability of the knee joint. After injury, the biomechanical structure of the knee joint is disordered, and the knee joint shows anterior instability, which leads to the injury of intra-articular cartilage, meniscus, and other structures and accelerates the aging and degeneration of the knee joint. Therefore, it is very important to identify the risk factors of

ACL injury for its early prevention and treatment. The results showed that there was no significant difference in femoral bicondylar width between the two groups ($P > 0.05$). The intercondylar fossa width, intercondylar fossa width index, ratio of tibial intercondylar eminence width to intercondylar notch width in group B were lower than those in the control group ($P < 0.05$). Some studies have suggested that the intercondylar fossa can be used as a valuable predictor to predict ACL injury, and the intercondylar fossa width index is weakly correlated with ACL injury [20]. This reveals that the poorer the fit between the tibial intercondylar eminence and the femoral intercondylar fossa is, the more likely it is to lead to ACL rupture, but the specific mechanism of effect needs to be clarified by the sample size and biomechanical studies on this aspect.

5. Conclusion

MRI based on K-space data reconstruction algorithm was applied to diagnose ACL injury of the knee and assess the risk factors for its occurrence. The results showed that compared with the traditional SOS algorithm, the K-space-based SMASH algorithm could effectively improve the image quality, reduce the impact of corrupted data on the final synthetic image, and improve the image SNR. Compared with the arthroscopy results, the MRI based on the K-space data reconstruction algorithm was found to have certain reference value for ACL injury of the knee, but its accuracy needed to be further improved. The ratio of tibial intercondylar augmentation width to femoral intercondylar notch width could be used to evaluate the matching of tibial intercondylar augmentation and femoral intercondylar notch in clinical practice, so as to evaluate the risk of ACL rupture. However, due to the limitation of conditions, the sample size included in this experiment is small, and the accuracy of some results needs to be further confirmed.

Data Availability

The data used to support the findings of this study are available from the corresponding author upon request.

Conflicts of Interest

The authors declare that there are no conflicts of interest.

Authors' Contributions

Rui Chang and Angang Chen contributed equally to this work.

Acknowledgments

This work was supported by Chengdu Scientific Research Project of Health and Family Planning Commission (2020094).

References

[1] J. D. Hassebrock, M. T. Gulbrandsen, W. L. Asprey, J. L. Makovicka, and A. Chhabra, "Knee ligament anatomy and biomechanics," *Sports Medicine and Arthroscopy Review*, vol. 28, no. 3, pp. 80–86, 2020.

[2] S. R. Filbay and H. Grindem, "Evidence-based recommendations for the management of anterior cruciate ligament (ACL) rupture," *Best Practice & Research Clinical Rheumatology*, vol. 33, no. 1, pp. 33–47, 2019.

[3] J. C. Richmond, "Anterior cruciate ligament reconstruction," *Sports Medicine and Arthroscopy Review*, vol. 26, no. 4, pp. 165–167, 2018.

[4] D. Dimitriou, D. Zou, Z. Wang, N. Helmy, and T.-Y. Tsai, "Anterior cruciate ligament bundle insertions vary between ACL-rupture and non-injured knees," *Knee Surgery, Sports Traumatology, Arthroscopy*, vol. 29, no. 4, pp. 1164–1172, 2021.

[5] T. Diermeier, B. B. Rothrauff, B. B. Rothrauff, L. Engebretsen, and A. D. Lynch, "Treatment after anterior cruciate ligament injury: panther symposium ACL treatment consensus group," *Knee Surgery, Sports Traumatology, Arthroscopy*, vol. 28, no. 8, pp. 2390–2402, 2020.

[6] R. Coffey and B. Bordoni, "Lachman test," in *StatPearls [Internet]*StatPearls Publishing, Treasure Island, FL, USA, 2021.

[7] O. Onishi, K. Ikoma, M. Kido, and T. Kubo, "Early detection of osteoarthritis in rabbits using MRI with a double-contrast agent," *BMC Musculoskeletal Disorders*, vol. 19, no. 1, 81 pages, 2018.

[8] M. P. Brady and W. Weiss, "Clinical diagnostic tests versus MRI diagnosis of ACL tears," *Journal of Sport Rehabilitation*, vol. 27, no. 6, pp. 596–600, 2018.

[9] M. Laurens, E. Cavaignac, H. Fayolle et al., "The accuracy of MRI for the diagnosis of ramp lesions," *Skeletal Radiology*, vol. 51, no. 3, pp. 525–533, 2022.

[10] E. R. Floyd, J. K. Monson, and R. F. LaPrade, "Multiple ligament knee reconstructions," *Arthroscopy*, vol. 37, no. 5, pp. 1378–1380, 2021.

[11] T. Yousaf, G. Dervenoulas, and M. Politis, "Advances in MRI methodology," *International Review of Neurobiology*, vol. 141, pp. 31–76, 2018.

[12] M. Hu, Y. Zhong, S. Xie, H. Lv, and Z. Lv, "Fuzzy system based medical image processing for brain disease prediction," *Frontiers in Neuroscience*, vol. 15, Article ID 714318, 2021.

[13] Y. Li, J. L. Zhao, Z. Lv, and J. H. Li, "Medical image fusion method by deep learning," *International Journal of Cognitive Computing in Engineering*, vol. 2, pp. 21–29, 2021.

[14] M. Gu, C. Liu, and D. M. Spielman, "Parallel spectroscopic imaging reconstruction with arbitrary trajectories using k-space sparse matrices," *Magnetic Resonance in Medicine*, vol. 61, no. 2, pp. 267–272, 2019.

[15] M. Kazemi, Z. Kavehvash, and M. Shabany, "K-space aware multi-static millimeter-wave imaging," *IEEE Transactions on Image Processing*, vol. 28, 2019.

[16] C. Oh, D. Kim, J. Y. Chung, Y. Han, and H. Park, "A k-space-to-image reconstruction network for MRI using recurrent neural network," *Medical Physics*, vol. 48, no. 1, pp. 193–203, 2021.

[17] M. A. Griswold, P. M. Jakob, Q. Chen, and D. K. Sodickson, "Resolution enhancement in single-shot imaging using simultaneous acquisition of spatial harmonics (SMASH)," *Magnetic Resonance in Medicine*, vol. 41, no. 6, pp. 1236–1245, 2019.

[18] M. Bernhardt, V. Vishnevskiy, R. Rau, and O. Goksel, "Training variational networks with multidomain simulations: speed-of-sound image reconstruction," *IEEE Transactions on Ultrasonics, Ferroelectrics, and Frequency Control*, vol. 67, no. 12, pp. 2584–2594, 2020.

[19] S. Krasnoperov, "MRI assessment of anterolateral ligament injury of knee joint," *Ortopedia Traumatologia Rehabilitacja*, vol. 22, no. 6, pp. 421–425, 2020.

[20] D. Zbrojkiewicz, C. Scholes, E. Zhong, and C. Bell, "Anatomical variability of intercondylar fossa geometry in patients diagnosed with primary anterior cruciate ligament rupture," *Clinical Anatomy*, vol. 33, no. 4, pp. 610–618, 2020.

Hindawi
Contrast Media & Molecular Imaging
Volume 2022, Article ID 2464640, 9 pages
https://doi.org/10.1155/2022/2464640

WILEY | Hindawi

Research Article

Efficacy Evaluation of 64-Slice Spiral Computed Tomography Images in Laparoscopic-Assisted Distal Gastrectomy for Gastric Cancer under the Reconstruction Algorithm

Weiguang Yu [1], Xing Li [1], Hongbo Zhou [2], Yang Zhang [3], and Zhiguo Sun [1]

[1] *Department of General Surgery, Affiliated Hongqi Hospital of Mudanjiang Medical University, Mudanjiang 157011, Heilongjiang, China*
[2] *Internal Medicine Oncology, Affiliated Hongqi Hospital of Mudanjiang Medical University, Mudanjiang 157011, Heilongjiang, China*
[3] *Department of Anatomy, Mudanjiang Medical University, Mudanjiang 157011, Heilongjiang, China*

Correspondence should be addressed to Zhiguo Sun; 1531140599@xzyz.edu.cn

Received 21 March 2022; Revised 3 May 2022; Accepted 5 May 2022; Published 31 May 2022

Academic Editor: M. Pallikonda Rajasekaran

This study was aimed to analyze the application value of the filtered back-projection (FBP) reconstruction algorithm of computed tomography (CT) images in laparoscopic-assisted distal gastrectomy. In this study, 56 patients with gastric cancer were selected as research subjects and randomly divided into the control group (CT-guided laparoscopic radical gastrectomy) and the observation group (CT-guided laparoscopic radical gastrectomy with the FBP reconstruction algorithm), with 28 patients in each group. Fourier transform and iterative reconstruction were introduced for comparison, and finally, the postoperative curative effect and adverse events were compared between the two groups. The results showed that the CT image quality score processed by the FBP reconstruction algorithm (4.31 ± 0.31) was significantly higher than that of the iterative reconstruction method (3.5 ± 0.29) and the Fourier transform method (3.97 ± 0.38) ($P < 0.05$). The incidences of postoperative wound infection and gastric motility disorder (5.88% and 8.16%, respectively) in the observation group were significantly lower than those in the control group (8.21% and 10.82%, respectively) ($P < 0.05$). The levels of serum interleukin-6 (IL-6) (280.35 ± 15.08 ng/L) and tumor necrosis factor-α (TNF-α) (144.32 ± 10.32 ng/L) in the observation group after the treatment were significantly lower than those in the control group, which were 399.71 ± 14.19 ng/L and 165.33 ± 10.08 ng/L, respectively ($P < 0.05$). In conclusion, the FBP reconstruction algorithm was better than other algorithms in the processing of gastric cancer CT images. The FBP reconstruction algorithm showed a good reconstruction effect on CT images of gastric cancer; CT images based on this algorithm helped to formulate targeted surgical treatment plans for gastric cancer, showing a high clinical application value.

1. Introduction

Gastric cancer is one of the most common malignant tumors in China, which has a serious impact on human health and even life. The 5-year survival rate of such malignant tumors is generally low; however, if it can be detected early and treated aggressively, the 5-year survival rate can reach more than 90%. Therefore, early detection, early diagnosis, and early treatment of this type of malignant tumor are very important [1, 2]. According to 2018 global survey data, the incidence and mortality of gastric cancer ranked fifth and second in malignant tumors, respectively, and showed an increasing trend with age [3, 4]. Early gastric cancer may not show obvious clinical symptoms. When the patient develops symptoms such as abdominal pain or discomfort, anemia, indigestion, dysphagia or obstruction, and other symptoms, it has mostly become advanced gastric cancer [5, 6]. At present, gastric cancer is mainly treated by surgery, and radiotherapy and chemotherapy are performed before and after surgery to enhance the curative effect [7]. Radical surgery is the main treatment for early gastric cancer; palliative surgery can be used when the tumor cannot be completely removed in advanced gastric cancer [8, 9]. The resection rate of early gastric cancer is high, up to 90%. Once in the advanced stage, the progression is rapid, and the complete resection rate is extremely low [10, 11]. In addition, doctors need to formulate corresponding treatment plans according to their special circumstances and choose the most suitable therapy for patients with different tumor stages, tumor types, and physical conditions [12, 13].

With the continuous advancement of modern medical diagnosis technology, various types of medical equipment are also highly popularized, and various auxiliary inspection methods can be used in the medical field to take images, assist clinicians to determine the lesions of gastric cancer, and determine surgical planning [14, 15]. Among them, computed tomography (CT) imaging is an important means of gastric cancer detection, with high diagnostic accuracy and good adaptability. However, the current segmentation of conventional CT images has great limitations and challenges, and there are problems such as blurred lesion boundaries and insignificant differences in brightness [16, 17]. Image reconstruction technology plays an important role in many fields. Common CT image reconstruction algorithms include the Fourier transform method, the iterative reconstruction method, and the filtered back-projection (FBP) method. In the process of research and implementation of the FBP algorithm, there are a series of extremely complex image processing problems and mathematical calculation problems, which have the advantages of fast reconstruction speed and high image quality [18].

At present, algorithms such as image reconstruction and computer-aided medical image analysis have obvious advantages in major breakthrough in technology and the improvement of medical level and have also become an effective way to solve problems in the medical image. Therefore, to solve blurred edges and insignificant differences in brightness of traditional CT images, a FBP reconstruction algorithm was introduced for image processing, and applied in laparoscopic-assisted radical gastrectomy to analyze its clinical application value.

2. Materials and Methods

2.1. Research Objects and Their Grouping. In this study, 56 patients with gastric cancer, admitted to the hospital from October 2019 to October 2020, were selected as research subjects, including 26 male patients and 30 female patients, aged 48–65 years old. Patients were randomly divided into a control group (CT-guided laparoscopic radical gastrectomy) and an observation group (64-slice spiral CT-guided laparoscopic radical gastrectomy with the FBP reconstruction algorithm), with 28 patients in each group. The average age of patients in the control group was 53.21 ± 7.28 years old, and the average age of patients in the experimental group was 54.08 ± 6.87 years old. This study had been approved by the ethics committee of hospital, and these patients and their families understood the research content and signed the informed consent.

Inclusion criteria were as follows: patients diagnosed with gastric cancer who underwent laparoscopic-guided radical gastrectomy for gastric cancer without restriction of pathological type; patients with complete case data; and patients with no radiotherapy or chemotherapy before surgery.

Exclusion criteria were as follows: patients with liver and kidney dysfunction or other system and organ diseases; patients with abnormal coagulation function and blood routine; and patients with other types of gastric diseases such as gastritis and gastric ulcer.

2.2. CT Scanning. Patients were scanned with 64-slice spiral CT. Patients were required to fast for 5 hours before the CT scan, but could drink a small amount of water for half an hour before the scan. Patients were in the supine position, and the scanning range was from the top of the diaphragm to the lower poles of both kidneys. Scanning parameters were defined as follows: tube voltage was 120 kV, tube current was 120 mAs, gantry rotation time was 0.6 seconds, detector collimation parameter was 65×0.618 mm, field of view was 340 mm × 340 mm, and matrix was 521×521.

The obtained CT-enhanced images were sent to the workstation for processing. All patients underwent contrast-enhanced CT scans of the abdomen. CT images were interpreted by two attending doctors or radiologists with rich clinical experience. If there was any dispute between two doctors or radiologists, they can consult with the third doctor or radiologist.

2.3. Reconstruction of CT Images. The basis of CT image reconstruction was that the same X-ray intensity, passing through different substances, has different attenuations. Using this law, different substances in the human body can be distinguished.

The process of CT image reconstruction was described as follows. In simple terms, structures within each layer of the human body that were penetrated by X-rays in a CT scan can be divided into small cubes (called voxels: *Voxel*). Each small cube corresponded to a separate attenuation signal, which was input into the corresponding small grid (called pixel: *Pixel*) in the image plane matrix, and the attenuation signal of each voxel was input into the corresponding pixel. Then, it was reflected in different grayscale images, so as to realize the reconstruction of CT images. Figure 1 shows the flow of FBP reconstruction of CT images.

The central slice theorem of a two-dimensional image stated that the Fourier transform method $p(\varpi)$ of the projection and $p(s)$ of a two-dimensional function $f(x, y)$ was equal to the slice of the function $f(x, y)$ that passed through the origin in a direction parallel to the detector of the Fourier transform method $F(\varpi x, \varpi y)$.

The one-dimensional continuous Fourier transform method pair is

$$F(W) = \int_{-\infty}^{+\infty} f(t)e^{-iWt}\mathrm{d}t, \tag{1}$$

$$f(t) = \frac{1}{2}\pi \int_{-\infty}^{+\infty} f(W)e^{-iWt}\mathrm{d}W. \tag{2}$$

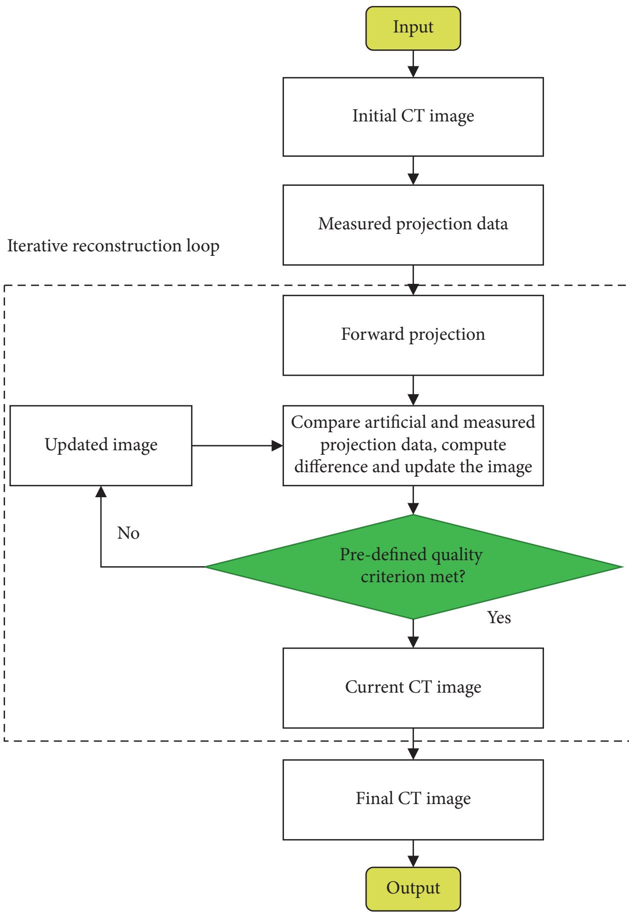

Figure 1: The flow of FBP reconstruction of CT images.

The two-dimensional continuous Fourier transform method and the corresponding Fourier transform are given as follows:

$$F(\mu,\nu)=\int_{-\infty}^{+\infty}\int_{-\infty}^{+\infty}F(t,z)e^{-j2\pi(\mu t,\nu z)}\mathrm{d}t\mathrm{d}z. \tag{3}$$

The inverse transform is as follows:

$$f(t,z)=\int_{-\infty}^{+\infty}\int_{-\infty}^{+\infty}F(\mu,\nu)e^{j2\pi(\mu t+\nu z)}\mathrm{d}\mu\mathrm{d}\nu. \tag{4}$$

In the above equation, f is a two-dimensional function; (μ,ν) represents the two-dimensional Fourier transform of the function; and the Fourier transform of projection of each angle was a straight line passing through the center of the frequency domain coordinates and finally formed a point scattering shape. The density of original points of the central segment in the plane $\varpi x-\varpi y$ was higher than that in the region farther from the origin, while the region near the origin of Fourier space was the low frequency region. Excessive weighting of low frequency components caused the image to become blurred. In order to eliminate the blurring effect, it should weight the Fourier space to make the density uniform. Therefore, a low frequency filter $|w|$ was used to suppress low frequency components and improve the clarity of the image.

The basic starting point of the R-L filter function was that the actual two-dimensional image function always had an upper frequency limit, so the filter function $|\theta|$ in frequency can be expressed as

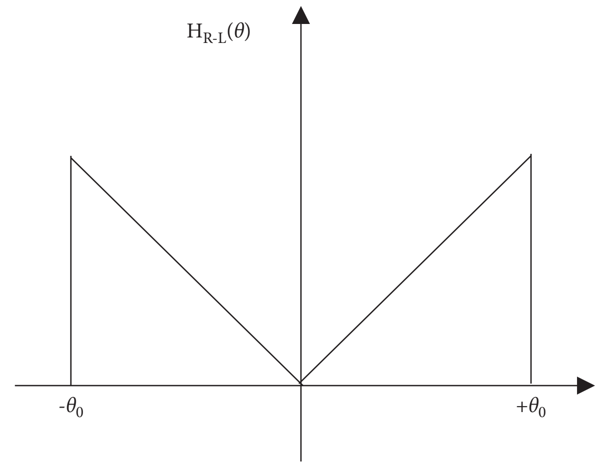

Figure 2: R-L filter function.

$$H_{R-L}(\theta)=\begin{cases}|\theta|, & |\theta|\le\theta_0,\\ 0. & \end{cases} \tag{5}$$

Its filter function is shown in Figure 2.

Then, the continuous R-L convolution function is expressed in

$$H_{R-L}(R)=\theta_0^2\left[2\mathrm{sinc}(2\theta_0R)-\mathrm{sinc}^2(\theta_0R)\right]. \tag{6}$$

The discretized R-L convolution function is shown in

$$H_{R-L}(nT)=\begin{cases}\dfrac{1}{4T^2}, & n=0,\\ 0, & \text{even number}(n),\\ -\dfrac{1}{\pi^2n^2T^2}, & \text{odd number}(n).\end{cases} \tag{7}$$

Different from the R-L filter function, the S-L filter function does not use a rectangular function to intercept the $|\theta|$ filter function in the frequency domain but uses some smoother window functions to constrain the filter function. The window function $W(\theta)$ is assumed as follows:

$$W(\theta)=\sin c\left(\frac{\theta}{2\theta_0}\right)\mathrm{rect}\left(\frac{\theta}{2\theta_0}\right). \tag{8}$$

Therefore, it could obtain that the S-L function could be expressed as follows:

$$H_{S-L}(\theta)=|\theta|\sin c\left(\frac{\theta}{2\theta_0}\right)\mathrm{rect}\left(\frac{\theta}{2\theta_0}\right). \tag{9}$$

The convolution function corresponding to the S-L filter function is expressed as follows:

$$H_{S-L}(R)=\frac{1}{2}\left(\frac{2\theta_0}{\pi}\right)^2\frac{1-4\theta_0R\sin(2\pi\theta_0R)}{1-(4\theta_0R)^2}. \tag{10}$$

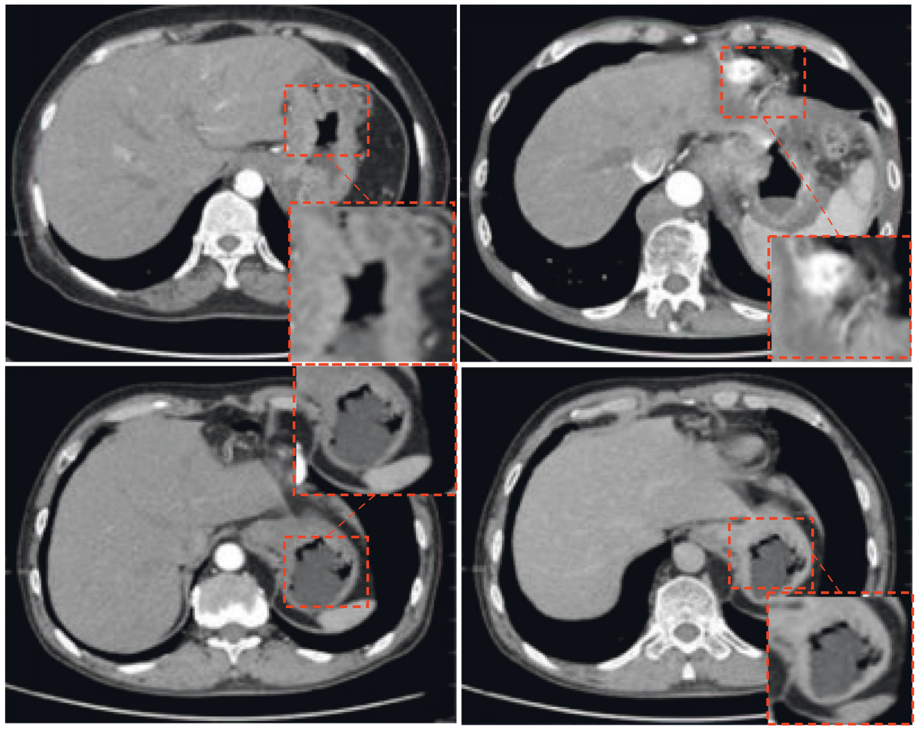

Figure 3: CT findings of four gastric cancer patients. The red marked area in the figure indicates irregular or diffuse thickening.

Its discretized convolution function is given as follows:

$$H_{S-L}(nT) = -\frac{2}{\pi^2 T^2 \left(4n^2 - 1\right)}. \tag{11}$$

2.4. Evaluation Indicators. All patients included underwent contrast-enhanced abdominal CT scans before laparoscopic-assisted distal gastrectomy. CT images of patients in the observation group underwent FBP reconstruction, and the reconstruction effect was analyzed by comparing the image quality scores.

Image quality was rated as follows: (1) the image quality was very poor, with blurred edges and large noise in structures such as the chest wall; (2) the image quality was poor, some artifacts were visible, and the diagnostic requirements cannot be met; (3) the image quality was general with low recognition; (4) the image quality was good with sharp edges; (5) the image quality was good with high recognition, and it can be used for diagnosis.

The incidence of adverse events and inflammatory response indexes of the two groups of patients were compared after surgery: serum interleukin-6 (IL-6) and tumor necrosis factor-α (TNF-α). Detection was completed according to the operation instructions of the IL-6 detection kit and the TNF-α detection kit, respectively.

2.5. Statistical Methods. SPSS 22.0 statistical software was used for data processing in this study. Measurement data were expressed as mean ± standard deviation (□$x \pm s$), and enumeration data were expressed as percentage (%). Pairwise comparisons were made using analysis of variance. The difference was statistically significant at $P < 0.05$.

3. Results

3.1. CT Manifestations of Gastric Cancer. Figure 3 shows CT images of 4 gastric cancer patients, including 2 male patients and 2 female patients, aged 52, 50, 50, and 54 years old, respectively. According to CT images of the four patients, the gastric wall of these patients was irregular or diffusely thickened, and the gastric cavity was deformed and narrowed. In addition, submucosal infiltration, thickening and sclerosis of the gastric wall, thick mucosal folds, and thinning or thickening of local blood vessels can be seen, and perigastric fat space appeared as a cord image.

3.2. The Reconstruction Effect of the CT Image Algorithm. To solve the noise and unclear image edges in conventional CT images under the premise of ensuring image quality, the initial image was reconstructed by introducing the Fourier transform method, the iterative reconstruction method, and the FBP reconstruction algorithm to compare the processing effects of different reconstruction algorithms on the image. The results are shown in Figure 4. CT reconstruction of different tumor node metastasis (TNM) stages of lung cancer suggested that CT images processed by the FBP reconstruction algorithm showed higher definition, clear edges, and no obvious noise.

3.3. Evaluation of Reconstruction Effect. Figure 5 shows the comparison results of CT images processed by the Fourier

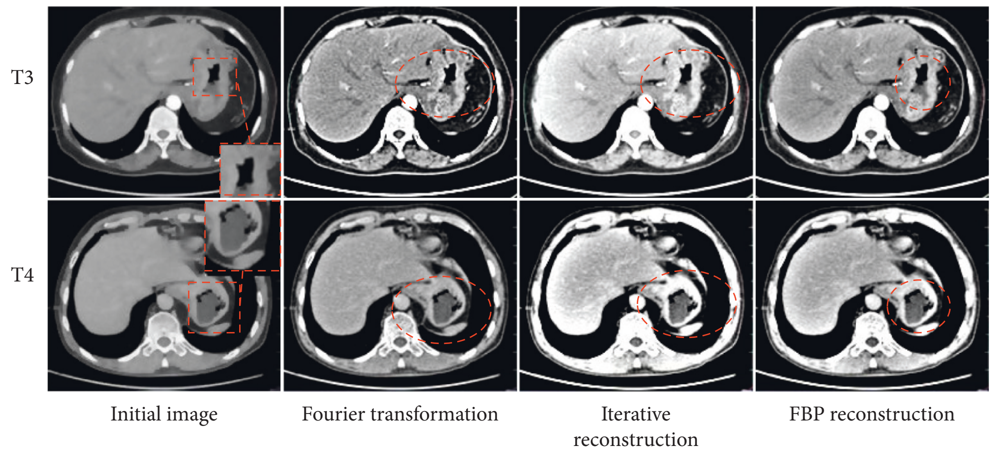

FIGURE 4: Processing effects of different algorithms. T3 and T4 represent different TNM stages. The red marked area in the figure indicates irregular or diffuse thickening.

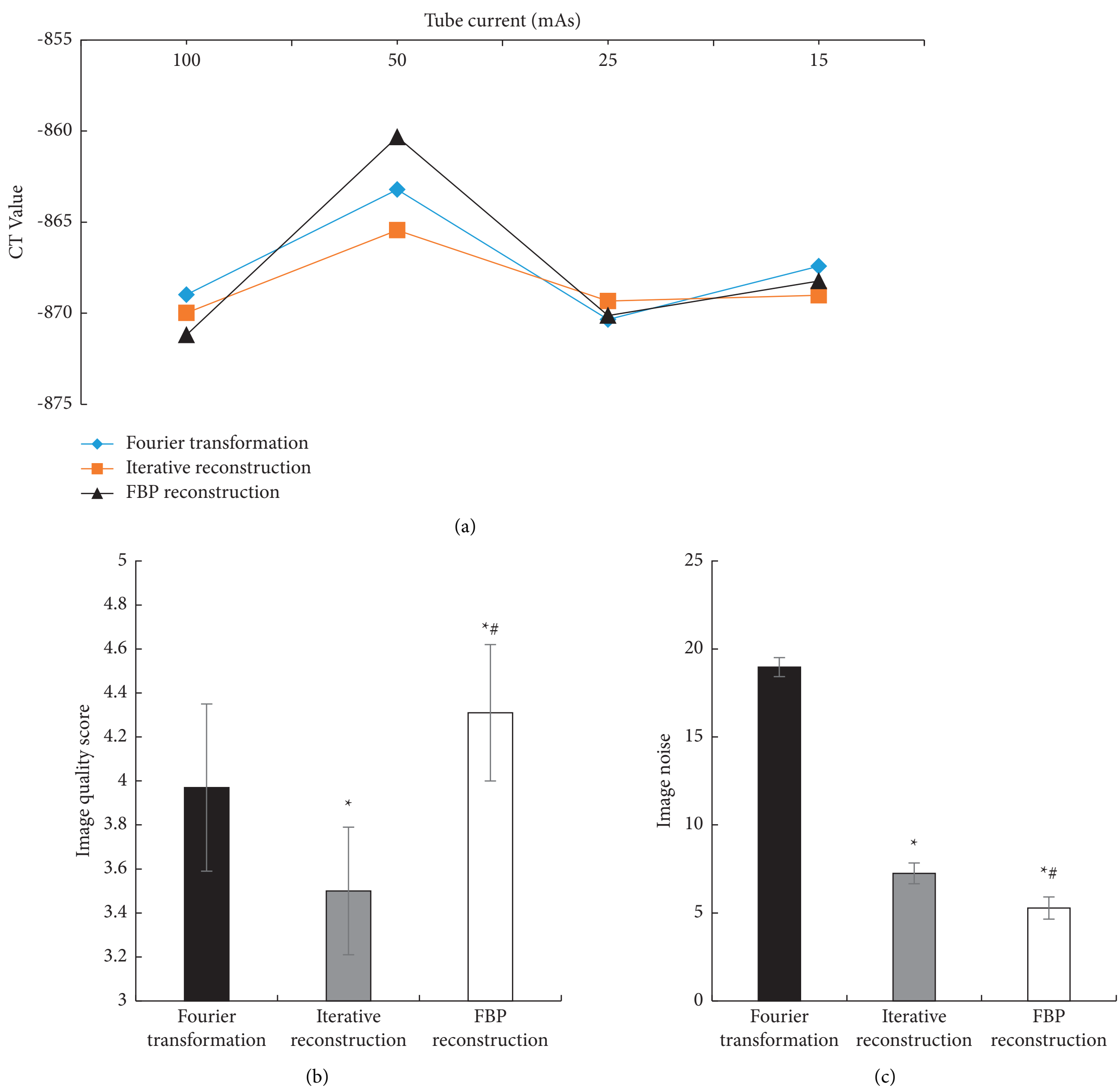

FIGURE 5: Evaluation of CT image reconstruction effect. (a) CT value. (b) Comparison of the image quality score. (c) Comparison of the image noise. ∗ meant significant difference compared with the Fourier transform method ($P < 0.05$) and # meant significant difference compared to the iterative reconstruction method ($P < 0.05$).

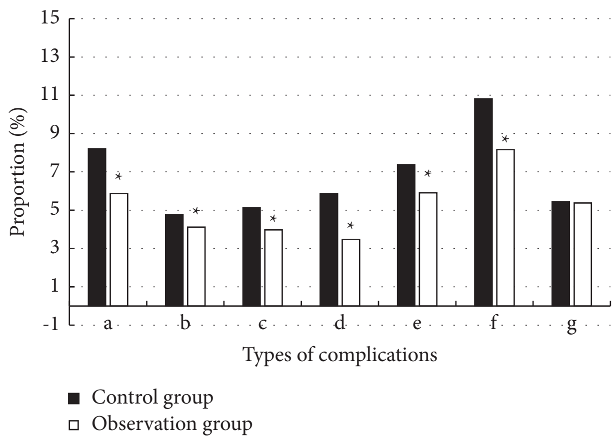

Figure 6: The incidence of postoperative adverse events in patients. (a–g) Postoperative wound infection, pulmonary infection, abdominal infection, severe abdominal pain, nausea and vomiting, gastric motility disorder, and other complications, respectively. $*$ indicates the difference was significant compared with the control group ($P < 0.05$).

transform method, the iterative reconstruction method, and the FBP reconstruction algorithm, respectively. Figure 5(a) shows the comparison of CT values of three algorithms with different tube currents. There was no statistically significant difference in CT values of three algorithms with different tube currents ($P > 0.05$), and there was no significant difference in CT values of three algorithms for the same tube current ($P > 0.05$). Figures 5(a) and 5(b) illustrate that the CT image quality score processed by the FBP reconstruction algorithm (4.31 ± 0.31) was significantly higher than that of the iterative reconstruction method (3.5 ± 0.29) and the Fourier transform method (3.97 ± 0.38) ($P < 0.05$). In addition, the CT image noise processed by the FBP reconstruction algorithm (5.28 ± 0.63) was significantly lower than that of the iterative reconstruction method (7.25 ± 0.59) and the Fourier transform method (18.97 ± 0.54) ($P < 0.05$).

3.4. Postoperative Adverse Events in Patients. After two groups of patients were treated by laparoscopic-assisted distal gastrectomy under the guidance of different CT images, the results of postoperative adverse events were compared. As illustrated in Figure 6, the more common postoperative adverse events included wound infection, abdominal pain, nausea and vomiting, gastric motility disorder, and pulmonary disorders. The incidences of gastric motility disorder and wound infection were higher. The incidence of postoperative wound infection (8.21% vs. 10.82%) and gastric motility disorder (5.88% vs. 8.16%) in the observation group were significantly lower than that in the control group ($P < 0.05$).

3.5. Changes of Postoperative Inflammatory Response Indicators in Patients. Figure 7 shows the comparison of changes in the inflammatory response indexes IL-6 and TNF-α before and after the treatment in the control group and the observation group. It demonstrates that there was no significant difference in the levels of IL-6 and TNF-α between the two groups before the treatment ($P > 0.05$). The serum levels of IL-6 and TNF-α in the observation group after the treatment (280.35 ± 15.08 ng/L, 144.32 ± 10.32 ng/L) were significantly lower than those in the control group (399.71 ± 14.19 ng/L, 165.33 ± 10.08 ng/L) ($P < 0.05$).

4. Discussion

Gastric cancer can be divided into early gastric cancer and advanced gastric cancer. Its CT has various manifestations, such as early gastric cancer is difficult to detect on CT due to its small lesions, and gastroscopic examination is required for diagnosis at this time [19]. For advanced gastric cancer, the cancer has invaded the submucosal layer and even entered the muscularis. On CT, main manifestations are localized or diffuse gastric wall thickening, the gastric wall thickening is usually uneven, and even ulcers can be seen, and the localized appearance of this cancer is rigid [20, 21]. CT can not only show changes of the gastric wall itself but it can also show the tumor's invasion to the surrounding, local or distant metastasis, such as the perigastric lymph node enlargement, ascites, thickening of the omentum and mesentery, and implanted nodules, showing a high application value in the diagnosis and the treatment of gastric cancer [22, 23]. Gastric cancer is divided into four stages according to CT manifestations. Stage I: a mass confined to the gastric cavity without metastasis or invasion to adjacent organs; stage II: the thickening of the gastric wall greater than or equal to 1 cm; stage III: gastric cancer that has invaded adjacent organs in addition to local manifestations; and stage IV: distant metastasis. Therefore, gastric cancer can be diagnosed by staging based on CT findings and then help clinicians to formulate corresponding treatment plans, so that patients can receive the most suitable treatment [24, 25]. The filtered back-projection reconstruction algorithm is developed on the basis of the back-projection method, and the image sharpness is solved by adding a filter function.

Tamura et al. [26] showed that the FBP reconstruction algorithm has fast reconstruction speed and high image quality and has become a commonly used CT image reconstruction method. CT images of gastric cancer patients

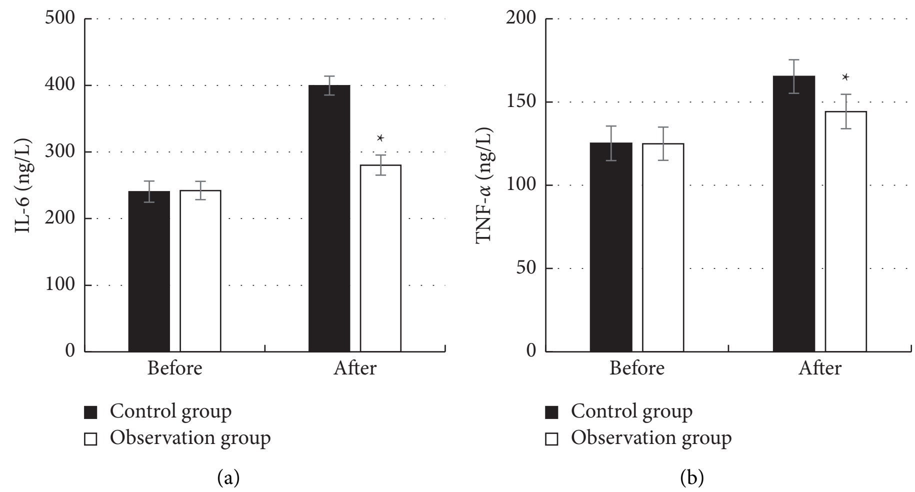

Figure 7: Comparison of inflammatory response indicators in patients: (a) comparison of the changes of IL-6 and (b) comparison of the changes of TNF-α. $*$ indicates a significant difference compared with the control group ($P < 0.05$).

were processed by introducing the Fourier transform method, the iterative reconstruction method, and the FBP reconstruction algorithm, respectively. The results showed that the CT image quality score processed by the FBP reconstruction algorithm was significantly higher than that processed by the iterative reconstruction method and the Fourier transform method ($P < 0.05$); and the CT image noise processed by the FBP reconstruction algorithm was significantly lower than that by the iterative reconstruction method and the Fourier transform method ($P < 0.05$). It is concluded that the FBP algorithm not only effectively solves the problems of large noise and unclear edges in conventional CT images but also its performance is significantly better than other algorithms. The research of Padole et al. [27] pointed out that although the iterative reconstruction algorithm was proposed earlier than filtered back-projection, it depended on the breakthrough of computer performance due to its huge computational load and slow reconstruction speed.

CT images reconstructed by the FBP algorithm were used for laparoscopic-assisted distal gastrectomy. The results showed that the incidence of postoperative surgical wound infection and gastric motility disorder in the observation group was significantly lower than that in the control group ($P < 0.05$). It may be because CT images reconstructed by the FBP algorithm better show stratification of lesions invading the gastric wall and make more accurate staging according to the degree of invasion, so as to formulate targeted treatment plans for patients, reducing the occurrence of various postoperative adverse events in patients [28, 29]. The levels of serum inflammatory response indexes IL-6 and TNF-α in the observation group after the treatment were significantly lower than those in the control group ($P < 0.05$). Similarly, reconstructed CT images helped doctors to better observe tumor metastasis in combination with images, make accurate staging diagnosis, and carry out corresponding treatment. Therefore, using it in laparoscopic-assisted distal gastrectomy for gastric cancer is of a high application value.

5. Conclusion

The results of this study found that the FBP reconstruction algorithm showed better reconstruction effect on CT images of gastric cancer; CT images based on the algorithm were helpful to formulate targeted surgical treatment plans for gastric cancer, showing a high clinical application value. However, this study only performed CT scan diagnosis and image reconstruction analysis for patients with advanced gastric cancer, and the sample sources were concentrated and lacked representativeness. Therefore, in the follow-up research, it would improve and optimize this aspect, and further analyze the reconstruction algorithm of CT images and its application value in the diagnosis and treatment of malignant tumors. In conclusion, this study could provide a reference for the early diagnosis and treatment of gastric cancer and other diseases.

Data Availability

The data used to support the findings of this study are available from the corresponding author upon request.

Conflicts of Interest

The authors declare that they have no conflicts of interest.

Acknowledgments

This work was supported by the scientific research start-up fund project of Mudanjiang Medical University (no. 2021-MYBSKY-026).

References

[1] D. Dong, L. Tang, Z.-Y. Li et al., "Development and validation of an individualized nomogram to identify occult peritoneal metastasis in patients with advanced gastric cancer," *Annals of Oncology*, vol. 30, no. 3, pp. 431–438, 2019.

[2] T. Fukagawa, "Role of staging laparoscopy for gastric cancer patients," *Annals of Gastroenterological Surgery*, vol. 3, no. 5, pp. 496–505, 2019.

[3] S. Mochizuki, L. Yamada, K. Kase et al., "A case of laparoscopic surgery for preoperatively diagnosed gastric metastasis of lung cancer," *Gan To Kagaku Ryoho*, vol. 48, no. 8, pp. 1057–1060, 2021.

[4] Z. Zhu, "Present status of preoperative staging and contemplation on preoperative precision staging for gastric cancer," *Zhonghua Wei Chang Wai Ke Za Zhi*, vol. 19, no. 2, pp. 126–131, 2016.

[5] Y. Wang, W. Liu, Y. Yu et al., "CT radiomics nomogram for the preoperative prediction of lymph node metastasis in gastric cancer," *European Radiology*, vol. 30, no. 2, pp. 976–986, 2020.

[6] K. Yoshikawa, M. Shimada, J. Higashijima et al., "Usefulness of diagnostic staging laparoscopy for advanced gastric cancer," *The American Surgeon*, vol. 26, 2021.

[7] B. Badgwell, P. Das, and J. Ajani, "Treatment of localized gastric and gastroesophageal adenocarcinoma: the role of accurate staging and preoperative therapy," *Journal of Hematology & Oncology*, vol. 10, no. 1, p. 149, 2017.

[8] E. C. Gertsen, A. S. Borggreve, H. J. F. Brenkman et al., "Evaluation of the implementation of FDG-PET/CT and staging laparoscopy for gastric cancer in The Netherlands," *Annals of Surgical Oncology*, vol. 28, no. 4, pp. 2384–2393, 2021.

[9] D. Takahashi, K. Hara, M. Tanabe et al., "[A case of remnant gastric necrosis after laparoscopy-assisted distal gastrectomy]," *Gan To Kagaku Ryoho*, vol. 48, no. 10, pp. 1281–1283, 2021.

[10] Z.-Q. Sun, S.-D. Hu, J. Li, T. Wang, S.-F. Duan, and J. Wang, "Radiomics study for differentiating gastric cancer from gastric stromal tumor based on contrast-enhanced CT images," *Journal of X-Ray Science and Technology*, vol. 27, no. 6, pp. 1021–1031, 2020.

[11] Q. Z. Gai, X. L. Li, N. Li, L. Li, Z. Meng, and A. F. Chen, "Clinical significance of multi-slice spiral CT, MRI combined with gastric contrast-enhanced ultrasonography in the diagnosis of T staging of gastric cancer," *Clinical and Translational Oncology*, vol. 23, no. 10, pp. 2036–2045, 2021.

[12] E. C. Gertsen, C. de Jongh, H. J. F. Brenkman et al., "The additive value of restaging-CT during neoadjuvant chemotherapy for gastric cancer," *European Journal of Surgical Oncology*, vol. 46, no. 7, pp. 1247–1253, 2020.

[13] B. Shi, H. Lin, M. Zhang, W. Lu, Y. Qu, and H. Zhang, "Gene regulation and targeted therapy in gastric cancer peritoneal metastasis: radiological findings from dual energy CT and PET/CT," *Journal of Visualized Experiments*, vol. 17, no. 131, Article ID 56526, 2018.

[14] D. Tsurumaru, Y. Nishimuta, T. Muraki et al., "Gastric cancer with synchronous and metachronous hepatic metastasis predicted by enhancement pattern on multiphasic contrast-enhanced CT," *European Journal of Radiology*, vol. 108, pp. 165–171, 2018.

[15] K. Nakajo, A. Chonan, R. Tsuboi et al., "A case of a glomus tumor of the stomach resected by laparoscopy endoscopy cooperative surgery," *Nihon Shokakibyo Gakkai zasshi = The Japanese journal of gastro-enterology*, vol. 113, no. 9, pp. 1557–1563, 2016.

[16] M. J. Willemink and P. B. Noël, "The evolution of image reconstruction for CT-from filtered back projection to artificial intelligence," *European Radiology*, vol. 29, no. 5, pp. 2185–2195, 2019.

[17] C. T. Quiñones, J. M. Létang, and S. Rit, "Filtered backprojection reconstruction for attenuation proton CT along most likely paths," *Physics in Medicine and Biology*, vol. 61, no. 9, pp. 3258–3278, 2016.

[18] R. N. Southard, D. M. E. Bardo, M. H. Temkit, M. A. Thorkelson, R. A. Augustyn, and C. A. Martinot, "Comparison of iterative model reconstruction versus filtered back-projection in pediatric emergency head CT: dose, image quality, and image-reconstruction times," *American Journal of Neuroradiology*, vol. 40, no. 5, pp. 866–871, 2019.

[19] J. H. Park, B. Kim, M. S. Kim et al., "Comparison of filtered back projection and iterative reconstruction in diagnosing appendicitis at 2-mSv CT," *Abdominal Radiology*, vol. 41, no. 7, pp. 1227–1236, 2016.

[20] C. Kim, K. Y. Lee, C. Shin et al., "Comparison of filtered back projection, hybrid iterative reconstruction, model-based iterative reconstruction, and virtual monoenergetic reconstruction images at both low- and standard-dose settings in measurement of emphysema volume and airway wall thickness: a CT phantom study," *Korean Journal of Radiology*, vol. 19, no. 4, pp. 809–817, 2018.

[21] Z. Deák, J. M. Grimm, M. Treitl et al., "Filtered back projection, adaptive statistical iterative reconstruction, and a model-based iterative reconstruction in abdominal CT: an experimental clinical study," *Radiology*, vol. 266, no. 1, pp. 197–206, 2013.

[22] J. E. Lee, S.-Y. Choi, J. A. Hwang et al., "The potential for reduced radiation dose from deep learning-based CT image reconstruction," *Medicine*, vol. 100, no. 19, p. e25814, 2021.

[23] L. Solaini, M. Bencivenga, A. D'ignazio et al., "Which gastric cancer patients could benefit from staging laparoscopy? A GIRCG multicenter cohort study," *European Journal of Surgical Oncology*, vol. S0748-7983, no. 22, pp. 00046–54, 2022.

[24] A. B. J. Borgstein, M. I. van Berge Henegouwen, W. Lameris, W. J. Eshuis, and S. S. Gisbertz, "Staging laparoscopy in gastric cancer surgery. A population-based cohort study in patients undergoing gastrectomy with curative intent," *European Journal of Surgical Oncology*, vol. 47, no. 6, pp. 1441–1448, 2021.

[25] E. C. Gertsen, H. J. F. Brenkman, R. van Hillegersberg et al., "18F-Fludeoxyglucose-Positron emission tomography/computed tomography and laparoscopy for staging of locally advanced gastric cancer," *JAMA Surgery*, vol. 156, no. 12, Article ID e215340, 2021.

[26] A. Tamura, E. Mukaida, Y. Ota, M. Kamata, S. Abe, and K. Yoshioka, "Superior objective and subjective image quality of deep learning reconstruction for low-dose abdominal CT imaging in comparison with model-based iterative reconstruction and filtered back projection," *British Journal of Radiology*, vol. 94, no. 1123, Article ID 20201357, 2021.

[27] A. Padole, S. Singh, J. B. Ackman et al., "Submillisievert chest CT with filtered back projection and iterative reconstruction techniques," *American Journal of Roentgenology*, vol. 203, no. 4, pp. 772–781, 2014.

[28] R. Tozzi, Z. Traill, G. Valenti, F. Ferrari, K. Gubbala, and R. G. Campanile, "A prospective study on the diagnostic pathway of patients with stage IIIC-IV ovarian cancer: exploratory laparoscopy (EXL) + CT scan VS. CT scan," *Gynecologic Oncology*, vol. 161, no. 1, pp. 188–193, 2021.

[29] Z. Y. Qian, Y. Wen, G. C. Lou et al., "Preliminary application of endoscopic titanium clip localization combined with three-dimensional CT reconstruction in the determination of resection margin of gastric central cancer under laparoscopy," *Zhonghua Wai Ke Za Zhi*, vol. 57, no. 10, pp. 38–43, 2019.

Hindawi
Contrast Media & Molecular Imaging
Volume 2022, Article ID 3936655, 9 pages
https://doi.org/10.1155/2022/3936655

Research Article

Intelligent Algorithm-Based MRI Image Features for Evaluating the Effect of Nursing on Recovery of the Neurological Function of Patients with Acute Stroke

Ding Wang [1,2] and Jingwei Dai [1,2]

[1] *Department of Neurosurgery, Shengjing Hospital of China Medical University, Liaoning 110000, Shenyang, China*
[2] *Third Department of Neurology Ward, Shengjing Hospital Affiliated to China Medical University, Liaoning 110000, Shenyang, China*

Correspondence should be addressed to Jingwei Dai; 202111114811042@zcmu.edu.cn

Received 4 March 2022; Revised 11 May 2022; Accepted 17 May 2022; Published 31 May 2022

Academic Editor: M. Pallikonda Rajasekaran

The aim of this study is to analyze the application of early rehabilitation nursing in nursing intervention of neurological impairment among patients with acute ischemic stroke. 116 patients with acute ischemic stroke were selected as the research subjects in this paper. The patients were divided into 58 experimental (early rehabilitation care) and 58 control (routine rehabilitation care) groups according to the difference of care protocols, all of which were performed magnetic resonance imaging on. An image resolution reconstruction algorithm on the basis of deep convolutional neural network is proposed for MRI image processing. The results show that peak signal to noise ratio (PSNR) and structural similarity index measure (SSIM) of the included algorithm were remarkably greater than those of compressed sensing (CS) algorithm and nonlocal similarity and block low rank prior-based NSBL algorithm. Running time was shorter than that of the latter two algorithms ($P < 0.05$). The neurological impairment scores of patients in the experimental group 3 and 5 weeks after treatment were obviously lower than those of patients in the control group ($P < 0.05$). The Barthel indexes of patients in the experimental group 3 and 5 weeks after treatment were obviously higher than those of patients in the control group ($P < 0.05$). FugI-Meyer assessment (FMA) and Disability of Arm-Shoulder-Hand (DASH) scores of patients in the experimental group 3 and 5 weeks after treatment were obviously lower than those of patients in control group ($P < 0.05$). The results show that the deep learning algorithm for MRI image processing performance is better than the traditional algorithm. It not only improves the image quality but also improves the processing efficiency. Early rehabilitation nursing and routine rehabilitation nursing can effectively improve the neurological deficit symptoms, limb motor function, and daily living ability of patients with acute ischemic stroke, and the effect of early rehabilitation nursing is the best.

1. Introduction

Acute stroke is due to various reasons that lead to blood supply disorders in local brain tissue, leading to ischemia and hypoxia in brain tissue and necrosis, resulting in corresponding symptoms and signs. It is a disease with high incidence, high recurrence rate, high death rate, high disability rate, and many complications. The common symptoms include weakness, numbness, or paralysis on one side or upper and lower limbs, weakness, numbness or paralysis on the face, blurred vision on one or both eyes, difficulty in language expression, dizziness, imbalance, and headache [1–3]. After treatment, about 70% of stroke patients have varying degrees of dysfunction. The severity of dysfunction depends on the damage to the brain structure [4, 5]. Clinical treatment of stroke mainly includes intravenous thrombolysis, vascular interventional therapy, antiplatelet anticoagulation and expansion, and improvement of cerebral vascular circulation. Conservative treatment and surgical treatment are also considered for acute stroke [6]. Statistics show that China has become one of the countries with the highest incidence of stroke. Its annual economic losses have reached more than 40 billion yuan [7]. Each year, the number of new patients reaches more than 2 million, of which ischemic stroke accounts for 70%. About 70%–80% of ischemic stroke patients lead to disability and cannot live independently [8]. With the aging of population, the development of the economic level and the change of lifestyle, the intervention of early nursing and rehabilitation therapy for patients with ischemic stroke is particularly important, so it is necessary to discuss.

Neuroimaging plays an important role in acute stroke. For example, to determine or exclude the diagnosis of cerebrovascular disease (ischemic or hemorrhagic) and to provide evidence of possible stroke pathogenesis (embolism, hemodynamics, etc.). Through the size and location of the lesion and vascular state, we provide important information about the prognosis and so on [9–11]. CT examination can be used as an accurate screening method. The differential point is that clinicians collect medical history and preliminarily determine that patients are involved in stroke after physical examination. Therefore, head CT is used in the first screening, which has the advantages of short time consumption and low cost [12]. MRI is superior to CT in differentiating acute ischemic stroke. The latest TTA report of the American Society of Neurology points out that DWI is determined to be useful for the diagnosis of acute ischemic stroke within 12 h of onset and should be more useful than nonenhanced CT [13, 14]. In addition, multiparameter MRI may prolong the treatment time window. The basis is the understanding of individual pathophysiological processes. MRI is used to identify patients most likely to benefit from treatment (those with ischemic penumbra or risk tissue) and those most likely to have complications (such as hemorrhagic transformation, malignant infarction) [15]. In clinical practice, due to the limitation of acquisition time, patient comfort, image signal-to-noise ratio, and other factors, it is often difficult to obtain ideal high-resolution magnetic resonance images. It is easy to affect the doctor's objective judgment [16]. At present, with the rapid development of deep learning, deep networks for image super-resolution problems emerge endlessly and have achieved very good results. Super-resolution (SR) reconstruction technology can reconstruct images with high resolution from low-resolution images, which has broad application prospects in the field of magnetic resonance. However, the traditional SR method belongs to supervised learning, which requires specific training data for image reconstruction with poor reconstruction effects.

In summary, the nursing treatment of neurological deficit symptoms in stroke patients still needs further discussion. This study selects 116 patients with acute ischemic stroke as the research subject. According to different nursing schemes, the patients were divided into 58 cases of experimental group (early rehabilitation nursing) and 58 cases of control group (routine rehabilitation nursing). All patients underwent MRI examination. An image resolution reconstruction algorithm on the basis of deep learning is proposed for MRI image processing. The therapeutic effect of early nursing rehabilitation on patients was comprehensively evaluated by comparing the neurological deficit symptoms, limb motor function, and daily living ability scores of the two groups before and after treatment.

2. Materials and Methods

2.1. Research Subjects. In this study, 116 patients with acute ischemic stroke admitted to hospital from June 1, 2019 to February 1, 2021 were selected as subjects. There were 72 males and 44 females aged 48–71 years. This study has been approved by the ethics committee of hospital. The family members of the patients signed the informed consent.

2.1.1. Inclusion Criteria. The inclusion criteria were as follows: (1) to meet the diagnostic criteria of cerebral infarction determined by the Fourth National Cerebrovascular Disease Conference in 1995. (2) Patients who have signed the informed consent. (3) Patients with lateral limb dysfunction. (4) Patients with limb muscle strength less than or equal to grade IV. (5) Patients with stable life weight. (6) Patients those who were willing to participate in rehabilitation training.

2.1.2. Exclusion Criteria. The exclusion criteria were as follows: (1) Patients with subarachnoid hemorrhage. (2) Patients with intracranial venous thrombosis. (3) Patients with severe pulmonary infection. (4) Patients with liver and kidney diseases, heart diseases, and other important organ damage. (5) Patients with limb muscle strength less than or equal to grade IV. (6) Patients with cognitive impairment. (7) Patients with neurological or musculoskeletal diseases affecting functional recovery.

2.2. Case Grouping and Nursing. According to different nursing schemes, the patients were divided into 58 cases of the experimental group (early rehabilitation nursing) and 58 cases of the control group (routine rehabilitation nursing).

Two groups of patients were responsible for rehabilitation training. Training began after the condition was stable and neurological symptoms were stable. Specific steps were as follows: (1) Teaching patients to make limbs in functional position. Family members and nursing staff adopted the correct posture for counseling: affected side position > healthy side position > supine position. Guide the patient to turn over every 2 hours and take back count. Avoid forming abnormal patterns of upper limb flexion, lower limb extension, and foot sag varus. (2) The hands and fingers crossed and held each other. The thumbs of the affected side were placed above, and the healthy limbs were used to drive the diseased limbs. Then, slowly put down the arms and placed in front of the abdomen. Upper limb joint activities include finger nose, lateral lifting, lower limb flexion brace bed hip lifting, namely, bridge movement. (3) Patients were encouraged to sit for training as early as possible after their condition stabilized. According to the patient' s muscle strength, patients should take the initiative as much as possible. Methods of family protection: the patient was moved laterally to the bedside, and the affected leg was

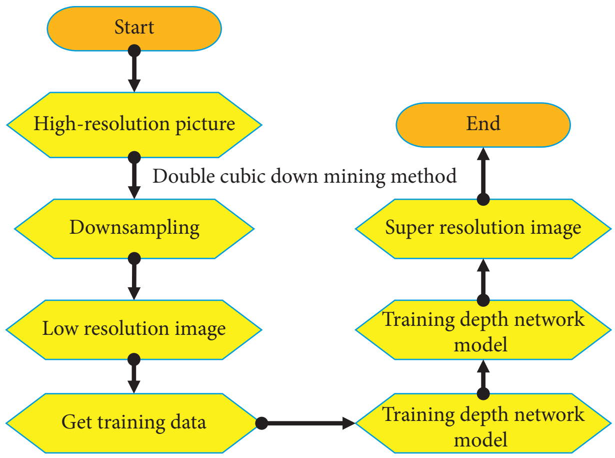

Figure 1: Conventional super-resolution image reconstruction method.

hooked with a healthy leg to move out of the bed, making the affected knee buckled to the bedside. Then, the body rotates to the affected side, and the healthy hand crosses the body. At the same time, the healthy arm strength pushed the bed to sit up. When the torso had certain control ability, it can gradually let the patient use the healthy hand to assist the patient to picked up or dropped the object. Then, gradually put out to increase the difficulty of sitting training. (4) Lower limb muscle strength grade 3 and above for standing training. When standing training, the therapist's protection method was as follows: the upper limbs forward, head and trunk forward, the center of gravity moved between the feet. Then, raise the patient's hips and knees were gradually stretched and made to stand up. The patient held the parallel bars by hand, gradually increased the time and tried to shift the center of gravity to the affected side. Moreover, gradually increased the standing balance training. (5) With the increase of lower limb weight-bearing muscle strength, walking training can be gradually carried out. Then, gradual transition to across different obstacles and stairs walking training was given. It mainly increases brain blood supply, activates brain cells, and improves local muscle spasm, twitch, and incomplete paralysis so as to improve muscle strength and motor function. The above rehabilitation exercise treatment was carried out every 20–30 min, 2-3 times a day, 4-5 days a week. Rehabilitation exercise therapy lasted 3 months.

Both groups were given drug treatment at the same time. Drug therapy was conducted in accordance with acute ischemic cerebrovascular disease diagnosis and treatment guidelines. Basic medications include aspirin, ginkgo dipyridamole, and edaravone.

2.3. MRI Examination. The patients were examined by 3.0 T superconducting magnetic resonance scanning, and the 12 - channel phased array head coil was used. Gradient echo sequence of magnetization preparation, scanning parameters were as follows: TE 900 ms, TR 2,200 ms, FOV $256 \times 256 \times 150$, 1 mm voxel collection. Planar echo imaging sequence, scanning parameters were as follows: TE 40 ms, TR 3,000 ms, FOV 215×215, 2 mm voxel acquisition, inversion angle 90°, scanning time 320 s. Finally, the obtained image data was input to the workstation for enhancement processing.

2.4. Deep Convolutional Neural Network (CNN)-Based Image Resolution Reconstruction Algorithm. With the rapid development of deep learning, deep networks for image super-resolution problems emerge in endlessly and have achieved very good results. However, most super-resolution methods on the basis of deep learning belong to supervised learning, which limits the reconstruction process to specific training data. The basic framework of these methods is illustrated in Figure 1. The specific downsampling method was used to process the high-resolution images to obtain the corresponding low-resolution image, and then the corresponding training data were collected. A deep network model was trained. Then, the low-resolution image to be tested was input into the model to obtain the reconstructed super-resolution image.

The purpose of super-resolution reconstruction is to recover high-resolution images from low-resolution images. Set the low-resolution image to P, which can be expressed as follows:

$$P_x = C\left(P_y; \theta\right). \tag{1}$$

where C represents the degradation process function, P_y represents the high-resolution image, θ represents the degradation process parameters. Then, the downsampling operation can be expressed as follows:

$$C\left(P_y; \theta\right) = \left(P_y\right)\downarrow_r, \tag{2}$$

$\downarrow_r$ represents the downsampling operation of r, and $\{r\} \in \theta$. In general, low-resolution images are obtained by bicubic anti-aliasing reduction of high-resolution images, so the degradation process can also be expressed as follows:

$$C\left(P_y; \theta\right) = \left(P_y \otimes \beta\right)\downarrow_r + u_\tau, \tag{3}$$

where β represents fuzzy kernel, $P_y \otimes \beta$ represents convolution operation between high-resolution image and fuzzy kernel, and u_τ represents Gaussian white noise. The objective function of super-resolution reconstruction can be expressed as follows:

$$\alpha * = \arg\min_{\alpha} \operatorname{loss}\left(P_y *, P_y\right) + \eta\Phi(\alpha), \tag{4}$$

where $\operatorname{loss}(P_y *, P_y)$ represents the loss function and $\Phi(\alpha)$ represents the regularization term. The above supervised image super-resolution algorithm can obtain good results. But a lot of paired training data are needed to train the network. For magnetic resonance imaging, which is limited by hardware conditions, it is difficult to obtain such data sets. Therefore, this paper regards super-resolution image reconstruction as an ill-posed inverse problem, that is, low-resolution images correspond to multiple different high-resolution images. Considering the actual operation process, image quality will be affected by many aspects. For example, the motion artifacts caused by the movement of the subjects in the data acquisition process, the black band artifacts caused by the inhomogeneity of the magnetic field, and the noise caused by the current fluctuation in the circuit, etc. So, introducing these factors into image degradation model can be expressed as follows:

$$P_L = C_{\mathrm{down}} T_H + \chi, \tag{5}$$

where P_L represents a low-resolution image, T represents degradation function, C_{down} represents the downsampling operator, and χ represents noise.

In magnetic resonance imaging, the degradation function can be seen as a part of the k-space center of the original high-resolution magnetic resonance image that intercepts the corresponding proportion. Therefore, a low-resolution magnetic resonance image is given to recover the image version as similar as the real collected high-resolution image. This study reconstructs super-resolution images by minimizing the following loss functions:

$$P_H^* = \arg\min P_H \left\| P_L - C_{\mathrm{down}} T_H \right\|, \tag{6}$$

where P_H^* represents the reconstruction of high-resolution images. The above formulation often leads to an unstable solution. So, it is necessary to give a suitable regularization term to limit the range of solution space, then the model can be updated to as follows:

$$P_H^* = \arg\min P_H \left\| P_L - C_{\mathrm{down}} T_H \right\|^2 + \eta \left\| P_H - l_0 e^{-\left(\mathrm{TIME}/P_\sigma\right)} \right\|^2. \tag{7}$$

TIME represents the spin locking time, l_0 represents the magnetization in equilibrium state, and P_σ represents the parameters to be fitted. The weighted images collected at different spin locking times were fitted by the second exponential decay model. $\arg\min P_H \| P_L - C_{\mathrm{down}} T_H \|^2$ ensures data consistency. $\| P_H - l_0 e^{-\left(\mathrm{TIME}/P_\omega\right)} \|^2$ ensures model consistency. Since the purpose of network learning is to learn the mapping from low-resolution images to high-resolution images, the above can also be expressed as follows:

$$P_H^* = \arg\min P_H \left\| P_L - \left(C_{\mathrm{down}} T\right)^{-1} P_L \right\|^2 + \eta \left\| P_H - l_0 e^{-\left(\mathrm{TIME}/P_\omega\right)} \right\|^2 P_\sigma, \tag{8}$$

where $\left(C_{\mathrm{down}} T\right)^{-1}$ represents the combination of the recovery operator and the sampling on the image.

2.5. Image Quality Assessment Indicators. In this study, peak signal-to-noise ratio (PSNR) [17] and structural similarity (SSIM) [18] are used as two parameters to evaluate image quality.

PSNR can be defined by the maximum pixel value and mean square error between images, which can be expressed as follows:

$$PSNR = 10 * \log_{10}\left(\frac{K^2}{(1/M)\left(\sum_{i=1}^{M}\left(P(i) - P^*(i)^2\right)\right)}\right). \tag{9}$$

where M represents pixels, P^* represents the reconstructed image, and P represents the original image.

SSIM is used to measure the structural similarity between images. The evaluation criteria are based on the brightness, contrast, and structure of the image, which can be expressed as follows:

$$\begin{aligned} \mathrm{SSIM} &= \left[R_1\left(P, P^*\right)\right]^a \left[R_2\left(P, P^*\right)\right]^b \left[R_3\left(P, P^*\right)\right]^c, \\ R_1\left(P, P^*\right) &= \frac{\left(2 \upsilon_P \upsilon_{P*} + R_0\right)}{\left(\upsilon_P^2 + \upsilon_{P*}^2 + R_0\right)}, \\ R_2\left(P, P^*\right) &= \frac{\left(2 \varsigma_P \varsigma_{P*} + R_{01}\right)}{\left(\varsigma_P^2 + \varsigma_{P*}^2 + R_{01}\right)}, \end{aligned} \tag{10}$$

where υ_P represents image brightness and ς_P represents contrast ratio.

2.6. Observation Indicators. The general data (age, gender, course of disease) of the two groups were recorded. The functional indexes before treatment, 3 weeks after treatment, and 5 weeks after treatment were recorded. The method suggested by National Institutes of Health Stroke (NIHSS) was used to assess the degree of neurological deficits. Activities of daily living were assessed by the modified Barthel Index (MBI). FugI-Meyer Assessment (FMA) was used to assess limb motor function. The DASH (disability of Arm-Shoulder-Hand) scale was used to score the patients before and after treatment [19].

2.7. Statistical Methods. The data in this study were analyzed by SPSS19.0. The measurement data are expressed as mean ± standard deviation ($\pm s$). Count data are expressed as percentage (%). One-way ANOVA was used for pairwise comparison. The difference was statistically significant with $P < 0.05$.

3. Results

3.1. Algorithm Performance Display. The MRI image reconstruction algorithm based on compressed sensing (CS) [20], the MRI image reconstruction algorithm based on nonlocal similarity and block low rank prior (NSBL) [21] are introduced, and compared with the algorithms designed in this study. It can be seen from the actual MRI image reconstruction (Figure 2) that the overall quality of the original image is poor, there are more artifacts and noises, and the resolution is low, and the clarity is obviously not enough. After the three algorithms, the quality has been significantly improved. Among them, the algorithm in this study has the best re-effect on MRI images, the clarity has been significantly improved, and the artifacts and noise have been greatly reduced.

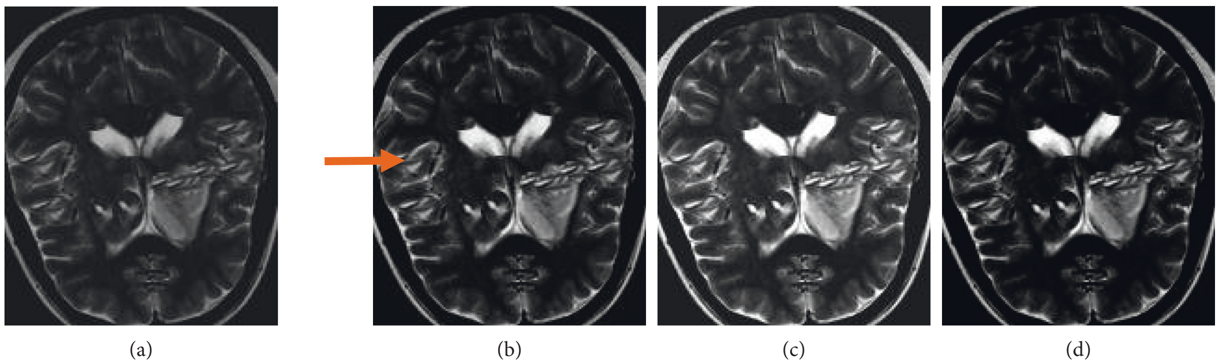

Figure 2: Performance of the algorithm. (a) is the original image, (b) is the image reconstruction for CS algorithm, (c) is the NSBL algorithm to reconstruct the image, and (d) is the reconstruction of images for the algorithm.

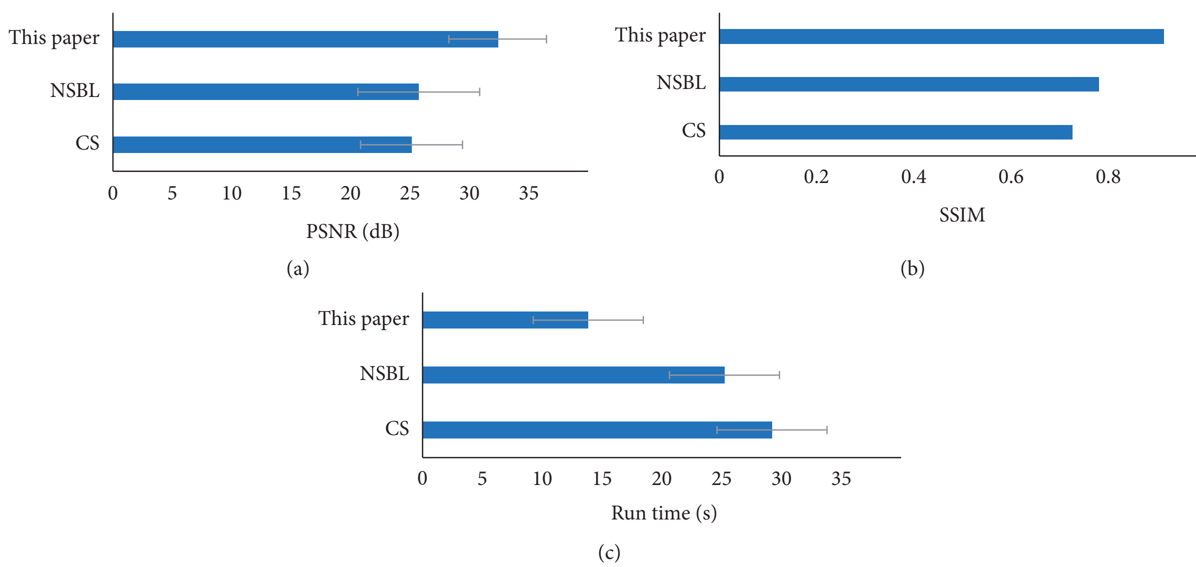

Figure 3: Quantitative analysis of algorithm performance. (a) is PSNR; (b) is SSIM; and (c) is the running time. * Compared with the proposed algorithm, $P < 0.05$.

From the quantitative data results (Figure 3), the PSNR and SSIM of the proposed algorithm are significantly greater than those of the CS algorithm and the NSBL algorithm. The difference was statistically significant ($P < 0.05$). The running time of the proposed algorithm is significantly shorter than that of the CS algorithm and NSBL algorithm. The difference was statistically significant ($P < 0.05$).

3.2. Comparison of Basic Data between the Two Groups of Patients. The basic data of the two groups were compared (Figure 4). There was no significant difference in age, gender, course of disease, location of disease (left hemisphere, right hemisphere, brainstem), and degree of nerve deficit (mild, moderate, and severe) between the two groups ($P > 0.05$).

3.3. MRI Imaging Data of Patients. As illustrated in Figure 5, the patient was a 59-year-old woman. The patient was treated for weakness and rigidity of the right lower limb. ADC map showed the low-signal region at the right parietal-occipital junction, FLAIR image showed a high signal in the corresponding region, T1WI showed a low signal in the corresponding region, and T1-enhanced scan showed brain parenchyma enhancement in the affected region.

Figure 6 reveals that the patient is a 70-year-old male. DWI displayed the low-signal region of the right occipital lobe, and the high signal edge was visible around it. This may be caused by the T2 penetration effect. The ADC map revealed a high signal in the corresponding region, SWI revealed the results of right occipital lobe hemorrhage, and T2WI revealed a high signal in the corresponding region of right occipital lobe.

3.4. Neurological Deficit Scores of the Two Groups before and after Treatment. Figure 7 shows that the difference in neurological deficit scores between the two groups before treatment was not statistically significant ($P > 0.05$). The neurological deficit scores of the two groups at 3 and 5 weeks after treatment were significantly lower than those before treatment, and the difference was statistically significant ($P < 0.05$). The neurological deficit score of the experimental

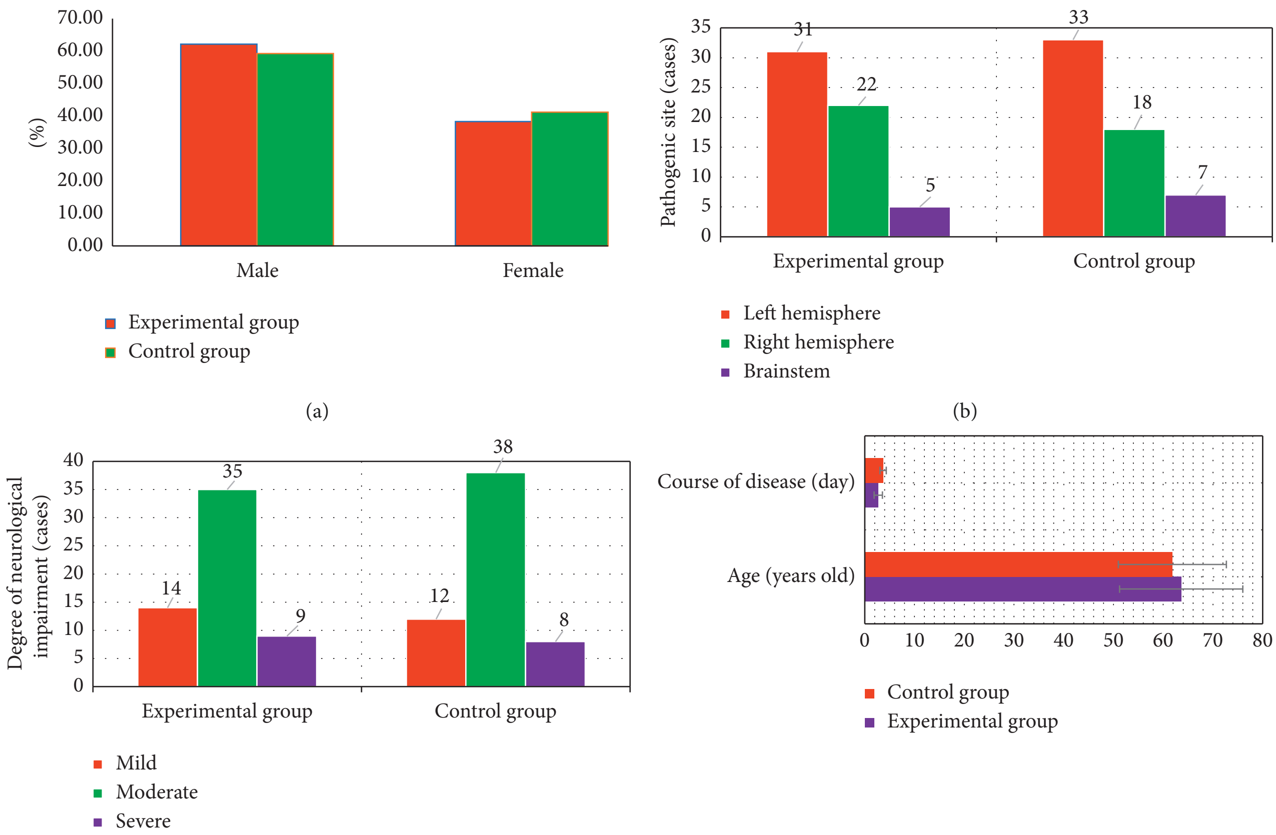

FIGURE 4: Comparisons of the data of the two groups. (a) is gender; (b) is the location of the disease; (c) is the degree of neurological deficit; and (d) is the age and course of disease. * Compared with the proposed algorithm, $P < 0.05$.

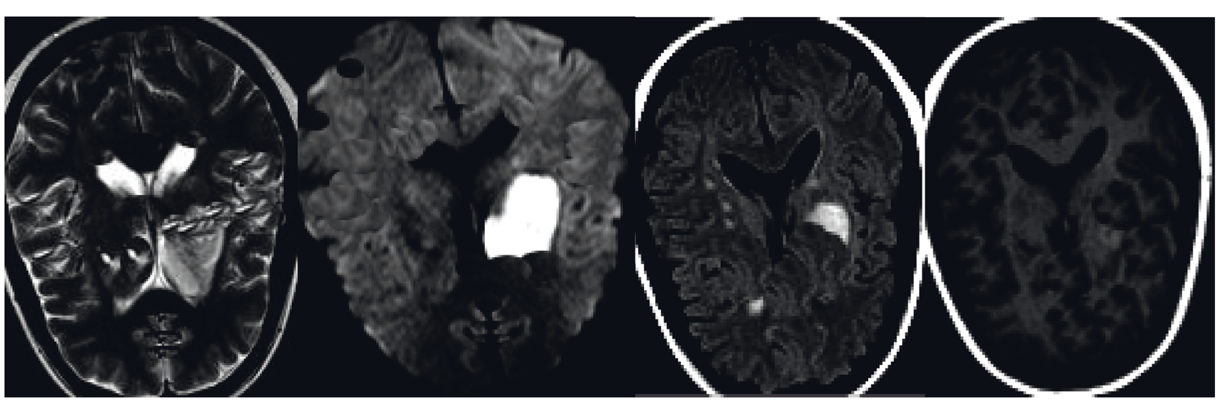

FIGURE 5: MRI images of early acute ischemic stroke.

group was significantly lower than that of the control group at 3 and 5 weeks after treatment, and the difference was statistically significant ($P < 0.05$).

3.5. Comparison of the Barthel Index before and after Treatment between the Two Groups. Figure 8 shows that the difference in the Barthel index between the two groups before treatment was not statistically significant ($P > 0.05$). The Barthel index of the two groups at 3 and 5 weeks after treatment was significantly higher than that before treatment, and the difference was statistically significant ($P < 0.05$). The Barthel index of the experimental group was significantly higher than that of the control group at 3 and 5 weeks after treatment, and the difference was statistically significant ($P < 0.05$).

3.6. Comparison of Motor Function Scores between the Two Groups before and after Treatment. Figure 9 shows that the

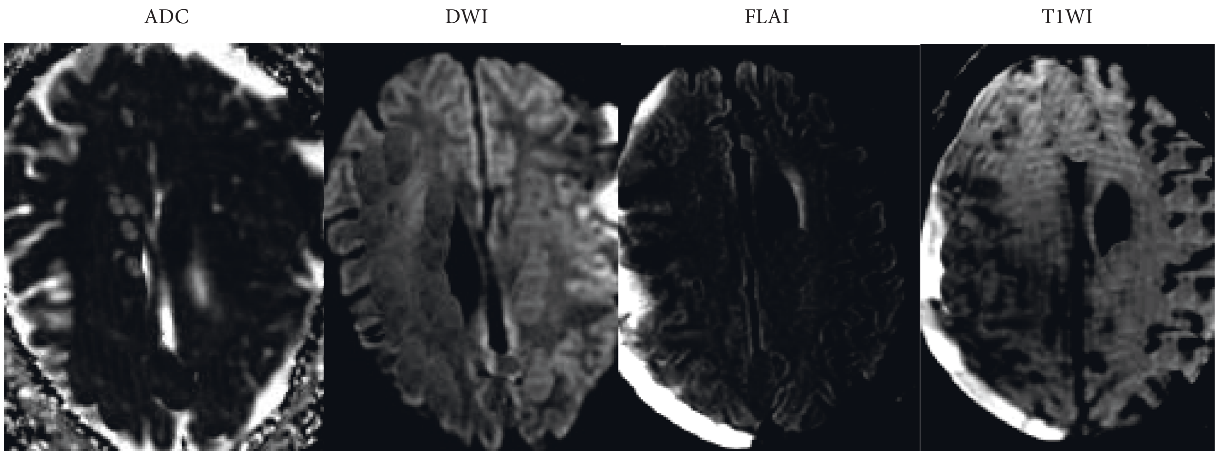

Figure 6: MRI images of early ischemic stroke in the subacute phase.

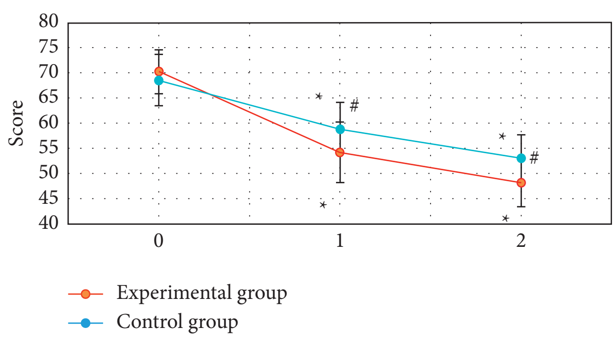

Figure 7: Two groups of patients before and after treatment neurological deficit score 0 is before treatment; 1 is three weeks after treatment; and 2 is five weeks after treatment. $^{\#}$Compared with that before treatment, $P < 0.05$; #compared with the experimental group, $P < 0.05$.

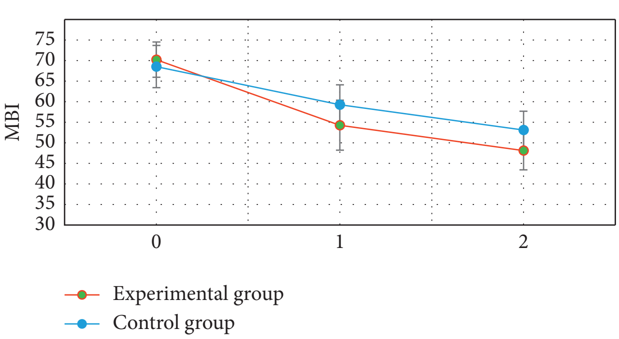

Figure 8: Barthel index of two groups before and after treatment. 0 is before treatment; 1 is three weeks after treatment; and 2 is 5 weeks after treatment. * Compared with that before treatment, $P < 0.05$; $^{\#}$compared with the experimental group, $P < 0.05$.

FMA difference between the two groups before treatment was not statistically significant ($P > 0.05$). FMA of the two groups at 3 and 5 weeks after treatment was significantly lower than that before treatment, and the difference was statistically significant ($P < 0.05$). FMA of the experimental group at 3 and 5 weeks after treatment was significantly lower than that of the control group, and the difference was statistically significant ($P < 0.05$).

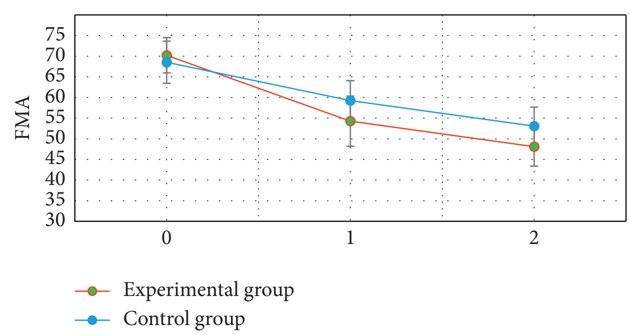

Figure 9: FMA scores of two groups before and after treatment. 0 is before treatment. 1 is three weeks after treatment. 2 is 5 weeks after treatment. * Compared with that before treatment, $P < 0.05$; $^{\#}$compared with the experimental group, $P < 0.05$.

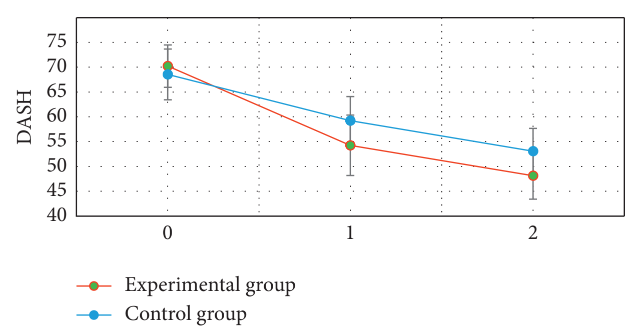

Figure 10: DASH scores of two groups before and after treatment. 0 is before treatment. 1 is three weeks after treatment. 2 is 5 weeks after treatment. * Compared with that before treatment, $P < 0.05$; $^{\#}$compared with the experimental group, $P < 0.05$.

3.7. Comparison of DASH between the Two Groups before and after Treatment. Figure 10 shows that the difference in DASH between the two groups before treatment was not statistically significant ($P > 0.05$). The DASH of the two groups at 3 and 5 weeks after treatment was significantly lower than that before treatment, and the difference was statistically significant ($P < 0.05$). The DASH of the experimental group was significantly lower than that of the control group at 3 and 5 weeks after treatment, and the difference was statistically significant ($P < 0.05$).

4. Discussion

Stroke is caused by a sudden rupture of blood vessels in the brain bleeding or cerebral vascular embolism caused by blood that cannot flow into the brain due to brain tissue damage. Stroke can lead to cerebral ischemia, hypoxia, necrosis, and other pathological changes, which lead to neurological deficits and other neurological symptoms. Its severity will directly affect the prognosis of patients, which is one of the topics of widespread concern in clinical practice [22]. Therefore, 116 patients with acute ischemic stroke were selected as the research subjects in this study. According to different nursing schemes, the patients were divided into 58 cases of the experimental group (early rehabilitation nursing) and 58 cases of the control group (routine rehabilitation nursing). The patients were examined by Avanto3.0 T superconducting magnetic resonance scanning in Siemens, Germany. The PSNR and SSIM of the proposed algorithm are significantly larger than those of the CS algorithm and NSBL algorithm. The running time was significantly shorter than that of the CS algorithm and NSBL algorithm, and the difference was statistically significant ($P < 0.05$). This is similar to the research results of Kopczak et al. (2020) [23]. It shows that the deep learning algorithm constructed in this paper has better processing performance than the traditional algorithm for MRI images, which not only improves the image quality but also improves the processing efficiency. The basic data of the two groups were compared, and it can be seen that there was no statistically significant difference in age, gender, course of disease, location of disease (left hemisphere, right hemisphere, and brainstem), and degree of nerve deficit (mild, moderate, and severe) between the two groups ($P > 0.05$). This provides feasibility for subsequent research.

The neurological deficit scores of the two groups at 3 and 5 weeks after treatment were significantly lower than those before treatment. The neurological deficit scores of the experimental group at 3 and 5 weeks after treatment were significantly lower than those of the control group, and the difference was statistically significant ($P < 0.05$). This is consistent with the research results of Lu et al. (2020) [24]. It indicated that early rehabilitation nursing and routine rehabilitation nursing could effectively improve the neurological deficit symptoms of patients with acute ischemic stroke, and the effect of early rehabilitation nursing was better. The Barthel index of the two groups at 3 and 5 weeks after treatment was significantly higher than that before treatment. The Barthel index of the experimental group was significantly higher than that of the control group at 3 and 5 weeks after treatment, and the difference was statistically significant ($P < 0.05$). This also reveals that early rehabilitation nursing can more effectively improve the daily living ability of stroke patients [25]. The FMA and DASH scores of the two groups at 3 and 5 weeks after treatment were significantly lower than those before treatment. The FMA and DASH scores of the experimental group were significantly lower than those of the control group at 3 and 5 weeks after treatment, and the difference was statistically significant ($P < 0.05$). This reveals that early rehabilitation nursing can more effectively improve the limb motor ability of stroke patients.

5. Conclusion

In this study, 116 patients with acute ischemic stroke were selected as subjects. According to different nursing schemes, the patients were divided into 58 cases of the experimental group (early rehabilitation nursing) and 58 cases of the control group (routine rehabilitation nursing). Patients were examined by magnetic resonance imaging on the basis of deep learning algorithm. The results show that the deep learning algorithm constructed in this paper has better processing performance than the traditional algorithm for MRI images, which not only improves the image quality but also improves the processing efficiency. Early rehabilitation nursing and routine rehabilitation nursing can effectively improve the neurological deficit symptoms, limb motor function, and daily living ability of patients with acute ischemic stroke, and the effect of early rehabilitation nursing is the best. However, only 116 patients with acute cerebral stroke were included. The sample size was small with single source. Besides, there was apparent regional limitations. Therefore, a wider range of cases needed to be included in subsequent studies to further discuss clinical nursing intervention paths in ischemic stroke. In summary, this study provides a theoretical support for the clinical nursing treatment of patients with ischemic stroke.

Data Availability

The data used to support the findings of this study are available from the corresponding author upon request.

Conflicts of Interest

The authors declare that they have no conflicts of interest.

References

[1] C. H. Suh, S. C. Jung, S. J. Cho et al., "MRI for prediction of hemorrhagic transformation in acute ischemic stroke: a systematic review and meta-analysis," *Acta Radiologica*, vol. 61, no. 7, pp. 964–972, 2020.

[2] C. Sun, X. Liu, C. Bao et al., "Advanced non-invasive MRI of neuroplasticity in ischemic stroke: techniques and applications," *Life Sciences*, vol. 261, Article ID 118365, 2020.

[3] N. Lakomkin, J. Pan, L. Stein, B. Malkani, M. Dhamoon, and J. Mocco, "Diffusion MRI reversibility in ischemic stroke following thrombolysis: a meta-analysis," *Journal of Neuroimaging*, vol. 30, no. 4, pp. 471–476, 2020.

[4] S. Tiedt, S. Brandmaier, H. Kollmeier et al., "Circulating metabolites differentiate acute ischemic stroke from stroke mimics," *Annals of Neurology*, vol. 88, no. 4, pp. 736–746, 2020.

[5] S. Camen, K. G. Haeusler, and R. B. Schnabel, "Cardiac imaging after ischemic stroke or transient ischemic attack," *Current Neurology and Neuroscience Reports*, vol. 20, no. 8, 36 pages, 2020.

[6] P. Naval-Baudin, I. Rodriguez Caamaño, C. Rubio-Maicas et al., "COVID-19 and ischemic stroke: clinical and

neuroimaging findings," *Journal of Neuroimaging*, vol. 31, no. 1, pp. 62–66, 2021.

[7] C. Provost, M. Soudant, L. Legrand et al., "Magnetic resonance imaging or computed tomography before treatment in acute ischemic stroke," *Stroke*, vol. 50, no. 3, pp. 659–664, 2019.

[8] A. Crofts, M. E. Kelly, and C. L. Gibson, "Imaging functional recovery following ischemic stroke: clinical and preclinical fMRI studies," *Journal of Neuroimaging*, vol. 30, no. 1, pp. 5–14, 2020.

[9] K. Macha, P. Hoelter, G. Siedler et al., "Multimodal CT or MRI for IV thrombolysis in ischemic stroke with unknown time of onset," *Neurology*, vol. 95, no. 22, pp. e2954–e2964, 2020.

[10] A. Vupputuri, S. Ashwal, B. Tsao, and N. Ghosh, "Ischemic stroke segmentation in multi-sequence MRI by symmetry determined superpixel based hierarchical clustering," *Computers in Biology and Medicine*, vol. 116, Article ID 103536, 2020.

[11] Z. Wang, M. Shaghaghi, S. Zhang et al., "Novel proton exchange rate MRI presents unique contrast in brains of ischemic stroke patients," *Journal of Neuroscience Methods*, vol. 346, Article ID 108926, 2020.

[12] X. H. Zhang and H. M. Liang, "Systematic review with network meta-analysis: diagnostic values of ultrasonography, computed tomography, and magnetic resonance imaging in patients with ischemic stroke," *Medicine (Baltimore)*, vol. 98, no. 30, Article ID e16360, 2019.

[13] D. Golubczyk, L. Kalkowski, J. Kwiatkowska et al., "Endovascular model of ischemic stroke in swine guided by real-time MRI," *Scientific Reports*, vol. 10, no. 1, Article ID 17318, 2020.

[14] H. Du, D. Wilson, G. Ambler et al., "Small vessel disease and ischemic stroke risk during anticoagulation for atrial fibrillation after cerebral ischemia," *Stroke*, vol. 52, no. 1, pp. 91–99, 2021.

[15] S. Wu, H. Zhang, J. Wang et al., "Iron sucrose as MRI contrast agent in ischemic stroke model," *Journal of Magnetic Resonance Imaging*, vol. 52, no. 3, pp. 836–849, 2020.

[16] Y. T. Chu, K. P. Lee, C. H. Chen et al., "Contrast-induced encephalopathy after endovascular thrombectomy for acute ischemic stroke," *Stroke*, vol. 51, no. 12, pp. 3756–3759, 2020.

[17] G. Zhu, C. Federau, M. Wintermark et al., "Comparison of MRI IVIM and MR perfusion imaging in acute ischemic stroke due to large vessel occlusion," *International Journal of Stroke*, vol. 15, no. 3, pp. 332–342, 2020.

[18] M. Grosser, S. Gellißen, P. Borchert et al., "Localized prediction of tissue outcome in acute ischemic stroke patients using diffusion- and perfusion-weighted MRI datasets," *PLoS One*, vol. 15, no. 11, Article ID e0241917, 2020.

[19] A. Subudhi, U. R. Acharya, M. Dash, S. Jena, and S. Sabut, "Automated approach for detection of ischemic stroke using Delaunay Triangulation in brain MRI images," *Computers in Biology and Medicine*, vol. 103, pp. 116–129, 2018.

[20] S. Ouchi and S. Ito, "Reconstruction of compressed-sensing MR imaging using deep residual learning in the image domain," *Magnetic Resonance in Medical Sciences*, vol. 20, no. 2, pp. 190–203, 2021.

[21] Y. Lv, G. Liang, H. Fan, J. Cheng, P. Xing, and L. Zhu, "Magnetic resonance imaging evaluation of hemangioma resection for encephalofacial angiomatosis (Sturge-Weber syndrome) in children under intelligent algorithm," *Contrast Media and Molecular Imaging*, vol. 2022, Article ID 7399255, 9 pages, 2022.

[22] A. Vupputuri, S. Ashwal, B. Tsao, E. Haddad, and N. Ghosh, "MRI based objective ischemic core-penumbra quantification in adult clinical stroke," in *Proceedings of the 2017 39th Annual International Conference of the IEEE Engineering in Medicine and Biology Society (EMBC)*, vol. 2017, pp. 3012–3015, Jeju, Korea (South), July 2017.

[23] A. Kopczak, A. Schindler, A. Bayer-Karpinska et al., "Complicated carotid artery plaques as a cause of cryptogenic stroke," *Journal of the American College of Cardiology*, vol. 76, no. 19, pp. 2212–2222, 2020.

[24] S. S. Lu, Y. Z. Cao, C. Q. Su et al., "Hyperperfusion on arterial spin labeling MRI predicts the 90-day functional outcome after mechanical thrombectomy in ischemic stroke," *Journal of Magnetic Resonance Imaging*, vol. 53, no. 6, pp. 1815–1822, 2021.

[25] B. Jiang, N. K. Hills, R. Forsyth et al., "Imaging predictors of neurologic outcome after pediatric arterial ischemic stroke," *Stroke*, vol. 52, no. 1, pp. 152–161, 2021.

Hindawi
Contrast Media & Molecular Imaging
Volume 2022, Article ID 3038308, 8 pages
https://doi.org/10.1155/2022/3038308

Research Article

Quantitative Evaluation of Extramural Vascular Invasion of Rectal Cancer by Dynamic Contrast-Enhanced Magnetic Resonance Imaging

Zheng Chen,[1] **Da Hu**,[2] **Guannan Ye**,[3] **and Dayong Xu**[1]

[1]*Department of General Surgery, The First Hospital of Changsha, Changsha 410005, Hunan, China*
[2]*Department of Radiology, The First Hospital of Changsha, Changsha 410005, Hunan, China*
[3]*Department of Gastroenterology, The First Hospital of Changsha, Changsha 410005, Hunan, China*

Correspondence should be addressed to Dayong Xu; 1400420839@xs.hnit.edu.cn

Received 4 March 2022; Revised 6 May 2022; Accepted 9 May 2022; Published 31 May 2022

Academic Editor: M Pallikonda Rajasekaran

This study was carried out to explore the preoperative predictive value of dynamic contrast-enhanced magnetic resonance imaging (DCE-MRI) in extramural vascular invasion (EMVI) in patients with rectal cancer. 124 patients with rectal cancer were randomly divided into two groups, with 62 groups in each group. One group used conventional magnetic resonance imaging (MRI) and was recorded as the control group. The other group used DCE-MRI and was recorded as the experimental group. The diagnostic value was evaluated by comparing the MRI quantitative parameters of EMVI positive and EMVI negative patients, as well as the area under the curve (AUC) of the receiver operating characteristic curve (ROC), diagnostic sensitivity, and specificity of the two groups. The results showed that the Ktrans and Ve values of EMVI positive patients in the experimental group and the control group were 1.08 ± 0.97 and 1.03 ± 0.93, and 0.68 ± 0.29 and 0.65 ± 0.31, respectively, which were significantly higher than those in EMVI negative patients ($P < 0.05$). The AUC of EMVI diagnosis in the experimental group and the control group were 0.732 and 0.534 ($P < 0.05$), the sensitivity was 0.913 and 0.765 ($P < 0.05$), and the specificity was 0.798 and 0.756 ($P > 0.05$), respectively. In conclusion, DCE-MRI has a higher diagnostic value than conventional MRI in predicting EMVI in patients with rectal cancer, which was worthy of further clinical promotion.

1. Introduction

Extramural vascular invasion (EMVI) refers to the presence of tumor plug attachment or tumor cell infiltration in the blood vessels outside the muscularis propria of the rectal wall [1–4]. It was first reported by Professor Talbot in 1981, and it was pointed out that EMVI could affect the prognosis of rectal cancer patients. For EMVI-positive rectal cancer patients, neoadjuvant chemoradiotherapy followed by surgical treatment can significantly reduce local recurrence and improve prognosis, so it is particularly important to complete accurate preoperative assessment of EMVI [5–8]. Conventional methods for preoperative rectal cancer patients include multi-row spiral CT, endorectal ultrasonography (ERUS), and dynamic contrast-enhanced magnetic resonance imaging (DCE-MRI). Preoperative accurate assessment of rectal cancer depends on the diagnosis and treatment level of radiologists and the development of imaging technology [9–11].

Multi-row spiral CT has poor resolution of pelvic soft tissues, making it difficult to accurately evaluate the depth of tumor invasion into the rectal wall and EMVI [12]. ERUS examination can accurately identify the hierarchical structure of rectal wall based on the principle of acoustic reflection, and has high accuracy in judging the depth of tumor invasion. However, when the tumor is large and late in stage, resulting in intestinal obstruction, the diagnostic accuracy of ultrasound is reduced because it cannot enter the intestinal lumen [13]. DCE-MRI is a noninvasive functional imaging technique that integrates morphologic and hemodynamic changes to reflect the characteristics of tumor microcirculation. Because DCE-MRI can quantify the parameters related to tumor microangiogenesis, perfusion, and permeability, it is widely used in the detection, prediction of EMVI and evaluation of neoadjuvant therapy response, tumor angiogenesis, biological invasiveness, and molecular markers [14]. As far as we know, there are few studies on the evaluation of EMVI of rectal cancer by DCE-MRI. In recent years, some scholars have reported the correlation between MRI evaluation of EMVI of rectal cancer (mrEMVI) and DCE-MRI parameters. The results showed that Kep values of mrEMVI positive patients were significantly lower than those in mrEMVI negative patients, while Ve values were higher than those in mrEMVI negative patients. However, the diagnostic efficacy of DCE-MRI quantitative parameters for EMVI remains unclear [15].

As an emerging area, imaging omics has attracted more and more attention. It mainly conducts quantitative analysis on imaging data and extracts a large number of quantitative features from medical images to provide nonvisual information related to tumor heterogeneity, which can be used for personalized treatment [16]. For rectal cancer, imaging omics is mainly applied to predict the cardiac resynchronization therapy (CRT) response, survival, and other pathological features, such as *T* stage, lymph node metastasis, and peripheral nerve invasion. However, to our knowledge, few studies have reported the use of imaging omics to predict EMVI in rectal cancer [17]. Therefore, in this study, DCE-MRI was used to evaluate EMVI of rectal cancer patients, aiming at exploring the preoperative predictive value of DCE-MRI for EMVI, and providing accurate preoperative risk stratification and individualized treatment for patients.

2. Materials and Methods

2.1. Research Subjects. In this study, 124 patients with rectal cancer diagnosed in hospital from May 2019 to October 2021 were divided into two groups according to the random number table method, with 62 patients in each group. Conventional MRI scanning was used in the control group, while DCE-MRI scanning was used in the experimental group. All patients and their families had fully understood the situation and signed informed consent, and this study had been approved by the ethics committee of hospital.

Inclusion criteria were as follows: (I) patients who were highly suspected of rectal cancer and confirmed by colonoscopy biopsy and histopathology; (II) patients who underwent the resection surgery within 14 days after DCE-MRI examination and had complete postoperative pathological data; and (III) those with no history of intraperitoneal tumor, and no history of intraperitoneal or anal surgery.

Exclusion criteria: (I) Patients with missing postoperative case data; (II) patients with diseases of the blood system, or patients with coagulation dysfunction or low immune function; (III) patients with serious dysfunction of heart, liver, and kidney; (IV) patients with contraindications for MRI; and (V) patients who did not cooperate with the examination.

2.2. Collection of MRI Imaging Data. The MRI scan was performed by a 3.0 T MRI machine. Before the scan, patients were asked to fast for 12 hours to keep the intestine empty. The patient was in a supine position with stable breathing. The scan range was from the lowest point of the symphysis pubis to the iliac crest line on both sides. The scan was carried out according to the DCE-MRI scan sequence specification for rectal cancer. (1) Coronal and sagittal T2-weighted imaging (T2WI) sequences: Fast Spin Echo (FSE) sequence was used for scanning. (2) Axial T2WI sequence: the tumor location was first determined by sagittal T2WI, and then horizontal FSE scan was performed along the long axis of the rectum perpendicular to the tumor. (3) Diffusion weighted imaging (DWI) sequence: tumor location was determined by sagittal T2WI, and horizontal scanning was performed using single excitation spin echo-planar imaging (EPI) technology. (4) Dynamically enhanced T1-weighted imaging (T1WI) scan sequence: according to the patient's body weight, the injection volume of the required contrast agent was calculated at a dose of 0.2 mL/kg, and the enhanced contrast agent-Gadolinium diamine injection was injected with a high-pressure syringe at a constant rate. Table 1 shows the specific scan parameters of each scan sequence.

2.3. DCE-MRI Image Processing. The imaging evaluation of each patient was agreed upon by two abdominal radiologists with more than 5 years of experience in pelvic MRI diagnosis, and the physician who evaluated the images was unaware of relevant laboratory and pathological findings. Pharmacokinetic analysis of DCE-MRI parameters was performed. The images were independently evaluated by two radiologists and regions of interest (ROI) were delineated layer by layer. Meanwhile, it should be noted to keep away from visible blood vessels, peripheral fat, necrosis or hemorrhage, and intestinal lumen contents should be avoided as far as possible. Then, the ROI of all layers should be fused to obtain the total ROI of the tumor, and the quantitative parameters below were recorded: volume transfer constant (Ktrans), rate constant (Kep), volume fraction of extravascular extracellular space (Ve), and volume fraction of plasma (Vp). Semiquantitative parameters: initial area under curve (iAUC), time to peak (TTP), rising slope (Max Slope), and maximum concentration of contrast agent (Max Conc).

The imaging evaluation of EMVI was conducted according to the MRI evaluation EMVI scoring system proposed by Leithner et al. [18]. 0: The tumor is non-nodular, infiltrating into the muscular layer, and there are no blood vessels outside the intestinal wall around the tumor; 1: The tumor is nodular, infiltrating into the muscle layer or having tiny blood vessels outside the intestinal wall, but not around the tumor; 2: there are blood vessels outside the intestinal wall around the tumor, but the size of the blood vessels is normal and there is no clear tumor signal in the blood vessels; 3: there was a moderate intensity signal in the blood vessels around the tumor, but the outline and diameter of the blood vessels only changed slightly; and 4: tumor signal appears in the blood vessels around the tumor, and the outline of the blood vessels is obviously irregular or the

Table 1: MRI scan sequence parameters.

	Sagittal T2WI	Coronal FS T2WI	Axial FS T2WI	Axial DWI
Repetition time (ms)	3000 ms	3000 ms	3000 ms	4000 ms
Echo time	(70–110) ms	(70–110) ms	(70–110) ms	(70–110) ms
Layer space	1.0 mm	2.0 mm	1.5 mm	1.5 mm
Layer thickness	5.0 mm	6.0 mm	5.0 mm	5.0 mm
Matrix	350 × 256	350 × 186	350 × 186	120 × 150
Field of view	(33–45) cm	(37–45) cm	(37–45) cm	(37–53) cm
Number of excitations	2	3	4	5

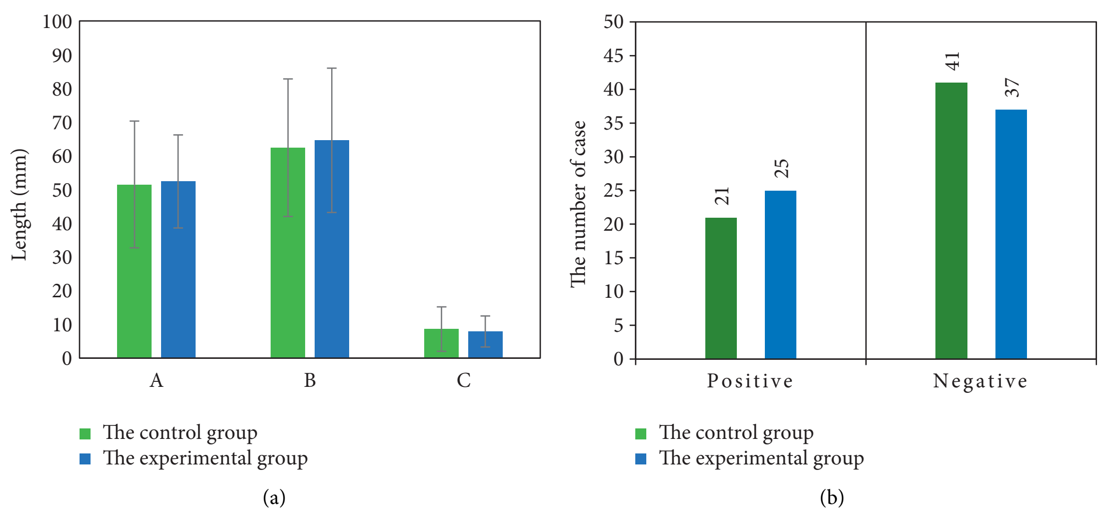

Figure 1: Clinical pathological characteristics of the two groups. In Figure (a), A represents the diameter of the tumor, B represents the distance between the lower margin of the tumor and the anal margin, and C represents the depth of tumor invasion. Figure (b) shows the number of EMVI cases.

blood vessels are nodular. 0~2 is EMVI negative, and 3~4 is EMVI positive.

2.4. Statistical Methods. The Shapiro–Wilk test is performed to determine whether the variables are normally distributed. The T test or Mann–Whitney U test is used for continuous variables, and Chi-square test or Fisher's exact test is used for categorical variables. Univariate and multivariate logistic regression analyses are carried out to determine independent predictors of EMVI. The receiver operating curve (ROC) is drawn and area under the curve (AUC) is calculated to evaluate the diagnostic efficacy of each imaging omics model, and internal verification is carried out in an independent verification set. The diagnostic efficacy of clinical, quantitative, and radiomic models are evaluated based on AUC, sensitivity, and specificity. Intraclass correlation coefficient (ICC) and 95% confidence interval (CI) are calculated to analyze the interobserver consistency of DCE-MRI quantitative perfusion parameters measured by two radiologists. $P < 0.05$ indicates that the difference is statistically significant.

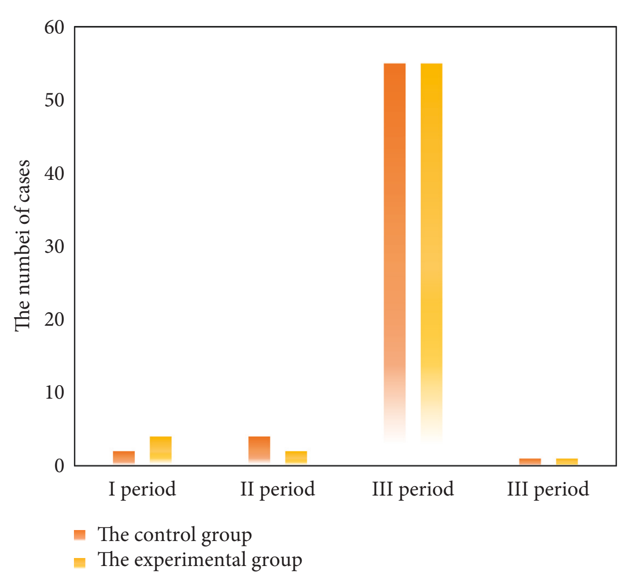

Figure 2: TNM staging in both groups.

3. Results

3.1. Clinical Pathological and Imaging Data of the Patients. The mean age of patients in the experimental group was (62.1 ± 11.4) years old and that in the control group was (61.9 ± 10.9) years old. In the control group, there were 21 positive EMVI cases and 41 negative EMVI cases. The numbers were 25 and 37 in the experimental group. There was no significant difference in age, tumor diameter, number of EMVI cases, and TNM stage between the two groups

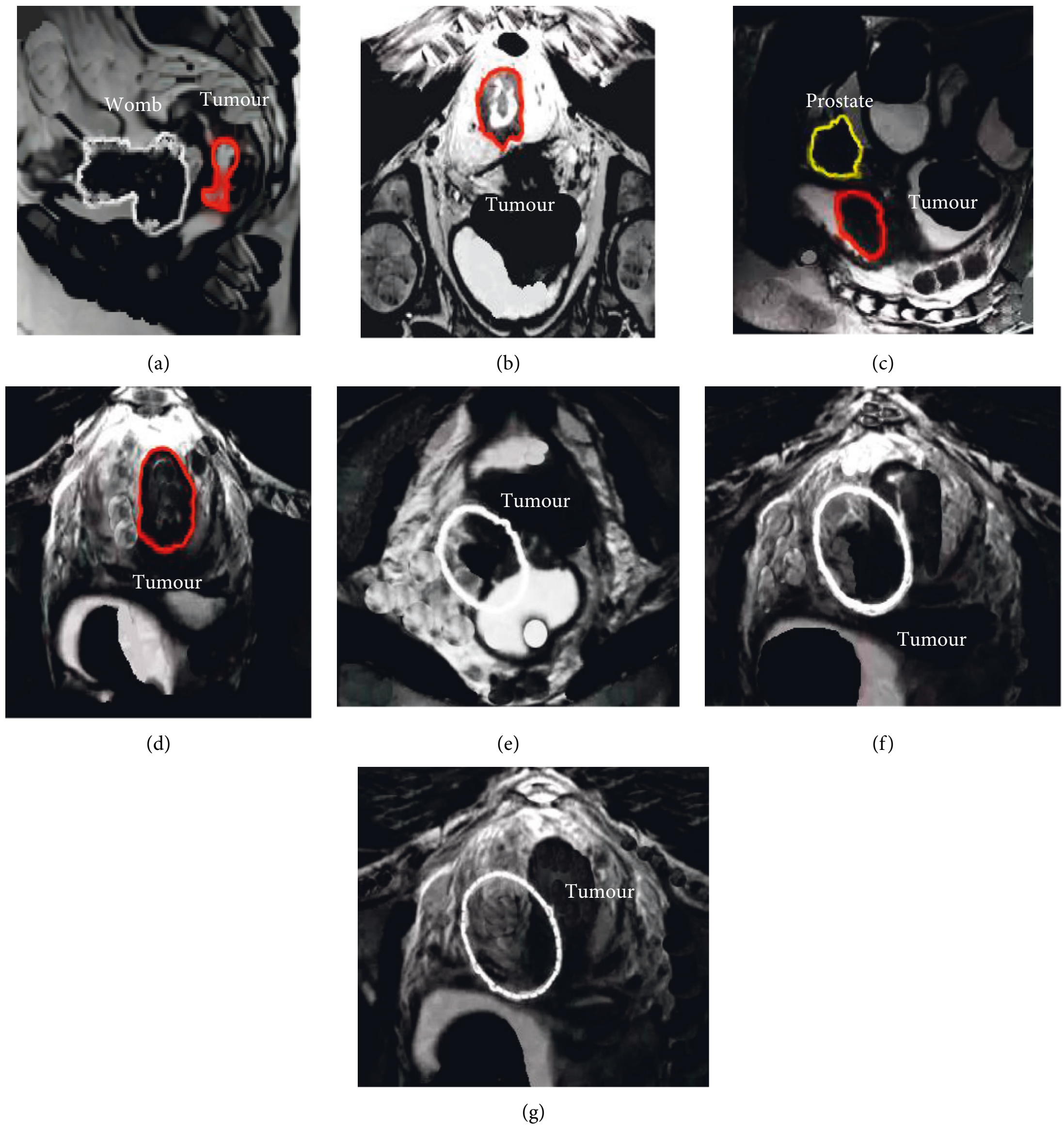

Figure 3: MRI images of a patient with rectal cancer. In Figure 3, arrows and dotted lines indicate cancerous sites. (a, c) show sagittal T2-weighted images. (b, d) Axial T2-weighted images. (e) Coronal T2-weighted image, and (f, g) show continuous axial MRI images. (e–g) Condition of a positive EMVI case. Under normal circumstances, the MRI images of large vessels outside the rectal wall should show a creeping distribution, while the blood vessels in (e–g) show signal loss on T2WI images due to blood flow in the vessels, also known as emptying phenomenon. When the external vascular lumen of rectum is enlarged, the irregular contour and the phenomenon of empty flow disappear and are replaced by tumor signal, namely, EMVI.

($P > 0.05$), which was comparable. Figures 1–3 show the clinical pathological characteristics of patients in the two groups, as well as the MRI images.

3.2. Comparison of DCE-MRI Parameters between the EMVI Positive Group and Negative Group. The consistency between two clinicians was good for the measurement of quantitative and semiquantitative parameters of DCE-MRI. The intra-group correlation coefficients of Ktrans, Kep, Ve, Vp, iAUC, TTP, Max Slope, and Max Conc were 0.78, 0.83, 0.86, 0.85, 0.88. 0.81, 0.75, and 0.73, respectively. Figures 4 and 5 show DCE-MRI parameters in the EMVI positive group and the EMVI negative group. Ktrans and Ve values in EMVI positive group were significantly higher than those in EMVI negative group, $P < 0.05$. There was no significant difference in Kep, Vp, and semiquantitative parameters between the EMVI positive group and EMVI negative group, $P > 0.05$.

The Ktrans value and Ve value of EMVI-positive patients in the experimental group and control group were 1.08 ± 0.97 and 1.03 ± 0.93, 0.68 ± 0.29 and 0.65 ± 0.31, respectively, which were significantly higher than those of EMVI-negative patients, $P < 0.05$, and the difference was statistically significant, as shown in Figure 6.

3.3. DCE-MRI Parameters of the Two Groups. In this study, the diagnostic efficacy of various parameters for EMVI was

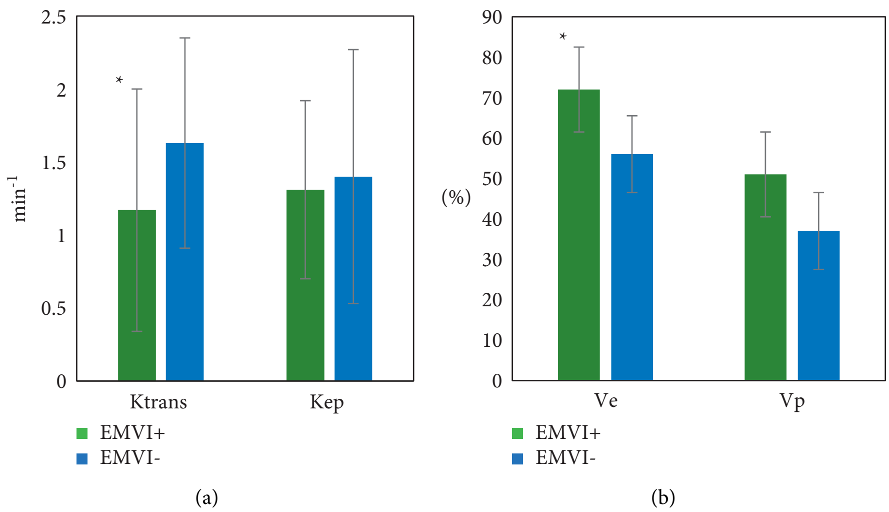

FIGURE 4: DCE-MRI parameters of the EMVI positive group and negative group. (a) Ktrans and Kep; (b) Ve and Vp. *means $P < 0.05$, the difference is statistically significant.

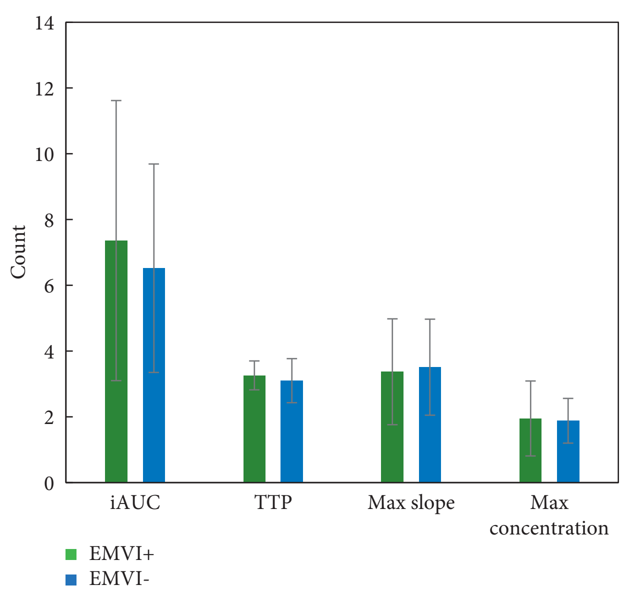

FIGURE 5: DCE-MRI parameters of the EMVI positive group and negative group.

evaluated by drawing ROC and calculating AUC. It was found that the DCE-MRI parameter performance (TNM staging, Ktrans, Ve) of the experimental group was significantly higher than that of the control group ($P < 0.05$), and the difference was statistically significant, as shown in Figure 7.

The AUC of EMVI diagnosis in the experimental group and the control group was 0.732 and 0.534, and the diagnostic sensitivity was 0.913 and 0.765, respectively. The values of the experimental group were significantly higher than the control group, $P < 0.05$. The specificity of diagnosis was 0.798 and 0.756, respectively, with no significant difference between the two groups ($P > 0.05$), as shown in Figure 8.

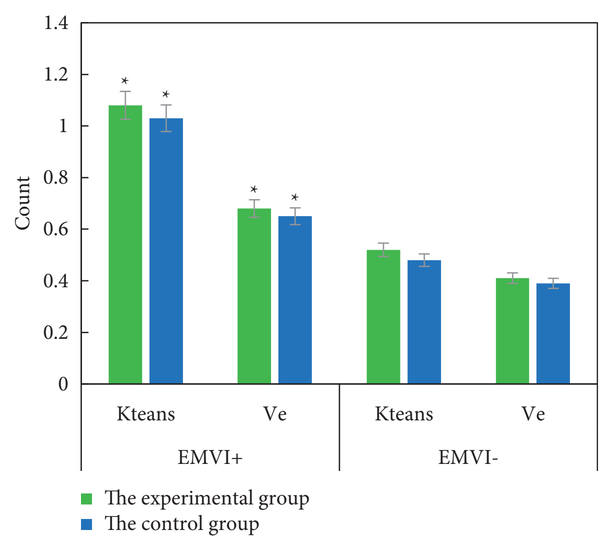

FIGURE 6: Ktrans and Ve values of EMVI positive and negative patients in the two groups. *means the difference is statistically significant, $P < 0.05$.

4. Discussion

According to statistics, EMVI can occur in about 1/3 of rectal cancer patients, and EMVI is very important for the prognosis of patients and the choice of treatment plan. The eighth edition of *American Joint Council on Cancer* (AJCC) include it as an independent adverse prognostic factor and as class I evidence. In addition, EMVI has been recommended as an imaging marker to predict the efficacy of neoadjuvant chemotherapy [19, 20]. Previous studies have shown that risk factors for EMVI include large tumor size and high T and N stages. In this study, the TNM stage was confirmed to be an independent predictor of EMVI, which was partially consistent with previous studies [21]. However, it was found that tumor size and TNM stage were not correlated with EMVI. In terms of tumor staging, this result may be due to

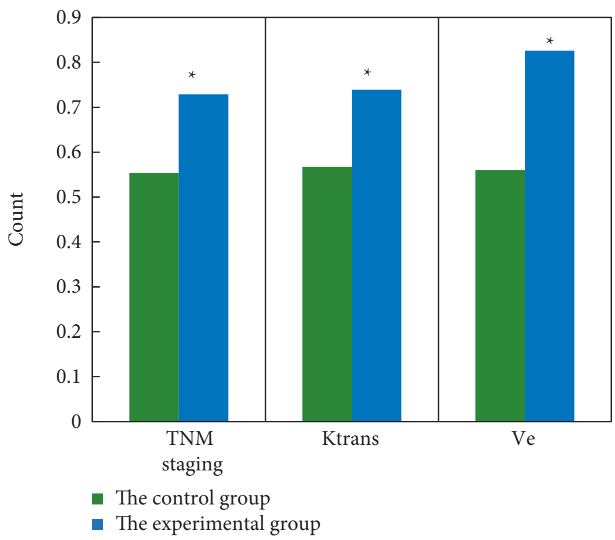

Figure 7: Diagnostic performance of different parameters in two groups. *means the difference is statistically significant, $P < 0.05$.

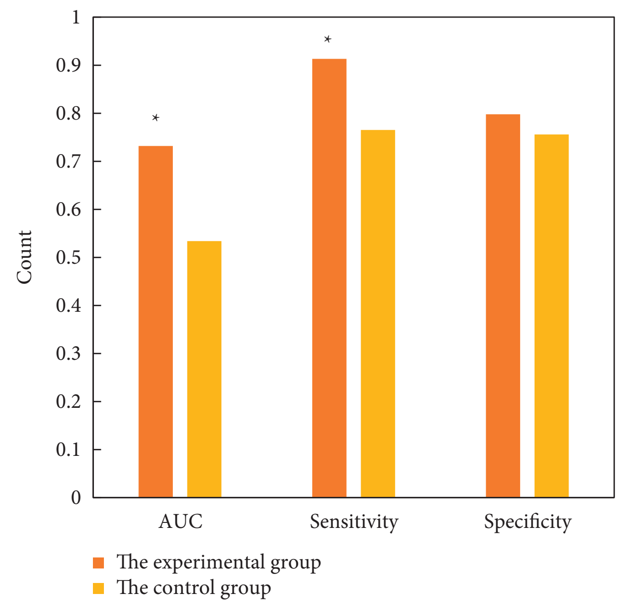

Figure 8: Comparison of AUC, sensitivity, and specificity of EMVI diagnosis between the two groups. *means the difference is statistically significant, $P < 0.05$.

selection bias, and the ROI of the tumor is manually delineated, which may be influenced by the individual factors of the delineator. Therefore, these factors cannot be used in preoperative decision making alone. Chen et al. showed that lymphovascular invasion (LVI) of rectal cancer could be evaluated preoperatively by measuring the total tumor volume on DWI and T2W images, and its AUC value was 0.899 and 0.877, respectively. However, volume measurement needs a lot of time, and cannot fully reflect the nature of EMVI, and the result remains to be verified [22]. Sun et al. attempted to explore the value of DWI as a potential quantitative method in the evaluation of rectal cancer EMVI, but the diagnostic efficacy was not significantly improved when DWI was added to detect EMVI [23].

In this study, the correlation between DCE-MRI parameters and EMVI in rectal cancer was analyzed, and only Ktrans and Ve values were significantly different between EMVI positive and EMVI-negative groups. The results showed that Ktrans and Ve values in EMVI positive group were significantly higher than those in negative group, and Ktrans and Ve values were positively correlated with EMVI, suggesting that these two parameters may be closely related to vascular invasion of tumor. Ve represents the volume fraction of extracellular extravascular space (EES). In the process of tumor progression, tumor cells secrete vascular endothelial factor, which increases the permeability of tumor vessels, and the function of cell-cell adhesion molecules is lost, leading to the expansion of cell space and EES. Therefore, it can be reasonably explained that the Ve value of EMVI positive group is significantly higher than that of EMVI negative group. This result was consistent with that of Leijssen et al. who reported increased Ve values in mrEMVI positive patients [24]. In terms of Ktrans, our findings are consistent with a recent study showing that LVI is associated with a high Ktrans value in rectal cancer patients [25].

Chinese Society of Clinical Oncology (CSCO) guidelines for the diagnosis and treatment of colorectal cancer recommend the use of rectal MRI to determine EMVI [26]. Other research results showed that the accuracy, sensitivity, specificity, positive predictive value, and negative predictive value of MRI detection of EMVI were 81%, 62%, 88%, 0.67, and 0.86, respectively [27]. Another study showed that the sensitivity and specificity of MRI for EMVI recognition were 28.2%–62.0% and 88.0%–94.0% [28]. In this study, DCE-MRI was used for preoperative prediction of EMVI in rectal cancer patients. It was found that the AUC of EMVI diagnosis in the experimental group and the control group was 0.732 and 0.534, respectively, and the diagnostic sensitivity was 0.913 and 0.765, respectively. Obviously, the values in the experimental group were significantly higher than the control group, $P < 0.05$. The specificity of diagnosis was 0.798 and 0.756, respectively, with no significant difference between the two groups ($P > 0.05$). Above, DCE-MRI is feasible and efficient and can assist imaging doctors in imaging diagnosis.

5. Conclusion

In this study, DCE-MRI was used for preoperative prediction of EMVI in patients with rectal cancer. DCE-MRI has a higher diagnostic value in predicting EMVI in rectal cancer patients than conventional MRI, which is worthy of further clinical promotion. However, in this study, tumor images below the level of levator ani muscle and above the peritoneal recursion are not included, so its applicability is limited. Besides, the sample size of this study is small, and an expanded sample size is necessary to strengthen the findings of the study. In a word, this study can provide theoretical basis for preoperative risk stratification and individualized treatment of patients.

Data Availability

The data used to support the findings of this study are available from the corresponding author upon request.

Conflicts of Interest

The authors declare that they have no conflicts of interest.

References

[1] S. Piawah and A. P. Venook, "Targeted therapy for colorectal cancer metastases: a review of current methods of molecularly targeted therapy and the use of tumor biomarkers in the treatment of metastatic colorectal cancer," *Cancer*, vol. 125, no. 23, pp. 4139–4147, 2019.

[2] A. Tverdal, G. Høiseth, P. Magnus et al., "Alcohol consumption, HDL-cholesterol and incidence of colon and rectal cancer: a prospective cohort study including 250,010 participants," *Alcohol and Alcoholism*, vol. 56, no. 6, pp. 718–725, 2021.

[3] A. M. D. Wolf, E. T. H. Fontham, T. R. Church et al., "Colorectal cancer screening for average-risk adults: 2018 guideline update from the American Cancer Society," *CA: A Cancer Journal for Clinicians*, vol. 68, no. 4, pp. 250–281, 2018.

[4] H. Chen, N. Li, J. Ren et al., "Participation and yield of a population-based colorectal cancer screening programme in China," *Gut*, vol. 68, no. 8, pp. 1450–1457, 2019.

[5] E. Saus, S. Iraola-Guzmán, J. R. Willis, A. Brunet-Vega, and T. Gabaldón, "Microbiome and colorectal cancer: roles in carcinogenesis and clinical potential," *Molecular Aspects of Medicine*, vol. 69, pp. 93–106, 2019.

[6] X. Deng, P. Liu, D. Jiang et al., "Neoadjuvant radiotherapy versus surgery alone for stage II/III mid-low rectal cancer with or without high-risk factors," *Annals of Surgery*, vol. 272, no. 6, pp. 1060–1069, 2020.

[7] J. Crippa, F. Grass, P. Achilli et al., "Risk factors for conversion in laparoscopic and robotic rectal cancer surgery," *British Journal of Surgery*, vol. 107, no. 5, pp. 560–566, 2020.

[8] S. Chen, N. Li, Y. Tang et al., "The prognostic value of MRI-detected extramural vascular invasion (mrEMVI) for rectal cancer patients treated with neoadjuvant therapy: a meta-analysis," *European Radiology*, vol. 31, no. 12, pp. 8827–8837, 2021.

[9] S. Yang, X. Zou, J. Li et al., "The application value of ceMDCT in the diagnosis of gastric cancer extramural vascular invasion and its influencing factors," *Journal of Healthcare Engineering*, vol. 2022, pp. 1–5, Article ID 4239600, 2022.

[10] A. Hamabe, M. Ishii, K. Onodera et al., "MRI-detected extramural vascular invasion potentiates the risk for pathological metastasis to the lateral lymph nodes in rectal cancer," *Surgery Today*, vol. 51, no. 10, pp. 1583–1593, 2021.

[11] J. A. Halpern, C. Oromendia, J. E. Shoag et al., "Use of digital rectal examination as an adjunct to prostate specific antigen in the detection of clinically significant prostate cancer," *The Journal of Urology*, vol. 199, no. 4, pp. 947–953, 2018.

[12] A. E. Obaro, A. A. Plumb, T. R. Fanshawe et al., "Post-imaging colorectal cancer or interval cancer rates after CT colonography: a systematic review and meta-analysis," *The Lancet Gastroenterology & Hepatology*, vol. 3, no. 5, pp. 326–336, 2018.

[13] C. Tsai, C. Hague, W. Xiong et al., "Evaluation of endorectal ultrasound (ERUS) and MRI for prediction of circumferential resection margin (CRM) for rectal cancer," *The American Journal of Surgery*, vol. 213, no. 5, pp. 936–942, 2017.

[14] X. Yu, W. Song, D. Guo et al., "Preoperative prediction of extramural venous invasion in rectal cancer: Comparison of the diagnostic efficacy of radiomics models and quantitative dynamic contrast-enhanced magnetic resonance imaging," *Frontiers in Oncology*, vol. 10, p. 459, 2020.

[15] J. M. Franklin, B. Irving, B. W. Papiez et al., "Tumour subregion analysis of colorectal liver metastases using semi-automated clustering based on DCE-MRI: Comparison with histological subregions and impact on pharmacokinetic parameter analysis," *European Journal of Radiology*, vol. 126, p. 108934, 2020.

[16] A. Khadidos, A. Khadidos, O. M. Mirza, T. Hasanin, W. Enbeyle, and A. A. Hamad, "Evaluation of the risk of recurrence in patients with local advanced rectal tumours by different radiomic analysis approaches," *Applied Bionics and Biomechanics*, vol. 2021, Article ID 4520450, 2021.

[17] D. R. Schmidt, R. Patel, D. G. Kirsch, C. A. Lewis, M. G. Vander Heiden, and J. W. Locasale, "Metabolomics in cancer research and emerging applications in clinical oncology," *CA: A Cancer Journal for Clinicians*, vol. 71, no. 4, pp. caac.21670–358, 2021.

[18] D. Leithner, J. V. Horvat, R. E. Ochoa-Albiztegui et al., "Imaging and the completion of the omics paradigm in breast cancer," *Radiologe, Der*, vol. 58, no. S1, pp. 7–13, 2018.

[19] X. J. Luo, Q. Zhao, J. Liu et al., "Novel genetic and epigenetic biomarkers of prognostic and predictive significance in stage II/III colorectal cancer," *Molecular Therapy: The Journal of the American Society of Gene Therapy*, vol. 29, no. 2, pp. 587–596, 2021.

[20] A. Chandramohan, R. Mittal, R. Dsouza et al., "Prognostic significance of MR identified EMVI, tumour deposits, mesorectal nodes and pelvic side wall disease in locally advanced rectal cancer," *Colorectal Disease*, vol. 24, no. 4, pp. 428–438, 2022.

[21] A. C. Lord, N. D'Souza, A. Shaw et al., "MRI-diagnosed tumour deposits and EMVI status have superior prognostic accuracy to current clinical TNM staging in rectal cancer," *Annals of Surgery*, vol. Publish Ahead of Print, 2020.

[22] Y. Chen, X. Yang, Z. Wen et al., "Association between high-resolution MRI-detected extramural vascular invasion and tumour microcirculation estimated by dynamic contrast-enhanced MRI in rectal cancer: preliminary results," *BMC Cancer*, vol. 19, no. 1, p. 498, 2019.

[23] H. Sun, Y. Xu, A. Song, K. Shi, and W. Wang, "Intravoxel incoherent motion MRI of rectal cancer: correlation of diffusion and perfusion characteristics with prognostic tumor markers," *American Journal of Roentgenology*, vol. 210, no. 4, pp. W139–W147, 2018.

[24] L. G. J. Leijssen, A. M. Dinaux, R. Amri et al., "Impact of intramural and extramural vascular invasion on stage II-III colon cancer outcomes," *Journal of Surgical Oncology*, vol. 119, no. 6, pp. 749–757, 2019.

[25] Y. Zhu, Y. Zhou, W. Zhang et al., "Value of quantitative dynamic contrast-enhanced and diffusion-weighted magnetic resonance imaging in predicting extramural venous invasion in locally advanced gastric cancer and prognostic significance," *Quantitative Imaging in Medicine and Surgery*, vol. 11, no. 1, pp. 328–340, 2021.

[26] T. Yoshino, D. Arnold, H. Taniguchi et al., "Pan-Asian adapted ESMO consensus guidelines for the management of patients with metastatic colorectal cancer: a JSMO-ESMO initiative endorsed by CSCO, KACO, MOS, SSO and TOS," *Annals of Oncology*, vol. 29, no. 1, pp. 44–70, 2018.

[27] A. Sofic, A. Selimovic, A. Efendic et al., "MRI evaluation of extramural venous invasion (EMVI) with rectal carcinoma using high resolution T2 and combination of high resolution T2 and contrast enhanced T1 weighted imaging," *Acta Informatica Medica*, vol. 29, no. 2, pp. 113–117, 2021.

[28] M. S. Cho, Y. Y. Park, J. Yoon et al., "MRI-based EMVI positivity predicts systemic recurrence in rectal cancer patients with a good tumor response to chemoradiotherapy followed by surgery," *Journal of Surgical Oncology*, vol. 117, no. 8, pp. 1823–1832, 2018.

Hindawi
Contrast Media & Molecular Imaging
Volume 2022, Article ID 4524958, 7 pages
https://doi.org/10.1155/2022/4524958

Research Article

Traumatic Brain Magnetic Resonance Imaging Feature Extraction Based on Variable Model Algorithm in Stroke Examination

Zhenghong Wu[1] **Dongqiu Wu**[2] **Weiwei Yang**[3] **Bing Wan**[1] **and Sibin Liu**[1]

[1]*Department of Radiology, Jingzhou Central Hospital, Jingzhou 434020, Hubei, China*
[2]*Department of Function, Jingzhou Chest Hospital, Jingzhou 434020, Hubei, China*
[3]*Department of Pulmonary and Critical Care Medicine, Jingzhou Chest Hospital, Jingzhou 434020, Hubei, China*

Correspondence should be addressed to Sibin Liu; 1431502102@post.usts.edu.cn

Received 22 February 2022; Revised 5 May 2022; Accepted 9 May 2022; Published 30 May 2022

Academic Editor: M Pallikonda Rajasekaran

The purpose of this study was to explore the diagnostic value of different sequence scanning of nonparametric variable model-based cranial magnetic resonance imaging (MRI) for ischemic stroke. A histogram analysis-based nonparametric variable model was proposed first, which was compared with the parametric deformation (PD) model and geometric deformation (GD) model. Then, 116 patients with acute ischemic stroke were selected as the research subjects. Routine MRI (T2WI, T1WI, FLAIR, DWI, SWI, and 3D TOF MRA) and MR SCALE-PWI were performed. The results showed that the nonparametric variable model algorithm was relatively complete in the actual segmentation results of MRI images, and the display clarity of lesions was better than PD and GD algorithms. The diagnostic sensitivity, specificity, and overall performance of the variable model algorithm were significantly higher than those of the other two algorithms ($P < 0.05$). According to ROC curve analysis, the AUC areas of DWI, SWI, 3D TOF MRA, and MR SCALE-PWI for the diagnosis of ischemic penumbra were 0.793, 0.825, 0.871, and 0.933, respectively. In summary, the segmentation results of MRI images by the nonparametric variable model based on histogram analysis were relatively complete, and the clarity of lesions was better than that of the traditional model. MRI images can effectively identify the occurrence of ischemic stroke. Moreover, MR SCALE-PWI had a good early identification effect on ischemic penumbra, which can reduce unnecessary treatment for patients.

1. Introduction

Stroke is the most common neurological disease that threatens human health and life in modern society [1]. Stroke refers to an acute cerebrovascular disease caused by a sudden rupture or obstruction of cerebral vessels that leads to cerebral blood circulation disorder, thereby causing brain tissue damage, which can be divided into ischemic stroke or hemorrhagic stroke [2, 3]. There are many causes of stroke, such as atherosclerosis, atrial fibrillation, heart valve disease, neck or brain tumors, and congenital vascular malformation. Hypertension, hyperlipidemia, diabetes, and bad habits are risk factors for stroke [4, 5]. The disease has the characteristics of high mortality, high incidence, high recurrence rate, high disability rate, and high prevalence rate, which has become the second leading cause of death in the world after ischemic heart disease. Therefore, it is necessary to diagnose and treat stroke early in clinic [6].

Medical imaging technology can present the internal structure of the human body in a noninvasive manner. Researchers and physicians can obtain potential information to save lives through it [7]. With the development of imaging technology these years, the use of imaging means to check stroke has been widely used [8–10]. With the improvement of imaging technology, doctors widely use computed tomography (CT) and magnetic resonance imaging (MRI) to show lesions. However, early brain CT examinations of stroke patients are mostly normal, and low-density lesions usually appear after 24–48 hours, which increases the difficulty of diagnosis and treatment [11]. MRI, an examination that uses strong magnets, radio waves, and a computer to generate detailed pictures of the human body, can accurately display early ischemic infarcts and has a high detection rate in the examination of cerebellar and brainstem infarcts [12, 13]. However, the original MRI images often have problems such as blurred tissue boundaries, spatial aliasing, and partial volume effect, which need to be enhanced by image segmentation technology [14]. The nonparametric deformation model can adapt to the variability of the anatomical structure over time and different individuals, so it can segment, match, and track anatomical structure targets and can consider the constraints from the image and the constraints on the location, size, and shape of the anatomical structure. Therefore, this study intends to optimize the skull MRI images of stroke patients with nonparametric variable model.

In summary, it is necessary to improve the quality of skull MRI images by using various image segmentation algorithms, but its effect still needs to be further improved. Therefore, a histogram analysis-based Gaussian mixture model was adopted in this research to fit the histogram, and a nonparametric variable model based on histogram analysis was proposed. 116 patients with acute ischemic stroke were selected as the research subjects for multisequence MRI scanning. By analyzing the diagnostic performance of MRI multimodal images for ischemic stroke, the evaluation value of different sequence scanning of skull MRI images based on a nonparametric variable model for ischemic stroke was discussed.

2. Materials and Methods

2.1. Research Objects. One hundred and sixteen patients with acute ischemic stroke admitted to the hospital from February 20, 2019, to July 10, 2021, were selected as subjects aged 25–71 years. The average age was 44.87 ± 2.6 years, including 73 males and 43 females. This study was approved by the ethics committee of the hospital and the patients and their families understood the study and signed informed consent.

Inclusion criteria were as follows: (i) patients with the first onset; (ii) patients without claustrophobia; (iii) patients with focal neurological deficits; (iv) patients only receiving medication; and (v) patients with good compliance.

Exclusion criteria were as follows: (i) patients with mental diseases; (ii) patients with poor image quality; (iii) patients with incomplete clinical data; and (iv) patients who quit the experiment halfway.

2.2. MRI Examination. Patients were examined by a 1.5 T superconducting magnetic resonance system with an 8-channel head coil. During the examination, the patient was in the supine position, wearing a matching headphone, and then, the sponge pad was placed between the subject's head and the MRI coil.

Conventional MRI examination included fast spin-echo sequence (T2WI), gradient-echo sequence (T1WI), fast spin-echo sequence (FLAIR), plane echo sequence (DWI), 3D gradient echo sequence (SWI), and 3D time of flight, magnetic resonance angiography (3D TOF MRA). The scanning parameters of each sequence are shown in Table 1.

MR SCALE-PWI scan: after routine scans, gadolinium injection of a glumine contrast agent (0.15 mmol/kg at 3.5 mL/s) was automatically injected with a high-pressure syringe 45 seconds later, followed by injection of 20 mL of normal saline at the same rate. The scan parameters are shown in Table 2. The generated qCBF and qCBV images were transferred to the workstation for processing; the intelligent segmentation model was used to delineate the region of interest (ROI) of lesions, and the size and quantitative values of the ROI were calculated.

2.3. Nonparametric Variable Model Based on Histogram Analysis. Based on the histogram analysis of the images, the Gaussian mixture model was employed to fit the histogram, and the obtained image's statistical characteristic parameters were taken as the constraint conditions to replace the stop term regarding image gradient information in the traditional method, thus guiding and controlling the evolution of the curve and completing the image segmentation.

Gaussian mixture model (GMM) is a probabilistic clustering method [15], which belongs to the generative model. It assumes that all data samples are generated by multivariate Gaussian distribution of a given parameter (Figure 1). Its definition can be expressed as follows:

$$\rho(x) = \sum_{l=1}^{L} \pi_l R\left(\frac{x}{\mu_l} \sum_l\right). \tag{1}$$

$R(x/\mu_l, \sum_l)$ is the Gaussian distribution, μ_l represents the mean, $\sum_l$ represents the covariance, π_l represents the mixing coefficient, and π_l satisfies $\sum_{l=1}^{L} \pi_l = 1$, $0 \leq \pi_l \leq 1$.

From the viewpoint of sum and product, edge density can be expressed as follows:

$$\rho(x) = \sum_{l=1}^{L} p(l) p\left(\frac{x}{l}\right). \tag{2}$$

$\pi_l = p(l)$ represents the prior probability that a data sample produces the l Gaussian component and $R(x/\mu_l, \sum_l) = p(x/l)$ represents the x probability under a given l rule. For a given GMM, it is also necessary to determine the unknowns contained in each Gaussian component of the model, such as mean, covariance, and mixing coefficient. This study uses the expectation-maximization algorithm based on maximum likelihood estimation to estimate the model parameters [16]. It is assumed that the sample set is $X = \{x_1, x_2, x_3, \cdots, x_m\}$ and the value set of the implied variable r is $R = \{r_1, r_2, r_3, \cdots, r_m\}$, and then, the logarithmic likelihood function of the sample set can be expressed as follows:

$$K(\alpha) = \sum_R p\left(X, \frac{R}{\alpha}\right). \tag{3}$$

$p(X, R/\alpha)$ represents a probability model with an unknown parameter α as the parameter, and $\alpha = \{\mu_l, \sum_l, \pi_l / l = 1, 2, \cdots, L\}$.

Table 1: Conventional MRI parameters.

Parameter	Axis position T2WI	Axis position T1WI	Axis position FLAIR	Sagittal position T1WI	Axis position DWI	SWI	3D TOF MRA
TR (ms)	4500	400	8400	200	2400	25	21
TE (ms)	97	2.5	105	2.48	50	18.5	3.5
FOV (mm)	250 × 250	250 × 250	250 × 250	250 × 250	250 × 250	250 × 250	220 × 220
Layer thickness (mm)	6	6	6	6	6	2	0.5
Number of incentives	1	1	1	1	1	1	1
Matrix	320 × 320	320 × 320	320 × 320	320 × 320	160 × 160	521 × 521	320 × 320
Scanning time (s)	62	48	115	50	64	216	216

Table 2: MR SCALE-PWI scan parameters.

Parameter	MR SCALE-PWI
TR (ms)	1500
TE (ms)	32
FOV (mm)	230 × 230
Layer thickness (mm)	6
Number of incentives	1
Matrix	125 × 125
Scanning time (s)	135

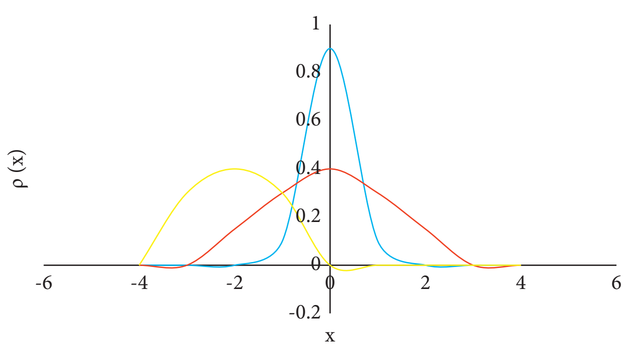

Figure 1: Gaussian mixture model (three Gaussian components).

By maximizing the logarithmic likelihood function, the maximum likelihood solution of the parameter can be obtained. The iterative process of the expectation-maximization algorithm is mainly divided into two steps. The first step is to calculate the expectation of the likelihood function according to the initial value of the parameter or the last iteration value. The second step is to maximize the likelihood function to obtain new parameter values.

When the sample size is M, the expectation obtained through the first step can be expressed as follows:

$$P\left(\frac{\alpha}{\alpha^m}\right) = \sum_{l=1}^{L}\sum_{i=1}^{m} p\left(\frac{l}{x_i,}\alpha^m\right)\log \pi_i + \sum_{l=1}^{L}\sum_{i=1}^{m} p\left(\frac{l}{x_i,}\alpha^m\right)\log p_l\left(\frac{x_i}{\alpha_l}\right). \tag{4}$$

$\rho_l(x_i/\alpha_l)$ corresponds to the l Gaussian component and $\rho(l/x_i,\alpha^m)$ represents the posterior probability of the l Gaussian component.

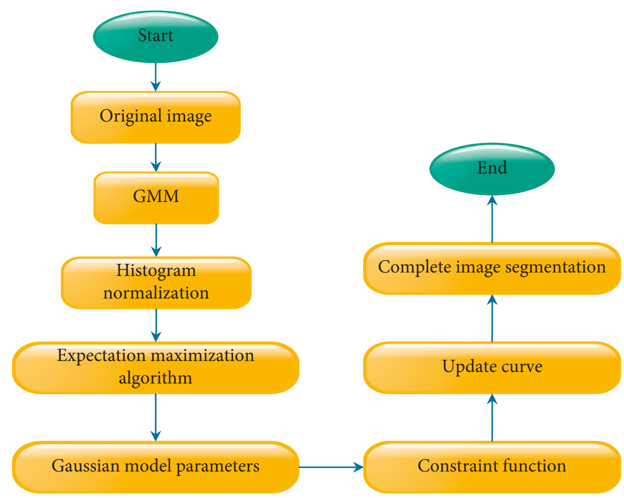

Figure 2: Nonparametric variable model image segmentation process based on histogram analysis.

$$p(l/x_i,\alpha^m) = \frac{\pi_l p_l(x_i/\alpha_l)}{\sum_{l=1}^{L}\pi_l p_l(x_i/\alpha_l)}. \tag{5}$$

After obtaining the expectation, the second step is used to calculate the model parameters.

$$\begin{aligned}
\pi_l^{m+1} &= \frac{\sum_{i=1}^{M} p_l(l/x_i,\alpha_l^m)}{M},\\
\mu_l^{m+1} &= \frac{\sum_{i=1}^{M} x_i p_l(l/x_i,\alpha_l^m)}{\sum_{i=1}^{M} p_l(x_i/x_i,\alpha_l^m)},\\
\sum_l^{m+1} &= \frac{\sum_{i=1}^{M}\left(x_i-\mu_l^{m+1}\right)^2 p_l(l/x_i,\alpha_l^m)}{\sum_{i=1}^{M} p_l(l/x_i,t\alpha_l^m)}.
\end{aligned} \tag{6}$$

The first step and the second step are iterated until the model parameters converge. Therefore, the nonparametric variable model image segmentation process based on histogram analysis is shown in Figure 2.

2.4. Algorithm Performance Indicators. The segmentation performance of the algorithm was assessed regarding sensitivity, specificity, and overall performance. Parametric

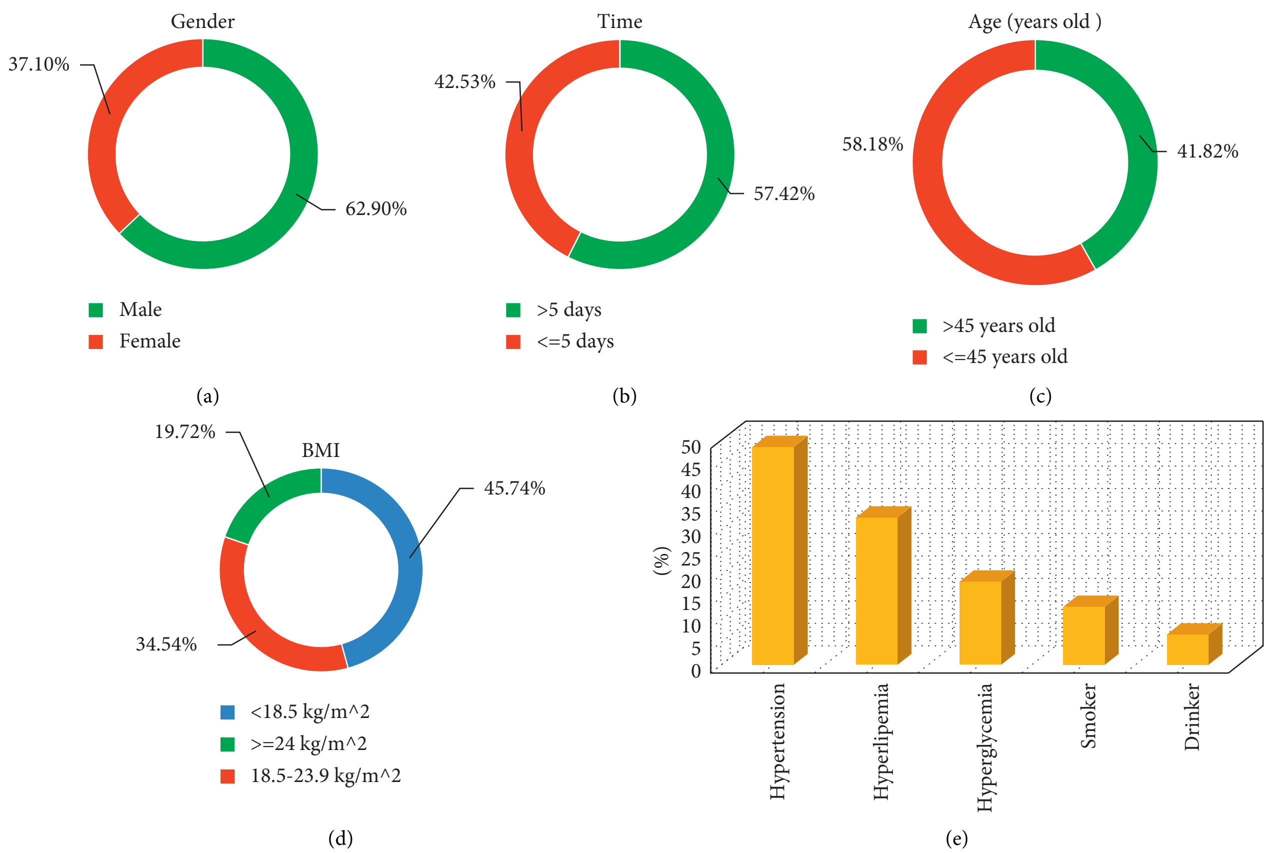

Figure 3: Basic information of patients. (a) Gender ratio; (b) the time interval from the onset of the first symptom to the follow-up MRI examination; (c) age; (d) BMI; (e) past medical history.

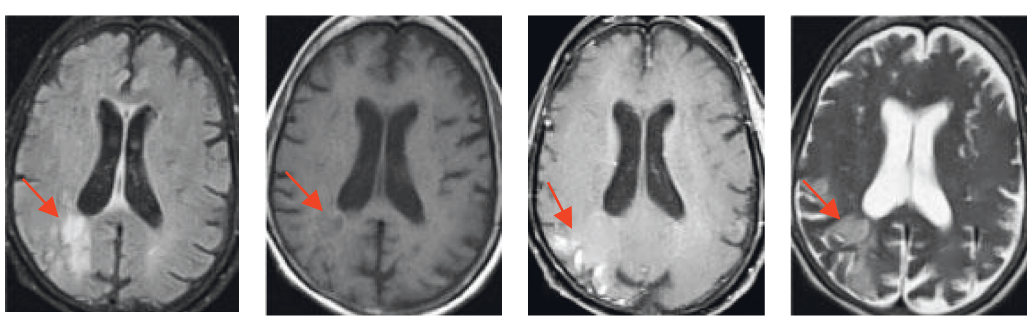

(a) (b) (c) (d)

Figure 4: MRI image of a 58-year-old female patient. The arrows in the images indicate the relevant stroke area.

deformation (PD) [17] and geometric deformation (GD) models [18] were compared with the proposed algorithm:

$$\text{sensitivity} = \frac{TP}{TP + FN},$$
$$\text{specificity} = \frac{TN}{FP + TN}, \qquad (7)$$
$$\text{overall performance} = \frac{TP + TN}{FN + FP + TP + TN},$$

where TP is true positive, TN is true negative, FP is false positive, and FN is false negative.

2.5. Clinical Data Collection. The age, gender, time interval from the onset of the first symptom to the follow-up MRI examination, past history (heart disease, stroke, transient ischemic attack, atherosclerosis, and other related diseases), National Institutes of Health Stroke Scale (NIHSS) score, and modified Rankin scale (mRS) score were collected.

2.6. Statistical Method. The data in this study were analyzed by SPSS 19.0. The measurement data were expressed as mean ± standard deviation ($\overline{x} \pm s$), and the count data were expressed as percentage. One-way analysis of variance was used for pairwise comparison. ROC curves were used to analyze the diagnostic effects of DWI, SWI, 3D TOF MRA, and MR SCALE-PWI sequences on ischemic penumbra in patients. The difference was statistically significant with $P < 0.05$.

3. Results

3.1. Basic Data of Patients. Figure 3 shows that the proportion of male patients (62.9%) was higher than that of female patients (37.1%). The proportion of patients with the first symptom onset to follow-up MRI examination interval greater than 5 days (57.42%) was higher than that of patients within 5 days (42.53%). The proportion of patients older than 45 years (58.18%) was higher than that of patients younger than 45 years (41.82%). The proportion of patients with BMI less than 18.5 kg/m^2 (45.74%) was the highest, followed by patients with BMI 18.5–23.9 kg/m^2 (42.53%), and the proportion of patients with BMI greater than 24 kg/m^2 (19.72%) was the lowest.

According to the past medical history of the 116 patients, 56 patients had hypertension, accounting for 48.51%. There were 38 patients with hyperlipidemia, accounting for 32.86%. There were 22 patients with hyperglycemia, accounting for 18.62%. There were 15 smokers, accounting for 13.09%. There were 8 drinkers, accounting for 6.96%.

3.2. MRI Images of Patients. Figure 4 shows MRI images of a 58-year-old female patient with early subacute ischemic stroke. FLAIR in image A shows hyperintensity in the corresponding area, T1W1 in image B shows hypointensity in the corresponding area, T1 enhanced scan in image C shows parenchymal enhancement in the affected area, and T2W1 in image D shows hyperintensity in the corresponding area.

3.3. Algorithm Performance Analysis. Figure 5 shows the comparison of the diagnostic sensitivity, specificity, and overall performance of the algorithm. The diagnostic sensitivity of the algorithm in this study was 98.41%, the specificity was 93.06%, and the overall performance was 95.58%. The diagnostic sensitivity of the GD algorithm was 91.07%, the specificity was 83.57%, and the overall performance was 85.02%. The diagnostic sensitivity, specificity, and overall performance of the PD algorithm were 89.93%, 85.91%, and 88.25%, respectively. The diagnostic sensitivity, specificity, and overall performance of the proposed algorithm were significantly higher than those of the GD algorithm and PD algorithm, and the difference was statistically significant ($P < 0.05$).

Figure 6 shows the segmentation effect of the algorithm on MRI images. The segmentation results of the algorithm on MRI images were relatively complete, the display clarity of the lesion was better than other algorithms, and the overall quality was the best.

3.4. ROC Curve Analysis. Figure 7 shows the ROC curve analysis of DWI, SWI, 3D TOF MRA, and MR SCALE-PWI sequences in the diagnosis of ischemic penumbra in patients.

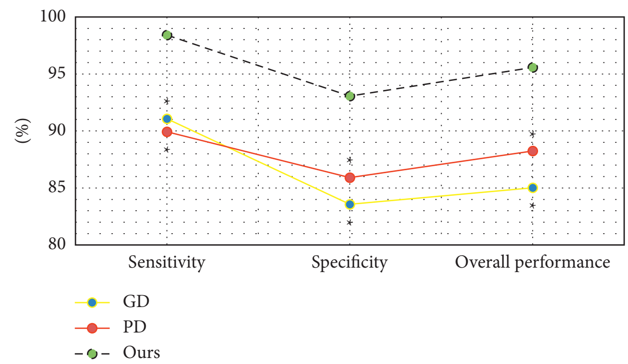

Figure 5: Diagnostic sensitivity, specificity, and overall performance of the algorithm. *Compared with the algorithm, $P < 0.05$.

The AUC of the DWI sequence in the diagnosis of ischemic penumbra was 0.793, that of SWI was 0.825, that of 3D TOF MRA was 0.871, that of MR SCALE-PWI was 0.933, and that of MR SCALE-PWI was the highest.

4. Discussion

Cerebral ischemia is caused by the decrease of local or diffuse cerebral blood flow. When the blood flow is lower than a certain value, ischemia becomes irreversible infarction. Ischemic stroke refers to an acute neurological dysfunction caused by a single or multiple focal cerebral infarction [19]. At present, neuroimaging examination is a common clinical method for the diagnosis of ischemic stroke. Early use of CT, CT angiography, conventional MRI, DWI, and other means is helpful to prevent the occurrence and development of stroke, and MRI multimodal imaging is the most widely used [20]. The original image often has the problems of more noise, more artifacts, and low quality. It is necessary to introduce a mathematical model for enhancement processing. A nonparametric variable model based on histogram analysis is proposed, and its performance is compared with the PD and GD models. The diagnostic sensitivity, specificity, and overall performance of the proposed algorithm are significantly higher than those of the GD and PD algorithms, and the difference is statistically significant ($P < 0.05$), which is similar to the results obtained by Mathukumalli et al. [21]. It shows that the nonparametric variable model based on the histogram analysis designed in this study has a good segmentation effect on MRI images and can effectively improve the quality of the original image. By comparing the segmentation results of the algorithm for MRI images, the segmentation results of the algorithm in this study for MRI images are relatively complete, and the clarity of the lesion is better than that of other algorithms. The overall quality is the best, which is consistent with the results of quantitative data [22].

116 patients with acute ischemic stroke were selected as the subjects. Routine MRI (T2WI, T1WI, FLAIR, DWI, SWI, and 3D TOF MRA) and MR SCALE-PWI were performed. The data of patients were analyzed, and it was found that the proportion of male patients (62.9%) was higher than that of female patients (37.1%), which may be due to the large

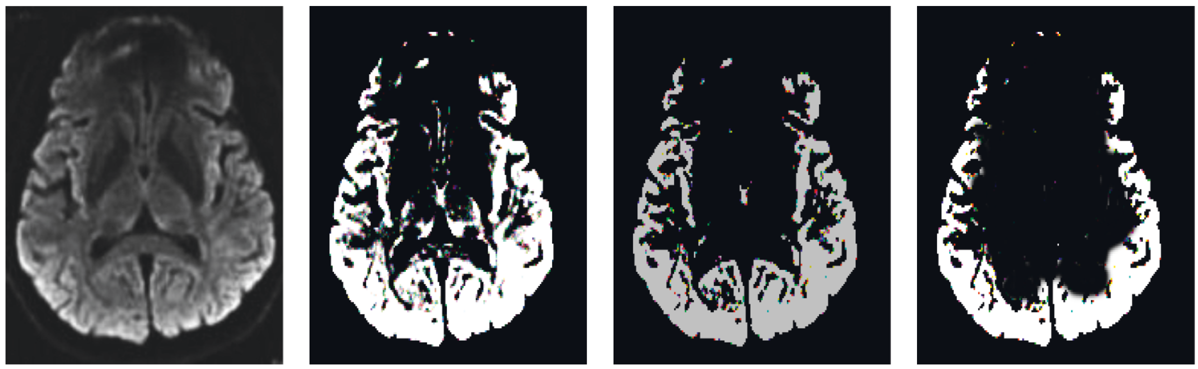

Figure 6: Segmentation effect of MRI images by the algorithm. (a) The original image; (b) the algorithm result; (c) the segmentation result of the GD algorithm; (d) the segmentation result of the PD algorithm.

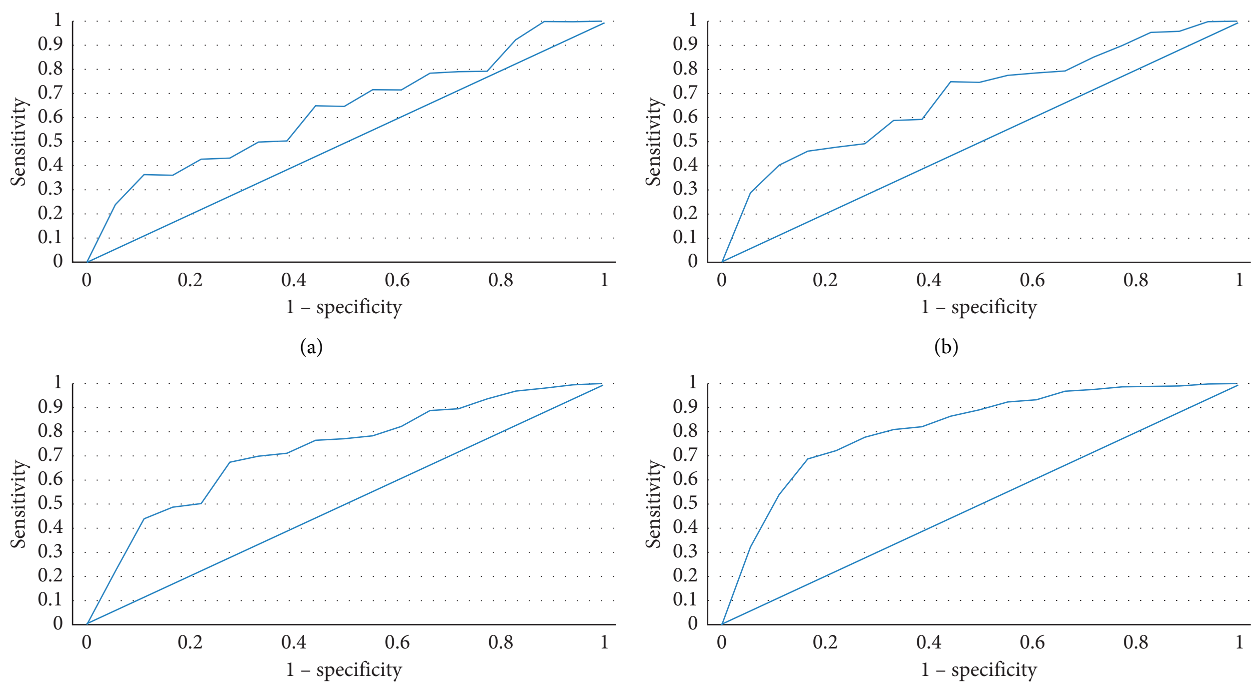

Figure 7: ROC curves of DWI, SWI, 3D TOF MRA, and MR SCALE-PWI sequences in the diagnosis of ischemic penumbra in patients. (a) DWI sequence; (b) SWI sequence; (c) 3D TOF MRA sequence; (d) MR SCALE-PWI sequence.

number of male smokers [23]. The proportion of patients older than 45 years(58.18%) was higher than that of patients younger than 45 years (41.82%), indicating that the incidence of ischemic stroke in the elderly population was higher. Among 116 patients, 56 patients were with hypertension, 38 patients with hyperlipidemia, 22 patients with hyperglycemia, 15 cases of smokers, and 8 cases of drinkers. The medical history was correlated with the occurrence of ischemic stroke [24]. ROC curve analysis showed that the AUC area of the DWI sequence in the diagnosis of ischemic penumbra was 0.793. The AUC area of the SWI sequence in the diagnosis of ischemic penumbra was 0.825. The AUC area of the 3D TOF MRA sequence in the diagnosis of ischemic penumbra was 0.871. The AUC area of the MR SCALE-PWI sequence in the diagnosis of ischemic penumbra was 0.933. This indicates that MR SCALE-PWI has a good effect on the early identification of ischemic penumbra, which can reduce unnecessary treatment and prolong the time window for patients to receive recanalization or neuroprotective treatment [25].

5. Conclusion

In this work, the nonparametric variable model based on histogram analysis was compared with PD and GD models, and 116 patients with acute ischemic stroke were given routine MRI scans at the same time. The results showed that the variable model algorithm had a strong ability to completely segment MRI images and display lesions and can effectively identify the occurrence of ischemic stroke. Moreover, the MR SCALE-PWI sequence had a better early identification effect on the ischemic penumbra, regarding which an effective treatment plan can be formulated. However, the disadvantage is that the sample size of patients is small, and the results may be biased. The PET data of patients are not collected, and the evaluation value of the gold standard and MRI cannot be compared. Third, the MRI equipment used is the latest purchase, and the LOVARS MRI data are not collected. In the future, the sample size of patients will be expanded, and the identification performance of the MR SCALE-PWI sequence in ischemic core and ischemic penumbra will be further explored. In conclusion, this study provides a reference for the clinical diagnosis of ischemic stroke patients.

Data Availability

The data used to support the findings of this study are available from the corresponding author upon request.

Conflicts of Interest

The authors declare no conflicts of interest.

Authors' Contributions

Zhenghong Wu and Dongqiu Wu contributed equally to this work.

References

[1] E. Zhang and P. Liao, "Brain-derived neurotrophic factor and post-stroke depression," *Journal of Neuroscience Research*, vol. 98, no. 3, pp. 537–548, Mar 2020.

[2] C. Sampaio-Baptista, Z.-B. Sanders, and H. Johansen-Berg, "Structural plasticity in adulthood with motor learning and stroke rehabilitation," *Annual Review of Neuroscience*, vol. 41, no. 1, pp. 25–40, Jul 8 2018.

[3] P. E. Turkeltaub, "A taxonomy of brain-behavior relationships after stroke," *Journal of Speech, Language, and Hearing Research*, vol. 62, no. 11, pp. 3907–3922, 2019.

[4] A. Baldassarre, L. E. Ramsey, J. S. Siegel, G. L. Shulman, and M. Corbetta, "Brain connectivity and neurological disorders after stroke," *Current Opinion in Neurology*, vol. 29, no. 6, pp. 706–713, Dec 2016.

[5] A. Crofts, M. E. Kelly, and C. L. Gibson, "Imaging functional recovery following ischemic stroke: clinical and preclinical fMRI studies," *Journal of Neuroimaging*, vol. 30, no. 1, pp. 5–14, Jan 2020.

[6] X. Ayrignac, N. Gaillard, C. Carra-Dallière, and P. Labauge, "Microangiopathie cérébrale: du diagnostic à la prise en charge small vessel disease of the brain: diagnosis and management," *La Revue de Medecine Interne*, vol. 41, no. 7, pp. 469–474, Jul 2020.

[7] J. Jiang, X. Huang, Y. Zhang, W. Deng, F. Shen, and J. Liu, "Total MRI burden of cerebral vessel disease correlates with the progression in patients with acute single small subcortical strokes," *Brain and Behavior*, vol. 9, no. 1, e01173 pages, Jan 2019.

[8] K. J. Wenger and E. Hattingen, "Schnelle MRT-Sequenzen für die akute neurologische Abklärung," *Radiologe, Der*, vol. 60, no. 3, pp. 208–215, Mar 2020.

[9] W. Lin and W. J. Powers, "Oxygen metabolism in acute ischemic stroke," *Journal of Cerebral Blood Flow and Metabolism*, vol. 38, no. 9, pp. 1481–1499, Sep 2018.

[10] D. A. Ferro, S. J. van Veluw, H. L. Koek, L. G. Exalto, and G. J. Biessels, "Cortical cerebral microinfarcts on 3 tesla MRI in patients with vascular cognitive impairment," *Journal of Alzheimer's Disease*, vol. 60, no. 4, pp. 1443–1450, 2017.

[11] B. Hordacre, B. Moezzi, and M. C. Ridding, "Neuroplasticity and network connectivity of the motor cortex following stroke: a transcranial direct current stimulation study," *Human Brain Mapping*, vol. 39, no. 8, pp. 3326–3339, Aug 2018.

[12] J.-P. Nicolo, T. J. O'Brien, and P. Kwan, "Role of cerebral glutamate in post-stroke epileptogenesis," *NeuroImage: Clinica*, vol. 24, p. 102069, 2019.

[13] D. A. Ferro, H. J. Mutsaerts, S. Hilal et al., "Cortical microinfarcts in memory clinic patients are associated with reduced cerebral perfusion," *Journal of Cerebral Blood Flow and Metabolism*, vol. 40, no. 9, pp. 1869–1878, Sep 2020.

[14] Q. Y. Zhao, Y. Zheng, and X. M. Wang, "[Clinical and imaging features of cerebral infarction in children]," *Zhong Guo Dang Dai Er Ke Za Zhi*, vol. 21, no. 4, pp. 354–358, Apr 2019.

[15] W. L. Nowinski, "Human brain atlases in stroke management," *Neuroinformatics*, vol. 18, no. 4, pp. 549–567, Oct 2020.

[16] J. J. Lee-Jayaram, L. N. Goerner, and L. G. Yamamoto, "Magnetic resonance imaging of the brain in the pediatric emergency department," *Pediatric Emergency Care*, vol. 36, no. 12, pp. 586–590, Dec 2020.

[17] P. Cui, L. D. McCullough, and J. Hao, "Brain to periphery in acute ischemic stroke: mechanisms and clinical significance," *Frontiers in Neuroendocrinology*, vol. 63, p. 100932, Oct 2021.

[18] C. D. Maida, R. L. Norrito, M. Daidone, A. Tuttolomondo, and A. Pinto, "Neuroinflammatory mechanisms in ischemic stroke: focus on cardioembolic stroke, background, and therapeutic approaches," *International Journal of Molecular Sciences*, vol. 21, no. 18, p. 6454, Sep 4 2020.

[19] E. Sidorov, C. Iser, N. Kapoor et al., "Criteria for emergency brain MRI during stroke-alert," *Journal of Stroke and Cerebrovascular Diseases*, vol. 30, no. 8, p. 105890, Aug 2021.

[20] M. Zhang, Y. Cao, F. Wu et al., "Characteristics of cerebral perfusion and diffusion associated with crossed cerebellar diaschisis after acute ischemic stroke," *Japanese Journal of Radiology*, vol. 38, no. 2, pp. 126–134, Feb 2020.

[21] S. Kaul, N. Mathukumalli, R. Dandu, and M. Kanikannan, "Clinicoradiological profile of superficial middle cerebral vein thrombosis," *Neurology India*, vol. 68, no. 2, pp. 373–377, Mar-pr 2020.

[22] A. S. Luthman, L. Bouchez, D. Botta, M. I. Vargas, P. Machi, and K.-O. Lövblad, "Imaging clot characteristics in stroke and its possible implication on treatment," *Clinical Neuroradiology*, vol. 30, no. 1, pp. 27–35, Mar 2020.

[23] R. McKinley and R. Marshall, "Advanced MRI in acute stroke," *Neurology*, vol. 92, no. 21, pp. 983-984, May 21 2019.

[24] D. Mallon, L. Dixon, T. Campion et al., "Beyond the brain: extra-axial pathology on diffusion weighted imaging in neuroimaging," *Journal of the Neurological Sciences*, vol. 415, p. 116900, Aug 15 2020.

[25] L. L. Lehman, A. R. Danehy, C. C. Trenor et al., "Transient focal neurologic symptoms correspond to regional cerebral hypoperfusion by MRI: a stroke mimic in children," *American Journal of Neuroradiology*, vol. 38, no. 11, pp. 2199–2202, Nov 2017.

Hindawi
Contrast Media & Molecular Imaging
Volume 2022, Article ID 3315121, 9 pages
https://doi.org/10.1155/2022/3315121

Research Article

Value of Magnetic Resonance Images and Magnetic Resonance Spectroscopy in Diagnosis of Brain Tumors under Fuzzy C-Means Algorithm

Huaiqin Liu, Qi Zhang, Shujun Niu, and Hao Liu

Department of Radiology, Zibo Central Hospital, Zibo 255000, Shandong, China

Correspondence should be addressed to Hao Liu; 201772350@yangtzeu.edu.cn

Received 21 March 2022; Revised 3 May 2022; Accepted 5 May 2022; Published 30 May 2022

Academic Editor: M. Pallikonda Rajasekaran

This study was aimed to explore the diagnostic value of magnetic resonance imaging (MRI) and magnetic resonance spectroscopy (MRS) in brain tumors under the fuzzy C-means (FCM) algorithm. The two-dimensional FCM hybrid algorithm was improved to be three-dimensional. The MRI images and MRS spectra of 127 patients with brain tumors (low-grade glioma group) and 54 healthy people (healthy group) were analyzed. The results suggested that the membership matrix of the improved algorithm had lower ambiguity, higher segmentation accuracy, closer relationship of intrapixels, and stronger irrelevance of interclass pixels. Through the analysis of gray matter volume, it was found that, compared with the healthy group, the gray matter and white matter volumes in the brain of high-grade glioma were higher, and those of low-grade glioma group were lower. The improved FCM algorithm could obtain a higher accuracy of 88.64% in segmenting images. It had a higher sensitivity to gray matter changes in brain tumors, reaching 92.72%; its specificity was not much different from that of traditional FCM, which were 83.61% and 88.06%, respectively. In the diagnostic value, the area under the curve of mean kurtosis was the largest, which was 0.962 ($P < 0.001$). The best critical value was 0.4096, which had a greater reference significance for clinical treatment and prognosis. The ratio of choline/N-acetyl-aspartate and the ratio of choline/creatine also showed significant differences in high- and low-grade gliomas ($P < 0.05$), but the specificity and sensitivity were slightly lower. It also had guiding significance for the grading of gliomas. Overall, the improved FCM algorithm had obvious advantages in the segmentation process of MRI images, which provided help for the clinical diagnosis of brain tumors.

1. Introduction

Brain tumors are made up of primary and secondary ones. Among various types of intracranial tumors, gliomas occupy the first place in the morbidity, which is about 40%–45% [1]. Glioma originates from human neuroepithelium and commonly includes astrocytoma, astroblastoma, and glioblastoma multiforme. Glioma is usually caused by the interaction of congenital genetic high-risk factors and environmental carcinogenic factors [2]. Due to its space-occupying effect, patients will have symptoms such as headache, nausea and vomiting, epilepsy, and blurred vision. Different pathological types of gliomas can also cause different clinical symptoms. For example, patients with optic glioma will lose vision to some extent, while patients with spinal glioma have symptoms such as limb pain, numbness, and muscle weakness [3, 4]. The degree of malignancy also affects the speed at which symptoms occur. Patients with low-grade gliomas often have a medical history of months or even years, while patients with high-grade gliomas usually have the history of weeks to months [5]. As the tumor continues to develop, the difficulty of surgical resection increases. Thus, early detection and diagnosis of glioma is very important to prevent the further development of the disease.

Medical imaging technology can be applied to detect abnormal changes in tissues of the body, and it becomes a necessary means for the determination of the treatment plan for brain tumors. There are many medical imaging technologies nowadays, including computed tomography (CT), magnetic resonance imaging (MRI), functional magnetic resonance imaging (FMRI), positron emission tomography (PET), and diffusion tensor imaging (DTI) [6]. Due to the diverse types of brain tumors, the development of imaging technologies, and the limitations of three-dimensional data, manual segmentation of brain tumor images showed the long time-consumption, inexperience, and poor repeatability. To deal with the brain tumor image segmentation effectively, many scholars have come up with some segmentation algorithms [7], but so far, the segmentation of brain tumor images has not been maturely applied clinically [8]. Magnetic resonance spectroscopy (MRS) is the only examination technology for noninvasive detection of chemical components in the body using the principle of chemical shift. Diffusion kurtosis imaging (DKI) is a new MRI technology on the basis of DTI technology, and it can reflect the water molecular diffusion in non-Gaussian distribution in biological tissues [9]. It has been found that the complexity of biological tissue structure is positively correlated with the DKI parameter value [10].

The different membership functions were adopted to set the target under fuzzy clustering algorithm here, and then the connection point of the functions was determined as the threshold by optimizing the target function [11]. The image segmentation process can also be regarded as a clustering process, and the advantage of fuzzy clustering is to utilize different membership functions to classify data points into multiple clusters. The commonly used clustering methods include fuzzy *C*-means (FCM) clustering, *K*-means algorithm, and expectation maximization algorithm [12]. It was to study MRI images of brain tumor and MRS spectra on the basis of FCM algorithm in this work. The two-dimensional hybrid of FCM algorithm was optimized to the three-dimensional one, and the spectra were expanded to the distribution in the two-dimensional or even three-dimensional space. The improved algorithm was applied to the cerebral MRI images of 127 brain tumor patients in the low-grade glioma group as well as 54 healthy volunteers in the healthy group. This study was intended to provide a valuable reference for the clinical diagnosis of brain tumors.

2. Materials and Methods

2.1. Principles of FCM Algorithm. FCM algorithm is a kind of clustering algorithm, which is improved from the hard clustering. The core idea of the clustering algorithm was to find the appropriate membership and clustering center. That is, when the variance and iteration error of the clustering cost function were minimized, as a result, the value of the cost function was the weighted cumulative summation of the 2-norm measure from the pixel to the clustering center. It is assumed that $M = \{m_1, m_2, \ldots, m_n\}$ is the grayscale or eigenvalue of the image pixels, and f is the number of clusters (number of clustering centers) that divide M. The clustering centers are expressed as $A = \{a_1, a_2, \ldots, a_f\}$, $b = \{b_{xy}\}$ denotes the membership matrix, and b_{xe} means m_x belongs to the membership degree of the e-th class area. The cost function of FCM is expressed as

$$\min E_l B, A = \sum_{x=1}^{F} \sum_{y=1}^{n} b_{xy}^{l} r_{xy}^{2}. \tag{1}$$

This equation satisfied the following equations:

$$\sum_{x=1}^{f} b_{xy} = 1,\ 1 \leq y \leq n, \tag{2}$$

$$\sum_{y=1}^{f} b_{xy} > 0,\ 1 \leq x \leq f, \tag{3}$$

$$b_{xy} = 1 \leq x \leq f,\ 1 \leq e \leq n. \tag{4}$$

In the equations, $B = b_{xy}$ is an $n \times x$ fuzzy membership matrix, which represents the size of the membership value of the y-th sample m_y belonging to the x-th class, with a range of 0–1. l is the weighted index, and $A = \{a_1, a_2, \ldots, a_f\}$ is the $h \times f$ matrix composed of f clustering center vectors. $r_{xy} = \|m_y - a_x\|$ means the Euclidean distance from the sample point m_y to the clustering center a_x, which is just the 2-norm measure from the pixel m_y to the clustering center.

For the minimization of the cost function E (B, A), the Lagrange multiplier method was used to construct the objective optimization function. The partial derivative of the clustering center a_x and the membership degree b_{xy} of the objective function was obtained, and the derivative result was set to zero. Then, the iterative update expressions for the clustering center and membership degree were worked out as

$$a_x = \left(\sum_{y=1}^{f} b_{xy}^{l} \right)^{-1} \sum_{y=1}^{f} \left(b_{xy}\right)^{l} m_y, \quad x = 1, 2, \ldots, f, \tag{5}$$

$$T_y = \{(x, y) | m_y = a_x, 1 \leq x \leq f\}. \tag{6}$$

If $T_y = \beta$, then the following equation can be obtained.

$$b_{xy} = \frac{1}{\left[\sum_{g=1}^{f} r_{gy}{}^{-1} r_{xy}\right]}, x = 1, 2, \ldots, f,\ y = 1, 2, \ldots, n, \tag{7}$$

If $T_y \neq 0$, then b_{xy} is any nonnegative real number satisfying

$$\sum_{x=1}^{f} b_{xe} = 1,\ b_{xe} \in [0, 1]. \tag{8}$$

The iterative equation for membership degree is a mapping from points to sets. In the actual calculation process, the following membership update equations are usually used.

$$b_{xy} = \left[\sum_{x=1}^{f} r_{gy}{}^{-1} r_{xy}^{2/l-1} \right]^{-1}, \quad T_y \neq \beta \tag{9}$$

$$b_{xy} = \left|T_y\right|^{-1}, \quad T_y \neq \beta, \quad x \in T_y, \tag{10}$$

$$b_{xy} = 0, \quad T_y \neq \beta, \quad x \notin T_y. \tag{11}$$

In the equations, I represents the number of iterations of the function. It is assumed that the iteration equations (3) and (7) met the iteration termination conditions, that is, the iteration ended when $i > I$ or $max_x = a_x^{i+1} - a_x^i < \alpha$. After the iteration ended, the pixels were classified according to the principle of the maximum membership degree. If $b_{yx} > b_{ye}$, m_y is classified into the region of x-th class of clustering centers, where $e = 1, 2, \ldots, f;\ x \neq e$.

2.2. Improvement of FCM Algorithm. The FCM algorithm usually used Euclidean distance for clustering. The Euclidean distance metric function was suitable for clustering whose distribution was in spherical or ellipsoid shape. But when the clustering distribution did not belong to a specific shape, the Euclidean distance ignored the relationship among sample dimension features. It was inappropriate to use Euclidean distance in this case, so the kernel function was introduced to measure the distance between pixels in the space. The low-dimensional space was mapped to the high-dimensional space, and the complex nonlinear issue was transformed into the linear issue of kernel space [13, 14], enhancing the noise immunity of the algorithm. The steps of improving the FCM algorithm were given as follows.

Firstly, the images were intuitively blurred.

The original image was converted from the spatial domain to the fuzzy domain, and grayscale processing was performed on each pixel. For a grayscale image with a size of $C \times D$, the grayscale level was in the interval $[m_{\min}, m_{\max}]$. The image was represented by an intuitionistic fuzzy set as

$$Q = \{m_{xe}, b(m_{xe}), a(m_{xe}), \pi(m_{xe})\}, \quad 0 < x \leq C,\ 0 < e \leq D. \tag{12}$$

In the equation, $b(m_{xe})$ is the membership degree of m_{xe}, and m_{xe} is the gray level of the pixel (x, e), which described the degree of brightness of the grayscale value of the pixel. The membership and nonmembership were expressed as equations (13) and (14), respectively.

$$b(m_{xe}) = (b(m_{xe}))^2, \tag{13}$$

$$a(m_{xe}) = (1 - b(m_{xe}))^2. \tag{14}$$

The hesitation of the image after intuition fuzzification is expressed as

$$\pi(m_{xe}) = 2b(m_{xe})(1 - b(m_{xe})). \tag{15}$$

The grayscale value of each pixel could be computed through

$$m_e = (b(m_{xe}), a(m_{xe}), \pi(m_{xe})). \tag{16}$$

Secondly, the initialization parameters were given.

The membership matrix was extended to the grayscale range, and the intuitive fuzzification was performed on the grayscales of the image. The initial membership matrix M was then obtained. The number of clustering categories f, the spatial constraint parameter θ, the weighted index l, δ in the kernel function, and the neighborhood radius p, stopping threshold α of the iteration, and the maximum iteration number I were all set. The initial iteration number was set to be 0.

Thirdly, the local information of the pixel was calculated according to its principles.

Fourthly, the clustering center $A^{*(I)} = a_x^{*(I)}$ was updated according to equations (3) and (4):

$$a_x^{*(I)} = \frac{\sum_{y=1}^{n} \left(b_{xy}^{*(I)}\right)^l \left(m_y + \theta \overline{m}_y\right)}{\sum_{y=1}^{n} (1+\theta)\left(b_{xy}^{*(I)}\right)^l}. \tag{17}$$

Fifthly, the membership function matrix $B^{|I+1|} = b_{xy}^{|I+1|}$ was updated according to equation (5).

$$b_{xy}^{|I+1|} = \sum_{I=1}^{f} \left[\left(\frac{\left\|\varphi(m_y) - \varphi(a_x)\right\|^2 + \theta\left\|\varphi(m_y) - \varphi(\overline{a}_x)\right\|^2}{\left\|\varphi(m_y) - \varphi(a_p)\right\|^2 + \theta\left\|\varphi(m_y) - \varphi(\overline{a}_p)\right\|^2}\right)\right]^{-1/l-1} \tag{18}$$

Sixthly, the generated hesitation $\pi_{xy}^{(I+1)}$ was applied to modify the membership function matrix $B^{(I+1)} = b_{xy}^{(I+1)}$,and then the following equations were obtained.

$$b_{ey}^{(I+1)} = \max\left\{b_{xy}^{(I+1)}\right\}, \tag{19}$$

$$\begin{cases} b_{ey}^{(I+1)} = 1 - \pi_{xy}^{(I+1)} \sum\limits_{y \neq e} b_{xy}^{(I+1)} \\ b_{xy}^{(I+1)} = \pi_{xy}^{(I+1)} b_{xy}^{(I+1)} \end{cases}. \tag{20}$$

Seventhly, it was judged whether the condition for iteration stopping, $B^{(I+1)} - B^I < \alpha$, was satisfied. If the condition was met, the iteration ended. Otherwise, the fifth step was repeated for the next iteration in the case of $i = i + 1$.

Eighthly, defuzzification of the image was done. The membership degree of the corresponding the grayscale level of the obtained intuitionistic fuzzy partition matrix was substituted into the image, and the classification of pixels was made according to the principles of maximum membership degree.

2.3. Verification of Segmentation Performance of the Algorithm. It was not objective enough to judge whether the improved algorithm was successful only by manual judgment. It was more convincing to judge the improved algorithm from the segmentation effect images and, on the other hand, from the quantitative analysis by introducing some evaluation indexes. For the comparison of the segmentation performance of the algorithm, three evaluation indexes—partition coefficient (Vpc), partition entropy (Vpe), and Xie-Beni index (Vxb)—were introduced to analyze the segmentation performance of the improved algorithm.

2.4. MRI Data. Common formats of MRI image data mainly include DICOM, Analyze, and NIFTI. 127 patients with brain tumor (low-grade glioma group) and 54 healthy people (healthy group) were included as the objects. All raw collected data were in the standard DICOM common format. Since the collected data was in DICOM format, it was necessary to process the collected data before extraction of the brain tissues. In this process, the MRIconvert (http://www.nitrc.org/projects/mricron) software was used to process the 164-layer images of the same object. The image was converted from a two-dimensional space in DICOM format to a three-dimensional space image in NITH format. 3T-MRI instrument scanning equipment was used, and the T1 structural images of the heads of all objects were obtained. The specific imaging parameters are shown in Table 1.

MRI had three imaging modes of $\theta 1$-weighted, $\theta 2$-weighted, and proton density-weighted images. After the values of $\theta 1$, $\theta 2$, θa, and θb were given, the image pixels of human tissues are

$$S(\theta 1, \theta 2, \theta a, \theta b) = \sum_n \beta_n \left(1 - e^{-\frac{\theta a}{\theta 1} n}\right) e^{-\frac{\theta b}{\theta 2}} \tag{21}$$

2.5. Preprocessing Procedure. Before segmentation, registration, analysis, and visualization of brain MRI images, the images must be preprocessed, including head movement correction, edge detection, and morphological optimization. The brain tissues in the image were extracted, but some nonbrain tissue parts such as scalp, muscles, and skull would have a certain impact on the segmentation results, resulting in mis-segmentation. Moreover, in the researches of diseased tissue in some brain areas, the brain was usually used as the research objects. If brain tissue image was to be segmented, the scalp, skull, and other nontissue components must be removed first, which would greatly reduce the effect of nonbrain tissue components on the segmentation [15, 16]. Then, the brain tissue image was further divided into gray matter and white matter, and the obtained results were more conducive to subsequent quantitative analysis. For the same type of image data, the demand angles were different, and the advantages and disadvantages of the segmentation methods were also different. In the process of brain MRI image segmentation, it was very important to remove nontissue components in the segmentation. The border-based segmentation method could effectively remove the interference of other information, and the method was simple and fast. The raw brain MRI images could be observed as shown in Figure 1.

Figure 2 shows the brain MRI images of a male patient with a clinical diagnosis of low-grade glioma. The tumor region could be clearly displayed by MRI technology.

For the experimental environment, CPU was Intel i7, and the memory was 8 g. The operating system adopted Windows 10, and the programming environment adopted MATLAB 2015b. All MRI data (including those of 127 brain tumor patients and 54 healthy people) were segmented using the FCM-based segmentation method. An image segmented by the improved method was randomly selected. The segmentation process is shown in Figure 3.

2.6. Statistical Analysis. All experimental data were statistically analyzed by SPSS 26.0, and measurement data were expressed as the mean + standard deviation ($x(\_) \pm s$), while enumeration data were statistically inferred by χ^2 test. The measurement data conformed to normal distribution were tested using t-test, the rank sum test was performed for those did not conform to normal distribution, and a difference was considered statistically significant as $P < 0.05$. The receiver operator characteristic (ROC) curve was utilized for analyzing the sensitivity, specificity, and optimal diagnostic threshold of each index for grading diagnosis of glioma. The calibration level $\alpha = 0.05$, $P < 0.05$, indicated the difference to be statistically significant.

3. Results

3.1. Verification Results of the Algorithm. As shown in Figure 4, the improved FCM algorithm had the higher Vpc and lower Vpe compared with the original algorithm. This suggested that the membership matrix of the proposed improved algorithm had a lower degree of ambiguity and a higher segmentation accuracy. The results also showed that the Vxb was lower, indicating that the intraclass pixels were more closely related and the interclass pixels were more irrelevant. In general, the improved algorithm had obvious advantages in the process of image segmentation.

3.2. Experimental Results of Image Segmentation. The original FCM algorithm, the U-Net algorithm, and the improved FCM algorithm were used for the processing of the brain tumor MRI images. As the segmentation results are presented in Figure 5, the segmentation effect of the improved FCM algorithm was better than other algorithms.

Usually, the segmentation result would be compared with the gold standard to complete the analysis of the segmentation. However, brain MRI images represented complex brain tissue structures, and the gold standard segmentation became time-consuming and labor-intensive, making it difficult to realize. Therefore, statistical methods were usually used for analysis, and the experimental results were evaluated and analyzed from an indirect perspective to verify the validity and accuracy of the segmentation. With the continuous development of computer technology, machine learning methods have been widely used in medical image analysis with their own advantages. Medical image processing methods could be better evaluated, and the accuracy of their analysis results could also be improved. Therefore, the FCM segmentation method and the improved FCM segmentation method were compared and analyzed from the aspects of volume calculation and machine learning classification. The segmented data were divided into groups of low-grade glioma, high-grade glioma, and healthy control objects for analysis and comparison, to verify the accuracy of the improved segmentation method.

Volume calculation has been often used in quantitative analysis methods. It was simple in operation and accurate in results and widely used in the analysis of medical images, especially brain MRI images. Here, the segmented and

Table 1: Imaging parameters of MRI.

Items	Parameters	Functions
Time of repetition (θa)	1980 ms	It determined the value of $\theta 1$.
Delay time of echo (θb)	2.28 ms	The contrast of $\theta 2$ would be affected.
Frequency encoding direction	245 mm*245 mm*165 mm	The smaller the value, the higher the resolution.
Flip angle	8°	It defined echo pulse sequence.
Volume of a unit voxel in a brain image	1 mm³	

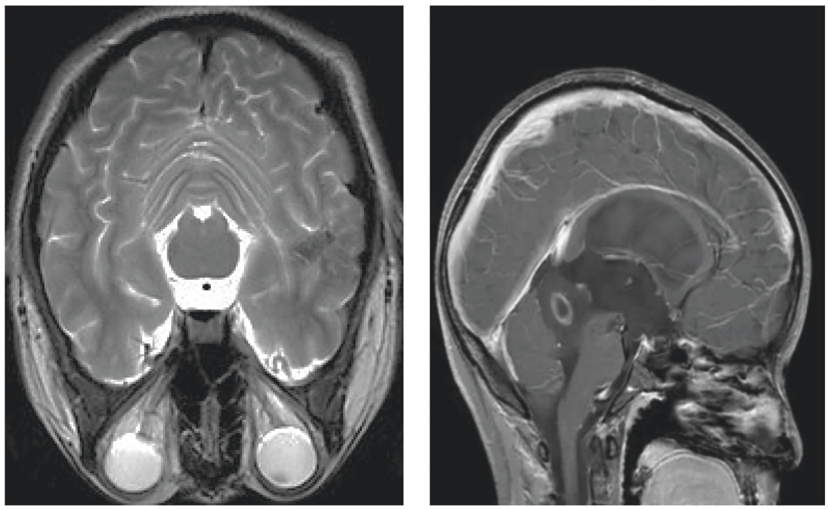

(a) (b)

Figure 1: MRI image of brain structure. Image (a) is in the coronal plane, and (b) is in the sagittal plane.

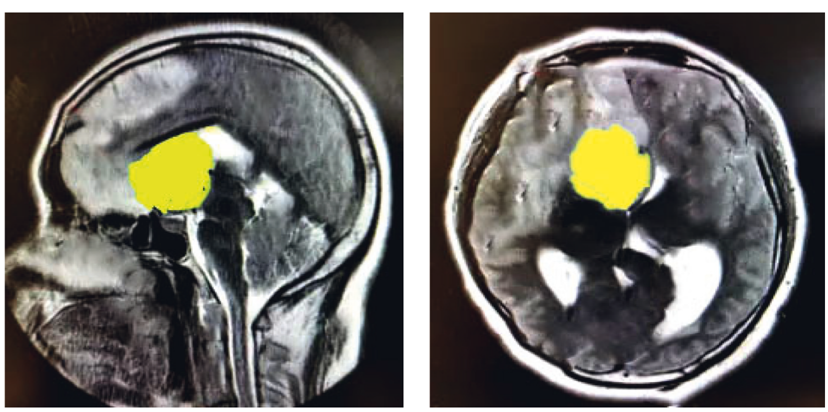

(a) (b)

Figure 2: MRI images of brain tumor, where (a) is in the sagittal plane and (b) is in the coronal plane. The yellow part in the images indicated the tumor region.

registered images were statistically organized in groups and categories, and the average volume of gray matter in each group was calculated. Compared with the healthy group, high-grade glioma showed the higher gray matter volume and white matter volume, while those of lower-grade glioma group were lower. Figure 6 shows the gray matter volume in different groups.

For the comparison of classification results, there have been more and more types of medical images, and related medical aided diagnosis technologies were also widely used. As medical images were closely combined with computer-aided diagnosis technology, the use of computer-aided diagnosis could improve the accuracy of diagnosis. It could also recognize and process various medical images and detect lesion areas. After feature extraction, the method of using pattern recognition and classification has become one of the important methods for diagnosis in medical images with the aid of computers. The comparison of classification results is shown in Figure 7.

Figure 7 shows that the improved FCM could give a higher accuracy in segmenting images, which reached 88.64%. It had a higher sensitivity to gray matter changes in

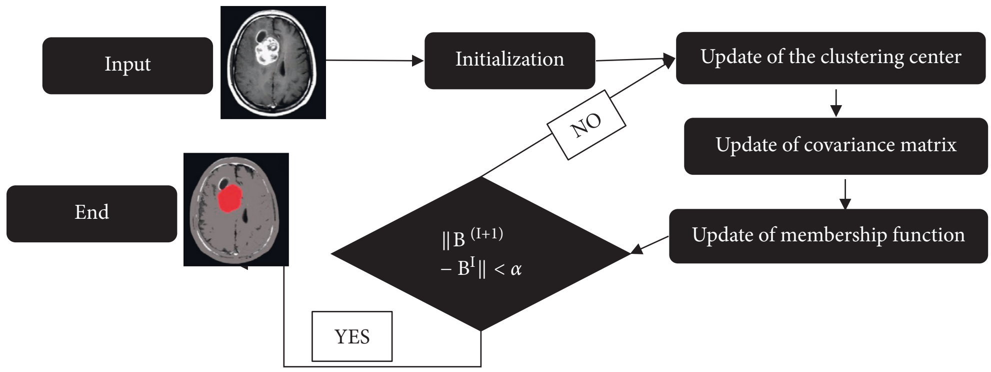

Figure 3: Segmentation flow chart.

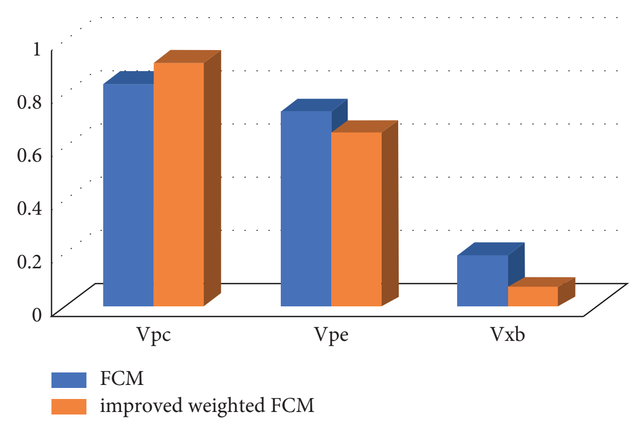

Figure 4: Performance comparison between the original algorithm and the improved FCM algorithm in image segmentation.

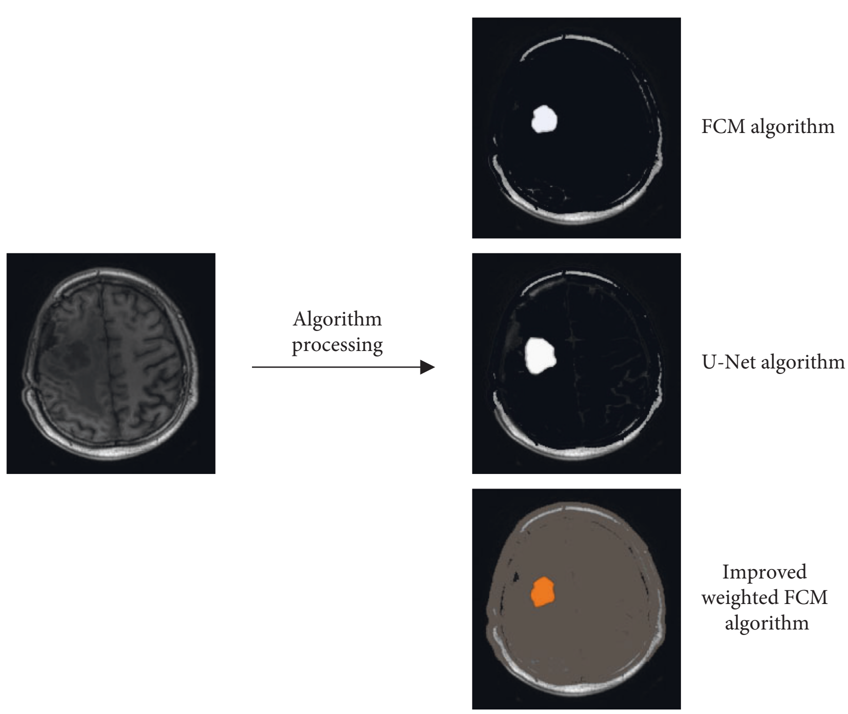

Figure 5: The brain tissue image segmented by the improved FCM method.

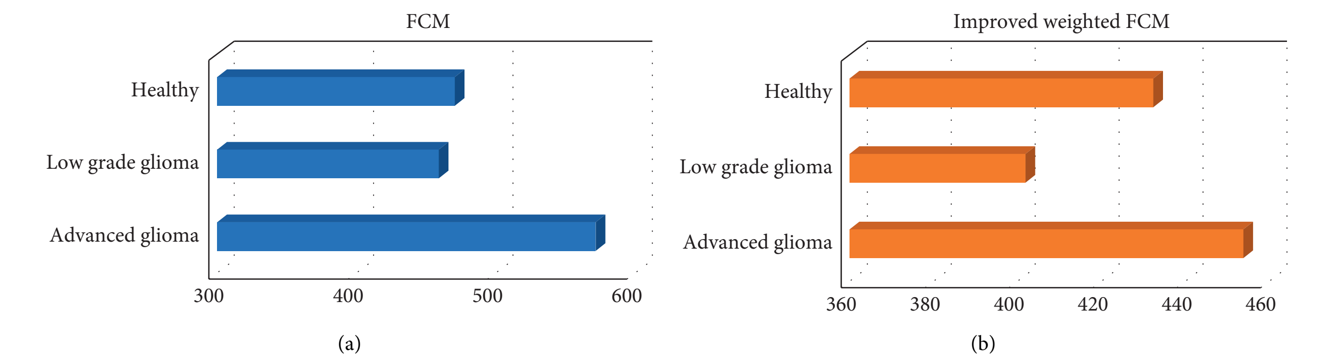

FIGURE 6: Comparison of gray matter volume in different groups. (a) The gray matter volume calculated by the FCM algorithm; (b) the gray matter volume calculated by the improved FCM algorithm.

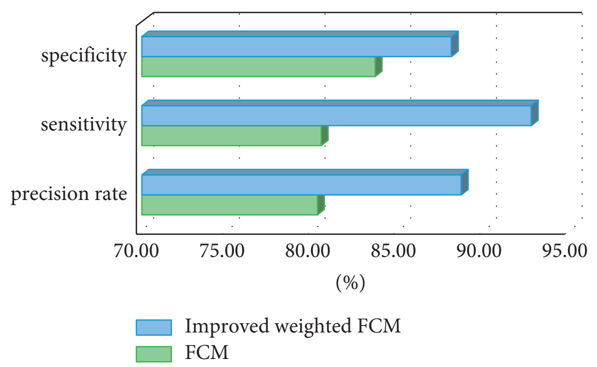

FIGURE 7: Comparison of specificity, sensitivity, and accuracy.

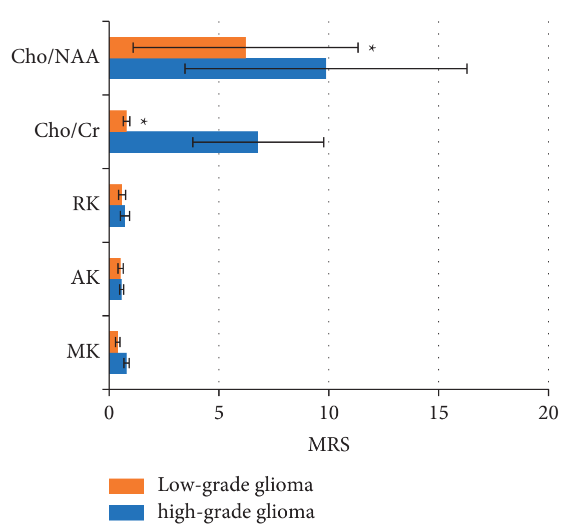

FIGURE 8: Comparison of parameters between high-grade gliomas and low-grade gliomas.

brain tumors, reaching 92.72%. Its specificity was not much different from that of traditional FCM, which were 83.61% and 88.06%, respectively.

3.3. Analysis Results of MRS. After statistical analysis, the mean kurtosis (MK), axial kurtosis (AK), and radial kurtosis (RK) values of high-grade gliomas and low-grade gliomas were of statistically significance. The differences in the ratio of choline/creatine (Cho/Cr) and the ratio of choline/N-acetyl-aspartate (Cho/NAA) were statistically significant. The results are shown in Figure 8.

TABLE 2: Comparison of the diagnostic value of different parameters for high-grade and low-grade gliomas.

Parameters	ROC	Critical value	Sensitivity	Specificity	*P*
MK	0.962	0.4096	0.928	0.867	<0.001
AK	0.834	0.6435	0.742	0.546	0.024
RK	0.792	0.5641	0.646	0.642	0.007
Cho/Cr	0.841	6.8752	0.725	0.545	0.018
Cho/NAA	0.803	2.6843	0.762	0.531	0.009

The diagnostic value of the five parameters was compared, and the ROC curve was used as shown in Table 2. The area under the curve (AUC) of the MK was the largest, which was 0.962, $P < 0.001$, and the best critical value was 0.4096. It was followed by RK, AK, Cho/NAA, and Cho/Cr, whose AUC value was 0.834, 0.792, 0.841, and 0.803, respectively; P values were all less than 0.05, and the best critical values were 0.6435, 0.5641, 6.8752, and 2.6843, respectively.

4. Discussion

Brain tumor is one of the major diseases that threaten human health. In its clinical diagnosis, MRI is one of the most common imaging methods. The MRI images of brain tumors are three-dimensional, and different types of brain tumors showed different characteristics and presented different states. The manual segmentation of brain tumor images is a heavy and time-consuming task, so it is the current trend to study the brain tumor image segmentation [17]. The outcome of clustering coincides with the goal that people want to achieve using image segmentation, so clustering algorithms are widely used in image segmentation [18]. FCM algorithm is one of the classic algorithms; it utilizes fuzzy thinking to describe the ambiguity of the objective world. FCM algorithm is widely applied because of its simple process and easy implementation, but it still has defects in many aspects [19].

To get better segmentation effect of FCM, the FCM algorithm was improved in this work, as the two-dimensional hybrid algorithm was improved to a three-dimensional one. In this case, MRI images of brain tumors and MRS were taken for analysis, which were of 127 brain tumor patients in the low-grade glioma group as well as 54 healthy persons in the healthy group. The results show that the improved FCM algorithm had a higher Vpc (0.9154, 0.8352) and a lower Vpe (0.6516, 0.7326), and the cluster validity index Vxb (0.0621, 0.1931) was lower. Such a result was consistent with the views of Hua et al. [20]. The improved FCM algorithm had obvious advantages in the image segmentation process, which were mainly reflected in lower ambiguity of membership matrix, higher segmentation precision, and the correlation between intraclass pixels and interclass pixels.

The analysis of gray matter volume suggested that compared with the healthy group, the gray matter volume of the high-grade glioma was higher (453.87), and that of the low-grade glioma group was lower (401.99). The improved FCM algorithm had a high accuracy in segmenting images, which reached 88.64%. It also had a higher sensitivity to gray matter changes in brain tumors, reaching 92.72%. Its specificity was not much different from that of the original FCM, which were 83.61% and 88.06%, respectively. Halder and Talukdar [21] also mentioned in their article that the pattern recognition classification method at current was one of the important methods for the diagnosis of medical images with the aid of computers. The improved FCM algorithm had high accuracy and sensitivity, which allowed it better assist doctors in medical image recognition processing, lesion area detection, etc., improving the accuracy of doctors' clinical diagnosis. For studying the diagnostic value, the results demonstrated that the AUC of the MK value was the largest, which was 0.962; and the optimal critical value was 0.4096, which had a greater reference significance for clinical treatment and prognosis. Significant differences were also found in Cho/NAA and Cho/Cr between the high-grade and low-grade gliomas, but the specificity and sensitivity were slightly poorer. Therefore, a certain guiding significance could be offered for the grading of gliomas.

5. Conclusion

The improved FCM algorithm was applied to the MRI images of low-grade glioma patients as well as healthy people in this research, and the performance detection and diagnostic value of the improved FCM algorithm were studied. As a result, the improved FCM algorithm had a better image segmentation effect and the higher accuracy and sensitivity compared with the original FCM. It was helpful to clinicians in diagnosing brain tumors. The disadvantages of this work were that the details were not fully handled, and there was no complete data comparison. In the future, it was planned to improve the segmentation theory in this work, further promoting the accuracy of the segmentation outcomes. On the other hand, the glioma was simply classified into the high-grade and low-grade types merely for the limitation of experimental data. There was not a detailed classification according to the classification of World Health Organization and the specific types of gliomas. Thus, the classification would be studied in detail as a large number of cases would be collected subsequently. This work provided a theoretical reference for the computer-based clinical diagnosis of brain tumors.

Data Availability

The data used to support the findings of this study are available from the corresponding author upon request.

Conflicts of Interest

The authors declare no conflicts of interest.

References

[1] I. Bae, J.-H. Chae, and Y. Han, "A brain extraction algorithm for infant T2 weighted magnetic resonance images based on fuzzy c-means thresholding," *Scientific Reports*, vol. 11, no. 1, p. 23347, 2021.

[2] S. A. P. S. Blessy and C. H. Sulochana, "Performance analysis of unsupervised optimal fuzzy clustering algorithm for MRI brain tumor segmentation," *Technology and Health Care*, vol. 23, no. 1, pp. 23–35, 2014.

[3] H. Chen, Z. Xie, Y. Huang, and D. Gai, "Intuitionistic fuzzy C-means algorithm based on membership information transfer-ring and similarity measurement," *Sensors*, vol. 21, no. 3, p. 696, 2021.

[4] Y. Chen, H.-M. Zhou, and Q. Jiang, "The application value of magnetic resonance imaging (MRI)in the clinical diagnosis in hospital management," *Pakistan Journal of Medical Sciences*, vol. 37, no. 6-WIT, pp. 1710–1713, 2021.

[5] Z. Lv and L. Qiao, "Analysis of healthcare big data," *Future Generation Computer Systems*, vol. 109, pp. 103–110, 2020.

[6] A. Fathi Kazerooni, M. Mohseni, S. Rezaei, G. Bakhshandehpour, and H. Saligheh Rad, "Multi-parametric (ADC/PWI/T2-w) image fusion approach for accurate semi-automatic segmentation of tumorous regions in glioblastoma multiforme," *Magnetic Resonance Materials in Physics, Biology and Medicine*, vol. 28, no. 1, pp. 13–22, 2015.

[7] S. Xie, Z. Yu, and Z. Lv, "Multi-disease prediction based on deep learning: a survey," *Computer Modeling in Engineering and Sciences*, vol. 128, no. 2, pp. 489–522, 2021.

[8] M. Hu, Y. Zhong, S. Xie, H. Lv, and Z. Lv, "Fuzzy system based medical image processing for brain disease prediction," *Frontiers in Neuroscience*, vol. 15, p. 714318, 2021.

[9] Q. Hu, H. M. Whitney, and M. L. Giger, "Radiomics methodology for breast cancer diagnosis using multiparametric magnetic resonance imaging," *Journal of Medical Imaging*, vol. 7, no. 04, p. 044502, July 2020.

[10] B. D. Weinberg, M. Kuruva, H. Shim, and M. E. Mullins, "Clinical applications of magnetic resonance spectroscopy in brain tumors," *Radiologic Clinics of North America*, vol. 59, no. 3, pp. 349–362, 2021.

[11] Y. Li, J. Zhao, Z. Lv, and J. Li, "Medical image fusion method by deep learning," *International Journal of Cognitive Computing in Engineering*, vol. 2, pp. 21–29, 2021.

[12] L. Jin and K. Chang, "Optimized fuzzy C-means algorithm-based coronal magnetic resonance imaging scanning in tracheal foreign bodies of children," *Journal of Healthcare Engineering*, vol. 2021, pp. 1–9, 2021.

[13] I. E. Kaya, A. Ç. Pehlivanlı, E. G. Sekizkardeş, and T. Ibrikci, "PCA based clustering for brain tumor segmentation of T1w MRI images," *Computer Methods and Programs in Biomedicine*, vol. 140, pp. 19–28, 2017.

[14] C. Ma, H. Li, K. Zhang, Y. Gao, and L. Yang, “Risk factors of restroke in patients with lacunar cerebral infarction using magnetic resonance imaging image features under deep learning algorithm,” *Contrast Media and Molecular Imaging*, vol. 2021, p. 2527595, 2021.

[15] K. S. Manic, R. Biju, W. Patel, M. A. Khan, N. S. M. Raja, and S. Uma, “Extraction and evaluation of corpus callosum from 2D brain MRI slice: a study with cuckoo search algorithm,” *Computational and Mathematical Methods in Medicine*, vol. 2021, p. 5524637, 2021.

[16] F. Palesi, M. Ferrante, M. Gaviraghi et al., “Motor and higher-order functions topography of the human dentate nuclei identified with tractography and clustering methods,” *Human Brain Mapping*, vol. 42, no. 13, pp. 4348–4361, 2021.

[17] S. Prabha, K. Sakthidasan @ Sankaran, and D. Chitradevi, “Efficient optimization based thresholding technique for analysis of alzheimer MRIs,” *International Journal of Neuroscience*, pp. 1–14, 2021.

[18] J. Yin, H. Chang, D. Wang, H. Li, and A. Yin, “Fuzzy C-means clustering algorithm-based magnetic resonance imaging image segmentation for analyzing the effect of edaravone on the vascular endothelial function in patients with acute cerebral infarction,” *Contrast Media and Molecular Imaging*, vol. 2021, p. 4080305, 2021.

[19] C. Zhang, X. Shen, H. Cheng, and Q. Qian, “Brain tumor segmentation based on hybrid clustering and morphological operations,” *International Journal of Biomedical Imaging*, vol. 2019, p. 7305832, 2019.

[20] L. Hua, Y. Gu, X. Gu, J. Xue, and T. Ni, “A novel brain MRI image segmentation method using an improved multi-view fuzzy c-means clustering algorithm,” *Frontiers in Neuroscience*, vol. 15, p. 662674, 2021.

[21] A. Halder and N. A. Talukdar, “Brain tissue segmentation using improved kernelized rough-fuzzy C-means with spatio-contextual information from MRI,” *Magnetic Resonance Imaging*, vol. 62, pp. 129–151, 2019.

Hindawi
Contrast Media & Molecular Imaging
Volume 2022, Article ID 1199841, 9 pages
https://doi.org/10.1155/2022/1199841

Research Article

Computed Tomography Imaging under Artificial Intelligence Reconstruction Algorithm Used in Recovery of Sports Injury of the Knee Anterior Cruciate Ligament

Heng Zhang[1], **Haiming Zheng**[2], **Ren Deng**[2], **Kaiwen Luo**[2], and **Shukai Duan**[3]

[1]*College of Mathematics and Statistics, Southwest University, Chongqing 400715, China*
[2]*Department of Military Logistics, Army Logistics Academy, Chongqing 401331, China*
[3]*College of Artificial Intelligence, Southwest University, Chongqing 400715, China*

Correspondence should be addressed to Shukai Duan; rockyzhang@swu.edu.cn

Received 9 February 2022; Revised 23 April 2022; Accepted 26 April 2022; Published 28 May 2022

Academic Editor: M Pallikonda Rajasekaran

This study aimed to analyze the influence of artificial intelligence (AI) reconstruction algorithm on computed tomography (CT) images and the application of CT image analysis in the recovery of knee anterior cruciate ligament (ACL) sports injuries. A total of 90 patients with knee trauma were selected for enhanced CT scanning and randomly divided into three groups. Group A used the filtered back projection (FBP) reconstruction algorithm, and the tube voltage was set to 120 kV during CT scanning. Group B used the iDose4 reconstruction algorithm, and the tube voltage was set to 120 kV during CT scanning. In group C, the iDose4 reconstruction algorithm was used, and the tube voltage was set to 100 kV during CT scanning. The noise, signal-to-noise ratio (SNR), carrier-to-noise ratio (CNR), CT dose index volume (CTDI), dose length product (DLP), and effective radiation dose (ED) of the three groups of CT images were compared. The results showed that the noise of groups B and C was smaller than that of group A ($P < 0.05$), and the SNR and CNR of groups B and C were higher than those of group A. The images of patients in group A with the FBP reconstruction algorithm were noisy, and the boundaries were not clear. The noise of the images obtained by the iDose4 reconstruction algorithm in groups B and C was improved, and the image resolution was also higher. The agreement between arthroscopy and CT scan results was 96%. Therefore, the iterative reconstruction algorithm of iDose4 can improve the image quality. It was of important value in the diagnosis of knee ACL sports injury.

1. Introduction

The anterior cruciate ligament (ACL) of the knee is a fibrous connective tissue connecting the femur and tibia, and its main function is transmitting tension and enhancing joint stability [1]. ACL injury has a high incidence in the population, and ACL fractures caused by noncontact mechanisms are common [2]. During exercise, sudden torsion, sudden stop, and weight-bearing can lead to ACL overload, resulting in ACL tear or even fracture [3]. Ligament injury can not only cause joint pain, cartilage and meniscus damage, and other soft tissue damage in the joint but may also even induce osteoarthritis if not treated in time [4]. At present, the degree of ligament relaxation, patient activity, individual clinical symptoms, and treatment strategies for injured ligaments are also different [5]. Conservative treatment mainly includes pain relief and waiting for self-healing under the protection of auxiliary devices [6]. ACL injuries mainly occur in sports and are relatively serious and difficult to treat in knee injuries [7]. It is more common than the initial belt injury of the posterior crossing, and the injury of the ACL of the knee will lead to a decrease in the stability of the knee and also accelerate the wear or injury of the articular cartilage and meniscus [8]. The fracture of the ACL inevitably has a significant impact on the stability of the knee [9]. Osteoarthritis of the knee is an aseptic and chronic arthritic disease characterized by degenerative changes in the articular cartilage and regeneration of joint margins and subchondral bones. The disease begins in the cartilage, and the degeneration of the articular cartilage is the core, which then affects the subchondral bone, synovium, joint capsule, and muscle belt. Eventually, joint pain, limited activity, and even unstable changes will be caused, thus affecting people's daily activity, ability, and quality of life [10].

Early, rapid, and accurate diagnosis of ACL injury is very important in clinical diagnosis and treatment. At present, the diagnosis of ACL injury mainly includes physical examination, such as front drawer test, axial shift test, and examination. However, in the acute phase of injury, it is affected by the patient's pain, joint swelling, and other factors that can affect the accuracy of the diagnosis. In addition, the gold standard for the diagnosis of ACL injury is arthroscopy. However, arthroscopy is not only expensive and slow but also traumatic to the patient. Using imaging can not only avoid these problems but also obtain information about the patient's knee. Computed tomography (CT) is adopted as a noninvasive imaging diagnostic method for patients with knee injuries. CT scan has the advantages of fast scanning speed, wide scanning range, and high scanning image resolution, which can provide reliable information for clinical judgment of knee injury types [11]. With the upgrading of CT in recent years, many researchers found that image reconstruction algorithms can be used to reduce the radiation risk of CT scans [12]. As artificial intelligence advances, technologies like deep learning and big data are widely used in the medical field. As a medical auxiliary diagnostic system, artificial intelligence medical imaging not only has high accuracy but also can improve the work efficiency of doctors. The traditional filtered rear projection (FBP) algorithm is very sensitive to noise and artifacts, thus limiting the reduction of the radiation dose. The iDose4 iterative reconstruction algorithm is one of the emerging computer intelligence algorithms. The introduction of the CT iDose4 iterative reconstruction algorithm can significantly optimize image quality and reduce noise while reducing the radiation dose of a CT scan [13]. Some scholars used iDose4 and FBP algorithms to process renal artery CT angiography and found that iDose4 reconstruction images were significantly better [14]. Currently, few studies applied the iDose4 iterative reconstruction algorithm to CT scan images of patients with ACL injuries of the knee joint.

This research was developed to compare the effect of original images obtained by different algorithms for patients with ACL injury of the orthopaedic knee joint with different doses of multislice spiral CT. The image quality after processing was compared with the FBP algorithm, hoping to provide a reference for the application of CT imaging in the recovery of the ACL of the knee joint.

2. Methods

2.1. Research Objects. A total of 90 patients with ACL motor injuries were recruited from September 2019 to October 2020, all of whom underwent enhanced CT scanning. Among them, 54 were male patients and 36 were female patients. All patients were between 23 and 58 years old, with an average age of 39 years. The patients were randomly rolled into groups A, B, and C. In group A, 30 patients were treated with the FBP reconstruction algorithm, and tube voltage was set to 120 kV during CT scanning. In group B, 30 patients were treated with the iDose4 reconstruction algorithm, and the tube voltage was set at 120 kV during CT scanning. In group C, 30 patients were treated with the iDose4 reconstruction algorithm, and tube voltage was set at 100 kV during CT scanning. This study had been approved by the ethics committee of the hospital, and all patients and their families had signed informed consent.

Inclusion criteria were as follows: (i) patients diagnosed with acute knee ACL sports injury according to the clinical diagnosis and treatment guidelines for ACL injury; (ii) patients who can receive a CT scan; (iii) patients without contraindications for allergy to contrast media; (iv) patients over 23 years old and younger than 58 years old; and (v) patients who signed the informed consent. Exclusion criteria were as follows: (i) patients with other concomitant fractures and knee lesions; (ii) patients with other infectious diseases or bone and joint diseases such as rheumatoid arthritis; (iii) patients suffering from serious cardiovascular and cerebrovascular diseases or liver and kidney dysfunction; (iv) patients with mental disorders; and (v) patients with communication disorders.

2.2. CT Scanning. The CT scanner used was a 128-slice helical CT scanner. CT scan parameter settings were given as follows: the layer thickness was 3 mm, the layer distance was also 3 mm, the rotation speed of the tube was set to 2 rpm, the pitch was 0.984, the contrast agent was iohexol, the tube current was 500 mAs, and the tube voltage was subject to the three different parameters of A, B, and C. The patient was in a supine position, and the scan range was from the distal end of the patient's femur to the proximal end of the knee joint.

2.3. Basic Methods of iDose4 Iterative Reconstruction Algorithm. The iDose4 iterative reconstruction algorithm belongs to a class of AI algorithms. It can not only iteratively reorganize in the projection space but also iteratively reorganize in the image space. The general flow of the iDose4 reconstruction algorithm is to reconstruct the projection data using the FBP method and construct the multinoise model and anatomical model of the obtained image data. In the process of repeated iterations, and the noise data is continuously removed to improve the image quality. Compared with the FBP algorithm, the main feature of the iDose4 algorithm is that it has a dual-space model. The iterative reconstruction expanded in the dual-space can be realized when the image texture remains unchanged, the artifacts and noise ratio of the image are reduced, and the image quality can be increased.

2.4. Observation Indicators. General information of patients was collected, including gender, age, body mass index (BMI), and disease location of patients in the three groups. The calculation method of BMI is shown in (1), where W is the weight and H is the height.

$$\mathrm{BMI} = \frac{W}{H}. \tag{1}$$

Subjective image rating was performed by two professional imaging physicians. The highest score was 5. A score of 1 indicated that the image quality was poor, the lesions cannot be displayed or the lesions and boundaries were not clear, and the artifacts showed great influence. A score of 2 indicated that the image quality was normal, the lesions and boundaries were blurred, but the lesions were visible. A score of 3 indicated good image quality, clear lesions and artifacts, but did not affect the diagnosis. A score of 4 indicated that the image quality was good, the influence of noise and artifacts was small, and the lesions were clear. A score of 5 indicated that the image quality was very good, without noise and artifacts, with clear lesions and clear boundaries, which can be used for diagnosis.

Two radiologists with more than three years of clinical imaging experience were invited to objectively evaluate the CT images of all patients and calculate the signal-to-noise ratio (SNR) and carrier-to-noise ratio (CNR). Three regions of interest (ROI) of the bone, adjacent muscle layer, and subcutaneous fat layer with an area of 50–100 mm^2 were selected to calculate the mean CT values and standard deviation (SD). SD was the objective noise of the image. The smaller the SD, the less image noise and the better the image quality. The SNR and CNR calculation methods are shown in (2) and (3), where $\mathrm{CT_a}$ represents the average CT value of the bone, $\mathrm{CT_V}$ represents the average CT value of the muscle, $\mathrm{CT_{avg}}$ refers to the average CT value of the bone and muscle, and $\mathrm{SD_{avg}}$ represents the average SD value of the bone and muscle.

$$\mathrm{SNR} = \frac{\mathrm{CT_{avg}}}{\mathrm{SD_{avg}}}, \tag{2}$$

$$\mathrm{CNR} = \frac{\mathrm{CT}_a - \mathrm{CT}_v}{\mathrm{SD_{avg}}}. \tag{3}$$

ACL injury in all patients was analyzed by arthroscopy and CT scan results of all patients. The radiation dose of patients was assessed by effective radiation dose (ED), CT dose index volume (CTDI), and dose length generation (DLP). The calculation method of effective radiation dose (ED) is shown in

$$\mathrm{ED} = DL\ P \times 0.0054. \tag{4}$$

The coincidence rate of CT diagnosis results and arthroscopic diagnosis results was counted. The calculation of the coincidence rate is shown in (5), where Y is the number of coincidences and Z is the total number.

$$\text{coincidence rate} = \frac{Y}{Z}. \tag{5}$$

2.5. Statistical Analysis. All data in this study were analyzed by SPSS 20.0 statistical software; the difference between the groups was analyzed by the chi-square test method. When $P < 0.05$, it meant that the difference was statistically significant.

3. Results

3.1. Basic Information of the Two Groups of Patients. The general clinical data of all patients are shown in Table 1. The three groups of patients showed obvious differences in gender, age, body mass index (BMI), and disease site ($P > 0.05$), and they were comparable.

3.2. Results of Image Evaluation Indicators

3.2.1. Subjective Evaluation Results. As illustrated in Figure 1, the image quality scores of group B and group C were higher than those of group A, and the comparison between group B and group A was statistically obvious ($P < 0.05$). It showed that the image quality obtained by the iDose4 reconstruction algorithm was better than the image quality obtained by the FBP algorithm.

3.2.2. Objective Evaluation Results. SD, SNR, and CNR were used as indicators for objective evaluation of the images. The result is shown in Figure 2. It was found that the noise of group B and group C was less than that of group A, which was statistically great ($P < 0.05$), and it was also statistically obvious compared with that of group B ($P < 0.05$). The SNR and CNR of groups B and C were higher than those of group A. However, the comparison of SNR and CNR between groups B and C was not statistically significant. At the same time, Figure 3 illustrates that the images of patients in group A using the FBP reconstruction algorithm were noisy, the lesions were difficult to identify, and the boundaries were not clear; while the image noise obtained by the iDose4 reconstruction algorithm in groups B and C was improved, and the image resolution was improved.

3.3. Evaluation of Results of Radiation Dose. The evaluation results of the three groups of radiation doses are shown in Figure 4. Compared with group A, the three radiation dose parameters of groups B and C were effectively reduced ($P < 0.05$). The EDs of group A, group B, and group C were

Table 1: Comparison of general data of all patients.

Group	Gender (male/female)	Age (years)	BMI (kg/m^2)	Disease site (left knee/right knee)
A ($n = 30$)	18/12	38 ± 4.1	23.34 ± 2.41	20/10
B ($n = 30$)	20/10	39 ± 5.9	23.53 ± 2.73	13/17
C ($n = 30$)	13/17	38 ± 4.6	24.48 ± 1.98	9/21
P	0.236	0.672	0.745	0.082

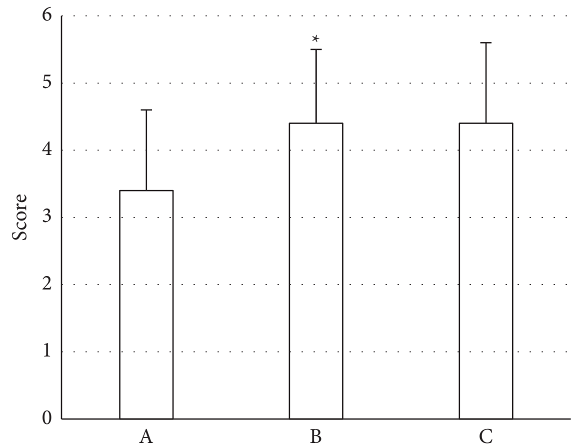

Figure 1: Subjective evaluation results on the image quality of the three groups of patients. $*$ indicates compared with group (A), $P < 0.05$.

4.46 ± 1.21, 3.39 ± 1.02, and 3.45 ± 1.32, respectively. Compared with group A, the ED of group B was reduced by 24.0%, and the ED of group C was reduced by 22.6%.

3.4. Comparison of CT Diagnosis Results with Arthroscopy. The comparison of CT diagnosis results and arthroscopic examination results of 90 patients with knee ACL injury is shown in Table 2. The arthroscopy results were undertaken as the gold standard to judge the diagnosis results. The coincidence rate between CT diagnosis results and arthroscopy diagnosis results was 96.6%. For diagnoses with normal results, the coincidence rate between CT diagnosis results and arthroscopy diagnosis results was 50%, and the coincidence rate between arthroscopy results and CT scan results was 96% (58/60).

4. Discussion

ACL injury is a common and frequently occurring disease of knee joint injury, which has a great impact on the normal life of patients [15]. Arthroscopy is currently considered the gold standard for diagnosing ACL injuries. However, arthroscopy is expensive, time-consuming, and invasive. Due to the implementation of arthroscopy, it brings additional pain to a considerable number of cases with negative results of arthroscopy, prolonging the recovery time and increasing the financial burden of the patient [16]. Therefore, early and accurate noninvasive examination has very important clinical significance. Currently, there are three main imaging methods for displaying muscle ligaments, namely, magnetic resonance imaging, ultrasound, and CT [17]. CT has obvious advantages in density and spatial resolution, and the operation is rapid, which provides a high-value imaging basis for the diagnosis and treatment of clinical diseases. However, increased radiation doses may breach the upper limit of the deterministic effect jeopardizing the health of patients. Therefore, how to significantly reduce the radiation dose on the basis of obtaining high-quality image data has become a focus of clinical research. Intelligent algorithms have been widely used in the field of medical image processing [18, 19].

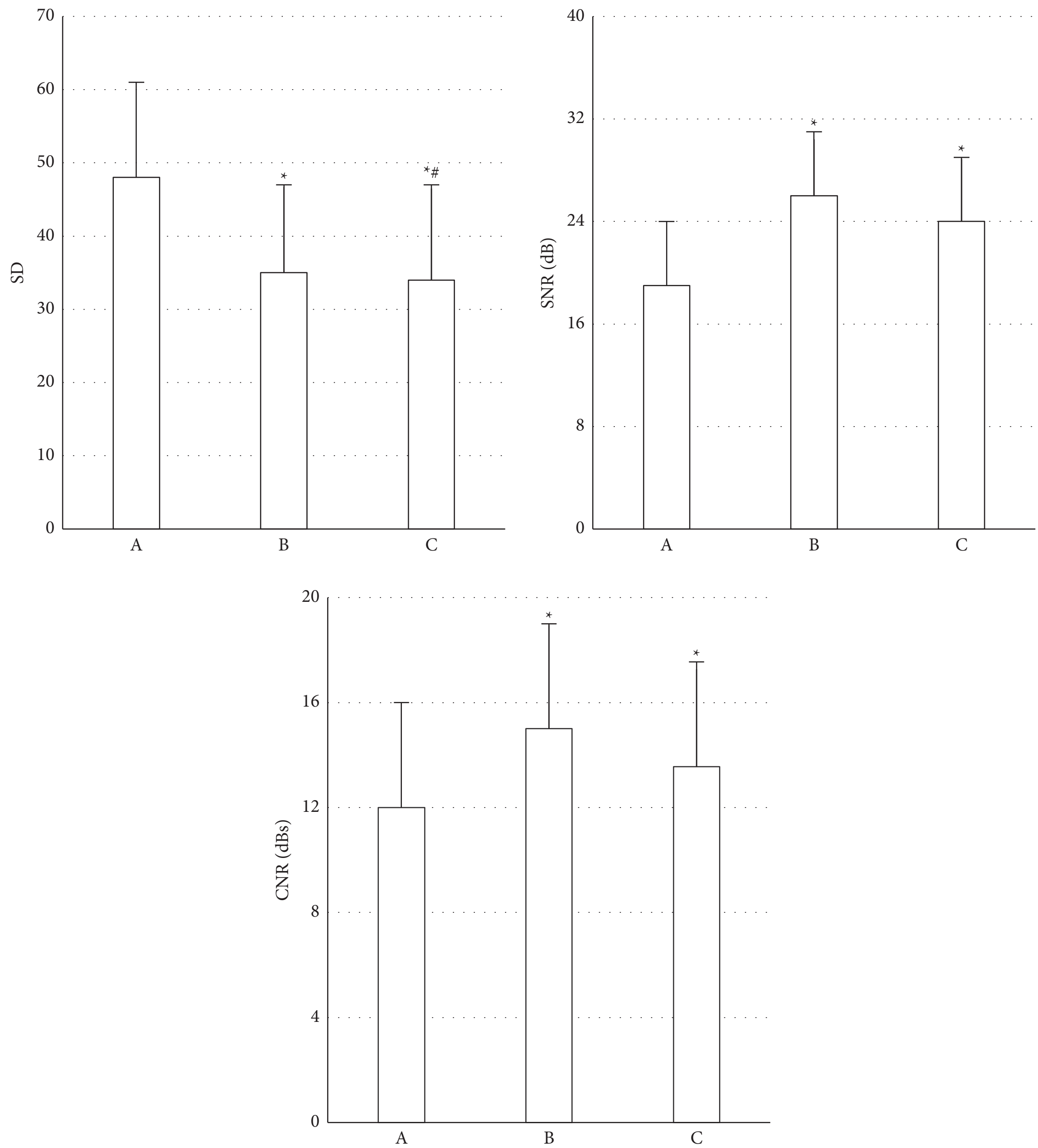

Figure 2: Comparison results of SD, SNR, and CNR of the three groups of patients. A is SD, B is SNR, and C is CNR. ∗ represents that the comparison difference between group A, group B, and group C, $P < 0.05$; # indicates the difference between group B and group C showed $P < 0.05$.

Compared with traditional FBP reconstruction algorithm, CT image iterative reconstruction techniques, such as the iDose4 algorithm, that have appeared in recent years can significantly reduce image noise and improve image contrast and image quality [20–22]. Moreover, there are also relevant materials to study the application of CT in the diagnosis of sports injuries in the recovery of the knee anterior cruciate ligament. Some scholars studied patients with knee trauma and performed

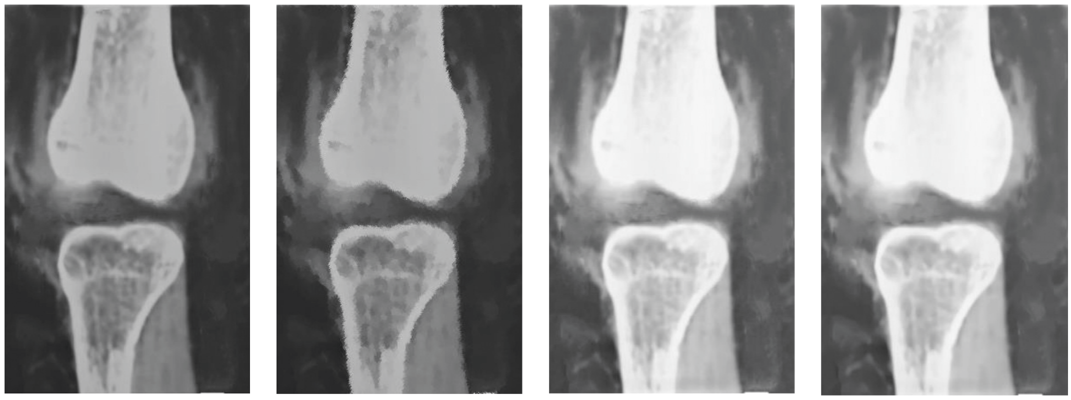

(a) (b) (c) (d)

Figure 3: CT image of a patient with a knee ACL injury. (a) Original CT image. (b) Image processed by the FBP algorithm. (c) Image of the patient in group B. (d) Image of the patient in group C.

dual-source CT or MRI scans. Finally, it was concluded that dual-source CT was safe, rapid, and accurate in diagnosing anterior cruciate ligament injury of the knee joint and can provide a reliable basis for cruciate ligament reconstruction surgery, showing very good application value [23]. CT images of MPR and VRT were processed in patients with ACL injury, and it was found that MPR and VRT images had a positive clinical value in the diagnosis of anterior cruciate ligament injury. Dual-source CT can measure the CT value of the ACL and the thickness of each segment through MPR and VRT postprocessing techniques to diagnose ACL in an objective, quantitative, and noninvasive manner. The degree of ligament injury can be more intuitively predicted using dual-energy staining techniques [24].

The results showed a 96% coincidence rate of CT scan results compared with the gold standard for knee injury examination. It can be explained that CT scanning showed a very good application value in the recovery of knee anterior cruciate ligament sports injury. The results showed that the image quality scores of groups B and C were higher than those of group A, and the comparison between groups B and A was statistically significant. The noise of groups B and C was smaller than that of group A, which was statistically significant ($P < 0.05$). The comparison between groups C and B was also statistically significant ($P < 0.05$). The SNR and CNR of groups B and C were higher than those of group A, but the SNR and CNR of groups B and C were not statistically significant. At the same time, the image noise of patients in group A using the FBP reconstruction algorithm was high, the lesions were difficult to identify, and the boundary was not clear. However, the image noise obtained by the iDose4 reconstruction algorithm in groups B and C was improved, and the image resolution was also higher. The ED of groups A ~ C were 4.46 ± 1.21, 3.39 ± 1.02, and 3.45 ± 1.32, respectively. Compared with group A, the ED of group B decreased by 24.0%, and the ED of group C decreased by 22.6%. Using the iDose4 reconstruction algorithm in image processing can not only ensure the quality of the image but also reduce the radiation risk to the patient.

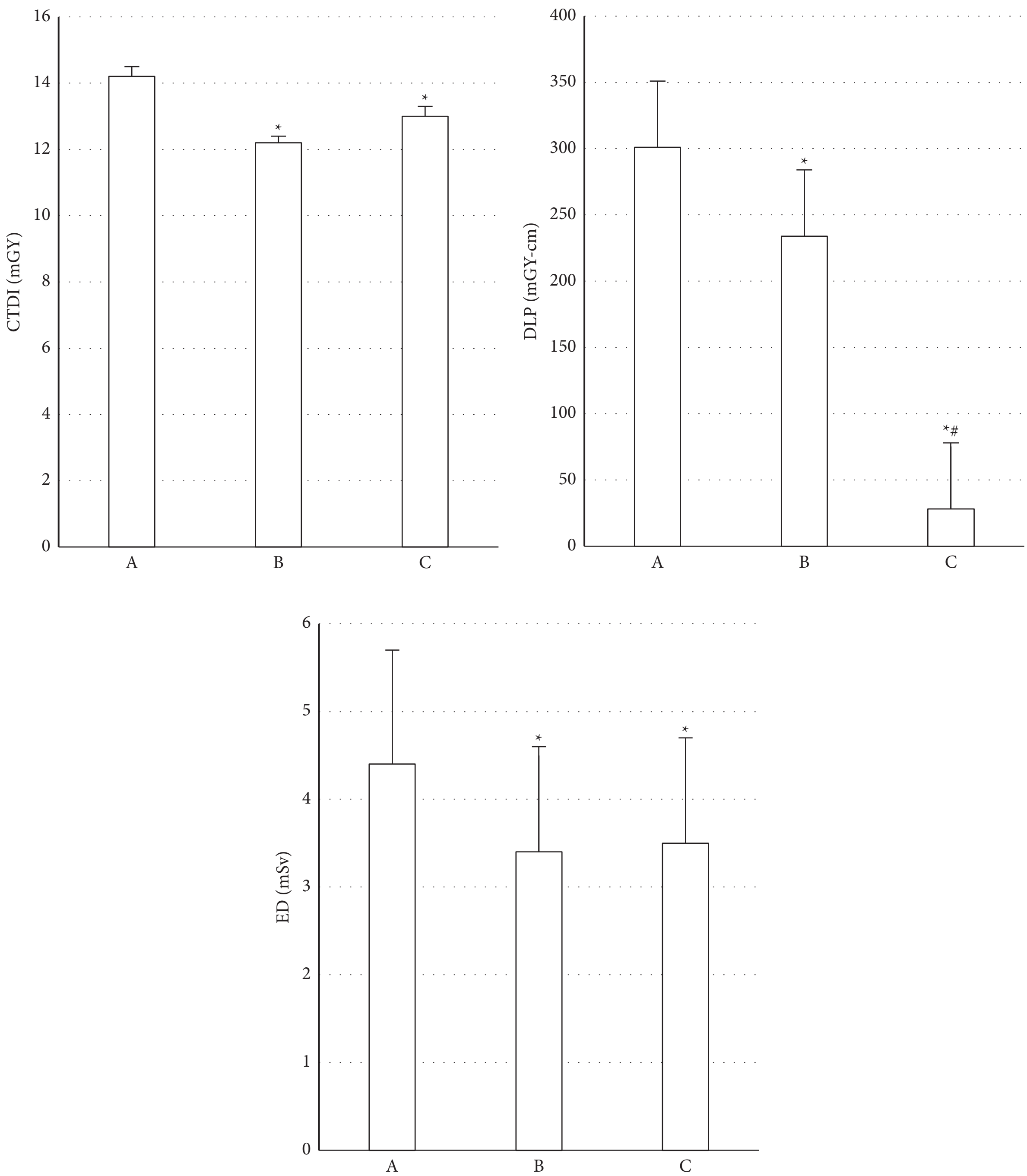

Figure 4: Comparison of radiation dose-related indicators among the three groups of patients. (a) CTD; (b) DLP; (c) ED. $*$ represents that the comparison difference between group A, group B, and group C $P < 0.05$; # indicates the difference between group B and group C, $P < 0.05$.

Table 2: Comparison of CT diagnosis results and arthroscopy results of all patients.

		CT examination results		
		Damage	Normal	Total
Arthroscopy results	Damage	82	5	87
	Normal	2	1	3
Total		84	6	90

5. Conclusion

In this study, the application value of CT imaging based on the artificial intelligence reconstruction algorithm in the recovery of knee ACL sports injury was explored. It was found that the image quality obtained by the iDose4 reconstruction algorithm was superior to other algorithms. CT imaging based on artificial intelligence reconstruction algorithm was applied in the diagnosis of ACL sports injury of the knee, the patient's ED was significantly reduced, the radiation dose was reduced by 24.0%, and the result of the CT examination was consistent with that of arthroscopy. Using the iDose4 reconstruction algorithm in image processing had a positive application effect. Nevertheless, the deficiency of this study was that the sample size is too small, which needs further exploration and verification.

Data Availability

The data used to support the findings of this study are available from the corresponding author upon request.

Conflicts of Interest

The authors declare that they have no conflicts of interest.

Authors' Contributions

Heng Zhang and Haiming Zheng contributed equally to this work.

Acknowledgments

This work was supported by the Chongqing special project for technological innovation and application development—Chongqing Bureau of Science and Technology (no. cstc2020jscx-cylhX0001).

References

[1] W. T. Hardaker, W. E. Garrett, and F. H. Bassett, "Evaluation of acute traumatic hemarthrosis of the knee joint," *Southern Medical Journal*, vol. 83, no. 6, pp. 640–644, 1990.

[2] V. A. van de Graaf, J. C. A. Noorduyn, N. W. Willigenburg et al., "Effect of early surgery vs physical therapy on knee function among patients with nonobstructive meniscal tears," *JAMA*, vol. 320, no. 13, pp. 1328–1337, 2018.

[3] S. L. Y. Woo, R. E. Debski, J. Zeminski, S. D. Abramowitch, S. S. Chan, and J. A. Fenwick, "Injury and repair of ligaments and tendons," *Annual Review of Biomedical Engineering*, vol. 2, no. 1, pp. 83–118, 2000.

[4] D. R. Bijukumar, C. McGeehan, and M. T. Mathew, "Regenerative medicine strategies in biomedical implants," *Current Osteoporosis Reports*, vol. 16, no. 3, pp. 236–245, 2018.

[5] N. T. Mabvuure, M. Malahias, B. Haddad, S. Hindocha, and W. S. Khan, "State of the art regarding the management of multiligamentous injuries of the knee," *The Open Orthopaedics Journal*, vol. 8, no. 1, pp. 215–218, 2014.

[6] S. F. El-Amin, M. V. Hogan, A. A. Allen, J. Hinds, and C. T. Laurencin, "The indications and use of bone morphogenetic proteins in foot, ankle, and tibia surgery," *Foot and Ankle Clinics*, vol. 15, no. 4, pp. 543–551, 2010.

[7] B. T. Samuelsen, K. E. Webster, N. R. Johnson, T. E. Hewett, and A. J. Krych, "Hamstring autograft versus patellar tendon autograft for ACL reconstruction: is there a difference in graft failure rate? A meta-analysis of 47,613 patients," *Clinical Orthopaedics and Related Research*, vol. 475, no. 10, pp. 2459–2468, 2017.

[8] B. R. Southam, A. J. Colosimo, and B. Grawe, "Underappreciated factors to consider in revision anterior cruciate ligament reconstruction: a current concepts review," *Orthopaedic Journal of Sports Medicine*, vol. 6, no. 1, Article ID 232596711775168, 2018.

[9] S. Seiwerth, R. Rucman, B. Turkovic et al., "BPC 157 and standard angiogenic growth factors. Gastrointestinal tract healing, lessons from tendon, ligament, muscle and bone healing," *Current Pharmaceutical Design*, vol. 24, no. 18, pp. 1972–1989, 2018.

[10] M. Krause, F. Freudenthaler, K.-H. Frosch, A. Achtnich, W. Petersen, and R. Akoto, "Operative versus conservative treatment of anterior cruciate ligament rupture," *Deutsches Ärzteblatt international*, vol. 115, no. 51-52, pp. 855–862, 2018.

[11] Y. Tsutsui, S. Awamoto, K. Himuro, T. Kato, S. Baba, and M. Sasaki, "Evaluating and comparing the image quality and quantification accuracy of SiPM-PET/CT and PMT-PET/CT," *Annals of Nuclear Medicine*, vol. 34, no. 10, pp. 725–735, 2020.

[12] H. Murazaki, Y. Funama, M. Hatemura, C. Fujioka, and S. Tomiguchi, "Quantitative evaluation of calcium (content) in the coronary artery using hybrid iterative reconstruction (iDose) algorithm on low-dose 64-detector CT: comparison of iDose and filtered back projection," *Japanese Journal of Radiological Technology*, vol. 67, no. 4, pp. 360–366, 2011.

[13] F. Pontana, S. Henry, A. Duhamel et al., "Impact of iterative reconstruction on the diagnosis of acute pulmonary embolism (PE) on reduced-dose chest CT angiograms," *European Radiology*, vol. 25, no. 4, pp. 1182–1189, 2015.

[14] Y. Xu, T. T. Zhang, T.-t. Zhang et al., "Effect of iterative reconstruction techniques on image quality in low radiation dose chest CT: a phantom study," *Diagnostic and interventional radiology*, vol. 25, no. 6, pp. 442–450, 2019.

[15] T. Hagino, S. Ochiai, S. Senga et al., "Meniscal tears associated with anterior cruciate ligament injury," *Archives of Orthopaedic and Trauma Surgery*, vol. 135, no. 12, pp. 1701–1706, 2015.

[16] K. M. Dale, J. R. Bailey, and C. T. Moorman 3rd, "Surgical management and treatment of the anterior cruciate ligament/medial collateral ligament injured knee," *Clinics in Sports Medicine*, vol. 36, no. 1, pp. 87–103, 2017.

[17] M. Hu, Y. Zhong, S. Xie, H. Lv, and Z. Lv, "Fuzzy system based medical image processing for brain disease prediction," *Frontiers in Neuroscience*, vol. 15, Article ID 714318, 2021.

[18] B. Wang and H. Liu, "FBP-Net for direct reconstruction of dynamic PET images," *Physics in Medicine and Biology*, vol. 65, no. 23, Article ID 235008, 2020.

[19] Y. Hou, X. Liu, S. Xv, W. Guo, and Q. Guo, "Comparisons of image quality and radiation dose between iterative reconstruction and filtered back projection reconstruction algorithms in 256-MDCT coronary angiography," *American Journal of Roentgenology*, vol. 199, no. 3, pp. 588–594, 2012.

[20] J. Wu, X. Wang, X. Mou, Y. Chen, and S. Liu, "Low dose CT image reconstruction based on structure tensor total variation using accelerated fast iterative shrinkage thresholding algorithm," *Sensors*, vol. 20, no. 6, p. 1647, 2020.

[21] P. B. Noël, S. Engels, T. Köhler et al., "Evaluation of an iterative model-based CT reconstruction algorithm by intra-patient comparison of standard and ultra-low-dose examinations," *Acta Radiologica*, vol. 59, no. 10, pp. 1225–1231, 2018.

[22] P. Prakash, M. K. Kalra, S. R. Digumarthy et al., "Radiation dose reduction with chest computed tomography using adaptive statistical iterative reconstruction technique,"

Journal of Computer Assisted Tomography, vol. 34, no. 1, pp. 40–45, 2010.

[23] G. Laurent, N. Villani, G. Hossu et al., "Full model-based iterative reconstruction (MBIR) in abdominal CT increases objective image quality, but decreases subjective acceptance," *European Radiology*, vol. 29, no. 8, pp. 4016–4025, 2019.

[24] C. Ji, Y. Chen, L. Zhu, and J. Zhang, "Arthroscopic anterior cruciate ligament injury in clinical treatment of joint complications and CT observation," *Journal of Healthcare Engineering*, vol. 2021, Article ID 6667046, 10 pages, 2021.

Hindawi
Contrast Media & Molecular Imaging
Volume 2022, Article ID 5871385, 8 pages
https://doi.org/10.1155/2022/5871385

Research Article

Computed Tomography Image Features under Denoising Algorithm for Benign and Malignant Diagnosis of Renal Parenchymal Tumor

Zhongxiao Zhang [1] and Zehua Wang [2]

[1]*Department of Urology, Qilu Hospital (Qingdao), Shandong University, Qingdao 266035, Shandong, China*
[2]*Department of Urology, Qilu Hospital, Shandong University, Jinan 250012, Shandong, China*

Correspondence should be addressed to Zehua Wang; wangzehua@sdu.edu.cn

Received 8 February 2022; Revised 23 April 2022; Accepted 26 April 2022; Published 27 May 2022

Academic Editor: M. Pallikonda Rajasekaran

To improve the quality of computed tomography (CT) images and provide help for benign and malignant diagnosis of renal parenchymal tumors, the independent component analysis (ICA) denoising algorithm was used. An improved ICA X-ray CT (X-CT) medical image denoising algorithm was proposed. ICA provided a higher signal-to-noise ratio for CT image denoising. Forty patients with renal tumor were selected as the observation group. The CT image performance of patients was evaluated by the denoising algorithm and compared with the wavelet transform algorithm, and the peak signal-to-noise ratio of the proposed algorithm was analyzed and compared. The results showed that among the 40 patients with renal tumors, 12 were renal clear cell carcinoma cases and 28 were cystic renal carcinoma cases. The accuracy of the enhanced CT image was 93.8%, and that of the CT image using the denoising algorithm was 96.3%; the difference between the two was significant ($P < 0.05$). The peak signal-to-noise ratio (PSNR) of the algorithm proposed was higher than the PSNR values of CT and noisy images. The PSNR of the proposed algorithm was significantly higher than that of mean filtering. The root mean square error (RMSE) algorithm of the proposed algorithm was significantly lower than that of the mean algorithm in image data processing ($P < 0.05$), which showed the superiority of the proposed algorithm. Enhanced CT can be staged significantly. In conclusion, the algorithm had a significant effect on the edge contour of detailed features, and the accuracy of CT images based on intelligent calculation was significantly higher than that of conventional CT images for benign and malignant renal parenchyma tumors, which was worth promoting in clinical diagnosis.

1. Introduction

Renal malignant tumor accounts for about 3% of all malignant tumors, which is a kind of primary renal cells and a relatively rare malignant tumor. Malignant tumors often have necrosis, ulceration, bleeding, and other conditions. However, benign tumors are mostly characterized by secondary changes, such as hemorrhage, necrosis, and ulcers [1, 2]. Malignant tumors can cause organ failure, infection, invasion, and destruction of tissues and organs [3–5]. Renal solid tumors are more likely to develop into renal cancer, and magnetic resonance imaging (MRI), enhanced computed tomography (CT), and renal puncture biopsy can be selected for detection without definite examination. For benign tumors, resection can be considered; for malignant tumors, radical resection is required [6]. As the disease progresses, the patient may develop hematuria, pain, or a mass. Any of these symptoms may indicate that the tumor has advanced. In adults, hematuria is an early and common symptom. Hematuria is mostly visible, whereas some hematuria can only be seen under a microscope. It is generally painless in patients when hematuria occurs. Hematuria is mostly intermittent and can often stop by itself [7]. The commonly used imaging methods for diagnosis of renal tumor include B ultrasound, X-ray, CT, and MRI. The accuracy of CT/MRI was the highest in a single examination, followed by B ultrasound. The accuracy of CT for renal cancer staging was better than that of X-ray and B ultrasound. CT is a noninvasive imaging method that can distinguish vascular, inflammatory, and cystic lesions.

Compared with traditional X-ray examination, CT has a higher density resolution and can clearly display soft tissues, joints, and other parts. With the continuous updation of high-tech medical equipment, the development of CT images is also changing rapidly. Studies on intelligent algorithms combined with CT images have mushroomed, which has expanded the scope of examination and improved the diagnostic level [8, 9]. However, interference of external signals often occurs in medical images, and the signals will be weakened during transmission. The image transmission process will be affected by imaging equipment, resulting in insufficient image clarity. Moreover, the feature display is not obvious, and the focus is not prominent, which cannot adapt well to the automatic analysis of the machine. The image is noisy and ambiguous, which makes it impossible to accurately locate the relevant lesions, thus reducing the judgment rate of doctors [10, 11]. X-ray CT medical imaging can filter out the noise in the image and provide a good visual environment for the analysis/observation of the image. X-CT images can eliminate irrelevant information in the image, enhance the detectability of relevant information by filtering out noise, and maintain clear contour lines while removing noise. The improvement of image scanning technology is helpful to reduce the influence of artifact and noise on CT examination, reduce X-ray radiation, and improve the quality of CT image. After the image is processed by the intelligent algorithm, it is conducive to data extraction, highlighting target features, and providing more reliable information [12–14].

Traditional denoising algorithms mainly include median filter, mean filter, and spatial wiener. In the process of noise elimination, these traditional denoising algorithms cannot retain the details of the image well and the image edge information is damaged. Thus, they cannot achieve a good denoising effect, which directly affects the diagnosis of the disease by doctors [15, 16]. The image denoising method of wavelet transform can save the details of the image well and retain most of the signal information, but there will be a fuzzy situation at the edge of the image. The X-CT image algorithm can recover useful real information, eliminate irrelevant information, and enhance the detectability of relevant information after noise filtering [17, 18]. Independent component analysis (ICA) is an efficient blind separation method, which can treat the polluted image as a mixture of the source image and noise during image denoising. Regardless of the noise intensity, it can be filtered out by some analysis methods and the restored image can retain the loss of image details. At present, ICA has been applied in face and character recognition [19], noise filtering [20], feature extraction [21], and other aspects, showing good results. The basic theoretical framework of ICA has been perfected, but there are still many problems that need to be further discussed, such as the ICA model with noise. The assumption that the model has many uncertainties needs to be optimized.

Therefore, the ICA denoising algorithm was used to denoise CT images, and separated original images and noise images were obtained by ICA to obtain a higher peak signal-to-noise ratio. The denoised images were used to accurately diagnose the benign and malignant renal substantial tumors, providing a reference for clinical diagnosis and treatment of diseases.

2. Data and Methods

2.1. Clinical Data. Forty patients with renal tumor admitted to hospital were included in the observation group, including 27 males and 13 females, aged 26–69 years. All patients underwent CT examination before surgery to accurately understand the size of tumors. Another forty healthy patients during the same period of physical examination were selected as the control group, including 21 males and 19 females, aged 27–70 years. The clinical data of the two groups of patients were complete. There was no significant difference in general data between the two groups ($P > 0.05$), indicating comparability. This study had been approved by the ethics committee of the hospital, and all the patients who participated signed informed consent.

Inclusion criteria were as follows: (i) patients with complete clinical data; (ii) patients with skin lesions, (iii) patients with no immune system diseases and no infectious diseases; (iv) patients who volunteered to join this research. Exclusion criteria were are follows: (i) patients with incomplete clinical data; (ii) patients unwilling to participate in this study; (iii) patients with heart, liver, kidney, and hematopoietic system diseases, diabetes, and other diseases; (iv) patients with congenital lesions; (v) patients with sites that did not meet the inclusion criteria.

2.2. Enhanced CT Scan. Patients were scanned with a spiral CT machine. The contrast agent was injected into the cubital vein with a high-pressure syringe at a rate of 3 mL/s in a single stage, with an injection volume of 90–100 mL. CT scans were performed from the patient's liver to the upper ureter. The first stage of the whole liver scan was performed 25–30 seconds after the contrast agent injection, the second stage was performed 60–70 seconds later, and the third stage was performed 120–180 seconds later. The pattern of lesion enhancement was recorded during the scan, and all the data were imported into a computer. The examination of the enhanced CT was performed by two physicians, and the data of departure were analyzed. The physician should have at least five years of experience and be able to master the procedure. If there were different opinions during the diagnosis process, the final judgment should be made after discussion.

2.3. Wavelet Transform Denoising Algorithm. The wavelet transform denoising method processes the image containing noise through the corresponding regular wavelet coefficients. According to different coefficient characteristics of the processing, it can retain the wavelet coefficient of the image signal. The wavelet theory image denoising process mainly includes the wavelet transform, the wavelet coefficient processing, and finally the inverse transformation of the coefficient after processing (Figure 1).

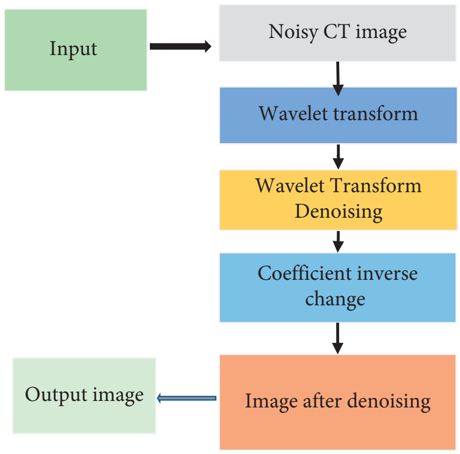

FIGURE 1: Wavelet transform denoising flowchart.

X-CT uses the X-ray beam received by the detector, and the X-ray signal is converted into an electrical signal, the photoelectric capacity is then converted into an electrical signal, digital analog is converted into a digital signal, and the digital signal is processed by a computer. X-CT medical images are arranged in a matrix, and the pixels reflect the X-ray absorption coefficient. The image sizes range from 0.5×0.5 mm to 1.0×1.0 mm. The X-CT devices corresponding to different pixel sizes are different, and the number and size of the images are also different. For images with high resolution, the number of pixels is more and the information stored is richer. The high resolution of X-ray CT images is also a significant feature, which can clearly present the pathological images under a good anatomical image background. X-CT image quality is also affected by a variety of factors; the main factors include scanning technical parameters, mechanical calibration, and image quality parameters, and these factors also restrict each other. Noise is an unpredictable random signal produced by human visual organs. To analyze image noise from the point of view of mathematics, a mathematical model needs to be established and the function information expressed by the function is used to degrade the noise image. If the signal under the influence of noise is $z(x, y)$, $n(x, y)$ represents noise, and the output signal is represented by $g(x, y)$, then the mean value of the total intensity of the image noise can be expressed as follows:

$$\mu = E(\mathrm{n}(x, y)) + \frac{1}{\mathrm{A} \times \mathrm{B}} \sum_{x=1}^{A} \sum_{y-1}^{B} \mathrm{n}(x, \mathrm{y}). \tag{1}$$

A is the row of the image matrix, and B is the column of the image matrix.

The variance of image noise is expressed by the following equation, that is, the fluctuation of image noise intensity:

$$\eta^2 = E(\mathrm{n}(x, y) - \mu)^2 + \frac{1}{\mathrm{A} \times \mathrm{B}} \sum_{x=1}^{A} \sum_{y-1}^{B} [\mathrm{n}(x, \mathrm{y}) - \mu]^2. \tag{2}$$

Two mathematical models represent image degradation, (3) represents additive noise, and (4) represents multiplicative noise. In the actual image, the noise and the image signal are independent of each other. The calculation of multiplicative noise is to transform the logarithmic change into additive noise, and the calculation process is relatively easy. After the image is denoised, the index can be selected and then converted.

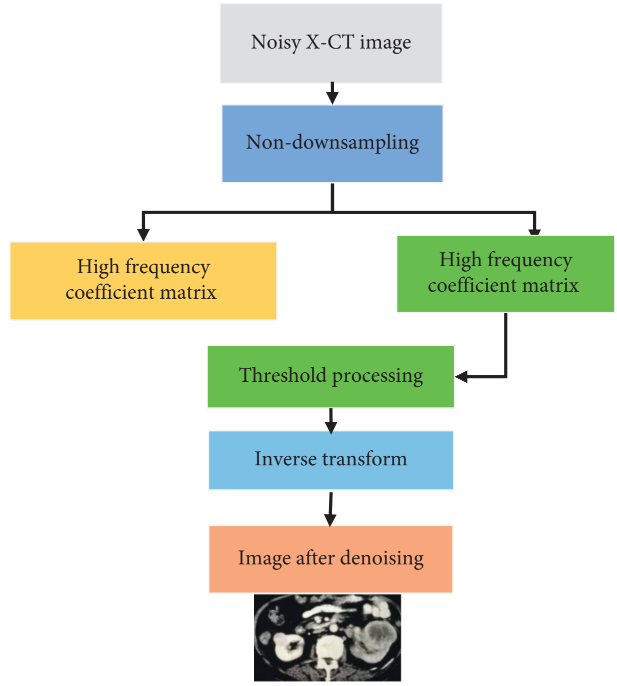

FIGURE 2: Flow chart of the X-CT denoising algorithm.

$$\mathrm{g}(x, y) = z(x, y) + n(x, y), \tag{3}$$

$$\mathrm{g}(x, y) = z(x, y)(1 + n(x, y)). \tag{4}$$

Quantum noise and photon noise are the main noises in X-CT images, and both can use Gaussian white noise as the model. The one-dimensional probability density function of Gaussian noise can be expressed as follows:

$$P(\mathrm{Q}) = \frac{1}{\sqrt{2\pi}\varphi} \mathrm{e}^{-(\mathrm{q}-\mu)^2/2\varphi^2}. \tag{5}$$

Here, Q represents the gray level φ of noise points and the standard deviation of Q, φ^2 represents the variance of Q, and μ represents the mean value of Q. The noise of different pixels in an image is irrelevant.

The algorithm flow chart is shown in Figure 2. The image containing noise is first sampled and then divided into a low-frequency coefficient matrix and a high-frequency coefficient matrix, and the inverse transformation is processed by the threshold value. Finally, the denoised image is obtained.

2.4. ICA Image Denoising Algorithm. The objective function equation of the ICA image algorithm is expressed as follows, and the calculation is easy to achieve universally:

$$U(y) = \left| E_y[G(y)] - E_y[G(v)] \right|^P. \tag{6}$$

V is a standard Gaussian random variable, the index $p = \log 2$, and G represents a nonquadratic and sufficiently smooth function. The nonquadratic function G is expressed as follows:

$$G_1(\mu) = \text{logcosh}a_1\mu. \tag{7}$$

Or, G is expressed as follows:

$$G_1(\mu) = \exp\left(-\frac{\text{a}_2\mu^2}{2}\right). \tag{8}$$

For the Sub-Gaussian variable, take $G1$. For Sub-Gaussian, take $G2$.

The iterative process of image preprocessing is expressed as follows:

$$W(\text{k}) = E\left\{xg\left[w(k-1)^T x\right]\right\} - E\left\{g\left[w(k-1)^T x\right]\right\}w(k-1). \tag{9}$$

After each iteration, a new W is obtained for normalization and the equation can be expressed as follows:

$$w(k) = -\frac{w(k)}{\|w(k)\|}. \tag{10}$$

2.5. Evaluation of Image Denoising Performance. X-CT medical imaging requires high image quality, and the loss of a little detail will have a certain impact on diagnosis. Enhancing the image information of interest is an important part of image processing, and qualitative and quantitative analysis and evaluation are carried out after image processing. Generally, subjective image analysis is based on people's sense and vision, with different reference standards and some differences in image cognition (Table 1).

Quantitative indexes were selected for objective evaluation. The root mean square error (RMSE), peak signal-to-noise ratio (PSNR), and mean square error (MSE) are some commonly used objective evaluation indexes, which can reflect the gray difference between the original image and the processed image. PSNR provides information and noise ratio for the image, while RMSE is the gray difference between the denoised image and the original image. The greater the signal-to-noise ratio of the image, the better the image quality.

$$\text{PSNR} = \text{lol}\frac{L^2}{1/AB\sqrt{\sum_{\text{i}=1}^{A}\sum_{j=1}^{B}\left(z_{ij} - z_{ij}'\right)}}$$

$$\text{RMSE} = \frac{1}{AB}\sqrt{\sum_{\text{i}=1}^{A}\sum_{j=1}^{B}\left(z_{ij} - z_{ij}'\right)^2} \tag{11}$$

$$\text{MSE} = \frac{1}{AB}\sum_{\text{i}=1}^{A}\sum_{j=1}^{B}\left(z_{ij} - z_{ij}'\right)^2.$$

Here, L is the gray value range, Z_{ij} is the value of the original image at (i, j), A is the number of pixels in the image in the y direction, and B is the number of pixels in the image in the x direction.

Table 1: Subjective evaluation image criteria.

Level	Standard	Evaluation
1	Changes in image quality affect the observation	Poor
2	The deterioration of image quality can be directly observed	General
3	Slight changes in image quality were observed but did not affect the observation	Good
4	The quality of the image did not change	Excellent

The experiment was carried out in the Windows operating system, the language was Mlab7.13 compilation environment, with 8 GB internal storage, the main frequency was 3.0 GHz (Inter quad-core), and the image size was 512×521.

2.6. Statistical Methods. SPSS 22.0 was used for data processing, and analysis methods were selected according to different situations. The paired sample t test was used to compare the changes of patient-related indicators, the independent sample t test was used for intergroup differences, ANOVA was used for multiple data, and $P < 0.05$ was used to determine whether there was statistical significance.

3. Results

3.1. Clinical Data Statistics of Patients. After CT examination, the malignant tumor showed uneven linear enhancement and increased pseudocapsule display, with liquefaction necrosis. After comparison, there was no significant difference in the basic information between the two groups ($P > 0.05$, Table 2).

3.2. Image Denoising Comparison with Different Methods. The result of mean filtering algorithm was compared with the image filtering results of the algorithm used in this work, and the results are shown in Figure 3. The PSNR of the proposed algorithm was significantly higher than that of the mean filtering algorithm, and the RMSE of the proposed algorithm was significantly lower than that of the mean filtering algorithm for image data processing ($P < 0.05$), indicating the superiority of the proposed algorithm. Figure 4(a) shows the original image with obvious fine particles. Compared with the original image, Figures 4(b) and 4(c) had a lighter sense of granularity and significantly enhanced clarity.

3.3. PSNR Comparison of Denoising Algorithms. Different sigma values (10, 20, 30, and 40) were selected to compare the PSNR of the algorithm, and the results are shown in Figure 5. The value of the proposed algorithm was higher than the PSNR values of CT and noisy images, which also showed that the algorithm had a significant effect on the detailed feature edge contour.

Table 2: Comparison of clinical data of patients.

Group	Cases	Male	Female	Age (years)	Cystic renal cancer	Clear cell carcinoma of the kidney
Observation group	40	27	13	56.3 ± 5.6	28 cases	12 cases
Control group	40	21	19	57.1 ± 6.0	0	0
T		−0.133		0.284	—	—
P		0.672		0.759	—	—

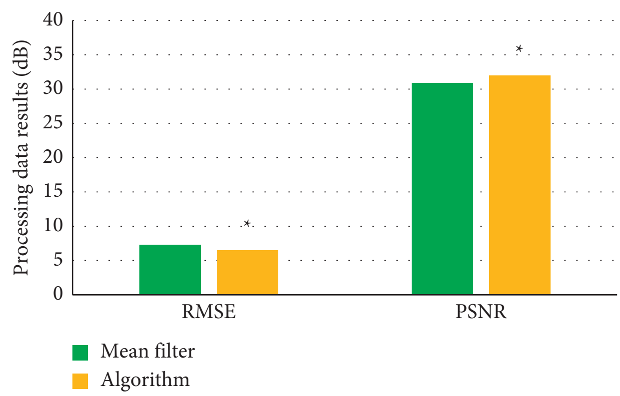

Figure 3: Comparison of image denoising. *A significant difference, $P < 0.05$.

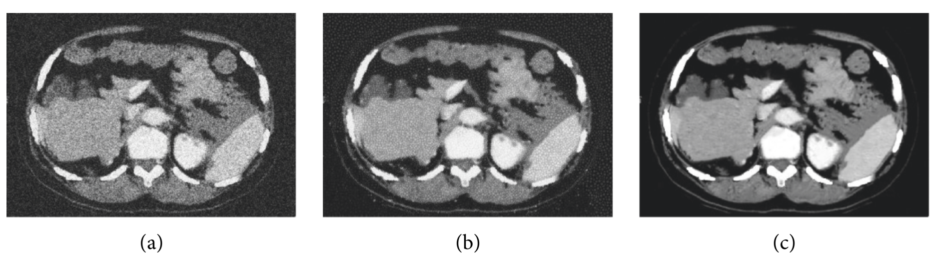

Figure 4: Comparison of CT images. (a) The image before CT enhancement. (b) The CT image after PSNR denoising. (c) The CT image after mean filtering algorithm denoising.

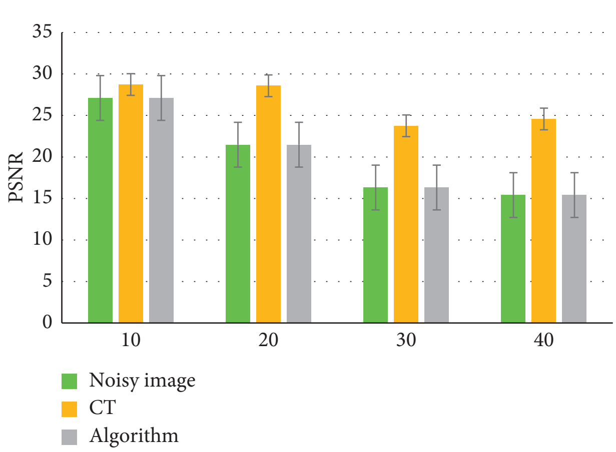

Figure 5: PSNR comparison of different algorithms.

3.4. Accuracy. The CT images of enhanced CT and those that underwent denoising algorithm treatment were compared, and the diagnostic results were analyzed as shown in Table 3. The accuracy of the enhanced CT was 93.8%, while that of CT images using the denoising algorithm was 96.3%. The difference between the two was significant ($P < 0.05$).

3.5. Contrast-Enhanced CT Images. The CT value was 20 Hu higher than that of the plain scan. The contrast agent in the medulla phase was partially excluded. The pseudocapsule sign, in which the renal tissue around the tumor was deformed and fibrotic under pressure, shows thin linear shadows without enhancement. Persistent filling defects of the renal vein and inferior vena cava were tumor emboli. Figure 6(a) shows the dermal medulla junction (30 s), Figure 6(b) shows the dermal medulla enhancement (100 s), and Figure 6(c) shows the development period of the collection system (5 min).

4. Discussion

Imaging examination is the most basic method for disease detection. With the continuous progress of the times, examination technology is also developing. The emergence of enhanced CT has further improved the accuracy of

Table 3: Comparison of diagnostic results.

Treatment	Cases	Malignant tumor	Sensitivity (%)	Specificity (%)	Accuracy
Enhanced CT	40	37	90.0	97.5	93.8%
Denoising algorithm treated-CT	40	39	95.0	97.5	96.3%*

Note: *a significant difference, $P < 0.05$.

(a) (b) (c)

Figure 6: Enhanced CT images.

ultrasound diagnosis, which plays a very important role in the diagnosis of malignant tumor-related diseases [22]. The earlier a tumor disease is discovered, the easier it is to be treated. More attention is paid to renal malignant tumors, and the accuracy, specificity, and sensitivity of tumor detection are also improving [23]. CT renal scan is usually performed by plain CT scan followed by enhanced CT scan. There are two stages in the enhanced scan: the renal cortex medulla stage (arterial stage) and the renal parenchyma stage (venous stage). In the medulla stage, because of the low density of the medulla, the boundary between medulla and cortex is very clear. In the renal parenchymal stage, the medulla images tend to be uniform due to the gradual influx of contrast agents into the cortex. Kang et al. [24] used CT to differentiate renal clear cell sarcoma from nephroblastoma, and the specificity was 86%, which was of significant value in differentiating renal clear cell sarcoma. In this study, the optimized algorithm based on denoising can distinguish irregular and difficult inflammatory responses with clearer two-dimensional boundaries. The classification of cystic renal carcinoma was proposed by radiologist Hartman et al. [25] in 1986, which mainly refers to renal cell carcinoma with cystic changes in imaging and gross pathology, as well as renal cell carcinoma with cystic changes found during surgery. According to pathophysiology, there are four types of cystic renal cell carcinoma, namely, cystic renal cell carcinoma, unilocular cystic renal cell carcinoma, cystic changes in renal cell carcinoma, and simple cyst canceration. The tumor is a cystic growth, derived from a cyst or a canceration of the cyst, and is absorbed by hemorrhage to form a cyst. In this study, the accuracy of enhanced CT was 93.8%, and the accuracy of the denoising algorithm was 96.3%. The accuracy of each algorithm did not reach 100%. In clinical practice, CT imaging still needs to be considered from many aspects and multiple case treatment plans should be referred to. The intelligent CT imaging algorithm can diagnose benign and malignant tumors. In case of poor conventional ultrasound diagnosis or suspected cases, the intelligent algorithm should be used to present auxiliary diagnosis.

There will be different degrees of reinforcement in the essence stage, which is expressed as “fast forward slow retreat” or “fast forward fast retreat.” The enhancement of the tumor smooth muscle and vascular components was obvious, showing onion skin, grid, and vortex enhancement. There were 12 patients with renal clear cell carcinoma which originated from the renal parenchyma, easily invaded adjacent tissue, often metastasized, could be calcified, and had obvious heterogeneous enhancement. Cortical enhancement in some renal cell carcinoma may approach or be higher than the renal cortex. Cystic nephroma showed complete intracapsular segmentation, no obvious mural nodules, equal or slightly low density, and mild to moderate continuous enhancement. The cystic contents were mainly myxomatous and closely connected with fibrous septa. Cystic renal carcinoma changes occurred in 5–7% of renal carcinomas and in 0.5% of renal cysts associated with renal carcinoma. In the first stage, the tumor was confined to the renal capsule with prominent limitations but smooth margins. In the second stage, the tumor was prominent, with a rough surface and a protrusion of 1 cm. In the third stage, the lymph nodes were enlarged and the inferior vena cava was thrombolytic. The abundance of blood vessels in tumor body can be reflected in CT image to a certain extent. The application of intelligent denoising algorithm preserves the details of the image better, improves the visual effect of the image effectively, and improves the quality of CT medical image. The CT image accuracy of denoising algorithm used in this study is 97.5%, significantly higher than that of enhanced CT (92.5%). Xu et al. [26] analyzed the CT image denoising algorithm with low overlapping sparse coding, and the proposed method has advanced denoising performance in terms of visual quality and objective standards. The X-CT denoising algorithm was introduced into the CT images of renal tumor patients to reduce the noise of CT images and significantly improve the image clarity. Conventional ultrasound elastography showed that the yellow and red cover of the tissue around the mass was malignant, which would cause the existence of misdiagnosis. The intelligent algorithm-based ultrasound imaging showed a significant difference in the elastic coefficient of the infiltrating catheter, and the lesions were judged as benign and malignant according to the score. The diagnostic effect was higher than that of ordinary CT images, and the diagnostic accuracy was higher.

5. Conclusion

The application of the ICA denoising algorithm in medical X-CT images implied corresponding variables under specific conditions and achieved better image denoising effect, which can accurately diagnose renal parenchymal tumors. The PSNR of this algorithm was significantly higher than that of the mean filtering algorithm, and it had a significant effect on the edge contour of detail features. This study has significant implications for this field. However, further research is needed to develop and innovate unified medical image denoising algorithms. There are many kinds of intelligent algorithms. Different denoising algorithms show different effects in image denoising. To explore more new intelligent algorithms suitable for medical imaging, it remains to be further studied by researchers.

Data Availability

The data used to support the findings of this study are available from the corresponding author upon request.

Conflicts of Interest

The authors declare that they have no conflicts of interest.

References

[1] R. J. Motzer, K. Penkov, J. Haanen et al., "Avelumab plus axitinib versus sunitinib for advanced renal-cell carcinoma," *New England Journal of Medicine*, vol. 380, no. 12, pp. 1103–1115, 2019.

[2] C. Nicolau, N. Antunes, B. Paño, and C. Sebastia, "Imaging characterization of renal masses," *Medicina*, PMCID, vol. 57, no. 1, , p. 51, 2021.

[3] C. Calandrini, F. Schutgens, R. Oka et al., "An organoid biobank for childhood kidney cancers that captures disease and tissue heterogeneity," *Nature Communications*, PMCID, vol. 11, no. 1, , p. 1310, 2020.

[4] D. F. McDermott, M. A. Huseni, M. B. Atkins et al., "Clinical activity and molecular correlates of response to atezolizumab alone or in combination with bevacizumab versus sunitinib in renal cell carcinoma," *Nature Medicine*, vol. 24, no. 6, pp. 749–757, 2018.

[5] J. Roth, I. Blaha, D. Bitter-Suermann, and P. U. Heitz, "Blastemal cells of nephroblastomatosis complex share an onco-developmental antigen with embryonic kidney and Wilms' tumor. An immunohistochemical study on polysialic acid distribution," *American Journal Of Pathology*, vol. 133, no. 3, pp. 596–608, 1988.

[6] N. Wake, J. S. Wysock, M. A. Bjurlin, H. Chandarana, and W. C. Huang, ""Pin the tumor on the kidney:" an evaluation of how surgeons translate CT and MRI data to 3D models," *Urology*, PMCID, vol. 131, , pp. 255–261, 2019.

[7] G. G. Re, D. J. Hazen-Martin, D. A. Sens, and A. J. Garvin, "Nephroblastoma (Wilms' tumor): a model system of aberrant renal development," *Seminars in Diagnostic Pathology*, vol. 11, no. 2, pp. 126–135, 1994.

[8] K. R. Moon, D. van Dijk, Z. Wang et al., "Visualizing structure and transitions in high-dimensional biological data," *Nature Biotechnology*, vol. 37, no. 12, pp. 1482–1492, 2019.

[9] T. R. Moen, B. Chen, D. R. Holmes et al., "Low-dose CT image and projection dataset," *Medical Physics*, vol. 48, no. 2, pp. 902–911, 2021.

[10] H. Choi, W. Chang, J. H. Kim et al., "Dose reduction potential of vendor-agnostic deep learning model in comparison with deep learning-based image reconstruction algorithm on CT: a phantom study," *European Radiology*, vol. 32, no. 2, pp. 1247–1255, 2021.

[11] D. Li, B. Mikela Vilmun, J. Frederik Carlsen et al., "The performance of deep learning algorithms on automatic pulmonary nodule detection and classification tested on different datasets that are not derived from LIDC-IDRI: a systematic review," *Diagnostics*, PMCID, vol. 9, no. 4, , p. 207, 2019.

[12] C. Yan, J. Lin, H. Li et al., "Cycle-consistent generative adversarial network: effect on radiation dose reduction and image quality improvement in ultralow-dose CT for evaluation of pulmonary tuberculosis," *Korean Journal of Radiology*, PMCID, vol. 22, no. 6, pp. 983–993, 2021.

[13] Z. Wang, J. Cai, W. Guo, M. Donnelley, D. Parsons, and I. Lee, "Backprojection Wiener deconvolution for computed tomographic reconstruction," *PLoS One*, vol. 13, no. 12, Article ID e0207907, 2018.

[14] S. Naganawa, R. Nakamichi, K. Ichikawa et al., "MR imaging of endolymphatic hydrops: utility of iHYDROPS-mi2 combined with deep learning reconstruction denoising," *Magnetic Resonance in Medical Sciences*, vol. 20, no. 3, pp. 272–279, 2021.

[15] M. Hu, Y. Zhong, S. Xie, H. Lv, and Z. Lv, "Fuzzy system based medical image processing for brain disease prediction," *Frontiers in Neuroscience*, PMCID, vol. 15, , Article ID 714318, 2021.

[16] Z. Yu, S. U. Amin, M. Alhussein, and Z. Lv, "Research on disease prediction based on improved DeepFM and IoMT," *IEEE Access*, vol. 9, Article ID 39043, 2021.

[17] C. Jaudet, K. Weyts, A. Lechervy, A. Batalla, S. Bardet, and A. Corroyer-Dulmont, "The impact of artificial intelligence CNN based denoising on FDG PET radiomics," *Frontiers in Oncology*, PMCID, vol. 11, , Article ID 692973, 2021.

[18] J. Amin, M. A. Anjum, M. Sharif, A. Rehman, T. Saba, and R. Zahra, "Microscopic segmentation and classification of COVID 19 infection with ensemble convolutional neural network," *Microscopy Research and Technique*, PMCID, vol. 85, no. 1, pp. 385–397, 2022.

[19] K.-C. Kwak and W. Pedrycz, "Face recognition using an enhanced independent component analysis approach," *IEEE Transactions on Neural Networks*, vol. 18, no. 2, pp. 530–541, 2007.

[20] D. Carone, G. W. J. Harston, J. Garrard et al., "ICA-based denoising for ASL perfusion imaging," *NeuroImage*, PMCID, vol. 200, , pp. 363–372, 2019.

[21] S. Kijima, T. Sasaki, K. Nagata, K. Utano, A. T. Lefor, and H. Sugimoto, "Preoperative evaluation of colorectal cancer using CT colonography, MRI, and PET/CT," *World Journal of Gastroenterology*, PMCID, vol. 20, no. 45, , Article ID 16964, 2014.

[22] E. Ishii, J. Fujimoto, S. Hara, S. Tanaka, and J. Hata, "Human sarcomatous Wilms' tumor lines: evidence for epithelial differentiation in clear cell sarcoma of the kidney," *Cancer Research*, vol. 49, no. 19, pp. 5392–5399, 1989.

[23] K. Bensalah, P. Bigot, L. Albiges et al., "Recommandations françaises du Comité de cancérologie de l'AFU - actualisation 2020-2022: prise en charge du cancer du rein," *Progrès en Urologie*, vol. 30, no. 12, pp. S2–S51, 2020, French.

[24] C. Kang, H. J. Shin, H. Yoon, J. W. Han, C. J. Lyu, and M.-J. Lee, "Differentiation between clear cell sarcoma of the kidney and wilms' tumor with CT," *Korean Journal of Radiology*, PMCID, vol. 22, no. 7, pp. 1185–1193, 2021.

[25] D. S. Hartman, C. J. Davis, T. Johns, and S. M. Goldman, "Cystic renal cell carcinoma," *Urology*, vol. 28, no. 2, pp. 145–153, 1986.

[26] D. Xu, T. Liu, Z. Zhou et al., "A denoising algorithm for CT image using low-rank sparse coding," *Medical Imaging 2018: Image Processing*, vol. 10574, 2018.

Hindawi
Contrast Media & Molecular Imaging
Volume 2022, Article ID 8952791, 10 pages
https://doi.org/10.1155/2022/8952791

Research Article

Artificial Intelligence Algorithm-Based High-Resolution Computed Tomography Image in the Treatment of Children with Bronchiolitis Obliterans by Traditional Chinese Medicine Method of Resolving Phlegm and Removing Blood Stasis

Xiaoning Shi[1] and Qing Zhou[2]

[1]*Child Health Section, Hunan Province Directly Affiliated TCM Hospital, Zhuzhou, Hunan 412000, China*
[2]*Department of Orthopedics and Traumatology, Zhuzhou 331 Hospital, Zhuzhou, Hunan 412000, China*

Correspondence should be addressed to Qing Zhou; j12021320@st.sandau.edu.cn

Received 28 February 2022; Revised 13 April 2022; Accepted 18 April 2022; Published 27 May 2022

Academic Editor: M. Pallikonda Rajasekaran

This research was aimed to explore the application of high-resolution computed tomography (HRCT) based on intelligent iterative reconstruction technique in the early diagnosis and treatment of bronchiolitis obliterans (BO) in children and to explore the efficacy of traditional Chinese medicine (TCM) in resolving phlegm and removing blood stasis. Sixty pediatric patients with BO were selected as the study subjects and diagnosed by HRCT scanning, and the scanned images were processed by iterative reconstruction technique. The patients were treated with TCM therapy of resolving phlegm and removing blood stasis alone (group A), HRCT-guided TCM therapy of resolving phlegm and removing blood stasis (group B), and iterative reconstruction HRCT-guided TCM therapy of resolving phlegm and removing blood stasis (group C). The results showed that the lung HRCT image after iterative reconstruction was closer to the original image than that after filtered back projection reconstruction, and the edge of the image after filtered back projection reconstruction was more blurred and the noise was higher. The image obtained by iterative reconstruction technique was smoother and clearer, and the image stability after iterative reconstruction was higher. The treatment results showed that the proportion of moderate and severe obstruction in group C was 5.18%, which was significantly lower than that in group A (18.75%) and group B (11.29%), and group B was significantly lower than that in group A (18.75%) ($P < 0.05$). The proportion of clinical effect in group C after treatment was 70.18%, significantly higher than that in group A (55.5%) and group B (63.34%), and that in group B was significantly higher than that in group A (55.5%) ($P < 0.05$). In summary, the lung HRCT after iterative reconstruction can more clearly and intuitively show the lesion site, which has a key role in guiding the early diagnosis and treatment planning of BO; the HRCT image based on iterative reconstruction technique combined with TCM treatment of removing blood stasis and resolving phlegm has a better therapeutic effect on children, with a high application value.

1. Introduction

Bronchiolitis obliterans (BO), also known as constrictive bronchiolitis, is a chronic airflow obstruction syndrome associated with inflammatory injury of small airways and belongs to a rare, fatal, and irreversible obstructive pulmonary disease that manifests as bronchiolar narrowing or obstruction due to inflammation or fibrosis [1, 2]. Since BO is usually caused by secondary respiratory tract infection, of which the more common is viral infection, and adenovirus is predominant, the disease is also used to specifically refer to a severe subtype of bronchiolitis in children caused by adenovirus or is considered to be a pulmonary manifestation in the chronic phase of transplant rejection [3, 4]. The main clinical characteristics of the disease are recurrent or persistent shortness of breath, wheezing or coughing, poor motor ability, and fine rales and wheezing in the lungs [5, 6]. Relevant studies indicated that the target of the pathogen causing bronchiolitis obliterans is respiratory ciliary cells. Due to the immune response mediated, inflammatory reaction and fibrosis occur in the repair process of epithelial cells, resulting in bronchiolitis obliterans [7, 8].

The treatment of bronchiolitis obliterans is generally treated with anti-inflammatory therapy so that the occlusion of bronchiolitis can be relieved. For bronchiolitis caused by bacterial infection, antibiotics should be used for treatment [9]. In addition, according to clinical experience, the combination of TCM treatment can often well improve the symptoms of children, improve the symptoms of cough, wheezing, and shortness of breath, and reduce the frequency of recurrent respiratory tract infections. TCM believes that bronchitis belongs to the category of lung or asthma syndrome [10, 11].

High-resolution computed tomography (HRCT) is widely used in clinical diagnosis of pulmonary nodules and nodules with special imaging [12, 13]. HRCT can clearly display fine structures, such as pulmonary lobules, airways, blood vessels, and interstitium, and does not require contrast enhancement during scanning [14]. HRCT is mainly used in the diagnosis of unexplained acute or chronic dyspnea, hemoptysis, lymphangitis cancer, emphysema, idiopathic interstitial fibrosis, and other diseases [15, 16]. Compared with conventional computed tomography (CT), HRCT has the advantage of high resolution, but its wide application in clinical diagnosis and treatment has certain limitations due to its high radiation dose [17, 18]. Iterative reconstruction algorithm (ART) refers to reconstructing images by solving linear equations. Starting from a hypothetical initial image, the method of gradual approximation is adopted. The theoretical projection value is constantly compared with the actual measured projection value and updated iteratively until the optimal solution is finally obtained. It was first used in positron emission tomography imaging, which can obtain high-quality images under the condition of low radiation dose [19, 20].

Therefore, a foreign study proposed the concept of low radiation dose scanning; however, reducing the radiation dose will increase the noise of the image to some extent. In order to solve the problem of increased image noise caused by the use of low radiation dose scanning, an iterative reconstruction algorithm was used for the reconstruction of HRCT images of the lungs so as to study the therapeutic effect of HRCT images based on iterative reconstruction algorithm combined with TCM for resolving phlegm and removing blood stasis on BO.

2. Materials and Methods

2.1. General Data and Grouping. Sixty patients with pediatric (32 males and 28 females) with BO admitted to hospital from September 2018 to November 2020 were randomly divided into group A (TCM treatment of resolving phlegm and removing blood stasis alone), group B (HRCT-guided TCM treatment of resolving phlegm and removing blood stasis), and group C (iterative reconstruction of HRCT-guided TCM treatment of resolving phlegm and removing blood stasis), with 20 patients in each group. The study was approved by the ethics committee of hospital. The patients and their families understood the study content and methods and signed the corresponding informed consent form.

TCM syndrome diagnosis criteria: cough weakness, increased sputum volume, fatigue, and sluggishness; tongue purple dark or spotted, thin and white coating.

Inclusion criteria: (i) children who met the clinical diagnostic criteria of bronchiolitis obliterans in children and were in stable stage; (ii) TCM syndrome differentiation belongs to deficiency of spleen and lung and internal obstruction of phlegm and blood stasis; and (iii) the age ranges from 4 to 15.

Exclusion criteria: (i) patients with diseases of other systems or organs; (ii) children with bronchial asthma, foreign body inhalation, and congenital bronchopulmonary dysplasia; and (iii) patients with severe liver and kidney insufficiency and primary diseases.

2.2. HRCT Scanning of Lung. During flat scan, the child was supine, arms up. It first scanned the positioning film and then determined the scanning range on the positioning film. HRCT scanning was employed. The scanning was performed in the transverse position, usually from the tip of the lung to the bottom of the lung, with layer thickness of 8–10 mm and layer spacing of 10 mm. Scanning was performed after deep inspirations and after breath-holding or after calm breathing. The scanning time was generally 0.7–3 s. HRCT scan: large matrix (512×512), thin layer (1~2 mm), and small field of view (15~30 cm in two lung scanning fields, 15~20 cm in the first). Image reconstruction was performed using iterative reconstruction technology; scanning field of view (FOV): 25~35; scan time <1 s.

2.3. Treatment of BO. Patients were treated with resolving phlegm and removing blood stasis decoction orally; the prescription composition was as follows: 15 g Radix Astragali, 10 g Radix Codonopsis, 10 g Poria, 10 g Rhizoma Dioscoreae, 10 g Pericarpium Citri Reticulatae, 9 g processed Pinellia Tuber, 10 g Rhizoma Dilong, 10 g Rhizoma Zelan, 6 g unprocessed Radix Glycyrrhizae, and so on. The specific dosage was added and subtracted according to the syndrome. The patients in group B and group C were diagnosed by HRCT and HRCT after iterative reconstruction, and the treatment plan was formulated according to the diagnosis results: 1 month as a course of treatment and continuous treatment for more than 5 courses.

2.4. HRCT Image Reconstruction. Image reconstruction algorithms can be roughly divided into transform method and series expansion method; the most used series expansion method is iterative reconstruction. Algebraic reconstruction method, simultaneous iterative reconstruction method, and maximum entropy method are widely used in iterative reconstruction algorithm [21]. Mathematical principle of image reconstruction: the radon transform $[Rf](L,\theta)$ of image function $f(r,\phi)$ is a line integral along the line L. It is the sum of the attenuation coefficients of each body element on the ray path, namely, the measured projection data. The essence of image reconstruction problem can be summarized as follows: according to projection data $P(L,\theta)$ (equation), the function image $f(r,\phi)$ can be obtained as follows.

$$[Rf](L,\theta) = \int_{-\infty}^{\infty} f(r,\phi)\mathrm{d}z, \tag{1}$$
$$\int_{-\infty}^{\infty} f(r,\phi)\mathrm{d}z = P(L,\theta).$$

The essence of algebraic reconstruction method is to solve the discrete projection equation approximately by iterative method, and the deviation is continuously corrected until satisfactory results are obtained. The algebraic reconstruction method is mathematically to solve a certain mathematical problem (to find a vector that satisfies a given linear inequality), and its basic idea is illustrated in Figure 1.

In Figure 1, the pixel value (gray scale or density) of pixel j is represented with x_j, and the overlapping area of ray i and pixel j is the intersection area of the shaded part in the figure, and its area (R) ratio to pixel δ^2 is as follows.

$$R_{ij} = \frac{S_{\text{dashed area}}}{\delta^2}. \tag{2}$$

The ray projection contribution (T) of pixel j to ray i is shown as follows.

$$T_{ij} = R_{ji}X_j. \tag{3}$$

Ray j also passes through other pixels and its total ray projection is as follows.

$$\begin{aligned} P_{ij} &= \sum_{1}^{N} P_{ij}, \\ &= \sum_{1}^{N} R_{ij}X_j. \end{aligned} \tag{4}$$

Equation (4) can be expressed by the following matrix.

$$P = R_X, \tag{5}$$

$$P = \left[P_1, P_2, \ldots, P_j\right]^T, \tag{6}$$

$$X = \left[X_1, X_2, \ldots, X_i\right]^T, \tag{7}$$

$$R = \begin{bmatrix} r_{11} & r_{12} & \cdot & \cdot & \cdot & r_{1j} \\ r_{21} & r_{22} & \cdot & \cdot & \cdot & r_{2j} \\ \cdot & \cdot & \cdot & \cdot & \cdot & \cdot \\ \cdot & \cdot & \cdot & \cdot & \cdot & \cdot \\ \cdot & \cdot & \cdot & \cdot & \cdot & \cdot \\ r_{i1} & r_{i2} & \cdot & \cdot & \cdot & r_{ij} \end{bmatrix}. \tag{8}$$

P is a j-dimensional vector (measurement vector); x is an i-dimensional vector, called image; and R is a ij-dimensional matrix (projection matrix). According to the measured P and the known matrix R (R can be obtained when the pixel arrangement and the geometric structure of ray are specified), X is obtained. Giving the actual situation and inevitable measurement error, (5) can be modified as follows.

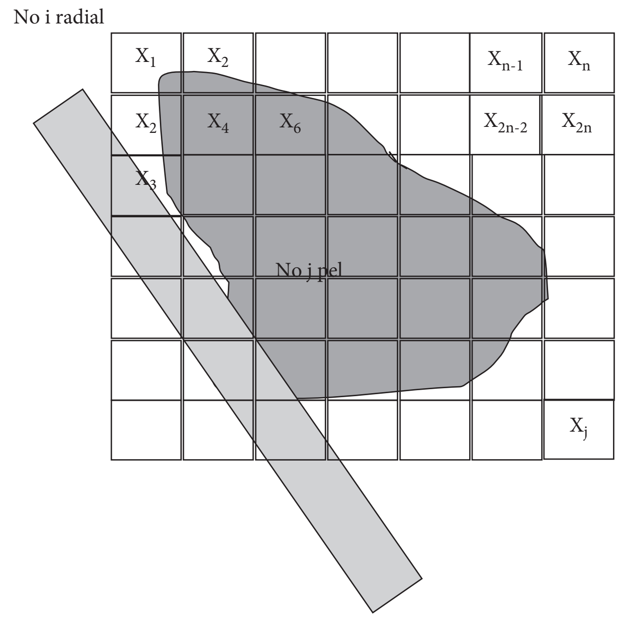

FIGURE 1: Basic idea of iterative reconstruction algorithm.

$$P = R_X + e, \tag{9}$$

where e is the error vector. An image vector $\widehat{X}$ is selected to minimize the objective function $\phi_1\{\widehat{x}\}$ (called the main criterion); if there are more than one x-value, one of which $\widehat{x}$ is selected to minimize the other objective function $\phi_2\{\widehat{x}\}$ (called the auxiliary criterion). $\phi_1\{\widehat{x}\}$ and $\phi_2\{\widehat{x}\}$ are the best criteria by used images. The commonly used optimal criteria include least squares criterion, maximum uniformity criterion, smoothing criterion, and maximum entropy criterion.

The least squares criterion: the following functions are minimized to solve $\widehat{x}$. The physical meaning of this criterion is to select $\widehat{x}$ to minimize the sum of squares of errors between the generated rays and the measured values.

$$\begin{gathered} \phi_1(x) = \sum_{i=1}^{I}\left(P_i - \sum_{j=1}^{J} r_{ij}\widehat{X}_j\right), \\ \sum_{i=1}^{I}\left(P_i - \sum_{j=1}^{J} r_{ij}\widehat{X}_j\right) = \|P - \mathrm{R}\widehat{X}\|^2, \\ \|P - R\widehat{x}\|^2 = (P - R\widehat{x})^T(P - R\widehat{x}). \end{gathered} \tag{10}$$

Maximum uniformity criterion and smoothness criterion are as follows.

$$\begin{aligned} \phi_2(x) &= \phi_{21}(x) + \widetilde{\phi_{22}}(x) \\ &= X^T\mathrm{BX} + X^TX \\ &= X^T(B+i)X. \end{aligned} \tag{11}$$

The physical meaning of (11) is the local uniformity between each pixel and its adjacent pixel and the uniformity of the whole image. If the least squares criterion is considered, the objective function can also be composed.

$$\widetilde{\phi}_1(x) = (P - R\hat{x})^T (P - R\hat{x}) + x^T (B + I)x, \tag{12}$$

where minimum $\widehat{X}$, $\widetilde{\phi}_1(\widehat{x})$ are selected so that the least squares criterion, maximum uniformity criterion, and smoothness criterion are integrated. Iterative reconstruction technique can be expressed as below.

$$\begin{aligned} Ax &= p, \\ x &= [x_1, x_2, \ldots, x_n]T, \\ p &= [p_1, p_2, \ldots, p_m]T, \end{aligned} \tag{13}$$

x is the one-dimensional vector of n elements, each element represents the pixel of a 2D object, p is the one-dimensional vector of m elements, each element represents the measurement carried out by a detector in a projection direction, A is called the projection matrix, and each value in this matrix called the projection rate defines the contribution of specific pixels to specific projection values.

The implementation of iterative reconstruction algorithm is as follows.

$$X^{(k+1)} = X^{(k)} + \lambda_k \frac{P_i - \langle a_i, x_k \rangle}{\|a_i\|^2} a_i^T, \tag{14}$$

where λ is the relaxation factor that determines the convergence rate. The whole iterative process is given in Figure 2.

$\overrightarrow{x}^0$ is an arbitrary initial value. The first step is to project the point $\overrightarrow{x}^0$ vertically to L1 to get a new value $\overrightarrow{x}^1$. The next step is to project the point $\overrightarrow{x}^1$ vertically to L2 to get new a value $\overrightarrow{x}^2$, and so on in a similar fashion. Each step is to project the currently estimated point onto the next line so that it satisfies the next equation. Eventually, the algorithm will converge on the solution of the equation group [22]. Figure 2(a) is a compatible equation group; that is, there is an exact solution for the equation group. When the number of iterations is sufficient, a convergence value can be obtained. Figure 2(b) is a system of incompatible equation group that will jump all the time within the triangular region in the middle after the number of iterations to a certain value. It means that any point in the triangular region is a numerical solution of the equation group, and the better way is to obtain multiple solutions and then calculate their average values.

2.5. Evaluation Indicators of Image Quality. The reconstructed image sharpness and noise will vary due to different image processing methods, so the mean square error (MSE) and structural similarity (SSIM) are used to evaluate the processed images.

$\mathrm{MSE}_{\mathrm{out}}$ represents the MSE between the result obtained by the reconstruction algorithm and the standard result. If the $\mathrm{MSE}_{\mathrm{out}}$ value is >1, it indicates that the new reconstruction algorithm is better. The greater the value, the better the effect. $\mathrm{MSE}_{\mathrm{in}}$ represents the *MSE* between the result obtained by the reconstruction algorithm for contrast and the standard result, and the improvement in signal-to-noise ratio (ISNR) is expressed as follows.

$$\mathrm{ISNR} = 10 \log_{10}\left(\frac{\mathrm{MSE}_{\mathrm{in}}}{\mathrm{MSE}_{\mathrm{out}}}\right). \tag{15}$$

MSE represents the mean square error between the reconstruction result and the target image, and μ^2max represents the maximum pixel value in the reconstruction result. The peak signal-to-noise ratio (PSNR) can be expressed as follows.

$$\mathrm{PSNR} = 10 \log_{10}\left(\frac{\mu^2 \max}{\mathrm{MSE}}\right). \tag{16}$$

MSE is the variance between the reconstructed image and the reference image, and *EMSE* equation is expressed as below.

$$\mathrm{EMSE} = \sqrt{\mathrm{MSE}}. \tag{17}$$

SSIM is a measure of the similarity between images. The closer the value is to 1, the higher the similarity between images is. In image reconstruction, the similarity between the reconstructed image and the original image can be measured. If a,b represent the results obtained by the new reconstruction method and standard results in the window, respectively, μ_a and μ_b represent the mean corresponding to a,b, β_a and β_b represent the standard deviation corresponding to a,b, and k_1 and k_2 are two very small constants so as not to divide by zero. *SSIM* is expressed as follows.

$$E(\mathrm{a}, b) = \frac{(2\mu_{\mathrm{a}}\mu_{\mathrm{b}} + \mathrm{k}_1)(2\beta_{\mathrm{ab}} + \mathrm{k}_2)}{(\mu_{\mathrm{a}}^2 + \mu_{\mathrm{b}}^2 + \mathrm{k}_1)(\beta_{\mathrm{a}}^2 + \beta_{\mathrm{b}}^2 + \mathrm{k}_2)}. \tag{18}$$

2.6. Statistical Methods. Statistical software SPSS 24.0 was used for statistical processing in this study. The measurement data were expressed as mean ± standard deviation. The measurement data in accordance with normal distribution were compared with single factor and multiple means, and the independent sample t-test was used between the two groups. The counting data were expressed as percentage or percentage by chi-square test. $P < 0.05$ was considered as statistically significant difference.

3. Results

3.1. Low-Dose HRCT Image Reconstruction. Figures 3(a) and 3(d) show adding noise through the Poisson distribution and then performing an iterative reconstruction. The image sharpness was very low at this time. Figure 3(b) is the original HRCT picture, and Figure 3(e) is the figure after one iteration rendering, which is still blurred compared to the original image. Figures 3(c) and 3(f) are the images obtained by reconstructing the projection data based on 90° projection angle using filtered back projection (FBP) and algebraic reconstruction technique (ART), respectively. The reconstructed

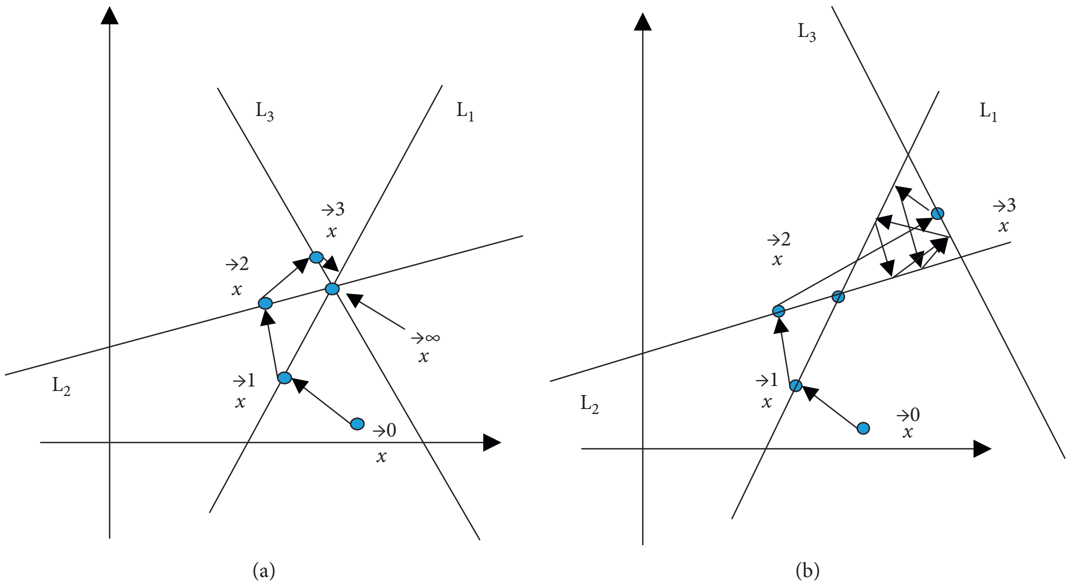

Figure 2: Iterative process. (a) Compatible equation group. (b) Incompatible equation group.

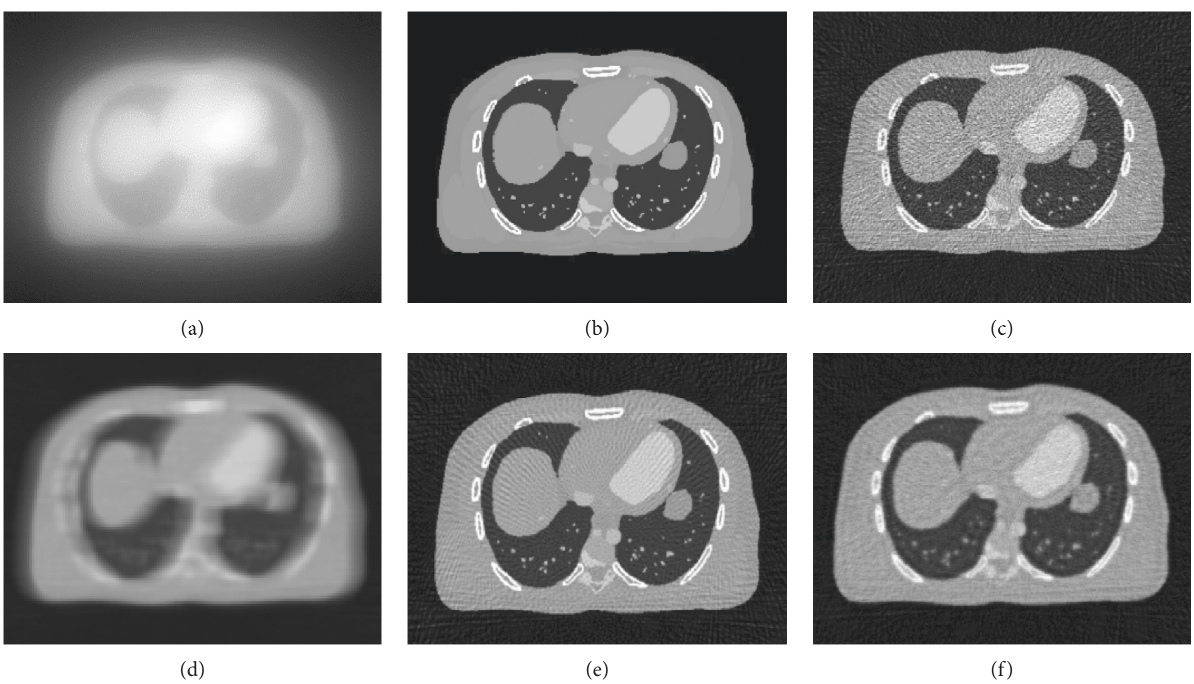

Figure 3: Low-dose HRCT image reconstruction: (a, d) images added with noise; (b) original image; and (e, c, f) reconstructed images.

image was compared with the original image. The image after iterative reconstruction was closer to the original image, and the edge of the image after FBP reconstruction was more blurred and noisier, and the image obtained by iterative reconstruction technique was smoother and clearer.

3.2. Comparison of Image Reconstruction Effect. From Figures 4(a) and 4(b), it can be found that after the number of iterations exceeded a certain value, the MSE no longer continues to decrease but begins to grow. It may be because the projection data obtained with only a 90° projection angle, the complexity of the projection data was less than that of the image to be reconstructed. After a certain number of iterations, due to the excess expression ability of the model, some features that can only meet the projection data but cannot meet the original image were trained, which led to the increase of MSE. Figures 4(c) and 4(d) are the contrast curves of FBP, ART, and original images, respectively. The FBP reconstructed image fluctuates greatly, while the ART

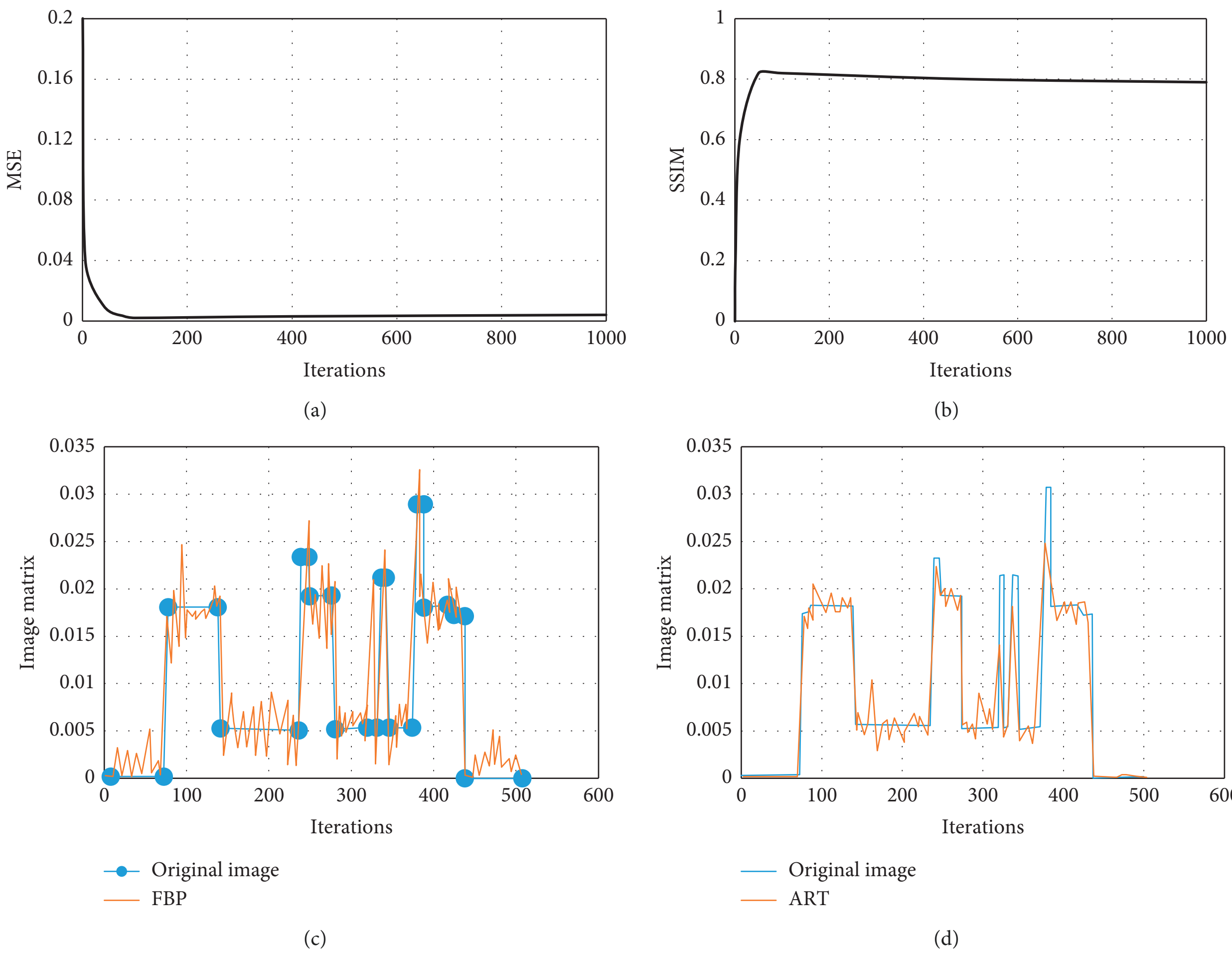

FIGURE 4: Evaluation of image reconstruction effect. (a), (b) The reconstructed images MSE and SSIM, respectively. (c) The image matrix of original image and FBP image. (d) The image matrix of original image and iterative reconstruction image.

reconstructed image is more stable. Although the FBP image fluctuated greatly, there was no energy loss. Although the ART curve performs better at the smooth, there is a large gap with the curve of the original image at the peak, which will lead to loss of image details.

3.3. Imaging Findings of BO. HRCT of BO are typically characterized by decreased lung density, accompanied by decreased vascular caliber. The features are called mosaic perfusion or mosaic reduction, suggesting bronchial or bronchiolar air trapping, which can be displayed by HRCT scanning in the expiratory phase. In patients with disease progression, there will be bronchiectasis characterized by airway wall thickening and caliber expansion. From the HRCT images of children after iterative reconstruction in Figure 5, the peripheral bronchiole wall was thickened, bronchiole dilatation was accompanied by secretion retention, and lobular central bronchial nodules were observed. Figures 5(c) and 5(d) show that the left pulmonary artery is smaller than the right pulmonary artery, the volume of the left pulmonary artery is reduced, the pulmonary transparency is enhanced, and the blood vessels are thinner.

3.4. Basic Information of Patients. Table 1 showed the basic information, such as age and course of disease, of the children included in the study. The children aged 8–11 accounted for a relatively high proportion (38.79%). Most of the patients (46.8%) had a course of disease from five to ten months. There was no statistical significance in patients' basic information ($P > 0.05$). Figure 6 suggests the analysis results of the main causes and symptoms of the children. All the children included in the study had wheezing symptoms, and more than 97% of the children had cough symptoms. The other common symptoms were shortness of breath, dyspnea, and so on, mainly including adenovirus, mycoplasma *pneumoniae*, and influenza virus.

3.5. Improvement of Pulmonary Function Obstruction. Children with BO are generally accompanied by obstructive ventilatory dysfunction mainly with small airway involvement, which can be divided into mild obstruction, moderate obstruction, and severe obstruction according to the degree of obstruction. Figure 7 suggests the comparison results of the degree of pulmonary function obstruction among the three groups after different ways of guided TCM treatment. The proportion of patients with moderate-to-severe obstruction

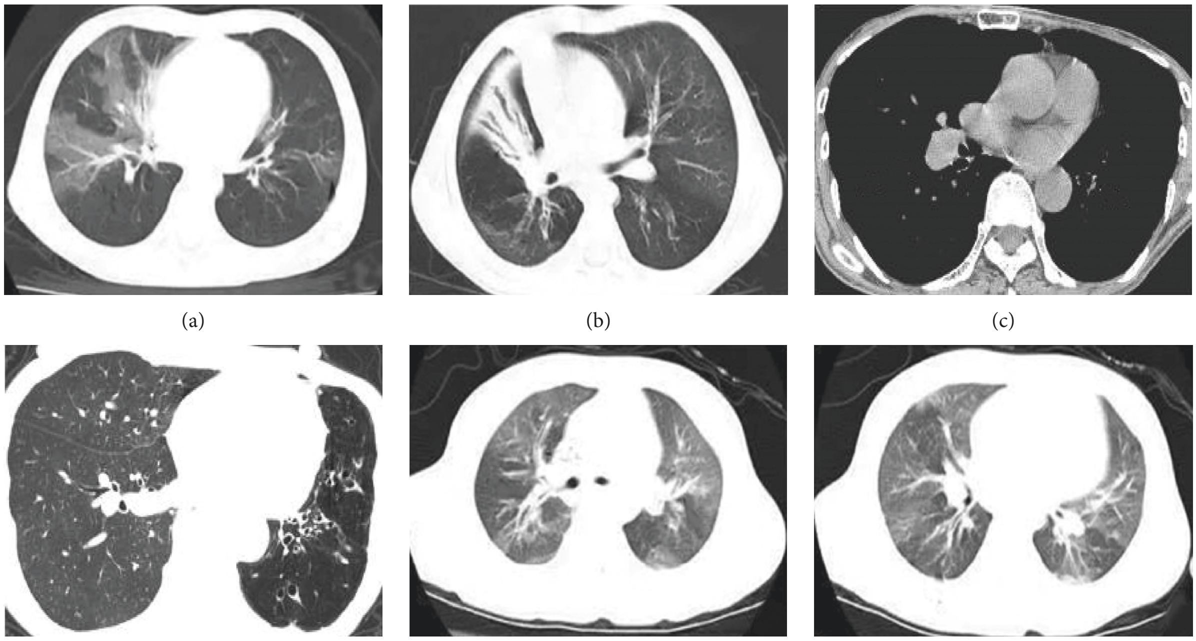

Figure 5: HRCT iterative reconstruction image of BO. (a, b, e, and f) HRCT plain scan images; (c, d) Expiratory phase HRCT images.

Table 1: Basic information of patients.

Item	Category	Proportion (%)
Age (years)	4~7	25.33
	8~11	38.79
	12~15	35.88
Gender	Male	53.33
	Female	46.67
Course of disease (month)	<5	33.4
	5~10	46.8
	>10	19.8

in group C was 5.18%, obviously inferior than that in group A (18.75%) and group B (11.29%), and significantly lower in group B than that in group A ($P < 0.05$). The proportion of patients with mild obstruction in group C was 56.38%, which was significantly superior than that in group A (34.93%) and group B (46.21%), and the proportion in group B was significantly higher than that in group A ($P < 0.05$).

3.6. Clinical Efficacy Analysis. After the three groups of patients were treated with TCM guided by different ways, the efficacy was evaluated according to the improvement of patients' symptoms and expressed by three levels: clinically significantly effective, clinically effective, and clinically ineffective. Figure 8 reveals the efficacy comparison results of the three groups of patients. The proportion of clinically significant effect after treatment in group C was 70.18%, which was clearly higher than that in group A (55.5%) and group B (63.34%), and the proportion in group B was clearly higher than that in group A ($P < 0.05$).

4. Discussion

At present, the treatment of bronchiolitis obliterans in children is mainly treated with glucocorticoids and bronchodilators, and the key stage of clinical treatment of this disease is the early stage. Therefore, accurate and early diagnosis also plays a key role in its efficacy. Katsura et al. [23] found that the application of TCM therapy can significantly improve the clinical symptoms and pulmonary ventilation function of children. In addition, TCM therapy has less impact and side effects on children, so it has good application value and research prospects [24]. Early chest radiographs of patients with BO are often unremarkable, and pulmonary hyperinflation and linear shadows and reticular shadows indicating alveolar wall thickening lack specificity for their diagnosis. Without contrast agent, HRCT plain scan at the end of inspiratory and end of exhalation is an effective method for noninvasive diagnosis of BO. Before and at the early stage of the clinical manifestations of BO, HRCT mosaic perfusion sign cannot be used as the basis for its early diagnosis. However, if the children are accompanied by abnormal changes in the bronchus (e.g., thickening of the bronchial wall and gas retention in the expiratory phase), it has a key role in prompting the diagnosis of BO.

The results showed that the HRCT image of lung after iterative reconstruction was closer to the original image than the filtered back projection reconstruction. The edge of the image reconstructed by filtered back projection was more blurred and the noise was greater. The image obtained by iterative reconstruction technique was smoother and clearer. The image stability after iterative reconstruction was higher. HRCT of the lung after iterative reconstruction can display the lesion site more clearly and intuitively, which has a key

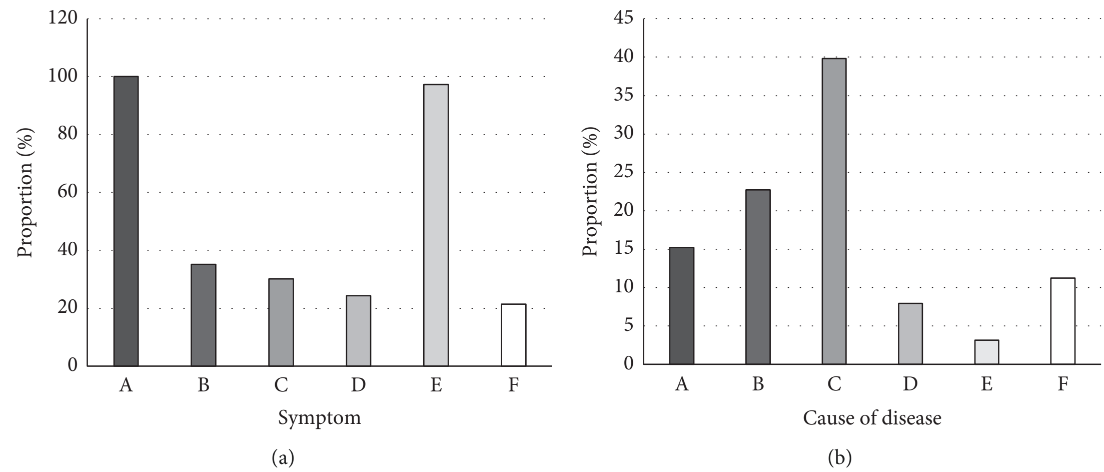

Figure 6: Etiology and symptoms of the patients. In Figure (a), A, B, C, D, E, and F indicated wheezing, shortness of breath, dyspnea, wheezing or rind in the lungs, cough, and cyanosis around the lips, respectively. In Figure (b), A, B, C, D, E, and F represented mycoplasma *pneumoniae*, adenovirus with mycoplasma *pneumoniae*, adenovirus, influenza virus, parainfluenza virus, and other causes, respectively.

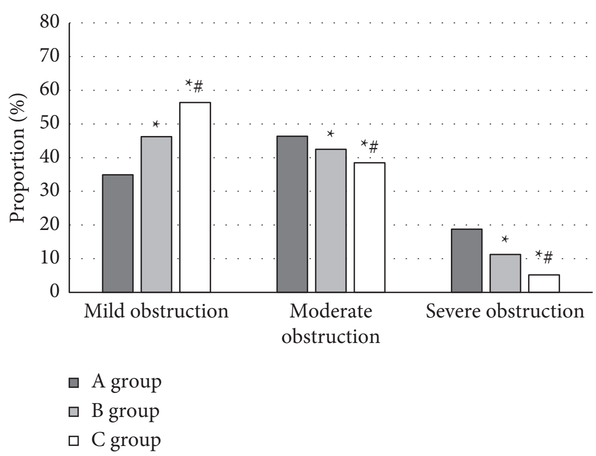

Figure 7: Degree of pulmonary function obstruction in patients. *Compared to group A ($P < 0.05$). #Compared to group B ($P < 0.05$).

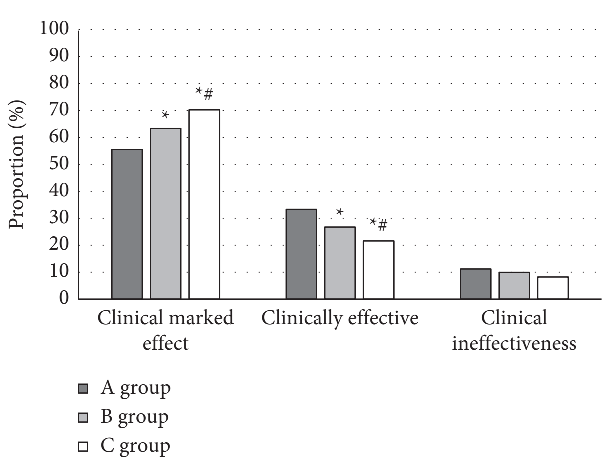

Figure 8: Analysis of clinical efficacy in patients. *Compared to group A ($P < 0.05$). #Compared to group B ($P < 0.05$).

guiding role in the early diagnosis and treatment of bronchiolitis obliterans. After treatment, the proportion of patients with moderate and severe obstruction in group C was significantly lower than that in group A and group B, and that in group B was significantly lower than that in group A ($P < 0.05$). The proportion of patients with mild obstruction in group C was significantly higher than that in groups A and B, and that in group B was significantly higher than that in group A ($P < 0.05$), which was similar to the results of Weng et al. [25]. Under the guidance of HRCT images after iterative reconstruction, a targeted TCM treatment plan for eliminating phlegm and removing blood stasis was developed, which had better efficacy for children with bronchiolitis obliterans and significantly improved their lung ventilation function. The proportion of clinical effect in group C was significantly higher than that in group A and group B ($P < 0.05$). The TCM therapy of resolving phlegm and removing blood stasis showed good efficacy and safety in improving the symptoms, signs, and pulmonary ventilation function of children with bronchiolitis obliterans. Moreover, guided by the HRCT images after iterative reconstruction, the targeted formulation of TCM treatment plan for resolving phlegm and removing blood stasis further improved its comprehensive efficacy.

5. Conclusion

The results showed that the HRCT of the lung after iterative reconstruction could display the lesion site more clearly and intuitively, which played a key guiding role in the early diagnosis and treatment of bronchiolitis obliterans. HRCT image based on iterative reconstruction technology combined with TCM therapy to remove blood stasis and remove phlegm had a good therapeutic effect on children with high application value. However, the HRCT image processing in this study lacks comparison with other intelligent algorithms, and the samples included in the study are few and are of low representativeness. Therefore, these aspects will be improved and optimized in the subsequent experiments, and the application of HRCT images based on artificial intelligence algorithm in the diagnosis and treatment of bronchiolitis obliterans in children will be further studied. In conclusion, this study provides a reference for the early diagnosis and treatment of bronchiolitis obliterans in children.

Data Availability

The data used to support the findings of this study are available from the corresponding author upon request.

Conflicts of Interest

The authors declare that they have no conflicts of interest regarding the publication of this paper.

References

[1] Y.-N. Li, L. Liu, H.-M. Qiao, H. Cheng, and H.-J. Cheng, "Post-infectious bronchiolitis obliterans in children: a review of 42 cases," *BMC Pediatrics*, vol. 14, no. 1, p. 238, 2014.

[2] C. Zhao, J. Liu, H. Yang, L. Xiang, and S. Zhao, "Mycoplasma pneumoniae-associated bronchiolitis obliterans following acute bronchiolitis," *Scientific Reports*, vol. 7, no. 1, p. 8478, 2017.

[3] S. O. Tomikawa and J. C. Rodrigues, "Current research on pediatric patients with bronchiolitis obliterans in Brazil," *Intractable & Rare Diseases Research*, vol. 4, no. 1, pp. 7–11, 2015.

[4] C. Chen, S. Hsu, W. Chen et al., "Post-infectious bronchiolitis obliterans: HRCT, DECT, pulmonary scintigraphy images, and clinical follow-up in eight children," *Frontiers in Pediatrics*, vol. 8, Article ID 622065, 2020.

[5] S. Walther, E. Rettinger, H. M. Maurer et al., "Long-term pulmonary function testing in pediatric bronchiolitis obliterans syndrome after hematopoietic stem cell transplantation," *Pediatric Pulmonology*, vol. 55, no. 7, pp. 1725–1735, 2020.

[6] M. Driskel, A. Horsley, L. Fretwell, N. Clayton, and M. Al-Aloul, "Lung clearance index in detection of post-transplant bronchiolitis obliterans syndrome," *ERJ Open Research*, vol. 5, no. 4, Article ID 02019, 2019.

[7] X. W. Chen, D. H. Chen, S. Z. Wu et al., "Value of anti-neutrophil cytoplasmic antibody in assessing the severity of bronchiolitis obliterans in children," *Zhong Guo Dang Dai Er Ke Za Zhi*, vol. 22, no. 9, pp. 990–995, 2020, Chinese.

[8] O. Sardón, E. G. Pérez-Yarza, A. Aldasoro, P. Corcuera, J. Mintegui, and J. Korta, "Bronquiolitis obliterante. Evolución a medio plazo," *Anales de Pediatría*, vol. 76, no. 2, pp. 58–64, 2012, Spanish.

[9] M. Zhang, Z. Lu, W. Yang, L. Qian, B. Wang, and B. Zhang, "Clinical features of postinfectious bronchiolitis obliterans in children undergoing long-term nebulization treatment," *World Journal of Pediatrics*, vol. 14, no. 5, pp. 498–503, 2018.

[10] X. Y. Wu, Z. X. Luo, Z. Fu, E. M. Liu, J. Luo, and L. He, "Clinical analysis of 28 cases of bronchiolitis obliterans," *Zhong Guo Dang Dai Er Ke Za Zhi*, vol. 15, no. 10, pp. 845–849, 2013, Chinese.

[11] N. M. Caballero-Colón, Y. Guan, H. Yang, S. Zhao, and W. De Jesús-Rojas, "Bronchiolitis obliterans and primary ciliary dyskinesia: what is the link?" *Cureus*, vol. 13, no. 6, Article ID e15591, 2021.

[12] D. H. Chen, Y. N. Lin, S. L. Lan et al., "Clinical characteristics of bronchiolitis obliterans in pediatric patients," *Zhonghua Er Ke Za Zhi*, vol. 50, no. 2, pp. 98–102, 2012.

[13] X. Wang, C. Liu, M. Wang, Y. Zhang, H. Li, and G. Liu, "Clinical features of post-infectious bronchiolitis obliterans in children undergoing long-term azithromycin treatment," *Experimental and Therapeutic Medicine*, vol. 9, no. 6, pp. 2379–2383, 2015.

[14] L. Gazourian, A. M. F. Coronata, A. J. Rogers et al., "Airway dilation in bronchiolitis obliterans after allogeneic hematopoietic stem cell transplantation," *Respiratory Medicine*, vol. 107, no. 2, pp. 276–283, 2013.

[15] H. Yazan, F. Khalif, L. A. Shadfaan et al., "Post-infectious bronchiolitis obliterans in children: clinical and radiological evaluation and long-term results," *Heart & Lung*, vol. 50, no. 5, pp. 660–666, 2021.

[16] Z. P. Oo, A. Bychkov, Y. Zaizen, M. Yamasue, J. I. Kadota, and J. Fukuoka, "Combination of pleuroparenchymal fibroelastosis with non-specific interstitial pneumonia and bronchiolitis obliterans as a complication of hematopoietic stem cell transplantation - clues to a potential mechanism," *Respiratory Medicine Case Reports*, vol. 26, pp. 244–247, 2019.

[17] M. Akagi, Y. Nakamura, T. Higaki et al., "Deep learning reconstruction improves image quality of abdominal ultra-high-resolution CT," *European Radiology*, vol. 29, no. 11, pp. 6163–6171, 2019.

[18] S. Muramatsu and K. Sato, "Quantitative analysis of emphysema in ultra-high-resolution CT by using deep learning reconstruction: comparison with hybrid iterative reconstruction," *Japanese Journal of Radiological Technology*, vol. 76, no. 11, pp. 1163–1172, 2020, Japanese.

[19] K. Yasaka, M. Katsura, S. Hanaoka, J. Sato, and K. Ohtomo, "High-resolution CT with new model-based iterative reconstruction with resolution preference algorithm in evaluations of lung nodules: comparison with conventional model-based iterative reconstruction and adaptive statistical iterative reconstruction," *European Journal of Radiology*, vol. 85, no. 3, pp. 599–606, 2016.

[20] K. Narita, Y. Nakamura, T. Higaki, M. Akagi, Y. Honda, and K. Awai, "Deep learning reconstruction of drip-infusion cholangiography acquired with ultra-high-resolution computed tomography," *Abdominal Radiology*, vol. 45, no. 9, pp. 2698–2704, 2020.

[21] H.-j. Lim, M. J. Chung, K. E. Shin, H. S. Hwang, and K. S. Lee, "The impact of iterative reconstruction in low-dose computed tomography on the evaluation of diffuse interstitial lung disease," *Korean Journal of Radiology*, vol. 17, no. 6, pp. 950–960, 2016.

[22] A. Nakamoto, M. Hori, H. Onishi et al., "Ultra-high-resolution CT urography: importance of matrix size and reconstruction technique on image quality," *European Journal of Radiology*, vol. 130, Article ID 109148, 2020.

[23] M. Katsura, J. Sato, M. Akahane, Y. Mise, K. Sumida, and O. Abe, "Effects of pure and hybrid iterative reconstruction algorithms on high-resolution computed tomography in the evaluation of interstitial lung disease," *European Journal of Radiology*, vol. 93, pp. 243–251, 2017.

[24] P. H. F. Togni, J. L. M. Casagrande, and H. M. Lederman, "Utility of the inspiratory phase in high-resolution computed tomography evaluations of pediatric patients with bronchiolitis obliterans after allogeneic bone marrow transplant: reducing patient radiation exposure," *Radiologia Brasileira*, vol. 50, no. 2, pp. 90–96, 2017.

[25] T. Weng, X. Lin, L. Wang, J. Lv, and L. Dong, "Follow-up on the therapeutic effects of a budesonide, azithromycin, montelukast, and acetylcysteine (BAMA) regimen in children with post-infectious bronchiolitis obliterans," *Journal of Thoracic Disease*, vol. 13, no. 8, pp. 4775–4784, 2021.

Hindawi
Contrast Media & Molecular Imaging
Volume 2022, Article ID 5847589, 5 pages
https://doi.org/10.1155/2022/5847589

Research Article

Diagnostic Value of Emission Computed Tomography Combined with Computed Tomography for Metastatic Malignant Tumor of Spine

Feng Qin,[1] Yapei Feng,[2] Panpan Zhang,[1] Yuemei Li,[1] and Weiqiang Fan[1]

[1]*Department of Spinal Surgery, Dongying Shengli Oilfield Central Hospital, Dongying City 257100, Shandong Province, China*
[2]*Department of Reproductive Medicine, Dongying Shengli Oilfield Central Hospital, Dongying City 257100, Shandong Province, China*

Correspondence should be addressed to Weiqiang Fan; fanweiqiang@slchos.cn

Received 22 March 2022; Revised 28 April 2022; Accepted 5 May 2022; Published 26 May 2022

Academic Editor: M. Pallikonda Rajasekaran

Objective. To explore the diagnostic value of emission computed tomography (ECT) combined with computed tomography (CT) for metastatic malignant tumor of spine. *Methods*. By means of retrospective study, a total of 102 patients with extraskeletal primary malignant tumor treated in our hospital from February 2019 to February 2021 were selected as the subjects. All patients had single lesion of the spine, of which 72 were malignant and 30 were benign according to the results of pathological examination. ECT and CT examinations were performed to all patients, and by taking the pathological findings as the gold standard, the sensitivity, specificity, positive predictive value and negative predictive value of ECT, CT, and their combination were calculated, and their efficacy in diagnosing metastatic malignant tumor of spine was analyzed. *Results*. A total of 68 (94.4%) metastatic malignant spinal tumors were detected by ECT combined with CT, with a detection rate of 100% in breast cancer and lung cancer, 94.1% in liver cancer, and 78.6% in prostate cancer, respectively; the combined diagnosis had a diagnostic sensitivity of 94.4%, specificity of 73.3%, positive predictive value of 89.5%, negative predictive value of 84.6%, and diagnostic accuracy rate of 88.2%, and AUC (95% CI) = 0.839 (0.739–0.939). *Conclusion*. Combining ECT with CT has a good diagnostic efficacy for metastatic malignant spinal tumors.

1. Introduction

Metastasis is a typical manifestation of the progression of malignant tumors to the middle and late stages, and lung, liver, and bones are the most common metastatic sites, with 66.7% of bone metastases belonging to spinal metastasis [1], that is, primary malignant tumors form secondary tumors by invading the spine through vascular, lymphatic, and other routes. Metastatic malignant spinal tumors not only cause patients to experience symptoms such as bone pain but may also trigger functional disorders such as fractures, reducing their quality of survival and increasing the risk of death [2, 3]. Since there is no cure for spinal metastasis, early diagnosis and targeted treatment are important measures to alleviate the clinical symptoms of patients [4], which is of great significance to improve the patient outcome. At this stage, pathological examination is still the gold standard for testing the nature of spinal tumors, but it is traumatic, and biopsy puncture is not feasible in some patients (such as those with coagulation disorder or poor compliance) [5], so minimally invasive and convenient imaging tests are gaining attention in clinic. Computed tomography (CT), X-rays, and emission computed tomography (ECT) are all common imaging modalities for the diagnosis of spinal tumors, and among them, X-ray films can clarify the nature of the lesion based on its morphology, presence or absence of bone destruction, etc., but some lesions that appear abnormal on ECT often require months to be visualized on X-ray films [6], so X-rays are generally used in the initial examination. CT has better sensitivity for the detection of metastatic spine tumors compared to X-rays and is especially valuable for suspected metastatic lesions with X-ray negative and ECT positive, because it is capable of visualizing the involvement of bone trabecula, cortical bone, and surrounding soft tissues. However, the efficacy of CT is also limited by the time that malignant cells invade the spine, and it cannot effectively detect the invaded bone without significant changes in physiological structure and osseous characteristics [7]. Unlike CT and X-rays, ECT evaluates the lesion mainly based on the abnormalities of radionuclides so that the nature of the lesion can be distinguished by the difference in radioactivity concentration, and its early diagnostic efficacy is superior to that of conventional imaging modalities.

According to the published works, the sensitivity of ECT for the diagnosis of metastatic malignant spine tumors ranges from 64.4% to 82.1% [8], and its specificity is relatively low [9], so the atypical lesions should be diagnosed using a combination of multiple imaging tests. Because ECT and CT have differences in imaging mechanism, both of them may give play to the effect of information complementation and improve the clinical detection rate of atypical lesions. By reviewing previous studies, it is found that the literature of combining ECT with CT for the diagnosis of metastatic malignant spine tumors is very few, and although some works explored the diagnostic value of SPECT/CT fusion imaging in single lesion of the spine [10], the sample size was small, causing difficulty in providing a sufficient basis for clinical application. Based on this, 102 patients with malignant tumors were included herein, and the diagnostic value of ECT combined with CT for metastatic malignant spine tumors was analyzed by exploring the detection rate in different malignant tumors, aiming to offer greater theoretical support for clinical practice.

2. Materials and Methods

2.1. General Data. Inclusion criteria are as follows: (1) the patients had extraskeletal primary malignant tumor; (2) single lesion of spine was found in the patients after whole-body bone imaging; (3) the patients were treated in our hospital in the whole course and had complete clinical data; (4) the patients were at least 18 years old; (5) the patients agreed to undergo puncture biopsy, and the nature of their single lesion in the spine was determined by pathological examination; and (6) the patients received follow-up for over half a year. Exclusion criteria are as follows: (1) the patients had primary malignant tumor of spine; (2) the patients had confirmed metastatic lesions at other sites in addition to the skeletal system; (3) according to the whole-body bone imaging, the patients had other bone abnormal concentrated focus other than single lesion of spine and obvious benign concentrated focus; (4) the patients were under the age of 18; and (5) the nature of patients' single lesion of spine was unclear.

A total of 102 patients with extraskeletal primary malignant tumor treated in our hospital from February 2019 to February 2021 were selected as the subjects. All patients had single lesion of the spine, of which 72 were malignant and 30 were benign according to the results of pathological examination. Among the patients with metastatic malignant tumor of spine, there were 42 females and 30 males, the mean age was (50.29 ± 5.19) years, 18 cases had breast cancer, 23 cases had lung cancer, 17 cases had liver cancer, and 14 cases had prostate cancer; and among the patients with benign tumor of spine, there were 12 females and 18 males, the mean age was (50.13 ± 3.80), 6 cases had breast cancer, 10 cases had lung cancer, 8 cases had liver cancer, and 6 cases had prostate cancer.

2.2. Moral Consideration. The study met the principles of World Medical Association Declaration of Helsinki [11], and the study team explained the study purpose, meaning, content, and confidentiality to the patients and asked the patients to sign the informed consent.

2.3. Methods

2.3.1. Examination Methods. All patients received the ECT and CT examinations.

ECT: the ECT tester made by GE Medical Systems Israel Ltd. (NMPA registration (I) no. 20163064732) was used, the $^{99\,m}$ TC-MDP tracer agent (provided by Beijing Xinke Sida Pharmaceutical Technology Co. Ltd.; labeling yield: 95%) was administered by intravenous injection, after that, the patients were told to drink more water and urinate more often 3 hours before ECT. During the examination, the patients were in the whole-body imaging position, the low-energy high-resolution collimator was applied, and two probes collected the anterior and posterior views at the same time, with the acquisition matrix of 256×512, scanning speed of 20 cm/min, window width of 20%, energy peak of 140 keV, voltage of 120 kV, and the sum of anterior and posterior acquisition counts ≥3.0 M. Then, 7100 A/DI was selected for whole-body bone SPECT scan with anterior and posterior views, and tomographic and local planar views were performed when necessary.

CT: first, X-ray positioning film scanning was performed to determine the scanner field, which centered on the vertebral body of the lesion shown by bone imaging, including 3 adjacent vertebral bodies on either side. After the position was determined, CT scan was performed with the CT scanner (Brilliance CT Big Bore; NMPA (I) 20093300931) made by Philips (China) Investment Co. Ltd., with the matrix of 256×256, slice thickness of 5 mm, tube voltage of 130 kV, tube current of 60 mA, automatic exposure tracking, collimator width of 2.5 mm, pitch of 1.5, and rotation time of 0.8 s.

2.3.2. Diagnostic Methods. ECT: (1) criteria for benign lesion: focal uptake was noted in the anterior part of the vertebral bodies, the end plates of the vertebral bodies and the facet joints, and radioactive concentration ≤ anterior superior iliac spine. (2) Criteria for malignant lesion: focal uptake was noted in the posterior part of the vertebral bodies, pedicle of vertebral arch, and radioactive concentration > anterior superior iliac spine.

CT: (1) criteria for benign lesion: hyperostosis, osteophyte formation at the edge of the vertebral bodies; coarse and indistinct cartilaginous surfaces of the vertebral bodies; degeneration of the intervertebral disc, narrowing of intervertebral space; facet wear with blurring of articular surfaces; spondylolisthesis, scoliosis, and spondylolysis. (2) Criteria for malignant lesion: bone resorptive lesions without sclerotic margins; osteoblastic focus; bone resorptive-osteoblastic mixed focus.

2.4. Efficacy Analysis. By the blind method, 2 experienced nuclear medicine physicians interpreted the ECT and CT images of 102 patients, and the 102 lesions were classified as benign (both ECT and CT showed benign) and malignant (ECT or CT showed malignant). The diagnostic efficacy of ECT and CT was calculated by comparing the physicians' interpretation results and pathological findings and plotting the ROC cures as follows. (1) Sensitivity: number of true positive cases/(number of true positive cases + number of false negative cases) × 100%; (2) specificity: number of true negative cases/(number of true negative cases + number of false positive cases) × 100%; (3) positive predictive value (PPV): number of true positive cases/(number of true positive cases + number of false positive cases); (4) negative predictive value (NPV): number of true negative cases/(number of false negative cases + number of true negative cases).

2.5. Statistical Processing. In this study, the data processing software was SPSS20.0, the picture drawing software was GraphPad Prism 7 (GraphPad Software, San Diego, USA), the items included were enumeration data and measurement data, the methods used were the X^2 test and t-test, and differences were considered statistically significant at $P < 0.05$.

3. Results

3.1. Comparison of ECT and CT Diagnostic Results. Tables 1–3 showed the diagnostic results of ECT, CT, and their combination.

3.2. Comparison of Detection Rates of Metastatic Malignant Spinal Tumors in Different Malignancies. ECT + CT had a detection rate of 100% of metastatic malignant spinal tumors in breast cancer and lung cancer, 94.1% in liver cancer, and 78.6% in prostate cancer, respectively (see Table 4).

3.3. Analysis of Diagnostic Efficacy of ECT and CT. ECT combined with CT had a diagnostic sensitivity of 94.4%, specificity of 73.3%, PPV of 89.5%, NPV of 84.6%, and diagnostic accuracy rate of 88.2% (see Table 5). Also, according to the ROC curves, the combined diagnosis obtained AUC (95% CI) = 0.839 (0.739–0.939) (see Figure 1).

Table 1: Diagnostic results of ECT.

ECT	Pathological examination		Total
	Malignant	Benign	
Malignant	54	6	60
Benign	18	24	42
Total	72	30	102

Table 2: Diagnostic results of CT.

CT	Pathological examination		Total
	Malignant	Benign	
Malignant	50	5	55
Benign	22	25	47
Total	72	30	102

Table 3: Diagnostic results of ECT combined with CT.

ECT + CT	Pathological examination		Total
	Malignant	Benign	
Malignant	68	8	76
Benign	4	22	26
Total	72	30	102

4. Discussion

When the malignant tumors progress to the middle and late stages, tumor cells will metastasize to other tissues through lymphatic, vascular, body cavity, and other routes, and although different malignant tumors may metastasize to different tissues, the metastatic lesions more likely occur in tissues with rich blood supply [12, 13], so bones are one of the most common tissues with distant metastasis. It has been reported in relevant investigations that breast cancer and prostate cancer patients are most likely to present with bone metastasis, 80.0% of female breast cancer patients died due to bone metastasis [14] and 90.0% of male prostate cancer patients had increased risk of death [15], and therefore, it is extremely important to enhance the prevention and treatment of bone metastasis. Because the red marrow is mainly distributed in the axial bone, which has a capillary network suitable for tumor embolus growth and no venous valve inside its venous network, so any factors that trigger the elevation of pelvic and thoracic pressure will cause the tumor embolus to enter the venous plexus [16]. Hence, the spine is the most susceptible skeletal tissue to metastasis, and early screening for spinal metastasis is the focus in the prevention and treatment of bone metastasis. At this stage, pathological examination is still the gold standard to examine the nature of spinal tumors, but not all patients can undergo puncture or surgical sampling, and it is difficult to obtain the pathological results of all lesions in practice, so some scholars advocate the combination of multiple imaging examinations to screen metastatic malignant spinal tumors and the implementation of regular follow-up of patients to avoid non-necessary pathological examinations [17, 18].

Table 4: Comparison of detection rates of metastatic malignant spinal tumors in different malignancies.

	Breast cancer	Lung cancer	Liver cancer	Prostate cancer	Total
Number of cases	18	23	17	14	72
Number of positive cases	18	23	16	11	68
Detection rate	100.0%	100.0%	94.1%	78.6%	94.4%

Table 5: Analysis of diagnostic efficacy of ECT and CT.

Group	Sensitivity (%)	Specificity (%)	PPV (%)	NPV (%)	Accuracy rate (%)
ECT	75.0 (54/72)	80.0 (24/30)	90.0 (54/60)	57.1 (24/42)	76.5 (78/102)
CT	69.4 (50/72)	83.3 (25/30)	90.9 (50/55)	53.2 (25/47)	73.5 (75/102)
ECT + CT	94.4 (68/72)	73.3 (22/30)	89.5 (68/76)	84.6 (22/26)	88.2 (90/102)

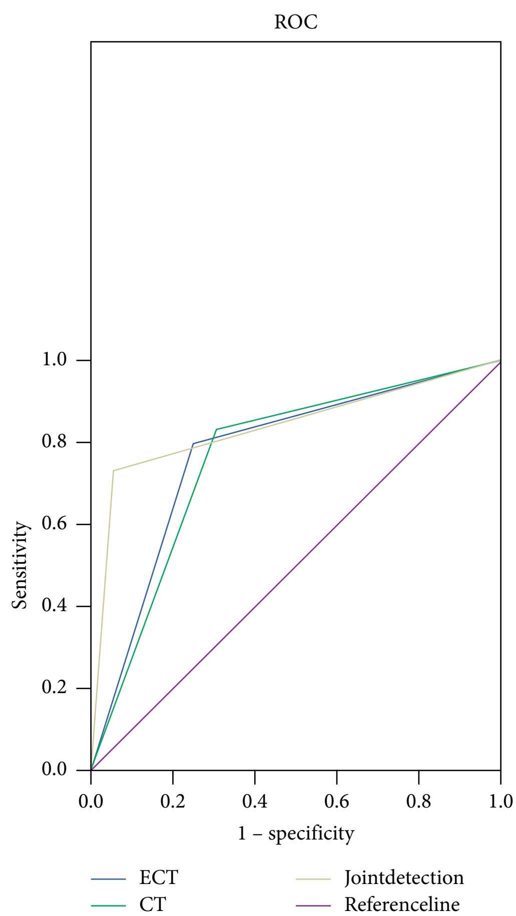

Figure 1: ROC curves of ECT, CT, and their combination.

X-rays, CT, and ECT are the most common examination modalities for metastatic spine tumors, in which X-rays and CT reflect the presence of metastasis based on the osteolytic changes of bone tissue and decalcification condition at the lesion site [19], but bone density changes on X-rays can be found only in case of more than 30.0% of the decalcification condition [20], so the possibility of tumor metastasis cannot be excluded for those without abnormalities in X-rays and further CT examination is needed. This study showed that CT had a sensitivity of 69.4% and NPV of 53.2% for the diagnosis of metastatic malignant spine tumors, which was due to the fact that although CT can clearly demonstrate the anatomy of the spine, it fails to sufficiently show the overlapping sites of lesions and microlesions as there are more overlapping sites in the spine, and diseases such as osteoporosis may also affect the accuracy of the results [21], resulting in a low NPV. After applying ECT examination, a total of 68 metastatic malignant spine tumors were detected, and the diagnostic sensitivity, accuracy, and NPV obviously rose, indicating that ECT combined with CT can play a role of mechanism complementation and improve the diagnostic accuracy for spine tumors. ECT is based on the technique of radioactive nuclear element tracing, which can make the diseased tissue present different radioactivity concentrations from normal tissue by the way of injecting radiopharmaceuticals, thus helping physicians to judge the metastasis of malignant tumors [22, 23]. Because of the wide distribution of glands within the breast, the detection rate of combined examination of metastatic malignant spinal tumors in breast cancer is 100.0%. Although the detection rate in lung cancer is also 100.0%, the mechanism is not clear and may be related to the rich blood vessels. In comparison, the detection rates in liver cancer and prostate cancer were relatively low, which were respectively 94.1% and 78.6%. Liu et al. adopted ECT examination alone to obtain a bone metastasis detection rate of 80.0% in liver cancer and 50.0% in prostate cancer [24], demonstrating that the combined examination has application value in spinal metastasis of different types of malignancies.

To sum up, ECT, as the most common nuclear medicine examination method, achieves a sensitivity that has been recognized by the academic community [25], but there is still an important meaning in combining ECT with CT for comprehensive judgment in most malignant tumors. ECT examination can be applied to localized subtle lesions, and lesions that are difficult to define by ECT can be morphologically distinguished with CT to confirm whether or not they are metastatic malignant spinal tumors. If the patient has significant bone destruction, the CT examination may be used to make up for ECT. The study results showed that combining ECT with CT obtained AUC (95% CI) = 0.839 (0.739–0.939), implying a good diagnostic efficacy of the combined diagnosis for metastatic malignant spine tumors. Besides, this diagnostic modality is convenient and high-efficient, which can greatly improve the efficacy of diagnosing metastatic malignant spine tumors.

Data Availability

The data used to support the findings of this study are available on reasonable request from the corresponding author.

Conflicts of Interest

The authors have no conflicts of interest to declare.

References

[1] L. Ge, K. Arul, and A. Mesfin, "Spinal cord injury from spinal tumors: prevalence, management, and outcomes," *World Neurosurgery*, vol. 122, Article ID e1551, 2019.

[2] E. Maj, B. Szemplińska, W. Prokopienko et al., "Role of diffusion tensor imaging parameters in the characterization and differentiation of infiltrating and non-infiltrating spinal cord tumors: preliminary study," *Clinical Neuroradiology*, vol. 30, pp. 739–747, 2020.

[3] S. Muraoka, K. Yamane, H. Haruo Misawa et al., "Assessment of the concordance rate between intraoperative pathological diagnosis and the final pathological diagnosis of spinal cord tumors," *Acta Medica Okayama*, vol. 75, no. 4, pp. 455–460, 2021.

[4] M. Ottenhausen, G. Ntoulias, I. Bodhinayake et al., "Intradural spinal tumors in adults-update on management and outcome," *Neurosurgical Review*, vol. 42, pp. 371–388, 2019.

[5] Y. Yuan, N. Lang, and H. S. Yuan, "[CT spectral curve in differentiating spinal tumor metastasis and infections]," *Beijing Da Xue Xue Bao Yi Xue Ban*, vol. 53, pp. 183–187, 2020.

[6] Y. Wang, A. Yin, T. Bian et al., "Observation of efficacy of internet-based chronic disease management model combined with modified therapy of bushenyiliu decoction in treating patients with type 2 diabetes mellitus and prostate cancer and its effect on disease control rate," *Evidence-based Complementary and Alternative Medicine*, vol. 2021, Article ID 7767186, 9 pages, 2021.

[7] M. M. Safaee, J. F. Burke, C. L. Dalle Ore et al., "Evaluating the clinical utility and cost of imaging strategies in adults with newly diagnosed primary intradural spinal tumors," *World Neurosurgery*, vol. 147, pp. e239–e246, 2021.

[8] M. M. Abd-El-Barr, K. T. Huang, Z. B. Moses, J. B. Iorgulescu, and J. H. Chi, "Recent advances in intradural spinal tumors," *Neuro-Oncology*, vol. 20, no. 6, pp. 729–742, 2018.

[9] A. Subramanian, B. R. Nair, and V. Rajshekhar, "Functional outcomes and temporal profile of recovery in patients with intradural extramedullary spinal cord tumors with poor nurick grade," *World Neurosurgery*, vol. 146, pp. e691–e700, 2021.

[10] M. H. Bilsky, Z. Gokaslan, J. H. Shin, N. Dea, and F. Ynoe de Moraes, "Introduction. Treatment of spinal cord and spinal axial tumors," *Neurosurgical Focus*, vol. 50, no. 5, p. E1, 2021.

[11] World Medical Association, "World medical association declaration of Helsinki," *JAMA*, vol. 310, no. 20, pp. 2191–2194, 2013.

[12] H. Zhuo, Y. Zhou, X. Chai, Q. Chang, and G. Rao, "The application of ultrasonic bone curette in laminoplasty of spinal canal after resection of intraspinal tumors," *Zhongguo Xiu Fu Chong Jian Wai Ke Za Zhi*, vol. 33, pp. 61–65, 2019.

[13] M. Formo, C. M. Halvorsen, D. Dahlberg et al., "Minimally invasive microsurgical resection of primary, intradural spinal tumors is feasible and safe: a consecutive series of 83 patients," *Neurosurgery*, vol. 82, no. 3, pp. 365–371, 2018.

[14] Y. Ma, L. Chen, X. Li et al., "Rationally integrating peptide-induced targeting and multimodal therapies in a dual-shell theranostic platform for orthotopic metastatic spinal tumors," *Biomaterials*, vol. 275, Article ID 120917, 2021.

[15] R. Jakubovic, M. Ruschin, C. L. Tseng, A. Pejović-Milić, A. Sahgal, and V. X. D. Yang, "Surgical resection with radiation treatment planning of spinal tumors," *Neurosurgery*, vol. 84, no. 6, pp. 1242–1250, 2019.

[16] Y. Kobayashi, S. Kawabata, Y. Nishiyama et al., "Changes in sagittal alignment after surgical excision of thoracic spinal cord tumors in adults," *Spinal Cord*, vol. 57, no. 5, pp. 380–387, 2019.

[17] F. Pessina, P. Navarria, G. A. Carta et al., "Long-term follow-up of patients with metastatic epidural spinal cord compression from solid tumors submitted for surgery followed by radiation therapy," *World Neurosurgery*, vol. 115, pp. e681–e687, 2018.

[18] J. J. Sun, J. Yang, J. C. Xie et al., "Comparative clinical study on seldom segment with multiple segment intramedullary primary spinal cord tumors," *Beijing da xue xue bao. Yi xue ban = Journal of Peking University. Health sciences*, vol. 51, pp. 840–850, 2019.

[19] K. Tsunoda, "Spinal cord tumors:classification, treatment, and prognosis," *Noshinkeigeka*, vol. 49, no. 6, pp. 1331–1345, 2021.

[20] W. Xiong, Y. Xu, Z. Fang, and F. Li, "Total en bloc spondylectomy for lumbar spinal tumors by paraspinal approach," *World Neurosurgery*, vol. 120, pp. 28–35, 2018.

[21] V. S. Klimov, V. V. Kel'makov, N. V. Chishchina, and A. V. Evsyukov, "Effectiveness of intraoperative monitoring of motor evoked potentials for predicting changes in the neurological status of patients with cervical spinal cord tumors in the early postoperative period," *Voprosy neirokhirurgii imeni N.N. Burdenko*, vol. 82, no. 1, pp. 22–32, 2018.

[22] M. Benesch, K. Nemes, P. Neumayer et al., "Spinal cord atypical teratoid/rhabdoid tumors in children: clinical, genetic, and outcome characteristics in a representative European cohort," *Pediatric Blood and Cancer*, vol. 67, no. 1, Article ID e28022, 2020.

[23] W. Hongyu, C. Dong, J. Wu, Y. Zhu, and H. Ma, "Total en bloc spondylectomy combined with the satellite rod technique for spinal tumors," *Journal of Orthopaedic Surgery and Research*, vol. 15, p. 536, 2020.

[24] P. Liu, Y. Liang, C. Bian et al., "Diagnostic accuracy of MR, CT, and ECT in the differentiation of neoplastic from non-neoplastic spine lesions," *Asia-Pacific Journal of Clinical Oncology*, vol. 16, no. 5, pp. e192–e197, 2020.

[25] H.-R. Zhang, R.-Q. Qiao, X.-G. Yang, and Y.-C. Hu, "A multicenter, descriptive epidemiologic survey of the clinical features of spinal metastatic disease in China," *Neurological Research*, vol. 42, no. 9, pp. 749–759, 2020.

Hindawi
Contrast Media & Molecular Imaging
Volume 2022, Article ID 9223928, 11 pages
https://doi.org/10.1155/2022/9223928

Research Article

Intelligent Algorithm-Based Magnetic Resonance for Evaluating the Effect of Platelet-Rich Plasma in the Treatment of Intractable Pain of Knee Arthritis

Bing Huang, Yun Huang, Xin Ma, and Yuequn Chen

Department of Orthopaedics, Jiangyin Lingang Hospital, Jiangyin 214443, Jiangsu, China

Correspondence should be addressed to Yuequn Chen; wangxiaohui@zzu.edu.cn

Received 28 February 2022; Revised 13 April 2022; Accepted 18 April 2022; Published 26 May 2022

Academic Editor: M. Pallikonda Rajasekaran

The application of intelligent algorithms in the treatment of intractable pain of patients with platelet-rich plasma (PRP) knee osteoarthritis by magnetic resonance was investigated. The automatic diagnosis of magnetic resonance knee osteoarthritis was established with multiple intelligent algorithms, including gray projection algorithm, adaptive binarization algorithm, and active shape model (ASM). The difference between automatic magnetic resonance detection indexes of the patients with knee osteoarthritis and artificial measurement results was analyzed. The included patients received PRP treatment. Knee osteoarthritis MRI osteoarthritis knee scores (KOA MOAKS) and Western Ontario and McMaster Universities arthritis index (WOMAC) before and after treatment were compared. The results showed that the results of knee osteoarthritis scores, inferior angle of femur, superior angle of tibia, and tibiofemoral angle (TFA) by automatic magnetic resonance diagnostic model were entirely consistent with artificial detection results. After the treatment, the total scores of knee lateral area, interior area, central area, and patellar area were all remarkably lower than those before the treatment ($P < 0.05$). After the treatment, knee KOA MOAKS scores and WOMAC scores were both lower than those before the treatment ($P < 0.05$). Visual analogue scale (VAS) scores 1 week, 2 weeks, and 3 weeks after the treatment were decreased compared with those before the treatment ($P < 0.05$). Relevant studies indicated that intelligent algorithm-based automatic magnetic resonance diagnostic knee osteoarthritis model showed good utilization values, which could provide the reference and basis for the treatment of the patients with knee osteoarthritis.

1. Introduction

Osteoarthritis (OA) is a common articular disease, which usually among middle-aged and elderly people. The main clinical symptoms include acute pain and mobility loss. The main pathological features of OA are articular cartilage degeneration, subchondral bone changes, and nonbacterial synovitis [1]. The pathological basis of knee OA (KOA) is cartilage degeneration [2]. The main therapeutic methods for KOA patients include drug therapy, articular cavity injection therapy, and surgical therapy. Surgical therapy is adopted mainly for the patients with stage IV KOA and some patients with stage III KOA. The cost of surgical therapy is high. Total knee arthroplasty (TKA) is a surgical therapeutic method of improving the pains among the patients with KOA at middle and late stages and restoring their functions. KOA can alleviate patients' pains and cure inflammation as quickly as possible. However, 8% to 13% of patients suffer from continuous intractable pain after TKA [3]. There is no effective therapeutic scheme for unknown intractable pain. Substance P (SP) and calcitonin gene-related protein (CGRP) may be the cause of pains after TKA. Relevant studies show that botulinum toxin A (BoNT/A) has anti-cholinergic and analgesic effects and can relieve patients' pains [4]. In addition, drug therapy also results in the incidence of complications. Long-term use of nonsteroidal anti-inflammatory drugs may cause gastrointestinal reaction and other side effects [5]. Platelet-rich plasma (PRP) is a platelet concentrate from the patient's own blood. According to relevant studies, PRP can effectively improve the clinical symptoms of KOA patients by regeneration repair and elimination of inflammation [6]. Besides, Louis et al. [7] pointed out that PRP showed no obvious therapeutic effects in KOA treatment compared with sodium hyaluronate. The clinical effect of PRP in KOA treatment was still controversial.

At present, the main methods of diagnosing KOA include X-ray image, magnetic resonance imaging (MRI), computed tomography (CT) image, and ultrasonic image. CT with high-density resolution can display the minor changes in articular structure. However, it cannot show synovial membrane and cartilage structures because it has ionizing radiation [8]. Ultrasound is fast, noninvasive, and cheap. It can be used for the diagnosis of OA. Nevertheless, it cannot fully show the minor changes of joints [9]. Plain X-ray can better show skeletons and soft tissues and recognize narrow articular space. Magnetic resonance can measure the thickness and volume of cartilage accurately. Besides, it possesses good application values in the measurement of lesion positions [10]. In recent years, intelligent algorithms are applied in medical image processing and analysis more and more widely. Currently, a large number of intelligent algorithms are applied in MRI image processing, mainly including spectrum-based segmentation methods, region-based segmentation methods, clustering-based segmentation methods, and deep learning-based segmentation methods. Intelligent algorithms show positive application values in the processing and segmentation of MRI images. Traditional machine learning method requires precise feature extraction. The establishment of medical image models requires considerable professional knowledge. Once the feature model is established, it can hardly vary with image data. Its quality has great influences on image segmentation effects. In addition, it shows poor portability with inconvenient application. Deep learning technology has strong feature learning capacity, and it shows more significant advantages with higher application values compared with these machine learning algorithms.

In summary, the clinical effect of PRP in the treatment of KOA is still controversial, and there is no effective magnetic resonance image segmentation method. In this study, the knee region of interest (ROI) was segmented and extracted by a variety of intelligent algorithms to achieve automatic diagnosis of magnetic resonance KOA. Moreover, 23 KOA patients were treated with PRP to evaluate the clinical effect of PRP in magnetic resonance diagnosis of KOA intractable pain and provide a reference for the diagnosis and treatment of KOA patients.

2. Materials and Methods

2.1. Study Object. Twenty-three patients with KOA admitted to hospital between July 2020 and August 2021 were selected as the study objects. All patients were performed with PRP and MRI detection before and after treatment. There were 14 male patients aged between 43 and 75, and their average age was 53.44 ± 6.15. There were 9 female patients aged between 42 and 73. Their average age was 52.6 ± 5.82. This study had been approved by Ethics Committee of Hospital, and the included patients had signed informed consent forms.

Inclusion criteria: patients performed with image detection and the assessment of degenerative change level of knee joint before and after treatment; patients conforming to KOA diagnostic standards revised by American College of Rheumatology [11]; patients with pain history for over 6 months; and patients with complete clinical and imaging data.

Exclusion criteria: patients suffering from knee articular lesions for reasons other than KOA; patients with incomplete functions of essential organs, such as heart, liver, and kidney; pregnant or lactating women; and patients suffering from severe primary diseases, including cardiovascular, liver, and hemopoietic system diseases.

2.2. ROI Segmentation of Knee Joint on Account of Intelligent Algorithm. Before analyzing magnetic resonance images of the knee, segmentation of magnetic resonance images of different sequences was required. In this study, images of different sequences were segmented using a gray projection algorithm. The gray projection value obtained by summing the pixels in the whole image could reflect the gray-level information. Method of calculating pixels projected onto the horizontal axis is shown in the following equation:

$$G_i = \sum \operatorname{pixel}(x, y)\big|_{x=i}. \tag{1}$$

In the above equation, G_i was the sum of the pixels projected onto $x = i$, and $\operatorname{pixel}(x, y)$ was the pixel value at coordinate (x, y). The projection to the vertical axis could be shown in the following equation:

$$G_i = \sum \operatorname{pixel}(x, y)\big|_{y=i}. \tag{2}$$

In this study, the sharpness [12] was adopted to detect the ribbon area, which could be shown in the following equation:

$$S_n = \sum_{i=-55}^{55} \left| \frac{G_n - G_{n+i}}{i} \Big|_{i \neq 0} \right|. \tag{3}$$

ROI segmentation of knee joint mainly included longitudinal and transverse segmentation. In the process of vertical ROI segmentation, relaxation constants were introduced to segment it on account of relaxation principle [10]. The ROI boundary of knee joint on account of relaxation principle could be shown in the following equation:

$$\begin{cases} E_t = E_j - A, \\ E_b = E_j + B. \end{cases} \tag{4}$$

In the above equation, E_t was the upper boundary of ROI of knee joint, E_b was the lower boundary of ROI of knee joint, and E_j indicated that the relaxation principle determined the upper and lower boundaries of ROI. A was upper boundary relaxation constant, and B was lower boundary relaxation constant.

The maximum entropy threshold method determined the binarization threshold by measuring the entropy of the gray histogram of the image. It had obvious advantages in background interference removal. If $P(x)$ was the probability of occurrence of x, the information entropy could be shown in the following equation:

$$I(x) = -\int_{-\infty}^{\infty} P(x)\log P(x)\mathrm{d}x. \quad (5)$$

If the probability of occurrence of gray level i was $P(i)$, the segmentation threshold was T, $[0, T]$ was the background gray level value, and $[T+1, 255]$ was the foreground of pixel points, the probability of gray level in the background and foreground could be shown in the following equation:

$$\begin{cases} P_i = \dfrac{P_i}{P_T}, & i \in [0, T], \\ P_i = \dfrac{P_i}{(1-P_T)}, & i \in [T+1, 255]. \end{cases} \quad (6)$$

In the above equation, P_T represented the proportion of pixels within the range of $[0, T]$ to pixels in the whole image.

D stood for background and E stood for foreground, and the information entropy of background and foreground could be shown in the following equation:

$$\left\{ I_D = -\sum_{i=0}^{T} P(i)\log P(i), I_E = -\sum_{i=T+1}^{255} P(i)\log P(i). \right. \quad (7)$$

Gray histogram reflected the occurrence frequency of each gray level in the image [13]. If the gray level is i, and $i \in [0, 255]$ and $N(i)$ were the number of pixels in the image, the calculation method of $N(i)$ could be shown in following equations:

$$N(i) = \sum_{x=0}^{W-1}\sum_{y=0}^{H-1} P[G(x,, y)], \quad (8)$$

$$P[G(x,, y)] = \begin{cases} 0, & G(x, y) \neq i, \\ 1, & G(x, y) = i. \end{cases} \quad (9)$$

In the above equation, $G(x, y)$ pixel point was gray value of (x, y). W was image width, and H was the height of the image.

Due to the gray projection algorithm of the initial magnetic resonance, images of different sequences were segmented. Relaxation constants were introduced to segment the knee preselected ROI region vertically and horizontally on account of the relaxation principle. Finally, ROI segmentation image was obtained. The specific process of knee ROI segmentation on account of intelligent algorithm in this study is shown in Figure 1.

2.3. Magnetic Resonance Knee Feature Point Extraction Based on Intelligent Algorithm. Most initial magnetic resonance images were exposed to unbalanced and uneven gray distribution phenomena [14]. If the gray level of X-ray image was set as 0~255, it was the gray-level distribution range of initial magnetic resonance image and the gray-level distribution range of transformed magnetic resonance image, then the gray value of the image pixels transformed by the algorithm could be shown in the following equation:

$$H(x, y) = \frac{(j-k)[F(x, y) - g]}{f - g}. \quad (10)$$

$F(x, y)$ represented the gray value of pixel (x, y) before linear transformation, and $H(x, y)$ was the gray value of pixel (x, y) after linear transformation.

In this study, Gaussian smoothing operator was used to denoise MRI, and one-dimensional Gaussian function could be shown in the following equation:

$$G(x) = \frac{1}{\sqrt{2\pi\sigma}}\exp\left(\frac{-x^2}{2\sigma^2}\right). \quad (11)$$

The two-dimensional Gaussian function could be shown in the following equation:

$$G(v, \mu) = \frac{1}{2\pi\sigma}\exp\left[\frac{-(v^2 + \mu^2)}{2\sigma^2}\right]. \quad (12)$$

The preprocessed image mainly realized edge detection according to the gray level of edge pixels. In this study, the algorithm was optimized on account of gradient operator to increase the precision of edge detection. If $F(x, y)$ was the gray value of pixel (x, y), and the difference between the gray value of the pixel on the horizontal axis and the vertical axis was $dF(x, y)$, the calculation method of gradient operator H_x and H_y could be shown in following equation:

$$\begin{bmatrix} H_x \\ H_y \end{bmatrix} = \begin{bmatrix} \dfrac{dF(x, y)}{F(x, y)} \\ \dfrac{dF(x, y)}{F(x, y)} \end{bmatrix}. \quad (13)$$

Canny operator had the finest edge detection and good integrity, but it was difficult to select an appropriate threshold [15]. Active shape model (ASM) could represent contour shape through a vector and had significant advantages in image edge detection [16]. Therefore, this study extracted fine edge features on account of Canny edge detection results and ASM model. The shape vector of the image with l feature point was shown in the following equation:

$$K_i = (x_{i1}, y_{i1}, x_{i2}, y_{i2}, \cdots, x_{il}, y_{il}). \quad (14)$$

(x_{il}, y_{il}) represented the coordinate of the l feature point in the i^{th} image, and then, n sample sets of shape vectors with length $2l$ were shown in the following equation:

$$J = (K_1, K_2, \ldots, K_n). \quad (15)$$

General alignment method and principal component analysis were used to eliminate the interference of nonshape information such as bone size and body position. Then, the edge contour was iterated on account of the local gray model. Then, the local texture of the i^{th} feature point was shown in the following equation:

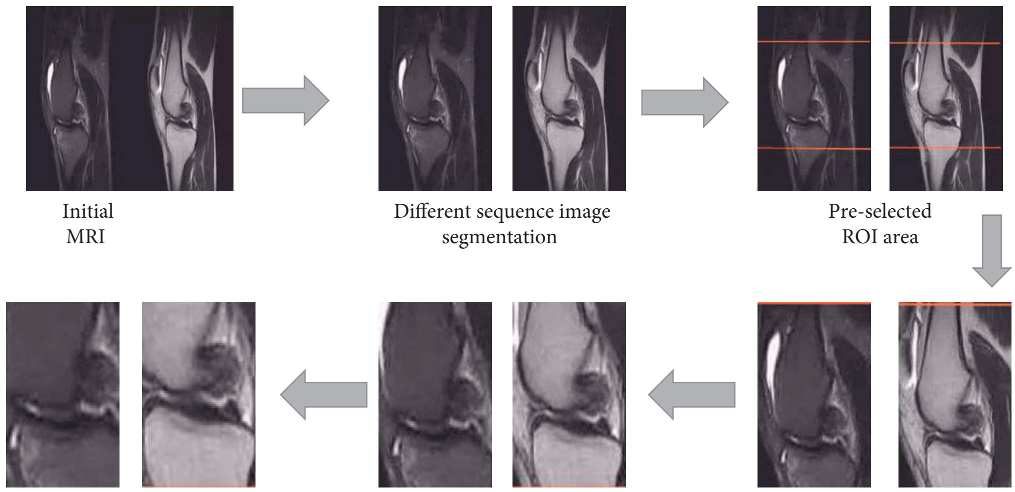

Figure 1: Specific flow chart of ROI segmentation of knee joint on account of intelligent algorithm.

$$G_{ij} = \left[G_{ij1}, G_{ij2}, \ldots G_{ij(2n+1)}\right]^T. \quad (16)$$

In the above equation, $G_{ij(2n+1)}$ represented the gradient characteristic parameter of the $2n+1$ adjacent point of the i^{th} feature point of the j^{th} image. Then, the mean and variance of m local textures was shown in following equations:

$$\widetilde{G}_i = \frac{1}{m}\sum_{j=1}^{m} G_{ij}, \quad (17)$$

$$S_i = \frac{1}{m}\sum_{j=1}^{m}\left(G_{ij} - \widetilde{G}_i\right)\left(G_{ij} - \widetilde{G}_i\right)^T. \quad (18)$$

Mahalanobis distance was shown in the following equation:

$$D_s = \left(G - \widetilde{G}_i\right)S_{i-1}\left(G - \widetilde{G}_i\right)^T. \quad (19)$$

In the above equation, G was the new feature of feature point i. If the displacement generated by each feature point was arranged into vectors, it could be shown in the following equation:

$$M_x = \left(M_{x1}, M_{x2}, \ldots, M_{xk}\right). \quad (20)$$

ROI segmentation image was enhanced by linear grayscale transformation. Then, Gaussian operator was used to denoise the image and Gaussian smoothing was obtained. Canny operator was used to detect the edge of knee joint. Finally, the extraction map of knee joint feature points was obtained by local search strategy.

2.4. Preparation and Treatment of PRP. 36 mL of peripheral venous blood was collected from patients, and 1/9 volume ratio sodium citrate injection was added for anti-coagulation treatment. Red blood cells were extracted and centrifuged at 870 g for 15 min after centrifugation at 275 g for 10 min. The upper platelet-poor plasma was discarded. PRP was diluted with 0.9% normal saline, and then, 10% calcium chloride was added to activate platelets in PRP.

Patients were supine and partially disinfected. The point at which the lateral and upper edges of the patella met was selected as the entry point for puncture. All patients were injected with 2 mL PRP at (1500~1800) $\times 10^9$/L. The knee joint of patients was passively flexion and extension for 3~5 times after injection, and the puncture point was covered and wrapped with sterile dressing. The treatment was performed once a week for 3 consecutive weeks.

2.5. Test Methods and Evaluation Indicators of Knee Joint Magnetic Resonance. 1.5 T magnetic resonance system was adopted. To be specific, the patients were instructed to take supine position. The examination was started after the knee was cut to 10° to 15°. During the examination, different sequences were applied according to different sections, such as PDWI-FS and T1-weighted image (T1WI) sequences in the coronal plane, PDWI-FS sequences in the sagittal plane, and T1WI and T2-weighted image (T2WI)-FS sequences in the transverse plane. The parameters were adjusted as follows: (1) PDWI-FS: time of echo (TE) of 34 ms and time of repetition (TR) of 3,800 ms; (2) T1WI: TE of 9.8 ms and TR of 500 ms; (3) T2WI-FS: TE of 85 ms and TR of 5,480 ms; and (4) interslice distance of 0.5 mm, matrix of 256×256, field of view of 18 cm, and slice thickness of 3 mm.

The distance of medial or external space of the knee joint, the ratio of medial or lateral space, and the amount of osteophyte of femoral or tibial bone, upper femoral angle, lower tibial angle, and tibial and femoral angle were obtained on the magnetic resonance films. These indicators were completed jointly by more than 1 attending orthopedic surgeon and radiologist. The calculation method of the ratio of medial and lateral space was shown in the following equation:

$$d = \frac{D_i}{D_o}. \quad (21)$$

In the above equation, D_i and D_o were medial joint and lateral joint space, respectively.

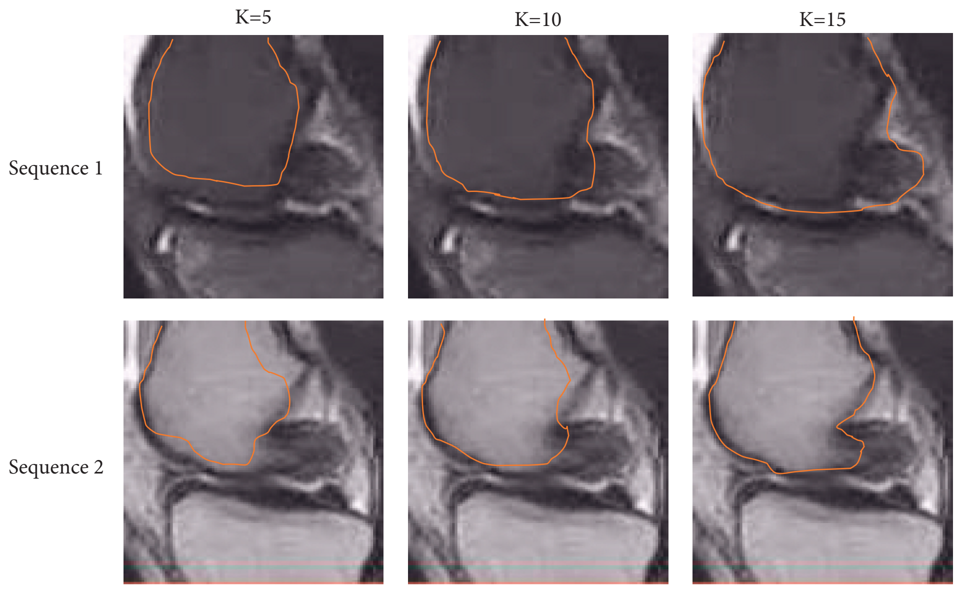

Figure 2: Results of MRI edge detection of knee joint based on intelligent algorithm.

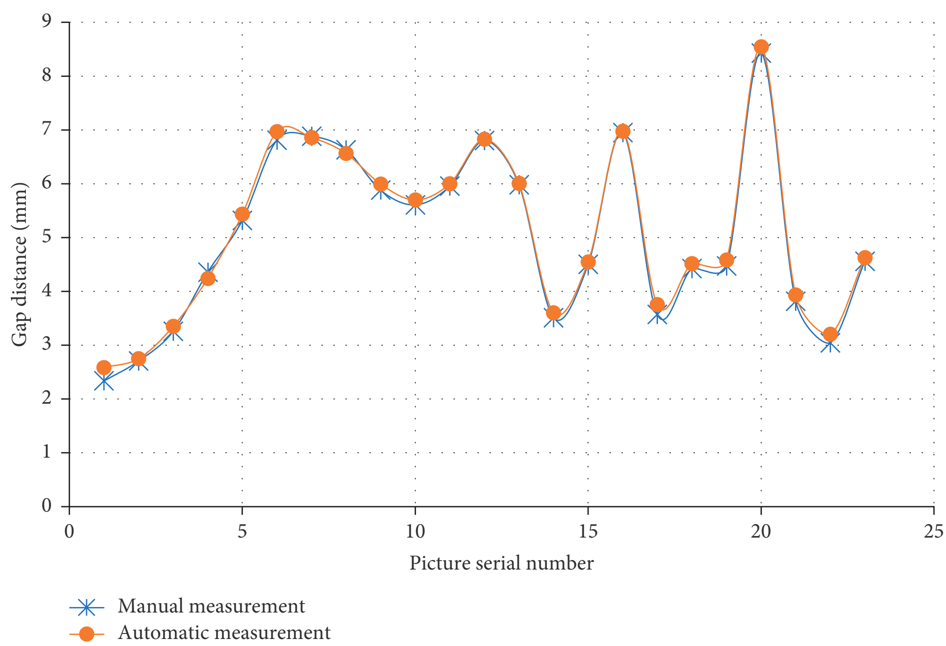

Figure 3: Measurement results of joint space by different methods.

The Western Ontario and McMaster Universities arthritis index (WOMAC) score was used to assess daily life difficulty before and after treatment. Knee osteoarthritis MRI osteoarthritis knee score (KOA MOAKS) was adopted to evaluate the degree of joint injury. Visual analogue scale (VAS) was used to assess the degree of pain in KOA patients and to compare the difference before and after treatment.

2.6. Statistical Methods. SPSS 19.0 statistical software was used for data processing. *T*-test was used to compare the differences. Spearman correlation coefficient was adopted to analyze the correlation between MOAKS score and WOMAC OA index. $P < 0.05$ indicated statistically significant difference.

3. Results

3.1. Analysis of Edge Detection Results of Knee Joint Magnetic Resonance Based on Intelligent Algorithm. The analysis of the edge detection results of knee joint magnetic resonance based on intelligent algorithm is given in Figure 2. With the increasing number of iterations *K*, the fit of the magnetic resonance contour extraction line was higher for the knee (marked in red) and the lower edge of the femur. It suggests that the accuracy of magnetic resonance knee edge detection becomes higher as the number of iterations increases.

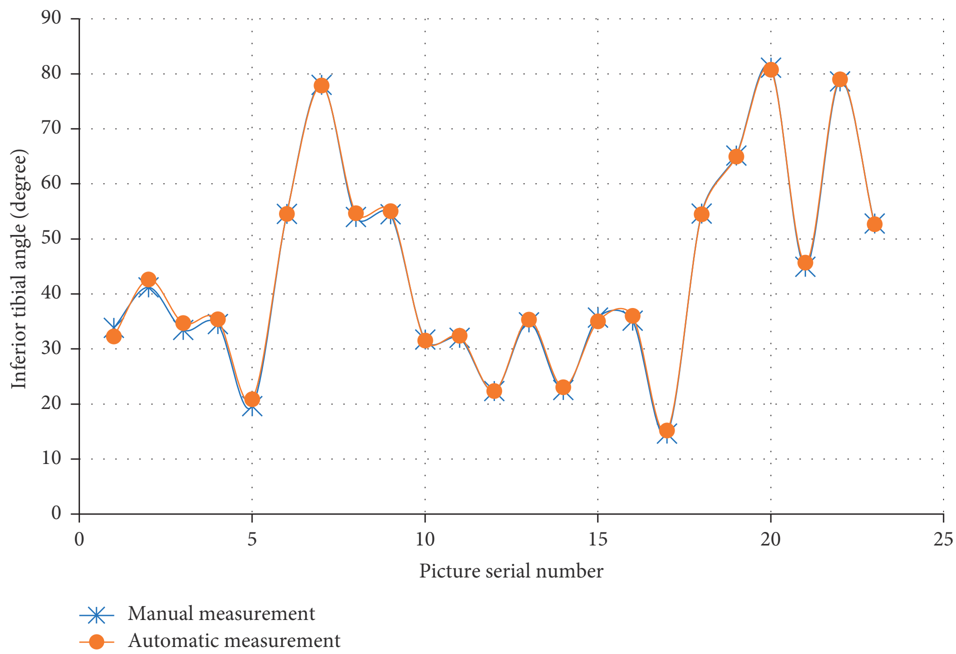

Figure 4: Comparison of inferior angle of femur measurement results with different methods.

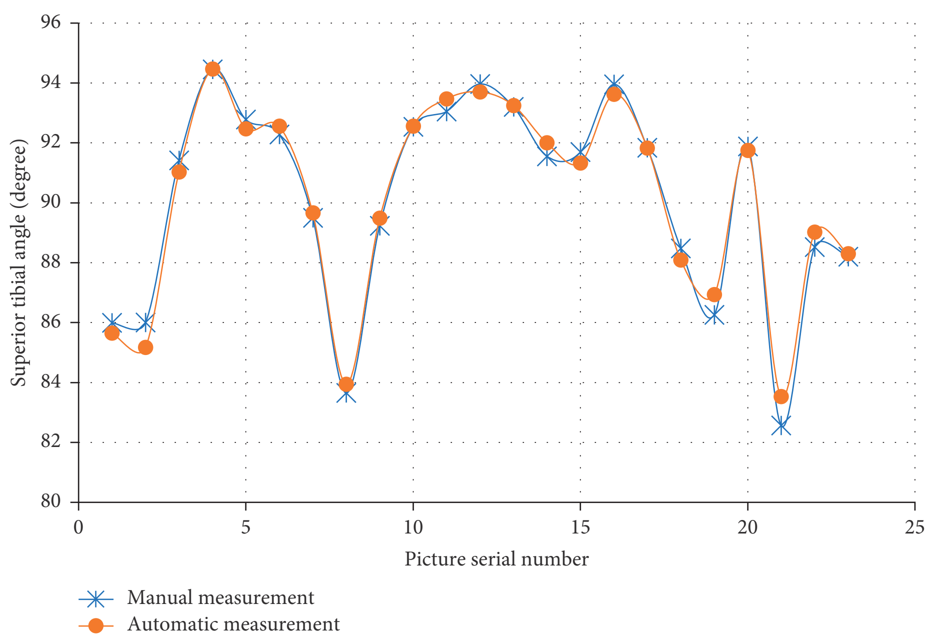

Figure 5: Comparison of superior angle of tibia measurement results with different methods.

3.2. Measurement and Analysis of Knee Joint Space Distance on Account of Intelligent Algorithm. Measurement and analysis of knee joint space distance on account of intelligent algorithm is shown in Figure 3. The results of automatic and manual detection of 23 knee joint space measurement had good consistency.

3.3. Analysis of Measurement Results of Knee Joint Correlation Angle on Account of Intelligent Algorithm. The analysis of detection results of inferior angle of femur, superior angle of tibia, and tibiofemoral angle (TFA) of the right leg in 23 images were analyzed, which are shown in Figures 4–6. The results of automatic detection and manual measurement of inferior angle of femur, superior angle of tibia, and TFA had good consistency.

3.4. Comparison of WOMAC Scores of KOA Patients before and after Treatment. Figure 7 shows the comparison of WOMAC scores of KOA patients before and after PRP treatment. After PRP treatment, the pain score, stiffness score, disability score, and WOMAC total score of patients

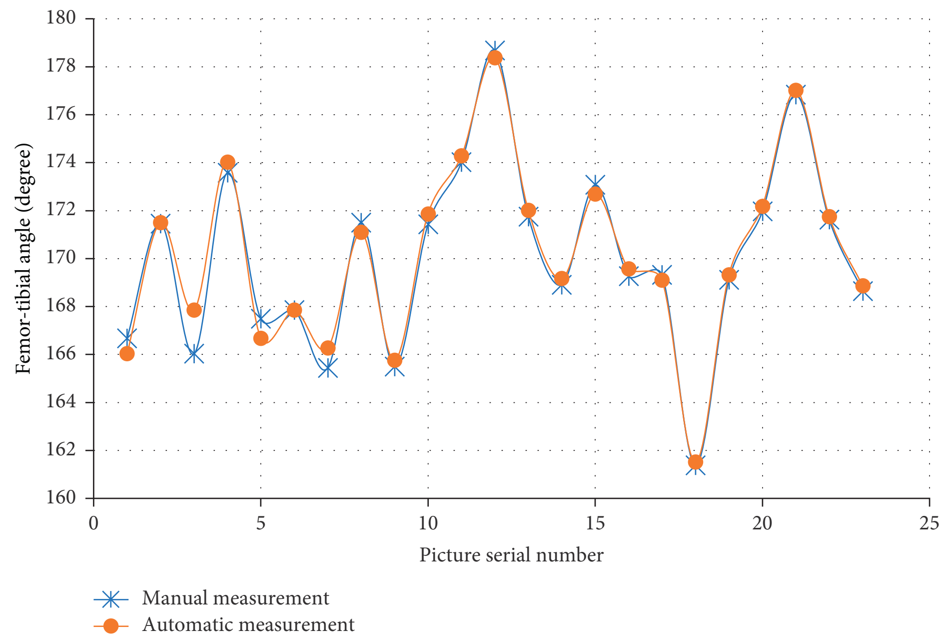

Figure 6: Comparison of TFA measurement results with different methods.

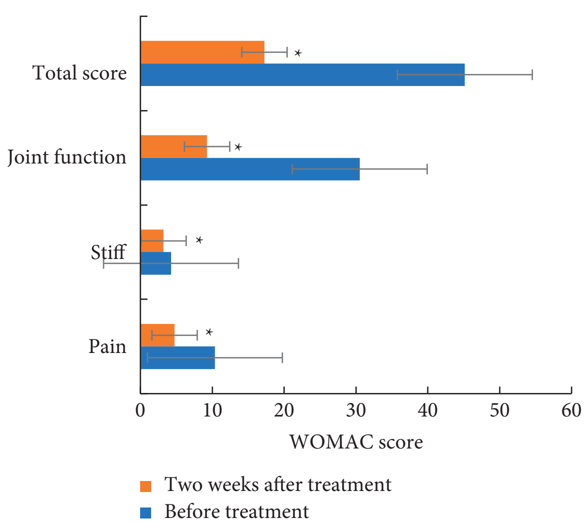

Figure 7: Comparison of WOMAC scores of KOA patients before and after treatment. *indicated that the comparison with WOMAC scores before treatment showed statistical difference ($P < 0.05$).

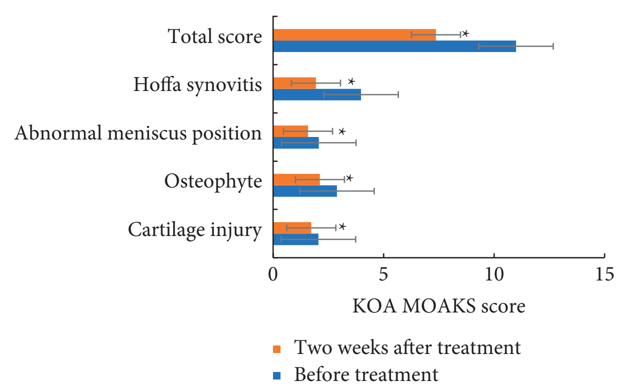

Figure 8: Comparison of KOA MOAKS scores of KOA patients before and after treatment. *suggested that the comparison with KOA MOAKS scores before treatment demonstrated statistical differences ($P < 0.05$).

were significantly decreased ($P < 0.05$), and the disability decrease was the highest.

Figure 8 indicates the comparison of KOA MOAKS scores of KOA patients before and after treatment. After PRP treatment, the cartilage injury score, osteophyte score, meniscus malposition score, Hoffa synovitis score, and KOA MOAKS total score of patients were obviously decreased ($P < 0.05$). The greatest decrease occurred in Hoffa synovitis score.

3.5. Correlation Analysis between MOAKS Score and WOMAC OA Index. Figure 9 reveals the correlation analysis of MOAKS score with pain score, stiffness score, disability score, and WOMAC OA total score after PRP treatment. MOAKS score has a good correlation with pain score, stiffness score, disability score, and WOMAC total score ($P < 0.05$) of which the correlation coefficient between bone marrow injury and pain is the highest ($r = 0.825$), and the correlation coefficient between MOAKS total score with pain and WOMAC total score is higher, 0.752 and 0.759, respectively.

3.6. Comparison of VAS Scores before and after Treatment. The comparison and analysis of VAS scores of KOA patients before and after PRP treatment are shown in Figure 10. VAS scores of patients decreased first and then stabilized with the extension of time after treatment. VAS scores of patients at 1, 2, and 3 weeks after treatment were all lower than that before treatment ($P < 0.05$).

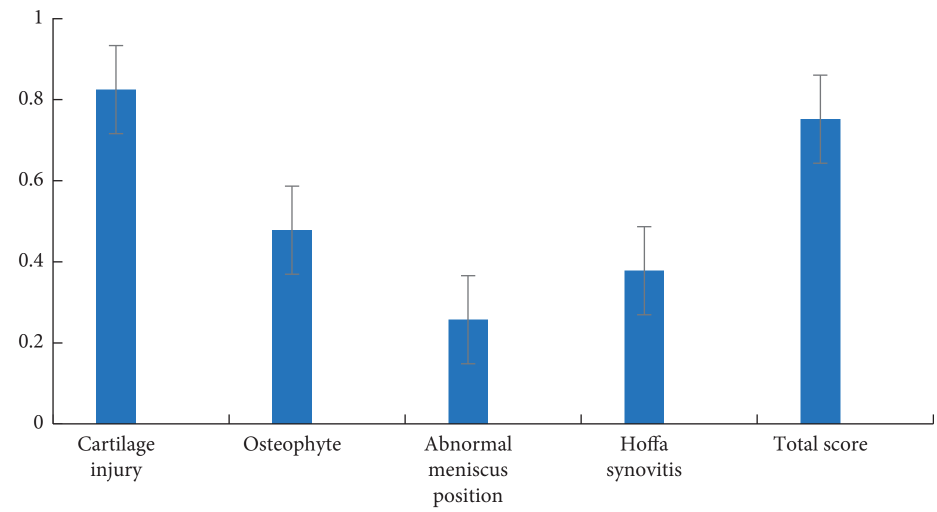

(a)

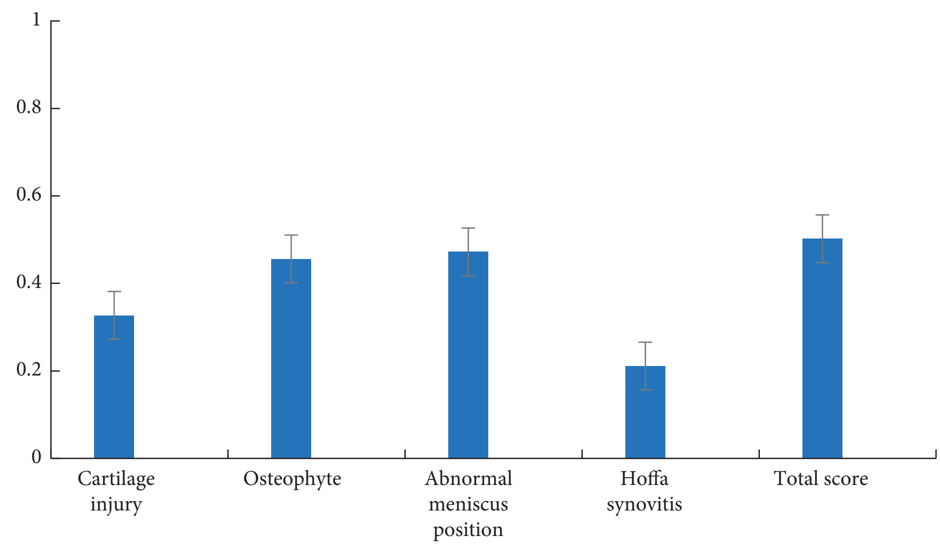

(b)

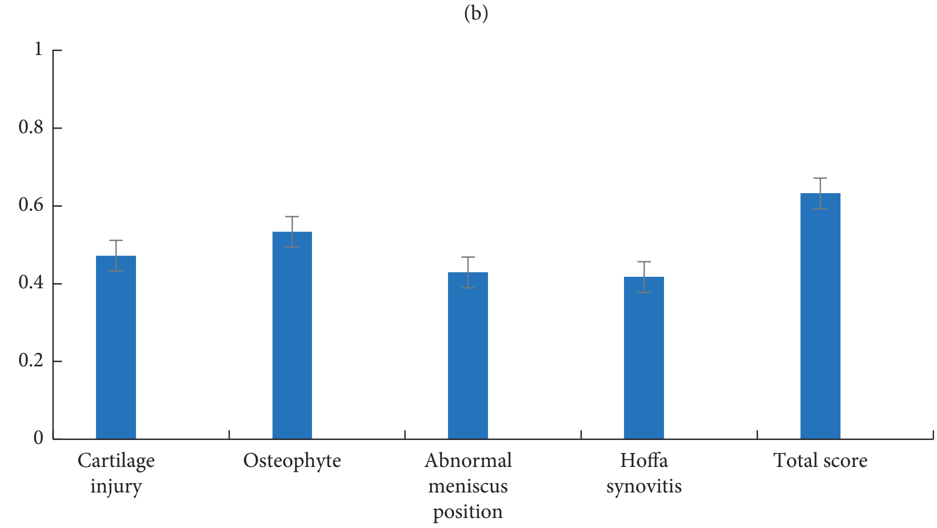

(c)

Figure 9: Continued.

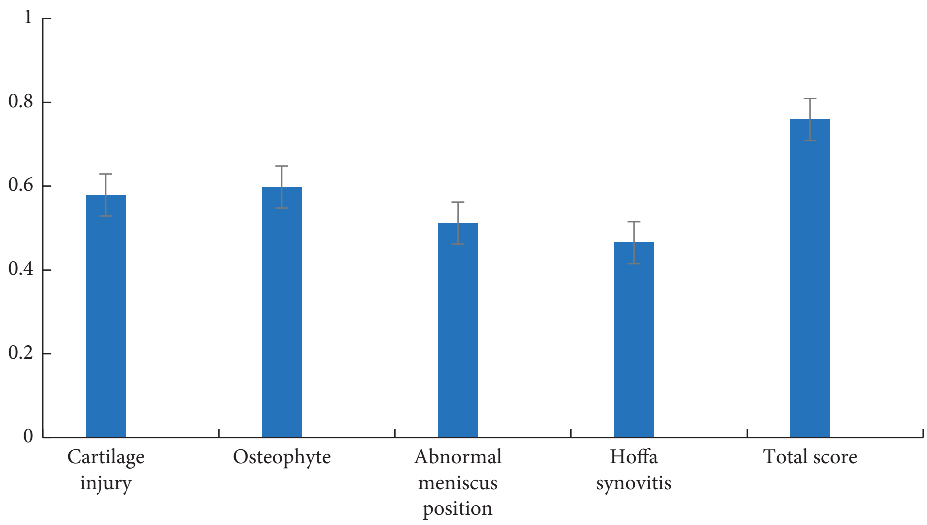

(d)

Figure 9: Correlation analysis between MOAKS score and WOMAC OA score for patients after PRP treatment. (a) The correlation between MOAKS score and pain score; (b) the correlation between MOAKS score and stiffness score; (c) the correlation between MOAKS score and disability score; (d) the correlation between MOAKS score and WOMAC OA total score.

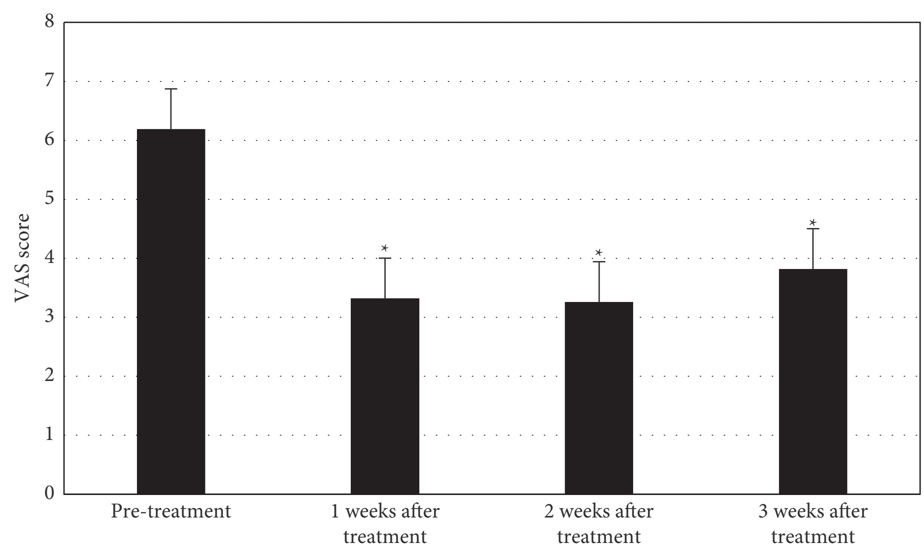

Figure 10: Comparison of VAS scores before and after treatment. *represented statistical differences compared with those before treatment ($P < 0.05$).

4. Discussion

KOA is a degenerative disease involving synovial membrane and knee joint. The main clinical manifestations are articular cartilage osteogenesis and cartilage destruction [10, 12]. KOA is common and frequent among elderly patients. The incidence of KOA among female patients is obviously higher than that among male patients [13, 14]. The current main therapeutic methods of Western medicine include oral drugs, local application, physiotherapy and rehabilitation, articular cavity injection, and knee joint replacement. The main therapeutic methods of Chinese medicine include treatment based on syndrome differentiation-based oral Chinese medicine decoction, plaster application, acupuncture, massage, and various special stitches. Pain is the most significant clinical manifestation among KOA patients. Relevant studies reveal that ozone combined with sodium hyaluronate treatment can be analgesic and anti-inflammatory. Besides, the therapy can obviously improve soft tissue functions, repair soft tissue damage, and show positive significance in accelerating the recovery of patients with KOA.

Among the examination methods for KOA, magnetic resonance examination is clearer than X-ray examination. It can judge and grade patients' signs, such as articular space by K-L classification. After treatment, the knee articular space becomes narrow [11, 15, 16]. Magnetic resonance shows good effects in the detection of knee articular space, inferior angle of femur, and superior angle of tibia [17, 18].

Intelligent algorithm-based automatic detection algorithm is very effective in the segmentation of MRI images. Among KOA patients, cartilage and osteophyte damage form at the joint edges [19]. Magnetic resonance can show different levels of narrow articular space, especially interior articular space [20]. Current clinical drug therapies are usually repeated so that it can cure KOA. The current study results reveal that PRP can promote the proliferation of osteoblast, the synthesis of cartilage and bone matrix, and the healing of soft tissues [21]. In addition, it was also found that PRP is anti-inflammatory in the treatment of KOA [22]. PRP can promote cartilage repair and shows potential utilization value in KOA treatment [23]. PRP is applied in orthopedics department more and more widely with various advantages. It is easy to obtain PRP, which does little harm to human body. Platelets with high concentrations are rich in a variety of growth factors and can effectively promote tissue healing [24].

Intelligent algorithm-based magnetic resonance segmentation algorithm was used to detect the clinical therapeutic effects of PRP on KOA. The difference between automatic magnetic resonance detection indexes of KOA patients and artificial measurement results was analyzed. Besides, KOA MOAKS and WOMAC before and after PRP treatment were compared. The research results showed that the detection results of knee articular space scores, inferior angle of femur, superior angle of tibia, and TFA by automatic magnetic resonance KOA diagnostic model were entirely consistent with artificial detection results. The results indicated that magnetic resonance played a positive role in the diagnosis of KOA and showed high clinical application values. Relevant studies suggested that the combined application of hyaluronic acid (HA) and PRP could repair degraded cartilage and delay the progression of KOA [22]. Raeissadat et al. [25] compared the short-term and long-term therapeutic effects of articular injection of HA, PRP, plasma rich in growth factor (PRGF), and ozone for patients with KOA. Consequently, they found out that the improvement of the symptoms of the patients only in PRP and PRGF groups lasted for 12 months, which showed long-term therapeutic effects. After the treatment, the total scores of knee lateral area, interior area, central area, and patellar area after treatment were all remarkably lower than those before the treatment ($P < 0.05$). After treatment, knee articular KOA MOAKS score and WOMAC were both lower than those before treatment ($P < 0.05$). MOAKS score and WOMAC score showed good correlation ($P < 0.05$). Barrow injury and pain-related coefficient were the highest, and the relevant coefficients of total MOAKS pain score and total WOMAC score were high. VAS score for patients after treatment was apparently lower than that before treatment ($P < 0.05$). The above results demonstrated that PRP could effectively improve the pain and articular pain among KOA patients and restore the functions of knee joint. PRP played a positive role in the treatment of KOA patients.

5. Conclusion

This study was on account of gray projection algorithm, adaptive binarization algorithm, ASM algorithm, and other intelligent algorithms to establish automatic diagnosis of MRI KOA. It aimed to discuss evaluation of MRI on account of intelligent algorithm on clinical effect of treatment of refractory pain in KOA with PRP. The results showed that the automatic diagnostic model of MRI KOA detection results on account of intelligent algorithm was highly consistent with those of manual detection. KOA patients were treated with PRP, and changes in knee KOA MOAKS scores and WOMAC scores were detected in magnetic resonance examinations before and after treatment. However, there were still some deficiencies in this study. In this study, the running time of automatic diagnostic model on account of intelligent algorithm and its specific detection accuracy were not further analyzed. In future experiments, the sample size will be further expanded to verify the running time, detection accuracy, sensitivity, and other parameters of the model established in [26] this study. In summary, automatic diagnostic model of MRI KOA on account of intelligent algorithm in this study could effectively evaluate the clinical efficacy of PRP in treating refractory pain in KOA. This provided a reference basis for the diagnosis and treatment of KOA patients.

Data Availability

The data used to support the findings of this study are available from the corresponding author upon request.

Conflicts of Interest

The authors declare no conflicts of interest.

References

[1] E. Charlier, C. Deroyer, F. Ciregia et al., "Chondrocyte dedifferentiation and osteoarthritis (OA)," *Biochemical Pharmacology*, vol. 165, pp. 49–65, 2019.

[2] T. Georgiev and A. K. Angelov, "Modifiable risk factors in knee osteoarthritis: treatment implications," *Rheumatology International*, vol. 39, no. 7, pp. 1145–1157, 2019.

[3] J. Li, Y. X. Li, L. J. Luo et al., "The effectiveness and safety of acupuncture for knee osteoarthritis: an overview of systematic reviews," *Medicine*, vol. 98, no. 28, Article ID e16301, 2019.

[4] G.-M. Song, X. Tian, Y.-H. Jin et al., "Moxibustion is an alternative in treating knee osteoarthritis," *Medicine*, vol. 95, no. 6, Article ID e2790, 2016.

[5] J. Charlesworth, J. Fitzpatrick, N. K. P. Perera, and J. Orchard, "Osteoarthritis- a systematic review of long-term safety implications for osteoarthritis of the knee," *BMC Musculoskeletal Disorders*, vol. 20, no. 1, p. 151, 2019.

[6] M. J. Salzler, "Editorial commentary: platelet-rich plasma: fountain of youth, cart before the horse, or both?" *Arthroscopy: The Journal of Arthroscopic & Related Surgery*, vol. 34, no. 5, pp. 1541-1542, 2018.

[7] M. L. Louis, J. Magalon, E. Jouve et al., "Growth factors levels determine efficacy of platelets rich plasma injection in knee osteoarthritis: a randomized double blind noninferiority trial compared with viscosupplementation," *Arthroscopy: The Journal of Arthroscopic & Related Surgery*, vol. 34, no. 5, pp. 1530–1540, 2018.

[8] A. Tsukada, K. Uchida, J. Aikawa et al., "Unilateral-dominant reduction in muscle volume in female knee osteoarthritis patients: computed tomography-based analysis of bilateral

sides," *Journal of Orthopaedic Surgery and Research*, vol. 15, no. 1, p. 543, 2020.

[9] Y. Huang, Q. Deng, L. Yang et al., "Efficacy and safety of ultrasound-guided radiofrequency treatment for chronic pain in patients with knee osteoarthritis: a systematic review and meta-analysis," *Pain Research and Management*, vol. 2020, Article ID 2537075, 11 pages, 2020.

[10] X. Zhao, J. Ruan, H. Tang et al., "Multi-compositional MRI evaluation of repair cartilage in knee osteoarthritis with treatment of allogeneic human adipose-derived mesenchymal progenitor cells," *Stem Cell Research & Therapy*, vol. 10, no. 1, p. 308, 2019.

[11] B. A. de Vries, R. A. van der Heijden, J. Verschueren et al., "Quantitative subchondral bone perfusion imaging in knee osteoarthritis using dynamic contrast enhanced MRI," *Seminars in Arthritis and Rheumatism*, vol. 50, no. 2, pp. 177–182, 2020.

[12] W.-S. Lee, H. J. Kim, K.-I. Kim, G. B. Kim, and W. Jin, "Intra-articular injection of autologous adipose tissue-derived mesenchymal stem cells for the treatment of knee osteoarthritis: a phase IIb, randomized, placebo-controlled clinical trial," *Stem Cells Translational Medicine*, vol. 8, no. 6, pp. 504–511, 2019.

[13] D. Shakoor, S. Demehri, F. W. Roemer, D. Loeuille, D. T. Felson, and A. Guermazi, "Are contrast-enhanced and non-contrast MRI findings reflecting synovial inflammation in knee osteoarthritis: a meta-analysis of observational studies," *Osteoarthritis and Cartilage*, vol. 28, no. 2, pp. 126–136, 2020.

[14] A. G. Culvenor, B. E. Øiestad, H. F. Hart, J. J. Stefanik, A. Guermazi, and K. M. Crossley, "Prevalence of knee osteoarthritis features on magnetic resonance imaging in asymptomatic uninjured adults: a systematic review and meta-analysis," *British Journal of Sports Medicine*, vol. 53, no. 20, pp. 1268–1278, 2019.

[15] J. Liu, L. Chen, Y. Tu et al., "Different exercise modalities relieve pain syndrome in patients with knee osteoarthritis and modulate the dorsolateral prefrontal cortex: a multiple mode MRI study," *Brain, Behavior, and Immunity*, vol. 82, pp. 253–263, 2019.

[16] D. Hayashi, F. W. Roemer, and A. Guermazi, "Magnetic resonance imaging assessment of knee osteoarthritis: current and developing new concepts and techniques," *Clinical & Experimental Rheumatology*, no. 5, pp. 88–95, 2019.

[17] G. Cai, F. Cicuttini, D. Aitken et al., "Comparison of radiographic and MRI osteoarthritis definitions and their combination for prediction of tibial cartilage loss, knee symptoms and total knee replacement: a longitudinal study," *Osteoarthritis and Cartilage*, vol. 28, no. 8, pp. 1062–1070, 2020.

[18] C. L. Daugaard, R. G. Riis, E. Bandak et al., "Perfusion in bone marrow lesions assessed on DCE-MRI and its association with pain in knee osteoarthritis: a cross-sectional study," *Skeletal Radiology*, vol. 49, no. 5, pp. 757–764, 2020.

[19] A. Prien, S. Boudabous, A. Junge, E. Verhagen, B. M. A. Delattre, and P. M. Tscholl, "Every second retired elite female football player has MRI evidence of knee osteoarthritis before age 50 years: a cross-sectional study of clinical and MRI outcomes," *Knee Surgery, Sports Traumatology, Arthroscopy*, vol. 28, no. 2, pp. 353–362, 2020.

[20] W. M. Oo, J. M. Linklater, K. L. Bennell et al., "Superb microvascular imaging in low-grade inflammation of knee osteoarthritis compared with power Doppler: clinical, radiographic and MRI relationship," *Ultrasound in Medicine and Biology*, vol. 46, no. 3, pp. 566–574, 2020.

[21] M. S. Dhillon, S. Patel, and T. Bansal, "Improvising PRP for use in osteoarthritis knee- upcoming trends and futuristic view," *Journal of Clinical Orthopaedics and Trauma*, vol. 10, no. 1, pp. 32–35, 2019.

[22] J. Zhao, H. Huang, G. Liang, L.-f. Zeng, W. Yang, and J. Liu, "Effects and safety of the combination of platelet-rich plasma (PRP) and hyaluronic acid (HA) in the treatment of knee osteoarthritis: a systematic review and meta-analysis," *BMC Musculoskeletal Disorders*, vol. 21, no. 1, p. 224, 2020.

[23] F. Migliorini, A. Driessen, V. Quack et al., "Comparison between intra-articular infiltrations of placebo, steroids, hyaluronic and PRP for knee osteoarthritis: a Bayesian network meta-analysis," *Archives of Orthopaedic and Trauma Surgery*, vol. 141, no. 9, pp. 1473–1490, 2021.

[24] C. O'Donnell, E. Migliore, F. C. Grandi et al., "Platelet-rich plasma (PRP) from older males with knee osteoarthritis depresses chondrocyte metabolism and upregulates inflammation," *Journal of Orthopaedic Research*, vol. 37, no. 8, pp. 1760–1770, 2019.

[25] S. A. Raeissadat, P. Ghazi Hosseini, M. H. Bahrami et al., "The comparison effects of intra-articular injection of platelet rich plasma (prp), plasma rich in growth factor (prgf), hyaluronic acid (ha), and ozone in knee osteoarthritis; a one year randomized clinical trial," *BMC Musculoskeletal Disorders*, vol. 22, no. 1, p. 134, 2021.

Hindawi
Contrast Media & Molecular Imaging
Volume 2022, Article ID 1886406, 8 pages
https://doi.org/10.1155/2022/1886406

Research Article

Diagnosis of Nonperitonealized Colorectal Cancer with Computerized Tomography Image Features under Deep Learning

Xiaohong Wang[1] **Changyi Guo**[2] **Yufeng Zha**[3] **Kai Xu**[4] **and Xiaochao Liu**[5]

[1]*Department of Critical Care Medicine, The Second Affiliated Hospital of Shaanxi University of Chinese Medicine, Xianyang 712000, Shaanxi, China*
[2]*Image Center, The Second Affiliated Hospital of Shaanxi University of Chinese Medicine, Xianyang 712000, Shaanxi, China*
[3]*Department of General Surgery, The Second Affiliated Hospital of Shaanxi University of Chinese Medicine, Xianyang 712000, Shaanxi, China*
[4]*Department of Medical Imaging, Baoji Central Hospital, Baoji 721000, Shaanxi, China*
[5]*Department of Gastroenterology, Shaanxi Hanzhong Centre Hospital, Hanzhong 723000, Shaanxi, China*

Correspondence should be addressed to Xiaochao Liu; 3321020797@stu.cpu.edu.cn

Received 5 February 2022; Revised 23 April 2022; Accepted 4 May 2022; Published 25 May 2022

Academic Editor: M Pallikonda Rajasekaran

This study aimed to explore the value of abdominal computerized tomography (CT) three-dimensional reconstruction using the dense residual single-axis super-resolution algorithm in the diagnosis of nonperitonealized colorectal cancer (CC). 103 patients with nonperitonealized CC (the lesion was located in the ascending colon or descending colon) were taken as the research subjects. The imagological tumor (T) staging, the extramural depth (EMD) of the cancer tissues, and the extramural vascular invasion (EMVI) grading were analyzed. A dense residual single-axis super-resolution network model was also constructed for enhancing CT images. It was found that the CT images processed using the algorithm were clear, and the peak signal-to-noise ratio (PSNR) and structural similarity (SSIM) were 33.828 dB and 0.856, respectively. In the imagological T staging of CC patients, there were 17 cases in the T3 stage and 68 cases in the T4 stage. With the EMD increasing, the preoperative carcinoembryonic antigen (CEA) highly increased, and the difference was statistically significant ($P < 0.05$). The postoperative hospital stays of patients were also different with different grades of EMVI. The hospital stay of grade 1 patients (19.45 days) was much longer than that of grade 2 patients (13.19 days), grade 3 patients (15.36 days), and grade 4 patients (14.36 days); the differences were of statistical significance ($P < 0.05$). It was suggested that CT images under the deep learning algorithm had a high clinical value in the evaluation of T staging, EMD, and EMVI for the diagnosis of CC.

1. Introduction

Colorectal cancer (CC) is one of the most common malignant tumors clinically, ranking third in the incidence of malignant tumors and fourth in the mortality of malignant tumors around the world [1, 2]. About 1.2 million people suffer from CC every year, and about 600,000 people lose their lives as a result. Its incidence is higher in Europe and America, but lower in Asia; the incidence is higher in men than in women [3]. In China, the incidence of CC in urban areas and rural areas is about 31.29/105 and 16.99/105, respectively, ranking third and sixth among malignant tumors. In urban areas, the 5-year survival period of CC patients is about 50%; in rural areas, the 5-year survival period is less than 40% [4, 5]. So far, even if there is no specific statistical data on the incidence of CC, the incidence of CC in China has shown an increasing trend year by year due to the changes in people's living standards in recent years and the westernization of living habits. Surgery is still the most effective way to treat CC [6]. Nonperitonealized CC refers to a tumor located on the posterior wall of the ascending colon or descending colon, where the posterior wall of the intestine is not covered by the peritoneum [7]. With the clinical staging and diagnosis of nonperitonealized CC, there have been many studies on the circumferential resection margin (CRM) of this disease. However, the CRM is caused by a sharp separation during surgical resection. The scope of surgical resection has a great influence on it, and it cannot truly reflect the infiltration of cancer tissues [8]. For the development and popularization of complete mesorectal excision (CME) surgery in China, the scope of surgical resection is more thorough than that of traditional radical surgery, significantly improving the surgery quality. On the contrary, the CRM of some deeply infiltrated cancer tissues may still be negatively affecting the correct evaluation of the CRM [9].

As one of the most commonly used clinical imaging techniques, computerized tomography (CT) has been applied in the examination of various diseases. Plain CT scanning is the basis of all CT examinations, with a relatively simple operation and a faster scanning speed. Most diseases can be detected without injection, such as craniocerebral hemorrhage, cerebral infarction, brain tumor, and fracture. Enhanced CT scanning is a further examination of plain CT scanning. When an issue is found in plain CT scanning, enhanced CT scanning is required; it is clearer than plain scanning to evaluate the blood supply of the lesions [10]. In recent years, deep learning has made great achievements in digital image processing. The deep convolutional neural network can learn the structural feature information of high and low frequencies in complex images, and it can give better results than traditional algorithms in the processing of medical images. The three-dimensional reconstruction algorithm of tomographic images eliminates the volume effect to a certain extent on the basis of deep learning, while maintaining the isotropy of the volume data [11, 12]. In the method of edge super-resolution depth slice interpolation, some scholars proposed a single-axis super-resolution method by combining the content of the orthogonal direction of the slice to obtain the reconstructed imaging image of the coronal plane and the sagittal plane [13]. From this, the idea of developing a three-dimensional reconstruction of abdominal CT images under the single-axis super-resolution reconstruction algorithm came up. It aimed to reduce the radiation intensity of CT tomographic images and improve the quality of the three-dimensional reconstruction model.

With CT imaging principles and deep learning-based super-resolution reconstruction technology, it was proposed to construct a feature-enhanced residual dense network model with a single axis and super-resolution [14]. The uniaxial super-resolution was utilized to perform three-dimensional reconstruction of abdominal CT images and evaluate its application value in the diagnosis of nonperitonealized CC trying to provide a certain theoretical basis for the clinical diagnosis of the disease.

2. Data and Methods

2.1. General Data of Patients. One hundred and three patients with nonperitonealized CC admitted to the hospital from March 2018 to March 2020 were included. Their general information and clinicopathological information were collected and recorded. The patients consisted of 49 males and 54 females, with an average age of 67.67 ± 14.32 years. There were 85 cases with lesions in the ascending colon and 18 cases with that in the descending colon. This study had been approved by the ethics committee of the hospital. The patients and their family members fully understood the status and signed the informed consent forms.

Inclusion criteria were as follows: patients who were diagnosed with CC according to the pathological diagnosis; patients who were in phase II of the pathological staging; patients who underwent the colon surgery for the first time; the surgery for patients was radical resection.

Exclusion criteria were as follows: patients who underwent emergency surgery; patients who died during the perioperative period; patients who had cachexia complications, or did not have the complete data.

2.2. CT Examination and Image Processing. The 64-slice spiral CT instrument was used for examinations. Patients were asked to fast for 4 hours before the examination, and drink 1L of purified water 30 minutes before the examination. The injected contrast agent was an iohexol injection with a dose of 80–100 mL, and the injection speed was 3 mL per second. CT scanning was performed 30 seconds after the start of the injection. The scanning range was from the top of the diaphragm to the plane of the pubic symphysis; the slice thickness was 5 mm, the scanning voltage was 125–145 kV, the scanning current was 150–220 mA, the interval was 0.984 : 1, and the scanning time was about 5 minutes. During the process, patients needed to minimize their movements, reduce mood swings, and calm their breathing. Finally, the obtained image data were uploaded to the computer, and the dense residual single-axis super-resolution network algorithm was applied to process the images.

2.3. Evaluation of the Results. For the imagological tumor (T) staging of patients, 2 radiologists with rich clinical imaging experience were invited, and the multislice spiral CT instrument was used [15]. The staging standards are shown in Table 1.

In the process of reading the images, both radiologists divided the stages with the independent double-blind principle. If the staging results of the two radiologists were different, a third radiologist was asked to stage. If the result of the third radiologist was the same as that of one of the first two radiologists, the stage was determined.

The imagological grading standards of extramural vascular invasion (EMVI) [16] are shown in Table 2 for details.

Both radiologists determined the EMVI grading independently and double-blindly. If the two results were different, a third radiologist was involved. When the result of the third radiologist was the same as that given by one of the first two radiologists, the EMVI grade was confirmed.

Two radiologists were invited to measure the extramural depth (EMD) of cancer tissues. The vertical distance between the cancer tissue outside the farthest end of the intestinal

Table 1: T staging of nonperitonealized CC imaging.

T staging	Specific manifestations
T1 stage	There was no significant imaging change in the intestinal wall of the diseased side
T2 stage	The intestinal wall of the diseased side was thickened asymmetrically, protruding into the intestinal cavity. But the muscular layer of the intestinal wall was smooth and contiguous, and the surrounding adipose tissues did not change.
T3 stage	The intestinal wall was smooth or thickened by the nodular discontinuously, the muscle layer of the lesion was discrete, and the adjacent adipose tissues were infiltrated
T4 stage	Cancer tissues infiltrated the muscular layer to the peritoneum, or the anterior edge of cancer nodules infiltrated adjacent organs (when the distance between the cancer tissue and the fused fascia was less than 1 mm, it was also present in the T4 stage).

Table 2: Imagological grading of EMVI for CC patients.

EMVI grading	Specific manifestations
Grade 1	No obvious EMVI occurred
Grade 2	The blood vessels adjacent to the cancer tissues became slightly curved
Grade 3	The small blood vessels adjacent to the cancer tissues showed nodular changes (the nodular manifestations had the same enhancement degree within the small blood vessels and the cancer tissues)
Grade 4	The large blood vessels adjacent to the cancer tissues were significantly infiltrated (tumor embolus could be observed in large enhanced veins)

wall and the intestinal wall was measured, and the EMD was calculated by taking the average value.

2.4. Model Construction of Dense Residual Single-Axis Super-Resolution Network. The original low-resolution image E^{LR} is the input, and a multiscale feature convolution layer was used to extract the shallow mapping layer, which is expressed as

$$M_{-1} = G_{SFE1}\left(E^{LR}\right). \tag{1}$$

G_{SFE1} represents a convolution operation of the multiscale feature extraction. Then, it came to the deep feature learning part of the dense residual block for further extraction of the shallow map and the global residual map. It is expressed as

$$M_0 = G_{SFE2}\left(M_{-1}\right). \tag{2}$$

G_{SFE2} is the convolution operation of the secondary shallow feature extraction, and M_0 is taken as the input of the deep feature extraction module. Thus, (3) is obtained.

$$M_{\mathrm{n}} = G_{RDB,\mathrm{n}}\left(M_{\mathrm{n}-1}\right) = G_{RDB,\mathrm{n}}\left(G_{RDB-1}\left(\ldots\left(G_{RDB,1}\left(M_0\right)\right)\ldots\right)\right). \tag{3}$$

$G_{R\ DB\ ,n}$ is the nth dense residual block. $G_{R\ DB\ ,n}$ is the iterative nesting method, including convolution and activation functions. Each dense residual block had a corresponding M_n; therefore, M_n refers to the local information in the feature map.

Afterward, the staircase features of a series of dense residual blocks were learned, and the results of all layer features extracted in the feature extraction stage were used for global residual learning and global dense feature fusion. The features of different layers were merged using Concat and convolution operations, and then, they were merged for dense feature fusion (DFF). In this case, DFF could be expressed as

$$M_{\mathrm{DF}} = G_{\mathrm{DFF}}\left(M_{-1}, M_0, M_1, \ldots, M_D\right). \tag{4}$$

F refers to the feature image after depth mapping. It was sent to the feature enhancement module to obtain the final feature image, which is expressed as

$$M_{LR} = G_{FE}\left(M_{LR-1}\right). \tag{5}$$

G stands for the operation of weighted reinforcement learning in the image. When the feature extraction ended, the feature map M was regarded as the multiscale upsampling layer *VM-Meta* of any scaling factor. It is described as

$$M_{SR} = G_{V-MMeta}\left(M_{LR}\right). \tag{6}$$

In (6), G is the upsampling operation. The size of the feature image in the vertical axis direction became n times of that of the input image (n represented the magnification times). 3×3 convolution was used to perform the feature compression operation, which is shown as

$$E_{SR} = G_{REC}\left(M_{SR}\right). \tag{7}$$

The output of the model was thus obtained, that was, the high-resolution image *SR*.

In the model optimizer, the *L1* loss function was adopted for $\left\{E_{LR}^i, E_{HR}^i\right\}_{i=1}^K$ of K pairs of data that were taken as the training set. The loss function was then expressed as

$$L(\gamma) = \frac{1}{K}\sum_{i=0}^{K}\left|G_{\mathrm{model}}\left(E_{LR}^i\right) - E_{HR}^i\right|. \tag{8}$$

γ is the network parameter set optimized using the Adam optimizer algorithm.

2.5. Statistical Analysis. SPSS22.0 was used to perform statistical analysis on the data. Quantitative data were compared using the χ^2 test or the Fisher exact probability method. The relationship among variables was shown by

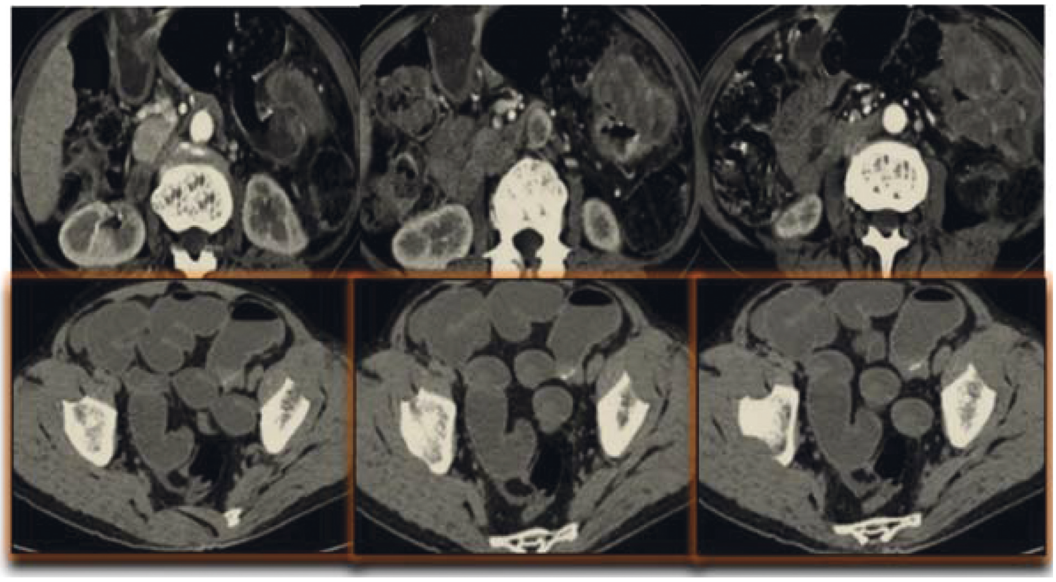

Figure 1: CT images of the patients before being processed by the single-axis super-resolution algorithm. All were enhanced arterial-phase scanning images.

correlation analysis, and the consistency evaluation was performed by the Kappa test. When $P < 0.05$, it meant that the difference was of statistical significance.

3. Results

3.1. General Information. Figures 1–3 show some CT images of the patients before and after being processed by the single-axis super-resolution algorithm, as well as the structural similarity (SSIM) and peak signal-to-noise ratio (PSNR) of the processed images.

From Figures 1–3, the CT images of patients were manifested with obvious thickening of the colorectal wall, showing irregular localization or diffuse thickening. Obvious enhancement was observed using CT-enhanced scanning, with colonic lumen stenosis and low-density necrotic zones inside the cancer tissues. After super-resolution reconstruction, the obtained images were clearer, and the PSNR and SSIM were 33.828 dB and 0.856, respectively.

3.2. Imagological T Staging. Figure 4 shows the imagological T staging results of the 103 patients with CC, which were determined by two radiologists. It was found that all the staging results of the two radiologists were in the T3 and T4 stages, having nothing to do with T1 and T2 stages. Radiologist 1 gave the results of 27 cases in the T3 stage and 76 cases in the T4 stage. Radiologist 2 gave the results of 25 cases in the T3 stage and 78 cases in the T4 stage. The consistency analysis of the results of the two radiologists was made for the common staging results, which shows 17 cases in the T3 stage and 68 cases in the T4 stage. From the Kappa consistency analysis, it was found that the imagological T staging of the two radiologists had generally poor consistency ($\kappa = 0.499$, $P < 0.05$).

As shown in Figure 5, the patients were divided into the T3 stage group and the T4 stage group according to imagological T staging. Their age, preoperative body mass index (BMI), preoperative carcinoembryonic antigen (CEA), preoperative carbohydrate antigen-199 (CA-199), time of surgery, postoperative hospital stays, and the statistical analysis results of lymph node examinations were compared. It was shown that all the terms of the T3 stage group were less than those of the T4 stage group, but the differences between the two groups were not statistically significant ($P > 0.05$).

3.3. EMD of Cancer Tissues. Figure 6 shows the imagological EMD measurement of 103 patients with CC by 2 radiologists. For the EMD measurement results of radiologist 1, EMD <1 mm was observed in 22 cases, $1 < \text{EMD} < 5$ mm in 27 cases, $5 < \text{EMD} < 15$ mm in 32 cases, and EMD >15 mm in 22 cases. For those of radiologist 2, there were 21, 27, 32, and 23 cases with EMD <1 mm, $1 < \text{EMD} < 5$ mm, $5 < \text{EMD} < 15$ mm, and EMD >15 mm, respectively. The Kappa method was adopted to analyze the consistency of the results of the two radiologists, and it was found to be generally poor ($\kappa = 0.384$, $P < 0.05$). The average values of the results of both doctors were taken, thus, there were 16 cases with EMD <1 mm, 34 cases with $1 < \text{EMD} < 5$ mm, 31 cases with $5 < \text{EMD} < 15$ mm, and 22 cases with EMD >15 mm.

According to the imagological measurement results of the EMD, the patients were divided into 4 groups, which were <1 mm group, 1–5 mm group, 5–15 mm group, and >15 mm group. The age, preoperative BMI, preoperative CEA, preoperative CA-199, time of surgery, postoperative hospital stays, and the number of lymph nodes were obtained. As shown in Figure 7, with the increase of the EMD, the preoperative CEA also increased, and the differences were statistically significant ($P < 0.05$). Through the correlation test, it was found that there was a certain correlation between the EMD and preoperative CEA ($P < 0.05$).

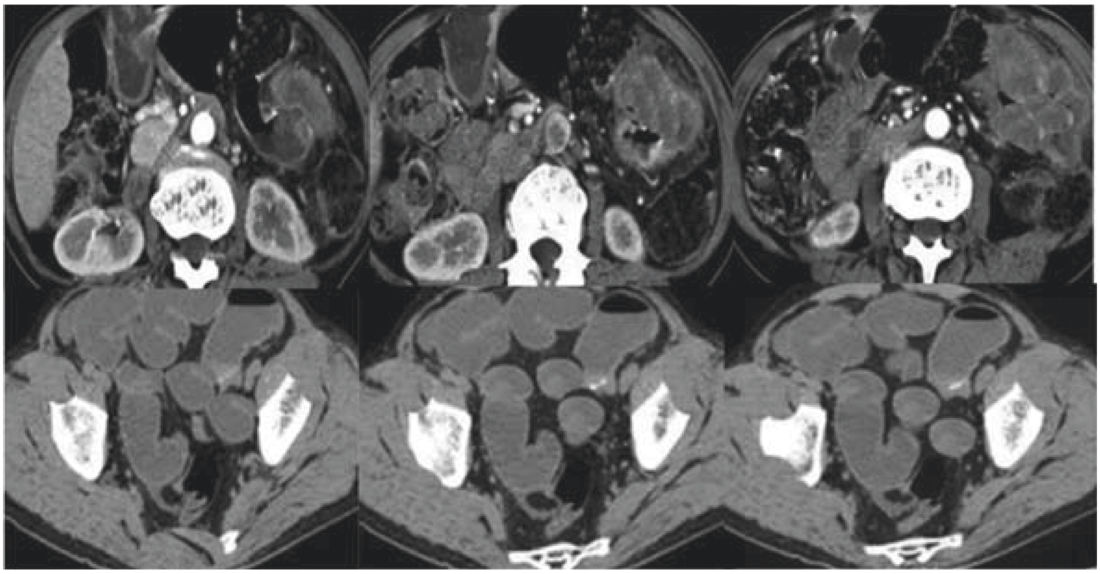

Figure 2: CT images of the patients after being processed by the single-axis super-resolution algorithm.

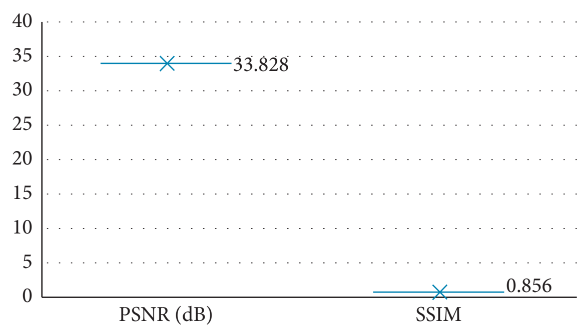

Figure 3: PSNR and SSIM of the obtained images after being processed by the single-axis super-resolution algorithm.

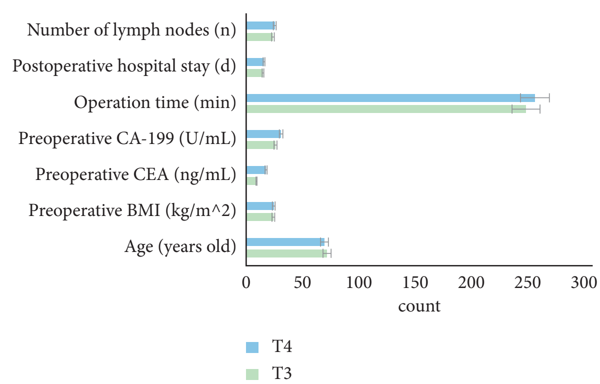

Figure 5: Comparison of clinical data of imagological T staging.

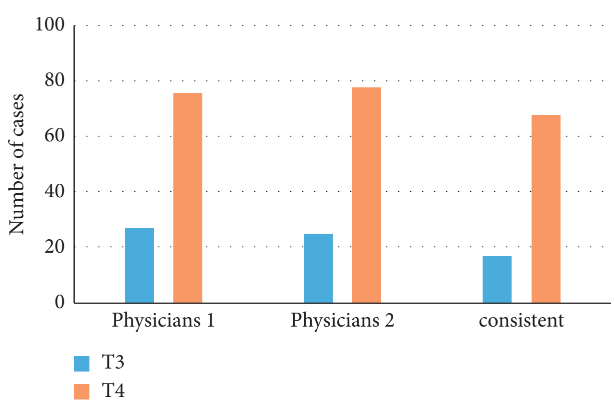

Figure 4: T staging results of imaging.

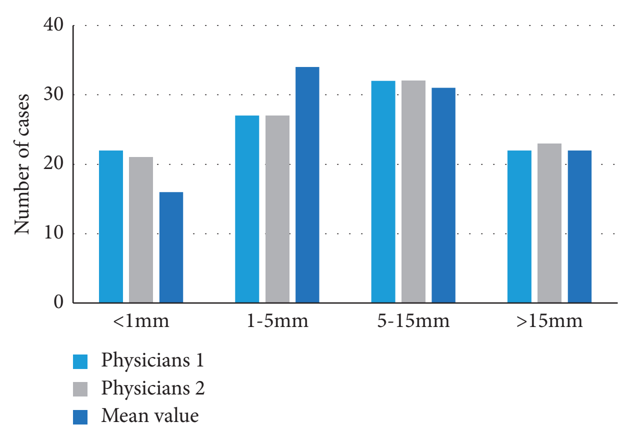

Figure 6: Evaluation results by the two radiologists on the EMD.

3.4. EMVI Evaluation Results. Figure 8 shows the imagological EMVI evaluation results of 103 patients with CC made by the two radiologists. The EMVI results of radiologist 1 are as follows: 27 cases were judged in grade 1, 33 cases in grade 2, 28 cases in grade 3, and 15 cases in grade 4. As for the EMVI results of radiologist 2, 14, 35, 33, and 21 cases were in grade 1, grade 2, grade 3, and grade 4, respectively. The consistency of the EMVI results of radiologist 1 and radiologist 2 was analyzed using the Kappa method,

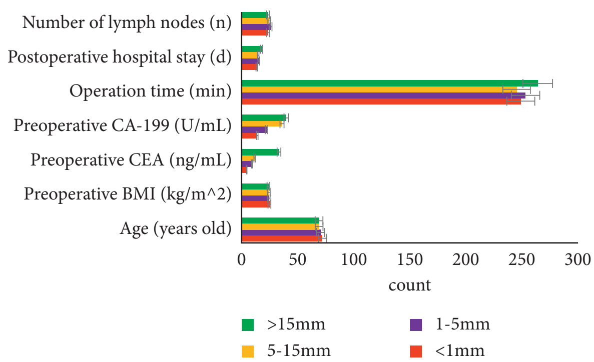

Figure 7: Comparison of clinical pathological data in imagological EMD.

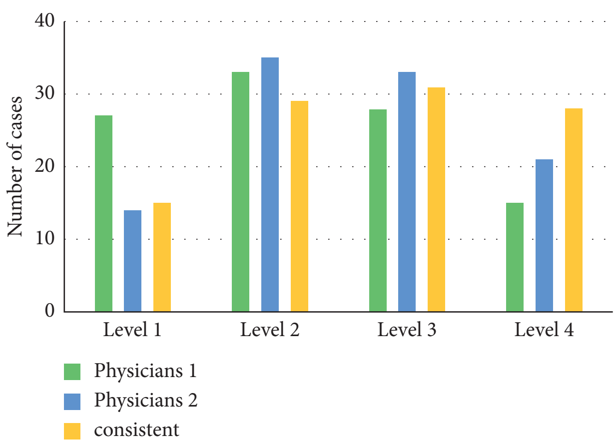

Figure 8: Imagological EMVI evaluation results by two radiologists.

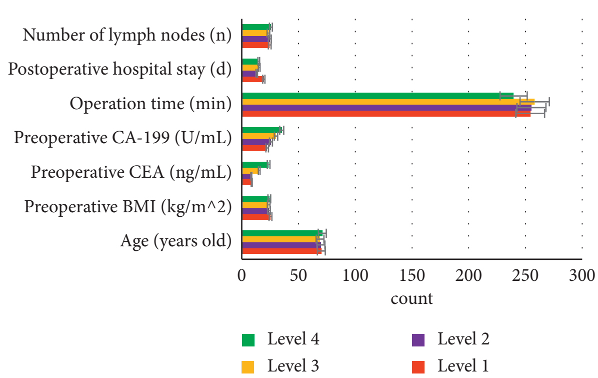

Figure 9: Comparison of clinical pathological data in imagological EMVI.

and it was found to be poor ($\kappa = 0.281$, $P < 0.05$). The final EMVI results are as follows: 15, 29, 31, and 28 cases were in grade 1, grade 2, grade 3, and grade 4, respectively.

With the evaluation results of EMVI, Figure 9 shows the comparisons of the age, preoperative BMI, preoperative CEA, preoperative CA-199, time of surgery, postoperative hospital stays, and the number of lymph nodes. There were differences in the postoperative hospital stays of patients in different EMVI grades, which were statistically significant ($P < 0.05$). However, no correlation was found between the EMVI grading and the postoperative hospital stays ($P < 0.05$) via the correlation test.

4. Discussion

The clinical examinations of CC patients generally include a barium meal, fiber colonoscopy, and imaging examinations [17]. A literature suggested that intestinal barium meal examination can show the characteristics of intestinal mucosal injury clearly, but there are certain limitations in showing changes in the outer lumen and the intestinal wall [18]. With fiber colonoscopy, the color of the intestinal mucosa and ulcers or bleeding on the surface of the intestinal mucosa can be observed directly. For suspected lesions, the tissues can be directly taken for medical examination. But the lesions outside the intestinal cavity and the infiltration of the surrounding tissues and organs cannot be shown [19].

Some scholars have proposed that CT scanning can obtain the data of the entire abdomen of patients and process them. It can not only clarify the location of the number of lesions, the situation inside and outside the intestinal cavity of the lesion, the invasion of adjacent organs and tissues, and the distant metastasis, etc.; it can also perform the staging of tumors [20, 21]. To improve the quality of CT images, the dense residual single-axis super-resolution network model was also constructed for the processing of CT images. The processing performance of this algorithm was analyzed, and the CT images obtained by this algorithm were clearer, with the PSNR of 33.828 dB and SSIM of 0.856. These indicated that the algorithm designed in this research had a better performance in processing CT images, worthy of promotion and application. It was shown from data analysis that, for CT imagological T staging of CC patients before surgery, there were 17 cases in the T3 stage and 68 cases in the T4 stage. The age, preoperative BMI, preoperative CEA, preoperative CA-199, time of surgery, postoperative hospital stays, and the number of lymph nodes of patients were analyzed. From the statistical analysis results, all the parameters in the T3 stage were less than those in the T4 stage. For the EMD of cancer tissues, EMD <1 mm was observed in 16 cases, $1 < \text{EMD} < 5$ mm in 34 cases, $5 < \text{EMD} < 15$ mm in 31 cases, and EMD >15 mm in 22 cases. Meanwhile, the preoperative CEA also increased with the increasing EMD, and the difference was statistically significant ($P < 0.05$). By the correlation test, it was discovered that there was a certain correlation between the EMD and preoperative CEA ($P < 0.05$). It was indicated that CT examination had a high clinical value for the imagological staging of CC and the diagnosis of cancer tissue invasion, which was exactly similar to the results of Flor et al. [22].

In the diagnosis of EMVI, 15 cases were assessed in grade 1, 29 cases were in grade 2, 31 cases were in grade 3, and 28 cases were in grade 4. The patients in different grades of EMVI had different hospital stays after surgery, and the differences were statistically significant ($P < 0.05$). However, the correlation test found that the EMVI grading had no correlation with the postoperative hospital stays ($P < 0.05$). Therefore, CT examination had a great clinical value for the diagnosis of CC invasion before surgery. There are also studies that show that the diagnostic efficiency and the sensitivity of EMVI evaluation with imaging are relatively low. For example, poor accuracy is obtained in the preoperative evaluation of tumors, so that it is of no clinical practical significance [23]. Some researchers believe that, even though imaging is less sensitive to the diagnosis of EMVI, it has a positive significance in the diagnosis of adjacent vascular infiltration of cancer tissues, showing an important significance in improving the prognosis of the disease [24].

5. Conclusion

The uniaxial super-resolution algorithm was used to perform three-dimensional reconstruction of abdominal CT, and its application value in the diagnosis of nonperitonealized CC was evaluated by analyzing the imagological T staging, the EMD of cancer tissues, and the EMVI grading. It was concluded that the CT images processed by the deep learning algorithm were clearer, and the PSNR and SSIM were measured as 33.828 dB and 0.856, respectively. CT can do well in preoperative staging of nonperitonealized CC, imagological T staging, and the evaluation of EMD and EMVI, having a high clinical value in the diagnosis of CC. However, some shortcomings were also exposed. The sample size was relatively small, and there was not a prospective experiment with large samples. In the future, the sample should be expanded for further research. Altogether, the results provided a theoretical basis for the clinical imaging diagnosis of nonperitonealized CC.

Data Availability

The data used to support the findings of this study are available from the corresponding author upon request.

Conflicts of Interest

The authors declare that they have no conflicts of interest.

References

[1] E. Saus, S. Iraola-Guzmán, J. R. Willis, A. Brunet-Vega, and T. Gabaldon, "Microbiome and colorectal cancer: roles in carcinogenesis and clinical potential," *Molecular Aspects of Medicine*, vol. 69, pp. 93–106, 2019.

[2] S. La Vecchia and C. Sebastián, "Metabolic pathways regulating colorectal cancer initiation and progression," *Seminars in Cell & Developmental Biology*, vol. 98, pp. 63–70, 2020.

[3] M. Arnold, M. S. Sierra, M. Laversanne, I. Soerjomataram, A. Jemal, and F. Bray, "Global patterns and trends in colorectal cancer incidence and mortality," *Gut*, vol. 66, no. 4, pp. 683–691, 2017.

[4] R. S. Zheng, K. X. Sun, S. W. Zhang et al., "[Report of cancer epidemiology in China, 2015]," *Zhonghua Zhongliu Zazhi*, vol. 41, no. 1, pp. 19–28, 2019, Chinese.

[5] H. Zhou, X. Zhang, Z. H. Shen et al., "[Screening of colorectal cancer in Kunming urban residents from 2014 to 2017]," *Zhonghua Wei Chang Wai Ke Za Zhi*, vol. 22, no. 11, pp. 1058–1063, 2019, Chinese.

[6] S. J. van Rooijen, M. A. Engelen, C. Scheede-Bergdahl et al., "Systematic review of exercise training in colorectal cancer patients during treatment," *Scandinavian Journal of Medicine & Science in Sports*, vol. 28, no. 2, pp. 360–370, 2018.

[7] K. Lee, H. R. Kim, D. Kim, S. I. Park, Y. H. Kim, and S. Choi, "Surgical outcome of colon interposition in esophageal cancer surgery: analysis of risk factors for conduit-related morbidity," *The Thoracic and Cardiovascular Surgeon*, vol. 66, no. 05, pp. 384–389, 2018.

[8] L. G. Yuan and Y. S. Mao, "[Current status of prognostic evaluation of esophageal cancer patients by circumferential resection margin]," *Zhonghua Zhongliu Zazhi*, vol. 41, no. 4, pp. 241–245, 2019.

[9] X. Y. Tang, M. X. Huang, S. Q. Han et al., "The circumferential resection margin is a prognostic predictor in colon cancer," *Frontiers In Oncology*, vol. 10, p. 927, 2020.

[10] Z. Li, X. Li, R. Tang, and L. Zhang, "Apriori algorithm for the data mining of global cyberspace security issues for human participatory based on association rules," *Frontiers in Psychology*, vol. 11, Article ID 582480, 2021.

[11] A. A. Kalinin, G. A. Higgins, N. Reamaroon et al., "Deep learning in pharmacogenomics: from gene regulation to patient stratification," *Pharmacogenomics*, vol. 19, no. 7, pp. 629–650, 2018.

[12] Z. Wan, Y. Dong, Z. Yu, H. Lv, and Z. Lv, "Semi-supervised support vector machine for digital twins based brain image fusion," *Frontiers in Neuroscience*, vol. 15, Article ID 705323, 2021.

[13] S. X. Xie, Z. C. Yu, and Z. H. Lv, "Multi-disease prediction based on deep learning: a survey," *Computer Modeling in Engineering and Sciences*, vol. 128, no. 2, pp. 489–522, 2021.

[14] Z. Zhang, Z. Tang, Y. Wang, C. Zhan, Z. Zha, and M. Wang, "Dense Residual Network: enhancing global dense feature flow for character recognition," *Neural Networks*, vol. 139, pp. 77–85, 2021.

[15] X. Zhang, H. Shen, and Z. Lv, "Deployment optimization of multi-stage investment portfolio service and hybrid intelligent algorithm under edge computing," *PLoS One*, vol. 16, no. 6, Article ID e0252244, 2021.

[16] S. Balyasnikova, N. Haboubi, A. Wale et al., "Session 2: extramural vascular invasion and extranodal deposits: should they be treated the same?" *Colorectal Disease*, vol. 20, no. Suppl 1, pp. 43–48, 2018.

[17] A. Tachimori, K. Yonemitsu, Y. Fukui et al., "[Clinical significance of preoperative chemotherapy for advanced colorectal cancer]," *Gan To Kagaku Ryoho*, vol. 47, no. 13, pp. 2021–2023, 2020.

[18] L. Zhao, W. Lu, Y. Sun et al., "Small intestinal diverticulum with bleeding: case report and literature review," *Medicine*, vol. 97, no. 9, Article ID e9871, 2018.

[19] A. M. Leszczynski, K. L. MacArthur, K. P. Nelson, S. A. Schueler, P. A. Quatromoni, and B. C. Jacobson, "The association among diet, dietary fiber, and bowel preparation at colonoscopy," *Gastrointestinal Endoscopy*, vol. 88, no. 4, pp. 685–694, 2018.

[20] A. E. Obaro, D. N. Burling, and A. A. Plumb, "Colon cancer screening with CT colonography: logistics, cost-effectiveness, efficiency and progress," *British Journal of Radiology*, vol. 91, no. 1090, Article ID 20180307, 2018.

[21] G. Pan, D. Li, X. Li, Y. Peng, T. Wang, and C. Zuo, “SPECT/CT imaging of HER2 expression in colon cancer-bearing nude mice using 125I-Herceptin,” *Biochemical and Biophysical Research Communications*, vol. 504, no. 4, pp. 765–770, 2018.
[22] N. Flor, A. P. Ceretti, C. Luigiano et al., “Performance of CT colonography in diagnosis of synchronous colonic lesions in patients with occlusive colorectal cancer,” *American Journal of Roentgenology*, vol. 214, no. 2, pp. 348–354, 2020.
[23] L. G. J. Leijssen, A. M. Dinaux, R. Amri et al., “Impact of intramural and extramural vascular invasion on stage II-III colon cancer outcomes,” *Journal of Surgical Oncology*, vol. 119, no. 6, pp. 749–757, 2019.
[24] E. E. van Eeghen, M. J. Flens, M. M. R. Mulder, and R. J. L. F. Loffeld, “Extramural venous invasion as prognostic factor of recurrence in stage 1 and 2 colon cancer,” *Gastroenterology Research and Practice*, vol. 2017, Article ID 1598670, 6 pages, 2017.

Hindawi
Contrast Media & Molecular Imaging
Volume 2022, Article ID 3790269, 9 pages
https://doi.org/10.1155/2022/3790269

Research Article

Magnetic Resonance Imaging Features on Deep Learning Algorithm for the Diagnosis of Nasopharyngeal Carcinoma

Ruijie Huang,[1] **Zhanmei Zhou**,[2] **Xintao Wang**,[3] **and Xiaohua Cao**[1]

[1]*Department of Otorhinolaryngology, Jingdezhen Second People's Hospital, Jingdezhen 333000, Jiangxi, China*
[2]*Department of Image, Jingdezhen Second People's Hospital, Jingdezhen 333000, Jiangxi, China*
[3]*Department of Otorhinolaryngology, Ganzhou People's Hospital, Ganzhou 341000, Jiangxi, China*

Correspondence should be addressed to Ruijie Huang; 201711111121683@stu.hubu.edu.cn

Received 8 February 2022; Revised 3 May 2022; Accepted 4 May 2022; Published 25 May 2022

Academic Editor: M Pallikonda Rajasekaran

The objective of this research was to investigate the application values of magnetic resonance imaging (MRI) features of the deep learning-based image super-resolution reconstruction algorithm optimized convolutional neural network (OPCNN) algorithm in nasopharyngeal carcinoma (NPC) lesion diagnosis. A total of 54 patients with NPC were selected as research objects. Based on the traditional CNN structure, OPCNN was proposed. Besides, MRI processed by the traditional CNN model and the U-net network model was introduced to be analyzed and compared with its algorithm. The used assessment parameters included volume transfer constant (K^{trans}), rate constant (K_{ep}), volume fraction (V_e), and apparent diffusion coefficient (ADC). The results showed that the values of Dice coefficient, peak signal-to-noise ratio (PSNR), and structural similarity (SSIM) of the OPCNN algorithm were significantly higher than those of the traditional CNN model and the U-net network model. Meanwhile, the difference was statistically significant ($P < 0.05$). K^{trans}, K_{ep}, and V_e in tumor lesions were significantly higher than those in the healthy side, while the ADC was significantly lower than that in the healthy side ($P < 0.05$). The sensitivity, specificity, and accuracy of dynamic contrast-enhancement magnetic resonance imaging (DCE-MRI) in the diagnosis of nasopharyngeal carcinoma staging were slightly higher than those in T2-weighted imaging (T2WI) and diffusion-weighted imaging (DWI). The diagnostic sensitivity of DCE-MRI was more than 85%, its diagnostic specificity was more than 75%, and its diagnostic accuracy was more than 90%. The AUC area of NPC diagnosed by combination of the three was significantly different from that diagnosed by single T2WI, DWI, and DCE-MRI ($P < 0.05$). The diagnostic accuracy of MRI based on the OPCNN algorithm for nasopharyngeal carcinoma (93.2%) was significantly higher than that of single MRI (76.4%). In summary, the OPCNN algorithm proposed in this study could improve the quality of MRI images, and the effect was better than the traditional deep learning model, which had the value of clinical promotion. The application value of DCE-MRI in the diagnosis of pathogenic lesions of nasopharyngeal carcinoma was better than conventional MRI. The combined application of T2WI, DWI, and DCE-MRI in the screening of nasopharyngeal carcinoma lesions could greatly improve the diagnostic accuracy of nasopharyngeal carcinoma.

1. Introduction

Nasopharyngeal carcinoma is a malignant tumor occurring on the top and sidewalls of the nasopharynx. It is one of the most frequent malignant tumors in China. The incidence rate is the first of the otorhinolaryngology malignant tumors. The lesions of nasopharyngeal carcinoma can be nodular, ulcerative, and submucosal invasive. The pathological type is mainly squamous cell carcinoma, and the other types are relatively rare [1–3]. Clinically, it is considered that the occurrence of nasopharyngeal carcinoma is mainly related to Epstein–Barr virus (EBV) infection, genetic factors, chemical factors, and environmental factors. In addition, individual factors also include long-term smoking, long-term drinking, and eating pickled food [4]. There are obvious gender and ethnic differences in nasopharyngeal carcinoma. Among them, the incidence rate of the yellow race is the highest, and the incidence rate of the black race is lower than that of the yellow race. The incidence rate of the white race is the lowest. Besides, the incidence rate of men is two times higher than that of women [5, 6]. Nasopharyngeal carcinoma grows in the nasopharynx behind the nasal cavity. Its location is hidden, and it is often asymptomatic in the early stage, which is easy to be ignored. With the development of the disease, patients may have symptoms such as tinnitus, deafness, hearing loss, nasal congestion, headache, facial paralysis, cranial nerve paralysis, and distant metastasis. Most patients were diagnosed only after finding neck mass or other metastatic symptoms, so they lost the best time for the treatment [7–9]. Therefore, to achieve early diagnosis and timely treatment, the early signal of nasopharyngeal carcinoma needs attention and vigilance.

There are many clinical diagnostic methods of NPC, such as physical examination, nasopharyngeal endoscopy, EBV serum examination, magnetic resonance imaging (MRI), computed tomography (CT), and positron emission tomography-computed tomography (PET-CT) [10]. Complete physical examination, especially examinations on 12 pairs of cranial nerves and lymph nodes of the neck, can effectively affect the therapeutic effects on NPC. Pharyngorhinoscopy can detect patients' lesser tubercles, granulomatous eminence, or frequent hemorrhage. EB virus is closely related to the incidence of NPC and can be adopted as the effective index of the adjuvant diagnosis of NPC [11, 12]. However, the above laboratory examination operations are complicated, and the accuracy of the results fluctuates greatly. In terms of imaging, chest CT is suitable for patients aged above 50, and they can effectively display lung metastasis or mediastinal lymph node metastasis among patients [13, 14]. PET-CT is suitable for patients with late NPC, and it can clearly show neck lymphadenectasis or distant metastasis. MRI imaging is a widely applied imaging technology at present and is characterized by a wide scanning range, numerous parameters, noninvasion, and high-resolution soft tissue [15].

Deep learning is a new research direction of machine learning. It is a series of algorithms created by data processed and decision-making mode created by the human brain [16, 17]. Convolutional neural network (CNN) is a feedforward neural network (FNN), which usually includes data input layer, operation layer, activation layer, pooling layer, and fully connected layer. It is a neural network. Convolution operation replaces traditional matrix multiplication operation. CNN can recognize the spatial relationship between data very well and show good application prospect in image classification, video recognition, and medical image processing [18]. The traditional CNN model adopts the convolution kernel method to extract features. Each convolution kernel represents a network training operator. Feature extraction is a digital process. The original image is transformed into the model for recognition and processing to obtain the most effective image features. However, its advantage is the attraction of extra parameters to increase the computation amount. The MRI image contains very rich and subtle structural information. The computation amount of algorithm is huge, and the operation lasts long when the traditional CNN model is used. Hence, a multipath dense connection structure (MDCS) was proposed to optimize the operation of feature extraction and the traditional CNN algorithm. Besides, the image super-resolution reconstruction algorithm optimized CNN (OPCNN) algorithm was designed and combined with the MRI image to investigate the diagnosis of NPC lesions, which is expected to provide help for clinical imaging diagnosis.

Deep learning is a new research direction of machine learning. It is a series of algorithms born by human brain processing data and creating patterns for decision-making. Convolutional neural network (CNN) is a feedforward neural network, which usually includes the data input layer, operation layer, activation layer, pooling layer, and fully connected layer. It is a neural network in which convolution operation replaces traditional matrix multiplication operation. CNN can well-identify the spatial relationship between data and has good application prospects in image classification, video recognition, medical image processing, etc. Therefore, this study combines the deep learning algorithm and MRI images to study the diagnosis of nasopharyngeal carcinoma lesions, in expectation to provide help for clinical imaging diagnosis.

2. Materials and Methods

2.1. Research Object. Fifty-four patients with nasopharyngeal carcinoma treated in the hospital from March 15, 2019, to July 20, 2021, were collected in this study, comprising 37 males and 17 females. All patients participated voluntarily and signed informed consent before the implementation of the project. All the contents in the research had been approved by ethics committee of the hospital.

Inclusion criteria were stated as follows: (1) patients with squamous cell carcinoma diagnosed by pathology; (2) patients who had not received radiotherapy and chemotherapy; (3) patients without metal dentures; (4) patients who voluntarily signed informed consent; (5) patients with good inspection compliance.

Exclusion criteria were stated as follows: (1) patients with contraindications to MRI; (2) patients with a history of drug allergy; (3) patients with surgical treatment; (4) patients with mental diseases; (5) patients with incomplete clinical data.

2.2. Magnetic Resonance Imaging Examination Method. 3.0T superconducting magnetic resonance scanning equipment was used in the study. The patient was placed in the supine position on the examination table, the patient's nose tip was placed in the center of the head and neck coil, and the laser positioning line was located at the nose tip for routine MRI and dynamic MRI enhanced scanning.

Conventional MRI: (1) axial fat-suppressed T2-weighted imaging (T2WI) sequence: repetition time, 7500 ms; echo time, 90 ms; visual field, 230×230 mm; layer spacing, 1.2 mm; layer thickness, 5 mm; and excitation time, 3 times; (2) axial diffusion-weighted imaging (DWI): repetition time, 3200 ms; echo time, 80 ms; visual field, 230×230 mm; layer spacing, 1.2 mm; layer thickness, 5 mm; and excitation time, 10 times.

Dynamic MRI enhancement (DCE-MRI): the contrast agent was gadopentetic-diethylenetriamine pentaacetic acid (Gd-DTPA) (specification: 100 mL/bottle; flow rate: 3 mL/s;

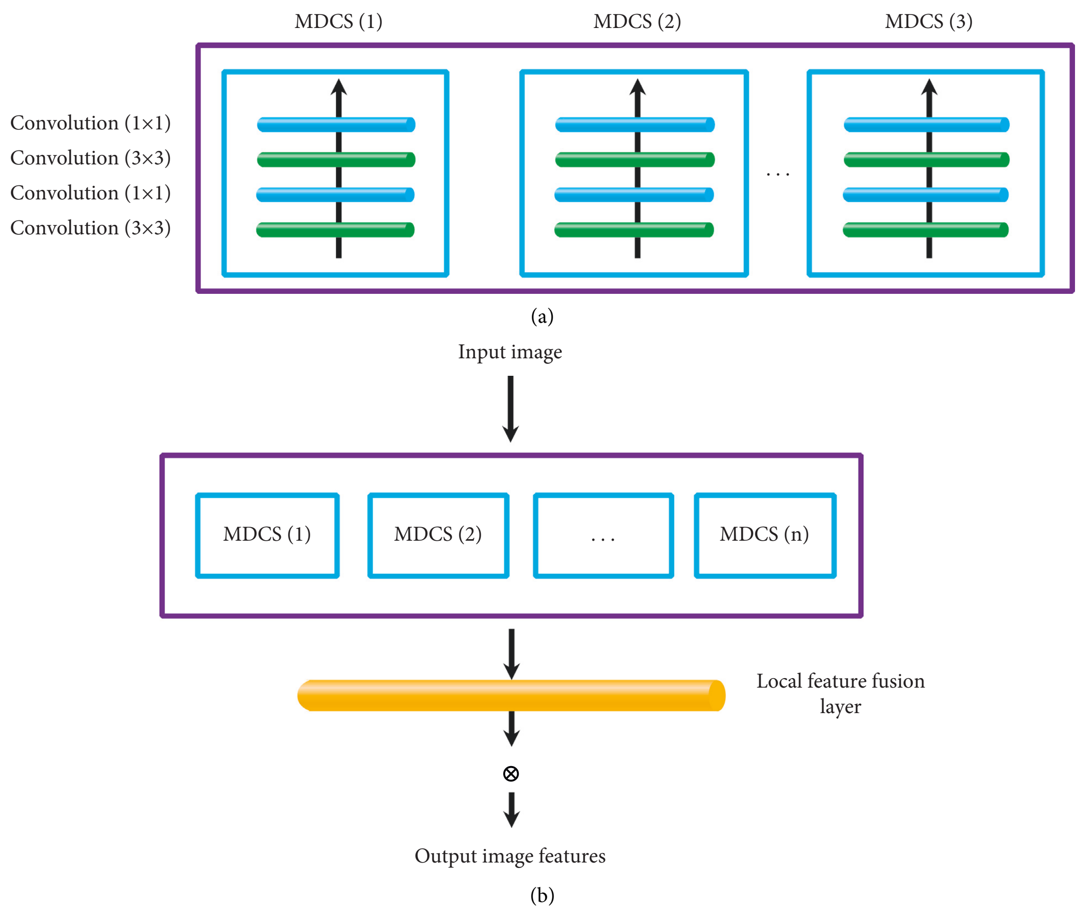

FIGURE 1: MDCS framework. (a) Schematic diagram of the multipath dense convolution block. (b) Schematic diagram of the multichannel dense connection structure.

dose, 0.2 mmol/kg; and fire rate, 2.1 mL/s). Axial 3D-T1 fast gradient self-selected echo sequence: repetition time, 3.52 ms; echo time, 1.42 ms; visual field, 230 × 230 mm; layer spacing, 1.2 mm; layer thickness, 5 mm; and excitation time, 1 time.

Each sequence of images was sent to the workstation for processing. The quantitative parameters of permeability and tumor focus were measured as follows: K^{trans} (the amount of contrast medium entering the extracellular space from blood per unit volume of tissue in unit time), K_{ep} (the amount of contrast medium entering the blood vessel from the extracellular space in unit time), V_{e} (the volume of extracellular space in unit volume of tissue), and the apparent diffusion coefficient (ADC) value.

2.3. Image Super-Resolution Reconstruction Algorithm Based on Optimized Convolutional Neural Network. Conventional neural network (CNN) was generally composed of the input layer, convolution layer, and activation layer. The convolution operation in the convolution layer could be regarded as the inner product operation of image and convolution kernel. It is assumed that the sliding step size is l , the convolution kernel size is r, the boundary filling is u , and the input image size is $p * q$. Equations (1) and (2) could be obtained as follows:

$$p' = \frac{(p - r + 2u)}{l} + 1, \tag{1}$$

$$q' = \frac{(q - r + 2u)}{l} + 1. \tag{2}$$

Here, $p' \times q'$ indicates the size of the output feature map. ReLU activation function was used by the activation layer to complete the mapping of features, introduce nonfeature expression for features, and enhance the expression ability of the network. The expression of ReLU activation function could be expressed as

$$h(x) = \begin{cases} 0, & x < 0, \\ x, & x \geq 0. \end{cases} \tag{3}$$

The feature extraction part was a digital process that could be recognized and processed by converting the original image into a model to obtain the most effective image features. The traditional CNN model used the convolution kernel method for feature extraction, and each convolution kernel represented an operator for network

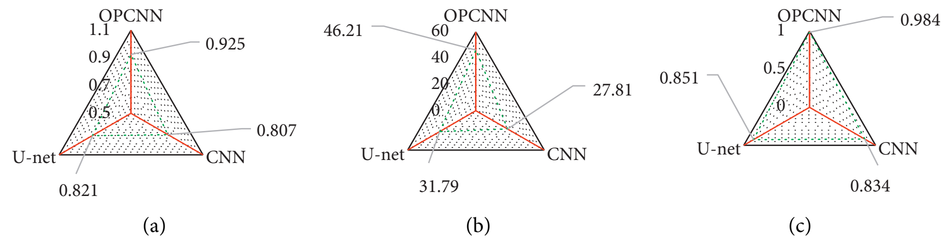

FIGURE 2: Quality comparison of tumor segmentation results of different algorithms. (a) Dice coefficient; (b) PSNR; (c) SSIM. * indicated that the difference was statistically significant compared with the OPCNN algorithm ($P < 0.05$).

training, to finally obtain richer image features, but the disadvantage was that it would attract additional parameters and increase the amount of calculation. It was considered that there was very rich and subtle structural information being contained in MRI images. Thus, a multipath dense connection structure (MDCS) (Figure 1) was designed in this study to optimize the feature extraction operation. Figure 1(a) shows a multipath dense convolution block. It could be observed that the size of the convolution block was 2×2 and 4×4. Figure 1(b) reveals the complete MDCS framework.

For the multipath dense convolution block, the image features extracted at layer j could be expressed as

$$H_j' = \lambda\left[v_j \times \langle H_0, H_1, H_2, \cdots H_{j-1}\rangle + c_j\right]. \quad (4)$$

In (4), H_j' represents the image features extracted by layer j, $\langle H_0, H_1, H_2, \cdots H_{j-1}\rangle$ represents the sum of the output features of the input layer and the previous layer $j-1$, v_j represents the weight of layer j, c_j represents the offset of layer j, and λ represents the activation function.

In addition, the adjustment of parameters was realized through a reverse neural network, which could lead to the problem of gradient disappearance. Therefore, this study also added local residual connection in multipath dense convolution blocks, which can be expressed as

$$H = H_{j-1} + H', \quad (5)$$

which indicated that H_{j-1} and H' could be quickly connected to reduce the computational complexity.

A multiway dense convolution block could greatly enrich the extracted image features, but it could also increase the parameters and produce many redundant features. Therefore, this study also introduced a local feature fusion block (LFFB) to reduce the dimension of image features. Then, the final output result could be expressed as

$$H' = \lambda\left[v_{LFFB} \times \langle h_0, h_1, h_2, \cdots h_{n-1}, h_n\rangle + c_{LFFB}\right]. \quad (6)$$

In (6), v_{LFFB} represents the weight of the local feature fusion block and c_{LFFB} represents the offset of the local feature fusion block. In this study, the image super-resolution reconstruction algorithm based on optimized CNN was set as OPCNN.

2.4. Image Evaluation Index. To analyze the performance of the OPCNN algorithm proposed in this study, the traditional CNN model and the U-net network model [19] were introduced as a comparison.

Dice coefficient, peak signal-to-noise ratio (PSNR), and structural similarity (SSIM) were used as indexes to evaluate the accuracy of segmentation results.

$$\begin{aligned}
\text{Dice} &= \frac{2TP}{(2TP + FP + FN)},\\
\text{PSNR} &= 10\log_{10}\left[\frac{(\text{maximum pixel value})2}{\text{MSE}}\right],\\
\text{MSE} &= \frac{\sum_{i=1}^{M}\sum_{j=1}^{N}\left(G^* - G\right)^2}{M \times N},\\
\text{SSIM} &= A_1(x, y) \times A_2(x, y) \times A_3(x, y),\\
A_1(x, y) &= \frac{\left(2\eta_x\eta_y + a_1\right)}{\left(\eta_x{}^2 + \eta_y{}^2 + a_1\right)},\\
A_2(x, y) &= \frac{\left(2\kappa_x\kappa_y + a_2\right)}{\left(\kappa_x{}^2 + \kappa_y{}^2 + a_2\right)},\\
A_3(x, y) &= \frac{\left(2\kappa_{xy} + a_3\right)}{\left(\kappa_x\kappa_y + a_3\right)}.
\end{aligned} \quad (7)$$

TP represents true positive, FP represents false positive, FN represents false negative, *MSE* represents the mean square error, G^* and G represent two images, $M \times N$ represents image size, η represents image pixel value mean, κ represents image pixel standard deviation, $A_1(x, y)$ represents brightness similarity, $A_2(x, y)$ represents contrast similarity, $A_3(x, y)$ represents structural similarity, and a_1, a_2, and a_3 were all parameters.

2.5. Statistical Methods. An SPSS19.0 version statistical software was used for data processing and analysis in this study. The measurement data were expressed by mean $\pm$ standard deviation, and counting data were expressed by percentage (%). One-way ANOVA was used for pairwise comparison. The difference was statistically significant ($P < 0.05$).

3. Results

3.1. Quality Comparison of Tumor Segmentation Results with Different Algorithms. Figure 2 shows the comparison of quality of tumor segmentation results of different

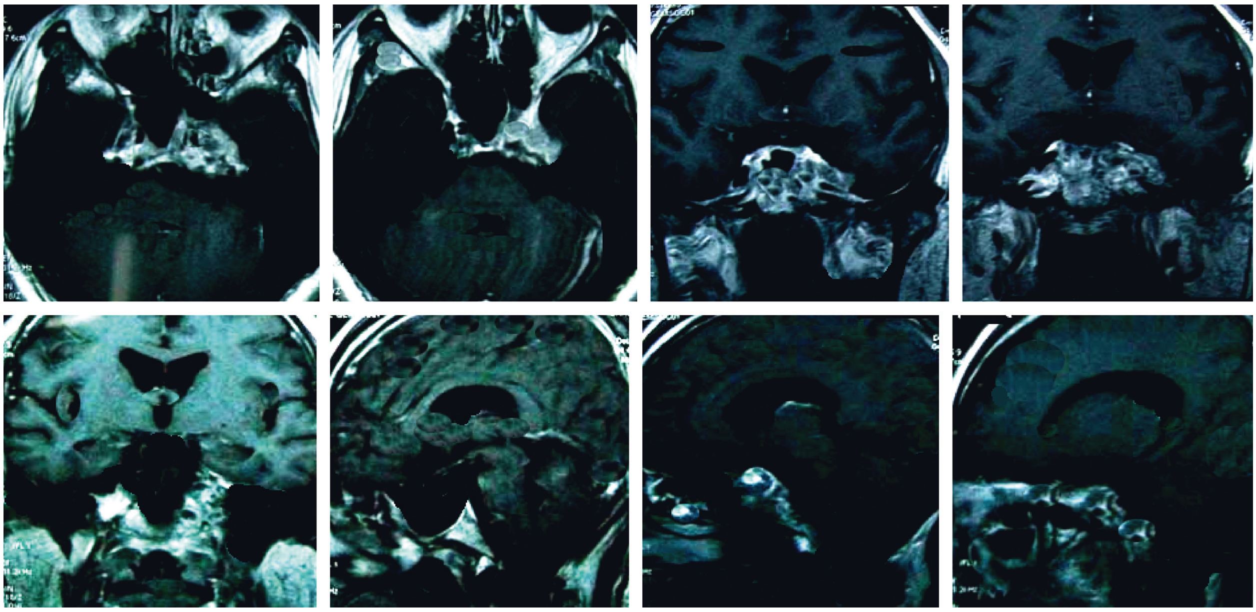

Figure 3: Conventional MRI scanning image of a patient with nasopharyngeal carcinoma.

algorithms. According to the results, Dice coefficients of the traditional CNN model, U-net network model, and OPCNN algorithm were 0.807, 0.821, and 0.925, respectively. PSNR of the traditional CNN model, U-net network model, and OPCNN algorithm reached 27.81, 31.79, and 46.21, respectively. SSIM of the traditional CNN model, U-net network model, and OPCNN algorithm amounted to 0.834, 0.851, and 0.984, respectively. The comparison showed that Dice coefficient, PSNR, and SSIM of the OPCNN algorithm were remarkably higher than those of the traditional CNN model and U-net network model. The differences demonstrated statistical significance ($P < 0.05$).

3.2. Image Features of Patients with Routine Magnetic Resonance Imaging. Figure 3 gives the conventional MRI scanning image of a patient with nasopharyngeal carcinoma. It was suggested that there were irregular abnormal signals on the outer wall of the posterior wall of the top of the nasopharynx. The image shows that the eustachian tube and parapharyngeal space narrowed, the mass involved the left sphenoid sinus upward, the left nasal muscle space, and carotid sheath forward. There were soft tissue shadows.

Figure 4 indicates that, among the 54 patients, 25 showed equal signal on T2WI image and 29 showed low signal; 18 cases of stage I, 22 cases of stage II, and 14 cases of stage III were diagnosed by routine MRI.

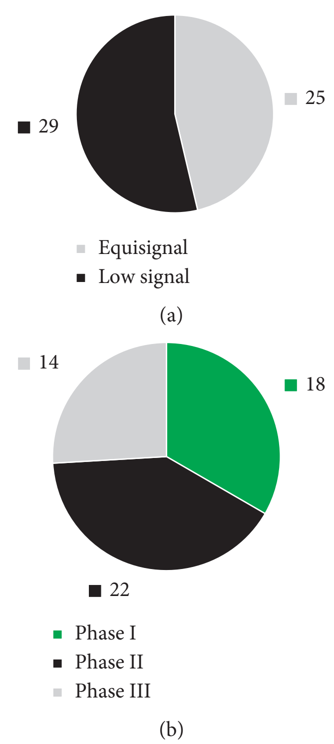

Figure. 4: Routine MRI scanning diagnosis results of nasopharyngeal carcinoma. (a) MRI features. (b) Staging diagnosis results.

3.3. Results of Quantitative Parameters of Tumor Focus and Healthy Side of Patients. Figure 5 shows the comparison of quantitative parameters (K^{trans}, K_{ep}, V_e, and ADC) between the tumor focus and the healthy side. It can be observed that K^{trans}, K_{ep}, and V_e in the tumor focus were significantly higher than those in the healthy side, and the difference was statistically significant ($P < 0.05$); ADC in the tumor focus was significantly lower than that in the healthy side, and the difference was statistically significant ($P < 0.05$).

3.4. Comparison of Diagnostic Effects between Conventional Magnetic Resonance Imaging and Dynamic Contrast-Enhanced Magnetic Resonance Imaging. Figure 6 displays the comparison of the sensitivity, specificity, and accuracy of T2WI, DWI, and DCE-MRI in staging diagnosis of NPC. According to Figure 6, DCE-MRI showed high diagnostic sensitivity, specificity, and accuracy of NPC staging, reaching over 85%, 75%, and 90%, respectively.

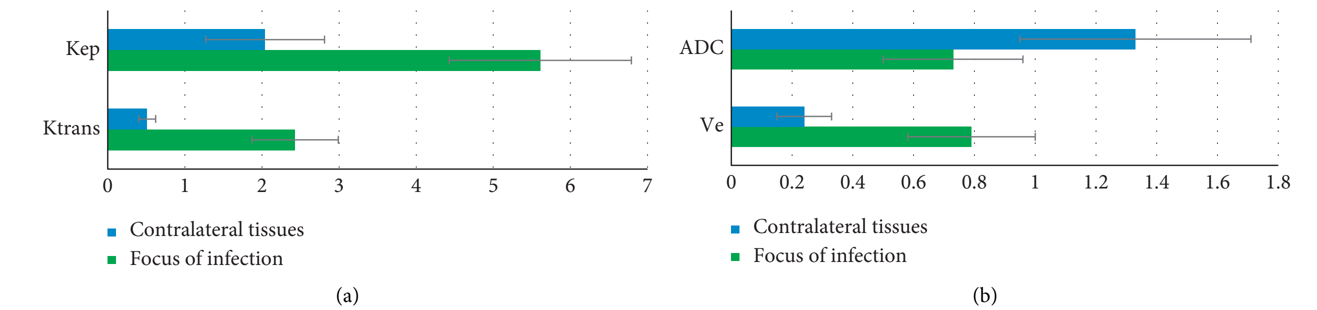

Figure 5: Comparison of quantitative parameters of tumor focus and healthy side of patients. (a) K^{trans} and K_{ep}; (b) V_e and ADC. * indicated that the difference was statistically significant compared with the tumor focus ($P < 0.05$).

3.5. Comparison of T2-Weighted Imaging, Diffusion-Weighted Imaging, Dynamic Contrast-Enhancement Magnetic Resonance Imaging, and Their Combined Detection in the Diagnosis of Nasopharyngeal Carcinoma. Figure 7 shows the comparison of diagnostic effects of T2WI, DWI, DCE-MRI, and their combined detection on nasopharyngeal carcinoma. It was suggested that the diagnostic sensitivity, specificity, and accuracy of T2WI for nasopharyngeal carcinoma were 87.14%, 74.08%, and 86.03%, respectively. The sensitivity, specificity, and accuracy of DWI in the diagnosis of nasopharyngeal carcinoma were 91.86%, 79.61%, and 89.41%, respectively. The sensitivity, specificity, and accuracy of DCE-MRI in the diagnosis of nasopharyngeal carcinoma were 93.07%, 81.31%, and 93.73%, respectively. The sensitivity, specificity, and accuracy were 96.08%, 84.14%, and 97.41%, respectively. The sensitivity, specificity, and accuracy of the combined detection of the three were slightly higher than those of T2WI, DWI, and DCE-MRI, which were 96.08%, 87.14%, and 97.41%, respectively.

3.6. Receiver Operating Characteristic Curve Analysis. Figure 8 indicates that the AUC area of T2WI for nasopharyngeal carcinoma diagnosis was 0.833, DWI for nasopharyngeal carcinoma diagnosis was 0.851, DCE-MRI for nasopharyngeal carcinoma diagnosis was 0.891, and the AUC area of combined three for nasopharyngeal carcinoma diagnosis was 0.942. The analysis of variance suggested that the AUC area of NPC diagnosed by combination of the three was significantly different from that diagnosed by single T2WI, DWI, and DCE-MRI ($P < 0.05$).

3.7. Comparison of Diagnostic Performance between Magnetic Resonance Imaging Based on Optimized Convolutional Neural Network Algorithm and Single Magnetic Resonance Imaging. Figure 9 illustrates that the diagnostic accuracy of MRI based on the OPCNN algorithm for nasopharyngeal carcinoma (93.2%) was significantly higher than that of single MRI (76.4%). The difference was statistically significant ($P < 0.05$).

4. Discussion

NPC is one of the conventional head and neck malignant tumors. Because its early symptom is not specific, the early diagnostic effect is usually unsatisfactory. Early detection of NPC lesions is beneficial to the clinical treatment effect and the prognosis of patients' quality of life [20–22]. At present, deep learning combined with the MRI technology is applied in tumor screening more significantly. The images obtained by different sequences show their respective advantages. Hence, a traditional CNN structure-based image super-resolution reconstruction algorithm OPCNN was proposed at first, and the traditional CNN model and U-net network model were introduced, compared, and analyzed.

The results revealed that Dice coefficient, PSNR, and SSIM of the OPCNN algorithm were all, obviously, higher than those of the traditional CNN model and U-net network model, and the differences showed a statistical meaning ($P < 0.05$). The results were consistent with that obtained by Ai et al. [23]. It was indicated that the segmentation effect of the OPCNN algorithm on MRI images was superior to that of the traditional CNN model and U-net network model, and it demonstrated application and promotion values.

Based on the analysis of the imaging features of conventional MRI and OPCNN algorithm-based dynamic enhanced MRI of 54 NPC patients, 25 cases showed equal signal on T2WI and 29 showed low signal on T2WI. The comparison of quantitative parameters of tumor focus and health side tissues suggested that K^{trans}, K_{ep}, and V_e of tumor focus tissues were significantly higher than those of healthy side tissues, while ADC was apparently lower than that of healthy side tissues. The differences were statistically significant ($P < 0.05$), which indicated that MRI quantitative parameters, including K^{trans}, K_{ep}, V_e, and ADC could be viewed as the effective indexes of diagnosing NPC [24, 25]. In terms of single-sequence MRI images, it was found out in the research that the diagnostic sensitivity (over 85%), specificity (over 75%), and accuracy (over 90%) of DCE-MRI in the NPC staging were all slightly higher than those of T2WI and DWI. The results showed that the application effect of DCE-MRI in NPC diagnosis was superior to that of conventional MRI. The combination of multiple detection methods was also common in clinical disease diagnosis [26].

Besides, it was also shown in the research that the sensitivity, specificity, and accuracy of the three combined methods in NPC detection were all slightly higher than those of T2WI, DWI, and DCE-MRI alone (96.08%, 87.14%, and 97.41%, respectively). Analysis of receiver operating characteristic (ROC) curves revealed that areas under curves

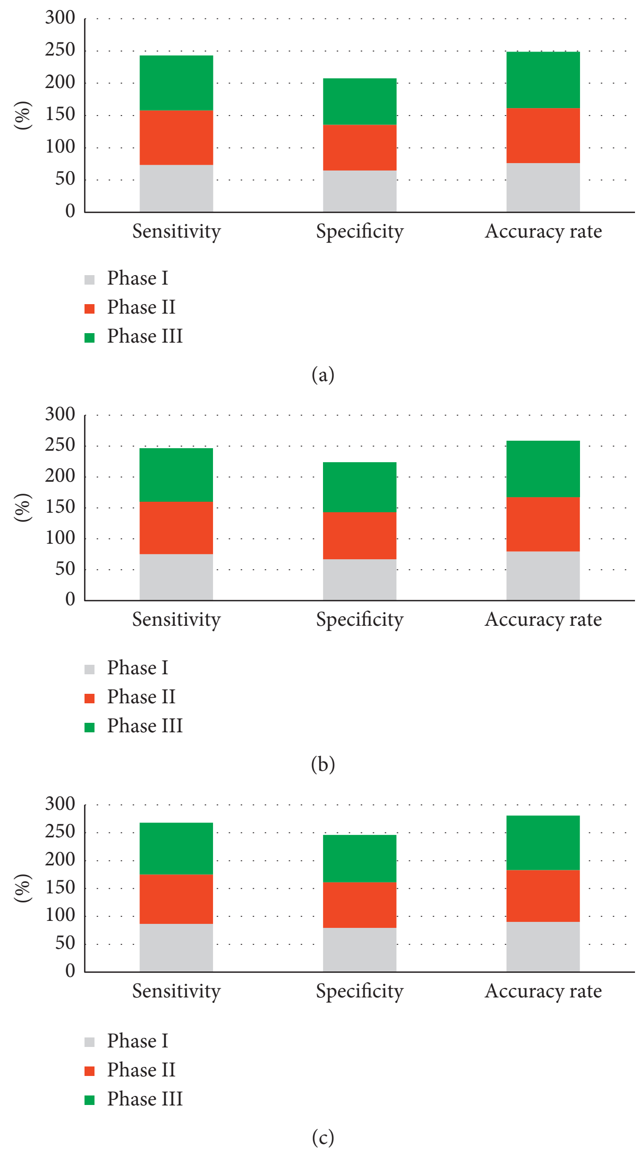

Figure 6: Sensitivity, specificity, and accuracy of T2WI, DWI, and DCE-MRI in the diagnosis of nasopharyngeal carcinoma stage. (a) The diagnosis result of T2WI for nasopharyngeal carcinoma stage; (b) the diagnosis result of DWI for nasopharyngeal carcinoma stage; (c) the diagnosis result of DCE-MRI for nasopharyngeal carcinoma stage; (d) the diagnosis result of T2WI, DWI, and DCE-MRI for nasopharyngeal carcinoma stage.

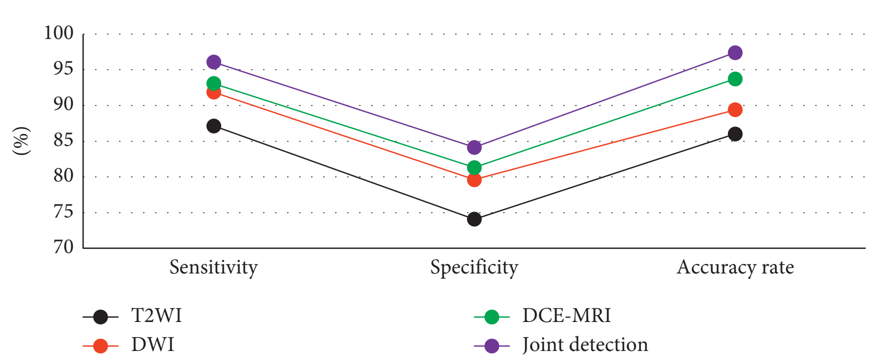

Figure 7: Comparison of T2WI, DWI, DCE-MRI, and their combined detection in the diagnosis of nasopharyngeal carcinoma.

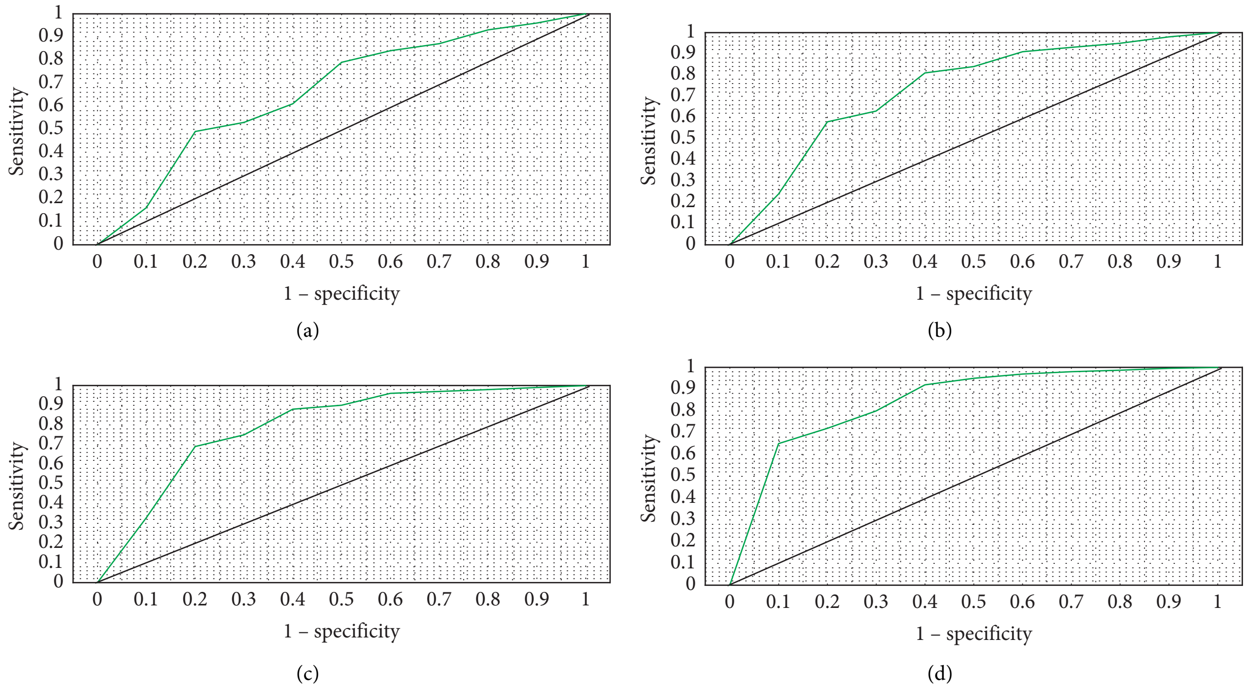

Figure 8: ROC curves of T2WI, DWI, DCE-MRI, and their combined detection. (a) T2WI; (b) DWI; (c) DCE-MRI; (d) their combined detection.

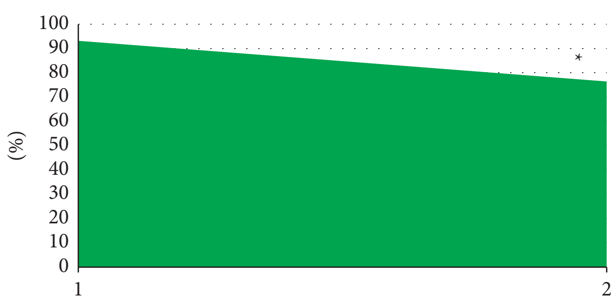

Figure 9: Comparison of diagnostic accuracy between MRI based on the OPCNN algorithm and single MRI. * indicated that the difference was statistically significant compared with MRI based on the OPCNN algorithm ($P < 0.05$).

(AUC) of three combined diagnosis showed statistical meaning ($P < 0.05$) compared with those of T2WI, DWI, and DCE-MRI alone. Hence, the combination of T2WI, DWI, and DCE-MRI could enhance the accuracy of NPC diagnosis dramatically.

5. Conclusion

A traditional CNN structure-based image super-resolution reconstruction algorithm OPCNN was proposed and applied in the clinical dynamic enhanced MRI scanning on 54 patients with NPC. The result showed that the diagnostic accuracy of OPCNN algorithm-based DCE-MRI remarkably improved. However, the diagnosis of NPC of different pathological types was not further divided and analyzed due to the small sample size of the included patients. In addition, only T2WI, DWI, and DCE-MRI were analyzed in combination without investigating the paired combination of three sequences. In subsequent studies, it is necessary to include and deeply discuss more NPC case data from different sources. To sum up, the research results provided the references for the development of the clinical diagnosis of NPC.

Data Availability

The data used to support the findings of this study are available from the corresponding author upon request.

Conflicts of Interest

The authors declare that they have no conflicts of interest.

References

[1] K. C. A. Chan, J. K. S. Woo, A. King et al., "Analysis of plasma Epstein–Barr virus DNA to screen for nasopharyngeal cancer," *New England Journal of Medicine*, vol. 377, no. 6, pp. 513–522, 2017.

[2] P. Sakthivel, A. Thakar, S. T. Arunraj, A. S. Bhalla, and R. Kumar, "Fusion 68Ga-Prostate-Specific membrane antigen PET/MRI on postoperative surveillance of juvenile nasal angiofibroma," *Clinical Nuclear Medicine*, vol. 45, no. 7, pp. 325-326, Article ID 32404701, 2020.

[3] F. E. Ucisik-Keser, T. L. Chi, Y. Hamid, A. Dinh, E. Chang, and D. Z. Ferson, "Impact of airway management strategies on magnetic resonance image quality," *British Journal of Anaesthesia*, vol. 117, no. 1, pp. 97–102, 2016.

[4] C. Rasch, R. Keus, F. A. Pameijer et al., "The potential impact of CT-MRI matching on tumor volume delineation in advanced head and neck cancer," *International Journal of*

Radiation Oncology, Biology, Physics, vol. 39, no. 4, pp. 841–848, Article ID 9369132, 1997.

[5] J.-H. Lee, "Huge tornwaldt cyst with otitis media with effusion," *Ear, Nose, & Throat Journal*, vol. 100, no. 5, pp. 528–530, Article ID 31760788, 2019.

[6] G. Yin, B. Tu, and L. Ye, "Correlation of intensity-modulated radiation therapy at a specific radiation dose with the prognosis of nasal mucous damage after radiotherapy," *Radiation and Environmental Biophysics*, vol. 59, no. 2, pp. 245–255, Article ID 32030481, 2020.

[7] B. Zhang, J. Tian, D. Dong et al., "Radiomics features of multiparametric MRI as novel prognostic factors in advanced nasopharyngeal carcinoma," *Clinical Cancer Research*, vol. 23, no. 15, pp. 4259–4269, Article ID 28280088, 2017.

[8] L. Zhao, J. Gong, Y. Xi et al., "MRI-based radiomics nomogram may predict the response to induction chemotherapy and survival in locally advanced nasopharyngeal carcinoma," *European Radiology*, vol. 30, no. 1, pp. 537–546, Article ID 31372781, 2020.

[9] B. Xiao, P. Wang, Y. Zhao, Y. Liu, and Z. Ye, "Nasopharyngeal carcinoma perfusion MRI," *Medicine*, vol. 99, no. 22, Article ID 32481470, 2020.

[10] C. Song, P. Cheng, J. Cheng et al., "Differential diagnosis of nasopharyngeal carcinoma and nasopharyngeal lymphoma based on DCE-MRI and RESOLVE-DWI," *European Radiology*, vol. 30, no. 1, pp. 110–118, Article ID 31372786, 2020.

[11] L. M. Wong, A. D. King, Q. Y. H. Ai et al., "Convolutional neural network for discriminating nasopharyngeal carcinoma and benign hyperplasia on MRI," *European Radiology*, vol. 31, no. 6, pp. 3856–3863, Article ID 33241522, 2021.

[12] J. Wei, S. Pei, and X. Zhu, "Comparison of (18)F-FDG PET/CT, MRI and SPECT in the diagnosis of local residual/recurrent nasopharyngeal carcinoma: a meta-analysis," *Oral Oncology*, vol. 52, pp. 11–17, Article ID 26547126, 2016.

[13] N. S. Voon, F. N. Lau, R. Zakaria et al., "MRI-based brain structural changes following radiotherapy of Nasopharyngeal Carcinoma: a systematic review," *Cancer Radiotherapie*, vol. 25, no. 1, pp. 62–71, Article ID 33414057, 2021.

[14] H. Ma, Y. Qiu, H. Li et al., "Prognostic value of nodal matting on MRI in nasopharyngeal carcinoma patients," *Journal of Magnetic Resonance Imaging*, vol. 53, no. 1, pp. 152–164, Article ID 32860315, 2021.

[15] M. Beker-Acay, "Editorial for "MRI-based deep learning model for distant metastasis-free survival in locoregionally advanced nasopharyngeal carcinoma"," *Journal of Magnetic Resonance Imaging*, vol. 53, no. 1, pp. 179-180, Article ID 32940967, 2021.

[16] M. Hu, Y. Zhong, S. Xie, H. Lv, and Z. Lv, "Fuzzy system based medical image processing for brain disease prediction," *Frontiers in Neuroscience*, vol. 15, Article ID 714318, 2021.

[17] Y. Li, J. Zhao, Z. Lv, and J. Li, "Medical image fusion method by deep learning," *International Journal of Cognitive Computing in Engineering*, vol. 2, pp. 21–29, 2021.

[18] Z. Yu, S. U. Amin, M. Alhussein, and Z. Lv, "Research on disease prediction based on improved DeepFM and IoMT," *IEEE Access*, vol. 9, no. 99, Article ID 39043, 2021.

[19] L. Zhang, X. Wu, J. Liu et al., "MRI-Based deep-learning model for distant metastasis-free survival in locoregionally advanced nasopharyngeal carcinoma," *Journal of Magnetic Resonance Imaging*, vol. 53, no. 1, pp. 167–178, Article ID 32776391, 2021.

[20] A. D. King, J. K. S. Woo, Q. Y. Ai et al., "Complementary roles of MRI and endoscopic examination in the early detection of nasopharyngeal carcinoma," *Annals of Oncology*, vol. 30, no. 6, pp. 977–982, 2019.

[21] G. Orman, B. H. Tran, N. Desai et al., "Neuroimaging characteristics of nasopharyngeal carcinoma in children," *Journal of Neuroimaging*, vol. 31, no. 1, pp. 137–143, Article ID 32862510, 2021.

[22] A. W. L. Mui, A. W. M. Lee, V. H. F. Lee et al., "Prognostic and therapeutic evaluation of nasopharyngeal carcinoma by dynamic contrast-enhanced (DCE), diffusion-weighted (DW) magnetic resonance imaging (MRI) and magnetic resonance spectroscopy (MRS)," *Magnetic Resonance Imaging*, vol. 83, pp. 50–56, Article ID 34246785, 2021.

[23] Q.-Y. Ai, A. D. King, J. S. M. Chan et al., "Distinguishing early-stage nasopharyngeal carcinoma from benign hyperplasia using intravoxel incoherent motion diffusion-weighted MRI," *European Radiology*, vol. 29, no. 10, pp. 5627–5634, Article ID 30903340, 2019.

[24] Y. Feng, C. Cao, Q. Hu, and X. Chen, "Grading of MRI-detected skull-base invasion in nasopharyngeal carcinoma with skull-base invasion after intensity-modulated radiotherapy," *Radiation Oncology*, vol. 14, no. 1, 10 pages, Article ID 30654807, 2019.

[25] X. Zhong, L. Li, H. Jiang et al., "Cervical spine osteoradionecrosis or bone metastasis after radiotherapy for nasopharyngeal carcinoma? The MRI-based radiomics for characterization," *BMC Medical Imaging*, vol. 20, no. 1, 104 pages, Article ID 32873238, 2020.

[26] A. D. King, A. C. Vlantis, T. W. C. Yuen et al., "Detection of nasopharyngeal carcinoma by MR imaging: diagnostic accuracy of MRI compared with endoscopy and endoscopic biopsy based on long-term follow-up," *American Journal of Neuroradiology*, vol. 36, no. 12, pp. 2380–2385, Article ID 26316564, 2015.

Hindawi
Contrast Media & Molecular Imaging
Volume 2022, Article ID 4938587, 10 pages
https://doi.org/10.1155/2022/4938587

Research Article

Deep Convolutional Neural Network-Based Brain Magnetic Resonance Imaging Applied in Glioma Diagnosis and Tumor Region Identification

Zhen Chen, Ning Li, Changtao Liu, and Shiwei Yan

Department of Neurosurgery,
The First People's Hospital of Lianyungang/The Affiliated Lianyungang Hospital of Xuzhou Medical University,
Lianyungang 222000, Jiangsu, China

Correspondence should be addressed to Shiwei Yan; 15211010189@stu.cpu.edu.cn

Received 24 March 2022; Revised 3 May 2022; Accepted 5 May 2022; Published 24 May 2022

Academic Editor: M Pallikonda Rajasekaran

The aim of this study was to explore the application value of dynamic contrast-enhanced magnetic resonance imaging (DCE-MRI) based on a convolutional neural network (CNN) algorithm in glioma diagnosis and tumor segmentation. 66 patients with gliomas who were diagnosed and treated in the hospital were selected as the research objects. The patients were rolled into the high-grade glioma group (HGG, 46 cases) and the low-grade glioma group (LGG, 20 cases) according to the World Health Organization glioma grading standard. All patients received a conventional plain scan and a DCE-MRI. Parameters such as volume transfer constant (K^{trans}), rate constant (K_{ep}), extracellular volume (V_e), and mean plasma volume (V_p) were calculated, and the parameters of patients of each grade were analyzed. The efficacy of each parameter in diagnosing glioma was analyzed through a receiver operating characteristic curve. All images were segmented by the CNN algorithm. The CNN algorithm showed good performance in DCE-MRI image segmentation. The mean, standard deviation, kurtosis, and skewness of K^{trans} and V_e, the standard deviation and skewness of K_{ep}, and the mean and standard deviation of V_p were statistically considerable in differentiating HGG and LGG ($P < 0.05$). ROC analysis showed that the standard deviation of K^{trans} (0.885) had the highest diagnostic accuracy in distinguishing HGG and LGG. The values of K^{trans}, V_e, and V_p were positively correlated with Ki-67 ($r = 0.346$, $P = 0.014$; $r = 0.335$, $P = 0.017$; $r = 0.323$, $P = 0.022$). In summary, the CNN-based DCE-MRI technology had high application value in glioma diagnosis and tumor segmentation.

1. Introduction

Glioma is one of the most common primary tumors in clinical practice. Clinical statistics showed that it is responsible for 81% of central nervous system malignancies [1–3]. In general, tumors are classified into low grade (grades I and II) and high grade (grades III and IV) according to the degree of malignancy. Clinical data showed that more than half of patients with glioma have glioblastoma, the most malignant form of brain cancer. In recent years, surgery and radiotherapy and chemotherapy have made continuous progress, but clinical data showed that the survival time of patients with comprehensive treatment is still less than 15 months, and their prognosis is also one of the worst among all tumor patients [4–6]. Almost all gliomas develop into the highest-grade gliomas. Clinical data showed that the average time for grade II and III gliomas to progress to IV is five years and two years, respectively. The incidence and mortality of glioma are high. Relevant clinical studies showed that the annual incidence of glioma in China is 3–6/100,000, and the annual death rate is as high as 30,000. In recent years, the incidence of this disease is also showing an increasing trend year by year. Statistics showed that the incidence of glioma in China is increasing by 1.2%. This disease poses a huge threat to human life and health [7, 8].

Once a glioma is diagnosed, patients do not survive for more than two years. Therefore, the early diagnosis of glioma is very important for the treatment and prognosis of the disease. At present, glioma can be graded by detecting molecular markers of glioma [9]. However, these methods are not widely used because of their high cost, the need for a large amount of tumor tissue, and the subjective influence of staining reagents and doctors. And these tests are invasive and cannot be used again in living tissue, which is why they are not widely available. With the rapid development of imaging technology, diseases can be diagnosed by various imaging methods. Magnetic resonance imaging (MRI) is one of the most important methods for the diagnosis of glioma [10–12].

How to segment tumor regions from brain MRI images of patients has always been a key and difficult point in the clinical diagnosis of glioma. At present, the most important method for regional segmentation of tumors is still manual segmentation by doctors. Such a segmentation method not only requires doctors to master strong professional knowledge but also wastes a lot of time and increases the workload of doctors. Therefore, the study of an automatic segmentation method of glioma has great positive significance for the diagnosis and treatment of glioma. However, the infiltration of tumor cells into surrounding tissues makes the tumor boundary blurred [13]. In addition, affected by the imaging principle of the MRI image itself, the grayscale range of images obtained by the same patient under different conditions is different. These characteristics of glioma lead to increased difficulty in image segmentation, so the traditional image segmentation methods cannot achieve good segmentation results. In recent years, the deep convolutional neural network (CNN) algorithm has shown considerable advantages in computer vision compared with other traditional machine learning algorithms. When the CNN algorithm performs image segmentation, it directly takes the original image as input and does not need to manually extract features. It can directly extract representative features from the image [14]. At present, many scholars have applied the CNN algorithm to glioma image segmentation [15, 16]. However, its segmentation effect varies greatly for different patients. In general, the CNN algorithm has a high application prospect and value in the segmentation of glioma. However, there is still a long way to go before it can be put into clinical application [17].

In this research, patients with glioma were taken as the research object, and dynamic contrast-enhanced (DCE)-MRI under the CNN algorithm was used to diagnose and segment patients with tumors, and the differences between the DCE-MRI-related parameters of patients with glioma of different grades were discussed and analyzed, to provide a good reference and basis for the diagnosis and treatment of clinically related diseases.

2. Research Methods

2.1. Research Objects. From March 2019 to March 2020, 66 patients with gliomas in hospital were selected as the research objects, including 36 male patients and 30 female patients. The mean age of the patients was 53.6 ± 11.3 years. According to the World Health Organization (WHO) glioma grading standard, the patients were rolled into the high-grade glioma group (HGG, 46 cases) and the low-grade glioma group (LGG, 20 cases). All studies obtained patient informed consent and this study had been approved by the ethics committee of the hospital.

Inclusion criteria were as follows: patients diagnosed with glioma after case diagnostic screening; patients with complete imaging and follow-up data; and patients with complete follow-up records. Exclusion criteria were as follows: patients with other malignant tumors at the same time; patients with other serious underlying diseases or with dysfunction of important organs such as the heart, lung, liver, and kidney; those who died of diseases or accidents other than glioma; and those who suffered from claustrophobia.

2.2. Imaging Studies. All cases were scanned by 3.0TMR with an 8-channel phased-array head coil. All patients underwent a routine plain scan and a DCE-MRI before surgery. Specific scanning parameters of conventional sequences were T1WI (TR/TE: 400 ms/2.48 ms, FOV: $230 \times 230\,mm^2$, matrix: 320×256, and bandwidth: 360 Hz/Px) and T2WI (TR/TE: 5,090 ms/91 ms, FOV: $230 \times 230\,mm^2$, matrix: 320×320, and bandwidth: 203 Hz/Px), with a layer thickness of 5 mm. DCE-MRI used cross-sectional T1 gradient 3D sequence scanning, and three groups of Tl-Vibe plain scans were performed before the examination (TR/TE: 3.89/1.31 ms, layer thickness: 3mm, FOV: $230 \times 230\,mm^2$; matrix: 224×161; flip angles: 5°, 10°, and 15°). A dynamic enhanced examination was then performed, including a total of 40 acquisitions. After the third collection, the contrast agent was injected through the cubital vein at a rate of 2.0–4.0 mL/s and a total amount of 0.1 mmol/kg. All localization levels of the DCE-MRI examination were consistent. The flip angle of the dynamic acquisition sequence was 15°, and the other parameters were the same as the previous plain scan sequence.

2.3. Image Processing. All MRI images were processed using the CNN algorithm. The specific image processing process includes the input image, CNN, heat map, CRF, output image, and other steps. The specific image processing process is shown in Figure 1. The CNN algorithm mainly includes a convolutional layer, a pooling layer, a fully connected layer, and a Softmax classification layer. The detailed CNN model is shown in Figure 2.

$$x_j^l = f\left(\sum_{i\in M_j} x_j^{l-1} \bullet K_{ij}^l + b_j^l\right), \tag{1}$$

where l is the number of layers, K is the convolution kernel, x_j^{l-1} is the feature map output by the previous layer, K_{ij}^l is the weight of the convolution kernel, b is the bias value, and $f(\bullet)$ is the activation function. The convolution operation has three modes of full convolution, same convolution, and valid convolution. The specific definitions are as follows.

(I) Full convolution

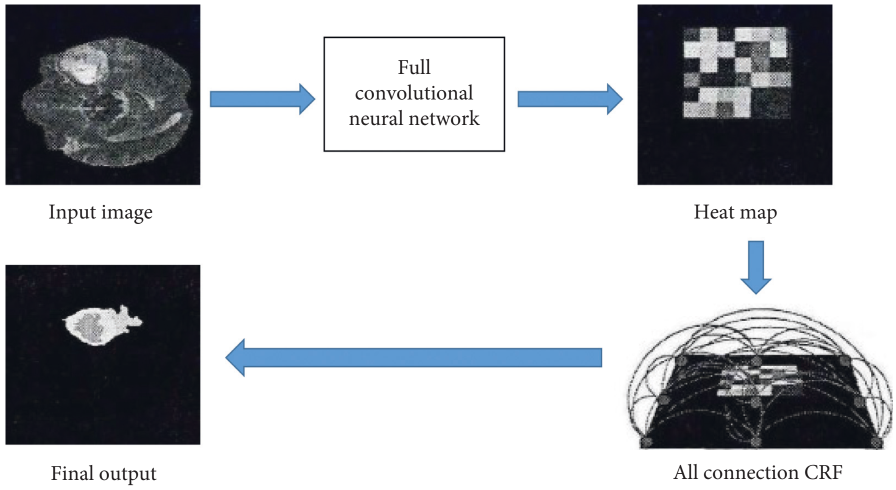

Figure 1: Image processing flow.

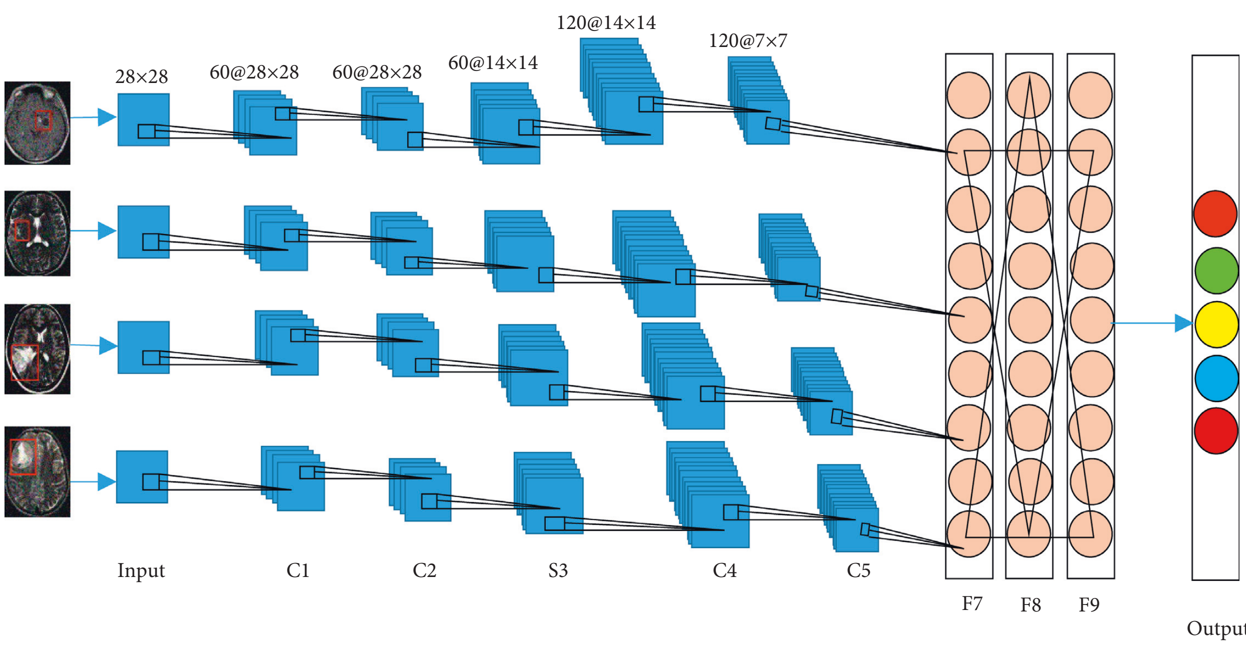

Figure 2: CNN model.

$$\begin{cases} y = \text{conv}\left(x, w, \prime\text{full'}\right) = \left(y(1), \ldots, y(t), \ldots, y(n+m-1)\right) \in R \\ y(t) = \sum_{i=1}^{m} x(t-i+1) \bullet w(i) \quad t = 1, 2, \ldots, n+m-1 \end{cases} . \tag{2}$$

(II) Same convolution

$$y = \text{conv}\left(x, w, \prime\text{same'}\right) = \text{center}\left(\text{conv}\left(x, w, \prime\text{full'}\right), n\right) \in R. \tag{3}$$

(III) Valid convolution

$$\begin{cases} y = \text{conv}\left(x, w, \prime\text{valid'}\right) = \left(y(l), \ldots, y(t), \ldots, y(n+m-1)\right) \in R \\ y(t) = \sum_{i=1}^{m} x(t+i-1) w(i) \quad t = 1, 2 \ldots, n+m-1 \end{cases} . \tag{4}$$

The pooling layer can reduce the possibility of overfitting and improve the fault tolerance of the model. The calculation of the pooling layer is as follows:

$$x_j^l = f\left(\beta_j^l \text{down}\left(x_j^{l-1}\right) + b_j^l\right). \tag{5}$$

do wn$(\bullet)$ is the downsampling function, and β and b are the multiplicative bias and the additive bias, respectively. There are two common pooling operations in deep learning-based multifeature fusion classification algorithms, namely, average pooling and maximum pooling. The average pooling refers to taking the mean value within the filter range as the pooled output. The maximum value pooling refers to using the maximum value within the filter range as the pooling output.

As for the full connection process, in the multifeature fusion classification algorithm under deep learning, the full connection layer is a network node arranged linearly and encodes the output result of the previous layer into a one-dimensional vector. The fully connected layer is defined as follows:

$$x^l = f\left(w^l x^{l-1} + b^l\right). \tag{6}$$

In the above equation, w^l is the network weight coefficient, x^{l-1} is the output feature map of the previous layer, and b^l is the fully connected layer bias item.

Softmax classification layer is a multiclassifier connected to the fully connected layer, which can complete more than two classification tasks and convert multiple outputs into probability values in the (0,1) interval. In logistic regression, the training set is $T = \{(x^{(1)}, y^{(1)}), \ldots, (x^{(m)}, y^{(m)})\}$, the input sample is $x^i \in R^n$, and $y^{(i)}$ is the sample label. Then, it is assumed that the function (hypothesis function) is defined as follows:

$$h_\theta(x) = \frac{1}{\left(1 + e^{-\theta_X^T}\right)}. \tag{7}$$

The cost function $J(\theta)$ is minimized as follows:

$$J(\theta) = -\frac{1}{m}\left[\sum_{i=1}^{m} y^{(i)}\log h_\theta\left(x^{(i)}\right) + \left(1 - y^{(i)}\right)\log\left(1 - h_\theta\left(x^{(i)}\right)\right)\right]. \tag{8}$$

The calculation of Softmax is as follows:

$$h_{(\theta)}\left(x^{(i)}\right) = \begin{bmatrix} p\left(y^{(i)} = 1|x^{(i)}, \theta\right) \\ p\left(y^{(i)} = 2|x^{(i)}, \theta\right) \\ \cdots \\ p\left(y^{(i)} = k|x^{(i)}, \theta\right) \end{bmatrix} = \frac{1}{\sum_{j=1}^{k} e^{\theta_j^T x^{(i)}}} \begin{bmatrix} e^{\theta_1^T x^{(i)}} \\ e^{\theta_2^T X^{(i)}} \\ \cdots \\ e^{\theta_K^T x^{(i)}} \end{bmatrix}. \tag{9}$$

Learning on the training sample T minimizes the damage function of Softmax. The expression of the minimum loss function is as follows:

$$J(\theta) = -\frac{1}{m} = \left[\sum_{i=1}^{m}\sum_{j=1}^{k} 1\left\{y^{(i)} = j\right\}\log\frac{e^{\theta_i^T x^{(i)}}}{\sum_{i=1}^{k} e^{\theta_i^T x^{(i)}}}\right], \tag{10}$$

where $1\{y^{(i)} = j\}$ indicates that if $y = j$, the value is 1; otherwise, it is 0; that is, the smaller the loss function, the closer the expected target.

The mean square error (MSE), peak signal-to-noise ratio (PSNR), and structural similarity (SSIM) are used to evaluate the segmentation effect quantitatively. The specific calculation methods of the three indicators are as follows:

$$\begin{aligned} \mathrm{MSE} &= \frac{1}{mn}\sum_{i=0}^{m-1}\sum_{j=0}^{n-1}[I(i,j) - K(i.j)]^2, \\ \mathrm{PSNR} &= 10\cdot\log_{10}\left(\frac{\mathrm{MAX}_I^2}{\mathrm{MSE}}\right) = 20\cdot\log_{10}\left(\frac{\mathrm{MAX}_I}{\sqrt{\mathrm{MSE}}}\right), \\ \mathrm{SSIM}(x,y) &= \frac{\left(2\mu_x\mu_y + c_1\right)\left(2\sigma_{xy} + c_2\right)}{\left(\mu_x^2\right) + \mu_y^2 + c_1)\left(\sigma_x^2 + \sigma_y^2 + c_2\right)}. \end{aligned} \tag{11}$$

2.4. Pathological Specimen Analysis. All patients' tumors were surgically removed, then the tumor specimens were analyzed, and the gliomas were classified into grades I to IV. Ki-67 immunohistochemical staining was performed on the obtained specimen, the whole specimen was browsed, and then the area with the highest positive expression density was selected. 1,000 tumor cells were counted under a 200× microscope, and the positive percentage of tumor cells was taken as the highest Ki-67 labeling index. The specific staining methods of Ki-67 were as follows: I. After samples were taken, the tissues were fixed with neutral formaldehyde for 24–48 hours, followed by conventional paraffin embedding treatment. II. The sample was sliced to 5~7 μm. III. The samples were put into 10 mM citric acid buffer and microwaved for 10 minutes. IV. The slices were cooled at room temperature for 20 minutes. V. Steps III and IV were repeated. VI. Slices were cooled at room temperature for 20 minutes before being removed from citric acid, washed twice with Tris-HCl buffer, and then left in Tris-HCl for staining. VII. Finally, Ki-67 labeling was carried out according to the conventional method.

2.5. Statistical Methods. Statistical analysis of all data relied on SPSS 11.0 to complete. Measurement data were expressed as the mean ± standard deviation ($\overline{x} \pm s$), and t-test was used to test the significance of patient data before and after surgery. The count data were expressed as actual number and percentage, and the significance test was carried out by χ^2 test. $P < 0.05$ was considered statistically considerable.

3. Results

3.1. Typical Case Image Display. The typical case images are shown in Figure 3. Analysis of Figure 3 shows that MRI can distinguish different grades of gliomas well. The CNN algorithm can segment lesions from MRI images of glioma patients more accurately.

3.2. Comparison of Histogram Parameters of K^{trans}, K_{ep}, V_e, and V_p Values in HGG and LGG. The comparison results of the histogram parameters of K^{trans}, K_{ep}, V_e, and V_p values of HGG and LGG are shown in Figure 4. Figure 4 shows that there were significant differences in mean value, standard deviation, kurtosis, and skewness of K^{trans} between the HGG group and the LGG group ($P < 0.05$). The mean value, kurtosis, and skewness of K_{ep} were significantly different between the two groups, $P < 0.05$. The mean value, standard deviation, kurtosis, and skewness of V_e were significantly different between the two groups, $P < 0.05$. There were significant differences in the mean and standard deviation of V_p between the two groups, $P < 0.05$.

3.3. Comparison of Histogram Parameters of Different Grades of Glioma. The comparison results of the histogram parameters of different grades of glioma are shown in Figure 5. There were significant differences in K^{trans} standard deviation, kurtosis, and skewness between grades II and III. K_{ep}

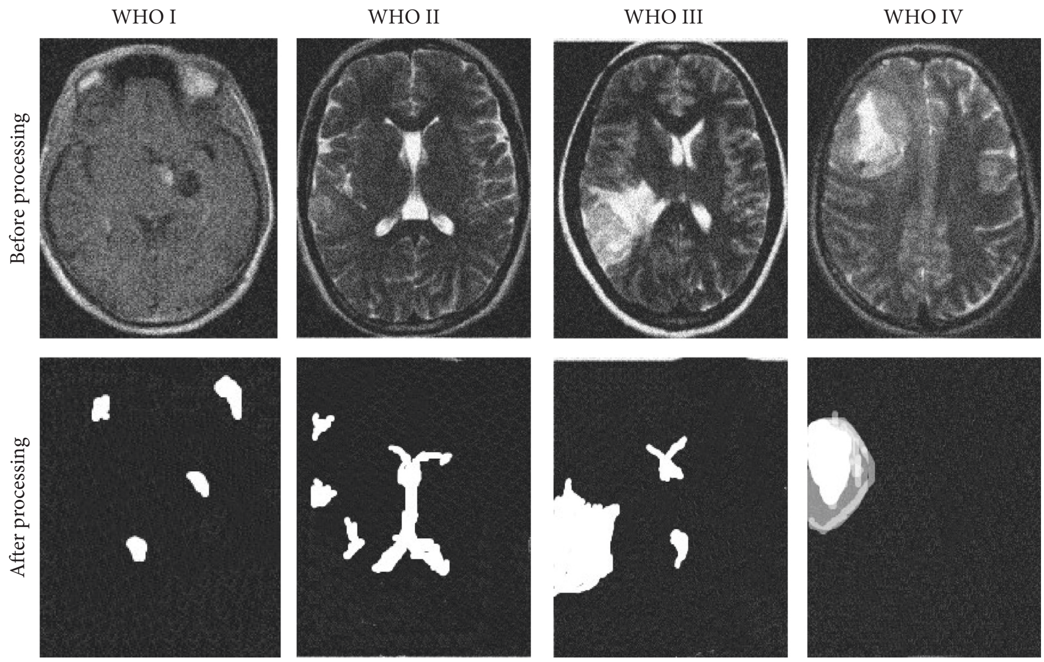

FIGURE 3: Typical case images.

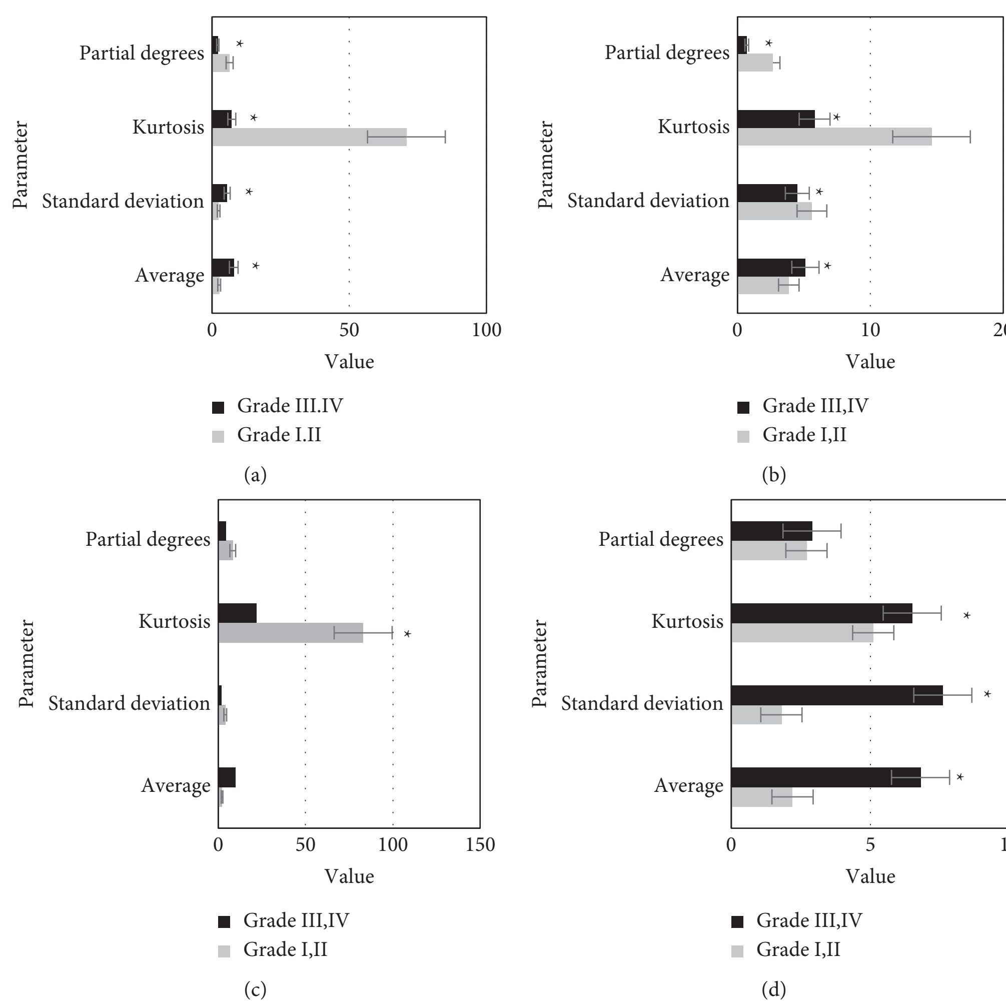

FIGURE 4: Comparison of histogram parameters of K^{trans}, K_{ep}, V_e, and V_p in HGG and LGG. (a) K^{trans}; (b) K_{ep}; (c) V_e; (d) V_p compared with the LGG group, $^*P < 0.05$.

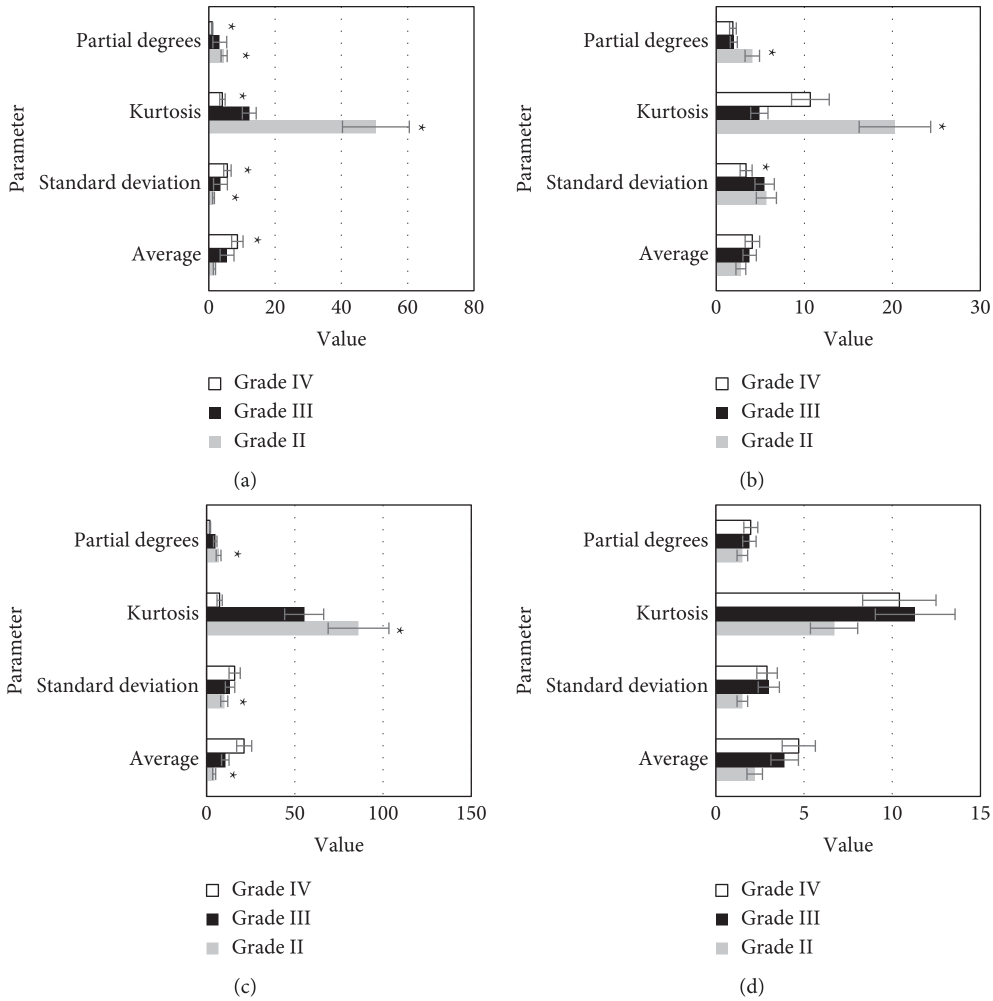

Figure 5: Comparison of histogram parameters of different grades of gliomas. (a) K^{trans}; (b) K_{ep}; (c) V_e; (d) V_p compared with grade III glioma, $^*P < 0.05$.

kurtosis and skewness were significantly different. The mean values of V_e were significantly different with $P < 0.05$. There were significant differences in K^{trans} average, kurtosis, and skewness between grades III and IV gliomas. K_{ep} standard deviation was significantly different. There were significant differences in mean value, standard deviation, kurtosis, and skewness of V_e, all $P < 0.05$.

3.4. Receiver Operating Characteristic (ROC) Analysis of K^{trans}, K_{ep}, V_e, and V_p Histogram Parameters in Glioma Grading. Table 1 and Figure 6 show the results of the efficacy analysis of K^{trans}, K_{ep}, V_e, and V_p histogram parameters for diagnosing glioma. The histogram parameters of K^{trans}, K_{ep}, V_e, and V_p all showed good performance in the diagnosis of glioma, especially the K^{trans} value had the best performance, and its standard deviation had the best diagnostic performance among all parameters.

3.5. Correlation between Ki-67 Index and Various Parameters in HGG and LGG. Figures 7 and 8 show the comparison results of the correlation between the Ki-67 index of HGG and LGG and various parameters, and the results of Ki-67 immunohistochemical staining. Analysis of Figure 7 shows that the Ki-67 index of patients with HGG was higher than that of patients with LGG. Analysis of Figure 8 shows that K^{trans}, V_e, and V_p were positively correlated with Ki-67, and K_{ep} had no correlation with Ki-67.

4. Discussion

Glioma is the most common intracranial primary tumor, which is characterized by high vascularization, high heterogeneity, and strong invasiveness. In recent years, despite the continuous advancement of surgical and chemotherapy techniques, the survival of glioma patients after comprehensive treatment is still very low [16]. Clinical studies showed that the survival of patients with gliomas will not exceed two years after diagnosis, and almost all LGG will develop into HGG [17]. The incidence of glioma has also shown an upward trend year by year. Glioma has high morbidity and mortality, which poses a huge threat to human life safety [18]. The diagnosis and grading of gliomas in the early stages of the disease have an important impact on

Table 1: The results of analysis of the efficacy of K^{trans}, K_{ep}, V_e, and V_p histogram parameters in diagnosing glioma.

		95% confidence interval (CI)	Sensitivity (%)	Specificity (%)
K^{trans}	Mean	0.88 (0.65,0.99)	88.6	85.1
	Standard deviation	0.88 (0.65,0.99)	84.2	85.7
	Kurtosis	0.88 (0.65,0.99)	93.8	77.7
	Skewness	0.88 (0.65,0.99)	95.5	77.7
K_{ep}	Standard deviation	0.88 (0.65,0.99)	44.3	100
	Skewness	0.81 (0.77,0.90)	88.1	86.2
V_e	Mean	0.83 (0.72,0.96)	83.9	94.1
	Standard deviation	0.78 (0.71,0.89)	77.2	68.8
	Kurtosis	0.85 (0.69,0.90)	74.4	85.5
	Skewness	0.83 (0.78,0.94)	79.8	86.7
V_p	Mean	0.88 (0.65,0.99)	88.2	77.3
	Standard deviation	0.77 (0.63,0.92)	95.5	70.1

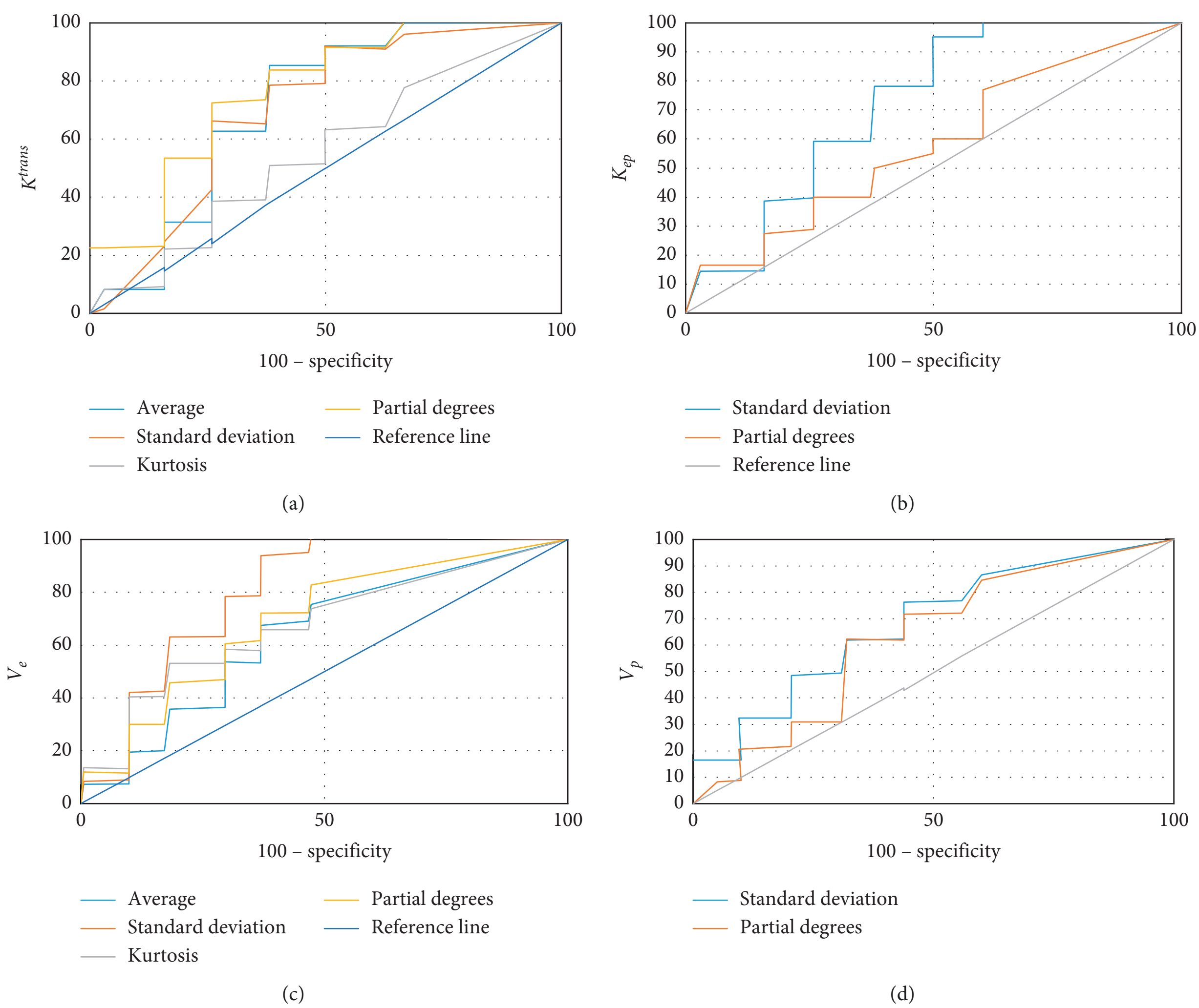

Figure 6: ROC curves of each parameter for diagnosing glioma. (a) K^{trans}; (b) K_{ep}; (c) V_e; (d) V_p.

the determination of the disease treatment plan and the prognosis of the disease. Many clinical studies suggested that microvascular proliferation is an important histological characteristic of gliomas in the brain, and the degree of microvascular proliferation also increases with the increase of tumor grade. Compared with normal blood vessels, tumor neovascularization is immature and its permeability is high, so it is easy to cause leakage of intravascular contrast agent. The above changes are one of the important indicators for the diagnosis of glioma [19].

In recent years, with the continuous progress and development of imaging technology, many new technologies

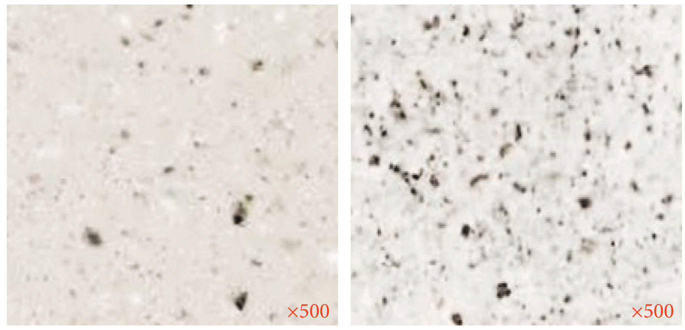

Figure 7: Comparison of Ki-67 index between HGG and LGG.

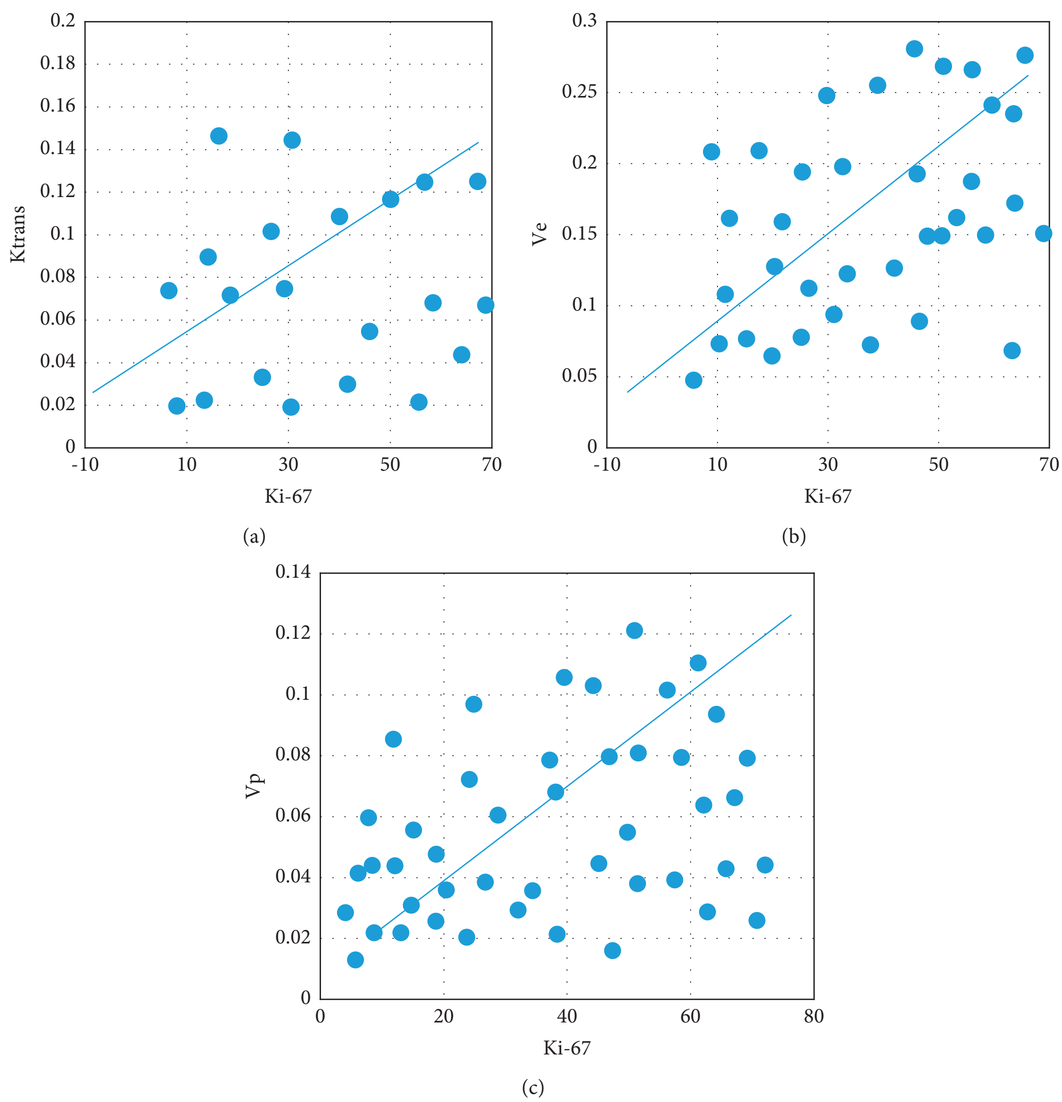

Figure 8: Correlation comparison between Ki-67 index and various parameters in HGG and LGG. (a) K^{trans}; (b) V_e; (c) V_p.

have been developed in the diagnosis of craniocerebral diseases. DCE-MRI is a novel functional MR imaging technique based on microvascular permeability and pharmacokinetic model assumptions. Based on the magnetic field changes caused by the leakage of contrast agent, it can quantitatively measure the microvascular permeability of gliomas and then noninvasively, dynamically, and quantitatively evaluate the functional properties of microvessels and improve the accuracy of glioma grading [20–22]. Quantitative parameters derived from the DCE-MRI hemodynamic model include the K^{trans}, K_{ep}, V_e, and V_p. In recent years, DCE-MRI has been widely used in the differential diagnosis of single brain metastases, primary central nervous system lymphoma (PCNSL), and glioma [23]. At present, the results are not uniform for the selection of optimal parameters and optimal thresholds for DCE-MRI in glioma grading. The reason may be that the quantitative parameters and arterial input function (AIF) are obtained in different ways in different studies, and the number of study cases will also have a certain impact on the results [24]. Therefore, the application value of DCE-MRI in the diagnosis of glioma needs further exploration and in-depth research. In this study, patients with glioma were diagnosed by DCE-MRI. The results showed that the mean, standard deviation, kurtosis, and skewness of K^{trans} and V_e, standard deviation and skewness of K_{ep}, and mean and standard deviation of V_p were statistically significant in differentiating HGG from LGG ($P < 0.05$). ROC analysis showed that the above values had good diagnostic performance for differentiating HGG from LGG, and K^{trans} had the highest standard deviation diagnostic accuracy. The standard deviation, kurtosis, and skewness of K^{trans}, kurtosis and skewness of K_{ep}, and mean value of V_e were statistically significant in differentiating grade II and III gliomas ($P < 0.05$). The mean, standard deviation, kurtosis, skewness of K^{trans} and V_e, and standard deviation of K_{ep} were statistically significant in differentiating grade III and IV gliomas ($P < 0.05$). K^{trans}, V_e, and V_p were positively correlated with Ki-67. This indicates that DCE-MRI histogram-related indicators are of great significance in the diagnosis and grading of glioma. This can provide important reference information for clinical treatment. This is consistent with the results of some previous studies.

In addition to grading gliomas after diagnosis, how to segment tumors from MRI images is also a focus and a difficulty in clinical research. At present, clinical segmentation of glioma tumor regions mainly relies on manual selection and division by doctors. This segmentation method is not only time-consuming and labor-intensive, but also the segmentation results are greatly influenced by the doctor's subjective opinion and require the doctor to have a strong professional knowledge reserve [25, 26]. This is a huge waste of time, manpower, and material resources. Therefore, it is necessary to develop an automatic tumor segmentation system. In recent years, deep CNN models have received extensive attention and applications in the field of medical image segmentation [27]. Abundant related research results showed that the CNN-based algorithm can directly use the original image as input, and automatically extract the characteristics of image features. It presented considerable advantages compared with traditional segmentation algorithms in the field of computer vision [28, 29]. At present, scientists have also done a lot of research on its application in glioma segmentation. For example, some scholars proposed a complex two-channel CNN model and applied it to the segmentation of glioma [30]. In this work, the CNN algorithm was applied to the segmentation of DCE-MRI images of glioma patients. The research results showed that CNN can better segment glioma lesions from the perspective of visual observation. In objective indexes, the CNN algorithm performed better than traditional segmentation algorithms on quantitative indexes such as MSE, PSNR, and SSIM. This shows that the CNN algorithm has high application value in DCE-MRI image segmentation.

5. Conclusion

Patients with glioma were taken as research objects, and MRI with the CNN algorithm was used to classify glioma and segment glioma. The results showed that the CNN algorithm had good performance in DCE-MRI image segmentation of glioma patients. The DCE-MRI histogram of glioma of different grades showed significant differences in K^{trans}, K_{ep}, V_e, and V_p, and other indicators, and the correlation between K^{trans} , K_{ep}, V_e, and V_p, and other indicators in Ki-67 also showed significant differences. In summary, CNN and DCE-MRI have high clinical application value in the diagnosis and differentiation of glioma. Nevertheless, there are still some defects in this work. For example, this research only analyzed the effect of DCE-MRI on the diagnosis of glioma and did not compare it with other diagnostic methods, which did not prove that DCE-MR is the best method for the diagnosis of glioma. In future studies and work, we will improve the above problems and further address them.

Data Availability

The data used to support the findings of this study are available from the corresponding author upon request.

Ethical Approval

This study was approved by the ethics committee of the hospital.

Consent

Informed consent was received from all patients who participated in this study.

Conflicts of Interest

The authors declare that there are no conflicts of interest.

References

[1] S. Xu, L. Tang, X. Li, F. Fan, and Z. Liu, "Immunotherapy for glioma: current management and future application," *Cancer Letters*, vol. 476, pp. 1–12, 2020.

[2] M. L. Suvà and I. Tirosh, "The glioma stem cell model in the era of single-cell genomics," *Cancer Cell*, vol. 37, no. 5, pp. 630–636, 2020.

[3] O. Gusyatiner and M. E. Hegi, "Glioma epigenetics: from subclassification to novel treatment options," *Seminars in Cancer Biology*, vol. 51, pp. 50–58, 2018.

[4] T. J. C. Wang and M. P. Mehta, "Low-grade glioma radiotherapy treatment and trials," *Neurosurgery Clinics of North America*, vol. 30, no. 1, pp. 111–118, 2019.

[5] C. J. Przybylowski, S. L. Hervey-Jumper, and N. Sanai, "Surgical strategy for insular glioma," *Journal of Neuro-Oncology*, vol. 151, no. 3, pp. 491–497, 2021.
[6] Z. Peng, C. Liu, and M. Wu, "New insights into long noncoding RNAs and their roles in glioma," *Molecular Cancer*, vol. 17, no. 1, p. 61, 2018.
[7] P. de Blank, P. Bandopadhayay, D. Haas-Kogan, M. Fouladi, and J. Fangusaro, "Management of pediatric low-grade glioma," *Current Opinion in Pediatrics*, vol. 31, no. 1, pp. 21–27, 2019.
[8] J. Bai, J. Varghese, and R. Jain, "Adult glioma WHO classification update, genomics, and imaging," *Topics in Magnetic Resonance Imaging*, vol. 29, no. 2, pp. 71–82, 2020.
[9] A. M. Miller, R. H. Shah, E. I. Pentsova et al., "Tracking tumour evolution in glioma through liquid biopsies of cerebrospinal fluid," *Nature*, vol. 565, no. 7741, pp. 654–658, 2019.
[10] T. M. Malta, C. F. de Souza, T. S. Sabedot et al., "Glioma CpG island methylator phenotype (G-CIMP): biological and clinical implications," *Neuro-Oncology*, vol. 20, no. 5, pp. 608–620, 2018.
[11] S. L. Hervey-Jumper and M. S. Berger, "Insular glioma surgery: an evolution of thought and practice," *Journal of Neurosurgery*, vol. 130, no. 1, pp. 9–16, 2019.
[12] A. Poff, A. P. Koutnik, K. M. Egan, S. Sahebjam, D. D'Agostino, and N. B. Kumar, "Targeting the Warburg effect for cancer treatment: ketogenic diets for management of glioma," *Seminars in Cancer Biology*, vol. 56, pp. 135–148, 2019.
[13] J. G. Nicholson and H. A. Fine, "Diffuse glioma heterogeneity and its therapeutic implications," *Cancer Discovery*, vol. 11, no. 3, pp. 575–590, 2021.
[14] E. Braganhol, M. R. Wink, G. Lenz, and A. M. O. Battastini, "Purinergic signaling in glioma progression," *Advances in Experimental Medicine & Biology*, vol. 1202, pp. 87–108, 2020.
[15] T. Nejo, A. Yamamichi, N. D. Almeida, Y. E. Goretsky, and H. Okada, "Tumor antigens in glioma," *Seminars in Immunology*, vol. 47, Article ID 101385, 2020.
[16] M. H. Hakar and M. D. Wood, "Updates in pediatric glioma pathology," *Surgical Pathology Clinics*, vol. 13, no. 4, pp. 801–816, 2020.
[17] M. C. Tom, D. P. Cahill, J. C. Buckner, J. Dietrich, M. W. Parsons, and J. S. Yu, "Management for different glioma subtypes: are all low-grade gliomas created equal?" *American Society of Clinical Oncology Educational Book*, vol. 39, no. 39, pp. 133–145, 2019.
[18] M. Norouzi, "Gold nanoparticles in glioma theranostics," *Pharmacological Research*, vol. 156, Article ID 104753, 2020.
[19] K. Terashima and H. Ogiwara, "[Pediatric glioma]," *Noshinkeigeka*, vol. 49, no. 3, pp. 640–646, 2021.
[20] A. Tsitlakidis, E. C. Aifantis, A. Kritis et al., "Mechanical properties of human glioma," *Neurological Research*, vol. 42, no. 12, pp. 1018–1026, 2020.
[21] A. Ellert-Miklaszewska, I. A. Ciechomska, and B. Kaminska, "Cannabinoid signaling in glioma cells," *Advances in Experimental Medicine & Biology*, vol. 1202, pp. 223–241, 2020.
[22] S. Feng and Y. Liu, "Metabolomics of glioma," *Advances in Experimental Medicine & Biology*, vol. 1280, pp. 261–276, 2021.
[23] H. Igaki, "[Radiotherapy for glioma]," *Noshinkeigeka*, vol. 49, no. 3, pp. 575–587, 2021.
[24] Y. Otani, T. Ichikawa, K. Kurozumi, and I. Date, "Dynamic reorganization of microtubule and glioma invasion," *Acta Medica Okayama*, vol. 73, no. 4, pp. 285–297, 2019.
[25] M. Hu, Y. Zhong, S. Xie, H. Lv, and Z. Lv, "Fuzzy system based medical image processing for brain disease prediction," *Frontiers in Neuroscience*, vol. 15, Article ID 714318, 2021.
[26] Z. Lv and L. Qiao, "Analysis of healthcare big data," *Future Generation Computer Systems*, vol. 109, pp. 103–110, 2020.
[27] S. Xie, Z. Yu, and Z. Lv, "Multi-disease prediction based on deep learning: a survey," *Computer Modeling in Engineering and Sciences*, vol. 128, no. 2, pp. 489–522, 2021.
[28] H. V. Chatwin, J. Cruz, and A. L. Green, "Pediatric high-grade glioma: moving toward subtype-specific multimodal therapy," *FEBS Journal*, vol. 288, no. 21, pp. 6127–6141, 2021.
[29] M. Ruff, S. Kizilbash, and J. Buckner, "Further understanding of glioma mechanisms of pathogenesis: implications for therapeutic development," *Expert Review of Anticancer Therapy*, vol. 20, no. 5, pp. 355–363, 2020.
[30] W. J. Wang, J. S. Ding, Q. Sun, X. Xu, and G. Chen, "Role of hyperbaric oxygen in glioma: a narrative review," *Medical Gas Research*, vol. 12, no. 1, pp. 1–5, 2022.

Hindawi
Contrast Media & Molecular Imaging
Volume 2022, Article ID 7197505, 7 pages
https://doi.org/10.1155/2022/7197505

Research Article

Application of Pelvic Magnetic Resonance Imaging Scan Combined with Serum Pyruvate Kinase Isozyme M2, Neutrophil Gelatinase-Associated Lipocalin, and Soluble Leptin Receptor Detection in Diagnosing Endometrial Carcinoma

Shizhong Su[1] and Liping Yin[2]

[1]*Obstetrics and Gynecology, People's Liberation Army 960th Hospital, Jinan City 250000, Shandong Province, China*
[2]*Imaging Department, Shandong Cancer Hospital and Institute, Shandong First Medical University and Shandong Academy of Medical Sciences, Jinan City 250117, Shandong Province, China*

Correspondence should be addressed to Liping Yin; yinliping@sd-cancer.org.cn

Received 22 March 2022; Accepted 28 April 2022; Published 21 May 2022

Academic Editor: M. Pallikonda Rajasekaran

Objective. To explore the application value of pelvic magnetic resonance imaging (MRI) scan combined with serum pyruvate kinase isozyme M2 (PKM2), neutrophil gelatinase-associated lipocalin (NGAL), and soluble leptin receptor (sOB-R) detection in diagnosing endometrial carcinoma (EC). *Methods*. The clinical data of 45 patients with pathologically confirmed EC treated in our hospital from May 2019 to May 2020 were retrospectively analyzed. All patients received pelvic MRI scan, serum PKM2, NGAL and sOB-R detection was performed, and the combination of the two was performed so as to analyze the diagnostic application value of the three modalities. *Results*. Compared with the joint detection, the number of true positive cases, sensitivity, specificity, and accuracy rate obtained by a single application of pelvic MRI or serum PKM2, NGAL, and sOB-R detection were obviously lower; the area under the ROC curve of the joint detection was obviously larger than that of single detection; the results of the joint detection were better than those of single detection ($P < 0.05$); the combined diagnosis obtained the highest sensitivity. *Conclusion*. Combining pelvic MRI with serum PKM2, NGAL, and sOB-4 detection can effectively promote the diagnostic accuracy for EC, presenting significant clinical diagnostic value.

1. Introduction

Endometrial carcinoma (EC) is an epithelial malignancy that occurs in the endometrium of women, which is classified into mucinous adenocarcinoma, endometrioid adenocarcinoma, papillary serous endometrial adenocarcinoma, adenocarcinoma with squamous cell differentiation, squamous carcinoma, and clear cell carcinoma [1, 2]. Relevant literature has pointed out that EC is one of the malignant tumors with high incidence worldwide, accounting for approximately 25% of malignant diseases of the female reproductive system [3]. Relevant data have revealed that EC, as a common pathological type, has a prevalence of 0.016%–0.019% [4]. In 2012, there were 319,588 new EC cases, ranking 6th in new cases of malignant tumors in women. Among them, 168,895 new EC cases were in European and American countries, ranking 4th, and 151,694 new EC cases were in developing countries, ranking 7th [5]. In the United States in 2015, there were 54,796 new EC cases and 10,109 cases died of EC, accounting for 55.79% of incidence and 33.38% of mortality among all gynecological cancers [6]. While in 2017, there were 61,379 new EC cases and 10,918 deaths from EC in the United States, the incidence was second only to colorectal cancer, lung cancer, and breast cancer, staying high in gynecological malignancies [7]. Recent studies have reported that the incidence of EC is increasing, and that its age of onset has been shown to be younger [8].

Although the incidence and mortality of EC are still high and the pathogenesis is still unclear, many scholars believe that EC is a gynecological tumor with a good prognosis [9]. EC is mainly characterized by abnormal vaginal bleeding and fluid drainage, and genetic factors, adverse lifestyles, and reproductive endocrine disorders are risk factors predisposing to the disease. Meanwhile, relevant literature has pointed out that currently about 69% of EC patients are diagnosed at an early stage of the disease, illustrating that the tumor is still located in the endometrium when diagnosed [10]. Such patients can achieve a 5-year overall survival rate of 93% after receiving clinical treatment [10]. Magnetic resonance imaging (MRI) has a high sensitivity in diagnosing EC, and its results have important implications in staging, providing guidance to clinical treatment [11]. However, MRI imaging is slower, requires more time and higher costs, and the diagnostic results of examination alone fail to meet clinical expectations. Also, some scholars believe that the detection of serum tumor markers in EC patients has similarly significant diagnostic value [12]. At present, clinical reports have confirmed the effectiveness of a single application of MRI as well as serum pyruvate kinase isozyme M2 (PKM2), neutrophil gelatinase-associated lipocalin (NGAL), and soluble leptin receptor (sOB-R) detection, while few reports focus on their combination. Based on this, the diagnosis modality combining MRI diagnosis with serum PKM2, NGAL, and sOB-R detection was adopted herein to provide more basis for future clinical treatment, with the results reported as follows.

2. Materials and Methods

2.1. General Data. The clinical data of 45 patients with pathologically confirmed EC treated in our hospital from May 2019 to May 2020 were retrospectively analyzed. The study met the World Medical Association Declaration of Helsinki [13].

2.2. Enrollment of Study Subjects

2.2.1. Inclusion Criteria. (1) The patients were diagnosed with EC for the first time according to the comprehensive medical history, re-examination, ultrasound, and pathologic examination of endometrium, with the clinical manifestations of abnormal vaginal bleeding and fluid drainage; (2) the patients did not receive antitumor treatments such as radiotherapy and chemotherapy before surgery, did not use sexual hormones 180 d before visiting the hospital, and had complete hematological indexes; (3) the patients did not have signs of chronic/acute infections; (4) the patients did not have hematological diseases and autoimmune diseases; and (5) the patients did not have mental illness and could normally communicate with others.

2.2.2. Exclusion Criteria. (1) The patients had endometriosis, endometrial polyp, and other benign lesions in the endometrium; (2) the patients had received dilatation and curettage; (3) the patients had incomplete clinical data and pathological examination results and were lost to postoperative follow-up; (4) the patients were complicated with tumor metastasis or other tumors; (5) the patients had pregnancy-related diseases and cervical diseases; (6) the patients were participating in other experiments.

2.3. Methods

2.3.1. MRI Scan. The superconducting MRI scanner (manufacturer: Philips Medical Systems Nederland B.V.; model: Gyroscan Panorama) was used to perform examination on the patients. Before examination, the patients were advised repeatedly to fast for 4–6 h, properly fill the bladder, and remove all metal objects. Scanning sequences: (1) Axial, coronal and sagittal spin-echo (SE) T1WI (TR500 ms, TE8.1 ms); (2) axial and sagittal fast spin-echo (FSE) T2WI (TR4500 ms, TE81 ms), and coronal T2WI (TR4800 ms, TE120 ms), with a slice thickness of 3 mm, slice interval of 1 mm, and the number of signal-averaged = 1; (3) DWI (TR3500, TE75 ms), the dispersed factor b values were 0 s/mm^2 and 1,000 s/mm^2, with slice interval of 1 mm, a slick thickness of 3 mm, FOV of 22 cm ∗ 22 cm, and a number of signal-averaged = 10; (4) a three-dimensional volumetric interpolated fast spoiled GRE T1WI (VIBE) sequence for DCE-MR, and the appropriate slice on the sagittal T2WI was selected, with TR4.05 ms, TE1.85 ms, slice thickness of 3 mm, FOV of 35 cm ∗ 35 cm, number of signal-averaged = 1, and total 20 time phases. The nonintermittent scanning was performed, with 10 s for each time phase. Gd-DTPA (0.1 mmol/kg) was injected through the cubital vein using a dual-barrel dual-channel special high-pressure injector for MR at a flow rate of 2 ml/s. Dynamic contrast-enhanced time-phase scans were initiated before drug injection, and the injection was finished after the end of the first time-phase scan. After dynamic contrast-enhanced scans, transaxial, sagittal, and coronal postenhancement scans were performed using a fat-suppressed sequence.

2.3.2. Serum PKM2, NGAL, and sOB-R Detection. Five ml of fasting venous blood was drawn from all patients and preserved in EDTA anticoagulation test tubes for 10-min centrifugation at 3,000 r/min and then let stand for 20 min, after that, the upper serum was separated and stored in the −80°C freezer and then sent for detection within 1 h. The patients' serum PKM2, NGAL, and sOB-R indicators were detected by the enzyme-linked immunosorbent assay (ELISA), the standard detection was carried out in strict accordance with the specification and instructions on the kits (manufacturer: MSK Biology Company).

2.4. Observation Indexes. The numbers of true-positive cases, false-positive cases, true-negative cases, and false-negative cases obtained by a single application of pelvic MRI scan, serum PKM2, NGAL, and sOB-R detection, and their combination were compared.

The sensitivity, specificity, and accuracy of single application of pelvic MRI scan, serum PKM2, NGAL, and sOB-

R detection, and their combination were compared. Sensitivity = number of true-positive cases/(number of true-positive cases + number of false-negative cases) ∗ 100%, specificity = number of true-negative cases/(number of true-negative cases + number of false-positive cases) ∗ 100%, and accuracy = number of accurately diagnosed cases/total number of cases ∗ 100%.

The utility of the three diagnosis modalities was compared by plotting the ROC curve.

2.5. Statistical Processing. In this study, the statistical analysis and processing of experimental data were conducted by the software SPSS21.0, the picture drawing software was GraphPad Prism 7 (GraphPad Software, San Diego, USA), the enumeration data were examined by X^2 test and expressed by (n (%)), the measurement data were examined by t-test and expressed by ($\overline{x} \pm s$), and differences were considered statistically significant at $P < 0.05$.

3. Results

3.1. Statistics of Baseline Data of All Subjects. Table 1 showed the statistics of baseline data of all subjects.

3.2. Comparison of Numbers of True-Positive Cases, False-Positive Cases, True-Negative Cases, and False-Negative Cases between Single Detection and Combined Detection. Table 2 showed that the numbers of true-positive cases of pelvic MRI scan and single detection of serum PKM2, NGAL, and sOB-R were obviously lower than that of combined detection.

3.3. Comparison of Sensitivity and Specificity between Single Detection and Combined Detection. Table 3 showed that the sensitivity, specificity, and accuracy rate of single detection were obviously lower than those of combined detection.

3.4. Area under ROC Curve of Single Detection and Combined Detection. Figure 1 showed that the area under the ROC curve of combined detection was obviously larger than that of single detection.

3.5. Comparison of Areas, S.E.[a], Asymp. Sig.[b], and Asymp. 95% CI of Various Indicators. The results of joint detection were better than those of single detection ($P < 0.05$) (see Table 4.

3.6. Comparison of Sensitivity and 1-Specificity. Table 5 showed that the joint detection obtained the highest sensitivity.

4. Discussion

Relevant literature has pointed out that the incidence of EC varies in different regions and countries, which is significantly higher in developed countries such as Europe and the United States than in developing countries, and accounts for approximately 49% of gynecological malignancies [14]. Fu et al. [15] stated that in China, the incidence of EC was significantly higher in more developed cities such as Shanghai and Beijing. Some published works demonstrated that in 2015, EC has become the malignant tumor with the highest incidence among the female reproductive system diseases in Beijing, ranking 5th in the female malignant tumors in Beijing, and its incidence shows an increasing trend (16.18/100,000 to 17.52/100,000) [16]. Antonio et al. [17] stated that the 5-year survival rates of EC patients at stage I, II, III, and IV were, respectively, 95.79%, 94.69%, 71.29%, and 23.79%, and considered that the survival rate of EC was significantly associated with pathological type, histological grade, and presence or absence of lymphatic metastasis. Meanwhile, Varol et al. [18] pointed out that the prognosis of EC disease is related to the degree of differentiation, clinical stages, and presence or absence of metastasis, and that the main cause of death of this disease is blood and lymph metastasis causing dysfunction in other organs. At present, the clinical treatment of the disease mainly focuses on "early diagnosis and early treatment," the prognosis of EC can be greatly improved if EC patients are diagnosed at an early stage due to clinical manifestations such as abnormal vaginal bleeding, and endometrial sampling followed by the pathological diagnosis is the most accurate way for EC diagnosis [19]. In recent years, MRI, as the optimal preoperative imaging examination, is widely used in clinical diagnosis. MRI exhibits high sensitivity in diagnosing EC and can provide effective staging data for clinical treatment, thereby providing correct guidance. In addition, the utility of MRI diagnosis has been confirmed in nasopharyngeal carcinoma, prostate cancer, breast cancer, and cervical cancer [20]. Endometrial tumors can be revealed by MRI imaging, by adjusting the imaging parameters, the tissue contrast can be effectively enhanced and the depth of tumor invasion into the uterine stroma can be better evaluated, and in this process, MRI can reveal the corresponding area by locating the required imaging plane, and at the same time, through enhanced T1WI, T2WI and dynamic contrast-enhanced MRI, patients' tumors and lesions can be determined. Therefore, MRI has a positive role in identifying EC [21]. Some studies have confirmed that MRI has a high diagnostic value in detecting adenomyosis and endometrial hyperplasia diseases [22]. Meanwhile, some scholars also believe that the detection of serum indicators in EC patients is also beneficial to the analysis of patient condition, and the reason is that PKM2 is a phosphorylase, which can phosphorylate more than 100 proteins in the human body, and it is also a marker of tumor energy metabolism conversion, presenting up-regulated expression in most cancers [23]. NGAL is a new member of the lipocalin family in human body. Its high expression is closely related to the migration, proliferation and invasion of malignant cells, so it is often used to aid the diagnosis of malignant tumors. High expression of sOB-R is associated with the occurrence and progression of EC, and all EC cell lines express higher levels of sOB-R. Although single application of MRI scan or serum detection presents higher diagnostic value, erroneous diagnosis or missed diagnosis may still occur in some patients.

Table 1: Statistics of baseline data of all subjects.

Item	Number of cases	Proportion (%)
Mean age ($\overline{x} \pm s$, years)	53.59 ± 10.40	—
BMI ($\overline{x} \pm s$, kg/m^2)	20.56 ± 0.84	—
Course of disease (months)	11.86 ± 6.17	—
Menopause		
Yes	30	66.67
No	15	33.33
FIGO stage (number of cases)		
Stage (0) carcinoma in situ	8	17.78
Stage I	11	24.44
Stage II	13	28.89
Stage III	7	15.56
Stage IV	6	13.33
Degree of tumor differentiation		
Poor	18	40.00
Moderate	17	37.78
Well	10	22.22
Complicated with lymphatic metastasis		
Yes	36	80.00
No	9	20.00
Occupation		
Teacher	11	24.44
Civil servant	10	22.22
Accountant	13	28.89
Self-employed	8	17.78
Others	3	6.67
Family economic status		
≥3,000 yuan/(month·person)	30	66.67
<3,000yuan/(month·person)	15	33.33
Place of residence		
Urban area	25	55.56
Rural area	20	44.44
Educational degree		
College	30	66.67
Middle school	10	22.22
Primary school	5	11.11
Nationality		
Han	40	88.89
Others	5	11.11

Table 2: Comparison of numbers of true-positive cases, false-positive cases, true-negative cases, and false-negative cases between single detection and combined detection (n (%)).

Detection modality	True positive (cases)	False positive (cases)	True negative (cases)	False negative (cases)
Pelvic MRI scan	33 (73.33%)*	4 (8.89%)	5 (11.11%)	3 (6.67%)
Serum PKM2, NGAL, and sOB-R	27 (60.00%)$^{\#}$	6 (13.33%)	5 (11.11%)	7 (15.56%)$^{\#\#}$
Combined detection	41 (91.11%)	1 (2.22%)	2 (4.44%)	1 (2.22%)

*Obvious difference in numbers of true-positive cases between pelvic MRI scan and combined detection ($x^2 = 4.865$, $P < 0.05$); $^{\#}$Obvious difference in numbers of true-positive cases between serum PKM2, NGAL, and sOB-R detection and combined detection ($x^2 = 11.791$, $P < 0.05$); and $^{\#\#}$Obvious difference in numbers of false-positive cases between serum PKM2, NGAL, and sOB-R detection and combined detection ($x^2 = 4.939$, $P < 0.05$).

Table 3: Comparison of sensitivity, specificity, and accuracy rate between single detection and combined detection (n (%)).

Detection modality	Sensitivity (%)	Specificity (%)	Accuracy rate (%)
Pelvic MRI scan	91.67	55.56	33 (73.33%)
Serum PKM2, NGAL, and sOB-R detection	79.41	45.45	27 (60.00%)
Combined detection	97.62	66.67	41 (91.11%)

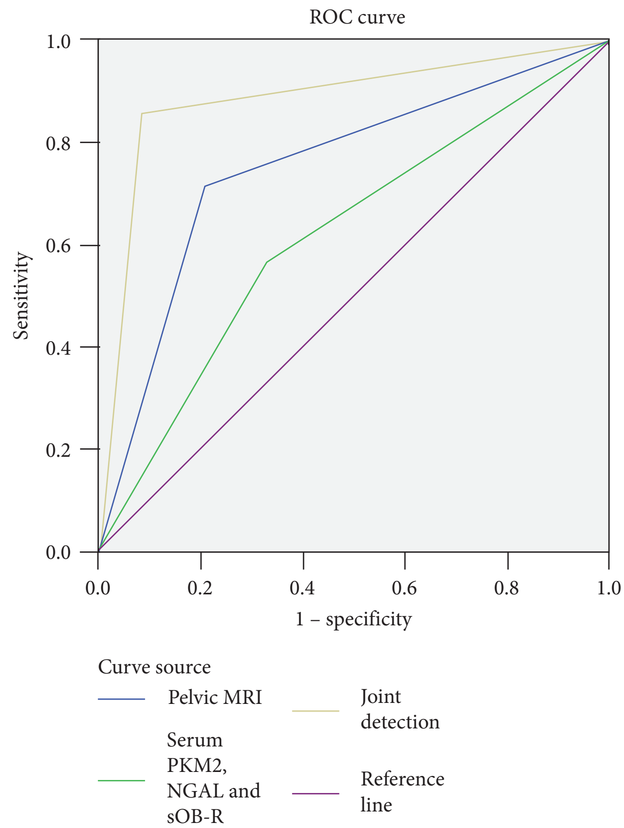

Figure 1: Area under ROC curve of single detection and combined detection.

Table 4: Comparison of areas, S.E.[a], Asymp. Sig.[b], and Asymp. 95% CI of various indicators.

				Asymp. 95% CI	
Test result variables	Area	S.E.[a]	Asymp. Sig.[b]	Lower limit	Upper limit
Pelvic MRI scan	0.753	0.075	0.004	0.605	0.901
Serum PKM2, NGAL, and sOB-R	0.619	0.085	0.172	0.453	0.785
Joint detection	0.887	0.056	<0.001	0.778	0.996

Table 5: Comparison of sensitivity and 1-specificity.

Test result variables	Positive[a] if greater than or equal to	Sensitivity	1-specificity
Pelvic MRI scan	−1.0000	1.000	1.000
	0.5000	0.714	0.208
	2.0000	<0.001	<0.001
Serum PKM2, NGAL, and sOB-R detection	−1.0000	1.000	1.000
	0.5000	0.571	0.333
	2.0000	<0.001	<0.001
Joint detection	−1.0000	1.000	1.000
	0.5000	0.857	0.083
	2.0000	<0.001	<0.001

With the advancement of medical technology, some scholars have pointed out that combining MRI scan with serum detection can obtain better results than single detection [24, 25]. In this study, the numbers of true positive cases detected by single detection of pelvic MRI scan and serum PKM2, NGAL, and sOB-R were obviously lower than that of joint detection, and the sensitivity, specificity and accuracy rate were also obviously lower in single detection than in joint detection, indicating that applying the diagnostic modalities such as pelvic MRI scan and serum PKM2, NGAL and sOB-R detection alone did not obtain desirable diagnostic efficacy and high diagnostic sensitivity, specificity and accuracy rate, and that the joint detection achieved better diagnostic results because it could provide more rich positive diagnostic information in clinic through different means. In addition, as many factors such as bacterial infection and other inflammations can affect serum indicators, the detection of serum PKM2, NGAL and sOB-R alone cannot accurately determine EC and needs to be used in combination with pelvic MRI scan to complement each other and improve the diagnostic performance. The study results also showed that compared with single detection, the joint detection had obviously larger area under ROC curve, better results ($P < 0.05$), and the highest sensitivity, which fully demonstrated that the joint detection has a higher accuracy rate and further improves the clinical diagnostic value. Shortcomings of the study: First, there was selection bias inherent to retrospective study, such as differences in staff technique for performing MRI examination and preoperative histopathologic examination; second, this trial did not include patients who received conservative treatment and nonsurgical treatment, and did not consider the prognosis of the patients; and finally, this study was based on the population within the region and did not include sufficient amount of patients from other provinces, so the results might be affected by the small sample size and regional culture. Therefore, it is necessary to further improve the study protocol, increase the sample size, and develop multicenter studies. In the near future, with the continuous improvement and advancement of medical technology, a technique for the effective diagnosis of EC disease may be explored to provide more evidence-based basis for the clinical treatment of such patients.

Data Availability

The data to support the findings of this study are available on reasonable request from the corresponding author.

Conflicts of Interest

The authors have no conflicts of interest to declare.

References

[1] L. G. Buchynska, T. V. Borykun, N. P. Iurchenko, S. V. Nespryadko, and I. P. Nesina, "Expression of microRNA in tumor cells of endmetrioid carcinoma of endometrium," *Experimental Oncology*, vol. 42, no. 4, pp. 289–294, 2020.

[2] Y. Norimatsu, S. Irino, Y. Maeda et al., "Nuclear morphometry as an adjunct to cytopathologic examination of endometrial brushings on LBC samples: a prospective approach to combined evaluation in endometrial neoplasms and look alikes," *Cytopathology*, vol. 32, no. 1, pp. 65–74, 2021.

[3] E. D. Euscher, D. Y Duose, C Lan et al., "Mesonephric-like carcinoma of the endometrium," *The American Journal of Surgical Pathology*, vol. 44, no. 4, pp. 429–443, 2020.

[4] R. Kaur, J. Mehta, and A. M. Borges, "Role of SMARCA4 (BRG1) and SMARCB1 (INI1) in dedifferentiated endometrial carcinoma with paradoxical aberrant expression of mmr in the well-differentiated component: a case report and review of the literature," *International Journal of Surgical Pathology*, vol. 29, no. 5, pp. 106689692095945–577, 2021.

[5] K. Sangwan, M. Garg, N. Pathak, and L. Bharti, "Expression of cyclin D1 in hyperplasia and carcinoma of endometrium and its correlation with histologic grade, tumor type, and clinicopathological features," *Journal of Laboratory Physicians*, vol. 12, no. 03, pp. 165–170, 2020.

[6] T. Iida, T. Muramatsu, H. Kajiwara et al., "Small cell neuroendocrine carcinoma of the endometrium with difficulty identifying the original site in the uterus," *Tokai Journal of Experimental & Clinical Medicine*, vol. 45, pp. 156–161, 2020.

[7] R. W. C. Wong, K. L. Talia, and W. G. McCluggage, "Endometrial gastric-type carcinoma," *The American Journal of Surgical Pathology*, vol. 44, no. 12, pp. 1736-1737, 2020.

[8] Y. Liu, Y. Chang, and Y.-x Cai, "Inhibition of lnc-OC1 induced cell apoptosis and decreased cell viability by releasing miR-34a and inhibiting PD-L1 in endometrial carcinoma," *Reproductive Sciences*, vol. 27, no. 10, pp. 1848–1856, 2020.

[9] D. M. Badary and H. Abou-Taleb, "Vitamin D receptor and cellular retinol-binding protein-1 immunohistochemical expression in normal, hyperplastic and neoplastic endometrium: possible diagnostic and therapeutic implications," *Annals of Diagnostic Pathology*, vol. 48, Article ID 151569, 2020.

[10] M. Tasuku, T. Kubo, H. Yoshihiko et al., "Less correlation between mismatch repair proteins deficiency and decreased expression of HLA class I molecules in endometrial carcinoma: a different propensity from colorectal cancer," *Medical Molecular Morphology*, vol. 54, pp. 14–22, 2021.

[11] K. Kazuhiro, K. Takako, Y Kawanaka et al., "Characteristics of MR imaging for staging and survival analysis of neuroendocrine carcinoma of the endometrium: a multicenter study in Japan," *Magnetic Resonance in Medical Sciences*, vol. 20, pp. 236–244, 2021.

[12] S. A. O'Toole, Y. Huang, L. Norris et al., "HE4 and CA125 as preoperative risk stratifiers for lymph node metastasis in endometrioid carcinoma of the endometrium: a retrospective study in a cohort with histological proof of lymph node status," *Gynecologic Oncology*, vol. 160, no. 2, pp. 514–519, 2021.

[13] World Medical Association, "World medical association declaration of Helsinki," *JAMA*, vol. 310, no. 20, pp. 2191–4, 2013 Nov 27.

[14] A. Travaglino, A. Raffone, A. Gencarelli et al., "Clinicopathological features associated with mismatch repair deficiency in endometrial undifferentiated/dedifferentiated carcinoma: a systematic review and meta-analysis," *Gynecologic Oncology*, vol. 160, no. 2, pp. 579–585, 2021.

[15] D.-J. Fu, A. J. De Micheli, M. Bidarimath et al., "Cells expressing PAX8 are the main source of homeostatic regeneration of adult endometrial epithelium and give rise to serous endometrial carcinoma," *Disease models & mechanisms*, vol. 13, 2020.

[16] S. Xu, Y. Yang, X. Wang et al., "γ-Glutamyl cyclotransferase contributes to endometrial carcinoma malignant progression and upregulation of PD-L1 expression during activation of epithelial-mesenchymal transition," *International Immunopharmacology*, vol. 81, Article ID 106039, 2020.

[17] T. Antonio, R. Antonio, G. Annarita, M. Antonio, Z. Fulvio, and I. Luigi, "Endometrial gastric-type carcinoma: an aggressive and morphologically heterogenous new histotype Arising from gastric metaplasia of the endometrium," *The American Journal of Surgical Pathology*, vol. 44, pp. 1002–1004, 2020.

[18] G. Varol, K. Mustafa, Ö. İsa Aykut, C. Ilker, S. Muzaffer, and G. Kemal, "Do estrogen, progesterone, P53 and Ki67 receptor

ratios determined from curettage materials in endometrioid-type endometrial carcinoma predict lymph node metastasis," *Current Problems in Cancer*, vol. 44, Article ID 100498, 2020.

[19] S. Christine and F. Oluwole, "High-grade endometrioid carcinoma of the endometrium with a GATA-3-positive/PAX8-negative immunophenotype metastatic to the breast: a potential diagnostic pitfall," *International Journal of Surgical Pathology*, vol. 28, pp. 631–636, 2020.

[20] Z. Xu, Y. Tian, J. Fu, J. Xu, D. Bao, and G. Wang, "Efficacy and prognosis of fertility-preserved hysteroscopic surgery combined with progesterone in the treatment of complex endometrial hyperplasia and early endometrial carcinoma," *Journal of B.U.ON.: Official Journal of the Balkan Union of Oncology*, vol. 25, pp. 1525–1533, 2020.

[21] D. Cuevas, A. Velasco, M. Vaquero et al., "Intratumour heterogeneity in endometrial serous carcinoma assessed by targeted sequencing and multiplex ligation-dependent probe amplification: a descriptive study," *Histopathology*, vol. 76, no. 3, pp. 447–460, 2020.

[22] G. Rivera, S. Niu, H. Chen, D. Fahim, and Y. Peng, "Collision tumor of endometrial large cell neuroendocrine carcinoma and low-grade endometrial stromal sarcoma: a case report and review of the literature," *International Journal of Surgical Pathology*, vol. 28, no. 5, pp. 569–573, 2020.

[23] K. M. Vroobel and A. D. Attygalle, "Sarcomatous transformation in undifferentiated/dedifferentiated endometrial carcinoma: an underrecognized phenomenon and diagnostic pitfall," *International Journal of Gynecological Pathology*, vol. 39, no. 5, pp. 485–492, 2020.

[24] Y. Dai, W. Chen, X. Xu et al., "Factors affecting adenoma risk level in patients with intestinal polyp and association analysis," *Journal of Healthcare Engineering*, vol. 2022, pp. 1–5, Article ID 9479563, 2022.

[25] C. Zhang, S. Shao, Y. Zhang et al., "LncRNA PCAT1 promotes metastasis of endometrial carcinoma through epigenetical downregulation of E-cadherin associated with methyltransferase EZH2," *Life Sciences*, vol. 243, Article ID 117295, 2020.

Hindawi
Contrast Media & Molecular Imaging
Volume 2022, Article ID 1613632, 8 pages
https://doi.org/10.1155/2022/1613632

Research Article

Evaluation of Nursing Effects of Pelvic Floor Muscle Rehabilitation Exercise on Gastrointestinal Tract Rectal Cancer Patients Receiving Anus-preserving Operation by Intelligent Algorithm-based Magnetic Resonance Imaging

Lijuan Zhang [1] and Feng Wang [2]

[1]*Department of Gastroenterology, Shanxi Province Cancer Hospital/Shanxi Hospital Affiliated to Cancer Hospital, Chinese Academy of Medical Sciences/Cancer Hospital Affiliated to Shanxi Medical University, Taiyuan 030013, Shanxi, China*
[2]*Clinical Laboratory, Shanxi Children's Hospital, Taiyuan 030013, Shanxi, China*

Correspondence should be addressed to Feng Wang; 201711111221535@stu.hubu.edu.cn

Received 4 March 2022; Accepted 18 April 2022; Published 19 May 2022

Academic Editor: M Pallikonda Rajasekaran

Based on magnetic resonance imaging (MRI) technology under artificial intelligence algorithm, the postoperative nursing effects of pelvic floor muscle rehabilitation exercise on gastrointestinal tract rectal cancer (RC) patients were investigated. A total of 88 patients receiving RC anus-preserving surgery in hospital were selected. The included patients were divided randomly into the experimental group (44 cases) and the control group (44 cases). Patients in the control group engaged in Kegel motion, while patients in the experimental group underwent self-designed comprehensive pelvic floor training. Anorectum function rating scale and quality of life questionnaire for colorectal cancer (EORTC QLQ-CR29) were utilized to compare and analyze anus functions and living quality of patients in the two groups. Besides, all patients in two groups received MRI examinations, and images were processed by a convolutional neural network (CNN) algorithm. The results showed that in MRI images, there were significant signal differences between lesion tissues and normal tissues. After being processed by an artificial intelligence algorithm, the definition of MRI images was remarkably enhanced with clearer lesion edges. The quality of images was also significantly improved. Besides, the comparison of anus functions of patients in two groups showed that the differences demonstrated statistical meaning after the intervention ($P < 0.05$). In conclusion, artificial intelligence algorithm-based MRI and comprehensive pelvic floor muscle exercise showed significant application prospects and values in the recovery of patients' intestinal functions after RC anus-preserving surgery.

1. Introduction

Rectal cancer (RC) is one of the most common malignant tumors and one of the most significant causes of death by cancer at present. Relevant statistics show that the incidence of RC is ranked in the 3rd place among cancers and the 5th place in mortality among cancers in China [1, 2]. At present, there is still no consensus on its pathogenesis, which may be due to heredity, environmental factors, and dietary habits [3]. Surgical treatment is the main therapeutic method of the disease [4]. However, anus-preserving is difficult in the surgical operations of RC because most tumors are located at the base of the pelvic floor and close to dentate lines. In recent years, anastomotic and surgical technologies are continuously developed and improved, and neoadjuvant therapy as well as total mesorectal excision (TME) are gradually proposed [5, 6]. RC anus-preserving surgery becomes the main method of treating RC gradually. The method saves many patients from carrying pockets for whole life. However, various intestinal dysfunctions and mental dysfunctions occur after surgery. As a result, the incidence of these symptoms seriously affects patients' living quality [7].

Although sphincter functions are completely preserved by RC anus-preserving surgery, intestinal anatomical structure and functions are impaired and disturbed in tumor excision. In addition, most patients suffer from multiple intestinal symptoms after surgery because of radiotherapy and other factors. According to considerable clinical data, about 50% to 90% of patients suffer from postoperative low anterior resection syndrome (LARS) [8, 9]. After the surgery, early symptoms are very significant with high incidence. However, these symptoms will probably last for a lifetime if treatment and recovery measures are not taken in time [10, 11]. At present, the common nursing methods include transanal irrigation, electrical stimulation of sacral nerves, biofeedback therapy, rectal balloon training, and Kegel motion [12, 13]. Foreign relevant studies are carried out at an earlier time, and most of them focus on the recovery of patients' intestinal functions by combining multiple training methods [14]. The improvement of patients' incontinence is also focused. In contrast, patients' living quality and other common symptoms are less focused. There is still no rehabilitation nursing method regarded as effective by the public. In addition, extensive and multi-center experimental validation is inadequate in most studies. Generally speaking, the scientificalness and safety of pelvic floor muscle training after RC anus-preserving surgery needed to be further verified and studied [15].

In recent years, imaging technology has constantly improved; RC diagnosis and therapeutic effect assessment methods have become more diversified gradually. Currently, the main assessment methods of diagnostic and therapeutic effects on RC include endorectal ultrasonography (ERUS), computed tomography (CT), and magnetic resonance imaging (MRI). For example, some scholars used MRI for the diagnosis of RC patients and an analysis of their diagnostic efficiency. The results showed that the accuracy, sensitivity, and specificity of MRI in diagnosing RC were 92%, 90%, and 85%, respectively. MRI has become the main method of clinical RC diagnosis. The extraction of effective features from numerous medical images is the focus of present studies to provide the basis for clinical diagnosis and treatment. The feature expression ability of traditional learning algorithms is weak because of their shallow training model level. As a result, the application of traditional learning algorithms is restricted in medical image feature extraction. On the contrary, deep learning algorithms make up for the defects of traditional learning algorithms [16]. In particular, the deep convolutional neural network (CNN) algorithm is a method with the most significant research values and potential in image processing and analysis. Furthermore, a large amount of research data demonstrates that the error rate of feature recognition is reduced to 3.5% [17]. To sum up, deep CNN shows significant advantages and application prospects in imaging processing and feature extraction. Nowadays, there are many studies on the application of CNN in medical imaging, including image segmentation, image classification, image registration, and target detection [18].

On the grounds of the previous researches, a set of pelvic floor muscle exercise methods was designed independently. Besides, artificial intelligence algorithm-based MRI technology was utilized to discuss postoperative recovery therapeutic effects of the method on RC patients receiving anus-preserving surgery, which aimed to provide new ideas and a reference basis for the diagnosis, treatment, and postoperative recovery of clinically relevant diseases.

2. Materials and Methods

2.1. Research Objects. A total of 88 patients receiving RC anus-preserving surgery in hospital between March 2019 and November 2020 were selected, including 58 male patients and 30 female patients. The average age of the included patients was 55.3 ± 11.3 years old, and they were divided randomly into the experimental group (44 cases) and the control group (44 cases). All the included patients had signed the informed consent forms and this research had been approved by the ethics committee of the hospital.

Inclusion criteria: patients who were diagnosed with RC by colonoscopy or pathological examination and the distance between the lower edge of the patient's tumors and dentate lines was equal to or shorter than 10 cm. Patients who accepted RC radical excision with anal sphincter retained. Patients who volunteered to engage in the research.

Exclusion criteria: patients who suffered from temporary or permanent stoma; patients who had anastomotic leak and other severe complications. Patients who got other complicated intestinal functional diseases before surgery, such as irritable bowel syndrome, Crohn's disease, and ulcerative colitis. Patients who took drugs that affected intestinal functions over 3 weeks within 1 month before surgery, such as antidiarrheal agents, laxatives, and morphine. Patients who received the auxiliary treatments of other intestinal functions imaging, such as biofeedback therapy. Patients who received the surgical treatment of other intestinal functions imaging, such as anorectal surgery, pelvic surgery, abdominal surgery, and spinal surgery. Patients who suffered from mental diseases. Patients who suffered from complications of severe heart, lung, kidney, and musculoskeletal diseases.

2.2. Postoperative Nursing Methods. Patients in both groups were offered medication, diet, and life guidance. Besides, they were also provided with anus peripheral skin care, anastomotic stoma expansion, regular defecation training, and other conventional nursing measures. Based on the above guidance and nursing measures, pelvic floor muscle rehabilitation training was carried out 1 week after postoperative defecation. Specific exercise intervention methods were as follows.

In the control group, patients were instructed to perform the Kegel motion. Before the exercise, patients were asked to empty their urinary bladders. After that, they needed to take a comfortable position, such as lying on their back or sitting. Patients should try to keep their leg, abdomen, and back muscles as relaxed as possible, and try their best to squeeze perineal muscles upward and inward until pelvic muscles and levator ani muscles were lifted upward. The squeezing action needed to be kept for 5 seconds, and then patients relaxed for 10 seconds. The above steps constituted a group of exercises. A total of 10 groups of exercises needed to be performed for each time. Each single exercise lasted for about 3 minutes and was performed 3 times each day.

In the experimental group, the training methods were improved and integrated based on considerable literature and data as well as the advice offered by anorectal surgery experts, rehabilitation therapists, and anorectal surgery nursing staff. The contents of the training included abdominal respiration, abdominal massage, Kegel motion, cross-leg anus lifting motion, and bridging anus lifting motion. Table 1 shows specific exercise methods below. Each single exercise lasted for 8 to 10 minutes, 3 times each day.

2.3. Observation Indexes. Patients' general data included social demography data (age, gender, education level, economic income, and payment methods of medical expenditure) and disease-related data (tumor differentiation levels, medical history, and surgical methods).

In terms of the anorectum function rating scale, the evaluation contents of the scale included defecation intention, defecation control, defecation sensory functions, defecation times, and defecation time. Each of the above five aspects included 3 levels, and each level was assigned with 0, 1, and 2 points, respectively. The total points for each level ranged from 0 to 10. Based on the general evaluations in five aspects, the anus functions were divided into four levels, including excellent level (9–10 points), good level (7–8 points), intermediate level (5–6 points), and poor level (0–4 points). Besides, excellent and good level rate = (excellent level rate + good level rate)/total number of cases × 100%.

The quality of life questionnaire for colorectal cancer (EORTC QLQ-CR29) included four aspects of body image: anxiety, weight, and sexual desire. Four aspects included a total of 19 items. In each item, there were four levels of answers which were none, a little, a lot, and quite a lot. The four levels corresponded to 1, 2, 3, and 4 points, respectively. The scoring method was polarization method.

2.4. Examination Methods. A Philips superconductive nuclear magnetic resonance instrument (Prodiva 1.5 T, No. 82307) was adopted with phased-array surface coils. Sagittal, axial, and coronal scanning were performed. The slice thickness was 4 mm without spacing. Before the examination, no intestinal preparation was required. During the examination, patients needed to take a supine position. The center of the surface coil was placed at the pubis symphysis. Besides, the middle axial slice should be kept perpendicular to the anal tubes, and sagittal and coronal slices needed to be balanced with the anorectal axis during the scanning. During the examination, patients needed to breathe calmly and minimize body movement as well. Table 2 demonstrated specific scanning parameters below.

2.5. Image Processing Methods. The denoising process was as follows. The array with $f(x, y)$ of the image being $M\times N$ was processed, and the image was $g(x, y)$. The gray level of the images was determined by the average value of the gray levels of several pixels including the field (x, y). The processed image is expressed by the following equation:

$$g(x, y) = \frac{1}{M}\sum_{(i,j)\in s} f(i, j). \tag{1}$$

In the above equation, $x, y = 0, 1, 2, \ldots, N\text{-}1$, S denoted the field collection with the point (x, y) as the center, and M referred to the total number of coordinate points in S. In terms of multiple images, the original image was set to be $f(x, y)$ and image noise was $n(x, y)$. Then, the noisy image $g(x, y)$ is expressed by the following equation:

$$g(x, y) = f(x, y) + n(x, y). \tag{2}$$

If noises were unrelated and the average value was 0, the equation generated is as follows:

$$f(x, y) = E[g(x, y)]. \tag{3}$$

In the below equation, $E\ g[(x, y)]$ represented the expected value of $g(x, y)$, and M noisy images were averaged to generate the following equations:

$$\begin{aligned} f(x, y) &= E[g(x, y)] \sim \bar{g}(x, y) \\ &= \frac{1}{M}\sum_{i=1}^{M} g_i(x, y). \end{aligned} \tag{4}$$

$$\delta^2_{g(x,y)} = \frac{1}{M}\delta^2_{n(x,y)}. \tag{5}$$

In the above two equations, $\delta^2_{\bar{g}(x,y)}$ and $\delta^2_{n(x,y)}$ were the variances of $\bar{g}$ - and n at the point (x, y).

The equations adopted for the edge detection process are as follows:

$$\begin{aligned} \psi^1(x) &= \frac{\mathrm{d}\theta(x)}{\mathrm{d}x}, \\ \psi^2(x) &= \frac{\mathrm{d}^2\theta(x)}{\mathrm{d}x^2}. \end{aligned} \tag{6}$$

$$\begin{aligned} w^1 f(s, x) &= f * \psi^1_s(x), \\ w^2 f(s, x) &= f * \psi^2_s(x). \end{aligned} \tag{7}$$

$$\begin{aligned} w^1 f(s, x) &= f * \left(s\frac{d\theta_s}{dx}\right)(x) \\ &= s\frac{\mathrm{d}}{\mathrm{d}x}(f * \theta_s)(x). \end{aligned} \tag{8}$$

$$\begin{aligned} w^2 f(s, x) &= f * \left(s^2\frac{d^2\theta_s}{dx^2}\right)(x) \\ &= s^2\frac{\mathrm{d}^2}{\mathrm{d}x^2}(f * \theta_s)(x). \end{aligned} \tag{9}$$

The membrane value of discrete binary wavelet transform $W^{1,d}_{2^j} f(n,m), W^{2,d}_{2^j} f(n,m)$ of point (n, m) is expressed by the following equation:

Table 1: Training plan of comprehensive pelvic floor muscle exercise in the experimental group.

Training order	Training items	Training methods
Part 1	Abdominal respiration	Patients were instructed to place hands on abdomen, and keep abdominal muscles relaxed as they inhaled. After that, they were allowed to pause for 1 to 2 seconds. As they exhaled, abdominal muscles were contracted with the hands on abdomen declining. Each group of training lasted for 5 seconds and 5 groups of training needed to be completed every time.
Part 2	Abdominal massage	Patients were asked to lie on their backs and press tianshu, qihai, and guanyuan acupuncture points successively. Each acupuncture point was pressed by the thumbs for 1 minute. When the acupuncture points become swollen and get fever, the degree of pressure should remain the same. Massage strength should be changed from light to heavy gradually with a moderate rate. Besides, the vertical tension of the surgical incision should not be increased.
Part 3	Kegel motion	Specific methods were the same as those for the control group, and the exercise was performed 5 times.
Part 4	Cross-leg anus lifting motion	Patients were asked to remain decubitus or in the standing position and keep thighs crossed. Besides, perinaeum needed to be clamped by hips and thighs, and the muscles around anus needed to be tightened and lifted upward slowly and gradually. The above actions should be kept for 5 seconds, and then patients were allowed to relax for 10 seconds. The group of exercise was performed 5 times.
Part 5	Bridging anus lifting motion	Patients were asked to lie on their backs in bed with their knees bent and the soles of their feet pushing the bed. With heads, elbows, and feet as the supporting points, hips were lifted by pelvic floor muscles, and hip muscles, and perineal muscles were contracted. Patients needed to try their best to keep the above actions for 5 seconds, and then they were allowed to lower their hips and relax for 5 seconds. The group of exercises was performed 5 times.
Part 6	Leg motion	Tsusanli was pressed and kneaded for 1 minute with the thumbs. When the acupuncture points become swollen and get a fever, the degree of pressure should remain the same. After that, two legs were lifted in turns. Besides, the thighs were kept at a 90° angle to the bodies. With a good physical condition, two legs could be gradually lifted, which should be repeated 5 times.

Table 2: MRI examination scanning parameters.

Sequence	Position	Time of repetition (TR)	Time of echo (TE)	Slice thickness/slice spacing	Matrix	Fat suppression
T2WI	Sagittal position	4400	80	4/0.9	330*330	Yes
T2WI	Axial position	4900	85	4/0.9	330*330	Yes
T2WI	Axial position	4900	80	4/0.9	330*330	No
T1WI	Axial position	673	23	4/0.9	330*330	Yes
T2WI	Coronal position	4100	95	4/0.9	330*330	No

$$M_{2^j}^d f(n,m) = \sqrt{\left|W_{2^j}^{1,d} f(n,m)\right|^2 + \left|W_{2^j}^{2,d} f(n,m)\right|^2}. \quad (10)$$

The phase angle is expressed as follows:

$$A_{2^j}^d f(n,m) = \arg\tan\left(\frac{W_{2^j}^{2,d} f(n,m)}{W_{2^j}^{1,d} f(n,m)}\right). \quad (11)$$

2.6. Statistical Analysis. The analysis of all the data was completed by the statistical product and service solution SPSS 19.0. Measurement data were expressed by the mean+standard deviation and tested by an independent sample t-test. The comparison of enumeration data was completed by the chi-square test. $P < 0.05$ indicated that the differences showed statistical significance.

3. Results

3.1. Patients' General Data. Table 3 shows patients' general data below. According to Table 3, the differences in age, gender, tumor differentiation, and anal edge tumor height of patients in the two groups demonstrated no statistical significance ($P > 0.05$).

3.2. Intelligent Algorithm-Based MRI Processing. Figure 1 displays MRI images of typical cases before and after the processing by an artificial intelligence algorithm. In Figure 1, the images were of Case 1, Case 2, Case 3, and Case 4, respectively, from left to right, and the scanning positions were sagittal, axial, coronal, and sagittal positions, respectively. The analysis of Figure 1 demonstrated that there were significant signal differences between lesion tissues and normal tissues in MRI images. After the processing by an artificial intelligence algorithm, the definition of MRI images was remarkably enhanced with clearer lesion edges. Obviously, image quality was also significantly improved.

3.3. Comparison of Anus Functions of Patients in Two Groups before and after Intervention. Figure 2 displays the results of the comparison of anus functions of patients in two groups

Table 3: General data on patients in two groups.

Items	Experimental group ($n = 44$)	Control group ($n = 44$)	Statistical values	P
Age (years old)	53.1 ± 10.5	55.8 ± 11.6	0.612	0.731
Gender (case)	—	—	0.044	0.939
Male	23 (52%)	18 (41%)	—	—
Female	21 (48%)	26 (59%)	—	—
Tumor level (case)	—	—	2.886	0.544
High differentiation	15 (34%)	10 (23%)	—	—
Moderate differentiation	20 (45%)	26 (59%)	—	—
Low differentiation	9 (20%)	8 (18%)	—	—
Anal edge tumor height	8.2 ± 2.6	7.3 ± 3.1	−1.127	0.485

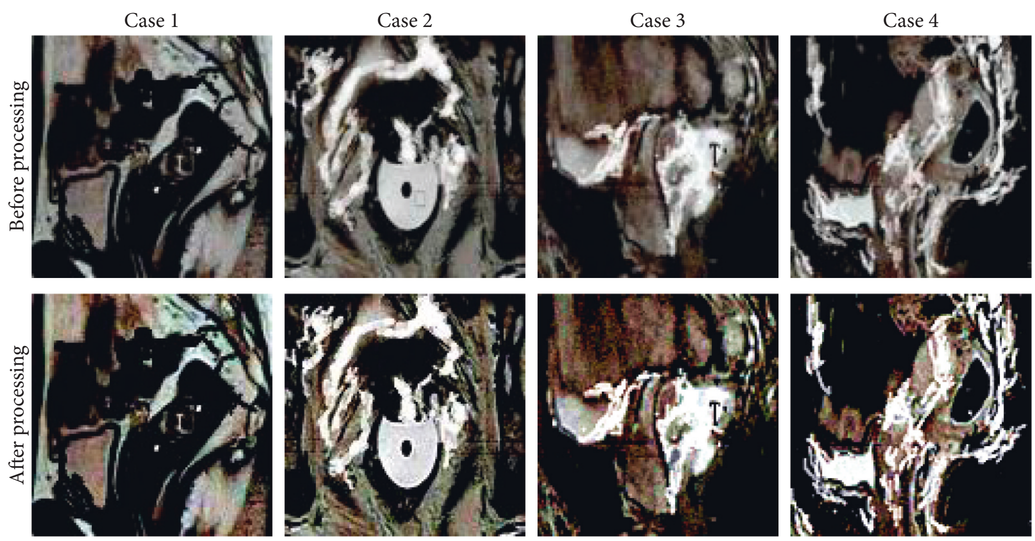

Figure 1: MRI images of typical cases.

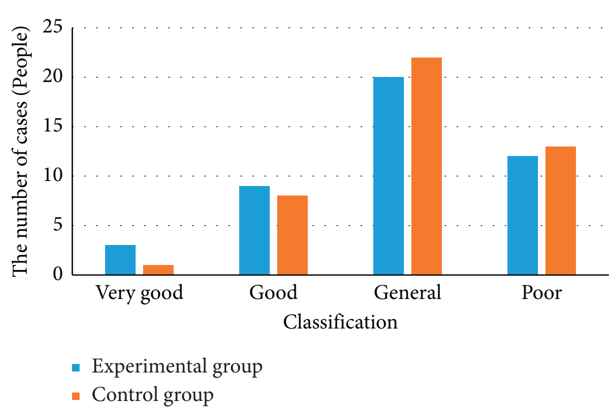

Figure 2: Comparison results of anus functions of patients in two groups before intervention. * Comparison to the control group, $(P) < 0.05$.

before the intervention. The analysis of Figure 2 revealed that the number of patients with excellent, good, intermediate, and poor levels of anus functions was 3, 9, 20, and 12, respectively, in the experimental group before the intervention. The excellent and good level rate reached 27%. In the control group, the number of patients with excellent, good, intermediate, and poor levels of anus functions was 1, 8, 22, and 13, respectively, and the excellent and good rates amounted to 20%. The comparison of anus functions in the two groups before the intervention showed no statistical significance ($P > 0.05$).

Figure 3 shows the comparison results of the anus functions of patients in two groups after the intervention. Figure 3 demonstrated that the number of patients with excellent, good, intermediate, and poor levels of anus functions in the experimental group 3 months after the intervention was 16, 22, 2, and 4, respectively. The excellent and good rates reached 86%. In the control group, the number of

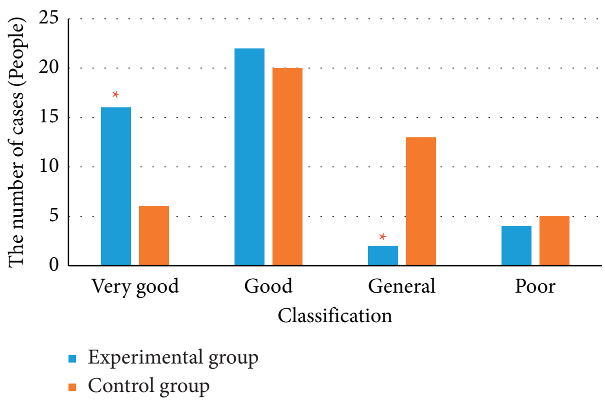

Figure 3: Comparison of anus functions of patients in two groups after intervention. * Comparison to the control group, $(P) < 0.05$.

patients with excellent, good, intermediate, and poor levels of anus functions was 6, 20, 13, and 5, respectively, and the excellent and good rate amounted to 59%. After the intervention, the comparison of anus functions between two groups showed statistical significance $(P > 0.05)$.

3.4. Comparison of Living Quality of Patients in Two Groups before and after Intervention. Figure 4 displays the comparison results of living quality of patients in two groups before the intervention. It was demonstrated in Figure 4(a) that the comparison of the score of each item in living quality between the experimental group and the control group before the intervention showed no significant difference. Besides, the comparison between groups showed no Figure 4(b) statistical significance as well $(P > 0.05)$. The above results indicated that the data of two groups were comparable.

3.5. Comparison of Living Quality of Patients in Two Groups after Intervention. Figure 5 illustrates the comparison results of the living quality of patients in two groups after the intervention. Figure 5(a) revealed that some symptoms of patients in the experimental group were significantly improved 3 months after the intervention, including (Figure 5(b)) frequent urination, defecate frequency, abdominal distension, dry mouth, fecal incontinence, and anus peripheral skin pain. The comparison of the scores in the above items showed significant differences and statistical meaning between the experimental group and the control group $(P < 0.05)$.

4. Discussion

RC is defined as malignant tumors appearing in the intestinal tracts about 15 cm away from the anal edges, and it is one of the main death causes related to cancers at present. Both the incidence and mortality of RC in cities are higher than those in rural areas, and the incidence and mortality of RC among males were higher than those among females as well [19]. In the early phase, there are usually no significant clinical symptoms. Defecation habits of patients are often changed in the middle phase of RC, such as slenderer or flatter stools. Some patients suffer from defecation frequency, tenesmus, anus discomfort, and hypogastrium pain [20]. At an advanced phase, bloody stool or mucus usually appears. If tumors further spread to the prostate, some complications of urethral stimulus will occur, such as frequent urination, urgent urination, dysuria, and hematuria [21]. Although traditional surgical treatment methods can radically cure tumors, it is usually difficult to retain an anus because of the short distance from dentate lines. As a result, patients need to carry pockets for their lifetime, which seriously reduces patients' living quality.

With the continuous development of adjuvant therapy and anastomat in recent years, anus-preserving surgery can not only radically cure RC but also can retain anus successfully. This surgery addresses the problems with traditional surgical methods and greatly improves patients' living quality [22]. According to relevant studies, the above symptoms of some patients will be alleviated 1 to 2 years after RC anus-preserving surgical treatment. However, the symptoms will last for a lifetime among most patients, which causes great damage to patients both psychologically and physically [23]. Hence, it is indispensable to carry out some pelvic floor muscle rehabilitation training to help patients recover their intestinal functions. The impacts of pelvic floor muscle rehabilitation training on the postoperative living quality of RC surgical patients were investigated, and the results showed that it could obviously improve patients' postoperative anus functions and living quality. Consequently, the results provided the reference for the improvement of RC patient prognosis. In this work, a comprehensive pelvic floor muscle rehabilitation training program was raised on the basis of reviewing a large number of literatures. As the training was applied to the postoperative recovery of patients with RC anus-preserving surgery, the results were analyzed. The scores of anal functions and living quality in the experimental group were higher than those in the control group. This suggested that the postoperative pelvic floor muscle rehabilitation training was beneficial to postoperative functional recovery and to reducing complications, which was consistent with the results of previous related studies.

In RC diagnosis and therapeutic effect judgment, ERUS, CT, and MRI are all main examination methods. MRI shows a high resolution of soft tissues and multiplane imaging capacity. As a result, it can recognize tumors and peripheral tissues accurately and has become one of the main methods for diagnosing RC. With the continuous improvement of imaging technology, the quality requirements of medical images get higher and higher. Besides, computer technology is also developed widely in medicine, with the processing of medical images as a significant branch [24]. The deep learning algorithm is the most concerned and promising algorithm, and also a CNN algorithm that can make up for the defects of traditional algorithms. In addition, it shows extremely significant advantages in image processing and feature extraction [25]. Artificial intelligence algorithm-based MRI technology was utilized to evaluate the therapeutic effects of this deep learning algorithm. There were obvious differences in MRI images processed by an artificial intelligence algorithm of RC patients between tumors and

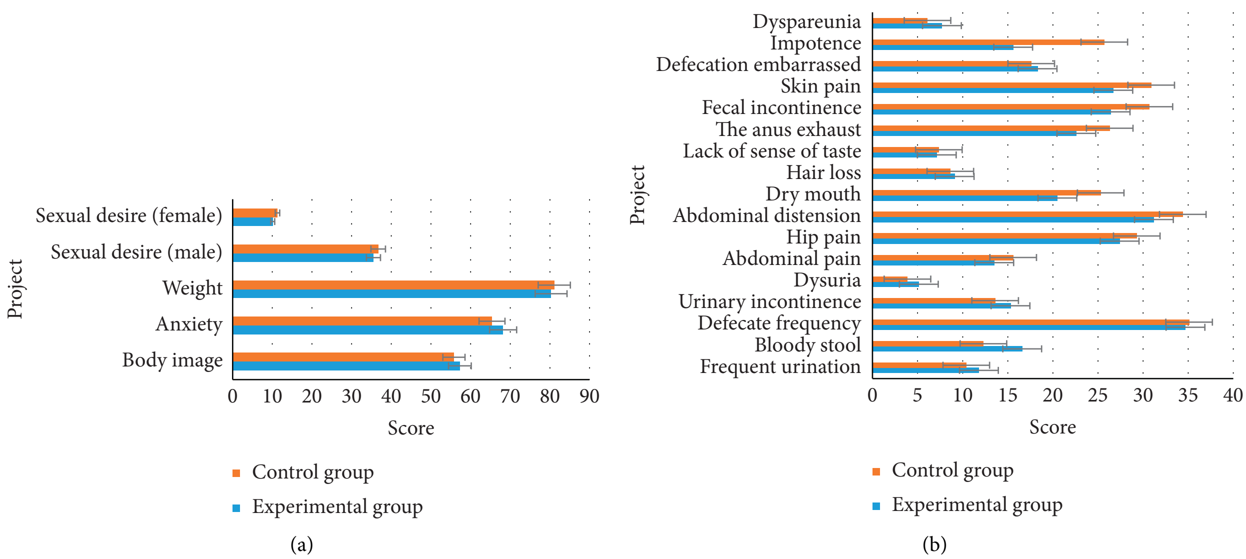

Figure 4: Comparison of living quality of patients in two groups before intervention. (a) function items; (b) symptoms.

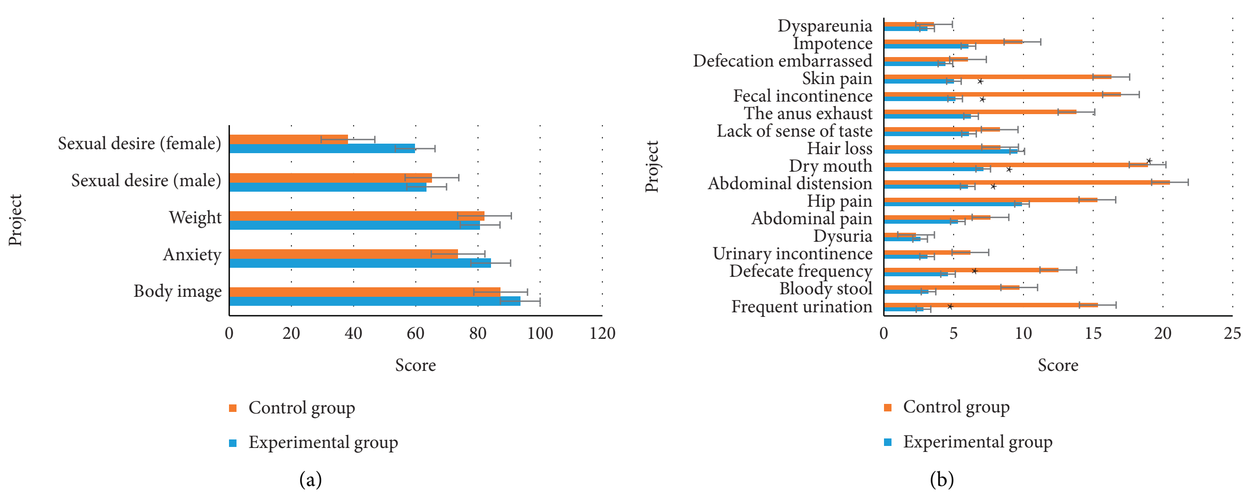

Figure 5: Comparison of living quality of patients in two groups after intervention: (a) function items; (b) symptoms. * Comparison to control group, $(P) < 0.05$.

peripheral tissues, and the quality of processed images was remarkably improved compared with that of the images to be processed. The differences indicated that artificial intelligence algorithm-based MRI showed significant application values and prospects in RC diagnosis and therapeutic effect assessment. MRI technology under an artificial intelligence algorithm was used for diagnosis and image processing of RC patients. The research results proved that the quality of processed MRI images was notably improved, the lesions were more prominent, and the boundary between the normal tissues and the lesions became clearer. It was illustrated that the method proposed in this work had a great application prospect in the diagnosis of RC.

5. Conclusion

Based on the reference to considerable literature, a comprehensive pelvic floor muscle training plan was proposed, and its therapeutic effects were evaluated by artificial intelligence algorithm-based MRI technology. The results demonstrated that there were obvious differences between MRI image tumors processed by an artificial intelligence algorithm of RC patients and peripheral tissues, and the quality of processed images was remarkably improved compared with that of the images to be processed. The differences revealed that artificial intelligence algorithm-based MRI showed significant application values and prospects in RC diagnosis and therapeutic effect assessment. What's more, the scores of anus functions and living quality of patients in the experimental group were both remarkably improved compared with those of patients in the control group after 3-month treatment.

Data Availability

The data used to support the findings of this study are available from the corresponding author upon request.

Conflicts of Interest

The authors declare that there are no conflicts of interest.

References

[1] G. Feeney, R. Sehgal, M. Sheehan et al., "Neoadjuvant radiotherapy for rectal cancer management," *World Journal of Gastroenterology*, vol. 25, no. 33, pp. 4850–4869, 2019.
[2] M. M. Symer and H. L. Yeo, "Recent advances in the management of anal cancer," *F1000Res.*vol. 7, 2018.
[3] O. A. Catalano, S. I. Lee, C. Parente et al., "Improving staging of rectal cancer in the pelvis: the role of PET/MRI," *European Journal of Nuclear Medicine and Molecular Imaging*, vol. 48, no. 4, pp. 1235–1245, 2020.
[4] U. I. Attenberger, J. Winter, F. N. Harder et al., "Height of rectal cancer: a comparison between rectoscopic and different MRI measurements," *Gastroenterol Res Pract*, vol. 2020, Article ID 2130705, 7 pages, 2020.
[5] G. Alvfeldt, P. Aspelin, L. Blomqvist, and N. Sellberg, "Rectal cancer staging using MRI: adherence in reporting to evidence-based practice," *Acta Radiologica*, vol. 61, no. 11, pp. 1463–1472, 2020.
[6] Y. E. Han, B. J. Park, D. J. Sung et al., "How to accurately measure the distance from the anal verge to rectal cancer on MRI: a prospective study using anal verge markers," *Abdominal Radiology*, vol. 46, no. 2, pp. 449–458, 2021.
[7] M. J. Corines, S. Nougaret, M. R. Weiser, M. Khan, and M. J. Gollub, "Gadolinium-based contrast agent during pelvic MRI: contribution to patient management in rectal cancer," *Diseases of the Colon & Rectum*, vol. 61, no. 2, pp. 193–201, 2018.
[8] A. Ogura, T. Konishi, C. Cunningham, and J G. Aguilar, H. Iversen, S. Toda, I K. Lee, H. X. Lee, K. Uehara, P. Lee, H. Putter, C. J. H v. d. Velde, G. L Beets, H. J T. Rutten, M. Kusters, L N S. Consortium, Neoadjuvant (Chemo)radiotherapy with total mesorectal excision only is not sufficient to prevent lateral local recurrence in enlarged nodes: results of the multicenter lateral node study of patients with low cT3/4 rectal cancer," *Journal of Clinical Oncology*, vol. 37, no. 1, pp. 33–43, 2019.
[9] J. J. C. Tersteeg, P. D. Gobardhan, R. M. P. H. Crolla et al., "Improving the quality of MRI reports of preoperative patients with rectal cancer: effect of national guidelines and structured reporting," *American Journal of Roentgenology*, vol. 210, no. 6, pp. 1240–1244, 2018.
[10] L. A. Min, Y. J. L. Vacher, L. Dewit et al., "Gross tumour volume delineation in anal cancer on T2-weighted and diffusion-weighted MRI - reproducibility between radiologists and radiation oncologists and impact of reader experience level and DWI image quality," *Radiotherapy & Oncology*, vol. 150, pp. 81–88, 2020.
[11] P. Manegold, J. Taukert, H. Neeff, S. Fichtner-Feigl, and O. Thomusch, "The minimum distal resection margin in rectal cancer surgery and its impact on local recurrence - a retrospective cohort analysis," *International Journal of Surgery*, vol. 69, pp. 77–83, 2019.
[12] X. Wang, W. Cao, D. Liu et al., "[The value of MRI with CUBE sequence in early evaluation of the efficacy of neoadjuvant therapy for locally advanced rectal cancer]," *Zhonghua Wei Chang Wai Ke Za Zhi*, vol. 21, no. 1, pp. 73–78, 2018.
[13] B. Huang, Z. Q. Zhou, H. Zhou et al., "[Analysis on clinical factors affecting transrectal natural orifice specimen extraction in rectal cancer surgery]," *Zhonghua Wei Chang Wai Ke Za Zhi*, vol. 23, no. 5, pp. 480–485, 2020.
[14] H. Kaur, H. Gabriel, M. Taggart et al., "MRI staging in an evolving management paradigm for rectal cancer, from the *AJR* special series on cancer staging," *American Journal of Roentgenology*, vol. 217, no. 6, pp. 1282–1293, 2021.
[15] Y. Huang, S. H. Huang, P. Chi et al., "[Rectum-preserving surgery after consolidation neoadjuvant therapy or totally neoadjuvant therapy for low rectal cancer: a preliminary report]," *Zhonghua Wei Chang Wai Ke Za Zhi*, vol. 23, no. 3, pp. 281–288, 2020.
[16] N. Horvat, C. Carlos Tavares Rocha, and B. Clemente Oliveira, "Etal. MRI of rectal cancer: tumor staging, imaging techniques, and management," *RadioGraphics*, vol. 39, no. 2, pp. 367–387, 2019.
[17] Z. Yang, G. Chunhua, Y. Huayan, J. Yang, and Y. Cheng, "Anatomical basis for the choice of laparoscopic surgery for low rectal cancer through the pelvic imaging data-a cohort study," *World Journal of Surgical Oncology*, vol. 16, no. 1, 199 pages, 2018.
[18] J. B. Yuval, H. M. Thompson, C. Firat et al., "MRI at restaging after neoadjuvant therapy for rectal cancer overestimates circumferential resection margin proximity as determined by comparison with whole-mount pathology," *Diseases of the Colon & Rectum*, vol. 65, no. 4, pp. 489–496, 2022.
[19] X. Li, H. Chen, B. Li, C. Wang, J. Zhang, and J. Hu, "[Application of improved anvil placement in laparoscopic resection of low rectal cancer with resection of anal eversion]," *Zhonghua Wei Chang Wai Ke Za Zhi*, vol. 21, no. 8, pp. 913–917, 2018.
[20] J. Chen, Y. Sun, P. Chi, and B. Sun, "MRI pelvimetry-based evaluation of surgical difficulty in laparoscopic total mesorectal excision after neoadjuvant chemoradiation for male rectal cancer," *Surgery Today*, vol. 51, no. 7, pp. 1144–1151, 2021.
[21] Y. Wang, "[Imaging diagnosis and imaging risk factors of anastomotic leakage after rectal cancer surgery]," *Zhonghua Wei Chang Wai Ke Za Zhi*, vol. 21, no. 4, pp. 404–408, 2018.
[22] J. S. Y. Hong, K. G. M. Brown, J. Waller, C. J. Young, and M. J. Solomon, "The role of MRI pelvimetry in predicting technical difficulty and outcomes of open and minimally invasive total mesorectal excision: a systematic review," *Techniques in Coloproctology*, vol. 24, no. 10, pp. 991–1000, 2020.
[23] M. Á Lorenzo Liñán, J. García Armengol, G. P. Martín Martín, V M. Sanjuán, and J V R. Vila, "Validation of pelvic magnetic resonance imaging as the method of choice to determine the distance to the anal margin in rectal cancer," *Cirugia Espanola*, vol. 29, pp. 245–251, 2021.
[24] D. W. Tan, F. Zhang, J. W. Ye et al., "[Initial report of laparoscopic single incision plus one port with simultaneous robotic-assisted transanal total mesorectal excision for low rectal cancer surgery]," *Zhonghua Wei Chang Wai Ke Za Zhi*, vol. 23, no. 6, pp. 605–609, 2020.
[25] S. Balcı, M. R. Onur, A. D. Karaosmanoğlu et al., "MRI evaluation of anal and perianal diseases," *Diagn Interv Radiol*, vol. 25, no. 1, pp. 21–27, 2019.

Hindawi
Contrast Media & Molecular Imaging
Volume 2022, Article ID 9410161, 6 pages
https://doi.org/10.1155/2022/9410161

Research Article

Diagnostic Value and Application of Prenatal MRI and Ultrasound in Fetal Cleft Lip and Palate

Xin Yan,[1] Guojing Xing,[1] Xin Wang,[2] Jun Li,[3] Qiuhong Sun,[4] and Xiaojie Shang[1]

[1]*Department of Ultrasound Medicine, Zibo Central Hospital, Zibo 255000, Shandong, China*
[2]*Department of Imaging,The Fourth People's Hospital of Zibo, Zibo 255000, Shandong, China*
[3]*Department of Neurosurgery, Zibo Central Hospital, Zibo 255000, Shandong, China*
[4]*College of Medical Technology, Zibo Vocational Institute, Zibo 255300, Shandong, China*

Correspondence should be addressed to Xiaojie Shang; shangxiaojie@zbzxyy.com.cn

Received 25 February 2022; Accepted 23 April 2022; Published 18 May 2022

Academic Editor: M. Pallikonda Rajasekaran

Objective. The purpose was to explore the diagnostic value and application of prenatal magnetic resonance imaging (MRI) and ultrasound (US) in fetal cleft lip and palate. *Methods*. From January 2018 to December 2019, 39 pregnant women without normal fetal maxillofacial structure or with fetal maxillofacial deformity under US examination in our hospital were selected as the study subjects. Not knowing the clinical data of the pregnant women, MRI and US physicians performed diagnostic analysis on the MRI or US images of all the study subjects and analyzed the results of prenatal MRI and US diagnosis and postpartum follow-up to compare the diagnostic efficacy and confidence of MRI and US. *Results*. The follow-up found that there were 20 cases of cleft lip, 15 cases of cheilopalatognathus, 3 cases of cleft palate, and 1 case of unilateral cleft lip with alveolar cleft, with a total of 39 cases having cleft lip and palate deformity. MRI and US had the same efficacy in the diagnosis of cleft lip. As for cleft palates, the diagnostic accuracy of MRI (94.87%) was significantly better than that of US (48.72%, $P < 0.001$). The diagnostic confidence of fetal cleft lip and palate by MRI (89.73%) was significantly better than that of US (43.59%, $P < 0.001$). The AUC of US (0.597) was significantly less than that of MRI (0.940), indicating that the diagnostic accuracy of US was not as good as that of MRI ($P < 0.05$). The sensitivity and 1 − specificity of MRI were significantly higher than those of US. *Conclusion*. MRI is more accurate than US in the diagnosis of fetal cleft lip and palate, and MRI can be the preferred method for prenatal detection of cleft lip and palate, thus providing more accurate opinions and information for perinatal pregnant women.

1. Introduction

Cleft lip and palate refers to a disease that causes clefts of soft and bone tissues of the lip or palate of the fetus during embryonic development. Fetal congenital facial malformation is a kind of congenital body surface malformation [1–3]. The malformation can appear at the birth of fetuses, which is not conducive to the growth and development of the children. Fetal cleft lip and palate is a common congenital facial malformation, which not only affects the appearance of children but also causes malnutrition in children with the difficulty of sucking milk, having a certain impact on the psychology of parents and children [4]. At the same time, most scholars believe that diabetes and malnutrition in pregnant women during pregnancy are the main factors contributing to fetal cleft lip and palate, but previous reports have shown that genetic factors and viral infection are also the main factors causing this disease [5]. In recent years, the reported incidence of cleft lip and palate has increased in various countries, with the incidence of 1/495–1/1995 worldwide and 1.8% in China. Epidemiological studies in developed countries such as the United States and Europe have shown that the incidence is higher in the yellow race than in the black and white races, and the incidence is influenced by geographical, ethnic, and socioeconomic factors [6]. Ultrasound (US) is currently the preferred method for clinical diagnosis of fetal cleft lip and palate. However, its detection results have certain limitations due to factors such as gestational age, amniotic fluid volume, and maternal obesity of pregnant women. Several studies have pointed out that MRI has a positive role in prenatal diagnosis of fetal cleft lip and palate [7, 8]. In addition, with the characteristics of multiple imaging, no ionizing radiation, and relatively objective diagnosis, MRI is less affected by the clinical experience of the operators, and its visual field is less affected by the fetal position. Therefore, MRI is widely used in the examination of fetal malformation. The purpose of this study was to explore the diagnostic value and application of prenatal MRI and US examinations in fetal cleft lip and palate, aiming to objectively analyze the accuracy of MRI and US in the diagnosis of fetal cleft lip and palate, specifically reported as follows.

2. Materials and Methods

2.1. General Information. From January 2018 to December 2019, 39 pregnant women without normal fetal maxillofacial structure or with fetal maxillofacial deformity under US examination in our hospital were selected as the study subjects. This study was in line with the principle of the Declaration of Helsinki [9].

2.2. Inclusion Criteria and Exclusion Criteria

2.2.1. Inclusion Criteria

(1) All pregnant women voluntarily received prenatal MRI and US diagnosis on the same day.
(2) All of them voluntarily accepted postpartum neonatal maxillofacial examination or the test results.
(3) This study was approved by the hospital ethics committee and the pregnant women signed a consent form after being informed.
(4) Pregnant women had a family history of cleft lip and palate.

2.2.2. Exclusion Criteria

(1) Pregnant women with severe pregnancy complications.
(2) Pregnant women with two or multiple pregnancies.
(3) Pregnant women who were transferred to other hospitals midway and no postdelivery results were obtained.

2.3. Methods

2.3.1. Diagnostic Confidence Scale and Cleft Lip and Palate Classification. The diagnostic results of cleft palate were classified into five grades, including definitely cleft palate (grade 5), probably cleft palate (grade 4), uncertain (grade 3), probably not cleft palate (grade 2), and certainly not cleft palate (grade 1), scored as 5, 4, 3, 2, and 1, respectively. Negative diagnosis was not cleft palate, and the nodes of diagnosis were definitely cleft palate, probably cleft palate, uncertain, and probably not cleft palate. Definite diagnosis included certainly not cleft palate and definitely cleft palate, with 100% of diagnostic confidence. Uncertain diagnosis included probably cleft palate, uncertain, and probably not cleft palate, with diagnosis confidence as 75%, 50%, and 25%, respectively.

In this study, MRI and US images were independently diagnosed by two diagnostic physicians with more than 10 years of diagnostic experience in our hospital. The diagnostic result was selected if two diagnostic physicians had same diagnosis. When the results were different, another two diagnostic physicians took a result after discussion. None of the four diagnostic physicians knew the clinical data and indicators of pregnant women and fetuses before diagnosis.

According to the different fetal development and cleft palate locations, cleft lip and palate was divided into cleft lip (CL), cleft palate (CP), cleft lip with alveolar cleft (CLA), and cleft lip with complete cleft palate (CLP), bilateral and unilateral.

2.3.2. US Detection Method. Experienced US diagnostic physicians used standardized methods to obtain the two-dimensional images of the fetal abdomen, chest, and limbs and to obtain the two-dimensional and three-dimensional images of the fetal head. Then, the images were stored in the picture archiving and communication system (PACS). The color Doppler ultrasonic diagnostic system (model: Philips HD7) was used for ultrasound examination with the activation of fetal protection key. The two-dimensional ultrasound emission capacity energy was less than $100\,mW/cm^2$, with 20 Hz–40 Hz as the frequency of exploration.

2.3.3. MRI Detection Method. The Amira 1.5 T superconducting scanner (Siemens) was used for MRI detection with spine coil and body coil. True FLSP (true fast imaging with steady-state precession) was used, with the scan reference data set as 1.93 ms of TE, 612 ms of TR, 256×256 of rectangle, 79° of flip angle, 4.0 mm of layer thickness, 1.00 of SNR, −50% of scanning interval, 380 mm of FOV, Averages 1, 484 Hz/PX of bandwidth, and 19 s of scan time. Pregnant women breathed freely in the supine position. The scan was performed in sagittal, axial, and coronal directions. Median sagittal/coronal scanning included maxillofacial region and brain. The axial scan was parallel to the deciduous dentition and included the fetal throat to the lower margin of mandible. The captured images were uploaded to picture archiving and communication system (PACS).

2.4. Observation Indexes. The postpartum follow-up results, the diagnostic accuracy of MRI and US, and diagnostic classification results were observed and recorded.

2.5. Statistical Processing. The data in this study were processed and analyzed by the data software SPSS20.0. The area under the curve (AUC) and receiver operating characteristic (ROC) were used to compare the diagnostic efficacy of prenatal MRI and US in the diagnosis of cleft lip and palate. The measurement data were measured by the *t*-test, expressed by ($\overline{x} \pm s$), and the count data were tested by $X2$, expressed by (n (%)). The difference was statistically significant when $P < 0.05$.

3. Results

3.1. Comparison of General Data. The baseline data of all subjects are shown in Table 1.

3.2. Postpartum Follow-Up Results. The follow-up found that 39 fetuses suffered from cleft lip and palate deformity, in which parents of 36 cases were informed of the detection results and parents of 3 cases were informed of autopsy results. There were 20 cases of cleft lip (18 unilateral and 2 bilateral), 15 cases of cheilopalatognathus (14 unilateral and 1 bilateral), 3 cases of cleft palate, and 1 case of unilateral cleft lip with alveolar cleft. None of the 39 children had concurrent malformations.

3.3. Diagnostic Accuracy of MRI and US. MRI and US had the same efficacy in the diagnosis of cleft lip. As for cleft palates, the diagnostic accuracy of MRI (94.87%) was significantly better than that of US (48.72%, $P < 0.001$), as shown in Table 2.

3.4. Follow-Up and Diagnostic Grading Results of MRI and US. In MRI, there were 35 cases of definite diagnosis, 1 case of missed diagnosis, and 3 cases of uncertain diagnosis (accounting for 7.69%). In US, there were 17 cases of definite diagnosis, 2 cases of missed diagnosis, and 20 cases of uncertain diagnosis (accounting for 51.28%). It could be seen that the diagnostic confidence of fetal cleft lip and palate by MRI (89.73%) was significantly better than that of US (43.59%), with statistical significance ($P < 0.001$). The follow-up and diagnostic grading results of MRI and US are shown in Table 3.

3.5. Analysis of AUC and ROC of MRI and US. The AUC of US (0.597) was significantly less than that of MRI (0.940), indicating that the diagnostic accuracy of US was not as good as that of MRI ($P < 0.05$), as shown in Table 4 and Figure 1.

3.6. Comparison of Sensitivity and 1 − Specificity. The sensitivity and 1 − specificity of MRI were significantly higher than those of US, as presented in Table 5.

4. Discussion

One of the most common facial congenital malformations is cleft lip and palate [10–12]. Relevant studies indicate that more than 50% of children with cleft lip suffer from cleft palates, but their causes are different [13]. During the fetal development, there are 2 mandibular processes, 2 maxillary processes, and 1 nasopalatine process around the original mouth of the embryo, and several protrusions will grow out along with the development. After 7 weeks of development, if the two globular processes from the nasopalatine process are not fused, a cleft lip will arise in the middle of the upper lip. If the globular process does not fuse with the maxillary process on one side, a unilateral cleft lip will arise. If the globular process does not fuse with the maxillary processes on both sides, a bilateral cleft lip will arise [14]. The palates are divided into secondary palate and primary palate. The primary palate is the anterior part of the palate, which is a small part of the palate and formed by fusion of the anterior palatal processes on both sides of the globular process. The secondary palate is formed by the fusion of two palatal processes toward the midline, which also fuses with the primary palate. After 8 weeks of development, if the nasal septum and bilateral palatal processes of the secondary palate do not fuse with the primary palate with bilateral anterior palatal processes, cleft palate will occur. Primary cleft palate is clinically referred to as alveolar cleft [15].

US is the preferred screening method for prenatal maxillofacial deformity clinically. However, it is difficult to make a clear judgment for US detection in cases of excessive obesity of pregnant women and small amniotic fluid volume. In addition, it is difficult for US detection to display clear images because echoes from protrusion of fetal maxillary alveolar and other parts are easily occluded. Relevant reports indicate that it is very safe to perform MRI detection on fetuses over 3 months of gestation, which can display the fine structure of the fetuses in any direction with a high anatomical resolution. Therefore, MRI is mostly used in clinic for further detection when US cannot be used for detection [16].

In clinical diagnosis, MRI is characterized by large soft tissue resolution, non-ionizing radiation, and large visual field imaging without limitations of maternal obesity, small amniotic fluid volume, and other factors. The rapid imaging of MRI greatly reduces fetal motion artifacts. According to the study of Werner et al. [17], MRI has a positive effect on prenatal imaging detection. Although prenatal MRI detection is widely used in clinic, MRI is not included in routine prenatal screening at present. MRI diagnosis is often performed after the US detection results in the diagnosis of cleft lip and palate are obtained, which directly improves the diagnostic efficiency of MRI. In order to analyze the diagnostic value and application of prenatal MRI and US examinations in fetal cleft lip and palate, 39 pregnant women without normal fetal maxillofacial structure or with fetal maxillofacial deformity under US examination in our hospital from January 2018 to December 2019 were selected as the study subjects. MRI and US physicians performed diagnostic analysis on the MRI or US images of all the study subjects without knowing the clinical data of the pregnant women, so that the diagnostic results of cleft lip and palate were more objective.

39 cases were studied in this study, with a gestation of 20–38 weeks. The results of this study found that MRI and US had the same diagnostic efficacy with the diagnostic accuracy, specificity, and sensitivity all as 100%. As for cleft palates, the diagnostic accuracy of MRI (94.87%) was significantly better than that of US (48.72%), with statistical significance ($P < 0.001$). According to the "The prenatal diagnosis and classification of cleft palate: the role and value of magnetic resonance imaging" studied by Zheng et al. [18], the diagnostic rates of US and MRI were 59.09% and 92.05%, respectively, which were consistent with the conclusion of this study, thus indicating that MRI diagnosis was more accurate than US diagnosis.

Table 1: Statistics of baseline data of all subjects (n (%)).

Items	N	Percentage
Age		
21–29 years old	31	79.49
30–40 years old	8	20.51
Average gestational age (weeks)	29.42 ± 5.56	—
Occupation		
Teachers	10	25.64
Financial practitioners	11	28.21
Accountants	12	30.77
Individual households	4	10.26
Other	2	5.13
Family income		
≥3000 yuan/(month·person)	30	76.92
<3000 yuan/(month·person)	9	23.08
Residence		
Urban area	25	64.10
Rural area	14	35.90
Education		
University	25	64.10
Middle school	12	30.77
Primary school	2	5.13
Nations		
Han	35	89.74
Other	4	10.26

Table 2: Diagnostic accuracy of MRI and US (n (%)).

Diagnosis	Misdiagnosis	Missed diagnosis	Uncertain diagnosis	Diagnostic accuracy
MRI diagnosis	0	0	2	(37/39) 94.87%
US diagnosis	0	6	14	(19/39) 48.72%
X^2				20.51
P				<0.001

Table 3: Follow-up and diagnostic grading results of MRI and US.

Number of cases	MRI diagnostic confidence grading	US diagnostic confidence grading	Follow-up results
12	1	1	11 cases of CL, 1 case of CLP
1	4	1	1 case of CLP
3	5	1	1 case of CP, 2 cases of CLP
7	1	4	7 cases of CL
2	3	3	2 cases of CP
4	5	3	1 case of CL, 1 case of CLA and 2 cases of CLP
1	1	4	1 case of CL
1	4	4	1 case of CLP
7	5	4	7 cases of CLP
1	5	5	1 case of CLP

Table 4: Statistical results of fetal cleft lip and palate diagnosed by MRI and US.

				Progressive 95% confidence interval	
Detection variables	Area	Standard error[a]	Progressive sig.[b]	Upper limit	Lower limit
MRI	0.940	0.051	<0.001	0.000	1.000
US	0.597	0.102	0.338	0.397	0.797

a = under nonparametric hypothesis; b = null hypothesis, real area = 0.5.

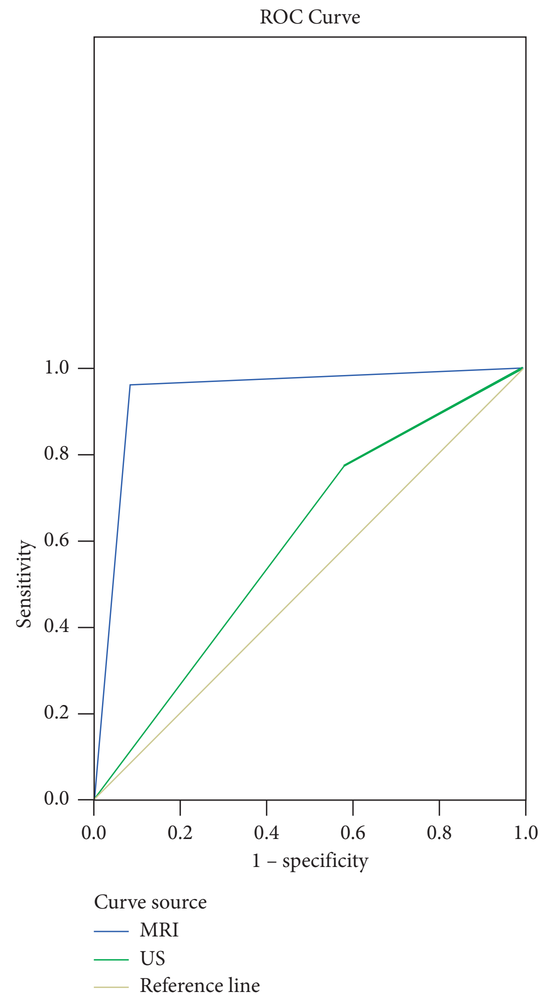

Figure 1: ROC analysis of MRI and US in the diagnosis of fetal cleft lip and palate.

Table 5: Comparison of sensitivity and 1 – specificity.

Detection variables	Positive[a] if greater than or equal to	Sensitivity	1 – specificity
	−1.0000	1.000	1.0001
MRI	0.5000	0.963	0.083
	2.0000	<0.001	<0.00
	−1.0000	1.000	1.000
US	0.5000	0.778	0.583
	2.0000	<0.001	<0.001

a = under nonparametric hypothesis.

In this study, both MRI and US could accurately diagnose unilateral cleft lip with complete cleft palate. MRI could clearly show the maxillofacial structure and brain parenchyma of a fetus with maternal obesity and isolated cleft palates without holoprosencephaly at 25 weeks of gestation, while US could not. There were 6 cases of missed diagnosis and 14 cases of uncertain diagnosis in US, mainly because maternal obesity covered the maxillofacial bones. There were 2 cases of uncertain diagnosis in MRI mainly due to the unclear display of the lip and palate caused by the artifacts generated by fetal motion. MRI diagnosis in this study showed that the cleft lip and palate of fetuses over 20 weeks of gestation was not significantly correlated with the gestational age of pregnant women while artifacts of fetal movement were the main influencing factors of MRI detection. The main factor affecting US detection was whether the maxillofacial area was covered or whether the mother was obese. In addition, the ROC curve analysis showed that the curve area of MRI was larger than that of US, suggesting that MRI can provide more information, with a lower number of misdiagnosis and missed diagnosis. Therefore, MRI diagnosis can be added to provide more accurate opinions for pregnant women when the results of US are unclear. This study also has some inadequacies. First, due to the limitations of relevant conditions, this study has a small sample size and limited sample source and lacks representativeness. Second, the different skills of staff in MRI and US examinations have a certain impact on the research results. Finally, this study is based on the patients within the region and did not include a sufficient number of patients from other provinces, so the results may be affected by the small sample size and regional culture.

In conclusion, MRI is more accurate than US in the diagnosis of fetal cleft lip and palate, and MRI can be the preferred method for prenatal detection of cleft lip and palate, thus providing more accurate opinions and information for perinatal pregnant women.

Data Availability

The data used to support the findings of this study are available from the corresponding author upon request.

Conflicts of Interest

The authors have no conflicts of interest to declare.

References

[1] A. Paula Pinho Matos, P. Teixeira Castro, L. de Barros Duarte et al., "Prenatal diagnosis of cervical masses by magnetic resonance imaging and 3D virtual models: perinatal and long-term follow-up outcomes," *Journal of Maternal-Fetal and Neonatal Medicine*, vol. 33, no. 13, pp. 2181–2189, 2020.

[2] T. Yamamoto, M. Kurabe, K. Matsumoto, S. Sugai, and H. Baba, "Congenital tracheal aplasia without prenatal diagnosis masked by maternal obesity and gestational diabetes: a case report," *A&A Practice*, vol. 14, no. 6, Article ID e01200, 2020.

[3] H. J. F. Milani, E. Q. d. S. Barreto, L. H. Chau et al., "Prenatal diagnosis of closed spina bifida: multicenter case series and review of the literature," *Journal of Maternal-Fetal and Neonatal Medicine*, vol. 33, no. 5, pp. 736–742, 2020.

[4] AMD, "Abstracts of MDSICON 2020: abstracts of the 5th annual conference of the movement disorders society of India (MDSICON 2020) 31st january to 2nd february, 2020, hotel uday samudra, kovalam, thiruvanthapuram, India," *Annals of Movement Disorders*, vol. 3, no. 4, pp. 1–42, 2020.

[5] D. Di Mascio, D. Buca, A. Khalil et al., "Outcome of isolated fetal talipes: a systematic review and meta-analysis," *Acta Obstetricia et Gynecologica Scandinavica*, vol. 98, no. 11, pp. 1367–1377, 2019.

[6] M. Lv, B. Zhao, and Q. Luo, "Prenatal diagnosis and prognosis assessment of fetal intra-abdominal cystic lesions: a retrospective study in 264 cases," *Journal of Obstetrics and Gynaecology*, vol. 39, no. 7, pp. 922–927, 2019.

[7] O. Nieto, M. Recio, A. Garicano et al., "EP06.20: prenatal diagnosis of two cases of isolated periventricular nodular heterotopia (PNH) by ultrasound and MRI in the second trimester," *Ultrasound in Obstetrics and Gynecology*, vol. 54, no. S1, p. 266, 2019.

[8] P. Rekawek, B. G. Coleman, A. Kamath, and J. L. Stone, "Prenatal sonography of multicentric infantile myofibromatosis: case report and review of the literature," *Journal of Clinical Ultrasound*, vol. 47, no. 8, pp. 490–493, 2019.

[9] C. D. Levant and C. Bâtiment, "World medical association declaration of Helsinki," *JAMA*, vol. 310, no. 20, pp. 2191–2194, 27.

[10] S. M. Ragaee, M. A.-F. Mourad, S. T. Hamed, and A. M. Abbas, "Fetal cerebellar vermis assessment by MRI. What does it add?" *Open Journal of Obstetrics and Gynecology*, vol. 09, no. 9, pp. 1290–1303, 2019.

[11] Q. Chang, Y. Peng, Q. Huang et al., "Prognosis of fetuses with ventriculomegaly: an observational retrospective study," *Prenatal Diagnosis*, vol. 39, no. 10, pp. 901–909, 2019.

[12] D. Di Mascio, F. G. Sileo, A. Khalil et al., "Role of magnetic resonance imaging in fetuses with mild or moderate ventriculomegaly in the era of fetal neurosonography: systematic review and meta-analysis," *Ultrasound in Obstetrics and Gynecology*, vol. 54, no. 2, pp. 164–171, 2019.

[13] H. F. Shieh, J. A. Estroff, C. E. Barnewolt, D. Zurakowski, W. H. Tan, and T. L. Buchmiller, "Prenatal imaging throughout gestation in Beckwith-Wiedemann syndrome," *Prenatal Diagnosis*, vol. 39, no. 9, pp. 792–795, 2019.

[14] K. M. Niles, S. Blaser, P. Shannon, and D. Chitayat, "Fetal arthrogryposis multiplex congenita/fetal akinesia deformation sequence (FADS)-Aetiology, diagnosis, and management," *Prenatal Diagnosis*, vol. 39, no. 9, pp. 720–731, 2019.

[15] A. E. Millischer, P. Sonigo, T. Attie et al., "Fetal MRI findings in a retrospective cohort of 26 cases of prenatally diagnosed CHARGE syndrome individuals," *Prenatal Diagnosis*, vol. 39, no. 9, pp. 781–791, 2019.

[16] M. S. Diallo, H. Poaty, S. Azonbankin, O. Faye, and F. Gangbo, "Fetal ventriculomegaly and outcomes: about 3 cases," *Open Journal of Pathology*, vol. 9, no. 3, pp. 41–49, 2019.

[17] H. Werner, P. Castro, and P. Daltro, "Prenatal Diagnosis of Apert Syndrome Using Ultrasound, Magnetic Resonance Imaging, and Three-Dimensional Virtual/physical Models: Three Case Series and Literature review," *Child\"s Nervous System*, vol. 34, 2018.

[18] B. Zheng, "The Prenatal Diagnosis and Classification of Cleft Palate: The Role and Value of Magnetic Resonance Imaging," *European Radiology*, vol. 29, 2019.

Hindawi
Contrast Media & Molecular Imaging
Volume 2022, Article ID 8998231, 5 pages
https://doi.org/10.1155/2022/8998231

Research Article

Diagnostic Value of Magnetic Resonance Imaging Scan, Multislice Spiral Computed Tomography Three-Dimensional Reconstruction Combined with Plain Film X-Ray in Spinal Injuries

Dajiang Xin[1] and Lei Lei[2]

[1]Department 3 of Trauma, Yantai Mountain Hospital, Yantai City 264000, Shandong Province, China
[2]Department of Medical Imaging, Hohhot First Hospital, Hohhot City 010059, Inner Mongolia Autonomous Region, China

Correspondence should be addressed to Lei Lei; leilei@hsdyyy.com.cn

Received 1 March 2022; Accepted 18 April 2022; Published 16 May 2022

Academic Editor: M. Pallikonda Rajasekaran

Objective. The main objective is to explore the diagnostic value of magnetic resonance imaging (MRI) scan, multislice spiral computed tomography (MSCT) three-dimensional reconstruction combined with plain film X-ray in spiral injuries. *Methods*. By means of retrospective study, the data of 100 patients with spiral injury treated in our hospital from January 2020 to December 2021 were retrospectively analyzed, and all patients received MRI scan, MSCT three-dimensional reconstruction, and plain film X-ray examination, and by taking the operation results as the reference, the diagnostic results of different diagnostic modalities were analyzed, and the accordance rates (diagnostic result/surgical result $\times$ 100%) of the three diagnostic modalities and their combination were calculated, respectively. *Results*. Among the 100 patients, 52 cases (52%) had a fracture at the anterior column of the spine, 28 cases (28%) had a fracture at the middle column of the spine, and 20 cases (20%) had a fracture at the posterior column of spine; 24 cases (24%) had simple flexion compression fracture, 60 cases (60%) had burst fracture, 6 cases (6%) had seat belt fracture, and 10 cases (10%) had fracture dislocation. The accordance rate of combined diagnosis for fracture site was 100%, and that for fracture type was 98.0%; MRI could visualize bone marrow injuries, ligamentous injuries, soft tissue injuries, and nerve root injuries that could not be visualized on X-ray plain films, and 3D reconstruction with MSCT could clearly demonstrate the 3D relationship of spinal fracture displacement, fracture line orientation, and spinal injury. *Conclusion*. Plain film X-ray is the basic method for diagnosing spinal injuries, while MRI and MSCT have their unique advantages in this regard, and patients with a negative result of X-ray plain film can be examined by MRI and MSCT to observe the spinal injury comprehensively.

1. Introduction

Spinal injuries, which result from indirect or direct external forces, are a common type of injury in the clinic [1]. Because of the complex anatomical structure, spinal injuries can cause curvature changes, displacement of fracture fragments, ligamentous injuries, soft tissue changes around the fractured vertebral bodies, etc., and for severe cases who are complicated with spinal cord injury (SCI), their movement, reflexes, and sphincters below the injury plane will be impaired [2, 3]. With the lifestyle changes of Chinese residents, the cause of injury to the spine has gradually increased, and the situation of spinal fractures is becoming more complex, so an accurate diagnosis of the site and type of spinal injuries in patients is beneficial to orthopedic physicians to develop the corresponding treatment plan, which is of great importance to reduce the disability and mortality of patients [4]. Plain film X-ray is the conventional diagnostic modality of spine injuries, which can clarify the compression of the vertebral body at the injured part, but may easily miss the cases with less severe compression [5], especially in patients with long-standing pain after trauma, X-ray plain films often fail to show the fracture signs, and they are usually diagnosed with soft tissue contusion, delaying their treatment time [6]. The current application of magnetic resonance imaging (MRI) and computed tomography (CT) further highlights the disadvantages of X-ray plain films, and more and more physicians prefer to choose MRI and CT to diagnose the injury condition of the spine [7, 8]. MRI has a unique diagnostic advantage for SCI, because paraspinal ligaments, disc injury, and paraspinal hematoma can only be detected by MRI, whereas conventional CT can only rely on the indirect signs to judge bone marrow and soft tissue injuries, with a poor clinical detection rate. The promotion of multislice spiral computed tomography (MSCT) in recent years has led to the improvement of CT examination results, and MSCT three-dimensional reconstruction can remove other bones and soft tissues, thus clearly showing the stereo image of the spine, facilitating physicians to observe the fracture line course in a full range and at many angles, and providing a good basis for determining the surgical plan and surgical path in the clinic [9]. At present, there are no studies in academia that combine plain film X-ray, MRI, and MSCT 3D reconstruction, but they all have their own advantages in diagnosing spinal injuries, and their combination may complement each other's advantages, improving the accuracy of spine injury diagnosis. Based on this, 100 patients with spinal injury were chosen as the subjects to explore the diagnostic value of combining MRI and MSCT three-dimensional reconstruction with plain film X-ray in spinal injury.

2. Materials and Methods

2.1. General Data. The data of spinal injury patients treated in our hospital from January 2020 to December 2021 were retrospectively analyzed, and 100 patients over 18 years old with a clear history of acute spinal trauma were selected, including 68 males and 32 females, with a mean age of (49.41 ± 8.90) years and a mean course of disease of (1.95 ± 0.71) d, and in terms of the cause of injury, 15 cases were caused by high-altitude falling, 30 cases were caused by a traffic accident, 38 cases were caused by a fall on the flat ground, 12 cases were caused by damage from the heavy object, and 5 cases were caused by other factors. All 100 patients presented with varying degrees of spinal pain and limited mobility, including 15 with paralysis of the lower extremities. All patients required surgical treatment and had the good cognitive ability to go along with MRI scan, MSCT three-dimensional reconstruction, and plain film X-ray examination.

Patients with spinal injury due to other reasons [10], with contraindications of relevant imaging examinations [11], complicated with other severe organic diseases and in pregnancy or lactation were excluded from the study.

2.2. Moral Consideration. The study was conducted under the guidance of the World Medical Association Declaration of Helsinki [12], and the patients and their family members understood the study objective, meaning, content, and confidentiality and signed the informed consent.

2.3. Methods

2.3.1. MRI Scan. The GE Signa Excite 1.5T superconducting MRI instrument (NMPA Registration (I) no. 20153333982) was used, patients were kept in a proper position with assistance, cervical coil and spinal surface coil were selected, and axial, sagittal, and coronal scans were determined based on the site of the spinal lesion in the patients, with the parameters of SE T_1WI TR/TE = 400/12 ms, FSE T_2WI TR/TE = 3200/105–120 ms, STIR TR/TE = 4000/56 ms, slice thickness of 4.0 mm, slice gap of 4.0 mm, interval of 1 mm, and 256×256 matrix.

2.3.2. MSCT 3D Reconstruction. The Philips MSCT scanner (NMPA Certified No. (2018) 3303600) was used, the patients were in the spine position with assistance, and ROIs were selected for scan based on the positioning image, with the set slice thickness of 2.5 mm, thin-layer reconstruction slice thickness of 2.0 mm, reconstruction interval of 1.5 mm, pitch of 1.5, tube voltage of 120 KV, and tube current of 120 mA. The acquired original cross-sectional CT images were transferred to a Philips Brilliance Workspace 2.0 workstation for 3D reconstruction, including multiplanar reconstruction volume reproduction (VR), with the built-in processing software. VR images hid the tissues that were not associated with the bone through adjustment of the threshold to clearly reveal the bones.

2.3.3. Plain Film X-Ray. The X-ray apparatus made by Shanghai Xin Huang Pu Medical Equipment Co., Ltd. (Shanghai Medical Products Administration Certified No. 20132301725) was used to regularly shoot the positive lateral plain film of the spinal segment at the lesion site, and the plain films of double oblique view were taken for some patients.

2.4. Observation Criteria. According to the three-column concept for classification [13], spinal injuries are divided into four types, that is, (1) simple flexion compression type, (2) burst type, (3) seat belt type, and (4) fracture-dislocation type.

The slides were read jointly by 2 radiologists and 1 orthopedic surgeon under double-blind conditions, and they reached a consensus conclusion through discussion. The results of the surgery were set as the standard in both groups, and the accordance of the results of imaging examinations with the standard was determined.

2.5. Statistical Processing. In this study, the data processing software was SPSS20.0, the picture drawing software was GraphPad Prism 7 (GraphPad Software, San Diego, USA), the items included were enumeration data and measurement data, the methods used were X^2 test and t-test, and differences were considered statistically significant at $P < 0.05$.

Table 1: Analysis of results of imaging examinations.

Group	MRI	MSCT	X-ray plain films	Joint examination
Anterior ligament injury	48	10	0	65
Posterior ligament injury	24	8	0	32
SCI	63	15	0	72
Soft tissue injury	76	86	20	86
Fracture line	92	95	78	95
Vertebral arch fracture	60	65	48	70
Nerve root injury	28	70	10	72

3. Results

3.1. Analysis of Results of Imaging Examinations. MRI. Vertebral fractures were shown as displacement of the vertebral bone fragments towards the front, displacement of the bone scraps at the posterior border into the posterior spinal canal, increased signal within the vertebral body, low or equal signal on T_1WI, and high signal on T_2WI. According to the MRI findings, 48 cases had injury of anterior ligament, which revealed as thickened anterior longitudinal ligament and increased signal on T_2WI and STIR; 24 cases had injury of posterior ligament, which revealed as thickened posterior longitudinal ligament and increased signal on T_2WI and STIR; 63 cases had SCI, with longitudinal strip isointensity and hypointensity in the spinal cord on T_1WI, slightly high signal on T_2WI, high signal on STIR, heterogeneous signal, and increased volume of the spinal cord in the injured segment; and 76 cases had injury of soft tissue, with patchy hyperintensity on T_2WI and STIR, and slightly low signal on T_1WI.

MSCT. Vertebral fractures were shown as flattening of the vertebral body with a wedge-shaped appearance, and in 82 cases, the fracture line and displaced bone were visible. The 3D reconstruction of MSCT could not fully reflect SCI, and only partial swelling and hemorrhage within the spinal cord could be revealed. MSCT only showed anterior longitudinal ligament thickening in 10 cases and posterior longitudinal ligament thickening in 8 cases, while the ligament injury in the remaining cases was failed to show directly.

X-Ray Plain Films. The fracture line appeared sharp in the lateral X-ray film. X-ray plain films failed to reveal injuries of the anterior ligament, posterior ligament, and spinal cord.

In short, MRI can reveal bone marrow injury, ligament injury, soft tissue injury, and nerve root injury that cannot be visualized on X-ray plain films, and MSCT 3D reconstruction can clearly demonstrate the 3D relationship of spinal fracture displacement, fracture line course, and spinal injury (see Table 1 for the analysis of the results of the three imaging examinations).

3.2. Comparison of Accordance Rates of Imaging Examinations. According to the three-column concept, among the 100 patients, 52 cases had fracture at the anterior column of the spine, 28 cases had fracture at the middle column of the spine, and 20 cases had fracture at the posterior column of the spine; 24 cases had simple flexion compression fracture, 60 cases had burst fracture, 6 cases had seat belt fracture, and 10 cases had fracture dislocation. The accordance rate of combined diagnosis for fracture site was 100%, and that for fracture type was 98.0% (see Table 2).

4. Discussion

Spinal injuries occupy an important position in systemic osteoarticular injuries, and vertebral fractures are more common in the clinic, accompanied by adnexal fractures in some patients, and their fracture rate is approximately 5.0%–6.0% of patients with systemic fractures [14]. Since the spine is a complex structure with multiple bones, in which joints and nerves are intricate, fracture patients may also suffer from complications such as SCI and nerve injury, which, in severe cases, seriously affect the physiological function of their internal organs and even make them lose the function of lower limbs and face the risk of paralysis or death [15, 16]. Accurate judgment of spinal injuries is beneficial for orthopedics to make surgical plans and improve patient outcomes, so intuitive and practical diagnostic modalities should be chosen in practice to enhance the diagnostic accuracy of spinal injuries. Plain film X-ray is the most basic diagnostic modality for spinal injuries, which can directly reflect the injured part in patients with vertebral fractures and is inexpensive, presenting a wide market value [17]. With the assistance of plain film X-ray, physicians can comprehensively analyze information such as the degree of compression and the interpedicular distance of the injured vertebral bodies of patients, so as to judge the fracture type. However, plain film X-ray is subject to the influence of spinal structure and cannot adequately detect fractures at overlapping sites, and in particular, it is difficult for plain film X-ray to distinguish whether the spinal canal is involved or not, and whether there is damage to soft tissues [18–20]. In this study, plain film X-ray failed to show the injuries of the anterior ligament, posterior ligament, and spinal cord. The utility of plain film X-ray is further limited by the complex patient condition, and there are often instances in practice in which patients are symptomatic and obtain negative X-ray results. To make up for the deficiencies of plain film X-ray, physicians usually advocate performing additional MRI or CT for patients with negative X-ray result [9]. MRI, due to its high soft-tissue resolution, can be used to accurately determine the injuries of soft tissue, ligament as well as bone marrow, and especially simple bone marrow injury and ligament injury. Scholars Shah et al. found that at the early

Table 2: Comparison of accordance rates of imaging examinations.

Group	MRI	MSCT	X-ray plain films	Joint examination
Fracture site	90 (90.0)	100 (100.0)	82 (82.0)	100 (100.0)
Fracture type				
Simple flexion compression fracture	20 (83.3)	22 (91.7)	18 (75.0)	24 (100.0)
Burst fracture	50 (83.3)	58 (96.7)	48 (80.0)	59 (98.3)
Seat belt fracture	4 (66.7)	5 (83.3)	3 (50.0)	5 (83.3)
Fracture dislocation	7 (70.0)	9 (90.0)	7 (70.0)	10 (100.0)

stage of ligament injury, MRI showed low signal on T_1WI and T_2WI, and the signal was more uniform [21]. According to the MRI findings of the study, 48 cases had injury of anterior ligament, which revealed as thickened anterior longitudinal ligament and increased signal on T_2WI and STIR, and 24 cases had injury of posterior ligament, which revealed as thickened posterior longitudinal ligament and increased signal on T_2WI and STIR. Bone marrow injury, as the most serious complication of spinal injury, can manifest as spinal cord edema, hemorrhage, contusion, and its early diagnosis can only be made by MRI [22]. Spinal cord lesions on MRI generally appear as longitudinal strips, patchy equal signals, or low signals. The MRI findings in this study showed that 63 cases had SCI, with longitudinal strip isointensity and hypointensity in the spinal cord on T_1WI, slightly high signal on T_2WI, high signal on STIR, heterogeneous signal, and increased volume of the spinal cord in the injured segment; in addition, 76 cases had injury of soft tissue, with patchy high signal on T_2WI and STIR, and slightly low signal on T_1WI.

Although MSCT had a detection rate for SCI and soft tissue injury inferior to that of MRI, it has the advantage of stereological imaging to adequately exclude overlapping interference [23]. MSCT has an independent postprocessing work station and includes a variety of reorganization ways, which can obtain the 3D images of bone and joint structure with only the cross-sectional data of CT, and physicians can observe the overall situation of fracture by 3D reconstruction of MSCT and analyze the anatomical relationship between the injured part and the adjacent structure, which effectively overcomes the deficiencies of MRI and X-ray plain films. According to the MSCT findings of the study, vertebral fractures were shown as flattening of the vertebral body with a wedge-shaped appearance, and in 82 cases, the fracture line and displaced bone were visible, 4 of which with minor fractures showed no trabecular bone density on conventional MSCT, and after 3D reconstruction, morphological changes could be found, and thus, the diagnosis was confirmed. MSCT 3D reconstruction compensates for the deficit of MRI insensitivity to the cortical bone and clearly and intuitively reveals the fracture site. Scholars Saman et al. found that this modality also has good diagnostic value for determining the size and number of vertebral fracture fragments [24]. Based on the three-column concept, among the 100 patients included in this study, 52 cases had fracture at the anterior column of the spine, 28 cases had fracture at the middle column of the spine, and 20 cases had fracture at the posterior column of the spine; 24 cases had simple flexion compression fracture, 60 cases had burst fracture, 6 cases had seat belt fracture, and 10 cases had fracture dislocation. The accordance rate of combining plain film X-ray, MRI, and MSCT 3D reconstruction for fracture site was 100%, and that for fracture type was 98.0%, confirming that the combined examination can make their respective advantages complementary to each other and effectively improve the detection accuracy of spinal injuries.

In short, MRI can reveal bone marrow injury, ligament injury, soft tissue injury, and nerve root injury that cannot be visualized on X-ray plain films, and MSCT 3D reconstruction can clearly demonstrate the 3D relationship of spinal fracture displacement, fracture line course, and spinal injury. Plain film X-ray, as the basic method of diagnosing spinal injuries, still cannot be replaced nowadays, but MRI and MSCT can make up for the shortcomings of plain film X-ray and play a role in drawing on each other's strengths. For patients with negative X-ray results, MRI and MSCT can be used to observe the spinal injury comprehensively, which is conducive to reducing the disability rate and mortality rate of patients with spinal injuries.

Data Availability

The data supporting the findings of this study are available on reasonable request from the corresponding author.

Conflicts of Interest

The authors declare that they have no conflicts of interest.

References

[1] T. Lurie, B. Schwartz, D. Najafali, P. Gandhi, M. Jackson, and Q. K. Tran, "Correlation of history and physical examination with imaging in traumatic near-shore aquatic head and spinal injury," *The American Journal of Emergency Medicine*, vol. 38, no. 10, pp. 2049–2054, 2020.

[2] G. V. Watane, B. Gosangi, R. Thomas et al., "Incidence and characteristics of spinal injuries in the victims of intimate partner violence (IPV)," *Emergency Radiology*, vol. 28, no. 2, pp. 283–289, 2021.

[3] S. Häckel, E. Hofmann, H. Anwander et al., "Anterior-posterior view by full-body digital X-ray to rule out severe spinal injuries in Polytraumatized patients," *BMC Emergency Medicine*, vol. 21, no. 1, p. 27, 2021.

[4] H. Wilde, A. S. Gamblin, J. Reese et al., "The effect of hospital transfer on patient outcomes after rehabilitation for spinal injury," *World Neurosurgery*, vol. 133, pp. e76–e83, 2020.

[5] M. A. Tafida, Y. Wagatsuma, E. Ma, T. Mizutani, and T. Abe, "Descriptive epidemiology of traumatic spinal injury in

Japan," *Journal of Orthopaedic Science*, vol. 23, no. 2, pp. 273–276, 2018.

[6] R. Mitchell, L. Harvey, R. Stanford, and J. Close, "Health outcomes and costs of acute traumatic spinal injury in New South Wales, Australia," *The Spine Journal*, vol. 18, no. 7, pp. 1172–1179, 2018.

[7] R. C. Sterner and N. P. Brooks, "Early decompression and short transport time after traumatic spinal cord injury are associated with higher American spinal injury association impairment scale conversion," *Spine*, vol. 47, no. 1, pp. 59–66, 2022.

[8] A. Bizhan, A.-D. Noori, C. Timothy et al., "Efficacy of ultra-early (< 12 h), early (12-24 h), and late (>24-138.5 h) surgery with magnetic resonance imaging-confirmed decompression in American spinal injury association impairment scale grades A, B, and C cervical spinal cord injury," *Journal of Neurotrauma*, vol. 37, pp. 448–457, 2020.

[9] A. Naduvanahalli Vivekanandaswamy, M. Kannan, V. Sharma et al., "Prognostic utility of magnetic resonance imaging (MRI) in predicting neurological outcomes in patients with acute thoracolumbar spinal cord injury," *European Spine Journal*, vol. 29, no. 6, pp. 1227–1235, 2020.

[10] A. L. Rabbitt, T. G. Kelly, K. Yan, J. Zhang, D. A. Bretl, and C. V. Quijano, "Characteristics associated with spine injury on magnetic resonance imaging in children evaluated for abusive head trauma," *Pediatric Radiology*, vol. 50, no. 1, pp. 83–97, 2020.

[11] Y. Bao, X. Zhong, W. Zhu et al., "Feasibility and safety of cervical kinematic magnetic resonance imaging in patients with cervical spinal cord injury without fracture and dislocation," *Orthopaedic Surgery*, vol. 12, no. 2, pp. 570–581, 2020.

[12] World Medical Association, "World medical association declaration of Helsinki," *JAMA*, vol. 310, no. 20, pp. 2191–2194, 2013.

[13] S. Shabani, M. Kaushal, H. M. Soliman et al., "AOSpine global survey: international trends in utilization of magnetic resonance imaging/computed tomography for spinal trauma and spinal cord injury across AO regions," *Journal of Neurotrauma*, vol. 36, no. 24, pp. 3323–3331, 2019.

[14] T. L. Wu, N. E. Byun, F. Wang et al., "Longitudinal assessment of recovery after spinal cord injury with behavioral measures and diffusion, quantitative magnetization transfer and functional magnetic resonance imaging," *NMR In Biomedicine*, vol. 33, no. 4, Article ID e4216, 2020.

[15] T. Dalkilic, N. Fallah, V. K. Noonan et al., "Predicting injury severity and neurological recovery after acute cervical spinal cord injury: a Comparison of cerebrospinal fluid and magnetic resonance imaging biomarkers," *Journal of Neurotrauma*, vol. 35, no. 3, pp. 435–445, 2018.

[16] J. Wang, Y. Li, T. Xu, J. Zhao, C. Yuan, and B. Wen, "Reconstructing nanohydroxyapatite prosthesis based on CT-scanning data and its application in spinal injury," *Journal of Biomedical Nanotechnology*, vol. 17, no. 9, pp. 1745–1753, 2021.

[17] M.-Yu Zhu, Ji-W. Tian, H. L. Teng et al., "[Application of Gemstone Spectrum Imaging for anterior spinal artery in patients with cervical spinal injury]," *Zhong Guo Gu Shang*, vol. 31, pp. 425–430, 2018.

[18] B. Fiani, R. A. Figueras, F. D. Stefano, N. Gautam, A. Khan, and M. Soula, "Nonmissile penetrating spinal injuries: mechanisms, expectations, and management," *Surgical Neurology International*, vol. 11, p. 406, 2020.

[19] W. Kim, N. Ahn, A. Ata, M. A. Adamo, P. Entezami, and M. Edwards, "Pediatric cervical spine injury in the United States: defining the burden of injury, need for operative intervention, and disparities in imaging across trauma centers," *Journal of Pediatric Surgery*, vol. 56, no. 2, pp. 293–296, 2021.

[20] S. Sikka, A. Vrooman, L. Callender et al., "Inconsistencies with screening for traumatic brain injury in spinal cord injury across the continuum of care," *The Journal of Spinal Cord Medicine*, vol. 42, no. 1, pp. 51–56, 2019.

[21] N. G. Shah, A. Keraliya, M. B. Harris, C. M. Bono, and B. Khurana, "Spinal trauma in DISH and AS: is MRI essential following the detection of vertebral fractures on CT?" *The Spine Journal*, vol. 21, no. 4, pp. 618–626, 2021.

[22] L. Zhang, F. R. López-Picón, Y. Jia et al., "Longitudinal [18F] FDG and [13N]NH3 PET/CT imaging of brain and spinal cord in a canine hemisection spinal cord injury model," *NeuroImage: Clinica*, vol. 31, p. 102692, 2021.

[23] P. C. Zambrano-Rodríguez, S. Bolaños-Puchet, H. J. Reyes-Alva et al., "High-resolution micro-CT myelography to assess spinal subarachnoid space changes after spinal cord injury in rats," *Journal of Neuroimaging*, vol. 31, no. 1, pp. 79–89, 2021.

[24] S. Shabani, B. P. Meyer, M. D. Budde, and M. C Wang, "Diagnostic imaging in spinal cord injury," *Neurosurgery Clinics of North America*, vol. 32, no. 3, pp. 323–331, 2021.

Hindawi
Contrast Media & Molecular Imaging
Volume 2022, Article ID 9684584, 8 pages
https://doi.org/10.1155/2022/9684584

Research Article

Deep Learning-Based Computed Tomography Perfusion Imaging to Evaluate the Effectiveness and Safety of Thrombolytic Therapy for Cerebral Infarct with Unknown Time of Onset

Minlei Hu,[1] Ning Chen,[1] Xuyou Zhou,[1] Yanping Wu,[2] and Chao Ma[3]

[1]*Department of Neurology, Affiliated Hospital of Jiaxing University, The First Hospital of Jiaxing, Jiaxing 314000, Zhejiang, China*
[2]*Department of Radiology, Affiliated Hospital of Jiaxing University, The First Hospital of Jiaxing, Jiaxing 314000, Zhejiang, China*
[3]*Department of Rehabilitation Medicine, Zhuji People's Hospital of Zhejiang Province, Zhuji 311800, Zhejiang, China*

Correspondence should be addressed to Chao Ma; 13858523198@139.com

Received 15 February 2022; Revised 3 April 2022; Accepted 8 April 2022; Published 9 May 2022

Academic Editor: M. Pallikonda Rajasekaran

This study was aimed to discuss the effectiveness and safety of deep learning-based computed tomography perfusion (CTP) imaging in the thrombolytic therapy for acute cerebral infarct with unknown time of onset. A total of 100 patients with acute cerebral infarct with unknown time of onset were selected as the research objects. All patients received thrombolytic therapy. According to different image processing methods, they were divided into the algorithm group (artificial intelligence algorithm-based image processing group) and the control group (conventional method-based image processing group). After that, the evaluations of effectiveness and safety of thrombolytic therapy for the patients with acute cerebral infarct in the two groups were compared. The research results demonstrated that artificial intelligence algorithm-based CTP imaging showed significant diagnostic effects and the image quality in the algorithm group was remarkably higher than that in the control group ($P < 0.05$). Besides, the overall image quality of algorithm group was relatively higher. The differences in the National Institute of Health stroke scale (NIHSS) scores for the two groups indicated that the thrombolytic effect on the algorithm group was superior to that on the control group. Thrombolytic therapy for the algorithm group showed therapeutic effects on neurologic impairment. The symptomatic intracranial hemorrhage rate of the algorithm group within 24 hours was lower than the hemorrhage conversion rate of the control group, and the difference between the two groups was 14%. The data differences between the two groups showed statistical significance ($P < 0.05$). The results demonstrated that the safety of guided thrombolytic therapy for the algorithm group was higher than that in the control group. To sum up, deep learning-based CTP images showed the clinical application values in the diagnosis of cerebral infarct.

1. Introduction

Cerebral infarction with unknown time of onset, known as "ischemic stroke," is a common disease of cerebral stroke, accounting for approximately 60%~80% among cerebral diseases. It arises from long-term insufficient cerebral blood supply. Eventually, it will lead to cerebral ischemia, insufficient oxygen uptake, and necrotic changes in the brain [1]. The identification of neurological dysfunction is very important for the early diagnosis of cerebral infarction so that blood circulation can be improved as soon as possible. For its clinical treatment, thrombolytic therapy is the most important method, and recombinant tissue plasminogen activator (rt PA) and urokinase are widely used thrombolytic drugs in clinic [2]. The time of rt PA treatment is 3–4.5 hours, and urokinase treatment takes 6 hours. Herpich and Rincon [3] showed that the treatment was effective within 6 hours of onset, but it was life-threatening after 6 hours. Due to the long onset time of patients, thrombolysis symptoms are mainly confused with clinical symptoms. Despite the limited treatment period for cerebral infarction, the traditional equipment for predicting cerebral blood flow and cerebral thrombosis is inaccurate. Patients not following the thrombolysis therapy can result in severe bleeding [4, 5].

According to the time and degree of vascular stenosis, there may be hypoperfusion tissue at the necrotic edge around the core infarction area. If the blood supply is restored in time, it is called ischemic penumbra (IP) [6]. The concept of IP is the theoretical basis of thrombolytic therapy. The thrombolysis is to protect ischemic shadow, preserve ischemic brain tissue as much as possible, and improve the prognosis of patients. Hence, it is important for clinical treatment to quickly detect the presence or absence of ischemic shadow [7, 8]. In recent years, computed tomography perfusion (CTP) imaging is the main method to evaluate the condition of acute ischemic stroke (AIS), although magnetic resonance imaging (MRI) is more accurate in examining ischemic brain tissue [9, 10]. Cerebral blood volume (CBV), cerebral blood flow (CBF), time-to-peak (TTP), mean transit time (MTT), and other pseudocolor perfusion parameters can be used to determine the condition of ischemic brain tissue [11, 12].

CT is a new technology that combines the most advanced technologies in many fields, such as radiation, informatics, microelectronics, and computer science. In 2004, the DRL reconstruction algorithm is constructed based on the common neural network algorithm. With the pervasiveness of computer technology, artificial intelligence (AI) algorithm has been widely used in the medical field. According to some research, the AI algorithm can improve the efficiency of refinement of the CT image of the lung. The DRL algorithm is mainly based on the deep convolutional neural network (DCNN) model for low-sampling image restoration. Simply put, DCNN model is a tool for image analysis and reconstruction using backward tracking propagation algorithm including backward analysis. Because CTP image data have three-dimensional data of height, weight, and time series, a DCNN model named DRL with three-dimensional convolution layer and active layer is constructed [13]. The DRL algorithm features accurate CT reconstruction using projection data truncated along the horizontal direction of the detector. Therefore, the DRL algorithm can be used to segment ROI [14]. DRL can obtain real high-resolution sectional images and analyze images quantitatively. To reconstruct images, the imaging system uses reconstructors to receive sampled and digitized X-ray data. Moreover, it can reduce the reconstruction time and radioactivity. Although CT technology has been developed for many years and the hardware has been greatly improved, the DRL reconstruction algorithm is scarcely used to process brain images [15].

In this study, the DRL model was optimized and applied in practice. Artificial intelligence-based CT image processing can improve the effectiveness and safety of the treatment for acute cerebral infarction. CTP images were analyzed factoring in peak signal-to-noise ratio to judge noise reduction efficiency and to study the characteristics of cerebral blood flow and dark zone of cerebral blood flow in acute cerebral infarction. The study was aimed at providing the theoretical references and basis for the clinical treatment of acute cerebral infarct.

2. Materials and Methods

2.1. Research Subjects. A total of 100 patients with cerebral infarct with unknown time of onset were selected as the research subjects. All patients underwent thrombolytic therapy. According to different image processing methods, the patients were divided into the algorithm group (artificial intelligence algorithm-based image processing group) and the control group (conventional method-based image processing group). Among 50 patients in the control group, there were 24 male patients and 26 female patients, and their average age was 58.0 ± 3.22. In the algorithm group, there were 28 male patients and 22 female patients, and their average age was 56.8 ± 3.41. The differences in general data on the patients in the two groups showed no statistical meaning ($P > 0.05$). This study had been approved by Ethics Committee of hospital. The patients' family members had signed informed consent forms.

Inclusion criteria were as follows: (i) CT examination of clinical symptoms of stroke; (ii) occlusion of large vessels in anterior circulation; (iii) MRI examination showed seizure symptoms; (iv) no intracranial hemorrhage was detected in brain CT. Besides, no obvious low-density shadow corresponding to neurologic impairment was found; (v) thrombolytic therapy could be performed within 6 hours after onset. The therapy for progressive stroke could be extended to 12 hours after onset; and (vi) patients and their family members had signed and consented.

Exclusion criteria were as follows: (i) patients who did not sign informed consent; (ii) patients with brain diseases such as intracranial hemorrhage and epilepsy; (iii) patients under 18 years old; (iv) with allergy to contrast agents; (v) acute cerebral infarct, subacute bacterial endocarditis, acute pericarditis, and severe heart failure came into being in the recent 90 days; and (vi) intracranial aneurysm, arteriovenous malformation, intracranial tumor, and suspected subarachnoid hemorrhage did not occur.

2.2. The Algorithm Processing of CT Perfusion Imaging. The noise model in the low-dose CT projection was regarded as the Gaussian noise with the mean-variance relationship, so the mathematical expression of the noise model was expressed as follows:

$$\sigma_i^2 = \frac{1}{P_{i0}} exp\left(\overline{a_i}\right)\left[1 + \frac{1}{P_{i0}}\left(\overline{a_i}\right)\left(\sigma_e^2 - 1.25\right)\right]. \quad (1)$$

In (1), P_{i0} represented the intensity of the incident ray, $\overline{a_i}$ represented the mean value of the chordal graph of ray penetration path i, σ_i^2 represented the variance of the chordal graph of ray penetration path i, and σ_e^2 represented the variance of the background electronic noise.

The adaptive chordal graph restoration method was used to reduce the noise and artifacts in the reconstructed CT images. In (2), the penalized weighted least squares (PWLS) were used to recover the projected data.

$$\Phi(p) = (y - p)^T \sum (y - p)^{-1} + \beta R(p). \quad (2)$$

In equation (2), p expressed the ideal chordal graph data to be estimated, $R(p)$ expressed the penalty term, and β expressed the smoothing parameter.

According to the probability theory in the statistical analysis, the median distribution was used to predict the central tendency ratio to the mean. Then, (3) showed the calculation of $R(p)$.

$$R(p) = \frac{1}{2}\sum_{i}\left(p_i - p(N_i)_{\text{median}}\right)^2. \quad (3)$$

In (3), N_i represented the four-neighborhood pixels in the two-dimensional chordal graph gridding, and $p(N_i)_{\text{median}}$ represented the mid-value.

The modified iterative Gauss–Seidel method was adopted to optimize and solve the PWLS function.

$$p_i^{m+1} = \frac{1}{1+\beta\sigma_i^2}\left[y_i + \beta\sigma_i^2 \cdot p^m(N_i)_{\text{median}}\right]. \quad (4)$$

In equation (4), m expressed the number of iterations.

To solve the problem of resolution loss in the images after the reconstruction, the adaptive projection data weighting method was adopted to process image data. If the original data containing the noise image were y, and the image data restored by the PWLS method were x, the constructed adaptive weighting framework could be expressed as follows:

$$\tilde{y}_i = \omega_i \cdot y_i + (1-\omega_i)\cdot x_i, \quad (5)$$

$$\omega_i = \begin{cases} 1, \sigma_i^2 \le \lambda, \\ 0, \sigma_i^2 > \lambda. \end{cases} \quad (6)$$

In (5) and (6), $\tilde{y}_i$ represented the image data after the weighted processing, ω_i represented the weight coefficient, σ_i^2 represented the noise variance, and λ represented the threshold factor.

The indexes of peak signal-to-noise ratio (PSNR), root mean square error (RMSE), and universal quality index (UQI) were used for the quantitative evaluation of the effects of image reconstruction. Equations (7)–(9) showed how the above indexes were defined [15].

$$PSNR = 20log_{10}\left(\frac{\overline{f}_{\max}}{\sigma}\right), \quad (7)$$

$$RMSE = \sqrt{\frac{\left[\sum_{i=1}^{n}\left(f_i - \overline{f}_i\right)^2\right]}{n}}, \quad (8)$$

$$UQI = \frac{\left[2Cov\left(f-\overline{f}\right)\cdot 2\mu_f\mu_{\overline{f}}\right]}{\left[\left(\sigma_f^2+\sigma_{\overline{f}}^2\right)\cdot\left(\mu_f^2+\mu_{\overline{f}}^2\right)\right]}. \quad (9)$$

In Equations (7)–(9), f expressed the perfusion parameter diagram after the restoration of the sequence, $\overline{f}$ expressed the reference to the perfusion parameter diagram, and σ expressed the standard deviation. σ_f^2 and $\sigma_{\overline{f}}^2$ expressed the contrast parameter in the region of interest and the variance of the reference parameter diagram. μ_f^2 and $\mu_{\overline{f}}^2$ expressed the contrast parameter in the region of interest and the mean value of the reference parameter diagram.

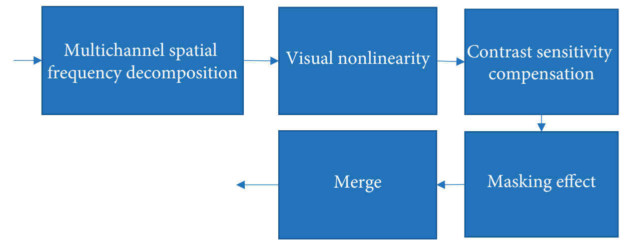

Figure 1: Abstract model of visual system.

The abstract model of visual system is shown in Figure 1.

2.3. Thrombolytic Scheme. According to *the Chinese Guidelines for the Diagnosis and Treatment of Acute ischemic Stroke 2014* [16], patients who met the inclusion and exclusion criteria accepted intravenous thrombolysis therapy within 4.5 hours of onset. *Usage.* Urokinase 0.9 mg/kg (the maximum dosage is 90 mg) was injected intravenously, and the dosage was 10% within 10 minutes. At the same time, the patient was monitored for physiological information, and abnormal physiological characteristics required symptomatic treatment. Aspirin 300 mg was taken orally 24 hours after thrombolytic therapy. Patients needed to be injected with 1 million to 1.5 million IU urokinase intravenously within 6 hours of onset.

2.4. CTP Examination Process. Spiral CT was employed to examine and scan the patients. Prior to the scanning, the patients needed to understand related precautions, and it should be ensured that no patients suffered from the contraindications of the examination. Before the operation, their height and weight should be recorded accurately. And trocar was inserted into anterior elbow vein. During the examination, the patients were instructed not to tilt their heads. Besides, they were told to keep body still without speaking or swallowing. In this case, good imaging effects could be obtained. The layer thickness of the scanning on head was required to be 5 mm, tube current was 100 mA, and tube voltage was 120 KV. CTP scanning was performed in dynamic reciprocating scanning mode. 40–50 mL of fluorine nonionic contrast agent was injected into anterior elbow venous double-tube high-pressure syringe at the flow rate of 4-5 mL/s. Besides, 20 mL of normal physiological saline was injected. CTP scanning was performed from the top of head to the side of foot, which lasted for 45 seconds and about 20 cycles. Tube voltage, tube current, scanning thickness, and matrix size were set to be 80 kV, 125 mA, 5 mm, and 512×512, respectively. The images scanned by CTP were transmitted to the perfusion analysis software at Brain Perfusion 4.0 EBW workstation by intelligent algorithm. After that, the software automatically output the images of cerebral perfusion parameters. Next, abnormal perfusion areas were divided by 3 doctors with more than 5 years of experience. The disagreement was settled by the negotiation with senior physicians.

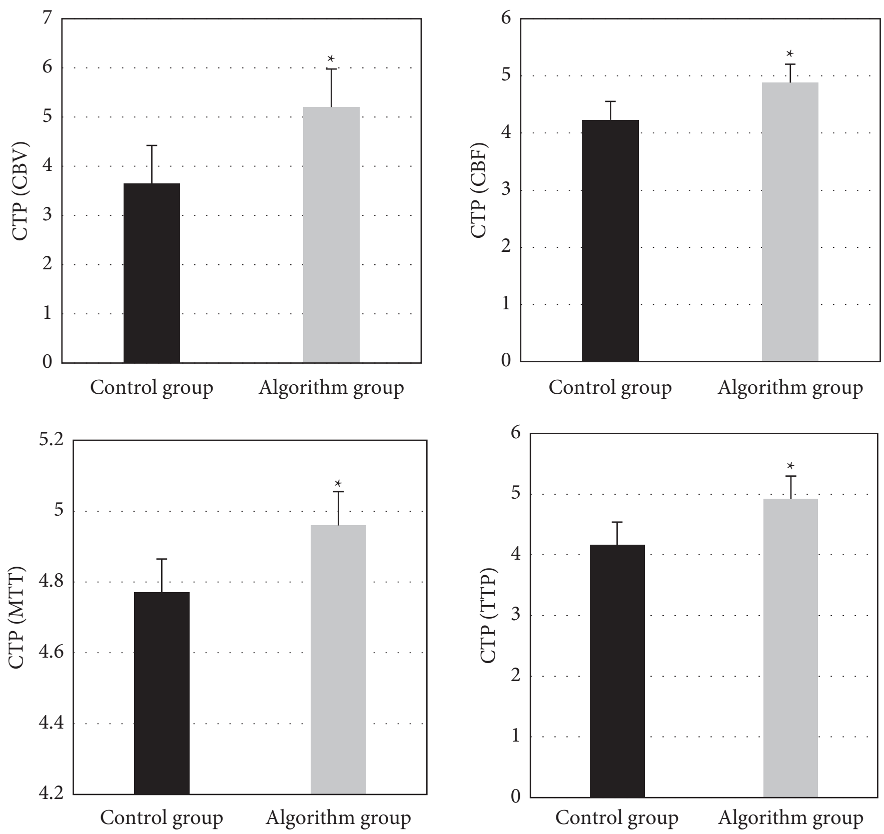

Figure 2: Comparison of accuracy of CBV, CBF, MTT, and TTP images between the two groups. * indicates statistically significant differences ($P < 0.05$).

2.5. Efficacy Evaluation. At one day, one week, half a month, and one month after the thrombolytic therapy, the NIHSS score was recorded, which was used as the evaluation standard of thrombolytic effect, and patients were evaluated for the brain nerve defects. One-month or three-month follow-up can reflect the long-term clinical results of thrombolytic therapy, while the NIHSS score can be used to evaluate patients' prognosis, and score ≤2 can be used as the obstacle threshold. A score of 0–2 means good prognosis, and a score of 3–4 means poor prognosis.

2.6. Safety Evaluation. After thrombolytic therapy combined with the NIHSS score (above 4 points), as well as CT or MRI examination, whether there is symptomatic cerebral hemorrhage is used as a safety evaluation index. In addition, the intracranial hemorrhage rates before and after thrombolytic therapy were compared. All indicators are recorded and classified by two doctors in strict accordance with the evaluation criteria to ensure the uniformity and accuracy.

2.7. Statistical Methods. GraphPad prism 5.0 software is used to process data expressed as mean ± standard deviation. SPSS 20.0 is used to analyze the differences among groups. *t*-Test for independent samples is performed for blood vessel diameter experiment and angiogenesis experiment. There is a statistical difference at $P < 0.05$.

3. Results

3.1. Comparison of Image Quality between Algorithm Group and Control Group. The pseudocolor image quality of CTP was evaluated factoring into the scores of CBV, CBF, MTT, and TTP. The image quality is divided into three grades: high (score >4), medium (score ≤4 and ≥2), and poor (score <2). As shown in Figure 2, for the image quality of the algorithm group, CBV was 5.2, CBF was 4.88, MTT was 4.96, and TTP was 4.92. The overall quality score was greater than 4, indicating high image quality. For the image quality in the control group, CBV was 3.65, CBF was 4.23, MTT was 3.77 MTT, and TTP was 4.16, with medium- and high-quality images. The overall image quality was better in the algorithm group.

The differences in PSNR, RMSE, and UQI indexes of patients' images processed by the compressed sensing reconstruction algorithm and the proposed algorithm were quantitatively evaluated. In Figure 3, compared with the compressed sensing reconstruction algorithm, PSNR and UQI values of images reconstructed by the proposed algorithm were remarkably higher, while the RMSE values were signally lower ($P < 0.05$).

3.2. Comparison of the Pseudocolor CTP Images Processed in the Algorithm Group and the Control Group. The pseudocolor CTP images of the two groups were compared for the

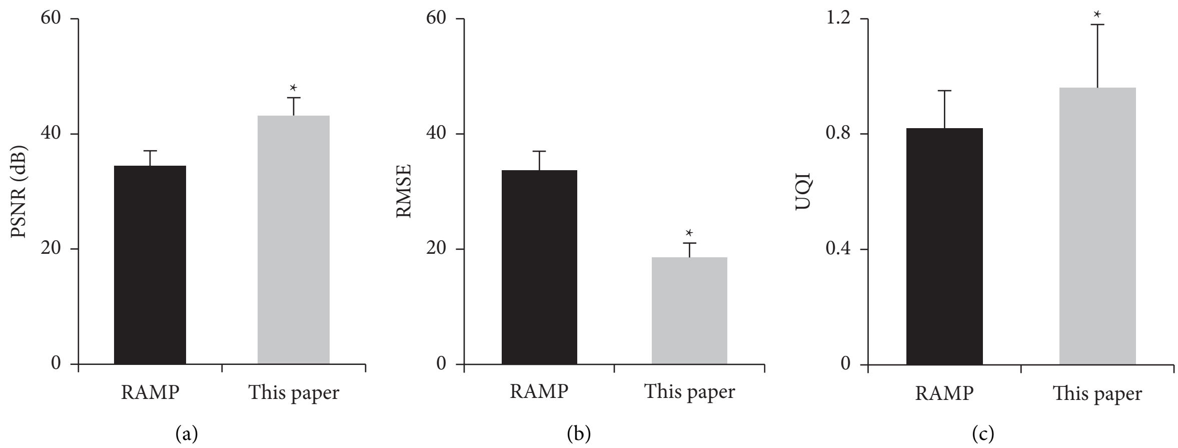

FIGURE 3: .Comparison of quantitative indexes of the images after the reconstruction. (a) comparison of PSNR; (b) comparison of RMSE; (c) comparison of UQI. * indicates statistically significant differences ($P < 0.05$).

ischemic area. The image of ischemic area and infarct core in perfusion image was very different from the normal image. As shown in Figures 4 and 5, the infarct core area in the image of the control group was slightly larger than that of the algorithm group, showing significant differences. In the algorithm group, the ischemic area and infarct core area in the original image were easier for doctors to distinguish, helpful for doctors to diagnose infarct lesions and blood flow. Figure 6 showed the myocardial infarction foci between the two groups, and it was noted that the algorithm group was more accurate in dividing the infarction area.

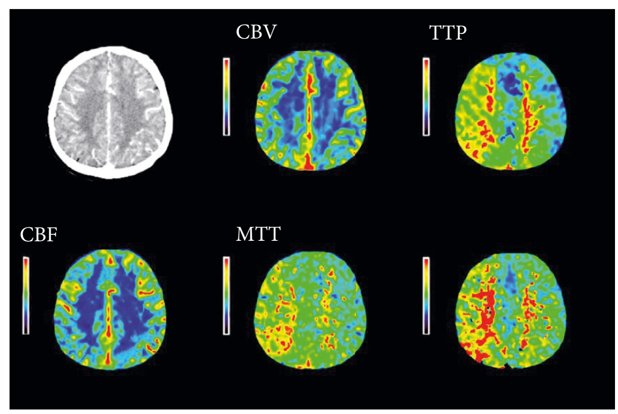

FIGURE 4: CTP pseudocolor image after processing by the algorithm.

3.3. Comparison of NIHSS Scores before and after Thrombolysis between the Two Groups. Figure 7 showed the NIHSS scores in the two groups. There was no significant difference between the control group and the algorithm group before thrombolysis ($P > 0.05$). On the day after thrombolytic therapy, the difference of the NIHSS scores between the algorithm group and the control group was 1.39, which was statistically significant ($P < 0.05$). One week after thrombolytic therapy, the difference of the NIHSS scores between the algorithm group and the control group was 0.91, which was statistically significant ($P < 0.05$). Half a month after thrombolytic therapy, the difference of the NIHSS scores between the algorithm group and the control group was 1.7, which was statistically significant ($P < 0.05$). One month after thrombolytic therapy, the difference of NIHSS scores between the algorithm group and the control group was 0.89, which was statistically significant ($P < 0.05$).

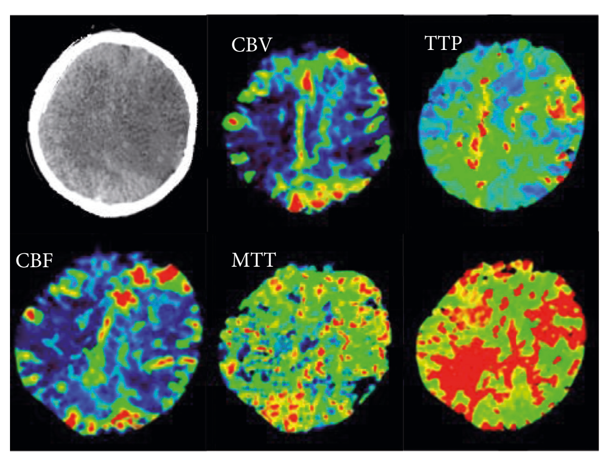

FIGURE 5: CTP pseudocolor image of control group after processing.

3.4. Comparison of Benign Prognosis Rate between Two Groups before and after Thrombolysis. As shown in Figure 8, one month after the thrombolytic treatment, the difference of benign prognosis rates between the algorithm group and the control group was 12%, with statistical differences ($P < 0.05$). After three months, the difference of benign prognosis rates between the algorithm group and the control group was 12%, with statistical difference ($P < 0.05$).

3.5. Comparison of Bleeding Conversion Rate between Two Groups before and after Thrombolysis. As shown in Figure 9, the symptomatic intracranial hemorrhage rate in the control group was 24% within 24 hours, and that was 10% in the

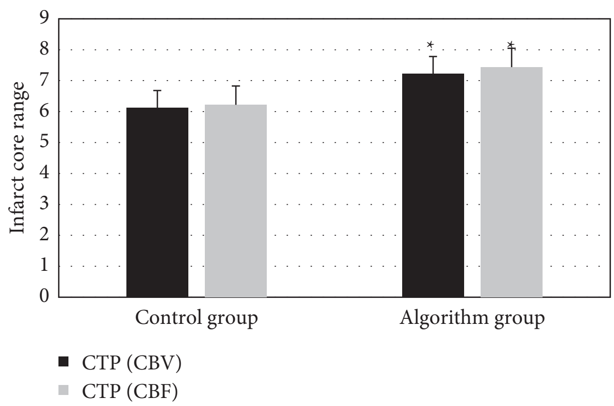

Figure 6: Comparison of myocardial infarction range between the two groups. * indicates statistically significant differences ($P < 0.05$).

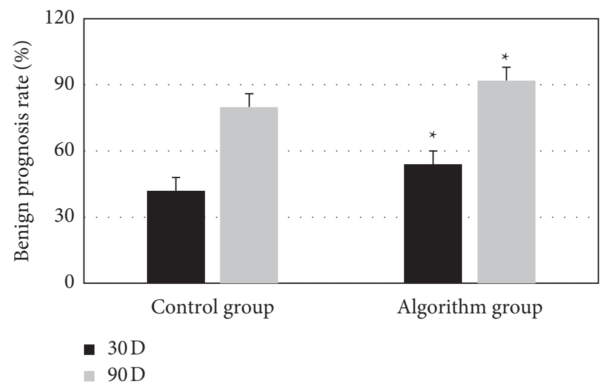

Figure 8: Comparison of benign prognosis rate between two groups before and after thrombolytic therapy. * indicates statistically significant differences ($P < 0.05$).

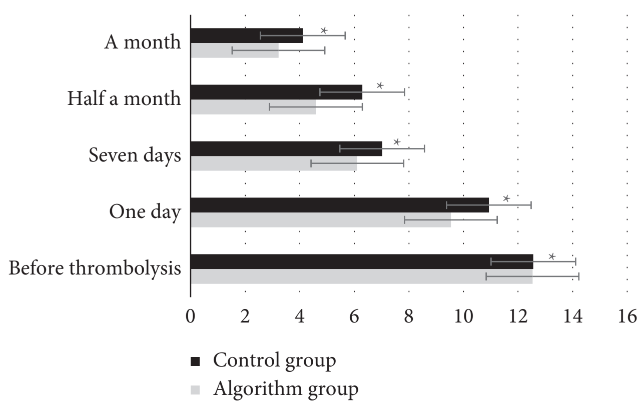

Figure 7: The NIHSS scores of the two groups at one day, one week, half a month, and one month after the treatment. * indicates statistically significant differences ($P < 0.05$).

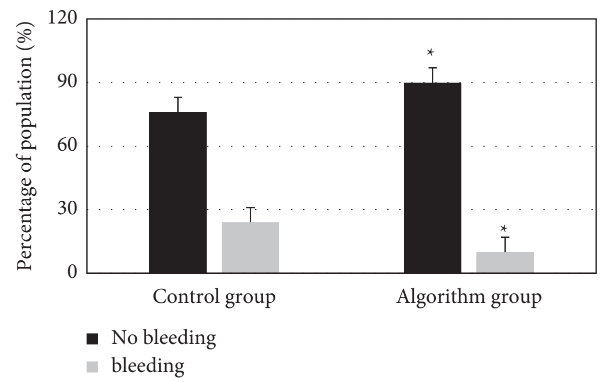

Figure 9: Comparison of bleeding conversion rate between two groups before and after thrombolytic therapy.

algorithm group. The conversion rate of the algorithm group was lower than that in the control group, and the difference was statistically significant ($P < 0.05$).

3.6. Comparison of Relative Values of Parameters in Ischemic Penumbra between Two Groups. Figure 10 shows the relative values of CBV, CBF, MTT, and TTP in ischemic penumbra between the two groups. It was found that the values in the algorithm group were significantly lower than the control group, with statistical differences ($P < 0.05$).

4. Discussion

The incidence of acute cerebral infarction has increased in recent years, with higher mortality and disability rate, which has affected residents' health and economic level [17]. CTP is a functional imaging that shows hyperacute abnormal perfusion areas of the brain. Related studies found that the abnormality appeared 30 minutes after ischemia [18]. Deep learning-based intelligent algorithm was applied in CTP imaging, and the results showed that the image quality was apparently superior to the quality of conventional CTP images. Artificial intelligence algorithm-based CTP images demonstrated remarkable diagnostic effects. In terms of the quality of the images in the algorithm group, CBV, CBF, MTT, and TTP reached 5.2, 4.88, 4.96, and 4.92, respectively. The values suggested that the scores for image quality were high. As to the quality of the images in the control group, CBV, CBF, MTT, and TTP amounted to 3.65, 4.23, 3.77, and 4, 16, respectively. Obviously, the overall quality of images in algorithm group was relatively higher, and the data differences between the two groups revealed statistical meaning ($P < 0.05$). The results indicated that deep learning-based CTP imaging was more beneficial to the diagnosis of diseases. CTP could offer clearer images for the analysis of diseases. Ischemic penumbra relative values of CBF images in the two groups were compared. The difference of the data between the two groups was 16. Ischemic penumbra relative values of MTT images in the two groups were compared, and the difference was 30. The values between the two groups showed statistical differences ($P < 0.05$). Besides, ischemic penumbra relative values of TTP images in the two groups were compared, and the difference was 23. The values between the two groups revealed statistical differences ($P < 0.05$). The above results indicated that the 4 parameters in ischemic penumbra of algorithm group were all decreased compared with those of the control group after thrombolysis, which suggested that infarct areas were correspondingly reduced and the therapy was effective.

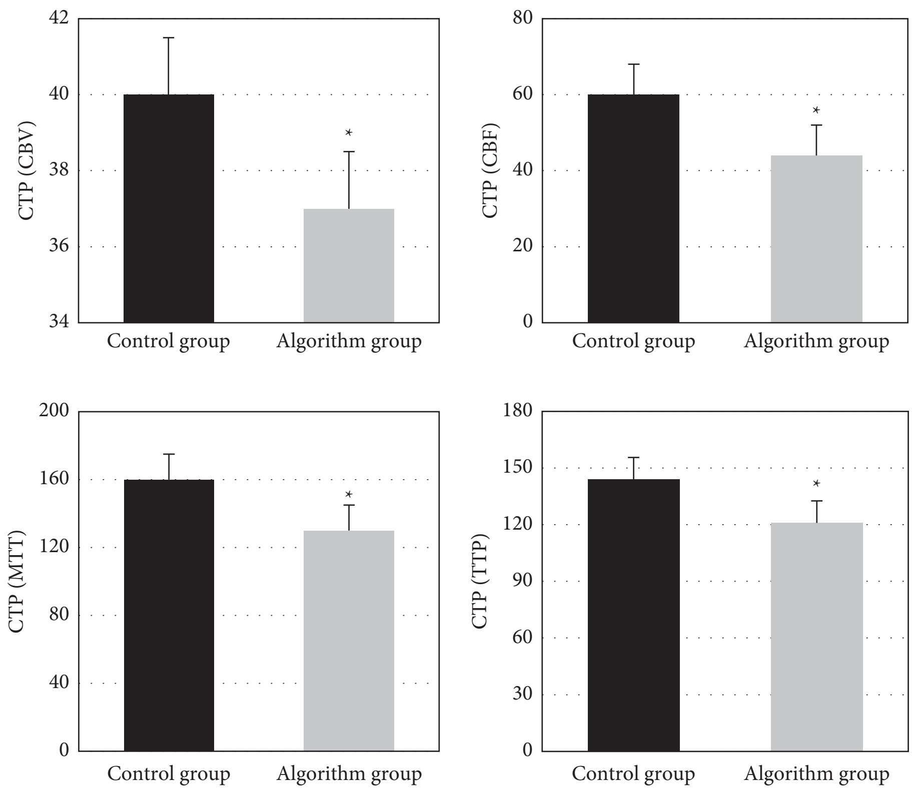

Figure 10: Comparison of parameters in ischemic penumbra of CBV, CBF, MTT, and TTP between two groups. * indicates statistically significant differences ($P < 0.05$).

Zhong et al. [19] proposed an accurate CT reconstruction algorithm based on back-projection filtering, which can accurately reconstruct the cross-sectional image of the object using the minimum projection data. DRL image optimization model has fewer learning cycles, shorter processing cycles, and higher image quality after processing, which can better meet clinical needs. Then, the quality of CTP pseudocolor images was evaluated in two groups, factoring into the scores of CBV, CBF, MTT, and TTP. The image quality is divided into three grades: high (score >4), medium (score ≤4 and ≥ 2), and poor (score <2). In the algorithm group, the image quality score was greater than 4, indicating high image quality. The overall image quality in the algorithm group was better. Based on the PSNR parameter, the noise in the image can be linearly indicated. The PSNR of DRL image was relatively high. In comparison of CTP pseudocolor images of two groups, the ischemic area and infarct core in the algorithm group were quite different from that of normal image. The ischemic area and infarct core area in the algorithm group were easier to identify, assisting doctors in diagnosing infarct focus and blood flow [20, 21]. The thrombolytic effect of the algorithm group was better than that of the control group. Thrombolysis demonstrated good curative effects on the nerve function defect in the algorithm group. The symptomatic intracranial hemorrhage rate in the control group was 24%, and that in the algorithm group was 10% within 24 hour, with a difference of 14% between the two groups, showing statistically significant differences ($P < 0.05$), indicating that thrombolytic therapy under the guidance of the algorithm group was safer than that in the control group. The limitation of this study is that CTP data need to be combined with MRI data to jointly evaluate the infarct core and ischemic range. In the future research, the data will be revised twice by combining MRI scan to expand the accuracy in the diagnosis of patients with acute ischemic stroke.

5. Conclusion

Artificial intelligence algorithm-based CTP images showed remarkable diagnostic effects. The results of the image quality in algorithm group revealed that the scores for image quality were high and the overall quality of the images in algorithm group was relatively higher. The differences in the NIHSS scores for the two groups showed that the thrombolytic effect on the algorithm group was superior to that on the control group. After the thrombolysis of algorithm group, the therapeutic effect on neurologic impairment was significant. The symptomatic intracranial hemorrhage rate of the algorithm group within 24 hours was dramatically superior to that of the control group. The deep learning-based algorithm group-guided thrombolytic therapy showed high safety and good clinical application prospects. Besides, it possessed guiding significance to the diagnosis of CTP images of patients with cerebral infarct. In addition, the sample size is small, which will reduce the power of the study. In the follow-up, an expanded sample size is necessary to strengthen the findings of the study [22].

Data Availability

The data used to support the findings of this study are available from the corresponding author upon request.

Conflicts of Interest

The authors declare no conflicts of interest.

Acknowledgments

This work was supported by the Jiaxing Science and Technology Plan (Livelihood Science and Technology Innovation Project) (No. 2019AD32181).

References

[1] G. Thomalla, C. Z. Simonsen, F. Boutitie et al., “WAKE-UP investigators MRI-guided thrombolysis for stroke with unknown time of onset,” *New England Journal of Medicine*, vol. 379, no. 7, pp. 611–622, 2018.

[2] M. T. Beckhauser, L. H. Castro-Afonso, F. A. Dias et al., “Extended time window mechanical thrombectomy for acute stroke in Brazil,” *Journal of Stroke and Cerebrovascular Diseases*, vol. 29, no. 10, Article ID 105134, 2020.

[3] F. Herpich and F. Rincon, “Management of acute ischemic stroke,” *Critical Care Medicine*, vol. 48, no. 11, pp. 1654–1663, 2020 Nov.

[4] J. J. Cirio, C. Ciardi, J. F. Vila et al., “Ataque cerebrovascular isquémico agudo de territorio anterior. Tratamiento endovascular [Acute ischemic stroke in anterior territory: endovascular treatment],” *Medicina*, vol. 80, no. 3, pp. 211–218, 2020.

[5] R. R. Leker, J. E. Cohen, D. Tanne et al., “Direct thrombectomy versus bridging for patients with emergent large-vessel occlusions,” *Interventional Neurology*, vol. 7, no. 6, pp. 403–412, 2018.

[6] M.-Y. Li, C. Chen, Z.-G. Wang, J.-J. Ke, and X.-B. Feng, “Effect of nalmefene on delayed neurocognitive recovery in elderly patients undergoing video-assisted thoracic surgery with one lung ventilation,” *Current Medical Science*, vol. 40, no. 2, pp. 380–388, 2020.

[7] E. Jiménez-Xarrié, B. Pérez, A. P. Dantas et al., “Uric acid treatment after stroke prevents long-term middle cerebral artery remodelling and attenuates brain damage in spontaneously hypertensive rats,” *Translational Stroke Research*, vol. 11, no. 6, pp. 1332–1347, 2020.

[8] V. Lopez-Rivera, S. Salazar-Marioni, R. Abdelkhaleq et al., “Integrated stroke system model expands availability of endovascular therapy while maintaining quality outcomes,” *Stroke*, vol. 52, no. 3, pp. 1022–1029, 2021.

[9] Z. Sun, Q. Xu, G. Gao, M. Zhao, and C. Sun, “Clinical observation in edaravone treatment for acute cerebral infarction,” *Nigerian Journal of Clinical Practice*, vol. 22, no. 10, pp. 1324–1327, 2019.

[10] Y. Zhao, Y. Zhang, and Y. Yang, “Acute cerebral infarction with adenomyosis in a patient with fever: a case report,” *BMC Neurology*, vol. 20, no. 1, 2020.

[11] W. Wu, C. Qiu, X. Feng et al., “Protective effect of paeoniflorin on acute cerebral infarction in rats,” *Current Pharmaceutical Biotechnology*, vol. 21, no. 8, pp. 702–709, 2020.

[12] L. G. F. Smith, E. Milliron, M.-L. Ho et al., “Advanced neuroimaging in traumatic brain injury: an overview,” *Neurosurgical Focus*, vol. 47, no. 6, p. E17, 2019.

[13] M. Hu, Y. Zhong, S. Xie, H. Lv, and Z. Lv, “Fuzzy system based medical image processing for brain disease prediction,” *Frontiers in Neuroscience*, vol. 15, Article ID 714318, 2021.

[14] I.-H. Lin, H.-T. Tsai, C.-Y. Wang, C.-Y. Hsu, T.-H. Liou, and Y.-N. Lin, “Effectiveness and superiority of rehabilitative treatments in enhancing motor recovery within 6 Months poststroke: a systemic review,” *Archives of Physical Medicine and Rehabilitation*, vol. 100, no. 2, pp. 366–378, 2019.

[15] F. Chen, J. Chen, Z. Peng et al., “Virtual-view PSNR prediction based on a depth distortion tolerance model and support vector machine,” *Applied Optics*, vol. 56, no. 30, pp. 8547–8554, 2017.

[16] K. Overgaard, T. Sereghy, G. Boysen, H. Pedersen, and N. H. Diemer, “Reduction of infarct volume and mortality by thrombolysis in a rar embolic strok model,” *Stroke*, vol. 23, no. 18, p. 1167, 1992.

[17] C.-N. Kao and Y.-W. Liu, “Acute cerebral infarction caused by atrial thrombus originating from left upper pulmonary vein stump after left upper lobe trisegmentectomy,” *General Thoracic and Cardiovascular Surgery*, vol. 68, no. 2, pp. 206-207, 2020.

[18] Y.-W. Wang and G.-M. Zhang, “New silent cerebral infarction in patients with acute non-cerebral amyloid angiopathy intracerebral hemorrhage as a predictor of recurrent cerebrovascular events,” *Medical Science Monitor*, vol. 25, pp. 418–426, 2019.

[19] B.-Y. Zhong, Z.-P. Yan, J.-H. Sun et al., “Prognostic performance of albumin-bilirubin grade with artificial intelligence for hepatocellular carcinoma treated with transarterial chemoembolization combined with sorafenib,” *Frontiers in Oncology*, vol. 10, Article ID 525461, 2020.

[20] J. Chen, W. Zhang, Y. Q. Wu, H. Chen, and J. F. Zhao, “Correlations of acute myocardial infarction complicated by cerebral infarction with insulin resistance, adiponectin and HMGB1,” *European Review for Medical and Pharmacological Sciences*, vol. 23, no. 10, pp. 4425–4431, 2019.

[21] S. C. van de Leemput, M. Prokop, B. van Ginneken, and R. Manniesing, “Stacked bidirectional convolutional LSTMs for deriving 3D non-contrast CT from spatiotemporal 4D CT,” *IEEE Transactions on Medical Imaging*, vol. 39, no. 4, pp. 985–996, 2020.

[22] A. Pu, H. Wang, and J. Ying, “Optimized backprojection filtration algorithm for postoperative reduction and analysis of respiratory infection-related factors of pelvic fractures by CT imaging,” *Scientific Programming*, vol. 2021, Article ID 3554718, 10 pages, 2021.

Hindawi
Contrast Media & Molecular Imaging
Volume 2022, Article ID 5373585, 10 pages
https://doi.org/10.1155/2022/5373585

Research Article

Early Diagnosis of Acute Ischemic Stroke by Brain Computed Tomography Perfusion Imaging Combined with Head and Neck Computed Tomography Angiography on Deep Learning Algorithm

Yi Yang[1] **Jinjun Yang**[2] **Jiao Feng**[1] **and Yi Wang**[1]

[1]*Department of Medical Imaging Centre, The First People's Hospital of Xianyang, Xianyang 712000, Shannxi, China*
[2]*Department of Ultrasound Medicine, The First People's Hospital of Xianyang, Xianyang 712000, Shannxi, China*

Correspondence should be addressed to Jinjun Yang; 2016218126@smail.jsut.edu.cn

Received 15 February 2022; Revised 13 April 2022; Accepted 16 April 2022; Published 9 May 2022

Academic Editor: M Pallikonda Rajasekaran

The purpose of the research was to discuss the application values of deep learning algorithm-based computed tomography perfusion (CTP) imaging combined with head and neck computed tomography angiography (CTA) in the diagnosis of ultra-early acute ischemic stroke. Firstly, 88 patients with acute ischemic stroke were selected as the research objects and performed with cerebral CTP and CTA examinations. In order to improve the effect of image diagnosis, a new deconvolution network model AD-CNNnet based on deep learning was proposed and used in patient CTP image evaluation. The results showed that the peak signal-to-noise ratio (PSNR) and feature similarity (FSIM) of the AD-CNNnet method were significantly higher than those of traditional methods, while the normalized mean square error (NMSE) was significantly lower than that of traditional algorithms ($P < 0.05$). 80 cases were positive by CTP-CTA, including 16 cases of hyperacute ischemic stroke and 64 cases of acute ischemic stroke. The diagnostic sensitivity was 93.66%, and the specificity was 96.18%. The cerebral blood flow (CBF), cerebral blood volume (CBV), and the mean transit time (MTT) in the infarcted area were significantly greater than those in the corresponding healthy side area, and the time to peak (TTP) was significantly less than that in the corresponding healthy side area ($P < 0.05$). The cerebral perfusion parameters CBF, TTP, and MTT in the penumbra were significantly different from those in the infarct central area and the corresponding contralateral area, and TTP was the most sensitive ($P < 0.05$). To sum up, deep learning algorithm-based CTP combined with CTA could find the location of cerebral infarction lesions as early as possible to provide a reliable diagnostic result for the diagnosis of ultra-early acute ischemic stroke.

1. Introduction

Ischemic stroke is the most common type of stroke, accounting for about 80% of all strokes. It is the softening and necrosis of brain tissue caused by blood circulation disorder, ischemia, and hypoxia in the local brain tissue, namely, vascular blockage [1–3]. The symptoms of acute ischemic stroke are mainly sudden skewing of the mouth and eyes with saliva secretion. Patients will not only have unclear speech but also have difficulty in pronunciation. In addition, some patients will have aphasia, dysphagia, weakness, or numbness of one limb [4]. At present, it is generally believed that the main factors causing acute ischemic stroke include large atherosclerosis, cardiogenic embolism, and arteriolar occlusion [5]. The inducing factors included age, race, heredity, hypertension, diabetes, dyslipidemia, heart disease, mental state, and so on [6, 7]. Acute ischemic stroke has the characteristics of high incidence rate, high mortality rate, high disability rate, and high recurrence rate. According to statistics, about one person dies of stroke every six seconds, and one person may be disabled by stroke every six seconds [8]. Therefore, early detection of the existence of early ischemic penumbra and diagnosis of acute ischemic stroke are very critical for the therapeutic effectiveness and prognosis of patients.

Imaging is used in the clinical diagnosis of acute ischemic stroke. Plain CT scan is the first choice for screening suspected stroke, which can distinguish intracranial hemorrhage and nonvascular lesions. However, it is difficult to find and diagnose the disease early. Generally, it cannot be found until 24 hours after ischemia [9–11]. Conventional MRI is effective in displaying acute small infarct and posterior circulation ischemic stroke. At present, the mismatch between PWI and DWI of MRI is a more effective method to judge the ischemic penumbra, but MRI has some limitations, such as long examination time, many contraindications, and high examination cost [12, 13]. CT perfusion imaging is a common method to evaluate acute ischemic stroke at present. It can early display the focus of cerebral ischemia and distinguish the inactivated brain tissue and ischemic penumbra. It has important clinical significance for timely diagnosis and guiding treatment [14]. CT angiography (CTA) is mainly through intravenous injection of drugs. When the drugs pass through the vascular arteries, they are scanned by CT. The formed images are imaged by computer synthesis. CTA can display the blocking site, vascular size, and blood flow compensation of patients with acute ischemic stroke [15]. Therefore, this study intends to use CT perfusion (CTP) imaging and CTA in the diagnosis of acute ischemic stroke.

Deep learning is a branch of machine learning. It is an algorithm that attempts to abstract data at a high level using multiple processing layers composed of complex structures or multiple nonlinear transformations. So far, several deep learning frameworks have been applied in the fields of computer vision, speech recognition, natural language processing, medicine, and bioinformatics [16].

Convolutional neural network (CNN) could share convolution kernels and process high-dimensional data without pressure. CNN enabled the image to still retain the original position relationship through convolutional operation with good image processing effects. However, it showed some disadvantages, including the high demand for sample size and strong hardware dependence. In summary, 88 patients with acute ischemic stroke were examined with CTP and CTA images, and the deep learning algorithm was applied to the original image processing. The diagnostic sensitivity, specificity, and cerebral perfusion parameters were analyzed to confirm the application value of CTP imaging based on a deep learning algorithm combined with head and neck CTA in the diagnosis of ultra-early acute ischemic stroke, which provided help for the clinical diagnosis and treatment of acute ischemic stroke.

2. Materials and Methods

2.1. Research Object. Eighty-eight patients with acute ischemic stroke in the hospital from May 2019 to May 2021 were collected as the research objects, including 54 males and 34 females, aged 33–79 years. According to this study, it was approved by the medical ethics committee of the hospital. The patients and their families understood the study and signed the informed consent.

Inclusion criteria: (1) patients diagnosed with acute ischemic stroke due to numbness, hemiplegia, weakness of one limb, and aphasia; (2) the time from symptom onset to baseline imaging examination was within 24 hours; (3) cranial CT excluded intracerebral hemorrhage; (4) complete clinical data; and (5) the National Institutes of Health Stroke Scale (NIHSS) score was greater than four.

Exclusion criteria: (1) complicated with mental diseases; (2) poor inspection compliance; (3) allergic constitution; and (4) patients who withdrew from the experiment halfway.

2.2. Inspection Method. CTP: after the cerebral hemorrhage was excluded by a routine CT plain scan, CTP imaging was performed. 42 mL of contrast agent iodopropane and 20 mL normal saline were injected through elbow vein at the rate of 6 ml/s. The scanning range was parietal bone, 15 cm. The time density curve was obtained. After image processing, the cerebral blood flow (CBF), cerebral blood volume (CBV), mean transit time (MTT), and time to peak (TTP) were obtained. The parameters such as CBF, CBV, TTP, and MTT in the corresponding areas of the affected side and the healthy side were measured by mirror technique, and the perfusion parameters in the lesion area (infarct core and penumbra) and the corresponding healthy side were compared.

CTA: scanning range was aortic arch cranial apex. 55 mL iopromide reagent was injected through the median elbow vein at the injection rate of 4.5–5.0 mL/s, and then 55 mL normal saline was injected. Scanning parameters: voltage 120 kV, current 240 mA, and layer thickness 0.45 mm. According to the location of the lesion, it was divided into: infratentorial lesion, paraventricular and basal ganglia lesions, frontoparietal lobe lesions, temporal occipital lobe lesions, and the lesions involving a large area of one cerebral hemisphere. The infarct volume was calculated.

2.3. Computed Tomography Perfusion Deconvolution Algorithm on Deep Learning. In CTP image processing, if the contrast agent concentration at the pulse input was D_{ca}, the region of interest was V_{RI}, and the corresponding average time density curve was TDC_{RI}; the relationship between D_{ca} and TDC_{RI} could be expressed as follows:

$$TDC_{RI}(t) = \left(D_{ca} \times U\right)(t). \tag{1}$$

In the above equation, $U(t)$ represents the residual function of blood flow scale. The above equation could be solved by deconvolution. In numerical implementation, the convolution equation (1) could be expressed by matrix multiplication after discretization. The volume of interest containing N voxels was taken as an example.

$$\widehat{U} = \arg_{U}^{\min\left(\|NU-D\|_2^2+\alpha E(U)/2\right)}. \tag{2}$$

In the above equation, N represents a block cyclic matrix, $N \in E^{K \cdot K}$ and K represent dynamic scanning parameters, $(\|NU - D\|_2^2/2)$ represent fidelity terms, $E(U)$ represent regular terms, and α represent weight parameters.

To solve (1), an auxiliary variable Z was introduced into the blood flow scale residual function and the alternating direction multiplier method (ADMM) [17] was used, and the process could be expressed as follows:

$$\begin{aligned}
U^{(n)} &= (1 - b_{su}\chi)U^{(n-1)} + b_{su}\chi\left(Z^{(n-1)} - \lambda^{(n-1)}\right) \\
&\quad - b_{su}N^{\tau}\left(NU^{(n-1)} - D\right), \\
Z^{(n)} &= (1 - b_{su}\chi)Z^{(n-1)} + b_{sz}\chi\left(U^{(n)} + \lambda^{(n-1)}\right) \\
&\quad - \alpha\Lambda E\left(Z^{(n-1)}\right), \\
\lambda^{(n)} &= \lambda^{(n-1)} + \kappa\left(U^{(n)} - Z^{(n)}\right).
\end{aligned} \tag{3}$$

In the above equations, λ represents a scaled Lagrange multiplier, χ represents a penalty hyperparameter, τ represents a transpose operator, b_{su} represents a step size $U^{(n)}$, b_{sz} represents a step size $Z^{(n)}$, Λ represents a regular term gradient operator, and κ represents a learning rate.

For the modular structure of ADMM algorithm, the regular term of (2) was separated from deconvolution. For example, $U^{(n)}$ was deconvolution process, $Z^{(n)}$ was denoising process, and $\lambda^{(n)}$ was iterative update auxiliary variable. Then, based on the idea of plug and play, the deconvolution process of low-dose CTP was constrained. The equations were improved as follows:

$$\begin{aligned}
U^{(n)} &= \left(1 - \tilde{\chi}^{(n)}\right)U^{(n-1)} + \tilde{\chi}^{(n)}\left(Z^{(n-1)} - \lambda^{(n-1)}\right) \\
&\quad - \tilde{b}_{su}^{(n)}N^{\tau}\left(NU^{(n-1)} - D\right), \\
Z^{(n)} &= \left(1 - \tilde{\chi}^{(n)}\right)Z^{(n-1)} + \tilde{\chi}^{(n)}\left(U^{(n)} + \lambda^{(n-1)}\right) \\
&\quad - \tilde{\alpha}\mathrm{Res}^{(n,l)}\left(Z^{(n-1)}\right), \\
\lambda^{(n)} &= \lambda^{(n-1)} + \kappa^{(n)}\left(U^{(n)} - Z^{(n)}\right), \\
\tilde{\chi} &= b_{su}\chi.
\end{aligned} \tag{4}$$

Compared with before, the update step size and penalty super parameters were combined into one parameter, and the performance of deconvolution network model could be improved by adaptively adjusting the parameters. The operation process of the deep learning deconvolution network model designed in this paper could be set as AD-CNNnet (Figure 1).

2.4. Simulation Experiment. The experiment was conducted on the platform of MATLAB 2015b. Table 1 revealed the parameter settings.

Block cyclic truncated singular value decomposition (bSVD) [18], sparse perfusion deconvolution (SPD) [19], and DenseSRNet [20] were used as comparison methods with AD-CNNnet.

Peak signal-to-noise ratio (PSNR), normalized mean square error (NMSE), and feature similarity (FSIM) were selected as evaluation indexes [21].

2.5. Statistical Methods. The data of this study were analyzed by SPSS19.0 statistical software. The measurement data were expressed by mean ± standard deviation ($\bar{x} \pm s$), and the counting data were expressed by percentage (%). One-way analysis of variance was used for pairwise comparison. The difference was statistically significant ($P < 0.05$).

3. Results

3.1. Performance Analysis Results of Network Model. Firstly, the optimal values of three parameters: the number of model filters, the number of residual blocks, and the number of ADMM iteration steps, were analyzed to live the best deconvolution network model for image processing.

If the number of filters was set to 5, 10, and 15, the loss curve of the model in network training could be illustrated in Figure 2. The loss curve under the three filter parameters decreased rapidly with the enhancement of network training times until it tended to be stable. Among them, the model with 15 filters has the best loss curve and the more stable learning ability.

If the number of residuals was set to 3, 5, and 7, the loss curve of the model in network training could be expressed in Figure 3. The loss curve under the three residual parameters decreased rapidly with the increase of network training times until it tended to be stable. Among them, the model with 7 residuals had the best loss curve and more stable learning ability.

If the number of ADMM iteration steps was set to 6, 9, and 12, the loss curve of the model in network training could be illustrated in Figure 4. The loss curve under the three iteration steps decreased rapidly with the increase of network training times until it tended to be stable. Among them, the model loss curve with 12 iterative steps of ADMM was the best and had more stable learning ability.

In terms of visual evaluation (Figure 5), the perfusion parameter map obtained by bSVD method was damaged by noise induced artifacts. The perfusion parameter map obtained by SPD and DenseSRNet methods was too smooth. The perfusion parameter map obtained by AD-CNNnet method performed best in suppressing artifacts and preserving details, which was closer to the reference image.

In terms of quantitative evaluation (Figure 6), PSNR and FSIM of AD-CNNnet method were significantly higher than those of other methods, while NMSE was significantly lower than other algorithms, and the difference was statistically significant ($P < 0.05$).

3.2. Computed Tomography Perfusion-Computed Tomography Angiography Inspection Results. Figure 7 shows that among the 88 patients, CTP-CTA was negative in 8 cases, including 2 cases of pons, 1 case of lacunar infarction in the left basal ganglia, 2 cases of multiple punctate acute cerebral infarction in the right frontal parietal lobe, and 3 cases of transient ischemic attack. CTP-CTA was positive in 80 cases,

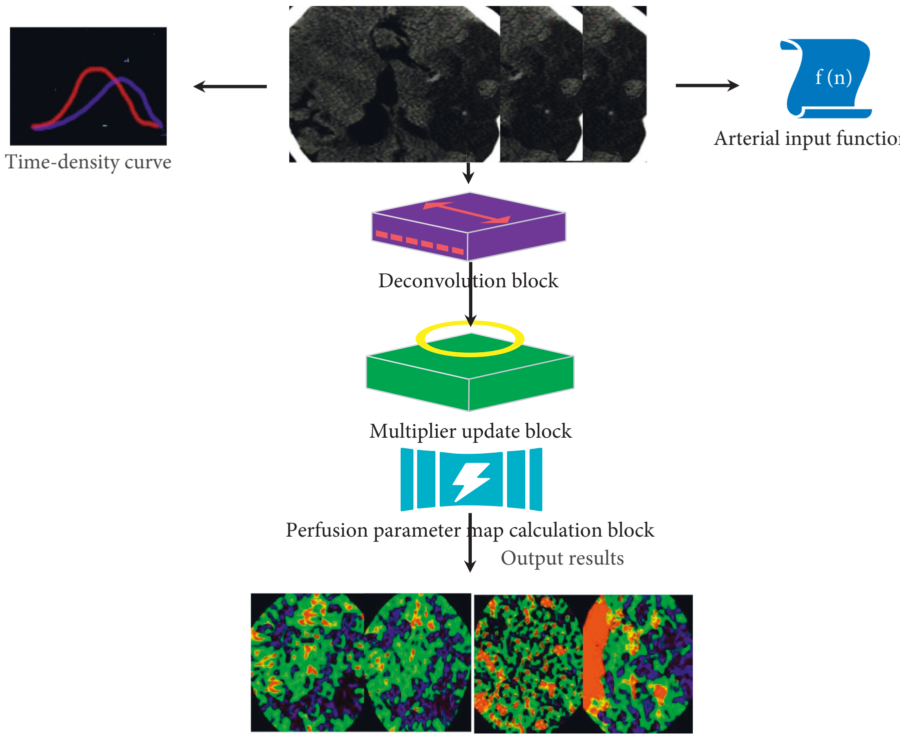

Figure 1: Improved deep learning deconvolution network model.

Table 1: Network model parameter setting.

Parameter	Numerical value
Number of network residual blocks	7
Number of network filters	15
Filter size	3 × 3
ADMM iteration steps	12
Initial learning rate	4500

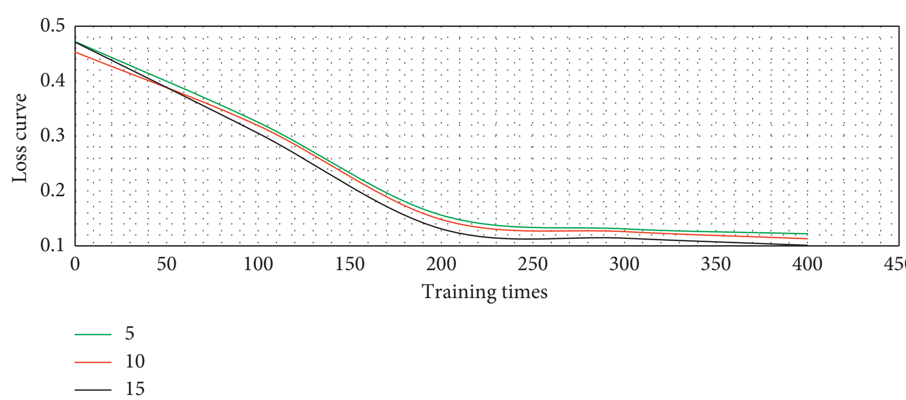

Figure 2: Loss curve of model training under different filter numbers.

including 16 cases of hyperacute ischemic stroke and 64 cases of acute ischemic stroke. The diagnostic sensitivity was 93.66%, and the specificity was 96.18%.

3.3. Comparison of Cerebral Perfusion Parameters between Infarcted Area and Contralateral Area. Figure 8 reveals that the cerebral perfusion parameters CBF, CBV, and MTT in the infarcted area were significantly greater than those in the corresponding contralateral area, and the difference was statistically significant ($P < 0.05$). The cerebral perfusion parameter TTP in the infarcted area was significantly lower than that in the corresponding contralateral area, and the difference was statistically significant ($P < 0.05$).

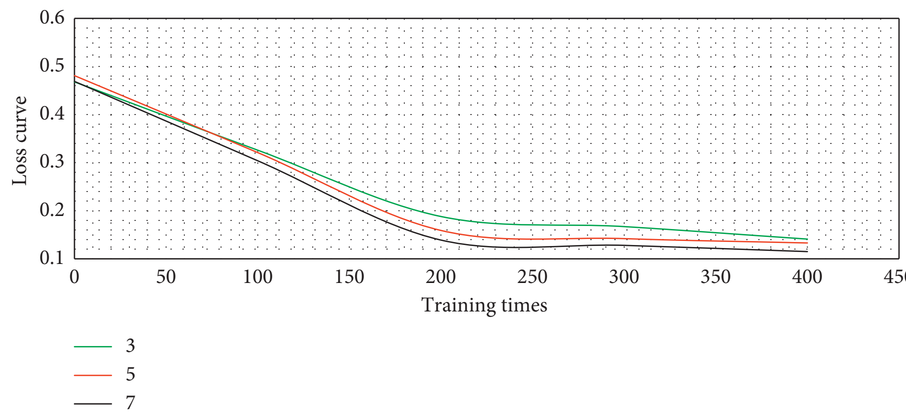

FIGURE 3: Loss curve of model training under different number of residual blocks.

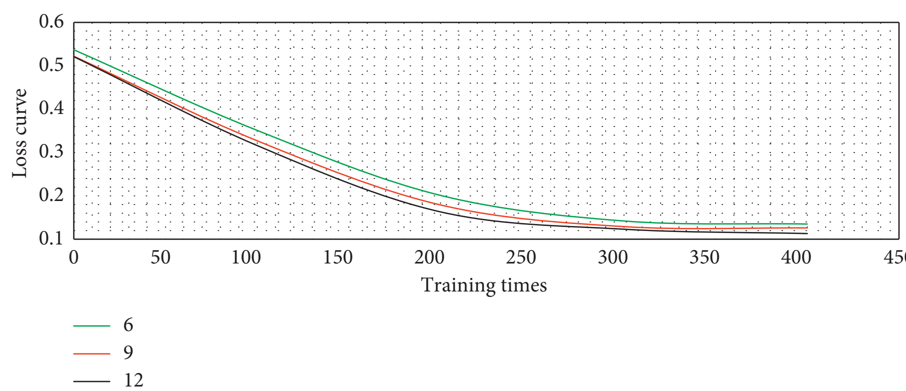

FIGURE 4: Loss curve of model training under different ADMM iteration steps.

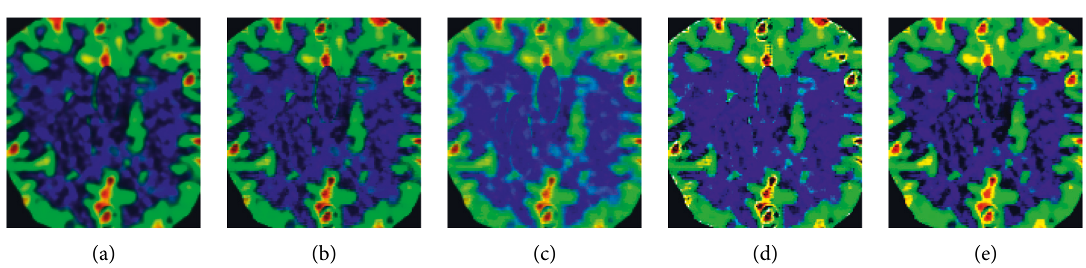

FIGURE 5: Perfusion parameters obtained by deconvolution network model. A was the reference image; B was SPD; C was bSVD; D was DenseSRNet; E was AD-CNNnet.

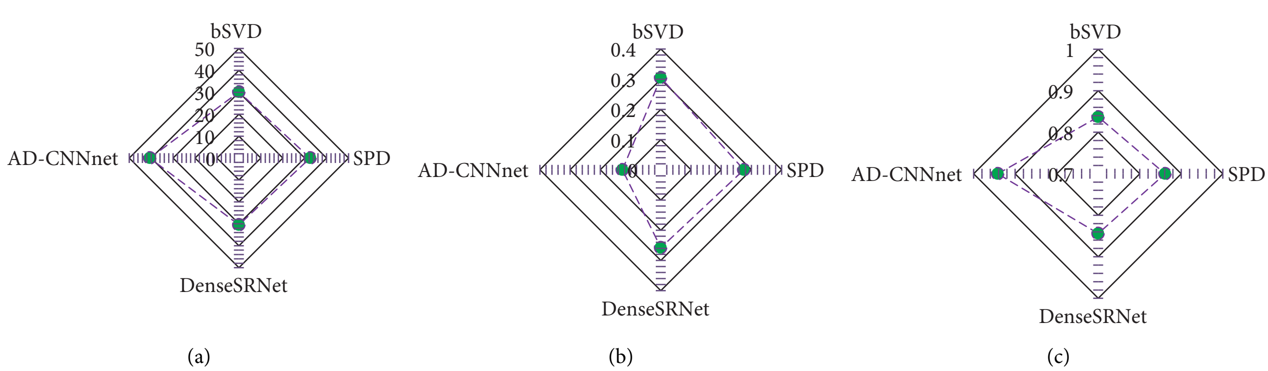

FIGURE 6: Quantitative evaluation indicators of deconvolution network model. (a) PSNR; (b) NMSE; (c) FSIM. ∗ indicates that the difference between AD-CNNnet and other methods was statistically significant ($P < 0.05$).

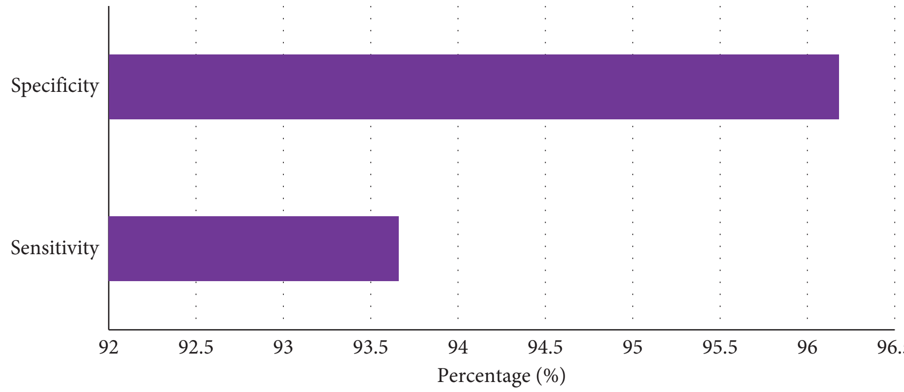

Figure 7: CTP-CTA results.

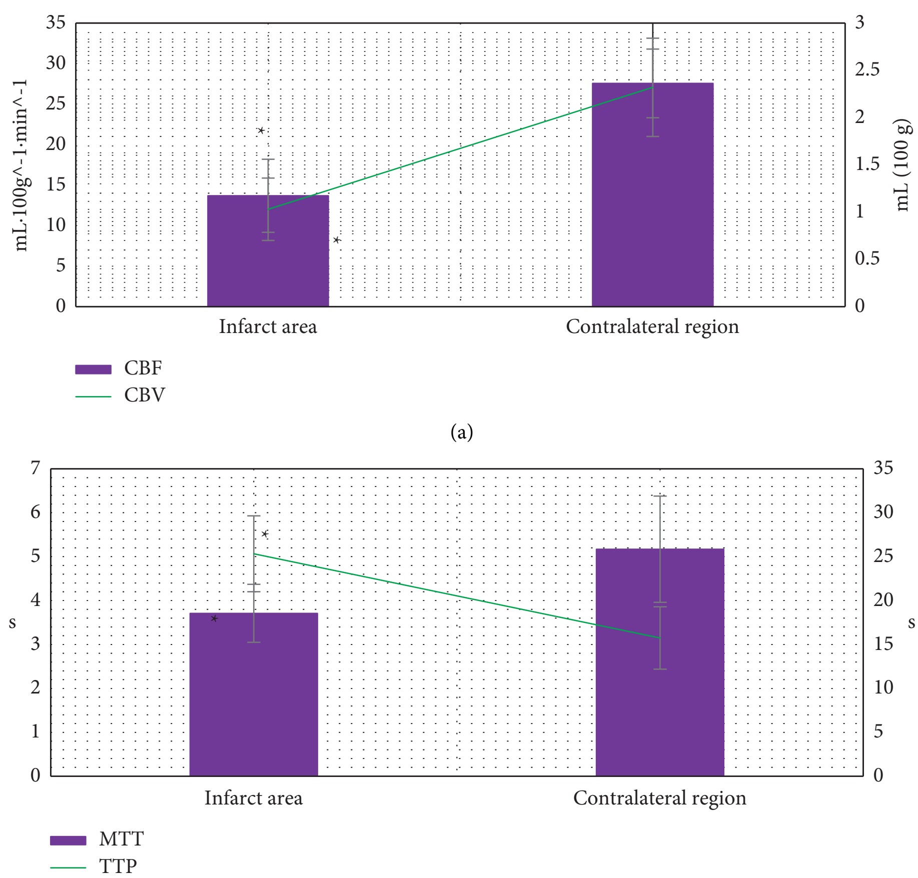

Figure 8: Comparison of cerebral perfusion parameters between infarcted area and contralateral area. A represents CBF and CBV; B represents MTT and TTP. ∗ indicates that there was significant difference between infarcted area and healthy side area ($P < 0.05$).

3.4. Comparison of Cerebral Perfusion Parameters in Penumbra, Infarct Center, and Contralateral Area. Figure 9 indicates that the cerebral perfusion parameters CBF, TTP, and MTT in the penumbra were significantly different from those in the infarct central area and the corresponding healthy side area ($P < 0.05$). The cerebral perfusion parameter CBV in the penumbra was significantly different from that in the infarct center ($P < 0.05$), but not from the corresponding healthy side ($P > 0.05$).

3.5. Analysis of Case Data of Some Patients. CTA indicated that the left anterior cerebral artery of male, 58, was thin (Figure 10), the distal end was not developed, and the P2 segment of the left posterior cerebral artery was blocked. CTP showed that CBV, CBF, and MTT decreased in the core area of cerebral infarction. TTP prolonged significantly. The volume of hypoperfusion area was 18.7 mL, and the penumbra was large.

CTA revealed the occlusion of the intracranial segment of the right internal carotid artery and the right middle

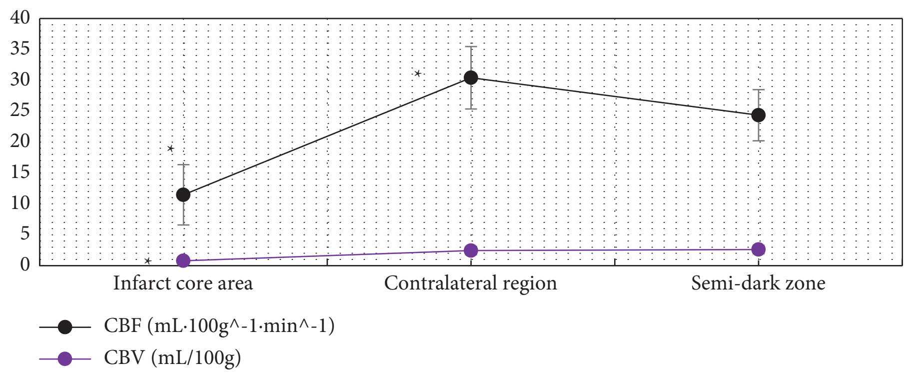

(a)

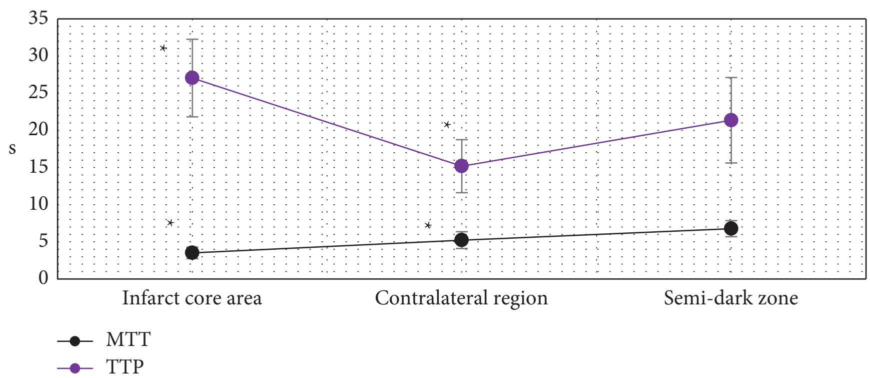

(b)

Figure 9: Comparison of cerebral perfusion parameters in penumbra, infarct center, and contralateral area of patients. A refers to CBF and CBV; B refers to MTT and TTP. $*$ indicates that the difference between the penumbra area, the infarcted area, and the contralateral area was statistically significant ($P < 0.05$).

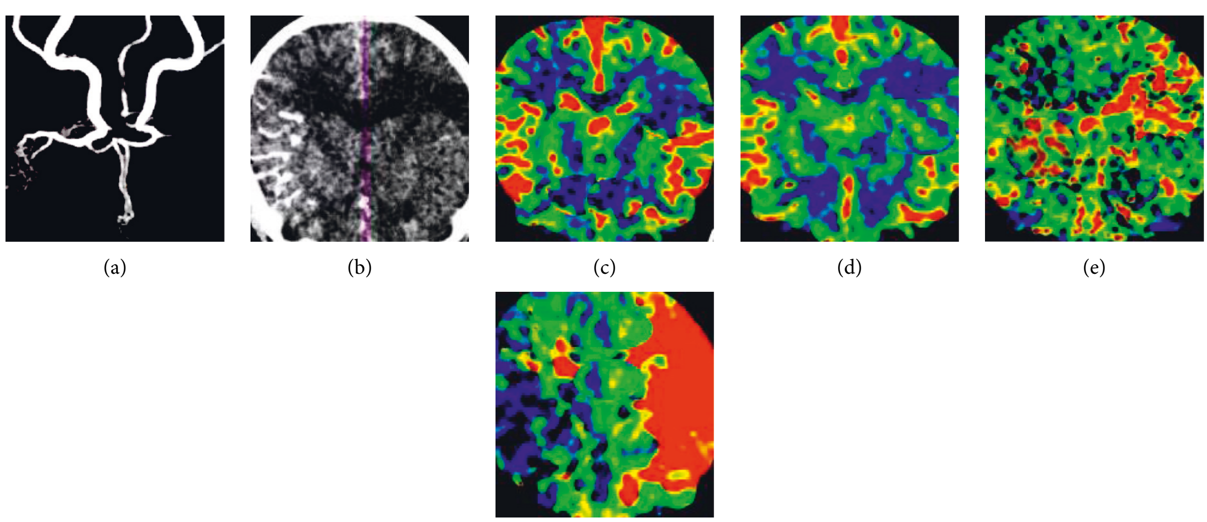

(a) (b) (c) (d) (e)

(f)

Figure 10: A 58-year-old male patient with left limb weakness and unclear speech was admitted to the hospital for 8 hours. A was CTA image; B was CTP image; and C-F was CBV, CBF, MTT, and TTP perfusion images, respectively.

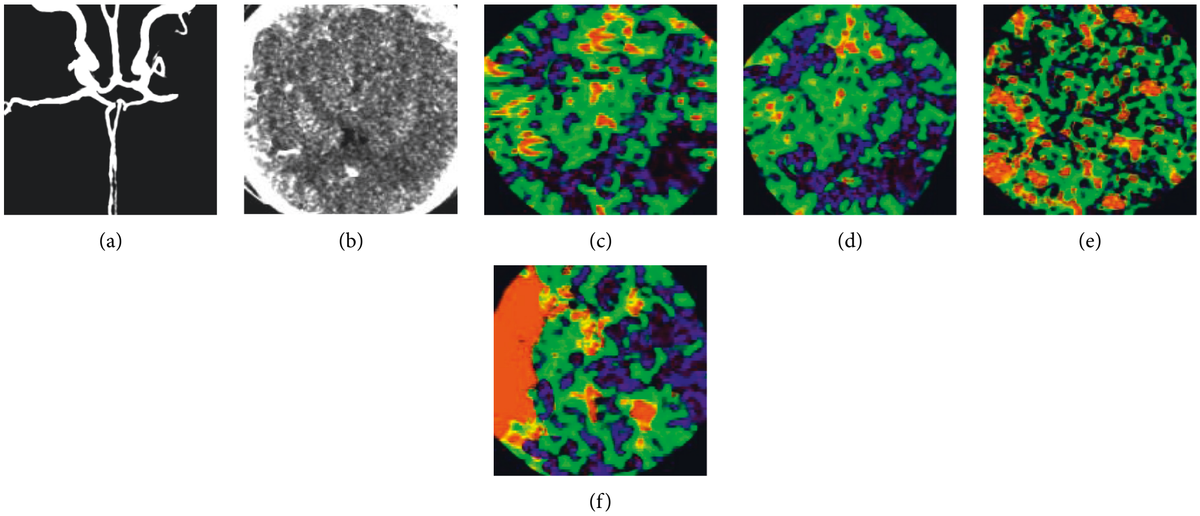

Figure 11: A 65-year-old male patient with sudden weakness of left upper limb and unclear consciousness was admitted to the hospital for 5 hours. A was CTA image; B was CTP image; C-F was CBV, CBF, MTT, and TTP perfusion images, respectively.

cerebral artery of a female, 65 (Figure 11). CTP showed that CBV, CBF, and MTT decreased in the core area of cerebral infarction, and TTP prolonged significantly.

4. Discussion

Cerebral infarction was the main cause of disability at present. Timely and rapid recovery of cerebral blood flow in patients with acute cerebral infarction has become an effective way to reduce the disability rate. Clinically, it was found that strict time limit can improve the effect of intravenous thrombolytic therapy by about 10%. Therefore, the limited time window has certain limitations. Rapid and accurate judgment of ischemic penumbra has become the key to the treatment of cerebral infarction [22]. In this study, 88 patients with acute ischemic stroke in the hospital were selected as the research object, and the brain CTP and CTA were examined by SOMATOM spirit double-slice spiral CT. To improve the effect of image diagnosis, a new deconvolution network model AD-CNNnet based on deep learning was proposed and used in actual CTP image evaluation. Firstly, the application effect of the model was analyzed. It was found that the perfusion parameter map obtained by AD-CNNnet method performs best in suppressing artifacts and preserving details, which was closer to the reference image, and has the best effect compared with other methods. In terms of quantitative evaluation, PSNR and FSIM of AD-CNNnet method were significantly higher than those of other methods, while NMSE was significantly lower than other algorithms ($P < 0.05$). PSNR and NMSE were two widely used objective image quality indicators. The larger the PSNR was, the smaller the NMSE was, and the better the image quality was. FSIM was used to measure the perceived similarity of two images. The closer the value was to 1, the higher the image similarity was proved [23]. The results gave that the proposed AD-CNNnet model showed more significant robustness in parameter calculation and could improve imaging quality more obviously compared with traditional algorithms.

CTP and CTA based on AD-CNNnet model were applied to the diagnosis of 88 patients with acute ischemia. It was found that 80 patients were positive for CTP-CTA, including 16 cases of hyperacute ischemic stroke and 64 cases of acute ischemic stroke. The diagnostic sensitivity was 93.66% and the specificity was 96.18%, which was similar to the results of Hakim A et al. (2019) [24]. Previous studies [25] showed that the low-density lesions could only be displayed by routine CT in patients with cerebral ischemia 24 hours after onset. In the early stage of acute cerebral infarction, especially in the hyperacute stage <6 h, the sensitivity and diagnostic rate of conventional CT plain scan were very low, indicating that CTP-CTA based on deep learning algorithm could find the location of cerebral infarction lesions as soon as possible. It provided a reliable clinical basis for the diagnosis of ultra early cerebral infarction and had a high clinical application value. By comparing the cerebral perfusion parameters in different regions, it was found that the CBF, CBV, and MTT in the infarcted area were significantly higher than those in the corresponding healthy side area. Besides, the TTP was significantly lower than that in the corresponding healthy side area. The difference was statistically significant ($P < 0.05$), indicating that the cerebral perfusion parameters CBF, CBV, MTT, and TTP can predict the occurrence of acute cerebral infarction to a certain extent [26]. Further analysis showed that the cerebral perfusion parameters CBF, TTP, and MTT in the penumbra were significantly different from the infarct central area and the corresponding contralateral area. TTP was the most sensitive ($P < 0.05$), which showed that the cerebral perfusion parameters CBF, TTP, and MTT had a good indicating significance for evaluating the penumbra area.

5. Conclusion

In this study, 88 patients with acute ischemic stroke in the hospital were taken as the research object, and the brain CTP and CTA were examined by SOMATOM Spirit double-slice spiral CT. To improve the effect of image diagnosis, a new deconvolution network model AD-CNNnet based on deep learning was proposed and used in patient CTP image evaluation. The results showed that CTP-CTA based on AD-CNNnet model could find the location of cerebral infarction as soon as possible, which provided a reliable clinical basis for the diagnosis of ultra early cerebral infarction and had a high clinical application value. In addition, its cerebral perfusion parameters CBF, CBV, MTT, and TTP can assist in judging the ischemic penumbra to a certain extent and provide guidance for individualized treatment of patients. However, there were few patients selected in this study and the source was single, which may have some impact on the results. In addition, the long-term follow-up data of patients were not collected, and the image evaluation of patient prognosis was not involved. More patient sample data will be collected in the later study to further explore the application value of CTP combined with CTA based on deep learning algorithm in the prognosis of patients with acute ischemic stroke. In conclusion, the results of this study provide a reference for the combined application of artificial intelligence technology and clinical imaging.

Data Availability

The data used to support the findings of this study are available from the corresponding author upon request.

Conflicts of Interest

The authors declare no conflicts of interest.

References

[1] G. S. Silva and R. G. Nogueira, "Endovascular treatment of acute ischemic stroke," *CONTINUUM: Lifelong Learning in Neurology*, vol. 26, no. 2, pp. 310–331, 2020.

[2] A. Vagal, M. Wintermark, K. Nael et al., "Automated CT perfusion imaging for acute ischemic stroke," *Neurology*, vol. 93, no. 20, pp. 888–898, 2019.

[3] D. Modin, B. Claggett, C. Sindet-Pedersen et al., "Acute COVID-19 and the incidence of ischemic stroke and acute myocardial infarction," *Circulation*, vol. 142, no. 21, pp. 2080–2082, 2020.

[4] X. Zhang, H. Shen, and Z. Lv, "Deployment optimization of multi-stage investment portfolio service and hybrid intelligent algorithm under edge computing," *PLoS One*, vol. 16, no. 6, Article ID e0252244, 2021.

[5] Z. Lv and L. Qiao, "Analysis of healthcare big data," *Future Generation Computer Systems*, vol. 109, pp. 103–110, 2020.

[6] A. E. Hassan, H. Shamim, H. Zacharatos et al., "Prospective Endovascular treatment in acute ischemic stroke evaluating non-contrast head CT versus CT perfusion (PLEASE No CTP)," *Interventional Neurology*, vol. 8, no. 2-6, pp. 116–122, 2019.

[7] W. Cao, Y. Ling, L. Yang, F. Wu, X. Cheng, and Q. Dong, "Assessment of ischemic volumes by using relative Filling time Delay on CTP source image in patients with acute stroke with anterior circulation large Vessel occlusions," *American Journal of Neuroradiology*, vol. 41, no. 9, pp. 1611–1617, 2020.

[8] M. A. Almekhlafi, W. G. Kunz, R. A. McTaggart et al., "Imaging Triage of patients with Late-window (6-24 hours) acute ischemic stroke: a Comparative study using Multiphase CT angiography versus CT perfusion," *American Journal of Neuroradiology*, vol. 41, no. 1, pp. 129–133, 2020.

[9] L. Lucas, F. Gariel, P. Menegon et al., "Acute ischemic stroke or Epileptic Seizure? Yield of CT perfusion in a "Code stroke" Situation," *American Journal of Neuroradiology*, vol. 42, no. 1, pp. 49–56, 2021.

[10] W. Brinjikji, A. M. Demchuk, M. H. Murad et al., "Neurons over Nephrons," *Stroke*, vol. 48, no. 7, pp. 1862–1868, 2017.

[11] F. Kauw, J. J. Heit, B. W. Martin et al., "Computed tomography perfusion data for acute ischemic stroke evaluation using rapid software," *Journal of Computer Assisted Tomography*, vol. 44, no. 1, pp. 75–77, 2020.

[12] Z. Li, X. Li, R. Tang, and L. Zhang, "Apriori algorithm for the data Mining of global cyberspace security issues for human participatory based on association rules," *Frontiers in Psychology*, vol. 11, Article ID 582480, 2021.

[13] J. Y. Han and I. Y. L. Tan, "Retrospective single-centre experience on the effect of the DAWN trial on the utilisation pattern, diagnostic yield and accuracy of CT perfusions performed for suspected acute stroke," *Journal of Medical Imaging and Radiation Oncology*, vol. 64, no. 4, pp. 477–483, 2020.

[14] M. Naccarato, M. Ajčević, G. Furlanis et al., "Novel quantitative approach for crossed cerebellar diaschisis detection in acute ischemic stroke using CT perfusion," *Journal of the Neurological Sciences*, vol. 416, Article ID 117008, 2020.

[15] R. M. Chesnut, S. Temkin, C. Rondina et al., "A method of Managing Severe Traumatic brain Injury in the absence of intracranial pressure monitoring: the imaging and clinical examination protocol," *Journal of Neurotrauma*, vol. 35, no. 1, pp. 54–63, 2018.

[16] M. Ajčević, G. Furlanis, A. Miladinović et al., "Early EEG alterations correlate with CTP hypoperfused volumes and neurological deficit: a wireless EEG study in hyper-acute ischemic stroke," *Annals of Biomedical Engineering*, vol. 49, no. 9, pp. 2150–2158, 2021.

[17] K. Nael, E. Tadayon, D. Wheelwright et al., "Defining ischemic core in acute ischemic stroke using CT perfusion: a multiparametric bayesian-based model," *American Journal of Neuroradiology*, vol. 40, no. 9, pp. 1491–1497, 2019.

[18] R. Khumtong, T. Krings, V. M. Pereira, A. Pikula, and J. D. Schaafsma, "Comparison of multimodal CT scan protocols used for decision-making on mechanical thrombectomy in acute ischemic stroke," *Neuroradiology*, vol. 62, no. 3, pp. 399–406, 2020.

[19] S. Lukas, S. Feger, M. Rief, E. Zimmermann, and M. Dewey, "Noise reduction and motion elimination in low-dose 4D myocardial computed tomography perfusion (CTP): preliminary clinical evaluation of the ASTRA4D algorithm," *European Radiology*, vol. 29, no. 9, pp. 4572–4582, 2019.

[20] C. C. McDougall, L. Chan, S. Sachan et al., "Dynamic CTA-Derived perfusion maps predict final infarct volume: the Simple perfusion reconstruction algorithm," *American Journal of Neuroradiology*, vol. 41, no. 11, pp. 2034–2040, 2020.

[21] L. Hu, D. W. Zhou, C. X. Fu et al., "Calculation of apparent diffusion coefficients in prostate cancer using deep learning algorithms: a pilot study," *Frontiers in Oncology*, vol. 11, Article ID 697721, 2021.

[22] M. Woisetschläger, L. Henriksson, W. Bartholomae, T. Gasslander, B. Björnsson, and P. Sandström, "Iterative reconstruction algorithm improves the image quality without affecting quantitative measurements of computed

tomography perfusion in the upper abdomen," *European Journal of Radiology Open*, vol. 7, Article ID 100243, 2020.
[23] L. Pennig, F. Thiele, L. Goertz et al., "Comparison of accuracy of arrival-time-insensitive and arrival-time-sensitive CTP algorithms for prediction of infarct tissue volumes," *Scientific Reports*, vol. 10, no. 1, p. 9252, 2020.
[24] A. Hakim, M. Pastore-Wapp, S. Vulcu, T. Dobrocky, W. J. Z'Graggen, and F. Wagner, "Efficiency of iterative metal artifact reduction algorithm (iMAR) applied to brain volume perfusion CT in the follow-up of patients after Coiling or clipping of ruptured brain aneurysms," *Scientific Reports*, vol. 9, no. 1, Article ID 19423, 2019.
[25] Y. Yao, D. Yang, Y. Huang, and M. Dong, "Predictive value of insulin-like growth factor 1-Child-Turcotte-Pugh score for mortality in patients with decompensated cirrhosis," *Clinica Chimica Acta*, vol. 505, pp. 141–147, 2020.
[26] T. Martin, J. Hoffman, J. R. Alger, M. McNitt-Gray, and D. J. Wang, "Low-dose CT perfusion with projection view sharing," *Medical Physics*, vol. 45, no. 1, pp. 101–113, 2018.

Hindawi
Contrast Media & Molecular Imaging
Volume 2022, Article ID 6460865, 9 pages
https://doi.org/10.1155/2022/6460865

Research Article

The Diagnostic Value of High-Resolution Computed Tomography Features Combined with Mycoplasma Pneumoniae Ribonucleic Acid Load Detection for Refractory Mycoplasma Pneumonia

Hongping Wei,[1] **Chunyan Wang**,[1] **Lili Ding**,[1] **and Min Wu**[2]

[1]*Department of Pediatrics, Yiwu Central Hospital, Yiwu 322000, Zhejiang, China*
[2]*Department of Pharmacy, Yiwu Central Hospital, Yiwu 322000, Zhejiang, China*

Correspondence should be addressed to Min Wu; 2019211614@mail.chzu.edu.cn

Received 3 March 2022; Revised 31 March 2022; Accepted 2 April 2022; Published 4 May 2022

Academic Editor: M Pallikonda Rajasekaran

The aim of this study was to investigate the value of high-resolution computed tomography (CT) images and mycoplasma *pneumoniae* (MP) ribonucleic acid (RNA) load detection in the early diagnosis of refractory mycoplasma *pneumoniae* (RMP) and provide more methods for the diagnosis and treatment of RMP. Seventy children with MP were divided into the RMP group (H1 group, 31 cases) and the MP group (H2 group, 39 cases) according to pathological findings, and all of them underwent CT scanning. MP-RNA load and genotype distribution were analyzed in both groups, and the diagnostic efficacy of CT combined with MP-RNA load for RMP was calculated. The sensitivity of children in the H1 group to erythromycin (59.17% vs 71.56%) and clarithromycin (53.21% vs 67.03%) was lower than that in the H2 group, and the resistance rate of children in the H1 group to erythromycin (71.43% vs 67.53%) and clarithromycin (64.24% vs 50.37%) was higher than that in the H2 group ($P < 0.05$); the regression coefficients between lactate dehydrogenase (LDH) and the MPLI value of RMP were −0.064 and −0.413, respectively, which were significantly negatively correlated ($P < 0.05$); the accuracy (96.5%), sensitivity (92.5%), and specificity (88%) of CT + MP-RNA in the diagnosis of RMP were significantly higher than those of CT alone (91%, 88%, and 82%) and MP-RNA alone (88%, 84.5%, and 74%), which were significantly different ($P < 0.05$). The results of high MP-RNA load detection can be used as an indicator to predict RMP, and the diagnostic efficacy is significantly improved after combination with high-resolution CT, with high clinical application value.

1. Introduction

Mycoplasma *pneumoniae* (MP) is mainly transmitted through the respiratory tract, mostly in late summer and early autumn [1–3]. Refractory mycoplasma pneumonia (RMP) is usually because the body's immunity is weakened and resistance is weakened, resulting in easy recurrent infection of the patient's lungs and symptoms such as obvious fever, irritable dry cough, and dyspnea [4, 5]. Macrolides, such as roxithromycin and erythromycin, are mostly used for the clinical treatment of RMP; if it is associated with bacterial infections, levofloxacin should be taken at the same time for combination therapy; if it is accompanied by a significant decrease in saturation, systemic oxygen therapy should be given [6, 7].

The clinical manifestations of RMP lack specificity, so pathogenic testing is required for diagnosis. Among them, the separation and cultivation of MP have always been the gold standard for true MP, but unfortunately there are some disadvantages such as time-consuming and harsh operating conditions [8–10]. Although the fast culture drug susceptibility (FCDS) method can diagnose the RMP within 24 hours, it is prone to bleeding and misdiagnosis. MP antibody detection is one of the commonly used clinical detection methods, but because the antibody itself needs to be detected about a week after infection and the waiting time is too long, it is not suitable for early diagnosis [11]. In addition, another method is to use real-time fluorescent PCR to detect MR-RNA from throat swabs. Its specific high sensitivity and specificity will not be affected by objective conditions such as disease course, degree of infection, and body immunity, so it is applicable for the diagnosis of early stage of MP [12, 13]. The RMP is largely reflected in MR resistance, and the resistance mechanism at the gene level has always been a hot topic for scholars. For example, literature indicated that the resistance of mycoplasma *pneumoniae* to macrolide antibiotics is mainly due to changes in the nucleotide sequence of the ribosomal 50S subunit 23S rRNA, domain V and II regions [14]. In addition, studies have shown that bacteria can produce inactivating enzymes against macrolide antibiotics, destroy the structure of macrolide antibiotics, and cause them to lose their antibacterial activity. Therefore, it is necessary to explore the effects of MP genotype and MP-RNA load on the early stage of MP.

With the development of imaging technology, the clinical diagnosis of MP has increasingly relied on imaging methods. Computed tomography (CT) uses precisely collimated X-ray beams, gamma rays, and ultrasound together with a very sensitive detector to scan a certain part of the human body one by one. The scanning time is fast, and the image is clear, which can be used for the inspection of a variety of diseases [15]. The thickness of ordinary CT is usually 5–10 mm, which is relatively thick, so it can only be reconstructed with low spatial frequency algorithms. The layer thickness of high-resolution CT scans can reach 1–1.5 mm, and on this basis, high-resolution algorithm reconstruction can be carried out, which shows the lesions more clearly, especially some fine structures. For example, it can display the lobules and bronchi, lobular spacing, lobular arteries, and veins of the lungs. It can be further examined and diagnosed on the basis of conventional CT. In particular, when some patients find small lung nodules, they usually choose to do high-resolution CT for further diagnosis [16].

In summary, the selection of the early diagnosis plan for RMP has always been a hot issue in clinical research. Therefore, 70 children with MP were selected as the research objects. The children were subjected to mycoplasma *pneumoniae* drug sensitivity test, high-resolution CT, MP-RNA load determination, and 23S rRNA V region 2063 genotype sequencing, to explore the application value of high-resolution CT images and MP-RNA load detection in the early diagnosis of RMP.

2. Materials and Methods

2.1. Research Objects and Grouping. In this study, 70 children with MP who were admitted to the hospital from October 2018 to October 2020 were selected as the research objects. There were 43 boys and 27 girls, aged 1–8 years, with an average age of 5.21 + 1.33 years. According to the results of pathological diagnosis, the samples were divided into the RMP (H1 group, 31 cases) and MP (H2 group, 39 cases) groups. MP-RNA load and genotype distribution were analyzed in both groups. In addition, the two groups of children were suitable for CT examination and then combined with MP-RNA load detection for the diagnosis of the two groups of children. The sensitivity, specificity, and accuracy of CT images combined with MP-RNA load in the diagnosis of MP were calculated and were compared with the single diagnostic results of the two examination methods. The study had been approved by the ethics committee of hospital, and the children and their families had understood the situation of the study and signed the informed consent forms.

Inclusion criteria are as follows: children with throat swab MP-RNA copy number >500; children who received relevant drug treatment before admission; and children who had understood the experiment and signed informed consents.

Exclusion criteria are as follows: patients with common respiratory tract infections; patients with mental illness; patients who had not been reviewed in hospital after treatment; patients who withdrew from the study due to personal reasons; and patients with atypical pathogens such as *Chlamydia pneumoniae* and *Chlamydia trachomatis*.

2.2. Culture and Drug Sensitivity Test of Mycoplasma Pneumoniae. The specific steps were given as follows. The sterile cotton swab treated with normal saline was tossed three times on the throat of the child, and the obtained sample was immediately placed in the freezing medium and restored to a liquid state at room temperature; 50 μL of sample was pipetted and dropped into the C-well of the drug-sensitive plate. The cotton swab was placed in the culture flask, stirred many times, and then squeezed against the bottle wall after taking it out; after the obtained liquid was mixed well, 50 μL was pipetted and dropped into the $C+$ well and other drug-sensitive holes. The drug-sensitive plate was placed in a 37 °C incubator for 24 hours. The wells of the drug-sensitive plate contained 12 kinds of antibiotics (erythromycin, azithromycin, clarithromycin, doxycycline, clindamycin, telithromycin, levofloxacin, enoxacin, sparfloxacin, grepafloxacin, gatifloxacin, and trovafloxacin). The drug resistance to microorganisms was analyzed based on the inhibition effect on growth of the microorganisms of different concentrations of antibiotics.

The interpretation criteria [17] were as follows. It can be evaluated based on the degree of discoloration of the drug-sensitive plate: it could be determined as positive result if the $C+$ well of the drug-sensitive plate changed from red to light blue, and it could be determined as negative result if the color remained unchanged. If the two drug-sensitive plate wells were all red, it meant that it was sensitive to the antibiotic; one red and one yellow well meant that it was mediator; and two yellow wells meant that it was resistant to the antibiotic.

2.3. Fluorescence Quantitative PCR Detection. The specific steps were as follows. The sterile cotton swab treated with saline was tossed over the throat of the child three times, and then, it was squeezed to dry. 1 mL of the swab liquid was sucked into a 2 mL centrifuge tube and centrifuged at 12,000 rpm for 10 minutes to obtain the precipitate. 50 μL of negative and positive quality control materials was placed into two 2 mL centrifuge tubes, which were added with 50 μL of nucleic acid extract, respectively. The mixture was mixed and lysed at 110 °C for 8 minutes and centrifuged at 12000 rpm for 10 minutes to collect the supernatant (20 μL) for PCR. The number of tubes required for the PCR was set as L, and then, L = Sample number + negative control + Positive control + Positive standard substance could be obtained. There were 1 negative control tube, 1 positive control tube, and 4 positive standard tubes. The L test tubes were added with the treated samples, MP-negative quality control substance, MP-positive quality control substance, and MP-positive quantitative standard substance (with 2 μL for each). Then, the tubes were capped and centrifuged at 2000 rpm for 15 seconds. After that, the test tubes were placed into the reaction tank of the PCR instrument one by one to perform the PCR amplification according to the set cycle conditions. PCR amplification conditions were set as follows: running at 95 °C for 3 minutes, denaturation at 95 °C for 50 seconds, and annealing at 55 °C for 1 minute (above operations were repeated for 10 cycles); and running at 93 °C for 30 seconds and annealing at 55 °C for 50 seconds (the operations were repeated for 30 times).

MP-RNA load can be determined according to the following procedures. The MPLI of positive samples was calculated by taking the content of H actin-RNA as the internal reference, so $\mathrm{MPLI} = -\lg(\text{Copy quantity}\ (MP - \mathrm{R}NA)/\text{Copy quantity}\ (\mathrm{Hactin} - \mathrm{R}NA))$ could be obtained. The smaller the MPLI value, the greater the MP-RNA load.

2.4. Sequencing. PCR was performed with reference to the primer sequence of the 23S rRNA V region in the previous literature [18, 19]. PCR amplification conditions were set as follows: denaturation at 95 °C for 5 minutes, run at 94 °C for 15 seconds, run at 52 °C for 30 seconds, and run at 72 °C for 30 seconds (above operations were cycled for 30 times), extension at 72 °C for 10 minutes, and storage at 4 °C. Then, 5 μL of the PCR product was taken for agarose gel electrophoresis, recovery purification, and sequencing. The sequencing result was compared with the reference sequence of the gene bank searched by the National Center for Biological Information (NCBI) to determine the 2063 genotype in the 23S rRNA V region.

2.5. CT Examination. In this study, the 16-slice spiral CT was adopted to scan the patient. Conventional CT was applied to scan the chest with a slice thickness of 10 mm and a slice distance of 10 mm, and some slices were selected for high-resolution CT scanning. The scan range was from the tip of the lung to the bottom of the lung. High-resolution CT scan parameters were defined as follows: collimation was 1.25 mm × 8 mm, pitch was 1.35, 0.8 seconds was required for each circle, tube voltage was 120 kV, tube current was 120 mA, and 13.5 mm was set per circle.

2.6. Observation Indicators. The basic data of the two groups of children were collected and recorded, including age, gender ratio, body mass index (BMI), white blood cells (WBCs), C-reactive protein (CRP), procalcitonin (PCT), lactate dehydrogenase (LDH), fever time, hospitalized time, cough time, IgA, IgG, IgM, and imaging data (CT and X-ray film). The drug resistance and sensitivity of MP of the children in two groups were recorded, including erythromycin, azithromycin, clarithromycin, doxycycline, clindamycin, telithromycin, levofloxacin, enoxacin, sparfloxacin, grepafloxacin, gatifloxacin, and trovafloxacin. The proportions of drug resistance gene mutation and the distributions of genotype mutations (A, C, G, and T) in the two groups of children were collected and recorded.

2.7. Statistical Analysis. The data in this study were analyzed by SPSS 19.0 version statistical software. The measurement data were expressed as mean ± standard deviation ($\bar{x} \pm s$), and the counting data were given in percentage (%). Pairwise comparison adopted a one-way analysis of variance. Origin 8.0 was adopted for drawing.

3. Results and Discussion

3.1. Comparison of Clinical Characteristics of Children in Two Groups. The clinical characteristics of children in the H1 and H2 groups were compared, and the results are illustrated in Table 1. The differences in age, gender ratio, BMI, WBC, CRP, fever time, hospitalized time, cough time, IgA, IgG, and IgM levels of children in the H1 and H2 groups were not statistically obvious ($P > 0.05$); the LDH, PCT, and antipyretic time of the children in the H1 group were much shorter than those of the children in the H2 group, showing statistical differences ($P < 0.05$).

3.2. Imaging Characteristics of Some Children. Figure 1 suggests the CT image of Case 1. Chest CT indicated that the lesion progressed rapidly and multiple lung-air sacs were formed.

Figure 2 shows the CT image of Case 2. Chest CT showed acinar nodules, tree-bud sign, tree-fog sign, and lesions distributed along the bronchi, accompanied by bronchial wall thickening and peribronchitis.

3.3. Comparison of Drug Sensitivity Test Results of Children in the H1 and H2 Groups. Figure 3 shows the comparison of drug sensitivity test results of children in the groups H1 and H2. It illustrated that the two groups of children with MP had higher resistance rates to erythromycin (71.43% vs 67.53%) and clindamycin (64.24% vs 50.37%) and had higher sensitivity rates to azithromycin (59.17% vs 71.56%), clarithromycin (53.21% vs 67.03%), and telithromycin (62.45% vs 65.49%). Among them, children in the H1 group showed a lower sensitivity rate to azithromycin and clarithromycin than the children in the H2 group, and the differences were statistically observable ($P < 0.05$). The two groups of children with MP all had high sensitivity rates to levofloxacin, enoxacin, sparfloxacin, grepafloxacin, gatifloxacin, and trovafloxacin, all of which were greater than 90%, and the drug resistance rates were extremely low (lower than 2%).

Table 1: Comparison of clinical characteristics of children in the H1 and H2 groups.

Projects	H1 group ($n = 31$)	H2 group ($n = 39$)	t or $\chi 2$	P
Age (years)	5.02 ± 1.21	5.10 ± 1.03	−0.134	0.343
Male (n/%)	19/61.29	24/61.54	−0.157	0.352
Female (n/%)	12/38.71	15/38.46	−0.216	0.491
BMI (kg/m^2)	18.67 ± 3.07	18.45 ± 3.14	−0.339	0.509
WBC ($\times 10^9$/L)	10.28 ± 2.37	11.43 ± 2.07	0.247	0.229
CRP (mg/L)	22.09 ± 4.36	20.17 ± 5.28	0.303	0.201
PCT (ug/L)	134.89 ± 10.62	120.67 ± 11.37	5.140	0.036
LDH (U/L)	271.22 ± 50.61	225.14 ± 48.93	6.783	0.025
Fever time (d)	8.15 ± 3.62	6.89 ± 4.25	0.241	0.232
Hospitalized time (d)	12.65 ± 5.17	11.03 ± 5.09	0.212	0.267
Antipyretic time (d)	16.07 ± 4.66	11.26 ± 4.71	6.546	0.028
Cough time (d)	17.95 ± 4.78	15.64 ± 4.43	0.398	0.187
IgA (g/L)	0.98 ± 0.45	0.91 ± 0.44	−0.211	0.413
IgG (g/L)	8.89 ± 0.97	8.63 ± 0.93	0.107	0.315
IgM (g/L)	1.64 ± 0.31	1.60 ± 0.44	−0.199	0.488

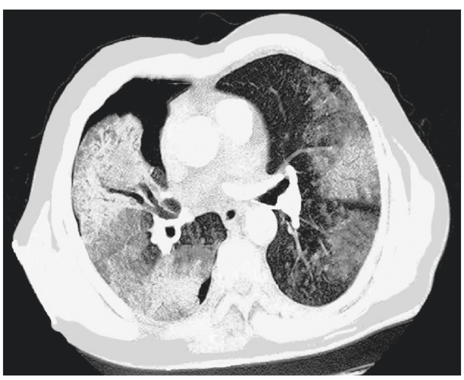

Figure 1: CT image of Case 1.

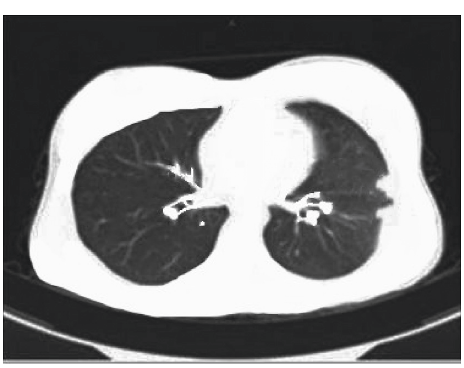

Figure 2: CT image of Case 2.

3.4. Comparison of MP-RNA Load of Children in the H1 and H2 Groups. The comparison of MP-RNA load of children in the H1 and H2 groups is illustrated in Figure 4. It revealed that the MPLI values of resistance to erythromycin, azithromycin, clarithromycin, clindamycin, and enoxacin in the H1 group were greatly lower than those in the H2 group, showing statistical differences ($P < 0.05$), while the MPLI values of resistance to doxycycline, telithromycin, levofloxacin, sparfloxacin, grepafloxacin, gatifloxacin, and trovafloxacin in children in the H1 group were not greatly different from those in the H2 group, showing no statistical significance ($P > 0.05$).

3.5. Comparison of Gene Sequencing Results of Children in the Groups H1 and H2. The comparison of drug resistance gene mutations in children in the H1 and H2 groups (Figure 5(a)) showed that the mutation rate of the 2063 gene in the 23S rRNA V region in the H1 group (96.42%) was greatly higher in contrast to that in the H2 group (73.51%), showing meaningful difference ($P < 0.05$); the non-gene mutation rate (3.58%) of children in the H1 group was obviously lower in contrast to the rate in the H2 group (26.49%), and the difference was remarkable ($P > 0.05$). Figure 5(b) shows the agarose gel electrophoresis of the PCR product. The rightmost was the marker from top to bottom: 600 bp, 500 bp, 400 bp, 300 bp, 200 bp, and 100 bp. On the right side of the marker was the target band. It was observed that the target band was brighter, clearly visible, and primer dimers under 200–300 bp and 100 bp.

The genotype distributions of antibiotic-resistant cases in the H1 and H2 groups are given in Figure 6. It illustrated that the erythromycin-, azithromycin-, clarithromycin-, doxycycline-, clindamycin-, and telithromycin-resistant cases showed A and *G* mutations in both groups of children, and the proportions of *G* mutation at 2063 in the H1 group of children resistant to erythromycin, azithromycin, clarithromycin, doxycycline, clindamycin, and telithromycin were obviously greater than that of the H2 group, while A mutation was the opposite, showing statistical differences ($P < 0.05$). The two groups of children showed A and *G* mutations in levofloxacin-, enoxacin-, sparfloxacin-, grepafloxacin-, gatifloxacin-, and trovafloxacin-resistant cases, but the mutation ratio was about 50%, and there was no dramatic difference between the two ($P > 0.05$).

3.6. Correlation of MP-RNA Load and Drug Resistance Gene Mutation to RMP. As shown in Table 2, RMP was normalized (1 referred to RMP and 0 for MP), and Pearson's correlation analysis was performed for MP-RNA load and drug resistance gene mutation. The results revealed that RMP and drug resistance gene mutation were extremely positively correlated ($r = -0.415$ and $P < 0.001$); RMP and

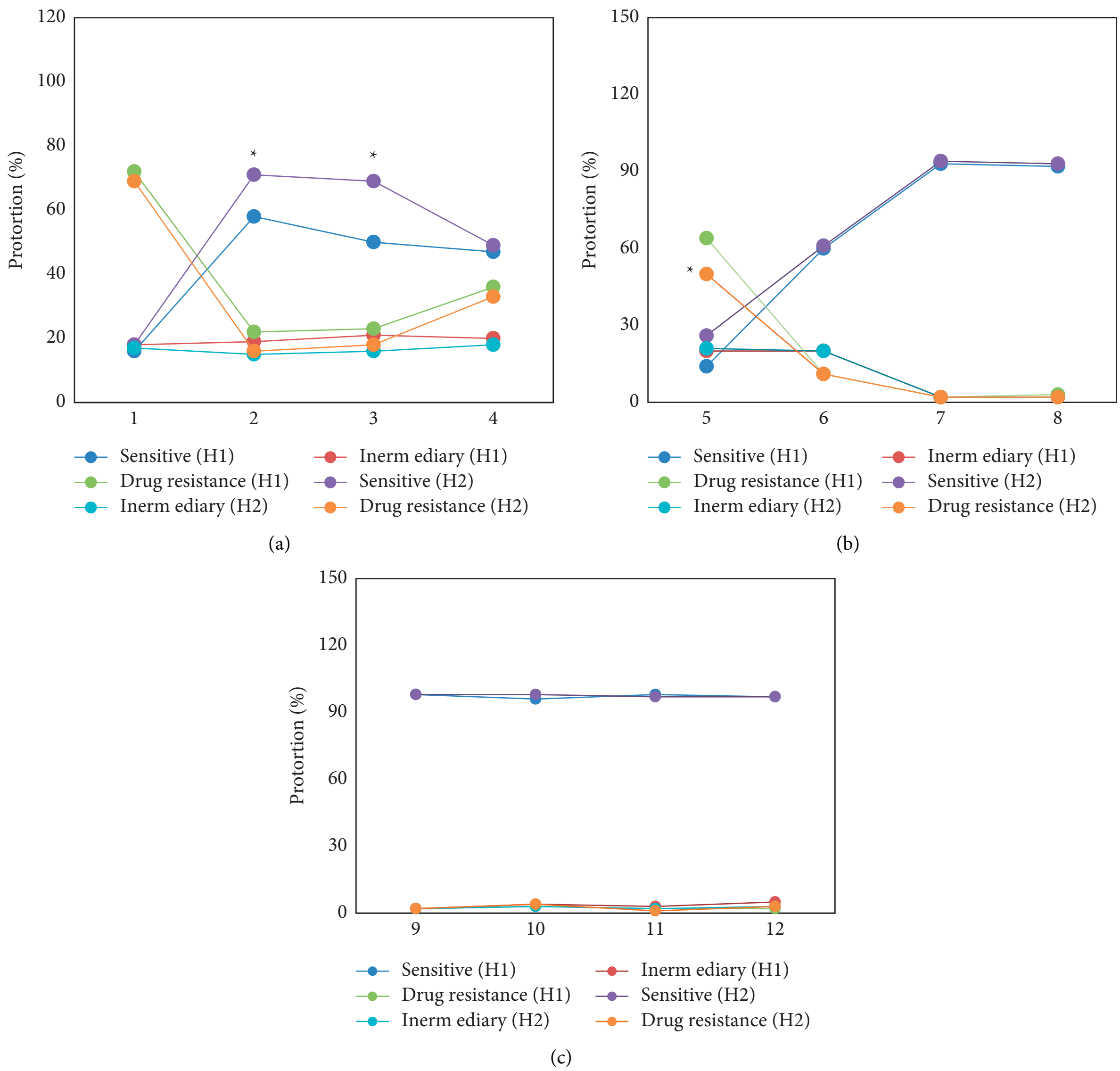

Figure 3: Comparison of drug sensitivity test results of children in the groups H1 and H2 (1–12 referred to erythromycin, azithromycin, clarithromycin, doxycycline, clindamycin, telithromycin, levofloxacin, enoxacin, pefloxacin, grepafloxacin, gatifloxacin, and trovafloxacin, respectively). (a) The sensitivity results of MP to erythromycin, azithromycin, clarithromycin, and doxycycline; (b) the sensitivity results of MP to clindamycin, telithromycin, levofloxacin, and enoxacin; and (c) the sensitivity results of MP to sparfloxacin, grepafloxacin, gatifloxacin, and trovafloxacin. $*$ he difference was visible statistically in contrast to the H1 group ($P < 0.05$).

MPLI resistance values showed an obviously negative correlation ($r = -0.399$ and $P < 0.05$).

To further explore the impacts of MPLI value and drug resistance gene mutation on RMP, different clinical indicators (LDH, PCT, and antipyretic time) and MP-RNA load and drug resistance gene mutation were incorporated into the multivariate regression analysis. As shown in Table 3, there was no obvious correlation between PCT and antipyretic time to the RMP ($P > 0.05$); the regression coefficients of RMP to LDH and MPLI were −0.064 and −0.413, respectively, and there was an extremely negative correlation ($P < 0.05$); the drug regression coefficient of resistance gene mutation to the RMP was 0.388, which showed a remarkably positive correlation ($P < 0.05$).

3.7. Diagnostic Performances of CT and MP-RNA Load for RMP. Figure 7 shows the accuracy (96.5%), sensitivity (92.5%), and specificity (88%) of CT + MP-RNA in the diagnosis of RMP were significantly higher than those of CT alone (91%, 88%, and 82%) and MP-RNA alone (88%, 84.5%, and 74%), and the differences were significant ($P < 0.05$).

4. Discussion

With the widespread use of antibiotics, the drug resistance of mycoplasma *pneumoniae* has received widespread clinical attention. Since 2000, the resistance rate of mycoplasma *pneumoniae* isolates to macrolides has increased year by year, which has made the treatment of MP became difficult

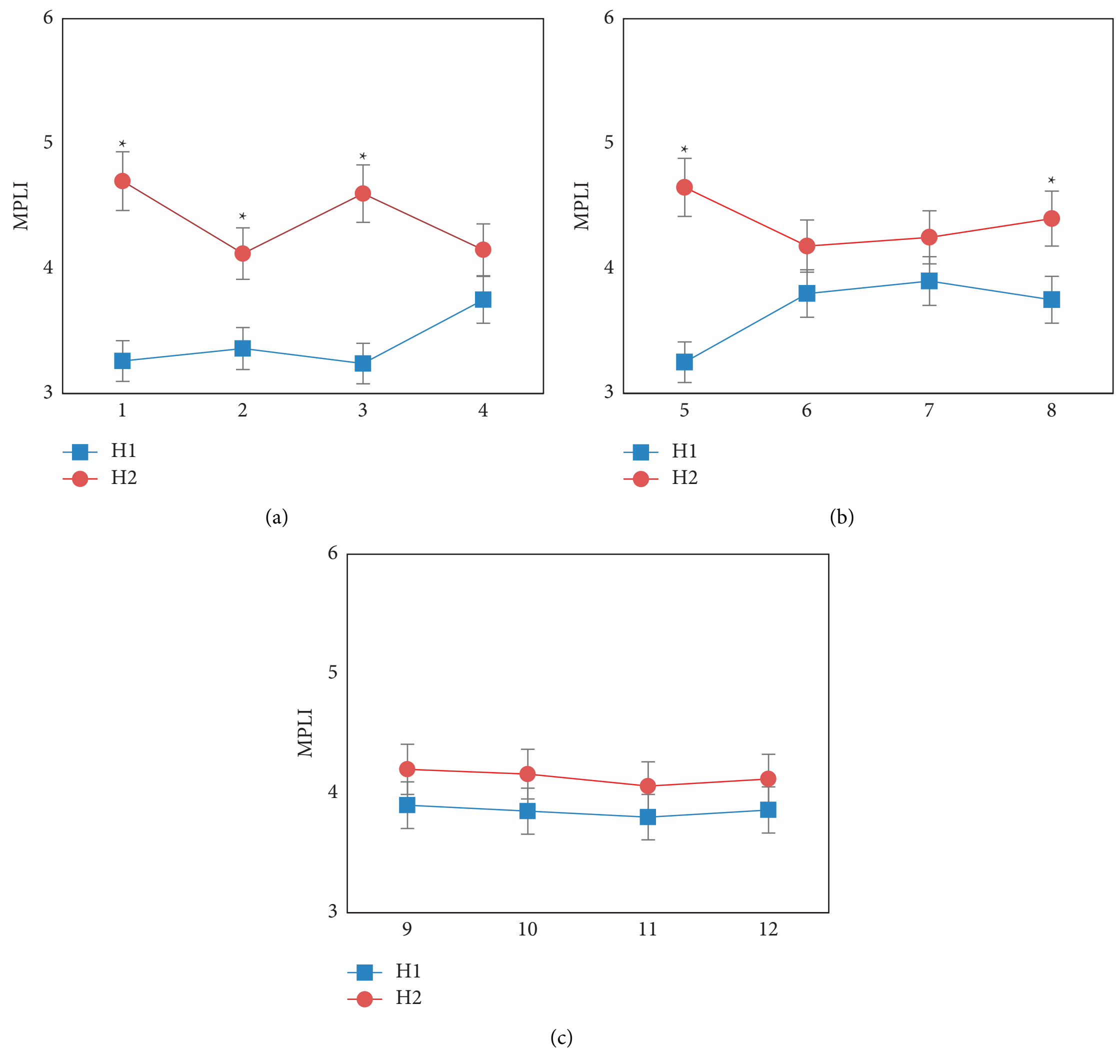

Figure 4: Comparison of MP-RNA load of children in the H1 and H2 groups (1–12 referred to erythromycin, azithromycin, clarithromycin, doxycycline, clindamycin, telithromycin, levofloxacin, enoxacin, sparfloxacin, grepafloxacin, gatifloxacin, and trovafloxacin, respectively). (a) showed the sensitivity results of MP to erythromycin, azithromycin, clarithromycin, and doxycycline; (b) showed the sensitivity results of MP to clindamycin, telithromycin, levofloxacin, and enoxacin; and (c) showed the sensitivity results of MP to sparfloxacin, grepafloxacin, gatifloxacin, and trovafloxacin. ∗ suggested that the difference was statistically remarkable compared with the H1 group ($P < 0.05$).

to be treated, based on which RMP is sourced [20, 21]. Because of the atypical early clinical manifestations of RMP, it is easy to be misdiagnosed and mistreated, so how to effectively make early diagnosis is very important. Compared with conventional CT, high-resolution CT shows clearer lesion display characteristics and a finer structure display, which can assist physicians in accurate diagnosis [22, 23]. In this study, 70 children with MP were selected as the research objects, including 31 cases of RMP (H1 group) and 39 cases of MP (H2 group). The clinical characteristics of the two groups of children were compared, and it was found that the LDH, PCT, and antipyretic time of children in the H1 group were much shorter than those of the H2 group, and the differences were statistically obvious ($P < 0.05$). Such results indicated that LDH, PCT, and antipyretic time may be related to the RMP [24]. The FCDS method found that the two groups of children's MPs were highly sensitive to azithromycin (59.17% vs 71.56%), clarithromycin (53.21% vs 67.03%), and telithromycin (62.45% vs 65.49%); the sensitivity rates of MP to azithromycin and clarithromycin in children in the H1 group were lower in contrast to the rates in children in the H2 group ($P < 0.05$). Such results were different from the findings of Mohanraj et al. [25], which may be because the abuse and irregular treatment of traditional macrolide antibiotics has reduced the sensitivity of MP to azithromycin, clarithromycin, and telithromycin, and RMP showed lower sensitivity [26]. The two groups of children with MP had higher sensitivity rates to levofloxacin, enoxacin, sparfloxacin, grepafloxacin, gatifloxacin, and trovafloxacin, all of which were higher than 90%, and the drug resistance rate was extremely low (lower than 2%), indicating that quinolone antibacterial drugs had good in

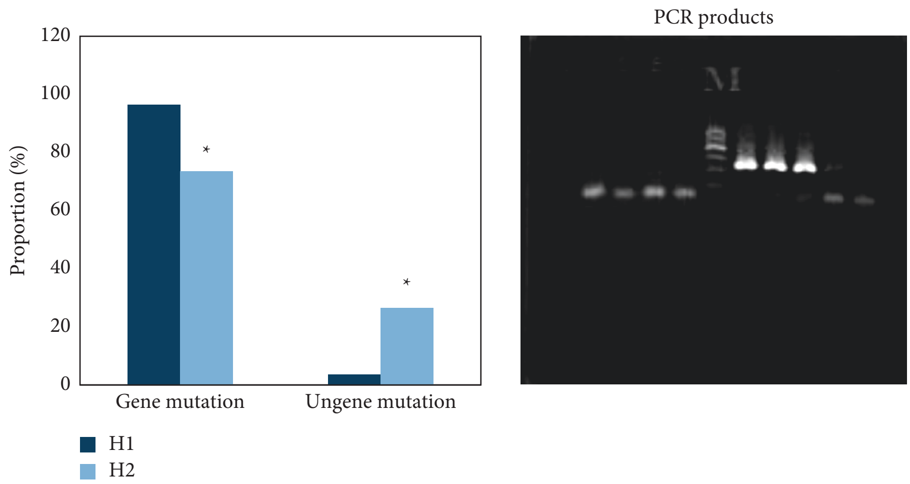

FIGURE 5: Comparison of gene sequencing results of children in the groups H1 and H2. ∗ suggested that there was a statistical difference compared with the H1 group ($P < 0.05$).

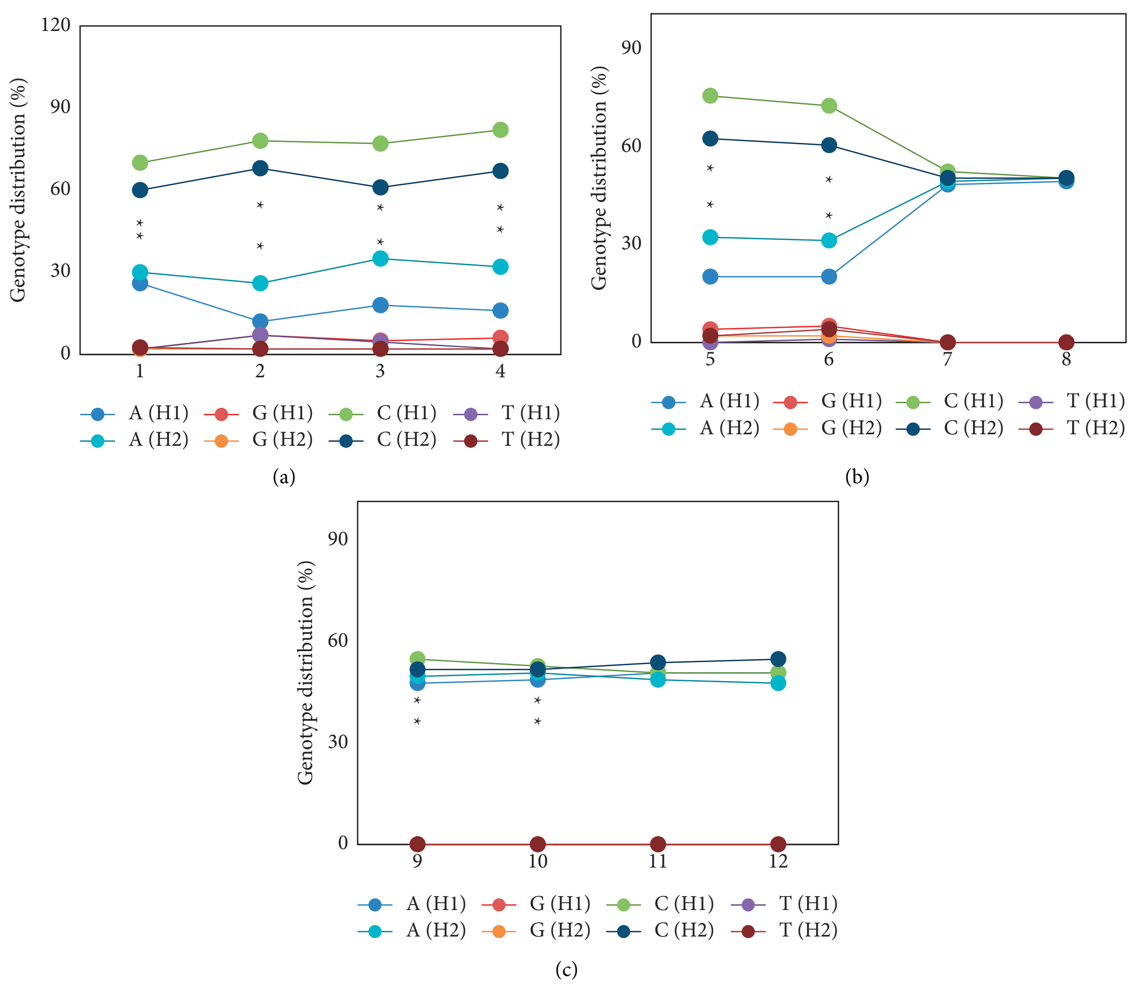

FIGURE 6: Distribution of genotype of antibiotic-resistant cases in children in the groups H1 and H2 (1–12 referred to erythromycin, azithromycin, clarithromycin, doxycycline, clindamycin, telithromycin, levofloxacin, enoxacin, sparfloxacin, grepafloxacin, gatifloxacin, and trovafloxacin, respectively). (a) showed the distribution of genotype in children with resistance to erythromycin, azithromycin, clarithromycin, and doxycycline; (b) showed the distribution of genotype in children with resistance to clindamycin, telithromycin, levofloxacin, and enoxacin; and (c) showed the distribution of genotype in children with resistance to sparfloxacin, grepafloxacin, gatifloxacin, and trovafloxacin. ∗ meant that the difference was statistically dramatic in contrast to the H1 group ($P < 0.05$).

Table 2: Correlation of MP-RNA load and drug resistance gene mutation to RMP.

Variable	RMP/MP	
	r	P
Drug resistance gene mutation	0.415	0.001
MPLI value	−0.399	0.011

Table 3: Multivariate regression analysis of MP-RNA load and drug resistance gene mutation to RMP.

Variable	RMP		
	Regression coefficient	*t* value	*P*
LDH	−0.064	3.461	0.027
PCT	0.139	2.552	0.059
Antipyretic time	0.266	2.815	0.071
MPLI value	−0.413	3.767	0.008
Drug resistance gene mutation	0.388	4.025	0.001

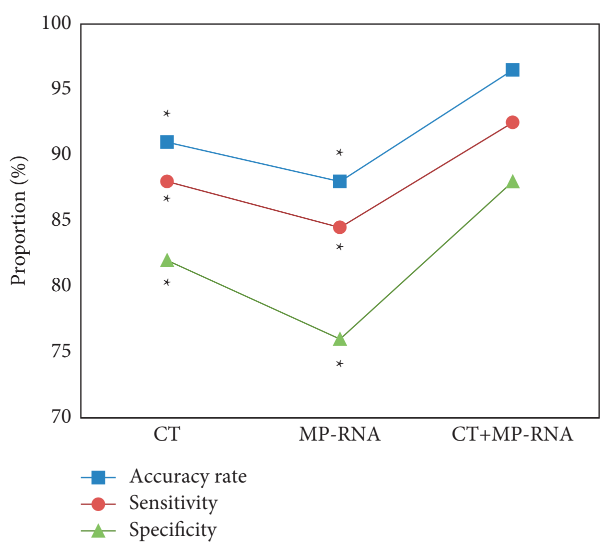

Figure 7: Diagnostic performances of CT and MP-RNA load for RMP. ∗ meant significant difference compared with CT + MP-RNA ($P < 0.05$).

vitro antimicrobial activity against mycoplasma *pneumoniae*. The results of Wei et al. [27] are consistent with the results of this exploration.

In addition, the MPLI values of children with resistance to erythromycin, azithromycin, clarithromycin, clindamycin, and enoxacin in the H1 group were lower than those in the H2 group, and the differences were great statistically ($P < 0.05$). Such results were similar to those of Lan et al. [28]. The smaller the MPLI value, the higher the MP-RNA load, which could objectively reflect the balance between MP and host immune clearance. Thus, the results indicated that RMP had a higher MP-RNA load. The proportions of *G* mutation at 2063 in children resistant to erythromycin, azithromycin, clarithromycin, doxycycline, clindamycin, and telithromycin in the H1 group were obviously greater in contrast to the proportions in the H2 group, while A mutation was the opposite, showing statistically obvious differences ($P < 0.05$). It suggested that A and *G* mutations at 2063 had greater impacts on the occurrence of RMP [29]. To further explore the impacts of MPLI value and drug resistance gene mutation on RMP, multifactor regression analysis was performed, and it was found that the regression coefficients of RMP to LDH and MPLI values were −0.064 and −0.413, respectively, showing an obviously negative correlation ($P < 0.05$); the regression coefficient of RMP to the resistance gene mutation was 0.388, showing a visibly positive correlation ($P < 0.05$). It indicated that high MP-RNA load, high drug resistance gene mutation, and low LDH levels could be deemed as indicators to predict RMP. It conforms to the conclusions of the study by Chen et al. (2021) [30]. The accuracy, sensitivity, and specificity of CT + MP-RNA in the diagnosis of RMP were significantly greater than that of single CT and MP-RNA, and the difference was statistically obvious ($P < 0.05$). This showed that high-resolution CT combined with MP-RNA load detection is better than a single detection method for the diagnosis of RMP.

5. Conclusion

It investigated the value of high-resolution CT images and MP-RNA load detection in the early diagnosis of RMP. The results showed that the detection results of high MP-RNA load could be used as an indicator to predict RMP, and the diagnostic efficacy was significantly improved after combining with high-resolution CT, with high clinical application value. However, there are still some shortcomings. The small sample size and single source of the selected patients resulted in a few different causes of drug resistance, which may have some impact on the results. The subsequent selection of patients will be increased for multicenter and large-sample analysis. In conclusion, the results can provide a reference for the selection of diagnostic indicators for RMP.

Data Availability

The data used to support the findings of this study are available from the corresponding author upon request.

Conflicts of Interest

The authors declare no conflicts of interest.

References

[1] M. J. M. Bonten, S. M. Huijts, M. Bolkenbaas et al., “Polysaccharide conjugate vaccine against pneumococcal pneumonia in adults,” *New England Journal of Medicine*, vol. 372, no. 12, pp. 1114–1125, 2015.

[2] L. Wu, M. Ye, X. Qin, Y. Liu, Z. Lv, and R. Zheng, “Diagnostic value of quantitative MP-IgG for Mycoplasma pneumoniae pneumonia in adults,” *Clinica Chimica Acta*, vol. 503, pp. 76–83, 2020.

[3] D. K. Chu, E. A. Akl, S. Duda et al., "Physical distancing, face masks, and eye protection to prevent person-to-person transmission of SARS-CoV-2 and COVID-19: a systematic review and meta-analysis," *The Lancet*, vol. 395, Article ID 10242, 1973–1987 pages 2020..

[4] J. Sadegh Tabrizi, M. Seyedhejazi, and A. Fakhari, "Preoperative education and decreasing preoperative anxiety among children aged 8 - 10 Years old and their mothers," *Anesthesiology and Pain Medicine*, vol. 5, no. 4, Article ID e25036, 2015.

[5] E. Lee, C. H. Kim, C.-H. Kim et al., "Annual and seasonal patterns in etiologies of pediatric community-acquired pneumonia due to respiratory viruses and Mycoplasma pneumoniae requiring hospitalization in South Korea," *BMC Infectious Diseases*, vol. 20, no. 1, p. 132, 2020.

[6] Y.-J. Choi, J.-H. Jeon, and J.-W. Oh, "Critical combination of initial markers for predicting refractory Mycoplasma pneumoniae pneumonia in children: a case control study," *Respiratory Research*, vol. 20, no. 1, p. 193, 2019.

[7] D. Colombi, F. C. Bodini, M. Petrini et al., "Well-aerated lung on admitting chest CT to predict adverse outcome in COVID-19 pneumonia," *Radiology*, vol. 296, no. 2, pp. E86–E96, 2020.

[8] G. Ruiz-Irastorza, J. I. Pijoan, and E. Bereciartua, "Second week methyl-prednisolone pulses improve prognosis in patients with severe coronavirus disease 2019 pneumonia: an observational comparative study using routine care data," *PLoS One*, vol. 15, no. 9, Article ID e0239401, 2020.

[9] Y. B. Cihan, "Ga-68-PSMA PET/CT ? or PET/MRI ?, Mp-MRI ? in diagnosis and radiotherapy planning in a patient with prostate cancer," *International Braz J Urol*, vol. 46, no. 6, pp. 1117–1119, 2020.

[10] Z. Wang, J. Sun, Y. Liu, and Y. Wang, "Impact of atopy on the severity and extrapulmonary manifestations of childhood Mycoplasma pneumoniae pneumonia," *Journal of Clinical Laboratory Analysis*, vol. 33, no. 5, Article ID e22887, 2019.

[11] B. Yilmaz, R. Turkay, Y. Colakoglu et al., "Comparison of preoperative locoregional Ga-68 PSMA-11 PET-CT and mp-MRI results with postoperative histopathology of prostate cancer," *The Prostate*, vol. 79, no. 9, pp. 1007–1017, 2019.

[12] T. Saraya, D. Kurai, K. Nakagaki et al., "Novel aspects on the pathogenesis of Mycoplasma pneumoniae pneumonia and therapeutic implications," *Frontiers in Microbiology*, vol. 5, p. 410, 2014.

[13] E.-A. Yang, H.-M. Kang, J.-W. Rhim, J.-H. Kang, and K.-Y. Lee, "Early corticosteroid therapy for mycoplasma pneumoniae pneumonia irrespective of used antibiotics in children," *Journal of Clinical Medicine*, vol. 8, no. 5, p. 726, 2019.

[14] M.-c. Zhao, L. Wang, F.-z. Qiu et al., "Impact and clinical profiles of Mycoplasma pneumoniae co-detection in childhood community-acquired pneumonia," *BMC Infectious Diseases*, vol. 19, no. 1, p. 835, 2019.

[15] K.-A. Chu, W. Chen, Y.-M. Hung, and J. C.-C. Wei, "Increased risk of ankylosing spondylitis after Mycoplasma pneumonia," *Medicine*, vol. 98, no. 27, Article ID e15596, 2019.

[16] G. D. Rubin, C. J. Ryerson, L. B. Haramati et al., "The role of chest imaging in patient management during the COVID-19 pandemic: a multinational consensus statement from the fleischner society," *Radiology*, vol. 296, no. 1, pp. 172–180, 2020.

[17] L. Q. Liu, Z. H. Wang, and H. Y. Yao, "Hepatocyte growth factor can guide treatment of Mycoplasma pneumoniae pneumonia in children," *Experimental and Therapeutic Medicine*, vol. 19, no. 5, pp. 3432–3438, 2020.

[18] P. M. Meyer Sauteur, J. Trück, A. M. C. van Rossum, and C. Berger, "Circulating antibody-secreting cell response during mycoplasma pneumoniae childhood pneumonia," *The Journal of Infectious Diseases*, vol. 222, no. 1, pp. 136–147, 2020.

[19] B. C. Chapman, B. Herbert, M. Rodil et al., "RibScore," *Journal of Trauma and Acute Care Surgery*, vol. 80, no. 1, pp. 95–101, 2016.

[20] W. J. Gu, X. X. Zhang, and Z. R. Chen, "Clinical significance of MP-DNA from endotracheal aspirates in diagnosis of Mycoplasma pneumoniae pneumonia in children," *Zhong Guo Dang Dai Er Ke Za Zhi*, vol. 17, no. 9, pp. 937–941, 2015.

[21] Y. Xiong, Q. Zhang, D. Sun, and W. Zhu, "Clinical and CT characteristics of healthcare workers with COVID-19," *Medicine*, vol. 99, no. 30, Article ID e21396, 2020.

[22] F. Tian, L.-P. Chen, G. Yuan, A.-M. Zhang, Y. Jiang, and S. Li, "Differences of TNF-α, IL-6 and Gal-3 in lobar pneumonia and bronchial pneumonia caused by mycoplasma pneumoniae," *Technology and Health Care*, vol. 28, no. 6, pp. 711–719, 2020.

[23] L. Scarfò, T. Chatzikonstantinou, G. M. Rigolin et al., "COVID-19 severity and mortality in patients with chronic lymphocytic leukemia: a joint study by ERIC, the European Research Initiative on CLL, and CLL Campus," *Leukemia*, vol. 34, no. 9, pp. 2354–2363, 2020.

[24] M. P. van der Meulen, I. Lansdorp-Vogelaar, S. L. Goede et al., "Colorectal cancer: cost-effectiveness of colonoscopy versus CT colonography screening with participation rates and costs," *Radiology*, vol. 287, no. 3, pp. 901–911, 2018.

[25] R. Mohanraj, S. Kumar, S. Jayakumar et al., "Where do mothers take their children for pneumonia care? Findings from three Indian states," *PLoS One*, vol. 14, no. 4, Article ID e0214331, 2019.

[26] D. Aguilera-Alonso, R. López Ruiz, and J. Centeno Rubiano, "Características clínicas y epidemiológicas de las neumonías adquiridas en la comunidad por Mycoplasma pneumoniae en una población española," *2010-2015 Epidemiological and clinical analysis of community-acquired Mycoplasma pneumonia in children from a Spanish population*, vol. 91, no. 1, pp. 21–29, 2019.

[27] R. Wei, H. Dou, L. Wang et al., "In vitro susceptibility test of xiao'er feire kechuan oral solution to mycoplasma pneumoniae," *Medicine*, vol. 98, no. 27, Article ID e16070, 2019.

[28] Y. Lan, S. Li, D. Yang et al., "Clinical characteristics of Kawasaki disease complicated with Mycoplasma pneumoniae pneumonia," *Medicine*, vol. 99, no. 19, Article ID e19987, 2020.

[29] T. Saraya, K. Ohkuma, Y. Tsukahara et al., "Correlation between clinical features, high-resolution computed tomography findings, and a visual scoring system in patients with pneumonia due to Mycoplasma pneumoniae," *Respiratory Investigation*, vol. 56, no. 4, pp. 320–325, 2018.

[30] J. Chen, F. Ji, Y. Yin, and S. Yuan, "Time to mycoplasma pneumoniae RNA clearance for wheezy vs. Non-wheezy young children with community-acquired pneumonia," *Journal of Tropical Pediatrics*, vol. 67, no. 1, 2021.

Hindawi
Contrast Media & Molecular Imaging
Volume 2022, Article ID 9107021, 9 pages
https://doi.org/10.1155/2022/9107021

Research Article

Three-Dimensional Reconstruction of a CT Image under Deep Learning Algorithm to Evaluate the Application of Percutaneous Kyphoplasty in Osteoporotic Thoracolumbar Compression Fractures

Jiameng Li, Zhong Xiang, Jiaqing Zhou, and Meng Zhang

Department of Spine Surgery, The Fourth Hospital of Changsha, Changsha 412002, Hunan, China

Correspondence should be addressed to Meng Zhang; 2013042107@stu.zjhu.edu.cn

Received 28 February 2022; Revised 31 March 2022; Accepted 2 April 2022; Published 28 April 2022

Academic Editor: M Pallikonda Rajasekaran

In order to investigate the therapeutic evaluation of percutaneous kyphoplasty (PKP) for the treatment of osteoporotic thoracolumbar compression fractures by three-dimensional (3D) reconstruction of computed tomography (CT) based on the deep learning V-Net network, the traditional V-Net was optimized first and a new and improved V-Net was proposed. The introduced U-Net, V-Net, and convolutional neural network (CNN) were compared in this study. Then, 106 patients with osteoporotic thoracolumbar compression fractures were enrolled, and 128 centrums were divided into the test group with 53 cases of PKP and the control group with 53 cases of percutaneous vertebroplasty (PVP) according to different surgical protocols. All patients underwent CT scan based on the improved V-Net, and data of centrum measurement indicators, pain score, and therapeutic evaluation results of the modified Macnab were collected. The Dice coefficient of the improved V-Net was observably higher than that of U-Net, V-Net, and CNN, while the Hausdorff distance was lower than that of U-Net, V-Net, and CNN ($P < 0.05$). The anterior height, central height, and posterior height of the centrum were significantly higher than those in the control group after operation (3, 5, and 7 days), while the Cobb angle of vertebral kyphosis was significantly lower than that in the control group ($P < 0.05$). The score of visual analog scale (VAS) and analgesic use score of patients in the test group were markedly lower than those in the control group (3, 5, and 7 days after operation), $P < 0.05$. Besides, the excellent and good rate of the test group was remarkably higher than that of the control group, $P < 0.05$. Hence, the improved V-Net had better quality of segmentation and reconstruction than the traditional deep learning network. Compared with PVP, PKP was helpful in restoring the height of the centrum in patients with osteoporotic thoracolumbar compression fractures and correct kyphosis, with better analgesic effect safety.

1. Introduction

With the increasing aging of population in China, the incidence of osteoporosis in the elderly is increasing. Osteoporotic vertebral fracture is one of the most pervasive complications of osteoporosis [1, 2]. Most patients have no obvious trauma or only mild trauma, such as sprains, bumps, flat falls, and even coughing, sneezing, bending, and other daily movements, which cause fractures easily, with a very high prevalence rate, higher than the hip, wrist, and proximal humerus fractures combined [3–5]. The main clinical symptoms of osteoporotic vertebral fracture are acute or chronic persistent pain in the lower back, chest and back, and chest and rib. The pain is relieved when patients lie down and have a rest but is intensified during activities with muscle convulsions and other phenomena simultaneously [6, 7]. Therefore, vertebral fractures are most common at the thoracolumbar junction and in the middle thoracic vertebrae. Moreover, conservative or surgical treatment is generally carried out according to the degree of patient's condition [8]. There are many conservative treatment methods, however, this treatment takes a quite long time to recovery. Besides, surgical treatment includes percutaneous kyphoplasty (PKP) and percutaneous vertebroplasty (PVP), both of which have such advantages as simple operation, less trauma, and fewer complications [9, 10].

With the pervasiveness of computer technology and imaging, the imaging technology is used in the clinical examination of orthopedic diseases. X-ray, as the most traditional imaging technology, is widely used and helps to show the status of vertebral fractures clearly, but it is prone to misdiagnose and missed diagnosis [11, 12]. The fracture condition is determined by magnetic resonance imaging (MRI) through a multiparameter condition and multiple signals, so MRI has high sensitivity and accuracy. However, MRI is expensive with complex operation, so it is not suitable for frequent use. Both computed tomography (CT) imaging and conventional X-ray use the principle of X-ray to diagnose the conditions of fracture effectively, whose operation is relatively simple and cost is acceptable [13]. Clinically, deep learning technology is often introduced to process original images to help doctors assess patients' conditions more precisely in order to improve the quality of the image [14, 15]. Deep learning is a set of algorithms that use various machine learning algorithms to solve various problems, such as images and texts on multilayer neural networks, which can be regarded as the most mainstream artificial intelligence (AI) at present. Furthermore, one of the hot topics of current research studies is the combinations of deep learning with clinical medical imaging [16]. Therefore, the 3D reconstruction model of CT imaging based on deep learning technology was explored to offer help for image evaluation of orthopedic diseases.

To sum up, osteoporotic vertebral fracture is a major clinical problem in the elderly. Surgical treatment is still advocated. Further studies are needed to evaluate the efficacy and safety of different surgeries. Therefore, traditional V-Net was optimized, and a new and improved V-Net was proposed in the study. The new and improved V-Net was used to scan CT images of 106 patients with osteoporotic thoracolumbar compression fractures who underwent PVP or PKP operation. Vertebral body measurements, pain scores, and efficacy assessment results of the modified Macnab were compared between test group and control group to investigate the clinical effect of PKP and PVP in the treatment of osteoporotic thoracolumbar compression fracture, which could provide some reference for clinical work of osteoporotic thoracolumbar compression fractures.

2. Materials and Methods

2.1. Subjects of the Study. One hundred six patients with osteoporotic thoracic and lumbar compression fractures who underwent PVP or PKP operation in hospital from June 1, 2018, to November 30, 2021, were included in the study. There were 128 centrums, including 63 males and 43 females. In accordance with the different surgical programs, the patients were divided into the test group with 53 cases of PKP and the control group with 53 cases of PVP. All the patients volunteered to participate and signed informed consent prior to the implementation of the study. This study had been approved by the ethics committee of the hospital.

The inclusion criteria were as follows: (I) patients diagnosed with severe osteoporosis by routine examination; (II) patients with intact posterior wall of centrums; (III) patients without the symptoms of spinal cord injury; and (IV) patients without the symptoms of nerve root damage.

The exclusion criteria were as follows: (I) patients with a compression fracture caused by a hemangioma; (II) patients with a compression fracture due to vertebral metastases; (III) patients with contraindications for operation; (IV) patients with poor compliance; and (V) patients with incomplete clinical data.

2.2. Therapeutic Schedule. Patients in the test group were placed in the supine position with pads placed on both sides of the hip. A unilateral pedicle approach was used to locate the responsible centrum with the X-rays on the C-arm machine and Kirschner wire (K-wire). Then, the projection of the pedicle to the transverse process was inserted with a puncture needle. When it reached the middle of the centrum, the puncture needle was immediately pulled out, the guide needle was inserted, and the prepared bone cement was slowly injected into the centrum. Meanwhile, CT was used to observe the distribution of bone cement. Additionally, after the distribution of bone cement was satisfied, the injection was stopped and hemostasis was performed. Antibiotics were applied 1-2 days after the operation. The patient was put on braces for activities 1 day later.

Patients in control group were placed in the supine position with pads placed on both sides of the hip. A unilateral pedicle approach was used to locate the responsible centrum with the X-rays on the C-arm machine and K-wire. Next, a puncture needle was placed in the line between the pedicle projection and the transverse process. When the middle of the centrum was reached, the needle was pulled out and a guide one was inserted. Along the guide needle, expansion casing and working casing were placed, and the fine drill was screwed in. After the fine drill was close to the anterior edge of the centrum, the drill was pulled out, and the pressurized balloon was put into the centrum. Then, the contrast agent was injected into the pressurized balloon with a syringe, and when the reduction was satisfactory, the injection was stopped. The contrast agent was pumped back and the balloon was pulled out. The prepared bone cement was slowly injected into the centrums. Meanwhile, the distribution of bone cement was observed by CT. The injection was stopped and hemostasis was performed after the distribution was satisfied. Antibiotics were applied one or two days after the operation. Additionally, patients were asked to put on braces for activities 1 day later.

2.3. Examination of CT Imaging. 128 slice spiral CT was used. Patients were asked to be in the supine position. The scan area was each centrum in the horizontal direction of the suspected injury, so that the scanning plane was perpendicular to the spinal canal. The parameters were set as follows: layer thickness was 0.521 mm, layer spacing was

1.2 mm, scanning dose was 120 kV, 250 mass, and measuring distance accuracy was 0.15 mm.

Then, the images obtained were transmitted to the workstation. After treatment, the leading edge, trailing edge, central height, and kyphosis Cobb angle of responsible centrums were measured.

2.4. Improved V-Net. The neural network is a mathematical model or computational model that imitates the structure and function of the biological neural network, which consists of the input layer, hidden layer, and output layer. As a technology oriented to 3D data processing, V-Net neural network [17] belongs to the coding-decoding structure. Moreover, the network on the left continuously helps to reduce the resolution of the image to extract features, and the right one is helpful to decode the image to restore it to the original size. A new V-Net based on the optimization of traditional V-Net is proposed in this study (Figure 1). The whole network structure is classified into the left side and the right side. The left side is the data compression part, and the right one is the data expansion part. Besides, each side has three feature channels, the input module is $120 \times 120 \times 56$, and the up-down sampling convolution kernel is $2 \times 2 \times 2$.

The activation function of convolution postsampling is parametric rectified linear unit (PReLU) function.

The function is as follows:

$$\mathrm{ReLU}(x) = \begin{cases} 0, & x \geq 0, \\ x, & x < 0. \end{cases} \tag{1}$$

When $x < 0$, the ReLU function is hard saturated. When $x = 0$, there is no saturation problem in the ReLU function. When $x > 0$, the ReLU function is not exhausted, and the gradient problem is solved. The ReLU function is improved to solve the problem of hard saturation, and the PReLU function is obtained, as shown in

$$\mathrm{PReLU}(x) = \begin{cases} 0, & x \geq 0, \\ x, & \beta x < 0. \end{cases} \tag{2}$$

In (2), β is a learnable parameter, not a fixed value. Then, the Softmax classifier is used to calculate the probability of the category of image pixels, as shown in

$$G(j) = \frac{e^{x_j}}{\sum_{j=1}^{M} e^{x_j}}. \tag{3}$$

In the (3), $G(j)$ represents the probability value that the pixel belongs to the j-th class, and x_j represents the j-th value in a pixel feature vector. The category corresponding to the maximum probability of each pixel is the category of the pixel, thus obtaining the final semantic segmentation result.

2.5. Evaluation Indicators. U-Net [18], V-Net, and CNN [19] were introduced for comparative analysis with the optimized V-Net designed in this study. The Dice coefficient, Hausdorff distance, and other indicators were used to evaluate the segmentation and reconstruction consequences of images by each deep learning network.

$$\begin{aligned}
\mathrm{Dice} &= \frac{2 \times |Z_1 \cap Z_2|}{|Z_1| + |Z_2|}, \\
\mathrm{Hausdorff} &= \max(\mathrm{Hausdorff}(C_1, C_2), \mathrm{Hausdorff}(C_2, C_1)), \\
\mathrm{Hausdorff}(C_1, C_2) &= \max_{c_1 \in C_1} \min_{c_2 \in C_2} \|c_1 - c_2\|, \\
\mathrm{Hausdorff}(C_2, C_1) &= \max_{c_2 \in C_2} \min_{c_1 \in C_1} \|c_2 - c_1\|.
\end{aligned} \tag{4}$$

In the abovementioned functions, Z_1 represented the actual result, Z_2 represented the segmentation results, and $|\cdots|$ represented all the pixel value. C_1 and C_2 represented the two sets. $\mathrm{Hausdorff}(C_1, C_2)$ represented the unidirectional Hausdorff distance from C_1 to C_2, and $\mathrm{Hausdorff}(C_2, C_1)$ represented the unidirectional Hausdorff distance from C_2 to C_1.

2.6. Therapeutic Evaluation. The visual analog scale (VAS), analgesic use score, and activity ability score of the patients were recorded before operation, and at 3, 5, and 7 days after operation. The modified Macnab was used to grade and evaluate the postoperative recovery of patients (excellent, good, medium, and poor).

2.7. Statistical Methods. SPSS 19.0 was employed for data statistics and analysis. Mean ± standard deviation ($\square x \pm s$) was how measurement data were expressed. The enumeration data were expressed in percentage. One-way analysis of variance was employed for pairwise comparison. When $P < 0.05$, it meant that the difference was statistically significant.

3. Results

3.1. Clinical Data of Patients. Figure 2 shows that there were no significant differences in sex ratio, symptom duration, the number of centrums (T8-T12 and L1-L5), age, height, and weight between test group and control group, $P > 0.05$.

3.2. Medical Records of Some Patients. Figures 3 and 4 show preoperative and postoperative CT images of different patients. The distribution of the fractured centrums was shown clearly through the preoperative CT images. The distribution of bone cement in centrums was shown through the postoperative CT images. Additionally, the centrums were fully filled with bone cement and the position of vertebral fracture was repaired.

3.3. Performance Comparison of Different Deep Learning Networks. In Figure 5, the Dice coefficient of the improved V-Net in this study was markedly higher than that of U-Net, V-Net, and CNN ($P < 0.05$). Furthermore, the Hausdorff distance of the improved V-Net was significantly lower than that of U-Net, V-Net, and CNN ($P < 0.05$). Figure 6 shows the spine 3D reconstruction images of the improved V-Net, where this deep learning network had a fabulous impact on

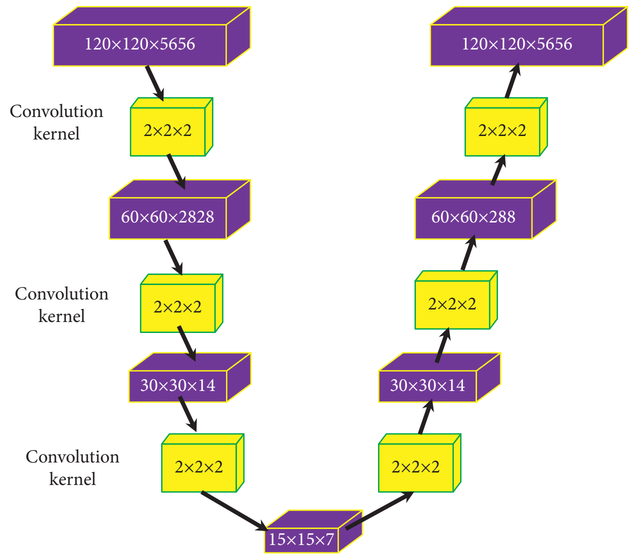

Figure 1: Structure of the improved V-Net.

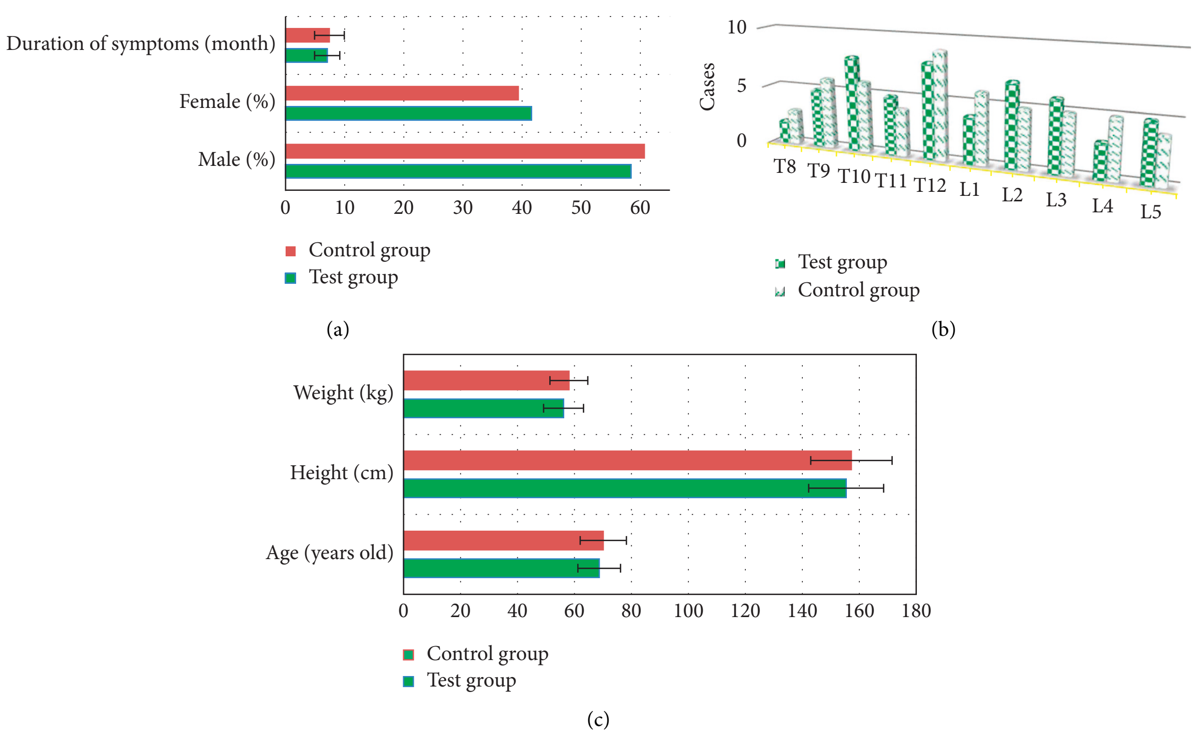

Figure 2: Clinical data of patients. (a) Sex ratio and symptom duration. (b) Number of centrums (T8-T12 and L1-L5). (c) Age, height, and weight.

3D reconstruction of CT images, which completely constructed the spine structure and retained good details.

3.4. Vertebral Imaging Results of the Two Groups. In Figure 7, before the operation, there were no statistically significant differences in vertebral anterior height, central height, posterior height, and kyphosis Cobb angle between the two groups. The anterior height, central height, and posterior height of centrums in test group were greatly higher than those in control group ($P < 0.05$). Besides, after the operation (3, 5, and 7 days), the Cobb angle of kyphosis of test group was observably smaller than that of control group ($P < 0.05$).

3.5. Comparison of the Scores of the Two Groups before and after Operation. In Figure 8, there were no significant differences in the preoperative VAS score, analgesic use score, and ability of activity score in both test group and control group, $P > 0.05$. At 3, 5, and 7 days after operation, the VAS

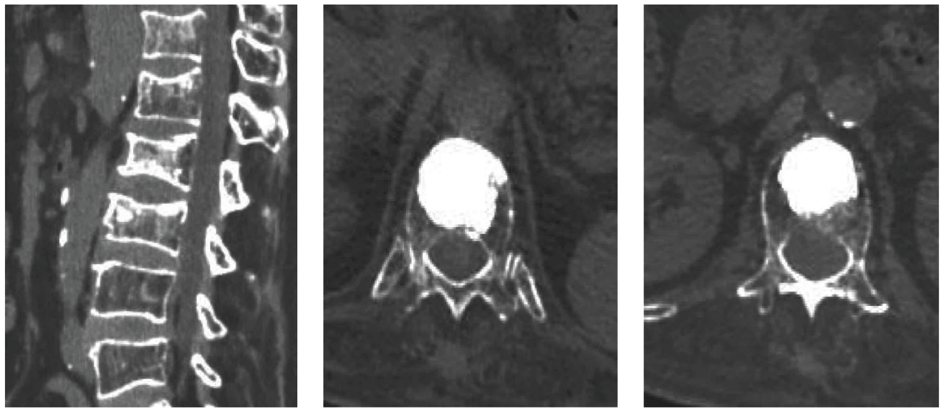

(a) (b) (c)

Figure 3: 70-year-old female with compression fractures of thoracic 12 and lumbar 1 vertebral body. (a) Preoperative CT. (b, c) Postoperative CT of thoracic 12 and lumbar 1 vertebral body.

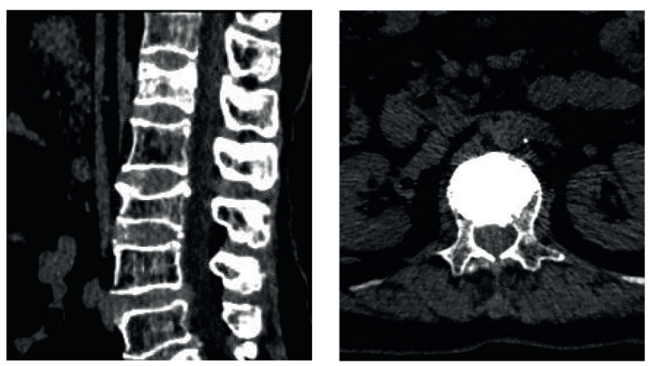

(a) (b)

Figure 4: 73-year-old female with a compression fracture of the first lumbar vertebra. (a) Preoperative CT. (b) Postoperative CT of lumbar 1 vertebral body.

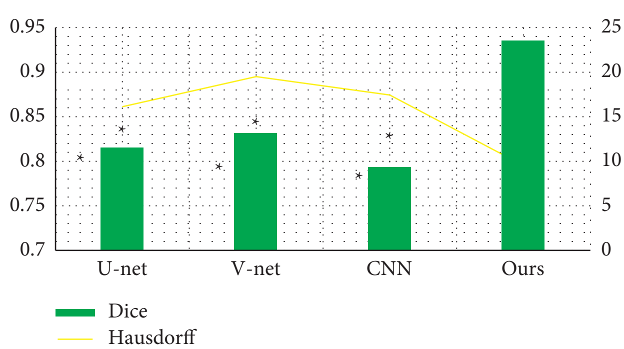

Figure 5: Comparison of the Dice coefficient and Hausdorff distance of different deep learning networks. Compared with the improved V-Net in this study, $P < 0.05$.

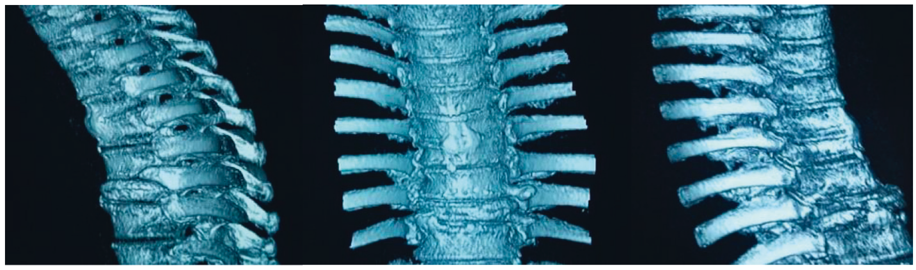

Figure 6: 3D reconstruction images of spine in the improved V-Net.

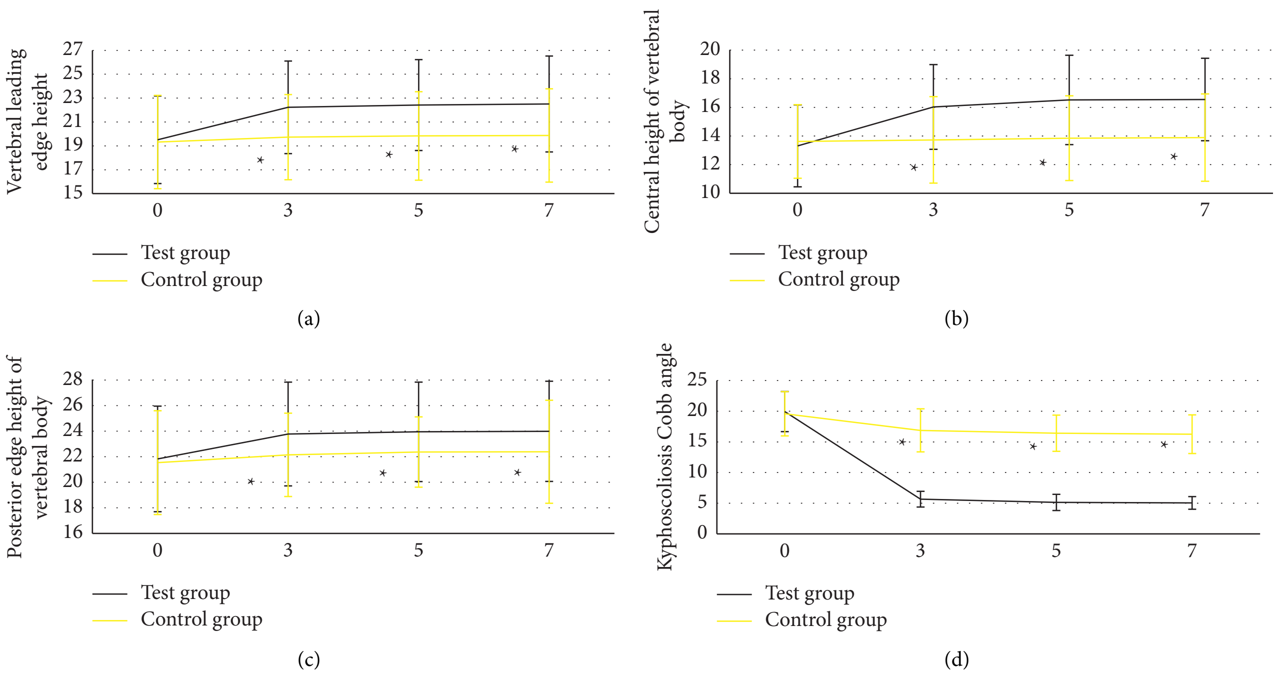

Figure 7: Vertebral imaging results of the two groups. (a) Anterior height, (b) central height, (c) posterior height, and (d) kyphosis Cobb angle, respectively. Besides, the numbers 0, 3, 5, and 7 meant before operation and 3, 5, and 7 days after operation, respectively. Compared with the test group, $P < 0.05$.

score and analgesic use score of patients in test group were evidently lower than those in control group, $P < 0.05$. Additionally, there was no statistically significant difference in activity scores between the two groups at 3, 5, and 7 days after operation.

3.6. Results of Postoperative Efficacy Evaluation of Modified Macnab in Two Groups. Figure 9 shows that there were 33 excellent cases, 13 good cases, 5 medium cases, and 2 poor cases of the modified Macnab in the test group. In the control group, there were 24 excellent cases, 17 good cases, 7 medium cases, and 5 poor cases. Therefore, the excellent and good rate of the test group was obviously higher than that of the control group ($P < 0.05$).

4. Discussion

Osteoporosis is a systemic disease of bone metabolism. The main manifestations were the increased bone brittleness, decreased elasticity, and decreased bone density. Osteoporotic vertebral compression fractures can seriously affect the patients' living quality and exercise ability, which requires aggressive rehabilitation [20, 21]. Deep learning combined with CT imaging technology is applied in the diagnosis and treatment of orthopedic diseases. Hence, the traditional V-Net was optimized first in the study. Then, a new improved V-Net was proposed. U-Net, V-Net, and CNN were introduced for comparison. The Dice coefficient of the improved V-Net was remarkably higher than that of V-Net, V-Net, and CNN. However, the Hausdorff distance was notably lower than that of U-Net, V-Net, and CNN, $P < 0.05$. The results were similar to the results of Kyriakou et al. (2019) [22]. Both the Dice coefficient and Hausdorff distance were effective indicators to evaluate the accuracy of image reconstruction. Therefore, the improve V-Net in this study had better segmentation and reconstruction quality than traditional deep learning network [23]. According to the 3D reconstruction results, the improved V-Net had

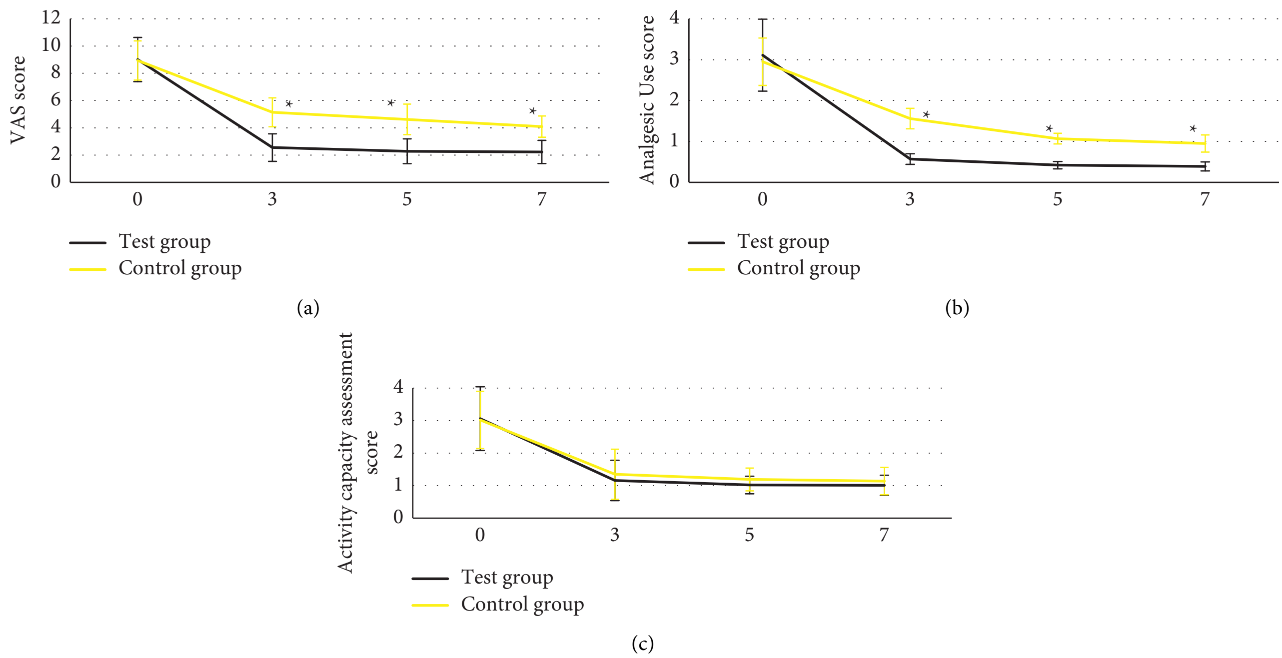

FIGURE 8: Comparison of preoperative and postoperative scores between the two groups. The numbers, 0, 3, 5, and 7 meant before operation and 3, 5, and 7 days after operation, respectively. (a) VAS score. (b) Analgesic use score. (c) Ability of activity score. *Compared with the test group, $P < 0.05$.

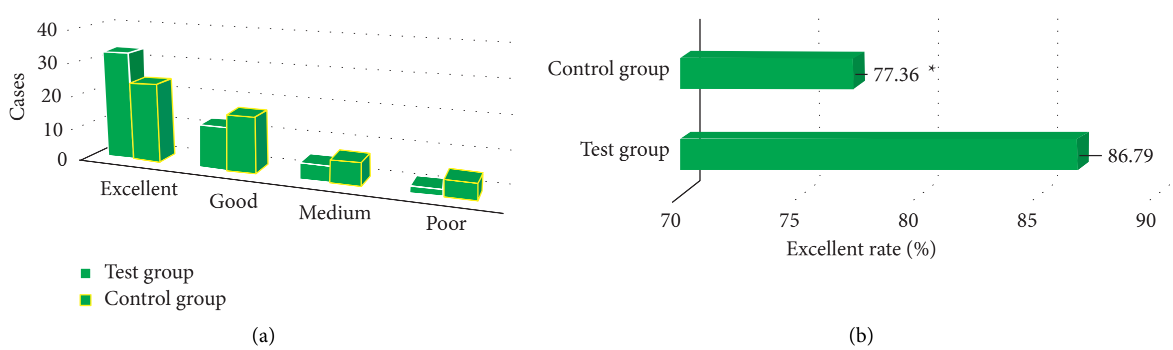

FIGURE 9: Comparison of postoperative adverse event between the two groups. (a) Number of the difference among the number of excellent, good, medium, and poor cases. (b) Excellent rate. ∗ Compared with the high-intensity group, $P < 0.05$.

excellent impacts of 3D reconstruction on CT images. Besides, it also constructed the spine structure and retained good details, which was consistent with the above quantities data.

106 patients with osteoporotic thoracolumbar compression fractures were selected. 128 centrums were divided into test group with 53 cases of PKP and control group with 53 cases of PVP. The clinical indicators of the two groups were recorded before and after operation. The anterior height, central height, and posterior height of centrums in test group were markedly higher than those in control group at 3, 5, and 7 days after operation. The Cobb angle of vertebral kyphosis was significantly lower than that in control group, $P < 0.05$. The consequences showed that compared with PVP, PKP treatment was helpful to restore the height of patients' diseased centrums effectively and correct kyphosis [24]. Moreover, at 3, 5, and 7 days after operation, the VAS score and analgesic use score of patients in test group were evidently lower than those in control group, $P < 0.05$. The consequences meant that compared with PVP, PKP treatment had more effective analgesic impact and safety, which was a safely and availably ideal method for the treatment of osteoporotic vertebral compression fracture. Additionally, there were no statistically significant differences in the scores of activity ability between test group and control group at 3, 5, and 7 days after operation, $P > 0.05$. Such results were quietly different from the previous studies. The reason probably was that the sample size included in this study was small, which caused the difference in activity ability between the two groups not obvious [25]. Finally, the modified Macnab was employed to evaluate the postoperative efficacy of the patients, and excellent and good rate of test group was

greatly higher than that of control group ($P < 0.05$). The results showed that PKP was more effective than PVP in the treatment of osteoporotic vertebral compression fractures.

5. Conclusions

The treatments of PKP and PVP were given to patients with osteoporotic thoracolumbar compression fractures in the experimental group and the control group, respectively. The CT image scanning based on the improved V-Net was performed on all the patients. Comprehensive evaluation results showed that PKP had a definite efficacy, analgesic effect, and good safety in patients with osteoporotic thoracolumbar compression fractures. The deficiency of this experiment is that the sample size of included patients is too small, which is limited to patients with thoracolumbar compression fractures. Moreover, the performance analysis of the improved V-NET network is not sufficient. A large number of data set samples are required for verification. The in-depth analysis will be considered later. In conclusion, the results of this study provided help for the clinical adoption of deep learning technology combined with imaging, which had a certain reference value for the clinical work of osteoporotic thoracolumbar compression fractures.

Data Availability

The data used to support the findings of this study are available from the corresponding author upon request.

Conflicts of Interest

The authors declare that they have no conflicts of interest.

References

[1] X.-H. Zuo, X.-P. Zhu, H.-G. Bao et al., "Network meta-analysis of percutaneous vertebroplasty, percutaneous kyphoplasty, nerve block, and conservative treatment for nonsurgery options of acute/subacute and chronic osteoporotic vertebral compression fractures (OVCFs) in short-term and long-term effects," *Medicine*, vol. 97, no. 29, Article ID e11544, 2018 Jul.

[2] Y. Long, W. Yi, and D. Yang, "Advances in vertebral augmentation systems for osteoporotic vertebral compression fractures," *Pain Research & Management*, vol. 2020, Article ID 3947368, 2020 Dec 7.

[3] J. Zhang, X. He, Y. Fan, J. Du, and D. Hao, "Risk factors for conservative treatment failure in acute osteoporotic vertebral compression fractures (OVCFs)," *Archives of Osteoporosis*, vol. 14, no. 1, p. 24, 2019 Feb 26.

[4] H. Zhang, C. Xu, T. Zhang, Z. Gao, and T. Zhang, "Does percutaneous vertebroplasty or balloon kyphoplasty for osteoporotic vertebral compression fractures increase the incidence of new vertebral fractures? A meta-analysis," *Pain Physician*, vol. 20, no. 1, pp. E13–E28, 2017 Jan-Feb.

[5] T.-K. Ahn, J. O. Kim, H. J. An et al., "3'-UTR polymorphisms of vitamin B-related genes are associated with osteoporosis and osteoporotic vertebral compression fractures (OVCFs) in postmenopausal women," *Genes*, vol. 11, no. 6, p. 612, 2020 Jun 2.

[6] H.-M. Li, R.-J. Zhang, H. Gao et al., "New vertebral fractures after osteoporotic vertebral compression fracture between balloon kyphoplasty and nonsurgical treatment PRISMA," *Medicine*, vol. 97, no. 40, Article ID e12666, 2018 Oct.

[7] X. Wu, X. Tang, M. Tan, P. Yi, and F. Yang, "Is Balloon kyphoplasty a better treatment than percutaneous vertebroplasty for chronic obstructive pulmonary disease (COPD) patients with osteoporotic vertebral compression fractures (OVCFs)?" *Journal of Orthopaedic Science*, vol. 23, no. 1, pp. 39–44, 2018 Jan.

[8] J. Lin, L. Qian, C. Jiang, X. Chen, F. Feng, and L. Lao, "Bone cement distribution is a potential predictor to the reconstructive effects of unilateral percutaneous kyphoplasty in OVCFs: a retrospective study," *Journal of Orthopaedic Surgery and Research*, vol. 13, no. 1, p. 140, 2018 Jun 7.

[9] K. Hinde, J. Maingard, J. A. Hirsch, K. Phan, H. Asadi, and R. V. Chandra, "Mortality outcomes of vertebral augmentation (vertebroplasty and/or balloon kyphoplasty) for osteoporotic vertebral compression fractures: a systematic review and meta-analysis," *Radiology*, vol. 295, no. 1, pp. 96–103, 2020 Apr.

[10] D. Noriega, S. Marcia, N. Theumann et al., "A prospective, international, randomized, noninferiority study comparing an implantable titanium vertebral augmentation device versus balloon kyphoplasty in the reduction of vertebral compression fractures (SAKOS study)," *The Spine Journal*, vol. 19, no. 11, pp. 1782–1795, 2019 Nov.

[11] Y.-B. Li, X. Zheng, R. Wang et al., "SPECT-CT versus MRI in localizing active lesions in patients with osteoporotic vertebral compression fractures," *Nuclear Medicine Communications*, vol. 39, no. 7, pp. 610–617, 2018 Jul.

[12] C. S. Wang, A. G. Liu, C. Z. Liu, and J. Tian, "[Application of three-dimensional CT and image classification in percutaneous vertebraplasty for osteoporotic vertebral compression fractures]," *Zhong Guo Gu Shang*, vol. 32, no. 7, pp. 635–640, 2019 Jul 25, Chinese.

[13] L. Zhang and P. Zhai, "A Comparison of percutaneous vertebroplasty versus conservative treatment in terms of treatment effect for osteoporotic vertebral compression fractures: a meta-analysis," *Surgical Innovation*, vol. 27, no. 1, pp. 19–25, 2020 Feb.

[14] H. Wang, P. Hu, D. Wu et al., "Anatomical feasibility study of unilateral percutaneous kyphoplasty for lumbar through the conventional transpedicular approach," *Medicine*, vol. 97, no. 37, Article ID e12314, 2018 Sep.

[15] Y. Li, J. Zhao, Z. Lv, and J. Li, "Medical image fusion method by deep learning," *International Journal of Cognitive Computing in Engineering*, vol. 2, pp. 21–29, 2021.

[16] T. Liu, Z. Li, Q. Su, and Y. Hai, "Cement leakage in osteoporotic vertebral compression fractures with cortical defect using high-viscosity bone cement during unilateral percutaneous kyphoplasty surgery," *Medicine*, vol. 96, no. 25, Article ID e7216, 2017 Jun.

[17] G. Osterhoff, G. Asatryan, U. J. A. Spiegl, C. Pfeifle, J.-S. Jarvers, and C.-E. Heyde, "Impact of multifidus muscle atrophy on the occurrence of secondary symptomatic adjacent osteoporotic vertebral compression fractures," *Calcified Tissue International*, vol. 110, no. 4, pp. 421–427, 2021 Oct 15.

[18] C. Chen and W. K. Kim, "The application of micro-CT in egg-laying hen bone analysis: introducing an automated bone separation algorithm," *Poultry Science*, vol. 99, no. 11, pp. 5175–5183, 2020 Nov.

[19] B. Chen, Z. Zhang, D. Xia, E. Y. Sidky, and X. Pan, "Algorithm-enabled partial-angular-scan configurations for dual-

energy CT," *Medical Physics*, vol. 45, no. 5, pp. 1857–1870, 2018 May.
[20] T. Wang, H. Kudo, F. Yamazaki, and H. Liu, "A fast regularized iterative algorithm for fan-beam CT reconstruction," *Physics in Medicine and Biology*, vol. 64, no. 14, Article ID 145006, 2019 Jul 11.
[21] Z. Lv and L. Qiao, "Analysis of healthcare big data," *Future Generation Computer Systems*, vol. 109, pp. 103–110, 2020.
[22] C. Kyriakou, S. Molloy, F. Vrionis et al., "The role of cement augmentation with percutaneous vertebroplasty and balloon kyphoplasty for the treatment of vertebral compression fractures in multiple myeloma: a consensus statement from the International Myeloma Working Group (IMWG)," *Blood Cancer Journal*, vol. 9, no. 3, p. 27, 2019 Feb 26.
[23] S. Xie, Z. Yu, and Z. Lv, "Multi-disease prediction based on deep learning: a survey," *Computer Modeling in Engineering and Sciences*, vol. 128, no. 2, pp. 489–522, 2021.
[24] H. Pan, S. Ding, X. Zhao et al., "[Bilateral percutaneous balloon kyphoplasty through unilateral transverse process-extrapedicular approach for osteoporotic vertebral compression fracture of lumbar]," *Zhongguo Xiu Fu Chong Jian Wai Ke Za Zhi*, vol. 35, no. 8, pp. 1007–1013, 2021 Aug 15, Chinese.
[25] Z. Chen, Y. Wu, S. Ning et al., "Risk factors of secondary vertebral compression fracture after percutaneous vertebroplasty or kyphoplasty: a retrospective study of 650 patients," *Medical Science Monitor*, vol. 25, pp. 9255–9261, 2019 Nov 19.

Hindawi
Contrast Media & Molecular Imaging
Volume 2022, Article ID 7730158, 7 pages
https://doi.org/10.1155/2022/7730158

Research Article

Application Effect of Combining Image-Text Communication-Based Healthcare Education with Shifting of Attention on Child Patients Undergoing Inguinal Hernia Repair under General Anesthesia

Sandong Chen, Wanshun Liang, Shuai Wang, and Yingping Jia

Department of Anesthesia and Perioperative Medicine, Children's Hospital Affiliated to Zhengzhou University, Zhengzhou 450000, Henan, China

Correspondence should be addressed to Yingping Jia; jiayingping@zzsetyy.org.cn

Received 18 March 2022; Revised 14 April 2022; Accepted 16 April 2022; Published 28 April 2022

Academic Editor: M Pallikonda Rajasekaran

Objective. To analyze the application effect of image-text communication-based healthcare education combined with shifting of attention on child patients undergoing inguinal hernia repair under general anesthesia. *Methods*. A total of 110 child patients with inguinal hernia treated in our hospital from January 2020 to January 2022 were selected as the study subjects and divided into the control group (CG, routine intervention measures) and the research group (RG, image-text communication-based healthcare education combined with shifting of attention) according to their preoperative intervention plans, with 55 cases each. After surgery, the child patients' psychological status, crying and shouting situation, and occurrence of complications were evaluated to compare and analyze the intervention effect of the two groups. *Results*. The child patients' positive rate and anxiety incidence rate of psychological status evaluation were obviously lower in RG than in CG ($P < 0.05$), and the daily frequency of crying and shouting was significantly lower in RG than in CG ($P < 0.05$); the single time of crying and shouting was significantly shorter in RG than in CG ($P < 0.05$); after surgery, child patients in the two groups had different degrees of infections, subcutaneous emphysema, and scrotal edema, but the total incidence rate of these complications was obviously lower in RG than in CG ($P < 0.05$); after surgery, no significant between-group difference in child patients' FLACC scores immediately after being transferred to the ward was observed ($P > 0.05$), and at postoperative 1 h, 3 h, and 5 h, the FLACC scores of RG were obviously lower than those of CG ($P < 0.05$); and according to the investigation results, the total satisfaction and number of very satisfied parents in RG were greatly higher than those in CG ($P < 0.05$). *Conclusion*. Before child patients undergoing inguinal hernia repair under general anesthesia, implementing image-text communication-based healthcare education combined with shifting of attention can effectively improve the child patients' postoperative psychological status and crying and shouting situation and is conducive to preventing postoperative infections, pain, and other complications and promoting postoperative recovery. The combined intervention has potential utility in reducing child patients' high-risk adverse reactions during the perioperative period and ensuring smooth operation, which is generally recognized by the child patients' family members.

1. Introduction

Inguinal hernia is a common surgical disease. The overall incidence of inguinal hernia is higher in children due to their unclosed or incomplete closed peritoneal vestigium processus combined with the factors such as crying and constipation [1–3]. Laparoscopic inguinal hernia repair is a relatively effective and safe procedure for the treatment of pediatric inguinal hernias in the clinic. However, the affected children with young age are prone to physiological and psychological traumatic stress reactions after surgery, which can then trigger adverse emotions and increase the risk of complications. Also, children have low tolerance for postoperative pain, which can very easily affect the efficacy of surgery [4–6]. At this stage, the affected children present poor acceptance to the conventional clinical nursing interventions, and their family members are mostly in a state of passive cooperation, and thus, the intervention efficacy is limited. Previous studies have shown that analgesic treatment, which is divided into pharmaceutical type and nonpharmaceutical type, can also alleviate postoperative stress reaction in children. However, common drugs are easy to trigger adverse effects such as nausea, vomiting, headache, and dizziness due to the low specificity, while the nonpharmaceutical measures mainly including shifting of attention are simple and easy, but its single application often shows insufficient intervention intensity [2, 7]. The emerging image-text communication-based healthcare education, which mainly uses pictures and words, is intuitive and efficient and obtains high child acceptance and adaptability, but its application is still somewhat controversial [8]. After analysis, the authors believed that such affected children have immature mind and body, extremely poor self-control, and high dependency on their parents, and therefore, the comprehensive intervention for such children should be based on their parents and implemented in advance. Based on this, the application effect of image-text communication-based healthcare education combined with shifting of attention on child patients undergoing inguinal hernia repair under general anesthesia was explored herein.

2. Materials and Methods

2.1. Inclusion Criteria

(1) The child patients met the clinical diagnosis criteria for pediatric inguinal hernia in the Medical Guidance for Children [1] and were diagnosed after ultrasonic testing and met the surgical indications
(2) The child patients received laparoscopic inguinal hernia repair under general anesthesia
(3) The child patients had unilateral lesion
(4) The child patients' parents had normal communication, cognition, and understanding abilities
(5) The child patients' parents understood the study plan, process, and significance and signed the informed consent.

2.2. Exclusion Criteria

(1) The patients had the history of chronic pain
(2) The patients were complicated with other internal medicine diseases
(3) The patients had the psychiatric history or cognitive impairment
(4) The patients had abnormal coagulation function
(5) The patients were less than 2 years old
(6) The patients had congenital diseases
(7) The patients had important visceral dysfunction
(8) The patients were crying persistently and could not receive anesthesia and surgery

2.3. Screening and Grouping of Child Patients. A total of 110 child patients with inguinal hernia treated in our hospital from January 2020 to January 2022 were selected as the study subjects and divided into the control group (CG, routine intervention measures) and the research group (RG, image-text communication-based healthcare education combined with shifting of attention) according to their preoperative intervention plans, with 55 cases each. The study met the World Medical Association Declaration of Helsinki (2013) [9].

2.4. Methods. After admission, all child patients received relevant physical examinations and laparoscopic inguinal hernia repair; and those in the control group (CG) accepted routine intervention measures, including education to their parents, nutritional support, and pacifying the emotions, and paying attention to position change, incision care, and prevention of intraabdominal hypertension and complications after surgery.

On the basis of CG, image-text communication-based healthcare education combined with shifting of attention was performed in the research group (RG). (1) Preparation: A special nursing intervention team was set up for centralized training, and after the team members passed the exam and reached the standard, relevant preparation works before implementing intervention were completed, including collecting and making textual and graphic files, mastering the psychological features of the affected children, formulating solutions for dealing with crying child patients, determining the education contents, and completing the documents, manuals, pictures, and audio data. (2) A good relationship with the affected children and their family members was established quickly with a kind, friendly, and positive attitude; in particular, more encouragement should be given to the affected children, so that they could increase the confidence in the medical staff, and for those with bad mood, consolation was given or psychological intervention was implemented. (3) Image-text communication: during the perioperative period, color graphic cards were distributed to the child patients mainly for soothing their emotions, and attention was paid to increasing the preoperative intervention intensity and laying the groundwork for postoperative intervention; during the intervention process, the child patients could be accompanied and assisted by their parents (for child patients who could not read on their own, reading could be completed with the assistance of their parents). (4) Image-text communication contents: when setting and selecting the contents, those that were popular and easy to understand, vivid, and interesting and rich in color should be used, e g., the cartoon preferred by children, so as to arouse the children's interest; in case of resentment, crying and shouting, and other bad emotions, interesting images and texts were used to shift the child patients' attention, and at the same time, consolation was performed to relieve their bad emotions, more appreciation and encouragement were given, and one-hour intervention was conducted daily before surgery [10]. (5) After the child patients were awake after surgery, images, texts, audios, videos, and other materials were used to shift their attention, so as to perform intervention before they experienced possible discomforts such as pain, and such intervention could correspond to the preoperative intervention contents for enhancing patients' psychological preparation and confidence to face the discomforts; after that, when the children were awake, movies and music preferred by them were played daily for 2-3 h and 30 min—1 h of image-text communication could be conducted. (6) Healthcare education: in addition to education and intervention implemented to the child patients, the healthcare education to their family members was also strengthened. During the perioperative period, basic knowledge of the disease, daily care precautions, complication prevention, postoperative off-bed activities, emotion soothing, healthy diet, and other knowledge were taught to the patients' family members; moreover, the family members' understanding of image-text communication, healthcare education, and shifting of attention was enhanced, so that they could better cooperate with the nursing personnel; after discharge, guidance and education mainly centered on children's psychological health, diet collocation, exercises, and physical fitness.

2.5. Observation Indexes

2.5.1. General Data. The data of child patients' age, weight, height, head circumference, gender, lesion location, surgery time, and ASA grade were recorded.

2.5.2. Psychological Status. According to the subjective evaluation method and scale evaluation method (SAS and SDS) [10], child patients' psychological status was evaluated by psychological tests after surgery. Subjective evaluation method: with the companion of family members, child patients were taken to the treatment room for evaluation of psychological status, the room was kept quiet and comfortable, and the nursing personnel directly communicated with the child patients and their family members and obtained information through sensory perception to judge the nature and extent of the child patients' psychological state. SAS and SDS were the standard scales to measure anxiety and depression in the clinic, which consisted of 20 symptom factors of anxiety and depression, each item was rated on a scale of 1–4 points, and the resulting crude scores were converted into the scale scores, with higher scores indicating more serious anxiety and depression.

2.5.3. Crying and Shouting Situation. The daily frequency and single time of crying and shouting of child patients were observed carefully.

2.5.4. Complication Incidence. The child patients' possible postoperative complications, such as infection, subcutaneous emphysema, and scrotal edema, were observed and recorded.

2.5.5. Pain. The FLACC scale was used to evaluate the child patients' pain degrees, which was suitable for the young children, and mainly included five areas: facial expression, leg movement, activity, cry, and consolability; each item was rated on a scale of 0–2 points, and the total score of the scale was 10 points, with higher scores indicating more serious pain.

2.5.6. Parent Satisfaction. By referring to the Newcastle Satisfaction with Nursing Scales (NSNS) [11], an Investigation Scale for Parent Satisfaction was proposed to investigate parent satisfaction with the intervention process. The total score was 100 points, and the degree of satisfaction was divided into dissatisfied, satisfied, and very satisfied according to the scores. The total satisfaction = (number of satisfied parents + number of very satisfied parents)/total number × 100%.

2.6. Statistical Processing. The between-group differences in data were calculated by the software SPSS 22.0, the picture drawing software was GraphPad Prism 7 (GraphPad Software, San Diego, USA), the items included were enumeration data and measurement data, which were expressed by (n (%)) and ($\overline{x} \pm s$) and examined by the X^2 test and t-test, respectively, and differences were considered statistically significant at $P < 0.05$.

3. Results

3.1. General Data. Table 1 provides that no statistical between-group differences in patients' general data such as age, weight, height, head circumference, gender, lesion location, surgery time, and ASA grades were observed ($P > 0.05$).

3.2. Psychological Status. According to the analysis of statistical data in Figure 1, the positive rate and anxiety incidence rate of psychological status evaluation were significantly lower in RG than in CG ($P < 0.05$), with statistically significant differences.

Note: the horizontal axis indicates the evaluation dimensions, and the vertical axis indicates the percentage (%). In CG, there were 25 cases with anxiety, 13 cases with depression, 10 cases with anxiety and depression, 7 normal cases, and 48 positive cases. In RG, there were 13 cases with anxiety, 7 cases with depression, 4 cases with anxiety and depression, 31 normal cases, and 24 positive cases. *Significant between-group difference in anxiety incidence of psychological status evaluation ($X2 = 5.790$, $P = 0.016$). **Significant between-group difference in positive rate of psychological status evaluation ($X^2 = 23.1579$, $P < 0.001$).

3.3. Crying and Shouting Situation. Table 2 provides that the daily frequency of crying and shouting was significantly lower in RG than in CG ($P < 0.05$), and the single time of

Table 1: Between-group comparison of patients' general data ($n = 55$).

Observation indicator	CG	RG	X^2/t	P
Age (years)	6.25 ± 2.10	6.10 ± 2.15	0.370	0.712
Weight (kg)	22.52 ± 2.47	21.70 ± 2.74	1.649	0.102
Height (cm)	117.26 ± 4.78	117.89 ± 5.02	0.674	0.502
Head circumference (cm)	50.14 ± 3.71	50.22 ± 4.10	0.107	0.915
Gender				
Male	43 (78.18)	45 (81.82)	0.227	0.634
Female	12 (21.82)	10 (18.18)		
Lesion location				
Left side	32 (58.18)	30 (54.55)	0.148	0.701
Right side	23 (41.82)	25 (45.45)		
Surgery time (min)	25.91 ± 1.55	26.18 ± 1.62	0.893	0.374
ASA grade				
I	28 (50.91)	31 (56.36)	0.329	0.566
II	27 (49.09)	24 (43.64)		

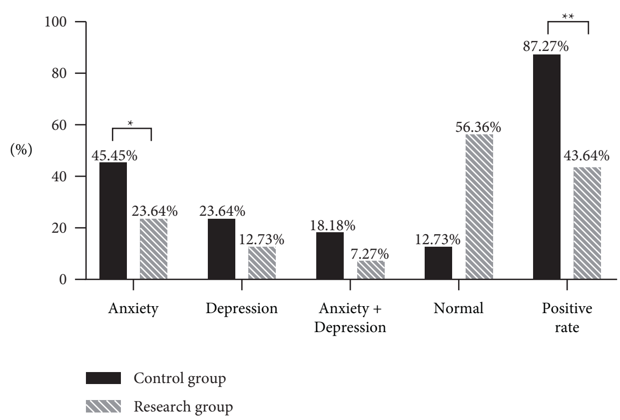

Figure 1: Psychological status evaluation positive rate ($n = 55$)

Table 2: Frequency and single time of crying and shouting of child patients in the two groups ($\bar{x} \pm s$).

Group	Cases	Frequency of crying and shouting (times/d)	Single time of crying and shouting (min)
CG	55	8.55 ± 2.31	2.37 ± 0.96
RG	55	3.16 ± 1.01	1.05 ± 0.55
t		15.855	8.848
P		<0.001	<0.001

crying and shouting was obviously shorter in RG than in CG ($P < 0.05$).

3.4. Complication Incidence. Table 3 provides that after surgery, the child patients in the two groups had different degrees of infection, subcutaneous emphysema, and scrotal edema, but the total incidence rate of these complications was significantly lower in RG than in CG ($P < 0.05$).

3.5. Pain Degree. Figure 2 shows that after surgery, no significant between-group difference in child patients' FLACC scores immediately after being transferred to the ward was observed ($P > 0.05$), and at postoperative 1 h, 3 h, and 5 h, the FLACC scores of RG were obviously lower than those of CG ($P < 0.05$).

Note: the horizontal axis indicates the time points, and the vertical axis indicates the score (points). In CG, the FLACC scores immediately after being transferred to the ward and at postoperative 1 h, 3 h, and 5 h were, respectively, (7.10 ± 0.41), (5.94 ± 0.48), (5.05 ± 0.46), and (4.08 ± 0.34). In RG, the FLACC scores immediately after being transferred to the ward and at postoperative 1 h, 3 h, and 5 h were, respectively, (7.02 ± 0.43), (5.03 ± 0.29), (4.03 ± 0.24), and (2.35 ± 0.47). * from left to right indicated significant between-group differences in the FLACC scores at postoperative 1 h, 3 h, and 5 h ($t = 12.254, 14.580, 22.117$, P all<0.001).

3.6. Parent Satisfaction. According to the investigation results, the total parent satisfaction and number of very satisfied parents were significantly higher in RG than in CG ($P < 0.05$), as given in Table 4.

Table 3: Statistics of complications in the two groups.

Group	Infection	Subcutaneous emphysema	Scrotal edema	Total incidence rate
CG ($n = 55$)	8 (14.55)	7 (12.73)	9 (16.36)	24 (43.64)
RG ($n = 55$)	2 (3.64)	1 (1.82)	3 (54.55)	6 (10.91)
X^2	3.960	4.853	3.367	14.850
P	0.047	0.028	0.067	<0.001

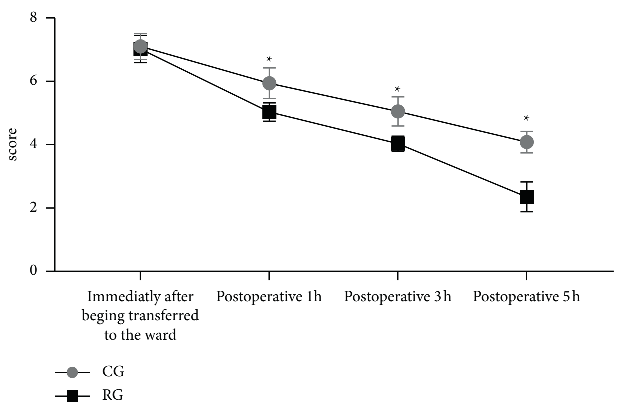

Figure 2: Analysis of patients' postoperative pain ($\bar{x} \pm s$)

Table 4: Analysis of parent satisfaction of the two groups (n (%)).

Group	Dissatisfied	Satisfied	Very satisfied	Total satisfaction
CG ($n = 55$)	19 (34.55)	17 (30.91)	19 (34.55)	36 (65.45)
RG ($n = 55$)	4 (7.27)	20 (36.36)	31 (56.36)	51 (92.73)
X^2			5.280	12.369
P			0.022	<0.001

4. Discussion

Inguinal hernia is one of the more common surgical diseases in pediatrics, and surgery is the main treatment means. With the continuous development of minimally invasive techniques, laparoscopy has gradually been used in inguinal hernia repair, and the clinical results are relatively satisfactory. But related investigations and studies found that the probability of developing chronic inguinal pain after inguinal hernia repair was about 3–6% and that the preoperative pain was also an important factor leading to postoperative concurrent chronic pain [12]. Postoperative pain will cause the body to abnormally release a series of inflammatory mediators that are painful in response to neuroendocrine stress, which can cause immunoglobulin decline in the affected children, affect postoperative recovery and children's sleep, and cause complications such as incision dehiscence and infection due to crying and shouting. In addition, because of incomplete physical and mental development of children and insufficient parental perception of the disease and other reasons, hernia surgery predisposes affected children to develop negative emotions such as fear, anxiety, and depression, which are not only detrimental to the smooth progress of surgery but also trigger psychological or physiological stress reactions and affect the prognosis [13]. Therefore, implementing effective perioperative intervention measures to child patients undergoing inguinal hernia repair has an active effect on prognosis.

Young children with incomplete perception of the disease may experience extreme fear of surgery as well as postoperative pain, and due to their strong dependency on their parents, they tend to cry and shout hardly after surgery because of pain [14, 15]. By analyzing the clinical features of previous cases, the study performed image-text communication-based healthcare education combined with shifting of attention in the perioperative period to child patients undergoing inguinal hernia repair under general anesthesia, and further education was given to their parents to assist the medical staff in better completing the intervention plan; such child patients were included in RG for comparative analysis with those received routine intervention in CG, and the results were as follows. The positive rate and anxiety incidence rate of psychological status evaluation were obviously lower in RG than in CG ($P < 0.05$); the daily frequency of crying and shouting was significantly lower in RG than in CG ($P < 0.05$), which was consistent with the research report by Damian et al. [16]; the single time of crying and shouting was obviously shorter in RG than in CG ($P < 0.05$); after surgery, child patients in the two groups had different degrees of infection, subcutaneous emphysema, and scrotal edema, but the total incidence rate of these complications was significantly lower in RG than in CG ($P < 0.05$); after surgery, no significant between-group difference in child patients' FLACC scores immediately after being transferred to the ward was observed ($P > 0.05$), and at postoperative 1 h, 3 h, and 5 h, the FLACC scores of RG were obviously lower than those of CG ($P < 0.05$); and according to the investigation results, the total parent satisfaction and number of very satisfied parents were significantly higher in RG than in CG ($P < 0.05$). The study results further confirmed that performing image-text communication-based healthcare education combined with shifting of attention in the perioperative period to child patients undergoing inguinal hernia repair under general anesthesia can effectively pacify their bad mood, improve their psychological status, and lower the frequency and time of crying and shouting; meanwhile, by shifting their attention, their pain sensation can be greatly reduced, which is conducive to preventing postoperative complications and accelerating recovery; hence, the parent satisfaction is higher.

With the image-text communication-based healthcare education combined with shifting of attention, the intervention plan meeting the interest of child patients was formulated to shift their attention and fear about disease, pain, and surgery, reduce their attention to pain, so that they could relax muscles and slow down the breathing frequency, which alleviated their pain sensation to some extent, and combined with the education to the child patients and their parents in the perioperative period, enhanced their confidence in fighting the disease and pain [17–19]. In addition, rich and interesting content, such as pictures, audios, and videos, could promote the interest of the child patients and directly improve the adverse emotions, and the child patients' trust in the medical staff could be enhanced with the positive encouragement of medical staff and their family members and effective communication. When the child patients behaved well, timely affirmation and encouragement could strengthen their positive cooperation with the medical staff, improve the crying and shouting situation, and significantly promote their compliance, which was conducive to lowering the occurrence rate of complications. In addition, because family members are a bridge between the child patients and the medical staff, necessary perioperative healthcare education was conducted to them, so that they could improve their perception of the disease and timely master postoperative-related care measures and simple care skills, avoid anxiety, and convey positive emotions to the child patients. Hence, the parent satisfaction was higher because child patients who were positively impacted could better assist the medical staff in implementing the intervention [20–23]. This intervention modality was simple and easy to execute, with less equipment and funding invested, which was easier to generalize, but the nursing personnel should pay attention to provide careful psychological counseling and effective communication to the child patients during the implementation process; in addition, the extremely special cases were excluded during the pathological screening; thus, there were certain limitations in the study. Future studies should expand the scope of research to analyze the methods that can control the adverse emotions and pain in child patients after surgery in many aspects and optimize the intervention program.

To sum up, before child patients undergoing inguinal hernia repair under general anesthesia, implementing image-text communication-based healthcare education combined with shifting of attention can effectively improve the child patients' postoperative psychological status and crying and shouting situation and is conducive to preventing postoperative infections, pain, and other complications and promoting postoperative recovery. The combined intervention has potential utility in reducing child patients' high-risk adverse reactions during the perioperative period and ensuring smooth operation, which is generally recognized by the child patients' family members.

Data Availability

The data used to support the findings of this study are available from the corresponding author upon request.

Conflicts of Interest

The authors declare that they have no conflicts of interest.

Acknowledgments

This research was funded by Henan Medical Science and Technology Research Plan (2018020611).

References

[1] C. Binger, K. Richter, A. Taylor et al., "Error patterns and revisions in the graphic symbol utterances of 3- and 4-year-old children who need augmentative and alternative communication," *Augmentative and Alternative Communication*, vol. 35, no. 2, pp. 95–108, 2019.

[2] I. Cohen Gerald, "A practical guide to graphic communication for quality assurance, education, and patient care in echocardiography," *Echocardiography*.vol. 36, no. 9, pp. 1747–1754, 2019.

[3] S. Huang, "The influence of digital multimedia communication forms on graphic design," *Computer Systems Science and Engineering*, vol. 35, no. 3, pp. 215–222, 2020.

[4] Y. Asada, H. Abel, C. Skedgel, and G. Warner, "On effective graphic communication of health inequality: considerations for health policy researchers," *The Milbank Quarterly*, vol. 95, no. 4, pp. 801–835, 2017.

[5] T. Turk, F. Newton, S. Choudhury, and M. S. Islam, "Predictors of quitting attempts among tobacco users in Bangladesh after a communication campaign to launch graphic warning labels on packaging," *Health Education & Behavior*, vol. 45, no. 6, pp. 879–887, 2018.

[6] M. Maria Laura, M. Damon, and R. Christiaan Erik, "Graphic user interfaces for communication," *Oceanography and Marine Biology an Annual Review*, vol. 55, pp. 403–420, 2017.

[7] S. Z. Ebigbagha, "3. The graphic communication actor: generating visual rhetoric for development initiatives," *Review of Artistic Education*, vol. 20, no. 1, pp. 262–279, 2020.

[8] R. Bernabei, "Wearable words: a case study applying jewellery theory and practice to the education of fine art, textiles innovation and design, graphic communication and illustration students," *The Design Journal*, vol. 20, no. 1, pp. 1503–1510, 2017.

[9] World Medical Association, "World Medical Association Declaration of Helsinki: ethical principles for medical research involving human subjects," *JAMA*, vol. 310, no. 20, p. 2191, 2013.

[10] H. Fernando, C. Garcia, T. Hossack et al., "Incidence, predictive factors and preventive measures for inguinal hernia following robotic and laparoscopic radical prostatectomy: a systematic review," *Journal of Urology*, vol. 201, no. 6, pp. 1072–1079, 2019.

[11] A. J. Perez, J. Arielle, E. E. Sadava, F. Gaber, and E. Emmanuel, "Nationwide analysis of inpatient laparoscopic versus open inguinal hernia repair," *Journal of Laparoendoscopic & Advanced Surgical Techniques*, vol. 30, no. 3, pp. 292–298, 2020.

[12] R. Alder, D. Zetner, and J. Rosenberg, "Incidence of inguinal hernia after radical prostatectomy: a systematic review and meta-analysis," *Journal of Urology*, vol. 203, no. 2, pp. 265–274, 2020.

[13] A. Piredda, E. Vellone, G. Piras et al., "Psychometric evaluation of the newcastle satisfaction with nursing scales," *Journal of Nursing Care Quality*, vol. 30, no. 1, pp. 84–92, 2015.

[14] M. Issa, M. Tacey, J. Geraghty et al., "Cyanoacrylate glue versus absorbable tacks in mesh fixation for laparoscopic extraperitoneal inguinal hernia repair: a randomized controlled trial," *Surgical Laparoscopy Endoscopy & Percutaneous Techniques*, vol. 31, no. 3, pp. 291–297, 2021.

[15] K. E. Chike-Harris, E. Katherine, A. Logan, G. Smith, R. DuBose-Morris, and R. DuBose-Morris, "Integration of telehealth education into the health care provider curriculum: a review," *Telemedicine and e-Health*, vol. 27, no. 2, pp. 137–149, 2021.

[16] N. Damian, I. Mocanu, and B. Mitrică, "Education and health care provision in the Romanian Danube Valley: territorial disparities," *Area*, vol. 51, no. 2, pp. 360–370, 2019.

[17] J. Brooke and D. Jackson, "An exploration of the support provided by prison staff, education, health and social care professionals, and prisoners for prisoners with dementia," *Journal of Forensic Psychiatry and Psychology*, vol. 30, no. 5, pp. 807–823, 2019.

[18] O. S. Sunde, K. R. Øyen, and S. Ytrehus, "Do nurses and other health professionals' in elderly care have education in family nursing?" *Scandinavian Journal of Caring Sciences*, vol. 32, no. 1, pp. 280–289, 2018.

[19] K. Forslund Frykedal, M. Barimani, M. Rosander, and A. Berlin, "Parents' reasons for not attending parental education groups in antenatal and child health care: a qualitative study," *Journal of Clinical Nursing*, vol. 28, pp. 3330–3338, 2019.

[20] K. Areskoug-Josefsson, A. C. Schindele, C. Deogan, and M. Lindroth, "Education for sexual and reproductive health and rights (SRHR): a mapping of SRHR-related content in higher education in health care, police, law and social work in Sweden," *Sex Education*, vol. 19, no. 6, pp. 720–729, 2019.

[21] H. Yonggang, Q. Changfu, W. Ping et al., "Single-port laparoscopic percutaneous extraperitoneal closure of inguinal hernia using "two-hooked" core needle apparatus in children," *Hernia*, vol. 23, no. 6, pp. 1267–1273, 2019.

[22] C. S. Olesen, S. Öberg, and L. Q. Rosenberg, "Risk of incarceration in children with inguinal hernia: a systematic review," *Hernia*, vol. 23, no. 2, pp. 245–254, 2019.

[23] M. Jukić, Z. Pogorelić, D. Šupe-Domić, and A. Jerončić, "Comparison of inflammatory stress response between laparoscopic and open approach for pediatric inguinal hernia repair in children," *Surgical Endoscopy*, vol. 33, no. 10, pp. 3243–3250, 2019.

Hindawi
Contrast Media & Molecular Imaging
Volume 2022, Article ID 8952355, 9 pages
https://doi.org/10.1155/2022/8952355

Research Article

Craniocerebral Magnetic Resonance Imaging Features of Benign Paroxysmal Positional Vertigo under Artificial Intelligence Algorithm and the Correlation with Cerebrovascular Disease

Hailong Xue,[1] **Yanli Jing**,[1] **Yingge Chen**,[1] **Cong Xi**,[2] **Na Bian**,[2] **and Yujuan Li**[2]

[1]*Department of Neurology, The 987th Hospital of the Joint Logistics Support Force of the People's Liberation Army, Baoji 721004, Shaanxi, China*
[2]*Department of Neurology, Baoji City People's Hospital, Baoji 721000, Shaanxi, China*

Correspondence should be addressed to Yujuan Li; 6180206050@stu.jiangnan.edu.cn

Received 5 February 2022; Revised 25 March 2022; Accepted 4 April 2022; Published 26 April 2022

Academic Editor: M Pallikonda Rajasekaran

This research aimed to discuss the characteristics of benign paroxysmal positional vertigo (BPPV) and the correlation with cerebrovascular disease. An artificial intelligence algorithm under a parallel dual-domain concatenated convolutional neural network (PDDC-CNN) was proposed to process the images of magnetic resonance imaging (MRI). MRI, magnetic resonance angiography (MRA), and susceptibility weighted imaging (SWI) were performed on all 60 research objects with a 3.0 MRI scanner. The number of cases with cerebral microbleeds (CMBs), SWI image display of small veins, the number of lacunar infarctions, vertebral artery dominance, and vertebrobasilar morphology were observed in the two groups. The number of lacunar infarctions was 2.400 ± 3.358 and 0.672 ± 0.251, respectively, in the BBPV group with 30 cases and the control group with the other 30 cases. The positive rates of CMBs on SWI images were 48% and 27% in the BBPV group and the control group, respectively, and the average CMBs were counted as 1.670 ± 2.326 and 0.487 ± 0.865. CMBs were shown as round or oval lesions of conventional sequence deletion in the images with a diameter of less than 1.5 cm. SWI images of the BBPV group showed a significant increase in intracerebral small veins compared to those of the control group. The curvature of the vertebrobasilar artery in the BBPV group was significantly higher than that in the control group, and the curvature of the basilar artery was slightly higher than that in the control group. In conclusion, the MRI features of BPPV patients were related to their own microvascular lesions closely, and it was speculated that the cerebrovascular factors might play a dominant role in the early onset of BPPV.

1. Introduction

Vertigo is a common symptom in emergency with various causes. Benign paroxysmal positional vertigo (BPPV) is one of the most common vertigoes clinically. It is more common in people over 60 years old, and about 30% of people over 70 years old have experienced it at least once in their lives. The symptoms of BBPV are rare in children and are classified as peripheral vestibular syndrome [1]. BPPV is caused by the rapid movement of relative gravity at a certain position of the head, accompanied with paroxysmal vertigo of short-positioning-angle-rotation linear nystagmus and relatively short time [2]. Its main clinical symptoms are the short-term rotational nystagmus caused by rapid head movement in a specific position, where the vertical line angle of relative gravity had a large change [3–5]. It is believed that BPPV is in a close relation to various vascular factors. These factors can cause serious damage to the blood vessels of the inner ear directly and may lead to the shedding of otoliths, which are likely to be the causes of BPPV [6]. Cerebral microbleeds (CMBs) are a kind of preclinical changes in microvascular fibrous hyaline change and hemosiderin deposits caused by slight extravasation of blood. It is also called old CMBs, type II lacunar hemorrhage, punctate hemorrhage, and so on [7]. The symptoms of CMBs patients are relatively insidious. However, as the patients' condition continues to develop, it may also cause more obvious early bleeding. As a potential bleeding disease state, CMBs are related to the sequelae of acute cerebrovascular disease and the decline of cognitive system function, and they can be taken as a marker in early disease screening [8]. Therefore, it is of great clinical value for the early diagnosis of CMBs.

In recent years, deep learning has made great breakthroughs in magnetic resonance imaging (MRI) reconstruction and has shown broad prospects. It has received extensive attention from researchers and has become one of the popular research methods [9, 10]. Convolutional neural networks have unique advantages in image processing. Compared with stacked autoencoders, deep confidence networks, and deep Boltzmann machines that can only input vectors, they can extract features and learn nonlinear mapping relationships [11]. The success of the early convolutional neural network AlexNet had attracted the attention of scholars; for the first time, Cao et al. [12] applied this classic deep learning network to compressed sensing MRI. The development of digital clinical medical imaging diagnosis technology in the 21st century has led to the technological advancement of modern clinical medicine in disease treatment and follow-up diagnosis. Thus, clinical imaging diagnostic medicine takes a leading position in the diagnosis of most clinical diseases [13]. The etiology of BPPV is complex, and it is difficult to be diagnosed and classified. The pathogenesis of BPPV is not yet clear, and research is mostly focused on the treatment of the disease. In addition, there is insufficient clinical understanding, which makes it difficult to diagnose correctly. There is little research on BPPV in imaging.

Susceptibility weighted imaging (SWI) is an emerging technology that has become more and more widely used in MRI contrast enhancement in recent years. Its biggest feature is that it can detect hemorrhages more sensitively than conventional MRI sequences, especially for microhemorrhages or punctate hemorrhages. The working principle of SWI vibration imaging lies in the highly differentiated imaging and the dependent effect of oxygen content in tissue blood, which are caused by the non-uniform magnetic field of the partial tissues. In intracranial vascular imaging, phase contrast (PC) and time-of-flight (TOF) methods are very sensitive to blood flow velocity and intracranial vascular distribution, and it is difficult to accurately distinguish between arteries and veins. It would not be limited by the many imaging conditions mentioned above when SWI is used, which can only present a clear visualization of intracranial venous vessels. Thereby, it has great technical advantages for intracranial venous vessel observation and vascular malformation detection [14].

In summary, how to diagnose BPPV accurately is a major issue that needs to be paid attention to in clinical practice. There are a number of research results showing that the treatment of BPPV is in connection with the local vascular motion factors. The conventional 3.0 t laser MRI scanning technology was used and combined with susceptibility and weighted MRI technology, to study in depth the correlation between intracranial local vascular movement factors and BPPV. It was expected to provide new help for the etiology, treatment, and early prevention of BPPV through the new perspective of clinical imaging.

2. Materials and Methods

2.1. Research Objects. Thirty patients with BPPV were selected, who were diagnosed in the hospital from early November 2019 to March 2020.12 males and 18 females were included, aged 20–68 years old with an average age of 41.37 ± 10.17 years. People who underwent normal physical examination without vertigo symptoms during the same period were selected as the control group, and a total of 30 cases were chosen. All patients signed an informed consent form, and this study had been approved by the ethics committee of the hospital.

Inclusion criteria: patients were diagnosed with BPPV through routine examinations. They agreed to cooperate with the hospital treatment and regular follow-up actively. They had a history of recurrent short-onset vertigo.

Exclusion criteria: patients took vestibular inhibitory drugs, antihistamines, and other anticholinergic drugs recently. They had a history of trauma, vascular diseases, metabolic diseases, or more. The patients failed to cooperate with hospitalization and long-term follow-ups.

2.2. Network Model Design. The new parallel dual-domain concatenated convolutional neural network (PDDC-CNN) was proposed under deep learning and compressed sensing. The overall structure of the network is shown in Figure 1.

The feature extractor and fusion module used in different domains had the same structure, but they did not share parameters. The parameters were not shared among the same modules in different stages. After the undersampling frequency domain and undersampling spatial data passed through the feature extractor and the data consistency layer, there was a cross-fusion process to fuse the feature maps from the two domains into those in one domain. The conversion from domain to domain was performed using Fourier forward and inverse transform.

The undersampling frequency domain and undersampling spatial domain data were used as input, and the reconstructed image was the output. The dual data streams were not only parallel but also cross-fused. The whole process was divided into five stages, which were five concatenated networks. Stages 1–4 had the same structure exactly, which were mainly used for artifact reduction and detail restoration. Stage 5 was to output the final reconstructed image, so the input and output of the fusion module were slightly different.

With the upgrading of hardware conditions, issues such as increased calculation, overfitting, gradient disappearance, and gradient explosion gradually emerged, when the network structure of the current deep learning model was deeper with more convolutional layers. The performance of image reconstruction reached saturation and was unable to continue to improve. Therefore, the residual was introduced into the convolutional neural network. The output of the previous layer of the convolutional neural network and the output of the last layer were added through a direct connection line. This connection neither increased the

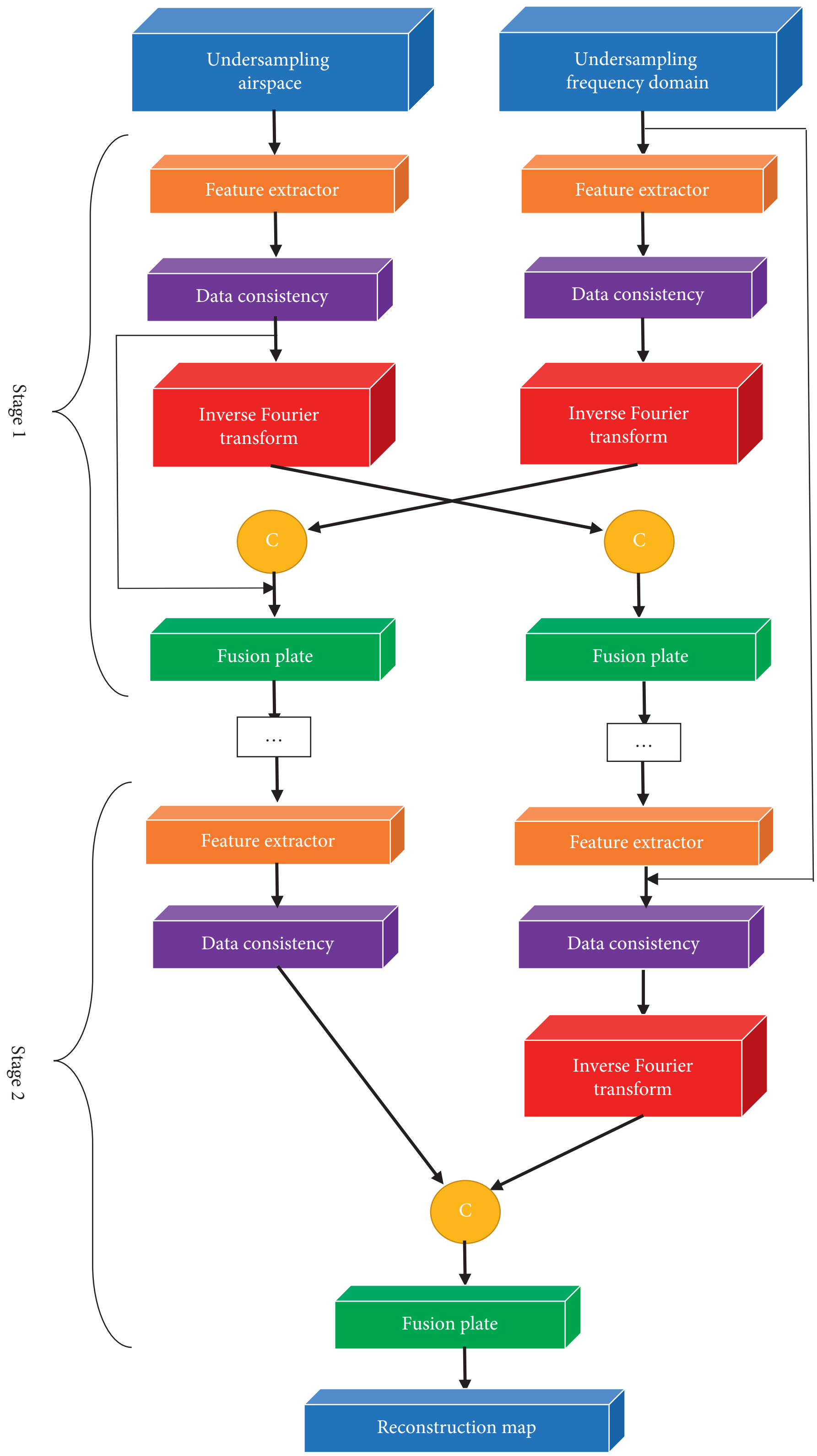

Figure 1: PDDC-CNN under deep learning and compressed sensing. The direction of the arrows indicated the direction of data flow.

parameters of the network nor increased the complexity of the calculation. The basic residual network was used to express, where a_m was the observed value, a_{m+1} was the predicted value, K_{a_m,c_m} was the residual, and c_m represented the mapping matrix. The residual network consisted of two parts, with $g(\cdot)$ representing the direct mapping part. The residual part corresponded to the convolution part, and it could be expressed as

$$a_{m+1} = g(a_m) + K_{a_m,c_m}. \quad (1)$$

In the multilayer residual structure, the predicted value of the M layer could be obtained from the observation value of any layer l shallower than it plus the sum of the residuals between them. It was expressed as

$$a_M = a_m \sum_{h=1}^{M-1} K_{a_m,c_m}. \quad (2)$$

It was supposed that the loss function was θ, to find the derivative with respect to a_m. The chain derivative equation was expressed as the

$$\frac{\partial_\theta}{\partial_{a_m}} = \frac{\partial_\theta}{\partial_{a_M}}\frac{\partial_{a_M}}{\partial_{a_m}} = \frac{\partial_\theta}{\partial_{a_M}}\left(1 + \frac{\partial}{\partial_{a_m}}\right)\sum_{h=m}^{M-1} K_{a_m,c_m}. \quad (3)$$

During the entire training process, the residual network would not have a gradient disappearance.

2.3. Image Examination and Image Processing. A superconducting 3.0MR automatic scanner was used, with a standard cranial 8-channel automatic scanning coil. The 60 objects underwent T1 weighted imaging (T1W1), T2 weighted imaging (T2W1), diffusion weighted imaging (DWI), T2-fluid attenuated inversion recovery (FLAIR), TOF, MRA, and SWI sequence scanning in cranial transverse axis. The imaging parameters included sensitivity encoding (SENSE), and three-dimensional T1 fast field echo (FFE). Time of repetition (TR) of 17.0 ms, time of echo (TE) of 25.0 ms, reversal angle of 15°, a layer thickness of 2 mm, no interval acquisition, a field of view (FOV) of 230 × 183 × 100 mm, matrix of 256 × 203, number of excitations of 1.0, and scanning time of 2 minutes and 38 seconds were also included.

SWI can produce the magnitude image (MI) and the phase image (PI) at the same time through one scanning. For obtaining the SWI image, the original MI and PI need to be transmitted to the workstation for processing. The PI was filtered by appropriate frequency, and 32 × 32 or 64 × 64 high-pass filter matrix was selected to filter out background low-frequency artifacts and retain the benefits of high-pass filtering. A high-pass filter map, the corrected PI, was obtained. The corrected PI and MI were integrated, and the SWI map was obtained through minimum density reconstruction.

2.4. Judgment of Cerebral Lacunar Infarction. MRI lacunar infarction was manifested as lesions in the bilateral subcortices with a diameter of less than 15 mm and clear boundaries with long T1 and long T2 signals. It was different from the enlargement of the perivascular Virchow–Robin spaces. It was common in the white matter, basal ganglia region, and their surrounding internal capsules of the brain. The total number of intracranial lacunar infarctions in each patient was counted.

2.5. CMBs Examination. The MI and SWI images showed low signal areas similar to an ellipse uniformly distributed on CMBs, which were not completely connected to the previous or next layer. The diameter was about 1.5–6.5 mm, and there was no obvious edema in the surrounding tissues. Intracranial calcifications and small blood vessel flow empty shadow should be eliminated in time. Intracranial calcifications were usually symmetrical, irregular in shape, and common in choroid plexus, globus pallidus, etc. Small blood vessel flow empty shadow was more common in the cerebral cortex area and was usually shown as short T2WI signals. By tracing the course of the blood vessels in the continuous layers, it could be distinguished. Figure 2 shows the images of CMBs.

2.6. Vertebrobasilar Artery Information. The measurement method of blood vessel width and diameter was described as follows. The sequential convergence point of the vertebrobasilar arteries was the starting point of the detection. The width of the bilateral vertebral arteries was measured with three points separated by 0.3 cm, and the average of their widths was taken as the measured value of the vertebral artery diameter standard. The following criterion was for judging the vertebral artery dominance. The difference in the diameter of the bilateral vertebral arteries was ≥0.3 mm, or was not much different in the image, and it was relatively closely connected with the basilar artery. According to the difference in the diameter of the bilateral vertebrobasilar arteries, it was divided into three grades. Grade I showed a difference between the bilateral artery diameters of 0.04–0.70 mm, Grade II had a difference of 0.71–1.17 mm, and Grade III had a difference of 1.18–2.67 mm.

A straight line was drawn between the junction of the bilateral vertebral basilar artery and the beginning of the basilar artery. This straight line was also called basilar artery length (BAL), which was the length standard line of the basilar artery. The bending length (BL) referred to the average distance from the most bending point of the basilar artery to the BAL. The types of abnormal vertebrobasilar curvature mainly included the C type, reverse C type, and S type.

2.7. Statistical Methods. The data analysis and processing were performed via Spss19.0. The measurement data were expressed as mean ± standard deviation. The comparisons between the measurement group and the control group were performed through an independent sample t-test. The ranked data were tested by the rank sum difference method. The chi-square test or Fisher's exact probability method was adopted to express the enumeration data. The inspection level of data analysis results was $\alpha = 0.05$.

3. Results

3.1. Statistical Results of Lacunar Infarctions. The average number of lacunar infarctions in the BPPV group was (2.400 ± 3.358), and that in the control group was (0.672 ± 1.252). As shown in Figure 3, the number of lacunar infarctions in the BPPV group was greater than that in the control group ($t = 2.410$, $P < 0.05$).

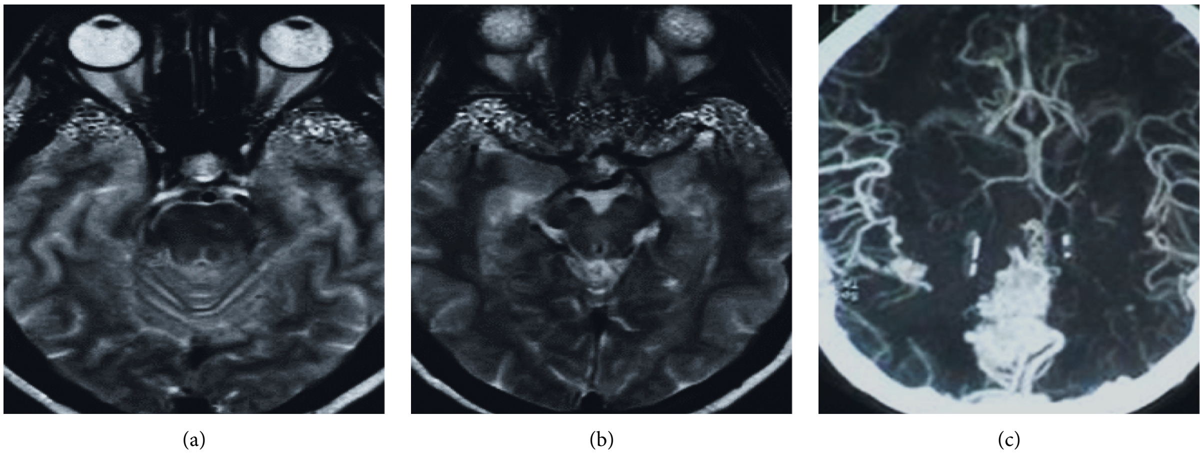

Figure 2: MI and SWI images of CMBs. The arrows pointed out CMBs. (a) The MI image. (b) The SWI image showing low-density signals. (c) The SWI image with clearer intracranial veins processed by the minimum density projection technology.

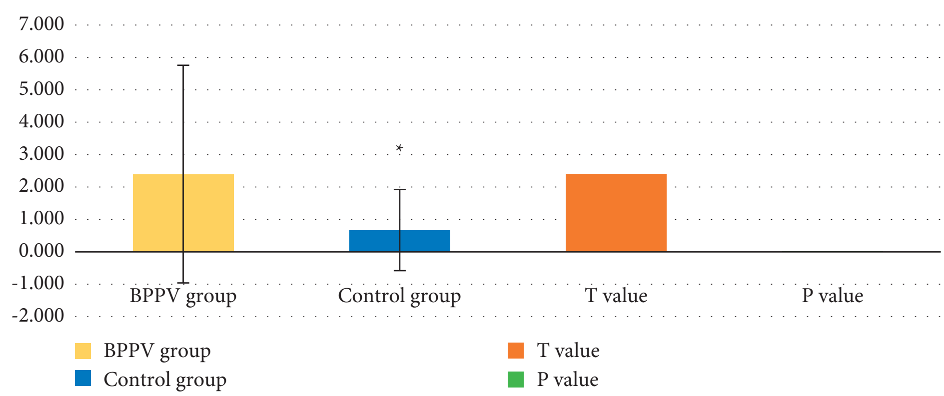

Figure 3: Comparison of the number of lacunar infarctions in the BPPV group and the control group. *The difference was statistically significant compared with the result of the BPPV group ($P < 0.05$).

3.2. The Positive Rate of CMBs. Among the 30 cases in the BPPV group, 14 cases (47%) were positive for CMBs; and among the 30 cases in the control group, 4 cases (13%) were detected positive for CMBs. The chi-square test was used to statistically analyze the positive rate of CMBs in both groups, and the results are shown in Figure 4.

The results of the positive rate and negative rate of CMBs were analyzed. It was found that the positive rate of CMBs in the BPPV group was higher than that of the control group ($\chi^2 = 3.309$, $P < 0.05$). Among the 18 positive cases, there were at most 10 and at least 1 CMBs lesion. The average number of CMBs in the BPPV group was (1.632 ± 3.017), while the number in the control group was (0.384 ± 0.898). There was statistical significance in the number of CMBs in both groups ($t = 1.982$, $P < 0.05$).

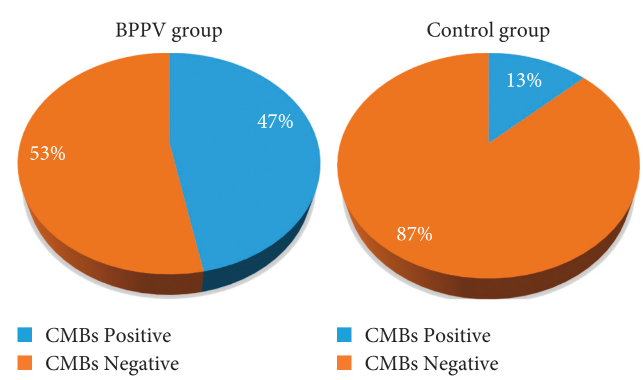

Figure 4: Comparison of the positive rate of CMBs between the BPPV group and the control group.

3.3. Comparison of the Detection Rate of CMBs by Conventional MRI and SWI Sequence. Among 60 examiners, 20 cases with CMBs were detected by SWI. 40 cases with CMBs were detected by conventional unenhanced MRI, which is shown in Figure 5.

Both the MI and SWI images of CMBs showed low-signal lesions with clear edges, as shown in Figure 6.

3.4. Correlation between Vertebral Artery Dominance as well as Basilar Artery Curvature and BBPV. MRA images of 60 objects were measured. It was shown that there were 19 cases with vertebral artery dominance in the BPPV group, among which 10 cases with left side dominance, 9 cases with right side dominance, and 10 cases with basilar artery morphological abnormalities. In the control group, there were 8 cases with vertebral artery dominance, including 3

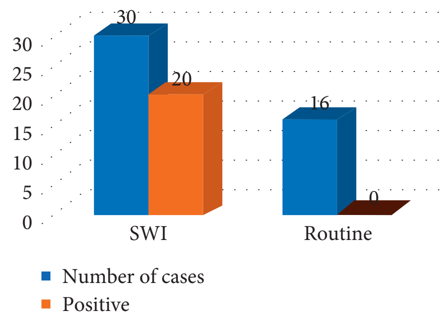

Figure 5: Comparison of the detection rate of CMBs by conventional MRI and SWI sequence.

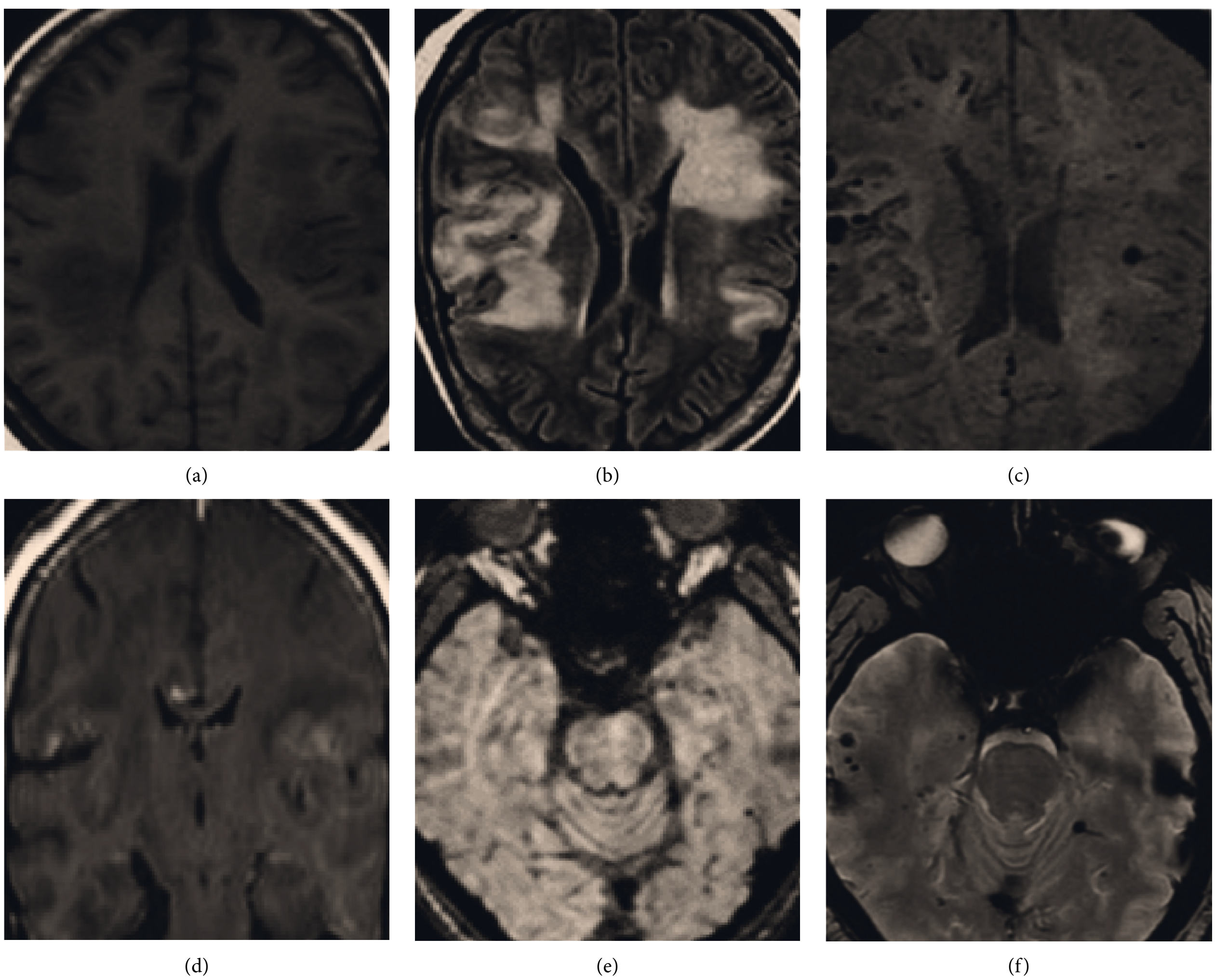

Figure 6: MI and SWI images of CMBs. (a–d) The image of T1WI, T2WI, T2-FLAIR, and DWI ($b = 1000$); these conventional MRI images showed no abnormality. (e) MI and (f) SWI image showed low-signal CMBs.

cases on the left side, 5 cases on the right side; 4 cases with abnormal basilar artery morphology, and the differences were statistically significant ($P < 0.05$). The comparisons of the dominance of the vertebral artery and the basilar artery curvature are shown in Figures 7–9.

4. Discussion

BPPV is a kind of motor hallucination or spatial image realization dislocation caused by head position changes. In recent years, some studies in China have paid great attention

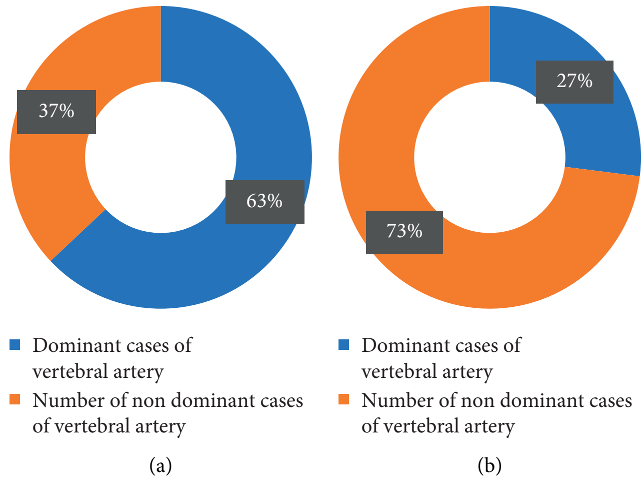

FIGURE 7: Comparative observation of the vertebral artery dominance in a total of 27 cases in the BPPV group (a) and the control group (b).

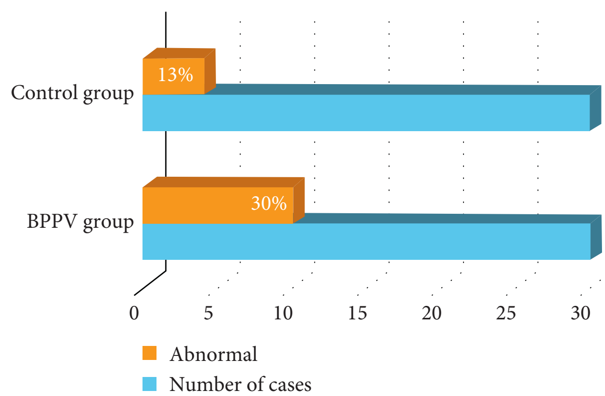

FIGURE 8: Morphological analyses of the vertebrobasilar artery.

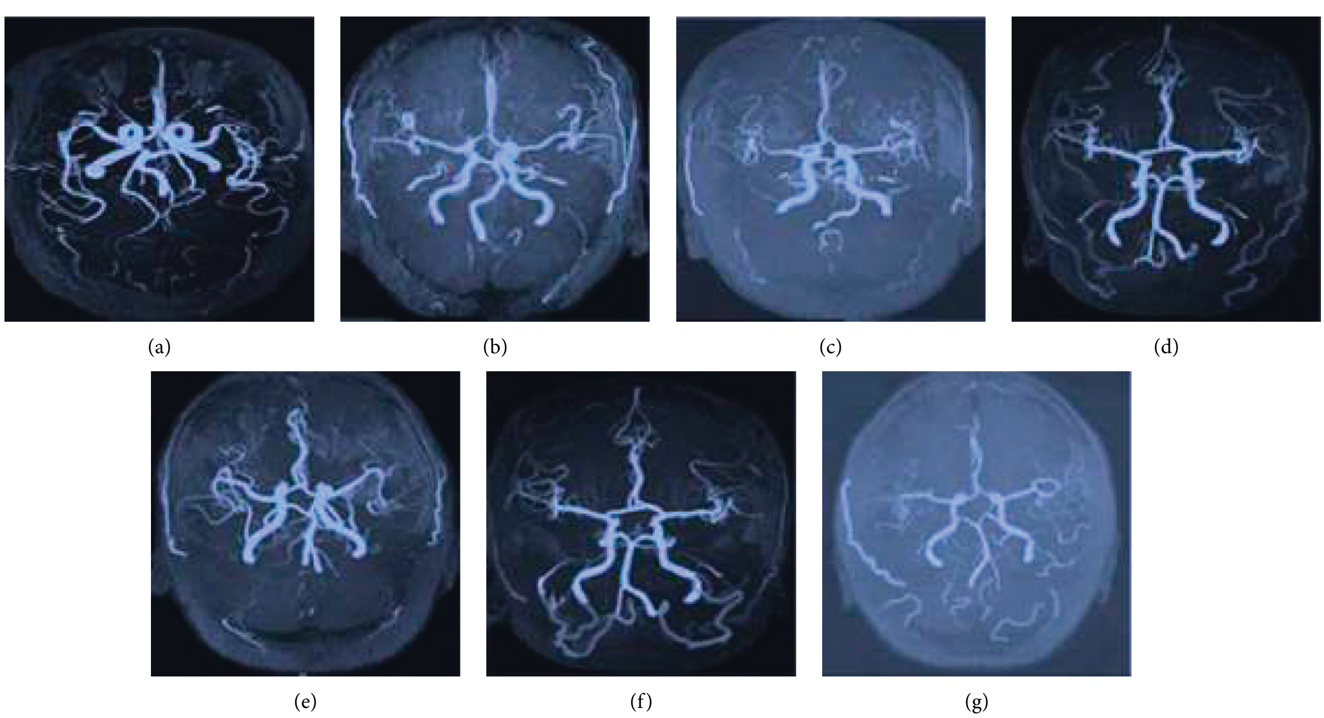

FIGURE 9: Basilar artery morphology. (a–g) The C type, S type, reverse C type, normal vertebral artery dominance, normality, left side dominance, and right side dominance.

to the serious impact of cerebrovascular risk factors in BPPV, especially in elderly patients with cerebrovascular diseases. There is a certain correlation between BPPV and cerebrovascular incident factors [15]. High blood pressure and diabetes may cause damage to the capillaries of the inner ear to a certain degree, leading to otolith shedding; it may directly participate in the pathogenesis of BPPV [16]. 30 patients with BPPV were selected as the research objects, and 39 patients without vertigo symptoms who received normal physical examination during the same period were chosen as the control group. All these patients underwent MRI scanning under the PDDC-CNN model. It was found that the average number of lacunar infarctions was (2.400 ± 3.358) in the BPPV group, and was (0.672 ± 1.252) in the control group, showing a remarkable difference between the two groups ($t = 2.410$, $P < 0.05$). This indicated that the cerebral lacunar infarction in BPPV patients was more severe than that in normal objects. The positive rate of CMBs in the BPPV group was higher than that in the control group significantly ($X^2 = 3.309$, $P > 0.05$), indicating that the incidence of a cerebral hemorrhage in BPPV patients was higher than that in normal people. Thus, it was speculated that the incidence of cerebral hemorrhage was related to the conditions of BPPV. The results of this work could also explain most of the concurrence of cerebral vascular risk factors and BPPV [17].

In the BPPV group, there were 19 cases of vertebral artery dominance, consisting of 10 cases of left dominance and 9 cases of right dominance. There were also 10 cases of abnormal basilar artery morphology. In the control group, 8 cases got vertebral artery dominance, with left dominance in 3 cases and right dominance in 5 cases; 4 cases got abnormal basilar artery morphology. The differences were of statistical significance ($P < 0.05$). Previous research has shown that cerebral small vessel diseases can directly damage the tiny arteries of the inner ear in patients, leading to microcirculation disturbance [18, 19]. This result suggested that BPPV patients may be complicated by cerebrovascular diseases, resulting in the vertebral artery dominance and the abnormality of the basilar artery, which could be diagnosed by imaging features of MRI. To sum up, it was of great significance for the clinical diagnosis and treatment of BPPV patients to explore the role of the vertebrobasilar artery on BPPV patients, and to find effective methods to delay the disadvantages caused by vertebral artery dominance and abnormal basilar artery [20]. Among the 60 patients, 20 cases with CMBs were detected by SWI, while 40 cases of CMBs were detected by conventional MRI scanning. It was proved that the SWI examination under the PDDC-CNN model had an excellent performance in diagnosing cerebral hemorrhage.

5. Conclusion

The artificial intelligence algorithm under PDDC-CNN was successfully applied. It was combined with conventional MRI scanning and MRA to explore the correlation between intracranial small blood vessels as well as vertebrobasilar arteries and BPPV in China. It was discovered that the MRI features of BPPV patients were in a close relation to their own microvascular lesions, and it was speculated that cerebrovascular factors might be dominant in the early onset of BPPV. Deep learning-based MRI could diagnose symptoms such as vertebral artery dominance and basilar artery abnormality more accurately in patients with BPPV, so it was worth being popularized clinically. However, the samples were relatively less, and the relationship between the location of CMBs, the abnormality of the vertebrobasilar artery and its branches, and the degree of BPPV had not been explored. The correlation and mechanism between the abnormalities of the basilar artery and its branches and the degree of BBPV could be investigated in the future with more samples and deeper methods. All in all, the results offered data reference for the imaging diagnosis of BPPV patients as well as the prevention and treatment of cerebrovascular diseases.

Data Availability

The data used to support the findings of this study are available from the corresponding author upon request.

Conflicts of Interest

The authors declare no conflicts of interest.

References

[1] Y. Lou, M. Cai, L. Xu, Y. Wang, L. Zhuang, and X. Liu, “Efficacy of BPPV diagnosis and treatment system for benign paroxysmal positional vertigo,” *American Journal of Otolaryngology*, vol. 41, no. 3, p. 102412, 2020.

[2] A. S. Bou Ghannam and S. Yassine, “Pediatric nystagmus,” *International Ophthalmology Clinics*, vol. 58, no. 4, pp. 23–65, 2018.

[3] P. Ranalli, “An overview of central vertigo disorders,” *Advances in Oto-Rhino-Laryngology*, vol. 82, pp. 127–133, 2019.

[4] C. Hammen, “Risk factors for depression: an autobiographical review,” *Annual Review of Clinical Psychology*, vol. 14, pp. 1–28, 2018.

[5] G. Eelen, L. Treps, X. Li, and P. Carmeliet, “Basic and therapeutic aspects of angiogenesis updated,” *Circulation Research*, vol. 127, no. 2, pp. 310–329, 2020 3.

[6] R. A. Bartholomew, R. J. Lubner, R. M. Knoll et al., “Labyrinthine concussion: historic otopathologic antecedents of a challenging diagnosis,” *Laryngoscope Investigative Otolaryngology*, vol. 5, no. 2, pp. 267–277, 2020.

[7] M. Pétrault, B. Casolla, T. Ouk, C. Cordonnier, and V. Berezowski, “Cerebral microbleeds: beyond the macroscope,” *International Journal of Stroke*, vol. 14, no. 5, pp. 468–475, 2019.

[8] T. F. D. Costa, C. J. L. Pimenta, M. M. L. D. Nóbrega et al., “Burden on caregivers of patients with sequelae of cerebrovascular accident,” *Revista Brasileira de Enfermagem*, vol. 73, no. 6, Article ID e20180868, 2020.

[9] C. Ribeiro-Silva, W. Vermeulen, and H. Lans, “SWI/SNF: complex complexes in genome stability and cancer,” *DNA Repair*, vol. 77, pp. 87–95, 2019.

[10] G. Zaharchuk, E. Gong, M. Wintermark, D. Rubin, and C. Langlotz, “Deep learning in neuroradiology,” *AJNR Am J Neuroradiol*, vol. 39, no. 10, pp. 1776–1784, 2018.

[11] M. Sarıgül, B. M. Ozyildirim, and M. Avci, "Differential convolutional neural network," *Neural Networks*, vol. 116, pp. 279–287, 2019.
[12] J. Cao, S. Liu, H. Liu, and H. Lu, "CS-MRI reconstruction based on analysis dictionary learning and manifold structure regularization," *Neural Networks*, vol. 123, pp. 217–233, 2020.
[13] Z. Li, X. Li, R. Tang, and L. Zhang, "Apriori algorithm for the data mining of global cyberspace security issues for human participatory based on association rules," *Frontiers in Psychology*, vol. 11, p. 582480, 2021.
[14] S. Xie, Z. Yu, and Z. Lv, "Multi-disease prediction based on deep learning: a survey," *Computer Modeling in Engineering and Sciences*, vol. 128, no. 2, pp. 489–522, 2021.
[15] M. Farooq and F. Anjum, "Sleep Paralysis," in *StatPearls*-StatPearls Publishing, Treasure Island (FL), 2021.
[16] A. L. McGuire, S. Gabriel, S. A. Tishkoff et al., "The road ahead in genetics and genomics," *Nature Reviews Genetics*, vol. 21, no. 10, pp. 581–596, 2020.
[17] J. C. Gore, "Artificial intelligence in medical imaging," *Magnetic Resonance Imaging*, vol. 68, pp. A1–A4, 2020 May.
[18] M. Hu, Y. Zhong, S. Xie, H. Lv, and Z. Lv, "Fuzzy system based medical image processing for brain disease prediction," *Frontiers in Neuroscience*, vol. 15, p. 714318, 2021.
[19] X. Zhang, H. Li, T. Xie, Y. Liu, J. Chen, and J. Long, "Movement speed effects on beta-band oscillations in sensorimotor cortex during voluntary activity," *Journal of Neurophysiology*, vol. 124, no. 2, pp. 352–359, 2020 Aug 1.
[20] Y. Chen, S. Hu, H. Mao, W. Deng, and X. Gao, "Application of the best evacuation model of deep learning in the design of public structures," *Image and Vision Computing*, vol. 102, p. 103975, 2020.

Hindawi
Contrast Media & Molecular Imaging
Volume 2022, Article ID 4574730, 8 pages
https://doi.org/10.1155/2022/4574730

Research Article

Plan-Do-Check-Action Circulation Combined with Accelerated Rehabilitation Nursing under Computed Tomography in Prevention and Control of Hospital Infection in Elderly Patients Undergoing Elective Orthopedic Surgery

Liguo Zhao,[1] **Lianghong Hu**,[2] **Zhangxian Li**,[3] **and Fenyan Deng**[2]

[1]*Fever Clinic, The Third Affiliated Hospital Hengyang Medical School, University of South China, Hengyang 421900, Hunan, China*
[2]*Department of Nursing, The Third Affiliated Hospital Hengyang Medical School, University of South China, Hengyang 421900, Hunan, China*
[3]*Department of Spinal Surgery, The Third Affiliated Hospital Hengyang Medical School, University of South China, Hengyang 421900, Hunan, China*

Correspondence should be addressed to Fenyan Deng; 19440113@smail.cczu.edu.cn

Received 15 February 2022; Revised 30 March 2022; Accepted 4 April 2022; Published 25 April 2022

Academic Editor: M. Pallikonda Rajasekaran

To explore the adoption of plan-do-check-action (PDCA) circulation combined with accelerated rehabilitation nursing based on gemstone spectral imaging computed tomography (GSICT) in the prevention and control of hospital infection in the elderly patients undergoing the elective orthopedic surgery, 80 elderly patients who underwent the elective orthopedic surgery in the hospital were selected. Then, according to the randomized controlled principle, these 80 patients were divided into control group (40 cases) with conventional nursing and observation group (40 cases) with accelerated rehabilitation surgical nursing combined with PDCA circulation. All the patients underwent the GSICT examination without any contraindicators. Compared with the conventional CT scan, metal artifacts in GSICT were considerably reduced. In the images processed by GSI and metal artifacts reduction system (MARS), metal artifacts were basically eliminated and the positions, forms, and edges of metal artifacts in the human body were clearly presented. Hospital infection occurred in 1 (2.5%) patient in the observation group and 5 (12.5%) patients in the control group, and the difference was statistically significant ($P < 0.05$). In terms of temperature increase, patients in control group (37.5%) had a remarkably higher value than that of observation group (7.5%). The increase rate of white blood cell (WBC) count in control group (12.5%) was obviously higher than that in observation group (2.5%). Besides, the differences were statistically significant ($P < 0.05$). After PDCA circulation combined with accelerated rehabilitation nursing mode was applied, the hospitalization time of observation group (5.3 ± 2.4 days) was markedly lower than that of control group (9.7 ± 3.8 days). Moreover, the total hospitalization cost of observation group (791.44 yuan) was notably lower than that of control group (4068.96 yuan), with significant differences ($P < 0.05$). Nursing satisfaction in observation group (92.5%) was higher than that in control group (77.5%), and the difference was statistically significant ($P < 0.05$). In short, GSICT could effectively reduce beam hardening artifacts and metal implant artifacts and improve image quality. Furthermore, accelerated rehabilitation nursing combined with PDCA circulation could effectively reduce the incidence of hospital infection and improve nursing satisfaction.

1. Introduction

Hospital infection refers to infections acquired by patients in hospital, including the infections acquired during hospitalization and the infections acquired in hospital and developed after discharge [1]. Patients who undergo the orthopedic surgery suffer from hunger, anesthesia, pain, and many other stimuli. Besides, the incidence of postoperative hospital infection is high, which seriously affects the rehabilitation process of patients [2]. The concept of surgical site infection (SSI) was first proposed by the U.S. Center of Disease Control in the late 20^{th} century. According to the data, the incidence of SSI ranked third in hospital infection, which accounts for about 15% of all hospital infection patients [3]. According to the domestic and international statistical data, during surgery, the overall incidence of SSI in patients is 2%–20%, and the incidence of SSI in clean surgery is the lowest [4–6]. Conventional perioperative orthopedic nursing is far from meeting patients' rehabilitation needs, and it is imperative to seek a new, rapid, and scientific nursing mode. The function of accelerated rehabilitation nursing in orthopedics is that it can effectively promote the rehabilitation of patients and reduce the incidence of hospital sense after orthopedics surgery [7–9]. In the process of clinical nursing, it is difficult to implement each step of accelerated rehabilitation surgery in nursing management work.

Accelerated rehabilitation nursing refers to a concept of accelerated physical and psychological rehabilitation in the perioperative period, based on a series of evidence of medicine and combined with multiple disciplines, on the premise of ensuring safety, reducing surgical stress response, hospitalization time, and cost [10]. Through systematic meta-analysis, Rao et al. [11] concluded that compared with conventional nursing, accelerated rehabilitation nursing could effectively reduce the occurrence of complications such as deep vein thrombosis and infection. Additionally, Shao et al. [12] found that accelerated rehabilitation nursing could effectively reduce the surgical trauma of patients who underwent the laparoscopic radical resection of rectal cancer and reduce the surgical inflammatory stress response, thus promoting the postoperative rehabilitation. At present, the main reason for accelerated rehabilitation nursing is providing intervention measures for various risk factors, and effectively reducing the hospitalization time and the risk of iatrogenic infection.

The plan-do-check-action (PDCA) circulation method is a quality management program proposed by Deming, an American management scientist. Through plan, do, check, and action, the implementation of the whole nursing step is mainly preformed in a circulation and improved continuously. According to effective research results, the potential nursing problems in the nursing work are found out. Then, the corresponding nursing interventions are given to address the existing nursing problems, so as to improve the risk awareness of nursing staffs, and effectively reduce the occurrence of adverse nursing events [13–15]. Xu et al. [16] found that due to the adoption of PDCA circulation management in the management of hospital infection in orthopedic surgery, the hospital infection rate and the surgical infection rate of patients were reduced, and the awareness rate of hospital infection and qualified rate of hand hygiene of medical staff were improved as well as the satisfaction rate of patients. Moreover, the adoption of PDCA circulation to implement cluster interventions was helpful to improve hand hygiene compliance effectively, thus reducing the incidence of hospital infections, which was explored by Demirel [17].

When patients who have undergone the elective orthopedic surgery receive the postoperative computed tomography (CT), radially diffused starlike and stepped artifacts are often found, due to the use of metal devices during internal fixation, such as intramedullary steel nails, metal replacement joints, and internal fixation plates. The great difficulties to the reconstruction of CT images are brought by the generation of artifacts, which causes misdiagnosis [18]. Gemstone spectral imaging computed tomography (GSICT) can solve the problem effectively. The dual energy process in the projection data space is completed by this technique. The metal artifacts are removed by the metal artifact elimination reconstruction technique. Furthermore, GSICT is widely used in postoperative examination of patients who have undergone the elective orthopedic surgery [19, 20].

The incidence of SSI after elective orthopedic surgery is influenced by many factors. Different surgical methods are varied with the incidence of SSI, but these factors can be prevented. Nurses are the ones who accompany orthopedic patients for the longest time during hospitalization. Therefore, according to these factors, certain preventive measures are implemented to avoid the occurrence of hospital infections. At present, there is no adoption of accelerated rehabilitation nursing under CT examination combined with PDCA circulation quality improvement in the prevention and control of postoperative hospital infections in elderly patients undergoing the elective orthopedic surgery. Hence, it was necessary to implement this adoption. Additionally, it could also provide a more safe, scientific, and effective accelerated rehabilitation nursing mode for the prevention and control of postoperative hospital infections in elderly patients who underwent elective orthopedic surgery. The level of prevention and control of orthopedic hospital infection in this region is improved, the medical resources are saved, and the burden of disease caused by hospital infection in orthopedic wards is also reduced. Therefore, accelerated rehabilitation nursing under CT examination combined with PDCA circulation is widely applied in the prospect.

2. Methods

2.1. Subjects of the Study. Eighty elderly patients who were admitted to the hospital from January 2019 to January 2021 for elective orthopedic surgery were selected. According to the randomized controlled principle, these 80 patients were divided into control group (40 cases) with conventional nursing and observation group (40 cases) with accelerated rehabilitation surgical nursing combined with PDCA circulation. There were 43 male patients and 37 female patients, and the mean age was 65.32 ± 9.74 years old. There is no difference in sex and age between the two groups, which is comparable. This study had been approved by the ethics committee of hospital. All the patients and their families knew about this study and signed the informed consent form.

The inclusion criteria were as follows: (i) patients older than 45 years old; (ii) patients scheduled for elective orthopedic surgery; (iii) patients in good physical condition and could tolerate surgery; and (iv) patients who informed about the study and agreed to participate in the study.0

The exclusion criteria were as follows: (i) those with poor compliance and (ii) those diagnosed with other organic diseases, such as mental disorders and liver and kidney dysfunction.

2.2. CT Examination. Patients were scanned by a high-definition energy spectrum CT, and the gemstone spectral imaging (GSI) mode was selected. The scan parameters were as follows. The tube current was 330 mA, the tube voltage was 120 kV, the scanning field was 25 cm, the tube speed was 350 ms, the spacing and layer thickness were 5 mm, the width of the single detector after reconstruction was 0.5 mm, and the pitch was 0.95 : 1. Besides, metal artifacts were removed by the metal-artifacts reduction system (MARS) technology. The window position was fixed at 420Hu and the window width was 2200Hu during the scanning process.

2.3. Specific Methods. In control group, patients were treated with conventional nursing, and they were informed to quit smoking and drinking before surgery, supple nutrition, and pay attention to postoperative wound care. Patients in observation group were treated with the improved PDCA circulation based on accelerated rehabilitation surgical nursing.

The specific contents of accelerated rehabilitation surgical nursing were as follows. Before the surgery: (i) Medical history was inquired in detail, and the recent history of respiratory tract infection (RTI) and periodontitis infection was also asked. (ii) Nutritional support was enhanced. Through the diet of high protein and high vitamin, patients' hypoproteinemia and anemia were corrected and their resistance was improved. (iii) Health education was emphasized. Two weeks before surgery, patients were told to quit smoking and they did cough exercises to improve lung function under the instrument. (iv) After admission, the skin of the surgical site was maintained clean every day. The prophylactic use of antibiotics was followed by doctor's advice before surgery, and intravenous infusion was started 30–60 minutes before surgery.

After the surgery: (i) Patients' anemia and hypoproteinemia were corrected continuously and promptly. The diet was the same as that before the surgery. (ii) Blood glucose of patients with diabetes was continuously monitored after surgery. Surgical stress could cause diabetic patients to develop insulin resistance and remain hyperglycemic for weeks. The risk of incision-related complications was increased. (iii) Incision management was strengthened. After surgery, it should strengthen muscle contraction exercise, promote venous and lymphatic reflux, and reduce edema of affected limbs. (iv) The management of hospital discharge. After discharge, patients were followed up closely 2-3 weeks, 1 month, 3 months, 6 months, 1 year after surgery, and every year thereafter, patients needed to come to the outpatient clinic for re-examination to check the surgical site for abnormal pain, redness, and skin temperature rise, and they were guided to do functional exercise.

PDCA circulation was classified into four stages: plan, implementation, inspection, and treatment. In the accelerated rehabilitation nursing of elderly patients who underwent elective orthopedic surgery, nursing was classified into four stages by the nurses in view of the existing problems. The first one was the planning stage, which included present situation analysis, cause investigation, finding the influencing factors, and correction and prevention. The second one was the implementation stage to implement the plan. The third one was the inspection stage to investigate the results. The last one was the treatment stage to summarize experience and set standards. This circulation was repeated to optimize the rehabilitation surgical nursing process after elective surgery and reduce the occurrence of orthopedic hospital infection.

2.4. Observation Indicators. Incision infection rate, body temperature elevation rate (body temperature elevation above 38°C) at three days after surgery, and white blood cell (WBC) elevation rate ($WBC > 10.0 \times 10^9$) were compared between the two groups. The length of hospital stay, total hospital cost, and nursing satisfaction were also compared between the two groups. Nursing satisfaction was evaluated by a self-made questionnaire of the department, with 0–100 points, which included satisfied score (>80 points), basically satisfied score (65–80 points), and dissatisfied score (<65 points). Total satisfaction = (satisfied cases + basic satisfied cases)/40 × 100%.

2.5. Image Processing and Observation Comparison. The conventional CT scan was not implemented repeatedly. Patients' pervious conventional CT scan data were transferred from hospital information system (HIS) online back to AW 4.5 post-processing workstation for a variety of recombination treatments, to reduce the amount of radiation to the patients including volume rendering (VR), maximum intensity projection (MIP), and multiplanar reformation (MPR). The obtained images were saved for comparison with those obtained from GSICT. The feasibility processing was implemented on the GSI scan image data transmitted to AW 4.5 post-processing workstation. The GSI viewer processing software was used for analysis, and the single energy image suitable for keV adjustment was selected. Then, images from the same layers as shoes from a conventional CT scan were found and compared. Furthermore, a different software was selected to process and observe the different cases, especially for careful reading and study of axial images, and to select the best way to evaluate the scanned images.

2.6. Statistical Methods. SPSS 22.0 was employed for data statistics and analysis. The measurement data ($\overline{x} \pm s$) were compared by the independent sample *t*-test. The enumeration data (n, %) were tested by χ^2 test. When $P < 0.05$, it meant that the difference was statistically significant.

3. Results

3.1. Results of the CT Scan. Through a variety of post-processing software, the metal artifacts caused by the presence of metal products in the body such as internal fixation nails and artificial joints could not be eliminated by the conventional CT scan. The accuracy of postoperative examination and diagnosis of orthopedic patients were reduced by the unclear relationship among artificial joints and the position of internal fixation nails, and even misdiagnosis was caused. The great difficulties were brought for orthopedic surgeons to follow-up patients after surgery (Figure 1).

Compared with the conventional CT scan, metal artifacts in GSICT were considerably reduced. In the images processed by GSI and MARS, metal artifacts were basically eliminated, and the positions, forms, and edges of metal artifacts in human body were clearly presented. GSICT helped to evaluate the effects of fracture reduction and internal fixation and improve the accuracy of diagnosis. Besides, it also helped to facilitate orthopedic surgeons to observe CT reexamination images and to evaluate the postoperative rehabilitation (Figure 2).

3.2. Results of Hospital Infection Incidence. In observation group, there was 1 patient (2.5%) who developed hospital infection, while in control group, there were 5 patients (12.5%) who developed hospital infection, including 1 patient with RTI, 2 patients with urinary tract infection (UTI), and 2 patients with incisional infection. Besides, the incidence of hospital infection in control group was evidently higher than that in observation group ($P < 0.05$) (Figure 3).

3.3. Rate of Elevated Body Temperature and Increased WBC Count. In observation group, there were 3 patients (7.5%) with elevated body temperature (higher than 38°C), while there were 15 patients (37.5%) with elevated body temperature. Hence, in Figure 4, the rate of elevated body temperature was notably higher than that in observation group ($P < 0.05$).

Increased WBC was observed in 4 patients (2.5%) in the observation group ($\text{WBC} > 10.0 \times 10^9$), and in 17 patients (12.5%) in control group. Therefore, in Figure 5, the rate of increased WBC count in control group was remarkably higher than that in observation group ($P < 0.05$).

3.4. Length of Stay and Total Cost of Stay. In Figure 6, after the adoption of PDCA circulation combined with accelerated rehabilitation nursing mode, the hospitalization time (5.3 ± 2.4 days) of the observation group was markedly lower than that of control group (9.7 ± 3.8 days) ($P < 0.05$).

In Table 1, the total hospitalization cost of observation group was 791.44 yuan, which was notably lower than that of control group (4,068.96 yuan) ($P < 0.05$).

3.5. Degree of Nursing Satisfaction. Table 2 and Figure 7 show that in observation group, 28 patients were very satisfied, 9 patients were basically satisfied, and 3 patients were dissatisfied, with a satisfaction rate of 92.5% (37/40). In control group, 16 patients were very satisfied, 15 patients were basically satisfied, and 9 patients were dissatisfied, with a satisfaction rate of 77.5% (31/40). Hence, the nursing satisfaction of observation group was higher than that of control group ($P < 0.05$).

4. Discussion

The imaging quality is determined by the detector which is the core part of CT. In the past 10 years, gemstones were used as detector materials for the GSICT developed by many scholars. The stability of gemstones is 20 times that of traditional rare Earth ceramic detectors and cadmium tungstate detectors. Gemstones have the characteristics of good air permeability and high purity, which ensure high quality of images and low dose of radiation. In the conventional CT scan, the diagnostic results are affected remarkably by artifacts caused by internal fixation plates and artificial joints [21]. Artifacts cause blurred imaging, which increases the difficulty of diagnosis. If diagnosis is wrong, premature exercise will cause the failure of elective orthopedic surgery. Additionally, delayed rehabilitation exercise will cause dyskinesia or muscle disuse atrophy [22]. Therefore, the removal of the artifacts becomes a vital issue to improve the image quality.

Compared with conventional CT equipment, HD energy spectrum CT imaging can realize single-photon imaging and material separation. HD energy spectrum CT can display fine lesions that cannot be found by conventional CT, which has been proved by several clinical cases. Meanwhile, density resolution has been improved. The sensitivity of small lesions is comparable to positron emission tomography (PET), and it has unique advantages in the specific diagnosis of lesions [23–25]. The HD energy spectrum CT scanning technology can effectively solve the problems of metal artifacts and improve the quality of CT images. Moreover, the technology requires that the CT scan is sampled at the same time to obtain double group projection data of objects. Hence, the conditions of high technology of hardware are necessary. MARS technology and single energy imaging technology are the main methods to remove artifacts by HD energy spectrum CT scanning technology. Furthermore, the MARS technology is designed to reduce image artifacts effectively by using software to control radiation through metal devices, generate low signals, and process the data simultaneously [26]. CT values of metal implants surrounding structures are precisely reflected by the single energy imaging technique combined with MARS. The CT value is proportional to the distance. The farther the distance is, the more it reflects the actual CT value of the tissue [27]. In the adoption of HD energy spectrum CT scanning technology, the region of 100–140 keV is the best region for GSI to eliminate metal implant artifacts. Additionally, this region is employed to improve the image quality obviously and to make the fine structures be imaged clearly.

PDCA circulation was born in the United States, based on the total quality management of the ideology and method. PDCA stands for plan, do, check, and action [28].

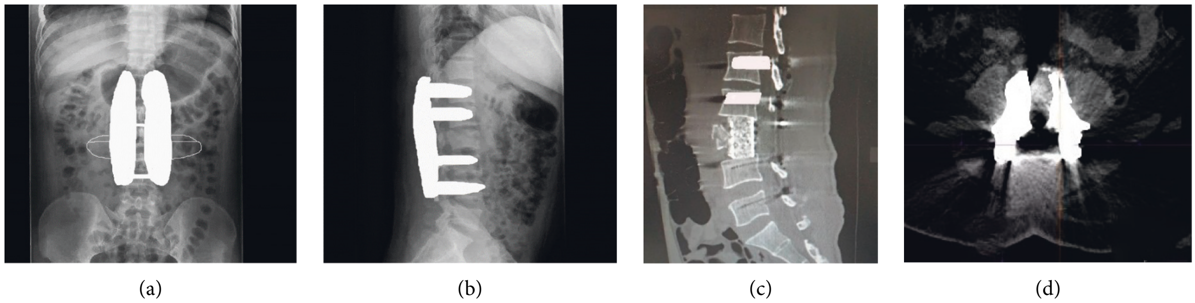

FIGURE 1: Conventional CT scan images. (a) Coronal position of lumbar vertebra. (b) Sagittal position of lumbar vertebra. (c) Sagittal position of thoracic vertebra. (d) Transverse position of lumbar vertebra. Many metal artifacts were observed, and the relationship among artificial joints and the position of internal fixation nails were blurred.

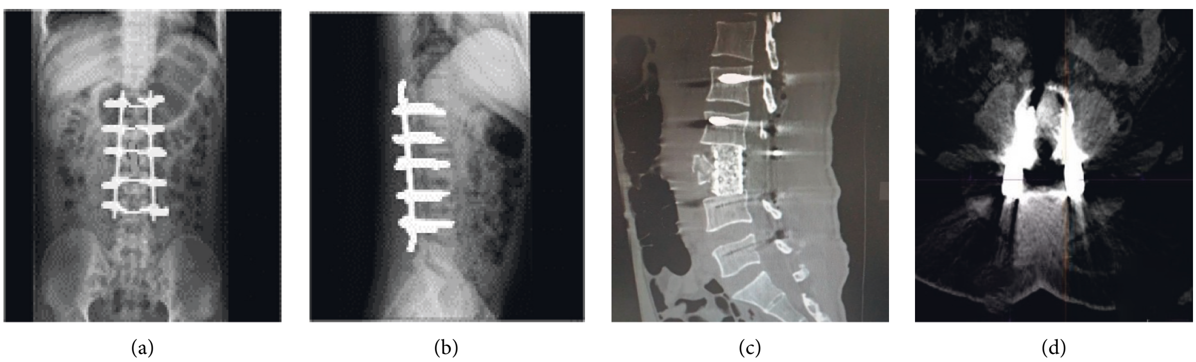

FIGURE 2: GSICT scan images processed by GSI and MARS. (a) Coronal position of lumbar vertebra. (b) Sagittal position of lumbar vertebra. (c) Sagittal position of thoracic vertebra. (d) Transverse position of lumbar vertebra. Compared with conventional CT scan images, the image clarity of the above four figures was obviously improved, and metal radial artifacts were basically eliminated. The relationship among artificial joints and the position of internal fixation nails were shown to facilitate observation.

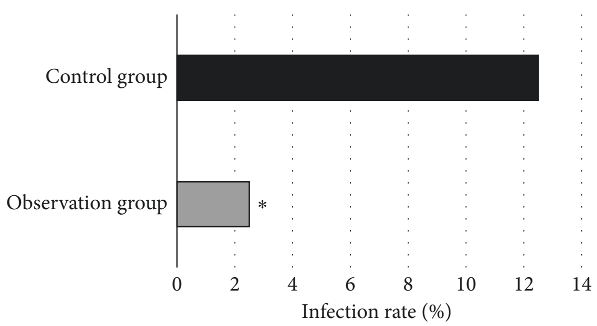

FIGURE 3: Incidence of hospital infection. *Compared with control group, $P < 0.05$.

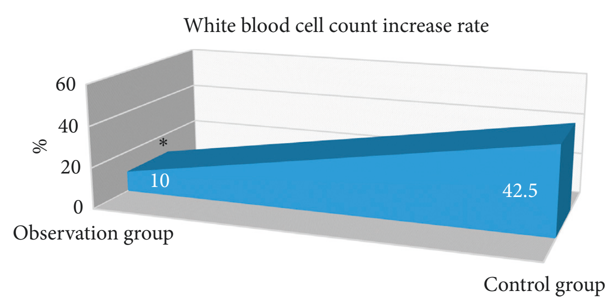

FIGURE 5: WBC count increase rate. *Compared with control group, $P < 0.05$.

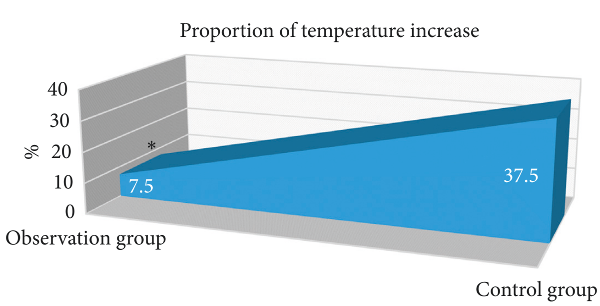

FIGURE 4: Proportion of temperature increase. *Compared with control group, $P < 0.05$.

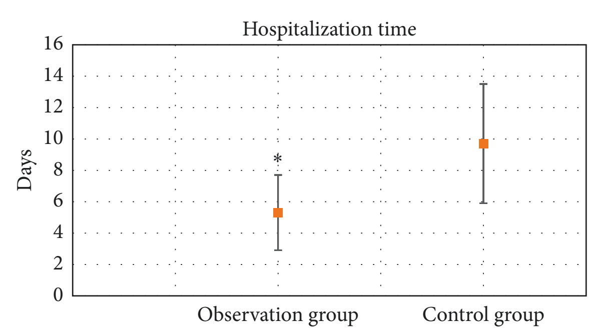

FIGURE 6: Comparison of hospitalization time. *Compared with control group, $P < 0.05$.

Table 1: Total costs of stay (yuan).

Group	Treatment costs	Drug costs	Bed costs	Examination costs	Total costs
Observation group	408.45	78.93	167.34	136.72	791.44
Control group	1,544.67	1,362.56	875.42	286.31	4,068.96
P	<0.05	<0.05	<0.05	<0.05	<0.05

Table 2: Degree of nursing satisfaction (n, %).

Group	Very satisfied	Basically satisfied	Dissatisfied	Degree of satisfaction (%)
Observation group	28 (70)	9 (22.5)	3 (7.5)	92.5
Control group	16 (40)	15 (37.5)	9 (22.5)	77.5
P	<0.05	<0.05	<0.05	<0.05

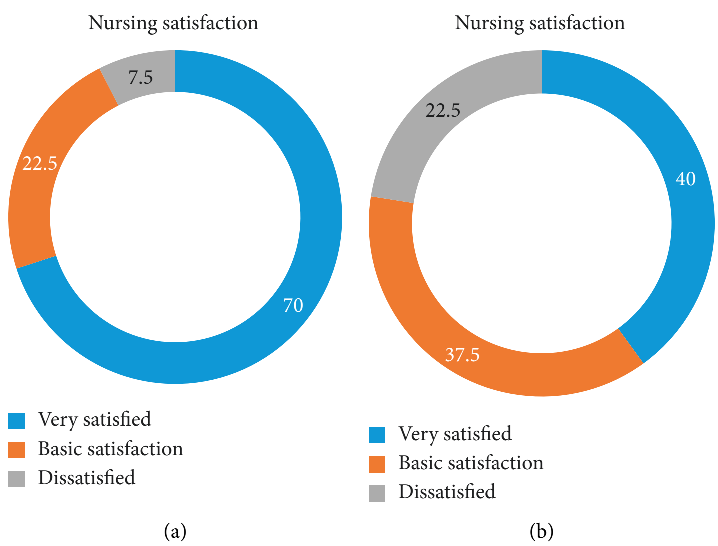

Figure 7: Nursing satisfaction. (a) Observation group. (b) Control group.

According to the adoption of PDCA circulation in the prevention and control of hospital infection in the surgical room, the various infection problems which have existed in the elderly patients are found out and solved in time, and the management quality of surgical room is improved because of the prevention and control function. Besides, the life safety of patients is also ensured. In the whole process of PDCA circulation nursing implementation, medical staff are required to have a high level of profession skills. The whole nursing structure is constantly optimized so that the quality of nursing work becomes more standardized and systematic. Moreover, the medical staff are also required to master the patients' disease development and postoperative recovery and to have an all-round communication with patients. With the deepening of the relationship of medical care, the quality of nursing work is improved. PDCA circulation combined with accelerated rehabilitation nursing was applied to patients who have undergone the elective orthopedic surgery, and the results were obtained as follows. The incision infection rate, body temperature, and WBC in observation group were lower than those in control group ($P < 0.05$). The length of hospitalization and total hospitalization cost in observation group were lower than those in control group ($P < 0.05$). The nursing satisfaction of observation group was higher than that of control group ($P < 0.05$). With the development of the PDCA circulation nursing model, the clinical manifestations of patients who underwent the elective orthopedic surgery were notably improved to shorten the hospital stay, which was investigated by Hua and Wang [29]. The results were consistent. According to PDCA circulation, the hospital stay was shortened, and the incidence of hospital infection was reduced. Furthermore, in the process of PDCA circulation nursing, problems were found and solved continually, and the implementations of every nursing detail were noticed. The executive ability of nursing was gradually improved while the incidence of hospital infection constantly decreased. The PDCA circulation nursing mode was applied in elective surgical treatment of orthopedics by Omar et al. [30]. The nursing quality was considerably improved, hospital stay was shortened, and the efficacy was improved. The results were also consistent.

Therefore, the adoption of PDCA circulation in the prevention and control of hospital infection in the surgical room is of high value, and it can be promoted and employed vigorously. Nevertheless, there are still some shortcomings. For instance, the sample size of the study was small; the HD energy spectrum CT scan required plenty of radiation energy, and the radiation dose received by patients was increased. Further studies and discussion are necessary in the future.

5. Conclusion

With the improvement of people's living standard and education level, people realize the importance of health and their demands for medical conditions and services increase accordingly. The beam hardening artifacts and metal implant artifacts were reduced effectively by the HD energy spectrum CT scan, thus improving image quality. Besides, the incidence of hospital infection was reduced by accelerated rehabilitation nursing combined with PDCA circulation, thereby improving nursing satisfaction. However, there are still deficiencies. For example, the sample size is small, so it is necessary to expand the sample for the prospective study. In addition, the HD energy spectrum CT scan required large ray energy, which increased the radiation dose of patients. To sum up, the adoption of accelerated rehabilitation nursing combined with PDCA circulation quality based on the HD energy spectrum CT scan in the prevention and control of hospital infection in elderly patients who underwent elective orthopedic surgery was improved.

Data Availability

The data used to support the findings of this study are available from the corresponding author upon request.

Conflicts of Interest

The authors declare that they have no conflicts of interest.

Acknowledgments

This work was supported by Hengyang Science and Technology Development Project in 2021 (No. 51(162)).

References

[1] H. Sun, L. Lv, Y. Bai et al., "Nanotechnology-enabled materials for hemostatic and anti-infection treatments in orthopedic surgery," *International Journal of Nanomedicine*, vol. 13, pp. 8325–8338, 2018.

[2] J. Skufca, J. Ollgren, M. J. Virtanen, K. Huotari, and O. Lyytikäinen, "Interhospital comparison of surgical site infection rates in orthopedic surgery," *Infection Control & Hospital Epidemiology*, vol. 38, no. 4, pp. 423–429, 2017.

[3] K. A. Cawcutt, J. R. Marcelin, and J. K. Silver, "Using social media to disseminate research in infection prevention, hospital epidemiology, and antimicrobial stewardship," *Infection Control & Hospital Epidemiology*, vol. 40, no. 11, pp. 1262–1268, 2019.

[4] P. Copanitsanou, "Recognising and preventing surgical site infection after orthopaedic surgery," *International Journal of Orthopaedic and Trauma Nursing*, vol. 37, Article ID 100751, 2020.

[5] S. Isguven, P. H. Chung, P. Machado et al., "Minimizing penile prosthesis implant infection: what can we learn from orthopedic surgery?" *Urology*, vol. 146, pp. 6–14, Article ID 3299190, 2020.

[6] A. I. Ribau, J. E. Collins, A. F. Chen, and R. J. Sousa, "Is preoperative Staphylococcus aureus screening and decolonization effective at reducing surgical site infection in patients undergoing orthopedic surgery? A systematic review and meta-analysis with a special focus on elective total joint arthroplasty," *The Journal of Arthroplasty*, vol. 36, no. 2, pp. 752–766, 2021.

[7] D. Y. Kim, Y.-M. Lee, K.-H. Park et al., "Clostridium difficile infection after orthopedic surgery: incidence, associated factors, and impact on outcome," *American Journal of Infection Control*, vol. 50, pp. 72–76, 2022.

[8] R. Ma, J. He, B. Xu et al., "Nomogram prediction of surgical site infection of HIV-infected patients following orthopedic surgery: a retrospective study," *BMC Infectious Diseases*, vol. 20, no. 1, p. 896, 2020.

[9] M. Ren, W. Liang, Z. Wu, H. Zhao, and J. Wang, "Risk factors of surgical site infection in geriatric orthopedic surgery: a retrospective multicenter cohort study," *Geriatrics and Gerontology International*, vol. 19, no. 3, pp. 213–217, 2019.

[10] H. Liang, J. Huang, J. Tong, and J. Wang, "Application of rapid rehabilitation nursing in thoracic surgery nursing," *Journal of healthcare engineering*, vol. 2021, Article ID 6351170, 9 pages, 2021.

[11] L. Rao, X. Liu, L. Yu, and H. Xiao, "Effect of nursing intervention to guide early postoperative activities on rapid rehabilitation of patients undergoing abdominal surgery," *Medicine*, vol. 100, no. 12, Article ID e24776, 2021.

[12] W. Shao, H. Wang, Q. Chen, W. Zhao, Y. Gu, and G. Feng, "Enhanced recovery after surgery nursing program, a protective factor for stoma-related complications in patients with low rectal cancer," *BMC Surgery*, vol. 20, no. 1, p. 316, 2020.

[13] Y. Jin, C. Li, X. Zhang, Y. Jin, L. Yi, and J. Cui, "Effect of FOCUS-PDCA procedure on improving self-care ability of patients undergoing colostomy for rectal câncer," *Revista da Escola de Enfermagem da USP*, vol. 55, 2021.

[14] X. Kong, X. Zhu, Y. Zhang, and J. Wu, "The application of plan, do, check, act (PDCA) quality management in reducing nosocomial infections in endoscopy rooms: it does work," *International Journal of Clinical Practice*, vol. 75, no. 8, Article ID e14351, 2021.

[15] Q. Jiang, D. Zhang, J. Majaw et al., "Minimization of the perianal infection rate of hematological malignancies with agranulocytosis by quality control circle activity and patient-hospital-student win-win concept," *Journal of International Medical Research*, vol. 46, no. 6, pp. 2338–2345, 2018.

[16] Y. Xu, Y. Hu, J. Xu, and M. Liu, "Study on the application of tracking methodology and PDCA circulation management in quality control of hospital infection management," *Panminerva Medica*, vol. 32, 2021.

[17] A. Demirel, "Improvement of hand hygiene compliance in a private hospital using the Plan-Do-Check-Act (PDCA) method," *Pakistan Journal of Medical Sciences*, vol. 35, no. 3, pp. 721–725, 2019.

[18] Y. Hu, S. Pan, X. Zhao, W. Guo, M. He, and Q. Guo, "Value and clinical application of orthopedic metal artifact reduction

algorithm in CT scans after orthopedic metal implantation," *Korean Journal of Radiology*, vol. 18, no. 3, pp. 526–535, 2017.

[19] Y.-X. Zhao, H.-N. Suo, Z.-W. Zuo, Y.-j. Xu, and J. Chang, "A comparison of the image quality and radiation dose with routine computed tomography and the latest gemstone spectral imaging combination of different scanning protocols in computed tomography angiography of the kidney," *Journal of Computer Assisted Tomography*, vol. 41, no. 2, pp. 263–270, 2017.

[20] Y. Wan, H. Guo, L. Ji, Z. Li, and J. Gao, "Gemstone spectral imaging dual-energy computed tomography for differentiation of renal cell carcinoma and minimal-fat renal angiomyolipoma," *Journal of Cancer Research and Therapeutics*, vol. 14, no. Supplement, pp. S394–S399, 2018.

[21] Y. Shinohara, M. Sakamoto, K. Kuya et al., "Carotid plaque evaluation using gemstone spectral imaging: comparison with magnetic resonance angiography," *Journal of Stroke and Cerebrovascular Diseases*, vol. 26, no. 7, pp. 1535–1540, 2017.

[22] T. Fang, W. Deng, M. W.-M. Law et al., "Comparison of image quality and radiation exposure between conventional imaging and gemstone spectral imaging in abdominal CT examination," *British Journal of Radiology*, vol. 91, no. 1088, Article ID 20170448, 2018.

[23] X.-H. Chen, K. Ren, P. Liang, Y. Chai, K.-S. Chen, and J.-B. Gao, "Spectral computed tomography in advanced gastric cancer: can iodine concentration non-invasively assess angiogenesis?" *World Journal of Gastroenterology*, vol. 23, no. 9, pp. 1666–1675, 2017.

[24] F. Yang, J. Dong, X. Wang, X. Fu, and T. Zhang, "Non-small cell lung cancer: spectral computed tomography quantitative parameters for preoperative diagnosis of metastatic lymph nodes," *European Journal of Radiology*, vol. 89, pp. 129–135, 2017.

[25] L. Li, Y. Zhao, D. Luo et al., "Diagnostic value of single-source dual-energy spectral computed tomography in differentiating parotid gland tumors: initial results," *Quantitative Imaging in Medicine and Surgery*, vol. 8, no. 6, pp. 588–596, 2018.

[26] V. Dunet, M. Bernasconi, S. D. Hajdu, R. A. Meuli, R. T. Daniel, and J.-B. Zerlauth, "Impact of metal artifact reduction software on image quality of gemstone spectral imaging dual-energy cerebral CT angiography after intracranial aneurysm clipping," *Neuroradiology*, vol. 59, no. 9, pp. 845–852, 2017.

[27] L. Li, S.-N. Cheng, Y.-F. Zhao, X.-Y. Wang, D.-H. Luo, and Y. Wang, "Diagnostic accuracy of single-source dual-energy computed tomography and ultrasonography for detection of lateral cervical lymph node metastases of papillary thyroid carcinoma," *Journal of Thoracic Disease*, vol. 11, no. 12, pp. 5032–5041, 2019.

[28] Y. Wei, M. Xu, W. Wang et al., "Effect analysis of Plan-do-check-act cycle method applied in nursing management of disinfection supply room," *Panminerva Medica*, vol. 64, no. 1, 2022.

[29] G. Hua and Q. Wang, "Analysis of the application value of PDCA circulation in nursing management of disinfection and supply room," *Minerva Surgery*, vol. 42, 2021.

[30] I. Omar, M. Shirazy, M. Omar, and A. Chaari, "Controlling nosocomial infection in adult intensive treatment unit: a quality improvement project," *The International Journal of Risk and Safety in Medicine*, vol. 31, no. 4, pp. 1–7, 2020.

Hindawi
Contrast Media & Molecular Imaging
Volume 2022, Article ID 3224939, 15 pages
https://doi.org/10.1155/2022/3224939

Review Article

IoT-Based Wearable Devices for Patients Suffering from Alzheimer Disease

Waleed Salehi,[1] **Gaurav Gupta**,[1] **Surbhi Bhatia**,[2] **Deepika Koundal**,[3] **Arwa Mashat**,[4] **and Assaye Belay**[5]

[1]*Yogananda School of Artificial Intelligence Computer and Data Sciences, Shoolini University, Bajhol Solan 173229, HP, India*
[2]*Department of Information Systems, College of Computer Science and Information Technology, King Faisal University, Al Hasa, Saudi Arabia*
[3]*Department of Systemics, School of Computer Science, University of Petroleum & Energy Studies, Dehradun, Uttrakhand, India*
[4]*Faculty of Computing and Information Technology, King Abdulaziz University, Rabigh, Saudi Arabia*
[5]*Department of Statistics, Mizan-Tepi University, Ethiopia*

Correspondence should be addressed to Assaye Belay; abstat23@gmail.com

Received 24 December 2021; Accepted 26 January 2022; Published 22 April 2022

Academic Editor: M Pallikonda Rajasekaran

The disorder of Alzheimer's (AD) is defined as a gradual deterioration of cognitive functions, such as the failure of spatial cognition and short-term memory. Besides difficulties in memory, a person with this disease encounters visual processing difficulties and even awareness and identifying of their beloved ones. Nowadays, recent technologies made this possible to connect everything that exists around us on Earth through the Internet, this is what the Internet of Things (IoT) made possible which can capture and save a massive amount of data that are considered very important and useful information which then can be valuable in training of the various state-of-the-art machine and deep learning algorithms. Assistive mobile health applications and IoT-based wearable devices are helping and supporting the ongoing health screening of a patient with AD. In the early stages of AD, the wearable devices and IoT approach aim to keep AD patients mentally active in all of life's daily activities, independent from their caregivers or any family member of the patient. These technological solutions have great potential in improving the quality of life of an AD patient as this helps to reduce pressure on healthcare and to minimize the operational cost. The purpose of this study is to explore the State-of-the-Art wearable technologies for people with AD. Significance, challenges, and limitations that arise and what will be the future of these technological solutions and their acceptance. Therefore, this study also provides the challenges and gaps in the current literature review and future directions for other researchers working in the area of developing wearable devices.

1. Introduction

The growing prevalence of dementia presents a major challenge to global health at different levels. Hurd and colleagues (2013) estimated at the financial level that dementia and, specifically, AD are among the diseases that are most expensive for the western region with a $160 billion per year price tag [1, 2]. Alzheimer's is a kind of disease that typically and slowly progresses in three main stages such as early, middle, and moderate or late [3]. Since this disease is affecting people in several different ways, so in that case, every affected person may experience different symptoms or go through the stages differently [3], as in Table 1 a short description of the activities that can be affected by AD is given.

A rapid digital revolution is taking place in the twenty-first century [4]. The Internet of Things is a buzz term in recent years very commonly called IoT. It is a relatively new idea that allows real-world physical devices or entities to be managed remotely via the Internet. We are witnessing the IoT applications it is used and how it serves humans in many aspects of life; nowadays, the applications such as remote controlling of smart homes, natural disasters alerting, health monitoring of patients, and location tracking. [5]. IoT generally refers to anything that can communicate and

Table 1: Three different stages of AD with their impacts.

SN	AD stages	Things causes by AD
1	Early stage	Having difficulty in speech, memory, work, and social skills or settings. Misplacing or losing a valuable object. Logical and judgmental thinking.
2	Mild stage	Not able to recall some basic information about their phone number, address, and the school they graduated from. Having difficulty in speech, memory, social skills, logical thinking, and senses.
3	Moderate stage	Losing the ability such as dressing themselves where in this stage the patient will be fully dependent on someone such as a caregiver or family member. Require assistance every time, having difficulties in communication, movement, and some other daily activities.

exchange data with other devices across a network infrastructure. Here the objects or things can be any embedded systems or sensors that connect with other systems to capture data such as the heart rate of a patient, location information, image recognition, and movements.

The wearable device is one of the major driving technologies of the IoT. Similarly, in entertainment, industrial logistics, sports, and many other fields, wearable computing has implemented and introduced new techniques, more productive processes, and creative goods [6]. However, no other sector, with interests ranging from well-being and prevention of disease to chronic patient care and various other disciplines in medical, anticipates and incorporates wearable technology as widely as healthcare [7] since a wearable IoT gadget combined with a mobile application could be a viable solution for healthcare services, acting as a patient's intelligent personal assistant.

Wearable assistive technology is the term that is used to define systems or devices that enable individuals with physical or communication and cognitive disabilities to improve the quality and capabilities of their life. The advent of wearable technology in recent years has motivated and allowed professionals in the healthcare sector to look beyond the clinic or office to help in identifying and detecting health risks, tracking or monitoring the development of diseases, for instance, patient with Alzheimer Disease (AD), and offer therapy or guidance [7].

The use of wearable devices has been adopted by many people, but we still need to involve IoT with more advanced AI-based techniques [8] for improving the quality of people with Alzheimer's [9].

In this study, we focus on wearable devices used specifically by AD patients that can also at the same time help their caregivers. The reason this study focuses on wearable devices is that rising healthcare expenses are a major concern; as we defined in the above section, wearable devices are sensors that can be used for remotely collecting health-related data. An example, a sensor passively collecting data on a person's physical activity is an accelerometer incorporated in the form of a wristband [10]. These devices are designed to monitor continually and convey data in real-time or on an ad hoc basis, and they have the potential to become an important component of the future of healthcare research development.

Medical imagings such as Positron Emission Tomography (PET), Magnetic Resonance Imaging (MRI) and so forth have shown a promising earlier detection and prediction of the disease. Currently, due to invasive nature and the cost of these tests, they are limited to research applications [11]. These constraints make it impossible to test an individual repeatedly and frequently, especially in the early stages of presymptomatic disease [12]. IoT-based sensors and wearable technologies have the potential to overcome these constraints, and their use in AD diagnosis has piqued attention [13]. These technologies provide unique services in an economical fashion due to the following reasons [11]:

(i) Use of such technology by a large number of people
(ii) Development and the variety of onboard sensors
(iii) This is the nature of such type of sensors, which are specially designed to investigate physical and cognitive symptoms
(iv) Although these gadgets are increasingly used by wide sectors of the population, this can have a major impact in healthcare system load, and to extremely lower the burden to the caregiver of a patient.

This study provides a concise study of IoT-based devices such as wearable assistive devices for AD patients and the simple approach to wearable device applications in healthcare for improving the quality of life of AD patients and to evaluate the previous research effort to demonstrate the potential use of these technological solutions for people suffering from the disease. Another main purpose of the study is to provide information on how these wearable devices can be used, what are the different functionalities they can offer, how can they help the patient and their caregivers. A wide range of advantages of using IoT-based sensors under various approaches is discussed. Furthermore, it is required to be pointed out that the use of these devices, however, shown challenges about durability, acceptability, ease of use. The following research questions are used as guidelines a guideline:

(i) What drives the adoption of wearable devices?
(ii) How effective are the applications of IoT-based wearable devices in patients with Alzheimer's disease?
(iii) Can these technological solutions ease the burden of caregivers of AD patients in the future?
(iv) Do these technological solutions with the use of some algorithms such as machine and deep learning help in more detection and monitoring of AD?

The organization of this study is as follows: an introduction and the research questions guidelines are given in the first section. The second section described the IoT and wearable devices concisely. Afterward, the literature review is done on various recent works in the field of IoT-based wearable devices for AD patients. Lastly, the result and discussion are done and followed by the conclusion section, and future scopes are suggested.

2. Materials and Methods

For achieving the research objectives, a review approach was used on the articles that are published in the area of wearables and IoT technologies and their applicability in elderly Alzheimer's patients. The study and process of targeting the papers are illustrated in Figure 1. Three large digital databases were chosen and searched to improve the odds of getting the best search results. In accordance with previous research studies [14, 15], researchers should always avoid scanning a single database for the literature in a review study; not a single database is likely to include all relevant papers; hence, supplemental searches are required [16].

2.1. Criteria for Inclusion

(i) Papers are published through a conference or a journal, and the text is written in the English language

(ii) The primary aim comes in various technological solutions in healthcare, such as devices, applications, algorithms, and methods

(iii) The technological solutions that are IoT-based and focused for Alzheimer's patients are considered

The case-control of these studies covers diagnosis, monitoring, adherence of medication, and tracking of AD patients. A flowchart is constructed for the identification of articles as follows in Figure 1.

In Figure 1, during the research and obtaining of papers, we have come across 95 papers that are collected from the various scientific sources. After that, we categorized papers in two groups important and not important based on each paper's abstract and conclusion sections, and the irrelevant and duplicate records of 71 have not been considered further. On the remaining research papers, a full-text reading of the paper is done, and 14 papers are excluded in this stage; finally a total number of 10 research-relevant articles are put together for further study.

3. Literature Review

Identifying and meeting the needs of people with cognitive disabilities is crucial for anyone, but it is particularly necessary for those who live alone, with the increased number of aged population around the world [17], the less support and stand from the family members, and a higher cost of formal look after of the patient. Such needs can be addressed by IoT-based wearable systems and enabling technologies and have the potential to do better far beyond them. Figure 2 gives a view of how these devices have emerged over the past years.

In recent years, various IoT-based and wearable assistive devices are developed and carried out for patients with AD. These devices are implemented and designed in different forms such as locating systems, tracking, and monitoring of the patients. The main aim behind all this is to ease the burden of the caregivers and help the patients and provide a convenient life for them. Ahmed and Al-Neami et al. [19] designed and developed an electronic device known as a smart biomedical assistant in which the aim is to provide continual monitoring of the AD patient's stability state that has the capabilities of reminding the patient automatically of the time of medication, showing the location on the map, and another very important feature that is a button that calls for an emergency case. The device is designed in such a way that one is wearable for the patient and the other one is used by the caregiver that is an IoT platform application that allows communication between the patient and the caregiver. The wearable device contains a global positioning sensor (GPS), motion unit sensor, sensor, and microcontrollers for heart rate and a display of LCD. Roopaei et al. [20] developed IoT-based wearable assistive glasses, and a deep learning approach is used and embedded for the AD patients. This ambient intelligence is based on facial perception for patients with memory difficulties. These face reminder glasses try to assist the patient in recognizing and identifying the people in a patient's family, colleagues', friends, and attempt to help the patient and improve their social skills via a visual understanding of various facial images of the patient's friends, family, and colleagues. For extracting the features of various facial images, the deep learning model is used, and an embedded personalized database is used for matching the facial images. Approximately 90.68% accuracy is achieved by the framework on a labeled face in the Wild dataset for verification of the faces. In another study, Takpoe et al. [21] presented a cost-effective solution of an intelligent assistive health system that can help elderly AD patients in medication adherence. They developed this intelligent assistive health system to give an audiovisual alert to the patients with memory loss disability to achieve medication adherence so that the users can take their right medication doses at the right time through the Liquid Crystal Display (LCD) being used in the system. Furthermore, the physician keyed in the prescriptions of drugs, and nonvolatile memory is used in the system to store the medication schedule. They also used a Subscriber Identity Module (SIM) and an integrated GSM modem so that the system can automatically send an alert message to the physician through an SMS in any case of nonadherences. Similar to the above-proposed system in this study, Oliveira et al. [22] developed an environment aware system in which this device is a wearable waist belt that is used for monitoring the environmental humidity and temperature, the location of the patient using GPS, and the movements of the patients as well. The devices are designed in such a way to send the information to the server and also to the caregiver through an SMS so that the caregiver can get access using an android application which is developed for the smartphone. Thus, the system serves as surveillance over the patient's status. Another monitoring device is designed and developed by Cazangiu et al. [23] for patients suffering from Alzheimer's to monitor their health parameters. A single sensor is used

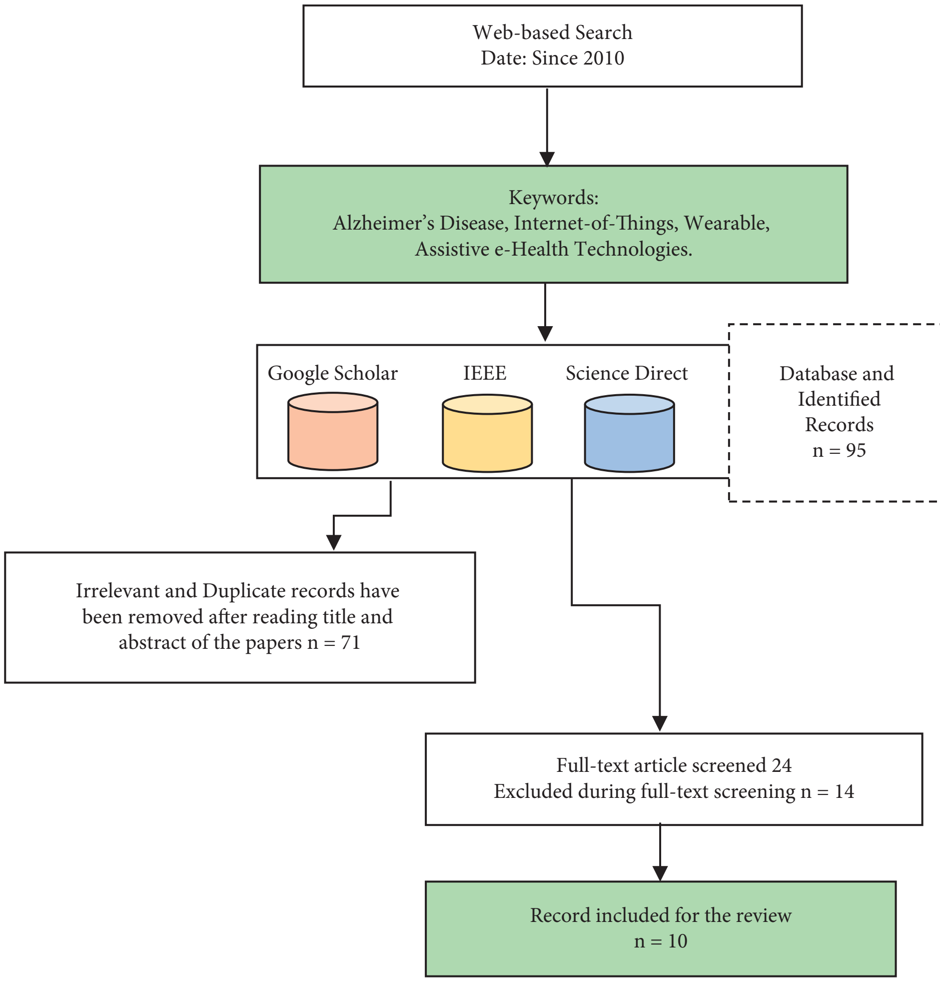

Figure 1: study and identification of relevant articles flowchart.

for environmental temperature, hearth pulse, and atmospheric pressure, it also generates an output in a screen to display all those health parameters that are used in the system. Furthermore, using a Bluetooth connection, the parameters can be displayed in a smartphone. Zellefrow et al. [24] presented a wearable solution that monitors and tracks the AD patient known as Halcyon along with a connected assistive indoor platform, which aids AD patients during the daily routine. The system contains four basic components: instruction assignments, detection of patient's engagement with any home appliances, instruction delivery, and tracking of the patient movement, and also, the system generates the patient's activities to the caregiver as a timed log. This system is customizable and prerecorded with the instruction given by the respective caregiver on how to do the routine activities. In this study, the authors Omar et al. [25] designed and developed an integrated autonomous system that includes all the necessary features, unlike the previews papers the features are included such as a reminder for medicine taking, monitoring the heart condition, constantly monitoring of the patient, and finding lost patient's items. In a single system, all the features are integrated, and second, to utilize those features efficiently, a mobile application was also developed. Hegde et al. [26] proposed and developed an autonomous, embedded low-cost wearable device using a concept called geofencing and GPS for tracking the real-time location that can help a caretaker in tracking the AD patient. The system then sends a text message real-time update to the caregiver or family member's mobile number. The alert is sent to the caregiver or a family member when the patient moves out of a safe area and following to that an update of such a situation even is sent after every 5 minutes. Gacem et al. [27] developed a pair of smart glasses that is equipped with a screen of Augmented Reality (AR) that is utilized in this study for performing the basic functions of a caretaker or caregiver and provide the features to the patients which can reduce the caregiving costs and increase the independence of the patient. The main features are the location and detection of misplaced objects and to help out the patient's location where they have been seen last, identifying and showing the relatives and friends names on the AR screen, monitoring the patient all the time if the patient lost his or her way, and the AR screen displays the way home and at the same time, the caregiver receives the location of the patient by an SMS, also in case the patient removes the glasses, detecting and predicting the cause of removal, and giving notification to the caregiver the patient's location and its predicted cause. Chen et al. [28] similar to above cited work

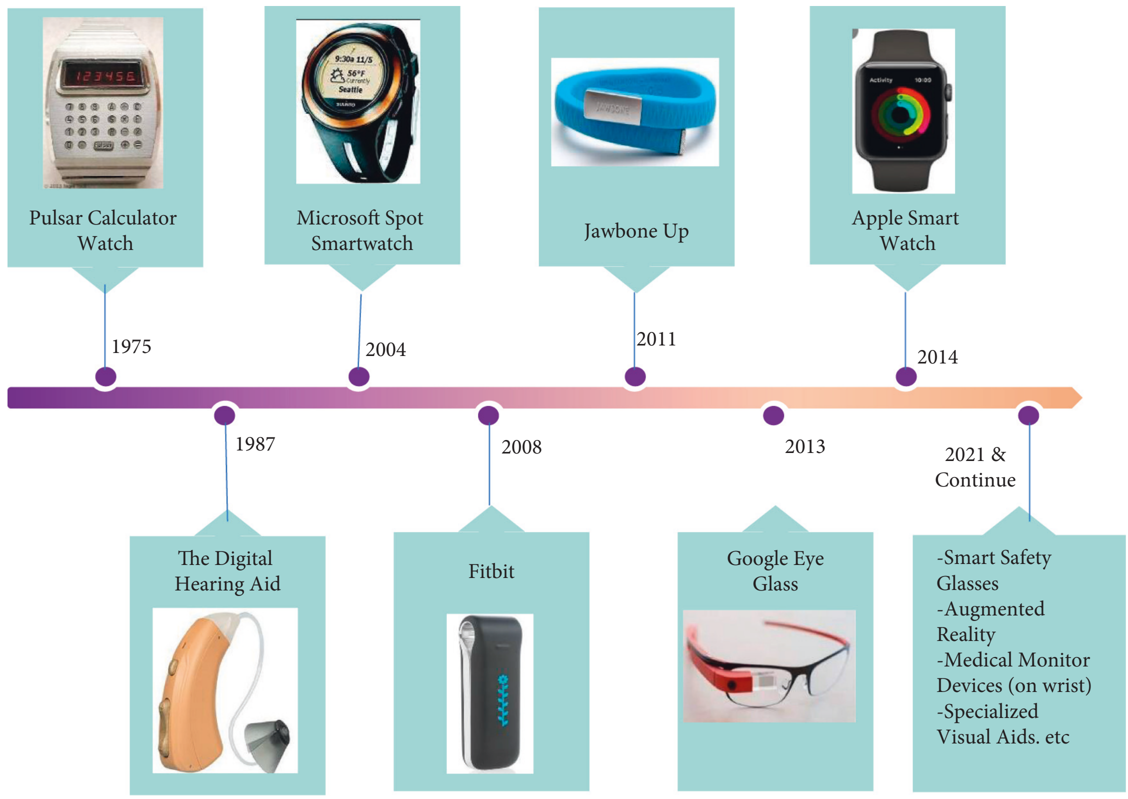

FIGURE 2: A look from 1975 to 2021 wearable technologies timeline [18].

in this study also utilized smart glasses; they have proposed a warning system for behavioral difference for dementia warning and early depression. The system is made of three parts smart glasses, cloud-based platform, and an indoor trilateration position that is BLE-based. This wearable device can be useful in recognizing daily movements such as running, walking, standing, lying down, sitting, and many other movements, and these parameters are obtained by a microelectromechanical system sensor (MEMS).

As we reviewed much-related research work, we have seen that none of them have developed a final wearable product to the market as shown in Table 2 Since some of the paper proposed models, some have developed prototypes to test the proposed work.

Sensors are one of the major and significant components of the IoT-based devices and wearables, and there are many sensors available in the market that are designed for the different specific purposes as detailed in Table 3 that depict what are the different types of sensors used in reviewed wearable devices.

The form factor is one of the main parts when it comes to wearables; as these devices are to be worn by AD patients considerable attention is required to build the wearable devices that will be acceptable and user friendly to the users. As shown in Table 4 we can observe that much work has been done, but when it comes to their design aspects, they are all facing the similar issues in which many of them test the prototype and get not so good feedback about the size, shape, design, and so on.

Table 5 shows various wearable devices with respect to the use of location tracking technology.

Table 6 shows different services and features provided by each wearable device.

When we talk about IoT that is where another important thing come to exist, that is the connectivity of various devices, how they communicate, send, and receive data, and most importantly, are these wearables integrated with some kinds of mobile application, Web-based application, Cloud, etc., in which these are the things that give more features so the patient and, most importantly, their caregivers and the doctor can benefit from them in assisting the patients. The user interface of each device is compared in Table 7.

Table 8 gives an overview of the contrast between various studied wearable devices, with respect to their availability, cost, sensor, IoT, connection, and their form factor. And in Table 9 a complete comparison has been made based on the various features with respect to each device.

Based on various features of each wearable device, a comparison chart is made in Figure 3.

4. Basics and Background: IoT Applications in Healthcare Industry

To begin with this new era of technology which is the IoT, first we need to understand the basic backbone of this technology that is Wireless Sensor Networks (WSN). The different aspects of IoT-based devices in digital health are described in Figure 4.

Table 2: Pricing of wearable devices and their availability.

SN	Wearable device	Cost	Availability
1	Smart biomedical system	N/A	N/A
2	Smart glasses	Cost-effective	N/A
3	Smart assistive mhealth system		N/A
4	Environment aware system	N/A	N/A
5	AD-patient monitoring device	40$	N/A
6	Halcyon device	Cost-effective	N/A
7	Intelligent assistive tool	N/A	N/A
8	Autonomous tracking device	Prototype cost □750 or $10	N/A
9	Smart assistive glasses	N/A	N/A
10	Smart glasses	N/A	N/A

Table 3: Sensors used in wearable devices.

SN	Wearable device	Used sensors
1	Smart biomedical system	Gyroscope, accelerometer
2	Smart glasses	NO
3	Smart assistive mhealth system	NO
4	Environment aware system	3axis accelerometer, HTU21D
5	AD-patient monitoring device	BPM sensor, MPL3115A2 pressure and altitude sensor, ADC, DFRobot heart-rate sensor, bluetooth module
6	Halcyon device	Accelerometer
7	Intelligent assistive tool	Pulse sensor
8	Autonomous tracking device	No
9	Smart assistive glasses	Accelerometer, gyroscope sensor
10	Smart glasses	Microelectromechanical, systems sensor, accelerometers

Table 4: Feature comparison of the wearable devices.

SN	Wearable device	Design aspects
1	Smart biomedical system	Implemented and designed with low-cost components but no miniaturize to wearable device
2	Smart glasses	Proposed but not developed the wearable device
3	Smart assistive mhealth system	Implemented and designed components but no miniaturize to wearable device
4	Environment aware system	Wearable waist-bag device
5	AD-patient monitoring device	Not wearable, autodesk FUSION 360 and a 3D printer is used for designing the case and printing it.
6	Halcyon device	Tag is used for detection of patient's engagement with home appliances
7	Intelligent assistive tool	The system built as a prototype
8	Autonomous tracking device	Design approached
9	Smart assistive glasses	Prototype designed
10	Smart glasses	Prototype designed

Table 5: Wearable device's location tracking.

SN	Wearable device	Location tracking
1	Smart biomedical system	GPS
2	Smart glasses	No
3	Smart assistive mhealth system	No
4	Environment aware system	GPS
5	AD-patient monitoring device	No
6	Halcyon device	Using the bluetooth tags
7	Intelligent assistive tool	GPS
8	Autonomous tracking device	GPS, geo-fencing
9	Smart assistive glasses	GPS, geo-fencing
10	Smart glasses	BLE gateway

Table 6: Various services provided by wearable devices.

SN	Wearable device	Service 1	Service 2	Service 3	Service 4	Service 5
1	Smart biomedical system	Clock monitoring	Location on the map	Medication time reminder	Emergency call button	Mobile app
2	Smart glasses	Facial perception model is being used in recognizing a person and to extract the features of facial accordingly	Micro database is used for recording the ground truth of facial features of related people around the patient	Matching metric is then used for comparing facial features from a real-time feature		
3	Smart assistive mHealth system	Audiovisual alert	Medication schedule is stored in the nonvolatile memory	e liquid crystal display (LCD) shows the medicine to be taken	Sound effect to get the attention	Sends message to the physician
4	Environment aware system	GPS localization	Environment monitoring	Activity	Fall detection	Mobile app service
5	AD-patient monitoring device	Environmental temperature				
	Atmospheric pressure	Heart pulse	Small screen display	Mobile app service		
6	Halcyon device	Detecting the patient's engagement with home appliances	Instruction assignment	Instruction delivery	Movement tracking	Mobile app service
7	Intelligent assistive tool	Heart rate monitoring	Reminder for taking medicine	Monitoring location of patient's	Finding lost items	Mobile app service
8	Autonomous tracking device	Real-time location tracking	Text message can be sent to the mobile number of caregivers	Alert is sent whenever the patient moves		
9	Smart assistive glasses	Location detection of misplaced objects	Monitoring and guiding the patient for their last seen location	Identification and display of the names of relatives, friends on the AR display	Sending patient location to caregiver simultaneously through SMS	Predicting if patient removed the wearable device and what is the cause
10	Smart glasses	Recognize daily movements				Web-based frontend server used to display

Table 7: The user interface of wearable device.

SN	Wearable device	Mobile supported OS	Remarks	Connection
1	Smart biomedical system	Mobile app android	Null	Wi-Fi, Bluetooth, GSM
2	Smart glasses	No	Wearable IoT with complex artificial perception embedding for AD patients	N/A
3	Smart assistive mhealth system	No	For optimal performance, the system can be further miniaturized into a wearable device	GSM, SIM (SMS is used to send message)
4	Environment aware system	Android application	To increase the acceptance, rate the authors stated that the proposed system can be decreased to a smaller size due to the feedback was uncomfortable by many of the patients.	DFRobot GPS/GPRS/GSM shield V3.0
5	AD-patient monitoring device	Software was written into AppInventor	It is suggested by the authors that by using higher performance sensors it can be upgraded, and for reducing the device size a PCB is needed.	Bluetooth

Table 7: Continued.

SN	Wearable device	Mobile supported OS	Remarks	Connection
6	Halcyon device	Full-fledged Android 4.2.2 OS is running on the "XTouch-Wave". Android mobile app	Since there are chances that a patient might takes of the wearable like watch and not wear it again that is where halcyon device can be effective solution	Near field communication (NFC), bluetooth, and RFID (radio frequency identifier-cation)
7	Intelligent assistive tool	Mobile app	As future work, it is suggested a few more features may be added and developing the system into a wearable device to provide more patient's medical details.	GPS-WiFi
8	Autonomous tracking device	Mobile text on number	In the future, the authors mentioned that more features can be added that are lacked now and improve the system.	GSM
9	Smart assistive glasses	No	The smart glasses were developed as a prototype and suggested to be a practical solution in the future that can help AD patients.	Wi-Fi, bluetooth
10	Smart glasses	Web-based frontend server	Null	BLE (bluetooth low energy) gateway

Table 8: Contrasting between the surveyed wearable devices.

SN	Wearable device	Availability	Cost	Sensor used	IoT	Connection via	Design aspect
1	Smart biomedical system	N/A	N/A	Gyroscope, accelerometer	Yes	GSM, W	Implemented and designed with low-cost components but no miniaturize to wearable device
2	Smart glasses	N/A	N/A	No	Yes	Null	Wearable glasses
3	Smart assistive mhealth system	N/A	N/A	No	No	GSM, SIM	Proposed but not developed the wearable device
4	Environment aware system	N/A	N/A	3axis accelerometerHTU21D	Yes	DFRobot GPS/GPRS/GSM shield V3.0	Wearable waist-bag device
5	AD-patient monitoring device	N/A	40$	BPM sensor, MPL311 A2 pressure and altitude sensor, ADC, DFRobot heart-rate sensor, bluetooth module	Yes	Bluetooth	Not wearable, autodesk FUSION 360 and a 3D printer is used for designing the case and printing it.
6	Halcyon device	N/A	Cost-effective	Accelerometer	Yes	Near field communication (NFC), bluetooth, and RFID (radio frequency Identifi-cation)	Tag is used for detection of patient's engagement with home appliances
7	Intelligent assistive tool	N/A	N/A	Pulse sensor	Yes	GSM	The system built as a prototype
8	Autonomous tracking device	N/A	Prototype cost □750 or $10	No	Yes	GSM	Designed approached
9	Smart assistive glasses	N/A	N/A	Accelerometer, gyroscope sensor	Yes	Wi-Fi, bluetooth	N/A
10	Smart glasses	N/A		Microelectromechanical, systems sensor, accelerometers	Yes	BLE (bluetooth low energy) gateway	Prototype designed

4.1. Wireless Sensor Network. Wireless Sensor Networks (WSNs) have emerged as a result of recent advancements and developments in wireless networks and electronics. WSNs have been hailed as one of the most transformative technologies in recent years that can change the future. WSN is a type of network that consists of interconnected devices, which are commonly known as nodes used to wirelessly communicate with each other to collect data of their environment [29]. Small and low battery-powered with minimal computing and radio communication capabilities make

Table 9: Comparison of various wearable devices based on their features.

Product	Design	Features						
		Alert/ reminder	Location tracking	Emergency call	Display	Connectivity	Sensor	Mobile app
Smart biomedical system	Wearable embedded	Yes	Yes	Yes	Yes	Wi-Fi, Bluetooth, GSM	Gyroscope, accelerometer	Yes
Smart glasses	Wearable	Yes	No	No	Yes	No	NO	No
Smart assistive mhealth system	System design	Yes	No	Yes	Yes	GSM, SIM card	No	No
Environment aware system	Waist wearable belt	Yes	Yes	Yes	No	Wi-Fi, GSM	3axis accelerometer, HTU21D	Yes
AD-patient monitoring device	Arduino nano-based device	Yes	Yes	No	Yes	Bluetooth	BPM sensor, pressure and environmental temperature sensor	Yes
Halcyon device	Wearable	Yes	Yes	No	No	Wi-Fi, SIM card, GSM, bluetooth	Null	Yes
Intelligent assistive tool	Conceptual design	Yes	Yes	No	Yes	Wi-Fi, GSM	Pulse sensor	Yes
Autonomous tracking device	Wearable embedded	Yes	Yes	No	Yes	GSM	Yes	Yes
Smart assistive glasses	Wearable	Yes	Yes	No	Yes	Wi-Fi, bluetooth	Accelerometer and gyroscope sensor	Yes
Smart glasses	Wearable	Yes	Yes	No	No	BLE (bluetooth low energy) gateway	Microelectromechanical systems sensor, accelerometers	No but display in server

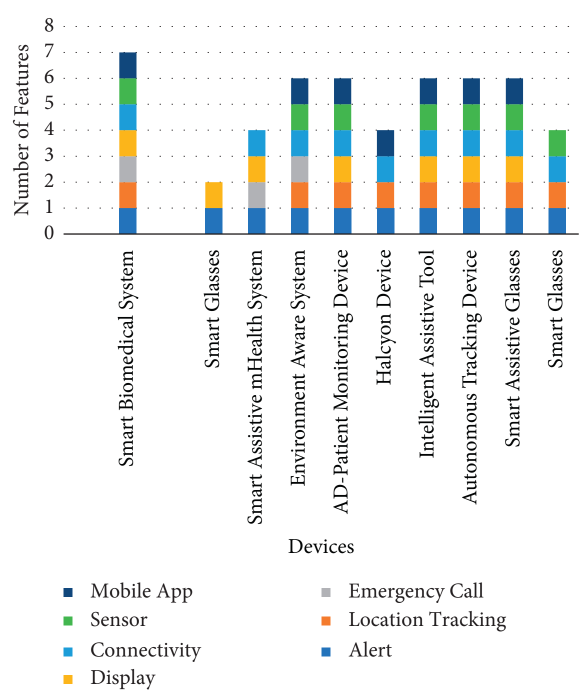

Figure 3: Feature-based comparison of wearable devices.

up these networks. This technology has been rapidly developing and plays an important role in different domains such as environmental, industrial operations, infrastructures, and healthcare.

WSN advancements have opened new possibilities in healthcare systems. Medical gadgets have been infiltrated by sensor-based technology, which has replaced hundreds of wired, connected devices in hospitals [30]. As we see the rapid

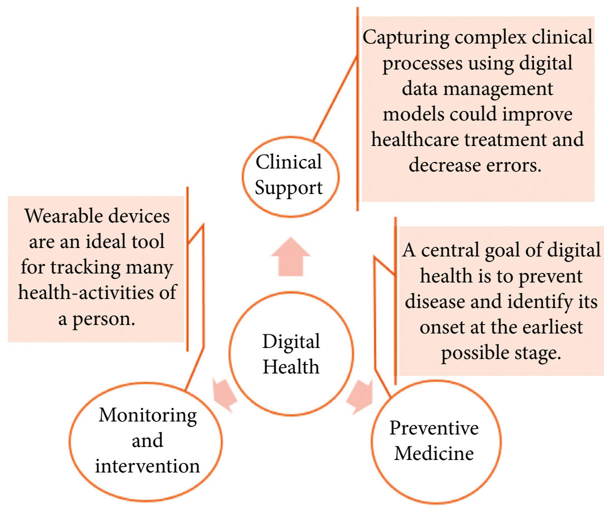

Figure 4: Different aspects in digital health.

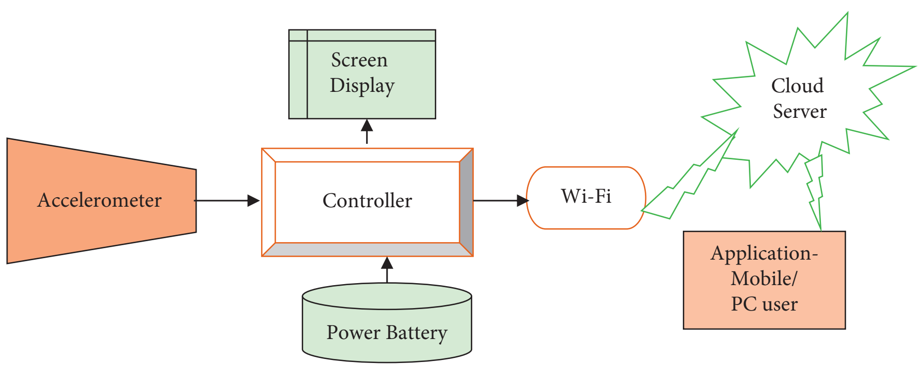

Figure 5: A typical intelligent wearable system block diagram.

Table 10: The basic components of an intelligent wearable device.

Component name	Description
Accelerometer	To keep track of all movements. The velocity and position of an accelerometer sensor are measured inertially [31]. It can detect inclination, tilt, and body orientation on three axes in most cases.
Power battery	Like any other electric devices, wearable devices also require battery power for the device to start functioning. Since wearables are expected to explode in popularity, and many semiconductor vendors are preparing for this by developing new level of battery-management technologies expressly for wearables [32].
Controller	Sensor network nodes and wearable devices are essentially small, attached devices. An analogue signal must be transformed into digital data before it can be broadcast over a wireless network or easily interfaced with other components of the wearable device. This job is done with something called controller or microcontroller that is attached to the wearable, and the main point here is every controller is consumed power so choosing a power efficient controller is the key [33].
Display	Wearable devices include everything from artificial heart monitors to fit bands that can track your daily steps. Many factors have aided this expansion [34], one of those factors is the liquid crystal display (LCD) panels, which enable high resolutions to be achieved even on tiny screens.
Internet	Wearables provide real-time user monitoring, any moment, and anywhere, in the digital-health ecosystem, enhancing care of patient and helping caregivers save time on their administrative works [35]. Wi-Fi plays a major role in wearables if we want to send the data to another system or connect to another platform like Cloud or mobile health application, and so on (The link between the cloud and wearable technology-compare the cloud, n.d).
Cloud computing	Data collection and analysis are at the heart of wearable technology and cloud computing is where one can store this data for further investigations and analysis [36]. Nowadays, cloud computing became an integral part of wearable technology and IoT-based devices [37]
Mobile application	Mobile applications are assistive technologies that are used in monitoring the health of an individual continuously, and these applications can be used in a variety of diseases, including AD (Sarkar and Lacusesta, 2019). There are various mobile health applications that have been developed over the past years for specific diseases like AD to assist and help the patient and their caregivers.

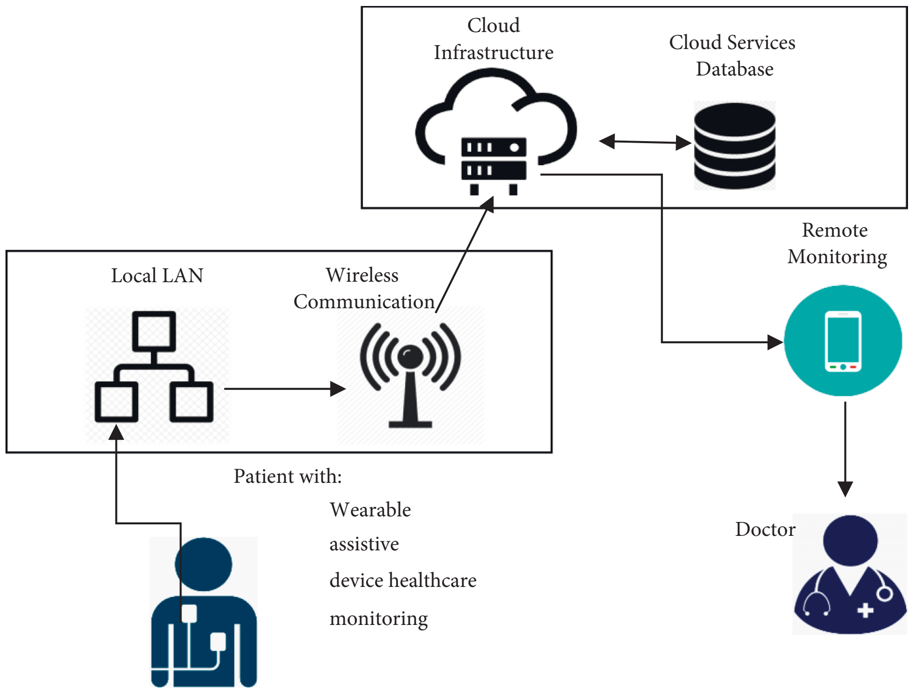

FIGURE 6: IoT and wearable device architecture.

TABLE 11: List of all the papers with their aims and their future scope and limitations.

Author's name and Ref	Title	Aim	Target stage	Future scope and limitation
(Ahmed and Al-Neami, 2020 [19]) Qayssar a et al.	Smart biomedical assisted system for AD patients	Wearable device and an IoT platform for the caregiver. Provide continual monitoring for AD patient's stability state. Capabilities are a reminder for medication time, location display on the map, emergency button call.	AD patient	—
(Roopaei et al., 2018 [20]) Mehdi et al.	Wearable IoT with complex artificial perception embedding for AD patients	IoT-based wearable glasses. To assist the patient in recognizing and identifying the people in a patient's family, colleagues, friends.	Memory-impaired (early stage)	—
(Temitope O. Takpor, Jimmy ademola, Segun I. Popoola, Joke A. Badejo, 2017) Temitope et al. [21]	Smart assistive system for adherence of medication for AD patients	An intelligent assistive system that can help elderly AD patients in medication adherence by an audiovisual alert and via an LCD to see the right medication at the right time.	Memory loss disability (Mild stage)	For optimal performance, the system can be further miniaturized into a wearable device
(Oliveira et al., 2014)Ana barreto et al. [22]	An environment aware system for AD patients	The aim of the waist-wearable belt device is to monitor the environment humidity and temperature, location and movement of the patient. The caregiver can receive information related to the patient.	Late stage	To increase the acceptance rate, the authors stated that the proposed system can be reduced to a smaller size owing to the feedback from many patients that they were uncomfortable to wear.

Table 11: Continued.

Author's name and Ref	Title	Aim	Target stage	Future scope and limitation
(Cazangiu et al., 2018) Teodor cazangiu et al. [23]	Monitoring device for AD patients	A single sensor for environmental temperature, heart pulse, and atmospheric pressure, and generating the output in a screen to display all those health parameters. And those parameters can be displayed in a smartphone using bluetooth.	Moderate stage	In the future, it is suggested by the authors that by using higher-performance sensors, it can be upgraded, and for reducing the device size a PCB is needed.
(Zellefrow et al, 2017) B.Zellefro et al. [24]	Assistive technology for AD patients-(halcyon)	A wearable smartwatch that is bluetooth-based can monitor and track AD patient along with a connected assistive indoor platform, which then can aid the AD patients during the daily routine.	Early stage	—
(Omar et al., 2019) Kazi Shahrukh Omar et al. [25]	An intelligent assistive tool for AD patients	Designed and developed an integrated autonomous system that includes features such as a reminder for taking medicine, heart condition monitoring, constant monitoring of the patients, and finding lost items of patients. For utilization of that feature, a mobile application is also developed.	Moderate stage	The system was built as a prototype and used in an academic environment and therefore, no evaluation study is done with real users. The module of the smart medicine box also has an issue that this cannot work when there is no Wi-Fi connectivity. As future work, it is suggested a few more features may be added and developed in the system of a wearable device to provide more patient's medical details.
(Hegde et al., 2019) Niharika Hegde et al. [26]	An autonomous lower cost tracking device for AD patients	A wearable device using a concept called geofencing and GPS for tracking the real-time location, which can help a caretaker in AD patient tracking has been developed.	Early and moderate stages	In the future, the authors mentioned that more features can be added that are lacking now and improve the system. The intended features to be added are logging of vital signs and monitoring, fall detection, communication in two ways with caregivers. The generated data from these can be used for analyzing and achieving the insights that are useful and can help in providing predictive and preemptive healthcare.
(Gacem et al, 2019) Mohamed ait Gacem et al. [27]	Smart assistive glasses for AD patients	Smart glasses are equipped with an AR screen to perform the basic functions of a caretaker. Features are location and detection of the misplaced object and help out the patient to locate what they have seen last, identifying, and showing the relatives and friends names on the screen, monitoring the patient all the time.	Early and moderate stages	The smart glasses were developed as a prototype and suggested to a practical solution in the future that can help AD patients.
(Chen et al, 2018)Wu-Lin Chen et al. [28]	Smart wearable glasses	Smart glasses is a warning system for behavioral difference for dementia warning and early depression.	Early stage	This wearable device can be useful in recognizing daily movements such as running, walking, standing, lying down, sitting, and many other movements.

growth of these technologies in recent years, we have witnessed a vast number of wireless devices has been adopted and integrated into the existing medical infrastructures.

4.2. Internet-of-Things. IoT refers to a network of linked devices that can use embedded sensors and communication protocols to collect and share data. In general, any kind of device that can connect to the network or Internet is considered to be part of the term called IoT [38]. For example, sensor systems, wearable health monitors, smart home security systems, smart factory equipment, connected appliances.

The difference between the IoT and WSN is all the sensors in an IoT system communicate their data straight to the Internet. A WSN, on the other hand, does not have a direct Internet connection. Rather, the numerous sensors are connected to a router or central node [39]. The data from the router or central node can then be routed as desired. Nowadays, IoT applications can serve in many areas of our lives, for example, alerting in natural disasters, remotely controlling smart homes, tracking of the location [5], and most importantly monitoring health. Even though WSNs and IoT technologies have grown in popularity and acceptance, there are still major risks attached such as limitations in terms of battery life, processing capacity, and bandwidth constraints. More importantly, security, any attacks on control, availability, and privacy can all be targets. Figure 5 described how digital technologies are used in the society and healthcare sector to enhance and improve the living quality of patients with different kinds of diseases [40, 41], delivering good healthcare services, more personalized and precise medicine, and clinical support.

4.3. Wearable Technology. Wearable devices are the next breakthrough in the world of technology, following the advent of smartphones. Wearable devices or wearable technology is a category of electronic devices that can be generally defined as devices that can be used to be worn externally as an embedded or accessory in the person's clothing or implanted in the person's body or even can be tattooed in the skin of the body [42]. These kinds of devices are usually used on a real-time basis to track the information. These devices contain motion sensors that are capable of taking day-to-day movement or activity snapshots and synchronizing that information with other devices such as laptops or mobiles [43], as shown in Table 10 a brief description of the basic components of an intelligent wearable device is given. Figure 5 depicts the various main components of a typical intelligent wearable system.

Wearable devices are an example of IoT, which is very useful and have been an integral part of the health and medical industry as shown in Figure 6. For instance, Smart Shirts {Formatting Citation} which are used for monitoring the well-being and health condition of a patient and send the information to the caregiver in a real-time manner. Wearable technologies are comprised of small [44, 45] embedded devices that are used to

(1) connect and interact with their environment using a variety of sensors,

(2) processing and storing the information, and

(3) transferring the data wirelessly to the desired destination for further analysis and processing.

Wearable devices are used to collect data about a person's health, such as

(1) Blood pressure

(2) Counted steps

(3) Burned Calories

(4) Time spends in exercise

(5) Physical strain [46].

5. Challenges and Limitations

Our review from the recent work identified the papers in which they proposed and developed assistive wearable technologies, and we have seen both basic and advanced devices, with their potential applications used for the care of AD patients in different ways and functionalities. Based on the review of literature in Section 3 of this study, the majority of the proposed assistive IoT-based tools focus on reducing the burden for the caregivers and services for individuals or elderly. Some of the developed systems or devices are also designed with detection mechanisms that are experimented with various methodologies of artificial intelligence (AI) such as classification algorithms, deep learning, and machine learning. It is obvious that these new AI-based techniques and algorithms can really impact and increase the capability of IoT-based wearable devices.

Some of the main limitations and advantages of this technological solution for Alzheimer's patients are listed and described below.

Advantages

(i) Advancement of social liability.
(ii) Increased patient's safeness.
(iii) Disability offsetting of AD patients.
(iv) Possibly declining treatment costs.
(v) Prolong the self-dependency of the patient at the residence.
(vi) Improved physical and psychological health of the patients.
(vii) Lastly, possible saving of money on expensive treatments for the community.

Major limitations:

(i) Deficiencies in the observance of cultural and social differences.

(ii) Lack of evidence on a clinical basis.

(iii) Primary financing is required.

(iv) Concerns regarding the privacy and security of the data.

There can be a negative reception risk by both caregivers and patient. A complete comparison of all the studied papers is put together in Table 11 with their future scope and limitations.

6. Conclusions and Future Trends

Wearable computing is changing the face of digital health in a variety of ways. First and foremost, these wearables are facilitating a shift away from the traditional IT-centralized systems for storage, processing, creation, and management of health-related data into a completely new model era, which is distributed data sharing with patients and the caretaker or the doctor. Second, the integration of wearables and IoT and the data they generate is leading us to use some of the powerful AI techniques for better treatments and automated diagnosis.

A personalized healthcare system is achievable using wearable computing technologies and enables information-sharing through distributed information environment. It also promotes the development of new health information and the development of more effective preventative measures. However, realizing the potential of wearable technologies and digital healthcare would contribute to numerous concurrent technology advancements.

This is an overview of the various technological solutions that are designed and developed for assistive wearable technologies by various researchers for patients suffering from Alzheimer's disease. The aim was to study the recent technological solutions and IoT-based wearable assistive devices accessible in the current time for helping the caregiver and assisting of the AD patients. Based on the current state of potential IoT and wearable applications, it is clear that the future healthcare technologies will rely substantially on the current research.

The limitations of the current research should be addressed in future research, and moreover, researchers could investigate how these IoT-based wearable devices are perceived by people. Similarly, more focus should be on the importance of their design characteristics such as shape, size and also functionalities to determine an effective, optimal, ease device for better usefulness. [47].

Data Availability

The data will be available on request.

Conflicts of Interest

The authors declare that there are no conflicts of interest regarding the publication of this article.

References

[1] M. D. Hurd, P. Martorell, A. Delavande, K. J. Mullen, and K. M. Langa, "Monetary costs of dementia in the United States," *New England Journal of Medicine*, vol. 368, no. 14, pp. 1326–1334, 2013.

[2] A. Wimo, L. Jönsson, J. Bond, M. Prince, and B. Winblad, "The worldwide economic impact of dementia 2010," *Alzheimer's and Dementia*, vol. 9, no. 1, pp. 1–11, 2013.

[3] G. Gupta, A. Gupta, P. Barura, V. Jaiswal, C. S. Engineering, and N. Delhi, *Mobile Health Applications and Android Toolkit for Alzheimer Patients , Caregivers and Doctors*, vol. 11, no. 1, pp. 199–205, 2019.

[4] M. Uppal, D. Gupta, S. Juneja, G. Dhiman, and S. Kautish, "Cloud-based fault prediction using IoT in office automation for improvisation of health of employees," *Journal of Healthcare Engineering*, vol. 2021, Article ID 8106467, 13 pages, 2021.

[5] S. Computer Society, "Institute of Electrical and Electronics Engineers," in *Proceedings of the 1st International Conference on Computer Applications & Information Security: ICCAIS'2018*, vol. 1–6, Kingdom of Saudi Arabia, April, 2018.

[6] M. Gupta, K. K. Gupta, M. R. Khosravi, P. K. Shukla, S. Kautish, and A. Shankar, "An intelligent session key-based hybrid lightweight image encryption algorithm using logistic-tent map and crossover operator for internet of multimedia things," *Wireless Personal Communications*, vol. 121, no. 3, pp. 1857–1878, 2021.

[7] O. Amft, "How wearable computing is shaping digital health," *IEEE Pervasive Computing*, vol. 17, no. 1, pp. 92–98, 2018.

[8] O. Obulesu, S. Kallam, G. Dhiman et al., "Adaptive diagnosis of lung cancer by deep learning classification using wilcoxon gain and generator," *Journal of Healthcare Engineering*, vol. 2021, Article ID 5912051, 2021.

[9] A. W. Salehi, P. Baglat, and P. Baglat, "Alzheimer's disease diagnosis using deep learning techniques," *International Journal of Engineering and Advanced Technology*, vol. 9, no. 3, pp. 874–880, 2020.

[10] E. S. Izmailova, J. A. Wagner, and E. D. Perakslis, "Wearable devices in clinical trials: hype and hypothesis," *Clinical Pharmacology & Therapeutics*, vol. 104, no. 1, pp. 42–52, 2018.

[11] L. C Kourtis, O. B Regele, J. M Wright, and G. B Jones, "Digital biomarkers for Alzheimer's disease: the mobile/wearable devices opportunity," *Npj Digital Medicine*, vol. 2, no. 1, pp. 1–9, 2019.

[12] P. Yadav, P. Kumar, P. Kishan, P. Raj, and U. Raj, "Development of pervasive IoT based healthcare monitoring system for alzheimer patients," *Journal of Physics: Conference Ser[3] ies*, vol. 2007, no. 1, 2021.

[13] S. Sharma, R. K. Dudeja, G. S. Aujla, R. S. Bali, and N. Kumar, "DeTrAs: deep learning-based healthcare framework for IoT-based assistance of Alzheimer patients," *Neural Computing & Applications*, vol. 8, no. 2018, 2020.

[14] M. Gusenbauer and N. R. Haddaway, "Which academic search systems are suitable for systematic reviews or meta-analyses? Evaluating retrieval qualities of Google Scholar, PubMed, and 26 other resources," *Research Synthesis Methods*, vol. 11, no. 2, pp. 181–217, 2020.

[15] S. Kraus, M. Breier, and S. Dasí-Rodríguez, "The art of crafting a systematic literature review in entrepreneurship research," *The International Entrepreneurship and Management Journal*, vol. 16, no. 3, pp. 1023–1042, 2020.

[16] A. S. Albahri, J. K. Alwan, Z. K. Taha et al., "IoT-based telemedicine for disease prevention and health promotion: state-of-the-Art," *Journal of Network and Computer Applications*, vol. 173, Article ID 102873, 2021.

[17] S. Shahrestani, "Assistive IoT: Deployment Scenarios and Challenges," *In: Internet of Things and Smart Environments*, vol. 35, pp. 75–95, 2017.

[18] A. Afyf, B. Larbi, F. Riouch, M. A. Sennouni, and Y. Nourdin, "Flexible antennas for wearable technologies," *Handbook of Research on Recent Developments in Intelligent Communication Application*, 2016.

[19] Q. A. Ahmed and A. Q. H. Al-Neami, "A smart biomedical assisted system for alzheimer patients," *IOP Conference Series: Materials Science and Engineering*, vol. 881, no. 1, 2020.

[20] M. Roopaei, P. Rad, and J. J. Prevost, "A Wearable IoT with Complex Artificial Perception Embedding for Alzheimer Patients," in *Proceedings of the World Automation Congress Proceedings*, pp. 28–33, Stevenson, WA, USA, 2018-June.

[21] T. O. Takpor, J. Ademola, S. I. Popoola, A. Joke, and A. A. A. Badejo, "R- Smart AssistivemHealthSystem for Medication Adherence in Patients with Alzheimer‟s

Disease.Pdf," *IoT-enabled Smart & Connected Communities*, vol. 2, 2017.

[22] R. Oliveira, A. Barreto, A. Cardoso, C. Duarte, and F. Sousa, "Environment-aware system for Alzheimer's patients," in *Proceedings of the 2014 4th International Conference on Wireless Mobile Communication and Healthcare – Transforming Healthcare Through Innovations in Mobile and Wireless Technologies (MOBIHEALTH)*, vol. 8–11, Athens, Greece, November 2014.

[23] T. Cazangiu, F. C. Argatu, B. A. Enache, V. Vita, and G. Stavros, "Device for monitoring people with Alzheimer's disease," *ISFEE*, in *Proceedings of the 2018 International Symposium on Fundamentals of Electrical Engineering*, p. 313, Bucharest, Romania, November 2018.

[24] B. Zellefrow, S. Shanaei, R. Salam, and A. El. Nasan, *Halcyon – Assistive Technology for Alzheimer ' S Patients*, Springer International Publishing, Manhattan, New York City, NY, USA, 2017.

[25] K. S. Omar, A. Anjum, T. Oannahary et al., *An Intelligent Assistive Tool for Alzheimer ' S Patient*, in *Proceedings of the 2019 1st International Conference on Advances in Science, Engineering and Robotics Technology (ICASERT)*, Dhaka, Bangladesh, May 2019.

[26] N. Hegde, S. Muralidhara, and D. V. Ashoka, "A low-cost and autonomous tracking device for Alzheimer's patients," *Journal of Enabling Technologies*, vol. 13, no. 4, pp. 201–211, 2019.

[27] M. A. Gacem, S. Alghlayini, W. Shehieb, M. Saeed, A. Ghazal, and M. Mir, "Smart Assistive Glasses for Alzheimer ' S Patients," in *Proceedings of the 2019 IEEE International Symposium on Signal Processing and Information Technology (ISSPIT)*, Ajman, United Arab Emirates, December 2019.

[28] W. L. Chen, L. B. Chen, W. J. Chang, and J. J. Tang, "An IoT-based elderly behavioral difference warning system," in *Proceedings of the 4th IEEE International Conference on Applied System Innovation 2018, ICASI*, pp. 308-309, Chiba, Japan, April 2018.

[29] E. S. Design, W. S. Networks, and Sanati-mehrizy, *Application of Wireless Sensor Networks in Health Care System Application of Wireless Sensor Networks in Health Care System*, Springer International Publishing, New York, NY, USA, 2013.

[30] A. Banerjee, C. Chakraborty, A. Kumar, and D. Biswas, "Chapter 5 - emerging trends in IoT and big data analytics for biomedical and health care technologies," in *Handbook of Data Science Approaches for Biomedical Engineering*Elsevier, Netherlands, 2020.

[31] G. Aroganam, N. Manivannan, and D. Harrison, "Review on wearable technology sensors used in consumer sport applications," *Sensors*, vol. 19, no. 9, p. 1983, 2019.

[32] S. Jhajharia, S. K. Pal, and S. Verma, "Wearable computing and its application," *International Journal of Computer Science and Information Technologies,*vol. 5, no. 4, pp. 5700–5704, 2014.

[33] O. Olorode and M. Nourani, "Reducing leakage power in wearable medical devices using memory nap controller," in *in Proceedings of the 2014 IEEE Dallas Circuits and Systems Conference (DCAS)*, pp. 1–4, IEEE, November 2014.

[34] W. Robin, L. Keith, and D. Harrison, "Wearable technology: If the tech fits, wear it," *Journal of Electronic Resources in Medical Libraries*, vol. 11, no. 4, pp. 204–216, 2014.

[35] C. Luka, R. Manivannan, and D. Magjarevic, "Seamless connectivity architecture and methods for IoT and wearable devices," *Automatika: časopis za automatiku, mjerenje, elektroniku, računarstvo i komunikacije*, vol. 61, no. 1, pp. 21–34, 2020.

[36] S. Ahmad Waleed, F. Noori, and R. Saboori, "Cloud computing security challenges and its potential solution," *American Journal of Engineering Research*, vol. 8, p. 10, 2019.

[37] G. -M. Iván, D. Sarkar, and R. Lacuesta, "Wearable technology and mobile applications for healthcare," *Mobile Information Systems*, vol. 2019, Article ID 6247094, , 2 pages, 2020.

[38] J. S. Talboom and M. J. Huentelman, "Big data collision: the internet of things, wearable devices and genomics in the study of neurological traits and disease," *Human Molecular Genetics*, vol. 27, no. 1, pp. 35–39, 2018.

[39] M. Kocakulak and I. Butun, "An Overview of Wireless Sensor Networks towards Internet of Things," in *Proceedings of the 2017 IEEE 7th Annual Computing and Communication Workshop and Conference (CCWC)*, Las Vegas, NV, USA, January 2017.

[40] A. W. Salehi, P. Baglat, and G. Gupta, "Materials Today: proceedings Review on machine and deep learning models for the detection and prediction of Coronavirus," *Materials Today Proceedings*, 2020.

[41] A. W. Salehi, P. Baglat, and G. Gupta, "A CNN model: earlier diagnosis and classification of alzheimer disease using MRI," in *Proceedings of the 2020 International Conference on Smart Electronics and Communication (ICOSEC)*, vol. 1, pp. 156–161, Trichy, India, September 2020.

[42] E. Bruno, S. Simblett, A. Lang et al., "Wearable technology in epilepsy: the views of patients, caregivers, and healthcare professionals," *Epilepsy and Behavior*, vol. 85, pp. 141–149, 2018.

[43] W. Devices, "New Ways to Manage Information," *Computer*, vol. 32, no. 1, pp. 57–64, 1999.

[44] A. Components and P. P. Healthcare, "Wearable Internet Of Things," in *Proceedings of the 2014 4th International Conference on Wireless Mobile Communication and Healthcare - Transforming Healthcare Through Innovations in Mobile and Wireless Technologies (MOBIHEALTH)*, vol. 2, pp. 304–307, Athens, Greece, November 2014.

[45] G. Srivastava and M. Khari, Eds., *Evaluation of Software Fault Proneness with a Support Vector Machine and Biomedical Applications,* Taylor & Francis Group, New York, NY, USA, 2021.

[46] H. Chouksey, "REVIEW OF AMBIENT ASSISTED LIVING APPLICATIONS FOR ALZHEIMER ' S DISEASE PATIENTS," *Himshi Chouksey*, vol. 1, pp. 34–45, 2019.

[47] W. T. Wearables, "Devices – Happiest Minds," 2019, https://www.happiestminds.com/Insights/wearable-technology/.

Hindawi
Contrast Media & Molecular Imaging
Volume 2022, Article ID 1985531, 7 pages
https://doi.org/10.1155/2022/1985531

Research Article

Diagnosis and Prognostic Analysis of *Mycoplasma pneumoniae* Pneumonia in Children Based on High-Resolution Computed Tomography

Jiangang Leng, Zemin Yang, and Wenhui Wang

Department of Pediatrics, Funan County People's Hospital, Funan County, Fuyang City 236300, Anhui Province, China

Correspondence should be addressed to Wenhui Wang; 20163052@ayit.edu.cn

Received 22 February 2022; Revised 3 April 2022; Accepted 6 April 2022; Published 22 April 2022

Academic Editor: M. Pallikonda Rajasekaran

Mycoplasma *pneumoniae* (MP) is defined as a common cause of pulmonary infections and accounts for up to four over ten of pneumonia in children over age 5. This study was aimed to explore the diagnosis and prognosis of mycoplasma *pneumoniae* pneumonia (MPP) in children using high-resolution computed tomography (CT) (HRCT). 71 children hospitalized with MPP were undertaken as the research objects to observe the incidence rate, occurrence time, and duration of the clinical symptoms and pathological signs. The chest HRCT and pulmonary ventilation function (PVF) were examined in the acute phase, the second phase re-examination period, and the third phase re-examination period. Relevant indicators were statistically analyzed to determine the change rules of chest HRCT and PVF and correlation between the two. Clinically, the children with MPP suffered from fever, cough, and sore throat. In addition to the above symptoms, children with MPP had different degrees of PVF impairment. Compared with the group with normal HRCT results, the forced vital capacity (FVC), forced expiratory volume in 1 second (FEV1), peak expiratory flow (PEF), forced expiratory flow at 25% forced expiratory volume (FEF25), forced expiratory flow at 50% forced expiratory volume (FEF50), forced expiratory flow at 75% forced expiratory volume (FEF75), and maximum mid-expiratory flow (MMEF75/25) of children in bronchopneumonia group, segmental pneumonia group, and lobar pneumonia group were obviously reduced, showing statistically great differences ($P < 0.05$). Compared with the case in acute phase, the PVF indicators of children in the re-examination phases were much higher, with greatly statistical differences ($P < 0.05$). In children with MPP, both the large and small airways were affected, but the recovery of the small airways was slow. Pulmonary HRCT and PVF can be undertaken as important indicators to judge the severity and prognosis of MPP in school-age children.

1. Introduction

Mycoplasma *pneumoniae* (MP) is well-known as an intracellular pathogen that can cause respiratory diseases and extra-pulmonary diseases of children, which is commonly named as mycoplasma *pneumoniae* pneumonia (MPP). The diseases are mostly spread by respiratory droplets, and sporadic infections occur throughout the year, especially in late autumn and early winter [1]. The incidence rate of MP infection has shown an upward trend year by year, which has been proved by related studies in recent years. Date for MPP in China is scarce. Data show that MP infection accounts for 10–40% of community-acquired pneumonia (CAP) in children at 9–14 years old, with a peak age of 4–6 years [2]. The clinical manifestations and chest X-ray examination of MPP are not characteristic, and the diagnosis cannot be made based on the clinical manifestations and chest X-ray examination alone. For a definitive diagnosis, testing for the pathogen is required. At present, the diagnosis of MPP in China mainly relies on serological tests. However, reports vary by age, region, year, and year of prevalence, so there are various reports with similar results. MPP has been well recognized as one of the most critical and dangerous health problems all over the China. With the changes in etiology, MPP shows new epidemiological characteristics, manifested as specific imaging changes that affect the pulmonary ventilation function (PVF), but the obvious pathogenesis is still unclear [3]. Current research believes that the pathogenesis of MPP is related to cell damage and immune inflammatory response caused by direct invasion, but the degree of damage and the duration of action are still unclear, and the clinical manifestations are often atypical. Studies have shown that the major and minor respiratory tract functions of children with MPP in acute phase have varying degrees of damage, the functions of both large and small airways are damaged in different degrees in children, especially when the MPP is in the acute phase. In addition, the lung function of most children can be improved significantly during the recovery period, but the PVF in small airway is more severe and slower to be recovered. Patients with markedly higher MP antibody titers may have more severe PVF impairment. The PVF impairments could be improved greatly after treatment, so they are reversible. MPP can induce asthma attacks in some patients with asthma. In addition, acute MP infection can not only promote acute attacks in children with asthma but also cause wheezing in nonasthmatic children [4]. MPP is mainly treated with antibiotics. Since cough is the most prominent clinical manifestation, low-dose antitussives and expectorants can be given appropriately. Those with severe symptoms of hypoxia should be given oxygen in time. For severe asthma, bronchodilators can be used. Adrenal corticosteroids can be used for patients with rapid and severe mycoplasma pneumonia in the acute stage or persistent pulmonary lesions resulting in atelectasis, pulmonary fibrosis, bronchiectasis, or extra-pulmonary complications.

Many new information on MPP infections is published in the last several years. Many studies have linked MP infection to asthma attacks. Therefore, MPP is currently considered to be an important cause of asthma exacerbations in nonasthmatic children [5]. Studies have shown that the abnormal rate of lung imaging of MPP patient is observably higher in contrast to the positive rate of lung signs. The lung imaging of patients with severe MPP often presents as large patchy shadows, possible atelectasis, pleural effusion, necrotizing pneumonia, pulmonary abscesses, and other pulmonary complications [6]. School-age children account for a higher proportion of MPP patients, with severe and diverse clinical manifestations and different degrees of PVF impairment [7]. Acute MPP can be developed into bronchiolitis obliterans if it is not controlled well in children, which can greatly affect the quality of life of children and is associated with MPP. Early identification and treatment of MPP is conductive to preventing the development of bronchiolitis obliterans. MP infection is impossible to be identified or confirmed based on a single clinical characteristic only. However, if the duration of pyrexia and severe fever is long, the blood oxygen saturation is reduced, and the ALT and LDH are increased, it can be determined as the MP infection. On the other hand, MP infection can be diagnosed by high-resolution computed tomography (HRCT) examination, because it can observe lung lesions from multiple levels, and it is easy to accurately locate and clarify the degree and scope of lesions. Pulmonary function suggests severe MPP involving the large airways, with concomitant stenosis and occlusion of the lower small airways [8]. Lung structural abnormalities are common in school-aged children after MPP surgery, but there are few studies on imaging, especially HRCT, and their correlation with PVF during the course of the disease (CoD). HRCT and PVF follow-up should be performed on school-age children with MPP at a fixed time. Chest HRCT and PVF test can be undertaken as important reference indicators for the diagnosis and prognosis of MPP [9]. Exploring the change rules of chest HRCT and PVF in children with MPP and correlation between the two can provide important support for clinical diagnosis, condition evaluation, treatment guidance, and prognosis judgment.

2. Materials and Methods

2.1. Objects. Seventy-one children were selected who admitted to hospital from October 2019 to December 2021. Inclusion criteria were given as follows: the patients were preschool and school-age children; children with MPP in acute onset, with a duration of less than 5 days on admission, accompanied by fever and respiratory symptoms; children whose X-ray examination of the chest showed patchy or patchy infiltrates or interstitial changes, with or without pleural effusion; and children with positive (+) result of serum MP-IgM antibody (diluted 1 : 39) diluted using microparticle agglutination method. Exclusion criteria were set as follows: children with autoimmune diseases and other chronic diseases and were taking some drugs that affected immune function; patients with respiratory diseases such as *tuberculosis* and previous bronchial asthma; patients with mixed infections determined by virus testing, sputum culture, and blood culture, and so on; and children whose parents refused to accept this experiment. Discontinuation criteria were set as follows: serious adverse events and feelings occurred during the treatment period; and the loss rate of subjects during the experiment was >19%. The experiment here complied with the ethical requirement and all children and their families had been aware of experimental procedure and signed the agreements.

2.2. CT Scanning. HRCT is believed to observe the fine structure of lesions, and it is an ideal supplement to conventional chest scans. HRCT examination was performed with 258-slice microplate rapid CT. The scanning voltage was 122 kV, and the fault was 1–1.8 mm. After diagnosis and treatment, the lung HRCT examination was performed again. It should scan continuously from the lung tip to the diaphragm. Before the HRCT examination, the patients were instructed with some key points to cooperate with the examinations. After the HRCT examination, the distribution and morphological characteristics of lung, pleura, and mediastinum were evaluated carefully by radiologists.

2.3. Treatment Methods and Follow-Up. The treatment included macrolide antibiotics (referring to pediatric medication methods); symptomatic treatment (like aerosol inhalation); bronchoscopy for lobar or segmental pneumonia according to the situation; and adrenal cortex hormone or gamma globulin for MPP at the extreme stage of inflammation. Patients who met the following conditions were discharged after oral medication and sequential treatment. If the cough was obviously relieved, the general condition was better; if the auxiliary temperature was <37.6°C for 72 h; and chest X-rays showed improvement in absorption. Patients with severe PVF impairment caused by MPP had to be supplied with oxygen in time. For patients with mild PVF impairment, bronchodilators can be used. Adrenal corticosteroids can be used for patients with rapid and severe MPP in the acute stage or persistent pulmonary lesions resulting in atelectasis, pulmonary fibrosis, bronchiectasis, or extra-pulmonary complications. The total course of treatment was 14–28 days and the follow-up was 3–6 months.

2.4. PVF Test (FVC Method). The environmental parameters and volume calibrations of the lung function instrument were checked before the examination. The predicted value was automatically generated by the PVF instrument software according to age, height, weight, and other basic parameters. The patient should keep his/her head stood naturally horizontally with the mouth closed, inhale deeply to the total lung volume (TLC) level, and maintain the exhalation to the functional residual capacity (FRC) level with the maximum volume and the fastest speed. In addition, it should observe the time-volume curve and flow-volume curve. The best test value should be kept three times (each time the difference was required to be <5% or < 0.2 L) to get the average value as the judgment result. The abovementioned operations were implemented by specialized staff trained in pulmonary function measurement so that the operations were professional enough and could be implemented correctly. In addition, the patient was trained to cooperate with the test in advance so that the test could be completed as smooth as possible.

2.5. Observation Indicators. The observation indicators included forced vital capacity (FVC), forced expiratory volume in 1 second (FEV1), peak expiratory flow rate (PEF), forced expiratory flow at 25% forced expiratory volume (FEF25), forced expiratory flow at 50% forced expiratory volume (FEF50), forced expiratory flow at 75% forced expiratory volume (FEF75), and maximum mid-expiratory flow (MMEF75/25). The PVF test results were as follows: first, the percentage of the FEV1 to the predicted value (FEV1%) < 79% indicated obstructive ventilation dysfunction (OVDF); FVC % < 79% suggested restrictive ventilation dysfunction (RVDF), and FEV1% < 79% and FVC% < 79% indicated mixed ventilation dysfunction (MVDF). Second, MMEF, FEF50%, FEF75%, and MMEF 75/25 of <80% indicated that the ventilation function of the small airway was affected. If FEV1, PEF, and FEF25 were normal, while FEF50 and FEF75 decreased <79%, it indicated early OVDF of small airway.

2.6. Statistical Analysis. Spss18 was adopted to complete statistics. The test results were expressed as mean ± standard deviation. The independent sample t-test and one-way analysis of variance were adopted between groups, and the test level was $a = 0.05$. $P < 0.05$ suggested the difference was obvious statistically.

3. Results

3.1. Basic Information of the Children. The clinical manifestations of 71 school-age children with MPP were analyzed. Among them, there were 37 males and 34 females; the mean age, height, and weight were 8.55 ± 1.84 years old, 141 ± 7.8 cm, and 28.9 ± 6.4 kg, respectively. PVF test was performed in 71 cases in acute stage (with CoD of 7.5 ± 2.1 days) and 62 cases in re-examination stages (with CoD of 30.2 ± 3.8 days). The HRCT was performed on 57 cases in acute stage (CoD was 7.5 ± 2.0 days) and 52 cases in re-examination stages (CoD was 30.2 ± 4.3 days). The main symptoms were fever (67/94.4%), cough (63/88.7%), and sore throat (47/66.2%). The specific data were shown in Figure 1. Among the clinical manifestations, fever appeared earliest and most frequently, with an average CoD of 1.48 ± 0.83 days; while cough lasted the longest (the average CoD was 11.51 ± 1.55 days). In addition, early lung signs were absent, and some cases may have transient wheezing and wet rales in the lungs, and may be accompanied by extra-pulmonary symptoms.

3.2. CT Image Characteristics of Children before and after Treatment. The chest CT images of the children before and after treatment were analyzed and compared, and the results were shown in Figure 2. The 1# child had high fever and severe cough before treatment, the MP-IgM antibody was 3.6 (positive >1.11), and only Azithromycin and other drugs (which were the commonly adopted drugs for MPP) were taken for clinical antibacterial treatment. The above clinical symptoms were found to decrease greatly after treatment with above operations. It indicated that Azithromycin was very effective to 1# child with MPP. Figures 2(a) and 2(b) showed that the CT images before and treatment, respectively. The 2# child claimed high fever, cough, and chest pain before treatment. After treatment with Moxifloxacin and other drugs, it was found that the absorption of the lesion improved to varying degrees. It meant that Moxifloxacin was effective for 2# child.

The chest HRCT manifestations of school-age children with MPP showed diversity, including increased lung texture, rod-shaped shadow, ground glass shadow, small patchy shadow, large patchy consolidation, atelectasis, bronchiectasis, chest cavity effusion, and hilar mediastinal lymph nodes swelling. In acute phase group, multiple lung lobes were involved more than a single lung lobe; while in the re-examination groups, more single lung lobes were found than multiple lung lobes, and the lesions in each group mainly involved the right lower lung. Increased lung texture was the most common in acute phase (26 cases, 45.6%). In addition, there were 25 cases with large-scale consolidation (accounting for 43.9%), and there were 17 children with atelectasis (29.8%), as shown in Figure 3. The lesions in the re-examination group had various degrees of absorption, of

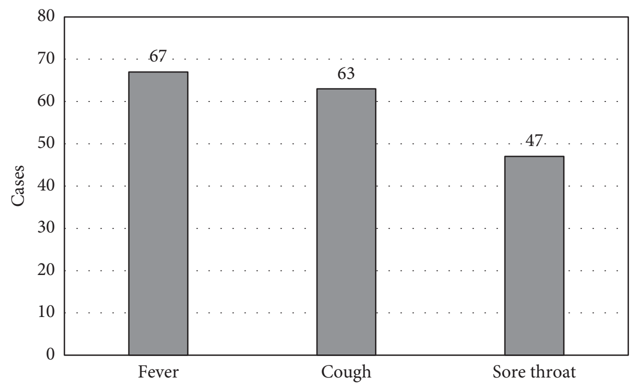

Figure 1: Statistics of the main clinical manifestations of children.

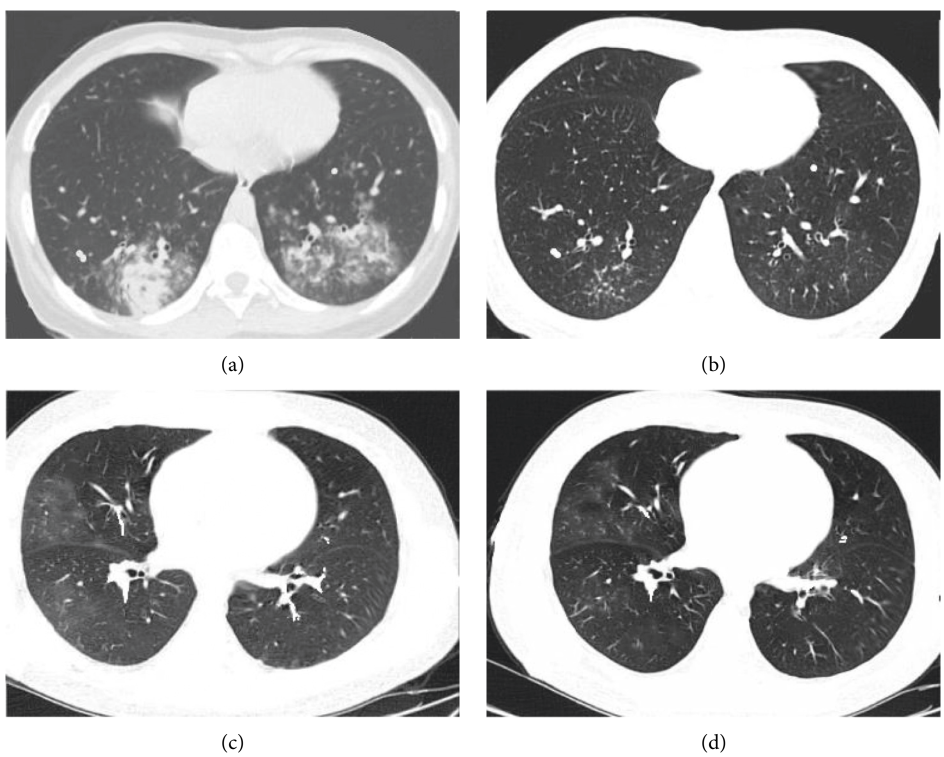

Figure 2: CT image characteristics of children before and after treatment.

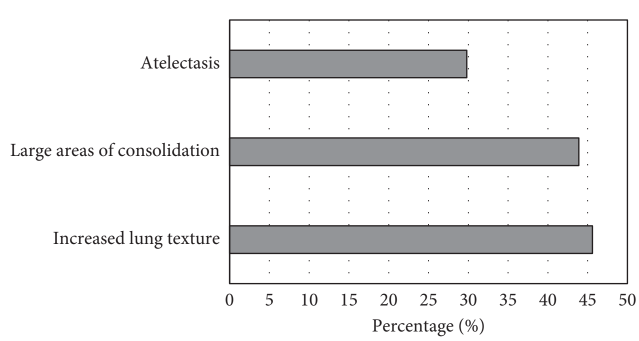

Figure 3: The main manifestations of chest HRCT in children with MPP in acute phase.

which 36 children (69.2%) had full absorption of the lesions. Figure 3 illustrated the specific results with exact data.

3.3. Comparison of PVF Indicators in Children with Different HRCT Manifestations. Based on the HRCT manifestations of MPP children, they were rolled into three different groups: a bronchopneumonia group, a segmental pneumonia group, and a lobar pneumonia group. The HRCT manifestations were different, which meant that the severity of the MPP was not the same, so children in each group had different degrees of PVF impairment. The OVDF was the major symptom in the bronchopneumonia group, which was found in large airways of the affected children. In the segmental pneumonia and lobar pneumonia groups, children were manifested as MVDF, which was concentrated on their small airways. The differences in PVF indicators of children with different manifestations were compared (as illustrated in Figure 4). It can be known that compared with the group with normal HRCT manifestations, all the PVF indicators in bronchopneumonia group, segmental pneumonia group, and lobar pneumonia group were all reduced, with statistically remarkable differences ($P < 0.05$). In addition, all above PVF indicators in children in lobar pneumonia group were always the lowest in contrast to the segmental pneumonia group and the bronchopneumonia group.

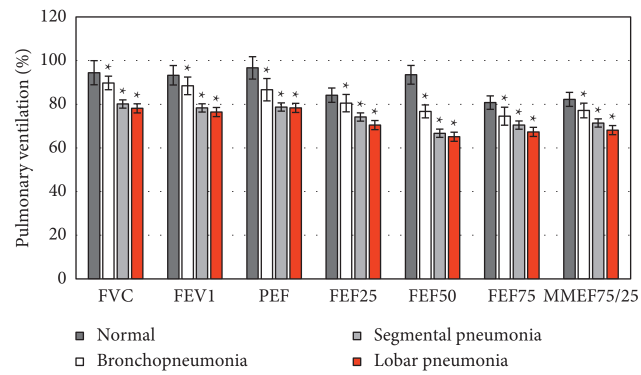

Figure 4: The correlation between different lung HRCT manifestations and PVF in children (*(P) < 0.05).

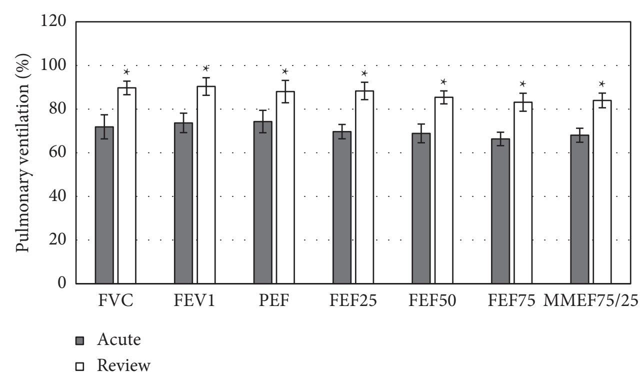

Figure 5: Comparison of PVF indicators in MMP children at different stages (*(P) < 0.05).

3.4. Comparison of PVF Indicators of Children before and after Treatment. School-age children with MPP showed different degrees of PVF impairment, of which OVDF was dominated. The changes of PVF indicators in different phases were compared, and the results were analyzed and displayed in Figure 5. From results in Figure 5, it can be observed that compared to the acute phase, the PVF indicators of children in the re-examination period increased sharply, and statistically visible differences could be found ($P < 0.05$).

4. Discussion

MPP is an acute lung inflammation caused by MP infection and is a disease commonly found in children's respiratory system. It is often accompanied by atelectasis and massive lung infiltration, which can cause extra-pulmonary complications. MPP can cause children to suffer from some flu-like symptoms, which can increase the burden on their health. The incidence of MP infection in children has shown an upward trend these years, and data show that MP infection accounts for 11%–41% of CAP in children, which may be even higher [10]. MP infection is a pathogen of pediatric respiratory infections in infants and adolescents, most of which are clinically manifested as respiratory tract infection syndrome, of which about 3% to 10% can develop into MPP. MPP is sporadic and prevalent throughout the year, with a high incidence in preschool and school-age. MPP due to MP infection is usually mild, but some cases develop a severe condition, so that the life is threatened. MPP is a frequent but underdiagnosed disease in children, and appropriate treatment cannot be given early. Patients with severe symptoms of PVF have to be intervened with oxygen supply in time. For severe PVF, bronchodilators can be used. Adrenal corticosteroids can be used for patients with rapid and severe MPP in the acute stage or persistent pulmonary lesions resulting in atelectasis, pulmonary fibrosis, bronchiectasis, or extra-pulmonary complications. MPP imaging findings in children are mostly unilateral lesions, accounting for more than 80%, mainly in the lower lobes, sometimes only in the shadow of the hilum, the shadow weight increases, irregular cloud-like lung infiltration, and the lung field extends from the hilum, especially in the lower lobes of both lungs. Both lungs may show diffuse network or nodular infiltration or interstitial pneumonia, and the lung segments or lobes are not consolidated. However, MPP has become a new epidemiological feature, due to changes in etiology, specific imaging changes affect lung function [11]. The chest radiograph has high spatial resolution and can display the overall status and the infection condition of the lung clearly. However, it is difficult to find the early or ultra-early pulmonary lesions due to the limitation of overlapping relationship. HRCT shows higher performance in displaying the fine structures of lung tissue (pulmonary lobular airways, blood vessels and interlobular septa, pulmonary interstitium, and millimeter-scale intrapulmonary nodules, etc.). Sometimes, it can display the morphological changes, which are similar to the gross specimen. Therefore, HRCT shows very high value in chest imaging examination. In addition, its another advantage is that no additional contrast enhancement is needed. HRCT uses thin-slice scanning to reduce the overlap caused by the volume effect and accurately collect lesion information [12]. Therefore, the local anatomy can be clearly displayed and the morphological changes of the small airway that cannot be detected by the lung function test can be observed. Early detection of injury, progress of injury, and improvement of injury after treatment can all be well evaluated. In addition, HRCT can be considered when the correlation between lung structure and lung function is assessed. Therefore, HRCT is a noninvasive, accurate, and reproducible imaging method [13], so it is especially beneficial for children, especially infants. The Philips 256-slice Micropanel CT (Brilliance NanoPanel iCT) can reduce the radiation dose of patients during the scanning process, which can be reduced by more than 80% compared with ordinary CT examinations. It shows obvious effect especially for infants and other radiation-sensitive populations. However, the potential risks of testing should be carefully evaluated.

In this work, the chest HRCT manifestations of school-age children with MPP showed diversity, including increased lung texture, rod-shaped shadow, ground glass shadow, small patchy shadow, large patchy consolidation, atelectasis, bronchus dilation, pleural effusion, and hilar mediastinal lymph nodes enlargement. More lung lobes were involved than a single lung lobe for children in the acute phase, while it was the opposite case for children in the re-examination periods. The lesions in each group mainly involved the right lower lung. Increased lung texture is the most common in acute phase, followed by large areas of consolidation and atelectasis. The multiple lesions have various degrees of absorption. A study on 207 children with MPP found that the most common manifestations of MPP on chest radiographs were lung parenchyma shadows (57%), large infiltrates (47.3%), and atelectasis (17.9%). A total of 75.1% of the children had different degrees of abnormal PVF, and most of them showed changes in small airway function. Such results are similar with the findings in this work. MPP chest radiographs are not specific, but they can show diffuse or reticular infiltration or consolidation. A total of 20% of patients have bilateral infiltration. Studies have observed the large and small airway ventilation indicators of MPP patients and found that they are significantly lower than expected, suggesting that respiratory mucosal injury and airflow limitation in children with MPP are caused by direct damage to the respiratory mucosa and immune damage caused by MP.

5. Conclusion

The clinical symptoms of MPP in school-age children were mainly fever, cough, and sore throat. In addition, it lacked positive signs in the early stage. The HRCT manifestations of MPP of school-age children were different, but there were some rules. There were varying degrees of lung ventilation function obstacles in MPP of school-age children, which was dominated by OVDF in small airways. Ventilation dysfunction in school-age children with MPP was related to the severity of HRCT manifestations. In children with MPP, both large and small airways were affected, but small airway mainly involved segmental pneumonia and lobular pneumonia, and its recovery was slowly. Pulmonary HRCT and PVF can be used as important indicators to judge the severity and prognosis of MPP in school-age children. However, sample included was less, so more children can be invited to participate in the experiment. Clinical trials should not be conducted in a single or small area, and it will get better performance by conducting it in multi-center hospitals.

Data Availability

The data used to support the findings of this study are available from the corresponding author upon request.

Conflicts of Interest

The authors declare no conflicts of interest.

References

[1] C. K. Kim, C. Y. Chung, J. S. Kim, W. S. Kim, Y. Park, and Y. Y. Koh, "Late abnormal findings on high-resolution computed tomography after Mycoplasma pneumonia," *Pediatrics*, vol. 105, no. 2, pp. 372–378, 2000.

[2] Y. Zhou, M. Hu, B. Ye, Z. Chen, and Y. Zhang, "Early prediction of necrotizing pneumonia from mycoplasma pneumoniae pneumonia with large pulmonary lesions in children," *Scientific Reports*, vol. 10, no. 1, Article ID 19061, 2020.

[3] Y. Y. Lu, R. Luo, and Z. Fu, "[Pathogen distribution and bacterial resistance in children with severe community-acquired pneumonia]," *Zhong Guo Dang Dai Er Ke Za Zhi*, vol. 19, no. 9, pp. 983–988, 2017, Chinese.

[4] L. Shi, Q.-G. Wu, J.-C. Zhang, G.-M. Yang, W. Liu, and Z.-F. Wang, "Mechanism of shuang-huang-lian oral liquid for treatment of mycoplasmal pneumonia in children on network pharmacology," *Combinatorial Chemistry & High Throughput Screening*, vol. 23, no. 9, pp. 955–971, 2020.

[5] J. Wang, C. Xia, A. Sharma, G. S. Gaba, and M. Shabaz, "Chest CT findings and differential diagnosis of mycoplasma pneumoniae pneumonia and mycoplasma pneumoniae combined with streptococcal pneumonia in children," *Journal of Healthcare Engineering*, vol. 2021, Article ID 8085530, 10 pages, 2021.

[6] M. Yang, D. H. Yang, X. Yang, Y. S. Wang, L. Wu, and Z. M. Chen, "Efficacy of bronchoalveolar lavage and its influence factors in the treatment of Mycoplasma pneumoniae pneumonia with atelectasis," *Zhonghua Er Ke Za Zhi*, vol. 56, no. 5, pp. 347–352, 2018, Chinese.

[7] M. Mathisen, S. Basnet, A. Christensen et al., "Viral and atypical bacterial detection in young Nepalese children hospitalized with severe pneumonia," *Microbiology Spectrum*, vol. 9, no. 2, Article ID e0055121, 2021.

[8] Y. Guo, W. Xia, X. Peng, and J. Shao, "Features discriminating COVID-19 from community-acquired pneumonia in pediatric patients," *Frontiers in Pediatrics*, vol. 8, Article ID 602083, 2020.

[9] Y. J. Liu, P. Chen, Z. S. Liu, Y. Li, H. Du, and J. L. Xu, "Clinical features of asymptomatic or subclinical COVID-19 in children," *Zhong Guo Dang Dai Er Ke Za Zhi*, vol. 22, no. 6, pp. 578–582, 2020, Chinese.

[10] F. Z. Zhang, J. X. Yuan, X. F. Tao, Z. M. Chen, and L. F. Tang, "Clinical features of pulmonary thromboembolism of eight children," *Zhonghua Er Ke Za Zhi*, vol. 58, no. 1, pp. 25–29, 2020, Chinese.

[11] Y. Ding, C. Chu, Y. Li et al., "High expression of HMGB1 in children with refractory Mycoplasma pneumoniae pneumonia," *BMC Infectious Diseases*, vol. 18, no. 1, p. 439, 2018.

[12] L. Chen, J. Liu, S. Zhao, Y. Yang, and J. Wu, "Clinical features and treatment ofrefractory Mycoplasma pneumoniae pneumonia unresponded to conventional dosemethylprednisolone in children," *Zhonghua Er Ke Za Zhi*, vol. 52, no. 3, pp. 172–176, 2014.

[13] L. Sharma, A. Losier, T. Tolbert, C. S. Dela Cruz, and C. R. Marion, "Atypical pneumonia," *Clinics in Chest Medicine*, vol. 38, no. 1, pp. 45–58, 2017.

Hindawi
Contrast Media & Molecular Imaging
Volume 2022, Article ID 7013703, 10 pages
https://doi.org/10.1155/2022/7013703

Research Article

Diagnostic Value of Coronary Computed Tomography Angiography Image under Automatic Segmentation Algorithm for Restenosis after Coronary Stenting

Xinrong He,[1] **Juan Zhao**,[2] **Yunpeng Xu**,[1] **Huini Lei**,[3] **Xianbin Zhang**,[4] **and Ting Xiao**[5]

[1]*Department of Cardiovascular Medicine 7, Xianyang Hospital of Yan'an University, Xianyang 712000, Shaanxi, China*
[2]*Department of Cardiovascular Medicine 2, Xianyang Hospital of Yan'an University, Xianyang 712000, Shaanxi, China*
[3]*Interventional Operating Room, Shangluo Central Hospital, Shangluo 726000, Shaanxi, China*
[4]*Department of Cardiology, Xi'an Changan Hospital, Xi'an 710000, Shaanxi, China*
[5]*Department of Cardiovascular Medicine, Shangluo Central Hospital, Shangluo 726000, Shaanxi, China*

Correspondence should be addressed to Ting Xiao; 201772218@yangtzeu.edu.cn

Received 8 February 2022; Accepted 23 March 2022; Published 16 April 2022

Academic Editor: M Pallikonda Rajasekaran

The diagnostic efficacy of coronary computed tomography angiography (CTA) images of coronary arteries in restenosis after coronary stenting based on the combination of the convolutional neural network (CNN) algorithm and the automatic segmentation algorithm for region growth of vascular similarity features was explored to provide a more effective diagnostic method for patients. 130 patients with coronary artery disease were randomly selected as the research objects, and they were averagely classified into the control group (conventional coronary CTA image diagnosis) and the observation group (coronary CTA image diagnosis based on an improved automatic segmentation algorithm). Based on the diagnostic criteria of coronary angiography (CAG), the efficacy of two kinds of coronary CTA images on the postoperative subsequent visit of coronary heart disease (CHD) stenting was evaluated. The results showed that the accuracy of the CNN algorithm was 87.89%, and the average voxel error of the improved algorithm was signally lower than that of the traditional algorithm (1.8921 HU/voxel vs. 7.10091 HU/voxel) ($p < 0.05$). The average score of the coronary CTA image in the observation group was higher than that in the control group (2.89 ± 0.11 points vs. 2.01 ± 0.73 points) ($p < 0.05$). The diagnostic sensitivity (91.43%), specificity (86.76%), positive predictive value (88.89%), negative predictive value (89.66%), and accuracy (89.23%) of the observation group were higher than those of the control group ($p < 0.05$). In conclusion, the region growth algorithm under the CNN algorithm and vascular similarity features had an accurate segmentation effect, which was helpful for the diagnosis of CTA image in restenosis after coronary stenting.

1. Introduction

With the rapid development of science and technology, economy, and culture, the types of diseases also increase. Due to the changes in people's daily living habits, the incidence of many diseases is increasing, and coronary heart disease (CHD) is one of them. In recent years, the incidence of CHD has increased with the trend of patients being young and the aging of the population [1, 2]. Angina pectoris and other symptoms of CHD bring great pain to patients [3, 4]. Coronary stent implantation is one of the most effective therapies at present [5]. About 2 million patients with CHD worldwide are treated with coronary stent implantation every year [6]. However, in-stent restenosis (ISR) occurs in some patients after surgery. Hence, rediagnosis is more crucial for these patients. The "gold standard" for the diagnosis of ISR is coronary angiography (CAG) [7]. Nevertheless, this method is not well accepted by patients because it is expensive, invasive, and the operation is complex. Nonetheless, coronary computed tomography angiography (CTA) [8] is a preferred method for people with simple operations, noninvasive examinations, and low inspection costs [9]. Besides, coronary CTA has a good diagnosis effect on CHD and postoperative restenosis [10].

In the past, CTA images of patients in clinical practice were examined or reviewed by doctors who observed the lesions through artificial segmentation [11]. Nevertheless, this method often causes the interference of subjective consciousness in the examination results, which leads to errors in the diagnosis results of diseases that can reduce the diagnostic accuracy [12]. To solve the abovementioned problems, an automatic segmentation technology is proposed through continuous exploration [13]. After continuous adoption and research, automatic segmentation technology has become a vital auxiliary means in the diagnosis of coronary CTA images for CHD. The segmentation algorithm is mainly classified into image denoising and image segmentation [14]. The segmentation algorithm based on the growth algorithm [15] is relatively ubiquitous. This method uses the similarity of pixels in different regions to classify regions, but the accuracy of segmentation is low [16]. Therefore, this method needs to be improved.

To sum up, coronary CTA images based on an improved automatic segmentation algorithm were employed for postoperative coronary stenting reexamination. The diagnostic value of CAG was evaluated with the diagnostic results as the gold standard to provide more accurate and effective examination methods for patients with CHD so that they could receive reasonable treatment.

2. Materials and Methods

2.1. Objects of Study. In this study, 130 patients who came to the hospital for the postoperative subsequent visit of CHD stenting between March 2019 and March 2021 were randomly selected as the research objects. There were 90 male patients and 40 female patients. The patients were 30–80 years old and the average age was 60.21 ± 9.55 years old. The diameter of the stent was 2mm–4 mm with an average diameter of 2.86 ± 0.19 mm. By the random number table, all the patients were classified into the control group (conventional coronary CTA image diagnosis) and the observation group (coronary CTA image diagnosis based on the improved automatic segmentation algorithm), each of which included 65 cases. The diagnostic results of CAG were taken as the standard to evaluate the effect of two kinds of CTA images on the postoperative subsequent visit of CHD stenting. This study has been approved by the ethics committee of the hospital. Patients and their families were aware of this research and signed informed consent.

The inclusion criteria were as follows: (i) patients who agreed to the CAG examination; (ii) patients whose reexamination was within 3 months after surgery; (iii) patients who signed the informed consent; and (iv) patients with single-vessel lesion.

The exclusion criteria were as follows: (i) patients with severe heart, liver, and renal insufficiency; (ii) patients who were allergic to iodine-containing contrast agents; (iii) patients with contraindications to coronary CTA examination; (iv) patients with hyperthyroidism; and (v) patients whose conditions were unstable.

2.2. Methods of Examination

2.2.1. The CAG Examination. Coronary angiography was performed by a digital subtraction angiography system for CAG. After the F sheath tube was introduced through radial artery puncture, 3,000–5,000 u of heparin as the anticoagulant was injected through the sheath tube before the imaging surgery. After the heparin injection was completed, an iodine-containing contrast agent (Ultravist) was injected by a Radial 5F TIG angiography catheter to perform angiography for the left and right coronary arteries. There were 6 positions of left coronary angiography, which were positive: left anterior oblique, right anterior oblique, spider, liver, and foot. Right coronary angiography was performed in two positions. One was the left anterior oblique position, and the other was head posture. The collected images were evaluated by several senior coronary interventional physicians. The evaluation methods were mostly visual observation. Figure 1 shows the evaluation criteria for ISR.

2.2.2. Coronary CTA Examination. Coronary CTA was examined by a 64-slice spiral CT. During the examination, the patient was placed in the supine position, and electrocardiogram (ECG) monitoring was required. The scanning range was from 1.4 cm below the tracheal bifurcation to 2 cm below the diaphragmatic surface of the heart. A contrast agent (pump speed: 5 mL/s and contrast agent: iohexol) was injected with a high-pressure syringe, and the dose was controlled at 55–70 mL according to the patient's weight. The injection time was 11 s–14 s. After that, 35 mL of normal saline was injected. Then, automatic scanning was performed, and images of each vessel were collected. Specific scanning parameters were as follows: tube voltage was −120 kV; tube current was −320 mA; revolving speed was −0.37 s/r; layer thickness was −0.65 mm; and pitch was −0.19. The images of the control group were directly analyzed and processed by professionals, while those of the observation group were processed by automatic segmentation technology. All the images were evaluated by the same team of senior imaging experts. Figure 2 shows the definition of ISR.

2.3. The Improved Automatic Segmentation Algorithm

2.3.1. Data Preprocessing. When the heart was scanned by CTA, many different tissues were involved, including the heart, bone, lung, and coronary artery [17, 18]. Different tissue densities were generated. The difference of Hounsfield unit (HU) values [19] was reflected in the CTA images. However, the CT values of coronary arteries that needed to be scanned were not markedly different from those of the surrounding tissues. To highlight the coronary arteries, it was necessary to preprocess the CTA images. In general, the CT values of coronary CTA ranged from 0 HU to 600 HU, and the window level and windowing were 300 HU and 600 HU, respectively. The relationship between them satisfied equations (1), (2), and (3):

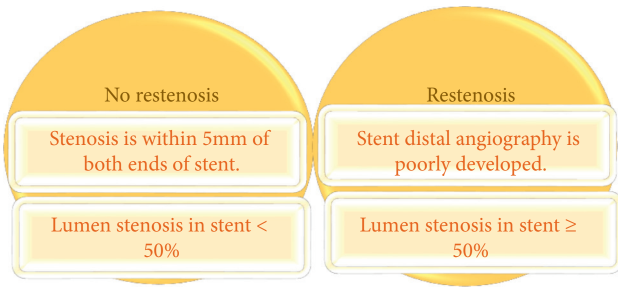

Figure 1: The evaluation criteria for ISR of CAG.

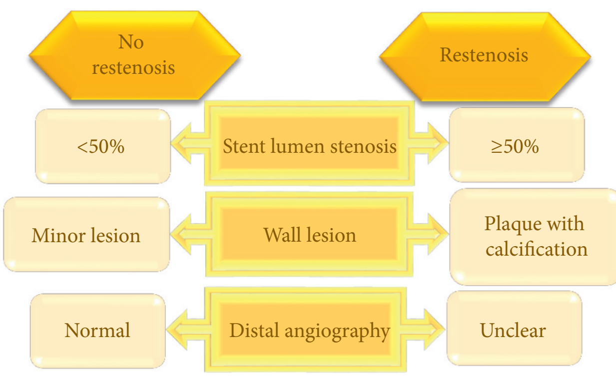

Figure 2: The evaluation criteria for ISR of CTA.

$$\begin{cases} y = 0 \\ x \in \left(0, wl - \dfrac{ww}{2}\right) \end{cases}, \tag{1}$$

$$\begin{cases} y = 128 + \dfrac{256 \cdot (x - wl)}{ww} \\ x \in \left[wl - \dfrac{ww}{2}, wl + \dfrac{ww}{2}\right] \end{cases}, \tag{2}$$

$$\begin{cases} y = 255 \\ x \in \left(wl + \dfrac{ww}{2}, 600\right) \end{cases}. \tag{3}$$

In the above equations, y represents the HU value of CTA image output, x represents the HU value of CTA image input, ww represents the windowing of CTA image, and wl represents the window level of CTA image. Then, the CT values of coronary CTA images were reduced to 0–245 by data enhancement.

2.3.2. Coronary CTA segmentation. The traditional region growth segmentation algorithm needed to manually set the initial point and threshold, so there was a great dependence. The region growth algorithm was combined with vascular similarity to improve the region growth and the accuracy of the segmentation algorithm. This algorithm includes three parts.

Firstly, the similarity features of blood vessels were extracted, which mainly involved the Hessian matrix [20] and the similarity function of blood vessels. The Hessian matrix of blood vessels was calculated by treating blood vessels as tubular structures. Then, three-dimensional data of vascular Hessian matrix were expressed as (7).

$$H_{(X-X)} = [I_{XX}(X), I_{XY}(X), I_{XZ}(X)], \tag{4}$$

$$H_{(X-Y)} = [I_{YX}(X), I_{YY}(X), I_{YZ}(X)], \tag{5}$$

$$H_{(X-Z)} = [I_{ZX}(X), I_{ZY}(X), I_{ZZ}(X)], \tag{6}$$

$$H_{(X)} = \begin{bmatrix} H_{(X-X)} \\ H_{(X-Y)} \\ H_{(X-Z)} \end{bmatrix}. \tag{7}$$

In equations (4), (5), (6), and (7), a series of $I_{xx}(X)$ represented the second derivative of point X along the X, Y, and Z directions of the graph. To improve the determination of vascular scale, the algorithm also introduced multiscale filtering, namely, the convolution of original data and the Gaussian kernels of different variances. The Gaussian kernel was expressed as follows:

$$G_{(X,\alpha)} = \left(\frac{1}{\left(\sqrt{2\pi\alpha^2}\right)^3}\right) \cdot e^{-\left(\frac{\|X\|^2}{2\alpha^2}\right)}. \tag{8}$$

In (8), α represents the variance, and $G\ (X, \alpha)$ represents that when the original data are at X, the variance is the Gaussian kernel of α. The Hessian matrix of the data of different scales was obtained by extracting the vascular features of different scales in the image through convolution. Then, the eigenvalue β_q $(q = 1, 2, 3)$ was calculated, and the corresponding eigenvector was χ_q $(q = 1, 2, 3)$. When $\beta_1 > \beta_2 > \beta_3$, based on voxels in blood vessels, β_3 would approach 0 infinitely, and χ_3 represented the radial direction of the vessel. β_1 and β_2 would be close and equal infinitely, χ_1 represents the tangential direction of the blood vessel, and χ_2 represents the normal direction of blood vessels. The features of tubular structures were screened according to the eigenvalues. In accordance with the above-mentioned calculation, some experts proposed the vascular similarity function under the eigenvalue, eigenvalue features, and vascular geometry features. The specific expression was as follows:

$$U_r(t) = \begin{cases} 0, & \text{if } \beta_1 > \dfrac{0}{\beta_3} > 0, \\ (1 - U_1) \bullet U_2 \bullet (1 - U_3), & \text{other} \end{cases}. \tag{9}$$

It was also expressed as (13).

$$S = \|H\|_F = \sqrt{\sum_{i=1}^{3} \beta_i^2}. \tag{10}$$

$$U_1 = \exp - \left[\frac{\left(|\beta_2| / |\beta_3|\right)^2}{\left(2\varepsilon^2\right)}\right]. \tag{11}$$

$$U_2 = \exp - \left[\frac{\left(|\beta_1| / \sqrt{|\beta_2 \beta_3|} \right)^2}{\left(2\phi^2\right)} \right]. \tag{12}$$

$$U_3 = \exp - \left[\frac{\left(S^2\right)}{\left(2\varphi^2\right)} \right]. \tag{13}$$

S represents the Gaussian Blur in (8). ε and ϕ represent the threshold that controlled the linear filter. φ needed to determine the threshold according to the gray level of the image.

Secondly, the seed point was located, and the root node of the coronary artery was automatically located according to the significance of the ascending aorta and the connection with the coronary artery to achieve the automatic segmentation of the coronary artery. Due to the irregularity of the ascending aorta circle, the segmentation method under convolutional neural network (CNN) was adopted. The idea of CNN is encoding (convolution-feature extraction)-decoding (deconvolution-feature mapping) mode. In the training process of ascending the aorta section by this mode, the loss function was DiceLoss. It was expressed as

$$\text{DiceLoss} = 1 - \left[\left(2 \sum_{j \in C} \left(\text{lab}_j \cdot \text{pre}_j \right) + \frac{\text{smooth}}{\sum_{j \in C} \text{pre}_j} + \sum_{j \in C} \text{lab}_j + \text{smooth} \right) \right]. \tag{14}$$

In (14), C represents a collection of pixels for the entire, *lab* represents the pixel label, and *pre* represents the predicted value of pixels. *Smooth* represents the constant in case that the denominator was zero.

The final part was the region growth. The conditions for the automatic implementation of region growth were provided by the abovementioned calculation. The specific steps of the region growth were as follows.

The first step was establishing the initial seed point.

The second step was fixing the voxel in the adjacent region of the seed point as the center and setting it as the point to be measured. It was calculated whether the growth conditions were satisfied. Then, the ones that were not satisfied were written down which were not calculated in the next growth. The other points that satisfied the requirements were cached.

The third step was extracting out one of the tested voxel points from the cache to update the initial seed points in the second step and repeat it.

The last step was to stop growing when the pixels to be measured satisfied the growth conditions when finished updating.

2.3.3. Methods of Evaluation. Image enhancement, extraction of similarity features of vessels at different scales, segmentation based on CNN, and the segmentation effect of the overall segmentation algorithm were analyzed. Based on the segmentation accuracy of CNN, the error between the pixels at the corresponding position on the output image and the original label image was evaluated. The calculation method was shown in (15). In (16), the segmentation effect of the overall segmentation algorithm was measured by the average voxel error [21].

$$\text{Acc} = \left(\frac{1}{P}\right) \cdot \sum_{j \in C} \left(\frac{V_i}{G_i}\right). \tag{15}$$

In (15), P represents the number of samples in the test set, C represents the collection of test set pixels, V represents the correct number of pixels in the predicted image, and G represents the number of pixels of positive samples in the annotation image.

$$\text{Error} = \left(\frac{1}{P}\right) \cdot \sum_{j \in C} \left(o_i - O_i\right). \tag{16}$$

In (16), P represented the population prime point, C represented the whole data, o represented the voxel points to be compared, and O represented the standard voxel point.

2.4. Observation Indexes

(I) Two or more cardiovascular imaging physicians evaluated the CTA image quality of the two groups. Table 1 shows the scoring criteria.

(II) The diagnostic sensitivity, specificity, positive predictive value, negative predictive value, and accuracy of CTA images of the two groups were evaluated based on the diagnostic results of CAG for coronary artery disease stenosis in postoperative review as the criteria.

2.5. Statistical Methods. SPSS 22.0 was employed for data statistics and analysis. The data were expressed as $\overline{x} \pm s$, and the two independent sample t-test was adopted for intergroup comparison. Percentage (%) or cases was how count data were expressed, and the intergroup comparison was tested by χ^2. The difference was statistically considerable with $P < 0.05$.

3. Results

3.1. The Algorithm Performance

3.1.1. The Effect of Image Enhancement. After enhanced processing, the CT value method of the coronary CTA image was compressed to 0–245 HU. Figure 3 shows the effect of processing. The comparison between the coronary artery

Table 1: Scoring criteria of CTA image.

Score (point)	ISR	Variant	Artifact
0	Invisible structure	——	——
1	Visible structure	Obvious	Obvious
2	Still clear structure	Mild	Mild
3	Clear structure	Not found	Not found

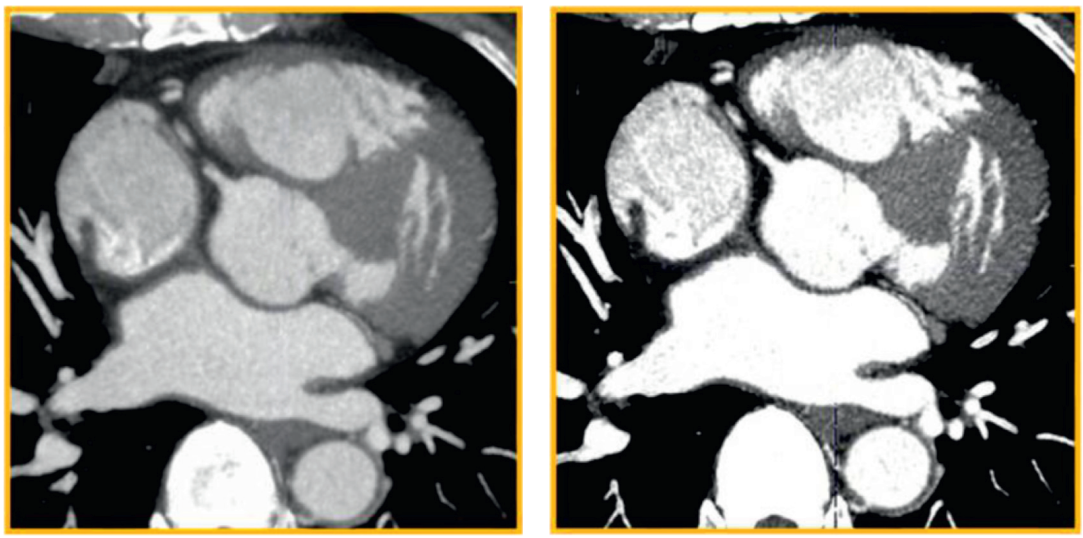

(a)

(b)

Figure 3: The effect of CTA data enhancement processing. (a) The original image; (b) the enhanced image.

and the surrounding tissue was evidently enhanced. The coronary artery area was more prominent, while the surrounding tissue was observably reduced, which was more helpful to observe the lesion.

3.1.2. Extraction of Similarity Features of Vessels of Different Scales. Figure 4 shows the fuzzy results of the Gaussian kernel with different variances ($\alpha = 0.5$, 1, 2). With the increase of α value, the response of small structural features was weakened gradually. After several tests, the resulting images of $\alpha = 0.5$, 1, and 2 were fused. The results showed that the details of various vessels in the fused images were reflected (Figure 4(e)).

3.1.3. CNN Algorithm Segmentation Effect. The CNN algorithm was used to segment ascending aorta slices. Figure 5 shows the segmentation effects of ascending aorta sections at different levels (if the highest layer was the first layer, Figure 5 was the first and second layer from top to bottom). After calculation, the segmentation accuracy of the CNN algorithm was 87.89%, which was at a high level.

3.1.4. The Improved Growth Automatic Segmentation Effect. The improved automatic growth segmentation and traditional region growth segmentation were compared regarding the average voxel error (HU/voxel). The results showed that the average voxel error of the improved segmentation method was 1.8921 (HU/voxel), while that of the traditional region growth method was 7.10091 (HU/voxel). The average voxel error of the improved segmentation method was obviously lower than that of the traditional growth algorithm ($P < 0.05$) (Figure 6).

3.2. Comparison of Basic Data. Figure 7 shows the comparison of the basic data between the two groups. In the control group, 72.31% were males, and 27.69% were females. In the observation group, 66.15% were males, and 33.85% were females. The mean age of the control group was 61.34 ± 8.85 years old, and that of the observation group was 60.01 ± 9.65 years old. The mean diameter of the stents in the control group was 2.56 ± 0.21 mm, and that of the observation group was 2.96 ± 0.13 mm, without any significant difference ($p > 0.05$). It suggested that the study had certain feasibility.

3.3. The Score of Image Quality. The score results of the CTA image quality were as follows: the mean CTA score of the control group was (2.01 ± 0.73) and that of the observation group was (2.89 ± 0.11), which was notably higher than that of the control group ($p < 0.05$) (Figure 8). Figure 8(a) shows the CTA image of reexamination results 2 months after surgery of a 56-year-old male patient in observation group, and Figure 8(b) shows the CTA image of reexamination results two months and one week after surgery of a 60-year-

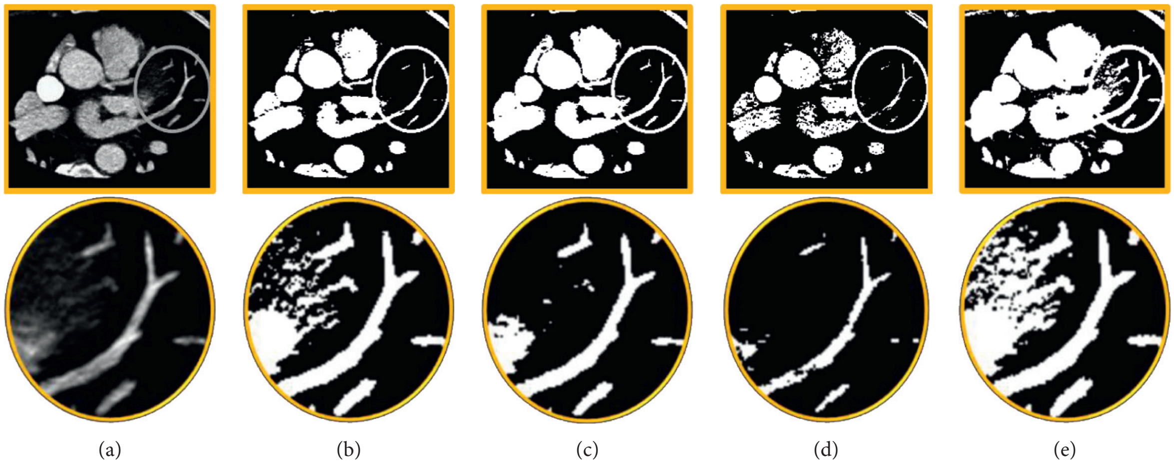

FIGURE 4: The images of extraction effect of vascular similarity features under different values of α. (a) Original image; (b) the image with $\alpha = 0.5$; (c) the image with $\alpha = 1$; (d) the image with $\alpha = 2$; (e) the fused image.

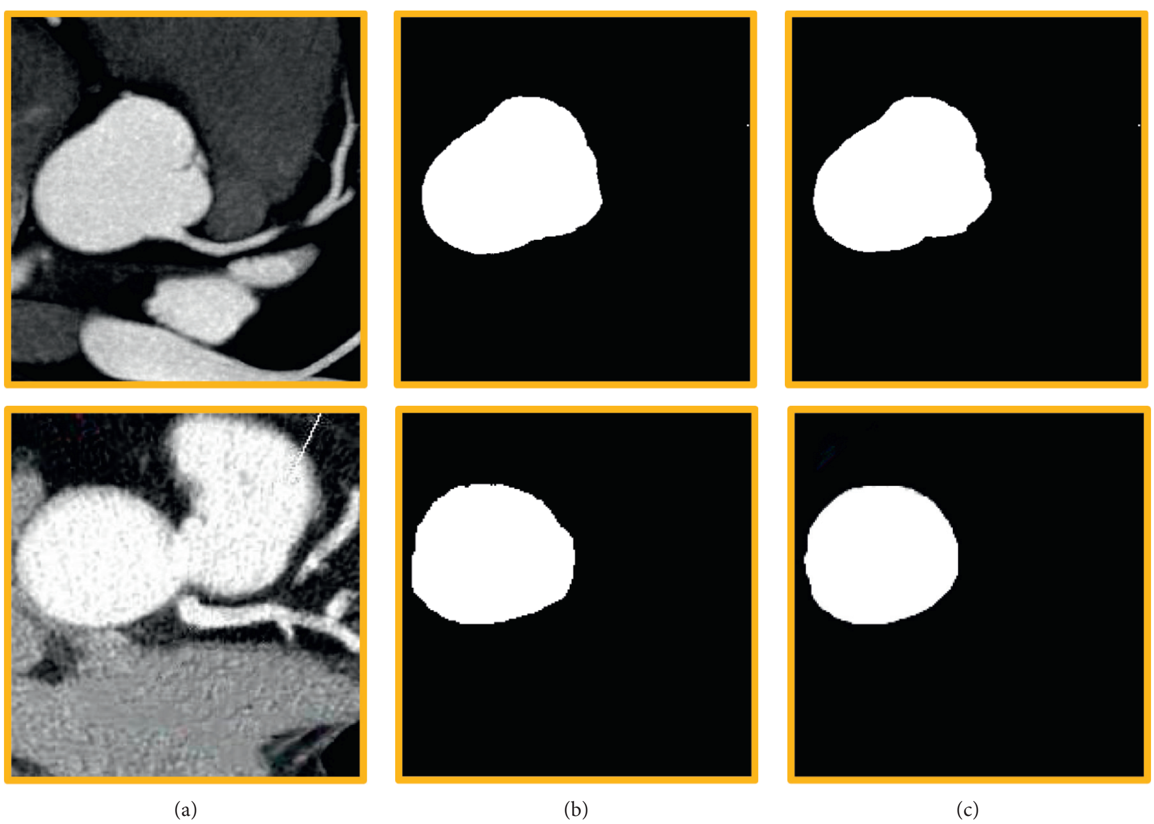

FIGURE 5: The segmentation effect of CNN algorithm. (a) The original image; (b) the labelling image; (c) the final effect image.

old male patient in control group. According to Figure 8, the lumen and wall plaques of the coronary arteries in the observation group were more obvious than those in the control group (the lesions were inside the yellow circle).

3.4. Comparison of Diagnostic Efficacy of Restenosis. Figure 9 shows the restenosis diagnostic efficacy results of the two groups' CTA images. In the control group, CTA diagnostic sensitivity was 74.29% (26/35), specificity was 60% (18/30), positive predictive value was 68.42% (26/38), negative predictive value was 66.67% (18/27), and accuracy was 67.69% (44/65). In the observation group, CTA diagnostic sensitivity was 91.43% (32/35), specificity was 86.76% (26/30), positive predictive value was 88.89% (32/36), negative predictive value was 89.66% (26/29), and accuracy was 89.23% (58/65). Consequently, the restenosis diagnosis sensitivity, specificity, positive predictive value, negative

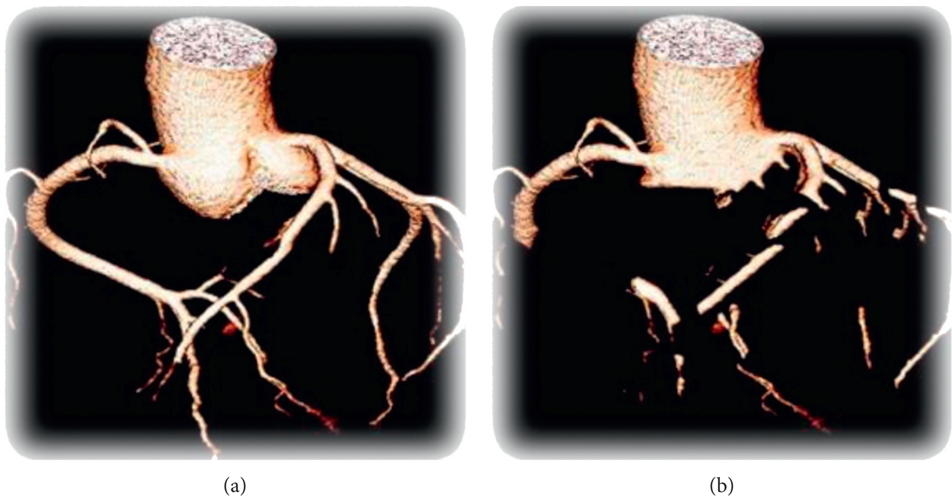

Figure 6: The effect images of regional growth segmentation. The image segmentation effect of (a) the improved region growth segmentation and (b) the traditional region growth segmentation.

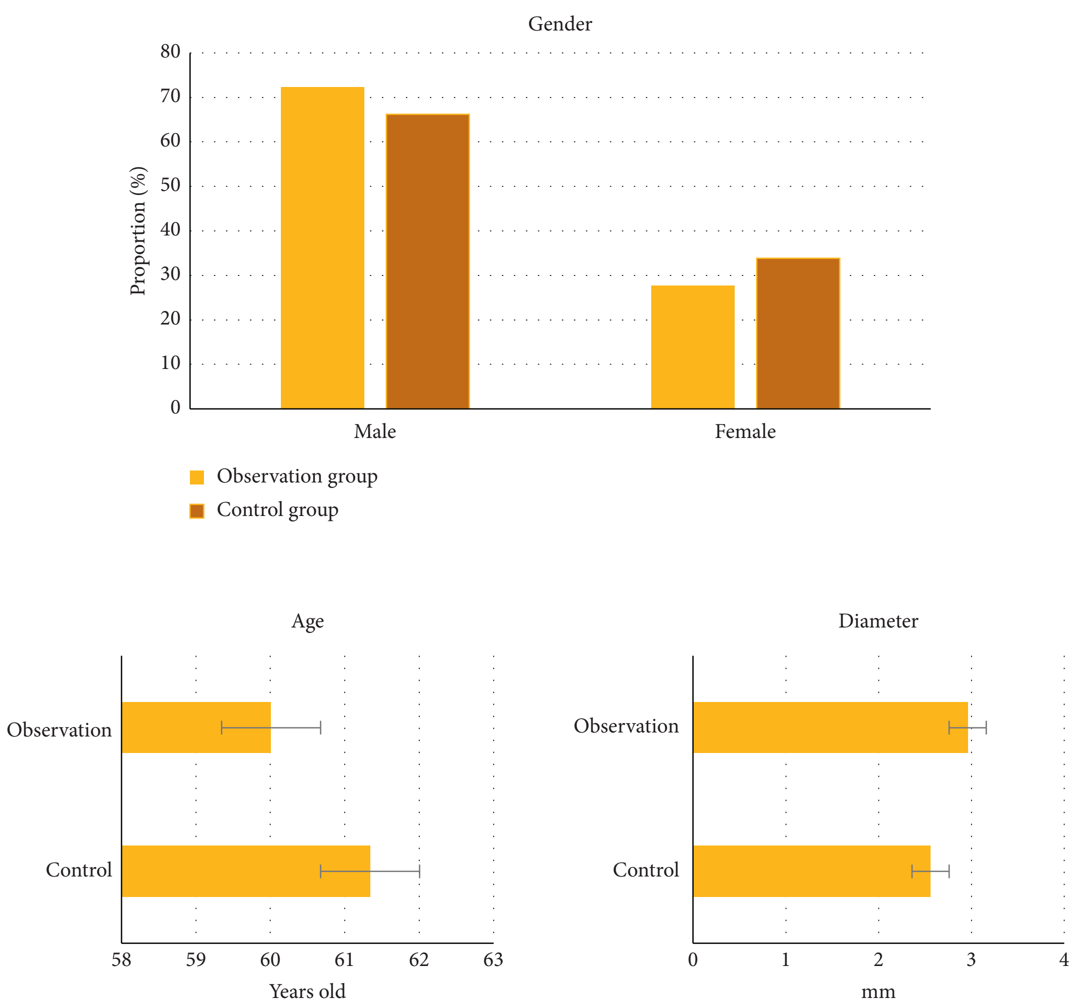

Figure 7: Comparison of basic data.

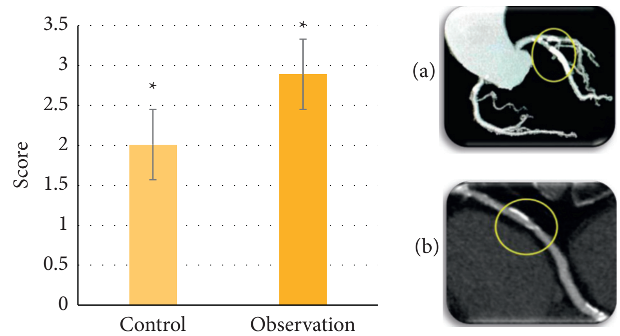

Figure 8: The score results of CTA image quality. *The comparison between the two groups was of statistical significance, $p < 0.05$.

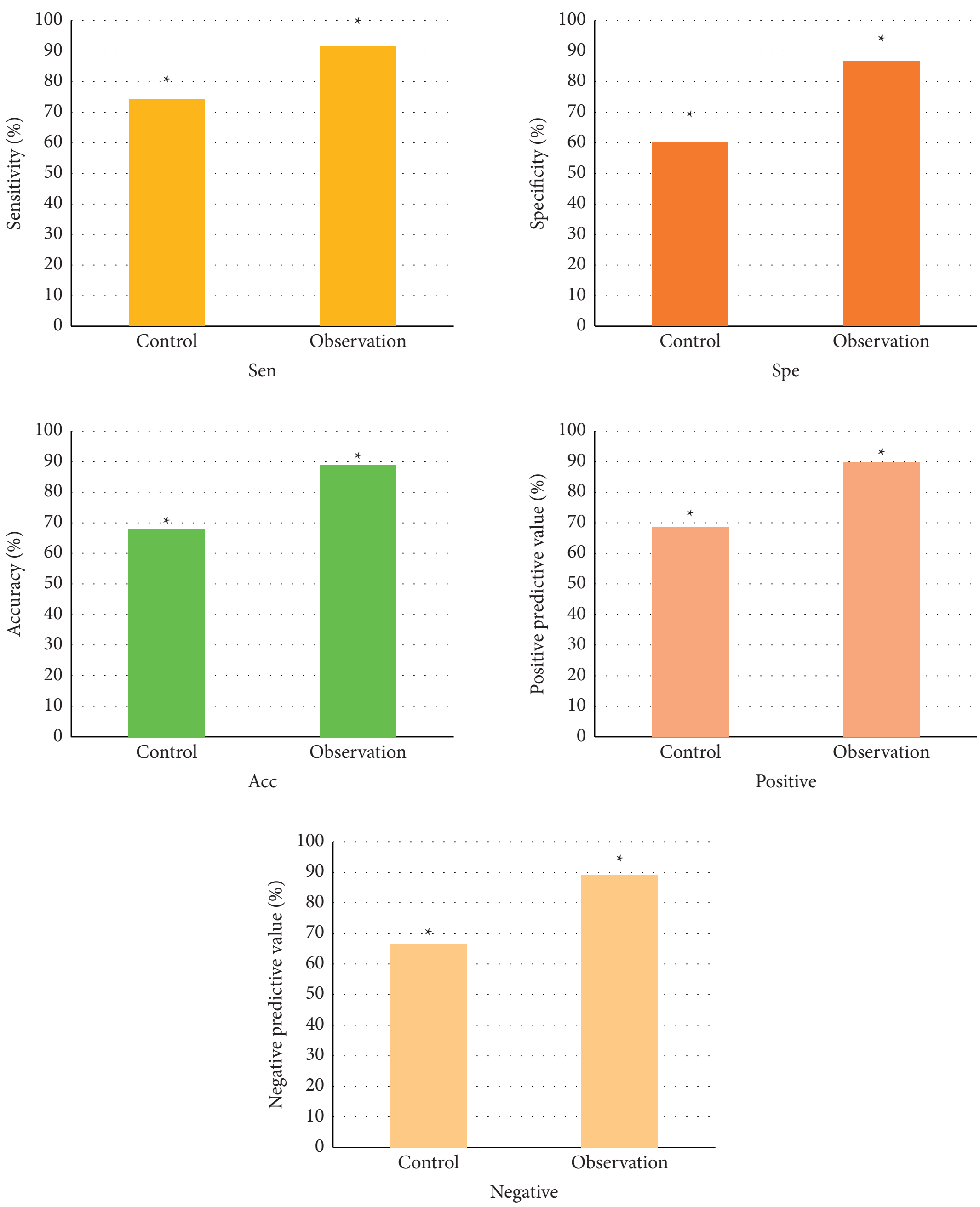

Figure 9: Comparison of diagnostic efficacy of CTA restenosis. *The comparison between the two groups was of statistical significance, $p < 0.05$.

predictive value, and accuracy of CTA images in the observation group were higher than those in the control group ($p < 0.05$).

4. Discussion

Region growth-based CTA images were used to diagnose restenosis after coronary stenting. To further improve the accuracy of image segmentation, the CNN algorithm and vascular similarity feature were combined to improve the region growth. The results showed that the segmentation accuracy of CNN algorithm could reach 87.89%, which was at a high level, indicating that the CNN algorithm had a good effect on image segmentation. Meijs et al. (2020) [22] proposed that the CNN algorithm had high performance in image segmentation. Moreover, the CNN segmentation algorithm was applied by many experts for CTA image diagnosis research, and the performance was affirmed [23–25]. However, in the extraction of vascular similarity features, the detailed vascular features could not be displayed with the gradual increase of the Gaussian kernel α. Nonetheless, after the fusion of the results of different scales, vessels of different sizes were revealed. Hence, multiscale vascular similarity feature extraction was more effective than single-scale vascular information extraction. The extraction of vascular similarity features involved the vascular similarity function, which was first proposed in 1998 and was widely used in the field of vascular segmentation [26]. Nevertheless, most of them were used for vascular segmentation of retinal images with high segmentation accuracy [27, 28]. Then, the improved region growth segmentation algorithm was compared with the traditional region segmentation algorithm. The results showed that the mean voxel error of the improved algorithm was manifestly lower than that of the traditional algorithm (1.8921 HU/voxel vs. 7.10091 HU/voxel) ($p < 0.05$). The smaller the mean voxel error was, the more accurate the segmentation result was. Consequently, the results indicated that the improved regional growth method could extract coronary arteries better. Region growth was a relatively common segmentation algorithm, which was involved in both magnetic resonance imaging (MRI) images [29] and CT images [30]. It was a segmentation method with great potential. The adoption effect of the improved method in clinical practice was explored.

Firstly, the quality scores of the two groups of CTA images were compared. The results showed that the mean score of CTA image in the observation group was higher than that in the control group (2.89 ± 0.11 points vs. 2.01 ± 0.73 points) ($p < 0.05$). Then, the diagnostic efficacy of CTA images in restenosis after coronary stenting was compared between the two groups. The results showed that the diagnostic sensitivity (91.43%), specificity (86.76%), positive predictive value (88.89%), negative predictive value (89.66%), and accuracy (89.23%) of the observation group were higher than those of the control group ($p < 0.05$). These results indicated that CTA images processed by an automatic segmentation algorithm were helpful to diagnose the restenosis after coronary stenting, and they also had good clinical adoption values, which reflected the adoption advantage of artificial intelligence (AI) in the field of medical imaging. In recent years, much attention has been paid to the adoption of segmentation algorithms in image processing, and lots of studies have shown that segmentation images are more conducive to the diagnosis of diseases. For instance, Liu et al. (2020) proposed that segmented MRI images could help doctors better observe a patient's heart health [31]. Furthermore, Pang et al. (2021) found that segmentation had great potential for clinical diagnosis and treatment of spinal diseases [32]. To sum up, the automatic segmentation algorithm was helpful to improve the diagnostic efficacy of CTA images with a good clinical adoption value.

5. Conclusion

In conclusion, the segmentation effect of the coronary CTA image was more precise by combining the CNN algorithm with the region growth algorithm of the vascular similarity feature. Besides, CTA images based on improved region growth segmentation algorithms had better clinical adoption value in the diagnosis of restenosis after coronary stenting. However, the type of patients selected in this study is relatively single, that is, only patients with single-vessel lesions, so it is not comprehensive enough and further comprehensive investigation is needed. The results of this study showed that the adoption of intelligent algorithms in the field of medical imaging had great potential, which was worth expecting and investigating.

Data Availability

The data used to support the findings of this study are available from the corresponding author upon request.

Conflicts of Interest

The authors declare no conflicts of interest.

References

[1] Y. Tian, P. Deng, B. Li et al., "Treatment models of cardiac rehabilitation in patients with coronary heart disease and related factors affecting patient compliance," *Reviews in Cardiovascular Medicine*, vol. 20, no. 1, pp. 27–33, 2019.

[2] M. Fioranelli, A. G. Bottaccioli, F. Bottaccioli, M. Bianchi, M. Rovesti, and M. G. Roccia, "Stress and inflammation in coronary artery disease: a review psychoneuroendocrineimmunology-based," *Frontiers in Immunology*, vol. 9, p. 2031, 2018.

[3] B. R. Pagliaro, F. Cannata, G. G. Stefanini, and L. Bolognese, "Myocardial ischemia and coronary disease in heart failure," *Heart Failure Reviews*, vol. 25, no. 1, pp. 53–65, 2020.

[4] J. E. Tamis-Holland, H. Jneid, H. R. Reynolds et al., "Contemporary diagnosis and management of patients with myocardial infarction in the absence of obstructive coronary artery disease: a scientific statement from the American heart association," *Circulation*, vol. 139, no. 18, pp. e891–e908, 2019.

[5] S. Li, L. Sun, L. Qi et al., "Effect of high homocysteine level on the severity of coronary heart disease and prognosis after stent

implantation," *Journal of Cardiovascular Pharmacology*, vol. 76, no. 1, pp. 101–105, 2020.

[6] A. Maehara, M. Matsumura, Z. A. Ali, G. S. Mintz, and G. W. Stone, "IVUS-guided versus OCT-guided coronary stent implantation," *Journal of the American College of Cardiology: Cardiovascular Imaging*, vol. 10, no. 12, pp. 1487–1503, 2017.

[7] L. Lin, L. Wang, X.-N. Zhang et al., "A clinical strategy to improve the diagnostic accuracy of 1.5-T non-contrast MR coronary angiography for detection of coronary artery disease: combination of whole-heart and volume-targeted imaging," *European Radiology*, vol. 31, no. 4, pp. 1894–1904, 2021.

[8] M. Garmer, M. Bonsels, F. Metz, O. Klein-Wiele, B. Brandts, and D. Grönemeyer, "Coronary computed tomography angiography and endocardial leads - image quality in 320-row CT using iterative reconstruction," *Clinical Imaging*, vol. 50, pp. 157–163, 2018.

[9] O. Ghekiere, R. Salgado, N. Buls et al., "Image quality in coronary CT angiography: challenges and technical solutions," *British Journal of Radiology*, vol. 90, no. 1072, Article ID 20160567, 2017.

[10] R. S. Driessen, I. Danad, W. J. Stuijfzand et al., "Comparison of coronary computed tomography angiography, fractional flow reserve, and perfusion imaging for ischemia diagnosis," *Journal of the American College of Cardiology*, vol. 73, no. 2, pp. 161–173, 2019.

[11] H. Du, K. Shao, F. Bao et al., "Automated coronary artery tree segmentation in coronary CTA using a multiobjective clustering and toroidal model-guided tracking method," *Computer Methods and Programs in Biomedicine*, vol. 199, Article ID 105908, 2021.

[12] Z. Wan, Y. Dong, Z. Yu, H. Lv, and Z. Lv, "Semi-supervised support vector machine for digital twins based brain image fusion," *Frontiers in Neuroscience*, vol. 15, Article ID 705323, 2021.

[13] J. Cui, H. Guo, H. Wang, F. Chen, L. Shu, and L. C. Li, "Fully-automatic segmentation of coronary artery using growing algorithm," *Journal of X-Ray Science and Technology*, vol. 28, no. 6, pp. 1171–1186, 2020.

[14] Q. Liu, H. Mohy-Ud-Din, N. E. Boutagy et al., "Fully automatic multi-atlas segmentation of CTA for partial volume correction in cardiac SPECT/CT," *Physics in Medicine and Biology*, vol. 62, no. 10, pp. 3944–3957, 2017.

[15] Y. Jiang, J. Qian, S. Lu, Y. Tao, J. Lin, and H. Lin, "LRVRG: a local region-based variational region growing algorithm for fast mandible segmentation from CBCT images," *Oral Radiology*, vol. 37, no. 4, pp. 631–640, 2021.

[16] G. Ma, J. Yang, and H. Zhao, "A coronary artery segmentation method based on region growing with variable sector search area," *Technology and Health Care*, vol. 28, no. S1, pp. 463–472, 2020.

[17] J. Liu, C. Wang, Q. Li et al., "Free-breathing, non-gated heart-to-brain CTA in acute ischemic stroke: a feasibility study on dual-source CT," *Frontiers in Neurology*, vol. 13, Article ID 616964, 2022.

[18] P. Poskaite, M. Pamminger, C. Kranewitter et al., "Self-navigated 3D whole-heart MRA for non-enhanced surveillance of thoracic aortic dilation: a comparison to CTA," *Magnetic Resonance Imaging*, vol. 76, pp. 123–130, 2021.

[19] A. Sudhyadhom, "On the molecular relationship between Hounsfield Unit (HU), mass density, and electron density in computed tomography (CT)," *PLoS One*, vol. 15, no. 12, Article ID e0244861, 2020.

[20] A. Denzel and J. Kästner, "Hessian matrix update scheme for transition state search based on Gaussian process regression," *Journal of Chemical Theory and Computation*, vol. 16, no. 8, pp. 5083–5089, 2020.

[21] Y. Zhao, A. M. Hernandez, J. M. Boone, and S. Molloi, "Quantification of airway dimensions using a high-resolution CT scanner: a phantom study," *Medical Physics*, vol. 48, no. 10, pp. 5874–5883, 2021.

[22] M. Meijs, F. J. A. Meijer, M. Prokop, B. v. Ginneken, and R. Manniesing, "Image-level detection of arterial occlusions in 4D-CTA of acute stroke patients using deep learning," *Medical Image Analysis*, vol. 66, Article ID 101810, 2020.

[23] J. Li, Y. Liu, Z. Zhang, B. Liu, and Y. Wang, "PmDNE: prediction of miRNA-disease association based on network embedding and network similarity analysis," *BioMed Research International*, vol. 2020, Article ID 6248686, 9 pages, 2020.

[24] H. O'Brien, J. Whitaker, B. Singh Sidhu et al., "Automated left ventricle ischemic scar detection in CT using deep neural networks," *Frontiers in Cardiovascular Medicine*, vol. 8, Article ID 655252, 2021.

[25] M. Hu, Y. Zhong, S. Xie, H. Lv, and Z. Lv, "Fuzzy system based medical image processing for brain disease prediction," *Frontiers in Neuroscience*, vol. 15, Article ID 714318, 2021.

[26] N. Anegondi, A. Kshirsagar, T. B. Mochi, and A. Sinha Roy, "Quantitative comparison of retinal vascular features in optical coherence tomography angiography images from three different devices," *Ophthalmic Surgery, Lasers and Imaging Retina*, vol. 49, no. 7, pp. 488–496, 2018.

[27] F. Tian, Y. Li, J. Wang, and W. Chen, "Blood vessel segmentation of fundus retinal images based on improved frangi and mathematical morphology," *Computational and Mathematical Methods in Medicine*, vol. 2021, Article ID 4761517, 11 pages, 2021.

[28] T. Mochi, N. Anegondi, M. Girish, C. Jayadev, and A. Sinha Roy, "Quantitative comparison between optical coherence tomography angiography and fundus fluorescein angiography images: effect of vessel enhancement," *Ophthalmic surgery, lasers & imaging retina*, vol. 49, no. 11, pp. e175–e181, 2018.

[29] E. S. Biratu, F. Schwenker, T. G. Debelee, S. R. Kebede, W. G. Negera, and H. T. Molla, "Enhanced region growing for brain tumor MR image segmentation," *Journal of Imaging*, vol. 7, no. 2, p. 22, 2021.

[30] S. Tan, L. Li, W. Choi, M. K. Kang, W. D. D'Souza, and W. Lu, "Adaptive region-growing with maximum curvature strategy for tumor segmentation in18F-FDG PET," *Physics in Medicine and Biology*, vol. 62, no. 13, pp. 5383–5402, 2017.

[31] D. Liu, Z. Jia, M. Jin et al., "Cardiac magnetic resonance image segmentation based on convolutional neural network," *Computer Methods and Programs in Biomedicine*, vol. 197, Article ID 105755, 2020.

[32] S. Pang, C. Pang, L. Zhao et al., "SpineParseNet: spine parsing for volumetric MR image by a two-stage segmentation framework with semantic image representation," *IEEE Transactions on Medical Imaging*, vol. 40, no. 1, pp. 262–273, 2021.

Hindawi
Contrast Media & Molecular Imaging
Volume 2022, Article ID 3080437, 13 pages
https://doi.org/10.1155/2022/3080437

Research Article

Impact of Music in Males and Females for Relief from Neurodegenerative Disorder Stress

Nilima Salankar,[1] **Anjali Mishra**,[1] **Deepika Koundal**,[1] **Vinh Truong Hoang**,[2] **Kiet Tran-Trung**,[2] **Atef Zaguia**,[3] **and Assaye Belay**[4]

[1]*School of Computer Science University of Petroleum and Energy Studies, Bidholi, Dehradun, India*
[2]*Faculty of Computer Science, Ho Chi Minh City Open University, Address: 97 Vo Van Tan Ward Vo Thi Sau District 3, Ho Chi Minh City, Vietnam Code Postal: 70000*
[3]*Department of Computer Science, College of Computers and Information Technology, Taif University, P.O. BOX 11099, Taif 21944, Saudi Arabia*
[4]*Department of Statistics, Mizan-Tepi University, Tepi, Ethiopia*

Correspondence should be addressed to Deepika Koundal; koundal@gmail.com

Received 21 January 2022; Accepted 5 March 2022; Published 12 April 2022

Academic Editor: M Pallikonda Rajasekaran

Neurological imbalance sometimes resulted in stress, which is experienced by the number of people at some moment in their life. A considerable measurement scheme can quantify the stress level in an individual, in which music has always been considered as the best therapy for stress relief in healthy human being as well in severe medical conditions. In this work, the impact of four types of music interventions with the lyrics of Hindi music and varying spectral centroid has been studied for an analysis of stress relief in males and females. The self-reported data for stress using state-trait anxiety (STA) and electroencephalography (EEG) signals for 14 channels in response to music interventions have been considered. Features such as Hjorth (activity, mobility, and complexity), variance, standard deviation, skew, kurtosis, and mean have been extracted from five bands (delta, theta, alpha, beta, and gamma) of each channel of the recorded EEG signals from 9 males and 9 females of the age category between 18 and 25 years. The support vector machine classifier has been used to classify three subsets: (i) male and female, (ii) baseline and female, and (iii) baseline and male. The noteworthy accuracy of 100% was found at the delta band for the first subset, beta and gamma bands for the second subset, and beta, gamma, and delta bands for the third subset. STA score has shown more deviation in the male category than in female, which gives a clear insight into the impact of music intervention with varying spectral centroid that has a higher impact to relieve stress in the male category than the female category.

1. Introduction

Any changes in the external or the internal environment that demands the human body to react and adjust often lead to stress that has usually been found in the college students. The external environment such as studies, job, society, and relationships are major impacting and internal environment like own thoughts and arised emotions with respective to thoughts. According to Alison Abbott, the stress can be threatening to both physical as well as mental health [1]. Stress causes many mental health problems such as hypertension [2], stroke [3], sleep disturbances [4], and depression/suicide [5]. It has also been found stress is one of the elements causing physical disorders such as cardiac attack [6], irritable bowel syndrome (IBS), back pain, and gastro-oesophageal reflux disease (GERD) [7]. Therefore, several responses have been used to measure the stress level. Clinically, the stress level of an individual is evaluated by the self-reported questionnaires with the rating scale such as relative stress scale, perceived stress scale (PSS) [8], and state-trait anxiety inventory (STAI) [9]. Apart from this, the physical features of an individual can also be used as one of the methods to compute and measure the stress such as facial expressions [10] and blink rate [11]. The stress causes dynamic alterations in the autonomous nervous system [12]. Also, it impacts the heart rate [13], skin conductance [14], and respiration [15]. According to neurologists, the stress majorly affects the human brain as it has a tendency to demonstrate the stressful situations [16, 17]. The electroencephalography (EEG) [18] and functional magnetic resonance imaging (FMRI) [19] are most commonly used tools to examine the brain activity. The EEG is the most preferred method because of inexpensive equipment with less disruption. In reference [20], the responses such as heart rate variability (HRV) and heart rate are very much associated with EEG in response to the stress.

Looking onto the effects caused by the stress on an individual's life, it is required to uncover the approaches, which could help to get relief from the stress and recuperate to the mental stability. Among the ample available approaches, music has been found as one of the therapies used for the mental disability treatment because of its power to change emotions and psychological behaviour of the human being [21, 22]. Listening to music is very common among the people for the mental relaxation in general [23, 24]. Moreover, it also helps to get into relaxing mode during anxiety or stressful situations irrespective of age and sex [25]. This therapy works very well on human beings [26, 27]. It plays a vital role in an individual's daily life for stress releasing as it directly impacts the brain activity [28]. Various methods have been used for visualizing the characteristics of the signals [29, 30]. Hippocampus and amygdala are the two brain structures, which are activated during the stressful situation, are known to be concerned with the regulation of the hypothalamic-pituitary-adrenal (HPA) axis, and are responsible for the tempting emotions with the music [31]. Another part of the human body, which is sensitive to the stress, is ANS, which provokes the physiological changes in response to music. Hence, this is the reason to study the impact of listening to music on the stress and anxiety levels extensively. According to various studies, music has a tendency to improve the emotional health of an individual by lowering down the stress level. The electrical signals generated in the human brain are captured by the EEG through the electrodes placed on the scalp. These EEG signals vary in the frequency and amplitude. Generally, the EEG signal frequency is classified into five frequency bands as delta (δ: up to 4 Hz), theta (θ: 4–8 Hz), alpha (α: 8–15 Hz), beta (β: 15–32 Hz), and gamma (γ: $\geq$ 32 Hz) waves. Each band indicates a different state of mind in response to any stimuli whether it is external or internal. Audio, as well as video, can be stimuli responsible for the activation of state of mind [32]. Although listening to music has enormous effect on the stress reduction, a definite conclusion of its effect cannot be drawn.

To the best of our knowledge, this is the first work that presents the musical intervention impact with varying spectral centroid and lyrics in emotion domain applied for stress relief in male and female categories. Motivation for carrying out this work is to identify an intensity of provoked stress in real-time environment. The contribution of this study is as follows:

(i) Identified an appropriate band and region where the impact of stimuli is more significant and requires to dig deep to analyze reduction in stress level.

(ii) To analyze the impact of Hindi music with lyrics and varying spectral centroid's impact on stress relief of male and female categories, the EEG signals of the healthy participants (male and female) have been recorded in our university laboratory setting using RMS EEG device. It is hypothesized that musical interventions used would reflect in recorded EEG signals and would help us to analyze the stress impacts in the light of variations in data. In this, four musical interventions have been considered whose goal is to analyze the nonmusical target. Eight features are extracted and fed to the classifier, that is, support vector machine (SVM) for the classification of the music intervention impact on male and female categories. It has been analyzed from experiments that males are more inclined towards triggered music intervention (MI-1, MI-2, and MI-3) as compared to females aged 18–25.

The study is designed in the four sections as follows: Section 2 discusses the related work, whereas Section 3 describes the material and method. Section 4 gives detailed information about the experiment results of the classification of the impact on the stress level in the male and the female category in response to different types of music along with the discussion of results, whereas Section 5 deals with the conclusion.

2. Related Work

According to the authors of reference [33], the left hemisphere's activities are taken over by the right hemisphere pointing to the regions of the stress detection. The beta and alpha bands denote the consciousness level, whereas delta and theta refer to the unconscious state of mind [34]. The prominent beta wave frequencies are known to be the indication of the stress and anxiety levels. Not only various features but also a number of classification methods have been employed by the researchers in the process of assessing the stress from the EEG brain signals. Researchers have used various features in order to assess the stress level using EEG signals such as frequency band power, peak frequency in alpha band, cross correlation between band powers, and Hjorth parameters, which are time-based characteristics of EEG waveform [35]. EEG signal is decomposed to bands with the help of signal processing method of discrete wavelet transformation method [36]. Listening to music initiates a number of cognitive processes in the human brain and is, hence, presumed that stress-related cognitive and psychological responses are influenced by the music [37]. Music listening helps reduce the psychological stress and increase the coping capacity of the stress in an individual [38, 39]. In most of the findings, music listening reduces the stress and anxiety level [40, 41], but not all findings show the reductions in the stress or anxiety level after listening to music [42, 43]. Listening to music has shown an impact on the stress and anxiety, which is an automatic response in any threatening or stressful situation. Music is found to activate the brain activities in terms of intense emotions [44–46]; hence, it has a tendency to change the anxiety levels caused by stressful situations or experiences. Several studies have considered different genres of music impact on the stress level and it has been found that classical music helps more in stress relieving than nonclassical music such as heavy metal and hard rock [40]. Not only music or noise but sedative music and silence also contribute to reducing the stress and help people to relax [47, 48]. Overall, there is merely no difference in the impact of silence, sedative, and simulative music on the stress relief [49]. In reference [50], the authors introduce the various perception of music. Music can be used for acquiring concentration or attention while doing some cognitive activities. In reference [51], the authors find that music has an impact on the performance of every participant while doing some cognitive activities. Not only has this but the results also helped to discriminate the genders of the participants. The difference in the characteristics of music leads to variations in the psychological regulation of the adolescents. The authors use EEG signals to prove this and claim that this conclusion could be used for treating the psychological disorders diseases [52]. In reference [53], the authors studied the EEG signals under the influence of favourite and the relaxed music stimuli and concluded that relaxing music has a better effect than the favourite one even listened for a longer period. EEG is used rapidly to acquire the stress level of an individual by analyzing the brain signals captured. In reference [54], the authors use time and frequency features from the EEG signals and applied supervised learning algorithms in order to get the worker's stress level while working and achieved 80.32% of accuracy. Many researchers have used EEG signals to compute the stress level by analyzing the brainwaves [55–57]. Responsible factors of stress in the job and its impact have been presented [58–60]. Hence, a relevant conclusion cannot be drawn about the effect of music on the brain activity or emotional behaviour of the stress response. Apart from the lack of discovering the impact of music on the stress, the existing literature contradicts the results when compared with the self-reported stress. The limitations that contradict could be a small sample size or different preferred types of music.

3. Material and Methods

3.1. Material. Data are acquired as EEG signals in response to the 4 Musical Interventions (MI-1, MI-2, MI-3, and MI-4) with Hindi lyrics and varying spectral centroid feature with a gap of 60 seconds between every intervention, and characteristics of the stimuli used are shown in Figure 1. Features have been extracted from five bands of every channel (14 channels). The feature file is then passed to the classifier and then inferred the results accordingly. A further explanation of the whole process is provided below.

3.2. Performance Evaluation Parameters. Statistical parameters sensitivity (Sen), specificity (Spec), and accuracy (Acc) have been computed to measure the performance of classifier. Good performance of a classifier model determines how efficiently classifier determines the correct and incorrect. To measure the performance of the classifier, percentage of correctly classified is defined as a ratio of correctly predicted class to the correctly predicted and incorrectly predicted as shown in the following equations:

$$\text{Sen} = \frac{\text{TP}}{\text{TP} + \text{FN}} * 100\%, \tag{1}$$

$$\text{Spec} = \frac{\text{TN}}{\text{TN} + \text{FP}} * 10, \tag{2}$$

$$\text{Acc} = \frac{\text{TP} + \text{TN}}{\text{TP} + \text{FN} + \text{TN} + \text{FP}} * 10, \tag{3}$$

where TP is the correct input correct output (CICO) (appropriate), FP is the incorrect input correct output (IICO) (misclassified), TN is the incorrect input incorrect output (IIIO) (appropriate), and FN is the correct input incorrect output (CIIO) (misclassified).

3.3. Methods

3.3.1. Data Acquisition. A total of 18 healthy participants, 9 male and 9 female, volunteered for the project were aged between 18 and 25 as this age group is most vulnerable in order to cope with stress. The consent form has been signed by all the volunteers and preliminary demonstration has been presented to make them acquainted with the entire procedure. The information such as name, age, gender, and self-reported emotions before listening/after listening to types of songs of the participant was collected through a set questionnaire. Subjects were not trained in music. STA questionnaire has also been filled out by the participant before/after the conduct of study to support the findings. The complete study protocol is as shown in Figure 2. Four types of music interventions (MI-1 to MI-4) have been used for experimentation where lyrics are in the Hindi language and all subjects involved in this study were well acquainted with the language and musical property considered is varying spectral centroid music is well associated with arousal of emotion. MI details are shown in Figure 1.

RMS EEG devices were used to capture the EEG signals of the participants in response to the four MIs with a sampling frequency of 256 Hz. Study involves two trials: trial-0 for the baseline and trial-1 for actual data capture when subjects were exposed to interventions. Duration for trail 0 is 2 minutes (eyes opened/closed 1 min each), and trail 2 is 8 minutes and divided into 4 chunks of 2 min duration in response to 4 MIs as shown in Figure 2. In addition to two trials, the rest time was given to subjects for 1 min in between each MI to avoid any overlapping of data in response to MI but has not been considered for analysis. Postdata recording STA form has been filled out by the volunteers along with the feedback form. The impedance limit set for the data capture is 20 k ohms. The considered channels in the study are C3 and C4 of the central region, F3, F4, F7, F8, FP1, and FP2 of the frontal region, P3 and P4 of the parietal region, and T3,

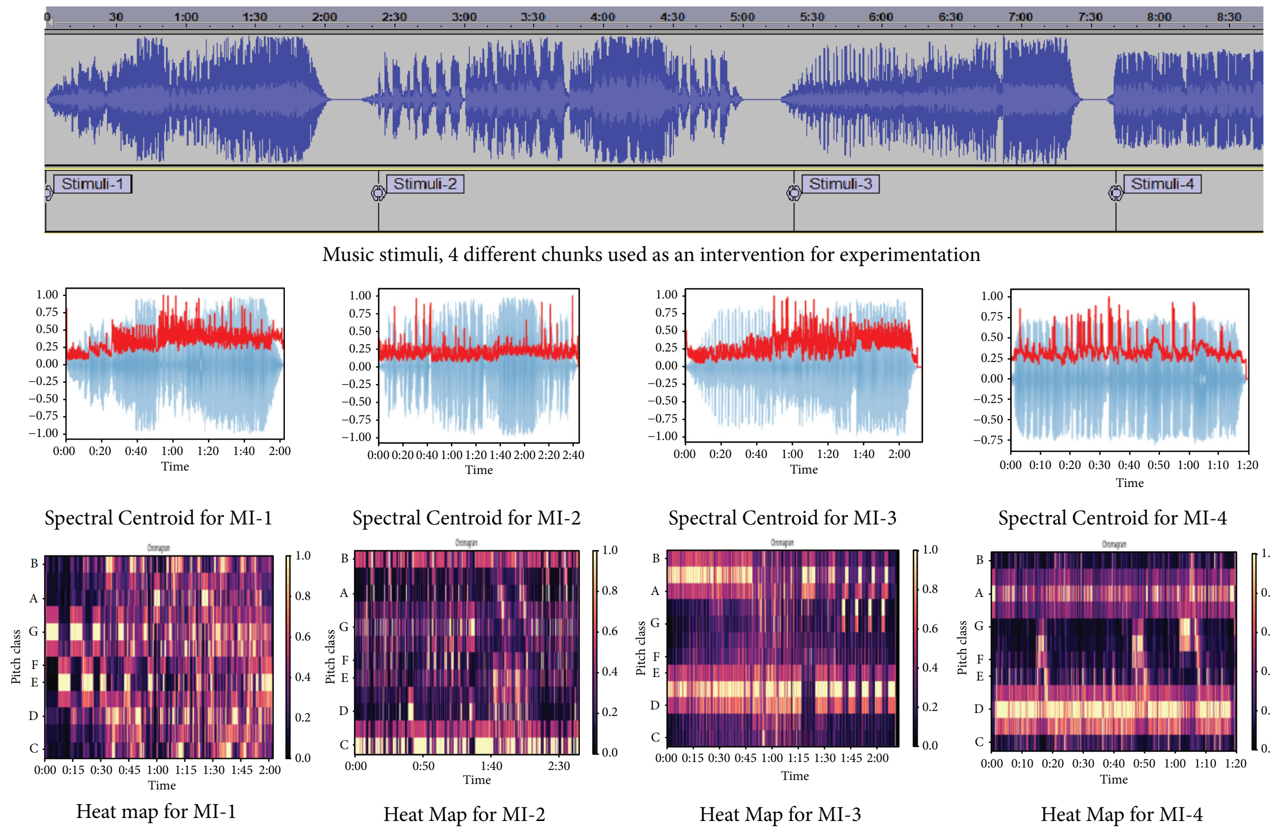

Figure 1: Characteristics of four musical interventions used in study.

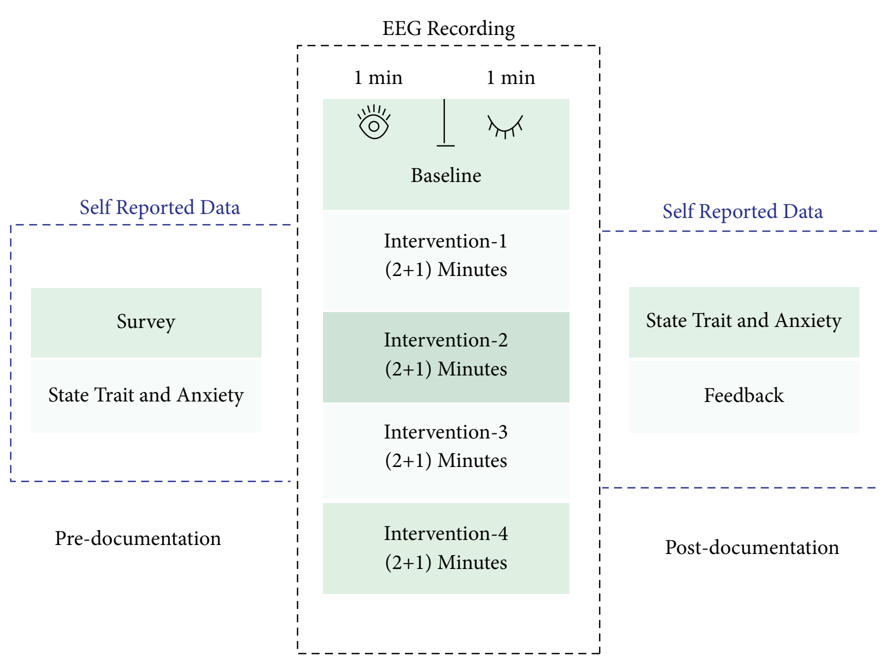

Figure 2: Flow of data acquisition.

T4, T5, T6 of the temporal region, as shown in Figure 3. Channel selections provide the 360-degree view of arousal/nonarousal of the signals in a particular region in response to interventions presented.

3.3.2. Preprocessing. Frequency till 60 Hz has been filtered by a butterworth filter. The device used in experimentation has not been associated with any filter, and thus it has generated the noise of 50 Hz and has removed the noise from

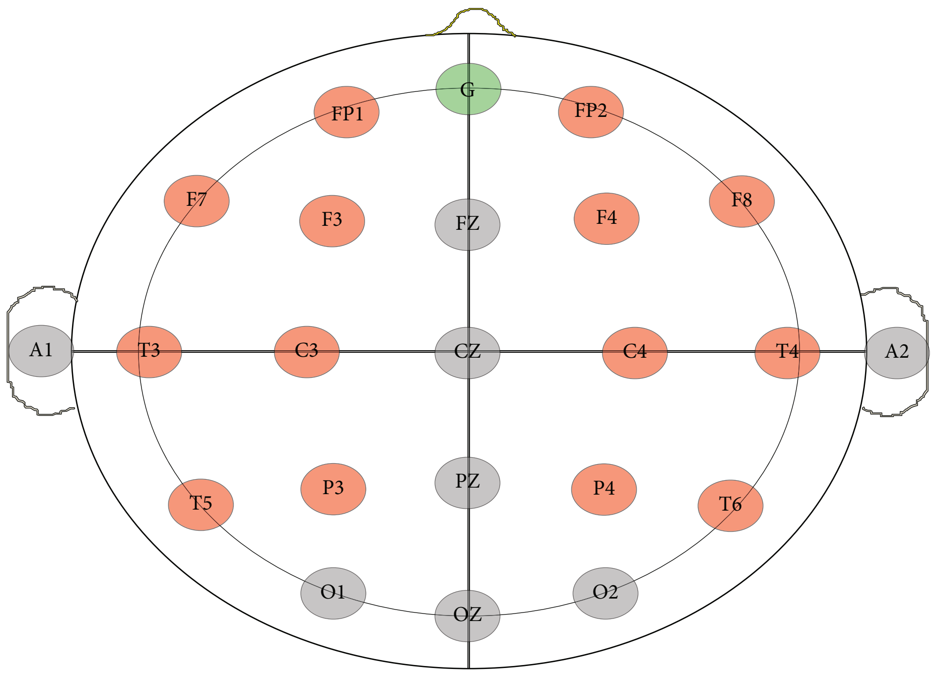

Figure 3: The channel selection.

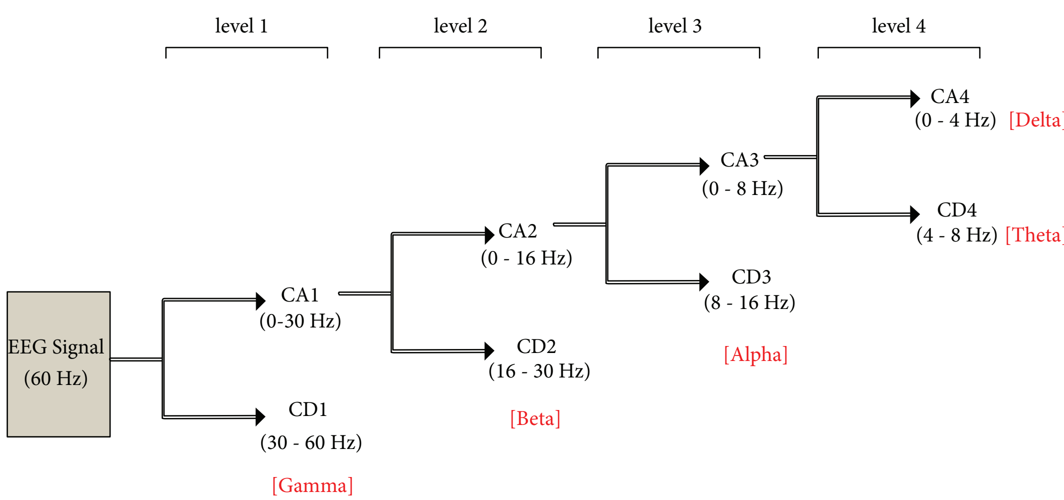

Figure 4: Decomposition of EEG signal into bands.

the data before generating the bands. After filtering, the data then passed through the discrete wavelet transformation using wavelet db7 to decompose the data into the bands as gamma waves (30–60 Hz, excluded 50 Hz), beta waves (16–30 Hz), alpha waves (8–16 Hz), theta waves (4–8 Hz), and delta waves (0–4 Hz) for each channel. The decomposition is shown in Figure 4.

3.3.3. Feature Extraction. Features were extracted from five bands of every channel for an entire individual participant in response to four musical interventions. From EEG signals, we can draw an ample amount of information relevant to the functional patterns of the brain. The channels taken for the study are 14, which are C4 and C3 of the central region, F3, F4, F7, F8, FP1, and FP2 of the frontal region, P3 and P4 of the parietal region, and T3, T4, T5, and T6 of the temporal region. Hjorth parameter and statistical features are used to quantify the stress level in male and female categories [61, 62]. The activity parameter represents the signal power and the variance of a time function. This can indicate the surface of the power spectrum in the frequency domain. This is represented by equation (4). The mobility parameter represents the mean frequency or the proportion of standard deviation of the power spectrum as in equation (5). The complexity parameter represents the change in frequency as in equation (6):

$$\text{Activity} = \mathrm{var}\,(y(t)), \tag{4}$$

$$\text{Mobility} = \sqrt{\frac{\mathrm{var}\,(\mathrm{d}y(t)/\mathrm{d}t)}{\mathrm{var}\,(y(t))}}, \tag{5}$$

$$\text{Complexity} = \sqrt{\frac{\text{Mobility}\,(\mathrm{d}y(t)/\mathrm{d}t}{\text{Mobility}\,(y(t))}};\ (t), \tag{6}$$

where *y(t)* is denoted as a signal.

(1) Statistical Features. It includes the feature standard deviation, variance, skew, kurtosis, and mean. Standard deviation measures how spread out the values are and is the square root of the variance and variance is the squared difference of the mean. Skew computes the symmetry of the dataset, whereas kurtosis checks whether the data are heavy tailed or light tailed to a normal distribution. The total sample size for each channel is 256 ∗ duration in sec. Thus, for each stimulus response, the dataset handled is of dimension 256 samples per second ∗ 120 sec duration ∗ 14 channels = 430080 samples for each subject. A total of eight features were extracted from each band of every channel for the entire subjects in the window size of 30 sec for each song. The obtained feature matrix for one band of a channel of single subject and individual song was 4×8. The nonparametric Wilcoxon Signed Rank Sum Test was used with $p \geq 0.05$ and features have been eliminated on the basis of the results. The null hypothesis for the study is there is no significant impact on the brain region as a response to MIs and alternate hypothesis set is intervention of MIs would derive a significant impact on the brain region and would support relieving from stress.

3.3.4. Classification. For classification, the support vector machine (SVM) has been used to perform a binary classification. The kernel used was polynomial. The feature dataset was segregated into training and testing data in the ratio of 8:2, total samples in feature file are 4 ∗ 8 for each subject/band, thus 80% for training involves approximately statistically significant 2048 samples for training and 512 samples for training at the stimuli level, and then linear classification is performed. Run time for classifier depends upon prominent features in selecting recording like number of spikes. The classifier used in this study is of binary nature and maximum iteration limit = 100 and numerical tolerance = 0.0010. For classification, subsets considered are the baseline vs. male (in response to MIs), baseline vs. female (in response to MIs), and male vs. female (in response to MIs).

4. Result Analysis and Discussion

4.1. Analysis of Proposed Work. Analysis of proposed work has been carried out at three subsets: level 1, male vs. female; level 2, baseline vs. male; and level 3, baseline vs. female. Commonly in all subsets out of seven extracted features, hjorth activity that signifies power associated with the signal has been found prominent.

For subset baseline vs. female and the impact of an intervention MI-1, baseline signal has shown tight spread in contrast to the response signal for the region's central, parietal, and temporal, whereas exactly reverse case has been identified for frontal regions, which motivates us analyze the statistical comparative statements at channel and band level as well. The impact of an intervention MI-3 and MI-4 on female in contrast to the baseline is more prominent, comparable, and contrast for central, frontal, and temporal regions of the brain, whereas in parietal, it has not shown any variability in acquired data. In central and frontal regions for MI-3, more variation in the median has been captured in contrast to the temporal region and the same results have been captured for intervention MI-4 as well.

For subset baseline vs. male and impact of intervention MI-1 in male category, data values are presented in comparative plots as shown in Figure 5 for all four regions (central, frontal, parietal, and temporal). Data variability patterns are different for all regions and the median is also showing a maximum difference in all regions except for the temporal region, reflecting the meaning of a higher impact of MI-1 on the male category. For baseline and impact of MI-2 in the male category, data values for all four regions (central, frontal, parietal, and temporal) are different, and median also exhibits maximum difference in all regions, reflecting the meaning of a higher impact of MI-2 in the male category. The baseline and impact of MI-3 data distributions are different for all region, and the median also exhibits the maximum difference in all regions except for the parietal region, reflecting the meaning of a higher impact of MI-3 in male category.

Similarly for the baseline and impact of MI-4 in the male category, data distributions for all four regions (central, frontal, parietal, and temporal) are different except for frontal region, showing less difference in the distribution pattern of well as the median variation reflecting minimum difference and median variation for all other regions showing maximum difference reflecting the meaning of a higher impact of an intervention MI-4 in male category.

The representation of the data values of the impact of MI-2 on male and female categories is as shown in comparative plots in Figure 6. The distribution pattern of the box is different for all the regions and the median variation is more, showing the maximum difference in the data values of the central region and parietal region.

Intervention MI-3 has achieved different distribution for the frontal region but is approximately similar to the central region. The median variation is much less, signifying the minimum difference in the data values lies in both central and frontal regions. Impact of MI-4 on subset male vs. female has achieved significant difference for both frontal and central region. The median variation is much less, signifying the minimum difference in the data values lies in both central and frontal regions.

A result obtained and detailed analysis done at channel and band level signify that majorly male is dominant in all scenarios as the result of an impact of interventions. Maximum variability have been found in male categories. Classifier performance according to interventions used for

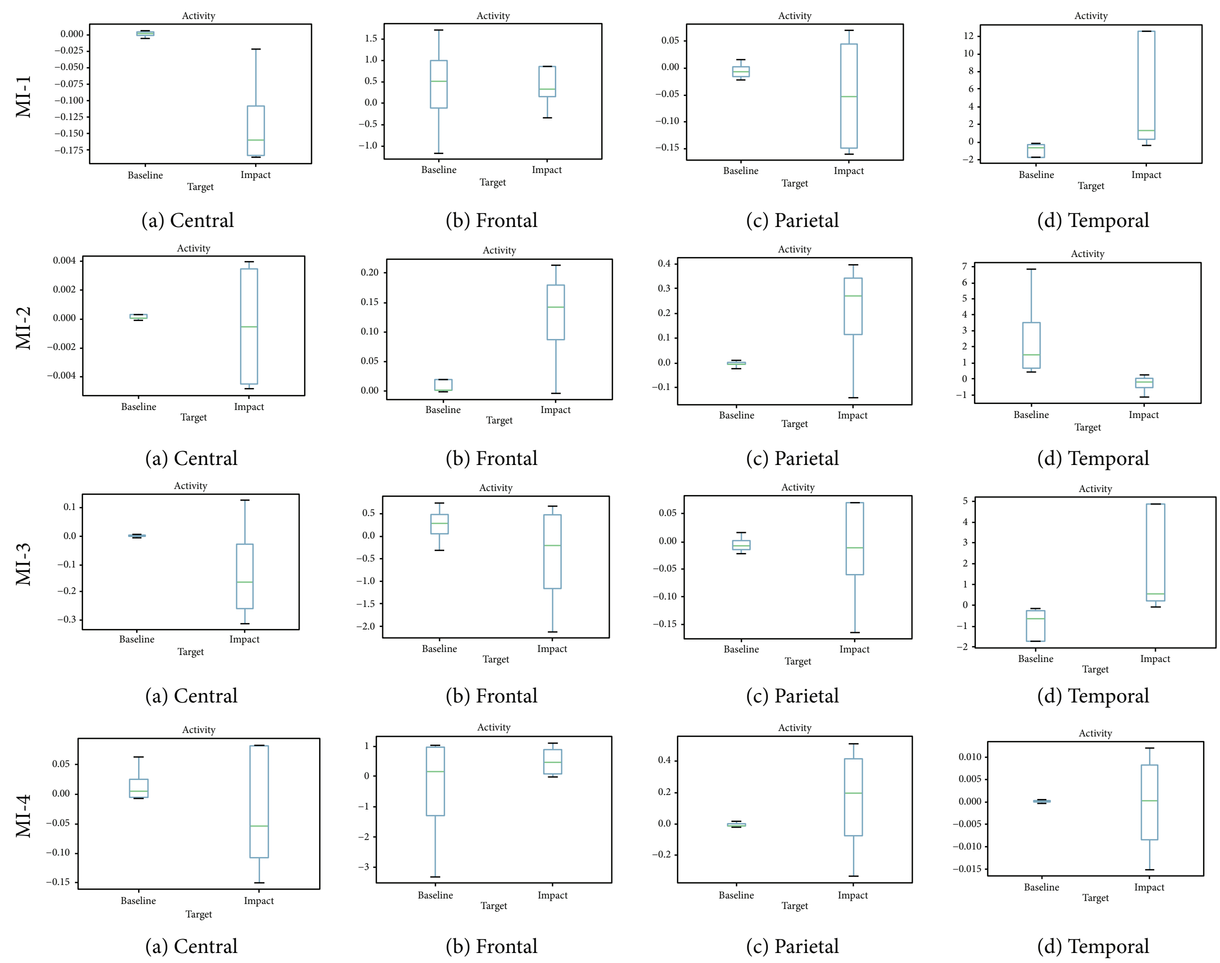

Figure 5: Comparative plots of the impact of interventions (MI-1 to MI-4) on the baseline and male category in (a) central region, (b) frontal, (c) parietal, and (d) temporal region with respect to the hjorth parameter activity.

three subsets: (1) male and female, (2) baseline and female, and (3) baseline and male. The objective is to carry the classification for subsets 1, 2, and 3 to identify prominent channels and bands out of the 14 channels and 5 bands for each channel with respect to musical interventions used for experimentation to relate our findings with the state-of-art work in the same domain. In reference [63], the results signify that activation of low-frequency band reflects the reduction in stress level, and results obtained by proposed methodology and interventions are completely in sync by showing activation of low-frequency band delta (0–4 Hz). In reference [64], music has a magical effect on stress reduction and affects highly stress population, and in proposed work, the results have been obtained in the male category rather than female. Interventions used are characteristically different with respect to the spectral centroid and lyrics are related to the emotional domain. For subset 1, in intervention 1, out of 14 channels, only four channels such as C4 (beta), F7 (gamma), FP2 (delta), and P3 (alpha) have achieved acceptable accuracy of above 70% and the rest all channels have been ignored as they have not exhibited prominent results. For subset 1, in intervention 2, out of 14 channels, only 3 channels have achieved acceptable accuracy such as C3 (delta), P3 (gamma), and T5 (theta) and the rest all channels have been ignored as they have not exhibited prominent results. Results of classifier accuracy are listed in Table 1.

Central region, which consists of two electrodes placement, has been analyzed, and the results achieved are for MI-1 at beta band is 72%, for MI-2 at the delta band is 100%, and for MI-3 at delta band is 100%. For MI-4 at theta/gamma band, accuracy obtained is 72%. Maximum accuracy has been achieved from MI-2, and MI-3 spectral centroid is prominent at the beginning and end and MI-3 spectral centroid is prominent at the center, which has a clear indication that in case of MI-2 and MI-3, male and female generate contrast EEG signals, and thus behaviour has been captured by the delta band region.

In frontal region, for experimentation, 6 electrodes have been placed, three on the left and three on the right side. The observation on the left side of the frontal region has revealed that for MI-1 on the left side of frontal region, maximum accuracy has achieved at FP2 electrode and delta band is 77%, for MI-2, no accuracy has been achieved as compared to other MIs. For MI-3, accuracy achieved is 77% of gamma band and for MI-4, accuracy achieved at gamma band is

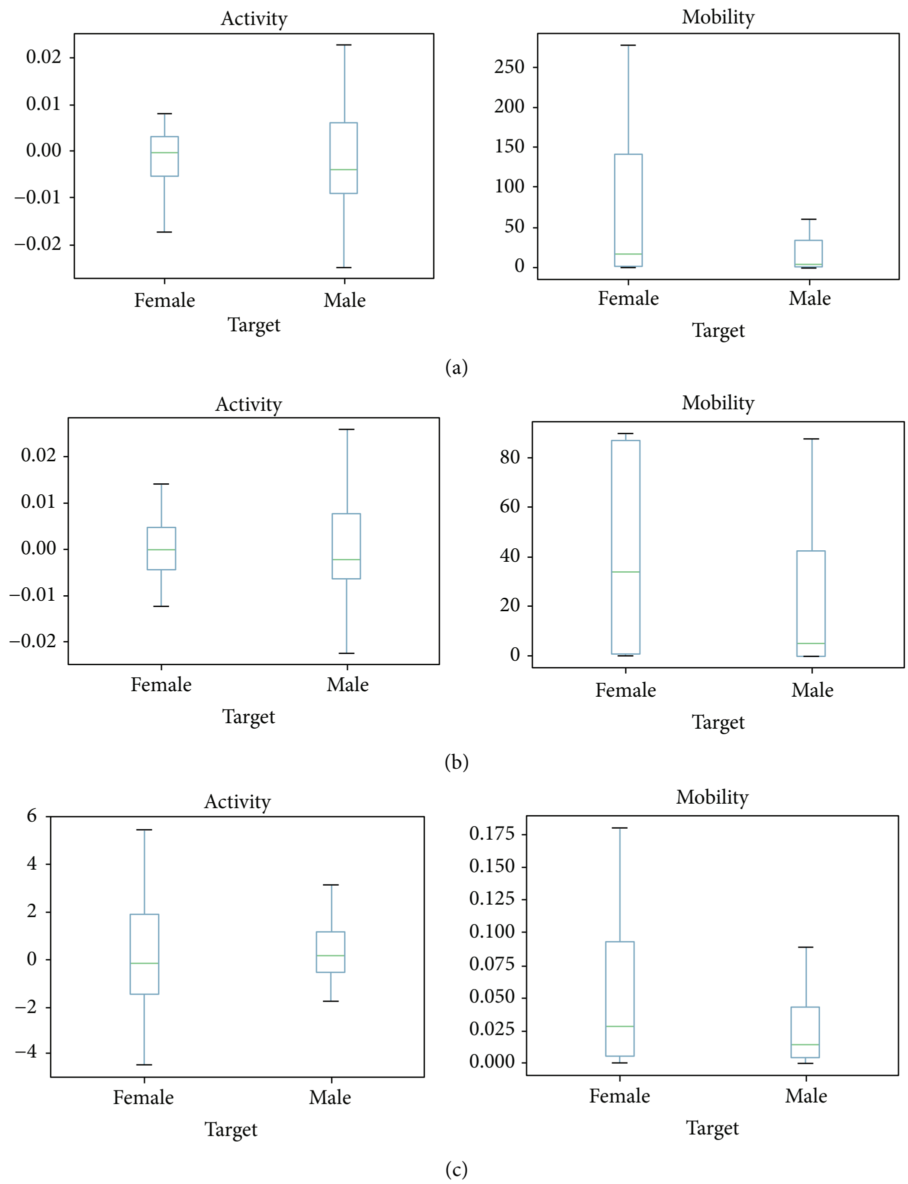

Figure 6: Comparative plots of the impact of MI-2 on male and female category in (a) central region, (b) parietal region, and (c) temporal region with respect to the hjorth parameter activity and mobility.

Table 1: Classification results for subset1 (male vs. female), subset 2 (baseline vs. female), and subset 3 (baseline vs. male).

Subset	Intervention	Channel	Bands	Accuracy	Sen	Spec
1	MI-1	FP2	Delta	77.78	100	60
	MI-2	C3	Delta, gamma	100, 83.33	100, 66.67	100, 100
	MI-3	C3	Delta	100	100	100
	MI-4	C4, F3	Theta, gamma	72.22	100, 0	100
2	MI-1	C4, P4, T3, T5, T6	Gamma	100	100	100
	MI-2	C3, F7, FP1, P4, T3	Beta	100	100	100
	MI-3	C4, FP1, T3	Beta	100	100	100
	MI-4	C3, C4, F7, T5	Beta	100	100	100
3	MI-1	C4, F3, T5	Beta	100	100	100
	MI-2	C3, F3, F7	Gamma	100	100	100
	MI-3	C4, P3	Beta	100	100	100
		C4, P3, T6	Beta	100	100	100
	MI-4	F3, Fp1, T5	Gamma	100	100	100
		T4	Delta	100	100	100

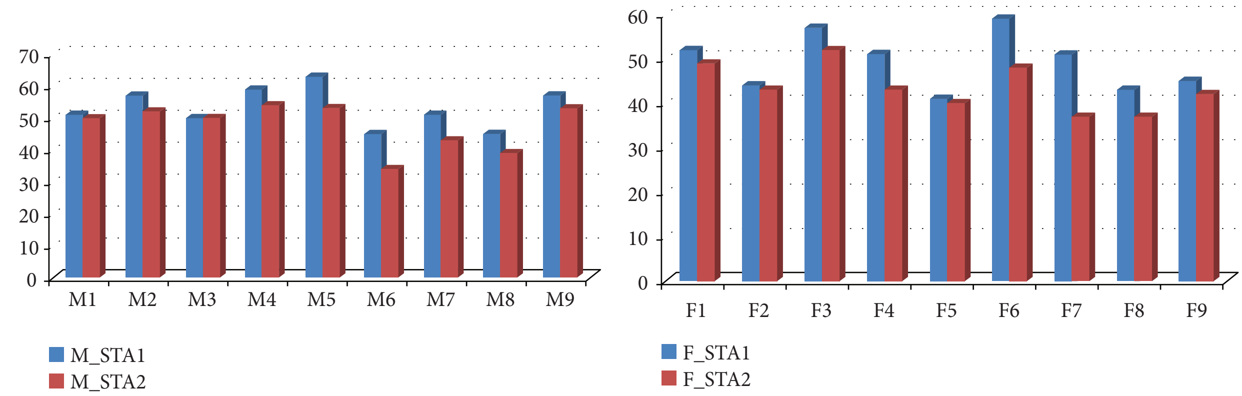

(a) (b)

Figure 7: State-trait anxiety analysis for (a) male and (b) female.

Table 2: Comparative analysis of proposed work with state of art.

Method Year	Number of subjects	Measures	Stimuli	Findings	Algorithm/methodology
2017 [64]	20 college students	EEG signals	Congruent test and incongruent test	The students with higher stress levels have seemed to be affected by the impact of music and the mean beta absolute power ratio increased by 0.246	Mean beta absolute power ratio
2018 [13]	80 infants	Heart rate, oxygen saturation, and neonatal infant pain scale (NIPS)	3 music interventions	The heart rate and pain perception are found to be reduced and oxygen saturation increases in the infants	Statistical analysis (ANOVA test)
2016 [25]	159 patients	State-trait anxiety inventory scale	Background music	Significant reduction found in the anxiety and stress level of the patients	Statistical analysis (Scheffe's test)
2018 [65]	7 subjects	EEG signals	Music	The model prediction for the participant's mental state has accuracy of 80% and with a small MSE loss up to 0.0882	Deep learning
2018 [63]	15 (average age 20.5 years)	EEG signals	15 different music	The findings during listening to music were increased in the spectral power in alpha band and decrease in high-frequency beta and gamma bands	Support vector machine
2019 [66]	15 males and 15 females, aged 20–35 years	EEG signals	4 English music tracks of metal, rock, electronic, and rap genres 5 Urdu music tracks of famous, melodious, patriotic, qawali, and ghazal genres	Urdu music tracks have more impact on stress reduction than English music tracks Females were more affected by the music than males	Minimal sequential optimization, stochastic gradient descent, logistic regression, and multilayer perception
[67–69]	Disabled cancer patients	EEG signals	Music	Effect on frontal lobe	Statistical test
Proposed	9 males and 9 females	EEG signals	4 musical interventions with Hindi lyrics and varying spectral centroid characteristics	Delta band is active for male, which is a clear indication of mindful state as an impact of musical intervention for MI-1, MI-2, and MI-3****	Support vector machine

72%. The observation on the right side of the frontal region has revealed that except for MI-1, none of the song has reported any difference in the male and female categories. For MI-1 on the right side of the frontal region, maximum accuracy achieved at delta band is 77% and it has been observed at FP2. For parietal section, for MI-1, maximum accuracy achieved at alpha band is 72%, and for MI-2, 77% accuracy has been achieved at gamma band, for MI-3 and

MI-4, no significant accuracy has been achieved as compared to MI-1 and MI-2. For temporal region, results have been analyzed for the left and right temporal regions. For left temporal, MI-2 has achieved maximum accuracy of 72% of theta band at T5, whereas other MIs have not shown any significant difference in the generated signal between male and female. For right temporal region, for MI-1, maximum accuracy obtained is 66% of gamma band, whereas accuracy achieved for MI-3 is 66% of beta band and for MI-4 is 61% of the delta band. For analysis of the baseline and MI-1 impact on female, the results retrieved have shown maximum accuracy of 100% at C4 gamma, F3 theta, FP1 beta theta, P3 beta, P4 gamma, T3 gamma, T4 beta, T5 gamma, and T6 gamma. It indicates that signals generated at baseline and MI-1 are not statistically different at central left and frontal right. For analysis of the baseline and MI-2 impact on female, the results retrieved have shown maximum accuracy of 100% C3 beta, F7 beta, FP1 beta, P3 gamma, P4 beta, T3 beta, and T5 gamma. It indicates that signals generated at baseline and MI-2 are not statistically different at central right, frontal right, and temporal right. For the analysis of the baseline and MI-3 impact on female, the results retrieved have shown maximum accuracy of 100% at C4 beta, F7 gamma theta, FP1 beta, FP2 gamma, T3 beta, T4 delta beta, and T5 beta gamma. It indicates that signals generated at baseline and MI-3 are not statistically different at central left and frontal right. Parietal has not shown any impact of music in this region. For the analysis of the baseline and MI-4 impact on female, the results retrieved have shown maximum accuracy of 100% C3 beta, C4 beta, F4 theta, F7 beta, and T5 beta. It indicates that signals generated at baseline and MI-4 are not statistically different at temporal right, and parietal has not shown any impact of intervention in this region. For the analysis of the baseline and MI-1 impact on males, the results retrieved have shown maximum accuracy of 100% at beta C4, beta, gamma F3, theta F4, delta gamma F7, alpha beta FP1, delta gamma FP2, beta gamma P3, theta T4, beta T5, and gamma T6. It indicates that signals generated at baseline and MI-1 are not statistically different at central left, and right parietal region has not shown any significant impact of intervention in this region. For analysis of the baseline and MI-2 impact on males, the results retrieved have shown maximum accuracy of 100% at C3 gamma, F3 gamma, F4 gamma theta, F7 gamma, FP2 beta, P3 beta, P4 beta gamma, T4 delta gamma, and T6 gamma theta. It indicates that signals generated at baseline, MI-2 is not statistically different at central right, and temporal left has not shown any significant impact of music. For analysis of the baseline and MI-3 impact on males, the results retrieved have shown maximum accuracy of 100% C4 beta, F3 alpha beta, FP2 delta, P3 beta, T4 theta gamma, T5 gamma, and T6 gamma. It indicates that signals generated at baseline and MI-3 are not statistically different at central left and parietal right. For the analysis of the baseline and MI-4 impact on males, the results retrieved have shown maximum accuracy of 100% C4 beta, F3 gamma, F4 beta gamma, F7 gamma, F8 beta delta, Fp1 gamma, FP2 beta gamma theta, P3 beta, T4 delta, T5 gamma, and T6 beta. The STA1 score recorded for male is in range of 45–63. The STA2 score recorded is in range of 34–54, which results in standard deviation of 7.12 for male category. The STA1 score recorded for female is in range of 41–59. The STA2 score recorded is in range of 37–52, which results in standard deviation of 6.38 for female category, as shown in Figures 7(a) and 7(b). According to the STA analysis, the deviation in the stress and anxiety level of the male category is found to be more as compared to females. Proposed interventions are most effective for male to reduce stress level as compared to female.

4.2. Comparative Study of the Proposed Work with State of the Art. Table 2 has listed the comparative analysis of the proposed work with state of the art. In the proposed work, band-wise and region-wise analysis have been carried out. Central region and delta band have shown major impact to reduce stress level. In references [70–72], interesting linear methods have been proposed.

Challenges in conducting this study are (i) to analyze the particular region that has a higher impact of an intervention, (ii) to deal with variations in intrasubjects of same category as well as different categories, (iii) to deal with intersubject variations because they are related to exact electrode position in multiple sessions, (iv) the impact of this variation has resulted into classification method to generalize for individual subjects as well, and (v) as used intervention has characterized with background music and considered removing and analyzing as suggested in reference [73]. MI details are shown in Figure 1, and survey data include the self-reported data.

5. Conclusion

The music interventions with Hindi lyrics and varying spectral centroid in this study have shown the impact on both male and female categories in reducing the stress, but higher impact has been observed in male category. Power associated with signals for delta band of central and frontal region of male category is more dominant in contrast to the female category for first three MIs and differentiated male and female categories. Delta, beta, and gamma bands' activation has been observed dominantly with respect to interventions in the male category, whereas only beta and gamma bands have been observed in the female category. Nonprominent delta band in the female category might be because of the mild impact of musical intervention to invoke the relaxation in the female category, and prominent visibility of delta wave in the temporal region for the male category gives an insight into mindful state in response to music interventions. In future, experimentation will be carried out with a greater number of subjects.

Data Availability

Dataset will be provided on request.

Conflicts of Interest

The authors declare that they have no conflicts of interest.

Acknowledgments

This work was supported by Taif University Researchers Supporting Project Number (TURSP-2020/114), Taif University, Taif, Saudi Arabia.

References

[1] A. Abbott, "Stress and the city: urban decay," *Nature*, vol. 490, no. 7419, pp. 162–164, 2012.
[2] T. G. Pickering, "Mental stress as a causal factor in the development of hypertension and cardiovascular disease," *Current Hypertension Reports*, vol. 3, no. 3, pp. 249–254, 2001.
[3] C. Espinosa-Garcia, I. Sayeed, S. Yousuf et al., "Abstract TP83: stress exacerbates global ischemia-induced inflammatory response: intervention by progesterone," *Stroke*, vol. 48, (suppl_1), p. ATP83, 2017.
[4] D. D. Wallace, M. H. Boynton, and L. A. Lytle, "Multilevel analysis exploring the links between stress, depression, and sleep problems among two-year college students," *Journal of American College Health*, vol. 65, no. 3, pp. 187–196, 2017.
[5] C. Brownson, M. S. Becker, R. Shadick, S. S. Jaggars, and Y. Nitkin-Kaner, "Suicidal behavior and help seeking among diverse college students," *Journal of College Counseling*, vol. 17, no. 2, pp. 116–130, 2014.
[6] A. P. Allen, P. J. Kennedy, J. F. Cryan, T. G. Dinan, and G. Clarke, "Biological and psychological markers of stress in humans: focus on the trier social stress test," *Neuroscience & Biobehavioral Reviews*, vol. 38, pp. 94–124, 2014.
[7] H. Mönnikes, J. Tebbe, M. Hildebrandt et al., "Role of stress in functional gastrointestinal disorders," *Digestive Diseases*, vol. 19, no. 3, pp. 201–211, 2001.
[8] S. Cohen, T. Kamarck, and R. Mermelstein, "A global measure of perceived stress," *Journal of Health and Social Behavior*, vol. 24, no. 4, pp. 385–396, 1983.
[9] C. D. Spielberger, "State-Trait Anxiety Inventory," *the Corsini Encyclopedia of Psychology*, p. 1, John Wiley & Sons, Inc, Hoboken, New Jersey, U.S, 2010.
[10] A. Deschênes, H. Forget, C. Daudelin-Peltier, D. Fiset, and C. Blais, "Facial expression recognition impairment following acute social stress," *Journal of Vision*, vol. 15, no. 12, p. 1383, 2015.
[11] S. Gowrisankaran, N. K. Nahar, J. R. Hayes, and J. E. Sheedy, "Asthenopia and blink rate under visual and cognitive loads," *Optometry and Vision Science*, vol. 89, no. 1, pp. 97–104, 2012.
[12] G. C. Dieleman, A. C. Huizink, J. H. M. Tulen et al., "Alterations in HPA-axis and autonomic nervous system functioning in childhood anxiety disorders point to a chronic stress hypothesis," *Psychoneuroendocrinology*, vol. 51, pp. 135–150, 2015.
[13] A. Rossi, A. Molinaro, E. Savi et al., "Music reduces pain perception in healthy newborns: a comparison between different music tracks and recoded heartbeat," *Early Human Development*, vol. 124, pp. 7–10, 2018.
[14] A. Liapis, C. Katsanos, D. Sotiropoulos, M. Xenos, and N. Karousos, "Recognizing emotions in human computer interaction: studying stress using skin conductance," in *Human-Computer Interaction - INTERACT 2015*, pp. 255–262, Springer, New York, NY, USA, 2015.
[15] J. Wielgosz, B. S. Schuyler, A. Lutz, and R. J. Davidson, "Long-term mindfulness training is associated with reliable differences in resting respiration rate," *Scientific Reports*, vol. 6, no. 1, Article ID 27533, 2016.
[16] J. D. Bremner, B. Elzinga, C. Schmahl, and E. Vermetten, "Structural and functional plasticity of the human brain in posttraumatic stress disorder," *Progress in Brain Research*, vol. 167, pp. 171–186, 2007.
[17] A. R. Subhani, W. Mumtaz, M. N. B. M. Saad, N. Kamel, and A. S. Malik, "Machine learning framework for the detection of mental stress at multiple levels," *IEEE Access*, vol. 5, Article ID 13545, 2017.
[18] D. Novák, L. Lhotská, V. Eck, and M. Sorf, "EEG and VEP signal processing," *Cybernetics, Faculty of Electrical Eng*, pp. 50–53, 2004.
[19] J. Dubois and R. Adolphs, "Building a science of individual differences from fMRI," *Trends in Cognitive Sciences*, vol. 20, no. 6, pp. 425–443, 2016.
[20] A. R. Subhani, L. Xia, A. S. Malik, and Z. Othman, "Quantification of physiological disparities and task performance in stress and control conditions," in *Quantification of Physiological Disparities and Task Performance in Stress and Control Conditions,* vol. 2013, pp. 2060–2063, IEEE, 2013.
[21] C. S. Pereira, J. Teixeira, P. Figueiredo, J. Xavier, S. L. Castro, and E. Brattico, "Music and emotions in the brain: familiarity matters," *PloS one*, vol. 6, no. 11, p. e27241, 2011.
[22] G. R. Watkins, "Music therapy: proposed physiological mechanisms and clinical implications," *Clinical Nurse Specialist*, vol. 11, no. 2, pp. 43–50, 1997.
[23] A. B. Haake, "Individual music listening in workplace settings," *Musicae Scientiae*, vol. 15, no. 1, pp. 107–129, 2011.
[24] N. Dibben and V. J. Williamson, "An exploratory survey of in-vehicle music listening," *Psychology of Music*, vol. 35, no. 4, pp. 571–589, 2007.
[25] G. Kipnis, N. Tabak, and S. Koton, "Background music playback in the preoperative setting: does it reduce the level of preoperative anxiety among candidates for elective surgery?" *Journal of PeriAnesthesia Nursing*, vol. 31, no. 3, pp. 209–216, 2016.
[26] A. Bowman, F. J. Dowell, N. P. Evans, and N. Evans, "'The effect of different genres of music on the stress levels of kennelled dogs'," *Physiology & Behavior*, vol. 171, pp. 207–215, 2017.
[27] A. Hampton, A. Ford, R. E. Cox III, C.-c. Liu, and R. Koh, "Effects of music on behavior and physiological stress response of domestic cats in a veterinary clinic," *Journal of Feline Medicine and Surgery*, vol. 22, no. 2, pp. 122–128, 2020.
[28] A. Linnemann, B. Ditzen, J. Strahler, J. M. Doerr, and U. M. Nater, "Music listening as a means of stress reduction in daily life," *Psychoneuroendocrinology*, vol. 60, pp. 82–90, 2015.
[29] N. Salankar, P. Mishra, and L. Garg, "Emotion recognition from EEG signals using empirical mode decomposition and second-order difference plot," *Biomedical Signal Processing and Control*, vol. 65, Article ID 102389, 2021.
[30] S. Gupta and N. Salankar, "An exploration of acoustic and temporal features for the multiclass classification of bird species," in *Book an Exploration of Acoustic and Temporal Features for the Multiclass Classification of Bird Species*, pp. 693–711, Springer, New York, NY, USA, 2021.
[31] S. Koelsch, "Brain correlates of music-evoked emotions," *Nature Reviews Neuroscience*, vol. 15, no. 3, pp. 170–180, 2014.
[32] A. M. Bhatti, M. Majid, S. M. Anwar, and B. Khan, "Human emotion recognition and analysis in response to audio music using brain signals," *Computers in Human Behavior*, vol. 65, pp. 267–275, 2016.
[33] R. Horlings, D. Datcu, and L. J. Rothkrantz, "Emotion recognition using brain activity," in *Proceedings of the Emotion Recognition Using Brain Activity*, p. 1, Gabrovo, Bulgaria, June 2008.

[34] E. Hoffmann, "Brain training against stress: theory, methods and results from an outcome study," *Stress Report*, vol. 4, no. 2, pp. 1–24, 2005.

[35] B. Hjorth, "EEG analysis based on time domain properties," *Electroencephalography and Clinical Neurophysiology*, vol. 29, no. 3, pp. 306–310, 1970.

[36] P. Gajbhiye, R. K. Tripathy, A. Bhattacharyya, and R. B. Pachori, "Novel approaches for the removal of motion artifact from EEG recordings," *IEEE Sensors Journal*, vol. 19, no. 22, Article ID 10600, 2019.

[37] I. Peretz and R. J. Zatorre, "Brain organization for music processing," *Annual Review of Psychology*, vol. 56, no. 1, pp. 89–114, 2005.

[38] J. Burns, E. Labbé, K. Williams, and J. McCall, "Perceived and physiological indicators of relaxation: as different as Mozart and Alice in chains," *Applied Psychophysiology and Biofeedback*, vol. 24, no. 3, pp. 197–202, 1999.

[39] K. Allen, L. H. Golden, J. L. Izzo et al., "Normalization of hypertensive responses during ambulatory surgical stress by perioperative music," *Psychosomatic Medicine*, vol. 63, no. 3, pp. 487–492, 2001.

[40] E. Labbé, N. Schmidt, J. Babin, and M. Pharr, "Coping with stress: the effectiveness of different types of music," *Applied Psychophysiology and Biofeedback*, vol. 32, no. 3, pp. 163–168, 2007.

[41] T. Ventura, M. C. Gomes, and T. Carreira, "Cortisol and anxiety response to a relaxing intervention on pregnant women awaiting amniocentesis," *Psychoneuroendocrinology*, vol. 37, no. 1, pp. 148–156, 2012.

[42] U. Nilsson, "The anxiety- and pain-reducing effects of music interventions: a systematic review," *AORN Journal*, vol. 87, no. 4, pp. 780–807, 2008.

[43] T. Richards, J. Johnson, A. Sparks, and H. Emerson, "The effect of music therapy on patients' perception and manifestation of pain, anxiety, and patient satisfaction," *Database of Abstracts of Reviews of Effects (DARE): Quality-Assessed Reviews [Internet]*, vol. 16, 2007.

[44] A. J. Blood and R. J. Zatorre, "Intensely pleasurable responses to music correlate with activity in brain regions implicated in reward and emotion," *Proceedings of the National Academy of Sciences*, vol. 98, no. 20, Article ID 11818, 2001.

[45] V. Menon, W. Butt, J. Thiercelin, R. Gomeni, P. Morselli, and D. London, "Effects in man of progabide on prolactin release induced by haloperidol or domperidone," *Psychoneuroendocrinology*, vol. 9, no. 2, pp. 141–146, 1984.

[46] S. Koelsch, "Towards a neural basis of music-evoked emotions," *Trends in Cognitive Sciences*, vol. 14, no. 3, pp. 131–137, 2010.

[47] J. Lingham and T. Theorell, "Self-selected "favourite" stimulative and sedative music listening - how does familiar and preferred music listening affect the body?" *Nordic Journal of Music Therapy*, vol. 18, no. 2, pp. 150–166, 2009.

[48] G. M. Sandstrom and F. A. Russo, "Music hath charms: the effects of valence and arousal on recovery following an acute stressor," *Music and Medicine*, vol. 2, no. 3, pp. 137–143, 2010.

[49] V. N. Stratton and A. H. Zalanowski, "The relationship between music, degree of liking, and self-reported relaxation," *Journal of Music Therapy*, vol. 21, no. 4, pp. 184–192, 1984.

[50] X. Li, K. Nie, N. S. Imennov, J. T. Rubinstein, and L. E. Atlas, "Improved perception of music with a harmonic based algorithm for cochlear implants," *IEEE Transactions on Neural Systems and Rehabilitation Engineering*, vol. 21, no. 4, pp. 684–694, 2013.

[51] A. R. Teixeira, A. Tomé, L. Roseiro, and A. Gomes, "Does music help to be more attentive while performing a task? A brain activity analysis," in *Proceedings of the 2018 IEEE International Conference on Bioinformatics and Biomedicine (BIBM)*, pp. 1564–1570, IEEE, Madrid, Spain, December, 2018.

[52] D. Wang, S. Liu, and X. Wang, "Study on the impact of different music education on emotional regulation of adolescents based on EEG signals," *Educational Sciences: Theory and Practice*, vol. 18, no. 5, 2018.

[53] R. Nawaz, H. Nisar, and Y. V. Voon, "The effect of music on human brain; Frequency domain and time series analysis using electroencephalogram," *Ieee Access*, vol. 6, Article ID 45191, 2018.

[54] H. Jebelli, S. Hwang, and S. Lee, "EEG-based workers' stress recognition at construction sites," *Automation in Construction*, vol. 93, pp. 315–324, 2018.

[55] F. Al-Shargie, T. B. Tang, N. Badruddin, and M. Kiguchi, "Towards multilevel mental stress assessment using SVM with ECOC: an EEG approach," *Medical, & Biological Engineering & Computing*, vol. 56, no. 1, pp. 125–136, 2018.

[56] G. Jun and K. G. Smitha, "EEG based stress level identification," in *Proceedings of the 2016 IEEE International Conference on Systems, Man, and Cybernetics (SMC)*, Article ID 003270, IEEE, Budapest, Hungary, October 2016.

[57] M. S. Kalas and B. Momin, "Stress detection and reduction using EEG signals," in *Proceedings of the 2016 International Conference on Electrical, Electronics, and Optimization Techniques (ICEEOT)*, pp. 471–475, IEEE, Chennai, India, March, 2016.

[58] K. Chienwattanasook and K. Jermsittiparsert, "Factors affecting job stress among employees in the banking sector of Malaysia," *International Journal of Innovation, Creativity and Change*, vol. 6, no. 2, pp. 288–302, 2019.

[59] C. Trisakhon and K. Jermsittiparsert, "Role of stressors and supervisory style in creative behaviour of employees with moderating role of organizational learning capability: a case of Thai pharmaceutical firms," *Systematic Reviews in Pharmacy*, vol. 10, no. 2, pp. 259–269, 2019.

[60] C. Kerdpitak and K. Jermsittiparsert, "The effects of workplace stress, work-life balance on turnover intention: an empirical evidence from the pharmaceutical industry in Thailand," *Systematic Reviews in Pharmacy*, vol. 11, no. 2, pp. 586–594, 2020.

[61] S.-H. Oh, Y.-R. Lee, and H.-N. Kim, "A novel EEG feature extraction method using Hjorth parameter," *International Journal of Electronic and Electrical Engineering*, vol. 2, no. 2, pp. 106–110, 2014.

[62] S. Bhat and D. Koundal, "Multi-focus Image Fusion Techniques: A Survey," *Artif Intell Rev*, vol. 54, pp. 5735–5787, 2021.

[63] H. Bo, L. Ma, Q. Liu, R. Xu, and H. Li, "Music-evoked emotion recognition based on cognitive principles inspired EEG temporal and spectral features," *International Journal of Machine Learning and Cybernetics*, vol. 10, no. 9, pp. 2439–2448, 2019.

[64] H. Nisar and S. J. Hong, "Study of cognitive flexibility at different stress levels with background music," in *Proceedings of the 2017 IEEE Life Sciences Conference (LSC)*, pp. 75–78, IEEE, Sydney, NSW, Australia, December, 2017.

[65] C.-Y. Liao, R.-C. Chen, and S.-K. Tai, "Emotion stress detection using EEG signal and deep learning technologies," in *Proceedings of the2018 IEEE International Conference on*

Applied System Invention (ICASI), pp. 90–93, IEEE, Chiba, Japan, April, 2018.
[66] A. Asif, M. Majid, and S. M. Anwar, "Human stress classification using EEG signals in response to music tracks," *Computers in Biology and Medicine*, vol. 107, pp. 182–196, 2019.
[67] M. De Witte, E. Lindelauf, X. Moonen, G. J. Stams, and S. V. Hooren, "Music therapy interventions for stress reduction in adults with mild intellectual disabilities: perspectives from clinical practice," *Frontiers in Psychology*, vol. 11, p. 3310, 2020.
[68] Y. J. Lee, M. A. Kim, and H.-J. Park, "Effects of a laughter programme with entrainment music on stress, depression, and health-related quality of life among gynaecological cancer patients," *Complementary Therapies in Clinical Practice*, vol. 39, Article ID 101118, 2020.
[69] M. S. d. Santos, F. d. M. Thomaz, R. T. Jomar, A. M. M. Abreu, and G. G. D. C. C. Taets, "Music in the relief of stress and distress in cancer patients," *Revista Brasileira de Enfermagem*, vol. 74, 2021.
[70] X. Chang, F. Nie, S. Wang, Y. Yang, X. Zhou, and C. Zhang, "Compound Rank- k projections for bilinear analysis," *IEEE Transactions on Neural Networks and Learning Systems*, vol. 27, no. 7, pp. 1502–1513, July 2016.
[71] Z. Li, F. Nie, X. Chang, L. Nie, H. Zhang, and Y. Yang, "Rank-constrained spectral clustering with flexible embedding," *IEEE Transactions on Neural Networks and Learning Systems*, vol. 29, no. 12, pp. 6073–6082, Dec. 2018.
[72] Z. Li, F. Nie, X. Chang, Y. Yang, C. Zhang, and N. Sebe, "Dynamic affinity graph construction for spectral clustering using multiple features," *IEEE Transactions on Neural Networks and Learning Systems*, vol. 29, no. 12, pp. 6323–6332, Dec. 2018.
[73] S. Mavaddati, "A novel singing voice separation method based on a learnable decomposition technique," *Circuits, Systems, and Signal Processing*, vol. 39, no. 7, pp. 3652–3681, 2020.

Hindawi
Contrast Media & Molecular Imaging
Volume 2022, Article ID 4476412, 10 pages
https://doi.org/10.1155/2022/4476412

Research Article

Exploration of CT Images Based on the BN-U-net-W Network Segmentation Algorithm in Glioma Surgery

Yongmei Yu,[1] **Zhaofeng Du**,[2] **Changxin Yuan**,[3] **and Jian Li**[1]

[1]*Department of Radiology, Jining First People's Hospital, No. 6 Jiankang Road, Jining, Shandong 272000, China*
[2]*Department of Imaging, Zaozhuang Traditional Chinese Medicine Hospital, No. 2666 Taihangshan South Road,Xuecheng District, Zaozhuang 277000, Shandong, China*
[3]*Military Sursery, Zaozhuang Traditional Chinese Medicine Hospital, No. 2666 Taihangshan South Road,Xuecheng District, Zaozhuang, Shandong, China*

Correspondence should be addressed to Jian Li; 1413490919@st.usst.edu.cn

Received 31 December 2021; Revised 19 February 2022; Accepted 21 February 2022; Published 11 April 2022

Academic Editor: M Pallikonda Rajasekaran

This study aimed to explore the application value of computed tomography (CT) imaging features based on the deep learning batch normalization (batch normalization, BN) U-net-W network image segmentation algorithm in evaluating and diagnosing glioma surgery. 72 patients with glioma who were admitted to hospital were selected as the research subjects. They were divided into a low-grade group (grades I-II, $N = 27$ cases) and high-grade group (grades III-IV, $N = 45$ cases) according to postoperative pathological examination results. The CT perfusion imaging (CTPI) images of patients were processed by using the deep learning-based BN-U-net-W network image segmentation algorithm. The application value of the algorithm was comprehensively evaluated by comparing the average Dice coefficient, average recall rate, and average precision of the BN-U-net-W network image segmentation algorithm with the U-net and BN-U-net network algorithms. The results showed that the Dice coefficient, recall, and precision of the BN-U-net-W network were 86.31%, 88.43%, and 87.63% respectively, which were higher than those of the U-net and BN-U-net networks, and the differences were statistically significant ($P < 0.05$). Cerebral blood flow (CBF), cerebral blood volume (CBV), and capillary permeability (PMB) in the glioma area were 56.85 mL/(min·100 g), 18.03 mL/(min·100 g), and 8.57 mL/100 g, respectively, which were significantly higher than those of normal brain tissue, showing statistically significant differences ($P < 0.05$). The mean transit time (MTT) difference between the two was not statistically significant ($P > 0.05$). The receiver operating characteristic (ROC) curves of CBF, CBV, and PMB in CTPI parameters of glioma had area under the curve (AUC) of 0.685, 0.724, and 0.921, respectively. PMB parameters were significantly higher than those of CBF and CVB, and the differences were statistically obvious ($P < 0.05$). It showed that the BN-U-net-W network model had a better image segmentation effect, and CBF, CBV, and PMB showed better sensitivity in diagnosing glioma tissue and normal brain tissue and high-grade and low-grade gliomas, among which PBM showed the highest predictability.

1. Introduction

Glioma is a common malignant tumor in the cranial nervous system, and its incidence accounts for about 40% of all intracranial tumors. At present, the pathogenesis of the disease is not clear. The common types are astrocytoma, oligodendroglioma, ependymoma, neuronal tumor, and medulloblastoma [1, 2]. Due to the different locations of the tumor in the brain, the clinical symptoms are also different. Most patients have headache, vomiting, and memory loss as the main symptoms of increased intracranial pressure [3]. Most of glioma grow infiltratingly, so the boundary with normal brain tissue is unclear; and the higher the tumor grade, the more unclear the boundary, the more serious the infiltration of peritumoral brain tissue [4, 5]. According to the classification criteria of glioma issued by the World Health Organization (WHO), it can be divided into grades I–IV, which were benign, borderline with a trend towards III and IV, and malignant [6]. Surgical resection is the main method for the treatment of glioma, but due to the different tumor grades, the prognosis varies greatly. Therefore, obtaining accurate glioma classification information is of great significance for the selection of treatment methods, surgical guidance, and the improvement of prognosis [6–8].

Clinically, the commonly used diagnostic methods for glioma are computed tomography (CT), magnetic resonance imaging (MRI), and other imaging examinations. However, the imaging characteristics of glioma lack specificity. The imaging of grades I–IV can be manifested as mixed signal images with different degrees of necrosis or cystic transformation. Therefore, conventional imaging examinations cannot accurately provide specific conditions that are not conducive to glioma grading, such as tumor angiogenesis, metabolism, and micronecrosis [9–12]. In recent years, CT perfusion imaging (CTPI) has shown superiority in reflecting the blood perfusion of tumors. Clinical scholars have used it in the diagnosis and classification of glioma patients, and the results have been significantly improved [13, 14]. However, each patient's craniocerebral condition is complex and changeable, with different manifestations in CT imaging. Clinicians diagnose and analyze the patient's condition by observing and analyzing each CT image. They are easily affected by certain objective factors, such as the doctor's experience, mental state, and the quality of CT imaging. This is not only time-consuming and labor-intensive but also causes risk of misdiagnosis and missed diagnosis [15–17].

With the development of science and technology and the enhancement of artificial intelligence computing capabilities, deep learning has begun to be widely used in visual image processing, data mining, and other fields and has achieved good results [18]. In clinical practice, some scholars use deep learning technology to analyze medical image maps to assist doctors in segmenting lesions, completing target detection and classification, and achieving good results [19, 20]. However, the traditional deep learning technology is difficult to achieve the purpose of more complex image segmentation such as glioma. Therefore, a 128-slice CT whole brain perfusion image segmentation method based on the U-net network was proposed in this study, which was used in the diagnosis and analysis of glioma patients.

In conclusion, obtaining accurate glioma grading information is of great significance for the selection of treatment methods, the guidance of surgery, and the improvement of prognosis. However, the U-net network in the clinical deep learning technology has shown good results in the processing of medical CT images at present. Therefore, this work proposed a segmentation algorithm of CT perfusion images based on the U-net network and applied it to the clinical diagnosis and analysis of glioma patients. It was hoped to explore the clinical practical value of the algorithm by comparing the imaging effects with the U-net and BN-U-net network algorithms that have been clinically proven to have good image segmentation effects, providing an effective reference for the diagnostic analysis and surgical treatment of glioma patients.

2. Materials and Methods

2.1. Research Objects and Their Grouping. In this study, 72 patients with glioma admitted to the hospital from July 2018 to June 2020 were selected as the research subjects. All patients were confirmed to be glioma by postoperative pathological biopsy and immunohistochemistry. Among them, 40 were males and 32 were females; and patients were 15–76 years old (with an average value of 42.75 ± 14.32 years old). All patients underwent 128-slice CT whole brain perfusion scan (Siemens SOMATOM definition AS 128-slice spiral CT machine) before surgery, and pathological examination was performed after operation to determine the pathological type and pathological grade. 72 patients were rolled into two groups based on postoperative pathological examination results and WHO pathological grading standards: 27 cases in the low-grade group (I-II) and 45 cases in the high-grade group (III-IV). This study had been approved by the ethics committee of hospital, and the patients and their families had understood the situation of the study and signed the informed consent forms.

Inclusion criteria: patients who were diagnosed as primary glioma by pathological examination, patients whose imaging data were well preserved, and patients with no contraindication to CT examination.

Exclusion criteria: patients who were allergy to iodine contrast agent, patients with hyperthyroidism, patients with intracranial tumor metastasis or multiple intracranial tumors, patients in the late stage of glioma with obviously increased intracranial pressure, patients with tendency to brain herniation, and patients with cardiopulmonary insufficiency.

2.2. CTPI. Before scanning, the patients had an iodine allergy test. Allergy rescue materials were prepared (epinephrine, dexamethasone, and nasal oxygen tube) for rescue at any time. 0.1 mL of iodine contrast agent was adopted for intradermal injection, and whether the subjects had allergic reactions should be observed after 15–20 minutes. The elbow vein was punctured with a 16G needle to ensure that the contrast agent was injected quickly and stably. The patient was instructed to lie supine, a routine brain scan was performed with the ear canthus line as the baseline to determine the extent of the lesion, and then a CT whole brain perfusion scan was performed. A high-pressure syringe was used to inject the contrast medium through the cubital vein at a speed of about 5.5 mL/s according to the subject's weight (1–1.5 mL/kg). Then, centering on the lesion, a continuous dynamic scan of 96 mm of the whole brain was performed. The scanning parameters were set as follows: scanning time was 40 seconds, scanning layer thickness was 0.6 mm, layer thickness was 1.0 mm, tube voltage was 80 kV, tube current was 120 mA, and 0.33 seconds for 1 cycle of tube rotation.

A three-dimensional postprocessing workstation was adopted to process the acquired data with a whole brain volume perfusion software package to obtain the pseudo-color maps of cerebral blood flow (CBF), cerebral blood volume (CBV), mean transit time (MTT), and capillary permeability (PMB).

2.3. Glioma CT Image Segmentation Algorithm Based on the U-net Network. The U-net network is an extension of the full

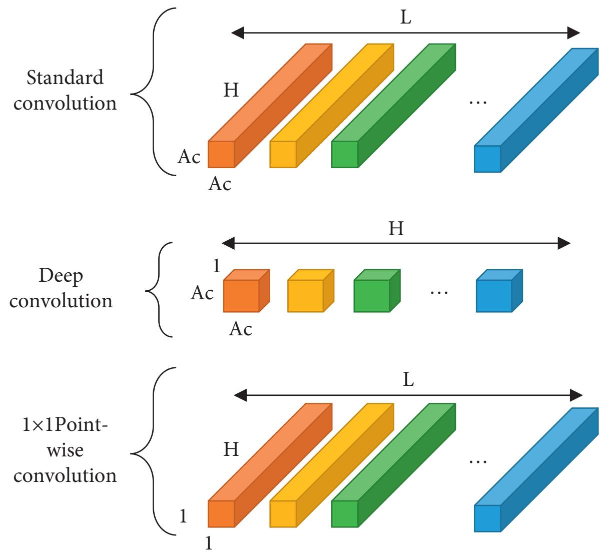

Figure 1: Schematic diagram of depth separable convolution.

convolutional neural network (FCN), which can be divided into two parts. The first half was used to extract image features, and the second half was used for sampling. Taking into account that the U-net network may have slower convergence speed and disappearance of gradients during training, the research had added a part of the norm layer to normalize it. At the same time, the research replaced the ordinary convolution in the U-net network with the depth separable convolution to improve the calculation speed, which improved the calculation speed of the model by reducing the network parameters and reducing the size of the network model. Therefore, a BN-U-net-W network model was designed.

The batch normalization (BN) was adopted for the normalization process to process the input value distribution of any neuron in each layer of the neural network into a standard normal distribution with a mean of 0 and a variance of 1, so as to improve the convergence speed and shorten the training time of the model. The process of BN normalization processing was mainly as follows.

It was assumed that the input was s, which was the number of all samples, and β was the parameter. If $\alpha = \{x_1 \ldots x_s\}$, the equation for calculating the mean value of the batch data can be expressed as follows:

$$\rho_\alpha = \frac{1}{s}\sum_{i=1}^{s} x_1 . \tag{1}$$

The data variance of each training batch can be expressed as

$$\sigma_\alpha^2 = \frac{1}{s}\sum_{i=1}^{s}\left(x_i - \rho_\alpha\right)^2. \tag{2}$$

The mean and variance of the data were adopted to perform BN on the training data to obtain a 0-1 normal distribution. In addition, ε was adopted to represent a very small positive number; then, the equation can be expressed as

$$\hat{x} = \frac{x_i - \rho_\alpha}{\sqrt{\sigma_\alpha^2 + \varepsilon}}. \tag{3}$$

It could multiply x_i by γ to adjust the size of the integer value and then add α to increase the offset to get m_i, where γ represents the scale factor, α represents the translation factor, and m_i can be expressed as

$$m_i = \gamma \hat{x}_i + \alpha. \tag{4}$$

Depth separable convolution can decompose the standard convolution into depth convolution and an $l \times 1$ point-by-point convolution. The principle is shown in Figure 1. Let A_c be the spatial dimension of the convolution kernel, and P_v be the size of feature map inputted by the convolution layer. The calculation amount of the standard convolution is as follows:

$$\text{Standard convolution} = A_c \times A_c \times H \times L \times P_v \times P_v. \tag{5}$$

The amount of calculation for deep convolution is as follows:

$$\text{Deep convolution} = A_c \times A_c \times P_v \times P_v. \tag{6}$$

The calculation amount of 1×1 point-by-point convolution is as follows:

$$1 \times 1 \text{ pointwise convolution} = H \times L \times P_v \times P_v. \tag{7}$$

Based on equations (5)–(7), the calculated ratio of depth separable convolution nuclear standard volume data can be obtained:

$$\frac{1}{L} + \frac{1}{A_c^2} = \frac{A_c \times A_c \times H \times P_v \times P_v + H \times L \times P_v \times P_v}{A_c \times A_c \times H \times L \times P_v \times P_v}. \tag{8}$$

The training dataset of the BN-U-net network model was the CT image, and the glioma standard was performed by experienced clinicians. Network training used NVIDIA GTX Titan V GPU for acceleration, the number of iterations was set to 50 epochs, the learning rate was 0.001, the batch size was set to 4, and the optimization function was RMSP_{rop}. The training process is shown in Figure 2. The training dataset was input to the BN-U-net network model for training after data enhancement, filtering, and histogram, and the segmentation results were output after segmentation. After the test dataset was filtered and histogram processed, it was directly segmented to output the segmentation results.

2.4. Observation Indicators. To compare the sensitivity, specificity, and accuracy of CTPI to the pathological classification of glioma, TP was used as the true positive of the test result, FN was false negative, FP was false positive, and TN was true negative:

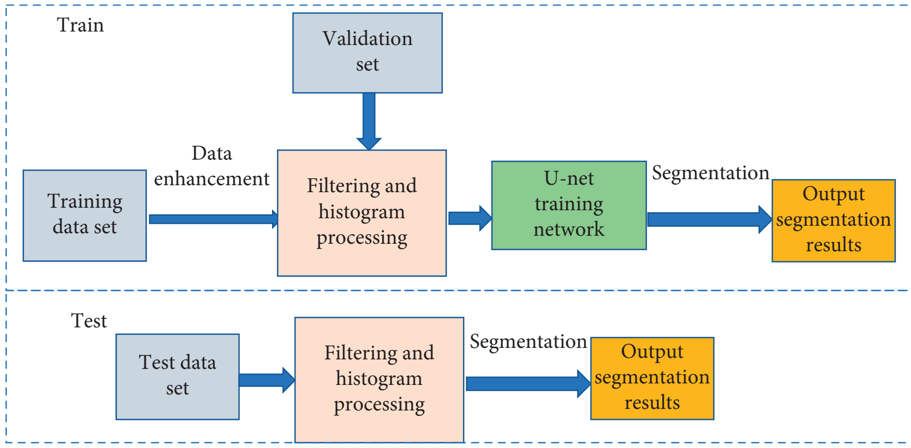

Figure 2: The training process of the BN-U-net-W network.

$$\text{Accuracy} = \frac{TP + TN}{TP + TN + FP + FN},$$
$$\text{Sensitivity} = \frac{TP}{TP + FN}, \tag{9}$$
$$\text{Specificity} = \frac{TN}{FP + TN}.$$

The effect of CTPI image segmentation was evaluated mainly using Dice similarity coefficient (DSC), recall, and precision, which could be calculated as follows:

$$DSC = \frac{2|Z \cap D|}{|Z| + |D|}. \tag{10}$$

In equation (10), Z was the result of manual segmentation by experts, and D was the segmentation result of the algorithm designed in this research. The value of Dice coefficient ranged from 0 to 1. The larger the value, the better the segmentation effect of the algorithm. The smaller the value, the poor the performance of the algorithm's glioma segmentation or the segmentation error. Precision and recall are calculated as follows.

$$\text{Precision} = \frac{TP}{TP + FP},$$
$$\text{Recall} = \frac{TP}{TP + FN}. \tag{11}$$

2.5. Statistical Analysis. SPSS 18.0 statistical software was adopted for data analysis, and the measurement data were expressed as mean ± standard deviation ($\overline{x} \pm s$). The independent sample t-test was used for comparison between groups, and $P < 0.05$ was considered statistically significant. The receiver operating characteristic (ROC) analysis was used to calculate the area under the ROC curve (AUC) and compare the diagnostic accuracy of CTPI parameters. The maximum value of Youden index (sensitivity + specificity-1) was selected as the cutoff point for diagnosing high and low-grade glioma, and the corresponding sensitivity and specificity were calculated.

3. Results

3.1. Basic Data. Figure 3 shows a comparison chart of the general data of the two groups of patients. As illustrated in the figure, the number of male patients in the low-dose group and the high-dose group was 24 and 16, respectively, and the number of female patients was 17 and 15, respectively. The average ages of the patients in the two groups were 42.96 ± 13.45 years old and 42.57 ± 15.13 years old, respectively; and the body mass index (BMI) was $22.15 \pm 2.14\,kg/m^2$ and $22.08 \pm 2.09\,kg/m^2$, respectively. After comparison, it was found that there was no significant difference in the ratio of male to female, average age, and BIM between patients in the two groups ($P > 0.05$).

3.2. The Processing Results of the BN-U-net-W Network Model. The Dice coefficient, recall rate, and precision of the BN-U-net-W network model in training sets 1, 2, and 3 were compared, and the results are shown in Figure 4. As shown in Figure 4, the Dice coefficient, recall rate, and precision of the BN-U-net-W network model algorithm in training set 1 were 92.13%, 94.41%, and 89.03%, respectively. In training set 2, the Dice coefficient, recall rate, and precision were 89.32%, 95.27%, and 89.94%, respectively. In training set 3, the Dice coefficient, recall rate, and precision were 77.26%, 92.16%, and 78.42%, respectively. Figure 4(d) shows the average values of Dice coefficient, recall rate, and precision for the three training sets, which were 86.24%, 93.95%, and 85.79%, respectively.

3.3. Comparison on Performances of Different Algorithms. In order to verify the performance of the algorithm, the U-net [21] and BN-U-net [22] networks were introduced and compared with the proposed algorithm in terms of the average Dice coefficient, average recall, and average precision of the three when testing 400 glioma CT images. The results are shown in Figure 5. The Dice coefficient, recall, and precision of the BN-U-net-W network were 86.31%, 88.43%, and 87.63%, respectively, which were higher than those of

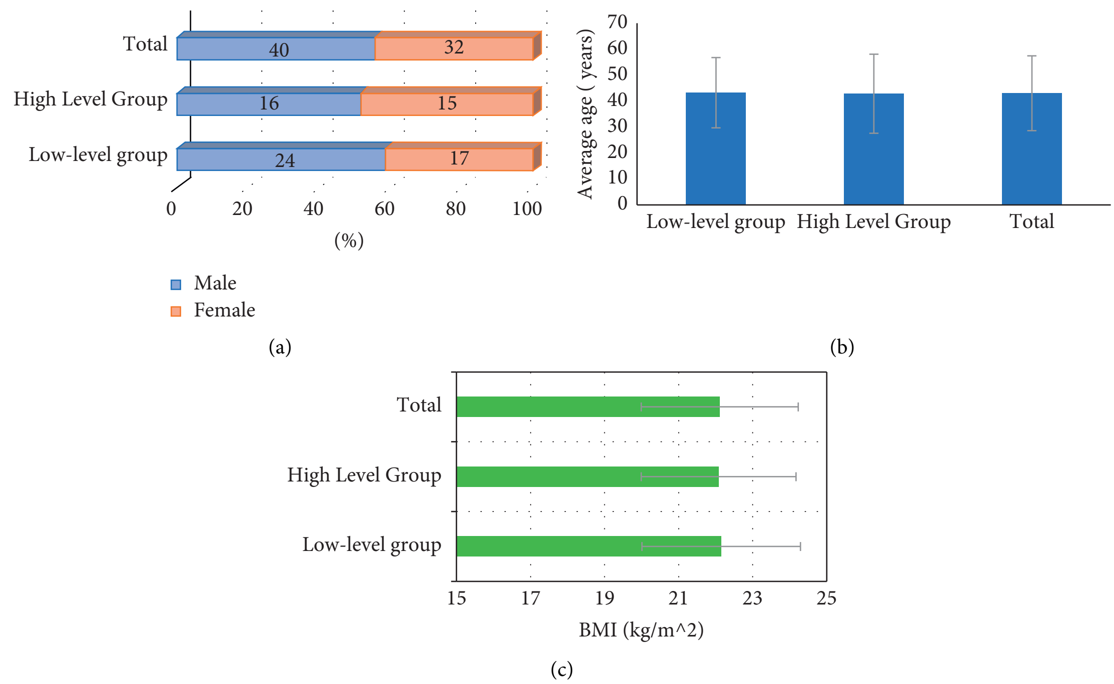

Figure 3: Comparison of the general data of the two groups of patients. (a) The gender distribution of the two groups of patients. (b) The comparison of the average age of the two groups of patients. (c) The comparison of the BMI of the two groups of patients.

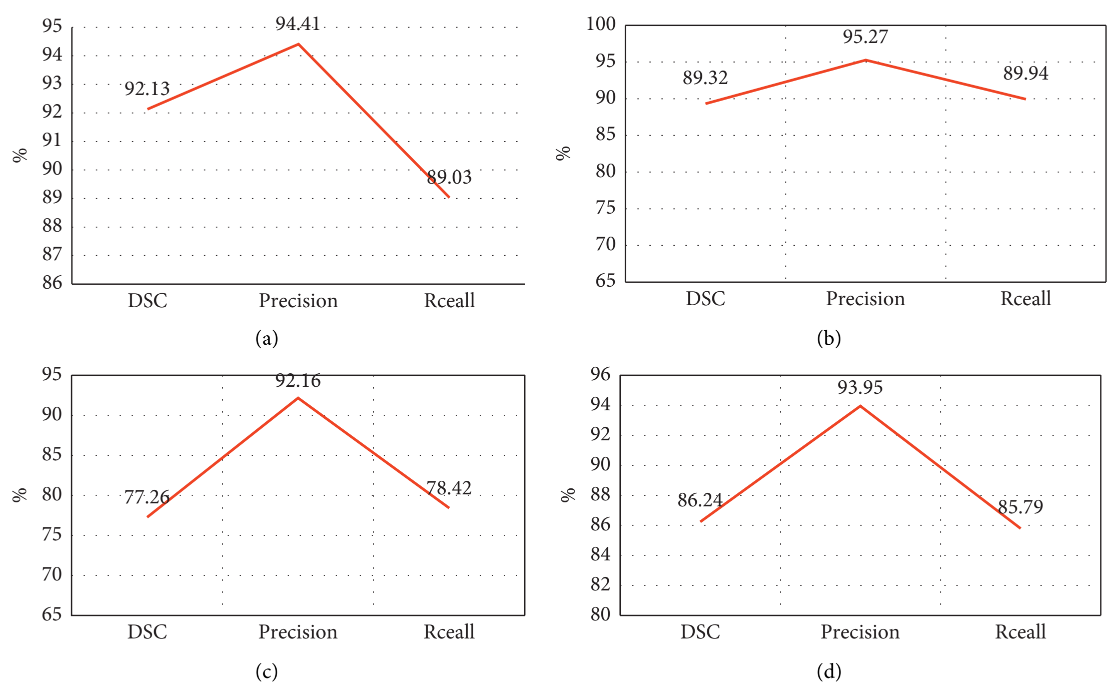

Figure 4: Processing results of the BN-U-net-W network model. (a)–(c) The performance analysis result of training set 1, training set 2, and training set 3, respectively. (d) The average result of performance analysis of three training sets.

U-net and BN-U-net networks, and the differences were statistically significant ($P < 0.05$).

The model sizes and the shortest time of the three networks required to segment a glioma CT image were calculated. The results are shown in Figure 6. Among the three types of networks, the U-net network took the shortest time to split a glioma CT, followed by the BN-U-net-W network, and the BN-U-net network took the longest time to be 0.59 seconds. Among the three networks, the model of the BN-U-net-W network was 142 M, which was significantly smaller than the other two, and the difference was statistically significant ($P < 0.05$).

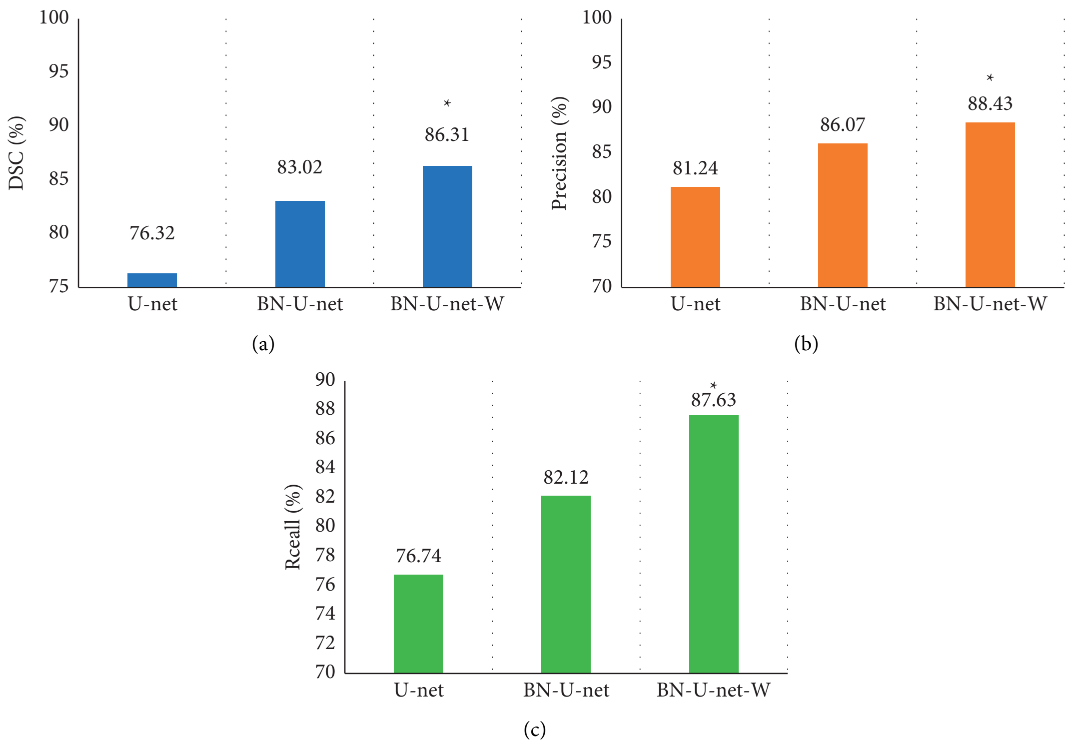

FIGURE 5: Comparison on performances of different algorithms. (a)–(c) The comparisons of Dice coefficient, recall, and precision, respectively. *The difference was statistically obvious in contrast to the BN-U-net-W algorithm ($P < 0.05$).

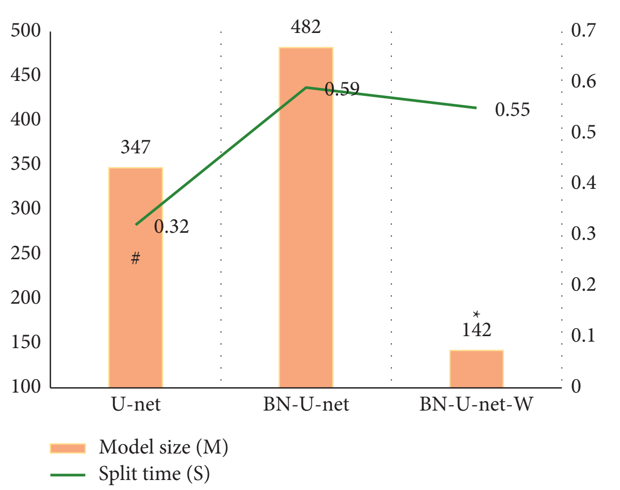

FIGURE 6: The model sizes and the shortest time of the three networks of three algorithms. * and # indicate that the difference was statistically great compared with BN-U-net-W and U-net, respectively ($P < 0.06$).

3.4. Comparison of CTPI Parameters between Normal Brain Tissue and Glioma Area. It statistically analyzed the CBF, PMB, CVB, and MTT of normal brain tissue and glioma tissue of 72 glioma patients, and the results are shown in Figure 7. The CBF, PMB, and CVB of glioma tissue were 56.85 (mL/(min 100 g)), 18.03 (mL/(min 100 g)), and 8.57 (mL/100 g), respectively, which were significantly higher than those in the normal brain tissue (19.87 (mL/(min·100 g)), 3.27 (mL/(min·100 g)), and 2.68 (mL/100 g), respectively), and the difference was statistically significant ($P < 0.05$). The MTT of normal brain tissue and glioma region of patients was 10.09 s and 9.02 s, respectively, and there was no significant difference between the two ($P > 0.05$).

3.5. Comparison on CTPI Parameters of Low-Grade and High-Grade Normal Brain Tissues. A total of 27 cases in the low-grade group (grades I-II) and 45 cases in the high-grade group (III-IV) of CBF, PMB, CVB, and MTT were counted in the study. The results are shown in Figure 8. There was no obvious difference in CBF, PMB, CVB, and MTT between low-grade normal brain tissue and high-grade normal brain tissue, and there was no statistical significance ($P > 0.05$).

3.6. Comparison on CTPI Parameters between Low-Grade and High-Grade Glioma Areas. A total of 45 cases in the low-grade group (grades I-II) and 45 cases in the high-grade group (III-IV) of CBF, PMB, CVB, and MTT were counted in the study. The results are shown in Figure 9. The CBF, PMB, and CVB in the glioma area were 81.04 mL/(min·100 g), 24.63 mL/(min·100 g), and 11.23 mL/100 g, respectively, which were significantly higher than those of normal brain tissue, and they were statistically significant ($P < 0.05$). There was no significant difference in MTT between the two ($P > 0.05$).

3.7. ROC Analysis on CTPI Parameters between Low-Grade and High-Grade Glioma Areas. The study analyzed the ROC

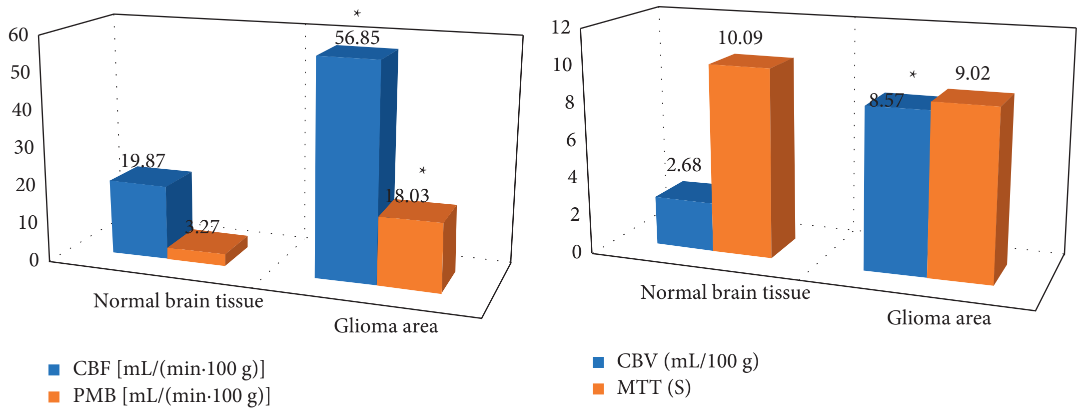

(a) (b)

Figure 7: Comparison on CTPI parameters between normal brain tissue and glioma area. (a) The comparisons of CBF and PMB. (b) The comparisons of CVB and MTT. ∗The difference was greatly significant compared with the glioma area ($P < 0.05$).

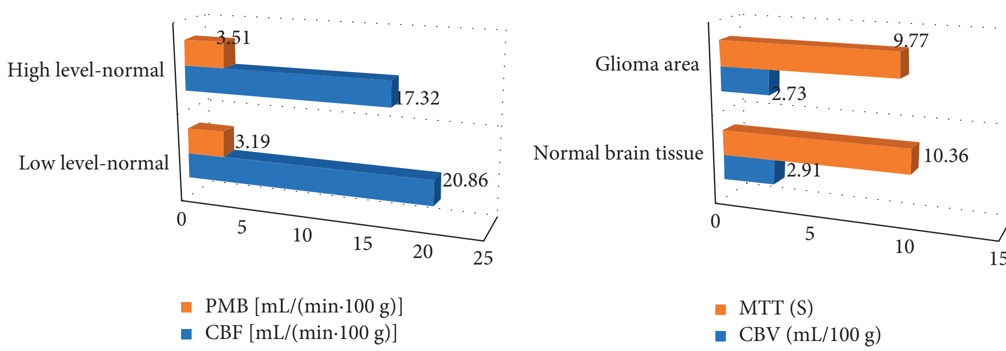

(a) (b)

Figure 8: Comparison on CTPI parameters of low-grade and high-grade normal brain tissues. (a) The comparisons of CBF and PMB. (b) The comparisons of CVB and MTT.

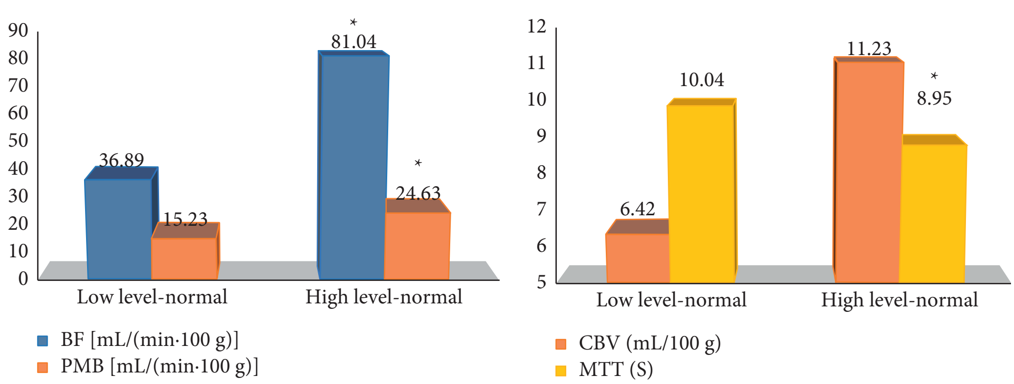

(a) (b)

Figure 9: Comparison on CTPI parameters between low-grade and high-grade glioma areas. (a) The comparisons of CBF and PMB. (b) Comparisons of CVB and MTT. ∗The difference was greatly significant compared with the glioma area ($P < 0.05$).

curves of CBF, CBV, and PMB in the high-grade and low-grade glioma CTPI parameters, and the results are shown in Figure 10. The AUC of CBF, CBV, and PMB was 0.685, 0.724, and 0.921, respectively.

3.8. Imaging Data of Patients. Figure 11 shows the CT imaging data of a 68-year-old female patient. The clinical symptoms of the patient were headache and nausea for 2 weeks, which worsened for two days. Figures 11(a) and 11(b)

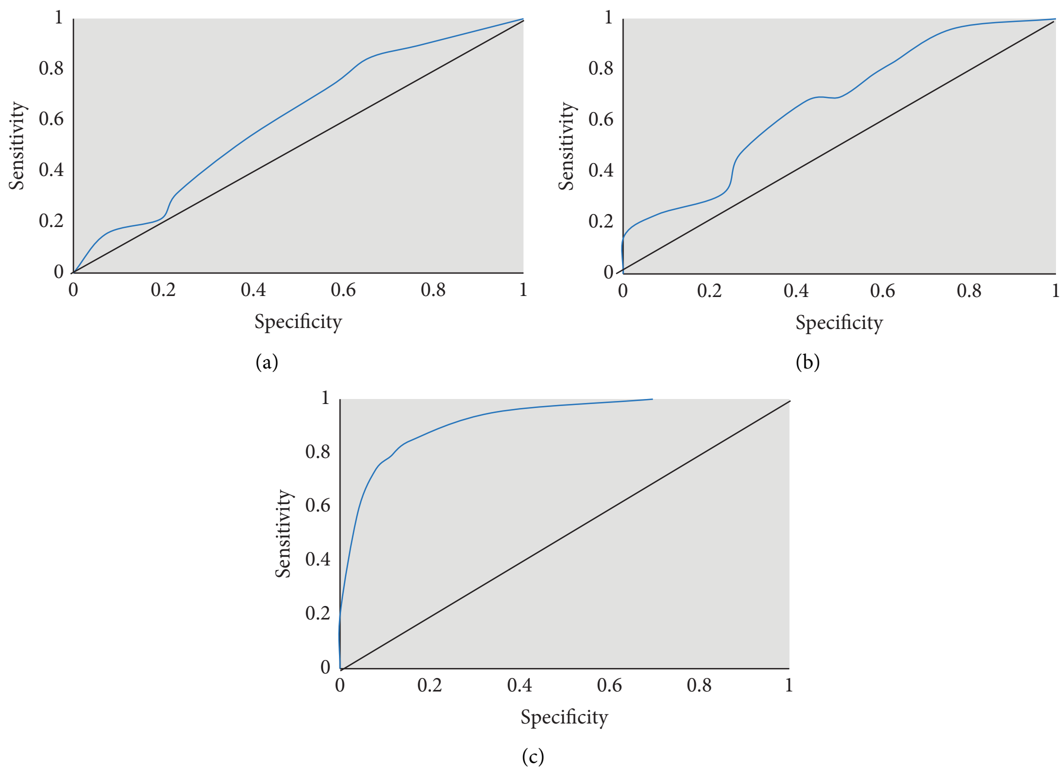

Figure 10: ROC analysis on CTPI parameters between low-grade and high-grade glioma areas. (a)–(c) The ROC results of CBF, CBV, and PMB, respectively.

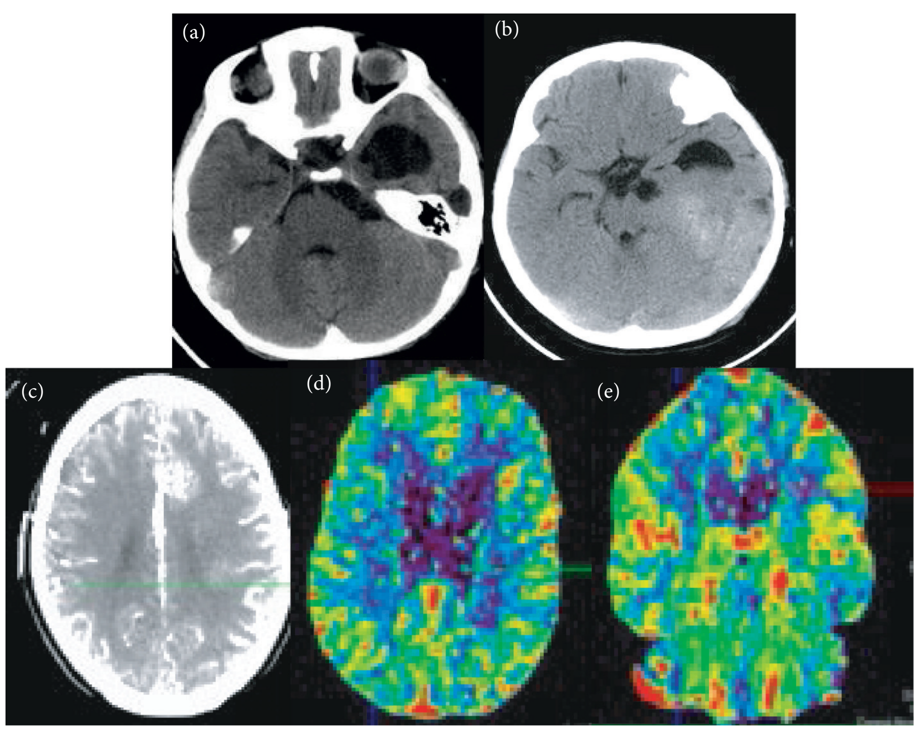

Figure 11: Imaging data of patients. (a)-(b) Ordinary CT. (c) Cranial enhanced CT. (d)-(e) CTPI.

show the normal CT, Figure 11(c) shows a brain enhanced CT, and Figures 11(d) and 11(e) show CT perfusion imaging. The figures demonstrated that the patient's glioma showed mixed density shadows, the glioma was irregular in shape, the boundary was unclear, and there were a small amount of cystic degeneration, hemorrhage, and necrosis. On contrast-enhanced CT, there were uneven enhancement, cystic degeneration, and hemorrhage, which showed that the patient's cerebral blood flow and surface infiltration were significantly aggravated.

4. Discussion

Glioma is a relatively common type of brain malignant tumors, which mainly occur in the central nervous system. Investigations have shown that the disease accounts for 40–50% of primary central nervous system tumors [7, 8]. The pathogenesis of glioma is not clear, but it is highly aggressive and has a high recurrence rate, so the clinical mortality rate is relatively high. Among the common glioma cell types, glioblastoma is the most common, accounting for about 50% of all gliomas, and the prognosis is extremely poor, with a recurrence rate close to 100% [23]. How to accurately obtain the specific type and classification of the patient's glioma is of great significance. Therefore, this study proposed a 128-slice CT whole brain perfusion image segmentation method based on the U-net network. In order to avoid the slowing down of the algorithm and the disappearance of the gradient, the research had added part of the norm layer and normalized it. At the same time, the ordinary convolution in the U-net network was replaced with depth separable convolution, which improved the speed of calculation, so a BN-U-net-W network model was designed.

In this study, the Dice coefficient, recall, and precision of the BN-U-net-W network model were calculated, and the average values were 86.24%, 93.95%, and 85.79%, respectively. In addition, in order to verify the performance of the algorithm, the study also introduced U-net and BN-U-net networks and compared the average Dice coefficient, average recall, and average precision of 400 glioma CT images tested by three network models. The results showed that the Dice coefficient, recall, and precision of the BN-U-net-W network were 86.31%, 88.43%, and 87.63%, respectively, which were higher than those of the U-net and BN-U-net networks, showing statistically obvious differences ($P < 0.05$). Such results were similar to the results of Wang et al. (2020) [24]. The BN-U-net-W network is added a norm layer to the full convolutional neural network (FCN) for normalization, which solved the problem that the U-net network may experience a decrease in convergence speed during training and testing. Slowness and gradient disappearance, in addition, the use of depthwise separable convolutional networks to replace ordinary convolutions can greatly reduce the size of the network model, reduce the parameters used in the network operation process, and greatly shorten the running time.

In addition, it also counted the model sizes of the three networks and the shortest time required to segment a glioma CT image in this study. Among them, the U-net network required the shortest time to segment a glioma CT, followed by the BN-U-net-W network. The longest time required for the BN-U-net network was 0.59 seconds; the model of the BN-U-net-W network was 142 M, which was much smaller than the other two, and the difference was statistically significant ($P < 0.05$). The study statistically analyzed the CTPI parameters of normal brain tissue and glioma area of 72 glioma patients. The results showed that the CBF, PMB, and CVB of glioma area were 56.85 mL/(min·100 g), 18.03 mL/(min·100 g), and 8.57 mL/100 g, respectively, which were much higher than those of normal brain tissue, and the differences were statistically significant ($P < 0.05$). This shows that these three parameters have better sensitivity in the diagnosis of glioma tissue and normal brain tissue, high-grade, and low-grade gliomas. The results of the study by Ahmad et al. (2016) [25] are also consistent with this work, indicating that CBF, PMB, and CVB show good detection sensitivity as monitoring indicators of neovascularization in patients with clinical glioma. In addition, using the correlation between the above indicators and glioma, the biological behavior of patients can be well evaluated. Finally, the study analyzed the ROC curves of CBF, CBV, and PMB in the high-grade and low-grade glioma CTPI parameters, and the AUCs were 0.685, 0.724, and 0.921, respectively. PMB parameters were significantly higher than CBF and CVB, and the differences were statistically significant, which showed that PBM had high predictability.

5. Conclusion

This study proposes a CT perfusion image segmentation algorithm based on the BN-U-net network and applies it to evaluate the application value of CT images in the diagnosis of glioma diseases. In order to verify the performance of the algorithm, the U-net and BN-U-net networks were introduced and compared with other algorithms in terms of Dice coefficient, recall, and precision. The results showed that the image segmentation effect of the BN-U-net-W network model designed in this study was better. Among the glioma CTPI parameters, CBF, CBV, and PMB were more sensitive in diagnosing glioma tissue and normal brain tissue and high-grade and low-grade glioma, and PBM had high predictability. However, this study did not make a detailed division of the pathological types of the study subjects and ignored the influence of different pathological types on CTPI parameters. In the follow-up study, the sample size can be increased to explore the impacts of different pathological types on CTPI parameters. In general, this study provided an effective reference for improving the survival rate and quality of life of patients with glioma.

Data Availability

The data used to support the findings of this study are available from the corresponding author upon request.

Conflicts of Interest

The authors declare that they have no conflicts of interest.

References

[1] R. Chen, M. Smith-Cohn, A. L. Cohen, and H. Colman, "Glioma subclassifications and their clinical significance," *Neurotherapeutics*, vol. 14, no. 2, pp. 284–297, 2017.

[2] T. J. C. Wang and M. P. Mehta, "Low-grade glioma radiotherapy treatment and trials," *Neurosurgery Clinics of North America*, vol. 30, no. 1, pp. 111–118, 2019.
[3] J. Bai, J. Varghese, and R. Jain, "Adult glioma WHO classification update, genomics, and imaging," *Topics in Magnetic Resonance Imaging*, vol. 29, no. 2, pp. 71–82, 2020.
[4] Z. Peng, C. Liu, and M. Wu, "New insights into long noncoding RNAs and their roles in glioma," *Molecular Cancer*, vol. 17, no. 1, p. 61, 2018.
[5] P. de Blank, P. Bandopadhayay, D. Haas-Kogan, M. Fouladi, and J. Fangusaro, "Management of pediatric low-grade glioma," *Current Opinion in Pediatrics*, vol. 31, no. 1, pp. 21–27, 2019.
[6] A. M. Miller, R. H. Shah, E. I. Pentsova et al., "Tracking tumour evolution in glioma through liquid biopsies of cerebrospinal fluid," *Nature*, vol. 565, no. 7741, pp. 654–658, 2019.
[7] A. Poff, A. P. Koutnik, K. M. Egan, S. Sahebjam, D. D'Agostino, and N. B. Kumar, "Targeting the Warburg effect for cancer treatment: ketogenic diets for management of glioma," *Seminars in Cancer Biology*, vol. 56, pp. 135–148, 2019.
[8] S. L. Hervey-Jumper and M. S. Berger, "Maximizing safe resection of low- and high-grade glioma," *Journal of Neuro-Oncology*, vol. 130, no. 2, pp. 269–282, 2016.
[9] T. J. Kruser, W. R. Bosch, S. N. Badiyan et al., "NRG brain tumor specialists consensus guidelines for glioblastoma contouring," *Journal of Neuro-Oncology*, vol. 143, no. 1, pp. 157–166, 2019.
[10] B. B. Kasten, K. Jiang, D. Cole et al., "Targeting MMP-14 for dual PET and fluorescence imaging of glioma in preclinical models," *European Journal of Nuclear Medicine and Molecular Imaging*, vol. 47, no. 6, pp. 1412–1426, 2020.
[11] M. Villena Martín, F. J. Pena Pardo, F. Jiménez Aragón, J. M. Borras Moreno, and A. M. García Vicente, "Metabolic targeting can improve the efficiency of brain tumor biopsies," *Seminars in Oncology*, vol. 47, no. 2-3, pp. 148–154, 2020.
[12] M. Riva, R. Wouters, A. Weerasekera et al., "CT-2A neurospheres-derived high-grade glioma in mice: a new model to address tumor stem cells and immunosuppression," *Biology Open*, vol. 8, no. 9, Article ID bio044552, 2019.
[13] M. Röhrich, K. Huang, D. Schrimpf et al., "Integrated analysis of dynamic FET PET/CT parameters, histology, and methylation profiling of 44 gliomas," *European Journal of Nuclear Medicine and Molecular Imaging*, vol. 45, no. 9, pp. 1573–1584, 2018.
[14] S. Kaczmarz, F. Hyder, and C. Preibisch, "Oxygen extraction fraction mapping with multi-parametric quantitative BOLD MRI: reduced transverse relaxation bias using 3D-GraSE imaging," *NeuroImage*, vol. 220, Article ID 117095, 2020.
[15] M. Orevi, O. Shamni, N. Zalcman et al., "[18F]-FDHT PET/CT as a tool for imaging androgen receptor expression in high-grade glioma," *Neuro-Oncology Advances*, vol. 3, no. 1, Article ID vdab019, 2021.
[16] N. Moshtaghi-Kashanian, H. Niroomand-Oscuii, and N. Meghdadi, "Simulating glioblastoma growth consisting both visible and invisible parts of the tumor using a diffusion-reaction model followed by resection and radiotherapy," *Acta Neurologica Belgica*, vol. 120, no. 3, pp. 629–637, 2020.
[17] D. Sasi S, R. K. Gupta, R. Patir, S. Ahlawat, S. Vaishya, and A. Singh, "A comprehensive evaluation and impact of normalization of generalized tracer kinetic model parameters to characterize blood-brain-barrier permeability in normal-appearing and tumor tissue regions of patients with glioma," *Magnetic Resonance Imaging*, vol. 83, pp. 77–88, 2021.
[18] M. Hu, Y. Zhong, S. Xie, H. Lv, and Z. Lv, "Fuzzy system based medical image processing for brain disease prediction," *Frontiers in Neuroscience*, vol. 15, Article ID 714318, 2021.
[19] Y. Li, J. Zhao, Z. Lv, and J. Li, "Medical image fusion method by deep learning," *International Journal of Cognitive Computing in Engineering*, vol. 2, pp. 21–29, 2021.
[20] Z Yu, S. U Amin, M Alhussein, and Z Lv, "Research on disease prediction based on improved DeepFM and IoMT," *IEEE Access*, no. 99, p. 1, 2021.
[21] Z. Zhang, C. Wu, S. Coleman, and D. Kerr, "DENSE-INception U-net for medical image segmentation," *Computer Methods and Programs in Biomedicine*, vol. 192, Article ID 105395, 2020.
[22] M. Lee, J. Kim, R. Ey Kim et al., "Split-attention U-net: a fully convolutional network for robust multi-label segmentation from brain MRI," *Brain Sciences*, vol. 10, no. 12, p. 974, 2020.
[23] M. C. Tom, D. P. Cahill, J. C. Buckner, J. Dietrich, M. W. Parsons, and J. S. Yu, "Management for different glioma subtypes: are all low-grade gliomas created equal?" *American Society of Clinical Oncology Educational Book*, vol. 39, no. 39, pp. 133–145, 2019.
[24] W Wang, H Feng, Q Bu et al., "MDU-net: a convolutional network for clavicle and rib segmentation from a chest radiograph," *J Healthc Eng*, vol. 2020, Article ID 2785464, 2020.
[25] N Ahmad, A Shaukat, A Rehan, and S Rashid, "Diagnostic accuracy of perfusion computed tomography in cerebral glioma grading," *Journal of the College of Physicians and Surgeons--Pakista: JCPSP*, vol. 26, no. 7, pp. 562–565, 2016.

Hindawi
Contrast Media & Molecular Imaging
Volume 2022, Article ID 2622316, 10 pages
https://doi.org/10.1155/2022/2622316

Research Article

CT Image Features Based on the Reconstruction Algorithm for Continuous Blood Purification Combined with Nursing Intervention in the Treatment of Severe Acute Pancreatitis

Yanyan Liu, Mingli Gu, Liping Liu, Lunmeng Cui, and Aimin Xing

Department of Critical Care Medicine, Affiliated Hongqi Hospital of Mudanjiang Medical University, Mudanjiang 157011, Heilongjiang, China

Correspondence should be addressed to Aimin Xing; 201711110410641@stu.hubu.edu.cn

Received 7 January 2022; Revised 25 February 2022; Accepted 28 February 2022; Published 28 March 2022

Academic Editor: M Pallikonda Rajasekaran

The aim of the study was to explore the CT images of the iterative reconstruction algorithm to evaluate the curative effect of continuous blood purification combined with nursing intervention in the treatment of severe acute pancreatitis (SAP). A total of 100 patients with SAP treated by the bedside continuous venous hemofiltration purification method in a hospital were selected. The control group ($n = 50$) was given a routine treatment, and the observation group ($n = 50$) was treated with the continuous blood filtration mode for blood purification based on the routine treatment. In the CT image scanning of periodontitis patients, the iterative reconstruction algorithm was introduced to reduce image noise, and the CT values under the algorithm were statistically analyzed. The results showed that IL-1, IL-6, and IL-8 after treatment were significantly lower than those before treatment ($P < 0.05$). The symptoms effectively improved with continuous blood purification combined with nursing intervention in patients with SAP. After the use of the iterative reconstruction algorithm, the image quality, image information, and image MSE significantly improved. The image noise with 50% dose reduction was the lowest, but the reconstruction algorithm improved the low contrast resolution ($P < 0.05$). CT images based on the reconstruction algorithm can clearly display the lesion characteristics of the patients, and the reconstruction algorithm is feasible to improve the spatial resolution of CT images.

1. Introduction

Acute pancreatitis (AP) is one of the common clinical abdomen pains with high mortality. The mortality rate of severe acute pancreatitis (SAP) in China is 25%–40%, and that in foreign countries is 15%–30%, mainly due to secondary infection caused by pancreatic and surrounding tissues [1]. The clinical manifestations of SAP are pancreatic edema, hemorrhage and necrosis, and systemic inflammatory response. SAP is one of the common critical illnesses in the emergency department. Active inflammatory factors in the body during the onset lead to the release of a large number of cytokines, leading to the aggravation of the disease [2]. The secondary infection of the pancreas and the peripancreatic tissue further develops into multiple organ failure, which seriously threatens the life of patients and produces a higher mortality [3]. At present, the effective treatment for SAP is mainly the continuous blood purification treatment, which can quickly purify the toxins in patients, so as to reduce the impact of the toxins on the bodies of these patients, and the inflammatory symptoms disappear [4]. SAP has a variety of causes. Excessive drinking and drinking can cause poor drainage of the pancreatic duct, increased pressure in the pancreatic and biliary systems, and a high concentration of protease excretion disorders, resulting in the rupture of pancreatic vesicles. Bile duct inflammation, stones, edema, and other lesions can cause ampulla obstruction, bile reflux into the pancreatic duct, and trypsinogen activation. In clinical practice, many infectious infections can also promote the occurrence of acute pancreatitis [5, 6]. Continuous blood purification is a new blood purification method that continuously and slowly removes the water and solute in patients. By inputting a large amount of replacement solution to the patients and giving them intravenous nutritional support, it can promote the recovery of the patient's condition, and has a good effect in severe cases[7, 8].

CT has been continuously applied in clinical diagnosis, and has proven to be an important method for the diagnosis of many diseases. In many cases, X-rays cannot provide sufficient information on the actual size of the lesion and the spatial position of the anatomical landmarks [9, 10]. CT scanning can show the volume increase of diffuse pancreas and the distribution of the pancreatic density, and enhanced scanning shows the pancreas has uneven mild enhancement, which can accurately observe the lesion site. Detecting acute pancreatitis using CT has advantages such as: fast CT scanning speed, strong ability of multiplanar reorganization and grading ability, avoiding respiratory movement artifacts and gastrointestinal gas influence, with high sensitivity and specificity. The severity of pancreatitis and the involvement of adjacent organs can be clearly judged, and the CT severity index score can be performed. However, in terms of the actual situation, the CT scan range is limited, and the scanned part is large, which leads to the detection data being truncated and not comprehensive. This situation will cause the possibility of inaccurate inspection results in the reconstruction of CT images. Moreover, due to the limitation of angles, CT images will produce a large number of artifacts in the scanning process. At present, how to reduce the generation of image artifacts in the case of reducing the radiation during CT examination has become a major research hotspot in the field of imaging examination.

With the development of algorithm technology, the iterative reconstruction algorithm has been widely studied and applied in CT images. It belongs to a new infrared imaging technology, and the conditions required for scanning imaging are relatively low. In the case of large calculation cost, the iterative reconstruction algorithm is still a good reconstruction method for projection data with incomplete information or noise [11–13]. CT image reconstruction is based on many mathematical and physical operations. Its purpose is to reduce image noise and improve image resolution. Therefore, it is very important to reasonably use the reconstruction algorithm and maximize the effect of the algorithm [14–16].

In summary, the data of CT images using the iterative reconstruction algorithm are reconstructed and applied in the diagnosis of GC diseases to improve the accuracy of the diagnosis, and reasonable analysis is carried out through research. It is hoped that CT images based on the reconstruction algorithm can clearly present the lesions of the patients, improve the detection method, and provide reference for the diagnosis of diseases in clinic settings.

2. Methods

2.1. General Information. One hundred patients with SAP treated in a hospital from January 2019 to December 2020 were randomly divided into an observation group and a control group. In the control group, there were 26 males and 24 females, aged 29–50 years, with an average age of (41.54 ± 2.18) years, including 32 patients with hypertension and 18 patients with simple periodontitis. There were 20 males and 30 females in the observation group, aged 28–52 years old, with an average age of (43.54 ± 2.76) years. There were 22 patients with hypertension and 28 patients with simple periodontitis. The causes of SAP in the two groups were biliary pancreatitis, hyperlipidemia, overeating, and excessive alcohol consumption. There was no significant difference in the general data of the patients ($P > 0.05$), indicating comparability. This study had been approved by the Ethics Committee of hospital and all patients signed the informed consent form.

Inclusion criteria: (1) Patients who conform to the diagnostic criteria of acute severe pancreatitis. (2) Patients voluntarily participated in the study. (3) Patients without immune system diseases or infectious diseases. Exclusion criteria: (1) Incomplete clinical data. (2) Patients who are unwilling participants. (3) Patients with mental illness.

2.2. Method. The control group was treated with conventional treatment, fasting, and continuous gastrointestinal decompression. Painkillers and antispasmodics could be selected to correct the water, electrolyte, and acid–base balance of the patients. Infected patients were treated with anti-infective drugs. If there were shock patients, shock drugs could be used and enteral and parenteral nutrition could be given to patients reasonably. The vital signs of the patients were comprehensively tested.

On the basis of the conventional treatment, the observation group was treated with the continuous blood filtration mode for blood purification. Cardiopulmonary bypass was established in the right femoral vein intubation of the patient, and continuous blood filtration was performed. The flow rate of the replacement solution was determined according to the patient, and 1500–2000 ml/h was located. The replacement solution formula was flexibly and reasonably formulated in combination with the electrolyte disorder and acid–base balance of the patient, and the dosage of sodium bicarbonate, calcium, and potassium in the replacement solution was personalized and adjusted. The blood flow was 150–200 ml/h, which could be adjusted according to the patient's capacity state. The purification time was 24 h, and the vital signs of the patients were closely monitored. If biochemical indexes were obviously normal, symptoms were significantly alleviated, and if serum amylase decreased, the blood purification treatment could be stopped. Continuous purification once a day or every other day according to the patient's condition, the cumulative treatment time was more than 72 hours.

Patients were examined by Dual source computed tomography. The examination process was described in detail to the patients before scanning. The patients were in supine position, and the peripheral venous pathway of the lower limb (any lower limb) was established to connect the ECG and the blood oxygen monitor. Before the examination, the patients were sedated by professional anesthesiologists. The dosage of the anesthetic was 2 mL/kg, and the duration was 10–15 minutes. In addition, the ECG, respiration, and peripheral blood oxygen saturation of the patients were monitored. The obtained CT images were transmitted to the workstation and processed by Functool II software. Post-processing workstation: Vitrea3.9 version post-processing workstation.

Firstly, the ECG gating technology was used. The tube voltage was 80 KV, and the tube current parameters were adjusted according to body weight. The machine automatically gave pitch, and the periodic exposure was automatic. The Ultravist (370 mg/mL) was used as the contrast agent, and the flow rate of the MEDRED double-tube high-pressure syringe was 0.12 mL/s/kg. After intravenous injection (the injection time was 20 seconds), the saline was injected at the same flow rate for 10 seconds. The range was then selected for scanning.

2.3. Observation Indicators. For the determination of inflammatory factors, 5 mL blood was collected on an empty stomach without anticoagulation, separated at 3, 000 r/min for 10 min, and stored at −20°C for later use. IL-6, IL-8, and IL-1 were determined by double-antibody Sandwich ELISA in Roche automatic chemiluminescence analyzer. Measurements were strictly in accordance with instructions.

PACHE II score: The physical condition of the patients was scored 72 hours before and after treatment. The higher the score, the more serious the disease. The score included chronic health status, age, and acute physiology score, with the highest score of 71 points.

The evaluation index of the algorithm was the mean square error (MSE).

$$\mathrm{MSE} = \frac{1}{M}\sum_{i=1}^{M}(yi - \hat{y}i)^2. \quad (1)$$

2.4. CT System Imaging Flow Chart. The imaging of CT is similar to X-rays. The X-ray passes through different tissues of the human body, and has different gray levels on CT images. After X-ray penetration, the corresponding attenuation of different tissues and organs is also different. X-ray projection data are the most primitive image information data. The CT image uses a highly collimated X-ray to scan a certain thickness of the patient's body. The detector records the attenuation information of the X-ray during the scanning process. Figure 1 shows the imaging flow chart of the CT system. The converter converts the analog information into digital information, and then enters the electronic calculation. The information flow is provided by the high-voltage generator to generate X-rays. The CT machine is also rotated at this time. The detector collects data continuously. According to the scanning of the patient's body, it is converted into electrical signals. The DAS system is converted into digital electrical signals. The slip ring system is used to reconstruct the image.

2.5. Improvement of Image Noise by the Iterative Reconstruction Algorithm. The complete CT iteration is called full iterative reconstruction, including back projection and front

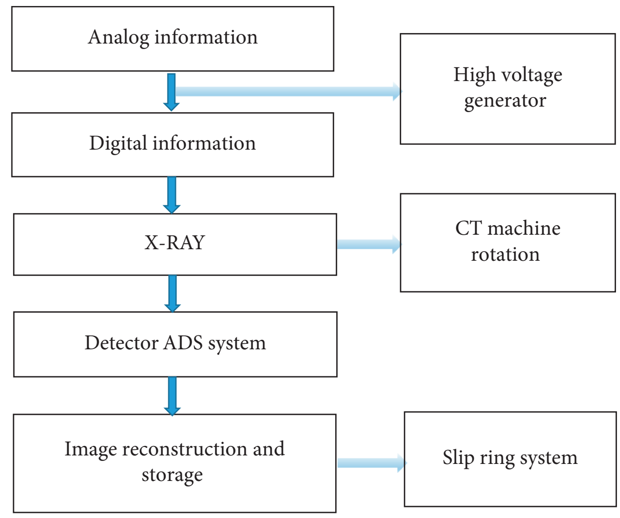

Figure 1: Flow chart of the CT system imaging.

projection. The connection of these two parts is also mainly completed by the iterative method. The working principle of the iterative algorithm is to reduce the noise in the front and rear projection domains. At the beginning of each calculation, image assumptions should be made, i.e., a similar initial value for each image is set, and then the possible projection value is calculated after the light passes through the human body. Firstly, a virtual image is constructed, and the iterative model is constructed including the construction of the noise model. According to the actual measurement value, the hypothetical image is continuously modified repeatedly. The calculation results and the real projection results are analyzed to obtain the corresponding correction results. The pixel value can be corrected many times until all the images are completed. The purpose of iterative reconstruction is to obtain a more realistic original image. The CT iterative image includes two parts: the front projection and the back projection. The principle of signal-to-noise ratio reduction is shown in Figure 2. The image is assumed, and then the initial value is set. The projection value of the light passing through the human body is calculated. The correction results show that the signal-to-noise ratio of the image is reduced, and the reconstructed image is obtained. The iterative reconstruction image is closer to the real image, and CT image reconstruction for patients can greatly reduce the scanning dose and effectively improve the image quality. The yellow arrow indicated the location of the lesion in Figure 2.

2.6. Application Principle. It is supposed that the size of the CT image is $h * w$, and the projection process can be expressed as follows:

$$U^{YX} = E^{YX\times hw} \bullet R^{hw^1}. \quad (2)$$

R^{hw^1} represents the image with size vector as hw^1; $E^{YX\times hw}$ represents the projection coefficient with matrix as $YX \times hw$; Y means the maximum projection value obtained at different angles, and X means different angles; U^{YX} is the projection vector with a size of YX.

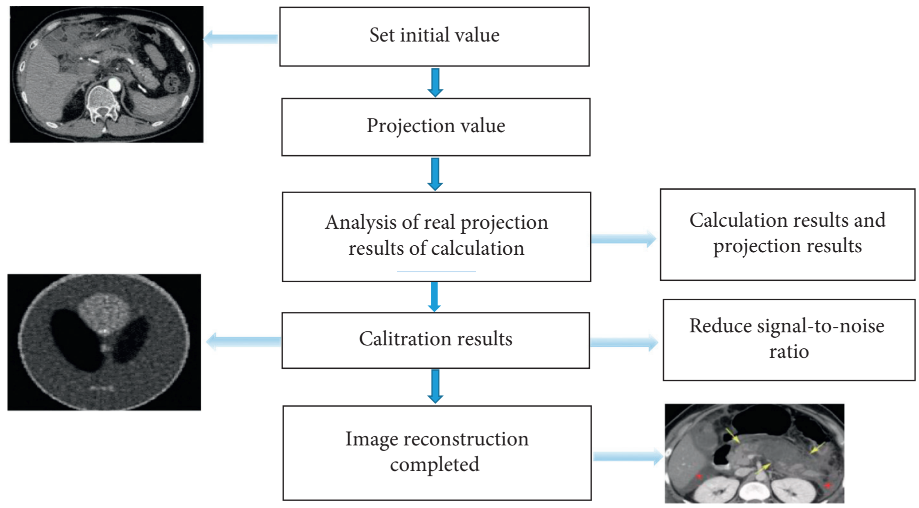

Figure 2: Process diagram of the iterative reconstruction algorithm.

The expression after image reconstruction is as below:

$$B^{hw*} = E^{YX\times hw*} \bullet U^{YX}. \tag{3}$$

B^{hw*} denotes the image with size hw^1; $E^{YX\times hw*}$ represents the generalized inverse of the projection coefficient as $E^{YX\times hw}$. However, due to the complexity and time-consuming nature of the $E^{YX\times hw*}$ calculation process, it needs to be improved. Therefore, it is replaced by another calculation method to save time.

Based on the following calculation principles, the first-order iterative method is used to obtain E^*.

When the $E^{YX\times hw*}$ initial estimation is P_0 and the residual is $C_0 = U^{YX}_{R(T)} - E^{YX\times hw} \bullet P_0$, $\gamma C_0 < 1$ and C_0 represents the radius of the spectrum; $U^{YX}_{R(T)}$ means the $E^{YX\times hw}$ orthogonal matrix. According to the above contents, the sequence $\{P_0, P_1, \ldots P_K, P_{K+1}, \ldots\}$ can be expressed as follows:

$$\begin{cases} P_{K+1} = P_K + P_0 - P_0 \bullet E^{YX\times hw} \bullet P_K \\ K = 0, 1, \ldots \end{cases}. \tag{4}$$

When $K \longrightarrow \infty$, the upper convergence $E^{YX\times hw*}$ is obtained, and the corresponding residual sequence can be expressed as

$$\begin{cases} \|C_{K+1}\| \leq \|C_0 \bullet C_K\| \\ K = 0, 1, \ldots \end{cases}. \tag{5}$$

The norm multiplication calculation of the matrix conforms to the following equation (6).

$$\|C_K\| = U^{YX}_{R(T)} - E^{YX\times hw} \bullet P_K. \tag{6}$$

In order to make the calculation simpler, the $E^{YX\times hw*}$ approximation can be set as follows:

$$P_0 = \theta E^{YX\times hw* \bullet t}. \tag{7}$$

$E^{YX\times hw*\bullet t}$ means a transposition of $E^{YX\times hw}$; θ represents a real value, consistent with $\theta E^{YX\times hw*\bullet t}$.

$$\theta \in \left(0, \frac{2}{\lambda_1 E^{YX\times hw}} \bullet E^{YX\times hw \bullet t}\right). \tag{8}$$

$\lambda_1 E^{YX\times hw} \bullet E^{YX\times hw\bullet}$ expresses the maximum non-zero eigenvalue of $E^{YX\times hw} \bullet E^{YX\times hw\bullet}$.

In order to reduce the difficulties in calculating $E^{YX\times hw}$ and $E^{YX\times hw\bullet q}$, the projection vector U^{YX} is added to both sides of equation (4) in the form of multiplication, and equation (9) can be obtained.

$$\begin{cases} P_{K+1}U^{YX} = P_K U^{YX} + P_0 U^{YX} - P_0 \bullet E^{YX\times hw} \bullet P_K \bullet U^{YX} \\ K = 0, 1, \ldots \end{cases}. \tag{9}$$

$P_{K+1}U^{YX}$ is the $K+1$ reconstructed image R^i_{K+1}; $N_K \bullet U^{YX}$ represents the K reconstructed image R^i_K; $P_0 \bullet U^{YX}$ denotes the original image R^i_0; $P_0 \bullet E^{YX\times hw} \bullet P_K \bullet U^{YX}$ denotes the projection of the image R^i, and then the image is reconstructed. The reconstruction times θ of $P_0 \bullet E^{YX\times hw} \bullet P_K \bullet U^{YX}$ are replaced with the FBP algorithm.

If $hw < YX$, $\theta = 1$; if $PP < YX$, $\theta < 2^{-(hw\div YX)}$.

In order to evaluate the application effect of the algorithm, the following experiments are carried out. It is supposed that the θ value is 1.

The schematic diagram of the iterative reconstruction algorithm is illustrated in Figure 3.

2.7. Application Steps. The application steps of the iterative reconstruction algorithm are as follows:

Step 1. θ is initialized and the condition φ is terminated.

Step 2. In the case of $K = 0$, the FBP algorithm is adopted to preprocess the original image, and $R^i_{fbp} R^i_0 = \theta R^i_{flp}$ is obtained.

Step 3. R^i_K is projected to get the projection value $U^{YX}{}_K$.

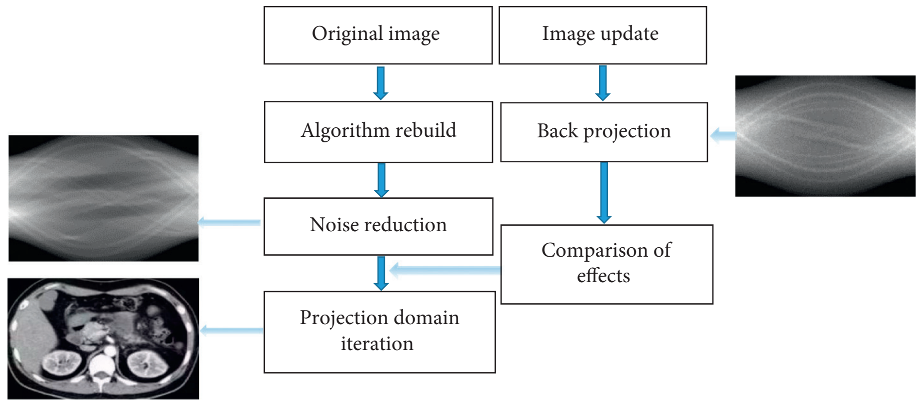

FIGURE 3: Schematic diagram of the iterative reconstruction algorithm.

Step 4. The reconstructed image combining $U^{YX}{}_K$ with the FBP algorithm is multiplied with θ to obtain R_r.

Step 5. The reconstructed image is corrected, and $R^i_{K+1} = R^i_K + R^i_0 - R^i_r$.

Step 6. $\Delta = \|R^i_{K+1} - R^i_K\|$, and $\begin{cases} \|R^i_{K+1} - R^i_K\| \leq K \\ K = k+1 \end{cases}$.

Step 7. If $\Delta > \varphi$, Step 3 is performed, conversely, end of calculation (Figure 4).

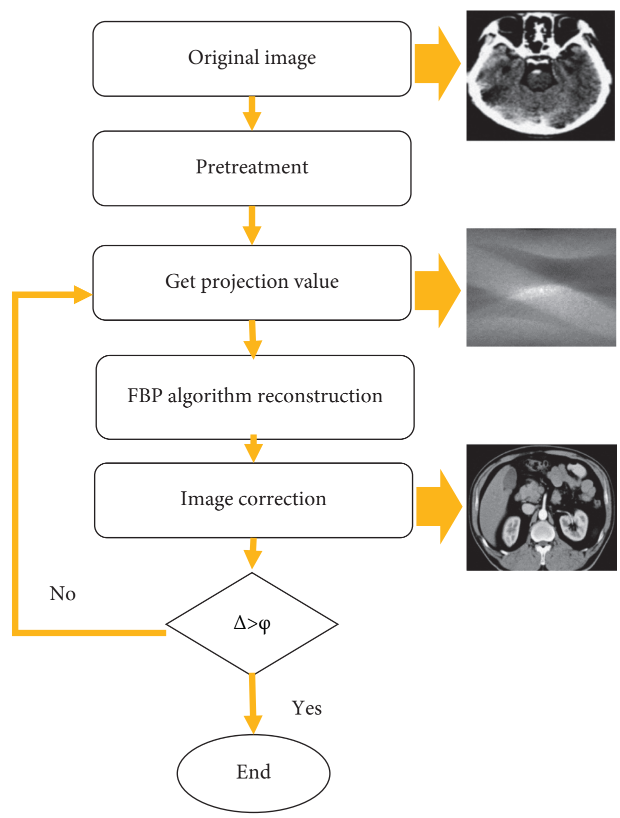

FIGURE 4: Flowchart of algorithm steps.

2.8. Statistical Analysis. Relevant data of chronic periodontitis patients were recorded by SPASS 21.0 statistical software. The measurement data were expressed as $(\overline{x} \pm s)$, and the t-test was used. The count data were expressed as (n, %), and $P < 0.05$, i.e., the difference was statistically significant.

3. Results

3.1. General Data. Table 1 shows the general data of the two groups of patients. There was no significant difference between the patients ($P > 0.05$). In the control group, the average age was (41.54 ± 2.18) years, including 8 cases of biliary pancreatitis, 11 cases of hyperlipidemia, 22 cases of overeating, and 9 cases of alcoholics. The average age of the patients in the observation group was (43.54 ± 2.76) years, including 10 cases of biliary pancreatitis, 9 cases of hyperlipidemia, 19 cases of overeating, and 12 cases of alcoholics.

3.2. CT Images. When the same dose was used in Figure 5, from the CT image, there was exudation around the pancreas, a small amount of effusion, and scattered cellular inflammatory changes. Figure C showed peripancreatic exudation in a case of simple pancreatitis. No obvious necrotic area was observed.

3.3. Iterative Algorithm CT Image Reconstruction. Iterative reconstruction algorithm is based on the estimation of the statistical model of observation data. The CT images of a patient with severe pancreatitis complicated with necrosis are shown in Figures 6(a) and 6(b). The secondary pancreatic abscess is formed on the basis of necrosis. There were obvious necrotic liquefaction foci in the abscess area, and the necrotic area was in the red box. The red arrow indicated the location of the lesion. Figure 6(c) shows the formation of pseudocysts around the spleen in the patients. Circular nodules in the red frame can be seen in the pseudocysts on the splenic hilum side, showing a significant enhancement similar to the large blood vessels in the abdominal cavity, which is the manifestation of pseudoaneurysm.

3.4. Comparison of the Reconstruction Algorithm Image Results. In CT imaging, the noise of the image decreases after applying the iterative reconstruction algorithm

Table 1: Comparison of general data between the two groups.

	Control group	Observation group
Male	26	20
Female	24	30
Age	41.54 ± 2.18	43.54 ± 2.76
Overeating	22	19
Alcoholic	9	12
Hyperlipidemia	9	11
Biliary pancreatitis	8	10
χ^2	8.357	
P	0.256	

(a) (b) (c)

Figure 5: CT images of acute pancreatitis (patient with acute simple pancreatitis, female, 57 years old).

(a) (b) (c)

Figure 6: Three-dimensional CT images of patients with SAP. (a, b) The CT images of a patient with severe pancreatitis complicated with necrosis. (c) The formation of pseudocysts around the spleen in the patients.

(Figure 7). With the reduction of the use dose, the spatial resolution of the image is effectively improved. The image noise with 50% dose reduction is the lowest (Figure 8), but the reconstruction algorithm improves the low-contrast resolution.

3.5. MSE of the Iterative Reconstruction Algorithm CT Images. The iterative reconstruction algorithm can restore the original image after a certain number of iterations (Figure 9). The MSE is closer to zero, and the representation effect is better. The image quality is better after the reconstruction algorithm.

3.6. Comparison of the Reconstructed Images. The simulation of low-dose CT image reconstruction was used. The template was 128×128 mm. The algorithm operating system was Window 10 32 bit SPI. The processor was Intelku 2 dual-core T6400@2.00 GHz processor, and the inner was 2G. The reconstruction image comparison shown in Figure 10(a) was an ideal projection domain image and was relatively clear. Figure 10(b) contained the noise projection domain image, and the particle sense was obvious.

3.7. APACHE II Score of the Two Groups. From Figure 11, the APACHE II scores of the two groups were decreased after treatment, indicating that the conditions of the two groups improved. After treatment, the difference between the observation group and the control group was significant ($P < 0.01$), indicating that the observation group showed better curative effect.

3.8. Comparison of the Survival Rate between the Two Groups. From Table 2, there were five deaths in the control group, of which two died of renal failure, one died of infective shock, and two died of fungal sepsis. One patient died of multiple organ failure in the observation group. The survival rate of the observation group was significantly higher than that of the control group ($P < 0.01$).

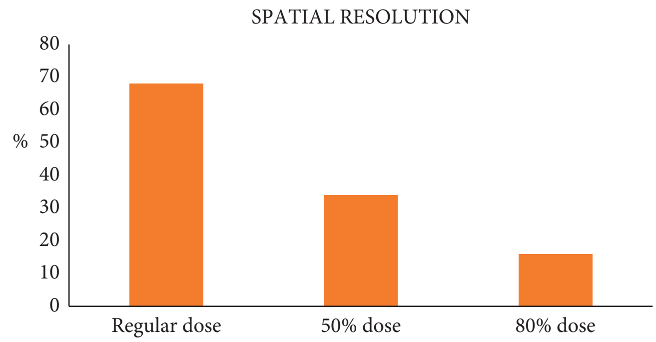

FIGURE 7: Image quality assessment of the iterative reconstruction algorithm.

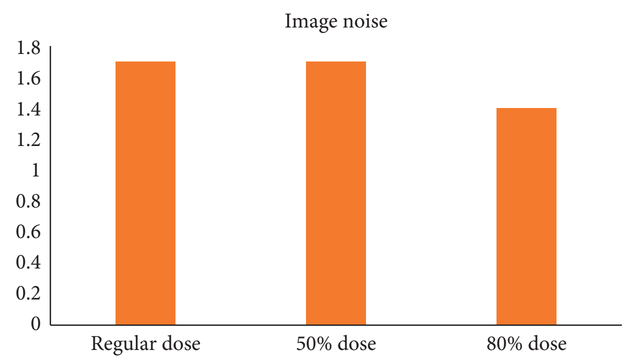

FIGURE 8: Improvement of signal to noise ratio.

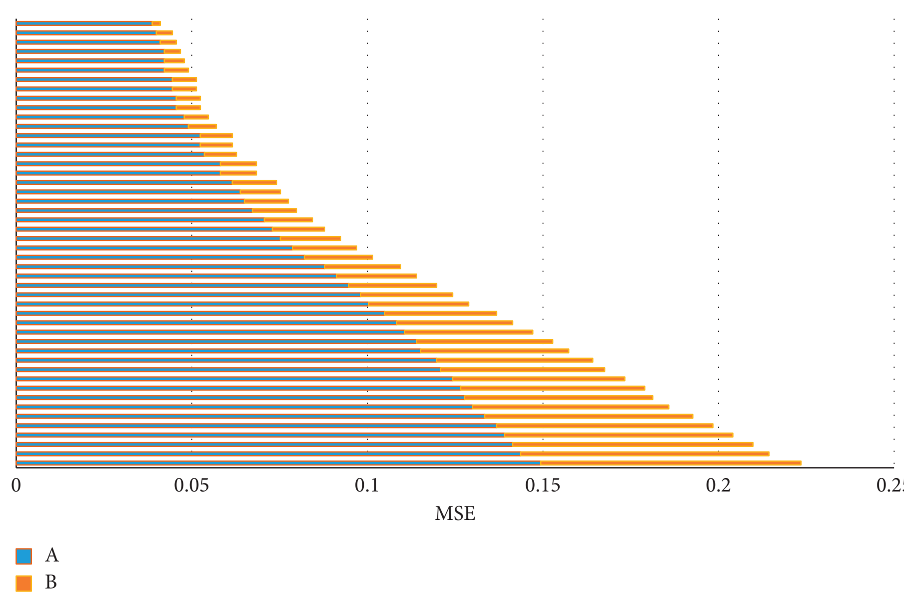

FIGURE 9: Image MSE distribution. (a) Iterative reconstruction algorithm CT group. (b) CT group without the algorithm.

3.9. Comparison of the Two Groups of Patients with Severe Factor Levels. As shown in Figure 12, the levels of inflammatory factors in the two groups were compared and analyzed. After treatment, the levels of the inflammatory factors were significantly decreased compared with those before treatment, and the levels of IL-1, IL-6, and IL-8 after treatment were significantly lower than those before treatment ($P < 0.05$), indicating that both treatments could improve the symptoms of the patients.

4. Discussion

Continuous blood purification is a new blood purification treatment method, which can continuously and slowly

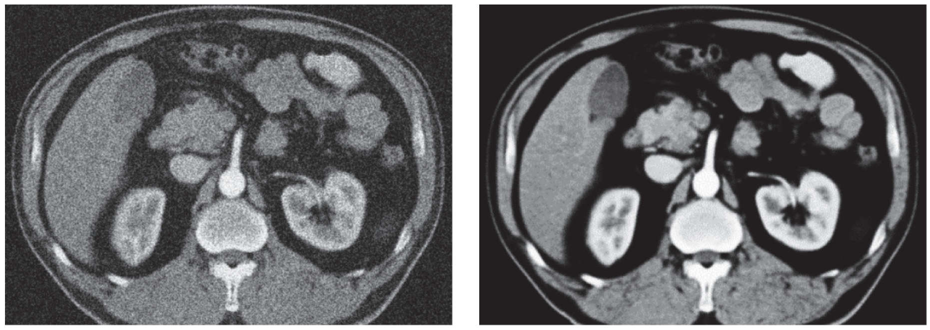

Figure 10: Comparison of the reconstructed images. (a) An ideal projection domain image and was relatively clear. (b) The noise projection domain image.

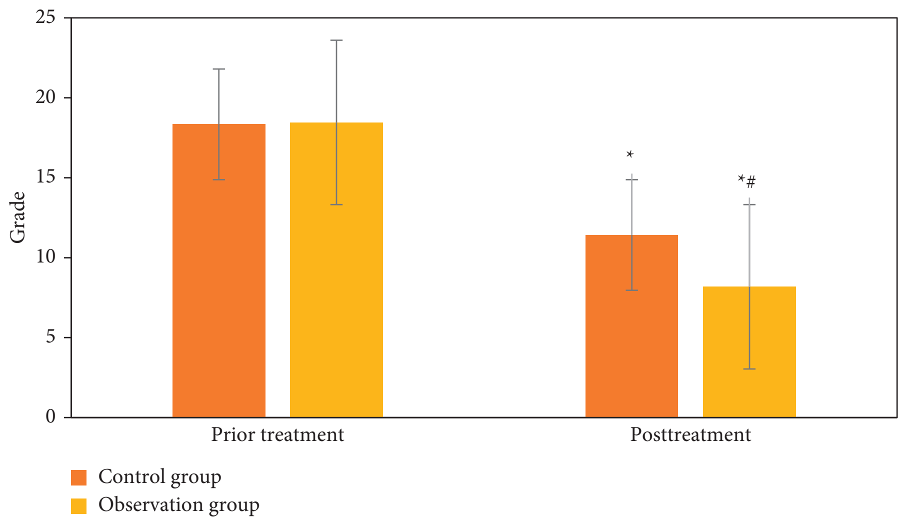

Figure 11: Comparison of the APACHE II scores between the two groups before and after treatment. *Significant difference compared with before treatment $P < 0.01$, #after treatment, the difference between the observation group and the control group was significant, $P < 0.01$.

Table 2: Comparison of the survival rate between the two groups after treatment.

	Control group	Observation group
Survival (case)	45	50
Death (case)	5	1
Died of fungal sepsis (case)	2	0
Died of infective shock (case)	1	0
Died of renal failure (cases)	2	0
Survival rate (%)	90%	98%
χ^2	5.89	
P	0.002	

remove the solute and water in the blood, improve the patient's immune system, and maintain the stability of the internal environment. Continuous blood purification treatment uses the strong adsorption of polymer material filter to remove IL-6, IL-1, IL-8 inflammatory factors and toxic metabolites during tissue injury, which can promote the recovery of organ function and regulate immune function [17–19]. Zhu et al. [20] found that continuous blood purification can rapidly reduce the blood amylase and lipase in children with SAP, help maintain the stability of the internal environment, block the systemic inflammatory response, improve organ function, and maintain fluid balance. In this study, the inflammatory factors of IL-6, IL-1, and IL-8 in the two groups reduced after treatment. Continuous blood purification can effectively improve patients with SAP.

As a fast-scanning technology, CT three-dimensional imaging can not only reduce the time of operation and imaging in the detection process, but also obtain more CT images and data information of lesions under the same scanning condition. Then, with the assistance of computers, more high-quality CT images are obtained for the diagnosis of patients' diseases. The processed CT images can not only be as intuitive as endoscopic images, but also improve the detection rate of small lesions. On this basis, further reconstruction of CT images by the iterative algorithm can improve the image quality. The iterative algorithm divides the whole image processing process into many times and gradually improves the image processing. During most low-dose scanning, the scanned image processing parameters must be optimized to maximize the image quality. The algorithm and various noise

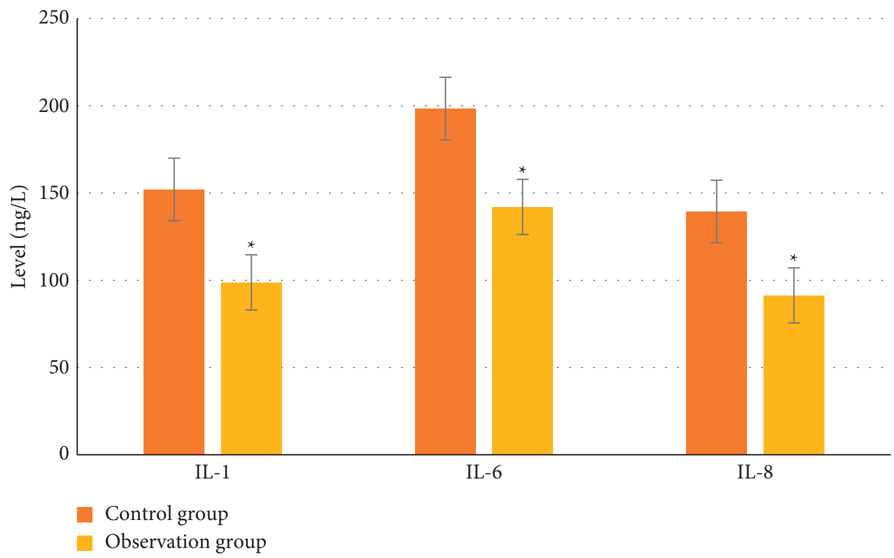

FIGURE 12: Comparison of severity factors in the patients of two groups. *Significant difference compared with before treatment, $P < 0.01$.

reduction technologies can smooth the image. It is found that the iterative reconstruction algorithm effectively optimizes the CT image quality, information quantity, and mean square error. Among them, the MSE is the optimal value with the result close to 0. The iterative algorithm was used to reconstruct and denoise CT images. The results showed that the image quality, image information, and image MSE significantly improved after the use of the iterative reconstruction algorithm. The CT image based on the reconstruction algorithm could clearly display the lesion characteristics of the patients, and the reconstruction algorithm was feasible to improve the spatial resolution of the CT images. Tirkes [21] stated in the literature that CT and MRI cholangiopancreatography are common cross-sectional imaging studies for the evaluation of chronic pancreatitis. The reconstruction algorithm is applied to CT three-dimensional imaging. With the reduction of the dose, the image spatial resolution is effectively improved. Comparing the image noise, it is found that the image noise with 50% dose reduction is the lowest, and the reconstruction algorithm can improve the low-contrast resolution. Gupta et al. [22] used CT to scan the gastrointestinal tract of patients with acute pancreatitis, and found CT features such as maximum thickness of the intestinal wall, extrapancreatic necrosis, and intestinal wall thickening. CT is helpful to predict gastrointestinal fistula in patients with acute pancreatitis. Abdullah et al. [23] applied the iterative reconstruction algorithm to CT angiography. The results show that the iterative reconstruction algorithm can effectively reduce the noise of CT images and improve the signal-to-noise ratio. The results show that the iterative reconstruction algorithm has a good-quality effect in the CT image scanning of SAP patients.

5. Conclusion

After the optimization of the iterative reconstruction algorithm, the quality of the CT image improved and the signal-to-noise ratio effectively improved. The reconstructed image algorithm can improve the quality of low-dose CT reconstructed images. This algorithm is feasible in the CT image application. The effect of continuous blood purification nursing intervention in the treatment of SAP patients is better than that of the ordinary routine treatment. There are many limitations, and the number of iterations of the algorithm is not repeated enough. In the future, the accuracy of the algorithm can be discussed from the number of iterations. Low-dose CT imaging is a research subject with a wide range. Compared with the actual situation, there must be differences in the simulated noise of low-dose CT. How to eliminate these differences can be studied in the next step.

Data Availability

The data used to support the findings of this study are available from the corresponding author upon request.

Conflicts of Interest

The authors declare no conflicts of interest.

References

[1] C. Xu, J. Liu, Z. Li, and X. Luan, "Efficacy analysis of continuous blood purification therapy for patients with severe acute pancreatitis and acute kidney injury," *Panminerva Medica*, vol. 20, 2020.

[2] Y. Guo, F. Cao, C. Li, H. Yang, S. Xia, and F. Li, "Continuous hemofiltration reduces mortality in severe acute pancreatitis: a meta-analysis," *Emerg Med Int*, vol. 2020, Article ID 6474308, 10 pages, 2020.

[3] D. Katagiri, M. Ishikane, T. Ogawa et al., "Continuous renal replacement therapy for a patient with severe COVID-19," *Blood Purification*, vol. 50, no. 1, pp. 129–131, 2021.

[4] H. B. Yao, M. B. Wen, G. Huang, D. G. Wu, and Z. J. Yang, "Effects of continuous blood purification on plasma cytokines in patients with severe acute pancreatitis," *Xi bao yu fen zi Mian yi xue za zhi*, vol. 27, no. 2, pp. 190-191, 2011.

[5] Y. Okita, T. Okahisa, M. Sogabe, M. Suzuki, Y. Ohnishi, and S. Ito, "Low-volume continuous hemodiafiltration with nafamostat mesilate increases trypsin clearance without decreasing plasma trypsin concentration in severe acute pancreatitis," *ASAIO Journal*, vol. 53, no. 2, pp. 207–212, 2007.
[6] P. G. Lankisch, M. Apte, and P. A. Banks, "Acute pancreatitis," *The Lancet*, vol. 386, no. 9988, pp. 85–96, 2015.
[7] Y. Aswani, S. M. Ansari, U. S. Chakraborty, P. Hira, and S. Ghosh, "Where there is pancreatic juice, there is a way: spontaneous fistulization of severe acute pancreatitis-associated collection into urinary bladder," *Indian Journal of Radiology and Imaging*, vol. 30, no. 04, pp. 529–532, 2020.
[8] M. Brand, A. Götz, F. Zeman et al., "Acute necrotizing pancreatitis: laboratory, clinical, and imaging findings as predictors of patient outcome," *American Journal of Roentgenology*, vol. 202, no. 6, pp. 1215–1231, 2014.
[9] Q. Lin, Y. f. Ji, Y. Chen et al., "Radiomics model of contrast-enhanced MRI for early prediction of acute pancreatitis severity," *Journal of Magnetic Resonance Imaging*, vol. 51, no. 2, pp. 397–406, 2020.
[10] J. Van den Bulcke, M. A. Boone, J. Dhaene et al., "Advanced X-ray CT scanning can boost tree ring research for earth system sciences," *Annals of Botany*, vol. 124, no. 5, pp. 837–847, 2019.
[11] A. Sinha, Y. A. Patel, M. Cruise et al., "Predictors of post-operative pain relief in patients with chronic pancreatitis undergoing the frey or whipple procedure," *Journal of Gastrointestinal Surgery*, vol. 20, no. 4, pp. 734–740, 2016.
[12] Y. Chen, C. K. Lin, Q. M. Fu, J. H. Huang, and C. Z. Huang, "Adoption of computed tomography images under iterative reconstruction algorithm in diagnosis of gastric cancer," *Scientific Programming*, vol. 11, no. 5, pp. 1–7, 2021.
[13] S. Chang, M. Li, H. Yu et al., "Spectrum estimation-guided iterative reconstruction algorithm for dual energy CT," *IEEE Transactions on Medical Imaging*, vol. 39, no. 1, pp. 246–258, 2020.
[14] T. Higaki, Y. Nakamura, J. Zhou et al., "Deep learning reconstruction at CT: phantom study of the image characteristics," *Academic Radiology*, vol. 27, no. 1, pp. 82–87, 2020.
[15] Y. Kubo, K. Ito, M. Sone et al., "Diagnostic value of model-based iterative reconstruction combined with a metal artifact reduction algorithm during CT of the oral cavity," *American Journal of Neuroradiology*, vol. 41, no. 11, pp. 2132–2138, 2020.
[16] T. Hamamura, Y. Hayashida, Y. Takeshita et al., "The usefulness of full-iterative reconstruction algorithm for the visualization of cystic artery on CT angiography," *Japanese Journal of Radiology*, vol. 37, no. 7, pp. 526–533, 2019.
[17] J. Wu, X. Wang, X. Mou, Y. Chen, and S. Liu, "Low dose CT image reconstruction based on structure tensor total variation using accelerated fast iterative shrinkage thresholding algorithm," *Sensors*, vol. 20, no. 6, Article ID 1647, 2020.
[18] D. Kefallonitou, K. Giannakou, A. Samartzis, I. Datseris, N. Karampelas, and I. Polycarpou, "[Comparative evaluation of Iterative and FORE-Iterative reconstruction algorithms for PET/CT]," *Hellenic Journal of Nuclear Medicine*, vol. 23, no. 1, pp. 97–107, 2020.
[19] Y. Hu, W. Xiong, C. Li, and Y. Cui, "Continuous blood purification for severe acute pancreatitis," *Medicine*, vol. 98, no. 12, Article ID e14873, 2019.
[20] Y. Zhu, Y. Cui, Y. C. Zhang et al., "[Efficacy of continuous blood purification in treatment of severe acute pancreatitis in children]," *Zhonghua Er Ke Za Zhi*, vol. 55, no. 5, pp. 338–342, 2017 May 4.
[21] T. Tirkes, Z. K. Shah, N. Takahashi et al., "Reporting standards for chronic pancreatitis by using CT, MRI, and MR cholangiopancreatography: the consortium for the study of chronic pancreatitis, diabetes, and pancreatic cancer," *Radiology*, vol. 290, no. 1, pp. 207–215, 2019 Jan.
[22] P. Gupta, G. Chayan Das, V. Sharma et al., "Role of computed tomography in prediction of gastrointestinal fistula in patients with acute pancreatitis," *Acta gastro-enterologica Belgica*, vol. 82, no. 4, pp. 495–500, 2019.
[23] K. A. Abdullah, M. F. McEntee, W. Reed, and P. L. Kench, "Evaluation of an integrated 3D-printed phantom for coronary CT angiography using iterative reconstruction algorithm," *Journal of Medical Radiation Sciences*, vol. 67, no. 3, pp. 170–176, 2020.

Hindawi
Contrast Media & Molecular Imaging
Volume 2022, Article ID 8464361, 7 pages
https://doi.org/10.1155/2022/8464361

Research Article

Intelligent Algorithm-Based Gastrointestinal X-Ray Examination in Evaluating the Therapeutic Effect of Probiotics Combined with Triple Therapy on Children with *Helicobacter* Infection

Qizheng Wang and Jiangshu Li

Department of Pediatrics, Huai'an Maternal and Child Health Care Hospital, Huai'an 223002, Jiangsu, China

Correspondence should be addressed to Jiangshu Li; 2014110123@stu.hznu.edu.cn

Received 28 December 2021; Revised 20 February 2022; Accepted 23 February 2022; Published 27 March 2022

Academic Editor: M. Pallikonda Rajasekaran

In this study, gastrointestinal X-ray imaging was processed based on the Ncut algorithm, the gastric signs of the children after probiotics combined with triple therapy were examined, the therapeutic effect of probiotics combined with triple therapy was evaluated, and the correlation between *Helicobacter pylori* (HP) infection and gastric disease was analyzed. The included children were randomly divided into group A (treated with standard triple therapy) and group B (pretreated with probiotics on the basis of the treatment method of group A) with 48 cases in each group. The gastrointestinal angiography results of children were observed. The accuracy of the gastrointestinal angiography based on intelligent algorithms was evaluated by taking the results of the urea breath test (UBT) as the gold standard. The results were as follows: first, gastrointestinal X-ray imaging before and after treatment showed that the recovery of the gastric body and gastric antral mucosa for children in group B was better than that of group A ($P < 0.05$); second, the incidence of gastrointestinal diseases in HP-positive patients was 78% and the incidence of HP-negative patients was 32%; third, the sensitivity, specificity, and accuracy of gastrointestinal X-ray imaging based on intelligent algorithm were 76.47%, 93.67%, and 90.63%, respectively. After treatment, tumor necrosis factor α (TNF-α) and interleukin 6 (IL-6) in group B were much lower than those in group A ($P < 0.05$), and the incidence of adverse reactions in group B was lower than that in group A ($P < 0.05$). In summary, gastrointestinal X-ray imaging based on intelligent algorithm had a reliable reference value for the judgment of gastrointestinal HP infection and probiotics combined with triple therapy was more effective for HP infection, which was worthy of clinical application.

1. Introduction

Helicobacter pylori (HP) infection is a global matter affecting the health of patients, and it increases with age, seriously affecting the health of children [1]. At present, the detection methods of HP infection mainly include gastroscopy and gastric mucosal pathological examination. Most scholars advocate active clinical treatment after childhood HP infection. In recent years, intestinal microecology studies have found that HP maintains close contact with gastric mucosal epithelial cells, so methods to correct the imbalance of gastrointestinal flora may be effective in the treatment and prevention of HP infection [2–4]. Traditional triple therapy has a certain degree of drug resistance due to the extensive use of drugs in clinical practice, and the effect is poor [5–7]. Studies have found that probiotics can release bacteriocins or organic acids and inhibit the growth of HP by destroying the cell wall or cytoplasmic membrane [8, 9]. Probiotics can also compete with HP to bind glycolipid receptors and adhere to gastric epithelial cells to reduce their mucosal damage to gastric epithelial cells [10]. In addition, probiotics can stabilize the gastric mucosal barrier, reduce inflammation, exert antioxidant effects, and promote the healing of damaged mucosa [11]. Endoscopic biopsy is also one of the most commonly used tests for HP infection. In addition, specific detection methods include rapid urease testing and silver-stained biopsies. However, there are few studies on X-ray imaging of the stomach and duodenum in patients with HP infection. Gastrointestinal X-ray combined with gas-barium double contrast filling compression method was adopted, and the patient's gastrointestinal tract was inflated by using a gas generating agent. Then, the patient is given a dry suspension of barium sulfate, and the patient's position is adjusted so that it can evenly apply the barium solution on the surface of the stomach cavity. Different body positions can be filmed under gas-assisted conditions to avoid omission of lesions. This study was applied to improve gastrointestinal X-ray imaging for the detection of HP-infected gastropathy.

In this work, the gastrointestinal X-ray imaging based on the Ncut algorithm was applied to evaluate the clinical efficacy of probiotics combined with triple therapy in the treatment of children with HP infection. Using the urea breath test (UBT) results as the gold standard, the accuracy of the test results and the relationship between HP infection and gastrointestinal X-ray imaging in children were evaluated. By detecting intestinal microecology and inflammatory factors, the effect of compound *Lactobacillus acidophilus* tablets was analyzed, the effects of different treatment methods on TNF-α and IL-6 in children were explored, and the incidence of adverse reactions of children with different treatment methods was analyzed. It aimed to provide treatment options for diseases caused by HP infection.

2. Research Methods

2.1. Research Objects. A total of 96 children with HP infection who were hospitalized from October 2019 to October 2020 were selected as the research objects. The children had upper gastrointestinal symptoms such as epigastric pain, discomfort, and anorexia. The children included were randomly divided into group A and group B, with 48 cases in each group. The children in group A were 3–12 years old, with an average age of 6.47 ± 2.78, while the children in group B were 3–11 years old, with an average age of 6.59 ± 2.13 years. The radiological approach did not pose a risk of radiation accumulation to the children. The study had been approved by the Ethics Committee of hospital, and the families of patients and children were informed about the study and signed informed consent.

The inclusion criteria were as follows: children whose 13C breath test was positive but with no proton pump inhibitor (PPI) within 2 weeks and no history of use of antibacterial drugs and bismuth within one month; children whose parents had signed the informed consent forms.

The exclusion criteria were as follows: children with severe liver, kidney, and cardiac dysfunction; children with mental system diseases; children with previous digestive system surgery; and children with history of allergy to the drugs in this study or similar drugs.

2.2. Grouping and Dosage Regimens of Children. Children in group A received standard triple therapy treatment: omeprazole with 0.6–1.0 mg/kg/d, amoxicillin with 50 mg/kg/d (maximum dose 1.0 g, 2 times/d), and clarithromycin with 15–20 mg/kg/d (maximum dose 0.5 g, 2 times/d). All of the above medicines were taken before breakfast and dinner with 10 days in total.

Children in group B received the following dosage regime. Before the triple therapy, the compound *Lactobacillus acidophilus* tablets (1 tablet/time, 0.5 g/tablet) were taken with cold boiled water after three meals for 2 weeks. Next, triple therapy (same as group A) was taken for 2 weeks. After completion, the compound *Lactobacillus acidophilus* tablets (1 tablet/time, 0.5 g/tablet) were taken again for 2 weeks.

2.3. Gastrointestinal X-Ray Imaging Based on Intelligent Algorithm. The noise gray value in the X-ray image was obviously different from its surrounding normal gray value, so the domain averaging algorithm in the spatial denoising algorithm was used to remove the noise in the image. First, it was assumed that the actual gray value in the image was $f(u, v)$, and the gray value of adjacent pixels can be expressed as $M_i\,(i = 1, 2, \ldots, n)$; then, it can be expressed as the following equation by using the domain average method:

$$g(u,v) = \begin{cases} \dfrac{1}{n}\displaystyle\sum_{i=1}^{n} M_i, & \left| f(u,v) - \dfrac{1}{n}\displaystyle\sum_{i=1}^{n} M_i \right| > \sigma, \\ f(u,v), & \text{other}. \end{cases} \tag{1}$$

In the above equation, s refers to the error threshold, which is a constant.

It was further assumed that the domain average was a low-pass filter of the image $f(u, v)$, and the discrete convolution was adopted for noise removal in the image. After the average value of the image was calculated, the image with noise smoothing function was finally obtained, which can be expressed as follows:

$$g(x,y) = \frac{1}{n}\sum_{k=1}^{n} [f(x,y)]_k. \tag{2}$$

To improve the effect of X-ray image denoising and enhancement, curvelet transform was adopted to process the image. Basic nonlinear enhancement operators included GAG operator, and then new operators can be proposed:

$$f(x,\mu) = \begin{cases} \dfrac{x - c\mu}{c\mu}\left(\dfrac{m}{c\mu}\right)^{\alpha} + \dfrac{2c\mu - x}{c\mu}, & x < 2c\mu, \\ \left(\dfrac{m}{x}\right)^{\alpha}, & 2c\mu \le x < m, \\ \left(\dfrac{m}{x}\right)^{\beta}, & x \ge m. \end{cases} \tag{3}$$

In the above equation, μ is the noise standard deviation, α is the determinant of the degree of nonlinear transformation, β refers to the determinant of the dynamic compression range, c represents the regularization parameter, and m is the threshold.

μ in (3) could be estimated as the following equation based on the wavelet analysis method:

$$\mu = \frac{\left[abs\left(C\{a\}\{b\}\right)_{\text{median}}\right]}{0.67}. \quad (4)$$

In equation (4), C is the subband coefficient of the image, a refers to the scale, b is the direction, and $abs\,(C\{a\}\{b\})_{\text{median}}$ represents the median of the absolute value of the subband coefficient.

Then, the Ncut algorithm was applied to segment the target area in the X-ray image. The similarity matrix of the traditional Ncut algorithm can be written as follows:

$$Z_{uv} = e^{\left(-F_u - F_{v2}^2/\sigma_l^2\right)} \begin{cases} e^{\left(-x_u - x_{v2}^2/\sigma_x^2\right)}, \; x(u) - x(v)_2 > r, \\ 0, \text{ other.} \end{cases} \quad (5)$$

In equation (5), F_u is the gray value of the pixel point u, $x(u)$ is the spatial position of the pixel point u, and σ_l and σ_x are the sensitivities of the gray level and position, respectively.

The specific image processing performance is shown in Figure 1.

2.4. Examinations. All patients received gastrointestinal X-ray angiography. In addition, all patients were required to take oral barium sulfate contrast agent before the examination. The time required for the entire inspection was about 10–15 minutes. First, a chest X-ray examination was performed to observe whether the heart and lungs had pathological changes, if there were foreign bodies that are not transparent to X-rays, and if there were contraindications such as obstruction or perforation. Second, the passage of the contrast agent in the esophagus was observed to examine whether there was ulcer of the esophagus and esophageal cancer. Third, the contrast agent passing through the cardia again was observed to check if there was achalasia and cardia cancer. After that, the patient was required to lay on the examination table and quickly turned 1 to 2 circles from right to left to observe the fundus of the stomach, the gastric antrum mucosa, and the gastric filling image. Finally, the patient was required to stand and scan from the esophagus to the stomach again. Then, the intelligent X-ray image segmentation method was adopted to process the obtained X-ray images.

The 13C breath test was performed, and HP routine examination required stopping antibacterial drugs for at least 4 weeks, stopping proton pump inhibitors for at least 2 weeks, and fasting on the day of the test. The 13C UBT delta over baseline (DOB) was used as an indicator, and DOB value > 4.4 was positive and DOB value < 3.6 was negative. They need to be taken orally with warm water completely, and do not crush them, so as not to affect the accuracy of the test results.

The intestinal microecological test was conducted as follows. Before and after treatment, 2 g of fresh fecal specimens were collected from all patients, which were diluted by the 10-fold dilution method, inoculated on the surface of the culture medium plate, and then evenly spread with L glass rods for routine aerobic and anaerobic culture. The most representative aerobic bacteria (*Enterococcus*, *Enterobacter*, and yeast) and anaerobic bacteria (*Bifidobacterium*, *Lactobacillus*, *Clostridium perfringens*, and *Bacteroides*) in the intestinal flora were selected for cultivation and bacterial identification using French bioMérieux identification system. The result was calculated as the logarithm (lgCFU/g) of the number of colonies (CFU) per gram of wet stool weight, the intestinal colonization resistance (B/E ratio) was calculated, and the B/E value was calculated by calculating the ratio of bifidobacteria and enterobacteria (B/E value) represented intestinal colonization resistance.

5 mL of fasting peripheral venous blood was collected from the two groups of patients before and after treatment and centrifuged at 3000 r/min for 10 minutes using the centrifuge to separate the serum. The enzyme-linked immunosorbent assay (ELISA) was applied to detect the serum tumor necrosis factor α (TNF-α) and interleukin 6 (IL-6) levels.

2.5. Observation Indicators. The gastrointestinal X-ray imaging results of the two groups of patients were compared before and after treatment, mainly to observe the thickening of the gastric body and gastric mucosal folds. The specific standards are shown in Table 1.

The 13C UBT DOB of patients between the two groups was compared before and after treatment. The judgment standard was as follows: DOB value > 4.4 was positive, and DOB value < 3.6 was negative. The negative test result was expressed as HP eradicate, and the occurrence of nausea and vomiting, diarrhea, abdominal distension, abdominal pain, rash, and other adverse reactions in the two groups of patients was recorded.

2.6. Statistical Analysis. The SPSS 22.0 was applied for statistical analysis. The measurement data were expressed as $\overline{x} \pm s$, the counting data were expressed as percentages, and the independent sample t-test and χ^2 test were applied, respectively. $P < 0.05$ indicated that the difference was statistically significant.

3. Results

3.1. Basic Data. In group A and group B, there were 48 cases in each group, and there was no statistically obvious difference in gender, age, average course of disease, and disease composition between the two groups, as shown in Table 2.

3.2. 13C Breath Test Results. Figure 2 shows the results of the 13C breath test of the two groups before and after treatment. Before treatment, the positive rates of HP infection in group B and group A were 95.57% and 96.21%, respectively, while they were 12.31% and 45.78%, respectively, after the treatment. After analysis and comparison, the improvement rate of group B HP infection (83.26%) was greatly higher than that of group A (50.34%), and the difference was statistically great ($P < 0.05$).

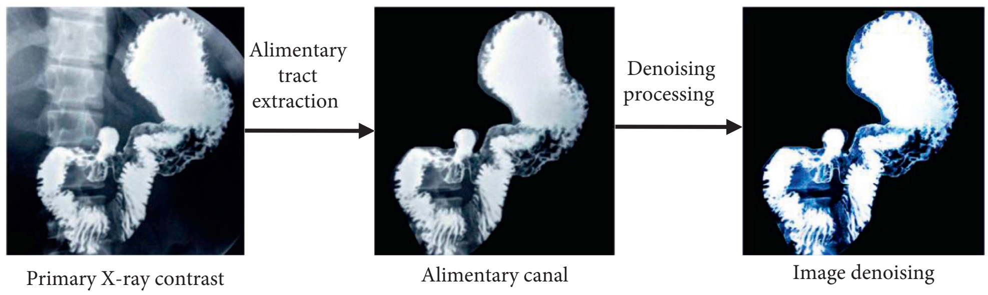

FIGURE 1: The processing process of gastrointestinal X-ray imaging using intelligent algorithm.

TABLE 1: Thickening criteria for gastric mucosal fold.

Position	Specific value
Antrum of stomach	≥0.5 cm
Gastric body	≥0.7 cm

TABLE 2: Basic data of patients in two groups.

	Group A	Group B
Age (years old)	7.38 ± 2.84	7.42 ± 2.69
Gender (male/female)	25/23	24/24
Average course of disease	5.38 ± 1.51	5.36 ± 1.49
Chronic gastritis	20	22
Gastric ulcer	11	11
Duodenal ulcer	17	15

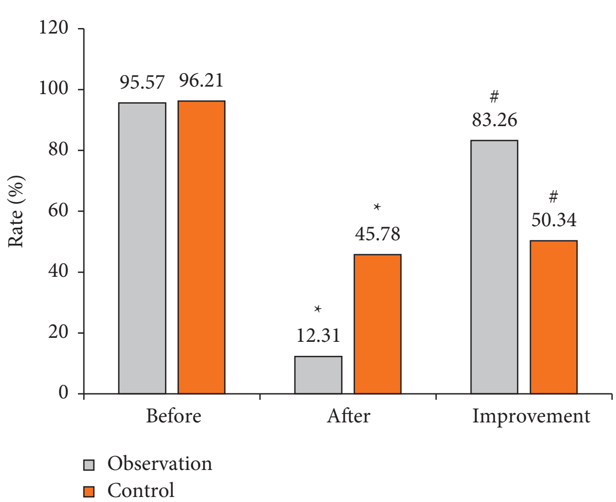

FIGURE 2: Comparison on 13C breath test results. *Comparison of positive rates between the two groups after treatment, $P < 0.05$. #Comparison of improvement rates between the two groups, $P < 0.05$.

3.3. Comparison on HP Removal Rate. The HP clearance rate of group A and group B was 52.08% and 89.58%, respectively, so the therapeutic effect of group B was much higher than that of group A ($P < 0.05$), as shown in Table 3.

TABLE 3: Comparison on HP removal rate in patients of two groups.

Group	Group A	Group B
HP removal rate (%)	52.08	89.58#

#The difference was statistically obvious in contrast to group A ($P < 0.05$).

3.4. Changes of Gastrointestinal X-Ray Imaging. Figure 3(a) is a normal X-ray image of the stomach, and the position indicated by the white arrow in Figure 3(a) refers to the folded part of the gastric mucosa. As shown, the outline of the stomach was smooth and tidy, the greater curvature of the stomach body was jagged, and the folds of the gastric mucosa can be seen in three obvious vertical and horizontal oblique shapes. The body of the stomach was parallel, the smaller curvature of the stomach was neat, and the stomach and greater curvature were grid-like. In addition, obvious vertical, horizontal, and oblique lines were also visible in the antrum. Figure 3(b) shows the HP-positive gastrointestinal changes in this study: stomach body and antral mucosal folds were thickened, disordered, and blurred, and gastric antrum folds were circular.

3.5. Gastrointestinal X-Ray Pattern in the Diagnosis of HP Infection. Table 4 shows the statistical results between the performance of gastrointestinal X-ray imaging after treatment and the HP-positive rate. After analysis and comparison, it was found that the probability of abnormal X-ray signs of HP-positive patients was 76.47% and that of those without abnormality was 23.53%, showing no statistical difference ($P < 0.05$). The probability of abnormalities in X-ray signs of HP-negative patients was 6.32%, and that of those without abnormalities was 93.67%, showing statistically great difference ($P < 0.05$), as shown in Figure 4. According to Table 4, the sensitivity, specificity, and accuracy of the X-ray examination results were 76.47%, 93.67%, and 90.63%, respectively.

3.6. Comparison of Changes in Intestinal Flora and Inflammatory Factors. Before treatment, there was no observable difference in the distribution of intestinal flora between the two groups of patients ($P > 0.05$). Compared with the condition before treatment, patients in group A showed a significant decrease in *Enterobacter*, yeast, *Clostridium perfringens*, *Bifidobacterium*, and *Lactobacillus* after treatment ($P < 0.05$) and a significant increase in enterobacteria ($P < 0.05$), and the B/E ratio was greatly reduced ($P < 0.05$). After treatment in group B patients, bifidobacteria and lactobacilli were remarkably increased ($t = 2.468$ and 3.887,

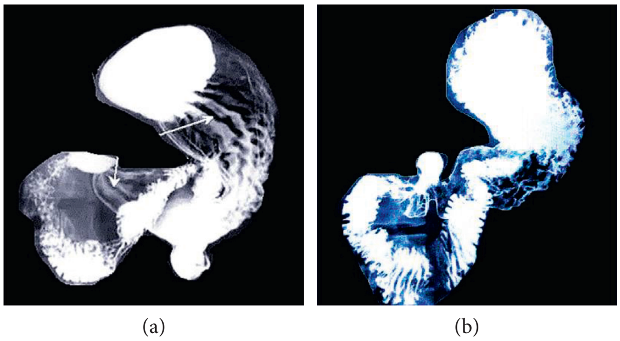

Figure 3: Results of gastrointestinal X-ray imaging. (a) Normal X-ray of gastrointestinal tract. (b) Positive gastrointestinal changes in HP.

Table 4: Gastrointestinal X-ray pattern in the diagnosis of HP infection.

Gastrointestinal X-ray signs	13C breath test results		Total number of cases
	Positive	Negative	
Number of children with abnormal results	13	5	18
Number of children with normal results	4	74	78
Total number	17	79	96

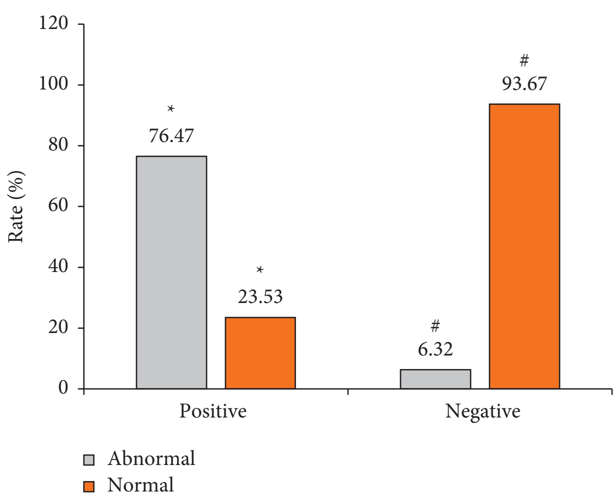

Figure 4: Comparison of HP results and X-ray imaging results. *Comparison of positive rates between the two groups after treatment, $P < 0.05$. #Comparison of improvement rates between the two groups, $P < 0.05$.

respectively, $P < 0.05$), *Clostridium perfringens* was greatly reduced ($P < 0.05$), enterococci and yeasts were reduced observably ($P < 0.05$), enterobacteria did not change observably ($P > 0.05$), and the B/E value was increased markedly ($P < 0.05$). The results revealed that the B/E value of group B patients after treatment was much higher than that of group A ($P < 0.05$). As shown in Table 5, there was no significant difference in TNF-α and IL-6 between the two groups of children before the treatment ($P > 0.05$), but those in group B were both greatly lower than group A after the treatment, showing statistically observable differences ($P < 0.05$) (Table 6).

3.7. Occurrence of Adverse Reactions. There were 3 cases of nausea and vomiting, 2 cases of diarrhea, 3 cases of abdominal distension and abdominal pain, 2 cases of loss of appetite, and 4 cases of rash in group A. There were 1 case of nausea and vomiting and 1 case of rash in group B. Therefore, the incidence of adverse reactions in group B was lower than that of group A ($P < 0.05$) (as given in Table 7).

4. Discussion

Under normal circumstances, the beneficial and harmful bacteria in the human gut are in a balanced state to maintain human health. When this balance is disrupted, the distribution of gut flora changes and the gut flora becomes unbalanced, which may lead to various diseases [12]. *Lactobacillus* and *Bifidobacterium* are beneficial bacteria in the human gut, while *Enterobacter* and *Enterococcus* are opportunistic pathogens in the human gut [13, 14]. Some studies have found that supplementary probiotic triple therapy has good efficacy and safety in eradicating HP in children. Fang et al. [15] conducted a meta-analysis of randomized controlled trials to supplement the efficacy of lactic acid bacteria triple therapy in the treatment of HP infected children, and the results showed that lactic acid bacteria as an adjunctive triple therapy can improve the eradication rate of HP and reduce the incidence of treatment-related diarrhea in children. Studies have shown that compound *Lactobacillus acidophilus* can promote the recovery of gastric mucosal permeability, protect the integrity of the mucosa, further prevent HP invasion, and form a mucosal barrier *in vivo* [16, 17]. The compound *Lactobacillus acidophilus* can reduce the production of inflammatory factors such as interleukin and interferon in the process of Th1 cell response, induce inflammatory factors such as interleukin produced by Th2 cell response, reduce mucosal inflammation, and enhance resistance to HP [18]. TNF-α and IL-6 are common inflammatory factors, and their blood levels show corresponding changes when inflammation occurs, and increases in its levels can be seen in various infectious diseases and have significant signs of illness in HP-infected patients [19, 20].

Among the medical image segmentation algorithms, the FCM algorithm has the advantages of being easy to execute, convenient, and fast and has become one of the mainstream segmentation algorithms [21]. The Ncut algorithm can promote the development of machine learning algorithms and is worthy of clinical application and promotion. Applying the Ncut algorithm to the medical field can help doctors solve some image processing tasks and help reduce the workload of doctors. The combination of Ncut algorithm and medical image processing is a combination of mathematics and medicine, which is beneficial to the progress of medical technology. Matsumoto et al. [22] used an

Table 5: Changes of intestinal flora before and after treatment in the two groups (lgCFU/g).

Group	Group A		Group B	
	Before treatment	After treatment	Before treatment	After treatment
Enterobacter	7.97 ± 0.72	$8.64 \pm 0.72^*$	7.96 ± 0.69	8.03 ± 0.75#
Enterococcus	6.48 ± 0.65	6.31 ± 0.75	6.50 ± 0.67	$6.10 \pm 0.85^*$#
Yeast	5.10 ± 0.67	$4.84 \pm 0.76^*$	5.06 ± 0.67	$4.33 \pm 0.74^*$#
Bifidobacterium	7.42 ± 0.63	$6.96 \pm 0.62^*$	7.41 ± 0.70	$7.98 \pm 0.81^*$#
Lactobacillus	6.47 ± 0.57	$5.77 \pm 0.61^*$	6.42 ± 0.63	$6.68 \pm 0.63^*$#
Clostridium perfringens	5.90 ± 0.42	$5.41 \pm 0.43^*$	5.87 ± 0.51	$5.13 \pm 0.47^*$#
B/E value	0.93 ± 0.12	$0.79 \pm 0.11^*$	0.93 ± 0.11	$0.99 \pm 0.12^*$#

$^*P < 0.05$ in contrast to the value before treatment in the same group; $^\#P < 0.05$ in contrast to the value in the same period between two different groups.

Table 6: Comparison of cytokines between the two groups of children.

Group	Group A		Group B	
	Before treatment	After treatment	Before treatment	After treatment
TNF-α (ng/L)	452.42 ± 43.28	$397.42 \pm 54.74^*$	462.46 ± 49.54	$225.85 \pm 61.47^*$#
IL-6 (ng/L)	59.74 ± 5.15	$43.08 \pm 10.33^*$	60.19 ± 4.80	$32.42 \pm 6.13^*$#

$^*P < 0.05$ in contrast to the value before treatment in the same group; $^\#P < 0.05$ in contrast to the value in the same period between two different groups.

Table 7: Comparison on occurrence of adverse reactions of children.

Group	Group A	Group B
Nausea and vomiting	3	1
Diarrhea	2	0
Bloating/abdominal pain	2	0
Loss of appetite	2	0
Rash	4	1
Total	13	2#

$^\#P < 0.05$ in contrast to group A.

intelligent algorithm to diagnose heart failure using chest X-ray images, and the results showed a diagnostic accuracy of 82%, suggesting that intelligent algorithms can help support the use of chest X-ray images to diagnose heart failure.

In this work, the gastrointestinal X-ray imaging based on intelligent algorithm was used to examine the digestive tract and the results of 13C breath test were used as the standard. The results of the 13C breath test showed that the improvement rates of the positive results of HP before and after treatment in group B and group A were 83.26% and 50.34%, respectively. Therefore, the improvement rate of group B was significantly higher than that of group A, indicating that the use of probiotics combined with triple therapy is superior to pure triple therapy. The sensitivity, specificity, and accuracy of X-ray examination results were 76.47%, 93.67%, and 90.63%, respectively, indicating that gastrointestinal X-ray imaging is feasible in the detection of HP infection. It was found that the serum levels of TNF-α and IL-6 in patients in group B were significantly lower than those in patients in group A, indicating that probiotics combined with triple therapy can significantly improve the intestinal flora of children with HP infection than triple therapy alone. In addition, the incidence of adverse reactions in group B was lower than that in group A ($P < 0.05$).

5. Conclusion

The intelligent X-ray image segmentation method had good effect in gastrointestinal X-ray image processing. Probiotics combined with triple therapy had a good clinical effect on children with *Helicobacter pylori* infection. It can better improve the clearance rate of *Helicobacter pylori*, improve the inflammatory response, and effectively improve the intestinal microecology of patients. The effect was remarkable, and it was worthy of clinical application.

Data Availability

The data used to support the findings of this study are available from the corresponding author upon request.

Conflicts of Interest

The authors declare no conflicts of interest.

References

[1] S. Mamishi, H. Eshaghi, S. Mahmoudi et al., “Intrafamilial transmission of Helicobacter pylori: genotyping of faecal samples,” *British Journal of Biomedical Science*, vol. 73, no. 1, pp. 38–43, 2016.

[2] A. Lewinska and M. Wnuk, “Helicobacter pylori-induced premature senescence of extragastric cells may contribute to chronic skin diseases,” *Biogerontology*, vol. 18, no. 2, pp. 293–299, 2017.

[3] P. G. Carolina, W. Rachel, C. Eunyoung et al., “Sa1609 - evaluation of mucosal lineage changes in the mouse gastric mucosa following infection with H.pylori and intestinal flora,” *Gastroenterology*, vol. 154, no. 6, 2018.

[4] A. Negovan, M. Iancu, E. Fülöp, and C. Bănescu, “*Helicobacter pylori* and cytokine gene variants as predictors of premalignant gastric lesions,” *World Journal of Gastroenterology*, vol. 25, no. 30, pp. 4105–4124, 2019.

[5] T. Kakiuchi, A. Mizoe, K. Yamamoto et al., “Effect of probiotics during vonoprazan \ ontaining triple therapy on gut

microbiota in H.pylori infection: a randomized controlled trial," *Helicobacter*, vol. 25, pp. 177–186, 2020.

[6] X. Shi, J. Zhang, L. Mo, J. Shi, M. Qin, and X. Huang, "Efficacy and safety of probiotics in eradicating H.pylori: a network meta-analysis," *Medicine*, vol. 98, no. 15, Article ID e15180, 2019.

[7] S. W. Lee, S. J. Moon, S. H. Kim et al., "The prolongation effect of ilaprazole-based standard triple therapy for *Helicobacter pylori*," *Medicine*, vol. 99, no. 38, Article ID e22137, 2020.

[8] P. Rezai, "Antibacterial activity of Lactobacilli probiotics on Clinical strains of H.pylori," *Iranian Journal of Basic Medical Sciences*, vol. 22, no. 20, pp. 1118–1124, 2019.

[9] C. Gutiérrez-Zamorano, M. González-Ávila, G. Díaz-Blas, C. T. Smith, C. González-Correa, and A. García-Cancino, "Increased anti- H.pylori effect of the probiotic Lactobacillus fermentum UCO-979C strain encapsulated in carrageenan evaluated in gastric simulations under fasting conditions," *Food Research International*, vol. 121, pp. 812–816, 2019.

[10] M. Zhang, C. Zhang, J. Zhao, H. Zhang, Q. Zhai, and W. Chen, "Meta-analysis of the efficacy of probiotic-supplemented therapy on the eradication of *H. pylori* and incidence of therapy-associated side effects," *Microbial Pathogenesis*, vol. 147, Article ID 104403, 2020.

[11] Y. Cha, Z. Wei, C. Ma, and L. Zhang, "Intelligent algorithm-based computed tomography image features in diagnosis of the effect of radiofrequency ablation in liver cancer," *Scientific Programming*, vol. 2021, Article ID 3422484, 9 pages, 2021.

[12] J.-R. Feng, F. Wang, X. Qiu et al., "Efficacy and safety of probiotic-supplemented triple therapy for eradication of *Helicobacter pylori* in children: a systematic review and network meta-analysis," *European Journal of Clinical Pharmacology*, vol. 73, no. 10, pp. 1199–1208, 2017.

[13] Z. Xu, Z. Lu, T. Soteyome et al., "Polymicrobial interaction between Lactobacillus and *Saccharomyces cerevisiae*: coexistence-relevant mechanisms," *Critical Reviews in Microbiology*, vol. 47, no. 3, pp. 386–396, 2021.

[14] Y. Xiao, Q. Zhai, H. Zhang, W. Chen, and C. Hill, "Gut colonization mechanisms of Lactobacillus and Bifidobacterium: an argument for personalized designs," *Annual Review of Food Science and Technology*, vol. 12, no. 1, pp. 213–233, 2021.

[15] H.-R. Fang, G.-Q. Zhang, J.-Y. Cheng, and Z.-Y. Li, "Efficacy of Lactobacillus-supplemented triple therapy for *Helicobacter pylori* infection in children: a meta-analysis of randomized controlled trials," *European Journal of Pediatrics*, vol. 178, no. 1, pp. 7–16, 2019.

[16] Y. Q. Du, T. Su, J. G. Fan et al., "Adjuvant probiotics improve the eradication effect of triple therapy for H.pylori infection," *World Journal of Gastroenterology*, vol. 18, no. 43, pp. 6302–6307, 2012.

[17] V. Ravichandra, S. Tanvi, M. D. Shastri et al., "A human origin strain Lactobacillus acidophilus DDS-1 exhibits superior in vitro probiotic efficacy in comparison to plant or dairy origin probiotics," *International Journal of Medical Sciences*, vol. 15, no. 9, pp. 840–848, 2018.

[18] C.-Y. Li, H.-C. Lin, C.-H. Lai, J. J.-Y. Lu, S.-F. Wu, and S.-H. Fang, "Immunomodulatory effects of Lactobacillus and Bifidobacterium on both murine and human mitogen-activated T cells," *International Archives of Allergy and Immunology*, vol. 156, no. 2, pp. 128–136, 2011.

[19] R. de Cássia Dos Santos, F. Bonamin, L. L. Périco et al., "Byrsonima intermedia A. Juss partitions promote gastroprotection against peptic ulcers and improve healing through antioxidant and anti-inflammatory activities," *Biomedicine & Pharmacotherapy*, vol. 111, pp. 1112–1123, 2019.

[20] S. Xu, X. Wu, X. Zhang, C. Chen, H. Chen, and F. She, "CagA orchestrates eEF1A1 and PKCδ to induce interleukin-6 expression in Helicobacter pylori-infected gastric epithelial cells," *Gut Pathogens*, vol. 12, no. 1, p. 31, 2020.

[21] M. Hu, Y. Zhong, S. Xie, H. Lv, and Z. Lv, "Fuzzy system based medical image processing for brain disease prediction," *Frontiers in Neuroscience*, vol. 15, p. 714318, 2021 Jul 30.

[22] T. Matsumoto, S. Kodera, H. Shinohara et al., "Diagnosing heart failure from chest X-ray images using deep learning," *International Heart Journal*, vol. 61, no. 4, pp. 781–786, 2020.

Hindawi
Contrast Media & Molecular Imaging
Volume 2023, Article ID 9875603, 1 page
https://doi.org/10.1155/2023/9875603

Retraction

Retracted: Artificial Intelligence-Based MRI in Diagnosis of Injury of Cranial Nerves of Premature Infant and Its Correlation with Inflammation of Placenta

Contrast Media & Molecular Imaging

Received 31 October 2023; Accepted 31 October 2023; Published 1 November 2023

This article has been retracted by Hindawi following an investigation undertaken by the publisher [1]. This investigation has uncovered evidence of one or more of the following indicators of systematic manipulation of the publication process:

(1) Discrepancies in scope
(2) Discrepancies in the description of the research reported
(3) Discrepancies between the availability of data and the research described
(4) Inappropriate citations
(5) Incoherent, meaningless and/or irrelevant content included in the article
(6) Peer-review manipulation

The presence of these indicators undermines our confidence in the integrity of the article's content and we cannot, therefore, vouch for its reliability. Please note that this notice is intended solely to alert readers that the content of this article is unreliable. We have not investigated whether authors were aware of or involved in the systematic manipulation of the publication process.

Wiley and Hindawi regrets that the usual quality checks did not identify these issues before publication and have since put additional measures in place to safeguard research integrity.

We wish to credit our own Research Integrity and Research Publishing teams and anonymous and named external researchers and research integrity experts for contributing to this investigation.

The corresponding author, as the representative of all authors, has been given the opportunity to register their agreement or disagreement to this retraction. We have kept a record of any response received.

References

[1] G. Liao, "Artificial Intelligence-Based MRI in Diagnosis of Injury of Cranial Nerves of Premature Infant and Its Correlation with Inflammation of Placenta," *Contrast Media & Molecular Imaging*, vol. 2022, Article ID 4550079, 9 pages, 2022.

Hindawi
Contrast Media & Molecular Imaging
Volume 2022, Article ID 4550079, 9 pages
https://doi.org/10.1155/2022/4550079

WILEY | Hindawi

Research Article

Artificial Intelligence-Based MRI in Diagnosis of Injury of Cranial Nerves of Premature Infant and Its Correlation with Inflammation of Placenta

Gui Liao

Department of Pediatrics, The Third People's Hospital of Yunnan Province, Kunming 650011, Yunnan, China

Correspondence should be addressed to Gui Liao; 171843163@masu.edu.cn

Received 6 January 2022; Revised 25 February 2022; Accepted 28 February 2022; Published 27 March 2022

Academic Editor: M Pallikonda Rajasekaran

The study focused on the effects of artificial intelligence algorithms in magnetic resonance imaging (MRI) for diagnosing cranial nerve inflammation of placenta and the correlation between cranial nerve injury with placental inflammation was explored. The subjects were selected from 132 premature infants in the hospital. According to the pathological examination of placenta, 81 cases with chorioamnionitis were taken as the experimental group and 51 cases without chorioamnionitis were taken as the control group. The incidence of cranial nerve injury in different groups of premature infants was analyzed by MRI diagnosis based on the principal component analysis (PCA) artificial intelligence algorithm, so as to analyze the correlation between cranial nerve injury and placental inflammation in premature infants. It was found that when the PCA artificial intelligence algorithm was incorporated into MRI examination of cranial nerve injury of premature infant, the A (accuracy), P (precision), R (recall), and $F1$ values under the PCA algorithm were 92%, 93.75%, 90%, and 92.87%, respectively. The A, P, R, and $F1$ of the control group were 54%, 54.1%, 52%, and 53.03%, respectively; there were statistically significant differences between the two groups, $P < 0.05$. As for the correlation of placental inflammation and cranial nerve injury, the positive detection rate of the experimental group was 53.09%, and the positive detection rate of the control group was 15.69%, and the difference was statistically significant, $P < 0.05$. In conclusion, the PCA artificial intelligence algorithm has high effectiveness and high accuracy in auxiliary diagnosis of premature brain nerve injury, and placental inflammation greatly increases the chance of premature infant suffering from brain nerve injury.

1. Introduction

Premature infant refers to live-born babies with a gestational age less than 37 weeks, weighed less than 2.5 kg [1], and having a head circumference of 33 cm or less. Its organ function and adaptability are relatively poor compared to full-term premature infant, and some organs are immature [2]. It has been found that except for perinatal hypoxia-ischemia or asphyxia, hyperbilirubinemia, and hypoglycemia, cranial nerve injury is also related to premature infant placental inflammation [3, 4]. There are many types of placental inflammation, and chorioamnionitis is a common one [5, 6]. It results from pathogens infecting the chorion, amniotic membrane, and decidua of the placenta. Morphologically, it manifests as neutrophils infiltrating the villi membrane [7, 8]. Maternal chorioamnionitis can cause fetal inflammatory response syndrome, which is a subclinical state caused by the activation of the fetal immune system and release of a large number of inflammatory factors (IL-6, IL-1, IL-8, and TNF-α). These inflammatory factors can interfere with the normal expression of fetal brain cytokines, leading to brain damage in premature infants [9].

In recent years, although the survival rate of premature infant has increased, the probability of cranial injury has also increased. Currently, cranial injury of premature infant is mainly diagnosed by doctors assisted by imaging examination. The commonly used imaging examination methods include ultrasound, electronic computed tomography (CT), and magnetic resonance imaging (MRI). CT image has limited resolution [10], and the radiation will do harm to people's health. Hence, it is not recommended. Ultrasound examination is safe and has high repeatability, and it can dynamically observe the progress of the disease, but it has many shortcomings [11]. MRI is an advanced medical imaging examination method introduced in the early 1980s, which combines the latest research results in the fields of biology [12, 13], chemistry, physics, and medicine [14, 15]. Additionally, it is sensitive to motion and prone to artifacts [16, 17].

MRI can accurately, sensitively and noninvasively reflect the location, scope, and histological basis of brain lesions, and it is a well-recognized imaging examination method to evaluate cranial injury of premature infant. Incorporating intelligent algorithms into MRI imaging can effectively improve its shortcomings and better assist doctors in diagnosing cranial injury of premature infant. Principal component analysis (PCA) is a common data analysis method. It is often used for dimensionality reduction of high-dimensional data and can improve the quality of MRI images by extracting the main feature components of the data, thus elevating the accuracy of diagnosis [18, 19]. Leviton et al. [20] introduced the main analysis algorithm of multivariate statistical analysis into brain nerve injury and adopted statistical pattern recognition brain image feature extraction, which greatly simplified the calculation.

There have been a large number of reports of cranial injury of premature infant, but there are not many studies on placental inflammation [21, 22]. To prevent and diagnose cranial injury of premature infant caused by placental inflammation, the correlation between cranial nerve injury and placental inflammation was analyzed through MRI based on PCA, expected to provide reference for the clinical prevention, diagnosis, and treatment of cranial nerve injury of premature infant.

2. Materials and Methods

2.1. Research Subjects and Grouping. The subjects were selected from 132 premature infants in the hospital from April 2018 to April 2020. According to the pathological examination of placenta, 81 cases with chorioamnionitis were taken as the experimental group and 51 cases without chorioamnionitis were taken as the control group. The incidence of cranial nerve injury in different groups of premature infants was analyzed by MRI diagnosis based on the principal component analysis (PCA) artificial intelligence algorithm, so as to analyze the correlation between cranial nerve injury and placental inflammation in premature infants. Placental inflammation was divided into stage 0, stage I, stage II, and stage III. The study had been approved by the ethics committee of hospital, and the subjects and their family members understood the content of the study and signed an informed consent form.

Inclusion criteria were as follows: premature infants with a gestational age less than 37 weeks, the bodyweight was under 2.5 kg, and the head circumference was under 33 cm.

Exclusion criteria were as follows: premature infant with congenital malformations, those with chromosomal abnormalities and metabolic genetic diseases, and those with craniocerebral abnormalities confirmed by prenatal examination.

2.2. Pathological Examination of Placental Inflammation. After delivery of premature infants, 3×3 cm fetal membrane tissue was taken from the placenta tear as the center to make fetal membrane rolls, and then, samples were taken from the center, middle, and edge of the placenta. Amniotic membrane, chorionic plate, villi, and decidua were selected. Specimens were fixed with 10% formaldehyde, embedded in paraffin, sliced, stained with hematoxylin-eosin (H&E), and read by experienced physicians in the department of pathology.

2.3. Staging Diagnostic Criteria of Placental Inflammation. Placental histology is mainly chorioamnionitis (HCA), that is, maternal neutrophils infiltrate into amniotic membrane, chorion, and decidua. Inflammation stages are as follows. Stage 1: neutrophil infiltration is less and scattered, almost all confined to the chorionic space. Stage 2: neutrophil infiltration increased and extended to the chorionic plate in the chorionic tissue, but did not enter the amniotic membrane. Stage 3: neutrophils infiltrated into amniotic epithelial cells. Stages represent the progress of the disease.

2.4. Principal Component Analysis Artificial Intelligence Algorithm. The mathematical derivation of PCA can be carried out from the two aspects of maximum separability and nearest reconstruction. The optimization condition of the former is that the variance is the largest after division, and the optimization condition of the latter is that the distance from the point to the division plane is the smallest. This study is from the perspective of maximum separability. The inner product of two vectors A and B is expressed as follows.

$$(a_1, a_2, \ldots, a_n) \cdot (b_1, b_2, \ldots, ab_n)^T = a_1 b_1, a_2 b_2, \ldots, a_n b_n. \tag{1}$$

The inner product operation maps two vectors to real numbers. Geometrically, assuming that A and B are two-dimensional vectors expressed as follows, its geometric representation is shown in Figure 1.

$$\begin{aligned} A &= (X_1, Y_1); B = (X_2, Y_2) \\ A \cdot B &= |A||B|\cos b. \end{aligned} \tag{2}$$

The inner product of B and A is equal to the projection length from B to A multiplied by the modulus of B. Assuming that the modulus of A is 1, namely, $|A| = 1$, as shown in equation (4), the inner product of B and A is equal to the scalar size of B projected to the line where A is located.

$$A \cdot B = |B|\cos b. \tag{3}$$

In the coordinate system, the vector (3, 2) defined as the projection on the x-axis is 3 and the projection on the y-axis

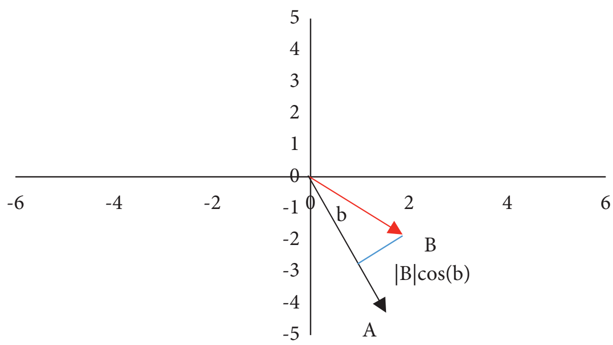

Figure 1: Vector geometry representation.

is 2. The projection is scalar, which can be negative. Therefore, for the vector (3, 2), to find its coordinates under (1, 0) (0, 1), it is just needed to solve the inner product. Above, to describe a vector accurately, a set of bases is determined first and then the projection value on each line where the basis is located is given. For the sake of convenience, the modulus length of the group basis vector is generally taken as 1, so that the inner product can directly represent the projection. For the vector (3, 2), the new coordinates in the group base is calculated as given in the following equation, which can be expressed by matrix multiplication.

$$\begin{pmatrix} \frac{1}{\sqrt{2}} & \frac{1}{\sqrt{2}} \\ -\frac{1}{\sqrt{2}} & \frac{1}{\sqrt{2}} \end{pmatrix}\begin{pmatrix} 3 \\ 2 \end{pmatrix} = \begin{pmatrix} 5\sqrt{2} \\ -\frac{1}{\sqrt{2}} \end{pmatrix}. \tag{4}$$

The two rows of the left matrix are two bases, which are multiplied by the original vector to obtain the new base coordinates. If there are m two-dimensional vectors, they are arranged into a two-row m-column matrix, which is multiplied by the base matrix to get the value under the new base. For data points (1, 1), (2, 2), and (3, 3), the equation is expressed as follows.

$$\begin{pmatrix} \frac{1}{\sqrt{2}} & \frac{1}{\sqrt{2}} \\ -\frac{1}{\sqrt{2}} & \frac{1}{\sqrt{2}} \end{pmatrix}\begin{pmatrix} 1 & 2 & 3 \\ 1 & 2 & 3 \end{pmatrix} = \begin{pmatrix} \frac{2}{\sqrt{2}} & \frac{4}{\sqrt{2}} & \frac{6}{\sqrt{2}} \\ 0 & 0 & 0 \end{pmatrix}. \tag{5}$$

The general representation is as the following equation, where P_i is a row vector, which represents the i^{th} basis, and A_j is a column vector, which represents the j^{th} original data.

$$\begin{pmatrix} P_1 \\ P_2 \\ \vdots \\ P_R \end{pmatrix}(a_1, a_2, \ldots, a_m) = \begin{pmatrix} P_1a_1 & P_1a_2 & \ldots & P_1a_m \\ P_2a_1 & P_2a_2 & \ldots & P_2a_m \\ \vdots & \vdots & \vdots & \vdots \\ P_Ra_1 & P_Ra_1 & \ldots & P_Ra_m \end{pmatrix}. \tag{6}$$

To multiply two matrices is to transform each column vector in the right matrix into each row vector in the left matrix. In other words, a matrix can represent a linear transformation. Variance describes the degree of dispersion of the value, and the variance of the variable is expressed as follows.

$$\mathrm{Var}(a) = \frac{1}{m}\sum_{i=1}^{m}(a_i - \mu)^2. \tag{7}$$

If the variable mean is 0, the variance can be expressed by the sum of squares of the elements divided by the number of elements, as shown in the following equation.

$$\mathrm{Var}(a) = \frac{1}{m}\sum_{i=1}^{m}a_i^2. \tag{8}$$

One-dimensional space uses variance to indicate the degree of data dispersion. In order to allow the two variables to represent the original information as much as possible, it is a must that there is no linear correlation between them. The covariance is expressed as follows.

$$Cov(a, b) = \frac{1}{m-1}\sum_{i=1}^{m}(a_i - \mu_a)(b_i - \mu_b). \tag{9}$$

Since the mean value is 0, the covariance is calculated as given in equation (10). A covariance of 0 means that the two variables are linearly uncorrelated. For the covariance to be 0, the second basis is selected in the direction orthogonal to the first basis. The dimensionality reduction optimization is to reduce n-dimensional vectors to K-dimensional.

The ultimate result is related to the variance within the variables and the covariance between variables. Both can be expressed in the form of inner product, and the inner product is related to the matrix multiplication. Assuming there are only two variables, a and b, they form a matrix by rows, as shown in equation (11).

$$Cov(a, b) = \frac{1}{m}\sum_{i=1}^{m}a_ib_i, \tag{10}$$

$$X = \begin{pmatrix} a_1 & a_2 & \ldots & a_m \\ b_1 & ab_2 & \ldots & b_m \end{pmatrix}. \tag{11}$$

The diagonals of the matrix are the variances of the two variables, and the other elements are the covariances of a and b. The two are included in a matrix, as shown in the following equation.

$$\frac{1}{m}XX^T = \begin{pmatrix} \frac{1}{m}\sum_{i=1}^{m} a_i^{\,2} & \frac{1}{m}\sum_{i=1}^{m} a_i b_i \\ \\ \frac{1}{m}\sum_{i=1}^{m} a_i b_i & \frac{1}{m}\sum_{i=1}^{m} b_i^{\,2} \end{pmatrix}. \tag{12}$$

To deduce, if there are m and n-dimensional data and they are arranged in a matrix $X_{n,m}$, as shown in equation (13), C is a symmetric matrix.

$$C = \frac{1}{m}XX^T. \tag{13}$$

According to the optimization conditions, the other elements except the diagonal are 0, and the elements are arranged on the diagonal by size from top to bottom. To describe the relationship between the original matrix and the matrix covariance matrix after the basis transformation, let the covariance matrix corresponding to the original data matrix X be C, and P is a set of matrixes. Let $Y = PX$, then Y is the data after base transformation of P by X. Supposing the covariance matrix of Y is D, the relationship between D and C is derived as follows.

$$\begin{aligned} D &= \frac{1}{m}YY^T \\ &= \frac{1}{m}(PX)(PX)^T \\ &= \frac{1}{m}PXX^TP^T \\ &= P\left(\frac{1}{m}XX^T\right)P^T \\ &= PCP^T. \end{aligned} \tag{14}$$

Then, it is necessary to complete the diagonalization. It is known that the covariance matrix C is a symmetric matrix. As is well-known, the eigenvectors corresponding to different eigenvalues of the real symmetric matrix must be orthogonal. Let the eigenvector λ multiplicity be λ; then, there must be r linearly independent eigenvectors corresponding to λ, so the r eigenvector units can be orthogonalized. Therefore, a real symmetric matrix with n rows and n columns is formed. Supposing these n eigenvectors are e_1, $e_2, \ldots, e_n$, and they are arranged by columns: $E = (e_1, e_2, \ldots, e_n)$. Then, the covariance matrix C is expressed as follows.

$$E^TCE = \wedge = \begin{pmatrix} \lambda_1 & \lambda_1 \\ \ddots & \lambda_1 \end{pmatrix}, \tag{15}$$

where $\wedge$ is a diagonal matrix, and its diagonal elements are the eigenvalues corresponding to each eigenvector, so that P is obtained. P is the matrix arranged in rows after the eigenvectors of the covariance matrix are unitized, expressed as in equation (17). If P is arranged according to the eigenvalues in $\wedge$ from large to small, then the original data matrix X is multiplied by the matrix composed of the first K rows of P to obtain the data matrix Y after dimensionality reduction.

$$P = E^T. \tag{16}$$

Figure 2 is a flowchart of the algorithm.

2.5. MRI Examination. Routine preparation was carried out before MRI examination, which was generally carried out in the infants' natural sleep state. Premature infants who underwent MRI were given 2 μg/kg dexmedetomidine intravenously within 10 min, and 1-2 μg/(kg·h) was the maintenance dose. During examination, the cotton quilt was wrapped to keep warm, and patients with severe symptoms were provided with oxygen bag nasal mask. 3.0 T MRI and corresponding workstation, 8-channel orthogonal head coil, sequence, and imaging parameters were as follows: TlWI : FSE sequence, FOV: 18 × 18, TR/TE: 500/11 ms, matrix: 320 × 192; T2WI : FSE sequence, FOV: 18 × 18, TR/TE: 4780/100 ms, matrix: 320 × 192, excitation times 3NEX, and layer thickness/spacing: 4.0/0.5 mm. MRI images of all the infants were retrospectively analyzed by 2 radiologists who were unaware of the clinical manifestations and follow-up results using a double-blind method.

2.6. Evaluation Index. The PCA-processed MRI images were evaluated with the cranial nerve injury as a positive case and the healthy patient as a negative case. True positive (TP) means that the prediction is a positive case, and the actual case is also positive. False positive (FP) means that the prediction is a positive case, and the actual is a negative case. False negative (FN) means that the prediction is a negative case, and the actual is a positive case. True negative (TN) means that the prediction is a negative case, and the actual is a negative case.

$$A = \frac{\mathrm{TN} + \mathrm{TP}}{\mathrm{TN} + \mathrm{TP} + \mathrm{FP} + \mathrm{FN}}, \tag{17}$$

$$P = \frac{\mathrm{TP}}{\mathrm{TP} + \mathrm{FP}}, \tag{18}$$

$$R = \frac{\mathrm{TP}}{\mathrm{TP} + \mathrm{FN}}. \tag{19}$$

In this study, accuracy (A) is used to indicate the proportion of correct predictions, calculated as given in equation (17), precision (P) indicates the ratio of actual positive cases among positive predictions, calculated as given in equation (18), and recall (R) is the ratio of the correctly predicted positive cases to all positive cases, calculated as given in equation (19).

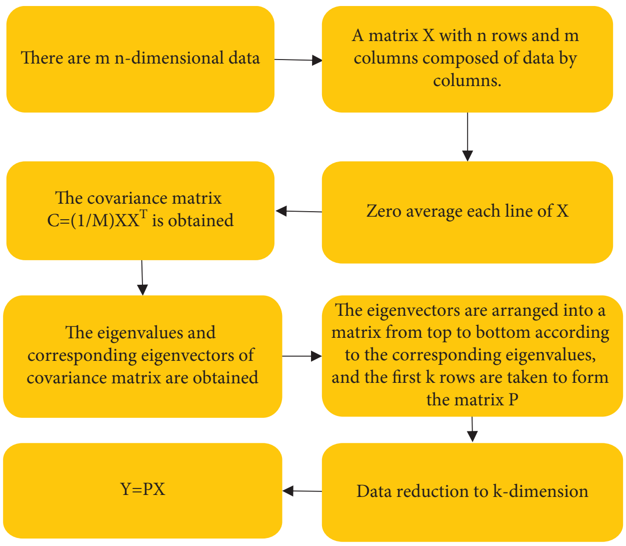

FIGURE 2: The flowchart of the PCA algorithm.

$$F = \frac{\left(\alpha^2 + 1\right) P \times R}{\alpha^2 (P + R)}, \quad (20)$$

$$F_1 = \frac{2P \times R}{P + R}. \quad (21)$$

When the P index and the R index are contradictory, the weighted harmonic average of P and R is used, that is, the F-measure method, expressed as follows. When the parameter $\alpha = 1$, it is the common $F1$, as shown in equation (21). A higher $F1$ value means the higher effectiveness of the algorithm. In an experiment to analyze the correlation between cranial injury of premature infant and placental inflammation, the positive detection rate is the ratio of the number of premature infants with cranial injury to the total number of cases multiplied by 100%.

2.7. Statistical Analysis. The research data were processed by SPSS version 19.0 statistical software. The collected measurement data were expressed as mean ± standard deviation ($\bar{x} \pm s$), and the count data were expressed by percentage (%). Pairwise comparison was performed by analysis of variance, and logistic regression was used to analyze the relationship between placental inflammation stage and the risk of brain injury in premature infants. Logistic regression analysis was used to analyze the relationship between placental inflammation stage and the risk of brain injury in premature infants, and $P < 0.05$ was a threshold for significance.

3. Results

3.1. MRI Image of Premature Infant with Cranial Nerve Injury. Figures 3–5 show the MRI images of three premature infants with cranial nerve injury. Figure 3 shows MRI images of a premature infant with mild hypoxic-ischemic encephalopathy (HIE). It was noted that the capillary endothelium was damaged and the permeability increased; and hypoxia led to the capillary reactive hyperemia and selective nerve necrosis.

Figure 4 shows MRI images of a premature infant with moderate HIE. It was noted that hypoxia led to congestion and expansion. The blood vessel development was immature, and basement membrane was damaged. Histologically, red blood cells and plasma proteins were exuded.

Figure 5 shows the MRI images of a premature infant with severe HIE. It was noted that the subcortical tissue was necrotic and brain atrophy occurred.

3.2. PCA Effectiveness Analysis. After MRI images of cranial nerve injury of premature infant were processed by the PCA algorithm, TP, FP, FN, and TN were 45, 3, 5, and 47, respectively; and when the control group was used for diagnosis, TP, FP, FN, and TN were 26, 22, 24, and 28, respectively, and the differences were statistically significant ($P < 0.05$). Figure 6 shows the comparison chart of the positive and negative cases of the two.

Figure 7 shows the results of A, P, and R. It was noted that A, P, and R of PCA-based MRI were 92%, 93.75%, and 90%, respectively; and the A, P, and R of the control group were 54%, 54.1%, and 52%, respectively, and the differences were statistically significant ($P < 0.05$). Obviously, the three indexes of the PCA-based MRI were better versus the control group.

As shown in Figure 8, the $F1$ value of the PCA algorithm was 92.87% and the F1 value of the control group was 53.03%. Obviously, the FI value of the PCA algorithm was significantly higher than the control group, and there were statistically significant differences, $P < 0.05$.

3.3. Positive Detection Rate of Cerebral Nerve Injury in Premature Infants with Placental Inflammation. As shown in Figure 9, in the experimental group of 81 patients with chorioamnionitis, there were 43 patients with cranial nerve injury, and the positive detection rate was 53.09%, and of 51 patients without chorioamnionitis in the control group, 8 had cranial nerve injury, and the positive detection rate was 15.69%. Obviously, there were statistically significant differences in the positive detection rate of the two groups, $P < 0.05$.

3.4. Correlation between Cerebral Nerve Injury and Placental Inflammation Stages in Premature Infants. Figure 10 shows the pathological sections of placental inflammation in premature infants. Logistic regression analysis showed that stage II and stage III of placental inflammation were risk factors for brain nerve injury in premature infants, as given in Table 1.

4. Discussion

There are many factors that will cause cranial nerve injury. Clinically, MRI is generally used to assist doctors in diagnosis [23]. It has good resolution for soft tissue and high contrast. The multiparameter and multiplane imaging technology is superior in positioning and quantification. It is a noninvasive method and has no radiation damage, without

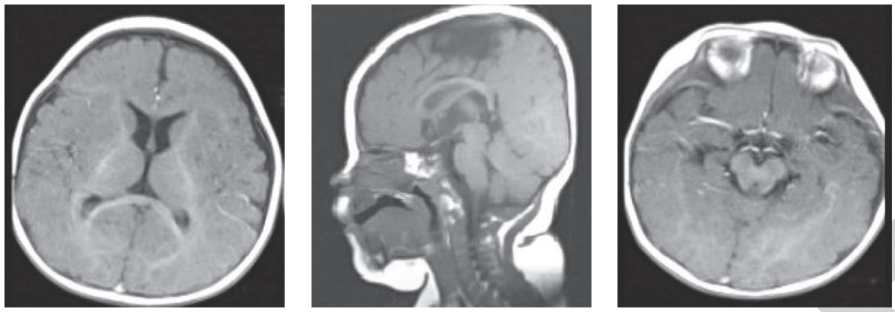

Figure 3: MRI images of mild HIE. (a)–(c) Images of transverse, sagittal, and coronal positions, respectively.

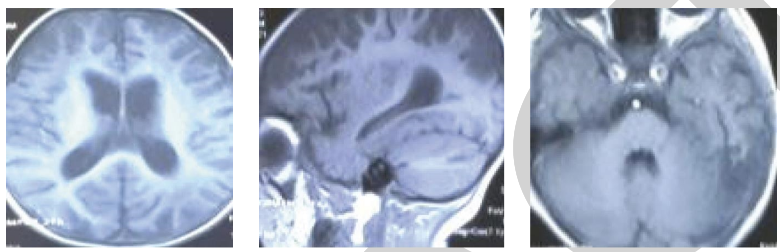

Figure 4: MRI images of moderate HIE. (a)–(c) Images of transverse, sagittal, and coronal positions, respectively.

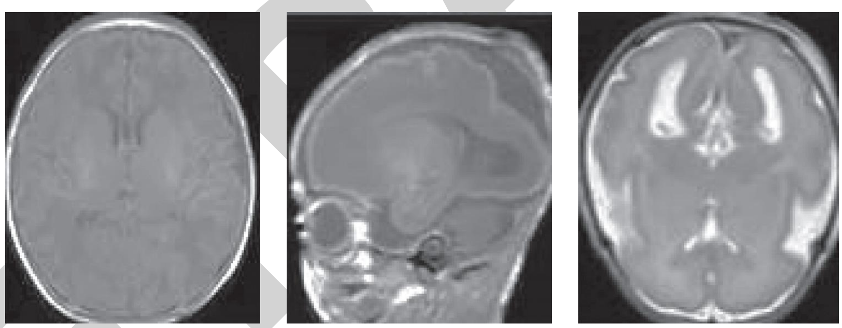

Figure 5: MRI images of severe HIE. (a)–(c) Images of transverse, sagittal, and coronal positions, respectively.

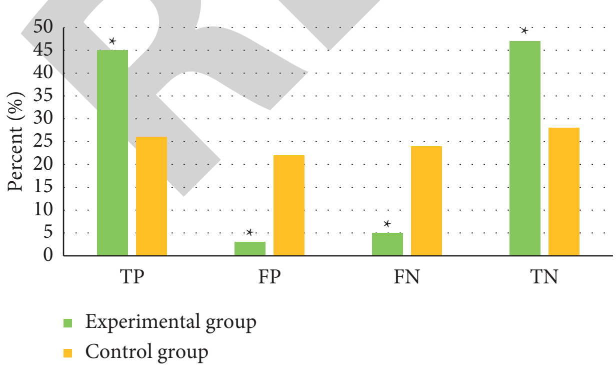

Figure 6: Comparison of positive and negative cases between PCA-based MRI and the control group. *Statistically significant difference compared with the control group ($P < 0.05$).

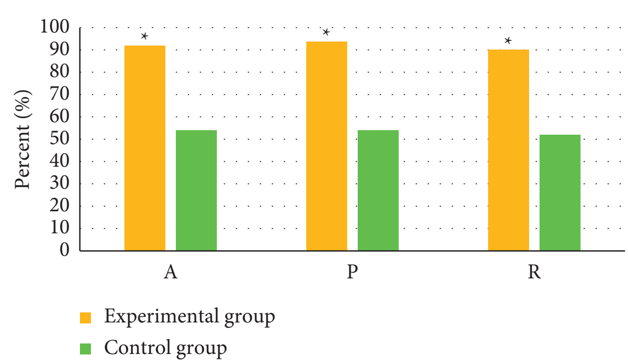

Figure 7: Comparison of A, P, R values between PCA-based MRI and the control group. *Statistically significant difference compared with the control group ($P < 0.05$).

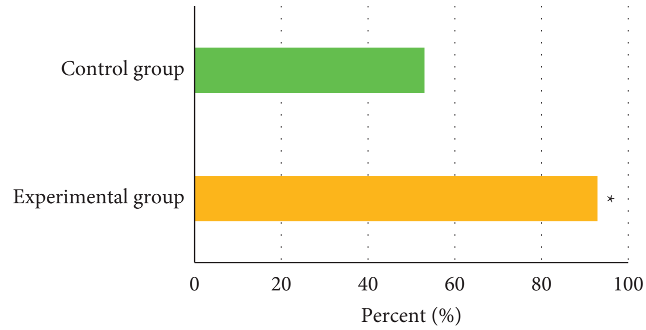

Figure 8: Comparison of $F1$ values between the PCA algorithm and the control group. *$F1$ value of the PCA algorithm was significantly different from that of the control group ($P < 0.05$).

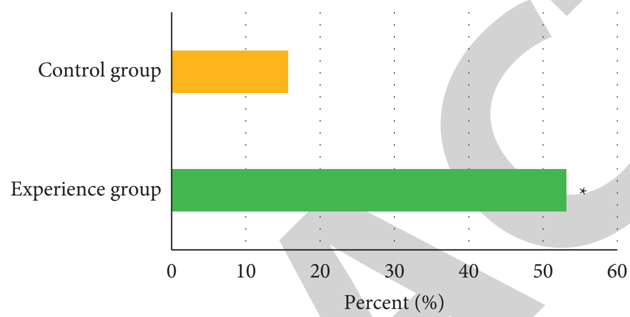

Figure 9: Comparison of positive detection rate between the experimental group and the control group. *Positive detection rate of the experimental group was significantly different from that of the control group ($P < 0.05$).

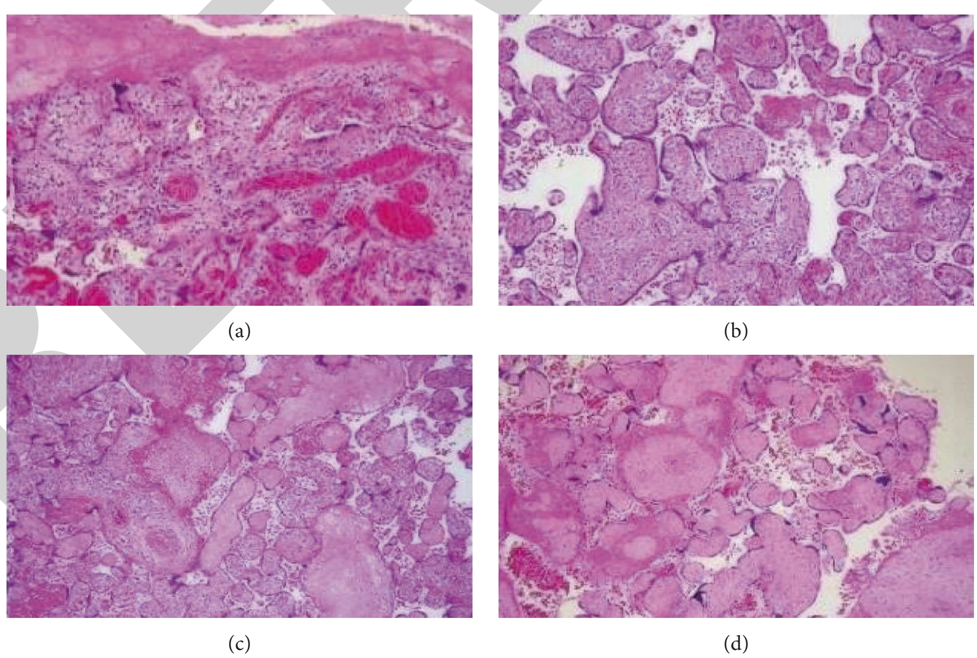

Figure 10: Stages of inflammation in pathological sections of placental tissue (H&E staining, ×200). (a) Stage 0, normal chorionic amniotic tissue. (b) In stage I, a few neutrophils infiltrate into the subchorionic amniotic membrane. (c) In stage II, moderate neutrophils infiltrate into the subchorionic amniotic membrane. (d) In stage III, a large number of neutrophils infiltrate into the lower layer of the chorionic amniotic membrane and parts of the amniotic epithelial cells are necrotic and fall off.

Table 1: Analysis of placental inflammation stage and risk of cerebral nerve injury in premature infants.

Inflammation of the placenta	Cases	Incidence probability of cerebral nerve injury (%)	OR	95% CI	P
Stage 0	51	4.25	1	—	—
Stage I	45	34.09	2.274	0.815–6.594	0.084
Stage II	39	29.55	5.267	1.256–18.952	0.002
Stage III	7	3.03	12.345	2.314–73.264	0.002

the need to use contrast agents. When MRI images are processed by the PCA algorithm, the sampling density is increased and the dimensionality is reduced by discarding some information. It is an important means to alleviate the dimensional disaster [24]. When the data are affected by noise, discarding the eigenvectors corresponding to the smallest eigenvalues can reduce noise to a certain extent because they are related to noise. PCA retains the main information [25] and may discard some seemingly useless information, but these seemingly useless information happens to be important information, so PCA may aggravate overfitting. PCA also makes the features of the data after dimensionality reduction independent of each other.

In this study, the application of the PCA algorithm in MRI diagnosis of cranial nerve injury of premature infant was analyzed, and the correlation between cranial nerve placental inflammation was explored, expected to provide reference for clinical prevention, diagnosis, and treatment of cranial nerve injury of premature infant. It was found that when the PCA algorithm was incorporated in MRI examination of cranial nerve injury of premature infant, the A, P, and R values of the PCA algorithm were 92%, 93.75%, and 90%, respectively, and the A, P, and R values of the control group were 54%, 54.1%, and 52%; the diagnosis accuracy rate under the artificial intelligence algorithm was higher, which is more conducive to the diagnosis of doctors. The $F1$ value of the PCA algorithm was 92.87%, and the $F1$ value of the control group was 53.03%. Obviously, the FI value of the PCA algorithm was significantly higher than the control group, and there were statistically significant differences, $P < 0.05$. As for the correlation between placental inflammation and cranial nerve injury, there were 43 patients with cranial nerve injury in the experimental group, with a positive detection rate of 53.09%, and of 51 patients without chorioamnionitis in the control group, 8 had cranial nerve injury, and the positive detection rate was 15.69%. Obviously, there were statistically significant differences in the positive detection rate of the two groups, $P < 0.05$, indicating that placental inflammation would greatly increase the chance of premature infant suffering from cranial nerve injury, and it was consistent with the results of Jablonska et al. [26].

Wu et al. [27] reported that hemodynamic disturbance after intrauterine infection may be related to the release of a large number of proinflammatory cytokines. These proinflammatory cytokines can eventually lead to brain injury by influencing the formation of microglia, oligodendrocytes, astrocytes, and myelin sheath, inducing other cytokines to produce cell damage, and mediating the neurotoxicity of nitric oxide and the cytotoxicity of excitatory amino acids. Rudie et al. [28] reported that based on the diagnosis of artificial intelligence MRI, the incidence of intraventricular hemorrhage in premature infants with chorioamnionitis in pregnant mothers can reach 16.1%, and the risk of intraventricular hemorrhage can be increased by 3.2 times due to placental inflammation and the third stage of inflammation. This study found that the second and third stage inflammation of placenta was a risk factor of brain injury in premature infants, which was consistent with the literature report.

5. Conclusion

In this study, the PCA artificial intelligence algorithm was incorporated into MRI examination of cranial nerve injury of premature infant, and its influence on MRI images was analyzed. Then, the correlation between cranial nerve injury with placenta inflammation was explored. It was found that the PCA algorithm demonstrates a high accuracy rate, and placental inflammation will greatly increase the chance of premature infant suffering from brain nerve injury. However, shortage of this study lies in the selection of sample size that is less and not considering premature infant brain injury caused by intrauterine infection, which may affect the result of the experiment, the sample, so in a follow-up experiment, it needs to expand further comprehensive analysis based on the artificial intelligence algorithm of MRI diagnosis of premature cranial nerve injury and its correlation with placental inflammation. The sample should be expanded in subsequent experiments to strengthen the findings of the study. In conclusion, this study provides reference for clinical prevention, diagnosis, and treatment of cranial nerve injury of premature infant.

Data Availability

The data used to support the findings of this study are available from the corresponding author upon request.

Conflicts of Interest

The author declares that there are no conflicts of interest.

References

[1] X. Liu, K. Chen, T. Wu, D. Weidman, F. Lure, and J. Li, "Use of multimodality imaging and artificial intelligence for diagnosis and prognosis of early stages of Alzheimer's disease," *Translational Research*, vol. 194, pp. 56–67, 2018.

[2] Y.-T. Chu, A. Hsu, C.-C. Wu, H.-D. Tsai, C. Tsung-Che Hsieh, and Y.-H. Hsiao, "Acute chorioamnionitis complicated with symmetrical peripheral gangrene," *Taiwanese Journal of Obstetrics & Gynecology*, vol. 59, no. 6, pp. 972–974, 2020.

Hindawi
Contrast Media & Molecular Imaging
Volume 2022, Article ID 3950641, 9 pages
https://doi.org/10.1155/2022/3950641

Research Article

Computed Tomography Images under the Nomogram Mathematical Prediction Model in the Treatment of Cerebral Infarction Complicated with Nonvalvular Atrial Fibrillation and the Impacts of Virus Infection

Yi Zhu,[1] **Hai Cheng**,[2] **Rui Min**,[1] **and Tong Wu**[1]

[1]*Department of Emergency, Geriatric Hospital of Nanjing Medical University, Nanjing 210024, China*
[2]*Department of Cardiology, Suzhou Kowloon Hospital, Suzhou 215000, China*

Correspondence should be addressed to Yi Zhu; 201309020133@stu.sdnu.edu.cn

Received 26 December 2021; Revised 20 February 2022; Accepted 23 February 2022; Published 27 March 2022

Academic Editor: M Pallikonda Rajasekaran

The aim of this work was to explore the effect of the nomogram mathematical model on the treatment of cerebral infarction complicated with nonvalvular atrial fibrillation (NVAF) and viral infection. The data were scanned by a circular trajectory fan beam isometric scanning mode system (scanning system), and the speckle noise of computed tomography (CT) images was smoothed by Lee filtering. 52 patients with postoperative recurrent viral infection (RVI group) and 248 patients without postoperative recurrent viral infection (NRVI group) were selected for retrospective analysis. The mathematical model curve was then analyzed through calibration plots and decision curves to predict the accuracy of the mathematical model. The results showed that the area under the receiver operating characteristic curve (AUC), sensitivity, specificity, and accuracy based on the training set were 0.7868, 0.7634, 0.6982, and 0.7146, respectively. The AUC, sensitivity, specificity, and accuracy based on the validation set were 0.7623, 0.7734, 0.6882, and 0.6948, respectively. There was no significant difference in the AUC between the two groups ($P > 0.05$), indicating that the nomogram mathematical prediction model had high repeatability. In conclusion, CT images based on the nomogram mathematical prediction model had good predictive ability in the treatment of cerebral infarction complicated with NVAF.

1. Introduction

Atrial fibrillation is a common persistent arrhythmia in clinical practice, and the stroke caused by it has the characteristics of high fatality rate and disability rate, especially in the elderly (10%) [1, 2]. Atrial fibrillation is not only an arrhythmia but also an important independent risk factor that causes cerebral infarction. The incidence and mortality of atrial fibrillation combined with cerebral infarction not only affect the survival of patients but also bring a heavy burden to the family [3, 4]. There are two types of atrial fibrillation, VAF and NVAF. NVAF is a common type of atrial fibrillation in clinical practice. It refers to atrial fibrillation without rheumatic heart disease, artificial valve replacement, or valve repair. Patients with NVAF have a higher risk of thromboembolism and are prone to merging cerebral infarction [5–7]. With the progress of pathophysiology research in the field of atrial fibrillation, various mechanisms such as ion channel mutation and myocardial fibrosis have been proved to be independent risk factors for atrial fibrillation. Viruses such as *Helicobacter pylori* (HP) and herpes simplex virus (HSV) can induce a large amount of release protein C from the body and trigger an inflammatory response, thereby increasing the risk of atrial fibrillation [8]. There are also some studies that only diagnose viral infection based on previous medical history, lacking the corresponding etiological evidence. Infections of viruses such as macrophage virus (MV), Coxsackie virus (CoxV), and parvovirus (PV) are all related to incidence of cardiovascular disease (CVD), but the relationship between the inflammatory responses caused by these viruses and the atrial fibrillation is still inconclusive [9]. In recent years, the prevention of stroke in patients with NVAF has received high attention, but the effect is not obvious. Because of the hidden nature of atrial fibrillation, real-time monitoring of patients has become a trend. With the development of big data technology, the collection of monitoring data of patients with atrial fibrillation can better help doctors summarize the characteristics of the disease, laying the foundation for the follow-up implementation of personalized treatment [10].

CT is one of the important bases for diagnosing cerebral infarction. Cerebral infarction can show abnormalities on CT images for 3–6 hours, mainly including increased aortic density [11, 12]. Although radiofrequency ablation and surgical management during the surgery have improved the survival rate after atrial fibrillation, the recurrence rate caused by viral infection still is not eliminated [13, 14]. Early recurrence prediction tools are still relatively lacking. A tool is needed for personalized assessment of recurrence caused by viral infection, and effective treatment measures can be taken by physicians to assess the probability of early postoperative recurrence [15, 16]. Mathematical models can make quantitative predictions based on the occurrence of diseases. For some specific objects, the mathematical models can be approximated according to the existence of some risk factors and expressed in mathematical structures, and then the statistical language and programming calculations can be adopted to make batch predictions. At this stage, there are mainstream methods of disease prediction, and these have become very popular methods for disease control and health policies. The American Heart Association (AHA) has used the establishment of CVD prediction models to propose prevention strategies, and many researchers have proposed prevention strategies for infectious disease prediction models. The application of mathematical prediction models is becoming more and more popular in medicine [17]. On the basis of multifactor analysis, a model that integrates multiple predictive indicators and predicts the probability of an outcome event individually and accurately has achieved lots of predictive effects in many diseases [18].

Therefore, in this experiment, the nomogram mathematical model was adopted to predict the probability of recurrence of atrial fibrillation after postoperative viral infection, so as to study the influencing factors of treatment of cerebral infarction combined with NVAF and postoperative viral infection. The individualized mathematical model could provide valuable information for clinical treatment. Statistical methods combined with computer software analysis finally got the experimental results. It was hoped that the application of the mathematical model in this study could provide an effective basis for evaluation of disease prevention, policy decision-making, and the effect of health intervention programs, so as to achieve the rational use of medical resources.

2. Methods

2.1. Research Objects. Patients with cerebral infarction combined with VAF who were admitted to hospital from June 2018 to June 2020 were selected as the research objects in this study. The family members of the patients all were given informed consent and signed the unified informed consent. This study had been approved by the Ethics Committee of the hospital. The screening process of research objects is presented in Figure 1.

Inclusion criteria. The diagnostic criteria of acute ischemic cerebral infarction were referred to the Chinese Acute Ischemic Stroke Diagnosis and Treatment Guidelines 2018: patients suffered from acute onset, neurological deficits, and ischemic lesions shown by imaging examination caused by nonvascular causes; patients with atrial fibrillation proved by the electrocardiogram (ECG) and no heart valvular disease proved by heart color Doppler ultrasound; patients whose onset was less than 72 hours; and patients who voluntarily participated in this research. According to the American College of Cardiology Atrial Fibrillation Management Guidelines 2014, the atrial fibrillation was defined as a supraventricular tachyarrhythmia characterized by the electrocardiogram, disappeared P wave, appeared irregular atrial fibrillation waves, and absolutely irregular R-R interval.

Exclusion criteria. Patients with severe organ dysfunction; patients with transient ischemic attack without infarction; patients with motor, sensory, language, or higher cerebral cortical dysfunction caused by other noncerebrovascular diseases; patients without vascular causes; patients who were critically ill and could not cooperate to improve relevant auxiliary examinations; and patients who had received other treatments within three months.

Fifty-two patients with postoperative recurrent viral infection (RVI group) were selected, including 30 males and 22 females, aged 32–63 years, with an average age of 52.01 ± 7.08 years. 248 patients without recurrent viral infection after surgery (NRVI group) were selected, including 130 males and 118 females, aged 31–63 years, with an average age of 52.01 ± 8.13 years. The research objects were retrospectively analyzed, and all patients underwent CT scan. The oral hematemesis and clinical baseline of all patients who met the inclusion criteria and did not meet the exclusion criteria should be collected within 24 hours of admission, and their diagnosis and treatment information during the hospitalization had to be completed within 24 hours of discharge or death. After screening, the clinical data of all eligible patients were recorded, including database number, admission time, gender, age, hospitalization number, and onset time. CT examination was performed for the heads of all patients.

According to the patient demographic data and entries on the CHA_2DS_2-VASC scale and HAS-BLED scale, the following factors of patients were observed. Congestive heart failure (CHF): the patient suffered from a clear history of CHF, was diagnosed as heart failure during the hospitalization, and was confirmed by the ECG to meet the Boston diagnostic criteria. Diabetes: the patients had a clear history of diabetes (treated by oral hypoglycemic drugs or insulin), previous bleeding or bleeding tendency, and hemorrhagic stroke.

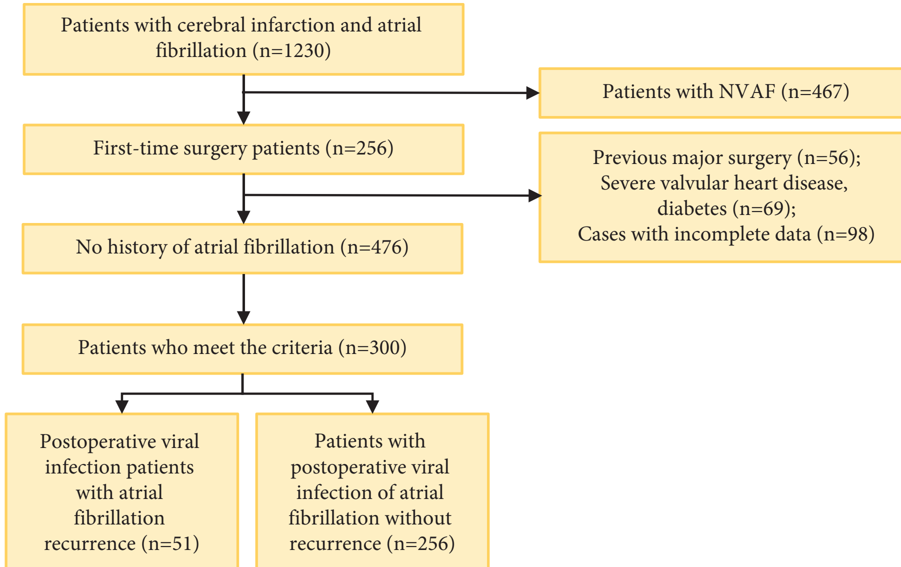

Figure 1: The screening process of research objects.

The patients in the observation group and the normal control group were descriptively analyzed. The distribution of each related factor in the cohort was calculated and performed with the single-factor analysis to clarify the statistical difference of each related variable in the distribution. *T* variable was applied for the linear variables, and the chi-square test was applied for the nonlinear variables. The CHF, hypertension, age ≥75 years, diabetes, and stroke/transient ischemic attack ($CHADS_2$) were scored from 5 indicators, as shown in Table 1.

2.2. Logistic Multivariate Regression Analysis. Logistic multivariate regression analysis was based on the premise of single-factor analysis to find relevant independent risk factors. The selection of independent variables of the logistic multivariate regression mathematical model was mainly based on Akaike information criterion (AIC) statistics.

The AIC was a trade-off between the complexity of the estimated model and the goodness of the model to fit the data, and it was a standard to measure the goodness of the statistical model. The calculation equation was AIC = 2k − 2ln(L), of which K represents the amount of model fitting parameters and *L* refers to the likelihood function.

Increasing the number of fitting parameters could effectively improve the goodness of model fitting, but it was prone to overfitting. The minimum AIC value was determined to select the fitting parameters and the corresponding model, which could effectively avoid overfitting when the model was excellent. AIC could find the model with the best interpretation of the data but with few free parameters.

2.3. CT Image Processing. Circular artifacts were more common in CT images, which were mainly due to the inconsistency of the detectors. There were many methods for image processing in the mathematical model, such as multifocus image fusion, Fourier transform, or high-pass filtering. The mathematical model of CT projection data was Radon transformation, which was actually some line integral values. The projection data were determined by the intensity of the object's ray, and the intensity was also related to the material composition of the object. If the initial intensity of the X-ray incident was E0, a binary function can be undertaken as the distribution of a certain fault of the detected object, and the emission intensity of the ray after passing through the object was E. The schematic diagram is shown in Figure 2.

According to Beer's law, the relationship between the initial intensity of the ray and the intensity of the ray was as follows:

$$E(L) = E_0 \exp\left\{-\int_L \mathrm{f}(x)\mathrm{d}l\right\}. \tag{1}$$

In equation (1), *L* represents the line where the ray lies, and d*l* was the integral element of the line. In equation (1), if r was expressed x, then the vector = (cos, sin), and the angle was the counterclockwise formed by the x1 axis and the normal of the straight line, r referred to the distance from the straight line to the origin of the coordinate. Then, the below equation could be obtained:

$$P(\delta, \mathrm{r}) = -\mathrm{In}\left(\frac{E}{E_0}\right) = \int_{LX\psi=r} \mathrm{f}(x)\mathrm{d}l. \tag{2}$$

The Radon change of the function *f(x)* was $P(\delta, \mathrm{r})$, which refers to the integral of *f(x)* along the straight line $r = \mathrm{x}\Psi$. When δ was fixed, $P(\delta, \mathrm{r})$ was a projection of *f(x)*.

In different scanning mathematical models, the projection data presented by the system were also different. In the current medical CT system, there was a spiral trajectory fan scan mode, and the original trajectory was equidistant. In this study, the circular track fan beam isometric scanning mode was used, and the schematic diagram of which is shown in Figure 3.

Table 1: Calculation methods of $CHADS_2$ score and derivative scores.

$CHADS_2$		CHA_2DS_2		R_2CHADS_2	
Risk factors	Score (s)	Risk factors	Score (s)	Risk factors	Score (s)
CHF	1	CHF	1	CHF	1
Diabetes	1	Diabetes	1	Diabetes	1
Age ≥75 years	1	Age ≥75 years	2	Age ≥75 years	1
Hypertension	1	Hypertension	1	Hypertension	1
Stroke/transient ischemic attack	2	Stroke/transient ischemic attack	2	Stroke/transient ischemic attack	2
		65 < age ≤ 75	1	Estimated glomerular filtration rate (GFR) ≤ 60	2
		Vascular disease	1		
		Female	1		
Total scores	6	Total scores	9	Total scores	8

Note: CHA_2DS_2 refers to CHF, hypertension, age ≥75 years [doubled], diabetes, stroke/transient ischemic attack. R_2CHADS_2 refers to renal dysfunction, CHF, hypertension, age ≥75 years, diabetes, stroke/transient ischemic attack.

Figure 2: The schematic diagram of Beer's law.

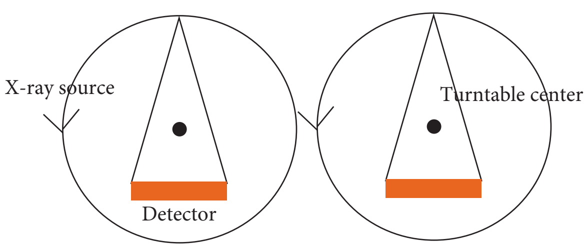

Figure 3: The schematic diagram of circular track fan beam isometric scanning mode.

Random speckle noise was a limitation of ultrasound images, caused by the interference of uneven fine tissue scattering. Due to the presence of noise, the spatial resolution of the image was reduced, and the interpretability of the image was reduced. Speckle noise was not conducive to the recognition of the image by the naked eye, and it concealed the effective features extracted by the image, so it was particularly important to effectively denoise the image. A better image denoising model was adopted in this study, and speckle noise was the correlation between multiplicative noise and image signal:

$$f(a,b) = g(a,b)\delta m(a,b). \quad (3)$$

In equation (3), *f(a, b)* represents the original image with noise, *g(a, b)* represents the uncertain noise-free image, and *δm(a, b)* refers to the multiplicative noise.

Image speckle denoising was also called multiplicative noise. Lee filtering was done to filter out image speckles based on the statistical characteristics of the image, select the length of the local area window on the speckle noise model, and obtain the prior mean and variance by calculating the local variance and mean.

$$\begin{aligned}
\hat{x} &= ax + by \\
\hat{x} &= \bar{x} + b(y + \bar{x}) \\
a &= 1 - \frac{\operatorname{var}(x)}{\operatorname{var}(y)} \\
b &= \frac{\operatorname{var}(x)}{\operatorname{var}(y)} \\
var(x) &= \frac{\operatorname{var}(y) - \beta_y^2 y^2}{1 + \beta_y^2}.
\end{aligned} \quad (4)$$

Equation (3) assumed the form of a linear filter; $\hat{x}$ and $\bar{x}$ were the minimum mean square estimate and the average value of x, respectively; and var(y) referred to the variance. If var(x) approached 0, it meant that the local area was uniform, and $\bar{x} = \hat{x}$ indicated the average pixel value in the window. If var(x) was relatively large, equal to y, it was the pixel value of the image itself, which meant that the noise in the marginal area could not be smoothed. The preprocess flow of the CT image is presented in Figure 4.

2.4. Model Evaluation. The AUC is defined as the area enclosed by the ROC curve and the coordinate axis, and the value of AUC ranges between 0.5 and 1. The closer the AUC is to 1.0, the higher the authenticity of the detection method. When it is equal to 0.5, the authenticity is the lowest. The recognition rate, sensitivity, and specificity were selected to evaluate the model construction, which were calculated using the below equations:

$$\begin{aligned}
\text{Accuracy} &= \frac{(TP + TN)}{(TP + TN + FP + FN)} \\
\text{Sensitivity} &= \frac{TP}{(TP + TN)} \\
\text{Specificity} &= \frac{TN}{(TN + FP)}.
\end{aligned} \quad (5)$$

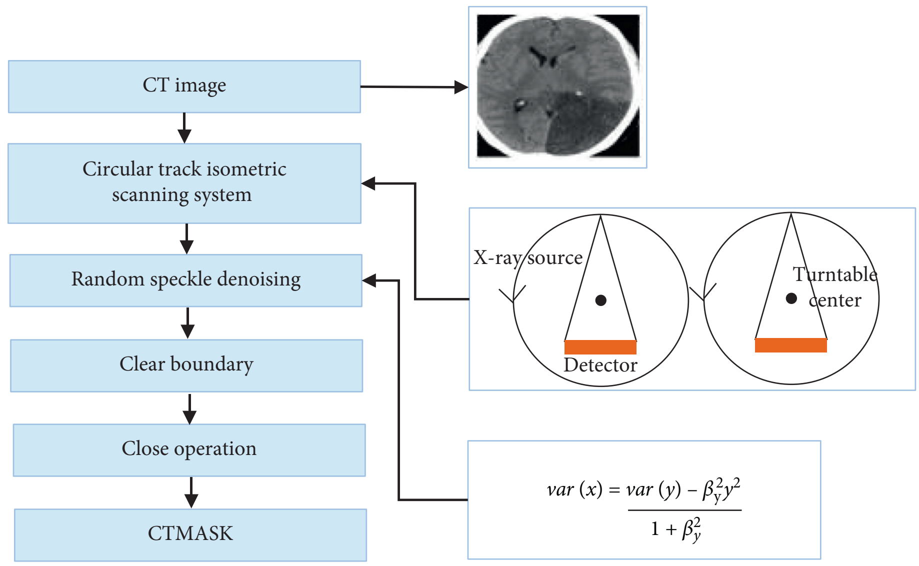

Figure 4: Preprocess flow of CT image.

Here, TP is the true positive, FP is the false positive, TN is the true negative, and FN is the false negative.

2.5. Statistical Methods. SPSS 22.0 software was adopted to perform statistical processing of the experimental data. Quantitative data were expressed in the form of mean ± standard deviation ($\overline{x} \pm S\,D$), and the independent sample t-test was used for difference comparison. The binary variables were given in the form of percentage (%), and the difference was compared using the chi-square test. $P < 0.05$ indicates that the difference between groups was statistically significant. On the basis of Logistic regression, the incidence probability of postoperative atrial fibrillation was predicted by using a line map, and the prediction ability and discrimination performance of the line map were evaluated. A consistent C-index Hull calibration curve was constructed. The larger the index, the more accurate the predicted value. The net income was quantified under different threshold probabilities to determine the clinical utility of the nomogram and verify the radical internal verification.

3. Results

3.1. Basic Data of Research Objects. The patient was followed up by telephone for three months after the onset of the disease to understand their quality of life in time, which was assessed using the modified Rankin Scale (mRS). The age, gender, coagulation function, cerebral infarction area, history of alcohol abuse, and CHF of the patients were assessed after admission, as shown in Table 2.

3.2. Analysis of Clinical Characteristics of the Two Groups. While the independent variables of the logistic multivariate regression model were selected, the Pearson correlation test can also be performed on the corresponding independent variables. If the two independent variables were statistically significantly correlated, the two independent variables and their interaction variables were put into the model, and the independent variables in the mathematical model were finally selected by AIC. It was necessary to further evaluate the nonlinearity of linear variables such as age to determine whether it was more suitable for the group model. The percentile was used to classify linear variables into nonlinear variables, which was subjective, so that some important information was lost. Therefore, the use of restricted cubic splines had a very good performance for the fitting of the model. The results of logistic multivariate regression analysis on the clinical characteristics between patients in the RVI group and NRVI group after atrial fibrillation are provided in Table 3.

3.3. Example of Nomogram. A 60-year-old patient was selected as an example. As illustrated in Figure 5, the corresponding score for the age variable was 50 and the score for peripheral arterial disease was 70. If the left atrium diameter increased by 43 mm when the patient was hospitalized, the corresponding score for the left atrium was 25. In the postoperative follow-up, if the AV-VP was less than 50%, the corresponding score of AP-VP was 0, and the sum of the above was 145. Analysis of the corresponding data on the total score axis and the new-onset AF axis showed that the risk of recurrence of atrial fibrillation was 50%.

3.4. Verification of Prediction Model. The prediction model showed higher effects on the recurrence of atrial fibrillation caused by viral infection on both the training set and the validation set (as shown in Figure 6). The AUC, sensitivity, specificity, and accuracy on the training set were 0.7868, 0.7634, 0.6982, and 0.7146, respectively; and those on the validation set were 0.7623, 0.7734, 0.6882, and 0.6948, respectively. There was no visible difference in the AUC between the two groups ($P > 0.05$), indicating that the nomogram prediction model showed high repeatability. The

Table 2: Basic data of research objects.

Factor	mRS ≤2	mRS >3	X^2/t	P
Score of stroke at admission	9.00 (4.00, 11.00)	10.00 (7.00, 14.00)	−4.138	≤0.001
Age	68.72 ± 5.62	70.35 ± 5.81	−1.321	0.136
Coagulation function	1.07 ± 0.05	1.06 ± 0.03	−1.876	0.043
Gender	54	43	0.028	0.812
Cerebral infarction area	49	20	4.861	0.011
History of alcohol abuse	60	51	1.621	0.172
CHF	72	50	0.065	0.658

Table 3: Comparison of clinical characteristics between patients in the RVI group and NRVI group after atrial fibrillation.

Variable	Patients in the RVI group ($n = 52$)	Patients in the NRVI group ($n = 248$)	P
Diabetes (%)	11 (21.15)	48 (19.35)	0.287
Hyperlipidemia (%)	7 (13.46)	26 (10.48)	0.072
Diuretics (%)	6 (11.54)	21 (8.47)	0.154
Beta blockers (%)	7 (13.46)	27 (10.89)	0.132
Lipid-lowering drugs (%)	23 (44.23)	68 (27.42)	0.045
COPD (%)	2 (0.038)	13 (0.052)	0.218
Antiplatelet drugs (%)	19 (36.54)	72 (0.29)	0.467
Active atrial electrode (%)	28 (53.85)	145 (58.47)	0.523
Active ventricular electrode (%)	38 (73.08)	208 (83.87)	0.765
Cardiac ultrasound			
LVEF (%)	5 (9.62)	8 (3.23)	0.231
LAD (%)	21 (40.38)	61 (24.90)	0.056
Laboratory indicators			
BUN (mg/L)	5.26 (±1.86)	5.89 (±2.12)	0.248
C-reactive protein (mg/L)	1.5 (0.5–3.9)	1.5 (0.5–4.2)	0.543
Follow-up parameters			
AP-VP ≥ 50 (%)	11 (21.15)	19 (7.66)	0.012
AP ≥ 50 (%)	28 (53.84)	82 (33.06)	0.038
VP ≥ 50 (%)	29 (55.77)	89 (35.89)	0.069

Note: COPD refers to chronic obstructive pulmonary disease; LEVF refers to left ventricular ejection fraction; BUN represents blood urea nitrogen; VP refers to the score of sepsis-related organ failure assessment; and AP is the short form of adapted physical activity and cardiac coherence in hematologic patients (APACCHE).

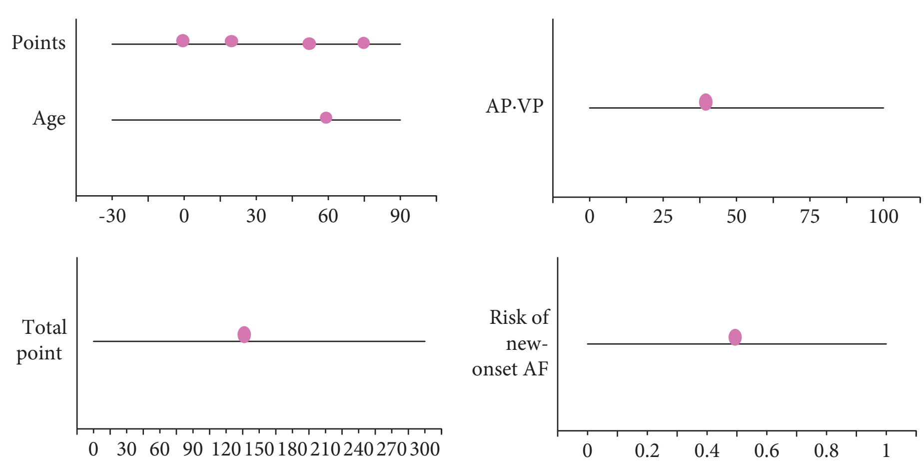

Figure 5: Nomogram figure of a patient with cerebral infarction combined with NVAF.

model calibration training graph revealed that the graph was closer to the diagonal, indicating that the prediction was highly consistent with the observation result, so the model had a good predictive ability.

3.5. CT Images of Cerebral Infarction. Figure 7 shows the CT images of patients with cerebral infarction combined with NVAF after viral infection after surgery. The cerebral sulcus around the infarcted vessel was swollen, the lenticular

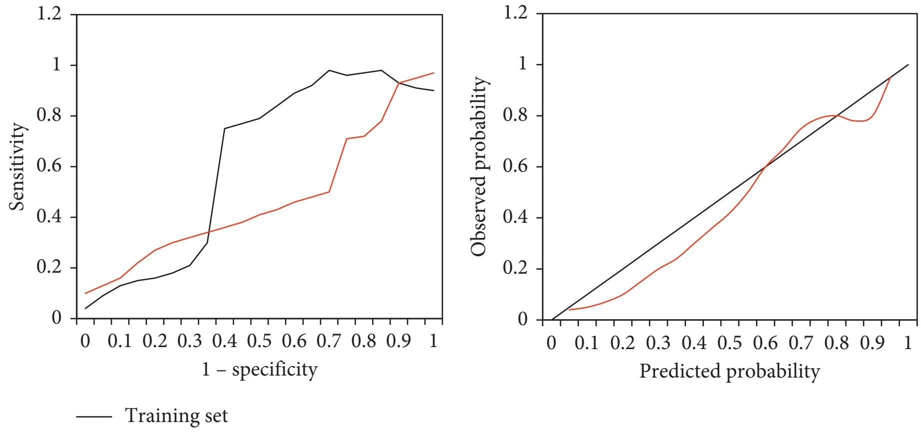

FIGURE 6: The ROC curve and model calibration curve of the prediction model on the training set and validation set. * indicates the difference was statistically obvious ($P < 0.05$).

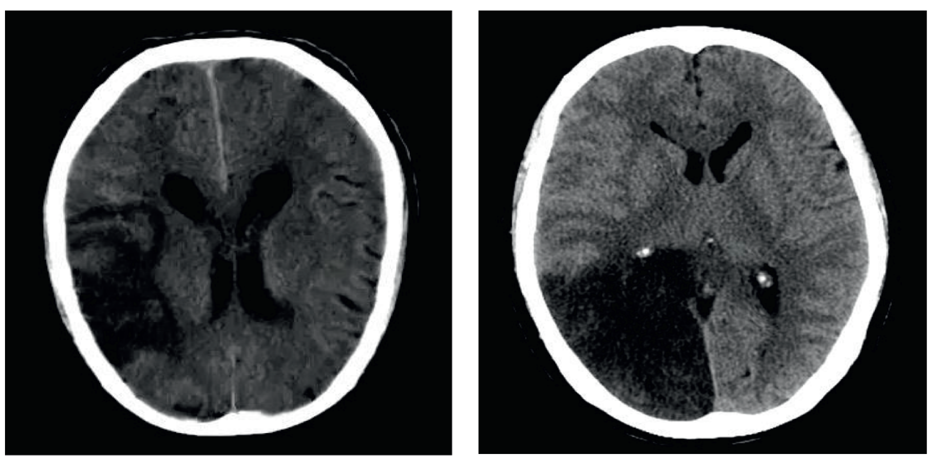

FIGURE 7: CT images of cerebral infarction.

nucleus was fuzzy, and the density of cerebrospinal fluid was greatly reduced.

3.6. The Clinical Value of Nomogram. In clinical application, the clinical decision curve is a new method for evaluating the predictive models. The nomogram of atrial fibrillation caused by viral infection is shown in Figure 8. The purple solid line represents the nomogram model of new-onset atrial fibrillation after postoperative viral infection, the yellow dashed line represents the single-factor predictive model of AP-VP ≥ 50%, and the red solid line indicates that all patients had postoperative new-onset cerebral infarction combined with NVAF. The X-axis represents the valve probability, and the Y-axis represents the net benefit. The range of the probability of occurrence was within the range of 12%–40%. The clinical net benefit of the mathematical prediction model of the nomogram in the study was higher than that of the single-factor model of AP-VP ≥ 50% and left atrial diameter. Such results indicated that the mathematical prediction model of this study had clinical application value.

4. Discussion

By staining atrial tissue from patients with atrial fibrillation, the researchers found macrophages, high expression of tumor-transforming factors, and other inflammatory factors. Inflammatory factors interfere with cardiomyocytes and induce fibroblast activation. Serum levels in patients with atrial fibrillation are affected by cardiovascular disease. Viral infection leads to recurrence of atrial fibrillation, which is associated with local inflammation caused by viral invasion of myocardial tissue. Ikeda et al. (2019) [19] analyzed the dose of oral anticoagulant rivaroxaban in patients with NVAF, and different doses had different clinical treatments for patients. In patients with acute ischemic stroke and nonvalvular atrial fibrillation, pre-event DOAC treatment was associated with smaller infarct volume and a reduced risk of proximal large-artery occlusion compared with no anticoagulation. During the postoperative follow-up of the patients in this work, if the AV-VP was less than 50%, the corresponding AP-VP score was 0, and the sum of the above scores was 145. Analysis of the corresponding data on the

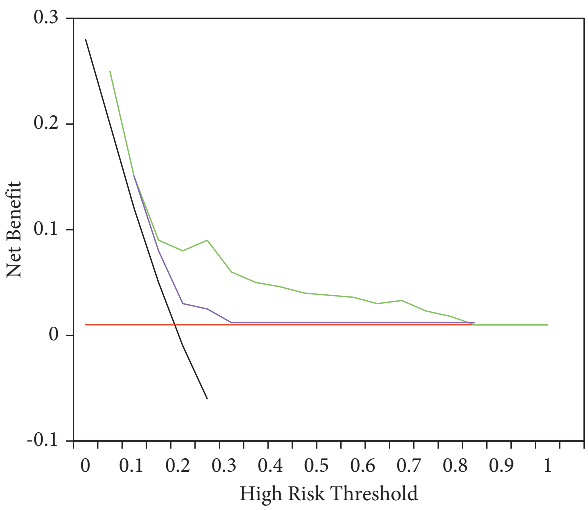

Figure 8: Clinical decision curve of the predictive model of atrial fibrillation after viral infection.

total score subaxis and the new-onset AF axis showed a 50% risk of AF recurrence.

The nomogram is an analysis method that integrates multiple predictive indicators. After a multifactor regression analysis is performed, the same square meter is drawn with a reference line graph, which can predict the resolution of the indicators and clarify the relationship between the indicators. This method is quickly applied clinically and achieved ideal prediction results. Borumandnia et al. (2021) [20] applied the nomogram to the survival prediction evaluation of patients with rectal cancer, and the results showed that it can help patients with rectal cancer to solve clinical decision-making and prognosis prediction. Xia et al. (2017) [21] applied the nomogram mathematical prediction model to the prediction of cardiovascular disease in peritoneal dialysis patients, and the nomogram can accurately predict the cardiovascular death factors of patients. In this study, the existing medical records were reviewed and analyzed, the risk factors were explored, and a simple nomogram was established as a tool to predict the occurrence of atrial fibrillation in viral infections, whose effectiveness was verified accordingly. A mathematical model was constructed to analyze the characteristics of the CT images of patients. After sorting, the characteristics of the normalized image were extracted. The algorithm ignored the difference in image intensity and autonomously recognized the interpretability of ultrasound images for a more detailed analysis of the risk factors of atrial fibrillation in patients with viral infection. In this study, the prediction model showed higher effects on the recurrence of atrial fibrillation caused by viral infection on both the training set and validation set. The accuracy on the training set was 0.7146, and the accuracy on the validation set was 0.6948. There was no observable difference in the AUC between the two groups ($P > 0.05$), indicating that the nomogram prediction model had high repeatability. The model calibration training graph revealed that the graph was closer to the diagonal, indicating that it had better predictive resolution. The range of the probability of occurrence was within the range of 12%–40%. The clinical net benefit of the mathematical prediction model of the nomogram in the study was higher than that of the single-factor model of AP-VP ≥ 50% and left atrial diameter. Such results indicated that the mathematical prediction model of this study had clinical application value.

5. Conclusion

In this study, the existing medical records were reviewed and analyzed, the risk factors were explored, and a simple nomogram was established as a tool to predict the occurrence of atrial fibrillation in viral infections, whose effectiveness was verified accordingly. A mathematical model was constructed to analyze the characteristics of the CT images of patients, so as to analyze the risk factors of atrial fibrillation in patients with viral infection. The prediction model showed higher effects on the recurrence of atrial fibrillation caused by viral infection on both the training set and validation set. The new nomogram used in this study had a good predictive efficiency and could help physicians identify the risk of atrial fibrillation due to viral infection in the clinic. However, there were still missing values and erroneous data in the model data set in this work, and the imputation of the data in the later stage would affect the analysis results of the data. Further validation of the nomogram prediction model from different data sets is required in future research [2, 21].

Data Availability

The data used to support the findings of this study are available from the corresponding author upon request.

Conflicts of Interest

The authors declare that there are no conflicts of interest.

Authors' Contributions

Yi Zhu and Hai Cheng contribute equally to this work.

References

[1] H.-Y. Guo, J.-T. Lin, H.-H. Huang et al., "Development and validation of a 18F-fdg PET/CT-Based clinical prediction model for estimating malignancy in solid pulmonary nodules based on a population with high prevalence of malignancy," *Clinical Lung Cancer*, vol. 21, no. 1, pp. 47–55, 2020.

[2] I. Deguchi, T. Osada, and M. Takao, "Prescription status of oral anticoagulants in patients with acute cerebral infarction with non-valvular atrial fibrillation at the time of stroke onset," *Journal of Cardiology*, vol. 75, no. 5, pp. 544–548, 2020.

[3] S. Yasuda, K. Kaikita, H. Ogawa et al., "Atrial fibrillation and ischemic events with rivaroxaban in patients with stable coronary artery disease (AFIRE): protocol for a multicenter, prospective, randomized, open-label, parallel group study," *International Journal of Cardiology*, vol. 265, pp. 108–112, 2018.

[4] C.-H. Lee, K.-H. Jung, D. J. Cho, and S.-K. Jeong, "Effect of warfarin versus aspirin on blood viscosity in cardioembolic stroke with atrial fibrillation: a prospective clinical trial," *BMC Neurology*, vol. 19, no. 1, p. 82, 2019.

[5] H. G. Woo, I. Chung, D. S. Gwak et al., "Recurrent ischemic stroke in atrial fibrillation with non-vitamin K antagonist oral anticoagulation," *Journal of Clinical Neuroscience*, vol. 64, pp. 127–133, 2019.

[6] K.-S. Hong, S. U. Kwon, S. H. Lee et al., "Rivaroxaban v s warfarin sodium in the ultra-early period after atrial fibrillation-related mild ischemic stroke," *JAMA Neurology*, PMCID, vol. 74, no. 10, pp. 1206–1215, 2017.

[7] Y. Zhu, H. Cheng, R. Min, and T. Wu, "WITHDRAWN: diagnosis of neural deterioration in patients with cerebral infarction combined with non-valvular atrial fibrillation under magnetic resonance imaging and exploration of the prognostic infection factors," *Neuroscience Letters*, vol. 15, Article ID 135213, 2020.

[8] T. Ikeda, S. Ogawa, T. Kitazono et al., "Real-world outcomes of the xarelto post-authorization safety & effectiveness study in Japanese patients with atrial fibrillation (XAPASS)," *Journal of Cardiology*, vol. 74, no. 1, pp. 60–66, 2019.

[9] G. Zapata-Wainberg, J. Masjuan, S. Quintas, Á. Ximénez-Carrillo, and Garc, A. a Pastor and Mart, M. nez Zabaleta, P. Cardona, M. M. Freijo Guerrero, L. Llull, and Benavente Fern, L. ndez, M. Castellanos Rodrigo, J. Egido, J. Serena, and J. Vivancos, The neurologist's approach to cerebral infarct and transient ischaemic attack in patients receiving anticoagulant treatment for non-valvular atrial fibrillation: ANITA-FA study," *European Journal of Neurology*, vol. 26, no. 2, pp. 230–237, 2019.

[10] S. H. Lee, K.-S. Hong, J. S. Lee et al., "Prediction of hemorrhagic transformation in patients with mild atrial fibrillation-associated stroke treated with early anticoagulation: post hoc analysis of the Triple AXEL Trial," *Clinical Neurology and Neurosurgery*, vol. 174, pp. 156–162, 2018.

[11] C. W. Park, H. S. Nam, J. H. Heo et al., "Non-vitamin K oral anticoagulants as first-line regimen for acute ischemic stroke with non-valvular atrial fibrillation," *Journal of Stroke and Cerebrovascular Diseases*, vol. 29, no. 9, Article ID 105025, 2020.

[12] J. Romero, R. C. Cerrud-Rodriguez, J. C. Diaz et al., "Uninterrupted direct oral anticoagulants vs. uninterrupted vitamin K antagonists during catheter ablation of non-valvular atrial fibrillation: a systematic review and meta-analysis of randomized controlled trials," *EP Europace*, vol. 20, no. 10, pp. 1612–1620, 2018.

[13] A. Desai, C. Escamilla-Ocanas, D. Dilip, H. Saber, and R. Damani, "Risk of stroke vs. Intracerebral hemorrhage in patients with non-valvular atrial fibrillation undergoing percutaneous coronary intervention: a systematic review and meta-analysis of randomized controlled trials comparing dual vs. Triple antithrombotic therapy," *Journal of Stroke and Cerebrovascular Diseases*, vol. 30, no. 4, p. 105654, 2021.

[14] S. Hanada, M. Pirzadeh, K. Y. Carver, and J. C. Deng, "Respiratory viral infection-induced microbiome alterations and secondary bacterial pneumonia," *Frontiers in Immunology*, PMCID, vol. 9, p. 2640, 2018.

[15] C. J. Klijn, M. Paciaroni, E. Berge, E. Korompoki, and K, J. rv, A. Lal, J. Putaala, and D. J. Werring, Antithrombotic treatment for secondary prevention of stroke and other thromboembolic events in patients with stroke or transient ischemic attack and non-valvular atrial fibrillation: a European Stroke Organisation guideline," *European Stroke Journal*, vol. 4, no. 3, pp. 198–223, 2019.

[16] I. Sakuma, S. Uchiyama, H. Atarashi et al., "Clinical risk factors of stroke and major bleeding in patients with non-valvular atrial fibrillation under rivaroxaban: the EXPAND Study sub-analysis," *Heart and Vessels*, vol. 34, no. 11, pp. 1839–1851, 2019.

[17] J. Steffel, P. Verhamme, T. S. Potpara et al., H. chel, G. Y. H. Lip, J. Weitz et al., The 2018 European Heart Rhythm Association Practical Guide on the use of non-vitamin K antagonist oral anticoagulants in patients with atrial fibrillation," *European Heart Journal*, vol. 39, no. 16, pp. 1330–1393, 2018.

[18] H. Heidbuchel, P. Verhamme, M. Alings et al., "Updated European Heart Rhythm Association practical guide on the use of non-vitamin-K antagonist anticoagulants in patients with non-valvular atrial fibrillation: executive summary," *European Heart Journal*, vol. 38, no. 27, pp. ehw058–2149, 2017.

[19] T. Ikeda, S. Ogawa, T. Kitazono et al., "Outcomes associated with under-dosing of rivaroxaban for management of non-valvular atrial fibrillation in real-world Japanese clinical settings," *Journal of Thrombosis and Thrombolysis*, PMCID, vol. 48, no. 4, pp. 653–660, 2019.

[20] N. Borumandnia, H. Doosti, A. Jalali et al., "Nomogram to predict the overall survival of colorectal cancer patients: a multicenter national study," *International Journal of Environmental Research and Public Health*, PMCID, vol. 18, no. 15, p. 7734, 2021.

[21] X. Xia, C. Zhao, Q. Luo et al., "Nomogram for predicting cardiovascular mortality in incident peritoneal dialysis patients: an observational study," *Scientific Reports*, PMCID, vol. 7, no. 1, Article ID 13889, 2017.

Hindawi
Contrast Media & Molecular Imaging
Volume 2022, Article ID 1183988, 10 pages
https://doi.org/10.1155/2022/1183988

Research Article

Implementation of Hospital-to-Home Model for Nutritional Nursing Management of Patients with Chronic Kidney Disease Using Artificial Intelligence Algorithm Combined with CT Internet +

Xing Chen[1], **Xueqin Huang**[1], **and Mingyuan Yin**[2]

[1]*Department of Internal Medicine, Hunan Provincial People's Hospital, Changsha 410005, Hunan, China*
[2]*Department of Nursing, Hunan Provincial People's Hospital, Changsha 410005, Hunan, China*

Correspondence should be addressed to Mingyuan Yin; 2018060000028@jlxy.nju.edu.cn

Received 31 December 2021; Revised 18 February 2022; Accepted 21 February 2022; Published 27 March 2022

Academic Editor: M Pallikonda Rajasekaran

The objective of this study was to evaluate the application value of "Internet + hospital-to-home (H2H)" nutritional care model using the improved wavelet transform algorithm based on computed tomography (CT) images in the nutritional care management of chronic kidney disease (CKD) stages 3-5. A total of 120 patients with CKD were the research objects and they were randomly divided into two groups. The normal nutritional nursing model was used for nursing of patients in the control group, and the "Internet + *H*2H″ model was used for the observation group (H2H group), with 60 cases in each group. The nursing effect was evaluated using 320-slice volume CT low-dose perfusion imaging images, anthropometry, laboratory biochemical tests, and other survey scores. The results showed that compared with the mean filter denoising (MFD) algorithm and the orthogonal wavelet denoising (OWD) algorithm, the mean square error (MSE) and signal noise ratio (SNR) values of the IWT algorithm were better (40.0781 vs 45.2891, 59.2123)/(20.0122 vs 18.2311, 15.7812) ($P < 0.05$). The arm muscle circumference (MAC) (239.77 ± 18.24 vs 243.94 ± 18.72 mm) and triceps skindold (TSF) value (8.87 ± 2.74 vs 10.04 ± 2.90 mm) of the patients in the H2H group were greatly improved after the nursing ($P < 0.05$). For biochemical indicators, serum albumin (ALB) (35.22 ± 4.98 vs 45.32 ± 4.21) g/L, prealbumin (PAB) (289.94 ± 72.99 vs 341.79 ± 74.45) mg/L, hemoglobin (Hb) (97.62 ± 24.87 vs 110.65 ± 28.83) g/L, and blood urea nitrogen (BUN) (15.74 ± 9.87 vs 11.06 ± 5.69) mmol/L of patients in H2H group were improved ($P < 0.05$). After nursing, the nutritional screening score of the H2H group was obviously improved (83.33% (before) vs 50% (after)), the total score of health quality assessment (114.89 ± 5.23) in the H2H group was much higher than that of the control group (87.22 ± 14.89), and the satisfaction on the nursing model was higher in the H2H group (100% vs 71.67%) ($P < 0.05$). The renal cortex BF before and after nursing was significantly different between the two groups of patients ($P < 0.05$), and the BE of the H2H group was significantly higher than that of the control group after treatment ((335.12 ± 52.74) $mL \cdot 100\,g^{-1} \cdot min^{-1}$ vs (289.90 ± 53.91) $mL \cdot 100\,g^{-1} \cdot min^{-1}$) ($P < 0.05$). In summary, the "Internet + *H*2H″ nutritional nursing model was more individualized, which can better improve the physical quality of patients with stages 3-5 of CKD, improve the psychological state of patients, and further enhance the prognosis of the disease. In addition, the IWT algorithm showed better effects in the processing of the image of 320-slice volume CT low-dose perfusion imaging, and it was worthy of clinical application.

1. Introduction

Chronic kidney disease (CKD) refers to the structure and function of the kidney caused by various reasons, and the onset time is more than 3 months [1, 2]. With the continuous increase in the number of CKD patients in recent years, the number of CKD patients worldwide has exceeded 850 million, and China has also exceeded 100 million [3]. It has been clinically found that patients with CKD 3-5 stages are prone to abnormal gastrointestinal function, endocrine dysfunction, metabolic acidosis, comorbidity [4], systemic microinflammatory state [5], decreased renal function, and accumulation of uremic toxins, causing a series of problems in the patient's body nutrition [6]. According to statistics, the disability rate and fatality rate of CKD rank first in chronic diseases, which is greatly related to the nutritional problems in the development of CKD [7]. Therefore, the improvement of nutritional problems is of great significance for improving the quality of life of patients and reducing the mortality and disability rate of patients.

At present, the commonly used clinical nutritional management method for chronic diseases is a continuous nutritional nursing model, which is called hospital to home (H2H). It is a hierarchical management model of hospital-community-home, emphasizing the continuity, individualization, and participation of patients and family members of nutritional management [8]. Studies have shown that the continuous and professional H2H management model meets the needs of patients in many ways and improves the overall effect of treatment [9]. In recent years, Internet technology has also been integrated into the H2H nutritional nursing model, forming an "Internet + $H2H''$ model. "Internet +" can use information technology and Internet platforms to deeply integrate various fields of society, so as to optimize the allocation and integration of social resources and create a new development ecology [10]. Studies have shown that a service platform based on "Internet +" can retain all nursing resources, which is convenient for patients to check repeatedly and enhance self-nursing awareness [11].

To further understand the application effect of the "Internet +" H2H nutrition care model in patients with CKD, CT was adopted to evaluate the renal status of the patients before and after the application of the nutrition care model. Clinical studies have shown that the blood flow status in the kidney can reflect its physiological and pathological conditions, and CT perfusion imaging of the kidney is an examination method that shows the microcirculation information of living tissues [12, 13]. At this stage, the radiation and the reproducibility of perfusion results in renal CT perfusion imaging technology are clinical research hotspots. The study proposed a 320-slice CT 16 cm wide detector. The scanning mode used by 320-slice CT is the nonmoving bed volume perfusion mode. The kidneys are in the same phase during the scanning process, which makes the measurement of renal cortex blood flow more accurate [14]. In order to reduce the amount of radiation in the CT examination process, low-dose perfusion can also affect people's perfusion. However, most of the images in the low-dose imaging process will have noise pollution, and the image display is not clear, which affects the accuracy of the examination results. In order to make the results of CT perfusion imaging more conducive to analysis and comparison, artificial intelligence algorithms were adopted in this study to denoise CT images. The wavelet transform denoising algorithm has been extensively studied in the optimization of CT images [15]. In order to improve their denoising performance, some research experts have carried out improved research on the wavelet transform algorithm. Research has shown that the improved wavelet transform denoising (IWT) algorithm can obtain effective application effects [16, 17].

In summary, this study used the Internet + $H2$H nutritional nursing model for patients with CKD in stages 3-5, adopted the 320-slice volume CT low-dose perfusion imaging examination image based on the IWT algorithm and other examination indexes for analysis and comparison, and evaluated the application value of the "Internet + $H2H''$ nutritional nursing model, aiming to provide a reasonable research basis for continuous nutrition management services for CKD patients in clinical practice.

2. Research Methods

2.1. Research Objects. In this study, 120 patients with CKD admitted to the hospital from March 2019 to March 2021 were randomly selected as the research objects. Among them, 66 were male patients and 56 were female patients. They were between 38 and 78 years old, with an average age of 62.34 ± 13.09 years old. There were 4 patients with an education level of elementary school and below, 34 with junior high school, 64 with high school/technical secondary school, and 18 with junior college and above. There were 25 patients with a family monthly income of less than RMB 3,000 and 95 patients with RMB 3,000 and above; there were 32 patients with CKD in stage 3, 58 patients with stage 4, and 40 patients with stage 5. A random number table method was used to divide 120 patients into two groups, which were set as the control group and the observation group (H2H group). The number of patients in both groups was 60. The patients in the control group used the conventional nutritional nursing model for nursing, and the patients in the H2H group use the "Internet +" H2H nutritional nursing model. Then the 320-slice volume CT low-dose perfusion imaging images based on the IWT algorithm, anthropometry, laboratory biochemical testing, and other survey scores were adopted to evaluate the application effect of the nutritional nursing model of the two groups of patients. This study had been approved by the ethics committee of hospital and all the research objects included in this study had signed the agreement.

Patients included in this study had to meet the following criteria: patients who met the diagnostic criteria of CKD [18], patients with CKD in stages 3-5 (the clinical staging criteria of CKD are listed in Table 1) and in stable condition. Patients whose main caregivers supported cooking at home or eating out <3 times/week, patients with clear consciousness and with certain language skills and smartphones, patients ≥18 years old, and patients who signed the informed consents and voluntarily participated in this study.

Patients who met the following criteria had to be excluded from this study: those with severe cognitive, mental, and language impairment; those with severe complications and severe damage to important organs; patients who received renal replacement therapy; those who were participating in other intervention studies.

2.2. Interventions. Patients in the control group received the conventional nutritional nursing model, while the patients in the H2H group were received the "Internet+" combined H2H management model.

Table 1: Comparison of the laboratory biochemical indexes of the two groups of patients before nutritional nursing and 6 months after nursing.

Biochemical indexes	Control group ($n = 60$)		H2H group ($n = 60$)	
	Before nursing	Six months after nursing	Before nursing	Six months after nursing
ALB (g/L)	34.32 ± 10.21	36.32 ± 9.89	35.22 ± 4.98	$45.32 \pm 4.21^*$
PAB (mg/L)	297.74 ± 71.82	307.12 ± 72.81	289.94 ± 72.99	$341.79 \pm 74.45^*$
Hb (g/L)	98.61 ± 24.87	103.61 ± 24.87	97.62 ± 24.87	$110.65 \pm 28.83^*$
BUN (mmol/L)	15.28 ± 12.34	15.40 ± 11.68	15.74 ± 9.87	$11.06 \pm 5.69^*$
SCr (μmol/L)	548.95 ± 115.50	547.98 ± 101.87	551.70 ± 115.28	$543.59 \pm 115.33^*$

$^*P < 0.05$ indicates the difference was statistically significant, compared with "H2H group before nursing."

2.2.1. Routine Nutrition Management Model

(i) Routine health education after admission: to inform patients and their families about the importance and continuity of nutritional support for CKD and the necessity of standardized treatment and follow-up outside the hospital.

(ii) To choose a variety of foods that are nutritionally sound: it should be emphasized that adequate energy intake should be ensured while appropriately restricting protein intake to prevent malnutrition.

(iii) Regular and quantitative meals: the energy of breakfast, lunch, and dinner can account for 20%–30% and 30%–35% of the total energy. The protein of three meals should be evenly distributed.

(iv) To limit the intake of plant proteins such as rice and noodles: it can take wheat starch (or other starches) as the staple food to replace ordinary rice and noodles and add appropriate amounts of milk, eggs, or various meats, soybeans, and other high-quality protein foods.

(v) When the disease requires restricting foods with high phosphorus content, it should carefully choose animal liver, nuts, dried beans, and various phosphorus-containing processed foods.

(vi) When the disease requires restricting foods with high potassium content, it should carefully choose fruits, potatoes and their starches, green leafy vegetables, etc.

(vii) Discharge guidance before discharge should be guaranteed with high quality, and regular telephone follow-up must be carried out after discharge to instruct patients to follow up on time.

2.2.2. Internet + H2H Care Model. First of all, the H2H management team and wechat management team should be established. The team consisted of 1 team leader (as the head nurse of the section), 1 consultant (as the section director), and 6 team members (1 nephrologist, 5 specialist nurses, and 1 dietitian). Secondly, all members of the team had to be trained. The training contents included kidney disease nutrition-related knowledge (9 credit hours), Internet nutrition management platform operation and common problem handling (1 credit hour), enrollment and data collection of patients (1 credit hour), and communication skills (1 credit hour).

The nephrologist was responsible for the overall treatment plan. The nutritionist was responsible for formulating individualized nutrition support plans and data collection for patients during and after discharge from the hospital and recorded clinical data of inpatients-including general data (name, gender, age, height, weight, blood pressure, blood sugar, etc.) and laboratory indicators (blood creatinine, urea nitrogen, uric acid, electrolytes, etc.) on the Internet platform. Specialist nurses were responsible for guiding patients to register on the Internet platform, providing platform operation guidance for patients and main caregivers (general data and laboratory index entry-data entry or uploading photos, online consultation, recipe viewing, etc.), ensuring that patients and the main caregiver were proficient in platform operation and other issues such as health education, data collection, assistance, and supervision of the implementation of the plan. Group members communicated and discussed the patient's situation once a month through video conferences and kept in close contact through WeChat groups during the rest of the period. After the initial treatment plan and nutrition plan of the patient were formulated, it was necessary to study and discuss it in the WeChat group to ensure that all members of the management team were fully aware and understood and to discuss the feasibility of the plan and the cooperation steps among members.

After the patient was admitted to the hospital, the nutritionist formulated individualized dietary prescriptions based on the patient's general information, laboratory indicators, allergy history, and communication with the nephrologist, explained the dietary prescriptions to the patient and the main caregivers in detail, and informed the precautions. The patient's general information and laboratory indicators were entered into the Internet platform. The platform automatically generated recipes for three meals a day, and the recipes were updated every three days. Group members patiently answered questions raised by patients.

On the day, the patient was discharged from the hospital, the specialist nurse urged the patient and the main caregiver to enter the patient's last laboratory indicators and the patient's weight, blood pressure, blood glucose, and other data into the Internet platform and checked whether the data entry was correct. After the patients discharged from the hospital, the Internet platform automatically sent three meals a day recipes and health education to the patients, reminded the patients to return to the clinic, and provided online consultation services to the patients. During the stay at home, patients should go to the community or hospital for re-examination according to the platform's re-examination reminder time limit and upload the re-examination laboratory indicators and general information to the Internet platform in time. Nutritionists assessed the nutritional status and support needs of the patients based on the results of the patient review and screened patients with malnutrition and high risk. Specialist nurses supervised and urged patients to implement nutritional programs. If patients had any questions, they can consult a doctor, nutritionist, or specialist nurse online on the platform.

2.3. IWT Algorithm. Among the wavelet transform algorithms, the image denoising method of OWD [19] has been widely used in image processing. However, this method can produce artificial noise, and the image reconstruction can affect a single wavelet coefficient due to the degree of translation. It has a strong dependence, which makes it difficult to choose the wavelet denoising threshold. Research shows that the dyadic wavelet transform (DWT) algorithm has translation invariance. Therefore, under the same misjudgment probability, the DWT algorithm has a better denoising effect [20].

In the processing of two-dimensional images, the DWT algorithm used multiple mother wavelet functions in different spatial directions for calculation, which could be specifically expressed as follows:

$$\left\{\varphi^{d}\right\}_{1\le d\le D}. \tag{1}$$

Here, d represented the airspace direction, $d = 1$ represented the horizontal direction, $d = 1$ represented the vertical direction, and φ referred to the wavelet function. The two-dimensional discrete function can be expressed as follows:

$$f(m,n)\in l^{2}\left(z^{2}\right). \tag{2}$$

Here, l represented the parameter in the horizontal direction and z represented the dispersion coefficient. Then, the corresponding finite-order dyadic wavelet transform can be expressed as follows:

$$W[f(m,n)]=\left\{W_j^d[f(m,n)]_{d=1,2;1\le j\le J},S_J[f(m,n)]\right\}. \tag{3}$$

Here, *(m, n)* represented the position, j represented the scale, $W_j^d[f(m,n)]$ referred to the transform coefficient of the wavelet function $f(m,n)$ at the location of *(m, n)*, scale of j, and direction of d, and $S_J[f(m,n)]$ was the approximate value of the location of *(m, n)* and the maximum scale of J.

In the denoising process of the DWT algorithm, the selection of the threshold is a key issue. The general threshold is easy to smooth the image, making the image too blurry. In this study, a new threshold was adopted, which could be calculated with the following equation:

$$\lambda_j=\sqrt{\log\frac{L_j}{J}\frac{\sigma_j^{2}}{\beta_j}}. \tag{4}$$

Here, J represented the number of decomposition layers of the scale, L_j represented the subband width on the j-th scale, σ_j represented the standard deviation of the noise on the j-th scale, and β_j was the variance of the coefficient component matrix on each scale.

From the decomposition structure of the wavelet transform, the noise variance expression of the j-th order can be obtained as follows:

$$\sigma_j^{2}=\sigma^2\left|\left(\sum_{i=0}^{j-2}*h_i\right)*g^{j-1}\right|_F\bullet\left|\left(\sum_{i=0}^{j-2}*h_i\right)\right|_F. \tag{5}$$

Here, σ^2 represented the variance of the original image noise, $*$ represented the convolution, $\|_F\bullet_F\|$ represented the norm, h_i referred to the filter coefficient formed by inserting 2^j-1 zeros after the filter coefficient h_{i-1}, and g^{j-1} represented the filter coefficient g^{j-2} formed by inserting 2^j-1 zeros before the filter coefficient. Since the variance of the noise of the original CT image was unknown, it needed to be estimated. If the wavelet coefficients on the smallest scale are used to estimate, the estimated value is as follows:

$$\sigma=\frac{\text{median}\left(\left|W_j^d f\right|\right)}{0.6745}. \tag{6}$$

Since there was a certain correlation between the wavelet coefficients, in order to prevent the wavelet coefficients from being incorrectly set due to the correlation, the window was set. The window was centered on the wavelet coefficient x_j,k that needed to be processed at the time, and the size was $m\times m\{m>1,|m\in 2n+1|n\ge 0\}$, ($2n+1$ was the representation method of an odd number) was recorded as $C_m(x_j,k)$, the maximum value $M_{j,k}$ of the absolute value of all wavelet coefficients in the current window is calculated, which can be expressed as follows:

$$M_{j,k}=\max\left|x_{m,n}\right|_{(m,n)\in C_m\left(x_j,k\right)}. \tag{7}$$

Then, the following equation could be obtained according to equation (4):

$$\begin{aligned}&x_j,k=x_j,k,\left|x_j,k\right|\ge\lambda,\\&x_j,k=x_j,k\left(1-\frac{\lambda-\left|x_j,k\right|}{M_{j,k}-\left|x_j,k\right|}\right),\left|x_j,k\right|<\lambda\&M_{j,k}\ge\lambda,\\&x_j,k=0,\ (\text{others}).\end{aligned} \tag{8}$$

The specific denoising effect was evaluated by mean square error (MSE) and signal-to-noise ratio (SNR). The specific calculation method was as follows:

$$\text{MSE}=\frac{1}{M\bullet N}\sum_{m=1,n=1}^{M,N}\left(f_{m,n}-\overrightarrow{f}_{m,n}\right)^2. \tag{9}$$

$$\text{SNR}=10lg\left[\frac{\sum_{m=1,n=1}^{M,N}f_{m,n}^2}{\sum_{m=1,n=1}^{M,N}\left(f_{m,n}-\overrightarrow{f}_{m,n}\right)^2}\right]. \tag{10}$$

Here, $f_{m,n}$ represented the original image, $\overrightarrow{f}_{m,n}$ represented the image after denoising, and $M \bullet N$ represented the size of the image.

2.4. CT Examination. The 320-row volumetric CT was used for inspection in this study. Before scanning, the patient was required to lie on their back and relax their breathing, and the patient was bound with an abdominal band to fix it to reduce the range of activity. Firstly, the positioning image was adopted to scan and locate the positions of both kidneys, so that the effective width of the detector (maximum 16 cm) included the entire kidneys on both sides. Secondly, it should perform dynamic volume perfusion enhanced scanning. The specific operation is shown in Figure 1. The scanning parameters were given as follows: tube voltage was −120 kV, tube current was −55 m As, rotation time was −0.6 S, collimation was −0.5 mm × 300, layer thickness was 0.6 mm, repetition time was 4 s, number of times was 15 times, and total time was 60 s. The examination table should not be moved during scanning.

2.5. Data Processing. The image was transferred to the vetra postprocessing workstation, and the scan information of the image was corrected and analyzed by the BODY RESITATION system. The region of interest (ROI) was set. According to the imaging characteristics, 2 ROIs were set in the renal cortex at the renal upper pole, lower renal pole, and renal hilum level. The time-density curve (TDC) of the ROI was drawn, and a perfusion function map that can reflect the perfusion state of the renal blood flow was obtained, which referred to the renal blood flow (BF) map.

2.6. Evaluation Tools. Anthropometric indicators were used for evaluation, so the triceps skindold (TSF) and arm muscle circumference (MAC) of the two groups of patients were measured and compared before nutritional nursing and 6 months after nursing.

It should test and compare the laboratory biochemical indicators of the two groups of patients before nutritional nursing and 6 months after nursing, including serum albumin (ALB), prealbumin (PAB), hemoglobin (Hb), blood urea nitrogen (BUN), and serum creatinine (SCr).

Nutrition risk screening 2002 (NRS 2002) [21] (total score ≥3 points to indicate that the patient has malnutrition or nutritional risk) and health survey summary (the MOS item short from health survey, SF-36) [22] were adopted. Satisfaction questionnaires were adopted to evaluate and compare the physical condition, quality of life, and nursing satisfaction of patients before and 6 months after nutritional nursing.

The 320-slice volume CT low-dose perfusion images based on improved wavelet transform denoising algorithm were selected in this study to examine the changes of renal cortex SF before nutritional nursing and 6 months after the nursing. Then, the renal recovery of the two groups of patients was compared.

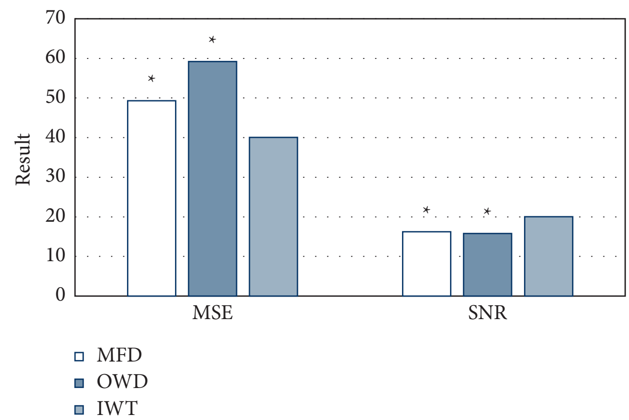

Figure 1: Comparison on MSE and SNR of different algorithms. $*P<0.05$ indicates the difference was statistically significant, compared with "IWT algorithm."

2.7. Statistical Analysis. SPSS 20.0 statistical software was used to analyze the data. The count data were expressed as n/%, and $\chi 2$ test was used. The measurement data were expressed as $\bar{x} \pm s$, and the t-test was used. $P<0.05$ indicates the difference was statistically significant.

3. Results

3.1. Comparison on General Data of Patients. The general clinical data of the two groups of patients were compared. In the control group, there were 34 males (51.52%) and 27 females (48.21%); there were 32 males (48.48%) and 29 females (51.79%) in the H2H group. The average age of patients in the control group was 61.72 ± 13.69 years, and that in the H2H group was 63.92 ± 13.29 years. In the control group, there were 2 patients with education level of elementary school and below, 18 with junior high school, 33 with high school/technical secondary school, and 10 with junior college or above. In the H2H group, there were 2 patients with primary school education and below, 16 cases with junior high school, 31 cases with high school/secondary school, and 8 cases with junior high school and above. In the control group, the number of patients with per capita monthly income of less than 3,000 yuan was 13 cases and 47 cases were those with 3,000 yuan and above; while those in the H2H group were 12 cases and 48 cases. In the control group, there were 15 patients in stage 3, 28 patients in stage 4, and 19 patients in stage 5; while in the H2H group, there were 17 patients in stage 3, 30 patients in stage 4, and 21 patients in stage 5. After analysis and comparison, the comparison of the general clinical data distribution between the two groups of patients was not statistically significant ($P<0.05$), suggesting the feasibility of the comparison of this study.

3.2. Comparison on Performance of Denoising Algorithms. The algorithm used in this work (IWT algorithm) was compared with the mean filter denoising (MFD) algorithm [23] and the orthogonal wavelet denoising (OWD) algorithm. Figure 1 shows the comparison of MSE and SNR of

CT images processed by three algorithms. Among them, the MSE values of the algorithm adopted in this work, the MFD algorithm, and the OWD algorithm were 40.0781, 45.2891, and 59.2123, respectively; the SNR values were 20.0122, 18.2311, and 15.7812, respectively. It can be found that the denoising effect of the algorithm used in this work was better than other algorithms ($P < 0.05$). Figure 2 shows the processing effect of the CT images of the three algorithms. It can be observed that the CT image processed by the algorithm used in this study showed a higher definition.

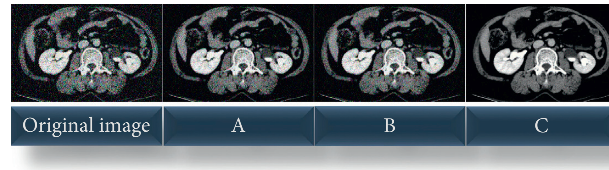

Figure 2: Processing effects of three algorithms. (a), (b), and (c) show the processing effects of MFD algorithm, OWD algorithm, and IWT algorithm, respectively.

3.3. Anthropometric Evaluation Results. Figure 3 shows that the MAC of the patients in the H2H group after nutritional care was significantly improved compared with that before the nursing ($(239.77 \pm 18.24$ vs $243.94 \pm 18.72)$ mm) ($P < 0.05$), and the nursing effect was better than that of the control group. Figure 4 shows that TSF after nursing was improved compared with before nursing ($(8.87 \pm 2.74$ vs $10.04 \pm 2.90)$ mm) ($P < 0.05$), and the nursing effect was better than that of the control group.

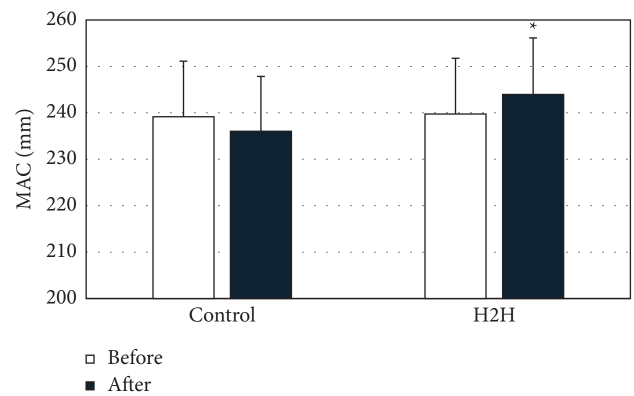

Figure 3: Comparison on MAC before and after nursing. $*P < 0.05$ indicates the difference was statistically significant, compared with "H2H group before nursing."

3.4. Laboratory Biochemical Test Results. Table 1 lists the comparison of the laboratory biochemical indexes (ALB, PAB, Hb, BUN, and SCr) of the two groups of patients before nutritional nursing and 6 months after nursing. It revealed that the various biochemical indicators of the control group patients had a certain improvement, and there was no significant difference in comparison ($P > 0.05$). ALB, PAB, Hb, and BUN of patients in the H2H group after nursing for 6 months were significantly improved compared with those before nursing ($P < 0.05$).

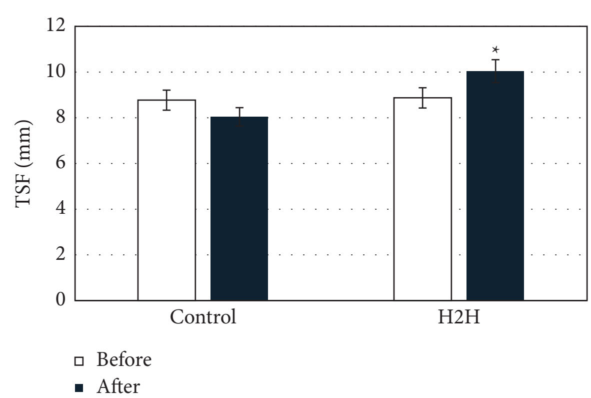

Figure 4: Comparison on TSF before and after nursing. $*P < 0.05$ indicates the difference was statistically significant, compared with "H2H group before nursing."

3.5. Questionnaire Evaluation Results. Figure 5 shows the statistical comparison of the NRS 2002 evaluation results of the two groups of patients before and after nursing. In the control group, 48 patients (80%) had an NRS 2002 score ≥3 before nursing and 45 patients (75%) after nursing, so the comparison was not significantly different ($P > 0.05$). In the H2H group, there were 50 patients (83.33%) with NRS 2002 score ≥3 before nursing and 30 patients (50%) after nursing, so there was a significant difference in comparison ($P < 0.05$).

Table 2 lists the scoring results of the four dimensions of the SF-36 summary table of the two groups of patients: mental function, physiological function, social relationship, and treatment status. Calculation and analysis showed there was no significant difference between the control group and H2H group in the total score of health quality assessment before nursing ($P > 0.05$); while the total score of health quality assessment in the H2H group after nursing was much higher than that of the control group ($P < 0.05$).

Table 3 lists the statistics of the survey results of the satisfaction of the two groups of patients with the nursing process. In the control group, 43 cases (71.67%) were satisfied with the nutritional nursing model and 60 cases (100%) were satisfied in the H2H group. There was a significant difference ($P < 0.05$).

3.6. CT Examination Results. Figure 6 shows the changes in renal cortex BF of the kidneys of the two groups of patients before and after 6 months of nursing. It can be observed that before nursing, the BF of the two groups was 236.53 ± 44.03 mL·100 g^{-1}·min^{-1} in the control group and 234.89 ± 45.11 mL·100 g^{-1}·min^{-1} in the H2H group, showing no significant difference ($P > 0.05$). After 6 months of nursing, the BF of the control group was 289.90 ± 53.91 mL 100 g^{-1}·min^{-1}, while that in the H2H group was 335.12 ± 52.74 mL·100 g^{-1} ·min^{-1}. The BF of the two groups of patients after 6 months of nursing was higher than before, and the H2H group was significantly higher than that of the control group ($P < 0.05$). Figure 7 shows the display of CT images before and after nursing.

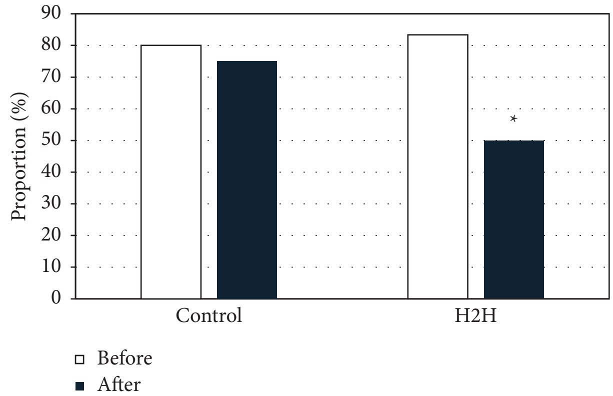

Figure 5: Comparison on NRS 2002 evaluation results. ∗ $P < 0.05$ indicates the difference was statistically significant, compared with "H2H group before nursing."

Table 2: Scoring results of the four dimensions of the SF-36 summary table of two groups of patients.

Biochemical indexes	Control group ($n = 60$)		H2H group ($n = 60$)	
	Before nursing	Six months after nursing	Before nursing	Six months after nursing
Mental function	36.45 ± 5.01	37.89 ± 4.29	35.98 ± 4.38	49.32 ± 3.21 ∗
Physiological function	18.32 ± 5.21	18.82 ± 4.81	18.22 ± 5.98	27.33 ± 4.67 ∗
Social relationship	16.33 ± 3.51	17.02 ± 3.67	15.23 ± 3.34	20.32 ± 1.01 ∗
Treatment status	11.21 ± 4.25	12.11 ± 3.49	10.87 ± 4.98	19.24 ± 1.89 ∗

∗ $P < 0.05$ indicates the difference was statistically significant, compared with "H2H group before nursing."

Table 3: Comparison on the satisfaction of the two groups of patients.

	Very satisfied	Satisfied	Not satisfied	Percentage
Control group ($n = 60$)	26	17	17	71.67
H2H group ($n = 60$)	42	18	0	100 ∗

∗ $P < 0.05$ indicates the difference was statistically significant, compared with the control group.

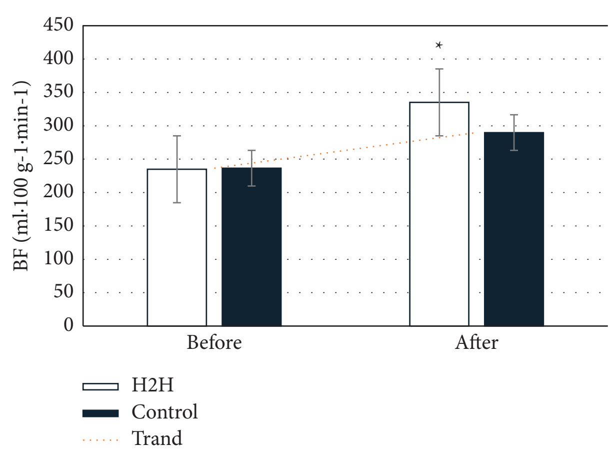

Figure 6: Changes in renal cortex BF before and after nursing. ∗ $P < 0.05$ indicates the difference was statistically significant, compared with the control group.

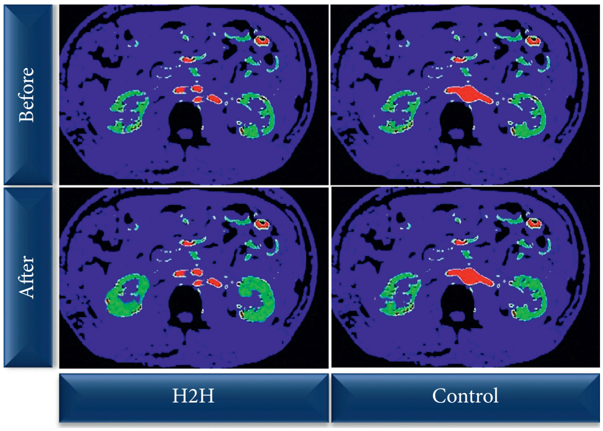

Figure 7: Image display of low-dose CT perfusion imaging.

4. Discussion

In this study, the "Internet + *H*2H" nutritional nursing model was compared with the conventional nursing model, and the anthropometric indicators, laboratory biochemical indicators, NRS 2002, SF-36 short form, satisfaction survey form, and 320-slice volume CT low-dose perfusion imaging technology were adopted to evaluate the effect of nursing. Malnutrition in CKD patients can cause abnormalities in the muscle tissue and blood biochemical indicators [24]. In this study, the MAC, TSF values, ALB, and PAB of the two groups of nursing provided support for this view. Moreover, the anthropometric indicators showed that the MAC and TSF values of patients in the H2H group were greatly improved after nursing; laboratory biochemical indicators showed that ALB, PAB, Hb, and BUN in the H2H group improved after nutritional nursing. The above results suggest that the nutritional nursing effect of patients in the H2H group is better, which is consistent with the research conclusion of Al-Kalaldeh et al. [25].

Some studies have proposed that the "Internet + *H*2H″ nutritional nursing model is not limited by time and space and has more continuity and pertinence in patients' nursing, which is lacking in traditional nursing methods [26]. The NRS 2002 evaluation results in this study showed that the proportion of patients in the H2H group who were malnourished or at risk of nutrition improved significantly after nursing. Another research suggests that the Internet can better realize effective interaction and resource sharing between nursing staff and patients, give patients individualized guidance, correct patients' unhealthy conditions timely and effectively, improve patients' physical and psychological conditions, and enhance patients' cure confidence [27, 28]. In this study, the SF-36 short form was adopted to evaluate, and it was found that the scores of mental function, physiological function, social relationship, and treatment status of patients in the H2H group were better than those of the control group after 6 months of nursing, so the patients in H2H group were more satisfied with the nursing. In addition, the study also used 320-slice volume CT low-dose perfusion imaging to detect the renal function of patients before and after nursing. There was a significant difference in renal cortex BF between the two groups before and after nursing ($P > 0.05$), and the BE of the H2H group was significantly higher than that of the control group after treatment (335.12 ± 52.74 mL·100 $\text{g}^{-1}\cdot\text{min}^{-1}$ vs 289.90 ± 53.91 mL·100$\text{g}^{-1}\cdot\text{min}^{-1}$) ($P < 0.05$). It was suggested that the prognosis of the patient's disease was related to the nutritional status of the body, and the application effect of the "Internet + *H*2H″ nutritional nursing model was better. Such results are in line with the research conclusions drawn by Lukaski et al. (2017) [29, 30]. The H2H nutritional care model is not only suitable for kidney care but also still applicable in neonatal care [31] and respiratory system disease care [32], and the application effect is good.

In order to improve the accuracy of the detection results, the IWT algorithm was used to denoise the CT image and analyze its performance. The results showed that compared with the MFD algorithm and the OWD algorithm, the MSE and SNR values of the denoising algorithm in this study were better. Hsieh et al. (2018) [30] improved the wavelet transform algorithm and used it for CT image processing and found that this method had higher SNR, better structural similarity index, and lower relative error.

5. Conclusion

In this study, the "Internet + *H*2H″ nutritional nursing model was adopted to perform nutritional nursing for patients with CKD in stages 3-5, and the CT images based on the IWT algorithm and other evaluations were adopted to evaluate their nursing effects, so as to compare with traditional nursing methods. The results showed that the Internet + *H*2H "nutritional nursing model was more individual and can better improve the physical quality of patients with stages 3-5, mental state of patients, and prognosis of the disease. In addition, the IWT algorithm had better results in the processing of 320-slice volume CT low-dose perfusion imaging and was worthy of clinical application. However, this study did not separately conduct targeted studies on patients in phases 3 to 5, and the records of the research indicators were not detailed enough, which are needed to be strengthened in subsequent studies. However, the overall results of the study showed that Internet technology had achieved an important position in the field, and the "Internet + *H*2H″ nutritional nursing model would also be widely recognized by patients and doctors in the application of nutritional nursing for patients in the future.

Data Availability

The data used to support the findings of this study are available from the corresponding author upon request.

Conflicts of Interest

The authors declare that they have no conflicts of interest.

Acknowledgments

This work was supported by the Scientific Research Project of Hunan Provincial Health Commission (202114010632).

References

[1] K. Vellanki and S. Hou, "Menopause in CKD," *American Journal of Kidney Diseases*, vol. 71, no. 5, pp. 710–719, 2018.

[2] Y. Sato and M. Yanagita, "Immune cells and inflammation in AKI to CKD progression," *American Journal of Physiology - Renal Physiology*, vol. 315, no. 6, pp. F1501–F1512, 2018.

[3] A. B. Reiss, N. Miyawaki, J. Moon et al., "CKD, arterial calcification, atherosclerosis and bone health: inter-relationships and controversies," *Atherosclerosis*, vol. 278, pp. 49–59, 2018.

[4] S. J. Rosansky, J. Schell, J. Shega et al., "Treatment decisions for older adults with advanced chronic kidney disease," *BMC Nephrology*, vol. 18, no. 1, p. 200, 2017.

[5] D. A. Drew, D. E. Weiner, and M. J. Sarnak, "Cognitive impairment in CKD: pathophysiology, management, and prevention," *American Journal of Kidney Diseases*, vol. 74, no. 6, pp. 782–790, 2019.

[6] D. M. Taylor, S. D. S. Fraser, J. A. Bradley et al., "A systematic review of the prevalence and associations of limited health literacy in CKD," *Clinical Journal of the American Society of Nephrology*, vol. 12, no. 7, pp. 1070–1084, 2017.

[7] S. Wongrakpanich, P. Susantitaphong, S. Isaranuwatchai, J. Chenbhanich, S. Eiam-Ong, and B. L. Jaber, "Dialysis therapy and conservative management of advanced chronic kidney disease in the elderly: a systematic review," *Nephron*, vol. 137, no. 3, pp. 178–189, 2017.

[8] T. Małecka-Massalska, R. Mlak, A. Smolen, and K. Morshed, "Bioelectrical impedance phase angle and subjective global assessment in detecting malnutrition among newly diagnosed head and neck cancer patients," *European Archives of Oto-Rhino-Laryngology*, vol. 273, no. 5, pp. 1299–1305, 2016.

[9] T. Kiran, D. Wells, K. Okrainec et al., "Patient and caregiver priorities in the transition from hospital to home: results from province-wide group concept mapping," *BMJ Quality and Safety*, vol. 29, no. 5, pp. 390–400, 2020.

[10] O. Aibana, C.-C. Huang, S. Aboud et al., "Vitamin D status and risk of incident tuberculosis disease: a nested case-control study, systematic review, and individual-participant data meta-analysis," *PLoS Medicine*, vol. 16, no. 9, 2019.

[11] L. Ran, W. Zhao, X. Tan et al., "Association between serum vitamin C and the blood pressure: a systematic review and meta-analysis of observational studies," *Cardiovasc Ther*, vol. 18, Article ID 4940673, 2020.

[12] S. Jeong, S. B. Park, I. H. Chang et al., "Estimation of renal function using kidney dynamic contrast material-enhanced CT perfusion: accuracy and feasibility," *Abdominal Radiology*, vol. 46, no. 5, pp. 2045–2051, 2021.

[13] D. Manoharan, A. Netaji, K. Diwan, and S. Sharma, "Normalized dual-energy iodine ratio best differentiates renal cell carcinoma subtypes among quantitative imaging biomarkers from perfusion CT and dual-energy CT," *American Journal of Roentgenology*, vol. 215, no. 6, pp. 1389–1397, 2020.

[14] Y. Asayama, A. Nishie, K. Ishigami et al., "Image quality and radiation dose of renal perfusion CT with low-dose contrast agent: a comparison with conventional CT using a 320-row system," *Clinical Radiology*, vol. 74, no. 8, 2019.

[15] Q. W. Oung, H. Muthusamy, S. N. Basah, H. Lee, and V. Vijean, "Empirical wavelet transform based features for classification of Parkinson's disease severity," *Journal of Medical Systems*, vol. 42, no. 2, p. 29, 2017.

[16] S. D. S. Fraser, P. J. Roderick, M. Casey, M. W. Taal, H. M. Yuen, and D. Nutbeam, "Prevalence and associations of limited health literacy in chronic kidney disease: a systematic review," *Nephrology Dialysis Transplantation*, vol. 28, no. 1, pp. 129–137, 2013.

[17] Z. Wan, Y. Dong, Z. Yu, H. Lv, and Z. Lv, "Semi-supervised support vector machine for digital twins based brain image fusion," *Frontiers in Neuroscience*, vol. 15, Article ID 705323, 2021.

[18] S. K. Venuthurupalli, W. E. Hoy, H. G. Healy, A. Cameron, and R. G. Fassett, "CKD screening and surveillance in Australia: past, present, and future," *Kidney International Reports*, vol. 3, no. 1, pp. 36–46, 2018.

[19] A. Zarei and B. M. Asl, "Automatic seizure detection using orthogonal matching pursuit, discrete wavelet transform, and entropy based features of EEG signals," *Computers in Biology and Medicine*, vol. 131, Article ID 104250, 2021.

[20] Y. Yu, Y. Xiao, J. Cheng, and B. Chiu, "Breast lesion classification based on supersonic shear-wave elastography and automated lesion segmentation from B-mode ultrasound images," *Computers in Biology and Medicine*, vol. 93, pp. 31–46, 2018.

[21] Z. Zhang, S. Pereira, M. Luo, and E. Matheson, "Evaluation of blood biomarkers associated with risk of malnutrition in older adults: a systematic review and meta-analysis," *Nutrients*, vol. 9, no. 8, p. 829, 2017.

[22] A. Bunevicius, "Reliability and validity of the SF-36 Health Survey Questionnaire in patients with brain tumors: a cross-sectional study," *Health and Quality of Life Outcomes*, vol. 15, no. 1, p. 92, 2017.

[23] M. Mafi, H. Rajaei, M. Cabrerizo, and M. Adjouadi, "A robust edge detection approach in the presence of high impulse noise intensity through switching adaptive median and fixed weighted mean filtering," *IEEE Transactions on Image Processing*, vol. 27, no. 11, pp. 5475–5490, 2018.

[24] P. Sharma, A. Rauf, A. Matin, R. Agarwal, P. Tyagi, and A. Arora, "Handgrip strength as an important bed side tool to assess malnutrition in patient with liver disease," *Journal of Clinical and Experimental Hepatology*, vol. 7, no. 1, pp. 16–22, 2017.

[25] M. Al-Kalaldeh, K. Suleiman, and O. Al-Kalaldeh, "Prognostic performance of NUTRIC score in quantifying malnutrition risk in the critically ill in congruence with the bioelectrical impedance analysis," *Nutrition in Clinical Practice*, vol. 35, no. 3, pp. 559–566, 2020.

[26] R. Caccialanza, E. Cereda, C. Klersy et al., "Bioelectrical impedance vector analysis-derived phase angle predicts survival in patients with systemic immunoglobulin light-chain amyloidosis," *Amyloid: International Journal of Experimental & Clinical Investigation*, vol. 27, no. 3, pp. 168–173, 2020.

[27] S. S.-L. Tan and N. Goonawardene, "Internet health information seeking and the patient-physician relationship: a systematic review," *Journal of Medical Internet Research*, vol. 19, no. 1, p. e9, 2017.

[28] R. Mieronkoski, I. Azimi, A. M. Rahmani et al., "The Internet of Things for basic nursing care-A scoping review," *International Journal of Nursing Studies*, vol. 69, pp. 78–90, 2017.

[29] H. C. Lukaski, U. G. Kyle, and J. Kondrup, "Assessment of adult malnutrition and prognosis with bioelectrical impedance analysis," *Current Opinion in Clinical Nutrition and Metabolic Care*, vol. 20, no. 5, pp. 330–339, 2017.

[30] G. Song and H. Liu, "Effect of Hospital to Home nutrition management model on postoperative clinical outcomes of

patients with laryngeal carcinoma," *Oncology Letters*, vol. 14, no. 4, pp. 4059–4064, 2017.
[31] D. Kabugo, H. Nakamura, B. Magnusson et al., "Mixed-method study to assess the feasibility, acceptability and early effectiveness of the Hospital to Home programme for follow-up of high-risk newborns in a rural district of Central Uganda: a study protocol," *BMJ Open*, vol. 11, no. 3, 2021.
[32] K. Parikh, M. Richmond, M. Lee et al., "Outcomes from a pilot patient-centered hospital-to-home transition program for children hospitalized with asthma," *Journal of Asthma*, vol. 58, no. 10, pp. 1384–1394, 2021.

Hindawi
Contrast Media & Molecular Imaging
Volume 2022, Article ID 9882532, 8 pages
https://doi.org/10.1155/2022/9882532

Research Article

Evaluation of Functional Magnetic Resonance Imaging under Artificial Intelligence Algorithm on Plan-Do-Check-Action Home Nursing for Patients with Diabetic Nephropathy

Qianqian Du,[1] **Dianchao Liang**,[2] **Lixin Zhang**,[3] **Guoyan Chen**,[4] **and Xueyan Li**[5]

[1]*Department of Endocrinology, the Second Hospital of Shijiazhuang, Shijiazhuang 050000, Hebei, China*
[2]*Community Health Service Centre of Zhentou, Shijiazhuang 050000, Hebei, China*
[3]*Department of Nursing, the Second Hospital of Shijiazhuang, Shijiazhuang 050000, Hebei, China*
[4]*Department of Nephrology, the Second Hospital of Shijiazhuang, Shijiazhuang 050000, Hebei, China*
[5]*Department of Peripheral Vascular Surgery, the Second Hospital of Shijiazhuang, Shijiazhuang 050000, Hebei, China*

Correspondence should be addressed to Qianqian Du; 131631437@m.gduf.edu.cn

Received 31 December 2021; Revised 25 February 2022; Accepted 28 February 2022; Published 25 March 2022

Academic Editor: M Pallikonda Rajasekaran

This study aimed to evaluate the effect of functional magnetic resonance imaging (fMRI) under the fuzzy C-means (FCM) clustering algorithm on plan-do-check-action (PDCA) home nursing for patients with diabetic nephropathy (DN). As the characteristics of fMRI image data were combined, the FCM algorithm was improved and applied into the clustering processing of fMRI activation regions of patients. 64 patients with DN were chosen as the research objects and were divided into the research group with PDCA home nursing and the control group with routine home nursing. The patients were randomly divided into the research group ($n = 32$) and the control group ($n = 32$). The curative effect, nursing satisfaction, and quality of life of patients after nursing were compared. The results showed that the coverage of fMRI activation points was significantly higher as being detected by the FCM algorithm, and the running time was shortened by 33.6 min. After nursing, the total effective rates in the research group and the control group were 87.5% vs. 34.4% in 3 months, 93.8% vs. 68.8% in 6 months, and 96.9% vs. 75.0% in 12 months, respectively; those in the research group were significantly higher than those in the control group ($P < 0.05$). The nursing satisfaction score (91.3 ± 4.5 vs. 80.9 ± 5.2) and nursing service quality score (89.7 ± 6.6 vs. 80.3 ± 7.1) in the research group were also significantly higher than those in the control group ($P < 0.05$). Meanwhile, the scores of each item after nursing in the research group were significantly higher than those in the control group ($P < 0.05$). The improved FCM algorithm detected the activation regions in the fMRI images more effectively, which could provide help for diagnosis and reduce error and misdiagnosis. At the same time, the PDCA home nursing also offered great help to the recovery of patients with DN, which was more superior for the curative effect of hospitalization, the promotion of recovery, and the improvement of patients' quality of life.

1. Introduction

Diabetic nephropathy (DN) is a kind of common diabetic complication. Pathologically, it is mainly observed in patients with glomerular sclerosis caused by microvascular disease, so it is also called diabetic glomerulosclerosis [1]. Statistics show that in recent years, the incidence of DN in China was increasing year by year, the prevalence has reached more than 17%, and the mortality of patients with uremia due to DN has also reached 30% or so [2]. More and more studies have proved that diabetes is one of the risk factors for end-stage kidney disease, and the current clinical methods for DN treatment are mostly to reduce blood urea nitrogen (BUN) and serum creatinine (Cr), which ignore nursing in the recovery [3]. Because DN is a type of chronic recurrent disease, only nursing during hospitalization cannot stabilize the patients' condition effectively in a long term. Therefore, an effective home nursing is of great significance to consolidate the curative effect, reduce the recurrence, and increase the quality of life of DN patients [4, 5]. The existing home nursing methods have the limitation without a flexible nursing plan, making the personalized nursing cannot be carried out depending on the characteristics of patients and specific diseases, so they have not achieved outstanding nursing advantages [6]. Plan-do-check-action (PDCA) nursing is a new kind of home nursing containing four parts, which are just the plan, do, check, and action [7]. Studies have shown that after PDCA home nursing, the clinical symptoms of patients can be significantly improved, and compared with other nursing methods, it is easier to be accepted by patients and their families [8].

Artificial intelligence technology brings new opportunities for the diagnosis of diseases. The diagnostic expert system developed on artificial intelligence technology is a program system that simulates the thinking process of medical experts in diagnosing diseases. The expert system has the ability to collect, organize, and record expert knowledge, so as to give medical advice. Besides, artificial intelligence is applied to the image processing of functional magnetic resonance imaging (fMRI) of diabetic patients, which can help doctors reduce misdiagnosis. The artificial intelligence-based diagnostic expert system not only reduces the computational time and cost of disease diagnosis but also improves the accuracy of disease classification. On the other hand, effective renal function monitoring and prognostic evaluation are also important for prolonging the survival time of patients. With the development of imaging technology, fMRI provides the possibility to monitor renal function and evaluate the prognosis of patients at the same time [9]. When fMRI is applied for the diagnosis and evaluation of the curative effect, the structures and functions are often assessed by parameters such as time series signals. However, in practical applications, the detected signals will be interfered by noise signals [10]. Therefore, it is very important to extract useful characteristic signals from the complex mixed signals. With the rapid development of computer science and technology, the intelligent algorithms can handle the difficult issues in various fields and provide new ideas for solving the issues of disease diagnosis and treatment in the medical field [11].

DN patients were taken as the research objects in this study, and the infinite norm algorithm (ICA) was introduced to scan and segment the fMRI images, so as to deal with the noise signal interference in fMRI images. Through observing and comparing differences in different imaging values in the clinical prognosis, it was expected to find a way for the evaluation of clinical prognosis of DN patients. Thereby, disease monitoring methods could be enriched to fill the gaps in this research field, and more importantly, help for clinical treatment could be offered to benefit the overall DN patients.

2. Methodology

2.1. Research Objects and Grouping. In this study, 64 patients with DN in hospital from January 2018 to December 2020 were selected as the research objects, including 38 males (59.4%) and 26 females (40.6%). Their average age was 46.37 ± 6.63 years old, and the average course of disease was 7.97 ± 3.73 years. The patients were randomly divided into the research group and the control group, with 32 cases in each group. The clinical data of patients in both groups were collected. After comparison, there was no significant difference in the average age, gender ratio, average course of disease, treatment method, renal function on discharge, and total score of SF-36 quality of life scale between the two groups ($P > 0.05$). Therefore, the two groups went with comparability. The study had been approved by the ethics committee of hospital, and the patients included and their families signed the informed consent forms.

Inclusion criteria: all objects met the Diagnostic Criteria and Staging Criteria for Diabetic Nephropathy formulated with reference to the Second National Academic Conference on Diabetes in 1999 and the diagnostic criteria of the World Health Organization. When the patients were discharged, their serum Cr and BUN were not higher than the twice of the normal levels, with mild clinical symptoms, and the total quality of life score <50 points. The total score of the patients' 36-item short form (SF-36) quality of life scale was not higher than 50 points. The patients did not have other somatic diseases, but with complete clinical data. The patients who did not meet the requirements were excluded. Exclusion criteria: the patients had other somatic diseases.

2.2. fMRI Examinations. 3.0 T MRI equipment was used for examinations. When scanning of diffusion weighted imaging (DWI) was performed, the echo sequence of the spin-echo diffusion weighted plane was used for imaging. The time of repetition (TR) was 3000 ms, the time of echo (TE) was 60.5 ms, the field of view (FOV) was $256 \times 256\ \text{mm}^2$, the layer thickness was 3 mm, and the flip angle was 90°. The patients were asked to fast for at least 6 hours the day before the examination and took the supine position for abdominal scanning in the examination. The scanning included those of T2-weighted imaging (T2WI) turbo field echo (TFE) sequence in the transverse and coronal positions. After the raw data were transmitted to the workstation, the Funtool was used to process and analyze the images.

2.3. Improvement of Fuzzy C-Means (FCM) Clustering Algorithm. With the characteristics of fMRI data signals, the HCC distance measurement method was obviously superior to the traditional Euclidean distance method. The HCC method was implemented on the Pearson correlation coefficient and could be described as

$$D\left(x_j, b_i\right) = \left(\frac{1 - p_{ij}}{1 + p_{ij}}\right)^{\beta}, \tag{1}$$

where p_{ij} is the Pearson correlation coefficient between the voxel point x_j and the central voxel point b_i, and β is the penalty factor, which could be set to 1.

Since the distance from the voxel point to the central voxel point was not a simple spatial distance, further improvements needed to be made on the basis of the HCC method. A function similar to the normal distribution was constructed for distance measurement and described as

$$Dd\left(x_j, b_i\right) = \left(1 - p_{ij}\right) \times \exp\left(-\alpha \times p_{ij}\right), \quad (2)$$

where α is the balance coefficient of the balance distance measurement function.

It was assumed that the fuzzy membership matrix in the FCM algorithm was $A = \left\{a_{ij} | 1 \le i \le n,\ 1 \le j \le m\right\}$, where n is the number of categories, the VoxEL dataset was $X = \{x_1, x_2, \ldots, x_n\}$, and the mean value matrix was $C = \{v_i | 1 \le i \le n\}$. At this time, the target equation of the improved FCM algorithm is

$$E_{\mathrm{FCM}}(X, A, C) = \sum_{i=1}^{n} \sum_{j=1}^{m} u_{ij}^{z} Dd^{2}\left(x_j, b_i\right). \quad (3)$$

$0 \le u_{ij} \le 1$ and $\sum_{i=1}^{n} u_{ij} = 1$ are assumed, and then, $D\ d(x_j, b_i)$ is the new distance measurement.

Finally, the coverage (accuracy) and running time were used to evaluate the algorithm. The coverage was the ratio of the sum number of correctly detected activated voxel points and nonactivated voxel points to the number of all voxel points in the measured region of fMRI images. The larger the ratio, the more accurate the regional function activation.

2.4. PDCA Home Nursing. After discharge from hospital, patients in the research group and the control group were required to take kidney-protecting drugs and hypoglycemic drugs routinely. Basic information such as gender, age, renal function on discharge, blood glucose, and accompanied symptoms were recorded to construct the health file of patients. The patients in the control group were treated with routine home nursing, including the telephone follow-up once a month, diet instruction, medication, exercise, rest, and follow-up visits specifically.

In addition to routine home nursing, patients in the research group were visited by specially trained full-time nurses in the follow-ups and received PDCA home nursing. According to the patients' health status, diet, nutritional level, living habits, cognitive status, and follow-up awareness, the targeted nursing plan was designed to standardize the treatment and health behaviors of patients. At the same time, the medication behavior of patients was also standardized, as a light, easy-to-digest, and high-vitamin diet was given, together with guided rest and work to avoid over fatigue. When patients suffered from the long-term, repetitive, and costly diseases, they had mental pressures, which required professional personnel to give timely psychological consultation to eliminate their anxiety, depression, and other unhealthy emotions, and help them build confidence in recovery. A home support model was established to help patients and their family members understand relevant knowledge of the disease and guide to establish communication between the family members and patients. Thus, the patients' physical and mental health could be maintained, their mental stress could be alleviated, and their ability to adapt to life was improved, thereby the compliance of the patients could be improved as well. At the first follow-up visit, relevant materials were given out to patients and their families, and the general information of the disease were introduced, making patients and their families understand the purpose, content, and expected outcome of this study. They were also guided in the implementation of the nursing plan. At the single-month follow-up, the nursing plan was revised and improved according to the issues encountered in the last month. At the even-month follow-up, the implementation effects of the nursing plan and the issues encountered were fully known and checked through the communication with the patients and their families, and the issues were then taken as the focus of nursing in the next month. At the last follow-up, the patients and their families were convened for a symposium to strengthen health education and other related knowledge, and they made evaluations on the effect of the implementation, recovery, and nursing satisfaction. The recurring and neglected issues during nursing for the patients were learned via follow-ups, and the optimal nursing plan was worked out under negotiation with patients and their family members. With the specific issues existing in implementation, the nursing plan was revised and improved, which was then transferred into the next PDCA nursing plan. After each cycle, the nursing plan became more complete and more comprehensive, so that the nursing effect will be more significant. The PDCA home nursing needed to be implemented continuously for one year to find a more effective home nursing model as well as the better effect.

2.5. Evaluation of Nursing Effect. 3 months, 6 months, and 12 months after nursing, the patients underwent renal function reexamination, and the improvements of the patients' clinical symptoms were recorded. The evaluation was mainly completed by fully trained personnel and was carried out according to the following criteria. If it was evaluated to be remarkedly effective, all the clinical symptoms disappeared, and the level of urinary albumin excretion returned to be normal or decreased by 50% or more. Meanwhile, the blood glucose and glycosylated hemoglobin level returned to be normal or decreased by 35% or more, and the 24 h quantitative level of urine protein decreased by 50% or more, with the normal renal function indicators. If it was evaluated as effective, the clinical symptoms were significantly improved. Urine albumin excretion, blood glucose, and glycosylated hemoglobin level were all reduced, but did not reach the standard of remarkedly effective. 24 h quantitative level of urine protein, with normal renal function indicators, also did not drop down by 50% compared with that before treatment. If it was evaluated to be ineffective, there was no improvement, but even an aggravation was found on the clinical symptoms; other laboratory indicators had not changed or increased.

12 months after nursing, the SF-36 scale developed by the U S. Medical Outcomes Study was adopted to evaluate the patients' quality of life [12]. The SF-36 scale contained 36 items, which could be classified into 8 dimensions of

physical functioning, role-physical, role-emotional, bodily pain, vitality, social functioning, mental health, and general health. The total score of the scale was 100 points. The higher the score, the better the quality of life of patients.

2.6. Statistical Analysis. SPSS 19.0 was applied for statistical analysis. The enumeration data were expressed by frequency (%), and the difference was compared under the χ^2 test. The measurement data were expressed by mean ± standard deviation $(\bar{x} \pm s)$, and the independent sample t-test was used for the difference comparison. When $P < 0.05$, the difference between groups was statistically significant.

3. Results

3.1. Basic Data Comparison of Patients. The basic data when the patients were discharged from the hospital were compared between the research group and the control group, and the results are given in Table 1. It was suggested that there was no significant difference between the two groups in the patients' average age, gender ratio, and body mass index ($P > 0.05$). In the laboratory examination indicators on discharge, there was also no significant difference between the two groups in hemoglobin, glycosylated hemoglobin, Cr, BUN, estimated glomerular filtration rate (eGFR), and urine protein by creatinine ratio of patients ($P > 0.05$). Therefore, the subsequent results are comparable.

3.2. fMRI Data Analysis under Improved FCM Algorithm. fMRI was used to examine the changes in the morphology of the patients' kidney structure before and after discharge. From the images of T2WI and DWI in Figure 1, it could be observed that compared to those on admission, the kidney morphology of the patient was fuller, and the boundary of cortex and medulla was very clear on discharge. The degree of fibrosis was low in the external kidney, and the diffusion of water molecules was very even.

The improved FCM algorithm was applied to analyze the fMRI image data of patients, and the results are shown in Figure 2. As 5 tests were carried out, the coverages of the improved FCM algorithm were always higher than those of the preimproved HCC method. The running time of the improved FCM algorithm was only 79.8 min, while that was 113.4 min without the improvement, showing a significant difference ($P < 0.05$).

3.3. Effect Evaluation of PDCA Home Nursing. The nursing effect was compared between the research group and the control group 3, 6, and 12 months after nursing, respectively. As shown in Figure 3, there was a significant difference between two groups, for the remarkedly effective rates of the research group and the control group were 56.3% vs. 18.8% in 3months, 71.9% vs. 53.1% in 6 months, and 87.5% vs. 56.3% in 12 months ($P < 0.05$). Both the remarkedly effective and effective rates pertain to the total effective rate, which was shown to be 87.5% vs. 34.4% in 3 months, 93.8% vs. 68.8% in 6 months, and 96.9% vs. 75.0% in 12 months, respectively, between the research group and the control group. The total effective rate of the research group was significantly higher than that of the control group ($P < 0.05$).

3.4. Evaluation of Satisfaction and Service Quality of PDCA Home Nursing. In 12 months of nursing, the scores of nursing satisfaction and nursing service quality were compared between patients in two groups, which are shown in Figure 4. It was observed that there were significant differences in scores of nursing satisfaction (91.3 ± 4.5 vs. 80.9 ± 5.2) and the nursing service quality (89.7 ± 6.6 vs. 80.3 ± 7.1) between the two groups, and those of the research group were significantly higher than those of the control group ($P < 0.05$).

3.5. Evaluation of Patients' Quality of Life after Home Nursing. After 12 months of nursing, the quality of life of patients in two groups was evaluated using the SF-36 scale. As shown in Figure 5, the scores of each item of patients in the research group after nursing were significantly higher than those in the control group, with statistically significant differences ($P < 0.05$).

4. Discussion

DN is a chronic disease that requires long-term treatment. Only the in-hospital treatment and nursing cannot stabilize the condition of this disease in a long term. Therefore, home nursing after discharge can help patients consolidate the treatment effect and improve the quality of life [4, 13]. fMRI was used in this study to evaluate the changes in renal functions on admission and discharge. It was found that the kidney morphology of patients on discharge was fuller than that on admission, and the boundary of cortex and medulla became quite clearer on discharge. In addition, the degree of kidney fibrosis was lower, and the diffusion of water molecules was even in images. As the improved FCM algorithm was applied to detect the fMRI activation regions, the detection result was closer to the confirmed state [14]. It proved that the in-hospital treatment controlled the deterioration of DN in patients, and the improved FCM algorithm could realize the analysis and processing of fMRI image data better.

DN patients must have long-term diet control and drug treatment. The home nursing should be carried out on many aspects, such as teaching patients to self-monitor blood glucose and urine glucose, insulin injection methods, and precautions for hypoglycemic drugs. The recording is very important of proper care for the skin and the amount of edema; while the social factors should also call attention to reduce the recurrence of DN and improve the quality of life of patients [15, 16]. The innovation of this research was to evaluate the impact of fMRI under the FCM clustering algorithm on PDCA home nursing in patients with DN. For PDCA home nursing, the

Table 1: Comparison of patients' basic data between two groups ($n = 64$).

Basic data	Research group ($n = 32$)	Control group ($n = 32$)	Value of P
Age (years old)	48.3 ± 5.2	49.1 ± 6.7	0.523
Gender (male, %)	18	20	0.482
Body mass index (kg/m^2)	23.8 ± 2.6	24.0 ± 3.1	0.544
Hemoglobin (g/L)	115.6 ± 8.9	117.2 ± 10.6	0.327
Glycosylated hemoglobin (%)	8.1 ± 1.2	7.9 ± 1.3	0.626
Cr (μmL/L)	153.2 ± 20.8	155.7 ± 18.4	0.411
BUN (mmol/L)	6.7 ± 1.5	6.6 ± 5.2	0.398
eGFR (mL/min/1.73 m^2)	71.4 ± 10.8	72.5 ± 12.6	0.339
Urine protein by creatinine ratio (mg/g)	563.2 ± 203.8	576.0 ± 182.5	0.298

eGFR, estimated glomerular filtration rate.

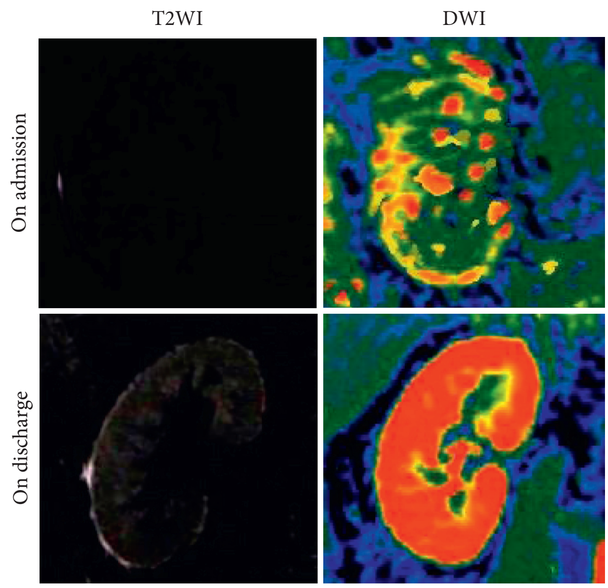

Figure 1: Changes in fMRI images of the patient's kidneys on admission and discharge.

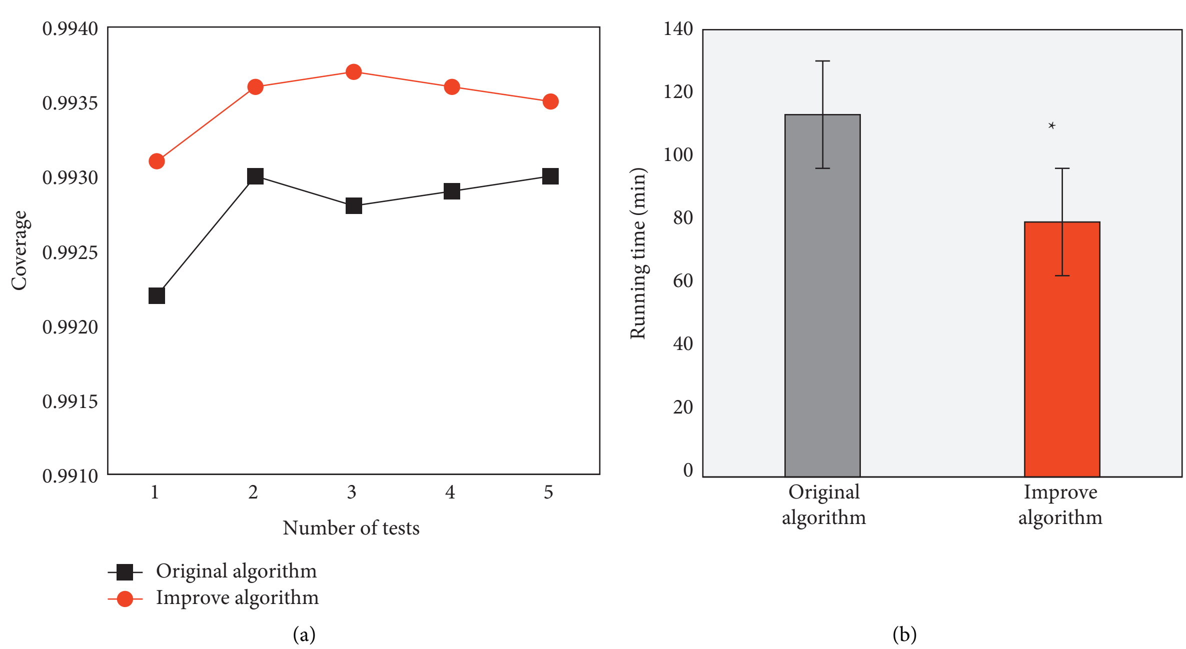

Figure 2: The processed results of fMRI data before and after the algorithm improvement. (a) The coverage comparison under different test times. (b) Comparison of the average running time. *Difference between groups was statistically significant ($P < 0.05$).

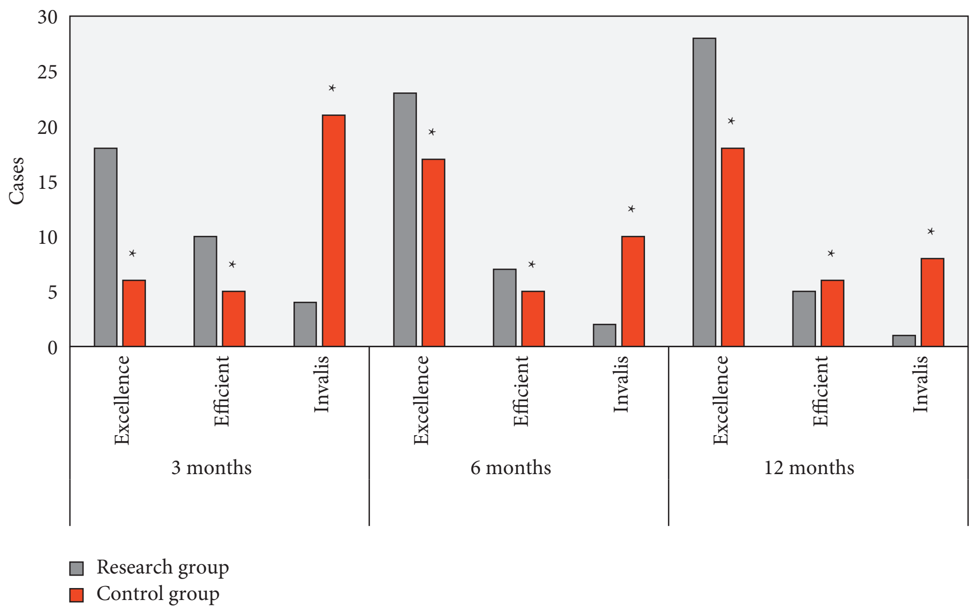

FIGURE 3: Nursing effect in different months. *Difference between groups was of statistical significance ($P < 0.05$).

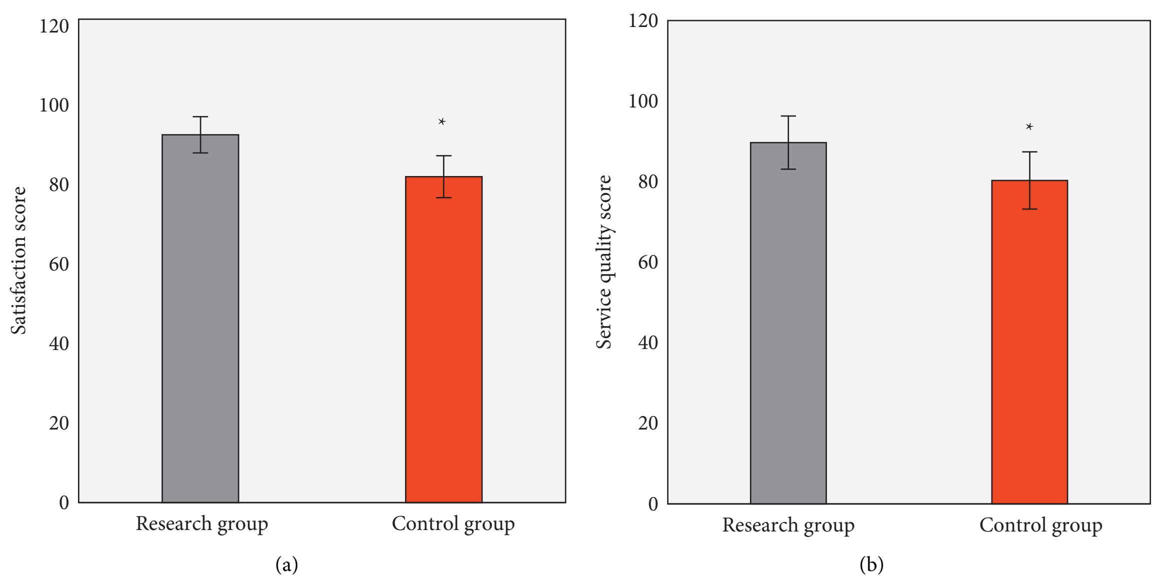

FIGURE 4: Satisfaction and service quality evaluations after nursing. (a) and (b) The scores of nursing satisfaction and the nursing service quality, respectively. *Statistically significant differences between groups ($P < 0.05$).

remarkedly effective rate of the research group and the control group was 56.3% vs. 18.8% within 3 months after nursing, 71.9% vs. 53.1% within 6 months, and 87.5% vs. 56.3% within 12 months ($P < 0.05$). PDCA nursing is a kind of planned, step-by-step, and very targeted approach, each cycle of which can make the quality of nursing improved [17]. Therefore, the effects of PDCA home nursing were analyzed and compared on the efficacy and quality of life of patients with DN after discharge from the hospital. It was shown that compared with routine home nursing, PDCA home nursing could maintain the treatment effect of patients significantly, and the scores of patients' satisfaction and service quality were significantly higher. Besides, the SF-36 scale was adopted to evaluate the quality of life of patients [18], the scores of which after PDCA home nursing were significantly higher in all dimensions than those of routine home nursing. Therefore, the PDCA home nursing could be carried out and adjusted according to the patients' personalities and disease characteristics, which was conducive to controlling the deterioration of the disease after discharge from hospital and improving the quality of life of the patients [19].

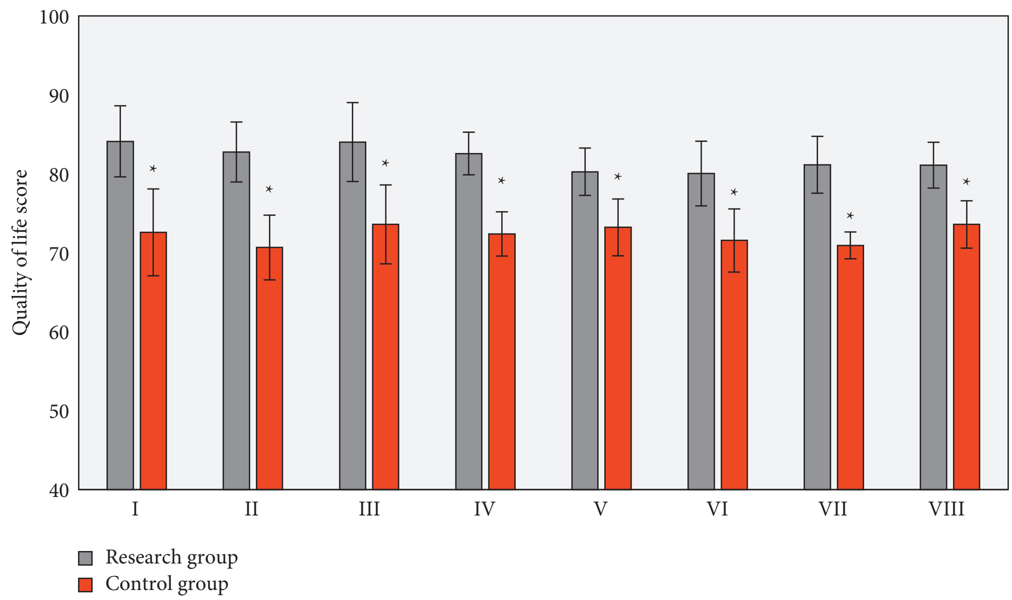

Figure 5: Comparison of patients' quality of life scores after nursing. I, II, III, IV, V, VI, VII, and VIII represent the general health, physical functioning, role-physical, bodily pain, social functioning, mental health, role-emotional, and vitality, respectively. *Statistically significant differences between two groups ($P < 0.05$).

5. Conclusion

This study was aimed to explore the effect of fMRI under the improved FCM algorithm on PDCA home nursing for patients with DN. The improved algorithm was used to detect the activation points in the fMRI images, which gave a result closer to the real situation. Thus, it could provide assistance in diagnosis and reduce errors and misdiagnosis. At the same time, PDCA home nursing offered the great help to the recovery of patients with DN. It was superior for the consolidation of the curative effect of hospitalization, the promotion of the recovery, and the improvement of quality of life. The shortcomings of this study were that the sample size was relatively small, and the impact of nursing on patients' diabetes and renal function indicators was not taken into consideration. Therefore, the research in this field needed to be further confirmed by multicenter and large-sample clinical studies.

Data Availability

The data used to support the findings of this study are available from the corresponding author upon request.

Conflicts of Interest

The authors declare that they have no conflicts of interest.

Acknowledgments

This work was supported by Hebei Youth Science and technology project (20160768).

References

[1] C. Qi, X. Mao, Z. Zhang, and H. Wu, "Classification and differential diagnosis of diabetic nephropathy," *Journal of Diabetes Research*, vol. 2017, Article ID 8637138, 2017.

[2] J. Wada and H. Makino, "Inflammation and the pathogenesis of diabetic nephropathy," *Clinical Science*, vol. 124, no. 3, pp. 139–152, 2013.

[3] N. Papadopoulou-Marketou, G. P. Chrousos, and C. Kanaka-Gantenbein, "Diabetic nephropathy in type 1 diabetes: a review of early natural history, pathogenesis, and diagnosis," *Diabetes*, vol. 33, no. 2, Article ID e2841, 2017.

[4] N. Helou, D. Talhouedec, M. Shaha, and A. Zanchi, "The impact of a multidisciplinary self-care management program on quality of life, self-care, adherence to anti-hypertensive therapy, glycemic control, and renal function in diabetic kidney disease: a Cross-over Study Protocol," *BMC Nephrology*, vol. 17, no. 1, p. 88, 2016.

[5] L. Y. Lee, H. H. Tung, S. L. Tsay, Y. C. Chen, H. H. Lee, and Y. X. Zeng, "Predictors for self-management in older adults with type 2 diabetic nephropathy," *Journal of Clinical Nursing*, vol. 29, no. 5-6, pp. 922–931, 2020.

[6] Y. Jin, C. Li, X. Zhang, Y. Jin, L. Yi, and J. Cui, "Effect of FOCUS-PDCA procedure on improving self-care ability of patients undergoing colostomy for rectal câncer," *Revista da Escola de Enfermagem da USP*, vol. 55, 2021 PMID: 34190882, Article ID e03729.

[7] Y. Si, H. Yuan, P. Ji, and X. Chen, "The combinative effects of orem self-care theory and PDCA nursing on cognitive function, neurological function and daily living ability in acute stroke," *American Journal of Tourism Research*, vol. 13, no. 9, pp. 10493–10500, 2021, PMID: 34650719; PMCID: PMC8507085.

[8] T. Fukui, "From evidence-based medicine to PDCA cycle," *Nihon Naika Gakkai Zasshi*, vol. 101, no. 12, pp. 3365–3367, 2012, PMID: 23356153.

[9] Y. Wang, L. Jiang, X.-y. Wang et al., "Evidence of altered brain network centrality in patients with diabetic nephropathy and retinopathy: an fMRI study using a voxel-wise degree centrality approach," *Therapeutic Advances in Endocrinology and Metabolism*, vol. 10, 2019.

[10] R. S. Brown, M. R. M. Sun, I. E. Stillman, T. L. Russell, S. E. Rosas, and J. L. Wei, "The utility of magnetic resonance imaging for noninvasive evaluation of diabetic nephropathy," *Nephrology Dialysis Transplantation*, vol. 35, no. 6, pp. 970–978, 2020.

[11] M. Hu, Y. Zhong, S. Xie, H. Lv, and Z. Lv, "Fuzzy system based medical image processing for brain disease prediction," *Frontiers in Neuroscience*, vol. 15, Article ID 714318, 2021.

[12] L. Lins and F. M. Carvalho, "SF-36 total score as a single measure of health-related quality of life: scoping review," *SAGE Open Medicine*, vol. 4, Article ID 205031211667172, 2016.

[13] A. Butt, N. Mustafa, A. Fawwad et al., "Relationship between diabetic retinopathy and diabetic nephropathy; a longitudinal follow-up study from a tertiary care unit of Karachi, Pakistan," *Diabetes & Metabolic Syndrome: Clinical Research Reviews*, vol. 14, no. 6, pp. 1659–1663, 2020.

[14] M. L. Seghier, "Clustering of fMRI data: the elusive optimal number of clusters," *PeerJ*, vol. 6, Article ID e5416, 2018.

[15] R. T. Varghese, I. Jialal, and C. Doerr, "Diabetic nephropathy (nursing)," in *StatPearls [Internet]*StatPearls Publishing, Treasure Island, FL, USA, 2021.

[16] L. Yu, X. Yang, and J. Hao, "Study on the effect of high quality nursing in patients with diabetic nephropathy," *Panminerva Medica*, vol. 25, 2021 Epub ahead of print. PMID: 34609118.

[17] Y. Wei, M. Xu, W. Wang et al., "Effect analysis of PDCA cycle method applied in nursing management of disinfection supply room," *Panminerva Medica*, vol. 2020, 2020 Epub ahead of print. PMID: 32550626.

[18] T. Tönnies, A Stahl-Pehe, C. Baechle et al., "Diabetic nephropathy and quality of life among youths with long-duration type 1 diabetes: a population-based cross-sectional study," *Pediatric Diabetes*, vol. 26, no. 5, pp. 613–621, 2019, Epub 2019 Apr 16. PMID: 30806008.

[19] C. Yi, X. Feng, and Y. Yuan, "Study on the influence of PDCA cycle nursing based on network service on the quality of life and nutritional status of hypertension patients in home care," *Evidence-based Complementary and Alternative Medicine*, vol. 2021, Article ID 6068876, 2021.

Hindawi
Contrast Media & Molecular Imaging
Volume 2022, Article ID 5411801, 9 pages
https://doi.org/10.1155/2022/5411801

Research Article

Artificial Intelligence Algorithm-Based Positron Emission Tomography (PET) and Magnetic Resonance Imaging (MRI) in the Treatment of Glioma Biopsy

Wei Wei,[1] **Liujia Ma**,[1] **Liying Yang**,[2] **Rong Lu**,[2] **and Cong Xi**[2]

[1]*Department of Neurosurgery, Affiliated Hospital of Yan'an University, Yan'an 716000, Shaanxi, China*
[2]*Department of Neurology, Baoji Municipal People's Hospital, Baoji 722204, Shaanxi, China*

Correspondence should be addressed to Cong Xi; 202072687@yangtzeu.edu.cn

Received 6 January 2022; Revised 21 February 2022; Accepted 23 February 2022; Published 23 March 2022

Academic Editor: M Pallikonda Rajasekaran

This study was aimed at exploring the application value of positron emission tomography (PET) + magnetic resonance imaging (MRI) technology based on convolutional neural network (CNN) in the biopsy and treatment of intracranial glioma. 35 patients with preoperatively suspicious gliomas were selected as the research objects. Their imaging images were processed using CNN. They were performed with the preoperative head MRI, fluorodeoxyglucose (FDG) PET, and ethylcholine (FECH) PET scans to construct the cancer tissue contours. In addition, the performance of CNN was evaluated, and the postoperative pathology of patients was analyzed. The results suggested that the CNN-based PET + MRI technology showed a recognition accuracy of 97% for images. Semiquantitative analysis was adopted to analyze the standard uptake value (SUV). It was found that the SUV_{FDG} and SUV_{FECH} of grade II/III glioma were 9.77 ± 4.87 and 1.82 ± 0.50, respectively, and the SUV_{FDG} and SUV_{FECH} of grade IV glioma were 13.91 ± 1.83 and 3.65 ± 0.34, respectively. According to FDG PET, the mean value of SUV on the lesion side of grade IV glioma was greater than that of grade II-III glioma, and the difference was significant ($P < 0.05$), and similar results were obtained on FECH PET. It showed that CNN-based PET + MRI fusion technology can effectively improve the recognition effect of glioma, can more accurately determine the scope of glioma lesions, and can predict the degree of malignant glioma to a certain extent.

1. Introduction

Neuroglioma can be referred to as glioma for short. It is a relatively common malignant tumor of the central nervous system from neuroepithelium, accounting for about 40% of intracranial tumors. It is the most common primary intracranial tumor, affecting approximately 3 to 8 out of 100,000 people each year, affecting all ages with a higher occurrence in men [1, 2]. According to the mortality rankings released by the World Health Organization (WHO) in 1998, glioma is the second leading cause of death in tumor patients under the age of 34 and the third leading cause of death between the ages of 35 and 54. Its symptoms are mainly characterized by sudden headaches accompanied by projective vomiting and increased intracranial pressure such as papilledema and some localized nerve damage [3, 4]. Aggressive growth is the main growth pattern of gliomas, which leaves no clear demarcation point between them and the surrounding adjacent normal brain tissue. To a large extent, the clinical effect of surgical treatment and the prognosis of patients are determined by the degree of resection of cancer tissue [5].

At present, the diagnosis of glioma is mainly based on imaging methods, such as magnetic resonance imaging (MRI) and positron emission tomography (PET). MRI is currently the most widely used clinical imaging for diagnosing neurosurgical gliomas, and it can construct the outline of cancer tissue by enhancing the range of enhanced lesions in the scan. However, whether the blood-brain barrier is damaged is a key factor in determining whether MRI images are enhanced or not. This means that MRI may not fully reflect the extent of cancer tissue. For most low-grade gliomas and a small number of high-grade gliomas, MRI does not show enhancement or only partial enhancement, which makes MRI insurmountable in describing the outline of cancer tissue, especially for low-grade gliomas [6–8]. PET can diagnose lesions through the metabolic differences between normal and diseased tissues and use different molecular imaging agents to perform noninvasive, dynamic, qualitative, and quantitative analysis of the metabolism and proliferation of brain tumor tissue. Therefore, it can supplement important information to CT/MRI images, but there are obvious deficiencies in tissue identification and anatomical localization [9].

PET and MRI fusion technology can combine the metabolic and anatomical data displayed by PET and MRI, which makes the localization information in the treatment of clinical gliomas more comprehensive and the treatment effect is more optimized [10, 11]. PET + MRI image fusion shows important clinical value for early diagnosis of glioma, precise localization of lesions, disease-based symptomatic treatment, and comprehensive evaluation. However, a large amount of image data increases the workload of doctors, which easily leads to fatigue, missed diagnosis, and misdiagnosis of disease diagnosis and is also susceptible to the images of doctors' experience and knowledge level in the reading process, making the results highly subjective [12]. Therefore, artificial intelligence algorithm-assisted diagnosis shows important research significance and application value in accurately diagnosing lesions. Convolutional neural network (CNN), which combines deep learning technology, is a learning method that can simulate the brain level. It uses four methods, namely, local receptive field, weight sharing, subsampling, and sparse connection, to process two-dimensional images. In addition, the advantage of CNN is that it can directly identify and feature the input original image, omitting the tedious process of preprocessing it, so CNN has extraordinary achievements in pattern recognition [13–15].

Taking glioma PET + MRI images as the research objects, this work constructed an artificial intelligence-based CNN auxiliary diagnosis model. The model was used in the classification and identification of gliomas to help clinicians make rapid diagnosis and treatment and to achieve the consistency of images and clinical research speculations. It aimed to promote the process of artificial intelligence, deepen its application in the medical field, and provide a certain theoretical basis for the diagnosis and treatment of neurosurgical gliomas in clinical practice.

2. Materials and Methodologies

2.1. General Data. From March 2018 to January 2020, 35 patients with highly suspected gliomas before surgery were treated in hospital. The general data about these patients is male in 23 cases and female in 12 cases. The age is from 23 to 67, with an average age of 45.3. The length of disease course is from 1 to 4 years. The main clinical manifestations of the patients were sudden headache with occasional projectile vomiting, general malaise, slurred speech, and seizures. The patients and their families had fully understood the situation and signed the informed consent forms, and this study had been approved by the medical ethics committee of the hospital.

Inclusion criteria were as follows: (i) patients whose diseases met the diagnostic criteria for glioma, which could be proved by definite pathological results of surgery or stereotactic needle biopsy; (ii) all patients who were first onset; (iii) patients with complete imaging data; and (iv) all patients who were aware of the study content and signed the informed consents.

Exclusion criteria were as follows: (i) patients with a history of brain space-occupying lesions; (ii) patients with a history of glioma treatment; and (iii) patients with a history of head trauma.

2.2. Preoperative Imaging Examination. PET scanning: all patients were performed with the examination 2 to 3 days before operation. The tracer 11C-Met 550–750 mBq was injected intravenously 6 hours after meal. After 20 minutes, PET was adopted for scanning, and cross sections, coronal planes, and sagittal planes were displayed, respectively.

MRI scanning: all patients were performed with MRI scanning on heads 1 day before the operation to determine the size of tumors. Conventional T1-weighted image (T1WI) and T2WI series examinations were implemented, respectively, by the 1.5 T intraoperative scanner. After gadopentetate dimeglumine (Gd-DTPA) was injected intravenously, T1WI enhancement scanning (T1-Gd) was conducted. In addition, some patients received magnetic resonance angiography (MRA) and diffusion tensor imaging (DTI). The grading criteria for gliomas in imaging examinations could be summarized as follows: for low-grade glioma (grade II), the diffuse astrocytoma showed relatively uniform signal, low signal on T1W, mostly no enhancement, and high signal on T2W and FLAIR. For, anaplastic glioma (grade III), when astrocytoma or oligodendrocytoma considered by MRI was enhanced, it indicated a high possibility of anaplastic. For glioma in grade IV, the main features of glioblastoma were irregular peripheral enhancement and massive central necrosis, and brain edema was visible outside the enhancement. Gliosarcoma, due to the predominance of sarcoma or glioma components, presented a real heterogeneously enhancing mass or a glioblastoma-like appearance, respectively.

2.3. Assessment of Uptake of PET Tracers. Visual analysis was adopted in the assessment. Combined with the lesion ranges of MRI images, the uptake of imaging agents was divided into three components as follows [16]:

(1) Low metabolism with uptake being lower or similar to white matters
(2) Intermediate metabolism with uptake being higher than white matters while significantly less than gray matters
(3) High metabolism with uptake being similar, equal to, or higher than gray matters

Apart from the concentration of imaging agents within lesion ranges, the assessment of uptake needed to be combined with the distribution forms and uniformity of imaging agents and the clear state of boundaries.

2.4. Preparation of CNN Model Structure

2.4.1. Convolutional Layer. As the core of the extraction of features in a convolutional neural network, the hidden layer has two special structures, including convolutional layer and subsampling layer. Local features of particular areas in local receptive fields are extracted by the convolutional layer. To be specific, a learnable kernel is convolved with the feature image on each layer to output the feature image on the next layer by the activated function. The convolution expression is shown in the following equation:

$$x_a^l = f\left(\sum_{i\in Ma} x_a^{l-1} \bullet k_{ia}^l + c_a^l\right). \quad (1)$$

In the above equation, l represents the number of layers, k stands for convolution kernel, x_a^{l-1} means a feature image on the upper layer, k_{ia}^l refers to the weight of convolution kernel, c means the offset item of each output feature image, and f() refers to the activated function. The incomplete connection mode is adopted in CNN, and this mode is featured with the sparse link between the neurons on upper and lower levels by local spatial correlation among layers. Hence, every output feature image may contain the convolution of multiple input images, which function differently due to the discrepancies of weights in convolution kernels.

2.4.2. Subsampling. Pooling calculation is performed for input by subsampling layer, and the feature dimension as well as the resolution can be reduced without repeated sampling. The number of input feature images and output feature images obtained by subsampling calculation are both n, but the original image is 2 times as large as the output feature images acquired by subsampling. The subsampling layer is expressed as

$$x_a^l = f\left(\beta_a^l \mathrm{down}\left(x_a^{l-1}\right) + c_a^l\right). \quad (2)$$

In the above equation, down (•) means subsampling function, β stands for multiplicative deviation, and c refers to additive deviation. After the features of images are obtained by using convolution, the classifier cannot categorize features directly because of large amounts of calculation, excessive time consumption, and easy fitting. To reduce the size of feature images, the subsampling layer is connected after the convolution layer. The neutrons input by the pooling layer is on the upper sampling window convolution layer in which neutrons gather form the value of neutrons. The value usually contains mean sampling and maximum pool sampling. The pooling results in a significant decrease of the number of neutrons in the model and shows the robustness in the horizontal movement and transformation of the input space.

2.4.3. Fully Connected Layer. In fully connected layers, all feature images (two-dimensional images), which are connected to the one-dimensional features, are used as the input to the fully connected network. The output of the fully connected layer is acquired by the input weighed sum and the response of the activated function.

$$x^l = f\left(v^l x^{l-1} + c^l\right). \quad (3)$$

In the above equation, v^l represents the weight coefficient of the fully connected network, x^{l-1} refers to feature images, and c^l means the offset items of the fully connected layer.

2.5. Softmax Classifier. Logical regression is the basis of the expansion of the Softmax regression classifier, and the training sample set of Softmax consists of m labelled samples: $\{x^{(1)}, y^{(1)}, x^{(2)}, y^{(2)}, \ldots, x^{(m)}, y^{(m)}\}$. Among these elements, $\mathrm{x}^{(\mathrm{i})}$ stands for input features and $x^{(i)} \in S^{n+1}$, $n+1$ is the dimension of eigenvector x, $y^{(i)}$ means classification labels, and logistic regression label is set as $y^{(i)} \in \{0, 1\}$.

If the loss function is expressed as (4), the cost function of the minimization of the parameter θ is expressed as (5).

$$p_\theta(x) = \frac{1}{1 + \exp\left(-\theta^T x\right)}, \quad (4)$$

$$A(\theta) = -\frac{1}{m}\left[\sum_{i-1}^{m} y^i \log\, p_\theta\left(x^i\right) + \left(1 - y^i\right)\log\left(1 - p_\theta\left(x^{(i)}\right)\right)\right]. \quad (5)$$

In the training samples of Softmax regression, different types of samples are denoted by a, the probability value of a is estimated by the function $p_\theta(x)$, and the probability value is shown as $q(y = a|x)$. $p_\theta(x)$ is presented as follows:

$$\mathrm{p}_\theta\left(\mathrm{x}^{\mathrm{i}}\right) = \begin{bmatrix} \mathrm{q}\left(\mathrm{y}^{\mathrm{i}} = 1|\mathrm{x}^{(\mathrm{i})}; \theta\right) \\ \mathrm{q}\left(\mathrm{y}^{\mathrm{i}} = 2|\mathrm{x}^{(\mathrm{i})}; \theta\right) \\ \\ \mathrm{q}\left(\mathrm{y}^{\mathrm{i}} = \mathrm{k}|\mathrm{x}^{(\mathrm{i})}; \theta\right) \end{bmatrix} = \frac{1}{\sum_{\mathrm{a}=1}^{\mathrm{k}} \mathrm{e}^{\theta_{\mathrm{a}}^T \mathrm{x}^{(\mathrm{i})}}} \begin{bmatrix} \mathrm{e}^{\theta_1^T \mathrm{x}^{(\mathrm{i})}} \\ \mathrm{e}^{\theta_2^T \mathrm{x}^{(\mathrm{i})}} \\ \\ \mathrm{e}^{\theta_{\mathrm{k}}^T \mathrm{x}^{(\mathrm{i})}} \end{bmatrix}. \quad (6)$$

In the above equation, $\theta_1, \theta_2, \ldots, \theta_k$ are parameters of the model and $\theta_1, \theta_2, \cdots, \theta_{\mathrm{k}} \in S^{\mathrm{n}+1}$. In the process of *Soft*max regression, θ is written in the column matrix as $\theta = \begin{bmatrix} \theta_1^T \\ \theta_2^T \\ \\ \theta_{\mathrm{k}}^T \end{bmatrix}$.

Based on the logistic regression, *Soft*max regression cost function is analyzed. In the function, 1 represents indicative function. 1{the expression value is true} = 1, and 1{the expression value is false} = 0, which demonstrate that the equation of cost function is expressed as follows:

$$A(\theta) = -\frac{1}{m}\left[\sum_{i=1}^{m}\sum_{a=0}^{1} 1\left\{y^{(i)} = a\right\}\log q\left(y^{(i)} = a|x^{(i)};\theta\right)\right]. \quad (7)$$

The cost function of *Soft*max is shown as follows:

$$A(\theta) = -\frac{1}{m}\left[\sum_{i=1}^{m}\sum_{a=1}^{k} 1\left\{a^{(i)} = a\right\}\log\frac{e^{\theta_a^T x^{(i)}}}{\sum_{l=1}^{k} e^{\theta_l^T x^{(i)}}}\right]. \quad (8)$$

The commonly used method of minimizing cost function is iterative optimization algorithm. The partial derivative of θ_a by $A(\theta)$ is shown as follows:

$$\frac{\partial A(\theta)}{\partial\theta_{al}} = \nabla_{\theta_a}A(\theta) = -\frac{1}{m}\sum_{i=1}^{m}\left[x^{(i)}\left(1\left\{y^{(i)} = a\right\} - q\left(y^{(i)} = a|x^{(i)},\theta\right)\right)\right]. \quad (9)$$

Later, the cost function $A(\theta)$ is minimized by the gradient descent algorithm. The gradient descent means the update of the parameter θ along with every iteration, which is shown as $\theta_a = \theta_a - z\nabla_{\theta a}A(\theta)\,(a = 1, 2, \cdots, k)$.

To avoid overfitting, a regularization item $\lambda/2\sum_{i=1}^{k}\sum_{a=0}^{n}\theta_{ia}^2$ is added behind the cost function and the excessively large parameter values are penalized, and then the equation for the regression cost function is derived, which is shown as follows:

$$A(\theta) = -\frac{1}{m}\left[\sum_{i=1}^{m}\sum_{a=1}^{k} 1\left\{a^{(i)} = a\right\}\log\frac{e^{\theta_a^T x^{(i)}}}{\sum_{l=1}^{k} e^{\theta_l^T x^{(i)}}}\right] + \frac{\lambda}{2}\sum_{i=1}^{k}\sum_{a=0}^{n}\theta_{ia}^2. \quad (10)$$

To achieve the *Soft*max regression and classification, the derivative of the minimized cost function is taken and shown as follows:

$$\frac{\partial A(\theta)}{\partial\theta_{al}} = \nabla_{\theta_a}A(\theta) = -\frac{1}{m}\sum_{i=1}^{m}\left[x^{(i)}\left(1\left\{y^{(i)} = a\right\} - q\left(y^{(i)} = a|x^{(i)};\theta\right)\right)\right] + \lambda\theta_a. \quad (11)$$

At the end, the Softmax regression classification model is generated by the minimization cost equation $A(\theta)$.

In the successive operations of convolutional neural networks and subsampling, the advantage of convolutional neural network in horizontal movement, scaling, and invariance in rotation as well as distortion is local receptive field, weight sharing, subsampling, and sparsity connection. While the convolution layer is connected to the neurons in a small neighborhood, weight sharing reduces the weight parameter obviously. The dimension of the subsampling features lowers, and the sparsity connection makes the network less complex, which enhances the generalization capacity and robustness of convolutional neural network in image comprehension.

2.6. Image Fusion. The 3D scan data of MRI and PET in DICOM format were imported into the system graphics workstation. The registration program automatically fused MRI T1-enhanced images, FDG PET images, and FECH PET images into the system. The accuracy of fusion was detected by craniofacial landmarks such as the nasal tip and inner conjunct, and manual fine-tuning can be performed if necessary. The fused images were still displayed in the form of MRI T1-enhanced images, FDG PET images, and FECH PET images, respectively, and lateral, sagittal, and coronal images can be displayed simultaneously as needed.

2.7. Formulation and Implementation of Operation. Formulation of operation: on the images of MRI (T1-Gd or T2WI) and 11C-Met PET cross sections, the contours of tumors were sketched, respectively. Concerning the cases whose lesions on the T1-Gd series were significantly enhanced, enhancement areas were regarded as tumor lesions. If the series did not enhance imaging or enhance it into punctiform shapes so that the contours of tumors could not be sketched, high signal areas of the T2WI series were viewed as tumor lesions. The areas where the uptake of 11C-Met PET images was obviously greater than peripheral normal gray matters were adopted as tumor lesions. When the contours of tumors were plotted, subjective visual manual drawing was utilized combined with the segmentation program and according to the image gray scale automatic plotting method. By the above methods, the contours of lesions in two images and the boundaries between intersection areas were sketched, respectively. The contributions of two different images in tumor sketch were described by the percentage (discrepancy-PET, %) of the volume of nonintersecting areas of PET and MRI images in that of the lesions shown by PET and the percentage (discrepancy-PET, %) of the volume of nonintersecting areas of MRI images and PET in that of the lesions shown by MRI, respectively.

Implementation of operation: the operation was implemented according to the postoperative operation plan and the relationship between tumors and normal brain tissues under the navigation microscope. Tumor excision was based on 11C-Met PET images or MRI images. To avoid brain tissue drift, intraoperative MRI scanning was performed on the cases with large intraoperative tumors and unclear boundaries between tumors and normal brain tissues hinted by the microscope. Besides, images were imported into the neurological system's computer workstation. After that, the same method was adopted to fuse and compare intraoperative MRI results with preoperative images to determine tumor excision.

2.8. Statistical Analysis. SPSS 23.0 software was used for statistical analysis of all data, measurement data were analyzed using independent samples *t*-test, count data were expressed as percentage, and $\chi 2$ test was used.

3. Results

3.1. Comparison of Performance of Convolutional Neural Networks. The parameter migration method was adopted to construct convolutional neural networks, and intracranial glioma with different modes of PET, MRI, and PET + MRI was identified. Figure 1(a), Figure 1(b), and Figure 1(c) show

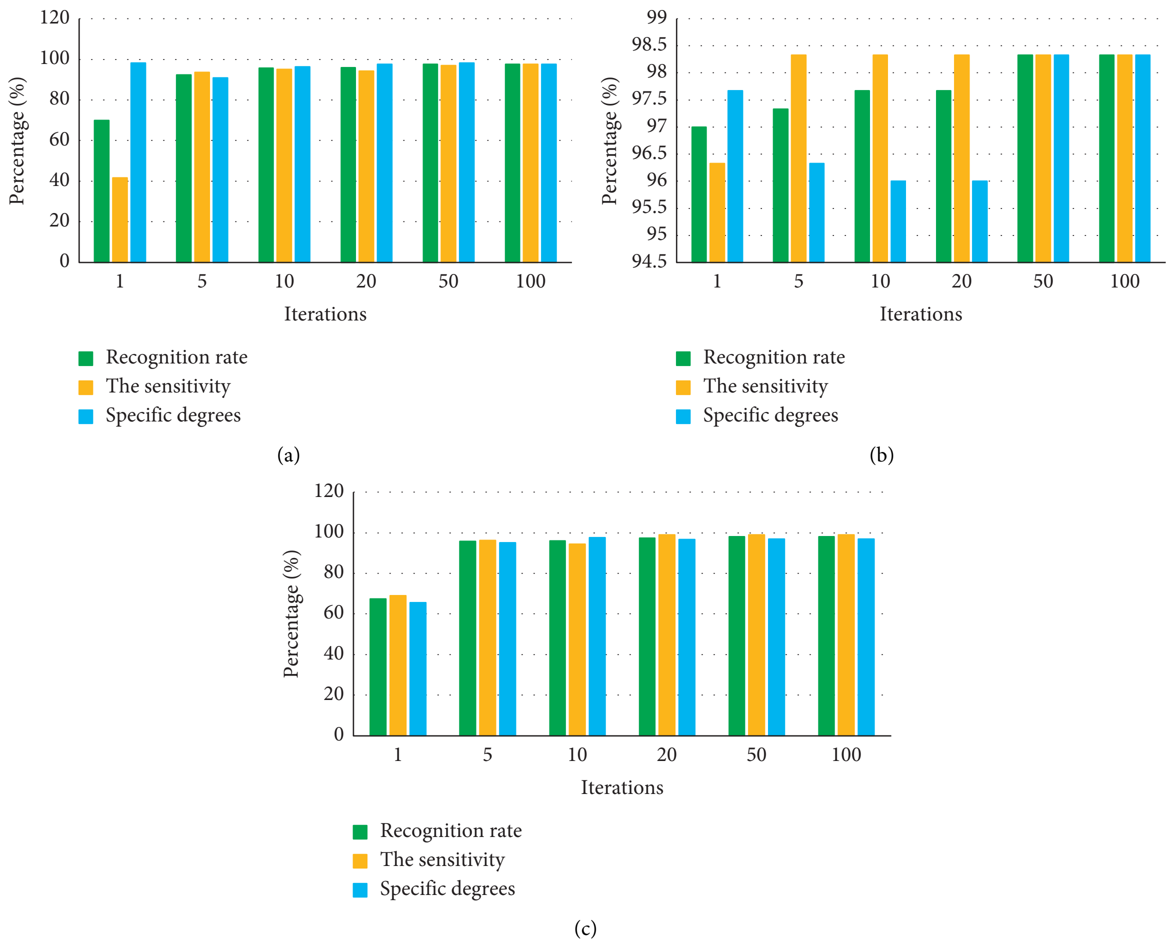

Figure 1: Comparison on the performance of CNNs. The performance evaluation results of (a) PET-CNN, (b) MRI-CNN, and (c) PET/MRI-CNN.

the evaluation results of performance of PET-CNN, MRI-CNN, and PET/MRI-CNN, respectively.

According to the above figures, the recognition accuracy of PET-CNN reached nearly 95% after the iteration occurred more than 10 times. Without the growing iteration numbers, accuracy was increased slightly, and it amounted to 97.67% after 50 iterations. In general, sensitivity was slightly lower than specific degree. In contrast, the recognition rate of MRI-CNN was higher with recognition accuracy reaching about 97%. After 10 iterations, it tended to be stable without being enhanced by the increasing iteration numbers. The recognition rate of fused PET/MRI images by PET/MRI-CNN reached 97%, while the specific degree was relatively low.

3.2. Imaging Performance. MRI of all patients showed T1 and T2 signals with different lengths. The enhancement scan demonstrated enhancement in 19 cases, and no obvious enhancement was detected in 16 cases. According to the type of pathology, enhancement was found in 4 cases with glioma of grade II and 6 cases with glioma of grade III. Enhancement was shown in all eight cases with glioblastoma multiforme, and obvious inhomogeneous enhancement was demonstrated in the other two patients with central nervous system vasculitis. Figures 2 and 3 show specific details. Figure 4 shows the PET images obtained after tracer injection in a 45-year-old male glioma patient. Figure 5 shows the PET + MRI fusion images of a 54-year-old female glioma patient after tracer injection.

On PDG PET, eight cases with the uptake greater than the contralateral gray matter were all patients with glioblastoma multiforme. Among 12 cases with the uptake close to the contralateral gray matter, six were patients with glioma of grade III, four were diagnosed with glioma of grade II, and 2 were patients with central nervous system vasculitis. Among 15 cases with the uptake less than the contralateral gray matter but greater than the contralateral white matter, nine were patients with glioma of grade III and six were diagnosed with glioma of grade II. On 18F-FECH PET, there were 21 cases with the uptake greater than background brain and 12 cases without obvious uptake. Obvious uptake of 11C-MET was observed in all eight cases with glioblastoma multiforme. Among 12 cases without uptake, five were patients with glioma of grade II and seven had glioma of grade III. Detailed information is shown in Figures 6(a) and 6(b).

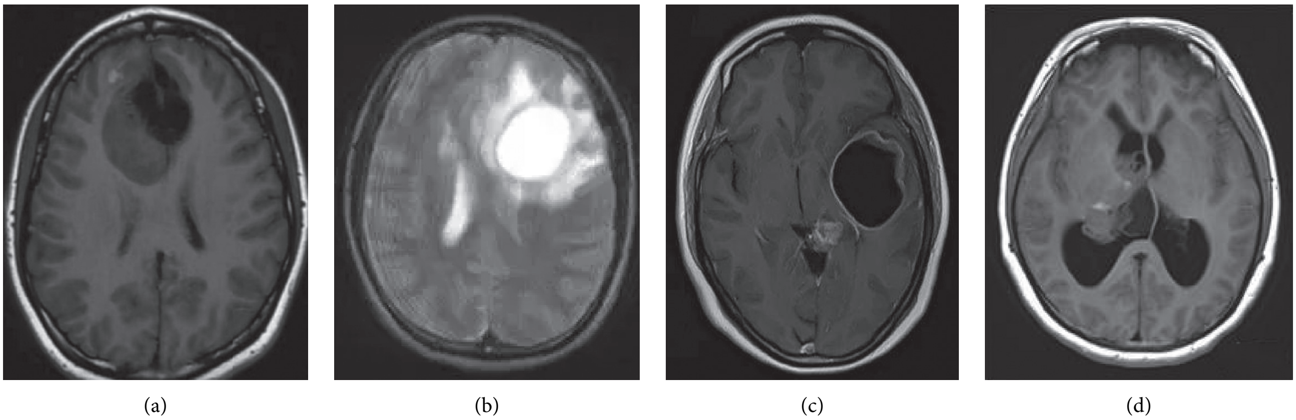

Figure 2: MRI images of patients with glioma in grade IV. The patient was a female, 62 years old. (a, b) MRI plain scan images and (c, d)MRI enhanced images.

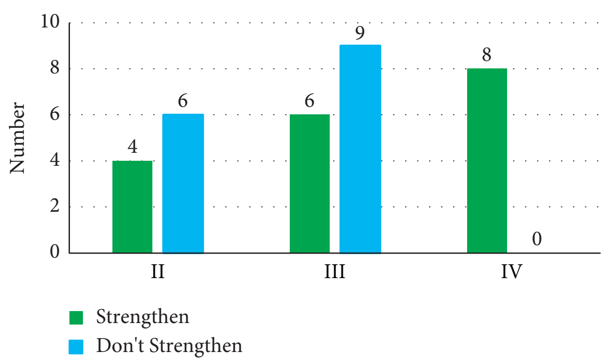

Figure 3: Enhancement of gliomas of different grades by MRI.

After measurement, it was found that the SUVFDG and SUVFECH of grade II/III glioma were 9.77 ± 4.87 and 1.82 ± 0.50, respectively, and the SUVFDG and SUVFECH of grade IV glioma were 13.91 ± 1.83 and 3.65 ± 0.34, respectively. The L/CFDG and L/CFECH values of grade II/III glioma were 2.00 ± 0.34 and 5.98 ± 3.88, respectively; and the L/CFDG and L/CFECH values of grade IV glioma were 2.68 ± 0.10 and 19.21 ± 6.30, respectively. See Figure 7 for details.

3.3. Construction of Contours of Cancer Tissues. According to the positional relationship of the contour lines of lesions on PDG PET and MRI, lesions were divided into the following six categories. (I) PET lesions within MRI lesions; (II) the contour lines of PET lesions and MRI lesions do not cross, but may overlap or not; (III) the contour lines of MRI lesions within PET lesions; (IV) the contour lines of PET and MRI lesions are roughly equal; (V) the contour lines of MRI are vague, so only PET lesions are detectable; and (VI) the contour lines of PET are vague, so only MRI lesions are detectable.

The number of gliomas in grades II, III, and IV was 2, 3, and 0 in class I; it was 0, 2, and 4 in class II, and it was 2 and 2 in class III. The number of cases in category IV was 0, 0, and 3, respectively. The number of cases in category V was 3, 5, and 0, and the number of cases in category VI was 3, 3, and 0, respectively (as shown in Figure 8).

Classification of the positional relationship of lesions on 18F-FECH PET and MRI was given as follows (as illustrated in Figure 9). The number of grade II, III, and IV gliomas were 2, 3, and 1 in class I, 0, 0, and 2 in class II, and 1 and 2 in class III. There are 1, 1, and 0 cases in category IV, 1, 0, and 1 in category V, and 4, 3, and 1 in category VI. The number of cases classified was 2, 5, and 1, respectively.

4. Discussion

The prerequisite for the embodiment of its one value of convolutional neural network is accurate imaging data. Conventional MRI imaging is the most applied imaging technique so far. The Gd-DTPA enhanced sequence is often applied in the construction of cancer tissues. However, enhancement is not shown on MRI or can be observed on only a few MRIs since blood-brain barriers are not impaired completely in most of gliomas of lower grade and a few gliomas of higher grade. It is hard to distinguish cancer tissues from pericancerous edema merely by normal T1WI or T2WI [17, 18]. In the research, it was found that the recognition rate of fused PET/MRI images by PET/MRI-CNN reached 97%. Because fused images themselves could enhance the discernibility degree of lesion areas, make images clearer as well as significant visual effects, and show lesion ranges more obviously, the recognition effects of glioma in neurosurgery by convolutional neural networks were enhanced. However, the specific degree of the networks was relatively low, which indicated a high misdiagnosis rate.

PET is a metabolic imaging method with which noninvasive, dynamic, qualitative, and quantitative analysis of the metabolism and proliferation of cancer tissues can be performed based on different molecular imaging agents. The use of this technique is an indispensable supplement to the presentation of anatomic information by CT/MRI. Metabolic and anatomic data provided by PET and MRI, respectively, can be combined effectively by the joint use of PET and MRI, which provides more complete location information and

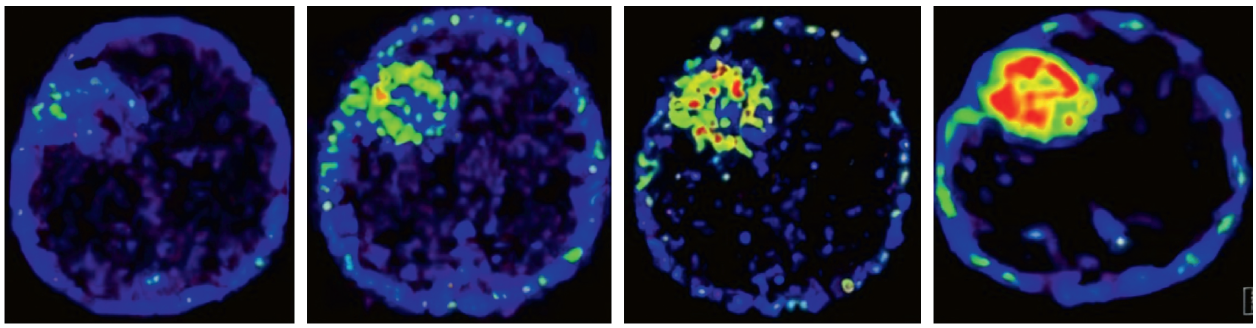

Figure 4: PET images of glioma patients. From left to right, they were the images of 1 h, 8 h, 12 h, and 24 h of injection of tracer, respectively.

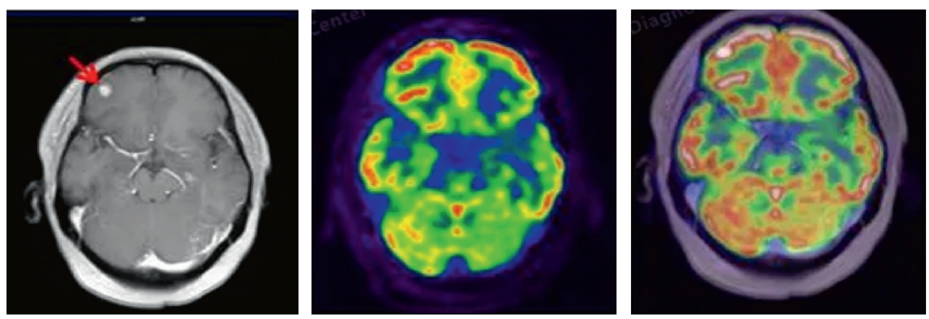

Figure 5: PET + MRI fusion images of glioma patients. From left to right, they were the fusion images and the images at 8 h and 24 h after the tracer injection. The arrows indicate the lesions.

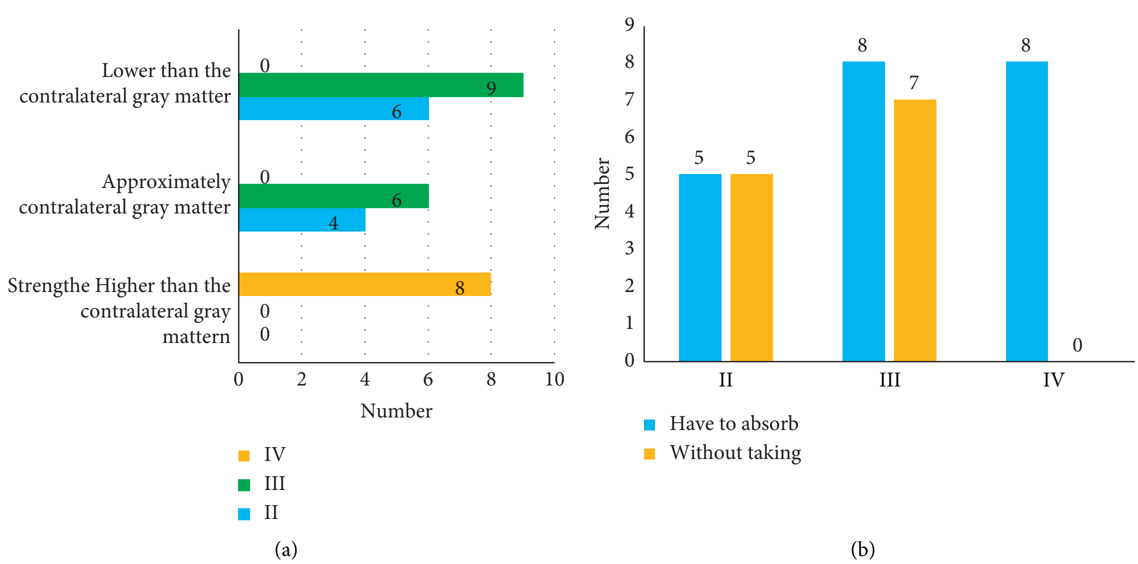

Figure 6: Uptake of tracers by gliomas of different grades. (a) The uptake of 18F-FDG and (b) the uptake of 18F-FECH.

qualitative information for the clinical treatment of glioma to optimize therapeutic effects [19]. Kebir et al. (2019) [20] performed surgical treatment on patients with gliomas of different grades with the navigation of 11C-MET PET fused with MRI. Without the enhanced MRI, PET tracers can be used to excise cancer tissues with high malignancy in locally concentrated areas. Hara et al. (2020) [21] made a statistical comparison of the tumor excision rate and the prognosis of patients between the PET/MRI navigation system and a single MRI navigation system, and 11C-MET was used as PET tracer. Totally, 36 surgeries were performed on 33 patients, 17 of which were navigated by PET/MRI and 19 were navigated by MRI. The results showed that PET/MRI could offer more information about the location of tumors, but there was no significant difference between the complications of the two surgeries. The total excision rate of the PET/MRI navigation system was higher than that of the MRI

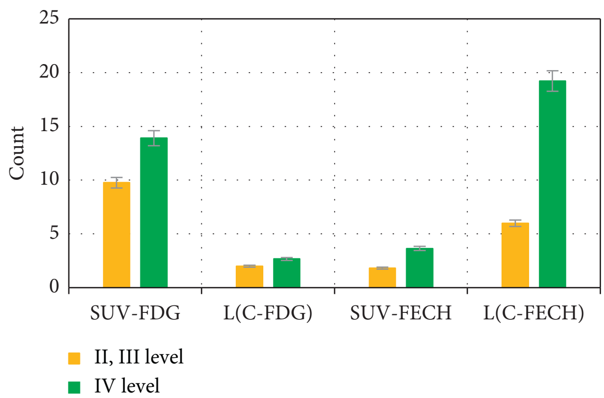

Figure 7: Semiquantitative analysis of the uptake of tracers by gliomas of different grades.

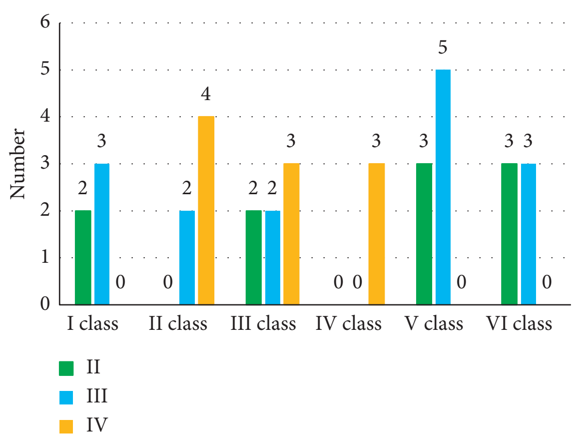

Figure 8: Classification of the manifestations of glioma of different grades on PDG PET.

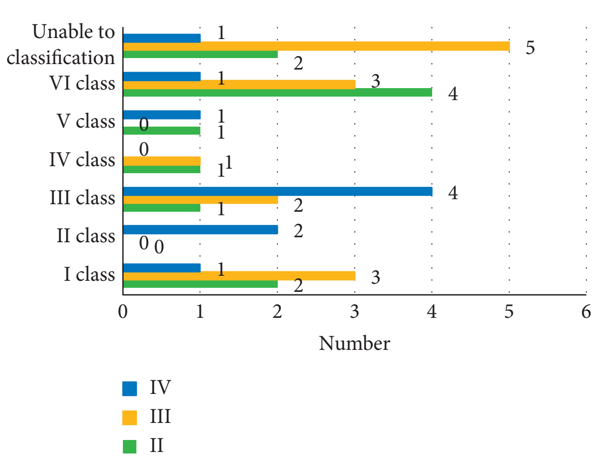

Figure 9: Classification of the manifestations of gliomas of different grades on FECH PET.

navigation system, and the PET/MRI navigation system survived longer than the MRI navigation system.

In this research, PET and MRI fusion technology was applied before surgeries to determine if biopsy or surgery should be performed on each of 35 patients suspected of glioma according to the location of lesions and imaging manifestations. The analysis of the manifestations of each case on MRI showed that glioblastoma multiforme in eight cases were all enhanced, but the enhancement of glioma could be observed only in 10 out of 25 cases with grades II-III, which proved that MRI enhancement could predict the severity of cancer tissues to some degree. However, the prediction was indirect because the judgement on if the blood-brain barrier was intact was necessary and closely related. This opinion was consistent with related literature reports [22, 23]. Meanwhile, eight cases with the uptake greater than the gray matter were all glioblastoma multiforme patients, and those with the uptake close to or less than gray matter were all diagnosed with glioma of grades II-III. In terms of the uptake of 18F-FECH (tracers), the obvious uptake of 18F-FECH was detected in all eight cases with glioblastoma multiforme, and the WHO grade of 12 glioma cases without obvious uptake were all II-III. According to the ratio of the standard uptake value of the lesions on FDG PET and the standard uptake value of lesions and contralateral brain tissues in semiquantitative analysis, the average of gliomas of grades II-III was lower than that of glioblastoma multiforme. These results were similar to the data obtained from FECH PET. Based on these analyses, it is shown that patients with the higher WHO grade of glioma probably means the higher uptake of two types of tracers. Unfortunately, the number of cases included in this research is small, and the analysis is not tested by statistics. The research shows that the PET uptake of tracers can better reflect the severity of glioma, which is consistent with some previous reports [24, 25].

In the comparison of the contours of lesions on PET and MRI, five PET lesions were smaller than those on MRI and seven PET lesions were larger than those on MRI on FDG PET. The result indicated that the range of lesions shown on PET was inclined to become larger than that presented by MRI. On FECH PET, tumor contours could not be determined by MRI and PET in eight cases, which showed the supplementary information provided for the cases with different tumor contours determined on MRI was not ideal. Nonetheless, a conclusion with statistical meaning could not be drawn because of the small number of cases. Katsanos et al. (2019) [26] reported that the range of lesions was smaller than that of lesions on MRI in nearly 85% of cases examined by FDG PET. The results showed an inconsistency with the results of the observation in this research. The appearance of the discrepancy may be related to different operating conditions of PET and the differences in subjective descriptions of constructing the contours of cancer tissues.

5. Conclusion

The PET + MRI fusion technology based on CNN can make the image clearer and the visual sense stronger. At the same time, it can improve the recognition effect of neurosurgical glioma and more accurately determine the scope of glioma lesions. In the absence of enhancement, there was a significant advantage especially in low-grade gliomas. However, due to the limited sample size, it lacked overall representativeness. In the future, it will increase the number of samples and conduct more in-depth studies on gliomas.

Data Availability

The data used to support the findings of this study are available from the corresponding author upon request.

Conflicts of Interest

The authors declare no conflicts of interest.

References

[1] J. Garland, B. Ondruschka, S. Stables et al., "Identifying fatal head injuries on postmortem computed tomography using convolutional neural network/deep learning: A feasibility study," *Journal of Forensic Sciences*, vol. 65, no. 6, pp. 2019–2022, 2020.

[2] F. Fahimi, Z. Zhang, W. B. Goh, T.-S. Lee, K. K. Ang, and C. Guan, "Inter-subject transfer learning with an end-to-end deep convolutional neural network for EEG-based BCI," *Journal of Neural Engineering*, vol. 16, no. 2, Article ID 026007, 2019.

[3] S. Braunstein, D. Raleigh, R. Bindra, S. Mueller, and D. Haas-Kogan, "Pediatric high-grade glioma: Current molecular landscape and therapeutic approaches," *Journal of Neuro-Oncology*, vol. 134, no. 3, pp. 541–549, 2017.

[4] A. Poff, A. P. Koutnik, K. M. Egan, S. Sahebjam, D. D'Agostino, and N. B. Kumar, "Targeting the Warburg effect for cancer treatment: Ketogenic diets for management of glioma," *Seminars in Cancer Biology*, vol. 56, pp. 135–148, 2019.

[5] J. Bai, J. Varghese, and R. Jain, "Adult glioma WHO classification update, genomics, and imaging: What the radiologists need to know," *Topics in Magnetic Resonance Imaging*, vol. 29, no. 2, pp. 71–82, 2020.

[6] Y. Leng, X. Wang, W. Liao, and Y Cao, "Radiomics in gliomas: A promising assistance for glioma clinical research," *Zhong nan da xue bao. Yi xue ban = Journal of Central South University. Medical sciences*, vol. 43, no. 4, pp. 354–359, 2018.

[7] M. Hu, Y. Zhong, S. Xie, H. Lv, and Z. Lv, "Fuzzy system based medical image processing for brain disease prediction," *Frontiers in Neuroscience*, vol. 15, Article ID 714318, 2021.

[8] J. Arzoine, C. Levé, C. Levé et al., "Anesthesia management for low-grade glioma awake surgery: A European low-grade glioma network survey," *Acta Neurochirurgica*, vol. 162, no. 7, pp. 1701–1707, 2020.

[9] X. Niu, T. Wang, X. Zhou et al., "Surgical treatment and survival outcome of patients with adult thalamic glioma: A single institution experience of 8 years," *Journal of Neuro-Oncology*, vol. 147, no. 2, pp. 377–386, 2020.

[10] M. Kim, S. Y. Jung, J. E. Park et al., "Diffusion- and perfusion-weighted MRI radiomics model may predict isocitrate dehydrogenase (IDH) mutation and tumor aggressiveness in diffuse lower grade glioma," *European Radiology*, vol. 30, no. 4, pp. 2142–2151, 2020.

[11] Z. Sui, X. Zhang, H. Li, D. Xu, and G. Li, "Magnetic resonance imaging evaluation of brain glioma before postoperative radiotherapy," *Clinical and Translational Oncology*, vol. 23, no. 4, pp. 820–826, 2021.

[12] T. Hofer, J. Kronbichler, H. Huber et al., "18F-Choline PET/CT, MRI, and software-based image fusion analysis in patients with primary hyperparathyroidism," *Clinical Nuclear Medicine*, vol. 46, no. 9, pp. 710–716, 2021.

[13] Z. Akkus, J. Cai, A. Boonrod et al., "A survey of deep-learning applications in ultrasound: Artificial intelligence-powered ultrasound for improving clinical workflow," *Journal of the American College of Radiology*, vol. 16, no. 9, pp. 1318–1328, 2019.

[14] Z. Lv and L. Qiao, "Deep belief network and linear perceptron based cognitive computing for collaborative robots," *Applied Soft Computing*, vol. 92, Article ID 106300, 2020.

[15] Z. Wang and A. Majewicz Fey, "Deep learning with convolutional neural network for objective skill evaluation in robot-assisted surgery," *International Journal of Computer Assisted Radiology and Surgery*, vol. 13, no. 12, pp. 1959–1970, 2018.

[16] C. Philippe, M. Zeilinger, M. Dumanic et al., "SNAPshots of the MCHR1: A comparison between the PET-tracers [18F] FE@SNAP and [11C]SNAP-7941," *Molecular Imaging and Biology*, vol. 21, no. 2, pp. 257–268, 2019.

[17] H. Zhang, Y. Li, Z. Lv, A. K. Sangaiah, and T. Huang, "A real-time and ubiquitous network attack detection based on deep belief network and support vector machine," *IEEE/CAA Journal of Automatica Sinica*, vol. 7, no. 3, pp. 790–799, 2020.

[18] X. Liu, Z. Li, W. Zhang et al., "Gadobutrol precedes Gd-DTPA in abdominal contrast-enhanced MRA and MRI: A prospective, multicenter, intraindividual study," *Contrast Media and Molecular Imaging*, vol. 2019, pp. 1–7, Article ID 9738464, 2019.

[19] H. Shao, X. Ma, Y. Gao et al., "Comparison of the diagnostic efficiency for local recurrence of rectal cancer using CT, MRI, PET and PET-CT," *Medicine*, vol. 97, no. 48, Article ID e12900, 2018.

[20] S. Kebir, M. Weber, L. Lazaridis et al., "Hybrid 11C-MET PET/MRI combined with "machine learning" in glioma diagnosis according to the revised glioma WHO classification 2016," *Clinical Nuclear Medicine*, vol. 44, no. 3, pp. 214–220, 2019.

[21] S. Hara, Y. Tanaka, Y. Ueda et al., "Detection of hemodynamic impairment on 15O gas PET using visual assessment of arterial spin-labeling MR imaging in patients with moyamoya disease," *Journal of Clinical Neuroscience*, vol. 72, pp. 258–263, 2020.

[22] H. Zhou, M. Vallières, H. X. Bai et al., "MRI features predict survival and molecular markers in diffuse lower-grade gliomas," *Neuro-Oncology*, vol. 19, no. 6, pp. 862–870, 2017.

[23] A. K. Narang, K. L. Chaichana, J. D. Weingart et al., "Progressive low-grade glioma: Assessment of prognostic importance of histologic reassessment and MRI findings," *World Neurosurgery*, vol. 99, pp. 751–757, 2017.

[24] T. Hirata, M. Kinoshita, K. Tamari et al., "11C-methionine-18F-FDG dual-PET-tracer-based target delineation of malignant glioma: Evaluation of its geometrical and clinical features for planning radiation therapy," *Journal of Neurosurgery*, vol. 131, no. 3, pp. 676–686, 2019.

[25] M. Sollini, R. Sghedoni, P. A. Erba et al., "Diagnostic performances of [18F]fluorocholine positron emission tomography in brain tumors," *The Quarterly Journal of Nuclear Medicine and Molecular Imaging*, vol. 62, no. 2, pp. 209–219, 2018.

[26] A. H. Katsanos, G. A. Alexiou, A. D. Fotopoulos, P. Jabbour, A. P. Kyritsis, and C. Sioka, "Performance of 18F-FDG, 11C-Methionine, and 18F-FET PET for glioma grading: A meta-analysis," *Clinical Nuclear Medicine*, vol. 44, no. 11, pp. 864–869, 2019.

Hindawi
Contrast Media & Molecular Imaging
Volume 2022, Article ID 8628668, 9 pages
https://doi.org/10.1155/2022/8628668

Research Article

Coronary Artery Magnetic Resonance Angiography Combined with Computed Tomography Angiography in Diagnosis of Coronary Heart Disease by Reconstruction Algorithm

Yun Ling, Jiapei Qiu, and Jun Liu

Department of Cardiovascular Surgery, Ruijin Hospital, Shanghai Jiaotong University School of Medicine, Shanghai 200025, China

Correspondence should be addressed to Jun Liu; 2016052063@stu.gzucm.edu.cn

Received 3 January 2022; Revised 21 February 2022; Accepted 23 February 2022; Published 23 March 2022

Academic Editor: M. Pallikonda Rajasekaran

This research aimed at discussing the diagnosis effect of coronary artery magnetic resonance angiography (MRA) combined with computed tomography (CT) angiography (CTA) based on the back-projection filter reconstruction (BPFR) algorithm in coronary heart disease (CHD), and its role in the diagnosis of coronary artery disease (CAD). Sixty patients with CHD were selected and randomly rolled into group A (undergone MRA examination), group B (undergone CTA examination), and group C (undergone MRA + CTA), with 20 cases in each group. Taking the diagnostic results of coronary angiography as the gold standard, the MRA and CTA images were reconstructed using a BPFR algorithm, and a filter function was added to solve the problem of image sharpness. In addition, the iterative reconstruction algorithm and the Fourier transform analysis method were introduced. As a result, the image clarity and resolution obtained by the BPFR algorithm were better than those obtained by the Fourier transform analytical method and the iterative reconstruction algorithm. The accuracy of group C for the diagnosis of mild coronary stenosis, moderate stenosis, and severe stenosis was 94.02%, 96.13%, and 98.01%, respectively, which was significantly higher than that of group B (87.5%, 90.2%, and 88.4%) and group C (83.4%, 89.1%, and 91.5%) ($P < 0.05$). The sensitivity and specificity for the diagnosis of noncalcified plaque in group C were 87.9% and 89.2%, respectively, and the sensitivity and specificity for the diagnosis of calcified plaque were 84.5% and 78.4%, respectively, which were significantly higher than those in groups B and C ($P < 0.05$). In summary, the BPFR algorithm had good denoising and artifact removal effects on coronary MRA and CTA images. The combined detection of reconstructed MRA and CTA images had a high diagnostic value for CHD.

1. Introduction

With the increasingly serious urban aging, more and more people suffer from cardiovascular disease (CVD) [1]. A recent epidemiological survey indicated that there are currently 290 million patients with CVD in China, of which more than 10 million are with coronary heart disease (CHD) and 4.5 million are patients with heart failure. The number of deaths from CVD accounts for the highest number of deaths from all diseases, far higher than other diseases such as tumors. For every 10 deaths, 4 patients die from CVD [2]. The most common CVD is CHD. The treatment cost of CHD patients has brought a huge burden to the family and society, and CHD has attracted more and more scholars' attention [3]. Early diagnosis and early prevention of CHD patients can effectively reduce the medical expenses of patients, while also avoiding the waste of medical resources. At present, the commonly used diagnostic methods for CHD include electrocardiogram (ECG) (to preliminary judge the location of myocardial ischemia or infarction), chest X-ray (to exclude lung disease, preliminary assessment of patients with suspected heart failure), myocardial markers (to determine the myocardial injury status and predict the time of myocardial ischemia of patients), computed tomography (CT) angiography (CTA), and magnetic resonance angiography (MRA) [4].

Stress echocardiography can determine whether the patient has signs of myocardial ischemia during exercise, so as to further clarify the diagnosis of stable CHD. CTA is a noninvasive inspection method to determine the degree of coronary artery stenosis (CAS) and its branches. If there is no stenosis on the coronary CT angiography, the invasive inspection is generally not necessary [5, 6]. Magnetic resonance angiography (MRA) is an examination method that uses electromagnetic waves to generate images of two-dimensional or three-dimensional structures of the body, and uses magnetic resonance phenomena to obtain electromagnetic signals from the human body and reconstruct human information [7]. It can be used for the diagnosis of heart disease, cardiomyopathy, pericardial effusion, mural thrombosis, etc. For the diagnosis of CHD, branches of coronary artery lesions can be intuitively found, which is of great significance for assessing the degree of branch obstruction and judging the severity of disease [8, 9]. Image reconstruction technology plays an important role in many fields, and there are a series of extremely complex image processing and mathematical calculation problems in the research and implementation of the reconstruction algorithm [10, 11]. The essence of back-projection reconstruction is to evenly erase (back projection) the ray projection taken from the finite object space onto all points in the infinite space where the ray reaches, including the point with the original pixel value of 0 [12, 13]. At present, algorithms such as image reconstruction and computer-assisted medical image analysis have obvious advantages in major breakthroughs in technology and improvement of medical level, and have also become an effective way to solve medical image problems [14, 15].

At present, CTA and MRA are widely used in the screening of CHD. However, there are few studies on the combination of the two in the diagnosis of CHD. In addition, the two diagnostic methods mentioned above have certain limitations, such as high false-positive rate and large amount of contrast agent. The resolution of coronary artery CTA is limited, and serious artifacts may exist during reconstruction, leading to inaccurate coronary artery assessment. Therefore, an attempt was made to construct a back-projection filter reconstruction (BPFR) algorithm, which convolved the Ramp-Lak filter with $\sin(x)/x$ to obtain the Sheep–Logan filter. The MRA images and noisy data of coronary artery were reconstructed by using the Sheep–Logan filter, so as to study the diagnostic value of coronary artery MRA and CTA combined detection based on the reconstruction algorithm for CHD.

2. Research Objects and Major Methods

2.1. General Data of Research Objects. In this study, there are 60 patients with CHD in hospital from November 2019 to October 2020, 38 males and 22 females, with an average age of 43.21 ± 8.37 years. The patients were randomly divided into group A (undergone MRA examination), group B (undergone CTA examination), and group C (undergone MRA + CTA), with 20 in each group. The study had been approved by the ethics committee of hospital, and the patients had been informed about this study and singed informed consents.

Inclusion criteria: patients without a history of CVD-related surgery; those with age between 50 and 70 years; and those taking no other drugs and antibiotics.

Exclusion criteria: patients with other system or organ diseases; those with cardiomyopathy; those who were allergic to iodine contrast agents; and those with serum creatinine above normal levels.

2.2. CTA and MRA Examinations. For patients in group A (undergone MRA examination), the coronary artery MRA used 1.5 T superconducting MR machine, the gradient field strength was 40 mT/m, the switching rate was 150 T/m per second, an 8-channel heart coil was adopted, and the heart electrical trigger and respiratory monitoring device were equipped. For the breath-hold three-dimensional (3D) fast steady-state balance precession sequence, the time of repetition (TR) was 4.1 ms, the time of echo (TE) was 1.9 ms, and the reversal angle was 65. The field of view (FOV) was 26×26 cm, the matrix was 256×192, partial K-space sampling was adopted, the layer thickness was 3.0 cm with 8–10 layers, and ECG-triggered mid-diastolic end-expiratory sampling was adopted. The maximum intensity projection coronary artery reconstruction method was used to reconstruct the coronary artery image.

For patients in group B (coronary artery CTA examination), the 16-slice spiral CT was used for CTA. The scanning range was determined by phase scanning, the upper tracheal carina was below the level, the lower boundary was 1 cm below the diaphragmatic surface, and the left and right sides were 1~2 cm larger than both sides of the heart edge. Layer selection was made by observing the left pulmonary trunk plane located on the calcification integral image. Scanning sequence: heart rate 50~60 beats/min was prospectively gated, and heart rate 60~70 beats/min was retrospectively gated. Maximum density projection recombination was used.

For patients in group C, coronary MRA and coronary CTA combined examination was performed. The diagnostic accuracy of coronary angiography was evaluated by the gold standard.

2.3. Image Reconstruction. Image reconstruction algorithms are roughly classified into Fourier transform (FT) algorithms and iterative reconstruction (IR) algorithms. With the increasing application of computer technology, there are various reconstruction algorithms with different characteristics. The BPFR algorithm, which is a FT theory-based spatial processing technology, was adopted as the basic algorithm of the model. It can perform convolution on the projection of each acquisition projection angle before back projection, thereby enhancing the quality of the reconstructed image. The reconstruction principle is shown in Figure 1.

In the process of the Fourier slice theorem, the one-dimensional FT of the projection and the 2D FT of the original image were equivalent. The Fourier slice theorem can perform the FT on the projections to obtain a 2D FT from a projection [16, 17]. Therefore, the projection image

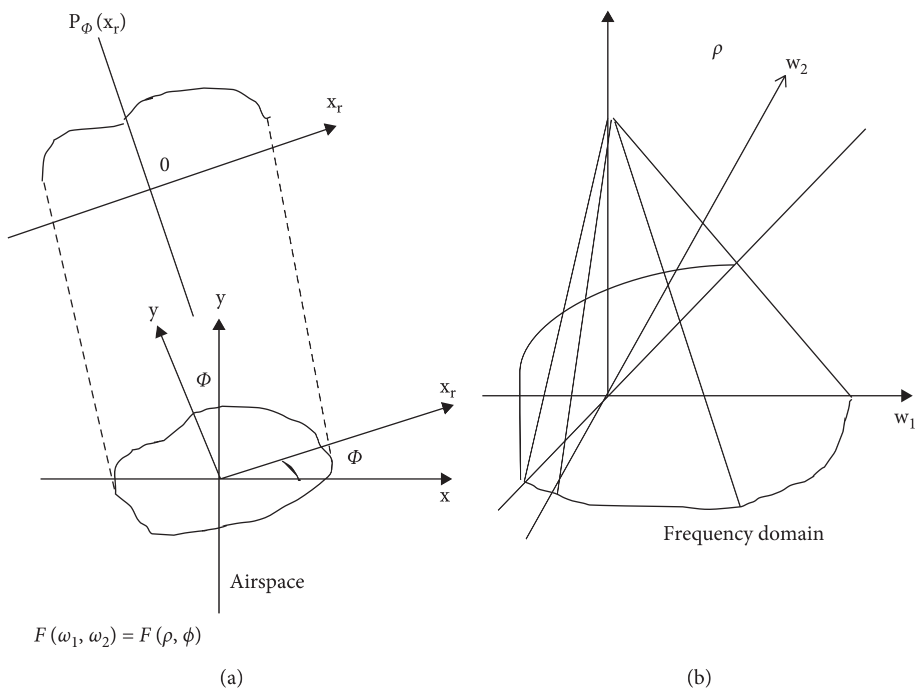

FIGURE 1: Principle of image reconstruction. (a) Before FT and (b) one-dimensional (1D) and two-dimensional (2D) FT.

can be reconstructed by collecting enough projections at different times (180 acquisitions generally), solving the 1D FT of each projection, combining abovementioned slices into the 2D FT of the image, and then using the inverse FT [18].

The BPFR algorithm back-projects the measured projection data along the scanning path "original path" to the pixels passed by the path. The value of a pixel in the tomographic plane is regarded as the accumulation (or average) of all the projection values of the rays passing through the pixel [19, 20]. The direct back-projection method is simple and easy to implement, but the image of Deba is very fuzzy, and it needs more time-consuming follow-up correction to restore the original image. In the parallel beam scanning mode, in addition to the fixed coordinate system *x-y* and the polar coordinate system (γ, ϕ), a rotating coordinate system *t-s* was adopted for easy principal explanation here. The coordinate system *t-s* coincided with the origin of the coordinate system *x-y*, and the angle was θ. Therefore, the ray position can be uniquely determined by the coordinate (t, θ), and (t, θ) corresponded to a ray projection value. The ray (t, θ) can pass (γ, ϕ) by satisfying thefollowing equation as follows:

$$t = r\cos(\phi - \theta). \tag{1}$$

In the translation/rotation scan mode, the scan operation is stepped by angular increment Δ and step distance d, so (t, θ) is often expressed as a discrete quantity $(n\ d, m\Delta)$, and m and n are integers. Corresponding projection data is given as follows:

$$p(t, \theta)(t = nd, \theta = m\Delta). \tag{2}$$

$t = nd, \theta = m\Delta$ was also discrete. $\triangle$ and d must be small enough; otherwise, those rays passing (γ, ϕ) will not pass the actual discrete ray position $(nd, m\Delta)$:

$$f(\gamma, \phi) = \frac{1}{m} \sum_{m=0}^{M-1} \tilde{p} m\Delta[r\cos(\phi - m\Delta)]. \tag{3}$$

In the above equation,

$$r\cos(\phi - m\Delta) \neq nd. \tag{4}$$

Therefore, the following equation cannot be directly obtained, and interpolation must be performed:

$$\tilde{p} m\Delta[r\cos(\phi - m\Delta)], \tag{5}$$

$$t = nd, \tag{6}$$

$$\theta = m\Delta. \tag{7}$$

The above two equations were both discrete. For a certain point (x_i, y_j) in space, there must be a ray t_m under a certain angle of view $\theta = \theta_m = m\Delta$, which was defined as

$$t_m = x_i \cos\theta_m + y_j \sin\theta_m. \tag{8}$$

Since (x_i, y_j) was the pixel coordinate of any point in space, t_m was not exactly an integer multiple of d and may be between $n_0 d$ and $(n_0 + 1)d$, that is,

$$t_m = (n_0 + \delta)d, 0 < \delta < 1. \tag{9}$$

After linear interpolation, the following equation is obtained:

$$\widetilde{p}(t_m, \theta_m) = \widetilde{p}m\Delta[(n_0 + \delta)d],$$
$$\widetilde{p}m\Delta[(n_0 + \delta)d] = \widetilde{p}m\Delta(n_0 d) + \frac{\widetilde{p}m\Delta[(n_0 + 1)d] - \widetilde{p}m\Delta[(n_0 d)]}{d}(t_m - n_0 d). \tag{10}$$

If $d = l$, and the fixed angle of view $\triangle$ was omitted, then the below equation could be obtained:

$$\begin{aligned}\widetilde{p}(n_0 + \delta) &= \widetilde{p}(n_0) + \delta[\widetilde{p}(n_0 + 1) - \widetilde{p}(n_0)] \\ &= (1 - \delta)\widetilde{p}(n_0) + \widetilde{\delta p}(n_0 + 1).\end{aligned} \tag{11}$$

Therefore, it needed to calculate n_0 and δ first. The image area is usually divided into NXN pixels. The beam rotates around the center of the image area after translation. For any pixel (x_i, y_j) and viewing angle θ, the following equations can be satisfied:

$$t = x_i \cos\theta + y_j \sin\theta,$$
$$x_i \cos\theta + y_j \sin\theta = \left(i - \frac{N}{2}\right)\cos\theta + \left(j - \frac{N}{2}\right)\sin\theta, \tag{12}$$
$$\left(i - \frac{N}{2}\right)\cos\theta + \left(j - \frac{N}{2}\right)\sin\theta = (i-1)\cos\theta + (j-1)\sin\theta - \frac{N}{2}(\cos\theta + \sin\theta).$$

After interpolation, the passed ray projection value can be obtained, as shown in the following equation:

$$\widetilde{p}(t_m, \theta_m) = \widetilde{p}m\Delta[(n_0 + \delta)d]. \tag{13}$$

After it was incorporated into $f(\gamma, \phi)$, the following could be acquired:

$$f(\gamma, \phi) = \frac{1}{m}\sum_{m=0}^{M-1}\widetilde{p}(t_m, \theta_m). \tag{14}$$

In concrete realization, it can be expressed as follows:

$$f(i, j) = \sum_{m=0}^{M-1}\widetilde{p}(\widetilde{t}_m(i, j), m\Delta). \tag{15}$$

When the above equation is executed on a computer, it can be calculated as follows:

$$\begin{aligned}f_m(i, j) &= f_{m-1}(i, j) + \widetilde{p}(\widetilde{t}_m(i, j), m\Delta), \\ m &= 1, 2, 3, \ldots, M.\end{aligned} \tag{16}$$

2.4. Image Reconstruction Results. A BPFR algorithm was used to reconstruct three-dimensional coronary MRA and CTA images of patients with CHD, and a filter function was added to solve the problem of image sharpness. The image acquisition process is shown in Figure 2. Among them, P, Q, R, S, and T represented the P wave, Q wave, R wave, S wave, and T wave in the ECG, respectively. PR and ST represented the P-R interval and ST segment, respectively, in the ECG. In addition, an iterative reconstruction algorithm (reconstructing the image by solving a system of linear equations) and an analytical method of Fourier transform were introduced. For patients with different degrees of coronary stenosis, coronary calcified plaque, and noncalcified plaque, the reconstructed three-dimensional images were used to present the lesions more clearly in a three-dimensional and visualized form to achieve the effect of simulation.

2.5. Statistical Methods. The data were analyzed and processed with SPSS 19.0. The measurement data and count data were expressed by the mean ± standard deviation (□$x \pm s$) and percentage (%), respectively. Pairwise comparison was realized by the analysis of variance. The difference was statistically significant at $P < 0.05$.

3. Results

3.1. Running Time of Different Algorithms. As given in Figure 3, the running time of the FT method and the IR algorithm was the shortest both when the overlap step (OLS) was 8 and the block size (BS) was 32^2 and when the OLS was 16 and the BS was 482. When the OLS was 16 and the BS was 32^2, the running time of the BPFR algorithm was the shortest.

3.2. Coronary CTA and MRA. After the R wave trigger delay of the ECG, the image acquisition was started, then coronary MRA angiography was started, then T2 prescan (inhibits venous and myocardial signals) was carried out, and then spectral presaturation inversion to restore fat saturation (inhibits fat signals) was performed, and navigation pulses were used for breathing exercises compensate. Figure 4 shows coronary CTA and MRA images in patients with CHD. Whole-heart coronary MRA images showed severe stenosis and occlusion of the left main coronary artery and proximal anterior descending artery. There was also significant stenosis in the posterior descending artery, and the results of coronary CTA and MRA were in good agreement.

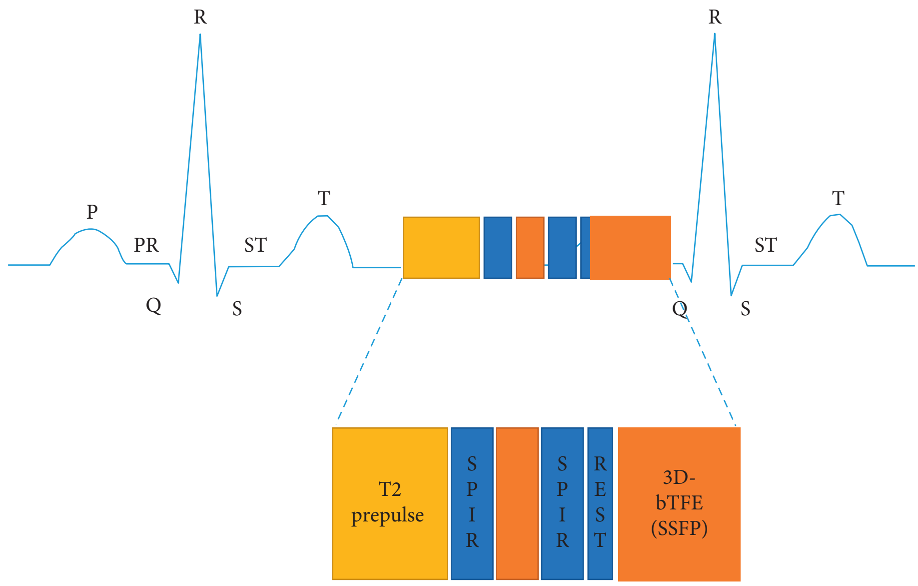

Figure 2: Image acquisition.

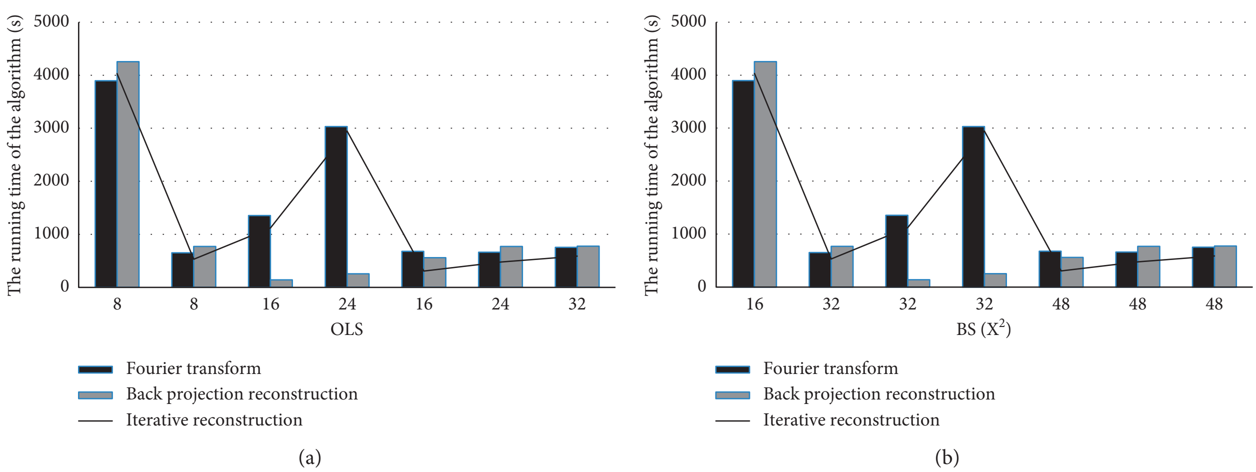

Figure 3: Running time for image reconstruction of different algorithms. (a) Running time at different OLSs and (b) running time at different BSs.

3.3. Reconstruction of Coronary Angiography Image. The BPFR algorithm applied the filter function to the original data, filtered signals in the image, removed the information that causes noise and artifacts, and reconstructed the image to remove the noise and artifacts of the image. Figure 5 shows the CTA images of CHD patients and reconstruction results of the FT method, IR algorithm, and BPFR algorithm. The clarity and resolution of the CTA image reconstructed by the BPFR algorithm were better than those of the FT method and IR algorithm, and the recognition rate of CAS and plaque was higher.

BPFR corrected the structural information of the target image block through the adaptive selection of images and super-resolution reconstruction, so as to obtain high-resolution images with higher definition, clear image edges, and significantly enhanced details. Then, the interference was eliminated to reconstruct a clearer image. Figure 6 shows the coronary artery MRA images of CHD patients and the reconstruction results of the FT method, IR algorithm, and BPFR algorithm. The red markers in the figure indicate severe stenosis and occlusion of LMCA and PADA branches. The clarity and resolution of the CTA image reconstructed by the BPFR algorithm are better compared with the FT method and IR algorithm, and the recognition rate of CAS and plaque was higher.

3.4. The Diagnosis Results of Coronary Artery Plaque. Figure 7 shows the comparison of the sensitivity and specificity of coronary artery noncalcified plaque and calcified plaque using coronary MRA examination, coronary CTA examination, and MRA combined with CTA examination in three groups of patients. The sensitivity and specificity of the noncalcified plaque diagnosis of group C

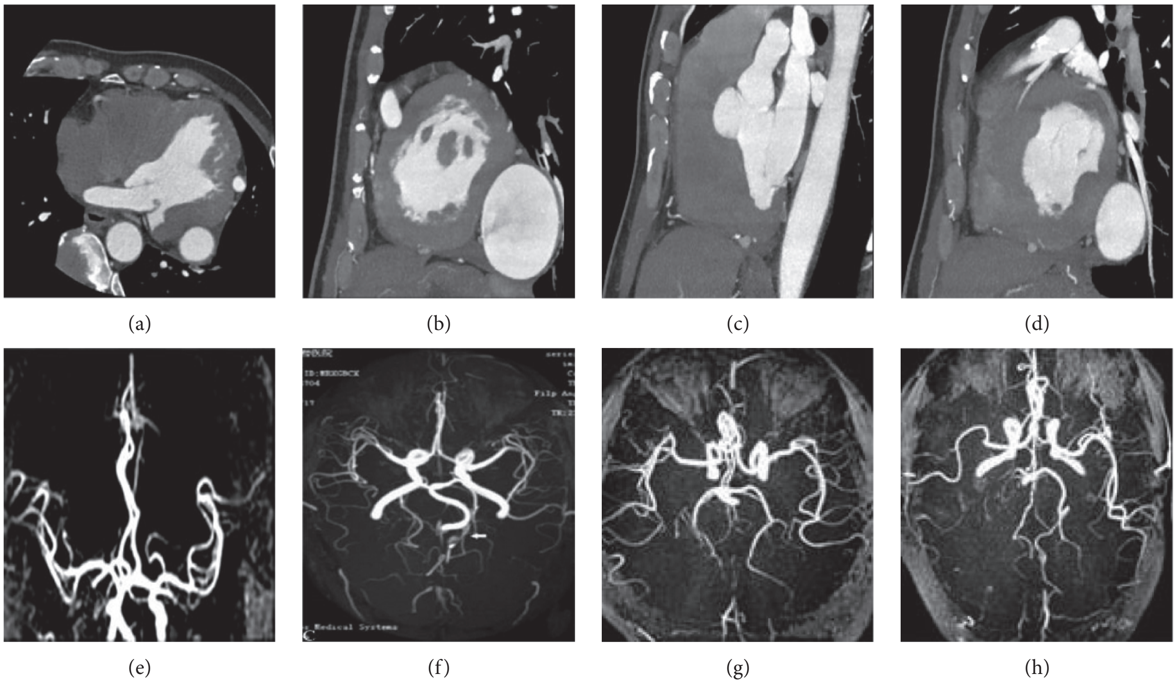

Figure 4: Coronary angiography images. (a–d) CTA images of four patients; (e–h) coronary MRA images of four patients.

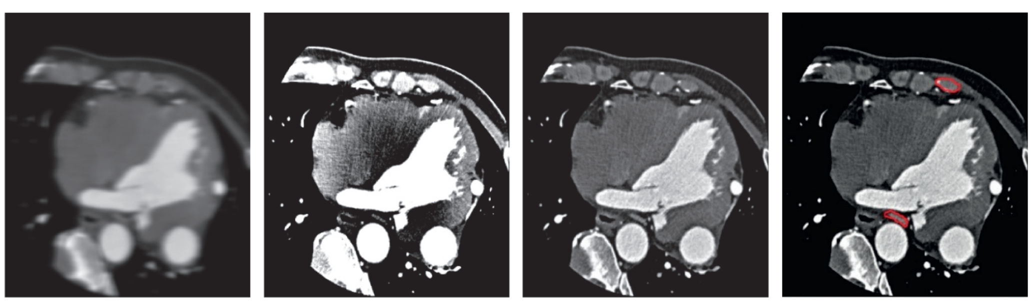

Coronary artery CTA | Fourier transform analytical method | Iterative reconstruction algorithm | Back projection reconstruction algorithm

Figure 5: Coronary CTA image reconstruction. (a) Coronary CTA image; (b) Fourier transform analysis method reconstructed image; (c) iterative algorithm reconstructed image; (d) BPFR-reconstructed image. The red area in the figure represents coronary stenosis and plaque.

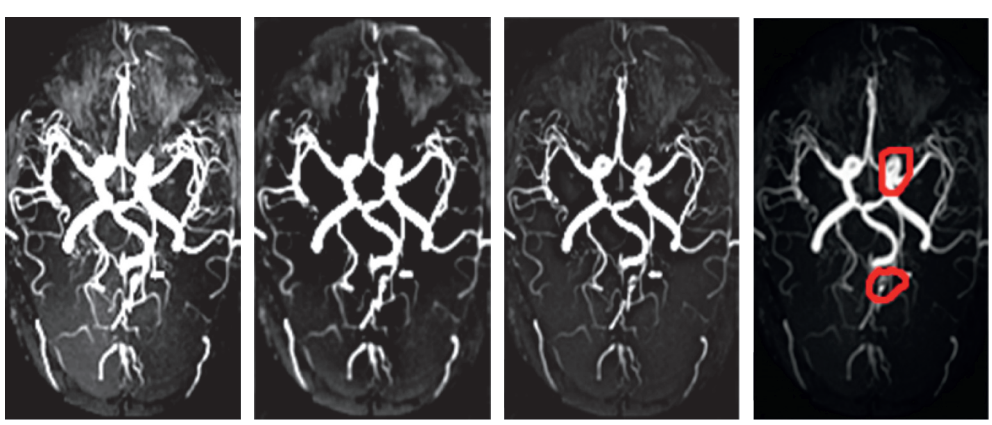

Coronary artery MRA | Fourier transform analytical method | Iterative reconstruction algorithm | Back projection reconstruction algorithm

Figure 6: Reconstruction of the coronary artery MRA image. (a) Coronary artery MRA image; (b–d) images reconstructed by the FT method, IR algorithm, and BPFR algorithm, respectively.

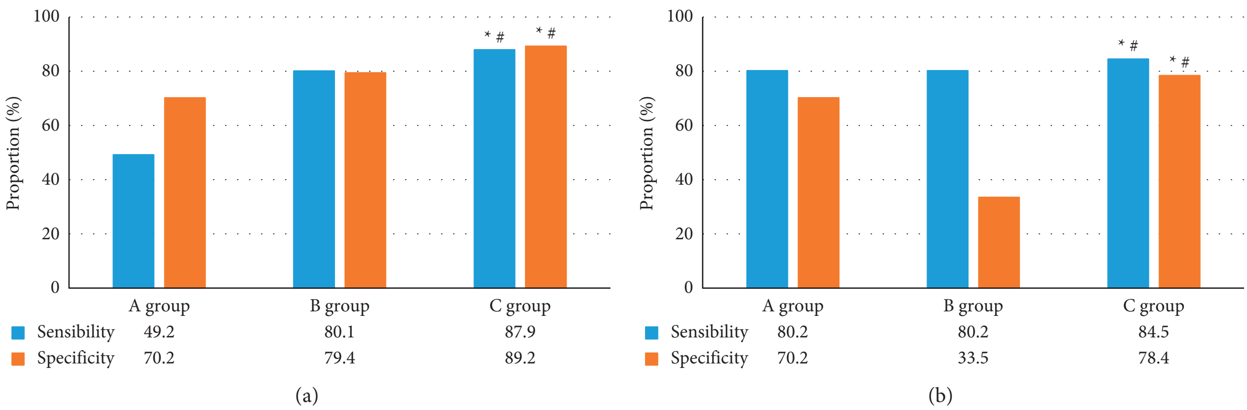

Figure 7: The diagnosis results of coronary artery plaque. (a, b) diagnosis results of noncalcified plaque and calcified plaque, respectively. * and # indicate $P < 0.05$ vs the group A and group B, respectively.

patients were 87.9% and 89.2%, respectively, which were obviously higher in contrast to the other two groups ($P < 0.05$). Sensitivity and specificity of the calcified plaque diagnosis in group C were 84.5% and 78.4%, respectively, which were higher dramatically than the values in the other two groups ($P < 0.05$).

3.5. The Diagnosis Results of CAS. Figure 8 illustrates the accuracy comparison results of patients in the diagnosis of mild, moderate, and severe CAS. The diagnosis accuracy of patients in group C for mild stenosis, moderate stenosis, and severe stenosis of the coronary arteries was 94.02%, 96.13%, and 98.01%, which were dramatically higher than those in group B (87.5%, 90.2%, and 88.4%) and group C (83.4%, 89.1%, and 91.5%), showing statistically obvious differences ($P < 0.05$).

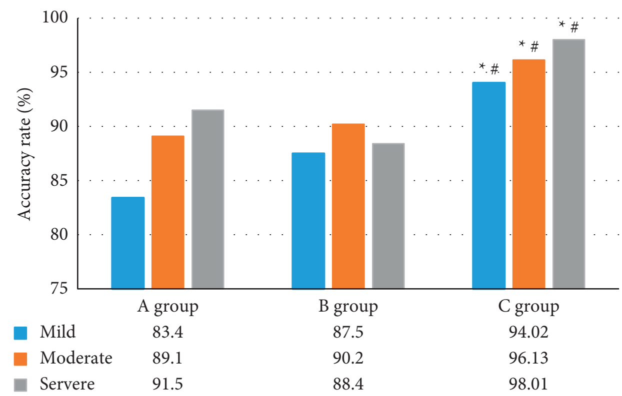

Figure 8: The diagnosis results of CAS. * and # indicate $P < 0.05$ compared with the group A and group B, respectively.

4. Discussion

Coronary MRA is a new method of coronary artery imaging without ionizing radiation and noninvasive, which is expected to replace the current coronary angiography technology. It is currently the most used method to obtain free-breathing 3D MRA by using respiration and ECG gating technology [21]. Shen et al. [22] found that MRA can detect significant CAD and predict serious cardiac adverse events. In addition, MRA has a long imaging time and low spatial resolution. However, with the application of new technologies such as high-field magnetic resonance imaging and multichannel cardiac coils, MRA can be imaged in a relatively short period of time to accurately diagnose coronary artery disease. The BPFR algorithm is developed based on back projection, solving the problem of image sharpness by adding filter function. Without the addition of filtering function, the reconstructed image is fuzzy, while the reconstructed image with the addition of filtering function can make it clearer [23]. Roh et al. [24] included patients with stable chest pain and compared them with standard treatment and coronary artery CTA. At 4.8 years of follow-up, the incidence of death from CHD or nonfatal myocardial infarction (2.3%) was significantly lower in patients treated with coronary CTA combination therapy. Coronary artery CTA may be used to determine the event risk of nonblocking CHD, which has a positive application value for the prevention and diagnosis of CHD. In this study, MRA and CTA images of coronary artery in patients with CHD were reconstructed by reverse projection image reconstruction algorithm, and filtering function was added to solve the problem of image sharpness. In addition, the iterative reconstruction algorithm and Fourier transform analytic method were introduced.

After the BPFR algorithm was employed to process MRA and CTA images, it was found that when the OLS was 16 and the BS is 32^2, the running time of the BPFR algorithm was the shortest. Therefore, BS was set to 32^2 and OLS length was set to 16 pixels to obtain a high-quality image and to prevent the parameters setting from affecting the reconstruction result. The sensitivity and specificity of patients in group C for diagnosing noncalcified plaques were 87.9% and 89.2%, respectively, and those for the diagnosis of calcified plaques were 84.5% and 78.4%, respectively, which were greatly higher than the values in other groups ($P < 0.05$). It may be because CTA is more conducive to judging the degree of stenosis of coronary arteries and their branches, while MRA is more conducive to identifying the diseased branches of coronary arteries and assessing the degree of branch obstruction. Both have high specificity, so their combined use can effectively improve the diagnostic effect. The accuracy of the combined detection of patients in group C for the diagnosis of mild, moderate, and severe CAS was 94.02%, 96.13%, and 98.01%, respectively, which were much higher ($P < 0.05$). Such findings show similarity to the results of Puz et al. [25], which may be due to the noninvasive inspection method of CTA, which is suitable for the degree of stenosis of coronary arteries and their branches. MRA can obtain electromagnetic signals, which is suitable for identifying the branch of coronary artery disease, assessing the degree of branch obstruction, and judging the severity of the disease. Therefore, the combination and application of MRA and CTA testing may be more conducive to improving the diagnosis of CHD.

5. Conclusion

In this study, the BPFR algorithm was constructed and applied to the MRA and CTA images of coronary artery patients with CHD, and the image was reconstructed to remove noise and artifacts. It was attempted to obtain the clear image and identify the lesion, so as to study the diagnostic value of coronary artery MRA and CTA combined detection based on the reconstruction algorithm. The results showed that the BPFR algorithm had good denoising and artifact removal effects on coronary MRA and CTA images. The combined detection of reconstructed MRA and CTA images has a high diagnostic value for CHD. However, the sample size included in this study is small and lacks certain representativeness. In addition, there is no in-depth study on whether the combined application of the two detection methods will cause certain side effects to patients. Therefore, this aspect will be improved and optimized in the follow-up study, and the application of coronary artery MRA and CTA combined detection based on the reconstruction algorithm in the diagnosis of CHD will be further analyzed. In conclusion, this study provides a reference for the application of intelligent algorithms in medical imaging and disease diagnosis.

Data Availability

The data used to support the findings of this study are available from the corresponding author upon request.

Conflicts of Interest

The authors declare no conflicts of interest.

Authors' Contributions

Yun Ling and Jiapei Qin contributed equally to this work.

References

[1] M. H. Albrecht, A. Varga-Szemes, U. J. Schoepf et al., "Diagnostic accuracy of noncontrast self-navigated free-breathing MR angiography versus CT angiography: a prospective study in pediatric patients with suspected anomalous coronary arteries," *Academic Radiology*, vol. 26, no. 10, pp. 1309–1317, 2019.

[2] C. Pirlet, L. Piérard, P. Lancellotti et al., "Contribution du scanner coronaire au diagnostic de maladie coronarienne [CT coronary angiography for the diagnosis of coronary heart disease]," *Revue Medicale de Liege*, vol. 69, no. 7-8, pp. 422–427, 2014.

[3] M. Pamminger, C. Kranewitter, C. Kremser et al., "Self-navigated versus navigator-gated 3D MRI sequence for non-enhanced aortic root measurement in transcatheter aortic valve implantation," *European Journal of Radiology*, vol. 137, Article ID 109573, 2021.

[4] T. Hickethier, J. R. Kröger, J. Von Spiczak et al., "Non-invasive imaging of bioresorbable coronary scaffolds using CT and MRI: first in vitro experience," *International Journal of Cardiology*, vol. 206, pp. 101–106, 2016.

[5] T. L. Bair, H. T. May, K. U. Knowlton, J. L. Anderson, D. L. Lappe, and J. B. Muhlestein, "Predictors of statin intolerance in patients with a new diagnosis of atherosclerotic cardiovascular disease within a large integrated health care institution," *Journal of Cardiovascular Pharmacology*, vol. 75, no. 5, pp. 426–431, 2020.

[6] K. E. Emmanuel, M. Nassar, and N. Nso, "Prognostic value of cardiovascular testing in asymptomatic patients with a history of cardiovascular disease: a review of contemporary medical literature," *Cureus*, vol. 13, no. 8, Article ID e16892, 2021.

[7] M. Ghadimi Mahani, "Diagnostic accuracy of noncontrast self-navigated free-breathing MR angiography versus CT angiography: a prospective study in pediatric patients with suspected anomalous coronary arteries," *Academic Radiology*, vol. 26, no. 10, pp. 1318-1319, 2019.

[8] A. N. Kazantsev, R. S. Tarasov, N. N. Burkov et al., "Progression of precerebral atherosclerosis and predictors of ischemic complications in cardiac patients," *Khirurgiya. Zhurnal im. N.I. Pirogova*, vol. 7, pp. 31–38, 2020.

[9] J. Gou, X. Wu, and H. Dong, "Reduced iteration image reconstruction of incomplete projection CT using regularization strategy through Lp norm dictionary learning," *Journal of X-Ray Science and Technology*, vol. 27, no. 3, pp. 559–572, 2019.

[10] T. Tsunekawa, M. Sawada, T. Kato et al., "The prevalence and distribution of occlusive lesions of the cerebral arteries in patients undergoing coronary artery bypass graft surgery," *Seminars in Thoracic and Cardiovascular Surgery*, vol. 30, no. 4, pp. 413–420, 2018.

[11] M. Jędrychowska, R. Januszek, W. Wańha et al., "Long-term prognostic significance of high-sensitive troponin I increase during hospital stay in patients with acute myocardial infarction and non-obstructive coronary arteries," *Medicina*, vol. 56, no. 9, p. 432, 2020.

[12] Y. Li, J. Zhao, Z. Lv, and J. Li, "Medical image fusion method by deep learning," *International Journal of Cognitive Computing in Engineering*, vol. 2, pp. 21–29, 2021.

[13] E.-J. Lee, C.-H. Chung, K.-H. Choi et al., "The impact of cerebral atherosclerosis according to location on prognosis after coronary artery bypass grafting," *Cerebrovascular Diseases*, vol. 46, no. 5-6, pp. 200–209, 2018.

[14] D. Piccini, L. Feng, G. Bonanno et al., "Four-dimensional respiratory motion-resolved whole heart coronary MR angiography," *Magnetic Resonance in Medicine*, vol. 77, no. 4, pp. 1473–1484, 2017.

[15] M. Hu, Y. Zhong, S. Xie, H. Lv, and Z. Lv, "Fuzzy system based medical image processing for brain disease prediction," *Frontiers in Neuroscience*, vol. 15, Article ID 714318, 2021.

[16] C. Morbach, M. Wagner, S. Güntner et al., "Heart failure in patients with coronary heart disease: prevalence, characteristics and guideline implementation - results from the German EuroAspire IV cohort," *BMC Cardiovascular Disorders*, vol. 17, no. 1, p. 108, 2017.

[17] S. B. Nam, D. W. Jeong, K. S. Choo et al., “Image quality of CT angiography in young children with congenital heart disease: a comparison between the sinogram-affirmed iterative reconstruction (SAFIRE) and advanced modelled iterative reconstruction (ADMIRE) algorithms,” *Clinical Radiology*, vol. 72, no. 12, pp. 1060–1065, 2017.

[18] A. Örgel, G. Bier, F. Hennersdorf, H. Richter, U. Ernemann, and T. K. Hauser, “Image quality of CT angiography of supra-aortic arteries : comparison between advanced modelled iterative reconstruction (ADMIRE), sinogram affirmed iterative reconstruction (SAFIRE) and filtered back projection (FBP) in one patients’ group,” *Clinical Neuroradiology*, vol. 30, no. 1, pp. 101–107, 2020.

[19] X. Wang, C. Zhu, J. Li, A. J. Degnan, T. Jiang, and J. Lu, “Knowledge-based iterative model reconstruction,” *Medicine*, vol. 97, no. 30, p. e11514, 2018.

[20] Q. Zhang, Q. Sun, Y. Zhang et al., “Three-dimensional image fusion of CTA and angiography for real-time guidance during neurointerventional procedures,” *Journal of Neurointerventional Surgery*, vol. 9, no. 3, pp. 302–306, 2017.

[21] M. H. Albrecht, A. Varga-Szemes, U. J. Schoepf et al., “Coronary artery assessment using self-navigated free-breathing radial whole-heart magnetic resonance angiography in patients with congenital heart disease,” *European Radiology*, vol. 28, no. 3, pp. 1267–1275, 2018.

[22] D. Shen, R. R. Edelman, J. D. Robinson et al., “Single-shot coronary quiescent-interval slice-selective magnetic resonance angiography using compressed sensing,” *Journal of Computer Assisted Tomography*, vol. 42, no. 5, pp. 739–746, 2018.

[23] R. R. Edelman, S. Giri, A. Pursnani, M. P. F. Botelho, W. Li, and I. Koktzoglou, “Breath-hold imaging of the coronary arteries using Quiescent-Interval Slice-Selective (QISS) magnetic resonance angiography: pilot study at 1.5 Tesla and 3 Tesla,” *Journal of Cardiovascular Magnetic Resonance*, vol. 17, no. 1, p. 101, 2015.

[24] J. W. Roh, B.-J. Kwon, S.-H. Ihm et al., “Predictors of significant coronary artery disease in patients with cerebral artery atherosclerosis,” *Cerebrovascular Diseases*, vol. 48, no. 3-6, pp. 226–235, 2019.

[25] P. Puz, A. Lasek-Bal, A. Warsz-Wianecka, and M. Kaźmierski, “Prevalence of atherosclerotic stenosis of carotid and cerebral arteries in patients with stable or unstable coronary artery disease,” *Polish Archives of Internal Medicine*, vol. 130, no. 5, pp. 412–419, 2020.

Hindawi
Contrast Media & Molecular Imaging
Volume 2022, Article ID 6495309, 8 pages
https://doi.org/10.1155/2022/6495309

Research Article

Diagnosis of Early Cervical Cancer with a Multimodal Magnetic Resonance Image under the Artificial Intelligence Algorithm

Zhenge Zhang, Chongyuan Zhang, Li Xiao, and Shuirong Zhang

Department of Gynecology Ward 2, Jingzhou Central Hospital, Jingzhou Hospital, Yangtze University, Jingzhou 434020, Hubei, China

Correspondence should be addressed to Shuirong Zhang; 201701111700031@stu.hubu.edu.cn

Received 16 January 2022; Revised 18 February 2022; Accepted 21 February 2022; Published 23 March 2022

Academic Editor: M. Pallikonda Rajasekaran

This research was conducted to explore the value of multimodal magnetic resonance imaging (MRI) based on the alternating direction algorithm in the diagnosis of early cervical cancer. 64 patients diagnosed with early cervical cancer clinicopathologically were included, and according to the examination methods, they were divided into A group with conventional multimodal MRI examination and B group with the multimodal MRI examination under the alternating direction algorithm. The diagnostic results of two types of multimodal MRI for early cervical cancer staging were compared with the results of clinicopathological examination to judge the application value in the early diagnosis of cervical cancer. The results showed that in the 6 randomly selected samples of early cervical cancer patients, the peak signal-to-noise ratio (PSNR) and structural similarity image measurement (SSIM) of multimodal MRI images under the alternating direction algorithm were significantly higher than those of conventional multimodal MRI images and the image reconstruction was clearer under this algorithm. By comparing MRI multimodal staging, statistical analysis showed that the staging accuracy of B group was 75%, while that of A group was only 59.38%. For the results of postoperative medical examinations, the examination consistency of B group was better than that of A group, with a statistically significant difference ($P < 0.05$). The area under the receiver operating characteristic (ROC) curve (AUC) of B group was larger than that of A group; thus, sensitivity was improved and misdiagnosis was reduced significantly. Multimodal MRI under the alternating direction algorithm was superior to conventional multimodal MRI examination in the diagnosis of early cervical cancer, as the lesions were displayed more clearly, which was conducive to the detection rate of small lesions and the staging accuracy. Therefore, it could be used as an ideal MRI method for the assistant diagnosis of cervical cancer staging.

1. Introduction

Cervical cancer is a malignant tumor with high incidence among gynecological diseases. It is one of the four most common cancers and poses a serious threat to women's life and health [1]. Epidemiological investigations have found that cervical cancer and its carcinoma in situ are closely related to factors such as sexually transmitted diseases, smoking, and premature sex (<16 years old). In addition, the diseased population is becoming younger and younger [2, 3]. Generally, cervical cancer has no significant feature in the early stage and occasionally manifests as increased vaginal discharge. The clinical methods for early cervical cancer diagnosis are the three examinations of colposcopy, cervical cytology, and cervical biopsy [4, 5]. However, biopsy is invasive and tissue sampling determines its accuracy. Early lesions in tumor tissues are not easy to find and occasionally appear as punctate lesions, which may lead to missed diagnosis. Therefore, an accurate and less traumatic diagnostic method is needed. The accuracy of early diagnosis and clinical staging of cervical cancer is of great significance for improving the prognosis and survival rate of cervical cancer patients, and overestimating or underestimating the severity of cancer tissue lesions will make an adverse effect on the prognosis [6].

Clinically, the initial diagnosis of cervical cancer is generally a gynecological examination, which is less reliable in the diagnosis of parauterine infiltration, degree of infiltration, tumor size, and the distant metastases of lymph nodes or pelvic cavity [7]. At present, clinical imaging methods, such as magnetic resonance imaging (MRI) plain scan, ultrasound, and computer tomography (CT), are used to evaluate the staging of cervical cancer [8, 9]. Ultrasound is simple, fast, and easy to operate, with a relatively cheap price. However, the anatomical scope of ultrasound is limited and the clarity of the tissue structure and lesions detected is much lower than that of CT and MRI [10]. CT can give a high density resolution, which can detect soft tissue structures or organs with small density differences accurately and can measure quantified CT parameter values, but it still cannot accurately observe the distant metastasis, pelvic infiltration, and the situation of rectum and bladder for cervical cancer [11]. MRI examination has the advantages of high tissue resolution and multisequence and multiparameter imaging, which are advantageous in the diagnosis and staging of cervical cancer. Currently, the monomodal, static, and planar MRI with morphological imaging has been developed to be three dimensional and dynamically multimodal with functional imaging [12]. The multimodal imaging summarizes the medical images under different modal imaging methods, so as to make up for deficiencies of each method; thereby, more effective data can be obtained, and finally, a clearer display of the lesions and efficient diagnosis can be realized. It combines functional imaging and anatomical imaging, so that the structural and functional information of the tissue are reflected, which is more conducive to the diagnosis of diseases [13].

However, compared with other medical imaging technologies, multimodal MRI also has some shortcomings and limitations. For example, the patient needs to burden high medical expenses, the scanning time is relatively longer, and the imaging resolution is low for it is easily affected by scanning time, signal-to-noise ratio, or more factors [14]. With the continuous development of computer intelligent algorithms, a new medical imaging technology called partial parallel imaging has emerged in the medical field. As an alternating direction algorithm, it is mainly applied and collects Fourier components concurrently in each receiver, as multiple receivers surround the scanned object, thereby the image quality and reconstruction speed are improved [15]. Without further processing, artifacts will appear in the final image, which will lead to the deteriorated image quality. For a higher-quality reconstructed image, a fast optimization algorithm is required to reconstruct the image.

Therefore, in this study, the alternating direction algorithm was applied in this study, as it has been used in the partial parallel imaging. Meanwhile, the algorithm was combined with multimodal MRI to diagnose patients with early cervical cancer. With the clinical pathological examination results, its application effect in diagnosis of early cervical cancer was evaluated.

2. Method

2.1. Research Subjects. In this study, 64 patients with early cervical cancer were selected in hospital from May 2018 to March 2021. They were 21–57 years old, with a median age of 43.8 years old. All cases were confirmed by postoperative pathological examinations. According to the examination methods, they were divided into two groups. In A group, the patients received conventional multimodal MRI examination, while in B group, they underwent multimodal MRI examination based on the alternating direction algorithm. The patients included in this study signed the informed consent forms, and the research process had been approved by the ethics committee of the hospital.

The patients in this study met the following inclusion criteria. They had no contraindications to MRI and were newly diagnosed with cervical cancer. Their MRI images are good in the quality without obvious distortion or artifacts. They could cooperate to complete the examinations and participate in the study voluntarily. With the exclusion criteria, patients had not undergone surgery without complete pathological data were excluded. Those who did not have complete data of MRI examination, those who have pelvic lymph node metastasis, and those with cervical cancer of stage II-B or above were also excluded.

2.2. Staging Standards of Cervical Cancer. A 3.0T superconducting magnetic resonance imaging system was used. All serial images of MRI were read blindly and staged by two senior doctors and a postgraduate imaging student. The images were analyzed and measured; if there was any divergence in the staging, it was determined after discussion. The staging standards of International Federation of Gynecology and Obstetrics (FIGO) [16] are shown in Table 1.

2.3. Alternating Direction Algorithm. In this study, the image reconstruction method based on image domain and coil sensitivity coding was applied, as shown below:

$$\mathrm{MFS}_j u = f_j. \tag{1}$$

According to the equation above, some k spatial data f_j obtained by the j-th receiver and the sensitivity mapping S_j were correlated with the mask M. F was the Fourier transform, f_j was the number of receivers, and S was the sensitivity mapping, which represented the vector of Fourier coefficients of the receiver.

According to (1), the reconstruction equation of image u was worked out by solving the least squares. The reconstruction equation was expressed as follows: .

$$\min_{u\in C^N} \sum_{j=1}^{k} \mathrm{MFS}_j u - f_{j2}^2. \tag{2}$$

In the above equation, $\|\cdot\|_2^2$ was 2-norm (also called Euclidean norm), and k was the number of channels (or receivers). Since the matrix obtained by MFS_j was ill-conditioned in (2), the minimization might be ill-conditioned as well. To reduce the influence of ill-condition, the recent SENSE model had been added into the energy functional function through a regularization term. Finally, the basic sparsity of the MR image in the finite difference region was utilized to optimize the rapid reconstruction of the image, by solving the optimization issue of the following equation:

$$\min_{u\in C^N} u_{TV} + \lambda \sum_{j=1}^{K} \left\| \mathrm{MFS}_j u - f_{j2}^2 \right\|. \tag{3}$$

Table 1: Cervical cancer staging standards.

FIGO staging		Tumor node metastasis (TNM)
	The carcinoma in situ was unassessable.	TX
	No evidence of primary cancer was found.	T0
Stage 0	Carcinoma in situ (pre-invasive carcinoma) was found.	Tisn0m0
Stage I	Cervical cancer was confined to the uterus (that spread to the uterus was not considered in staging.).	T1N0M0
I-A	Invasive carcinoma was found under a microscope, including superficial infiltration and any visible lesions.	T1a
I-A_1	Interstitial infiltration depth was <3 mm, and horizontal diffusion range was ≤7 mm.	T1a_1
I-A_2	Interstitial infiltration depth reached 3–5 mm, and horizontal diffusion range was ≤7 mm.	T1a_2
I-B	The microscopic lesion was larger than that of stage I-A_2, or visible cancer lesions were confined to the cervix.	T1b
I-B_1	The maximum diameter of the macroscopic cancer lesions was ≤4 cm.	T1b_1
I-B_2	The maximum diameter of the macroscopic cancer lesions was >4 cm.	T1b_2
Stage II	The cancer spread out of the uterus, but did not reach the pelvic wall or the lower third of the vagina.	T2N0M0
II-A	No parauterine infiltration was found.	T2a
II-B	Parauterine infiltration could be observed.	T2b

In (3), $\|\cdot\|_{TV}$ was the total variational norm, and $\lambda > 0$ was the parameter corresponding to the relative weight of the data fidelity term. Then, (4) was worked out.

$$\sum_{j=1}^{K} \left\| \mathrm{MFS}_j u - f_{j2}^2 \right\|. \tag{4}$$

In (3), $\|\cdot\|_{TV}$ controlled the solution, and the general form of the image reconstruction was expressed as follows:

$$\min_{u \in C^N} Y(u) + H(u), \tag{5}$$

where Y represented a convex function, perhaps a non-differentiable function, H was a convex function that was continuously differentiable. In the image reconstruction based on the total variational model, Y and H had the following form as shown below:

$$Y(u) = \|u\|_{TV}, H(u) = \lambda \left\| A_{tt} \right\|^2 f, \tag{6}$$

f was the measured data; and A was the matrix that described the imaging equipment or data acquisition mode, which might be complex and ill-conditioned. The matrix A in parallel MRI was expressed as below:.

$$\mathrm{A} = \begin{pmatrix} \mathrm{MFS}_1 \\ \vdots \\ \mathrm{MFS}_K \end{pmatrix}. \tag{7}$$

To solve the lack of smoothness of Y in (6), an auxiliary variable v was added to obtain the equivalent constraint issue, which was expressed as follows: .

$$\begin{aligned} &\min_{u \in C^N} \quad Y(v) + H(u), \\ &\mathrm{s.t}\, u = v, u, v \in C^N. \end{aligned} \tag{8}$$

After that, the equivalent constraint issue was transformed into an unconstrained issue through the second penalty, as shown in the following equation:.

$$\min_{u,v} Y(v) + H(u) + \alpha \|v - u\|_2^2. \tag{9}$$

In (9), α was a parameter, and an auxiliary variable v was introduced, so that the smooth term H and the non-differentiable term Y could be handled independently to a certain extent. At this time, the penalty term issue was dealt with preferentially: the minimized v was found first by fixing u, and then the minimized u was obtained by fixing v, which are shown in the following equation:

$$\begin{aligned} v^{k+1} &= \arg\min_{v} \|v\|_{\mathrm{TV}} + \alpha \|v - u\|_2^2, \\ u^{k+1} &= \arg\min_{u} \|\mathrm{Au} - f\|_2^2 + \alpha \|v - u\|_2^2, \end{aligned} \tag{10}$$

v^{k+1} in the (10) represented the first sub-issue under the total variation, and u^{k+1} represented the second sub-issue. The primal-dual mixed gradient (PDHG) algorithm could be introduced to solve the first sub-issue, then the v^{k+1} in (10) could be expressed as given below:

$$\min_{v} \sum_{i=1}^{N} \left\| D_i v \right\|_2 + \alpha \|v - u\| = \min_{v} \max_{p \subset X} \langle p, Dv \rangle + \lambda \|v - u\|_2^2. \tag{11}$$

As $X = \{p = (p_1 \cdots p_N)\} \in C^{2N}$, the primal and dual variables were iteratively updated through the PDHG algorithm, obtaining the following equation:

$$\begin{aligned} p^{k+1} &= \arg\max_{p} \varnothing\left(v^k, p\right) + \frac{1}{2\tau_k} \left\| p - p^k \right\|_2^2, \\ v^{k+1} &= \arg\min_{v} \varnothing\left(v, p^{k+1}\right) + \frac{1}{2\theta_k}. \end{aligned} \tag{12}$$

In this equation, $\varnothing(v^k, p) = \langle p, Dv \rangle + \alpha \|v - u^k\|_2^2$; and τ_k and θ_k represented the primal and dual step-size, respectively, corresponding to the total variational regularization term. The final iteration result was expressed as (13)

$$p^{k+1} = \prod_X \left(p^k + \tau_k D v^k\right), \left(\prod_X (p)\right)_i = \frac{p_i}{\max\left\{\left\|p_i\right\|_2, 1\right\}},$$
$$v^{k+1} = \left(1 + 2\alpha\theta_k\right)^{-1}\left(v^k - \theta_k D^T p^{k+1} + 2\alpha\theta_k u^k\right)\left(1 - \theta_k\right)v^k + \theta_k\left(u^k - \frac{1}{2\alpha}D^T p^{k+1}\right). \tag{13}$$

For the second sub-issue in (10), dual decomposition method could be used to solve them .

$$\min_u \lambda\|\mathrm{Au} - f\|_2^2 + \alpha\|v - u\|_2^2. \tag{14}$$

Then, the equation of the second sub-issue was obtained, which was expressed as follows:

$$\begin{aligned} u^{k+1} = \arg\min_u \lambda\Big(&2\left(Au^k - f\right)^T A\left(u - u^k\right) \\ &+ \delta_k\left\|u - u^k\right\|_2^2 + \alpha\|v - u\|_2^2\Big). \end{aligned} \tag{15}$$

In the equation, $\delta_k = \|A\,(u^k - u^{k-1})\|_2^2/\|u^k - u^{k-1}\|_2^2$. The matrix A had the very complicated and ill-conditioned structure in parallel MRI, in which under the total variational model the $S_j u$ in (3) could be replaced by X_j for variable decomposition. Then, (3) was transformed into the following:

$$\min_{u\in C^N} \|u\|_{TV} + \lambda \sum_{j=1}^{K} \left\|\mathrm{MFX}_j - f_j\right\|_2^2, X_j = S_j u. \tag{16}$$

With the augmented Lagrangian function, (16) could then be transformed into (17).

$$\begin{aligned} &\|u\|_{TV} + \lambda \sum_{j=1}^{K} \left\|MFX_j - f_j\right\|_2^2 + 2\alpha\langle d_j, X_j - S_j u\rangle \\ &\quad + \alpha\left\|X_j - S_j u\right\|_2^2. \end{aligned} \tag{17}$$

Then, (17) was iterated with the alternating direction multiplier method, and (18) was worked out.

$$\begin{aligned} X_j^{k+1} &= \arg\min_{X_j} \left\|\mathrm{MFX}_j - f_j\right\|_2^2 + 2\alpha\langle b_j^k, X_j - S_j u^k\rangle + \alpha\left\|X_j - S_j u\right\|_2^2, \\ u^{k+1} &= \arg\min_u \|u\|_{TV} + \lambda\alpha\langle b_j^k, X_j - S_j u^k\rangle + \alpha\left\|X_j - S_j u\right\|_2^2, \\ b_j^{k+1} &= b^k + \left(X_j^{k+1} - S_j u^{k+1}\right). j = 1 \cdots N. \end{aligned} \tag{18}$$

Since the solution of the matrix in the conventional equation was the product of the Fourier transform and the diagonal matrix, $F^T M^T MF + \alpha I = F^T\,(M^T M + \alpha I)F$ in the (18). The u-sub-issues of X_j^{k+1} in the (18) could be quickly calculated through the PDHG algorithm.

2.4. Image Evaluation Indicators. The peak signal-to-noise ratio (PSNR) could evaluate the quality of the processed images, which is commonly used in the fields of super-resolution, compression, and restoration of images. PSNR was expressed as the logarithm of the ratio of the mean square error (MSE) between the reconstructed image and the true image to the maximum possible pixel value of the image [17].

The MSE was a measure of the error between the reconstructed image and the true value image, and its specific definition was expressed as follows:

$$\mathrm{MSE} = \frac{1}{H \times W} \sum_{i=1}^{H} \sum_{j=1}^{W} \left(f\,(i, j) - g\,(i, j)\right)^2. \tag{19}$$

In this equation, *f(i,j)* and *g(i,j)* represented the reconstructed image and the true value image, respectively, with the height H and the width W. The PSNR of these two images could be calculated through the MSE and the maximum possible pixel value. PSNR was defined as the following:

$$\mathrm{PSNR} = 10\,\log_{10}\left(\frac{\left(2^n - 1\right)^2}{\mathrm{MSE}}\right). \tag{20}$$

In equation (20), n represented the number of bits of the image pixel, and 2^n-1 represented the maximum possible pixel value of the image. The unit of PSNR was dB; and the larger the PSNR, the better the reconstruction quality of the image.

Structural similarity image measurement (SSIM) consisted of three contrasts of the brightness, contrast, and structure. The calculation equation of this indicator is shown as (21) below:

$$\mathrm{SSIM}\,(x, y) = \frac{\left(2\mu_x\mu_y + C_1\right)\left(2\sigma_{xy} + C_2\right)}{\left(\mu_x^2 + \mu_{y+}^2 C_1\right)\left(\sigma_x^2 + \sigma_{y+}^2 C_2\right)}. \tag{21}$$

2.5. Multimodal MRI Examination Methods. Before the examination, all metal objects, such as bracelets and intrauterine devices, were removed. The bladder was filled appropriately to avoid fluctuation artifacts caused by excessive urine. The patients were in a supine position with hands raised above the head, and the head would enter the device range at first. The patients were comforted to stay relaxed, were trained to hold their breath or breath naturally, and an indwelling needle on the elbow was given to enhance the scanning of injection angiography.

A 1.5 T MRI instrument was used with a body-phased array surface coil. The scanning range was about from the horizontal line of the umbilical cord to the pelvic floor. The conventional plain scanning was carried out in order of T1, T2, diffusion weighted imaging (DWI), and dynamic contrast enhanced MRI (DCE-MRI). Conventional scanning in the coronal, sagittal, and axial positions were mainly included.

2.6. Statistical Methods. SPSS22.0 was used to process the relevant data. The medical examination results were taken as the gold standards. The coincidence and Kappa value of the two examination methods were compared, and their values in the diagnosis and staging of early cervical cancer were evaluated. The enumeration data were described by rate (%); and the measurement data, conformed to the normal distribution and the homoscedasticity, were compared under the paired t-test, and $P < 0.05$ was considered to be statistically significant.

3. Research Results

3.1. Result Analysis of Image Reconstruction Indicators. The imaging effect of multimodal MRI based on the alternating direction algorithm was compared with that of conventional multimodal MRI. The results showed that for the 6 randomly selected samples of early cervical cancer, the average PSNR and the average SSIM of the traditional algorithm was 34.82 dB and 0.9474, respectively. The average PSNR of the alternating direction algorithm was 38.98 dB, and the average SSIM was 0.9799. The MRI under the alternating direction algorithm had significant advantages in the image reconstruction. The PSNR and SSIM of the algorithm-based MRI were significantly higher than those of conventional MRI, with the reconstruction effect was significantly improved. The comparisons are shown in Figures 1 and 2.

As shown in Figure 3, the multimodal MRI images of the same patient with early cervical cancer were compared, between those of conventional MRI and those of MRI under the alternating direction algorithm. It can be observed that the multimodal MRI under the alternating direction algorithm gave the significantly clearer images than the conventional multimodal MRI in the corresponding level (the arrows pointed to the tumors).

3.2. Comparison of Multimodal MRI and Medical Examination. As shown in Figure 4, the results of conventional multimodal MRI showed that there were missed diagnoses in 2 cases, and the sensitivity reached 96.88% (62/64). With the postoperative pathological staging, it was suggested that the examination results of 38 of the 64 cases with early cervical cancer were consistent with the postoperative pathological staging results, and the staging accuracy was 59.38% (38/64).

The multimodal MRI examination under the alternating direction algorithm showed that there was no missed diagnosis, and the sensitivity reached 100% (64/64). As shown in Figure 5, the MRI examination results of 48 of the 64 cases with early cervical cancer were consistent with those of postoperative pathological staging, and the staging accuracy was 75% (48/64).

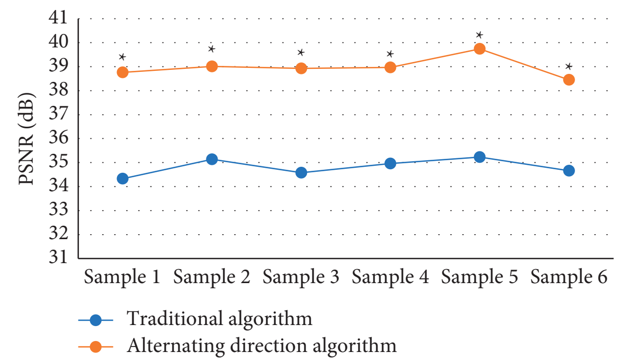

Figure 1: Comparison of PSNR under different image processing methods. *indicates that compared with the traditional algorithm, the differences were statistically significant as $P < 0.05$.

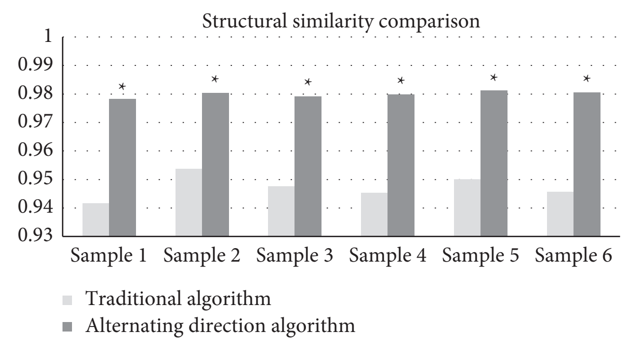

Figure 2: Comparison of SSIM under different image processing methods. *indicates that the differences were statistically significant compared with those of the traditional algorithm, $P < 0.05$.

3.3. Consistency between the Staging Obtained by the Two Methods and Postoperative Medical Examination. Generally speaking, the Kappa coefficient ranged between [−1,1]. When the Kappa coefficient was 0.4–0.75, it meant that the results were highly consistent; when the Kappa coefficient was ≤0.4, the consistency was relatively worse. According to the postoperative pathological results, the early cervical cancers in patients were staged at I-A, I-B, and II-A, respectively. The weighted Kappa coefficients of conventional MRI were 0.3748, 0.2885, and 0.0173, respectively, which were all less than 0.4, indicating that the consistency between them and the

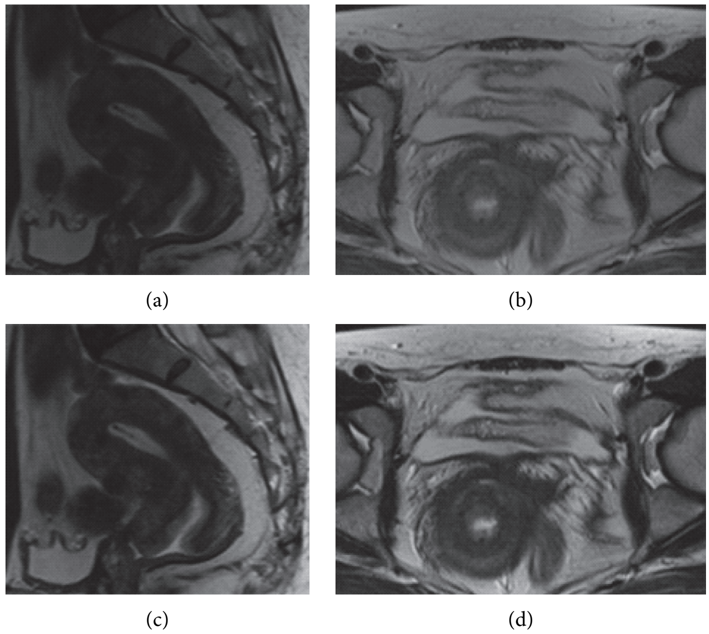

FIGURE 3: Imaging comparison of two algorithms. A and C are the images of conventional multimodal MRI; B and C are those of multimodal MRI under the alternating direction algorithm.

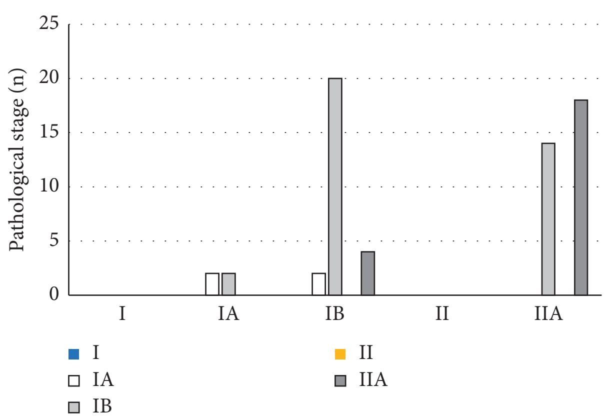

FIGURE 4: Result comparison of conventional MRI and medical examination.

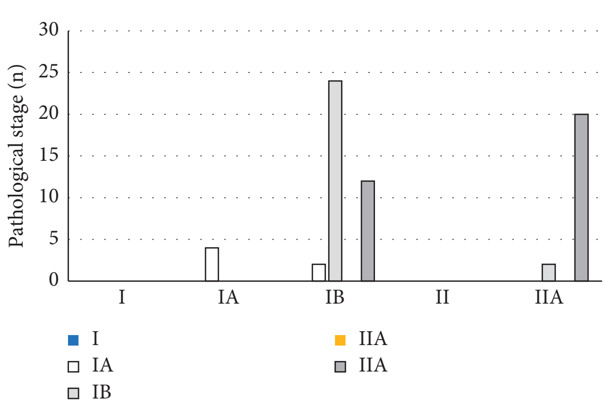

FIGURE 5: Result comparison of MRI under alternating direction algorithm and medical examination.

pathological results was poor. The Kappa coefficients of algorithm-based MRI were 0.4583, 0.4497, and 0.5152, respectively, which were all greater than 0.4. Thus, as shown in Figure 6, the staging of multimodal MRI under the alternating direction algorithm was significantly superior to that of conventional multimodal MRI in the diagnosis of early cervical cancer, with the statistically significant difference ($P < 0.05$).

3.4. Evaluation of the Diagnosis Results with the Two Examination Methods. The postoperative pathological results were taken as the gold standard. The sensitivity, specificity, positive predictive value, and negative predictive value of the two examination methods were calculated for the diagnosis of early cervical cancer. It is shown in Figure 7 with the results that the values of the four items of group A were 48.7, 65.1, 70.7, and 41.8, respectively; while those of group B were 71.5, 94, 97, and 66.4, respectively.

The two examination methods were drawn into the receiver operating characteristic (ROC) curves, as shown in Figure 8. The area under the ROC curve (AUC) was 0.617 of conventional multimodal MRI, and the standard error (SE) was 0.7, the 95% confidence interval (CI) of the area was (0.408, 0.716), the sensitivity was 0.503, and the misdiagnosis rate was 0.349. For the multimodal MRI under the alternating direction algorithm, the AUC, SE, the 95% CI, the sensitivity, and the misdiagnosis rate was 0.752, 0.048, (0.766, 0.957), 0.614, and 0.133, respectively. It could be observed that the AUC of the algorithm-based MRI in this study was larger than that of the conventional multimodal MRI, the sensitivity was significantly improved, and the misdiagnosis rate was significantly reduced.

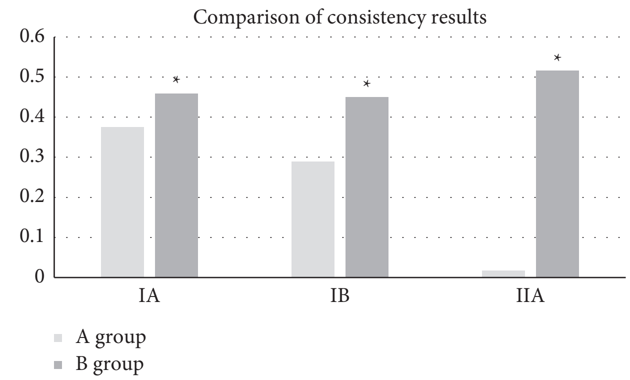

FIGURE 6: Consistency comparison among the two methods and medical examination. *indicates that compared with the Kappa coefficient of A group, the differences were statistically significant ($P < 0.05$).

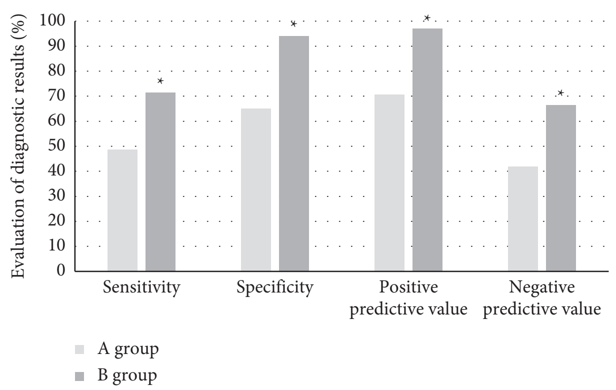

FIGURE 7: Evaluation of the diagnosis results with the two examination methods. *indicates that the differences were statistically significant, as the data were compared with those of A group ($P < 0.05$).

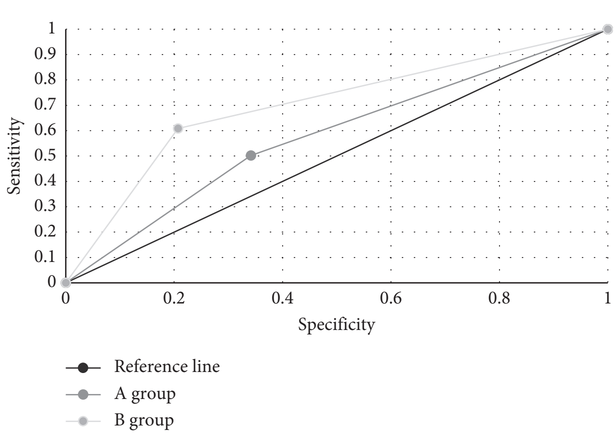

FIGURE 8: ROC curves of the two examination methods.

4. Discussion

Cervical cancer is the gynecological malignant tumor with the highest incidence. The morbidity and mortality of it remain high in developing countries, and the clinical staging determines the final treatment measures. The clinical staging of cervical cancer mainly relies on pelvic examination currently, and the diagnosis is also highly subjective. Together with the unreliable staging, it often makes patients miss the optimal treatment plan, leading to a poor prognosis [18]. With the medical development, MRI examination of cervical cancer is becoming more and more important for the diagnosis and staging of cervical cancer. The accurate staging depends on clearly showing of the anatomical structure of the various organs in the pelvic cavity, the levels among the various tissues, and the difference between the tumor and normal tissues [19]. Multimodal MRI with multidimensional and multiparameter imaging shows the anatomical relationship very clearly among various organs and tissue structures in the pelvic cavity. The high soft tissue resolution provides an intuitive anatomical basis for the judgment of cervical cancer invasion and the depth of infiltration. The clear structures shown make the preoperative evaluation of cervical cancer more accurate, but there are still many disadvantages [20]. Therefore, in this study, the MRI based on the alternating direction algorithm was applied for the examination of patients. The results of the algorithm-based MRI were compared with those of conventional MRI and clinical examination, to explore its application effect in the diagnosis of early cervical cancer.

It was shown that among the 6 randomly selected samples of early cervical cancer patients, the multimodal MRI under the alternating direction algorithm had a significant advantage in image reconstruction. For the traditional algorithm, the average values of PSNR and SSIM were 34.82 dB and 0.9474, respectively. For the alternating direction algorithm, the average PSNR and the average SSIM were 38.98 dB and 0.9799, respectively. The values were also significantly higher than those of conventional multimodal MRI. With the algorithm-based MRI, the reconstruction effect was significantly improved, and the reconstructed images were clearer. The multimodal MRI under the alternating direction algorithm was used to assist in the staging of early cervical cancer and then was compared with the staging of conventional multimodal MRI. The staging accuracy of B group was 75%, while that of A group was only 59.38%. For the postoperative medical examinations, it was shown from the postoperative staging results that the weighted Kappa coefficient of conventional multimodal MRI for cervical cancer stage IA, IB, and IIA were 0.3748, 0.2885, and 0.0173, respectively. The Kappa coefficients of multimodal MRI under the alternating direction algorithm were 0.4583, 0.4497, and 0.5152, respectively. The consistency with B group was far better than that with the A group, and the difference was statistically significant ($P < 0.05$), which proved that the algorithm-based MRI was more accurate in the staging of early cervical cancer than the conventional MRI. In addition, the AUC of conventional multimodal MRI was 0.617, the standard error was 0.7, the 95% confidence interval of the area was (0.408, 0.716), the sensitivity was 0.503, and the misdiagnosis rate was 0.349. For the multimodal MRI under alternating direction algorithm, the AUC, standard error, 95% confidence interval of the area, sensitivity, and the misdiagnosis rate was 0.752, 0.048, (0.766, 0.957), 0.614, and 0.133, respectively. The AUC of the algorithm-based MRI was larger than that of the conventional multimodal MRI, showing that the sensitivity of the algorithm-based MRI was significantly improved, and the misdiagnosis rate was significantly reduced. Therefore, it was more valuable for the diagnosis of early cervical cancer.

All in all, the multimodal MRI under the alternating direction algorithm was of great value in the diagnosis and staging of early cervical cancer. It was easier to find small lesions with the algorithm-based MRI, thereby the detection rate and staging accuracy of the lesions were improved. Thus, it could be taken as one of the routine examination methods for patients with cervical cancer.

5. Conclusion

Multimodal MRI under the alternating direction algorithm was superior to conventional multimodal MRI in the diagnosis of early cervical cancer. As the lesions were shown more clearly, the detection rate and staging accuracy of small lesions were improved. Therefore, it could be used as an ideal MRI method to assist in the staging of cervical cancer with the application value. Although this algorithm-based MRI made some improvement in the accuracy of examination, it still cannot achieve the effect of 100% accuracy of cervical cancer staging. In the follow-up researches, this technology needed to be further improved and developed.

Data Availability

The data used to support the findings of this study are available from the corresponding author upon request.

Conflicts of Interest

The authors declare that they have no conflicts of interest.

References

[1] J. Sheng, Y. Xiang, L. Shang, and Q. He, "Molecular alterations and clinical relevance in cervical carcinoma and precursors (Review)," *Oncology Reports*, vol. 44, no. 6, pp. 2397–2405, 2020.

[2] A. G. Siokos, O. Siokou-Siova, and I. Tzafetas, "Correlation between cervical carcinogenesis and tobacco use by sexual partners," *Hellenic Journal of Nuclear Medicine*, vol. 22, no. Suppl 2, pp. 184–190, 2019 Sep-Dec.

[3] K. Baskran, P. K. Kumar, K. Santha, and Sivakamasundari II, "Cofactors and their association with cancer of the uterine cervix in women infected with high-risk human papillomavirus in south India," *Asian Pacific Journal of Cancer Prevention*, vol. 20, no. 11, pp. 3415–3419, 2019 Nov 1.

[4] C. M. Rerucha, R. J. Caro, and V. L. Wheeler, "Cervical cancer screening," *American Family Physician*, vol. 97, no. 7, pp. 441–448, 2018 Apr 1.

[5] P. Ziemke and H. Griesser, "p16-/Ki-67 in der Zervix-Zytologie: Indikationen," *Pathologe, Der*, vol. 38, no. 1, pp. 38–44, 2017 Feb.

[6] S. Pimple, G. Mishra, and S. Shastri, "Global strategies for cervical cancer prevention," *Current Opinion in Obstetrics and Gynecology*, vol. 28, no. 1, pp. 4–10, 2016 Feb.

[7] A. Srivastava, J. Misra, S. Srivastava, B. Das, and S. Gupta, "Cervical cancer screening in rural India: status & current concepts," *Indian Journal of Medical Research*, vol. 148, no. 6, pp. 687–696, 2018 Dec.

[8] I. O. Lawal, K. O. Ololade, G. O. Popoola et al., "18F-FDG-PET/CT imaging of uterine cervical cancer recurrence in women with and without HIV infection," *The Quarterly Journal of Nuclear Medicine and Molecular Imaging*, vol. 6, 2019 May 8.

[9] T. Saida, A. Sakata, Y. O. Tanaka et al., "Clinical and MRI characteristics of uterine cervical adenocarcinoma: its variants and mimics," *Korean Journal of Radiology*, vol. 20, no. 3, pp. 364–377, 2019 Mar.

[10] A. Kumari, S. Pankaj, V. Choudhary et al., "Ultrasonic and histopathological evaluation to exclude premalignant and malignant lesions in perimenopausal and postmenopausal women presenting as abnormal uterine bleeding," *Journal of Obstetrics & Gynaecology of India*, vol. 69, no. S2, pp. 171–176, 2019 Oct.

[11] S. Liu, L. Xia, Z. Yang et al., "The feasibility of 18F-FDG PET/CT for predicting pathologic risk status in early-stage uterine cervical squamous cancer," *Cancer Imaging*, vol. 20, no. 1, p. 63, 2020 Sep 10.

[12] H. J. Meyer, S. Purz, O. Sabri, and A. Surov, "Cervical cancer: associations between metabolic parameters and whole lesion histogram analysis derived from simultaneous 18F-FDG-PET/MRI," *Contrast Media and Molecular Imaging*, vol. 2018, Article ID 5063285, 8 pages, 2018.

[13] M. Soltaninejad, G. Yang, T. Lambrou et al., "Supervised learning based multimodal MRI brain tumour segmentation using texture features from supervoxels," *Computer Methods and Programs in Biomedicine*, vol. 157, pp. 69–84, 2018 Apr.

[14] B. Liu, S. Gao, and S. Li, "A comprehensive comparison of CT, MRI, positron emission tomography or positron emission tomography/CT, and diffusion weighted imaging-MRI for detecting the lymph nodes metastases in patients with cervical cancer: a meta-analysis based on 67 studies," *Gynecologic and Obstetric Investigation*, vol. 82, no. 3, pp. 209–222, 2017.

[15] M. Hu, Y. Zhong, S. Xie, H. Lv, and Z. Lv, "Fuzzy system based medical image processing for brain disease prediction," *Frontiers in Neuroscience*, vol. 15, Article ID 714318, 2021 Jul 30.

[16] L.-C. Horn, C. E. Brambs, S. Opitz, U. A. Ulrich, and A. K. Höhn, "FIGO-Klassifikation für das Zervixkarzinom 2019 - was ist neu?" *Pathologe, Der*, vol. 40, no. 6, pp. 629–635, 2019 Nov.

[17] X. Duan, M. Gou, N. Liu, W. Wang, and C. Qin, "High-capacity image steganography based on improved xception," *Sensors*, vol. 20, no. 24, p. 7253, 2020 Dec 17.

[18] N. Beharee, Z. Shi, D. Wu, and J. Wang, "Diagnosis and treatment of cervical cancer in pregnant women," *Cancer Medicine*, vol. 8, no. 12, pp. 5425–5430, 2019 Sep.

[19] P. Balcacer, A. Shergill, and B. Litkouhi, "MRI of cervical cancer with a surgical perspective: staging, prognostic implications and pitfalls," *Abdominal Radiology*, vol. 44, no. 7, pp. 2557–2571, 2019 Jul.

[20] I. S. Haldorsen, N. Lura, J. Blaakær, D. Fischerova, and H. M. J. Werner, "What is the role of imaging at primary diagnostic work-up in uterine cervical cancer?" *Current Oncology Reports*, vol. 21, no. 9, p. 77, 2019 Jul 29.

Hindawi
Contrast Media & Molecular Imaging
Volume 2022, Article ID 6331206, 9 pages
https://doi.org/10.1155/2022/6331206

Research Article

Effect of Different Nursing Interventions on Discharged Patients with Cardiac Valve Replacement Evaluated by Deep Learning Algorithm-Based MRI Information

Jing Zhang [1] **and Qiong Zhou** [2]

[1] *Department of Cardiology Second Ward, Jingzhou First People's Hospital, No. 8 Hangkang Road, Jingzhou, Hubei Province 434000, China*
[2] *Department of Cardiology Third Ward, Jingzhou First People's Hospital, No. 8 Hangkang Road, Jingzhou, Hubei Province 434000, China*

Correspondence should be addressed to Qiong Zhou; 16030000204@pop.zjgsu.edu.cn

Received 31 December 2021; Revised 19 February 2022; Accepted 21 February 2022; Published 21 March 2022

Academic Editor: M. Pallikonda Rajasekaran

This study was aimed to explore the application of cardiac magnetic resonance imaging (MRI) image segmentation model based on U-Net in the diagnosis of a valvular heart disease. The effect of continuous nursing on the survival of discharged patients with cardiac valve replacement was analyzed in this study. In this study, the filling completion operation, cross entropy loss function, and guidance unit were introduced and optimized based on the U-Net network. The heart MRI image segmentation model ML-Net was established. We compared the Dice, Hausdorff distance (HD), and percentage of area difference (PAD) values between ML-Net and other algorithms. The MRI image features of 82 patients with valvular heart disease who underwent cardiac valve replacement were analyzed. According to different nursing methods, they were randomly divided into the control group (routine nursing) and the intervention group (continuous nursing), with 41 cases in each group. The Glasgow Outcome Scale (GOS) score and the Self-rating Anxiety Scale (SAS) were compared between the two groups to assess the degree of anxiety of patients and the survival status at 6 months, 1 year, 2 years, and 3 years after discharge. The results showed that the Dice coefficient, HD, and PAD of the ML-Net algorithm were (0.896 ± 0.071), (5.66 ± 0.45) mm, and (15.34 ± 1.22) %, respectively. The Dice, HD, and PAD values of the ML-Net algorithm were all statistically different from those of the convolutional neural networks (CNN), fully convolutional networks (FCN), SegNet, and U-Net algorithms ($P < 0.05$). Atrial, ventricular, and aortic abnormalities can be seen in MRI images of patients with valvular heart disease. The cardiac blood flow signal will also be abnormal. The GOS score of the intervention group was significantly higher than that of the control group ($P < 0.01$). The SAS score was lower than that of the control group ($P < 0.05$). The survival rates of patients with valvular heart disease at 6 months, 1 year, 2 years, and 3 years after discharge were significantly higher than those in the control group ($P < 0.05$). The abovementioned results showed that an effective segmentation model for cardiac MRI images was established in this study. Continuous nursing played an important role in the postoperative recovery of discharged patients after cardiac valve replacement. This study provided a reference value for the diagnosis and prognosis of valvular heart disease.

1. Introduction

Cardiac valve disease is a common cardiovascular disease with abnormal cardiac valve structure or function. There are about 15 million patients with cardiac valve disease worldwide, accounting for 50% of cardiovascular diseases [1]. Cardiac valve disease causes hemodynamic changes in patients, which eventually lead to heart failure, arrhythmia, embolism, and other complications [2]. Cardiac valve replacement is a common treatment for valvular heart disease, but long-term anticoagulation therapy is required after surgery [3]. Due to the limited awareness of the disease, thrombosis may occur due to lack of anticoagulant effect or bleeding due to excessive anticoagulant effect. Finally, the effects of the operation and the quality of life of patients are affected [4]. Continuous nursing is a kind of continuous nursing for patients after discharge under the guidance of medical staff to reduce the occurrence of postoperative adverse symptoms and improve the quality of life after operation [5]. Some studies showed that quality care for patients after heart valve replacement can significantly reduce the incidence of postoperative complications. Moreover, the guidance of professional nursing staff can reduce the incidence of adverse reactions in anticoagulant therapy and improve the prognosis of patients [6]. However, most studies were studying the influence of nursing methods on patients during hospitalization, and there were few studies on the influence of nursing methods on patients after discharge.

Ultrasound cardiogram (UCG) is a common imaging method in the diagnosis of valvular heart disease. UCG has the characteristics of good accuracy and being cost-effective, which is the gold standard for the diagnosis of valvular heart disease. However, it can only be semiquantitatively analyzed in the evaluation of differential pressure and reverse flow [7]. MRI can accurately quantify the differential pressure and reverse flow in the diagnosis of heart valve disease. MRI can accurately quantify the differential pressure and reverse flow in the diagnosis of heart valve disease. However, at present, most of the current cardiac MRI images are mostly divided manually, which has problems such as subjectivity, poor repeatability, and time-consuming. In addition, quantitative diagnosis of cardiac diseases is carried out [8]. Some researchers applied deep learning algorithms to MRI image segmentation. However, the heart structure is complex and the tissue boundary is blurred. And the images captured by the heart beat produced motion artifacts and noise [9]. These factors have brought great challenges to the accurate positioning and segmentation of cardiac structures. The U-Net in deep learning can obtain higher segmentation accuracy with less training times. Some researchers established a heart segmentation method based on the U-Net network with faster training speed and less memory occupation [10]. However, in the application process, it is found that due to uncontrollable factors in the process of MRI image acquisition, the distribution of image pixel values is different and the image data have problems such as noise. Directly using the original image leads to a certain deviation in segmentation [11]. Therefore, it needs to be further optimized.

In summary, there are few studies on the postdischarge care of patients after cardiac valve replacement. MRI technology still has the phenomenon of segmentation result deviation in the diagnosis process. The U-Net was optimized to increase its accuracy in MRI image segmentation, which was then applied to the diagnosis of heart valvular disease. Continuous nursing was used in patients after cardiac valve replacement to explore the impact of continuous nursing on postoperative quality of life. It was hoped to provide a reference value for the diagnosis and prognosis of clinical heart valvular disease.

2. Materials and Methods

2.1. Region of Interest (ROI) Detection Based on the U-Net Network. In order to increase the accuracy of MRI image segmentation, MRI images need to be preprocessed before ROI detection using the U-Net network. It mainly includes three parts, which are as follows: data normalization processing, image denoising, and image normalization. The data normalization is mainly normalizing the original image to the same size, so that each image voxel size is as consistent as possible [12]. ReLU is used as the activation function in the middle layer of a convolutional neural network. The calculation method of ReLU is expressed as follows:

$$G(X) = \max(0, X). \tag{1}$$

The input MRI image is mapped to $(0, \infty)$, and the final output layer uses softmax activation function. The calculation method is expressed as follows:

$$G_i(Y) = \frac{e^{zi}}{\sum_{j\in\text{group}} e^{zj}}. \tag{2}$$

The output probability is (0, 1), so the network input of image MRI after processing is normalized (0, 1).

Originally acquired MRI images include parts of the heart and organs around the heart. In order to ensure the accuracy of the whole heart structure segmentation network, the original labels need to be preprocessed. Its specific processing method can be expressed as follows:

$$L(i, j, k) = \begin{cases} 0, & d(i, j, k) = b, \\ 1, & d(i, j, k) = s_m, \quad m = 1, 2, L7. \end{cases} \tag{3}$$

In the equation, b is the background label value in the original label image, and s_m is the label value of the seven-seed structure of the heart in the original label image. They are the left ventricular chamber (LV), right ventricular chamber (RV), left atrial chamber (LA), right atrial chamber (RA), left ventricular myocardium (Myo), ascending aorta (aorta), and pulmonary artery (PA).

The main body of the U-Net network is composed of encoding and decoding structures. Coding and decoding structures play an important role in image processing. The convolution layer and pooling layer can be used to obtain the image feature map in MRI image processing [13]. Decoding is converting the feature map into the feature map required for a specific task through the convolution layer and the transposition convolution layer [14]. The encoding and decoding structure based on the U-Net network can ensure the reuse of feature maps of the same size and reduce the loss of information during the pooling process in the encoding phase [15]. In this study, the input and output sizes of the basic convolution unit were consistent throughout the filling and completion operations. The ROI detection structure based on the U-NET network is shown in Figure 1.

The last layer of the network uses the cross-entropy function and softmax. The cross-entropy function can be expressed as follows:

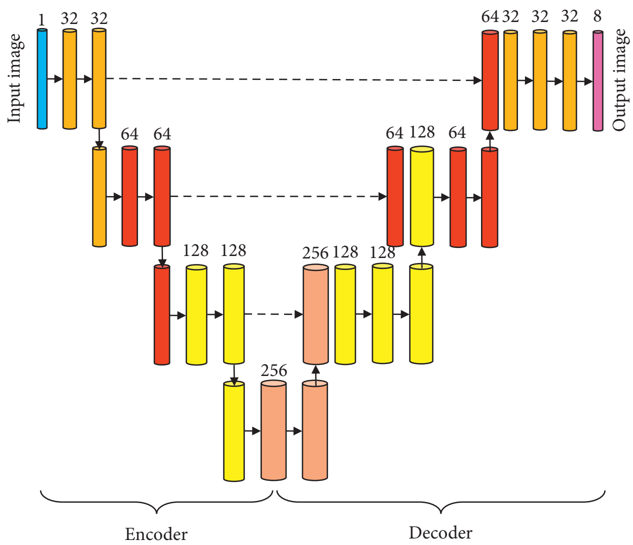

FIGURE 1: ROI detection structure based on the U-Net network.

$$E = \sum_{x\in\Omega} w(x)\log\left[p_{l(x)}(x)\right], \tag{4}$$

in the equation, $w(x)$ is the image weight, and its calculation method is expressed as follows:

$$w(x) = w_a(x) + w_0 \bullet \exp\left\{\frac{\left[d_1(x) + d_2(x)\right]^2}{2\beta^2}\right\}, \tag{5}$$

in the equation, w_a is used to balance the weight map of category frequency. d_1 represents the distance to the nearest cell boundary. d_2 represents the distance to the second nearest cell boundary. β is the network weight by Gaussian distribution parameters.

The loss function can show the difference between the target area segmented by the model and the actual target area [16]. Based on the classification objective of this study, the cross-entropy loss function was used as the model loss function. The calculation method of the cross-entropy loss function can be expressed as follows:

$$J(\delta) = -\frac{1}{m}\sum_{i=1}^{m}\left\{y^{(i)}\log\left[h_\delta\left(x^{(i)}\right)\right] + \left(1 - y^{(i)}\right)\log\left[1 - h_\delta\left(x^{(i)}\right)\right]\right\}, \tag{6}$$

in the equation, m denotes the number of categories. n is the number of voxels. $y^{(i)}$ is the true probability of the i-prime being class m. $x^{(i)}$ is the prediction probability of the i-prime being class m.

The original image is adjusted to a size suitable for the U-Net network inspection. The adjusted MRI image is input into the optimized U-Net network for heart segmentation. The external cube frame (the red boxes in Figure 2) of the heart region is calculated based on the preliminary heart segmentation results, and it is used as the initial ROI of the heart image. Then, it expands five voxels outward to restore the original image to obtain the final original image. Then, the ROI detection results of the original image are obtained. The ROI detection process based on the U-NET network is shown in Figure 2.

2.2. MRI Image Segmentation Model Based on the U-Net Network. Cardiac MRI images were further segmented by ROI detection results based on the U-Net network in this study. The U-Net networks typically update parameter weights through the last layer of output calculation errors. In the process of operation, due to the deep network, it led to a lack of guidance for the updating of low-level network parameters. In this study, each layer on the U-Net network expansion path was used as a label prediction with a certain resolution. Multiple outputs of different scales were increased on the expansion path. The guidance unit was introduced to establish a new heart MRI image segmentation method, and it was named ML-Net. The guidance unit can guide the high-level segmentation through the features extracted at the low level to increase the accuracy of image segmentation. Therefore, the higher the output, the finer the prediction results. The ML-Net heart segmentation network structure is shown in Figure 3.

The loss function of the ML-Net heart segmentation network is calculated based on the Dice coefficient. The calculation method is expressed as follows:

$$J(\delta) = 1 - \frac{2\times\left|y\cap g_\delta(x)\right|}{\left|y\cup g_\delta(x)\right|}. \tag{7}$$

In the equation, y is the real category of all voxels, and $g_\delta(x)$ is the predicted category of all voxels.

2.3. Performance Evaluation of MRI Image Segmentation. In this study, Dice coefficient, Hausdorff distance (HD), and percentage of area difference (PAD) were used as the evaluation indexes of model segmentation effect. The Dice coefficient measures the proximity between the target real area and the predicted area. The closer the Dice coefficient is to 1, the better the model segmentation performance is. The calculation method is expressed as follows:

$$\text{Dice} = \frac{2|C\cap D|}{|C| + |D|}. \tag{8}$$

HD is the symmetric distance measure of the maximum difference between the two contours. The smaller the HD value, the better the segmentation performance. The calculation method is expressed as follows:

$$H\ D(C, D) = \max_{a\in C}\left\{\max_{a\in D}\left[s(a, b)\right]\right\}. \tag{9}$$

PAD is also an evaluation index for medical image segmentation. The smaller the PAD value, the better the model segmentation performance. The calculation method is expressed as follows:

$$\text{PAD} = \frac{|C - D|}{C}. \tag{10}$$

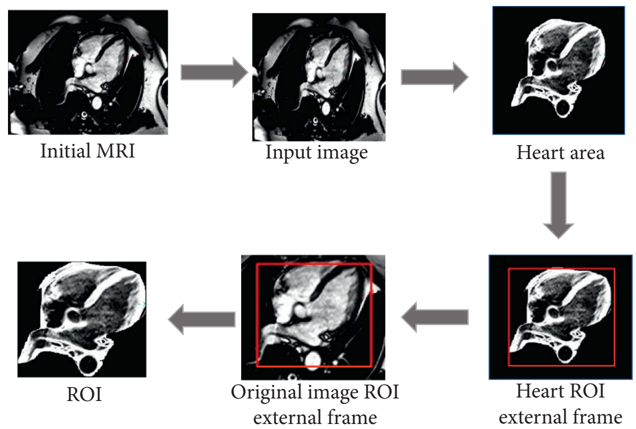

Figure 2: ROI detection process based on the U-NET network.

In equations (8)~(10), $s(a, b)$ is the Euclidean distance between two points a and b. C is the predictive output graph of the model. D is the gold standard drawn manually.

2.4. Research Subject and Grouping. A total of 82 patients who underwent cardiac valve replacement in hospital from December 2017 to June 2021 were selected as the study subjects. All patients underwent MRI examinations. There were 50 males and 32 females. The age of the patients ranged from 33 to 71 years. The average age was 50.64 ± 6.89 years. The inclusion criteria were as follows: (1) patients clinically diagnosed as rheumatic heart disease; (2) patients who underwent cardiac valve replacement for the first time; (3) patients with cardiac function of grade I–III; and (4) patients with hemiplegia, cerebral infarction, pulmonary function, and other diseases. The exclusion criteria were as follows: (1) patients with communication or disturbance of consciousness; (2) patients with severe liver and kidney dysfunction or other cancers; and (3) MRI images were not clear and did not meet the clinical application standards. All subjects were randomly divided into the control group (routine nursing) and the intervention group (continuous nursing) according to different nursing methods, with 41 cases in each group. In the conventional nursing group, there were 26 males and 15 females, ranging from 33 to 70 years old, with an average age of 50.87 ± 4.48 years old. There were 19 patients with grade I, 14 patients with grade II, and 8 patients with grade III cardiac function. In the continuous care group, there were 24 males and 17 females, ranging from 34 to 71 years old, with an average age of 49.93 ± 5.64 years old. There were 21 patients with grade I, 13 patients with grade II, and 7 patients with grade III cardiac function. There was no significant difference in age, sex ratio, and proportion of patients with different cardiac function grades between the two groups ($P > 0.05$). This study had been approved by the ethics committee of the hospital, and the subjects included in the study had signed the informed consent form.

2.5. MRI Examination Methods. All subjects were diagnosed using the superconducting MRI scanner with total image matrix (TIM) technology. The phase velocity coding film in the plane parallel to the blood flow direction was used to determine the blood flow state. The scanning parameters were as follows: repetition time (TR) was 65 ms, echo time (TE) was 2.8 ms, and deflection angle (FA) was 30°. A quantitative evaluation of the blood flow profile in the abdominal aorta with phase-coded cine-MR (VEC-MR) was performed. The scanning parameters were as follows: repetition time (TR) was 64 ms, echo time (TE) was 2.8 ms, and deflection angle (FA) was 30°. The scanning plane was set at the fastest flow rate or valve level, and the phase diagram of 20–25 frames in one cardiac cycle can be obtained by one scan.

Blood flow analysis software was used to manually analyze the blood flow phase map. The blood flow parameters such as maximum velocity, forward blood flow, unit time flow, average flow, average velocity, and cross-sectional area of blood flow were calculated in one cardiac cycle. According to the blood flow phase diagram, the forward flow and reverse flow of each cardiac cycle were obtained. The reflux index was calculated, 15%–20% for mild, 20%–40% for moderate, and more than 40% for severe.

2.6. Nursing Intervention Methods and Observation Indicators. The control group was given routine nursing care; that is, the nursing staff of the department gave guidance to the patients after discharge. The main contents included diet, medication, activities, and other matters needing attention. It was recommended that patients receive regular reviews. The intervention group was given continuous nursing intervention based on routine nursing in the control group. After patient discharge, full-time nursing staff regularly conducted family visits or telephone inquiries, and the frequency was 1 time/month. A systematic and standardized continuous nursing evaluation scale was developed with sleep quality, drug dosage, daily diet content, heart rate, and blood pressure changes as the main guidance content. Full-time nursing staff provided healthy diets for patients. Patients were instructed to perform regular wound reexamination, blood tests, MRIs, and electrocardiogram (ECG) examinations. The drug dosage was adjusted according to the test results.

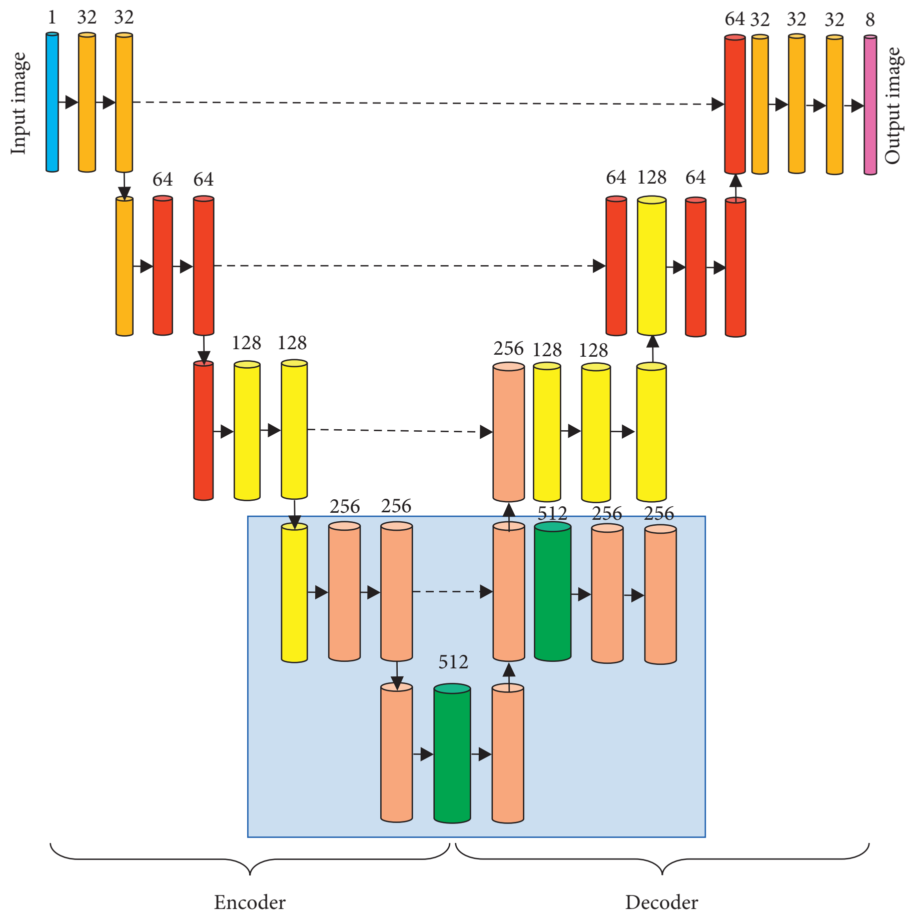

FIGURE 3: ML-Net heart segmentation network structure diagram.

The Glasgow Outcome Scale (GOS) was used to evaluate the prognosis of patients. 1 point represented death, 2 points represented severe disability, 3 points represented inability to take care of themselves, 4 points represented independent living, and 5 points represented normal living [17]. The Self-rating Anxiety Scale (SAS) was used to evaluate the anxiety degree of patients. The higher the SAS score, the more serious the anxiety [18]. The survival of the patients at 6 months, 1 year, 2 years, and 3 years after discharge was counted.

2.7. Statistical Methods. The experimental data were processed by SPSS19.0 statistical software. The measurement data were expressed as the mean ± standard deviation (x(−) ±s), the count data were expressed as percentage (%). The χ^2 test was used. $P < 0.05$ indicated that the difference was statistically significant.

3. Results

3.1. The ML-Net Heart Segmentation Results Analysis. Under the same training set, the influence of iteration times of the FCN, U-NET, and ML-NET on Dice value in the heart segmentation process was verified (Figure 4). As the number of iterations increased, the Dice values of FCN, U-Net, and ML-Net algorithms increased first and then tended to be stable. At the same iteration number, the Dice value of the ML-Net network was higher than that of the FCN and U-Net.

The Dice, HD, and PAD values of heart segmentation by CNN, FCN, SegNet, U-Net, and ML-Net algorithms were compared and analyzed (Figure 5). The maximum Dice coefficient of the ML-Net algorithm was (0.896 ± 0.071). HD and PAD were the smallest, which were (5.66 ± 0.45) mm and (15.34 ± 1.22) %, respectively. The Dice, HD, and PAD values of the ML-Net algorithm were statistically different from those of other algorithms ($P < 0.05$).

3.2. MRI Features of Valvular Heart Disease. MRI images of patients with valvular heart disease showed abnormalities in the atrium, ventricle, and main artery. And the patient's cardiac blood flow signal was abnormal. Aortic stenosis can be seen in patients with severe mitral valve disease (shown by the arrow), and the left ventricular wall was concentrically thickened (Figure 6(a)). Patients with mitral insufficiency caused by hypertrophic cardiomyopathy mainly showed left atrial enlargement (shown by the arrow), and the left ventricular cavity was not significantly increased (Figure 6(b)). MRI images of patients with mitral insufficiency caused by left ventricular dysfunction showed

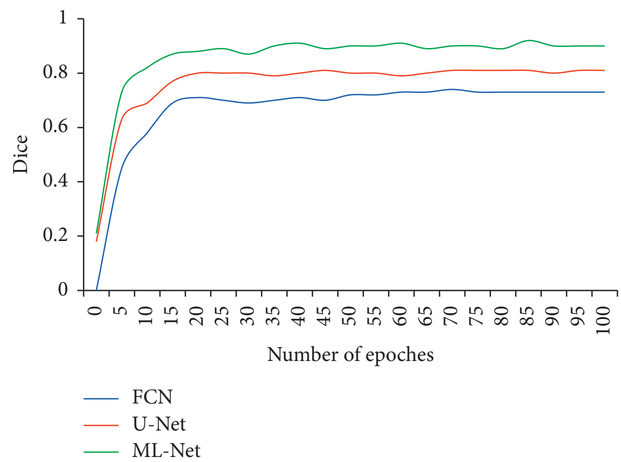

Figure 4: Curves of Dice values of different algorithms changing with iterations.

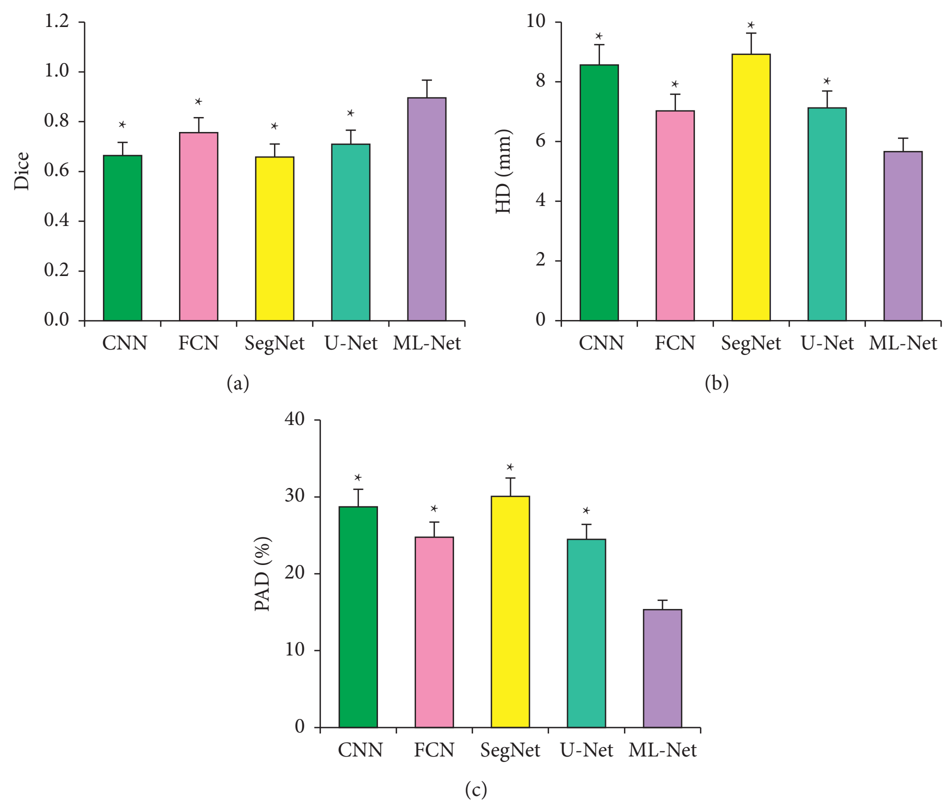

Figure 5: Analysis of heart segmentation results of different algorithms. (a) Dice coefficient comparison; (b) HD value comparison; (c) PAD value comparison. * Compared with the ML-Net algorithm, ($P < 0.05$).

enlargement of left atrium and left ventricular cavity (shown by arrow) (Figure 6(c)). In patients with severe mitral valve disease, the left atrium near the mitral valve orifice during the left ventricular systolic period showed obvious reflux of high-speed blood flow signals (shown by the arrow in Figure 6(d)).

3.3. Analysis of MRI Results. The diagnostic performance of MRI for valvular heart disease was analyzed using echocardiography (UCG) as the gold standard (Figure 7). The proportion of patients with mild, moderate, and severe reflux indexes detected by UCG was 12.20%, 42.68%, and 45.12%, respectively. The proportion of patients with mild, moderate, and severe reflux indexes detected by MRI was 12.20%, 50.00%, and 37.80%, respectively. There was statistical difference between them ($P < 0.05$).

3.4. Analysis of Nursing Results of Cardiac Valve Replacement. The GOS scores of the control group and the intervention group after intervention were compared and analyzed

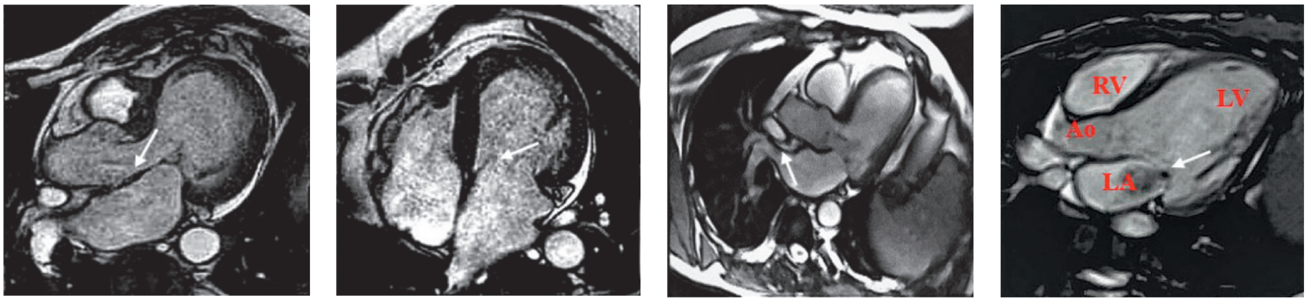

(a) (b) (c) (d)

Figure 6: (a) Patient with severe mitral valve disease, 61 years old, male. Left atrial height, enlargement, aortic stenosis; (b) a 54-year-old male patient with mitral insufficiency caused by hypertrophic cardiomyopathy. Left atrial enlargement; (c) patient with mitral insufficiency due to left ventricular dysfunction, 47 years old. Left atrium and left ventricle increased; (d) in patients with severe mitral valve disease, the left atrial (LA) and left ventricular (LV) cavities were significantly enlarged during the left ventricular systolic phase of the four-chamber view of the heart.

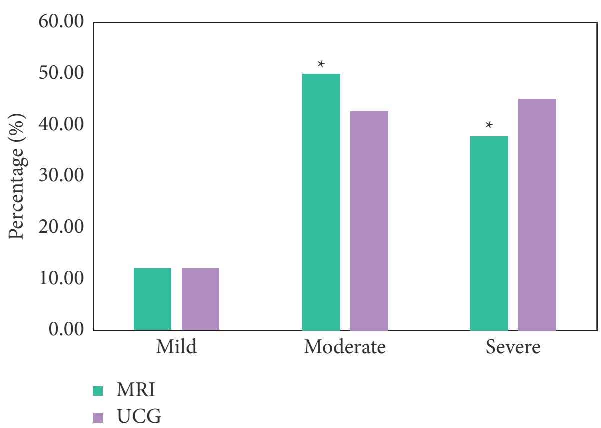

Figure 7: Comparison of MRI and UCG in the diagnosis of Cardiac Valvular Regurgitation Index. $*$ Compared to UCG, ($P < 0.05$).

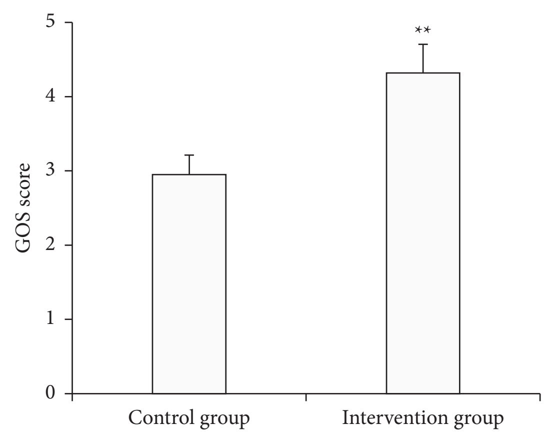

Figure 8: Comparison of the GOS scores of different nursing methods. ** Compared with the control group, ($P < 0.01$).

(Figure 8). The results showed that the GOS score of the intervention group was significantly higher than that of the control group ($P < 0.01$).

The SAS scores of the control group and the intervention group after intervention were compared and analyzed (Figure 9). The results showed that the SAS score of the intervention group was lower than that of the control group ($P < 0.05$).

The survival conditions of patients in the control group and the intervention group at different times after intervention were compared and analyzed (Figure 10). The results revealed that the survival rates of 6 months, 1 year, 2 years, and 3 years after discharge in the intervention group were significantly higher than those in the control group ($P < 0.05$).

4. Discussion

In this study, cardiac MRI images were preprocessed based on the U-Net network to make their data distribution more consistent and meet the data requirements of neural network training [19]. The results showed that the Dice value of the ML-Net network was higher than that of the FCN and U-Net under the same iteration number. Under the same number of iterations, the Dice value of the ML-Net network was higher than that of the FCN and U-Net. The Dice coefficient of the ML-Net algorithm was the largest (0.896 ± 0.071), and its HD and PAD were the smallest, which were (5.66 ± 0.45) mm and (15.34 ± 1.22) %, respectively. Compared with other algorithms, the Dice, HD, and PAD values of the ML-Net algorithm were all statistically different ($P < 0.05$). The segmentation accuracy of the ML-Net network obtained by the optimization of the U-Net network was significantly improved. The reason was that the guidance unit in the ML-Net network sampled the low-resolution output, which enhanced the network feature extraction ability [20]. Finally, the segmentation accuracy was significantly improved. Lee et al. (2021) [21] established a brain MRI segmentation algorithm based on the U-Net algorithm and found that the Dice value of the segmented MRI image was 0.93. The Dice value of the image segmented by the established method was significantly smaller than that in this study, and the reason may be that the segmentation parts of the two were different, and the large amount of tissue around the heart had a certain impact on the segmentation, resulting in a smaller Dice value. However, the Dice value of the

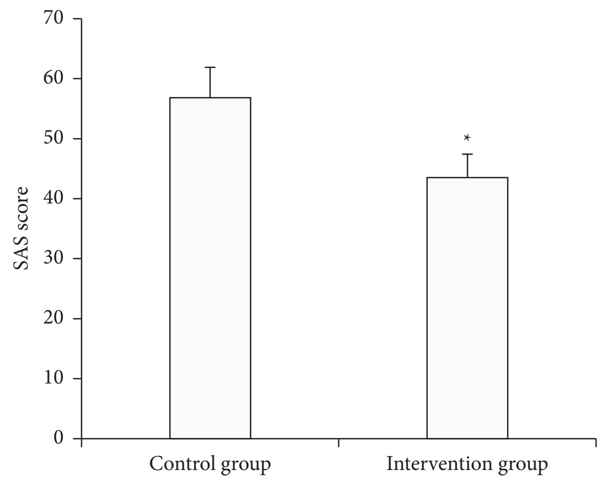

Figure 9: Comparison of the SAS scores of different nursing method. * Compared with the control group ($P < 0.05$).

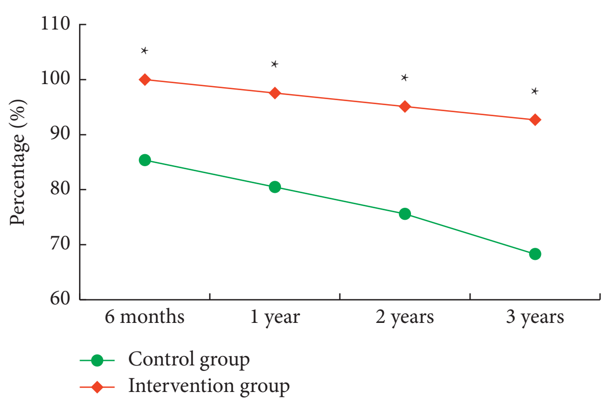

Figure 10: Comparison of the survival rate of different nursing methods. * Compared with the control group ($P < 0.05$).

established model was significantly higher than that of the ventricle segmentation method established by the researchers of Zhao et al. (2020) [22] based on the U-Net algorithm.

The blood flow sensitive MR technology in MRI diagnosis played an important role in the diagnosis of cardiac valve disease [23]. The results of this study showed that there was a statistically significant difference between patients with mild, moderate, and severe UCG detection reflux index and MRI ($P < 0.05$). The results showed that the proportion of patients with a moderate reflux index detected by MRI was higher than that of UCG. Its diagnostic accuracy was obviously higher than UCG. This was consistent with the research results of Francone et al. (2020) [24]. Anticoagulant drugs should be taken for life after heart valve replacement [25]. It was unable to ensure the effective use of anticoagulant drugs for some patients due to a lack of professional nursing knowledge after discharge, resulting in poor postoperative therapeutic effect and quality of life [26]. The results revealed that the GOS score of the intervention group was significantly higher than that of the control group ($P < 0.01$). The SAS score of the intervention group was lower than that of the control group ($P < 0.05$). Continuous nursing can effectively improve the psychological state of patients. Continuing care took patients who had been controlled and needed reasonable rehabilitation nursing as the research object and provided out-of-hospital nursing guidance for patients [27]. It can effectively alleviate the adverse emotions of patients and effectively improve the postoperative quality of life of patients.

5. Conclusion

A heart MRI image segmentation model ML-Net was constructed based on the U-Net network, and the influence of continuous nursing on discharged patients after cardiac valve replacement was analyzed. It was found that the ML-Net could effectively improve the segmentation accuracy of cardiac MRI images. Continuous nursing can effectively improve the psychological status of discharged patients with cardiac valve replacement and improve the postoperative survival rate. However, there were still some shortcomings in this study, and the quality of life of patients with continuous nursing was not analyzed. In the future, the influence of continuous nursing on the quality of life of patients will be further analyzed. In summary, this study established an effective cardiac MRI image segmentation model. Continuous nursing played an important role in the postoperative recovery of discharged patients after cardiac valve replacement. This theory provided a reference value for the diagnosis and prognosis of valvular heart disease.

Data Availability

The data used to support the findings of this study are available from the corresponding author upon request.

Conflicts of Interest

The authors declare no conflicts of interest.

References

[1] Z. Mrsic, S. P. Hopkins, J. L. Antevil, and P. S. Mullenix, “Valvular heart disease,” *Primary Care: Clinics in Office Practice*, vol. 45, no. 1, pp. 81–94, 2018.

[2] S. Gati, A. Malhotra, and S. Sharma, “Exercise recommendations in patients with valvular heart disease,” *Heart*, vol. 105, no. 2, pp. 106–110, 2019.

[3] K. L. Pan, D. E. Singer, B. Ovbiagele, Y. L. Wu, M. A. Ahmed, and M. Lee, “Effects of non-vitamin K antagonist oral anticoagulants versus warfarin in patients with atrial fibrillation and valvular heart disease: a systematic review and meta-analysis,” *Journal of American Heart Association*, vol. 6, no. 7, Article ID e005835, 2017.

[4] J. B. Chambers, “Valve disease and non-cardiac surgery,” *Heart*, vol. 104, no. 22, pp. 1878–1887, 2018.

[5] A. A. Mennander, “Commentary: when is repeated cardiac valve surgery justified during drug-associated infective endocarditis?” *The Journal of Thoracic and Cardiovascular Surgery*, vol. 159, no. 4, pp. 1271-1272, 2020.

[6] S. Saha, S. Varghese, A. A. Ahmad et al., “Complex valve surgery in elderly patients: increasingly necessary and surprisingly feasible,” *The Thoracic and Cardiovascular Surgeon*, vol. 68, no. 02, pp. 107–113, 2020.

[7] P. Lancellotti, R. Dulgheru, Y. Y. Go et al., “Stress echocardiography in patients with native valvular heart disease,” *Heart*, vol. 104, no. 10, pp. 807–813, 2018.

[8] S. Badiani, P. Waddingham, G. Lloyd, and S. Bhattacharyya, “Stress echocardiography in valvular heart disease,” *Expert Review of Cardiovascular Therapy*, vol. 16, no. 11, pp. 795–804, 2018.

[9] M. Habijan, D. Babin, I. Galić et al., “Overview of the whole heart and heart chamber segmentation methods,” *Cardiovascular Engineering and Technology*, vol. 11, no. 6, pp. 725–747, 2020.

[10] J. Sander, B. D. de Vos, and I. Išgum, “Automatic segmentation with detection of local segmentation failures in cardiac MRI,” *Scientific Reports*, vol. 10, no. 1, Article ID 21769, 2020.

[11] M. Paknezhad, M. S. Brown, and S. Marchesseau, “Improved tagged cardiac MRI myocardium strain analysis by leveraging cine segmentation,” *Computer Methods and Programs in Biomedicine*, vol. 184, Article ID 105128, 2020.

[12] B. Taslakian, A. Pires, D. Halpern, J. S. Babb, and L. Axel, “Stylus/tablet user input device for MRI heart wall segmentation: efficiency and ease of use,” *European Radiology*, vol. 28, no. 11, pp. 4586–4597, 2018.

[13] Q. Tong, C. Li, W. Si et al., “RIANet: recurrent interleaved attention network for cardiac MRI segmentation,” *Computers in Biology and Medicine*, vol. 109, pp. 290–302, 2019.

[14] Y. Li, J. Zhao, Z. Lv, and J. Li, “Medical image fusion method by deep learning,” *International Journal of Cognitive Computing in Engineering*, vol. 2, pp. 21–29, 2021.

[15] Z. Yu, S. U. Amin, M. Alhussein, and Z. Lv, “Research on disease prediction based on improved DeepFM and IoMT,” *IEEE Access*, vol. 9, pp. 39043–39054, 2021.

[16] M. Hu, Y. Zhong, S. Xie, H. Lv, and Z. Lv, “Fuzzy system based medical image processing for brain disease prediction,” *Frontiers in Neuroscience*, vol. 15, Article ID 714318, 2021.

[17] S. D. Yeatts, R. H. Martin, W. Meurer et al., “Sliding scoring of the glasgow outcome scale-extended as primary outcome in traumatic brain injury trials,” *Journal of Neurotrauma*, vol. 37, no. 24, pp. 2674–2679, 2020.

[18] X. Fan, C. Xing, L. Yang, J. Wang, and L. Feng, “Fatigue, self-efficacy and psychiatric symptoms influence the quality of life in patients with myasthenia gravis in Tianjin, China,” *Journal of Clinical Neuroscience*, vol. 79, pp. 84–89, 2020.

[19] Z. Lv, L. Qiao, Q. Wang, and F. Piccialli, “Advanced machine-learning methods for brain-computer interfacing,” *IEEE/ACM Transactions on Computational Biology and Bioinformatics*, vol. 18, no. 5, pp. 1688–1698, 2021.

[20] M. Lee, J. Kim, R. Ey Kim et al., “Split-Attention U-net: a fully convolutional network for robust multi-label segmentation from brain MRI,” *Brain Sciences*, vol. 10, no. 12, p. 974, 2020.

[21] B. Lee, N. Yamanakkanavar, and J. Y. Choi, “Automatic segmentation of brain MRI using a novel patch-wise U-net deep architecture,” *PLoS One*, vol. 15, no. 8, Article ID e0236493, 2020.

[22] M. Zhao, Y. Wei, Y. Lu, and K. K. L. Wong, “A novel U-Net approach to segment the cardiac chamber in magnetic resonance images with ghost artifacts,” *Computer Methods and Programs in Biomedicine*, vol. 196, Article ID 105623, 2020.

[23] K. Kyhl and P. L. Madsen, “[Heart valve disease evaluated with MRI],” *Ugeskr Laeger*, vol. 180, no. 11, Article ID V04170279, 2018.

[24] M. Francone, R. P. J. Budde, J. Bremerich et al., “CT and MR imaging prior to transcatheter aortic valve implantation: standardisation of scanning protocols, measurements and reporting-a consensus document by the European Society of Cardiovascular Radiology (ESCR),” *European Radiology*, vol. 30, no. 5, pp. 2627–2650, 2020.

[25] C. Mve Mvondo, M. Pugliese, J. C. Ambassa, A. Giamberti, E. Bovio, and E. Dailor, “Mechanical heart valve replacement in a low-middle income region in the modern era: midterm results from a sub-saharan center,” *The Thoracic and Cardiovascular Surgeon*, vol. 68, no. 02, pp. 099–106, 2020.

[26] A. J. Small, O. Aksoy, D. S. Levi, M. M. Salem, E. H. Yang, and J. A. Aboulhosn, “Combined transcatheter tricuspid and pulmonary valve replacement,” *World Journal for Pediatric and Congenital Heart Surgery*, vol. 11, no. 4, pp. 432–437, 2020.

[27] L. A. El-Khatib, H. De Feijter-Rupp, A. Janoudi, L. Fry, M. Kehdi, and G. S. Abela, “Cholesterol induced heart valve inflammation and injury: efficacy of cholesterol lowering treatment,” *Open Heart*, vol. 7, no. 2, Article ID e001274, 2020.

Hindawi
Contrast Media & Molecular Imaging
Volume 2022, Article ID 9322196, 10 pages
https://doi.org/10.1155/2022/9322196

Research Article

Characteristics of Computed Tomography Images for Patients with Acute Liver Injury Caused by Sepsis under Deep Learning Algorithm

Huijun Wang,[1] **Qianqian Bao**,[2] **Donghang Cao**,[1] **Shujing Dong**,[1] **and Lili Wu**[1]

[1]*Department of Anesthesiology, Taizhou Hospital of Zhejiang Province Affiliated to Wenzhou Medical University, No. 150 Linhai West Street, Taizhou 317000, Zhejiang, China*
[2]*Department of Operation, Taizhou Hospital of Zhejiang Province Affiliated to Wenzhou Medical University, No. 150 Linhai West Street, Taizhou 317000, Zhejiang, China*

Correspondence should be addressed to Lili Wu; 201801010522@stu.hnie.edu.cn

Received 31 December 2021; Revised 18 February 2022; Accepted 21 February 2022; Published 19 March 2022

Academic Editor: M Pallikonda Rajasekaran

This study was aimed at exploring the application of image segmentation based on full convolutional neural network (FCN) in liver computed tomography (CT) image segmentation and analyzing the clinical features of acute liver injury caused by sepsis. The Sigmoid function, encoder-decoder, and weighted cross entropy loss function were introduced and optimized based on FCN. The Dice value, precision, recall rate, volume overlap error (VOE), relative volume difference (RVD), and root mean square error (RMSE) values of the optimized algorithms were compared and analyzed. 92 patients with sepsis were selected as the research objects, and they were divided into a nonacute liver injury group (50 cases) and acute liver injury group (42 cases) based on whether they had acute liver injury. The differences in the proportion of patients with different disease histories, the proportion of patients with different infection sites, the number of organ failure, and the time of admission to intensive care unit (ICU) were compared between the two groups. It was found that the optimized window CT image Dice value after preprocessing (0.704 ± 0.06) was significantly higher than the other two methods ($P < 0.05$). The Dice value, precision, and recall rate of the optimized-FCN algorithm were (0.826 ± 0.06), (0.91 ± 0.08), and (0.88 ± 0.09), respectively, which were significantly higher than other algorithms ($P < 0.05$). The VOE, RVD, and RMSE values were (21.19 ± 1.97), (10.45 ± 1.02), and (0.25 ± 0.02), respectively, which were significantly lower than other algorithms ($P < 0.05$). The proportion of patients with a history of drinking in the nonacute liver injury group was lower than that in the acute liver injury group ($P < 0.05$), and the proportion of patients with a history of hypotension was greatly higher than that in the nonacute liver injury group ($P < 0.01$). CT images of sepsis patients with acute liver injury showed that large areas of liver parenchyma mixed with high-density hematoma, the number of organ failures, and the length of stay in ICU were significantly higher than those in the nonacute liver injury group ($P < 0.05$). It showed that the optimization algorithm based on FCN greatly improved the performance of CT image segmentation. Long-term drinking, low blood pressure, number of organ failures, and length of stay in ICU were all related to sepsis and acute liver injury. Conclusion in this study could provide a reference basis for the diagnosis and prognosis of acute liver injury caused by sepsis.

1. Introduction

Sepsis is one of the main causes of death in intensive care unit (ICU) patients. According to statistics, there are approximately 18 million new cases each year, with a mortality rate of 2%–40% [1]. As the target organ of sepsis, the liver plays an important role in the occurrence and development of sepsis [2]. Acute liver injury is one of the common acute and critical illnesses caused by sepsis, with a high fatality rate and poor prognosis [3]. However, there are few studies on the clinical characteristics of patients with sepsis complicated by acute liver injury. At present, the diagnosis of sepsis liver injury mainly uses a number of serological indicators to indirectly assess the severity of liver injury [4]. In imaging examination methods, CT examination has significant advantages in evaluating liver trauma or intra-abdominal blood volume. Compared with serological test indicators, CT can reflect the extent of liver parenchymal destruction and accurately determine the degree of liver damage [5]. However, there are abundant organs and blood vessels around the liver, and the boundary between normal tissue and the diseased area is blurred. Manually segmenting the diseased area with CT images is time-consuming and prone to segmentation errors [6].

As a new field of machine learning, deep learning can be established to imitate the human brain for data analysis and learning and has powerful feature learning and model representation capabilities. Convolutional neural network (CNN) has strong representation learning capabilities and has been widely used in speech recognition, language processing, and image processing [7]. CNN has been used in the detection of breast cancer, cell carcinoma and brain lesions, knee cartilage segmentation, brain tumor segmentation, and liver tumor segmentation in medical image processing [8]. However, CNN has the disadvantage of losing the spatial information of the original image in image segmentation [9]. Jiang et al. (2021) [10] pointed out that the full convolutional neural network (FCN) based on CNN can overcome the shortcomings of CNN in the liver segmentation process of CT images and avoid the repeated storage and calculation convolution caused using pixel blocks. However, the image results obtained by the upsampling of the FCN algorithm are smooth and blurred, which is not sensitive to the processing of details in the image [11]. At the same time, some studies pointed out that the relationship between pixels is not fully considered in the image processing process, and the spatial regularization step used in the usual pixel classification-based segmentation methods is ignored, which lacks spatial consistency [12]. Therefore, it needs to be further optimized to overcome the problems of inaccurate segmentation results and lack of spatial consistency of the FCN algorithm.

To sum up, CT shows significant advantages in acute liver injury. The FCN algorithm still has certain limitations in CT image liver segmentation, which needs to be optimized. Moreover, there are few studies on the analysis of CT imaging characteristics of patients with acute liver injury in sepsis. Therefore, the FCN algorithm was optimized to increase its image segmentation performance. It was then applied to liver segmentation of CT images in patients with acute sepsis liver injury, and the clinical characteristics and CT imaging characteristics of patients with acute liver injury in sepsis were discussed, aiming to provide reference basis for the diagnosis of patients with acute liver injury caused by sepsis.

2. Materials and Methods

2.1. Research Objects and Grouping. In this study, 92 patients with sepsis in hospital from December 2018 to March 2021 were selected as research objects, and all patients underwent CT examination. There were 51 males and 41 females. The age range of patients was 19–86 years, and the average age was 59.94 ± 10.18 years. The inclusion criteria of this study were defined as follows: patients who had performed with CT examination; and patients who were in line with the inclusion criteria of abnormal liver function [13]. Exclusion criteria were defined as follows: patients with past chronic liver damage; patients after liver tumor or partial liver resection; patients with obstructive jaundice and biliary tract disease; and patients with liver damage caused by nonseptic reasons such as drugs. According to whether they had acute liver injury, they were divided into nonacute liver injury group (50 cases) and acute liver injury group (42 cases). This study had been approved by the ethics committee of hospital, and all subjects included in the study had signed the informed consent forms.

2.2. CT Examination Method. All patients were instructed to fast for 4–6 hours before examination, and the clinical data such as blood pressure and pulse were measured about 20 minutes before scanning. Plain scan and enhanced examination were performed with CT machine. The patient was placed in supine position and scanned in transverse axial position, with both arms raised and head held, from the xiphoid process to the lower margin of the liver. To reduce the motion artifacts in the image, patients must hold the air with inhalation during scanning or hold the air with calm breathing. Scanning parameter setting was tube voltage of 100 kV, tube current of 100 mA, pitch of 1.0, layer spacing of 7.5 mm, layer thickness of 7 mm, window position of 45–75 HU, and window width of 150–250 HU. According to Becker classification [14], liver injury CT images were classified.

2.3. Liver Segmentation Framework Based on FCN. FCN has greatly improved image segmentation accuracy and segmentation speed from traditional CNN [15]. Based on the imprecise segmentation results in the FCN algorithm, the optimization was realized through the CT window and algorithm optimization, and a liver segmentation framework was established, as shown in Figure 1. The initially obtained CT image data set was randomly cropped and then subjected to FCN algorithm for segmentation, and finally the segmented liver CT image was output.

2.4. CT Image Preprocessing for Liver Segmentation. Image preprocessing can reduce the interference of a certain tissue or organ from unrelated tissues or organs. The CT value of different tissues and organs in the human body is different, and the CT value of liver tissue is between 50 and 70 HU [16]. For the initial CT image of the liver, it was inputted to the convolutional layer with a convolution kernel size of 1×1 for preprocessing, the Sigmoid function was used to activate it, and the preprocessed CT image was finally output. It was assumed that the upper limit of the serial port function of CT image processing was A, and the liver CT image preprocessing module can be expressed as follows:

$$G(x) = \frac{A}{1 + e^{-(Cx+b)}}. \tag{1}$$

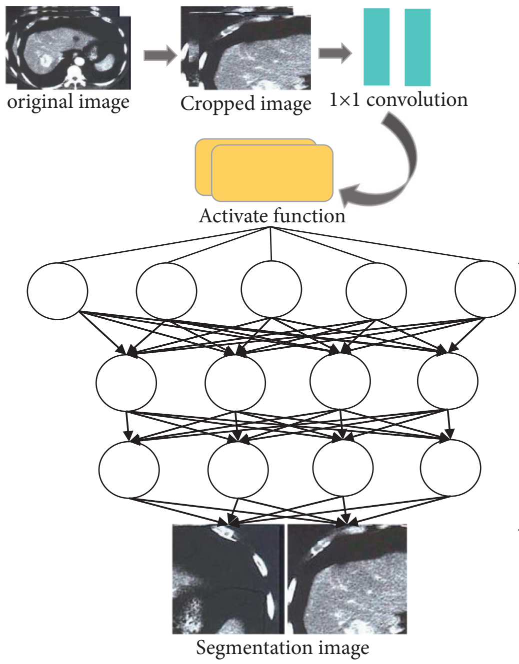

Figure 1: Liver segmentation process based on FCN.

In the equation above, C and b were convolutional layer parameters, and x was the CT value of the original CT image. In order to increase the efficiency of network training, the convolutional layer parameters C and b were optimized in the study. The specific algorithm was as follows:

$$C = \frac{2}{CC}\log\left(\frac{A}{\alpha} - 1\right),$$
$$b = \frac{-2CL}{CC}\log\left(\frac{A}{\alpha} - 1\right). \tag{2}$$

In the equations above, CC was the window width, CL was the window level, and α was the difference between the upper bound of the function and the right end of the window, which is related to the slope of the Sigmoid function.

2.5. Design of Liver CT Image Segmentation Network Based on FCN. The encoder-decoder structure can not only improve the feature expression ability in the image segmentation process, but also avoid the problem of gradient disappearance that may occur during the training process of the deep network [17]. Dense Net can avoid the training error caused by deep network training through the short-circuit connection in the residual module [18]. l was assumed to be the current number of layers, and the output of layer l can be expressed as follows:

$$x_l = B_l\{x_0, x_l, \ldots, x_{l-1}\}. \tag{3}$$

In (3), $B_l\{\,\}$ represented a combination of operations, and $x_0, x_l, \ldots, x_{l-1}$ was the splicing of the output of all layers before the layer l.

After the input image passed through the encoder, a low-resolution feature representation was produced, and the decoder network structure was related to the final image segmentation result [19]. In this study, the Dense connection among decoder modules was introduced, and the Skip connection in semantic segmentation was introduced to reduce the potential errors caused by the decoder's mesoscale modules, thereby improving the accuracy of segmentation. The structure of the liver CT image processing encoder optimized in this study is shown in Figure 2.

2.6. Design of Loss Function of Liver CT Image Segmentation Network Based on FCN. The segmentation evaluation index performance combining cross entropy and Lovász-Softmax's loss function was significantly higher than that of alone [20]. The calculation method of the cross entropy loss function was given as follows:

$$D(y, y') = -\frac{1}{N}\sum_{i=1}^{N}\sum_{h=1}^{H} y_i^h \log y_i'^h. \tag{4}$$

In (4), y_i^h referred to the binary label of pixel i to category h, $y_i'^h$ represented the probability value that pixel i belongs to category h, N was the sum of the number of pixels in a batch in the training process, and H was the total number of categories.

In liver CT image segmentation, a weighted cross entropy loss function is often used to solve the problem of category imbalance. The calculation method of weighted cross entropy loss function is shown in the following formula, where ω_i^h represented the weight of the category:

$$D(y, y') = -\frac{1}{N}\sum_{i=1}^{N}\sum_{h=1}^{H} \omega_i^h y_i^h \log y_i'^h. \tag{5}$$

During the operation of the cross entropy loss function, there was still rough segmentation of the edge area of the image. The Dice coefficient was a commonly used evaluation index for segmented images. The calculation method was given as follows:

$$\mathrm{Dice}(A, B) = \frac{2|A \cap B|}{|A| + |B|}. \tag{6}$$

In the above equation, A was the number of pixels in the prediction area, and B was the number of pixels in the labeling area. The optimized Dice coefficient can be used as a loss function to improve the rough edge of the segmented image. The Dice loss function can be expressed as

$$\mathrm{Dice} = \frac{2\sum_i^N P_i Q_i}{\sum_i^N P_i^2 + \sum_i^N Q_i^2}. \tag{7}$$

In (7), P represented the predicted probability value of pixel i, ${}_{Q}^{i}$ was the binary label value of pixel i, and N referred to the total number of pixels in a batch. The partial derivative of the predicted probability of the Dice coefficient to the j-th pixel and the optimized loss function (sDice) are, respectively, expressed as

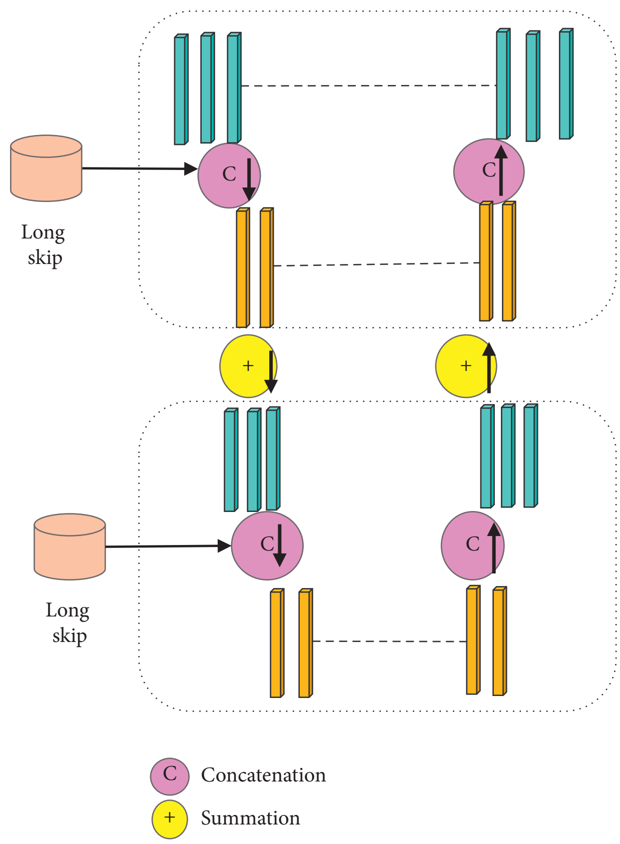

FIGURE 2: Encoder structure diagram after optimization.

$$\frac{\partial D}{\partial P_j} = 2\left[\frac{Q_j\left(\sum_i^N P_i^2 + \sum_i^N Q_i^2\right) - 2P_j\left(\sum_i^N P_i Q_i\right)}{\left(\sum_i^N P_i^2 + \sum_i^N Q_i^2\right)^2}\right], \tag{8}$$

$$sDice = 1 - Dice.$$

The Jaccard index is also a measure of the degree of regional overlap [21], and its calculation method was as follows:

$$\text{Jaccard} = \frac{|A \cap B|}{|A \cup B|}. \tag{9}$$

In semantic segmentation, the Jaccard index can be expressed as

$$J_c(y, y') = \left|\frac{\{y = h\} \cap \{y' = h\}}{\{y = h\} \cup \{y' = h\}}\right|. \tag{10}$$

In (10), y was the actual pixel category label vector and y' was the predicted pixel category label vector.

The calculation method of loss function based on Jaccard index was shown in

$$\Delta J_c(y, y') = 1 - J_c(y, y'). \tag{11}$$

In order to optimize the discrete Jaccard loss in continuous space, it needs to be expanded smoothly. It was assumed that the set of misclassified pixels was E_c, which could be expressed as

$$E_c(y, y') = \{y = c, y' \neq c\} \cup \{y \neq c, y' = c\}. \tag{12}$$

Jaccard loss could be expressed as

$$\Delta J_c\colon E_c \in \{0, 1\}P \mapsto \frac{|E_c|}{|\{y = c\} \cup E_c|}. \tag{13}$$

$H_i(x)$ was assumed to be the prediction score of the pixel by the segmentation network, and the Hinger loss of the pixel can be expressed as follows:

$$m_i = \max[1 - H_i(x) y_i, 0]. \tag{14}$$

Then, the final loss can be expressed as

$$\text{Loss}(H) = \overline{\Delta J_c}[m(H)]. \tag{15}$$

In the equation above, $\overline{\Delta J_c}$ referred to the Lovasz expanded item of ΔJ_c, and m was the vector number.

2.7. Test Data and Image Evaluation Indicators. In this study, the liver CT images were from 86 patients with liver disease collected. The original liver CT tomographic slice parameters were 1.25 mm ∗ 1.25 mm, and the slice spacing was 2 mm. All CT images were randomly divided into a training set (60 cases) and a test set (26 cases). The test environment was defined as follows: computer operating system Ubuntu 16.04 LTS 64 bit system, central processing unit (CPU) : Intel Core I7-2600 3.4 G HZ, memory: DDR 34 GB, hard disk 1 TB. The *Python* 3 was selected as a tool for implementing the DBN model code, and the deep learning framework was PyTorch.

The focus detection mainly used the focus detection precision and recall rate for evaluation, and the calculation methods were as follows:

$$\text{precision} = \frac{TP}{TP + FP} \times 100\%, \tag{16}$$

$$\text{recall} = \frac{TP}{TP + FN} \times 100\%. \tag{17}$$

In (16) and (17), TP represented the number of correctly detected lesions; FN represented the number of missed lesions; and FP represented the number of wrongly detected lesions.

Image segmentation evaluation indicators mainly used volume overlap error (VOE) and relative volume difference (RVD) for evaluation, and the calculation methods were as follows:

$$\begin{aligned} \text{VOE}(C, D) &= 1 - \left|\frac{C \cap D}{C \cup D}\right|, \\ \text{RVD}(C, D) &= \frac{|D| - |C|}{|C|}. \end{aligned} \tag{18}$$

In the equation above, C referred to the pixel set of the automatically segmented image, and D was the pixel set of the manually drawn image.

The root mean square error (RMSE) can be used to evaluate the burden of liver lesions. The calculation method of RMSE was given as follows:

$$\mathrm{RMSE} = \sqrt{\frac{1}{n}\sum_{i=1}^{n}\left(C_i - D_i\right)^2}. \tag{19}$$

2.8. Statistical Analysis. The test data processing was performed using SPSS19.0 statistical software, the measurement data were expressed as mean ± standard deviation ($\overline{x} \pm s$), and count data were expressed as percentage (%), using the χ^2 test. $P < 0.05$ indicated that the difference was statistically significant.

3. Results and Analysis

3.1. Analysis of CT Image Preprocessing Results. The segmented images without pretreatment (no pretreatment), traditional CT window pretreatment (tradition window), and optimized window pretreatment (optimized window) were compared and analyzed. The results were shown in Figure 3. The Dice value of the CT image preprocessed by the optimized window was (0.704 ± 0.06), and the Dice values of the CT image preprocessed by the no pretreatment and tradition window were (0.517 ± 0.05) and (0.583 ± 0.05), respectively. The Dice value of CT image preprocessed by optimized window was significantly higher than the other two methods ($P < 0.05$).

The output CT values of CT images under different preprocessing methods were compared further, and the results are illustrated in Figure 4. With the continuous increase of the initial CT value, the output CT values of no pretreatment and tradition window both show an obvious linear upward trend; and the output CT value of the optimized window shows an "S" curve with the continuous increase of the initial CT value. When the input CT value was greater than 200 HU, the output CT value no longer changed, showing a stable trend.

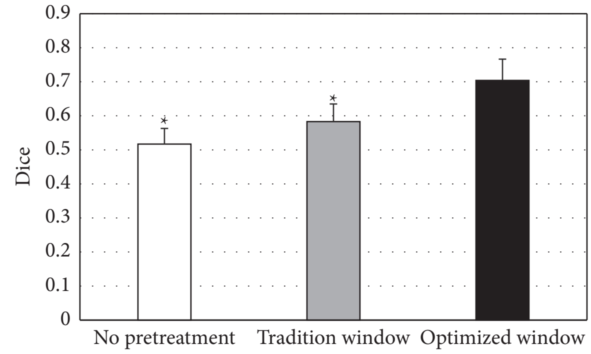

Figure 3: Comparison on the Dice value of CT images under different preprocessing methods. * indicates a statistical difference compared with the optimized window method ($P < 0.05$).

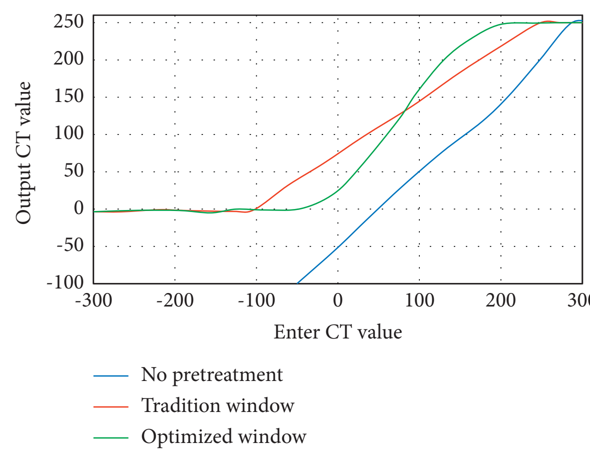

Figure 4: Curves of CT values of CT images under different preprocessing methods.

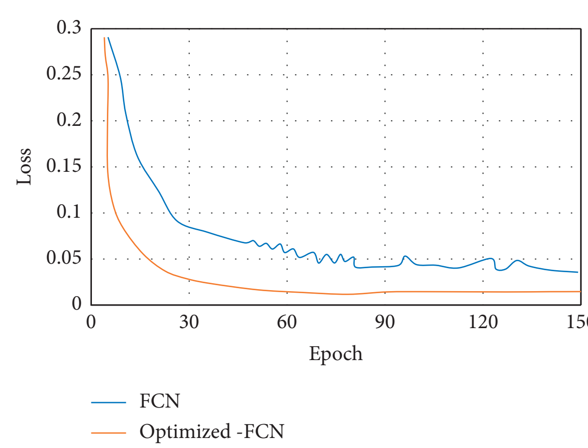

Figure 5: Changes in Loss values on training sets of different algorithms.

3.2. Analysis of CT Image Segmentation Effect. The Loss values of the FCN algorithm before optimization and the optimized-FCN algorithm in this study were analyzed and compared on the training set (Figure 5). As the Epoch value continued to increase, the Loss values of the two algorithms showed a tendency to first decrease and then stabilize. Under the same Epoch value, the Loss value of the Optimized-FCN algorithm was lower than that of the FCN algorithm.

A comparative analysis of the results of segmentation of CT images by the FCN algorithm before optimization and the Optimized-FCN algorithm is shown in Figure 6. It illustrated that, compared with the FCN algorithm, the Optimized-FCN algorithm had a higher degree of fit between the liver CT image lesion segmentation results and the manual segmentation results.

The Dice value of CT image segmentation between the FCN algorithm before optimization and the Optimized-FCN algorithm was compared. Figure 7 shows that the Dice values of the FCN algorithm and the optimized-FCN algorithm were (0.675 ± 0.07) and (0.826 ± 0.06), respectively, and the Dice value of the Optimized-FCN algorithm was much higher than that of the FCN algorithm ($P < 0.05$).

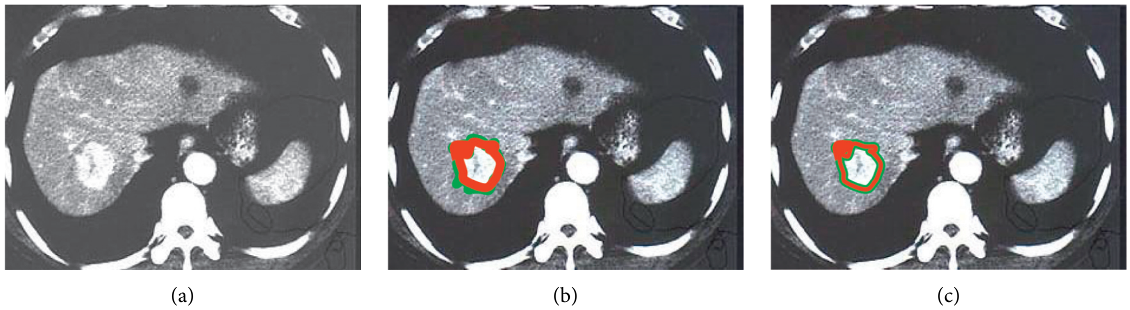

Figure 6: Comparison on segmentation results of liver lesions by different algorithms. (a) Initial CT image; (b) CT image segmented by FCN algorithm; (c) CT image segmented by Optimized-FCN algorithm.

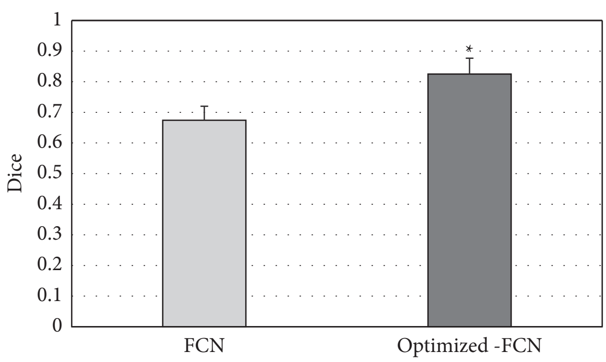

Figure 7: Comparison on Dice value before and after optimization. * suggests that the difference was statistically obvious ($P < 0.05$).

3.3. Comparative Analysis with Other Segmentation Methods. The results of Optimized-FCN algorithm segmentation of CT images with UNet, Res Net, Dense UNet, and the whole nested edge detection (HED) algorithm were compared (Figure 8). The detection precision, recall, VOE, RVD, and RMSE values of the optimized-FCN algorithm were (0.91 ± 0.08), (0.88 ± 0.09), (21.19 ± 1.97), (10.45 ± 1.02), and (0.25 ± 0.02), respectively. The detection precision and recall rate of Optimized-FCN algorithm were greatly higher than other algorithms ($P < 0.05$), and the values of VOE, RVD, and RMSE were significantly lower than other algorithms ($P < 0.05$).

3.4. Comparison of Basic Data. The basic data of the two groups of patients, such as age, gender, smoking history, drinking history, history of hypertension, history of diabetes, and history of low blood pressure, were compared and analyzed (Table 1). There was no significant difference between the two groups of patients in age, gender, the proportion of patients with smoking history, the proportion of hypertension history, and the proportion of diabetes history ($P > 0.05$). The proportion of patients with a history of drinking in the nonacute liver injury group was lower than that in the acute liver injury group ($P < 0.05$), and the proportion of patients with a history of low blood pressure in the acute liver injury group was significantly higher than that in the nonacute liver injury group ($P < 0.01$).

3.5. CT Imaging Results of Acute Liver Injury Caused by Sepsis. The CT imaging manifestations of patients with acute liver injury under different grades were analyzed, and the results are illustrated in Figure 9. Crescent-shaped high-density hematomas under the liver capsule can be observed in CT imaging of patients with grade I; the left liver lobe of grade II patients had a slightly low-density small hematoma; the right hepatic lobe of grade III patients was irregular and the boundary is blurred; and in the grade IV CT image, the right lobe of the liver can be seen with a patchy high-low density hematoma. The liver parenchyma showed a large mixed high-density hematoma under the grade V CT image, and the liver parenchymal lesions involved the right portal vein.

3.6. Clinical Characteristics of Patients with Acute Liver Injury Caused by Sepsis. The clinical characteristics of the two groups of patients were compared, and the results are revealed in Figure 10. There was no significant difference in the proportion of patients with different infection sites between the two groups ($P > 0.05$). The number of organ failures and length of stay in ICU in the acute liver injury group were much higher than that of the nonacute liver injury group ($P < 0.05$).

4. Discussion

Xu et al. (2019) [22] optimized it based on traditional window settings, and the results showed that image segmentation parameters have been improved. This study further optimized it based on the current research results to improve the segmentation performance. The results in the study showed that the Dice value of the CT image preprocessed by the optimized window was obviously higher than the other two methods ($P < 0.05$). It showed that the optimized CT window preprocessing method in this study can improve the performance of liver CT image segmentation. The Loss value of the Optimized-FCN algorithm was lower than that of the FCN algorithm, and the Dice value was higher than that of the FCN algorithm ($P < 0.05$). It showed that, under the same conditions, the loss function value of the optimized-FCN algorithm was lower, which may be related to the selection of weighted cross entropy loss function used in this study. The weighted cross entropy loss function can enable the segmented image to complete the

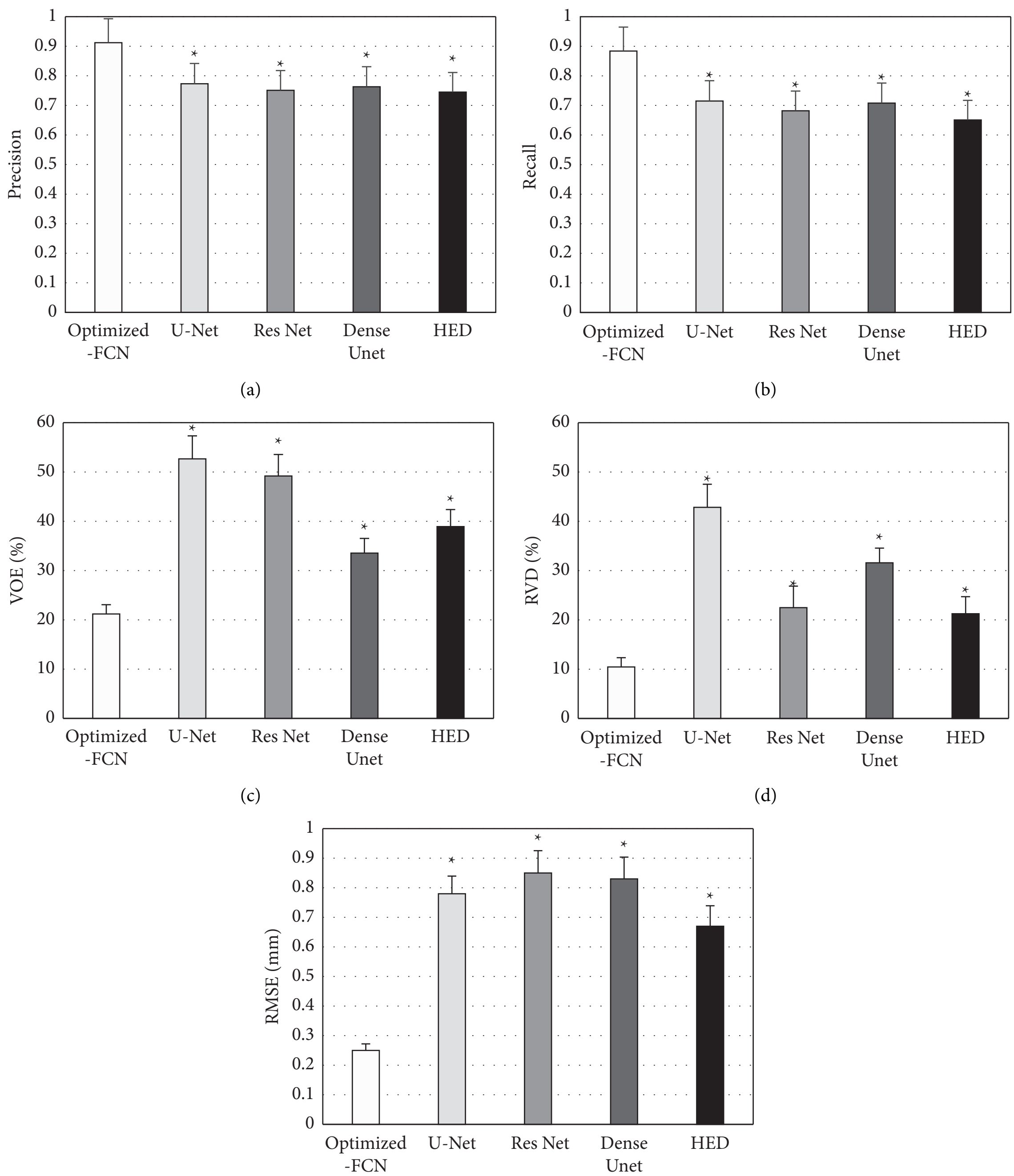

Figure 8: Comparison on image segmentation indexes of different algorithms. (a–e) showed the comparison on precision, recall, VOE, RVD, and RMSE, respectively. * means the difference was statistically obvious compared with the Optimized-FCN algorithm ($P < 0.05$).

rough segmentation and refined segmentation of the target object in different periods of training [23], improving the segmentation effect and reducing the Loss value. The detection precision and recall rate of the Optimized-FCN algorithm were significantly higher than other algorithms ($P < 0.05$), and the VOE, RVD, and RMSE values were significantly lower than other algorithms ($P < 0.05$). These results showed that the Optimized-FCN algorithm significantly improved the segmentation performance of liver CT images. Alirr (2020) [24] segmented the liver based on a machine learning algorithm and found that the Dice of the segmented CT image was 0.726. Weston et al. (2020) [25] established a liver segmentation method based on the CNN algorithm, and the results showed that the Dice value of this method for segmenting liver CT images was 0.79. Chen et al. (2021) [26] optimized the model based on the FCN algorithm and applied it to liver segmentation. The results showed that the Dice value of this method for segmenting liver CT images was 0.742. In this study, the Dice value of the Optimized-FCN algorithm for segmenting liver CT images

Table 1: Comparison of basic data of the two groups of patients.

Group	Nonacute liver injury group ($n = 50$)	Acute liver injury group ($n = 42$)	t value or χ^2 value	P value
Age (years old)	60.02 ± 5.78	59.96 ± 7.64	1.924	0.227
Males (cases, (%))	28 (56.00)	23 (54.76)	2.427	0.258
History of smoking (cases, (%))	14 (28.00)	12 (28.57)	2.337	0.265
History of drinking (cases, (%))	7 (14.00)	19 (45.24)	4.731	0.018*
History of hypertension (cases, (%))	16 (32.00)	14 (33.33)	2.019	0.198
History of low blood pressure (cases, (%))	24 (12.00)	38 (90.48)	5.213	0.008**
History of diabetes (cases, (%))	10 (20.00)	8 (19.05)	2.922	0.173

* indicated a statistical difference, $P < 0.05$; ** indicated a highly significant difference, $P < 0.01$.

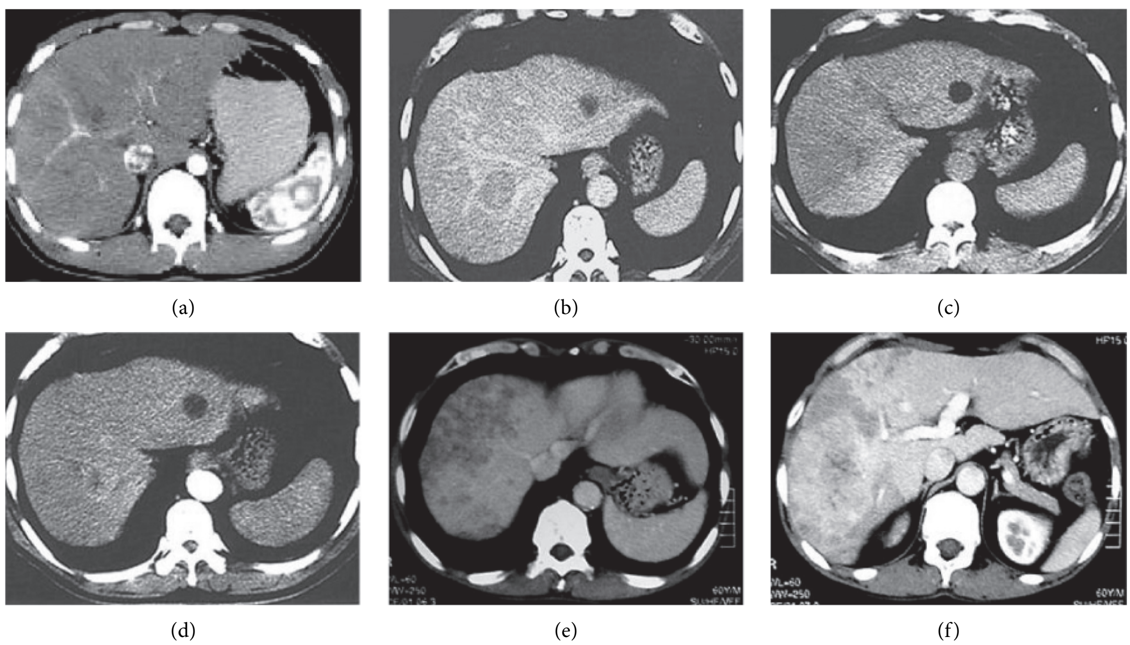

Figure 9: CT imaging results of acute liver injury caused by sepsis. (a–f) The CT images of patients with normal liver, grade I, grade II, grade III, grade IV, and grade V, respectively.

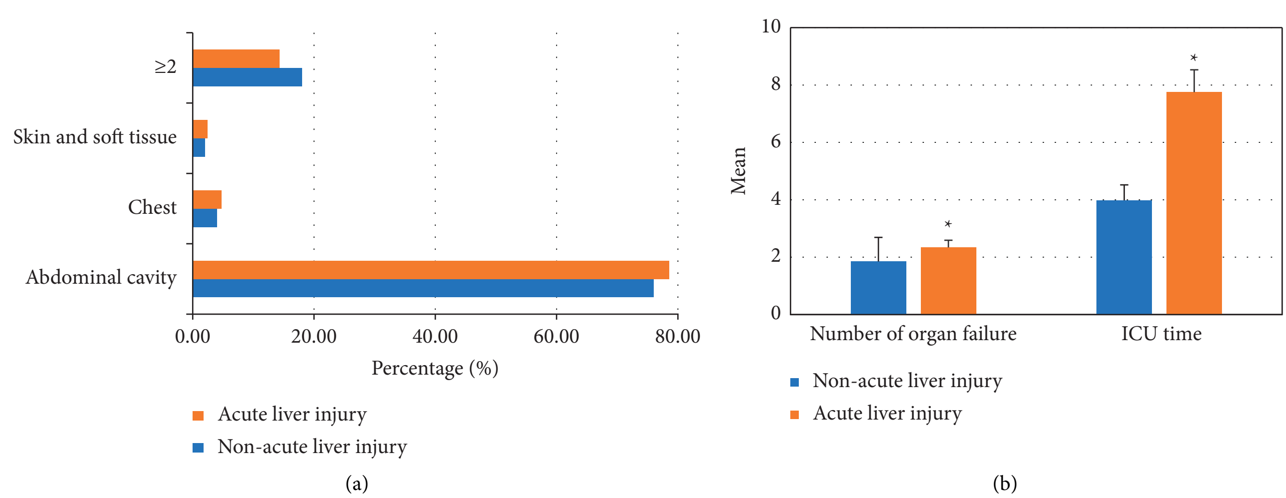

Figure 10: Comparison on infection site, number of organ failures, and length of stay in ICU between the two groups. (a) Comparison on the infection sites; (b) comparison on number of organ failures and length of stay in ICU. * suggests that the difference was statistically visible in contrast to the nonacute liver injury group ($P < 0.05$).

was 0.825, which was significantly better than these algorithms.

The typical CT appearance of liver injury is a well-defined low-density change on plain scan, which corresponds to the irradiation field and has nothing to do with liver anatomy [27]. The incidence of acute liver dysfunction in sepsis was about 25%. The results of this study showed that the proportion of patients with a history of drinking and low blood pressure in the nonacute liver injury group was lower than that in the acute liver injury group ($P < 0.05$). The reason was that long-term drinking can cause liver dysfunction, fatty degeneration, and liver compensatory ability to be significantly reduced. When the body develops sepsis, it is accompanied by liver function damage [28]. Insufficient tissue perfusion in patients with severe sepsis leads to hypoxia of weaving cells and ischemia of hepatocytes and ultimately leads to liver damage [29]. The number of organ failures and length of stay in ICU in the acute liver injury group were significantly higher than those in the nonacute liver injury group ($P < 0.05$). The more severe the liver damage, the longer the mechanical ventilation time [30]. Current research results showed that whether there is liver damage in the case of severe infection will affect the level of inflammatory response in the lungs. The incidence of acute lung injury is significantly increased if liver injury is present in sepsis patients, mainly due to the increased inflammatory response in the lung upon liver injury [31]. The results of this study were similar to that.

5. Conclusion

In this study, a liver CT image segmentation method based on FCN was established, and the clinical characteristics of acute liver injury caused by sepsis were analyzed. It was found that the optimized-FCN algorithm significantly improved the CT image segmentation performance. Long-term drinking, low blood pressure, number of organ failures, and length of stay in ICU were all related to acute liver injury caused by sepsis. However, there were some shortcomings in this study. It preliminarily analyzed the clinical characteristics of acute liver injury caused by sepsis. In addition, it was a retrospective study, lacking biochemical indicators and other data analysis. In the future work, the clinical features of acute liver injury caused by sepsis would be further analyzed. In conclusion, this work established an effective vertical liver CT image segmentation method based on the FCN algorithm and obtained the relevant influencing factors of sepsis acute liver injury, which provided a reference for the diagnosis and prognosis of sepsis acute liver injury.

Data Availability

The data used to support the findings of this study are available from the corresponding author upon request.

Conflicts of Interest

The authors declare no conflicts of interest.

Authors' Contributions

Huijun Wang and Qianqian Bao contributed equally to this work.

Acknowledgments

This work was supported by Taizhou Science and Technology Bureau Project (no. 20ywa15).

References

[1] M. Huang, S. Cai, and J. Su, "The pathogenesis of sepsis and potential therapeutic targets," *International Journal of Molecular Sciences*, vol. 20, no. 21, p. 5376, 2019, PMID: 31671729; PMCID: PMC6862039.

[2] J. Sun, J. Zhang, X. Wang et al., "Gut-liver crosstalk in sepsis-induced liver injury," *Critical Care*, vol. 24, no. 1, p. 614, 2020, PMID: 33076940; PMCID: PMC7574296.

[3] P. Strnad, F. Tacke, A. Koch, and C. Trautwein, "Liver - guardian, modifier and target of sepsis," *Nature Reviews Gastroenterology & Hepatology*, vol. 14, no. 1, pp. 55–66, 2017, Epub 2016, Dec 7. PMID: 27924081.

[4] M.-K. Hong, L.-L. Hu, Y.-X. Zhang et al., "6-Gingerol ameliorates sepsis-induced liver injury through the Nrf2 pathway," *International Immunopharmacology*, vol. 80, 2020, Epub 2020, Jan 21. PMID: 31978803, Article ID 106196.

[5] B. G. J. Surewaard, A. Thanabalasuriar, Z. Zeng et al., "α-Toxin induces platelet aggregation and liver injury during *Staphylococcus aureus* sepsis," *Cell Host & Microbe*, vol. 24, no. 2, pp. 271–284, 2018, Epub 2018, Jul 19. PMID: 30033122; PMCID: PMC6295203.

[6] E. Triantafyllou, K. J. Woollard, M. J. W. McPhail, C. G. Antoniades, and L. A. Possamai, "The role of monocytes and macrophages in acute and acute-on-chronic liver failure," *Frontiers in Immunology*, vol. 9, p. 2948, 2018, PMID: 30619308; PMCID: PMC6302023.

[7] M. Hu, Y. Zhong, S. Xie, H. Lv, and Z. Lv, "Fuzzy system based medical image processing for brain disease prediction," *Frontiers in Neuroscience*, vol. 15, 2021, PMID: 34393718; PMCID: PMC8361453, Article ID 714318.

[8] F. Schwendicke, T. Golla, M. Dreher, and J. Krois, "Convolutional neural networks for dental image diagnostics: a scoping review," *Journal of Dentistry*, vol. 91, Article ID 103226, 2019.

[9] R. D. MacDougall, Y. Zhang, M. J. Callahan et al., "Improving low-dose pediatric abdominal CT by using convolutional neural networks," *Radiology: Artificial Intelligence*, vol. 1, no. 6, PMID: 32090205; PMCID: PMC6884028, Article ID e180087, 2019.

[10] J. Jiang, Y. Luo, F. Wang, Y. Fu, H. Yu, and Y. He, "Evaluation on auto-segmentation of the clinical target volume (CTV) for graves' ophthalmopathy (GO) with a fully convolutional network (FCN) on CT images," *Current Medical Imaging Formerly Current Medical Imaging Reviews*, vol. 17, no. 3, pp. 404–409, 2021, PMID: 32914716.

[11] X. Zhou, "Automatic segmentation of multiple organs on 3D CT images by using deep learning approaches," *Advances in Experimental Medicine & Biology*, vol. 1213, pp. 135–147, 2020, PMID: 32030668.

[12] D. Abdelhafiz, J. Bi, R. Ammar, C. Yang, and S. Nabavi, "Convolutional neural network for automated mass segmentation in mammography," *BMC Bioinformatics*, vol. 21, no. S1, p. 192, 2020.

[13] C. L. Chowdhary, M. Mittal, K. Kumerasan, P. A. Pattanaik, and Z. Marszalek, "An efficient segmentation and classification system in medical images using intuitionist possibilistic fuzzy C-mean clustering and fuzzy SVM algorithm," *Sensors*, vol. 20, no. 14, p. 3903, 2020, PMID: 32668793; PMCID: PMC7411903.

[14] F. Tang, S. Liang, T. Zhong et al., "Postoperative glioma segmentation in CT image using deep feature fusion model guided by multi-sequence MRIs," *European Radiology*, vol. 30, no. 2, pp. 823–832, 2020, Epub 2019, Oct 24. PMID: 31650265.

[15] G. H. B. Miranda and J. C. Felipe, "Computer-aided diagnosis system based on fuzzy logic for breast cancer categorization," *Computers in Biology and Medicine*, vol. 64, pp. 334–346, 2015, Epub 2014, Oct 14. PMID: 25453323.

[16] Y. Todoroki, Y. Iwamoto, L. Lin, H. Hu, and Y.-W. Chen, "Automatic detection of focal liver lesions in multi-phase CT images using a multi-channel & multi-scale CNN," in *Proceedings of the 2019 41st Annual International Conference of the IEEE Engineering in Medicine and Biology Society (EMBC)*, pp. 872–875, PMID: 31946033, IEEE, Berlin, Germany, July 2019.

[17] A. Ben-Cohen, R. Mechrez, N. Yedidia, and H. Greenspan, "Improving CNN training using disentanglement for liver lesion classification in CT," in *Proceedings of the 2019 41st Annual International Conference of the IEEE Engineering in Medicine and Biology Society (EMBC)*, pp. 886–889, PMID: 31946036, Berlin, Germany, July 2019.

[18] K. Wang, A. Mamidipalli, T. Retson et al., "Automated CT and MRI liver segmentation and biometry using a generalized convolutional neural network," *Radiology: Artificial Intelligence*, vol. 1, no. 2, Epub 2019, Mar 27. PMID: 32582883; PMCID: PMC7314107, Article ID 180022, 2019.

[19] S. Lee, E. K. Choe, S. Y. Kim, H. S. Kim, K. J. Park, and D. Kim, "Liver imaging features by convolutional neural network to predict the metachronous liver metastasis in stage I-III colorectal cancer patients based on preoperative abdominal CT scan," *BMC Bioinformatics*, vol. 21, no. 13, p. 382, 2020, PMID: 32938394; PMCID: PMC7495853.

[20] S. Agrawal, R. K. Dhiman, and J. K. Limdi, "Evaluation of abnormal liver function tests," *Postgraduate Medical Journal*, vol. 92, no. 1086, pp. 223–234, 2016, Epub 2016, Feb 3. PMID: 26842972.

[21] D.-H. Chang, S. Brinkmann, L. Smith et al., "Calcification score versus arterial stenosis grading: comparison of two CT-based methods for risk assessment of anastomotic leakage after esophagectomy and gastric pull-up," *Therapeutics and Clinical Risk Management*, vol. 14, pp. 721–727, 2018, PMID: 29713180; PMCID: PMC5909785.

[22] M. Xu, S. Qi, Y. Yue et al., "Segmentation of lung parenchyma in CT images using CNN trained with the clustering algorithm generated dataset," *BioMedical Engineering Online*, vol. 18, no. 1, p. 2, 2019, PMID: 30602393; PMCID: PMC6317251.

[23] J. M. Wolterink, R. W. van Hamersvelt, M. A. Viergever, T. Leiner, and I. Išgum, "Coronary artery centerline extraction in cardiac CT angiography using a CNN-based orientation classifier," *Medical Image Analysis*, vol. 51, pp. 46–60, 2019, Epub 2018, Oct 22. PMID: 30388501.

[24] O. I. Alirr, "Deep learning and level set approach for liver and tumor segmentation from CT scans," *Journal of Applied Clinical Medical Physics*, vol. 21, no. 10, pp. 200–209, 2020.

[25] A. D. Weston, P. Korfiatis, K. A. Philbrick et al., "Complete abdomen and pelvis segmentation using U-net variant architecture," *Medical Physics*, vol. 47, no. 11, pp. 5609–5618, 2020.

[26] X. Chen, X. Wei, M. Tang et al., "Liver segmentation in CT imaging with enhanced mask region-based convolutional neural networks," *Annals of Translational Medicine*, vol. 9, no. 24, p. 1768, 2021.

[27] D. I. Cha, K. D. Song, S. Y. Ha, J. Y. Hong, J. A. Hwang, and S. E. Ko, "Long-term follow-up of oxaliplatin-induced liver damage in patients with colorectal cancer," *British Journal of Radiology*, vol. 94, no. 1123, Article ID 20210352, 2021.

[28] T. N. Bukong, Y. Cho, A. Iracheta-Vellve et al., "Abnormal neutrophil traps and impaired efferocytosis contribute to liver injury and sepsis severity after binge alcohol use," *Journal of Hepatology*, vol. 69, no. 5, pp. 1145–1154, 2018, Epub 2018, Jul 18. PMID: 30030149; PMCID: PMC6310218.

[29] H. Y. Zhou, C. X. Long, L. Luo, Y. Y. Chen, P. P. Liu, and Z. H. Xiao, "[Effect of mogroside VI on acute liver injury induced by sepsis in mice and related mechanisms]," *Zhong Guo Dang Dai Er Ke Za Zhi*, vol. 22, no. 11, pp. 1233–1239, 2020, Chinese.

[30] G. Chen, H. Deng, X. Song et al., "Reactive oxygen species-responsive polymeric nanoparticles for alleviating sepsis-induced acute liver injury in mice," *Biomaterials*, vol. 144, pp. 30–41, 2017, Epub 2017, Aug 11. PMID: 28820966.

[31] Z. Xu, S. Mu, X. Liao et al., "Estrogen protects against liver damage in sepsis through inhibiting oxidative stress mediated activation of pyroptosis signaling pathway," *PLoS One*, vol. 15, no. 10, Published 2020 Oct 1, Article ID e0239659, 2020.

Hindawi
Contrast Media & Molecular Imaging
Volume 2022, Article ID 9540701, 8 pages
https://doi.org/10.1155/2022/9540701

Research Article

Evaluation of the Effects of Folic Acid Combined with Atorvastatin on the Poststroke Cognitive Impairment by Low-Rank Matrix Denoising Algorithm-Based MRI Imaging

Yancui Li[1], **Zhou Fang**[1], **Jianghua Li**[2], **Jing Wang**[1], **Xi Wang**[1], **Xiang Li**[3] **and Fang Fang**[1]

[1]*Department of Pharmaceutics, The First Affiliated Hospital of Jiamusi University, Jiamusi 154002, Heilongjiang, China*
[2]*Department of Otolaryngology, The First Affiliated Hospital of Jiamusi University, Jiamusi 154002, Heilongjiang, China*
[3]*Department of Pharmaceutics, Hongda Hospital of Jiamusi University, Jiamusi 154002, Heilongjiang, China*

Correspondence should be addressed to Fang Fang; 6170206034@stu.jiangnan.edu.cn

Received 21 December 2021; Revised 28 January 2022; Accepted 31 January 2022; Published 4 March 2022

Academic Editor: M. Pallikonda Rajasekaran

This research aimed to study the optimization effects of the low-rank matrix denoising (LRMD) algorithm based on the Gaussian mixture model (GMM) on MRI images of stroke patients, aiming to evaluate the effects of atorvastatin combined with folic acid on poststroke cognitive impairment (PSCI) in patients with ischemic stroke. First, the GMM-based low-rank matrix denoising (LRMD) algorithm was constructed and applied to process MRI images of 64 patients with ischemic stroke. Then, the MRI images before and after processing were compared for the denoising degree and quality. An image with 5% noise was not as clear as an MRI image with 1% noise, and the effects of atorvastatin combined with folic acid on PSCI in patients with ischemic stroke were discussed. It was found that the denoising degree of MRI images processed by the GMM-based LRMD algorithm was significantly improved, the image quality was significantly enhanced ($P < 0.05$), and the diagnosis accuracy and efficiency of stroke patients were heightened. Atorvastatin combined with folic acid reduce the homocysteine (HCY) and total cholesterol (TC) levels, as well as Montreal Cognitive Scale (MOCA) scores of PSCI patients ($P < 0.05$). In conclusion, the MRI images processed by the LRMD algorithm have good quality. Folic acid combined with atorvastatin can effectively reduce HCY and TC levels, thereby alleviating PSCI of stroke patients.

1. Introduction

Stroke is a cerebrovascular disease, arising from the organic changes of the cerebral vessels, such as blockages and malformations. Its attack is sudden, which can lead to poststroke cognitive impairment [1]. Clinically, stroke usually falls into two types: ischemic stroke and hemorrhagic stroke. The former will cause muscle stiffness, weakness of the limbs, and damage to cognitive functions, such as memory and thinking, bringing great inconvenience to patients' daily lives [2]. PSCI is a kind of behavioral cognitive impairment caused by stroke, and it has attracted the attention of many researchers [3]. Studies have shown that the emergence of PSCI is related to the lack of nutrition in patients, and appropriate supplementation of nutrients can effectively prevent cognitive system dysfunction [4]. The research results of Ma et al. [5] showed that the lack of nutrients such as folic acid can accelerate the cognitive decline of patients with ischemic stroke. Enderami et al. [6] evaluated the folate levels of patients with cognitive impairment and found that patients with low folate levels are more likely to have memory problems, and either folic acid or in combination with other drugs can improve the body's cognitive level.

Nowadays, imaging technologies such as computed tomography (CT) and magnetic resonance imaging (MRI) are widely used in medical image analysis. As a result, the detection rate of malignant tumors has also generally increased, and the survival period of patients with malignant tumors begins to increase [7]. Among them, MRI imaging technology is a common method to diagnose brain tumors. Various imaging parameters produce various different modal maps, providing rich information for the diagnosis and treatment of brain tumors [8]. MRI is currently the only nonradiation and noninvasive imaging technology for cerebrovascular diseases, and it is sensitive in the differential diagnosis of intracranial aneurysms. It can show the vascular structure without using a contrast agent. Studies have pointed out that the traditional MRI imaging and transmission processes will be interfered by Rician noise, and effective denoising processing can improve the quality of MRI images, thereby improving the diagnostic efficiency [9].

There have been many reports on denoising algorithms for MRI images, including filtering methods, image block prior denoising algorithms, and low-rank matrix factorization (LRMF) based on image sparsity [10]. Xie et al. [11] found that the Gaussian mixture model (GMM) can easily construct prior noise-free images. Low-rank matrix factorization (LRMF) aims to find specific data items of a matrix that are infinitely close to a noisy image. In this study, a Gaussian mixture model (GMM)-based low-rank matrix denoising (LRMD) algorithm was used to process the MRI images of stroke patients, and its optimization effects were evaluated. Then, the effects of atorvastatin combined with folic acid on the PSCI of patients with ischemic stroke were explored, in order to further understand the role of folic acid combined with atorvastatin in the PSCI and treatment of stroke patients.

2. Materials and Methods

2.1. Research Subjects. Sixty-four patients with ischemic stroke from April 2019 to June 2020 were selected as research subjects, including 32 males and 48 females. All of them had the MRI examination. They were aged between 22 and 81 years old, with an average age of 52 years. After the patients were admitted to the hospital, their cognitive function was evaluated using Montreal Cognitive Assessment (MOCA) scale. All subjects were followed up at 3 and 6 months after the onset of ischemic stroke using the MOCA scale. This study has been approved by the ethics committee of hospital, and the patients and their families signed the informed consent form.

The inclusion criteria were as follows: (I) patients aged ≥18 years; (II) patients diagnosed with acute ischemic stroke as per the diagnostic criteria in *Neurology* (7th Edition, People's Medical Publishing House) [12]; (III) the time from first onset to admission was ≤7 days; (IV) those who can cooperate with medical staff to perform scale scoring and MRI examinations; (V) basic information was complete; and (VI) the patient was willing to cooperate in the follow-up.

The exclusion criteria were as follows: (I) cognitive function decline caused by previous nonvascular factors; (II) those accompanied by mental illnesses, such as depression and schizophrenia; (III) those accompanied by severe limb movement, hearing, and language impairment and unable to cooperate with the medical staff in the scale assessment; (IV) those who cannot complete head magnetic resonance examination due to the presence of metal foreign bodies such as steel plates, stents, cardiac pacemakers, and claustrophobia; (V) those suffering from malignant tumors, acute myocardial infarction, and other serious diseases of the system; and (VI) those who refused to participate in the registration investigation.

2.2. The Grouping Methods. The patients were divided into the non-PSCI group (group A) and the PSCI group according to MOCA results. According to whether to give atorvastatin combined with folic acid treatment, they were randomly divided into two groups: the PSCI untreated group (group B) and the PSCI treated group (group C). In group A, there were 20 subjects, including 14 males and 6 females, aged 66 years old. In group B, there were 22 cases, including 12 males and 10 females, aged 67 years. In group C, there were 22 patients, including 11 males and 11 females, aged 67 years old. Group A received placebo treatment; group B received placebo treatment; and group C took 15 mg of folic acid combined with 20 mg of atorvastatin orally, once a night. The drug intervention cycle lasted for 6 months. Then, the MOCA score, plasma and serum levels were detected.

2.3. Imaging Examination. After the patient was admitted to the hospital, the unenhanced MRI scan and susceptibility imaging were performed within 3 days. Cerebral microbleeds (CMBs) are an imaging manifestation of cerebral small vessel disease, showing circular uniform low signals with a diameter of 2~5 mm and clear borders [13]. This is due to the escape of red blood cells from the blood vessel and then being swallowed by macrophages to form hemosiderin [14]. Two imaging physicians who were blinded read the films to find the location of the cerebral infarction and whether there were CMBs. Any inconsistencies were resolved by inviting a senior medical imaging physician to arbitrate.

2.4. GMM-Based Clustering of MRI Images of Stroke Patients. The MRI images of different organs are similar, and it is difficult to distinguish image blocks because of the similar interference signals of different structures in intracranial MRI images of stroke patients. Therefore, the GMM-based clustering method is used to cluster the MRI images of intracranial cerebral hemangioma together with the prior method of noise-free MRI image blocks. First, the MRI image is set as S and then segmented based on structural similarity. Finally, the segmentation results are merged (n image blocks) into a set, that is, $PS = (P_1S\ ,\ \ldots, P_iS, \ldots, P_nS)$. In this set, P_iS represents the matrix corresponding to the first image block. If the image block PS can be divided into w categories, the probability of the P_iS image block can be expressed by GMM, and the equation is as follows:

$$p\left(P_iS|\Phi\right) = \sum_{h=1}^{H} w_h p_h\left(P_iS|\mu_{h,}\sum h\right), \quad (1)$$

where H represents the GMM containing H Gaussian classes, h represents the number of corresponding Gaussian classes, w represents the weight, μ represents the mean, Σ is the reference covariance matrix, and Φ represents the set composition of the mean. μ, covariance matrix Σ, and the weight w of each Gaussian class satisfy the following equation. In addition, the probability density function of the h^{th} Gaussian class is used, expressed as follows:

$$p\left(P_iS|\mu_{h,}\sum h\right) = c\cdot \exp\left(\left(-\frac{1}{2}(P_iS-\mu_h)^T\sum_h^{-1}(P_iS-\mu_h)\right)\right), \quad (2)$$

where c represents the normalization constant, and the negative exponent represents the correlation between P_iS and $\mu_{h,}$.On this basis, $D = (d_1, d_2, \ldots, d_h), d_i \in \{1, 2, \ldots, R\}$ class labels are used to simplify expressions. $p(P_iS, d_i = h|\Phi)$ indicates that $P_iS(i, \ldots, h)$ is independent under the GMM parameter setting. In the GMM parameter set, the probability of PS clustering to class R is calculated as follows:

$$p(\mathrm{PS}, D|\Phi) = \prod_{i-1}^{h} p(P_iS, d_i|\Phi). \quad (3)$$

The final clustering results of MRI images of cerebral aneurysms based on GMM are shown in Figure 1.

2.5. LRMF Denoising Algorithm Based on Image Block Prior. The MRI image of the brain aneurysm with given noise is divided into blocks, and then $P = (P_1S, P_iS, \ldots, P_hS)$ is obtained. Assuming that the GMM parameter set is obtained by learning the information of noise-free MRI image blocks, *PS* is divided into H categories according to the prior knowledge of GMM. $\bar{P}_aX = [P_{h_1}, \ldots, P_{h_{d(h)}}]$ refers to a matrix composed of all image blocks in the H^{th} category, and d(h) represents the number of all similar image blocks in the H^{th} category. The image blocks in the same Gaussian class contain similar structural information, so $\bar{P}_hS$ can be decomposed into the following equations:

$$\bar{P}_hS = Q_h + T_h, \quad (4)$$

where Q_h represents a low-rank *matrix*, T_h represents a noise matrix, and a low-rank matrix represents image data after denoising. Assuming that the noise of each pixel in the image is independent and uniformly distributed, the energy function can be expressed as follows:

$$E(Q_h) = \tau Q_{h*} + \frac{1}{\sigma^2}\bar{P}_hS - Q_{hF}^2, \quad (5)$$

where τ represents the normal number, and σ represents the standard deviation of the noise; Q_{h*} is the matrix kernel norm, and $\bar{P}_hS - Q_h{}_F^2$ is the norm of matrix Frobenius.The rank minimization in (5) can be solved by minimizing the weighted kernel norm. Hence, for a given noise MRI image, a noise-free MRI image can be reconstructed on the basis of a prior denoising model of the noise-free MRI image.

2.6. Evaluation Indexes of Stroke MRI Image Processed by the LRMD Algorithm. The quality of MRI images of cerebral aneurysms was evaluated by factoring into root mean square error (RMSE), peak signal-to-noise ratio (PSNR), and structural similarity (SSIM). MSE and PSNR describe the error between the target image z and the original image x from the perspective of pixel values, while SSIM takes into account the characteristics of the human visual system, making the evaluation results more in line with the human senses.

2.7. Cognitive Function Evaluation Indexes. The changes of plasma index homocysteine (HCY), serum index total cholesterol (TC), and MOCA scores before and after treatment were compared between untreated PSCI patients and non-PSCI patients.

The diagnostic criteria of PSCI were as follows: (I) PSCI that occurred within half a year after the occurrence of the stroke; (II) PSCI (MOCA total score <26 points) caused by the stroke.

For the determination of plasma HCY, 4 mL of early morning fasting blood was drawn from the cubital vein of the subject, and then transferred to a common desiccator, stored at 4°C. Then, it was centrifuged within 1 hour (3000 rpm, 10 min), and hemorrhagic cells and plasma were separated. Next, the 0.5 mL of plasma in the upper layer was transferred into a 1 mL centrifuge tube, and then stored at −20°C to facilitate the batch measurement of plasma HCY.

For determination of serum TC, 10 mL of fasting venous blood was drawn and transferred to an ordinary drying tube. After 15 minutes, the blood sample was centrifuged in a high-speed automatic balance for 10 minutes at 3000 rpm. Subsequently, the upper layer of plasma was taken and transferred into a test tube. An automatic biochemical analyzer was used to detect the level of serum TC.

2.8. Statistical Analysis. Statistical analysis was performed using SPSS 24.0 software, expressed as mean ± standard deviation ($\bar{x} \pm s$). The χ^2 test method was used to process the data, with $\alpha = 0.05$, and $P < 0.05$ was the threshold for significance.

3. Results

3.1. Changes in MRI Images of Stroke Patients before and after Processing by GMM-Based LRMD Algorithm. Figure 2 shows the MRI images of patients with ischemic stroke tumors before and after processing by the GMM-based LRMD algorithm. Compared with the MRI image before denoising, the texture of the MRI image after denoising was clearer.

Figure 3 shows the clarity of the MRI image of the same patient. The image with 5% noise was not as clear as the MRI image with 1% noise. Therefore, denoising processing can greatly change the visual clarity of the MRI image.

3.2. Comparison of MRI Image Quality Indexes of Stroke Patients under Different Noise Intensities. The MRI image quality indexes of stroke patients showed that under the same noise intensity, the difference of the PSNR under different K values was very small, as shown in Figure 4.

Figure 5 shows that as the noise intensity increased from 1% to 7%, the RMSE increased from 1.57 dB to 8.72 dB,

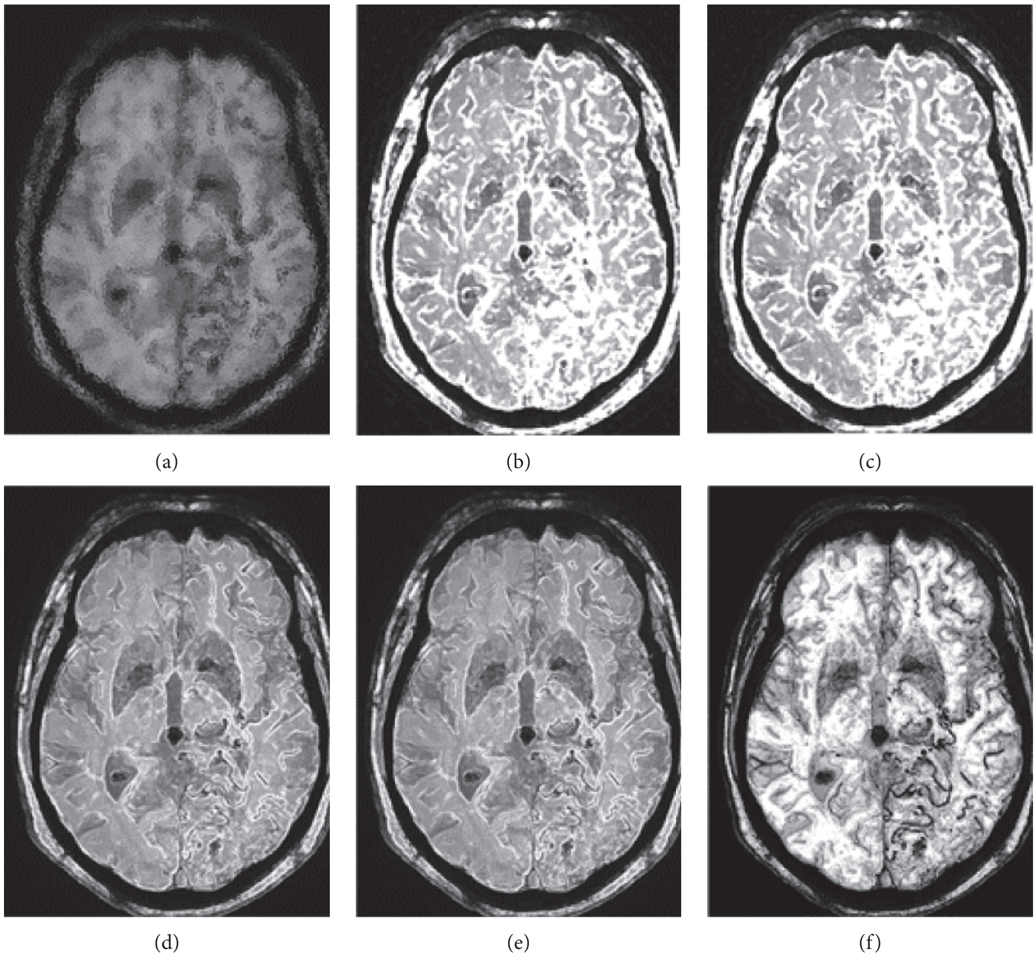

Figure 1: GMM-based clustering results of MRI images of stroke patients. *Note.* Figures (a), (b), (c), (d), (e), and (f) were images with 10% noise; clustering results of noisy images; clustering results generated by iterations; clustering results after 3 circles of iterations; clustering results after 6 circles of iterations and the denoised image.

indicating that greater noise intensity led to lower similarity between the processed MRI image and the original image.

3.3. MRI Image Quality Processed by a GMM-Based LRMD Algorithm. The PSNR value of the MRI image processed by the GMM-based LRMD algorithm was compared with that of the original MRI image, as shown in Figure 6. The PSNR value of the MRI images processed by the GMM-LRMD algorithm increased by an average of 12.5 dB, indicating that the LRMD algorithm can significantly improve PSNR and that the difference was statistically significant ($P < 0.05$). If the denoised MRI image is closer to the original image, the image quality is higher and it is easier to diagnose an ischemic stroke.

Figure 7 compares SSIM values of MRI images before and after being processed by the LRMD algorithm. As the degree of noise increased, the SSIM value of the LRMD algorithm was reduced from 0.9 to 0.6 dB, while it was always less than 1. A lower noise degree indicates that the closer SSIM value after denosing is closer to 1. In other words, higher similarity between the original image and the target image indicates higher quality of the original image.

3.4. HCY Levels the Three Groups of Patients before and after Treatment. Figure 8 shows the HCY values of the patients before and after treatment. Before treatment, the average HCY of patients in group A was $21.4 \pm 3.52\,\mu$mol/L, that of patients in group B was $33.8 \pm 2.44\,\mu$mol/L, and that in group C was $36.8 \pm 3.05\,\mu$mol/L. Obviously, the HCY levels of patients in groups A and B were significantly different ($P < 0.05$), the HCY levels of patients in groups A and C were also significantly different ($P < 0.05$), but the differences in HCY levels of patients in groups B and C were not significant ($P > 0.05$). After treatment, the average HCY of patients in group A was $22.3 \pm 2.78\,\mu$mol/L, that in group B was $37.6 \pm 2.56\,\mu$mol/L, and that in group C was $21.5 \pm 3.17\,\mu$mol/L. The HCY values of patients in groups A and B were not significantly different before and after treatment ($P > 0.05$), while the HCY values of patients in group C were significantly different before and after treatment ($P < 0.05$).

3.5. TC Levels of the Three Groups of Patients before and after Treatment. Figure 9 shows the serum TC values of the patients before and after the treatment. Before treatment, the

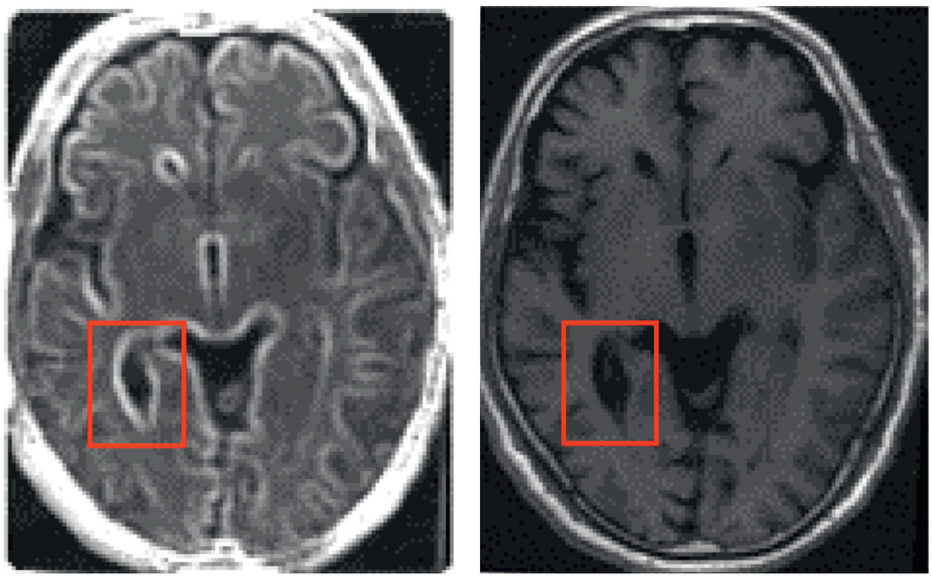

(a) (b)

Figure 2: Comparison of MRI images before and after being processed by the GMM-based LRMD algorithm. (a) The image before denoising, and (b) the image after denoising. The red box indicates intracranial hemorrhage.

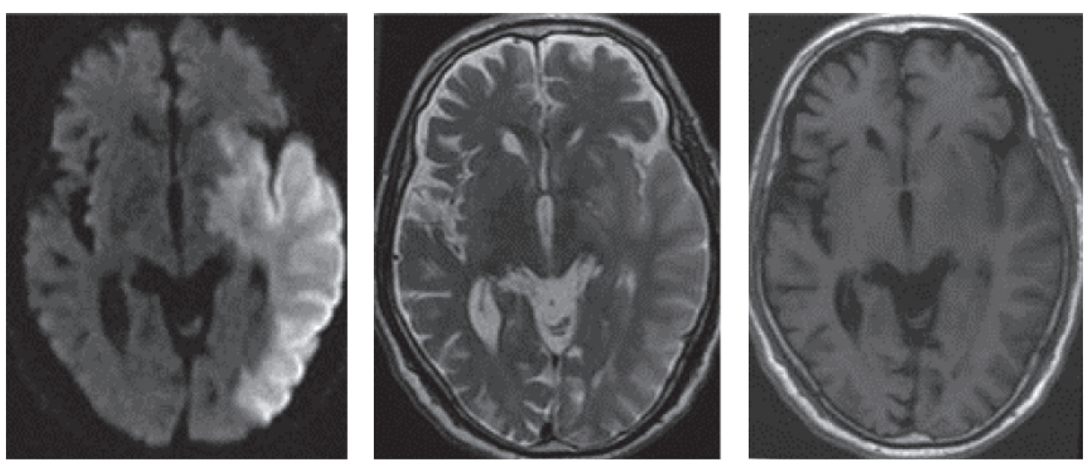

(a) (b) (c)

Figure 3: Comparison of MRI images of stroke patients under different noise intensities. (a) 5%, (b) 1%, and (c) noise-free MRI images.

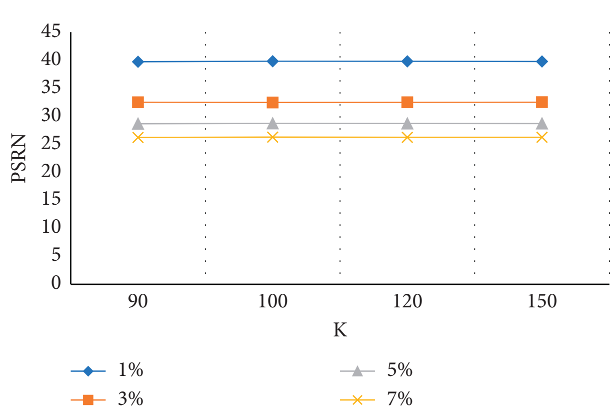

Figure 4: PSRN values at different K values.

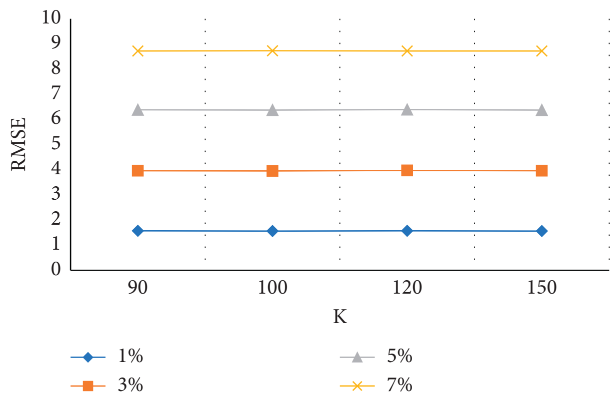

Figure 5: RMSE values at different K values.

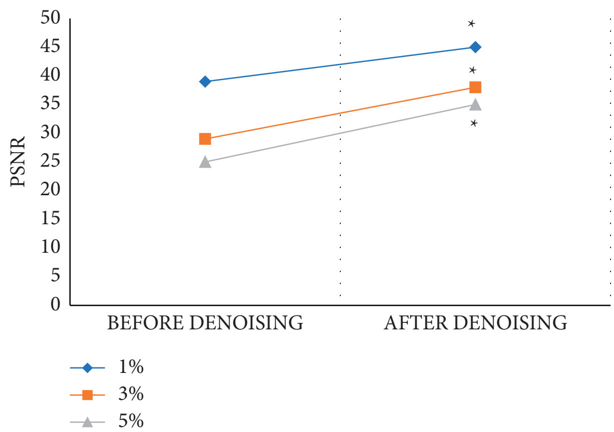

Figure 6: Comparison of PSNR scores of MRI images before and after denoising. Note: * indicates that there was a significant difference between the PSNR score after denoising and the PSNR score before denoising ($P < 0.05$).

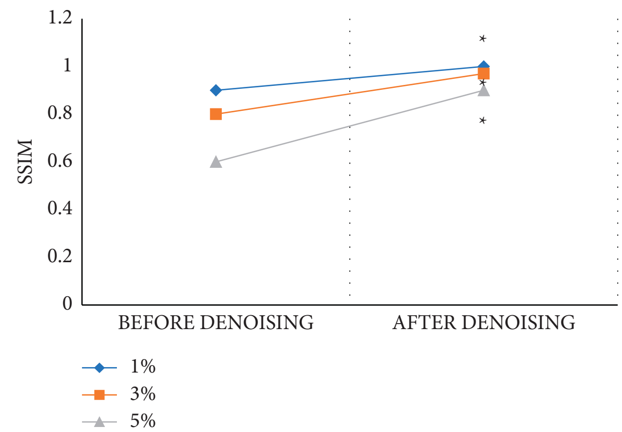

Figure 7: Comparison of SSIM scores of MRI images before and after denoising. Note: * indicates that there was a significant difference between the SSIM score after denoising and the SSIM score before denoising ($P < 0.05$).

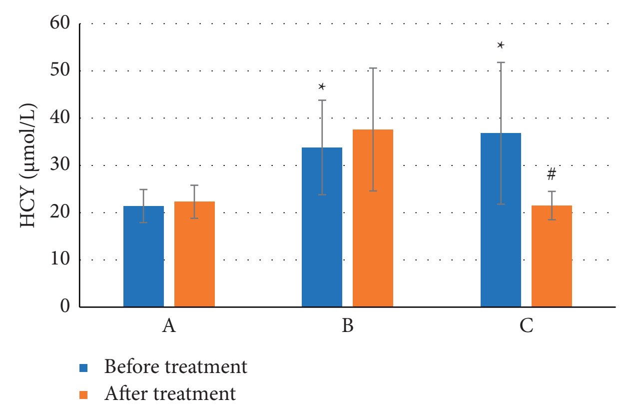

Figure 8: Comparison of the HCY levels of the three groups of patients before and after treatment. Note: * means there was a significant difference versus group A ($P < 0.05$). # indicates that there was a significant difference before and after treatment in the same group ($P < 0.05$).

average TC of the patients in group A was 5.23 ± 2.01 mol/L, that in group B was 6.14 ± 1.96 mol/L, and that in group C patients was 6.64 ± 1.87 mol/L. Obviously, the TC levels of patients in groups A and B were significantly different ($P < 0.05$). The TC levels of patients in groups A and C were also significantly different ($P < 0.05$), but the TC levels of patients in groups B and C were not significantly different ($P > 0.05$). After treatment, the average TC of patients in group A was 5.82 ± 1.47 mol/L, that in group B patients was 6.79 ± 1.77 mol/L, and that in group C patients was 5.33 ± 2.17 mol/L. There was no significant difference in TC values of patients in groups A and B before and after treatment ($P > 0.05$), while the difference in TC values of patients in group C before and after treatment was significant ($P < 0.05$).

3.6. Comparison of the MOCA Scores of the Three Groups of Patients before and after Treatment. Figure 10 shows the MOCA scores of the patients before and after the treatment. Before treatment, the average MOCA of patients in group A was 31.7 ± 0.58, that in group B was 25.3 ± 1.96, and that in group C was 25.4 ± 1.02. Obviously, the MOCA scores of patients in groups A and B were significantly different ($P < 0.05$), and the differences in MOCA scores of patients in groups A and C were also statistically significant ($P < 0.05$), but the differences in MOCA scores between groups B and C were not significant ($P > 0.05$). After treatment, the average MOCA of patients in group A was 31.3 ± 0.79, that in group B was 24.8 ± 1.23, and that in group C was 25.3 ± 1.22. The differences in MOCA scores of group A were not statistically significant before and after treatment ($P > 0.05$). The MOCA scores in group B differed significantly before and after treatment ($P < 0.05$), and the difference in MOCA scores in group C was not significant before and after treatment ($P > 0.05$). After treatment, there was a significant difference in the MOCA scores between groups B and C ($P < 0.05$).

4. Discussion

Stroke is a cerebrovascular disease with high morbidity, disability, and mortality. Studies have shown that the prevalence of PSCI in patients with severe stroke is as high as

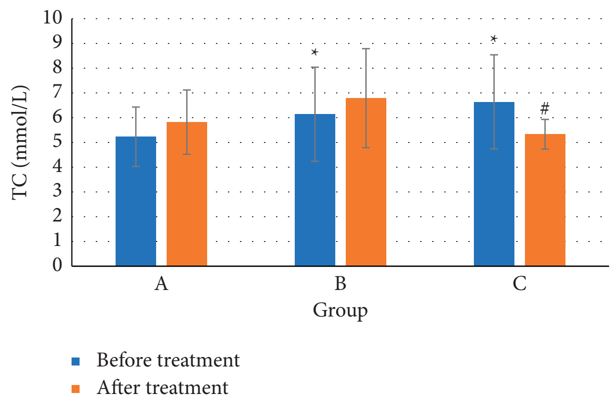

FIGURE 9: Comparison of the TC levels of the three groups of patients before and after treatment. Note: * means there was a significant difference versus group A ($P < 0.05$). # indicates that there was a significant difference before and after treatment in the same group ($P < 0.05$).

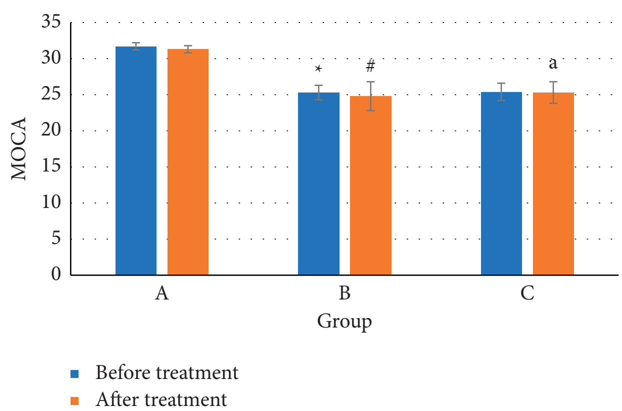

FIGURE 10: Comparison of MOAC levels before and after treatment in the three groups of patients. Note: * means there was a significant difference versus group A ($P < 0.05$). # indicates that there was a significant difference before and after treatment in the same group ($P < 0.05$). a means there was a significant difference versus group B ($P < 0.05$).

37%–80%, and it can be fatal in severe cases [15]. MRI is widely used in the examination and diagnosis of cerebrovascular diseases and has obvious advantages. However, in actual practice, it will be affected by objective factors such as the patient's breathing rate and the doctor's operations. The final MRI image quality is poor, so it is necessary to choose a suitable image segmentation algorithm [16]. In this study, the denoising degree of MRI images processed by the GMM-based LRMD algorithm was significantly improved, the image quality was significantly enhanced, and the diagnostic accuracy and efficiency of PSCI patients were heightened.

The increase in plasma HCY was related to cognitive impairment. Before treatment, the HCY levels of patients in groups A and B were significantly different ($P < 0.05$), and the HCY levels in groups A and C also differed significantly ($P < 0.05$), but there was no significant difference in HCY levels between groups B and C ($P > 0.05$). After treatment, the HCY values of patients in groups A and B were not significantly different before and after treatment ($P > 0.05$), and the HCY values of patients in group C were significantly different before and after treatment ($P < 0.05$). These results indicated that the HCY level of PSCI patients was significantly higher than that of non-PSCI patients, which was in line with the research conclusion of Ma et al. [17]. Folic acid is an important cofactor in the body's metabolic process. It can be supplemented with folic acid to reduce the level of HCY in the body and alleviate PSCI in patients [18]. After PSCI patients were treated with folic acid combined with atorvastatin, their own HCY levels were significantly reduced, which showed that folic acid combined with atorvastatin can lower patients' plasma levels, echoing the conclusions of previous studies.

Studies have shown that an increase in serum TC can inhibit brain metabolism by reducing cerebral blood flow, thereby increasing the probability of PSCI and dementia. In addition, high-level TC can also inhibit the deformation of related neurons to cause PSCI [19]. This is because the increase in serum TC will inhibit the metabolism of amyloid in nerve cells [20], resulting in the accumulation of amyloid protein in the patient's body, thus leading to PSCI. Meyer et al. [21] found that hyperlipidemia was a key cause of PSCI. In this study, it was found that before treatment, the TC levels of patients in groups A and B were significantly different ($P < 0.05$), and the differences in TC levels of patients in groups A and C were also significant ($P < 0.05$), but there was no significant difference in TC levels between groups B and C ($P > 0.05$). After treatment, the TC values of patients in groups A and B were not significantly different before and after treatment ($P > 0.05$), but the TC values of patients in group C were significantly different before and after treatment ($P < 0.05$). These results indicated that the increase in serum TC contributed to PSCI. The TC level of group C treated with folic acid combined with atorvastatin was significantly reduced. Therefore, folic acid combined with atorvastatin can reduce the plasma level of PSCI patients, thereby reducing PSCI.

The cognitive MOCA scores of the three groups of patients before and after treatment showed that after treatment, there was a significant difference in MOCA scores between the PSCI group treated by the folic acid combined with atorvastatin and the placebo-treated group B ($P < 0.05$). The scores of patients in group C decreased slowly, so the degree of PSCI in group C was smaller compared to group B. It is suggested that folic acid combined with atorvastatin can alleviate the PSCI of patients and can be used in the treatment of PSCI of stroke patients.

5. Conclusion

In this study, the GMM-based LRMD algorithm was applied to process MRI images of stroke patients. The images before and after processing were then compared. Next, the effects of atorvastatin combined with folic acid on the PSCI of patients with ischemic stroke were discussed in order to further understand the role of atorvastatin combined with folic acid in the PSCI and treatment of stroke patients. The results showed that the denoising degree of MRI images processed by the GMM-based LRMD algorithm was significantly improved, and the image quality was significantly enhanced.

Atorvastatin combined with folic acid can reduce HCY, serum TC, and MOCA scores. Therefore, the processed MRI images have good quality, and folic acid combined with atorvastatin can effectively reduce plasma and serum levels, thereby reducing the PSCI of stroke patients. It was of great significance for the early diagnosis and treatment of stroke patients. However, some limitations should be noted. The sample size is small, which will reduce the power of the study, and an expanded sample size is necessary in the follow-up to strengthen the findings of the study [22].

Data Availability

The data used to support the findings of this study are available from the corresponding author upon request.

Conflicts of Interest

The authors declare no conflicts of interest.

Authors' Contributions

Yancui Li and Zhou Fang contributed equally to this work.

Acknowledgments

This work was supported by the Scientific Research Project of Health Commission of Heilongjiang Province (number: 2020-326).

References

[1] X. Zhang and X. Bi, "Post-stroke cognitive impairment: a review focusing on molecular biomarkers," *Journal of Molecular Neuroscience*, vol. 70, no. 8, pp. 1244–1254, 2020 Aug.

[2] L. Zhao, J. M. Biesbroek, L. Shi et al., "Strategic infarct location for post-stroke cognitive impairment: a multivariate lesion-symptom mapping study," *Journal of Cerebral Blood Flow and Metabolism*, vol. 38, no. 8, pp. 1299–1311, 2018 Aug.

[3] Z. Teng, Y. Dong, D. Zhang, J. An, and P. Lv, "Cerebral small vessel disease and post-stroke cognitive impairment," *International Journal of Neuroscience*, vol. 127, no. 9, pp. 824–830, 2017 Sep.

[4] C. Y.-f. Hung, X.-Y. Wu, V. C.-h. Chung, E. C.-H. Tang, J. C.-y. Wu, and A. Y.-L. Lau, "Overview of systematic reviews with meta-analyses on acupuncture in post-stroke cognitive impairment and depression management," *Integrative Medicine Research*, vol. 8, no. 3, pp. 145–159, 2019 Sep.

[5] Y. Li, J. Zhao, Z. Lv, and J. Li, "Medical image fusion method by deep learning," *International Journal of Cognitive Computing in Engineering*, vol. 2, no. 6, pp. 21–29, 2021.

[6] A. Enderami, M. Zarghami, and H. Darvishi-Khezri, "The effects and potential mechanisms of folic acid on cognitive function: a comprehensive review," *Neurological Sciences*, vol. 39, no. 10, pp. 1667–1675, 2018 Oct.

[7] M. Hu, Y. Zhong, S. Xie, H. Lv, and Z. Lv, "Fuzzy system based medical image processing for brain disease prediction," *Frontiers in Neuroscience*, vol. 15, p. 714318, 2021 Jul 30.

[8] P. Mundada, M. Becker, V. Lenoir et al., "High resolution MRI of nail tumors and tumor-like conditions," *European Journal of Radiology*, vol. 112, pp. 93–105, 2019 Mar.

[9] G. S. Stacy, J. Bonham, A. Chang, and S. Thomas, "Soft-tissue tumors of the hand-imaging features," *Canadian Association of Radiologists Journal*, vol. 71, no. 2, pp. 161–173, 2020 May.

[10] R. B. Jeffrey, "Imaging pancreatic cysts with CT and MRI," *Digestive Diseases and Sciences*, vol. 62, no. 7, pp. 1787–1795, 2017 Jul.

[11] D. Xie, Y. Li, H. Yang et al., "Denoising arterial spin labeling perfusion MRI with deep machine learning," *Magnetic Resonance Imaging*, vol. 68, pp. 95–105, 2020 May.

[12] F. Herpich and F. Rincon, "Management of acute ischemic stroke," *Critical Care Medicine*, vol. 48, no. 11, pp. 1654–1663, 2020 Nov.

[13] Y. H. Zhong, Q. Yang, Z. Liu et al., "[The value of MRI plain scan and DWI in the diagnosis of brain metastases]," *Zhonghua Zhongliu Zazhi*, vol. 43, no. 4, pp. 466–471, 2021 Apr 23.

[14] Y. Qin, A. Bao, H. Li, X. Wang, G. Zhang, and J. Zhu, "Application value of CT and MRI in diagnosis of primary brain lymphoma," *Oncology Letters*, vol. 15, no. 6, pp. 8500–8504, 2018 Jun.

[15] V. Zietemann, A. Kopczak, C. Müller, F. A. Wollenweber, and M. Dichgans, "Validation of the telephone interview of cognitive status and telephone montreal cognitive assessment against detailed cognitive testing and clinical diagnosis of mild cognitive impairment after stroke," *Stroke*, vol. 48, no. 11, pp. 2952–2957, 2017 Nov.

[16] S. Xie, Z. Yu, and Z. Lv, "Multi-disease prediction based on deep learning: a survey," *Computer Modeling in Engineering and Sciences*, vol. 128, no. 2, pp. 489–522, 2021 Jul.

[17] F. Ma, Q. Li, X. Zhou et al., "Effects of folic acid supplementation on cognitive function and Aβ-related biomarkers in mild cognitive impairment: a randomized controlled trial," *European Journal of Nutrition*, vol. 58, no. 1, pp. 345–356, 2019 Feb.

[18] F. Ma, T. Wu, J. Zhao et al., "Folic acid supplementation improves cognitive function by reducing the levels of peripheral inflammatory cytokines in elderly Chinese subjects with MCI," *Scientific Reports*, vol. 6, no. 1, p. 37486, 2016 Nov 23.

[19] R. Haußmann, C. Sauer, S. Neumann, A. Zweiniger, J. Lange, and M. Donix, "Folsäure- und Vitamin-B12-Bestimmung in der Diagnostik kognitiver Störungen," *Nervenarzt, Der*, vol. 90, no. 11, pp. 1162–1169, 2019 Nov.

[20] D. Valera-Gran, E. M. Navarrete-Muñoz, M. Garcia de la Hera et al., "INMA Project. Effect of maternal high dosages of folic acid supplements on neurocognitive development in children at 4-5 years of age: the prospective birth cohort Infancia y Medio Ambiente (INMA) study," *The American Journal of Clinical Nutrition*, vol. 106, no. 3, 887 pages, 2017 Sep.

[21] D. G. Loughrey, M. E. Kelly, G. A. Kelley, S. Brennan, and B. A. Lawlor, "Association of age-related hearing loss with cognitive function, cognitive impairment, and dementia," *JAMA Otolaryngology-Head & Neck Surgery*, vol. 144, no. 2, pp. 115–126, 2018 Feb 1.

[22] N. Ciesielska, R. Sokołowski, E. Mazur, M. Podhorecka, A. Polak-Szabela, and K. Kędziora-Kornatowska, "Is the Montreal Cognitive Assessment (MoCA) test better suited than the Mini-Mental State Examination (MMSE) in mild cognitive impairment (MCI) detection among people aged over 60? Meta-analysis," *Psychiatria Polska*, vol. 50, no. 5, pp. 1039–1052, 2016 Oct 31.

Hindawi
Contrast Media & Molecular Imaging
Volume 2022, Article ID 1035619, 9 pages
https://doi.org/10.1155/2022/1035619

Research Article

Deep Learning Algorithm-Based MRI Image in the Diagnosis of Diabetic Macular Edema

Xiuping Han,[1] **Juan Tan**,[2] **and Yumei He**[1]

[1]*Department of General Medicine, Affiliated Hospital of Yan'an University, Yan'an 716000, Shaanxi, China*
[2]*Department of Traditional Chinese Medicine, Affiliated Hospital of Yan'an University, Yan'an 716000, Shaanxi, China*

Correspondence should be addressed to Yumei He; yadxfsyyhym@yau.edu.cn

Received 21 December 2021; Revised 28 January 2022; Accepted 31 January 2022; Published 4 March 2022

Academic Editor: M Pallikonda Rajasekaran

This study investigates the value of magnetic resonance imaging (MRI) based on a deep learning algorithm in the diagnosis of diabetic macular edema (DME) patients. A total of 96 patients with DME were randomly divided into the experimental group ($N = 48$) and the control group ($N = 48$). A deep learning 3D convolutional neural network (3D-CNN) algorithm for MRI images of patients with DME was designed. The application value of this algorithm was comprehensively evaluated by MRI image segmentation Dice value, sensitivity, specificity, and other indicators and diagnostic accuracy. The results showed that the quality of MRI images processed by the 3D-CNN algorithm based on deep learning was significantly improved, and the Dice value, sensitivity, and specificity index data were significantly better than those of the traditional CNN algorithm ($P < 0.05$). In addition, the diagnostic accuracy of MRI images processed by this algorithm was $93.78 \pm 5.32\%$, which was significantly better than the diagnostic accuracy of $64.25 \pm 10.24\%$ of traditional MRI images in the control group ($P < 0.05$). In summary, the 3D-CNN algorithm based on deep learning can significantly improve the accuracy and sensitivity of MRI image recognition and segmentation in patients with DME, can significantly improve the diagnostic accuracy of MRI in patients with DME, and has a good clinical application value.

1. Introduction

Diabetic retinopathy is currently one of the four leading causes of blindness in western developed countries. In recent years, the incidence of diabetic retinopathy in China has also gradually increased, seriously affecting the visual function and quality of life of diabetic patients [1]. According to statistics, 7% of patients with a history of diabetes for 10 years have retinopathy and about 25% for 15 years. In patients with type 2 diabetes for 20 years, the incidence of oral hypoglycemic agents is 60% and 84% for insulin injection. Diabetes mellitus is a multisystem disease dominated by glucose metabolism disorders, which easily lead to metabolic disorders in retinal tissue, resulting in abnormal retinal vascular function and structure [2, 3]. Diabetic macular edema (DME), defined as a retinal thickening or hard exudate deposition due to diabetes-induced extracellular fluid accumulation within the diameter of one optic disc of the fovea, is one of the common causes of visual impairment in diabetic patients [4, 5]. The Early Treatment Diabetic Retinopathy Study (ETDRS) believes that clinically significant DME (CSDME) needs to meet more than one of the following three conditions: (1) retinal edema thickening is in the 500 μm area from the center of the macula, or less than 500 μm; (2) hard exudation is located in the 500 μm area from the center of the macula, or less than 500 μm, accompanied by adjacent retinal thickening; (3) retinal thickening has at least one optic disc diameter (DD) range, and lesions at any site are within 1 DD from the center of the macula [6].

Current studies suggest that the factors affecting DME formation are as follows: severity of diabetic retinopathy, duration of diabetes, posterior vitreous detachment, pregnancy and cataract surgery, and metabolic control. The pathogenesis of DME may include disruption of the blood-retinal barrier, changes in periretinal vascular dynamics, and periretinal vascular hypoperfusion due to retinal macular ischemia [7, 8]. FFA is a seminal examination that can identify the extent of macular edema, identify the presence or absence of perfusion areas in macular capillaries or capillary rumen-like bulging, and locate the location of leakage points but cannot objectively quantify reactive retinal thickness changes [9]. OCT is currently recognized as the best method to identify the location and severity of retinal edema, and its sensitivity and specificity for detecting macular edema are about 90%, while due to the high cost of MRI examination, the diagnostic accuracy is not comparable to that of OCT, which makes the clinical use of MRI for the diagnosis of DME disease still relatively less [10].

In recent years, various deep learning algorithms have been fully applied in the field of medical image processing, and various image quality optimization algorithms, image fusion processing algorithms, and image segmentation algorithms have emerged endlessly, especially in the field of MRI image optimization [11]. As one of the most widely used and fastest iterative image processing algorithms, the deep learning algorithm is fully applied in the clinical diagnosis of various diseases such as brain tumors, liver cancer, lung cancer, and cervical cancer [12, 13]. However, there are still few reports on deep learning algorithms in the field of DME image processing. Based on this, this study hopes to design a targeted algorithm according to the characteristic information of MRI images of DME patients to realize the rapid segmentation of color vessel regions in the images and the accurate localization and extraction of the characteristic information of injury location.

In summary, this study used the MRI images of the 3D convolutional neural network (3D-CNN) algorithm based on deep learning to monitor DME and comprehensively evaluate the application value of this algorithm by detecting the MRI image quality and diagnostic accuracy of patients with DME. It hopes to provide some reference for the optimization of clinical MRI image diagnosis in patients with DME.

2. Materials and Methods

2.1. Research Objects and Groups. Ninety-six patients with DME who received treatment in hospital from March 2018 to March 2021 were selected as the subjects, including 54 male patients and 42 female patients, with the age range of 46–73 years, and the mean age was 59.1 ± 13.4 years. These 96 patients with DME included 34 patients with serous retinal detachment (SRD), 29 patients with diffuse retinal thickening (DRT), 17 patients with cystoid macular edema (CME), and 16 patients with mixed DME with coexistence of two or three types. All patients were diagnosed by OCT after admission. They were divided into control group (routinely monitored by MRI images) and experimental group (monitored by MRI images based on deep learning 3D convolutional neural network (CNN) algorithm) according to different treatment methods, with 48 cases for each group. This study has been approved by the ethics committee of hospital, and all subjects included in the study signed the informed consent form.

Inclusion criteria are as follows: (1) patients meeting the clinical diagnostic criteria of DME; (2) detailed records of FFA, OCT, and FP. Exclusion criteria were as follows: (1) macular edema caused by other causes; (2) severe ophthalmic diseases, such as senile macular degeneration, retinal vein occlusion, anterior ischemic optic neuropathy, retinal capillary dilation, retinal vasculitis, and retinal artery occlusion.

2.2. Sequence Parameters of MRI Image Diagnostic Examination for DME. The conventional MRI scans of the orbit for DME disease used in this study were located axially and sagittally, including transverse T1-weighted image (T1WI), transverse and sagittal T2-weighted image (T2WI), and transverse fluid-attenuated inversion recovery (FLAR). The scanning parameters of the setup in this study are as follows (Table 1).

2.3. Establishment of Segmentation Model of DME Lesions Based on 3D-CNN Algorithm Based on Deep Learning. In this study, the 3D-CNN algorithm based on deep learning is designed to segment DME lesions based on the traditional CNN. This model introduces the time dimension into the convolutional kernel operation. In addition, based on preserving the characteristic information of input data, three-dimensional data are added so that the output data after multiple operations are still arranged according to three-dimensional space.

In the model design, the basic framework architecture of the algorithm is carried out according to the CNN structure. The feature extractor is deployed in the overall structure of the network to make the input data enter the network, and the features of different levels of the image are gradually extracted through the convolution layer, pooling layer, and nonlinear function activation layer. The nonlinear activation function-ReLU function is introduced between the upper and lower input of the activation layer, and then the MRI image segmentation task of DME patients in this study is divided into different output categories. The Dice loss function is introduced to solve the problem of uneven classification in the data processing so as to better realize the MRI image segmentation of DME. Dice score coefficient (DSC) is one of the evaluation indexes based on pixel overlap [14]. The calculation equation of the convolution layer is shown in (1), the mathematical expression of the ReLU function is shown in (2), and the calculation equation of DSC is shown in (3).

$$K = k\left(K_{a-1}\right) * D_a + B_a. \tag{1}$$

K_{a-1} represents the feature map information of the previous layer, B_a represents the offset, and D_a represents the weight matrix. Each row in the matrix corresponds to the weight of the neuron connected to all the neurons in the previous layer.

$$\mathrm{ReLU} = \max(0, x), \tag{2}$$

$$D = \frac{2\sum_j^M g_j h_j}{\sum_j^M g_j^2 + \sum_j^M h_j^2}. \tag{3}$$

Table 1: MRI scanning parameters of DME.

	MRI scanning position			
	T1WI transverse position	T2WI sagittal position	T2WI transverse position	FLAR transverse position
Number of collections	Single	Single	Single	Single
Time of repetition (TR)	250 ms	440 ms	4000 ms	6000 ms
Time of echo (TE)	2.46 ms	2.46 ms	93 ms	96 ms
Flip angle (FA)	70°	90°	120°	130°
Matrix	320 × 320	320 × 320	320 × 320	256 × 256
Layer thickness	6 mm	4 mm	6.5 mm	6 mm
Layer spacing	0 mm	0 mm	0 mm	0 mm
Field of view (FOV)	320 mm × 320 mm	320 mm × 320 mm	240 mm × 240 mm	320 mm × 320 mm

In (3), g_j represents the pixel value of point j in the prediction results and h_j represents the pixel value of point j in the true value label. The sum of M pixels is calculated. The gradient equation is shown in (4). The loss function of DME image segmentation can be expressed as in (5).

$$\frac{\partial D}{\partial g_i} = 2\left[\frac{h_i\left(\sum_j^M g_j^2 + \sum_j^M h_j^2\right) - 2g_i\left(\sum_j^M g_j h_j\right)}{\sum_j^M g_j^2 + \sum_j^M h_j^2}\right], \tag{4}$$

$$N = \frac{2}{|V|}\sum v \in V\frac{\left(\sum_j g_{j,f} h_{j,v}\right)}{\sum_j g_j + \sum_j h_j}. \tag{5}$$

The number of pixels is represented by i in (4), V represents a category in (5), and v represents a category in the study of the DME segmentation task. g represents the segmentation result area predicted by the network, h represents the segmentation area calibrated by the true value label, j represents any pixel in the image, and $g_{j,f}h_{j,f}$ represents the numerical parameters of the predicted output and the output pixel of the true value label area at j.

In order to adapt to the dense connection operation in 3D CNN, the jump structure is used to connect the feature maps of each layer in this study, and then the feature maps of all layers are connected in series. On this basis, in order to solve the gradient dispersion problem in the data processing of deep convolution neural network, this study introduces the residual structure [15], and the results of the addition operation between the input data and the output data are correlated by a bypass (shortcut structure). Then the deep network model is constructed.

The corresponding expression of the jump structure is shown in (6), and the output expression of the residual unit is shown in (7).

$$S_1 = C\left(S_0, S_1, S_2 \ldots S_{j-1}\right), \tag{6}$$

$$C_1 = C\left(S_0\right) + V\left(S_1, \omega_1\right). \tag{7}$$

The $C(\cdot)$ function in (6) represents the fitting target in CNN, and $V(S_1, \omega_1)$ represents the convolution operation in (7), ω_1 represents the weight parameter in the network, and C_1 represents the network output of the first layer. If $H(\cdot)$ is an identity map, it is expressed as (8), then the network output C_1 of the residual structure of the first layer can be expressed as in (9).

$$H\left(S_1\right) = S_1, \tag{8}$$

$$Y_1 = S_1 + 1 = S_1 + F\left(S_1, \omega_1\right). \tag{9}$$

The overall output of the residual structure unit is a linear addition between the original data of the input image and the output data after the convolution operation. In this way, the output of the entire network can be represented by an addition algorithm. Assuming that there are a total of M residual structure network units in the network, the overall output of the residual network can be expressed by the following:

$$S_M = S_m + \sum_{j=m}^{M-1} F\left(S_1, \omega_1\right). \tag{10}$$

In this study, the convolution layer setting in the deep learning 3D convolution mode is used to the residual structure unit, and the batch normalization (BN) layer is changed to the group normalization (GN) layer operation in the residual structure. Firstly, the input MRI image information in this model will pass through the convolution layer whose convolution kernel size is set to $3 \times 3 \times 3$, then pass through the GN layer to accelerate the convergence ability of the network, then pass through the nonlinear activation function layer, and will be entered into a convolution layer whose convolution kernel size is set to $3 \times 3 \times 3$, which is used to extract the feature information of the interested target area in the data. The superposition of two 3D convolution layers deepens the depth of the network. Such a structure can greatly reduce the computational complexity without reducing the network performance in the MRI image segmentation task of DME. The structure pattern of the lesion feature extraction network of the DME MRI image is illustrated in Figure 1, and the final algorithm processing flow is illustrated in Figure 2.

2.4. MRI Image Quality Assessment Based on Artificial Intelligence 3D-CNN Algorithm. In this study, the experimental environment based on deep learning 3D-CNN algorithm is as follows: 12G Titanx device, Ubuntu16.04 system for related training, and BraTs2017 dataset for algorithm simulation training. The deep learning frameworks Tensorflow and Keras are used.

In this study, the lesion range of the DME area (S) outlined by two radiologists was compared with the lesion

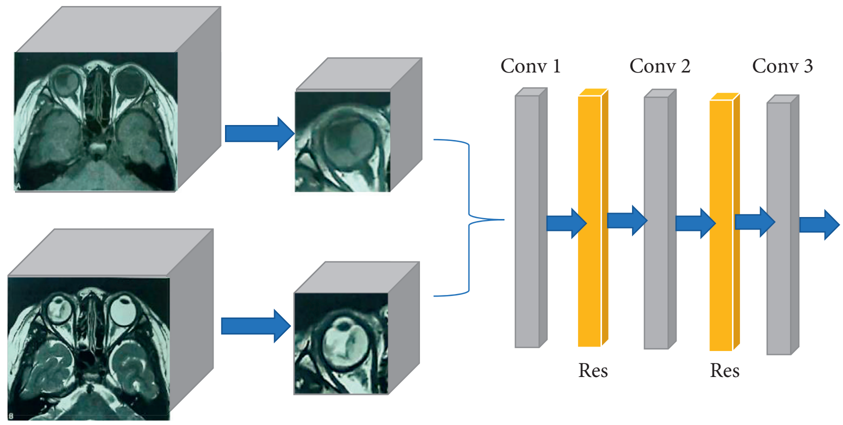

Figure 1: MRI image feature lesion extraction pattern of DME.

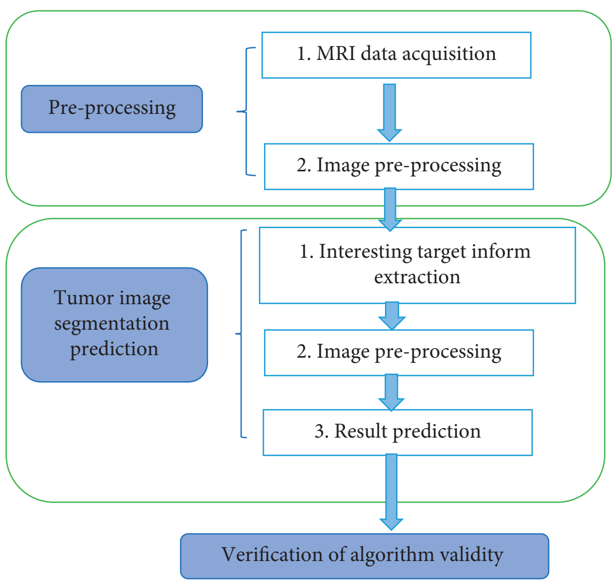

Figure 2: Flow chart of 3D-CNN algorithm based on artificial intelligence.

range determined by the image segmentation of the artificial intelligence algorithm (O). The coincidence degree between the true DME lesion area (Q) and the DME lesion area (O) determined by artificial intelligence algorithm was fitted to calculate the accuracy (Dice), sensitivity, specificity, and Haus distance of the algorithm for MRI imaging diagnosis of patients with DME. The Haus distance can evaluate the degree of fitting between the two different ways to determine the lesion area, which refers to the maximum value of the shortest distance from one point to another point set [16]. The mathematical expressions of Dice, sensitivity, specificity, and Haus distance are shown in (11)–(14).

$$Dice = \frac{|Q \cap O|}{|Q| + |O|/2}, \tag{11}$$

$$\text{Sensitivity} = \frac{|Q \cap O|}{|Q|}, \tag{12}$$

$$\text{Specificity} = \frac{|P \cap R|}{|P}. \tag{13}$$

P and R represent other locations outside the real DME lesion area and other locations outside the DME lesion area determined by an artificial intelligence algorithm. In addition, according to the different structural groups of DME, three overlapping tumor regions are divided, which are the whole lesion, the lesion core area, and the enhanced lesion area.

$$\text{Haus} = \max\{H(Q, O), H(O, Q)\}. \tag{14}$$

2.5. MRI Diagnosis Analysis of DME. In this study, the diagnostic results of MRI images and actual pathological results of patients with DME between the traditional CNN algorithm and artificial intelligence 3D-CNN algorithm were compared, the diagnostic accuracy of patients with DME before treatment and after treatment with the two algorithms was calculated, and the application value of 3D-CNN algorithm based on deep learning for MRI image diagnosis of patients with DME was comprehensively evaluated.

2.6. Statistical Methods. The test data were processed by SPSS 19.0 statistical software. The measurement data were expressed as mean ± standard deviation ($\overline{x} \pm s$). The comparison of mean between groups was performed by t-test. The enumeration data were expressed as percentage (%).. The χ^2 test was used. The differences were statistically significant when $P < 0.05$.

3. Results

3.1. Summary of Basic Information of Patients in the Two Groups. Figure 3 shows the comparison of basic information of two groups of patients with DME. There was no significant difference in gender distribution, mean age, type of DME, and mean duration of disease between the two groups of DME patients, with no statistical significance ($P > 0.05$).

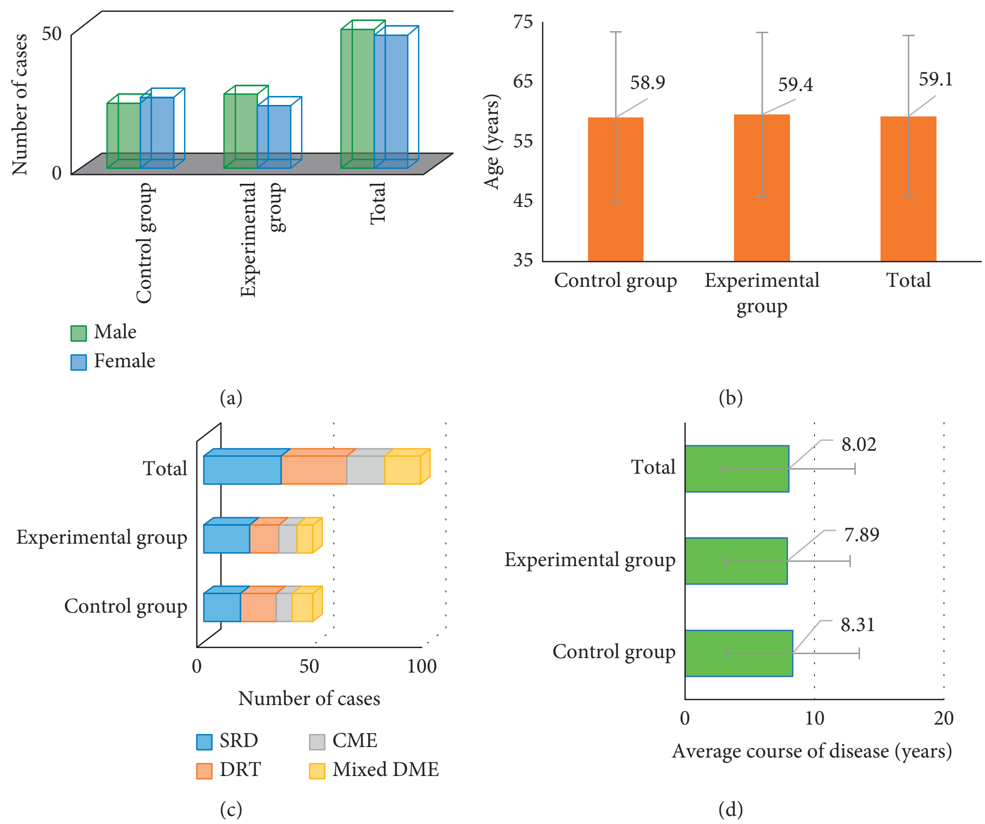

FIGURE 3: Comparison of basic information between the two groups. (Note: (a) is the gender distribution comparison figure of the two groups, (b) is the mean age comparison figure of the two groups, (c) is the DME type comparison figure of the two groups, and (d) is the mean disease course comparison figure of the two groups).

3.2. MRI Images of Patients with DME Processed by Different Algorithms. Figure 4 shows the MRI images of patients in the two groups, and Figure 5 shows the comparison of MRI images of patients with DME processed by different algorithms. Figures 4(a)–4(c) are the MRI images of the experimental group of patients (No. 32), which are the transverse T1WI, transverse T2WI, and oblique sagittal T2WI images of the patient. Figures 4(d)–4(i) are the MRI images of the control group of patients (No. 77) (processed by the deep learning 3D-CNN algorithm). Figures 4(d)–4(f) are the initial MRI images of the transverse T1WI, transverse T2WI, and oblique sagittal T2WI of the patient (No. 77). Figures 4(g)–4(i) are the transverse T1WI, transverse T2WI, and oblique sagittal T2WI MRI images of the patient (No. 77) after processing by the deep learning 3D-CNN algorithm. In the initial state, there was no significant difference in the MRI image quality between the experimental group and the control group. After processing by the deep learning 3D-CNN algorithm, the overall clarity and contrast of the MRI images of the experimental group were significantly improved, the recognition performance of the lesions in the MRI images of patients with DME was greatly increased, and the accuracy of the edge division of the lesion site was significantly improved, making the display of the ocular structure of the transverse and sagittal images of MRI clearer and intuitive, and the difficulty in the diagnosis of macular edema was further reduced.

Figures 5(a)–5(c) are the MRI images of patients from the experimental group, which are the initial MRI images without algorithm processing, the MRI images with conventional CNN algorithm processing, and the MRI images with deep learning 3D-CNN algorithm processing, respectively. Compared with Figure 5(a), the clarity of MRI images in Figures 5(b) and 5(c) is improved to some extent, and the MRI image quality in Figure 5(c) is relatively high. In addition, Figures 5(b) and 5(c) compare stereoscopic and intuitive for imaging the ocular structures of patients with DME, which is more helpful for disease diagnosis.

3.3. Evaluation of MRI Image Quality Based on Artificial Intelligence 3D Convolution Neural Network Algorithm Processing. Figure 6 shows a comparison of the diagnostic indicators for the conventional CNN algorithm and the MRI image processing based on the deep learning 3D-CNN algorithm. Figures 6(a)–6(d) are the comparison plots of Dice value, sensitivity value, specificity value, and Haus distance of the two algorithms. The mean Dice value of the MRI images processed by the traditional CNN algorithm is 0.6855, and the resulting interval is (0.58, 0.77). The mean Dice value of the MRI images processed by the deep learning 3D-CNN algorithm is 0.898, and the resulting interval is (0.83, 0.97), with a significant difference between the two groups ($P < 0.05$). The mean sensitivity of the traditional

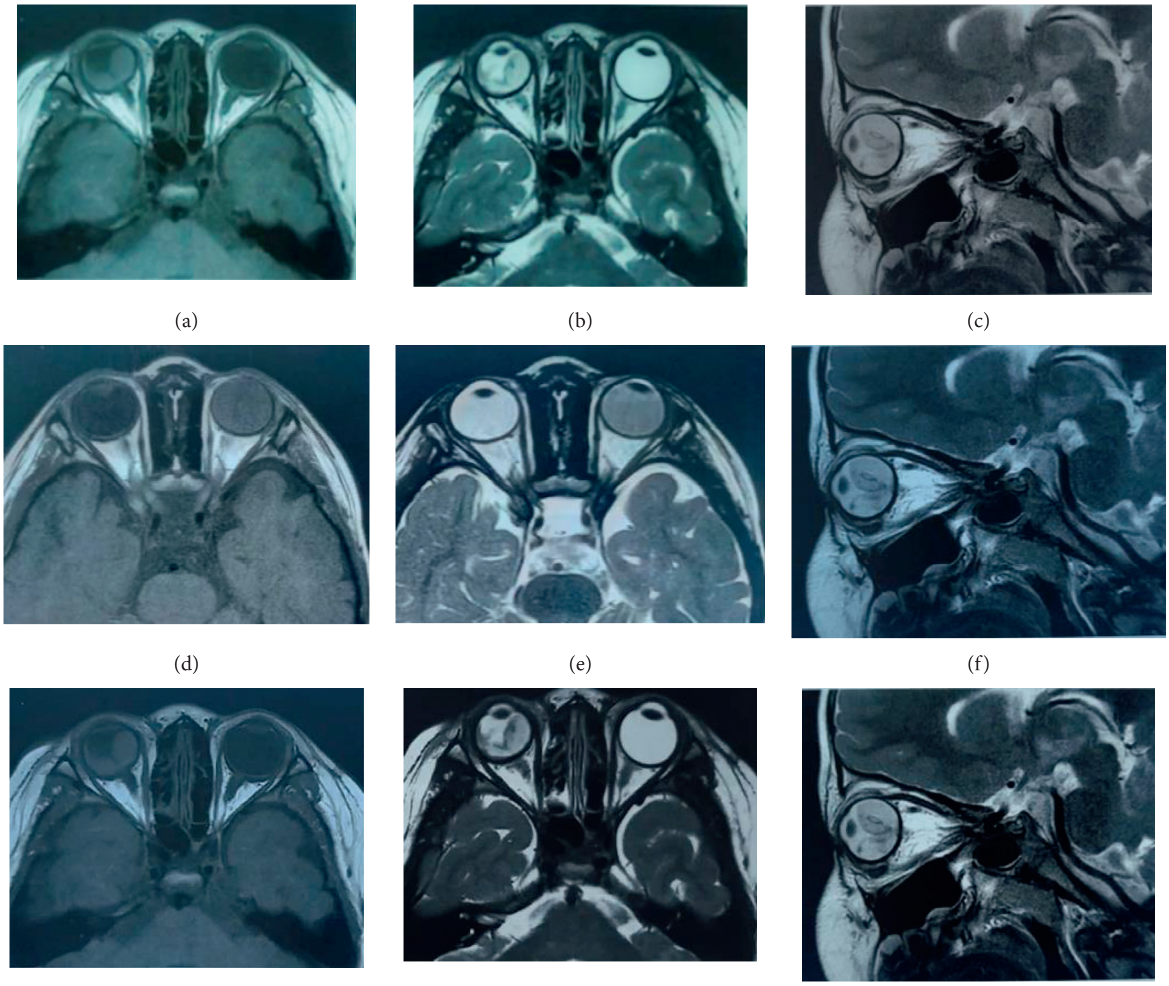

(a) (b) (c) (d) (e) (f) (g) (h) (i)

FIGURE 4: MRI image of patients in the two groups.

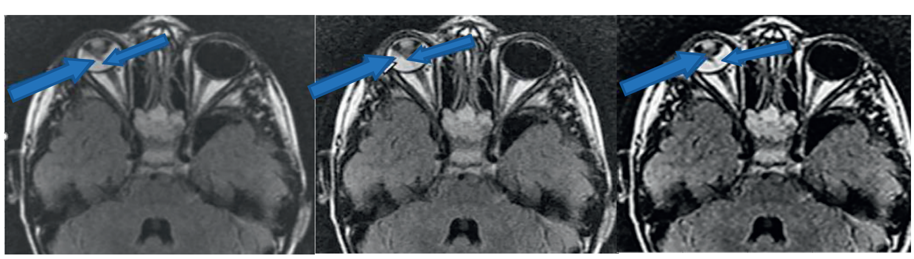

FIGURE 5: MRI images of patients with DME processed by different algorithms. (a) is sagittal T2WI image of conventional head MRI of a patient in the experimental group, (b) is sagittal T2WI image of head MRI of the patient processed by CNN algorithm, and (c) is sagittal T2WI image of head MRI of the patient processed by deep learning 3D-CNN algorithm. The blue arrow points to the lesion location for the patient.

CNN algorithm is 0.64, the resulting interval is (0.59, 0.72); the mean specificity is 0.67, and the resulting interval is (0.61, 0.74); the mean sensitivity of the deep learning 3D-CNN algorithm is 0.9, the resulting interval is (0.84, 0.96); the mean specificity is 0.8855, and the resulting interval is (0.84, 0.93), with significant difference between the specificity and sensitivity of two algorithms ($P < 0.05$). The mean values of Haus distance of traditional CNN algorithm and deep learning 3D-CNN algorithm are 0.920 and 0.916, respectively, and there is no significant difference.

3.4. MRI Image Diagnostic Accuracy Evaluation. Figure 7 shows the comparison of diagnostic accuracy of MRI images of DME patients with different algorithms. The diagnostic accuracy of conventional MRI images was $64.25 \pm 10.24\%$ in

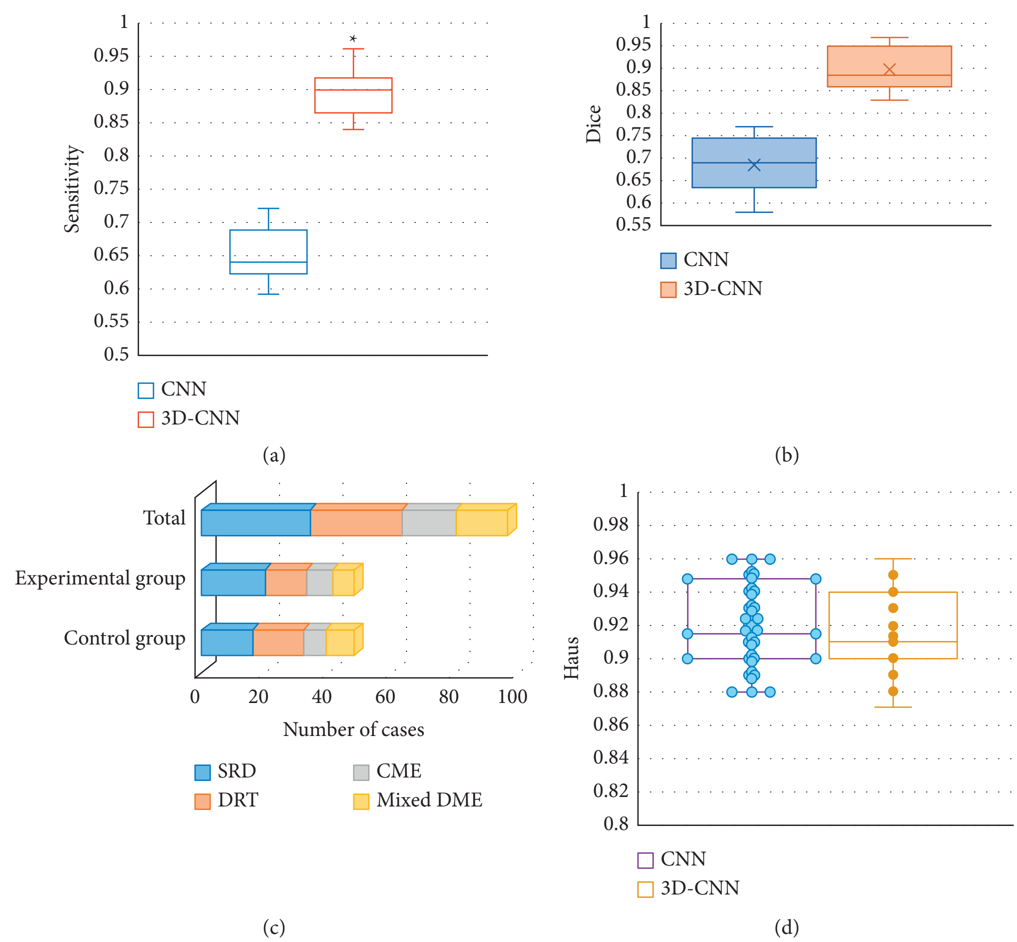

Figure 6: Comparison of image processing quality evaluation indicators of different algorithms. (Note: (a) was the Dice value comparison graph; (b) was the sensitivity value comparison graph; (c) was the specificity value comparison graph; (d) was the Haus distance comparison graph; * indicated that the difference was statistically significant).

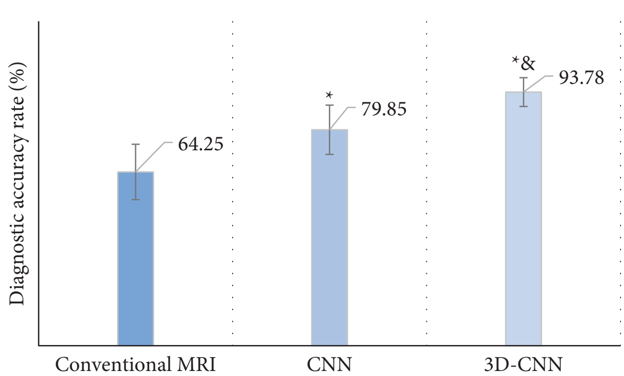

Figure 7: Comparison of imaging diagnostic accuracy of different algorithms. Note: * indicated that the difference in diagnostic accuracy compared with conventional MRI images was significant ($P < 0.05$); & indicated that the difference in diagnostic accuracy compared with CNN algorithm was significant ($P < 0.05$).

the control group and $79.85 \pm 9.11\%$ in the experimental group under the traditional CNN algorithm. However, the diagnostic accuracy of MRI images of DME patients in the experimental group processed by the 3D-CNN algorithm based on deep learning was $93.78 \pm 5.32\%$. Compared with the diagnostic accuracy of conventional multimodal MRI images, the diagnostic accuracy of the two algorithms increased significantly ($P < 0.05$), and the diagnostic accuracy of the artificial intelligence 3D-CNN algorithm also increased significantly compared with the traditional CNN algorithm ($P < 0.05$).

4. Discussion

In recent years, in-depth learning technology has been continuously updated and iterated and is used as an auxiliary diagnosis and treatment method in the imaging diagnosis process of various common clinical diseases. CNN algorithm based on deep learning has gradually replaced supervised learning as an effective computer-assisted artificial intelligence medical image processing method by virtue of its model learning ability and highly automated target feature information grasping ability [17,] is widely used in the field of medical image segmentation for various diseases such as brain tumors, lung cancer, liver cancer, breast cancer, and gastric cancer, and has achieved good experimental results [18]. At present, the main object of the artificial intelligence imaging algorithm for DME is OCT. Recently, Singh and Gorantla [19] mentioned that the CNN algorithm has a good effect on color fundus image screening in patients with DME.

In this study, a 3D-CNN algorithm based on deep learning was designed according to the MRI image characteristics of patients with DME and used in the clinical MRI image diagnosis of DME disease. The results showed that compared with the MRI images of the control group, the overall clarity and contrast of the MRI images of the experimental group treated with deep learning 3D-CNN algorithm were significantly improved, the recognition performance of the MRI image lesions and the accuracy of the edge division of the lesion site were significantly improved, and the ocular structure display of the transverse and sagittal images of the MRI images was more stereoscopic and intuitive. In addition, compared with the traditional CNN algorithm, the clarity of MRI images and the recognition performance of lesions of the 3D-CNN algorithm based on deep learning were significantly improved, and the Dice value, sensitivity, and specificity index data were significantly better than those of the traditional CNN algorithm ($P < 0.05$). The Haus distance data of the two algorithms were 0.920 and 0.916, respectively, and the difference was not statistically significant ($P > 0.05$). By comparing the clinical diagnostic accuracy of patients with DME treated with different processing methods, the diagnostic accuracy of MRI images processed with the 3D-CNN algorithm designed in this study based on deep learning was $93.78 \pm 5.32\%$, which was significantly better than the diagnostic accuracy of traditional MRI images in the control group ($P < 0.05$) and also significantly improved compared with the diagnostic efficacy of MRI images under the optimization of traditional CNN algorithm ($P < 0.05$). The results are consistent with the study conclusions of Zhang et al. [20], indicating that the MRI image algorithm based on deep learning can improve the MRI image quality to a great extent, optimize the identification process of disease characteristics images, and improve the efficiency of disease diagnosis. However, the relevant optimization procedure of the 3D-CNN algorithm based on deep learning is very complex and remains to be further studied.

It shows that the deep learning algorithm has a good utilization value in MRI image monitoring of DME and can well provide some expansion ideas for improving the clinical diagnostic accuracy of patients with DME from the imaging point of view.

5. Conclusion

A deep learning 3D-CNN algorithm for MRI image characteristics of DME patients is designed and applied to the clinical diagnosis of DME patients. The results showed that the intelligent recognition and segmentation performance of the 3D-CNN algorithm based on deep learning for MRI images in patients with DME was significantly improved compared with the traditional CNN algorithm, and the diagnostic accuracy was also significantly improved.

However, there are some shortcomings as follows: the sample size of patients with various types of DME is relatively small and the corresponding algorithm optimization analysis is not performed for the MRI image characteristics of patients with different types of DME. In addition, the monitoring index of MRI image segmentation quality based on the deep learning 3D-CNN algorithm used in this study was relatively small, and the performance evaluation of this algorithm was relatively single. Then, the algorithm will be further optimized, and more performance evaluation indexes will be included to perform multiangle comprehensive analysis for the application value of this algorithm. In conclusion, this study confirmed that the image characteristics of MRI based on deep learning algorithm have a good application value in the clinical diagnosis of DME patients, which is worthy of further clinical promotion and provides a reference basis for the imaging diagnosis, treatment, and monitoring of clinical DME patients.

Data Availability

The data used to support the findings of this study are available from the corresponding author upon request.

Conflicts of Interest

The authors declare no conflicts of interest.

References

[1] M. Stewart, D. Browning, and C. Lee, "Diabetic macular edema: Evidence-based management," *Indian Journal of Ophthalmology*, vol. 66, no. 12, pp. 1736–1750, 2018.

[2] A. Daruich, A. Matet, A. Moulin et al., "Mechanisms of macular edema: beyond the surface," *Progress in Retinal and Eye Research*, vol. 63, pp. 20–68, 2018.

[3] F. Bandello, M. Battaglia Parodi, P. Lanzetta et al., "Diabetic macular edema," *Macular Edema*, vol. 58, pp. 102–138, 2017.

[4] G. Holló, T. Aung, L. B. Cantor, and M. Aihara, "Cystoid macular edema related to cataract surgery and topical prostaglandin analogs: mechanism, diagnosis, and management," *Survey of Ophthalmology*, vol. 65, no. 5, pp. 496–512, 2020.

[5] P. Romero-Aroca, M. Baget-Bernaldiz, A. Pareja-Rios, M. Lopez-Galvez, R. Navarro-Gil, and R. Verges, "Diabetic macular edema pathophysiology: vasogenic versus inflammatory," *Journal of Diabetes Research*, vol. 2016, Article ID 2156273, 17 pages, 2016.

[6] E. J. Kim, W. V. Lin, S. M. Rodriguez, A. Chen, A. Loya, and C. Y. Weng, "Treatment of diabetic macular edema," *Current Diabetes Reports*, vol. 19, no. 9, p. 68, 2019.

[7] S. R. Cohen and T. W. Gardner, "Diabetic retinopathy and diabetic macular edema," *Developments in Ophthalmology*, vol. 55, pp. 137–146, 2016.

[8] A. Markan, A. Agarwal, A. Arora, K. Bazgain, V. Rana, and V. Gupta, "Novel imaging biomarkers in diabetic retinopathy and diabetic macular edema," *Therapeutic Advances in Ophthalmology*, vol. 12, Article ID 251584142095051, 2020.

[9] D. S. Kermany, M. Goldbaum, W. Cai et al., "Identifying medical diagnoses and treatable diseases by image-based deep learning," *Cell*, vol. 172, no. 5, pp. 1122–1131, 2018.

[10] Y. R. Chung, Y. H. Kim, S. J. Ha et al., "Role of inflammation in classification of diabetic macular edema by optical

Coherence Tomography," *Journal of Diabetes Research*, vol. 2019, Article ID 8164250, 2019.

[11] T. Higaki, Y. Nakamura, F. Tatsugami, T. Nakaura, and K. Awai, "Improvement of image quality at CT and MRI using deep learning," *Japanese Journal of Radiology*, vol. 37, no. 1, pp. 73–80, 2019.

[12] M. Hu, Y. Zhong, S. Xie, H. Lv, and Z. Lv, "Fuzzy system based medical image processing for brain disease prediction," *Frontiers in Neuroscience*, vol. 15, Article ID 714318, 2021.

[13] Y. Li, J. Zhao, Z. Lv, and J. Li, "Medical image fusion method by deep learning," *International Journal of Cognitive Computing in Engineering*, vol. 2, pp. 21–29, 2021.

[14] Z. Yu, S. U. Amin, M. Alhussein, and Z. Lv, "Research on disease prediction based on improved DeepFM and IoMT," *IEEE Access*, vol. 9, no. 99, pp. 39043–39054, 2021.

[15] F. Hoseini, A. Shahbahrami, and P. Bayat, "AdaptAhead optimization algorithm for learning deep CNN applied to MRI segmentation," *Journal of Digital Imaging*, vol. 32, no. 1, pp. 105–115, 2019.

[16] L. M. Jampol, "Classifications of diabetic macular edema," *European Journal of Ophthalmology*, vol. 30, no. 1, pp. 6-7, 2020.

[17] N. M. Bressler, W. T. Beaulieu, A. R. Glassman et al., "Persistent macular thickening following Intravitreous Aflibercept, Bevacizumab, or Ranibizumab for Central-Involved diabetic macular edema with vision impairment," *JAMA Ophthalmology*, vol. 136, no. 3, pp. 257–269, 2018.

[18] T. H. Rim, A. W. J. Teo, H. H. S. Yang, C. Y. Cheung, and T. Y. Wong, "Retinal vascular signs and cerebrovascular diseases," *Journal of Neuro-Ophthalmology*, vol. 40, no. 1, pp. 44–59, 2020.

[19] R. K. Singh and R. Gorantla, "DMENet: diabetic macular edema diagnosis using Hierarchical Ensemble of CNNs," *PLoS One*, vol. 15, no. 2, Article ID e0220677, 2020.

[20] M. Zhang, G. S. Young, H. Chen et al., "Deep-learning detection of cancer Metastases to the Brain on MRI," *Journal of Magnetic Resonance Imaging*, vol. 52, no. 4, pp. 1227–1236, 2020.

Hindawi
Contrast Media & Molecular Imaging
Volume 2022, Article ID 4147970, 8 pages
https://doi.org/10.1155/2022/4147970

Research Article

Artificial Intelligence Algorithm-Based Intraoperative Magnetic Resonance Navigation for Glioma Resection

Jianqiang Wei,[1] **Chunman Zhang**,[2] **Liujia Ma**,[2] **and Chunrui Zhang**[3]

[1]*Neurovascular Interventional Therapy Center, Affiliated Hospital of Yan'an University, Yan'an 716000, Shaanxi, China*
[2]*Department of Neurosurgery, Affiliated Hospital of Yan'an University, Yan'an 716000, Shaanxi, China*
[3]*Department of Neurology, Hanzhong People's Hospital, Hanzhong 723000, Shaanxi, China*

Correspondence should be addressed to Chunrui Zhang; 1722010272@stu.cpu.edu.cn

Received 25 December 2021; Revised 28 January 2022; Accepted 31 January 2022; Published 4 March 2022

Academic Editor: M Pallikonda Rajasekaran

The study aimed to analyze the application value of artificial intelligence algorithm-based intraoperative magnetic resonance imaging (iMRI) in neurosurgical glioma resection. 108 patients with glioma in a hospital were selected and divided into the experimental group (intraoperative magnetic resonance assisted glioma resection) and the control group (conventional surgical experience resection), with 54 patients in each group. After the resection, the tumor resection rate, NIHSS (National Institute of Health Stroke Scale) score, Karnofsky score, and postoperative intracranial infection were calculated in the two groups. The results revealed that the average tumor resection rate in the experimental group was significantly higher than that in the control group ($P < 0.05$). There was no significant difference in Karnofsky score before and after the operation in the experimental group ($P > 0.05$). There was no significant difference in NIHSS score between the experimental group and the control group after resection ($P > 0.05$). The number of patients with postoperative neurological deficits in the experimental group was smaller than that in the control group. In addition, there was no significant difference in infection rates between the two groups after glioma resection ($P > 0.05$). In summary, intraoperative magnetic resonance navigation on the basis of a segmentation dictionary learning algorithm has great clinical value in neurosurgical glioma resection. It can maximize the removal of tumors and ensure the integrity of neurological function while avoiding an increased risk of postoperative infection, which is of great significance for the treatment of glioma.

1. Introduction

Glioma is one of the most common diseases in neurosurgery, which belongs to malignant tumors. Glioma plays an important role in intracranial tumors. About half of intracranial tumors are gliomas clinically [1]. In recent years, the incidence of glioma has been increasing. According to statistics, there are up to 15,000 new glioma patients in the United States every year. The incidence of intracranial tumors in China is about 0.1%. Nearly half of the newly diagnosed patients were diagnosed with glioma [2–4]. The cancerous glial cells in glioma patients are derived from the neuroectodermal layer. Not only is the incidence higher than other intracranial tumors, but also the recurrence rate is very high after various treatments. Therefore, compared with other intracranial tumors, glioma has the characteristics of high mortality and a low cure rate [5–7]. In China, gliomas are divided into eight categories, among which astrocytoma has the highest incidence. Clinically, gliomas are divided into four grades according to the degree of malignancy of astrocytomas. Grade I is relatively mild. It is mainly manifested as hair cell astrocytoma, which accounts for about 5% of the incidence of glioma. Benign tumors are often diagnosed and can be cured by resection in theory. Grade II is more serious; mainly as astrocytoma and a small amount of astrocytoma, accounting for about 35% of glioma. Grade III is mostly developed from grade II glioma. Interstitial astrocytomas accounted for about 15–25% of gliomas. The disease is serious and highly malignant. Grade IV is the most serious malignancy, accounting for one third of all gliomas. It is mainly manifested as glioblastoma [8–12].

With the rapid development of science and technology and the improvement of medical level, more and more treatment methods for glioma are appearing in people's eyes. Drug therapy as one of the treatment methods has achieved good results. The selection of appropriate chemotherapy drugs according to the specificity of glioma can inhibit the growth of tumors and delay or limit the deterioration of tumors to a certain extent [13–15]. The disadvantages of chemical drug therapy are the side effects of drugs, which limit the development and application of drug therapy. Radiotherapy also plays a certain role in the clinical treatment of glioma. Radiotherapy can kill radiation-sensitive tumor cells and limit the development of tumors. In addition, radiotherapy has great advantages for deep tumors that cannot be reached by surgery [16–19]. The dose of the first two treatment methods needs to be strictly controlled, and there will be some damage to normal tissues, which is greatly limited in the treatment of glioma [20]. Therefore, surgical treatment is the most commonly used and effective treatment of glioma in clinics [21]. Gliomas with a low degree of deterioration are mostly cured by surgery, while gliomas with a high degree of deterioration can greatly prolong the life span of patients by surgical treatment. Glioma resection is the most critical in the treatment of glioma [22–25]. The resection can minimize the tumor volume, reduce the number of tumor cells, reduce intracranial hypertension and prolong the life of patients [26].

Magnetic resonance imaging (MRI) plays an important role in neurosurgical treatment and diagnosis. Intraoperative magnetic resonance imaging (iMRI) appeared in the late twentieth century [27]. MRI has a high resolution on the soft tissue of the body, which plays an important role in the diagnosis of glioma and postoperative review [28]. At present, iMRI technology can provide real-time imaging information during glioma surgery, which has a great role in promoting glioma resection and makes neurosurgical glioma resection enter a new period [29–31].

In this study, 108 patients with glioma were collected as research subjects, and two different methods were used to conduct experiments during surgery to analyze the application value of iMRI based on artificial intelligence algorithms in neurosurgical glioma resection.

2. Materials and Methods

2.1. Research Objects. This study selected 108 patients with glioma in hospitals from February 2, 2018 to June 2, 2021. Among them, there were 58 males and 50 females, ranging in age from 27 to 65 years old, with an average age of 40.28 ± 3.76 years old. The patients were randomly divided into an experimental group (patients with iMRI-assisted glioma resection) and a control group (patients with conventional surgical resection), with 54 cases in each group. All the subjects agreed to sign informed consent forms with the consent of their family members, and this study had been approved by the ethics committee of the hospital.

Inclusion criteria were as follows: (1) clinical symptoms and laboratory tests have been diagnosed with glioma patients; (2) no severe heart, lung, or abdominal diseases; (3) no other intervention measures were implemented before the operation; and (4) patients without any examination of contraindications.

The exclusion criteria were as follows: (1) critically ill patients; (2) patients with severe cardiopulmonary or abdominal diseases; (3) patients unable to cooperate with surgical treatment due to mental illness; (4) patients whose family members did not agree and did not sign the informed consent; and (5) older patients (older than 70 years) or patients who cannot undergo craniotomy.

2.2. Intraoperative Magnetic Resonance-Guided Neurosurgical Glioma Resection. Before surgery, the patients were scanned using magnetic resonance technology to obtain imaging data, determine the regional scope, boundary, and nerve conduction bundle in the adjacent region of glioma, and prepare for real-time navigation during surgery. The specific scanning sequence parameters are shown in Figure 1.

The glioma patients in the experimental group were prepared strictly according to the intraoperative magnetic resonance scanning navigation standard. First, patients need to wear earplugs. Then, it is important to ensure there is no skin contact between the upper and lower limbs, palms and fingers, and armpits. All kinds of instrument accessories including monitor and catheter, magnetic resonance coil wire, and arteriovenous infusion tube did not have any contact with the skin. Ensure that there is no metal in the surgical area. The patient is placed in the right position as required. The head is fixed, and the navigation frame is installed to ensure that the head area can be detected by the instrument. Patients were routinely disinfected, spread sheets were placed, skin incisions were made, and skull drilling was carried out after craniotomy. The doctor determined the surgical plan according to the navigation image and performed glioma resection. During iMRI scanning, the surgical area was covered with sterile gauze and then wrapped with a sterile cover. During the operation, magnetic resonance professionals were asked to verify the work, including patients during the operation, air and ground objects in the safe area, and all safety measures during the operation were closed. The screen door was opened, and intraoperative magnetic resonance scanning was performed after the magnet was removed to check the tumor resection at any time. The regional boundary of residual glioma was marked by neuronavigation, and the resection plan was formulated, which was completely resected under neuronavigation. At the same time, in order not to damage other functional areas, irreversible damage to nerve function was avoided.

2.3. Segmentation Dictionary Learning Algorithm. A segmented dictionary learning algorithm can overcome the problem of small signal and large differences between tissues in MRI reconstruction images. Before reconstruction, the image is segmented according to the characteristics, and the initial image classification is obtained based on the image gray level. The same type of organization uses

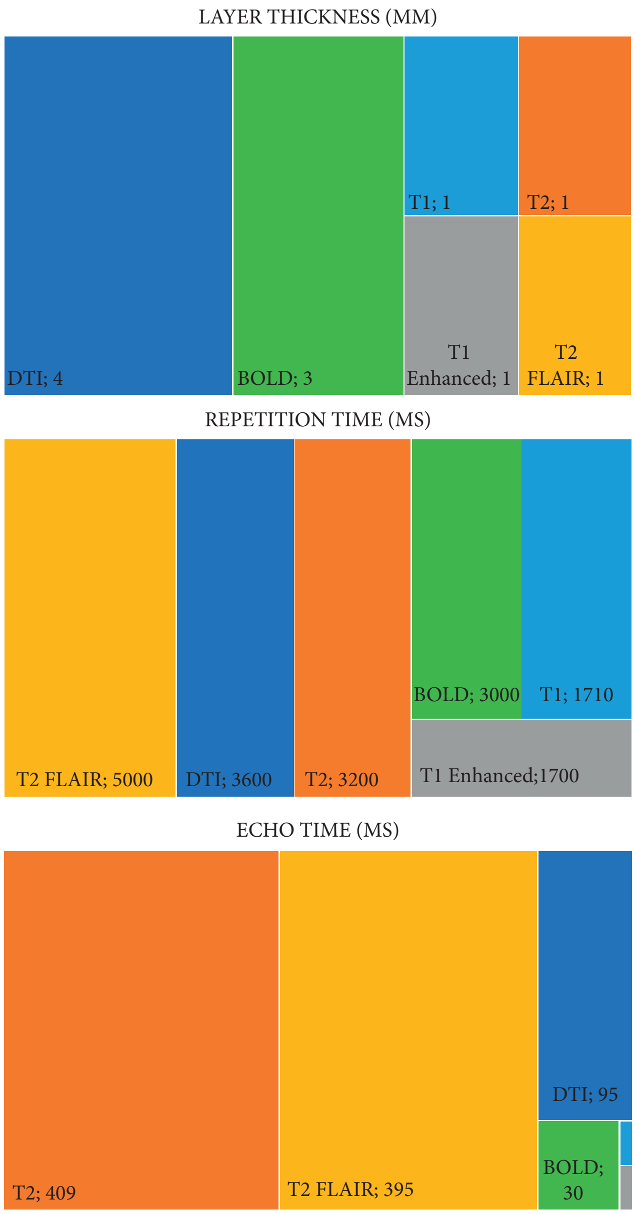

Figure 1: The parameters of MRI scanning sequence during operation.

a unified image gray mean to constrain, and then the image with the segmentation constraint is reconstructed to construct the dictionary. The specific process is shown in Figure 2.

2.4. Measurement of Glioma Resection. The glioma boundary was drawn under the enhanced MRI image, and the tumor volume before and after resection was obtained to calculate the tumor volume. The extent of glioma resection can be evaluated by tumor resection rate. The tumor resection rate was expressed as T, the preoperative glioma volume was expressed as F, and the postoperative tumor volume was expressed as L. The method of calculating the tumor resection rate was as follows:

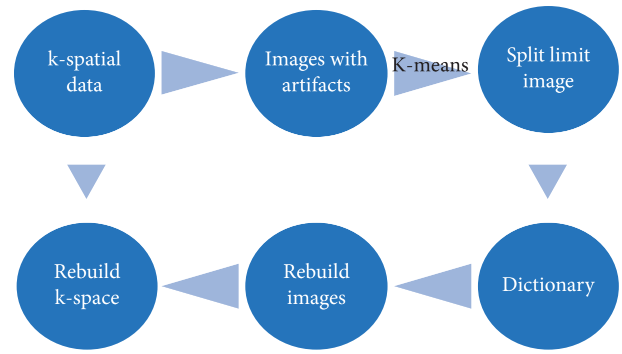

Figure 2: Flow chart of the segmentation dictionary learning algorithm.

$$T = \frac{F - L}{F} \times 100\%. \tag{1}$$

According to the calculated glioma resection rate, the degree of tumor resection is divided into four grades: total resection, near-complete resection, secondary resection, and partial resection. The corresponding tumor resection rates were 100%, 90%–99%, 50%–89%, and <50%, respectively.

2.5. Assessment of Neurological Function in Patients with Glioma. Before and after glioma resection, Karnofsky function status scores were performed on the patients. The higher the score was, the better the health status of the patients was. The patients had a strong tolerance for the side effects of surgical treatment and a greater probability of complete cure. The lower the score, the worse the patient's physical condition. Once the score is lower than 60, a variety of antitumor treatments are difficult to implement.

Two days after glioma resection, the NIHSS score was measured. They were evaluated and recorded from the aspects of consciousness level, gaze, vision, facial paralysis, upper limb movement, lower limb movement, ataxia, sensation, language, dysarthria, and neglect. The lower the score, the better the patient's health, the less neurological damage.

2.6. Evaluation of Postoperative Infection in Glioma Patients. The evaluation of postoperative infection in patients with glioma was based on fever and cerebrospinal fluid examination results. Specific criteria are as follows: patients with postoperative fever, vomiting, headache, and meningeal irritation sign positive symptoms. The results of cerebrospinal fluid examination showed that white blood cells > 10^6/L, while white blood cells > 10^{10}/L in peripheral blood. The results of cerebrospinal fluid specimen examination showed that the sugar content was 0.45 g/L. The results of bacterial culture of cerebrospinal fluid or intracranial drainage tube showed positive.

2.7. Statistical Method. SPSS software was used for the statistical analysis of the data. The data in line with normal distribution were expressed as mean ± standard deviation.

The t test was used to represent the measurement data, chi-square (χ^2) test was used to represent the count data, and $P < 0.05$ meant the difference was statistically significant.

3. Results

3.1. MRI Results. Figure 3 is a glioma patient with clinical manifestations of hyperactivity and low speech ability, and often seizures. Preoperative MRI showed a glioma located in the left temporal lobe, and neurosurgical glioma resection was performed under intraoperative magnetic resonance navigation based on a segmentation dictionary learning algorithm. Intraoperative magnetic resonance imaging revealed that the glioma was being cut, and there were some residual tumors. At the end of the operation, magnetic resonance imaging showed that the glioma had been completely resected.

Figure 4 shows MRI images of different glioma patients. Gliomas distributed in different parts of the brain are shown in Figure 4, where the yellow circle indicates the location of a glioma.

3.2. Results of Glioma Resection Degree. The degree of glioma resection was compared between the two groups by calculating the tumor resection rate of the experimental group and the control group. The results showed that the average tumor resection rate of the experimental group was significantly higher than that of the control group ($P < 0.05$). In addition, the resection rate in the control group was significantly lower than that in the experimental group ($P < 0.05$). The specific results are shown in Figure 5.

3.3. Neurological Function Score of Glioma Resection Patients. Karnofsky scores were compared between the two groups before and after surgery, and the results showed that there was no significant difference in Karnofsky scores before and after surgery in the experimental group ($P > 0.05$). The Karnofsky score in the control group was significantly lower than that before operation ($P < 0.05$). There was no significant difference in preoperative Karnofsky score between the two groups ($P > 0.05$), but there was a significant difference in postoperative Karnofsky score between the two groups ($P < 0.05$). The specific results are shown in Figure 6.

NIHSS was used to evaluate the postoperative neurological function of the two groups, and the results showed that there was no significant difference in NIHSS score between the experimental group and the control group ($P > 0.05$). In addition, the number of patients with different degrees of neurological deficit in the control group was close to half (24/54), and the number of patients with neurological deficit in the experimental group was less than that in the control group. The specific results are shown in Figures 7 and 8.

3.4. Evaluation Results of Postoperative Infection in Glioma Patients after Resection. The postoperative infection rates of the two groups were evaluated, and it was found that the postoperative infection rates of glioma patients in the experimental group and the control group were 7.4% (4/54). There was no significant difference in infection rate ($P > 0.05$). The results are shown in Figure 9.

4. Discussion

At present, the incidence and mortality of glioma are increasing. Gliomas play an important role in intracranial tumors, and about half of the intracranial tumor clinics are gliomas [32]. The effective treatment of glioma has become a hot research direction for researchers in China and abroad. The treatment of glioma needs to be determined based on the specific circumstances of each patient. It is extremely individualized treatment. The main treatment principle is surgery, supplemented by other treatments. Therefore, a smooth and effective operation is a prerequisite for the treatment of this disease. In this study, intraoperative magnetic resonance navigation on the basis of an artificial intelligence algorithm is applied to neurosurgical glioma resection, and the clinical application value of intraoperative magnetic resonance navigation in neurosurgical glioma resection is studied. A total of 108 patients with glioma were selected and divided into the experimental group (patients with intraoperative magnetic resonance assisted glioma resection) and the control group (patients with conventional surgical experience resection), with 54 in each group. In the experimental group, the tumor resection rate, NIHSS score, Karnofsky score, and postoperative intracranial infection were calculated by real-time reconstruction of intraoperative magnetic resonance images on the basis of a segmentation dictionary learning algorithm. To evaluate the application value of intraoperative magnetic resonance navigation on the basis of segmentation dictionary learning algorithm in neurosurgical glioma resection.

The tumor resection rate is crucial to evaluate the success of glioma resection. The decrease of resection rate indicates that the recurrence rate of tumor will be significantly reduced and the life expectancy of patients will be prolonged. The results of this study showed that the average tumor resection rate in the experimental group was significantly higher than that in the control group ($P < 0.05$). This shows that under the guidance of intraoperative magnetic resonance navigation, glioma resection can better achieve tumor resection, which is of great significance to other adjuvant therapies for patients. The complete neurological function of patients after glioma resection is also an important indicator for evaluating surgery. In this study, Karnofsky scores were compared between the two groups of patients before and after surgery, and the results showed that there was no significant difference in Karnofsky scores before and after surgery in the experimental group ($P > 0.05$). NIHSS was used to evaluate the postoperative neurological function of the two groups, and the results showed that there was no significant difference in NIHSS score between the experimental group and the control group ($P > 0.05$). The number of patients with postoperative neurological deficits in the experimental group was smaller than that in the control group. This shows that under the guidance of intraoperative

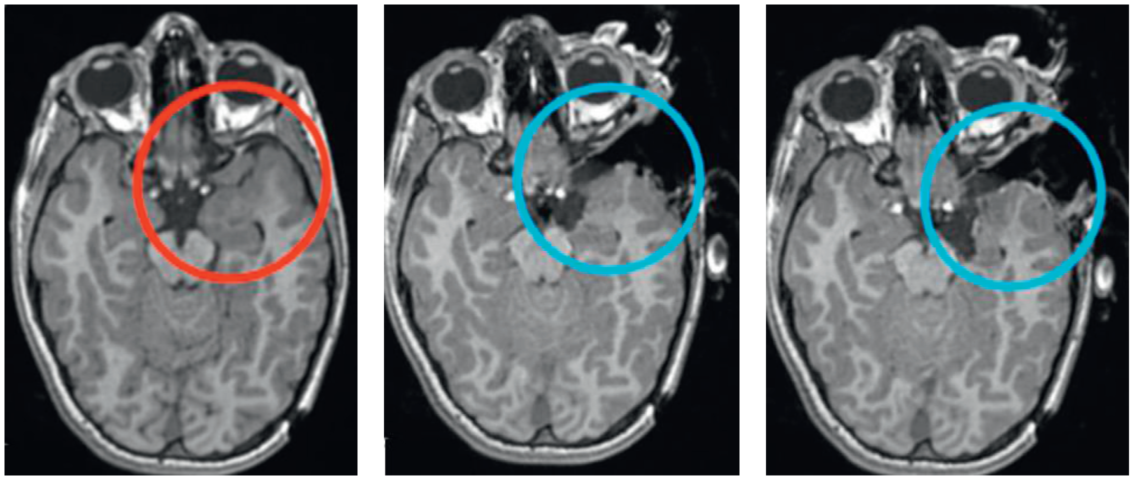

(a) (b) (c)

Figure 3: MRI of a patient with glioma before (a), during (b), and after (c) resection.

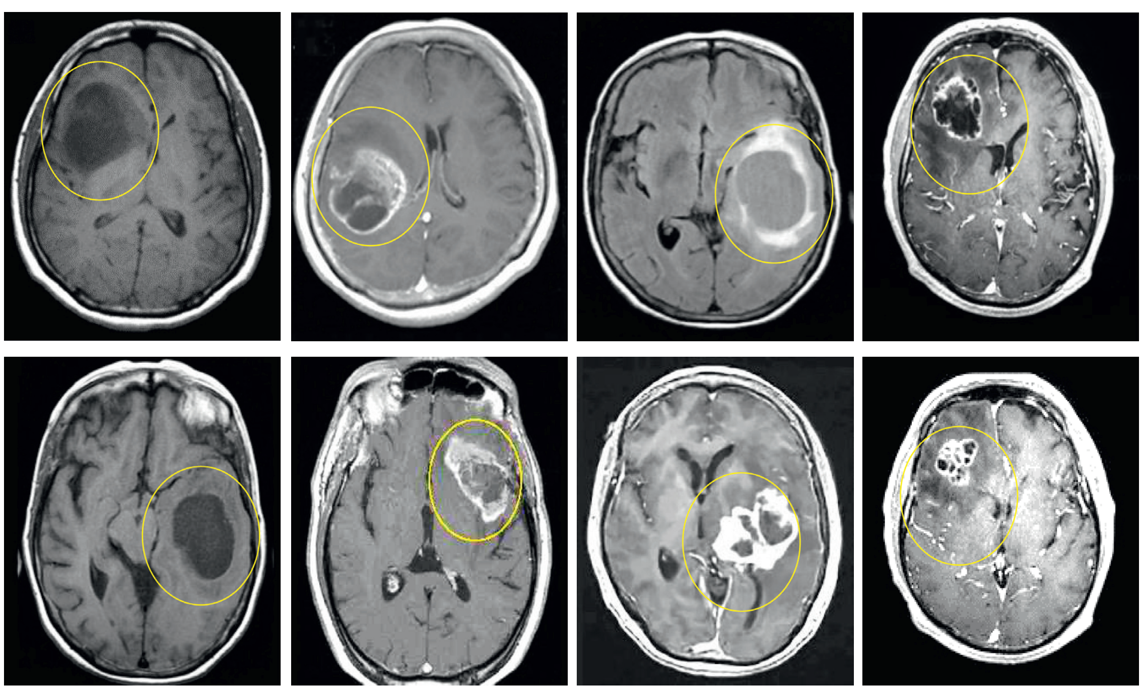

Figure 4: Magnetic resonance imaging results of glioma patients.

magnetic resonance navigation, the neurological function of patients after resection is relatively complete, which greatly guarantees the quality of life of patients after operation. In addition, the postoperative infection of the two groups was evaluated, and it was found that there was no significant difference in the infection rate between the patients with glioma guided by intraoperative magnetic resonance and the patients with conventional glioma resection ($P > 0.05$). Studies have found that intraoperative magnetic resonance scanning technology in glioma resection can significantly improve the tumor resection rate. Under the guidance of neural function navigation, real-time brain tissue functional images can be provided for the tumor resection process, and the resection area can be observed at any time to avoid damage to the neural function area or conduction bundle. Then, the most complete resection and the safest resection were achieved, which is consistent with the results of this study [33]. At the same time, the application of intra-operative MRI in tumor resection in this study did not increase the risk of postoperative infection. Therefore, the

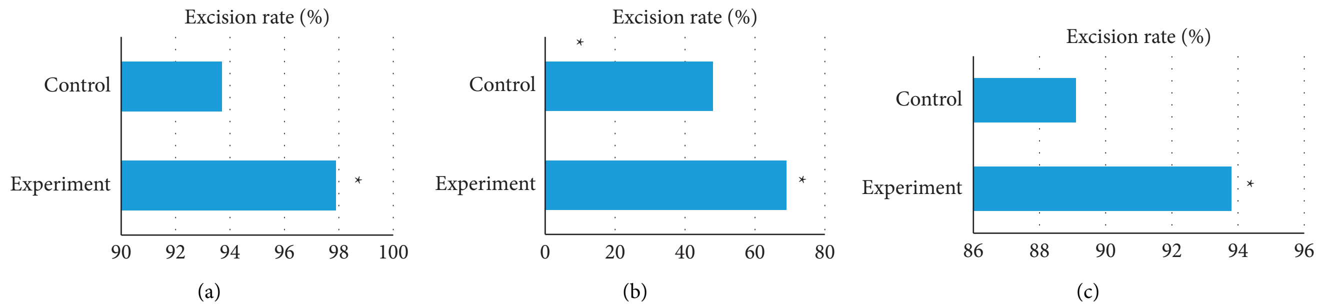

Figure 5: Comparison of tumor resection rate between the two groups. (a) The comparison of the average tumor resection rates of the two groups. (b) The comparison of the total tumor resection rates of the two groups. (c) The comparison of the subtotal tumor resection rates of the two groups. *significant difference: $P < 0.05$.

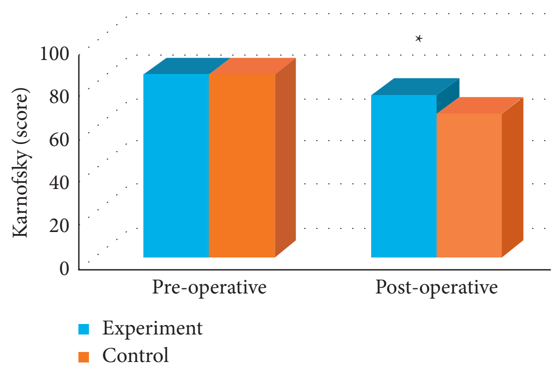

Figure 6: Comparison of Karnofsky scores between the two groups before and after glioma. Note: *significant difference, $P < 0.05$.

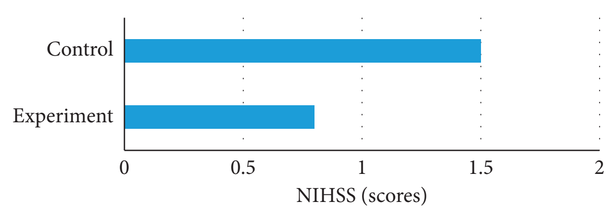

Figure 7: Comparison of NIHSS scores between the two groups after glioma resection.

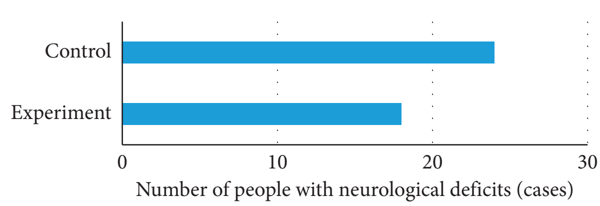

Figure 8: Comparison of neurological deficits between the two groups after glioma resection.

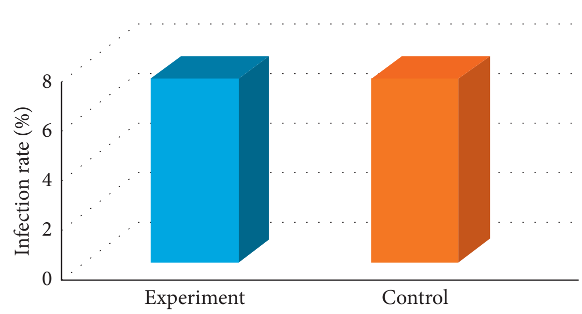

Figure 9: Comparison of infection rates between the two groups after glioma resection.

application of intraoperative MRI in glioma resection has great clinical value.

5. Conclusions

Intraoperative magnetic resonance navigation on the basis of an artificial intelligence algorithm was applied to neurosurgery glioma resection to study the clinical application value of intraoperative magnetic resonance navigation in neurosurgery glioma resection. A total of 108 patients with glioma were selected and divided into the experimental group (patients with intraoperative magnetic resonance assisted glioma resection) and the control group (patients with conventional surgical experience resection), with 54 in each group. In the experimental group, the tumor resection rate, NIHSS score, Karnofsky score, and postoperative intracranial infection were calculated by real-time reconstruction of intraoperative magnetic resonance images on the basis of a segmentation dictionary learning algorithm. The results revealed that under the guidance of intraoperative magnetic resonance navigation, glioma resection can better achieve tumor resection. In addition, the neurological function of patients after resection is relatively complete, which greatly ensures the quality of life of patients after operation. In addition, intraoperative MRI did not increase the risk of postoperative infection in patients undergoing tumor resection. Intraoperative magnetic resonance navigation on the basis of a segmentation dictionary learning algorithm has great application value in neurosurgery glioma resection. The deficiency of this study is that the sample size of the research object is too small, and the source is single, not random and widely applicable. In the subsequent studies, the analysis and research of multisite, multitype, and large sample sizes will be considered to provide a more practical and effective reference value for the application of intraoperative magnetic resonance navigation in neurosurgery glioma resection.

Data Availability

The data used to support the findings of this study are available from the corresponding author upon request.

Conflicts of Interest

The authors declare no conflicts of interest.

References

[1] K. Deland, J. S. Mercer, D. M. Crabtree et al., "Radiosensitizing the vasculature of primary brainstem gliomas fails to improve tumor response to radiation therapy," *International Journal of Radiation Oncology, Biology, Physics*, vol. 112, no. 3, Article ID S0360, 2022.

[2] H. Luo, C. Tao, X. Long, X. Zhu, and K. Huang, "Early 2 factor (E2F) transcription factors contribute to malignant progression and have clinical prognostic value in lower-grade glioma," *Bioengineered*, vol. 12, no. 1, pp. 7765–7779, 2021.

[3] L. Ye, Y. Xu, L. Wang et al., "Downregulation of CYP2E1 is associated with poor prognosis and tumor progression of gliomas," *Cancer Medicine*, vol. 10, no. 22, pp. 8100–8113, 2021.

[4] Y. Narita, Y. Muragaki, N. Kagawa et al., "Safety and efficacy of depatuxizumab mafodotin in Japanese patients with malignant glioma: a nonrandomized, phase 1/2 trial," *Cancer Science*, vol. 112, no. 12, pp. 5020–5033, 2021.

[5] Z. Zhao, Y. Wu, Z. Wang, J. Xu, Y. Wang, and Z. Zhao, "Establishment and validation of five autophagy-related signatures for predicting survival and immune microenvironment in glioma," *Genes & Genomics*, vol. 44, no. 1, pp. 79–95, 2021.

[6] M. M. J. Bauman, A. R. Bhandarkar, C. R. Zheng et al., "Management strategies for pediatric patients with tectal gliomas: a systematic review," *Neurosurgical Review*, 2021.

[7] A. Fukui, Y. Muragaki, T. Saito et al., "Impact of awake mapping on overall survival and extent of resection in patients with adult diffuse gliomas within or near eloquent areas: a retrospective propensity score-matched analysis of awake craniotomy vs. general anesthesia," *Acta Neurochirurgica*, vol. 164, no. 2, pp. 395–404, 2021.

[8] R. Chakrabarti, V. Gupta, S. Vyas, K. Gupta, and V. Singh, "Correlation of dual energy computed tomography electron density measurements with cerebral glioma grade," *The Neuroradiology Journal*, Article ID 197140092110474, 2021.

[9] C. A. Manju, K. Jeena, R. Ramachandran et al., "Intracranially injectable multi-siRNA nanomedicine for the inhibition of glioma stem cells," *Neuro-Oncology Advances*, vol. 3, no. 1, Article ID vdab104, 2021.

[10] X. Chen, C. Li, Y. Li et al., "Characterization of METTL7B to evaluate TME and predict prognosis by integrative analysis of multi-omics data in glioma," *Frontiers in Molecular Biosciences*, vol. 8, Article ID 727481, 2021.

[11] F. Wang, L. Dong, X. Wei et al., "Effect of gambogic acid-loaded porous-lipid/PLGA microbubbles in combination with ultrasound-triggered microbubble destruction on human glioma," *Frontiers in Bioengineering and Biotechnology*, vol. 9, Article ID 711787, 2021.

[12] Z. Y. Qi, L. L. Wang, and X. L. Qu, "lncRNA LINC00355 acts as a novel biomarker and promotes glioma biological activities via the regulation of miR-1225/FNDC3B," *Disease Markers*, Article ID 1683129, 2021.

[13] Z. Lv and L. Qiao, "Analysis of healthcare big data," *Future Generation Computer Systems*, vol. 109, pp. 103–110, 2020.

[14] A. Rayi, I. Alnahhas, S. Ong, P. Giglio, and V. K. Puduvalli, "Targeted therapy for BRAF mutant brain tumors," *Current Treatment Options in Oncology*, vol. 22, no. 11, p. 105, 2021.

[15] A. R. Giovagnoli, R. F. Meneses, C. Paterlini, A. Silvani, and A. Boiardi, "Cognitive awareness after treatment for high-grade glioma," *Clinical Neurology and Neurosurgery*, vol. 210, Article ID 106953, 2021.

[16] D. Raj, P. Agrawal, H. Gaitsch, E. Wicks, and B. Tyler, "Pharmacological strategies for improving the prognosis of glioblastoma," *Expert Opinion on Pharmacotherapy*, vol. 22, no. 15, pp. 2019–2031, 2021.

[17] C. J. Shen and S. A. Terezakis, "The evolving role of radiotherapy for pediatric cancers with advancements in molecular tumor characterization and targeted therapies," *Frontiers in Oncology*, vol. 11, Article ID 679701, 2021.

[18] G. Zhong, Y. Wang, Q. Wang et al., "Discovery of novel ID2 antagonists from pharmacophore-based virtual screening as potential therapeutics for glioma," *Bioorganic & Medicinal Chemistry*, vol. 49, Article ID 116427, 2021.

[19] W. W. Lin, G. Y. Ou, and W. J. Zhao, "Mutational profiling of low-grade gliomas identifies prognosis and immunotherapy-

related biomarkers and tumour immune microenvironment characteristics," *Journal of Cellular and Molecular Medicine*, vol. 25, no. 21, Article ID 10111, 2021.

[20] G. Li, Z. Zhang, L. Cai et al., "Fn14-targeted BiTE and CAR-T cells demonstrate potent preclinical activity against glioblastoma," *OncoImmunology*, vol. 10, no. 1, Article ID 1983306, 2021.

[21] F.-X. Tian, H.-F. Ma, and Q. Zhang, "Identification of mir-9 in glioma diagnosis and prognosis," *Clinical Laboratory*, vol. 66, no. 7/2020, 2020.

[22] F. Higuchi, H. Nagashima, J. Ning, M. V. A. Koerner, H. Wakimoto, and D. P. Cahill, "Restoration of temozolomide sensitivity by PARP inhibitors in mismatch repair deficient glioblastoma is independent of base excision repair," *Clinical Cancer Research*, vol. 26, no. 7, pp. 1690–1699, 2020.

[23] H.-L. Bai, C.-M. Kang, Z.-Q. Sun et al., "TTDA inhibited apoptosis by regulating the p53-Bax/Bcl2 axis in glioma," *Experimental Neurology*, vol. 331, Article ID 113380, 2020.

[24] A. Kumar, P. Chandra, and S. Kale, "Parietal transventricular approach for medial temporal glioma: a technical report," *Surgical Neurology International*, vol. 11, p. 22, 2020.

[25] H.-M. Chan, W. N.-H. Loh, T. T. Yeo, and K. Teo, "Awake craniotomy and excision of a diffuse low-grade glioma in a multilingual patient: neuropsychology and language," *World Neurosurgery*, vol. 128, pp. 91–97, 2019.

[26] S. Xin, K. Huang, and X.-G. Zhu, "Non-coding RNAs: regulators of glioma cell epithelial-mesenchymal transformation," *Pathology, Research & Practice*, vol. 215, no. 9, Article ID 152539, 2019.

[27] M. D. Jenkinson, D. G. Barone, A. Bryant et al., "Intraoperative imaging technology to maximise extent of resection for glioma," *Cochrane Database of Systematic Reviews*, vol. 2021, no. 5, Article ID CD012788, 2018.

[28] Y. Fujita, M. Kohta, T. Sasayama et al., "Intraoperative 3-T magnetic resonance spectroscopy for detection of proliferative remnants of glioma," *World Neurosurgery*, vol. 137, pp. 149–157, 2020.

[29] Z. Yu, S. U. Amin, M. Alhussein, and Z. Lv, "Research on disease prediction based on improved DeepFM and IoMT," *IEEE Access*, vol. 9, no. 99, Article ID 39043, 2021.

[30] A. Pichierri, M. Bradley, and V. Iyer, "Intraoperative magnetic resonance imaging-guided glioma resections in awake or asleep settings and feasibility in the context of a public health system," *World Neurosurgery: XL*, vol. 3, Article ID 100022, 2019.

[31] S. X. Xie, Z. C. Yu, and Z. H. Lv, "Computer modeling in engineering & sciences," *Tech SciencePress*, vol. 128, no. 2, pp. 489–522, 2021.

[32] Z.-J. Chen, J.-L. Zheng, W. Guan, W.-G. Liu, J.-Y. Zheng, and J.-D. Zuo, "Intraoperative perfusion-weighted imaging in non-enhanced glioma surgery," *Minerva Chirurgica*, vol. 74, no. 4, pp. 313–319, 2019.

[33] A. Kondo, O. Akiyama, S. Aoki, and H. Arai, "Application of intra-operative magnetic resonance imaging for intracranial epidermoid cysts," *British Journal of Neurosurgery*, pp. 1–5, 2020.

Hindawi
Contrast Media & Molecular Imaging
Volume 2022, Article ID 2214583, 10 pages
https://doi.org/10.1155/2022/2214583

Research Article

Artificial Intelligence Algorithm-Based Computed Tomography Image in Assessment of Acute Renal Insufficiency of Patients Undergoing Percutaneous Coronary Intervention

Xiuming Zhang, Tao Liu, and Chunhua Tian

Department of Nephrology, Inner Mongolia Baogang Hospital, Baotou 014010, Inner Mongolia Autonomous Region, China

Correspondence should be addressed to Chunhua Tian; 2020141030@stu.gzhmu.edu.cn

Received 26 December 2021; Revised 28 January 2022; Accepted 31 January 2022; Published 28 February 2022

Academic Editor: M Pallikonda Rajasekaran

This study was aimed to analyze the changes in renal function of patients undergoing percutaneous coronary intervention (PCI) surgery and the characteristics of their computed tomography (CT) image based on artificial intelligence algorithms. In this study, 104 patients with coronary atherosclerotic heart disease (CAHD) were treated as the research objects. They were divided into an experimental group (patients who underwent CAG and PCI within 1 week after enhanced coronary CT (ECCT)) and the control group (patients who underwent CAG and PCI within 1–3 weeks after ECCT). Renal imaging scans of patients were performed by CT based on discrete inseparable shear transform (DNST) optimized algorithm, which was named as O-DNST. The results showed that the serum creatinine (Scr), blood urea nitrogen (BUN), and urine protein (UP) levels of patients in the experimental group were significantly higher than those of the control group 24–72 hours after surgery, while the levels of endogenous creatinine clearance (Ccr) and estimated glomerular filtration rate (eGFR) were significantly lower than those of the control group ($P < 0.05$). The levels of $\beta 2$ microglobulin ($\beta 2$-MG), C-reactive protein (CRP), interleukin 6 (IL-6), and tumor necrosis factor (TNF-α) in the experimental group were significantly higher than those in the control group 24–72 hours after surgery ($P < 0.05$). The incidence of contrast-induced nephropathy (CIN) in the experimental group (15.38%) was significantly higher than that in the control group (5.8%), and the difference was statistically significant ($P < 0.05$). The results showed that repeated application of contrast agent in a short period of time can promote the increase of serum inflammation levels in PCI patients, which may be a risk factor for CIN in PCI patients.

1. Introduction

Coronary atherosclerotic heart disease (CAHD) is caused by atherosclerotic lesions in coronary arteries that cause stenosis or obstruction of the vascular lumen, resulting in myocardial ischemia, hypoxia, or necrosis, so it is often referred to as "coronary heart disease (CHD)" [1]. CHD is a common disease of middle-aged and elderly people, frequently occurring, and seriously endangering people's lives. Most people do not have any symptoms at ordinary times, work, study, and life are as usual, but they often have signs of myocardial ischemia, such as feeling frontal discomfort or symptoms of fatigue. Although the symptoms are mild, if the electrocardiogram is performed in time, myocardial ischemia will be found [2–4]. The treatment of CHD mainly includes drug therapy, interventional therapy, and surgical coronary artery bypass graft. Medical treatment is the cornerstone of CHD treatment, regardless of the degree of coronary artery stenosis or whether the patient has a stent or a heart bypass. Once diagnosed with CHD, patients need long-term adherence to oral prognostic drugs, but they can only relieve symptoms, stabilize plaques, and prevent acute myocardial infarction [5, 6]. Coronary artery bypass grafting refers to the use of the patient's own great saphenous vein or other arteries to connect the distal end of the narrowed coronary artery with the aorta to supply blood to the distal end of the myocardium to improve the symptoms of angina pectoris and improve life treatment, but the operation is complicated and risky [7]. Percutaneous coronary intervention (PCI) has the advantages of simple operation, small trauma area, and quick postoperative recovery. It can quickly rebuild coronary blood vessels in emergency situations, which can effectively alleviate the symptoms of patients and improve the quality of life [8].

With the extensive clinical application of contrast technology, especially in elderly patients with severe comorbidities, contrast-induced nephropathy (CIN) has become the third leading cause of hospital-acquired renal failure, accounting for the largest incidence of 11% [9, 10]. In many studies, CIN is defined as acute renal function decline that occurs after intravascular contrast media is used for no other reason. The specific manifestations are summarized as follows: 48–72 hours after using the contrast agent, the serum creatinine level rises by 44 μmol/L, or 25% higher than the baseline serum creatinine level [11]. As for the pathogenesis of CIN, it is still unclear. Some studies believe that renal blood flow reduction, especially renal medulla ischemia, direct cytotoxicity, and the osmotic pressure and viscosity of the contrast agent play an important role in the pathogenesis of CIN [12–14]. At present, it is believed that the original renal insufficiency is the most important risk factor for the occurrence of CIN. There is no evidence-based medicine to prove that a certain drug has a definite preventive effect on CIN. However, some studies have confirmed that certain drugs can play a role in reducing the incidence of CIN, such as adenosine antagonists, statins, vitamin C, and calcium channel blockers. Other preventive measures include: maintaining water and electrolyte balance, closely monitoring renal function indicators before and after angiography, actively dealing with complications, and strengthening nutritional support, which show differences in effect, so the focus of treatment of CIN is to prevent [15]. In recent years, CT enhancement has been widely used in clinical heart and coronary artery imaging and has become an important noninvasive imaging method for the diagnosis and detection of CHD. Water-soluble iodine contrast agents are commonly used in CT examinations, and the adverse reactions caused by iodine-containing contrast agents, especially contrast agent nephropathy, have attracted the attention and attention of clinicians and radiologists [16]. How to prevent contrast nephropathy and life-threatening reactions is an urgent issue that deserves attention and must be properly handled.

Intelligent medical imaging uses artificial intelligence technology to analyze and process the scanned images of commonly used medical imaging technologies such as X-ray, CT, magnetic resonance imaging (MRI), and ultrasound and provide diagnostic assistance and prompts [17]. Based on this, 104 patients with CAHD who underwent coronary angiography (CAG) and PCI surgery after the enhanced coronary CT (ECCT) were treated as the research objects. They were divided into an experimental group (patients who underwent CAG and PCI within 1 week after ECCT) and the control group (patients who underwent CAG and PCI within 1–3 weeks after ECCT). The preoperative and postoperative renal function indicators, inflammatory indicators, and the incidence of CIN in the two groups were compared to deeply analyze the clinicopathological characteristics of acute renal function injury caused by the application of contrast agents in PCI surgery, aiming to provide reference for selection of clinical prevention and treatment strategies for CIN.

2. Materials and Methods

2.1. Research Objects. In this study, 104 patients with CAHD who underwent CAG and PCI surgery in hospital from March 2018 to May 2021 were selected as the research subjects after coronary CT examination with enhanced coronary artery. There were 58 males and 46 females, with an age range of 20–72 years. This study had been approved by the ethics committee of the hospital, and the patients and their family members had understood the research situation and signed the informed consent forms.

Inclusion criteria were defined as follows: patients who signed the informed consents; patients with angina or severe coronary artery stenosis; patients who did not receive medication or surgical treatment; and patients older than 18 years old.

Exclusion criteria were given as follows: patients over 72 years old; patients with hyperthyroidism; patients who had received interventional therapy; patients who were allergic to iodine contrast agents; patients with severe renal dysfunction; patients recently taking a large number of nephrotoxic drugs; and patients who were suspected with severe left main stem disease.

2.2. Grouping. The included patients were randomly divided into an experimental group (52 cases) and a control group (52 cases). Patients in the experimental group underwent CAG and PCI surgery within 1 week after ECCT; whereas those in the control group underwent CAG and PCI surgery within 1–3 weeks after ECCT.

2.3. CT Examination. CT Scanner was adopted in this study. The patient was required to keep a supine position and scan from the diaphragm to the symphysis pubis. Scanning parameters were given as follows: tube voltage was 120 kV, tube current was 220 mA, matrix was 256 × 256, conventional scanning layer thickness was 5 mm, and layer spacing was 5 mm. The contrast agent iohexol was injected from the cubital vein at a flow rate of 2.5 mL/s, the scanning time of the arterial phase was 30 seconds, the scanning time of the parenchymal phase was 50 seconds, the scanning time of the delayed phase was 100 seconds, the reconstruction layer thickness was 1.5 mm, and the layer spacing was 1.5 mm.

2.4. Improved Image Denoising Algorithm Based on DNST (O-DNST). Shear wave transform [18] is a new type of multiscale geometric analysis method, which is constructed by affine transformations such as scaling, shearing, and translation of the basic function, which embodies the geometric and mathematical characteristics of the function. In this study, the discrete nonseparable shear wave transform

(DNST) was introduced as the core algorithm, and the inseparable shear wave generator can be expressed as follows:

$$\Phi_{\mathrm{no}}(\eta) = U\left(\frac{\eta_1}{2}, \eta_2\right)\Phi(\eta),$$

$$\inf_{\eta\in\Gamma}|U(\eta)| \geq a_1, \tag{1}$$

$$\Gamma = \left\{\eta \in \left[-\frac{1}{2},\frac{1}{2}\right]^2 : \frac{1}{4} \leq |\eta_1| \leq \frac{1}{2}, \frac{\eta_2}{\eta_1} \leq 1\right\}.$$

In the above three equations, U represented a two-dimensional sector filter, $a_1 \rangle 0$ was a constant, and Φ_{no} represents an inseparable shear wave generator. The shear wave generated by the inseparable shear wave generator can be expressed as follows:

$$\Phi_{\mathrm{no}\,(i,j,n)}(x) = 2^{\frac{3}{4}i}\,\Phi_{\mathrm{no}} B_j C_2 x - W_{d1} n. \tag{2}$$

$$W_{d1} = \mathrm{diag}\left(d_1^i, d_2^i\right). \tag{3}$$

In the (2) and (3), W_{d1} represents the sampling matrix, and d_1 and d_2 were the sampling constant for conversion.

The Bayesian algorithm based on the coefficient statistical model in the transform domain has always been a hot topic of image denoising. Constructing a prior probability distribution model for the coefficient edges makes the algorithm have the advantages of better balance of noise suppression and preservation of image details. The NIG distribution was introduced to determine the marginal statistical distribution of DNST coefficients.

It was assumed that the noise image was Q and the original image was P, then, the following equation could be obtained:

$$Q = P + Z. \tag{4}$$

In the above equation, Z represented Gaussian noise. After the DNST was introduced, the followingequation could be obtained:

$$q = p + z. \tag{5}$$

In equation (5), q represented the shear wave coefficient of the noise image through DNST change, p represented the shear wave coefficient of the noise-free image, and z represented the noise coefficient of the noise-free image. The Bayesian maximum posterior estimation lesson can be expressed as follows:

$$p*(q) = arg\max_p\left\{h_{p|q}(p|q)\right\}. \tag{6}$$

In equation (6), $h_{p|q}(p|q)$ represents the conditional density of observation of q versus p. Then, the Bayesian was adopted to simplify the processing:

$$p*(q) = arg\max_p\left\{h_n(q-p)\bullet h_p(p)\right\}. \tag{7}$$

$$h_n(n) = \frac{\exp\langle -n^2/2{\varphi_n}^2\rangle}{\sqrt{2\pi}\varphi_n}. \tag{8}$$

In the abovementioned equations, $h_n(\cdot)$ represented the probability distribution of the noise coefficient, $h_p(\cdot)$ referred to the prior distribution of the noise-free image coefficient, and ${\varphi_n}^2$ represented the Gaussian variance. After equation (8) was substituted into equation (7),

$$p*(q) = arg\max_p\left[-\frac{(q-p)^2}{2{\varphi_n}^2} + \lambda(p)\right]. \tag{9}$$

$$\lambda(p) = \ln h_p(p). \tag{10}$$

In equations (9) and (10), $\lambda(p)$ was a convex differentiable function. $-(q-p)^2/2{\varphi_n}^2 + \lambda(p)$ was set as the first derivative, and then $p*(q)$ can be calculated to obtain the maximum posterior estimate:

$$\frac{q-p^*}{{\varphi_n}^2} + \lambda'(p^*) = 0. \tag{11}$$

Next, an optimal linear interpolation shrink (OLIS) algorithm was proposed to ensure a good threshold effect, which could be expressed as follows:

$$\varphi_\alpha^{\mathrm{OLIS}} = \begin{cases} q - \tau(q-\beta) & |q| \leq K \\ 0 & |q| > K \end{cases}. \tag{12}$$

$$\tau = \frac{\chi_n^2}{\chi_q^2}. \tag{13}$$

In equations (12) and (13) above, □ represented the average value of the corresponding sub-band coefficients, K represented the calculated threshold, and χ^2 represented the noise variance.

The above showed an improved image denoising algorithm based on DNST, which was named as O-DNST. In summary, the O-DNST algorithm flow can be shown in Figure 1. Firstly, the discrete inseparable shear waves were adopted to divide the image into multiple high-frequency sub-bands and obtain the corresponding shear wave coefficients and a low-frequency sub-band. Secondly, the noise variance, threshold, and statistical parameters of the high-frequency sub-band were calculated. Thirdly, it could perform threshold processing on all high-frequency sub-band coefficients and perform mixed low-frequency denoising processing on the low-frequency sub-band. Finally, the inverse DNST reconstruction was performed on the low-frequency sub-band to obtain a denoised image.

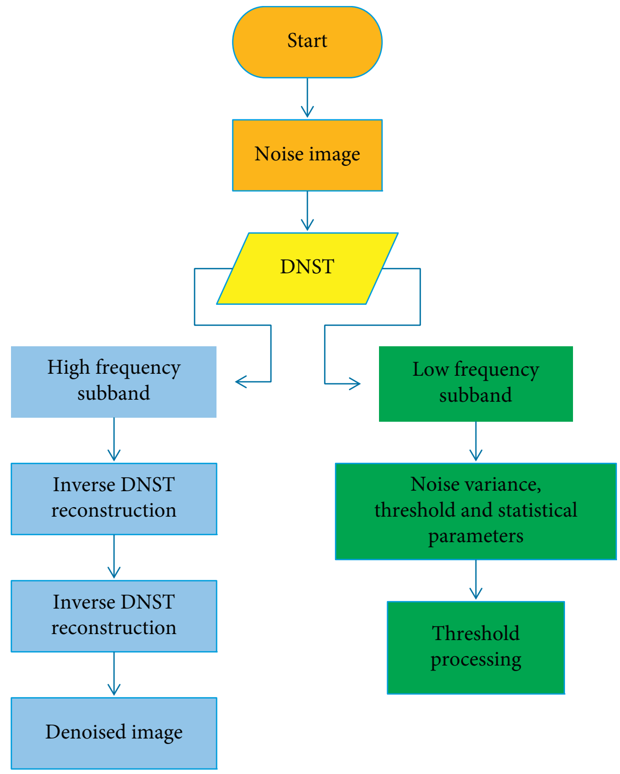

Figure 1: Improved image denoising algorithm process based on DNST.

2.5. Indicators of Algorithm Processing Effect. The root mean square error (RMSE) and running time were used as the performance indicators of the algorithm to process CT images.

It was supposed that the width of the image was L and the height was H, then,

$$RMSE = \sqrt{\frac{\sum_{i=1}^{H} \sum_{j=1}^{L} \left(v_{ij} - V\right)^2}{L \bullet H}}. \tag{14}$$

In equation (14), v_{ij} represented the gray value of the image, and V represented the average value of the gray value of the image.

Discrete separable shear wave transform (DSST) [19], wavelet transform (WT) [20], and DNST were used as controls to compare with the O-DNST algorithm.

2.6. Observation Indicators. The general information (gender, age, height, weight, diabetes, hypertension, hyperlipidemia, mild anemia, contrast dose, and Mehran score) of patients were recorded. The preoperative and postoperative (24, 48, and 72 hours) renal function indicators (serum creatinine (Scr), blood urea nitrogen (BUN), endogenous creatinine clearance (Ccr), estimated glomerular filtration rate (eGFR)), urine protein (UP), and inflammatory factors (β2 microglobulin (β2-MG), C-reactive protein (CRP), interleukin 6 (IL-6), and tumor necrosis factor-α (TNF-α)) of patients were recorded and compared.

2.7. Statistical Methods. The data processing of this study was analyzed by using the SPSS19.0 version statistical software, the measurement data was expressed by the mean ± standard deviation ($\bar{x} \pm s$), and the count data was expressed by the percentage (%). One-way analysis of variance was used for pairwise comparison. The difference was statistically significant at $P < 0.05$.

3. Results

3.1. Basic Data of Patients. The two groups of patients were compared in terms of basic information (gender, age, height, weight, diabetes, hypertension, hyperlipidemia, mild anemia, contrast agent dose, and Mehran score). As shown in Figures 2 and 3, the differences were all not statistically significant ($P > 0.05$).

Figure 4 was a CT image of a male patient (51 years old). The kidneys were enlarged on plain scan, and multiple wedge-shaped low-density areas appeared on enhanced scan. Figure 5 showed a CT image of a female patient (50 years old). The plain scan showed that the kidney is enlarged and the contour was irregular; and the enhanced scan showed the enhancement of the abscess wall, stones, and perinephric involvement.

3.2. Performance Analysis of O-DNST Algorithm. Figure 6 showed the comparison of image quality evaluation indicators of DSST, WT, DNST, and O-DNST algorithms. It illustrated that the RMSE and running time of the O-DNST

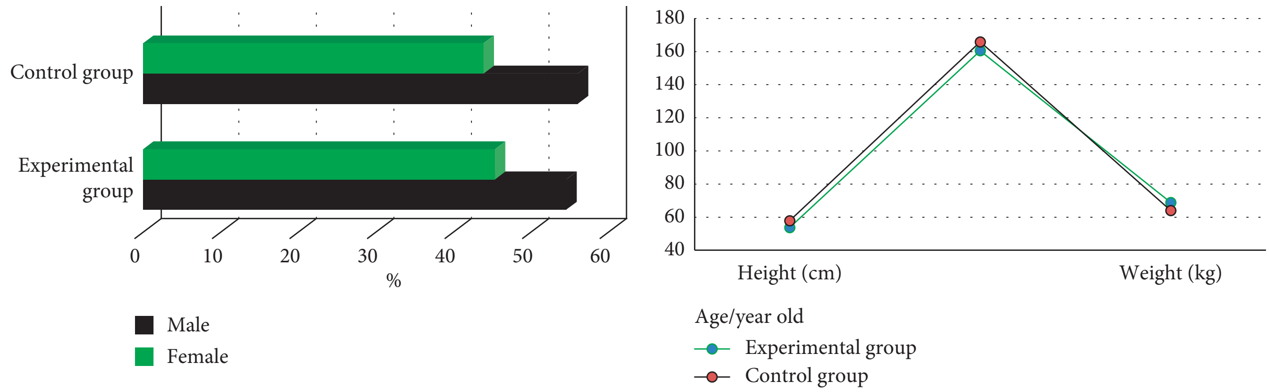

(a) (b)

Figure 2: Comparison of gender, age, height, and weight of the two groups of patients. (a) compared the ratio of men to women; and (b) compared the age, height, and weight.

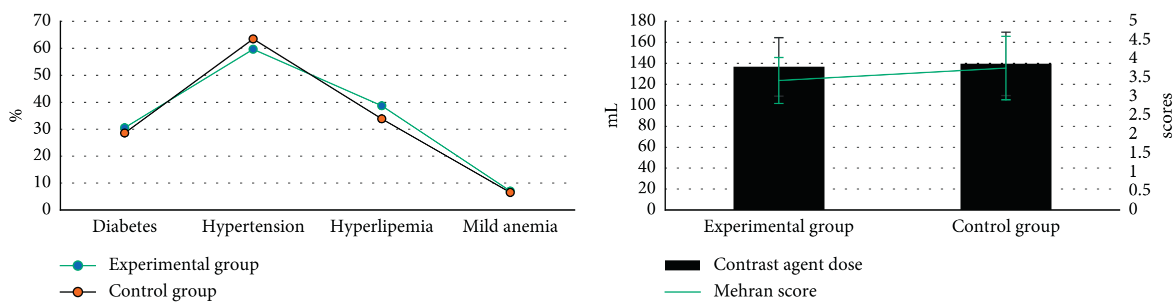

(a) (b)

Figure 3: Comparison of diabetes, hypertension, hyperlipidemia, mild anemia, contrast agent dosage, and Mehran score between the two groups. (a) showed the comparison on diabetes, hypertension, hyperlipidemia, and mild anemia; and (b) illustrated the comparison on contrast agent dose and Mehran score.

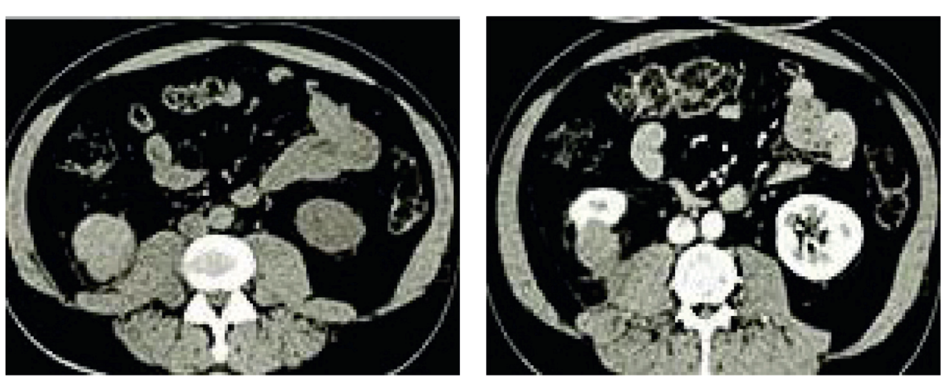

(a) (b)

Figure 4: CT image of a patient's kidney (male, 51 years old). The left image was the CT plain scan result, and the right image was the CT enhanced result.

algorithm were significantly lower than the DSST, WT, and DNST algorithms, and the differences were statistically significant ($P < 0.05$).

As shown in Figure 7 below, the images processed by the DSST, WT, DNST, and O-DNST algorithms showed a certain improvement compared with the original CT images. Among them, the resolution of image processed by WT algorithm was still low, and that of the DSST and DNST algorithms was higher, but there were artifacts, resulting in the subtle display of the organization was not clear. In addition, the O-DNST algorithm showed the best image clarity and tissue resolution, so the overall quality was better than other algorithms.

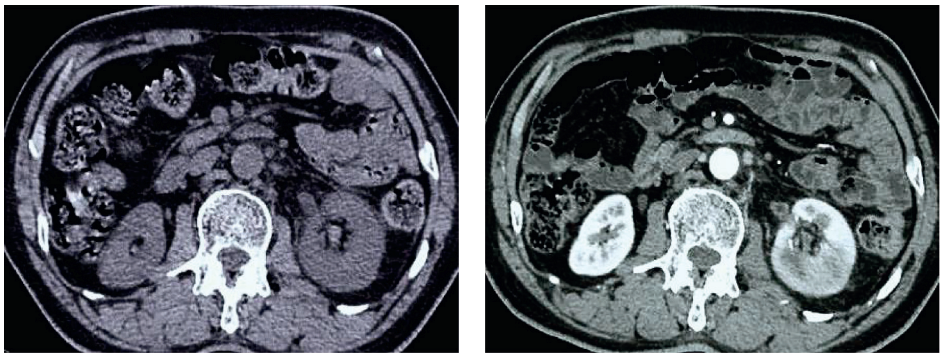

(a) (b)

Figure 5: CT image of a patient's kidney (female, 50 years old). The left image was the CT plain scan result, and the right image was the CT enhanced result.

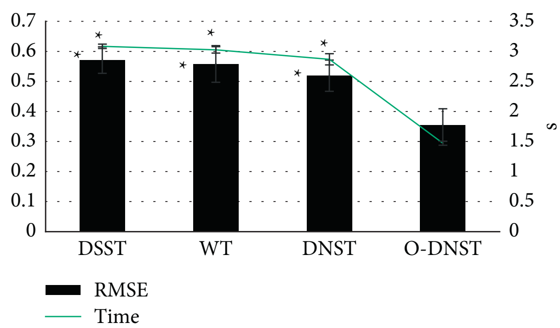

Figure 6: Comparison of image quality evaluation indicators of DSST, WT, DNST, and O-DNST algorithms. *Significant difference compared with the O-DNST algorithm ($P < 0.05$).

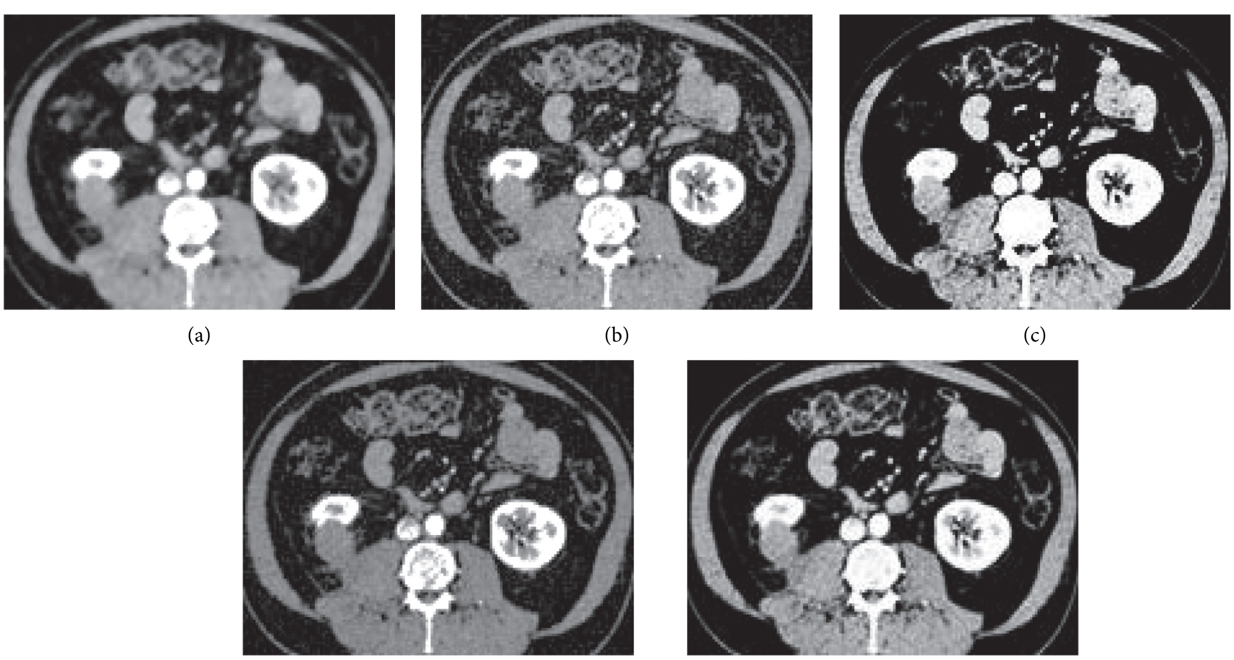

(a) (b) (c)

(d) (e)

Figure 7: Comparison of image processing effects of DSST, WT, DNST, and O-DNST algorithms. (a) showed the image of CT plain scan; and (b–e) were images processed by DSST, WT, DNST, and O-DNST algorithms, respectively.

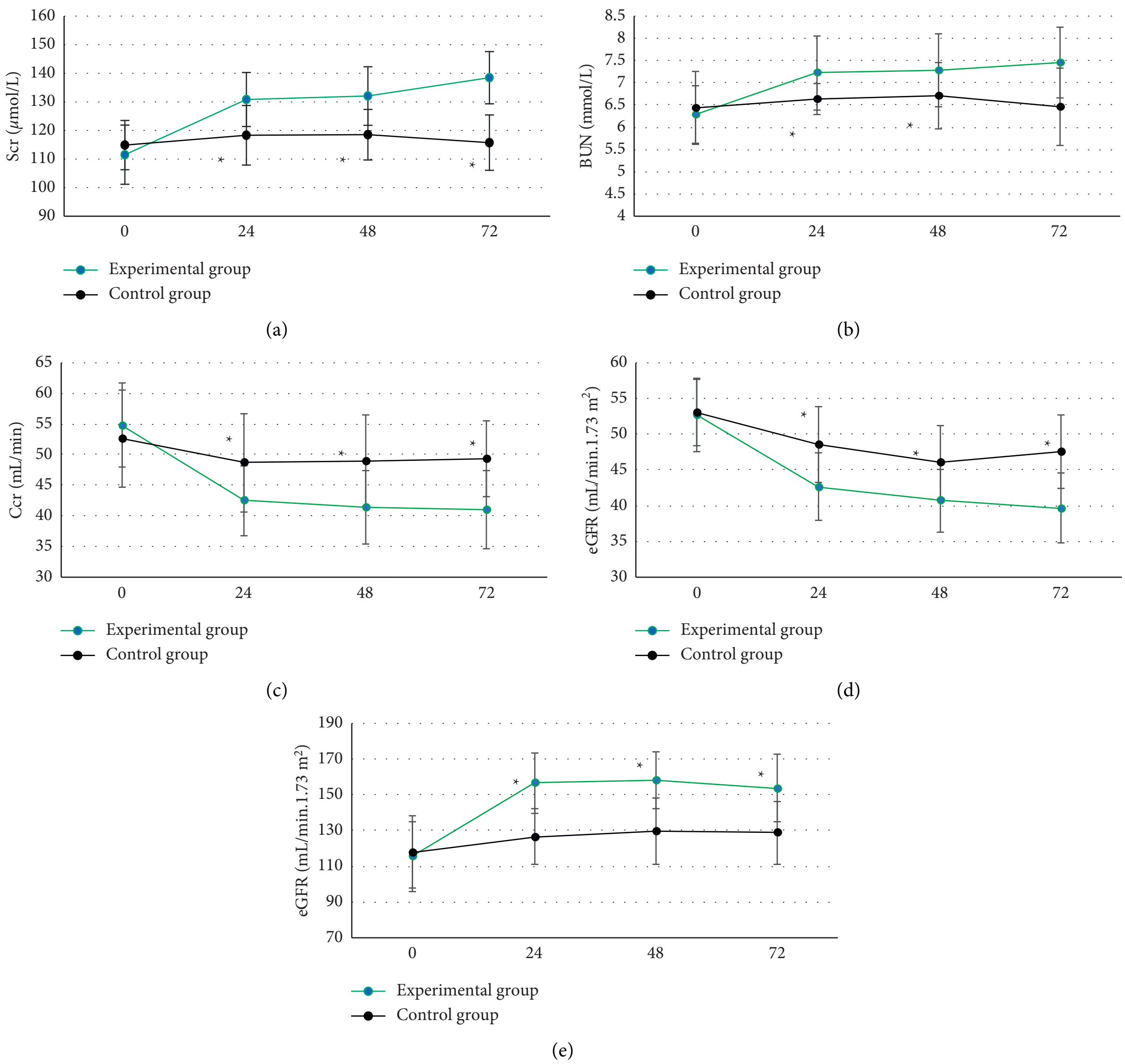

Figure 8: Comparison of renal function indicators between the two groups of patients (0–72 referred to "before surgery", 24 hours, 48 hours, and 72 hours after surgery, respectively). A ~ E showed the comparisons of Scr, BUN, Ccr, eGFR, and UP, respectively. *Significant difference compared with the experimental group ($P < 0.05$).

3.3. Comparison of Renal Function Indicators between Two Groups of Patients. As shown in Figure 8, the preoperative Scr, BUN, Ccr, eGFR, and UP levels of patients in the experimental group and the control group were not statistically different ($P > 0.05$). The levels of Scr, BUN, and UP in the experimental group were significantly higher than those in the control group at 24–72 hours after surgery, and the differences were statistically significant ($P < 0.05$). The Ccr and eGFR levels of patients in the experimental group were significantly lower than those in the control group at 24–72 hours after surgery, and the differences were statistically significant ($P < 0.05$).

3.4. Comparison of the Levels of Inflammatory Factors between the Two Groups. The preoperative β2-MG, CRP, IL-6, and TNF-α levels of the experimental group and the control group were not significantly different ($P > 0.05$). The levels of β2-MG, CRP, IL-6, and TNF-α in the experimental group were significantly higher than those in the control group for 24–72 hours after surgery, and the differences were statistically significant ($P < 0.05$). The specific comparison results are illustrated in Figure 9.

3.5. Comparison of the Incidence of CIN between the Two Groups. The incidence of CIN between the two groups was compared, and the results are given in Figure 10. 8 patients in the experimental group developed CIN with an incidence rate of 15.38%, and 3 patients in the control group developed CIN with an incidence rate of 5.8%. It can be inferred that the incidence of CIN in the experimental group was significantly higher than that in the control group, and the difference was statistically significant ($P < 0.05$).

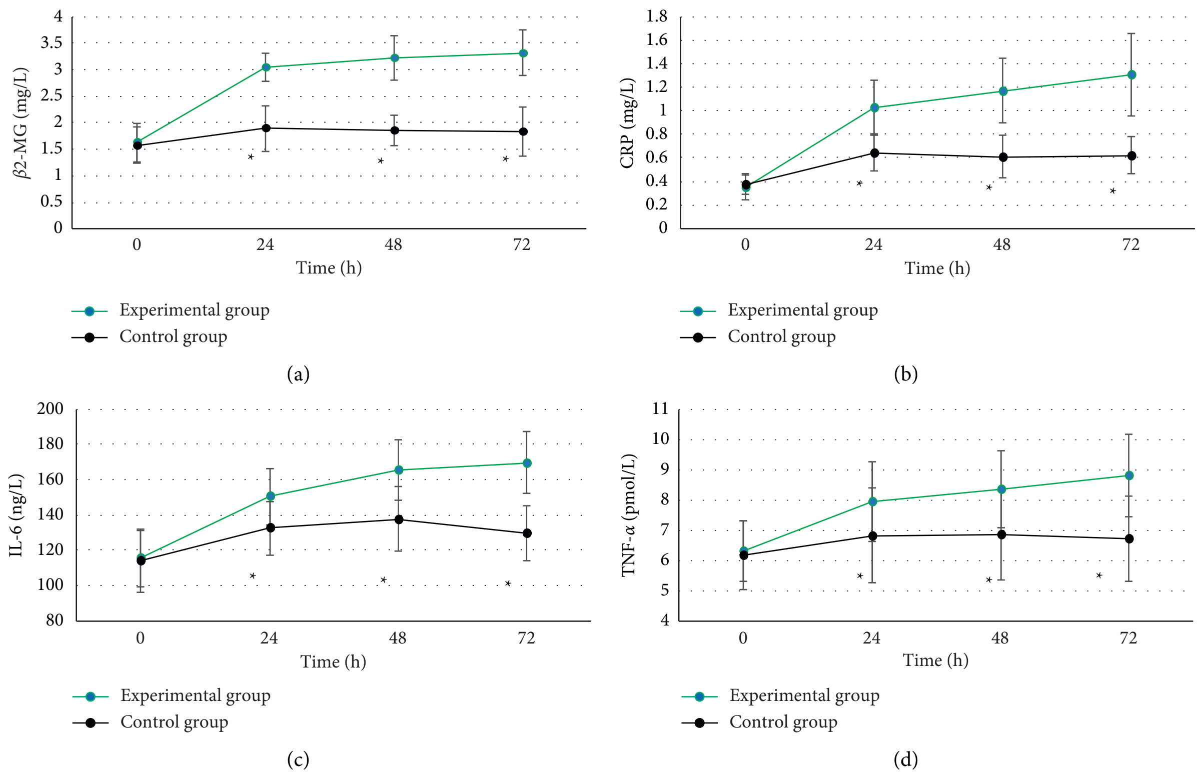

FIGURE 9: Comparison of levels of inflammatory factors between the two groups of patients (0–72 referred to "before surgery", 24 hours, 48 hours, and 72 hours after surgery, respectively). A ~ D showed the comparisons of β2-MG, CRP, IL-6, and TNF-α, respectively. *Significant difference compared with the experimental group ($P < 0.05$).

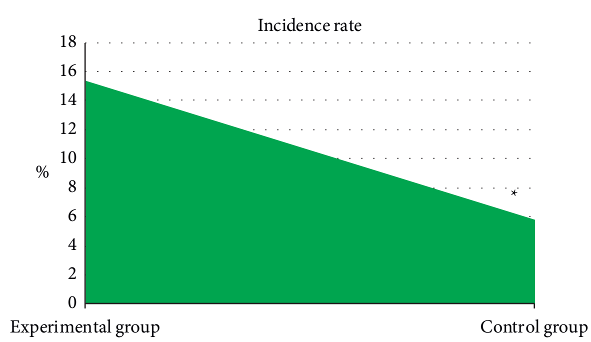

FIGURE 10: Comparison of incidence of CIN between the two groups. *Significant difference compared with the experimental group ($P < 0.05$).

4. Discussion

Contrast agents play an important role in the diagnosis and interventional treatment of coronary heart disease, and the occurrence of CIN has attracted more and more attention from clinicians [21]. At present, CIN has risen to the third leading cause of iatrogenic renal failure after decreased renal blood perfusion and nephrotoxic drugs. Therefore, early evaluation and prevention of CIN are necessary [22]. In this study, 104 patients with CAHD who underwent CAG and PCI surgery within 1 week after the ECCT were treated as the research objects. They were divided into an experimental group (patients who underwent CAG and PCI within 1 week after ECCT) and the control group (patients who underwent CAG and PCI within 1–3 weeks after ECCT). All the objects were performed with the kidney CT imaging scan. In order to improve image quality, an improved image denoising algorithm based on DNST (O-DNST) was firstly proposed and compared with DSST, WT, and DNST algorithms. It was found that the RMSE and running time of the O-DNST algorithm were significantly lower than those of the DSST, WT, and DNST algorithms, and the differences were statistically significant ($P < 0.05$). This is similar to the processing performance of the original dual algorithm proposed by Foygel et al. (2016) [23] for CT image data. It shows that the O-DNST algorithm can not only effectively reduce image noise but also improve the efficiency of image processing, and has a better optimization effect on the basis of traditional algorithms. Comparison of processing effects of different algorithms revealed that the image resolution processed by the WT algorithm was still low, and that of the DSST and DNST algorithm was higher, but there were artifacts, which led to the unclear display of the subtleties of the organization. In addition, the O-DNST algorithm shows the best image clarity and tissue resolution, and the overall quality is better than other algorithms. Such results are consistent with the abovementioned quantitative results and confirmed the superiority of the algorithm in this study.

The two groups of patients were compared in terms of basic data (gender, age, height, weight, diabetes, hypertension, hyperlipidemia, mild anemia, contrast agent dose, and Mehran score), and the differences were not statistically significant ($P > 0.05$). This shows that the sample grouping of this study is reasonable and the follow-up study is feasible. Comparison on renal function indicators revealed that the levels of Scr, BUN, and UP in the experimental group were significantly higher than those of the control group 24–72 hours after surgery, while the levels of Ccr and eGFR were significantly lower than those of the control group, showing statistically significant differences ($P < 0.05$). Scr, BUN, UP, Ccr, and eGFR are all indicators used to assess renal function [24, 25], which indicates that CAG again within 1 week after ECCT may be a factor that may cause renal function damage in patients undergoing PCI. The levels of β2-MG, CRP, IL-6, and TNF-α in the experimental group were significantly higher than those in the control group for 24–72 hours after surgery, and the differences were statistically significant ($P < 0.05$). β2-MG, CRP, IL-6, and TNF-α are all sensitive markers of inflammation. The increase in the levels of these markers indicates that the body is in a proinflammatory state, indicating that CAG again within 1 week after ECCT will promote PCI The patient's serum inflammation level is increased. The incidence of CIN in the experimental group was significantly higher than that in the control group, and the difference was statistically significant ($P < 0.05$), indicating that repeated application of contrast agent in a short period of time may be a risk factor for CIN in PCI patients.

5. Conclusion

In this study, 104 patients with CAHD who underwent CAG and PCI surgery within 1 week after the ECCT were treated as the research objects. They were divided into an experimental group (patients who underwent CAG and PCI within 1 week after ECCT) and the control group (patients who underwent CAG and PCI within 1–3 weeks after ECCT). All the objects were performed with the kidney CT imaging scan. At the same time, the renal function indicators, inflammation indicators, and incidence of CIN were compared between the two groups of patients before and after surgery. The results showed that repeated application of the contrast agent in a short period of time can promote the increase of serum inflammation levels in PCI patients, which may be a risk factor for CIN in PCI patients. However, it was a single-center clinical randomized study with a limited sample size. In addition, none of the included subjects had kidney disease and had no significant damage to basic renal function. In addition, patients with basic kidney disease were not discussed. A large-scale randomized double-blind clinical trial of the center for the prevention and treatment of CIN would be carried out later. In conclusion, the research in this study provided theoretical support for the clinical evaluation of patients with acute renal damage caused by contrast agents.

Data Availability

The data used to support the findings of this study are available from the corresponding author upon request.

Conflicts of Interest

The authors declare no conflicts of interest.

References

[1] M. R. Rudnick, A. K. Leonberg-Yoo, H. I. Litt, R. M. Cohen, S. Hilton, and P. P. Reese, "The controversy of contrast-induced nephropathy with intravenous contrast: what is the risk?" *American Journal of Kidney Diseases*, vol. 75, no. 1, pp. 105–113, 2020.

[2] H. H. N. Yan, H. C. Siu, S. Law et al., "A comprehensive human gastric cancer organoid biobank captures tumor subtype heterogeneity and enables therapeutic screening," *Cell Stem Cell*, vol. 23, no. 6, pp. 882–897, 2018.

[3] Y. Chen, S. Hu, H. Mao, W. Deng, and X. Gao, "Application of the best evacuation model of deep learning in the design of public structures," *Image and Vision Computing*, vol. 102, Article ID 103975, 2020.

[4] Y. Fukushima, H. Miyazawa, J. Nakamura, A. Taketomi-Takahashi, T. Suto, and Y. Tsushima, "Contrast-induced nephropathy (CIN) of patients with renal dysfunction in CT examination," *Japanese Journal of Radiology*, vol. 35, no. 8, pp. 427–431, 2017.

[5] Y. Zhu, S. Zhang, and Y. Shen, "Humble leadership and employee resilience: exploring the mediating mechanism of work-related promotion focus and perceived insider identity," *Frontiers in Psychology*, vol. 10, p. 673, 2019.

[6] S. Xie, Z. Yu, and Z. Lv, "Multi-disease prediction based on deep learning: a survey," *Computer Modeling in Engineering and Sciences*, vol. 128, no. 2, pp. 489–522, 2021.

[7] Z. Zhao, C. Ye, Y. Hu, C. Li, and X. Li, "Cascade and fusion of multitask convolutional neural networks for detection of thyroid nodules in contrast-enhanced CT," *Computational Intelligence and Neuroscience*, vol. 2019, Article ID 7401235, 2019.

[8] A. A. Bashir, V. Kong, D. Skinner et al., "Contrast-induced nephropathy following CT scan for trauma is not rare and is associated with increased mortality in South African trauma patients," *European Journal of Trauma and Emergency Surgery*, vol. 45, no. 6, pp. 1129–1135, 2019.

[9] A. Gökyer, A. Küçükarda, O. Köstek et al., "Contrast nephropathy in cancer patients receiving anti-VEGF therapy: a prospective study," *International Journal of Clinical Oncology*, vol. 25, no. 10, pp. 1757–1762, 2020.

[10] M. A. Escarcega-Tame, M. López-Hurtado, M. R. Escobedo-Guerra, E. Reyes-Maldonado, G. Castro-Escarpulli, and F. M. Guerra-Infante, "Co-infection between genotypes of the human papillomavirus and *Chlamydia trachomatis* in

Mexican women," *International Journal of STD & AIDS*, vol. 31, no. 13, pp. 1255–1262, 2020.

[11] C. Q. Lai, H. Ibrahim, A. I. Abd Hamid, M. Z. Abdullah, A. Azman, and J. M. Abdullah, "Detection of moderate traumatic brain injury from resting-state eye-closed electroencephalography," *Computational Intelligence and Neuroscience*, Article ID 8923906, 2020.

[12] M. M. Soliman, D. Sarkar, I. Glezerman, and M. Maybody, "Findings on intraprocedural non-contrast computed tomographic imaging following hepatic artery embolization are associated with development of contrast-induced nephropathy," *World Journal of Nephrology*, PMCID, vol. 9, no. 2, pp. 33–42, 2020.

[13] K. Wang, J. Fan, W. Lin et al., "Functional polymorphism of PIN1 rs2233679 is associated with the progression of CIN to early cervical cancer in Hunan Chinese," *Taiwanese Journal of Obstetrics & Gynecology*, vol. 59, no. 2, pp. 220–226, 2020.

[14] B. G. Abu Jawdeh, A. C. Leonard, Y. Sharma et al., "Contrast-induced nephropathy in renal transplant recipients: a single center experience," *Frontiers of Medicine*, vol. 4, p. 64, 2017.

[15] M. Quintas-Neves, J. M. Araújo, S. A. Xavier, J. M. Amorim, V. Cruz E Silva, and J. Pinho, "Contrast-induced neurotoxicity related to neurological endovascular procedures: a systematic review," *Acta Neurologica Belgica*, vol. 120, no. 6, pp. 1419–1424, 2020.

[16] M. A. Sadiq, M. S. Al Habsi, S. K. Nadar, M. M. Shaikh, and H. A. BaOmar, "Transient contrast induced neurotoxicity after coronary angiography: a contrast re-challenge case," *Pakistan Journal of Medical Sciences*, vol. 36, no. 5, pp. 1140–1142, 2020.

[17] S. O. Siri, J. Martino, and V. Gottifredi, "Structural chromosome instability: types, origins, consequences, and therapeutic opportunities," *Cancers*, vol. 13, no. 12, p. 3056, 2021.

[18] S. S. Mousavi Gazafroudi, M. B. Tavakkoli, M. Moradi et al., "Coronary CT angiography by modifying tube voltage and contrast medium concentration: evaluation of image quality and radiation dose," *Echocardiography*, vol. 36, no. 7, pp. 1391–1396, 2019.

[19] T. Hongo, M. Tsuchiya, M. Inaba et al., "Using kidney size for early detection of contrast-induced nephropathy in the emergency department setting," *Acute Medicine & Surgery*, vol. 5, no. 3, pp. 278–284, 2018.

[20] S. M. Tao, X. Kong, U. J. Schoepf et al., "Acute kidney injury in patients with nephrotic syndrome undergoing contrast-enhanced CT for suspected venous thromboembolism: a propensity score-matched retrospective cohort study," *European Radiology*, vol. 28, no. 4, pp. 1585–1593, 2018.

[21] R. M. Chesnut, N. Temkin, S. Dikmen et al., "A method of managing severe traumatic brain injury in the absence of intracranial pressure monitoring: the imaging and clinical examination protocol," *Journal of Neurotrauma*, vol. 35, no. 1, pp. 54–63, 2018.

[22] H. M. Ropiak, O. Desrues, A. R. Williams, A. Ramsay, I. Mueller-Harvey, and S. M. Thamsborg, "Structure-activity relationship of condensed tannins and synergism with trans-cinnamaldehyde against *Caenorhabditis elegans*," *Journal of Agricultural and Food Chemistry*, vol. 64, no. 46, pp. 8795–8805, 2016.

[23] R. Foygel Barber, E. Y. Sidky, T. Gilat Schmidt, and X. Pan, "An algorithm for constrained one-step inversion of spectral CT data," *Physics in Medicine and Biology*, vol. 61, no. 10, pp. 3784–3818, 2016.

[24] N. Nakamura, C. Aoyagi, H. Matsuzaki et al., "Role of computed tomography volumetry in preoperative donor renal function evaluation of living related kidney transplantation," *Transplantation Proceedings*, vol. 51, no. 5, pp. 1314–1316, 2019.

[25] S. Lawton and S. Viriri, "Detection of COVID-19 from CT lung scans using transfer learning," *Computational Intelligence and Neuroscience*, vol. 2021, Article ID 5527923, 2021.

Hindawi
Contrast Media & Molecular Imaging
Volume 2022, Article ID 1732915, 9 pages
https://doi.org/10.1155/2022/1732915

Research Article

Efficacy of Morphine Combined with Mechanical Ventilation in the Treatment of Heart Failure with Cardiac Magnetic Resonance Imaging under Artificial Intelligence Algorithms

Zhihai Geng,[1] Bolun Chen,[1] Qiang Li,[2] Xi Han,[3] and Xuelian Zhu[1]

[1]*Department of Anesthesiology, First Affiliated Hospital of Jiamusi University, Jiamusi 154003, Heilongjiang, China*
[2]*Department of Anesthesiology, Jiansanjiang Hospital of Beidahuang Group, Jiamusi 156399, Heilongjiang, China*
[3]*Department of Anatomy, School of Basic Medical Sciences, Jiamusi University, Jiamusi 154007, Heilongjiang, China*

Correspondence should be addressed to Xuelian Zhu; hanxi@jmsu.edu.cn

Received 3 December 2021; Revised 17 January 2022; Accepted 20 January 2022; Published 25 February 2022

Academic Editor: M. Pallikonda Rajasekaran

This study was aimed at exploring the efficacy of morphine combined with mechanical ventilation in the treatment of heart failure with artificial intelligence algorithms. The cardiac magnetic resonance imaging (MRI) under the watershed segmentation algorithm was proposed, and the local grayscale clustering watershed (LGCW) model was designed in this study. A total of 136 patients with acute left heart failure were taken as the research objects and randomly divided into the control group (conventional treatment) and the experimental group (morphine combined with mechanical ventilation), with 68 cases in each group. The left ventricular end-diastolic diameter (LVEDD), left ventricular end-systolic diameter (LVESD), left ventricular ejection fraction (LVEF), N-terminal pro-brain natriuretic peptide (NT-proBNP), arterial partial pressure of oxygen (PaO_2), and arterial partial pressure of carbon dioxide ($PaCO_2$) were observed. The results showed that the mean absolute deviation (MAD) and maximum mean absolute deviation (max-MAD) of the LGCW model were lower than those of the fuzzy k-nearest neighbor (FKNN) algorithm and local gray-scale clustering model (LGSCm). The Dice metric was also significantly higher than that of other algorithms with statistically significant differences ($P < 0.05$). After treatment, LVEDD, LVESD, and NT-proBNP of patients in the experimental group were significantly lower than those in the control group, and LVEF in the experimental group was higher than that in the control group ($P < 0.05$). PaO_2 of patients in the experimental group was also significantly higher than that in the control group ($P < 0.05$). It suggested that the LGCW model had a better segmentation effect, and morphine combined with mechanical ventilation gave a better clinical efficacy in the treatment of acute left heart failure, improving the patients' cardiac function and arterial blood gas effectively.

1. Introduction

Heart failure is the ventricular insufficiency caused by structural or functional diseases of the heart. It is usually classified into acute heart failure and chronic heart failure, and the former can be a sign of aggravation of the latter [1–3]. Heart failure is more common among the elderly aged more than 65 years, most of which are chronic heart failure [4]. Meanwhile, heart failure can also be divided into left heart failure and right heart failure. Acute left heart failure is clinically the most common, which manifests as severe dyspnea, orthopnea, expectoration with pink foamy sputum, dysphoria, fear, and so on. Hypoxemia may occur in patients with heart failure; for some severe cases, it would occur complicated with acute pulmonary edema or cardiogenic shock. [5, 6]. Therefore, the key to the treatment of heart failure is to improve cardiopulmonary function and oxygenation of patients timely.

Mechanical ventilation is the main method for the treatment of acute left heart failure, which can be divided into noninvasive and invasive mechanical ventilations [7]. Invasive mechanical ventilation brings some complications and is not easy to be accepted by patients, while noninvasive positive pressure mechanical ventilation can achieve the effect of increased ventilation in the alveoli without trachea cannula [8, 9]. Some studies have found that noninvasive positive pressure mechanical ventilation is effective to reduce the work of breathing in patients with left heart failure, thereby reducing oxygen loss and improving the ratio of ventilation to blood flow [10]. However, patients with left heart failure are often complicated by unhealthy emotions such as irritability and fear, and poor tolerance to noninvasive ventilation, which greatly reduces the efficiency of mechanical ventilation and gives a poor efficacy [11]. Morphine is a commonly used drug for the treatment of acute left heart failure. It diminishes the angiectasis of the peripheral blood vessels by inhibiting the sympathetic nerves, so as to reduce the returned blood volume as well as the pressure load on the heart of patients [12]. Meanwhile, morphine has a good sedative effect to ease the irritability, fear, and more of patients, induce them to fall asleep, and reduce their oxygen consumption [13]. As a result, morphine can make patients with acute left heart failure adapt to mechanical ventilation better, reduce human-machine asynchrony, and improve the effect of mechanical ventilation and the clinical prognosis [14].

Cardiac magnetic resonance imaging (MRI) is accurate to measure ventricular volume and functions, and is considered to be the gold standard for noninvasive assessment of cardiac function. MRI can not only present the cardiac anatomical structure clearly, but also show the structure of the myocardium, the ventricular wall thickness, and the surrounding blood vessels. It plays an important role in the diagnosis, treatment, and prognostic evaluation of heart failure [15, 16]. However, in the process of cardiac MRI, the artifacts due to blood flow would lead to gray inhomogeneity, and factors like breathing and sternocleidomastoid muscle would also cause the target boundary to be unclear or even broken [17]. Artificial intelligence algorithms have shown superior performances in image segmentation and gradually have a cross-combination with medical imaging. Li et al. [18] used the golden-angle radial data for real-time exercise stress cardiac MRI reconstruction, detecting the increase in stroke volume and ejection fraction caused by exercise in a healthy heart. Ammar et al. [19] applied the full convolutional neural network to achieve cardiac MRI sequence segmentation as it can handle the pixel-level classification. They calculated three key structural volume characteristics effectively of the left ventricular cavity, right ventricular cavity, and left ventricular myocardium for disease prediction. A watershed-based cardiac MRI segmentation algorithm was proposed in this study for cardiac MRI imaging, and it was used to evaluate the efficacy of morphine combined with noninvasive mechanical ventilation in the treatment of acute left heart failure. To deal with the issues of cardiac MRI, a watershed-based cardiac MRI segmentation algorithm was proposed to evaluate the efficacy of morphine combined with noninvasive mechanical ventilation in the treatment of acute left heart failure.

In summary, improving cardiopulmonary function timely and preventing vital organ failure are the keys to the treatment of acute left heart failure. Noninvasive positive pressure ventilation helps to improve the ratio of ventilation to blood flow effectively, and morphine can make patients with acute left heart failure adapt to noninvasive mechanical ventilation better. Therefore, the watershed-based cardiac MRI segmentation algorithm was proposed in this study, together with the local gray-scale clustering model (LGSCm) introduced, for the efficacy evaluation of morphine combined with mechanical ventilation in the treatment of acute left heart failure. It was expected to provide a theoretical support for the clinical treatment of patients with acute left heart failure.

2. Materials and Methods

2.1. Research Objects and the Grouping. One hundred and thirty-six patients with acute left heart failure, who were admitted to the hospital from March 2018 to February 2020, were selected as the research objects. According to the random number table method, they were divided into the experimental group and the control group, with 68 people in each group. The general clinical information of the patients, including their name, gender, and age, was collected. This study was approved and supported by the ethics committee of hospital. All participant patients signed the written informed consents and volunteered to participate in this study.

Patients included met the following inclusion criteria. They were 18–73 years old, could receive mechanical ventilation treatment, and were in line with the clinical diagnosis of acute left heart failure. The exclusion criteria were described as follows. The patients had a weak spontaneous breathing, were complicated with vital organ function failure, or had a poor compliance. They had the upper respiratory tract obstruction or were severely allergic to the drugs used in the study.

2.2. Therapeutic Methods. The patients in the control group received conventional treatments, which mainly included sedation, diuresis, heart strengthening, blood vessel expansion, airway spasm relief, and oxygen inhalation. The oxygen flow rate was 5–10 L/min and was adjusted according to the specific conditions of patients. In addition to the above conventional treatment, ventilator was given to the patients in the experimental group to assist breathing. 5–10 mg morphine was also given through subcutaneous injection or intravenous infusion. After 1–2 hours, the dosage was adjusted according to the patients' specific conditions.

2.3. Cardiac MRI Examination. Cardiac MRI examination was performed. The scanning acquisition was completed at the end expiration when the patients held their breath. The true steady-state precession sequence with retrospective electrocardiograph-gating was applied to scan layer by layer from the cardiac base to the apex, and multiple layers of images were continuously collected, and 25 frames of images were collected in each cardiac cycle. The scanning parameters were set as follows. The layer thickness was 6-8 mm, the number of layers was 10–12, the time of repetition (TR) was 3.5 ms, the time of echo (TE) was 1.8 ms, the flip angle (FA) was 45°, and the field of view was 320×320. Two experienced radiologists in the field of cardiac radiology analyzed the collected images independently. If there was a difference in the comments of them, the final results were obtained after discussion between them.

2.4. Establishment of Local Grayscale Clustering Watershed (LGCW) Segmentation Model. Watershed algorithm is commonly used in image segmentation, to deal with the issues such as blurred or missing image boundaries. It repairs the missing boundaries based on the existing boundaries of tissues and organs, to complete a closed contour boundary line so that tissues and organs are separated on the image. For a more accurate segmentation of noise-free cardiac MRI images, the LGSCm was introduced in this study [20]. Combined with the watershed algorithm, an LGCW segmentation model was designed. The segmentation process of the LGCW model is shown in Figure 1.

With the local gray-scale clustering criteria, a local area model in the local area of the image was obtained through LGSCm; thereby, the gray inhomogeneity was handled. *K(nm)* was assumed to represent the Gaussian kernel function, *P(m)* represented the image, *e(n)* represented the gray inhomogeneity feature of the approximated image, and $e(n)t_2$ represented the clustering center of average local grayscale values. As H represented the Heaviside function, its specific energy function is defined as follows:

$$E = \int \left(\int K(n-m)\left(P(m) - e(n)t_1\right)^2 H(\varphi(m))l_m \right) l_n + \int \left(\int K(n-m)\left(P(m) - e(n)t_2\right)^2 \left(1 - H(\varphi(m))l_m \right) l_n. \quad (1)$$

The LGSCm overcame the image noise and gray inhomogeneity, and segmented the tissues and organs of cardiac MRI images. However, it had the disadvantage of blurred or missing tissue boundaries. The watershed algorithm could solve this issue, so the LGCW segmentation model was designed by combining the two algorithms. The LGSCm was used for the cardiac MRI image segmentation, to obtain the initial contour at first. Then, the optimal solution was worked out via (1) iteratively, through which the contour line and the offset field were continuously corrected. After the gray inhomogeneity caused by the offset field and the noise were removed, the tissues and organs in the cardiac MRI image were segmented. The segmented cardiac MRI image was then binarized, and the threshold value within the contour area was fixed as 1, whereas the threshold value outside the area was 0. The Euclidean distance transform [21] was used to reconstruct the grayscale image, and the minimum grayscale areas were formed in different tissues and organs in the image. After that, the grayscale image was segmented through the watershed algorithm, to build a watershed between the tissues and organs so that the tissues and organs adhered to each other were divided. Finally, the accurate cardiac MRI segmentation was worked out. The segmentation was carried out in the experimental environment of MATLAB 2015a, CPU of 2.60 GHz, RAM of 3.0 GB, and Windows7 Professional.

2.5. Observation Indicators. The clinical efficacy and cardiac functional indicators of patients in the two groups were compared, and the indictors included left ventricular end-diastolic diameter (LVEDD), left ventricular end-systolic diameter (LVESD), left ventricular ejection fraction (LVEF), and N-terminal pro-brain natriuretic peptide (NT-proBNP). Vital sign indicators of respiratory rate, systolic blood pressure, and diastolic blood pressure, and arterial blood gas indicators of arterial partial pressure of oxygen (PaO_2), and arterial partial pressure of carbon dioxide ($PaCO_2$) were also observed. The criteria of different efficacies are described in Figure 2.

The total effective rate is expressed as follows:

$$\text{total effective rate } (\%) = \frac{\text{significantly effective (n)} + \text{effective (n)}}{\text{total people (n)}} \times 100\%. \quad (2)$$

The mean absolute deviation (MAD), maximum mean absolute deviation (max-MAD), and Dice metric (DM) were used to evaluate the performance differences among different algorithms. The MAD and max-MAD are expressed in the following equations:

$$\mathrm{MAD}(K, L) = \frac{1}{2}\left(\frac{1}{x}\left(\sum_{s=1}^{x} f(k_x, L) + \frac{1}{r}\sum_{t=1}^{x} f(l_t, K).\right.\right. \quad (3)$$

$$\mathrm{maxMAD}(K, L) = \max\left(\frac{1}{2}\left(f(k_x, L) + f(l_t, K),\right.\right. \quad (4)$$

where $f(k_x, L) = \min\|k_x - l_t\|$, $f(l_t, K) = \min\|l_t - k_x\|$, and $K = \{k_1, k_2, k_3 \ldots k_x\}$ were the points on the contour of the automatically segmented image; whereas $L = \{l_1, l_2, l \ldots l_x\}$ was the point on the contour of the manual segmentation image. The smaller the MAD value, the smaller the average difference between the automatic segmentation and the manual segmentation. The smaller the max-MAD value, the smaller the maximum difference between the automatic and the manual segmentations. DM was to calculate the similarity between the automatic and the manual segmentations, and it was expressed in the following equation:

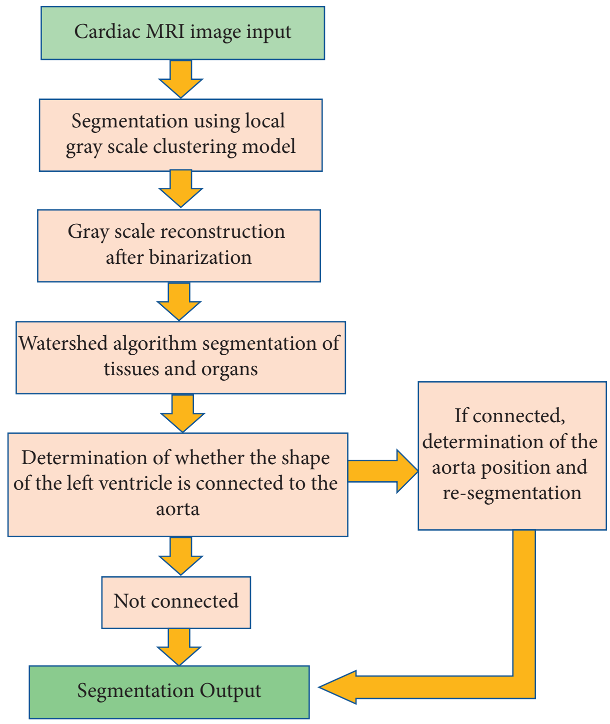

Figure 1: The segmentation flowchart of the LGCW model.

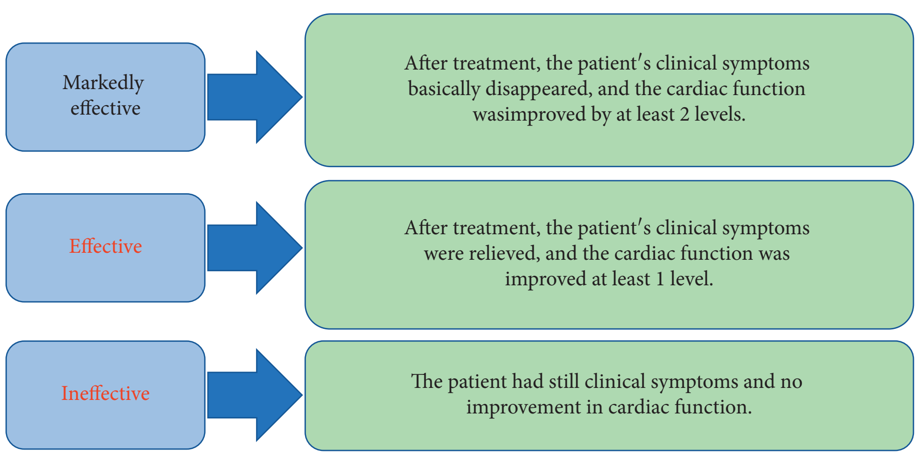

Figure 2: Evaluation criteria of the efficacies.

$$DM = \frac{2|Z \cap D|}{|Z| + |D|}, \tag{5}$$

where Z is the area manually segmented and D is the area automatically segmented by the algorithm. The value of DM ranged from 0 to 1; the larger the value, the better the segmentation effect by the algorithm; the smaller the value, the poorer the algorithmic segmentation effect or of the segmentation error.

2.6. Statistical Analysis. The data were processed via SPSS 22.0. Normally distributed data were recorded in the form of mean ± standard deviation, and nonnormally distributed data were recorded in median (P25-P75). Normal distribution values between groups were compared by t-test, nonnormally distributed values were compared by rank sum test, and categorical variables were compared by χ^2 test; $P < 0.05$ showed the difference was statistically significant.

3. Results

3.1. Performance Analysis of Algorithms. As the fuzzy k-nearest neighbor (FKNN) algorithm [22] was introduced in this study, the MAD, max-MAD, and DM of the FKNN, LGSCm, and LGCW were compared and analyzed, with the results shown in Figure 3. The MAD values of LGSCm, FKNN, and LGCW were 17.76 ± 10.8PT, 3.24 ± 2.27PT, and

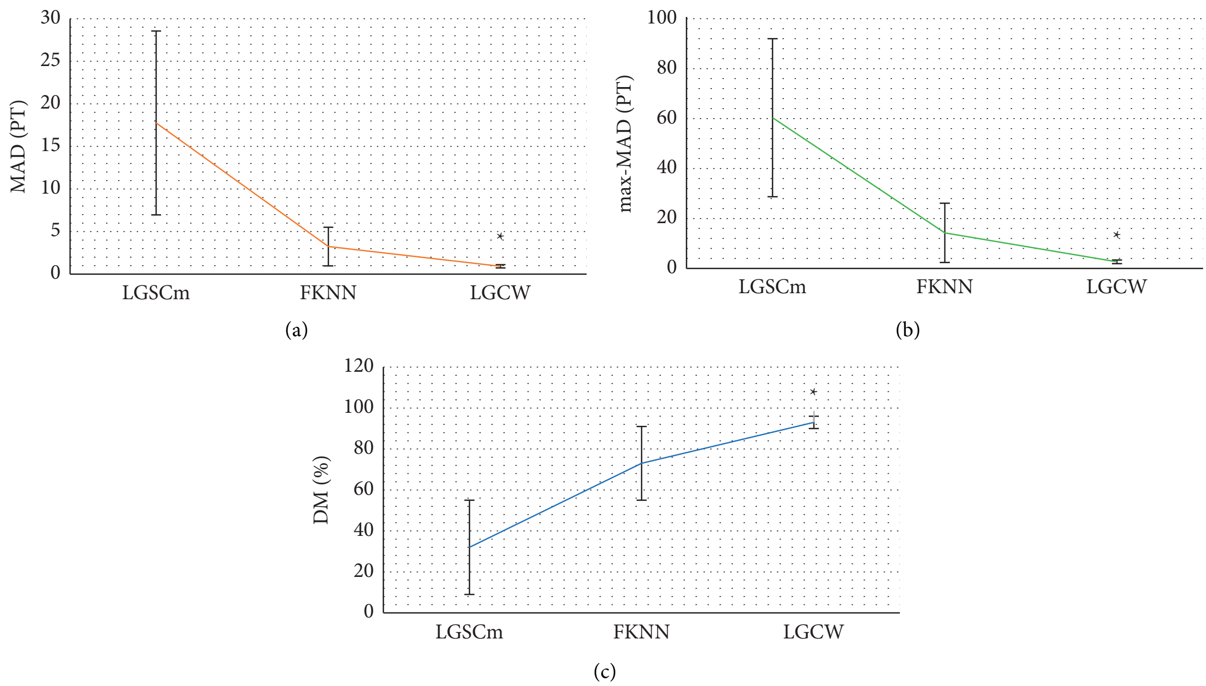

Figure 3: Performance analysis of the three algorithms. (a) The results of MAD; (b) results of max-MAD; (c) results of DM. * indicates that the differences were statistically significant compared to those of the LGCW algorithm ($P < 0.05$).

0.92 ± 0.19PT, respectively; the max-MAD values of them were 60.36 ± 31.64PT, 14.25 ± 11.87PT, and 2.65 ± 0.73PT, respectively; the DM values were $32 \pm 23\%$, $73 \pm 18\%$, and $93 \pm 3\%$, respectively. As the values were compared with those of the LGCW model, there were statistically significant differences ($P < 0.05$). It was suggested that the segmentation of the LGCW model differed very little from the manual segmentation, with a strong robustness and high similarity.

3.2. Images of Segmentation. The segmentation results of the three algorithms were compared, as shown in Figure 4. These images were the cardiac MRI images of a 67-year-old male patient. Compared with the manual segmentation, the LGCW model achieved the best segmentation effect, with the clearest boundary; the FKNN was the second.

3.3. General Clinical Data of the Patients. A total of 136 patients were included in the study. Their general clinical data are shown in Table 1. In the control group, there were 37 males and 31 females, aged 27–73 years, with an average age of 46.72 ± 12.4 years, the heart rate of $125.33 \pm 6.15 \mathrm{f/min}^{-1}$, and the urine volume of 39 ± 9 mL/h. In the experimental group of 36 males and 32 females, the patients were 26–72 years old with an average age of 47.21 ± 11.32 years, the heart rate of $126.24 \pm 6.21 \mathrm{f/min}^{-1}$, and the urine volume of 40 ± 10 mL/h; thus, there was no statistically significant difference ($P > 0.05$). The comparison is shown in Figure 5.

3.4. Comparison of Clinical Efficacy between Two Groups. The clinical efficacy on patients in the two groups was counted, as shown in Figure 5. In the control group, the patient number of the markedly effective, effective, and ineffective were counted as 20 (29.41%), 32 (47.06%), and 16 (23.53%), respectively; and the total effective rate was 76.47%. In the experimental group, there were 29 (42.65%), 34 (50%), and 5 (7.35%) patients were counted with the efficacy of the markedly effective, effective, and ineffective, respectively; and the total effective rate was 92.65%. The total effective rate of the experimental group was significantly higher than that of the control group, with a statistically significant difference ($P < 0.05$).

3.5. Comparison of Patients' Cardiac Function before and after Treatment. After treatment, the LVEDD, LVESD, and NT-proBNP of patients in both groups were significantly lower than those before treatment, and LVEF was significantly higher than those before treatment. LVEDD (57.36 ± 3.74 mm), LVESD (45.21 ± 6.24 mm), and NT-proBNP (369.85 ± 27.64 ng/mL) of patients in the experimental group after treatment were significantly lower than those in the control group. LVEF ($50.05 \pm 6.18\%$) in the experimental group after treatment was higher than that in the control group, showing statistically significant differences ($P < 0.05$). More details are shown in Figure 6.

3.6. Comparison of Vital Signs after Treatment. The vital signs of patients in the two groups after treatment are shown in Table 2. The respiratory rate of patients in the experimental group was $18.25 \pm 1.27 \mathrm{f/min}^{-1}$, the systolic blood pressure was 102.78 ± 4.81 mmHg, the diastolic blood pressure was 73.55 ± 4.55 mmHg, and the heart rate was $80.72 \pm 4.26 \mathrm{f/min}^{-1}$, which were all significantly smaller than those in the control group, with the statistically significant differences ($P < 0.05$).

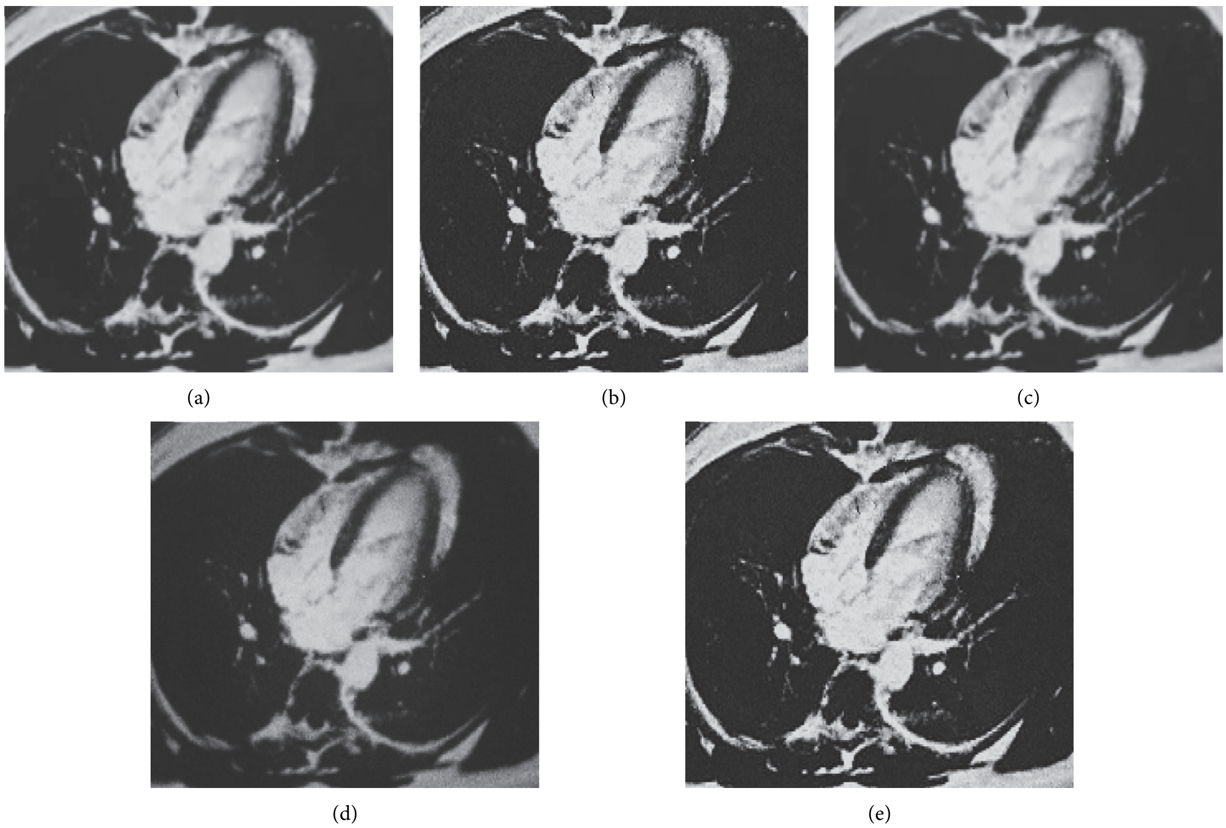

Figure 4: Segmentation results of three algorithms. (a) The image needed to be segmented; and (b–e) shows the images segmented by manual, LGSCm, FKNN, and LGCW algorithm, respectively.

Table 1: General clinical data of patients in the two groups.

Groups	Gender		Age (years)	Heart rate (f/min^{-1})	Urine volume (mL/h)
	Male (n)	Female (n)			
Control group ($n = 68$)	31	37	46.72 ± 12.4	125.33 ± 6.15	39 ± 9
Experimental group ($n = 68$)	32	36	47.21 ± 11.32	126.24 ± 6.21	40 ± 10

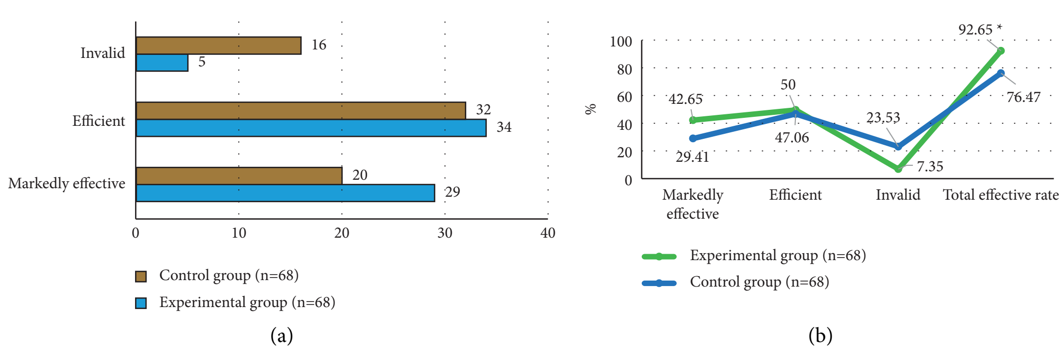

Figure 5: Comparison of clinical efficacy between the two groups. (a) The statistics of patient numbers with different efficacies. (b) The comparison of different efficacies. * indicates that there was a statistically significant difference compared to the data of the experimental group ($P < 0.05$).

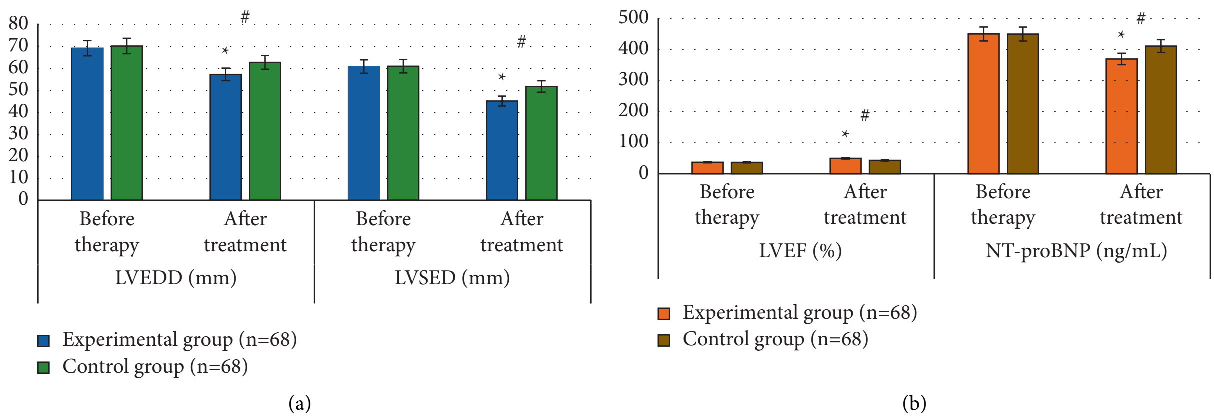

FIGURE 6: Comparison of cardiac function of patients before and after treatment. (a) The comparison of LVEDD and LVESD. (b) The comparison of LVEF and NT-proBNP. # indicates that the differences were statistically significant compared to the data before treatment in the same group, and * indicates the statistically significant differences compared to the data of the control group ($P < 0.05$).

TABLE 2: Comparison of vital signs of patients.

Groups	Respiratory rate (f/min^{-1})	Systolic blood pressure (mmHg)	Diastolic blood pressure (mmHg)	Heart rate (f/min^{-1})
Control group ($n = 68$)	$20.23 \pm 1.54^*$	$110.03 \pm 6.33^*$	$80.62 \pm 6.1^*$	$98.23 \pm 3.79^*$
Experimental group ($n = 68$)	18.25 ± 1.27	102.78 ± 4.81	73.55 ± 4.55	80.72 ± 4.26

Note. * indicates that the differences were statistically significant compared to corresponding data in the experimental group ($P < 0.05$).

3.7. Comparison of Arterial Blood Gas of Patients after Treatment. The arterial blood gas of patients in the two groups after treatment was compared and analyzed, as shown in Figure 7. The blood gas indicators of patients in both two groups were significantly different from those before treatment; the patients' PaO_2 was 86.27 ± 20.35 mmHg in the experimental group after treatment, which was significantly higher than that of the control group; the $PaCO_2$ of patients in the experimental group after treatment was 35.13 ± 6.81 mmHg, which was significantly lower than that of the control group, and the differences were all statistically significant ($P < 0.05$).

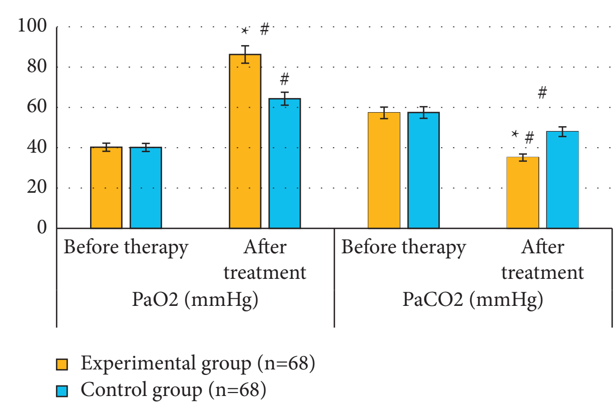

FIGURE 7: Comparison of arterial blood gas after treatment. Notes: # indicates that the differences in the same group were statistically significant compared to the data before treatment, and * indicates that the differences compared to those in the control group were statistically significant ($P < 0.05$).

4. Discussion

Heart failure is a kind of ventricular insufficiency due to various predisposing factors in the heart. Its clinical symptoms include dyspnea, coughing, and lack of strength, and in severe cases, it may also cause pulmonary edema or cardiogenic shock [23]. Acute left heart failure is common among heart failures, and it is manifested as a sudden increase in pressure load on the left heart and in pulmonary circulation resistance. Clinically, mechanical ventilation is commonly applied in the treatment of acute left heart failure [24]. Masip [25] evaluated the role of noninvasive ventilation in acute heart failure. It is found that noninvasive ventilation can improve respiratory distress quickly, reduce the need for intubation in patients with acute cardiogenic pulmonary edema, and decrease the mortality rate. Therefore, the intelligent algorithm-based cardiac MRI was proposed to evaluate the efficacy of morphine combined with mechanical ventilation in the treatment of acute left heart failure in this study. The LGSCm and the watershed algorithm were introduced, and on these bases, the LGCW model was designed and compared with the FKNN as well as LGSCm algorithms. It was shown that the MAD and max-MAD of the LGCW segmentation model were significantly smaller than those of other algorithms, the DM value was much higher than that of other algorithms, and the differences were statistically significant ($P < 0.05$). This indicated that the segmentation by LGCW had a small difference from the manual segmentation, with a strong robustness and high similarity. Roy et al.[26] applied the watershed algorithm in segmentation of lung lesion images and proposed a multi-view deep learning-driven iterative watershed algorithm, and finally, the similar results were obtained with those of this study.

Kawaguchi et al. [27] used morphine in the treatment of patients with advanced heart failure and drew a conclusion that applying morphine is feasible in the palliative care of patients with advanced heart failure complicated with refractory dyspnea. In this study, patients in the control group received conventional treatment, and patients in the experimental group were treated with morphine, which was to evaluate the efficacy of the two methods in the treatment of patients with acute left heart failure. The study found that the markedly effective rate, effective rate, ineffective rate, and total effective rate in the experimental group were 42.65%, 50%, 7.35%, and 92.65%, respectively. The total effective rate was significantly higher than that in the control group, and the difference was statistically significant ($P < 0.05$). It was indicated that morphine could alleviate the clinical symptoms effectively and improve cardiac function of patients, which was similar to the results of Johnson et al. [28]. After treatment, the LVEDD, LVESD, and NT-proBNP of patients in the two groups were significantly lower than those before treatment, and the LVEF was significantly higher than that before treatment; at the same time, the LVEDD, LVESD, and NT-proBNP of patients in the experimental group were significantly lower than those of the control group, and the LVEF of the experimental group was also significantly higher than that of the control group; the differences were statistically significant ($P < 0.05$). The vital signs of patients in the experimental group were close to normal values after treatment and were significantly lower than those in the control group with the statistically significant differences ($P < 0.05$). In the comparison of arterial blood gas, the PaO_2 of patients in the experimental group was 86.27 ± 20.35 mmHg, which was obviously higher than that of the control group; $PaCO_2$ was 35.13 ± 6.81 mmHg, which was significantly lower than that of the control group, showing statistically significant differences ($P < 0.05$). It was concluded that morphine combined with mechanical ventilation had a great the clinical efficacy in the treatment of acute left heart failure. The main reason was the sedative effect of morphine could maintain the patients' vital signs, reduce the stress responses, and make the patients more tolerant to mechanical ventilation, and then, the cardiac function and arterial blood gas were improved.

5. Conclusion

In this study, the efficacy of morphine combined with mechanical ventilation was researched in the treatment of acute left heart failure with the cardiac MRI based on the LGCW segmentation model. The FKNN and the LGSCm algorithms were also compared and analyzed; the clinical efficacy, the cardiac function, vital signs, and arterial blood gas were evaluated, as conventional treatments were applied in the control group and morphine was used in the experimental group. It was found from the results that the difference in segmentation effect between the LGCW model and manual segmentation was minimal, and the LGCW model had a strong robustness and high similarity. Morphine combined with mechanical ventilation in the treatment of acute left heart failure had a good clinical efficacy, and it could improve the cardiac function and arterial blood gas of patients effectively. However, the selected cases in this study were less relatively, which led to a lack of sample capacity, and follow-up investigations were not included, requiring further in-depth research. All in all, this study gave a theoretical support for the clinical treatment of patients with acute left heart failure.

Data Availability

The data used to support the findings of this study are available from the corresponding author upon request.

Conflicts of Interest

The authors declare that there are no conflicts of interest.

Acknowledgments

This work was supported by the Research Project of Heilongjiang Provincial Department of Education (2020-KYYWF-0291).

References

[1] M. Arrigo, M. Jessup, W. Mullens et al., "Acute heart failure," *Nature Reviews Disease Primers*, vol. 6, no. 1, p. 16, 2020.

[2] L. Sinnenberg and M. M. Givertz, "Acute heart failure," *Trends in Cardiovascular Medicine*, vol. 30, no. 2, pp. 104–112, 2020.

[3] K. E. Di Palo and N. J. Barone, "Hypertension and heart failure," *Heart Failure Clinics*, vol. 16, no. 1, pp. 99–106, 2020.

[4] D. Snipelisky, S. P. Chaudhry, and G. C. Stewart, "The many faces of heart failure," *Cardiac Electrophysiology Clinics*, vol. 11, no. 1, pp. 11–20, 2019.

[5] P. van der Meer, H. K. Gaggin, and G. W. Dec, "ACC/AHA versus ESC guidelines on heart failure," *Journal of the American College of Cardiology*, vol. 73, no. 21, pp. 2756–2768, 2019.

[6] V. D'orio, A. Ancion, and P. Lancellotti, "L'insuffisance cardiaque sévère et l'œdème pulmonaire aigu [Acute heart failure and acute pulmonary edema]," *Rev Med Liege*, vol. 73, no. 5-6, pp. 251–256, 2018.

[7] L. Adamo, C. Rocha-Resende, S. D. Prabhu, and D. L. Mann, "Reappraising the role of inflammation in heart failure," *Nature Reviews Cardiology*, vol. 17, no. 5, pp. 269–285, 2020.

[8] J. Masip, W. F. Peacock, S. Price et al., "Indications and practical approach to non-invasive ventilation in acute heart failure," *European Heart Journal*, vol. 39, no. 1, pp. 17–25, 2018.

[9] Z. Wan, Y. Dong, Z. Yu, H. Lv, and Z. Lv, "Semi-supervised support vector machine for digital twins based brain image fusion," *Frontiers in Neuroscience*, vol. 15, Article ID 705323, 2021.

[10] E. C. Goligher, M. Dres, B. K. Patel et al., "Lung- and diaphragm-protective ventilation," *American Journal of Respiratory and Critical Care Medicine*, vol. 202, no. 7, pp. 950–961, 2020.

[11] X. Zhang, H. Shen, and Z. Lv, "Deployment optimization of multi-stage investment portfolio service and hybrid intelligent algorithm under edge computing," *PLoS One*, vol. 16, no. 6, Article ID e0252244, 2021.

[12] M. C. J. Kneyber, D. de Luca, D. de Luca et al., "Recommendations for mechanical ventilation of critically ill children from the paediatric mechanical ventilation consensus conference (PEMVECC)," *Intensive Care Medicine*, vol. 43, no. 12, pp. 1764–1780, 2017.

[13] J. Geiseler and C. Kelbel, "Entwöhnung von der mechanischen Beatmung," *Medizinische Klinik - Intensivmedizin und Notfallmedizin*, vol. 111, no. 3, pp. 208–214, 2016.

[14] D. Orso, G. Boaro, E. Cassan, and N. Guglielmo, "Is morphine safe in acute decompensated heart failure? A systematic review of the literature," *European Journal of Internal Medicine*, vol. 69, pp. e8–e10, 2019.

[15] Ò. Miró, V. Gil, F. J. Martín-Sánchez et al., "Morphine use in the ED and outcomes of patients with acute heart failure," *Chest*, vol. 152, no. 4, pp. 821–832, Article ID 28411112, 2017.

[16] M. Hu, Y. Zhong, S. Xie, H. Lv, and Z. Lv, "Fuzzy system based medical image processing for brain disease prediction," *Frontiers in Neuroscience*, vol. 15, 2021.

[17] S. E. Petersen, M. Y. Khanji, S. Plein, P. Lancellotti, and C. Bucciarelli-Ducci, "European Association of Cardiovascular Imaging expert consensus paper: a comprehensive review of cardiovascular magnetic resonance normal values of cardiac chamber size and aortic root in adults and recommendations for grading severity," *European Heart Journal - Cardiovascular Imaging*, vol. 20, no. 12, pp. 1321–1331, 2019.

[18] Y. Y. Li, P. Zhang, S. Rashid et al., "Real-time exercise stress cardiac MRI with Fourier-series reconstruction from golden-angle radial data," *Magnetic Resonance Imaging*, vol. 75, pp. 89–99, 2021.

[19] A. Ammar, O. Bouattane, and M. Youssfi, "Automatic cardiac cine MRI segmentation and heart disease classification," *Computerized Medical Imaging and Graphics*, vol. 88, Article ID 101864, 2021.

[20] C. Chunming Li, R. Rui Huang, Z. Zhaohua Ding, J. C. Gatenby, D. N. Metaxas, and J. C. Gore, "A level set method for image segmentation in the presence of intensity inhomogeneities with application to MRI," *IEEE Transactions on Image Processing*, vol. 20, no. 7, pp. 2007–2016, 2011.

[21] M. Manduhu and M. W. Jones, "A work efficient parallel algorithm for exact euclidean distance transform," *IEEE Transactions on Image Processing*, vol. 28, no. 11, pp. 5322–5335, 2019.

[22] B. Wu, Y. Fang, and X. Lai, "Left ventricle automatic segmentation in cardiac MRI using a combined CNN and U-net approach," *Computerized Medical Imaging and Graphics*, vol. 82, Article ID 101719, 2020.

[23] J. Maciver and H. J. Ross, "A palliative approach for heart failure end-of-life care," *Current Opinion in Cardiology*, vol. 33, no. 2, pp. 202–207, 2018.

[24] A. González, E. B. Schelbert, J. Díez, and J. Butler, "Myocardial interstitial fibrosis in heart failure," *Journal of the American College of Cardiology*, vol. 71, no. 15, pp. 1696–1706, 2018.

[25] J. Masip, "Noninvasive ventilation in acute heart failure," *Current Heart Failure Reports*, vol. 16, no. 4, pp. 89–97, 2019.

[26] R. Roy, S. Mazumdar, and A. S. Chowdhury, "MDL-IWS: multi-view deep learning with iterative watershed for pulmonary fissure segmentation," in *Proceedings of the 2020 42nd Annual International Conference of the IEEE Engineering in Medicine & Biology Society (EMBC)*, vol. 2020, pp. 1282–1285, Montréal, Québec, July 2020.

[27] J. Kawaguchi, Y. Hamatani, A. Hirayama et al., "Experience of morphine therapy for refractory dyspnea as palliative care in advanced heart failure patients," *Journal of Cardiology*, vol. 75, no. 6, pp. 682–688, 2020.

[28] M. J. Johnson, S. Cockayne, D. C. Currow et al., "Oral modified release morphine for breathlessness in chronic heart failure: a randomized placebo-controlled trial," *ESC Heart Failure*, vol. 6, no. 6, pp. 1149–1160, 2019.